IREX III

Performance of Iris Identification Algorithms

NIST Interagency Report 8xxx - Appendices

P. Grother, G. W. Quinn, J. R. Matey

M. Ngan, W. Salamon, G. Fiumara, C. Watson

Information Access Division

National Institute of Standards and Technology

Figure 1: **Threshold calibration curves** for implementation I01A executing searches for single-eye enrolled populations $N = (0.16, 1.6, 4)$ million, and two-eye populations of $N = (0.16, 1.6)$ million individuals. While the large search sets S_{nb} were used used, with number of searches in the hundreds of thousands, the number of observed scores in the far tails is small: To get reduced uncertainty more searches would be necessary. Missing plots indicate the run is not yet complete.

Appendix C: Threshold Calibration Plots

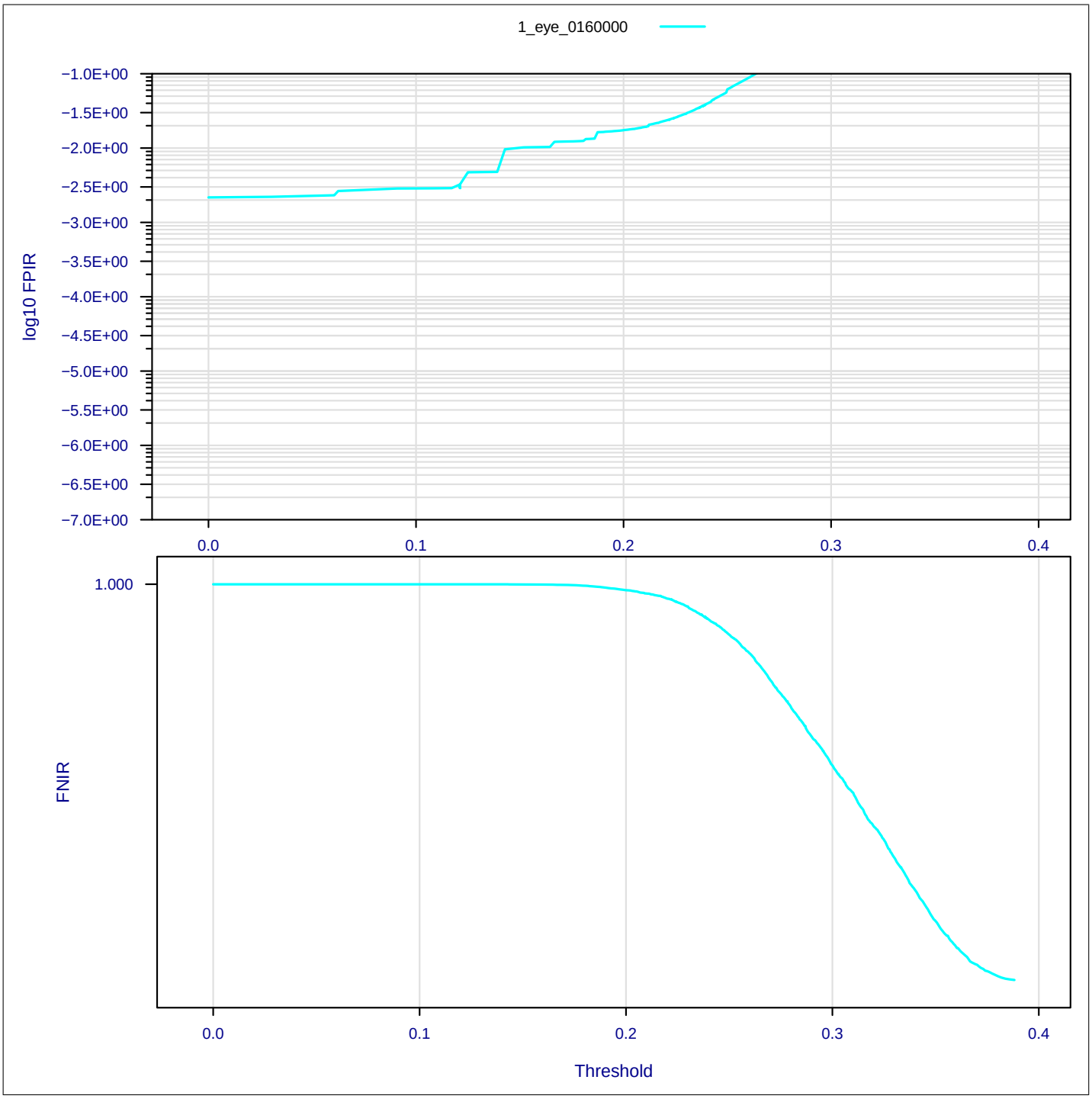

Figure 2: **Threshold calibration curves** for implementation I02A executing searches for single-eye enrolled populations $N = (0.16, 1.6, 4)$ million, and two-eye populations of $N = (0.16, 1.6)$ million individuals. While the large search sets S_{nb} were used used, with number of searches in the hundreds of thousands, the number of observed scores in the far tails is small: To get reduced uncertainty more searches would be necessary. Missing plots indicate the run is not yet complete.

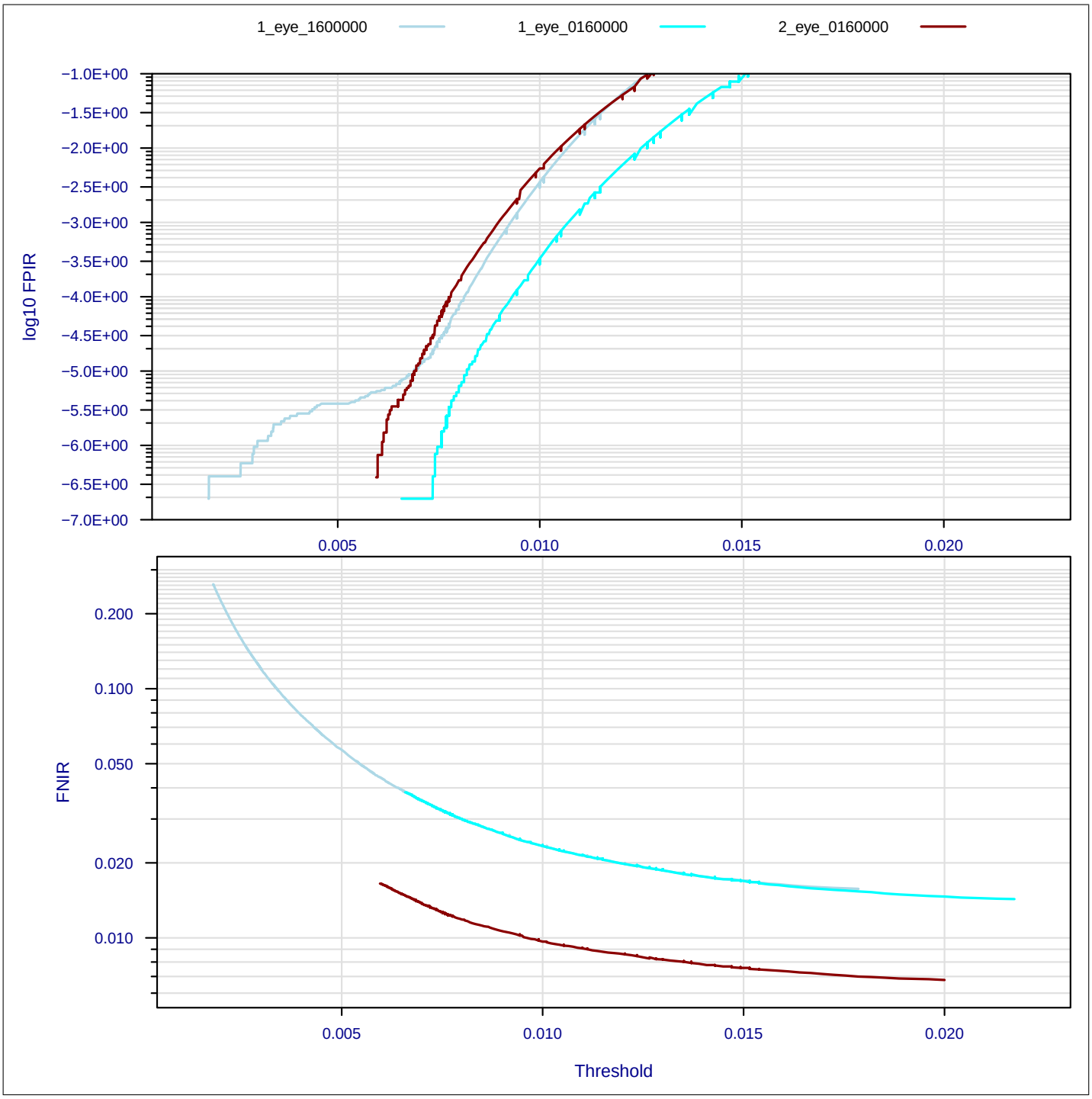

Figure 3: **Threshold calibration curves** for implementation N02A executing searches for single-eye enrolled populations $N = (0.16, 1.6, 4)$ million, and two-eye populations of $N = (0.16, 1.6)$ million individuals. While the large search sets S_{nb} were used used, with number of searches in the hundreds of thousands, the number of observed scores in the far tails is small: To get reduced uncertainty more searches would be necessary. Missing plots indicate the run is not yet complete.

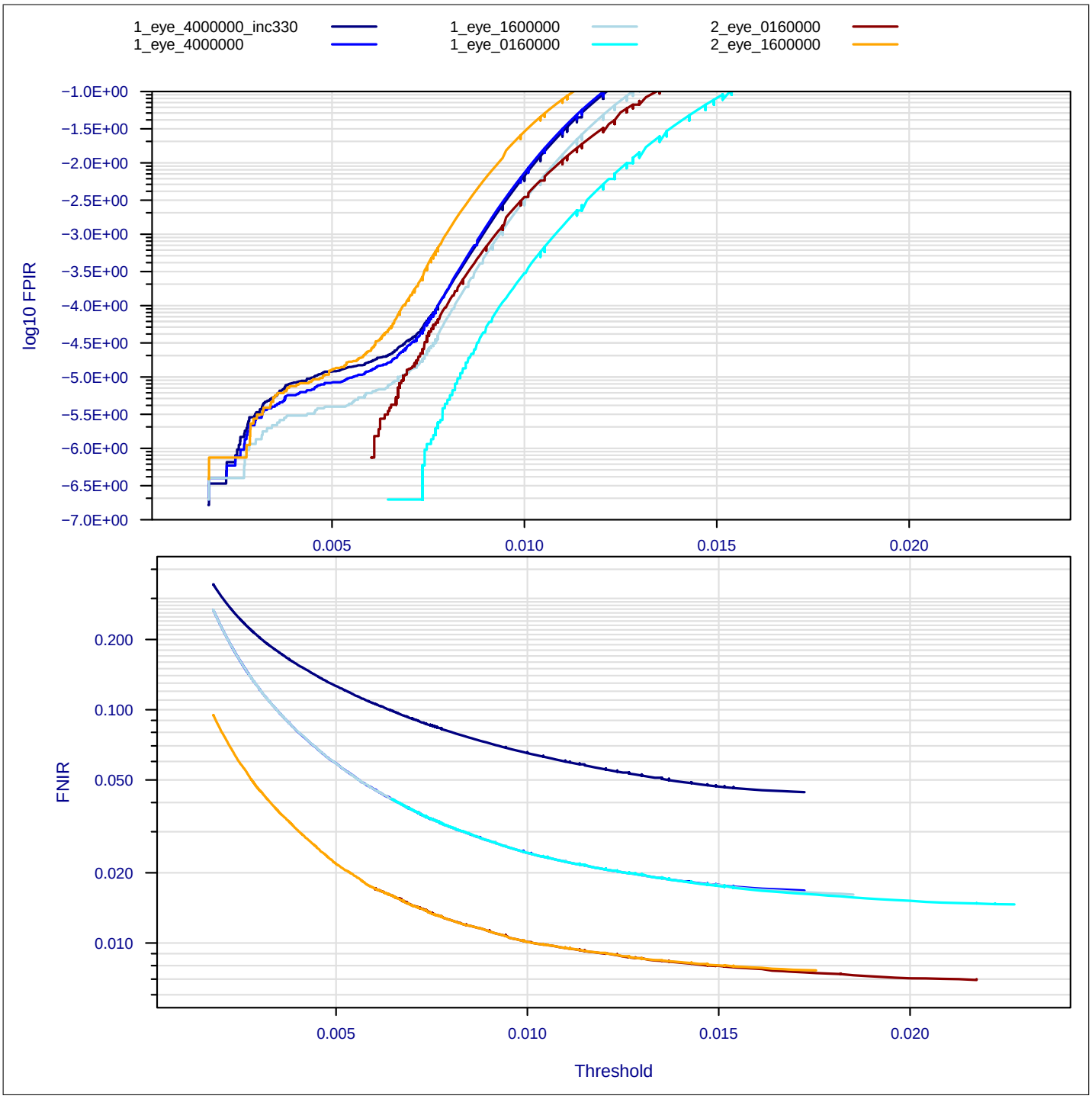

Figure 4: **Threshold calibration curves** for implementation N02B executing searches for single-eye enrolled populations $N = (0.16, 1.6, 4)$ million, and two-eye populations of $N = (0.16, 1.6)$ million individuals. While the large search sets S_{nb} were used used, with number of searches in the hundreds of thousands, the number of observed scores in the far tails is small: To get reduced uncertainty more searches would be necessary. Missing plots indicate the run is not yet complete.

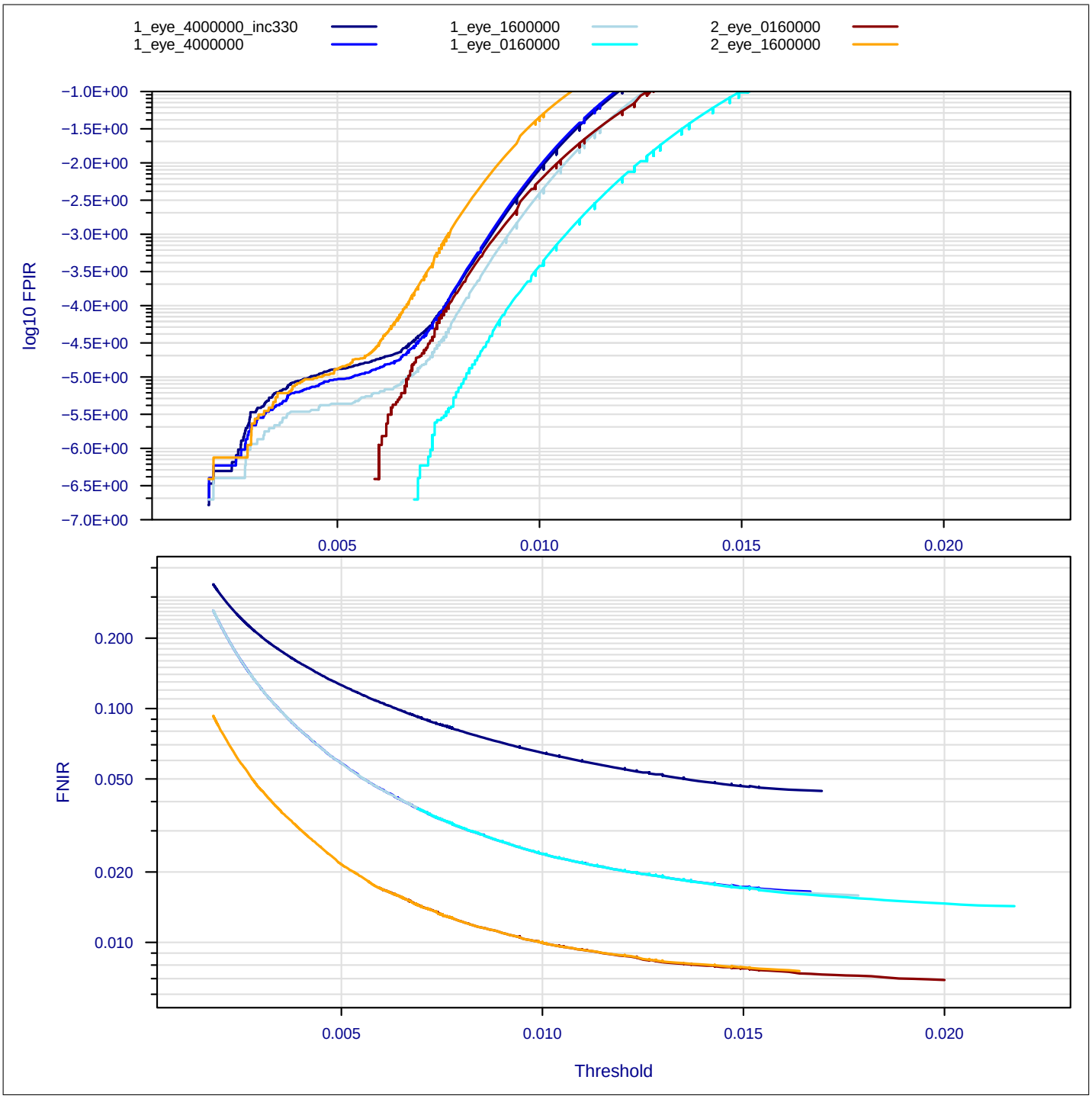

Figure 5: **Threshold calibration curves** for implementation N03A executing searches for single-eye enrolled populations $N = (0.16, 1.6, 4)$ million, and two-eye populations of $N = (0.16, 1.6)$ million individuals. While the large search sets S_{nb} were used used, with number of searches in the hundreds of thousands, the number of observed scores in the far tails is small: To get reduced uncertainty more searches would be necessary. Missing plots indicate the run is not yet complete.

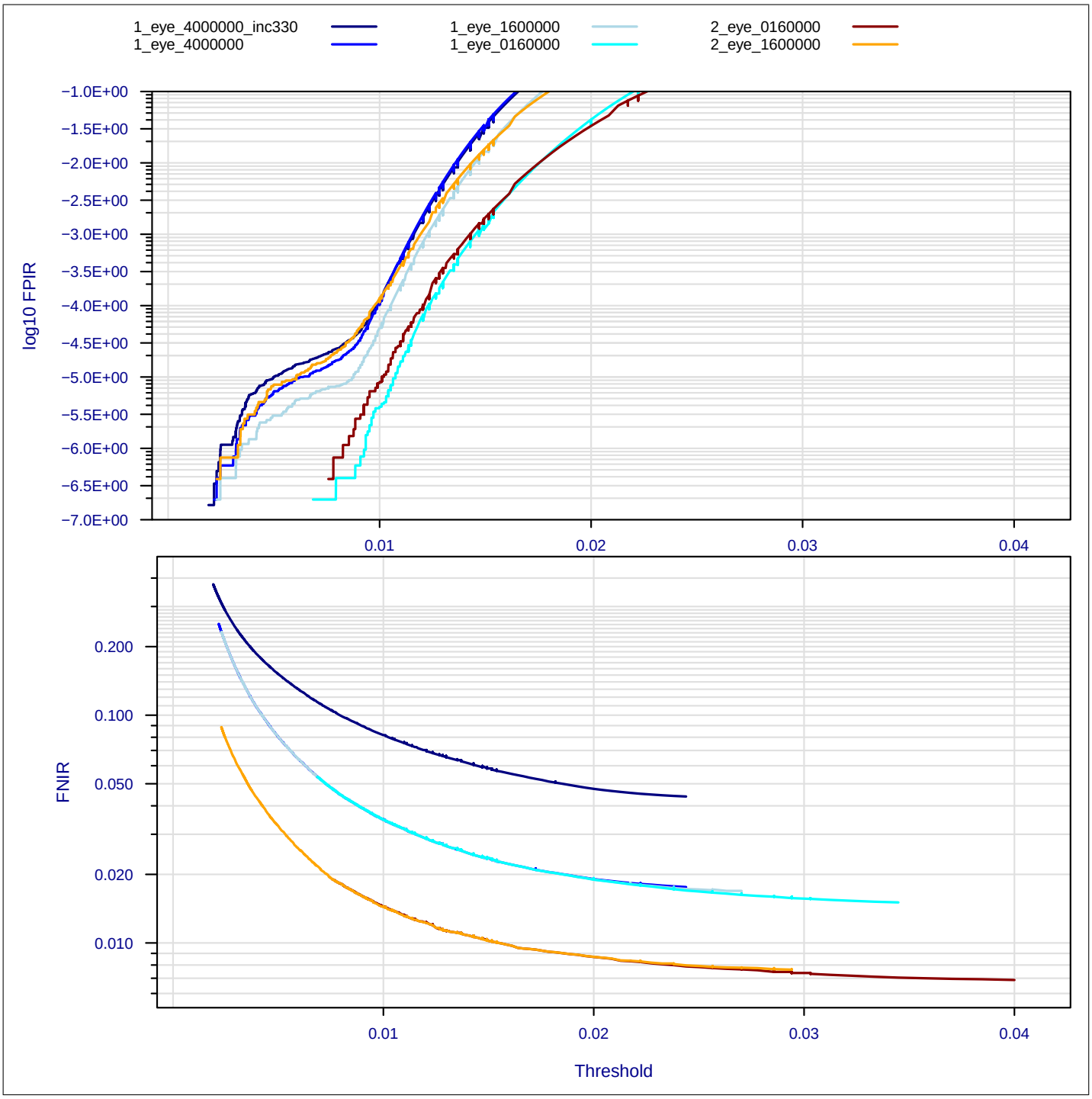

Figure 6: **Threshold calibration curves** for implementation N03B executing searches for single-eye enrolled populations $N = (0.16, 1.6, 4)$ million, and two-eye populations of $N = (0.16, 1.6)$ million individuals. While the large search sets S_{nb} were used used, with number of searches in the hundreds of thousands, the number of observed scores in the far tails is small: To get reduced uncertainty more searches would be necessary. Missing plots indicate the run is not yet complete.

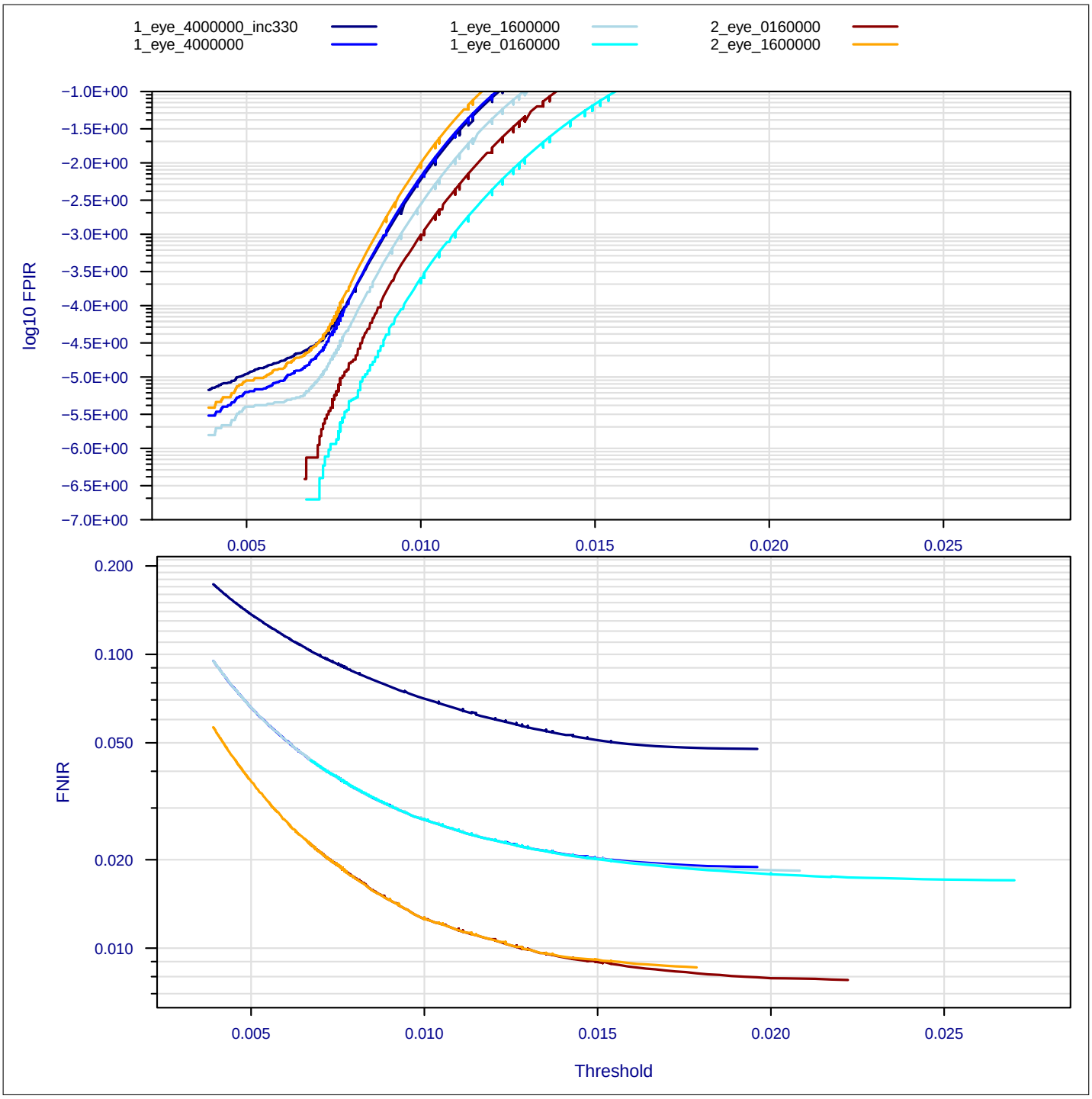

Figure 7: **Threshold calibration curves** for implementation N04A executing searches for single-eye enrolled populations $N = (0.16, 1.6, 4)$ million, and two-eye populations of $N = (0.16, 1.6)$ million individuals. While the large search sets S_{nb} were used used, with number of searches in the hundreds of thousands, the number of observed scores in the far tails is small: To get reduced uncertainty more searches would be necessary. Missing plots indicate the run is not yet complete.

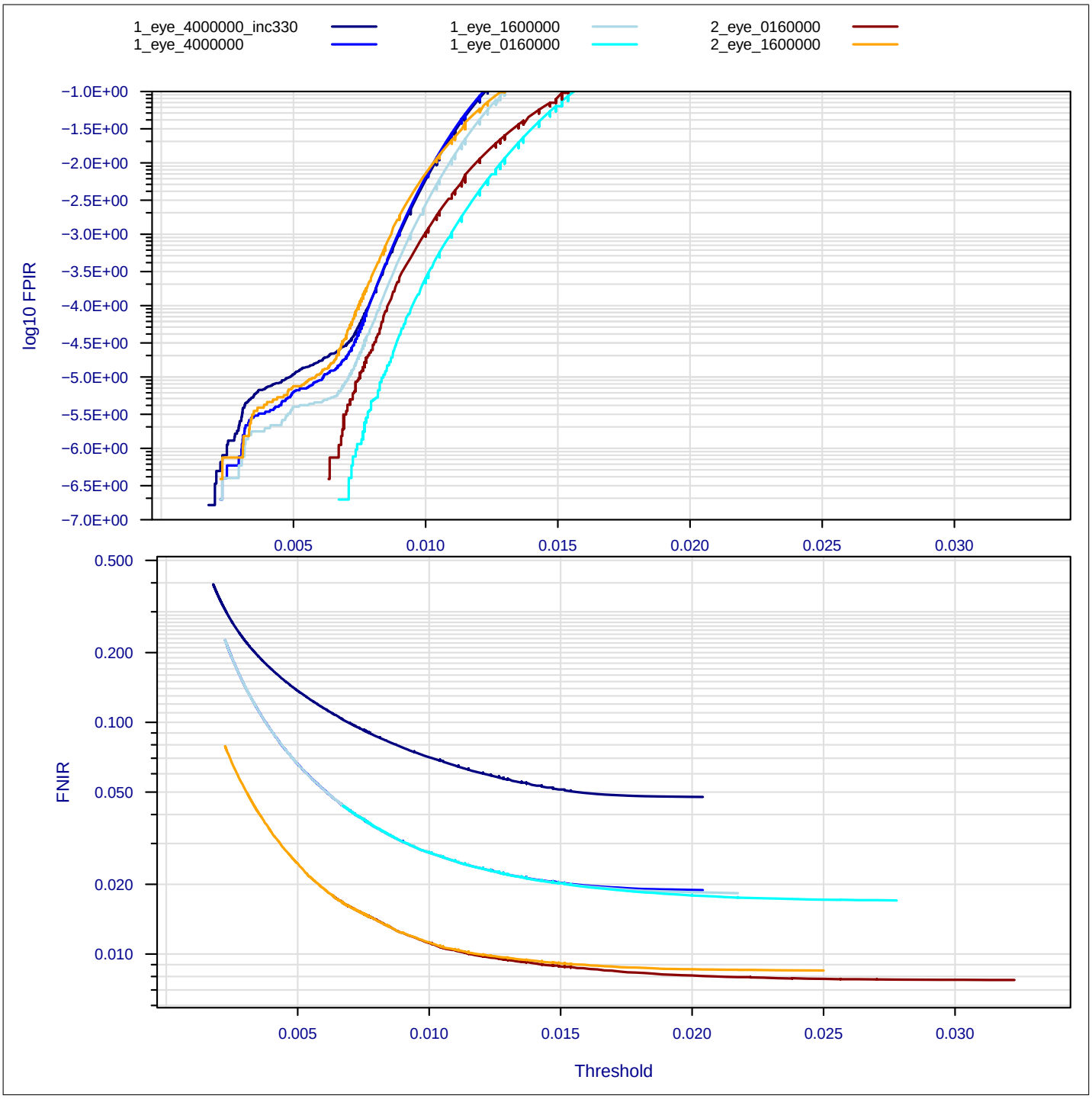

Figure 8: **Threshold calibration curves** for implementation N11A executing searches for single-eye enrolled populations $N = (0.16, 1.6, 4)$ million, and two-eye populations of $N = (0.16, 1.6)$ million individuals. While the large search sets S_{nb} were used used, with number of searches in the hundreds of thousands, the number of observed scores in the far tails is small: To get reduced uncertainty more searches would be necessary. Missing plots indicate the run is not yet complete.

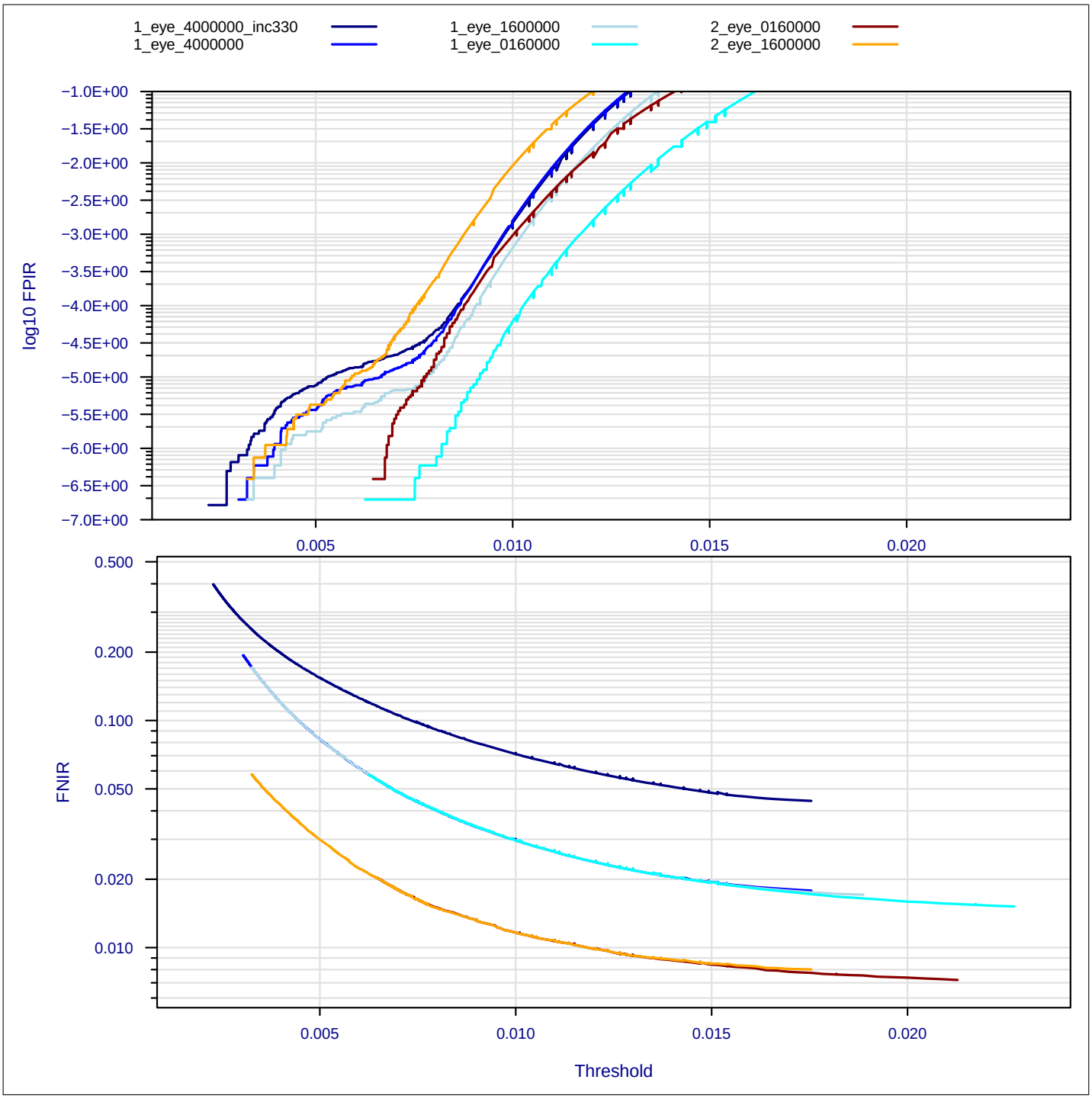

Figure 9: **Threshold calibration curves** for implementation N11B executing searches for single-eye enrolled populations $N = (0.16, 1.6, 4)$ million, and two-eye populations of $N = (0.16, 1.6)$ million individuals. While the large search sets S_{nb} were used used, with number of searches in the hundreds of thousands, the number of observed scores in the far tails is small: To get reduced uncertainty more searches would be necessary. Missing plots indicate the run is not yet complete.

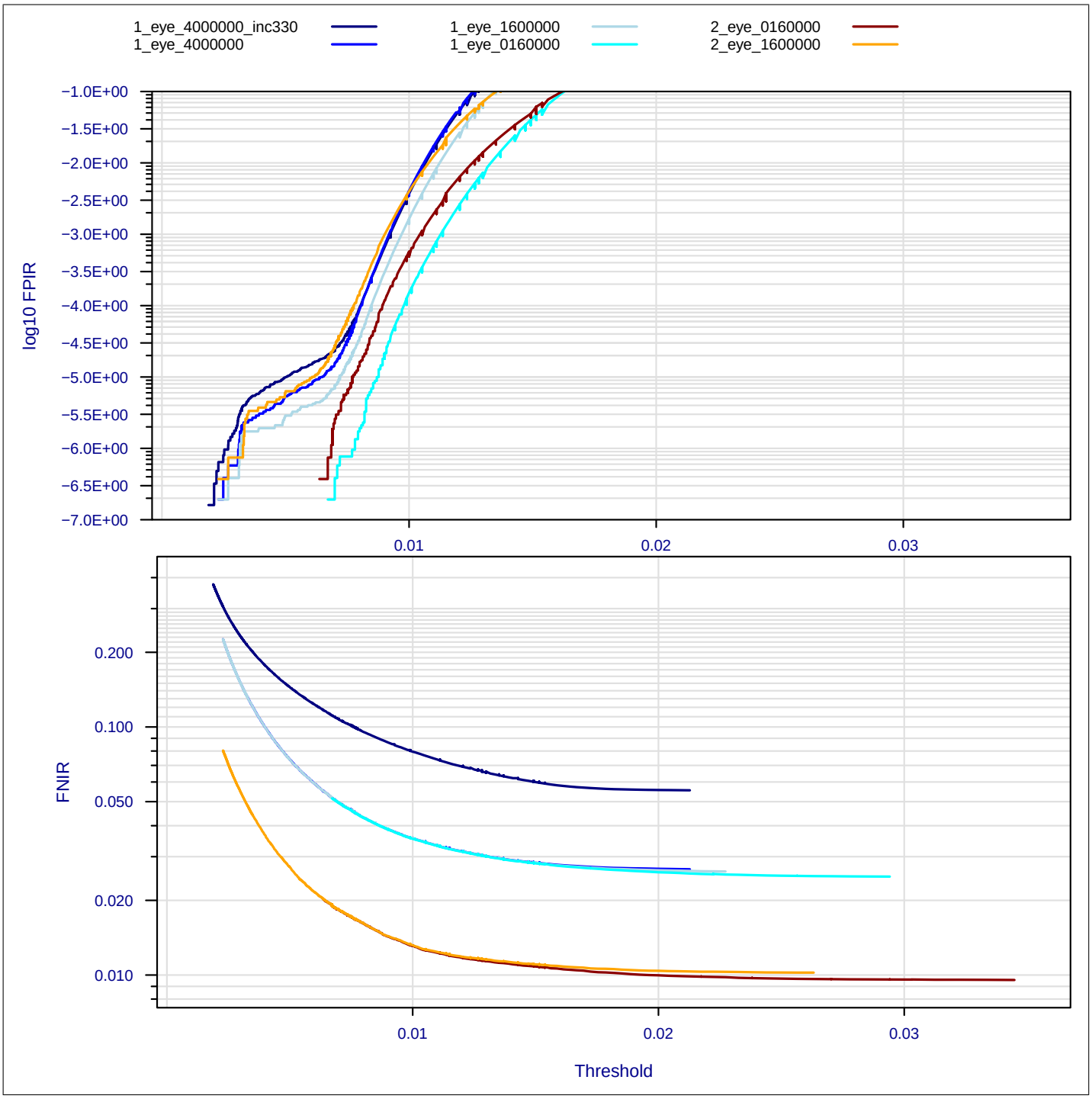

Figure 10: **Threshold calibration curves** for implementation N12A executing searches for single-eye enrolled populations $N = (0.16, 1.6, 4)$ million, and two-eye populations of $N = (0.16, 1.6)$ million individuals. While the large search sets S_{nb} were used used, with number of searches in the hundreds of thousands, the number of observed scores in the far tails is small: To get reduced uncertainty more searches would be necessary. Missing plots indicate the run is not yet complete.

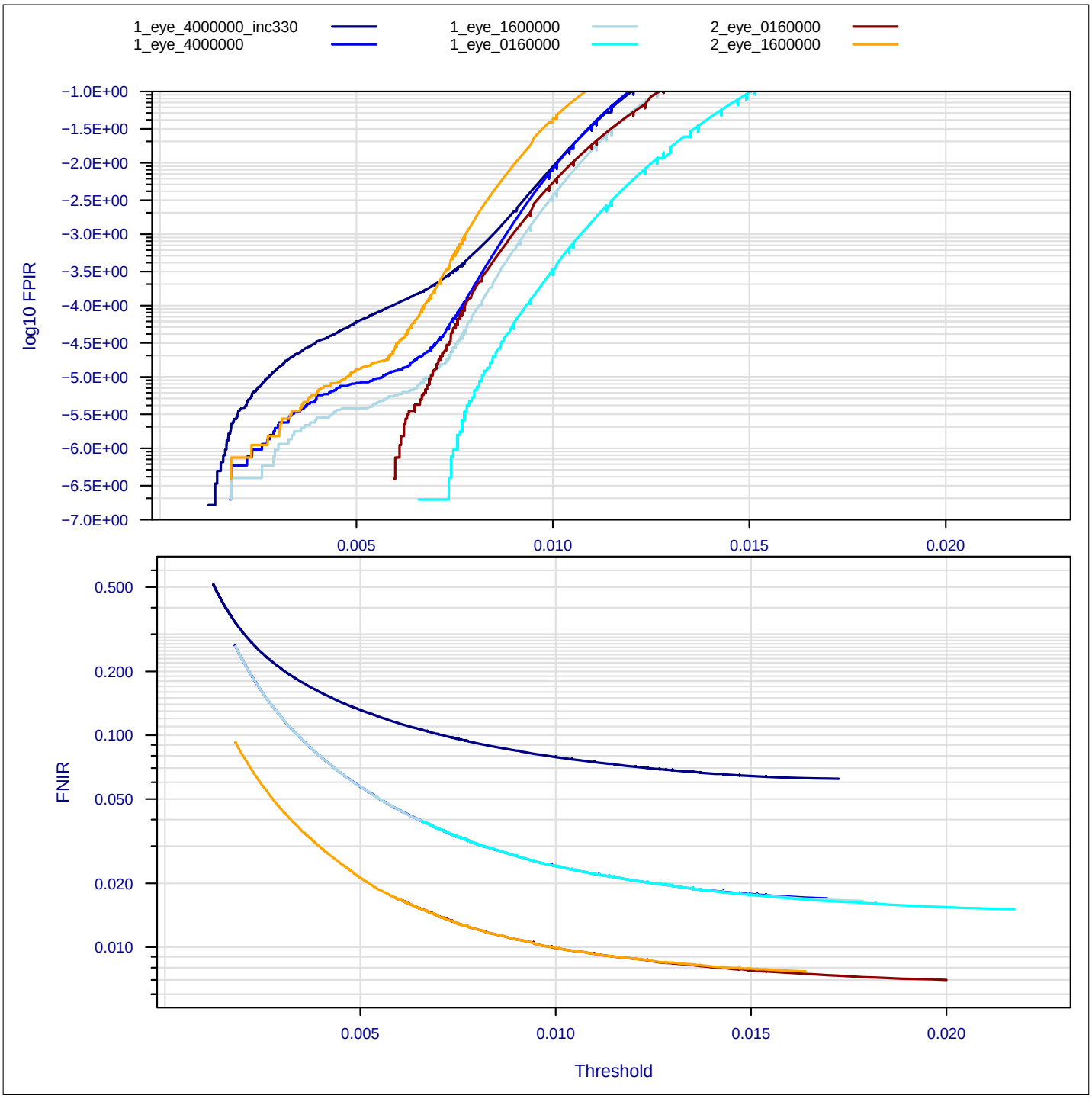

Figure 11: **Threshold calibration curves** for implementation N12B executing searches for single-eye enrolled populations $N = (0.16, 1.6, 4)$ million, and two-eye populations of $N = (0.16, 1.6)$ million individuals. While the large search sets S_{nb} were used used, with number of searches in the hundreds of thousands, the number of observed scores in the far tails is small: To get reduced uncertainty more searches would be necessary. Missing plots indicate the run is not yet complete.

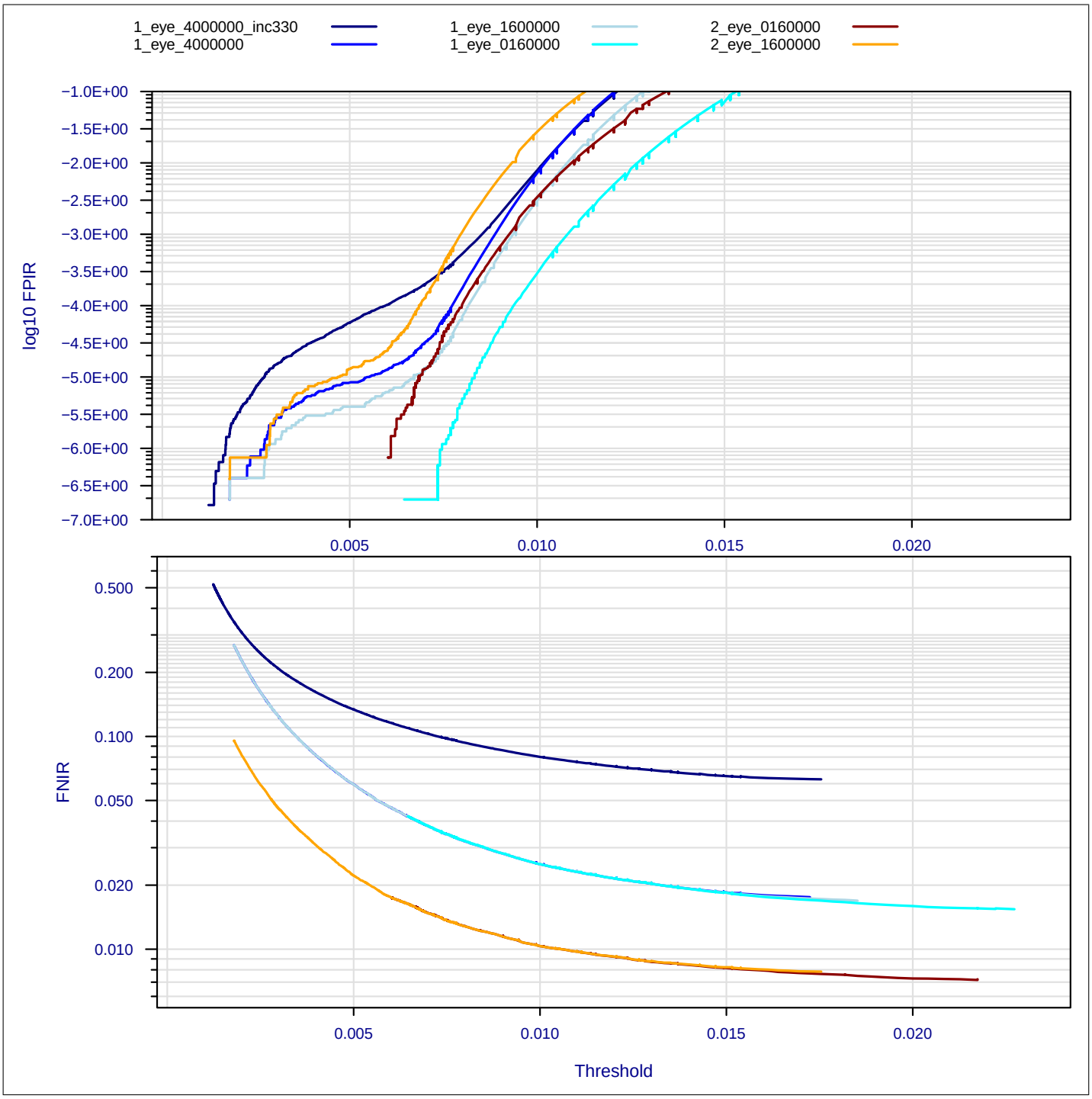

Figure 12: **Threshold calibration curves** for implementation N13B executing searches for single-eye enrolled populations $N = (0.16, 1.6, 4)$ million, and two-eye populations of $N = (0.16, 1.6)$ million individuals. While the large search sets S_{nb} were used used, with number of searches in the hundreds of thousands, the number of observed scores in the far tails is small: To get reduced uncertainty more searches would be necessary. Missing plots indicate the run is not yet complete.

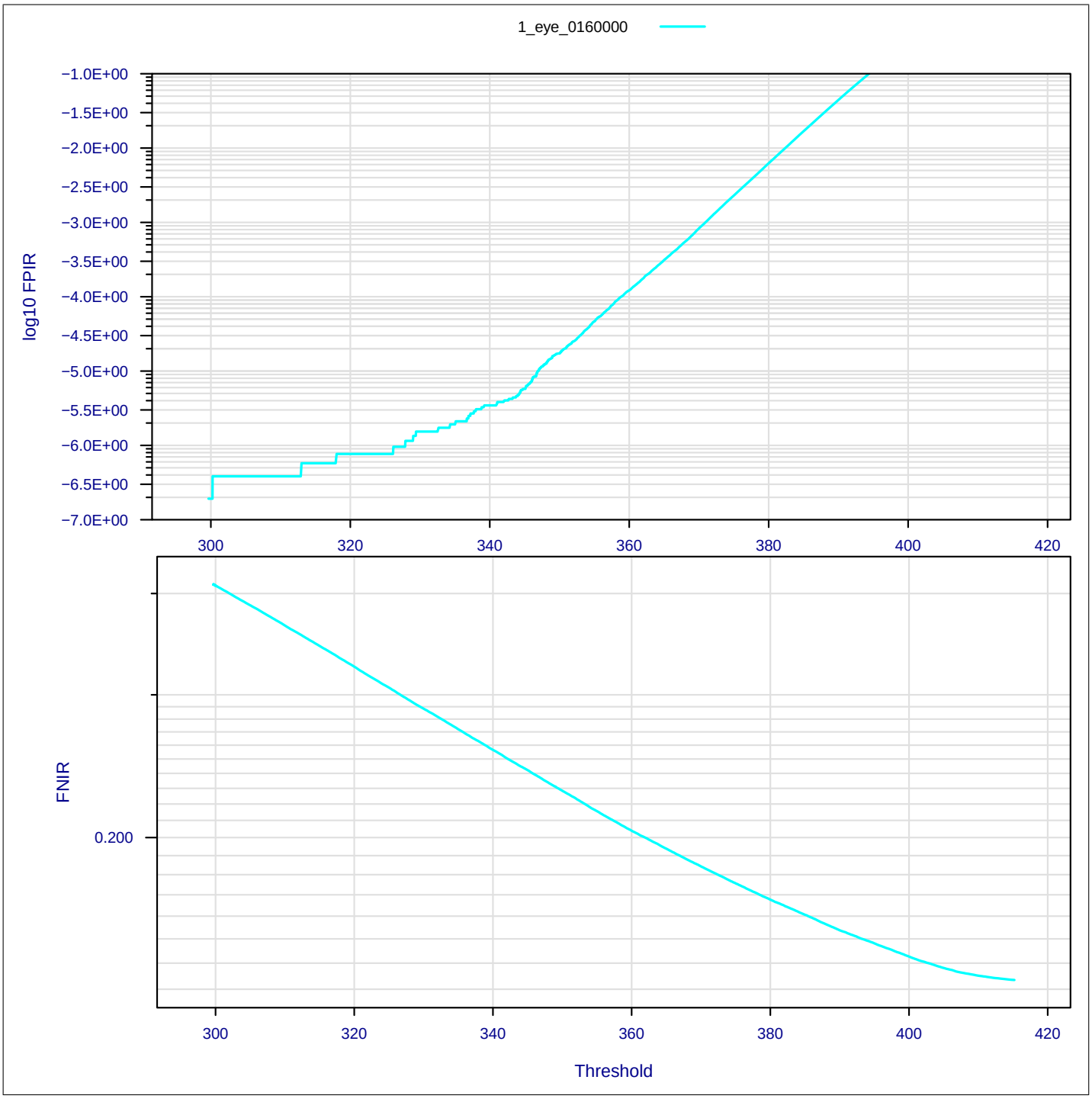

Figure 13: **Threshold calibration curves** for implementation P02A executing searches for single-eye enrolled populations $N = (0.16, 1.6, 4)$ million, and two-eye populations of $N = (0.16, 1.6)$ million individuals. While the large search sets S_{nb} were used used, with number of searches in the hundreds of thousands, the number of observed scores in the far tails is small: To get reduced uncertainty more searches would be necessary. Missing plots indicate the run is not yet complete.

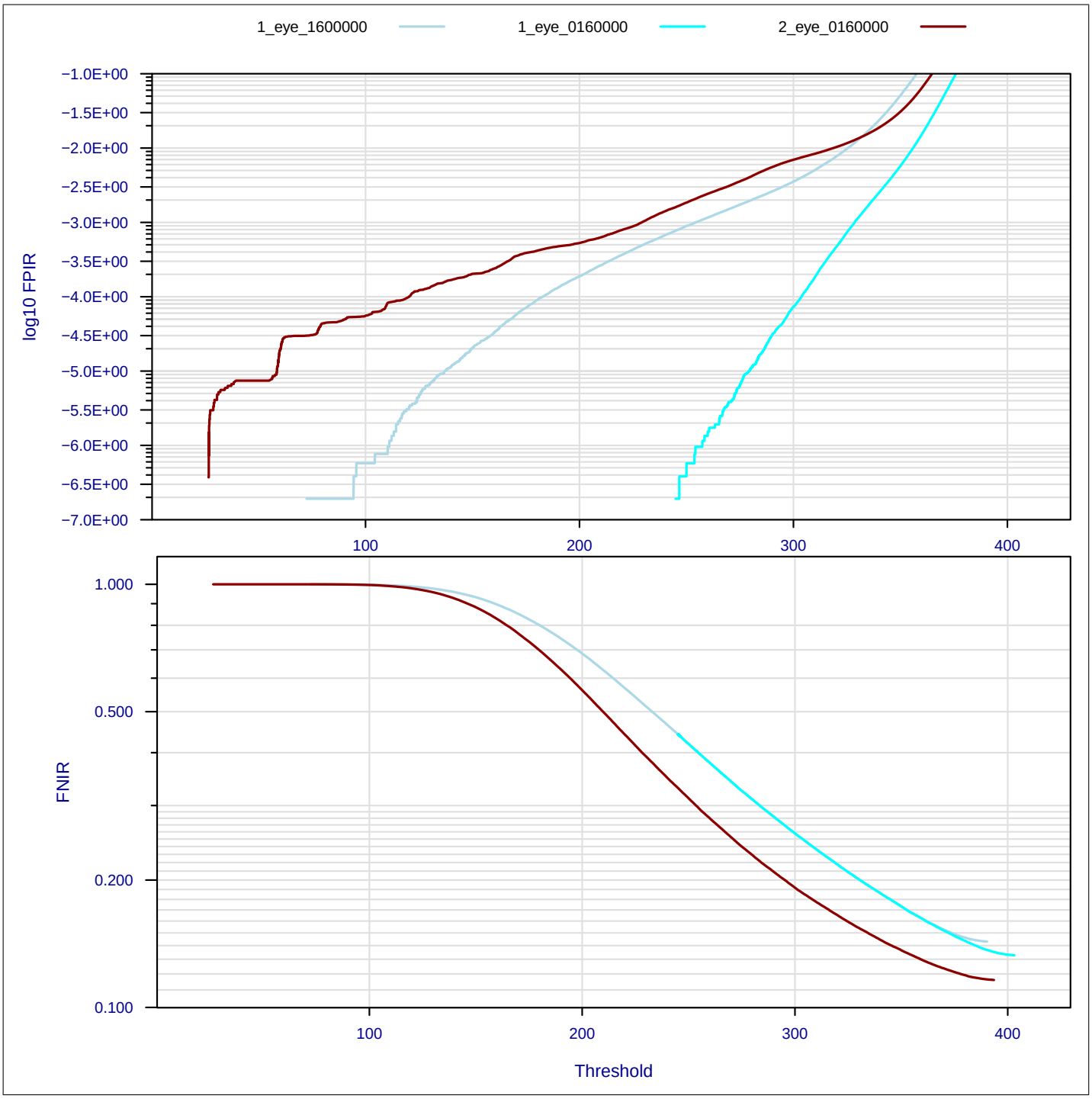

Figure 14: **Threshold calibration curves** for implementation P11A executing searches for single-eye enrolled populations $N = (0.16, 1.6, 4)$ million, and two-eye populations of $N = (0.16, 1.6)$ million individuals. While the large search sets S_{nb} were used used, with number of searches in the hundreds of thousands, the number of observed scores in the far tails is small: To get reduced uncertainty more searches would be necessary. Missing plots indicate the run is not yet complete.

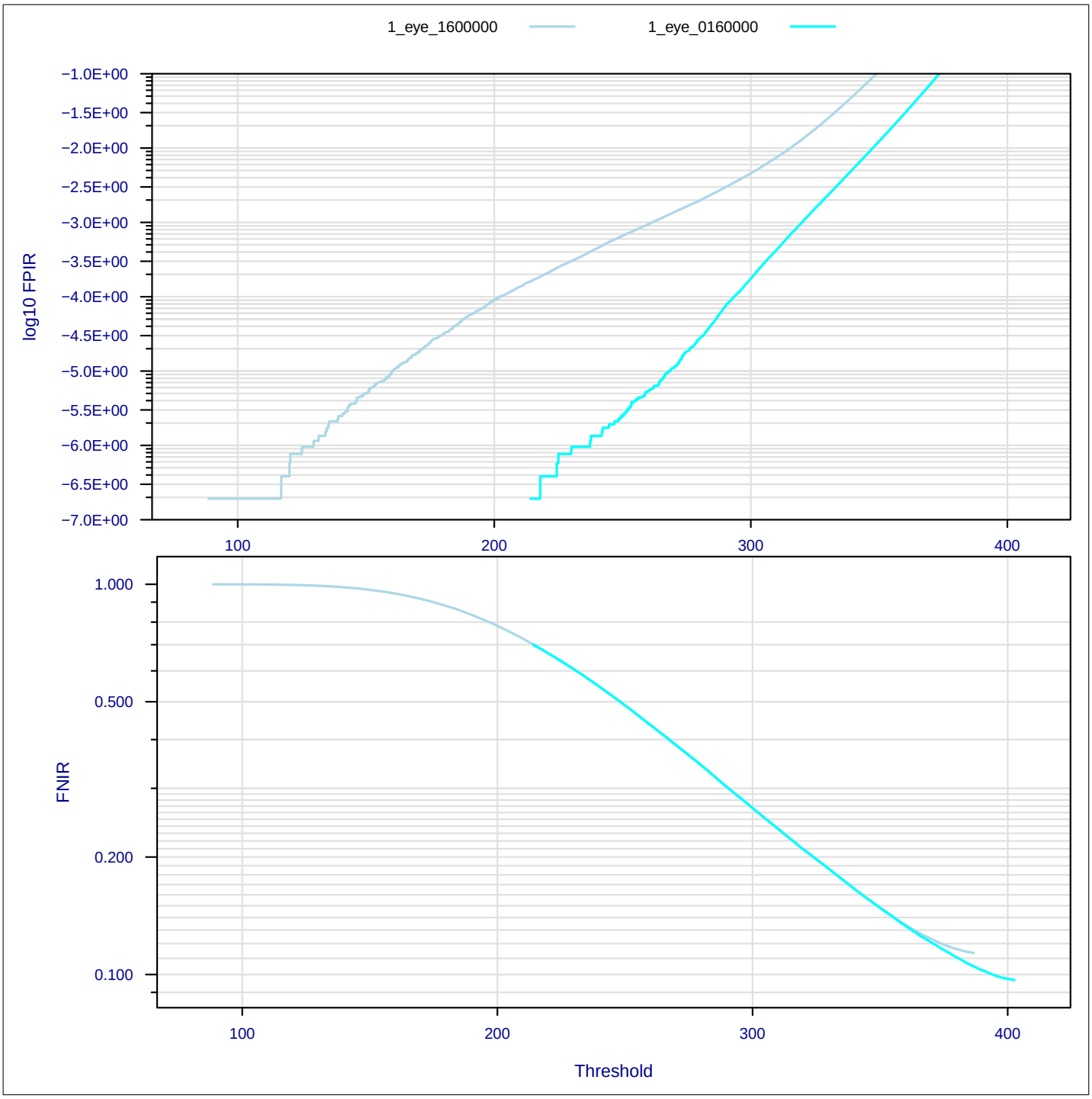

Figure 15: **Threshold calibration curves** for implementation P11B executing searches for single-eye enrolled populations $N = (0.16, 1.6, 4)$ million, and two-eye populations of $N = (0.16, 1.6)$ million individuals. While the large search sets S_{nb} were used used, with number of searches in the hundreds of thousands, the number of observed scores in the far tails is small: To get reduced uncertainty more searches would be necessary. Missing plots indicate the run is not yet complete.

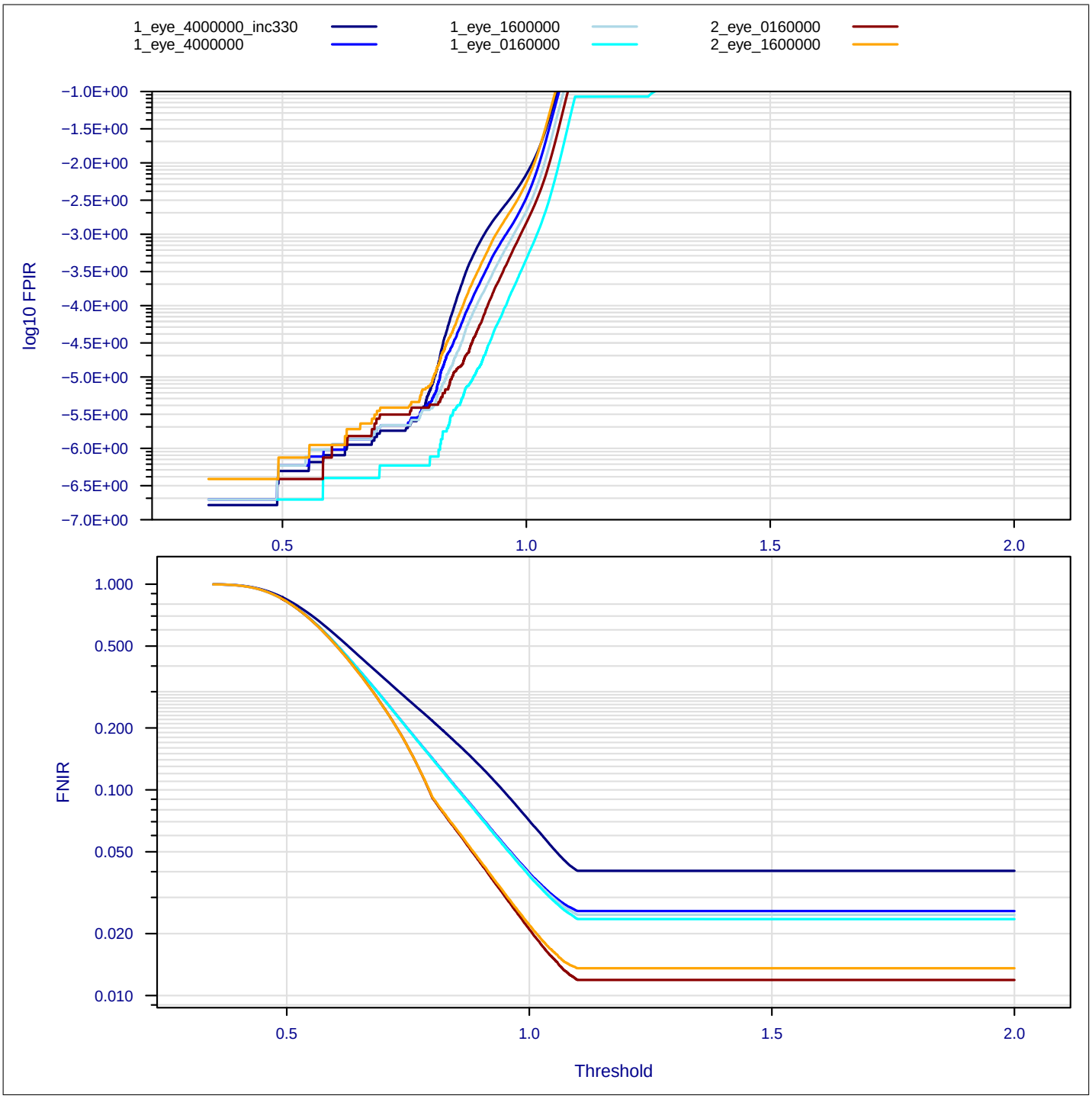

Figure 16: **Threshold calibration curves** for implementation Q02A executing searches for single-eye enrolled populations $N = (0.16, 1.6, 4)$ million, and two-eye populations of $N = (0.16, 1.6)$ million individuals. While the large search sets S_{nb} were used used, with number of searches in the hundreds of thousands, the number of observed scores in the far tails is small: To get reduced uncertainty more searches would be necessary. Missing plots indicate the run is not yet complete.

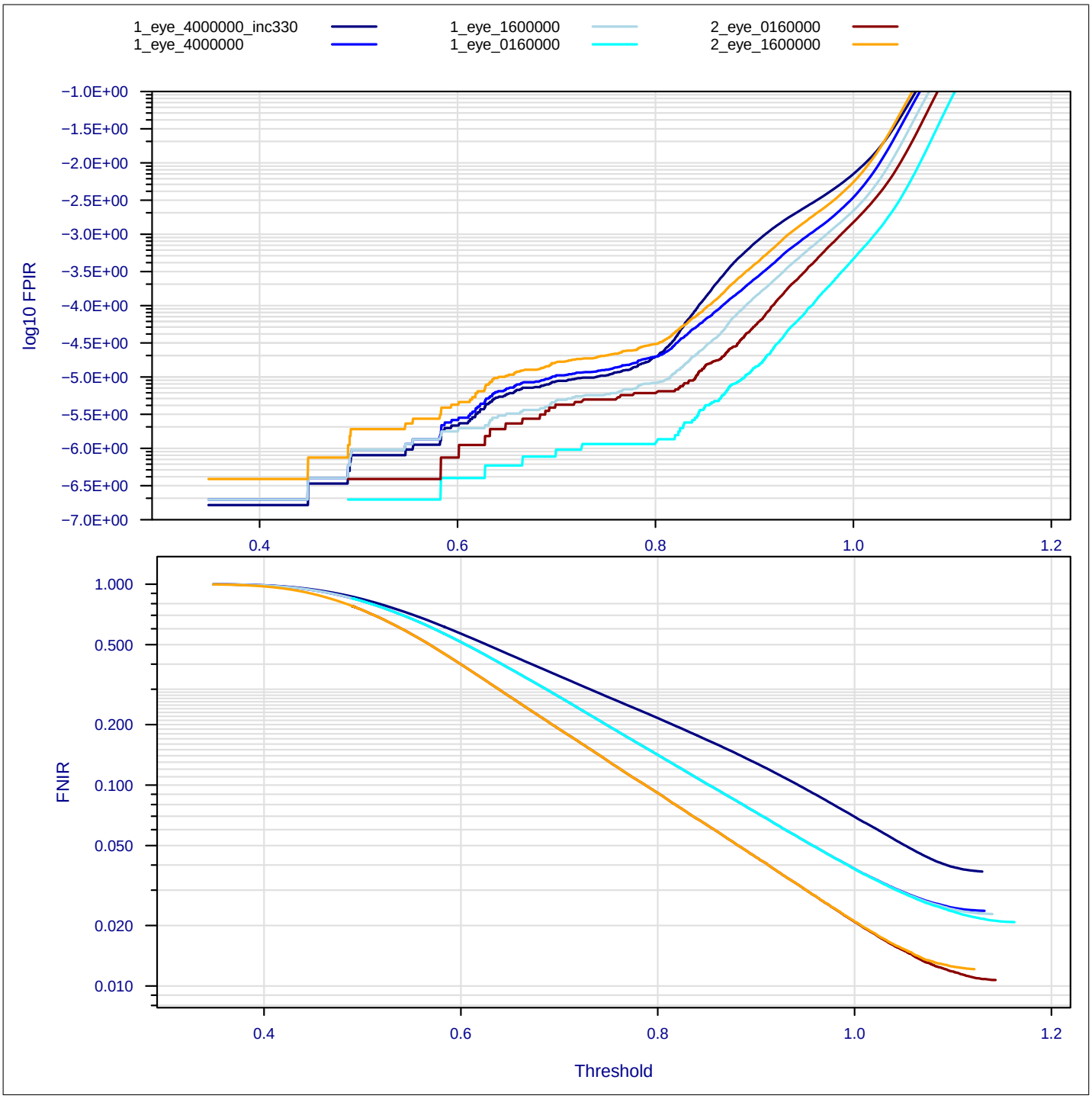

Figure 17: **Threshold calibration curves** for implementation Q02B executing searches for single-eye enrolled populations $N = (0.16, 1.6, 4)$ million, and two-eye populations of $N = (0.16, 1.6)$ million individuals. While the large search sets S_{nb} were used used, with number of searches in the hundreds of thousands, the number of observed scores in the far tails is small: To get reduced uncertainty more searches would be necessary. Missing plots indicate the run is not yet complete.

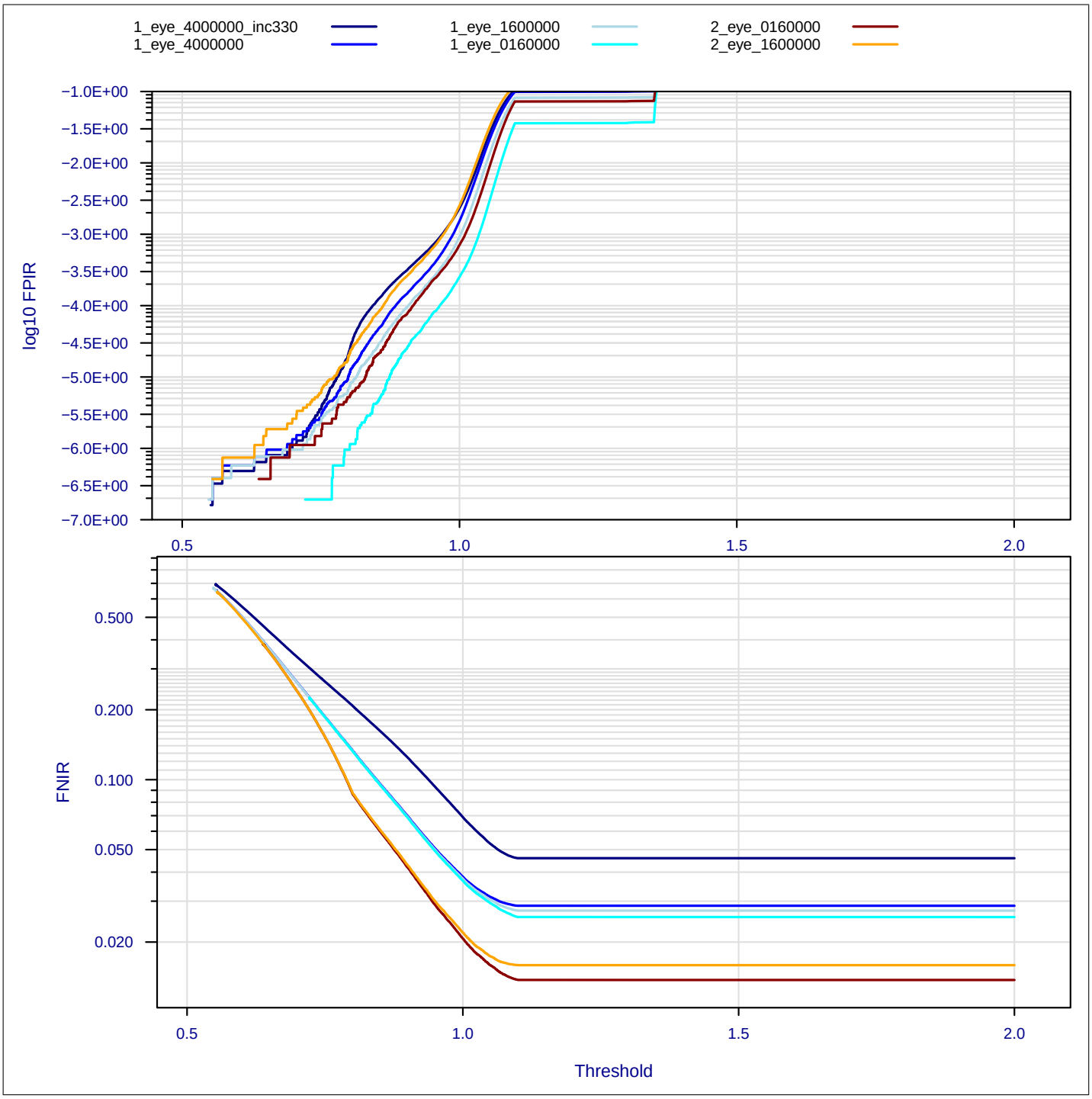

Figure 18: **Threshold calibration curves** for implementation Q03A executing searches for single-eye enrolled populations $N = (0.16, 1.6, 4)$ million, and two-eye populations of $N = (0.16, 1.6)$ million individuals. While the large search sets S_{nb} were used used, with number of searches in the hundreds of thousands, the number of observed scores in the far tails is small: To get reduced uncertainty more searches would be necessary. Missing plots indicate the run is not yet complete.

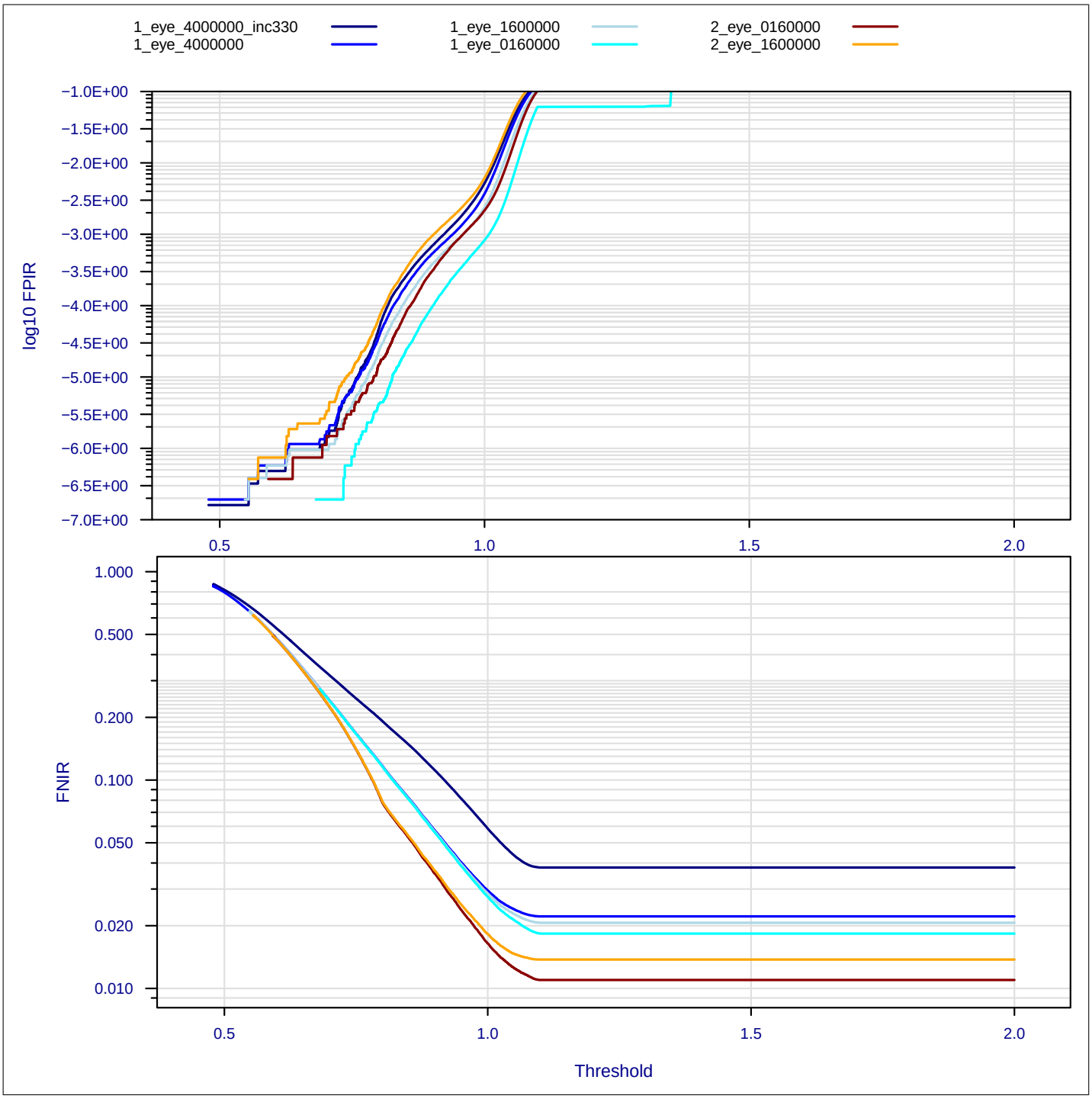

Figure 19: **Threshold calibration curves** for implementation Q03B executing searches for single-eye enrolled populations $N = (0.16, 1.6, 4)$ million, and two-eye populations of $N = (0.16, 1.6)$ million individuals. While the large search sets S_{nb} were used used, with number of searches in the hundreds of thousands, the number of observed scores in the far tails is small: To get reduced uncertainty more searches would be necessary. Missing plots indicate the run is not yet complete.

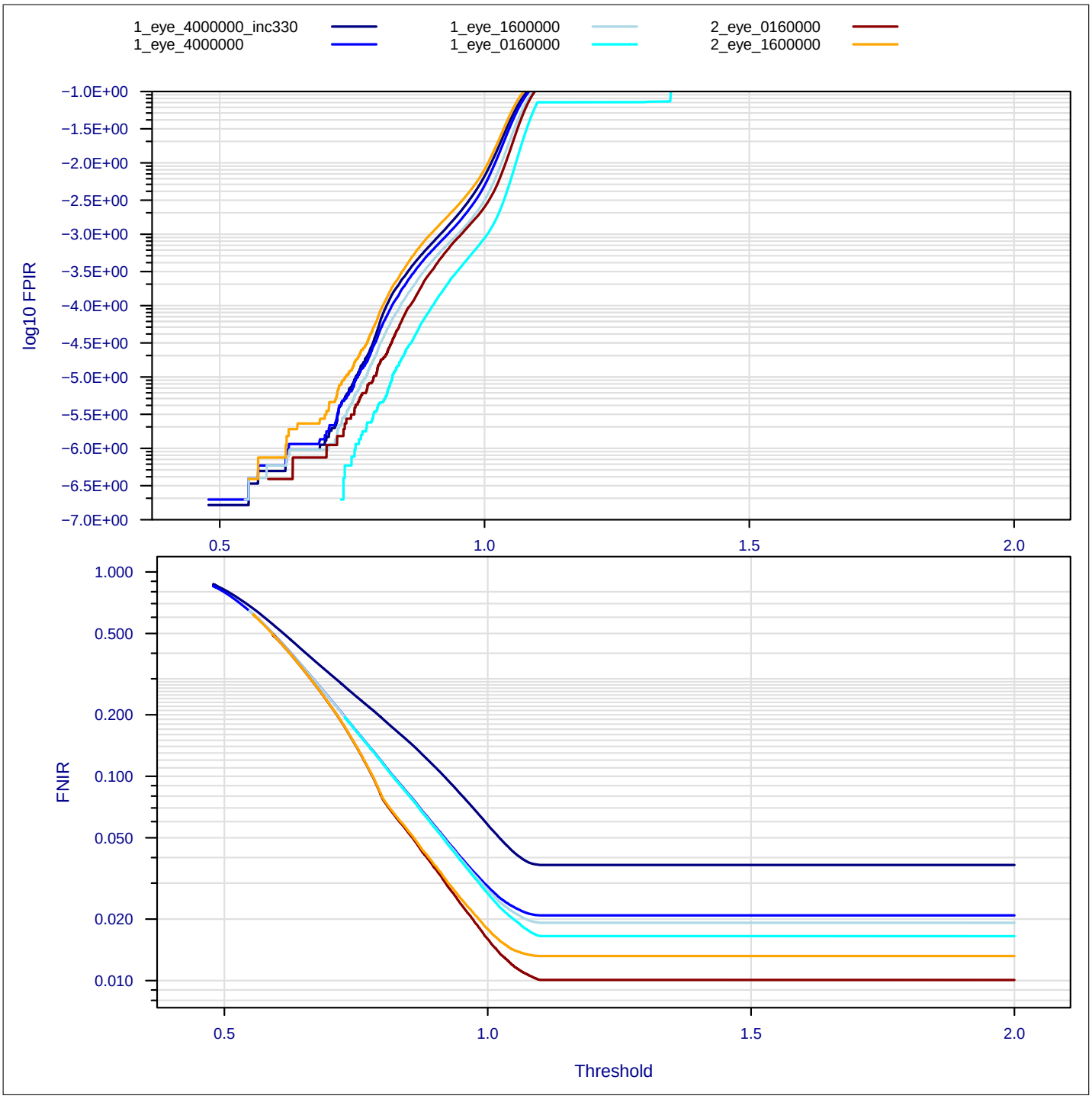

Figure 20: **Threshold calibration curves** for implementation Q04B executing searches for single-eye enrolled populations $N = (0.16, 1.6, 4)$ million, and two-eye populations of $N = (0.16, 1.6)$ million individuals. While the large search sets S_{nb} were used used, with number of searches in the hundreds of thousands, the number of observed scores in the far tails is small: To get reduced uncertainty more searches would be necessary. Missing plots indicate the run is not yet complete.

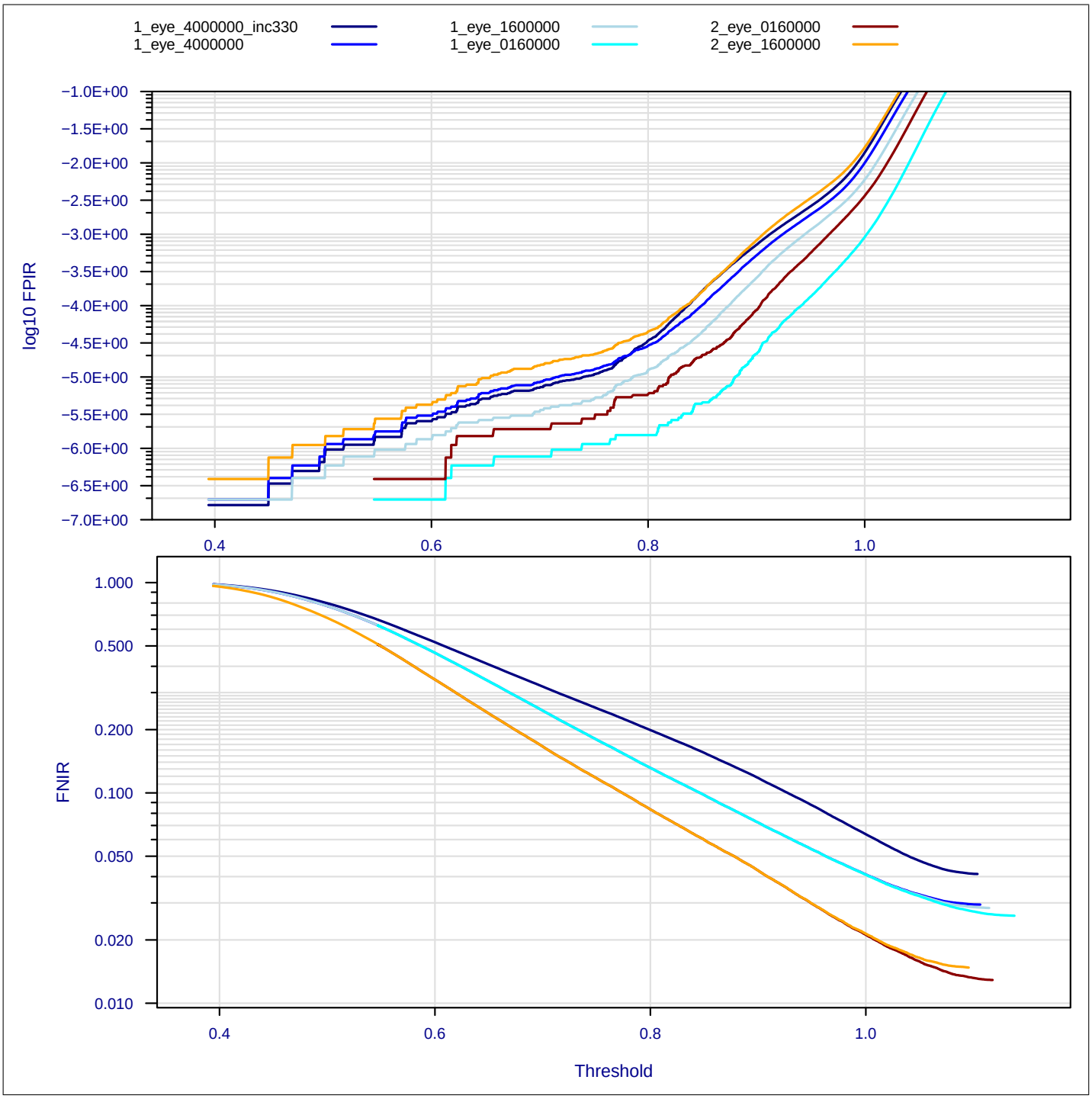

Figure 21: **Threshold calibration curves** for implementation Q11B executing searches for single-eye enrolled populations $N = (0.16, 1.6, 4)$ million, and two-eye populations of $N = (0.16, 1.6)$ million individuals. While the large search sets S_{nb} were used used, with number of searches in the hundreds of thousands, the number of observed scores in the far tails is small: To get reduced uncertainty more searches would be necessary. Missing plots indicate the run is not yet complete.

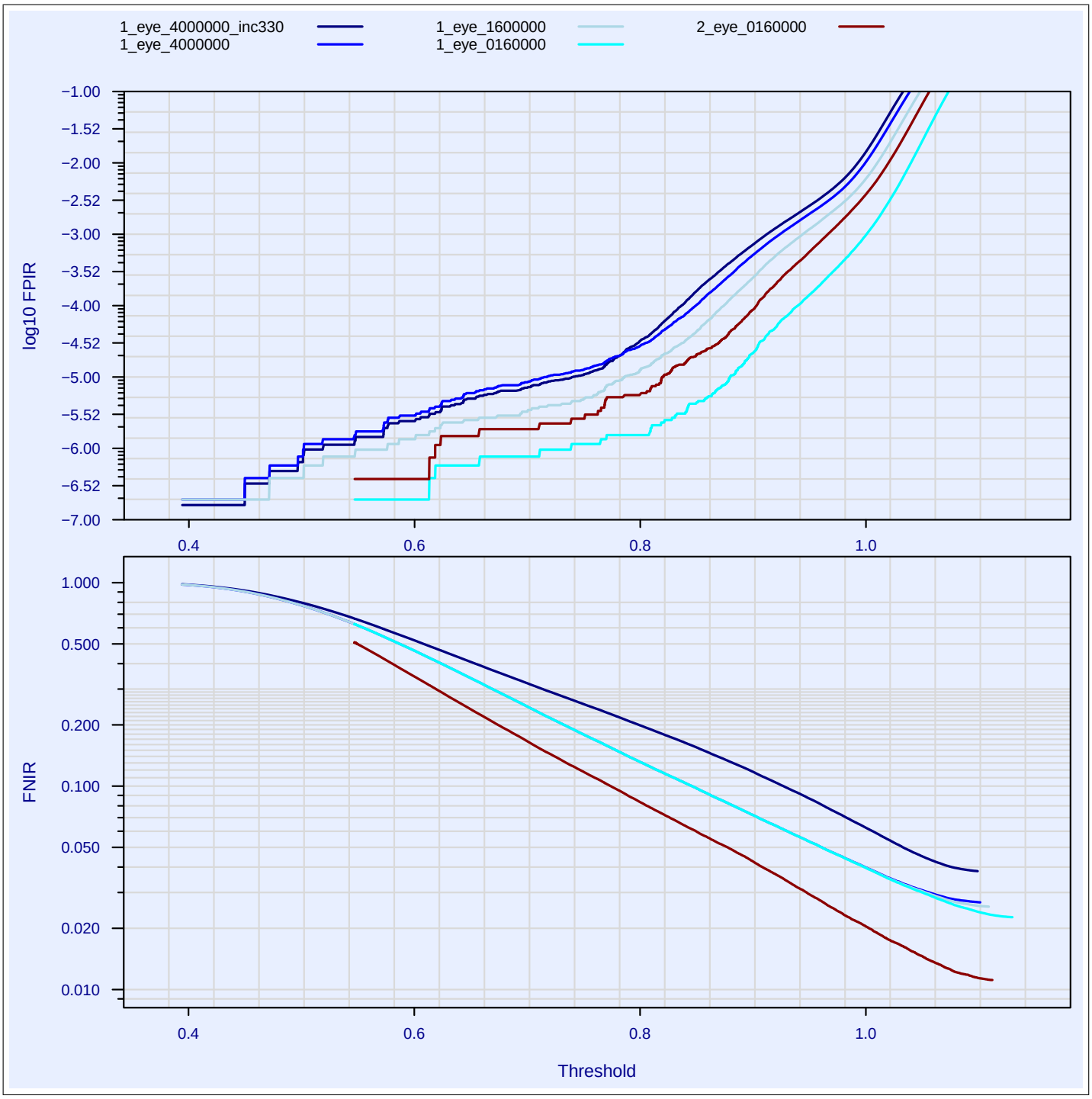

Figure 22: **Threshold calibration curves** for implementation Q12B executing searches for single-eye enrolled populations $N = (0.16, 1.6, 4)$ million, and two-eye populations of $N = (0.16, 1.6)$ million individuals. While the large search sets S_{nb} were used used, with number of searches in the hundreds of thousands, the number of observed scores in the far tails is small: To get reduced uncertainty more searches would be necessary. Missing plots indicate the run is not yet complete.

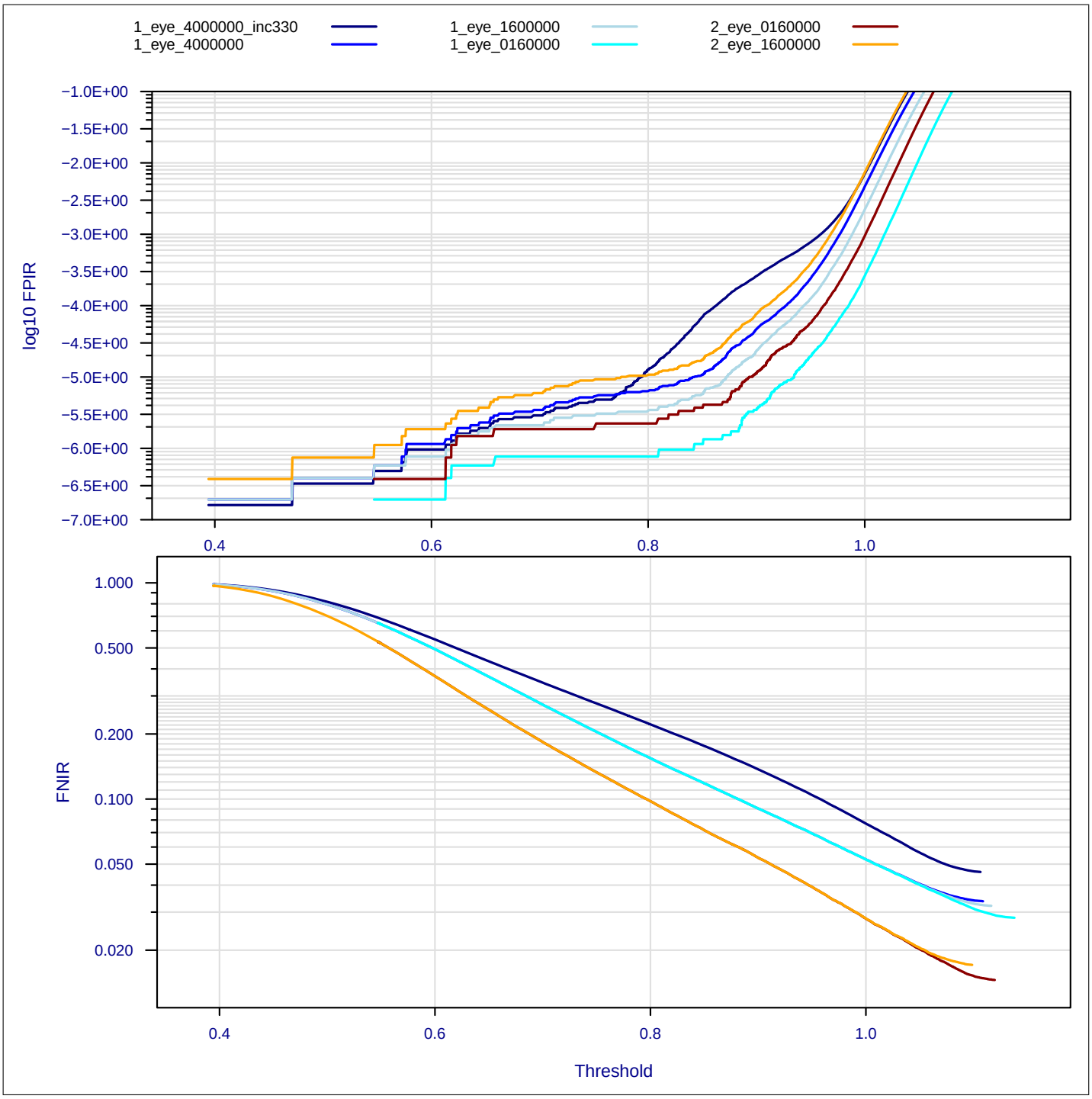

Figure 23: **Threshold calibration curves** for implementation Q13B executing searches for single-eye enrolled populations $N = (0.16, 1.6, 4)$ million, and two-eye populations of $N = (0.16, 1.6)$ million individuals. While the large search sets S_{nb} were used used, with number of searches in the hundreds of thousands, the number of observed scores in the far tails is small: To get reduced uncertainty more searches would be necessary. Missing plots indicate the run is not yet complete.

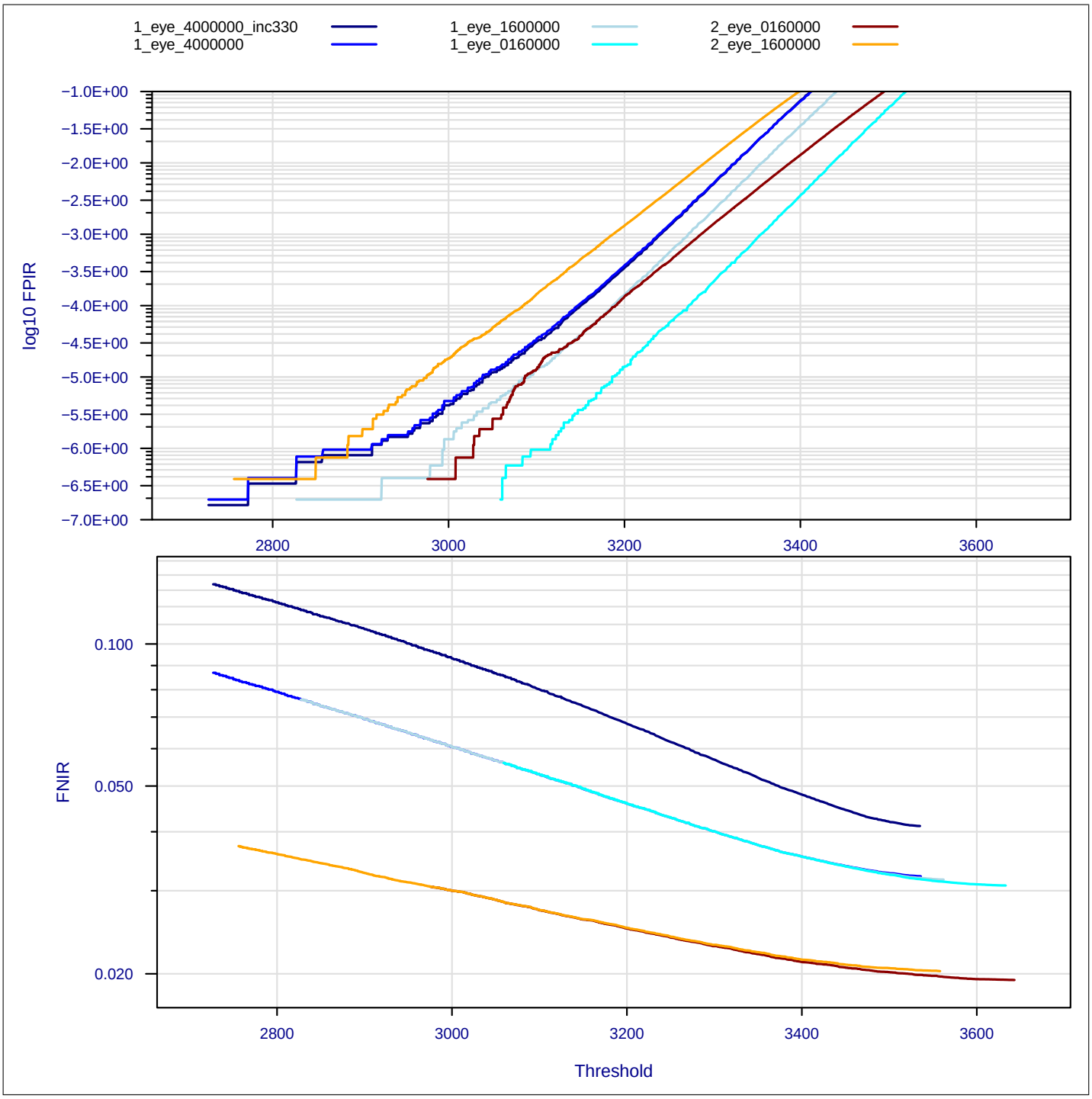

Figure 24: **Threshold calibration curves** for implementation R02A executing searches for single-eye enrolled populations $N = (0.16, 1.6, 4)$ million, and two-eye populations of $N = (0.16, 1.6)$ million individuals. While the large search sets S_{nb} were used used, with number of searches in the hundreds of thousands, the number of observed scores in the far tails is small: To get reduced uncertainty more searches would be necessary. Missing plots indicate the run is not yet complete.

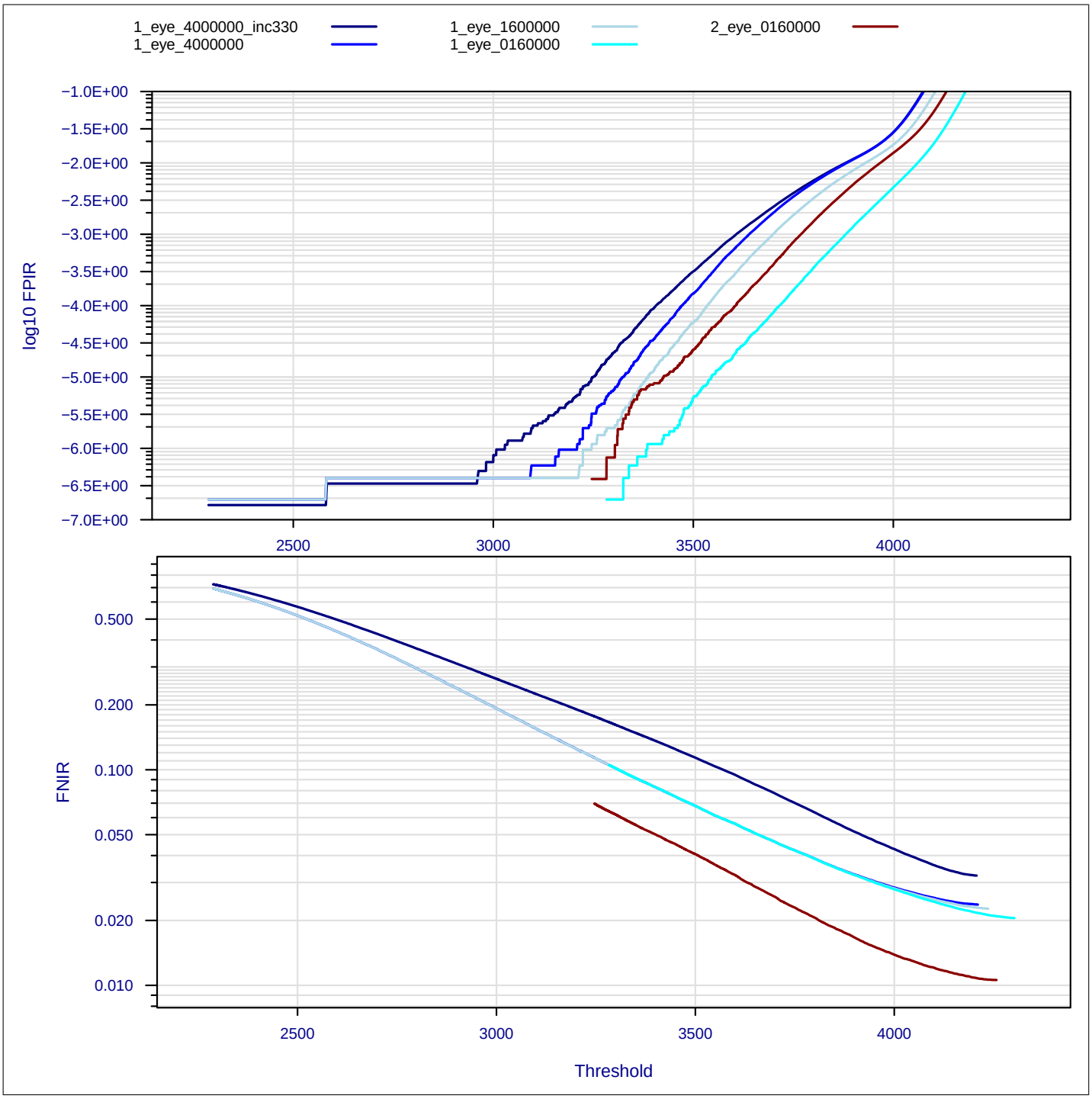

Figure 25: **Threshold calibration curves** for implementation R02B executing searches for single-eye enrolled populations $N = (0.16, 1.6, 4)$ million, and two-eye populations of $N = (0.16, 1.6)$ million individuals. While the large search sets S_{nb} were used used, with number of searches in the hundreds of thousands, the number of observed scores in the far tails is small: To get reduced uncertainty more searches would be necessary. Missing plots indicate the run is not yet complete.

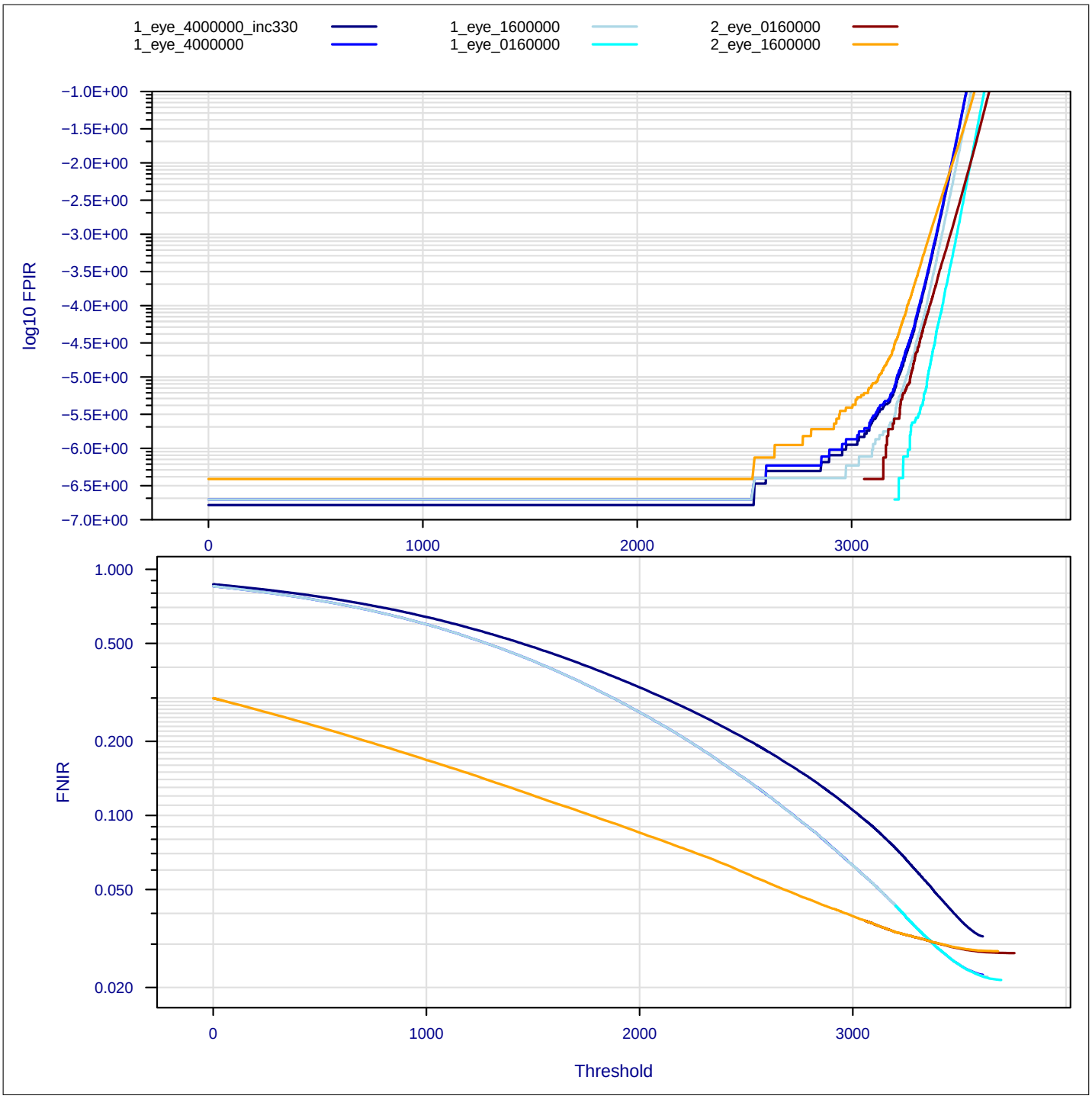

Figure 26: **Threshold calibration curves** for implementation R03A executing searches for single-eye enrolled populations $N = (0.16, 1.6, 4)$ million, and two-eye populations of $N = (0.16, 1.6)$ million individuals. While the large search sets S_{nb} were used used, with number of searches in the hundreds of thousands, the number of observed scores in the far tails is small: To get reduced uncertainty more searches would be necessary. Missing plots indicate the run is not yet complete.

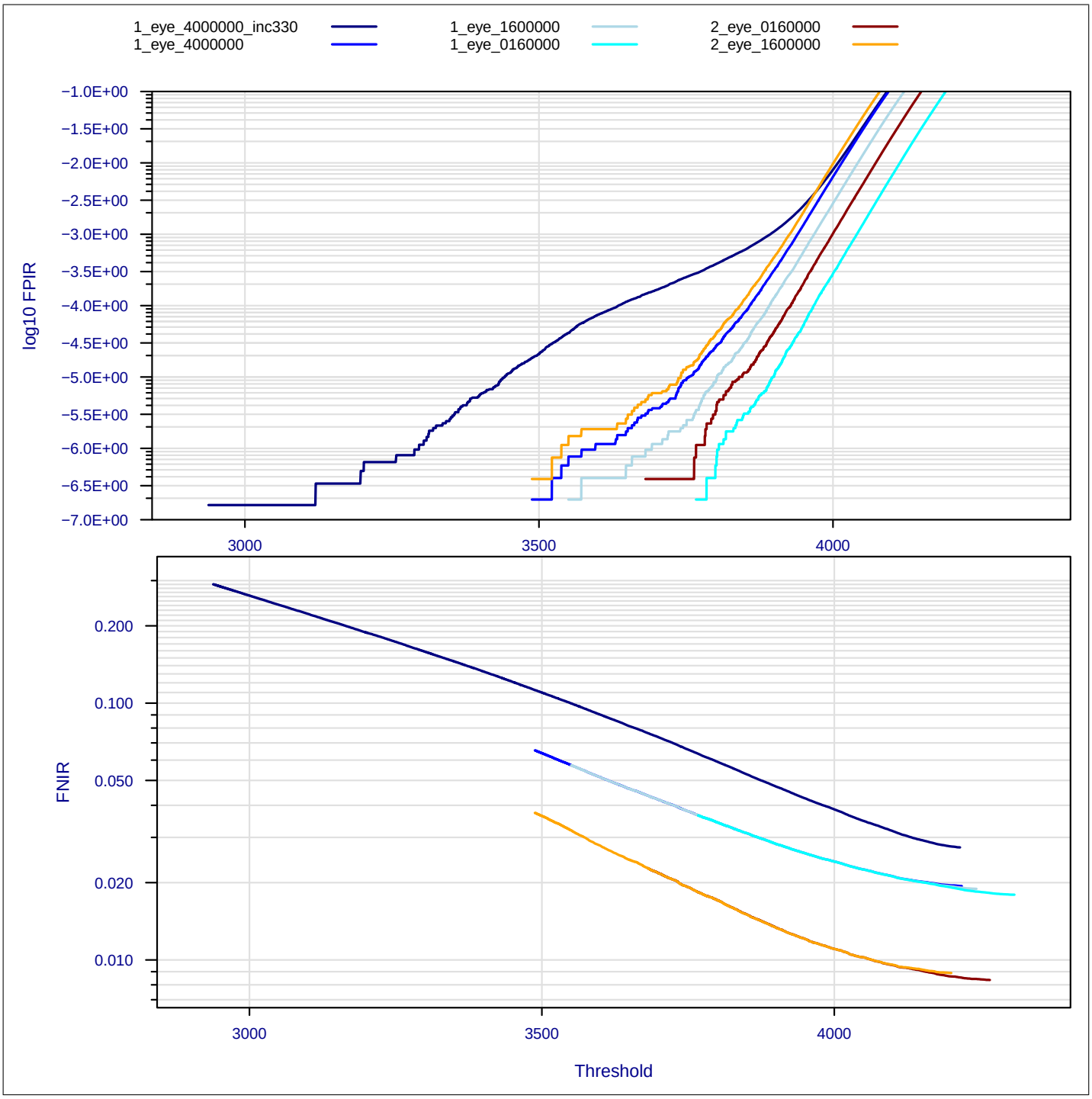

Figure 27: **Threshold calibration curves** for implementation R03B executing searches for single-eye enrolled populations $N = (0.16, 1.6, 4)$ million, and two-eye populations of $N = (0.16, 1.6)$ million individuals. While the large search sets S_{nb} were used used, with number of searches in the hundreds of thousands, the number of observed scores in the far tails is small: To get reduced uncertainty more searches would be necessary. Missing plots indicate the run is not yet complete.

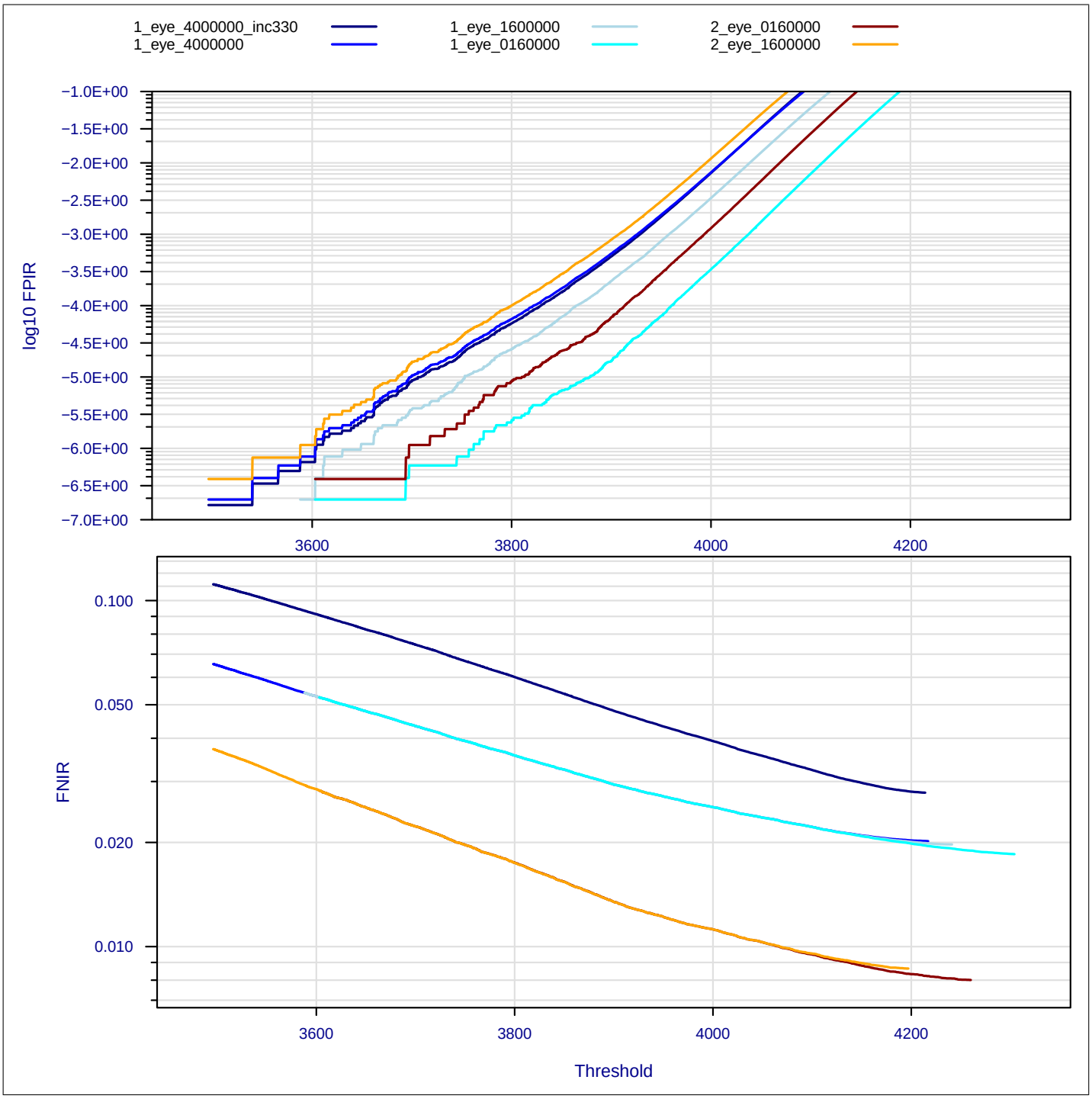

Figure 28: **Threshold calibration curves** for implementation R04B executing searches for single-eye enrolled populations $N = (0.16, 1.6, 4)$ million, and two-eye populations of $N = (0.16, 1.6)$ million individuals. While the large search sets S_{nb} were used used, with number of searches in the hundreds of thousands, the number of observed scores in the far tails is small: To get reduced uncertainty more searches would be necessary. Missing plots indicate the run is not yet complete.

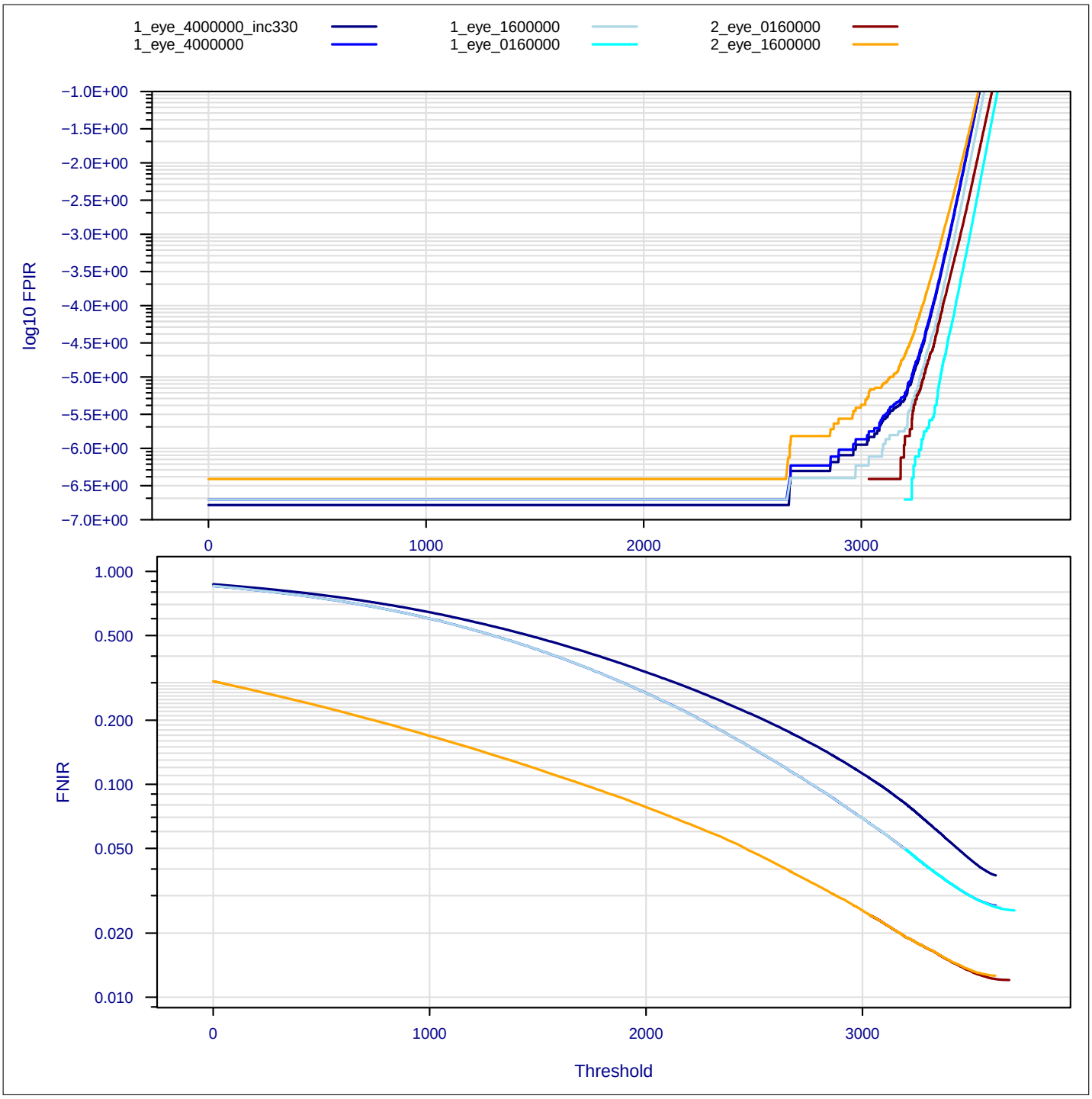

Figure 29: **Threshold calibration curves** for implementation R11A executing searches for single-eye enrolled populations $N = (0.16, 1.6, 4)$ million, and two-eye populations of $N = (0.16, 1.6)$ million individuals. While the large search sets S_{nb} were used used, with number of searches in the hundreds of thousands, the number of observed scores in the far tails is small: To get reduced uncertainty more searches would be necessary. Missing plots indicate the run is not yet complete.

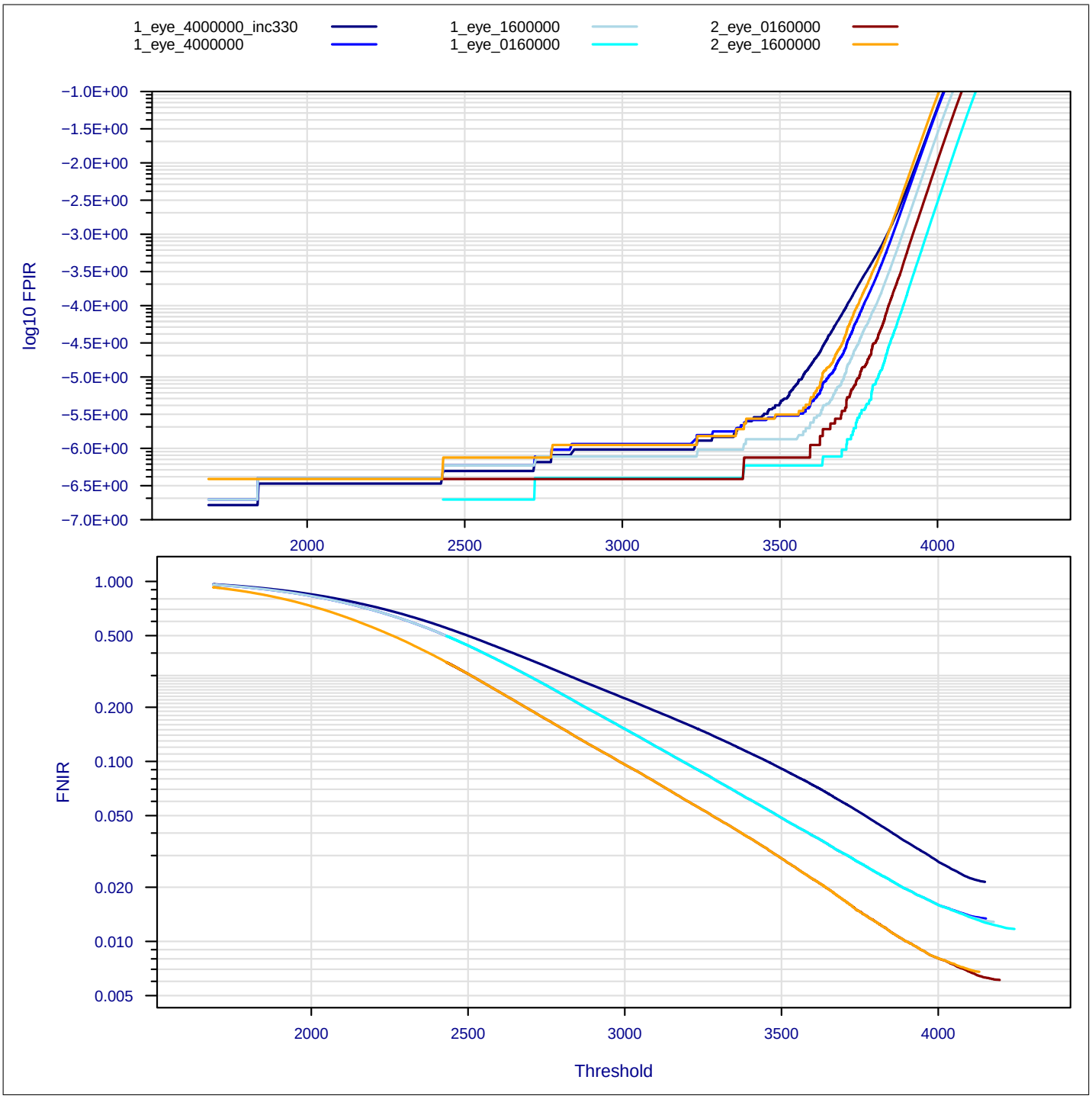

Figure 30: **Threshold calibration curves** for implementation R11B executing searches for single-eye enrolled populations $N = (0.16, 1.6, 4)$ million, and two-eye populations of $N = (0.16, 1.6)$ million individuals. While the large search sets S_{nb} were used used, with number of searches in the hundreds of thousands, the number of observed scores in the far tails is small: To get reduced uncertainty more searches would be necessary. Missing plots indicate the run is not yet complete.

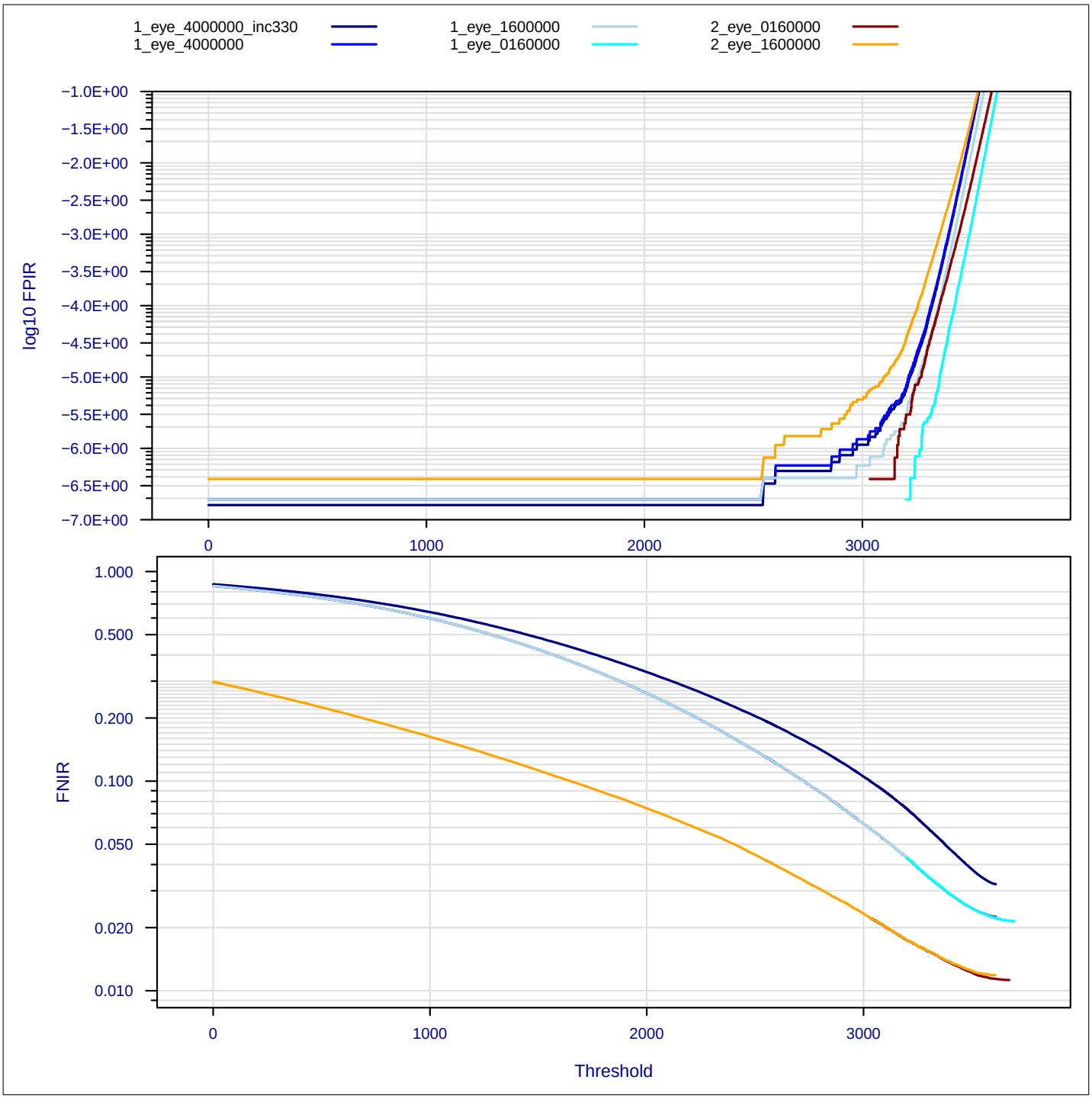

Figure 31: **Threshold calibration curves** for implementation R12A executing searches for single-eye enrolled populations $N = (0.16, 1.6, 4)$ million, and two-eye populations of $N = (0.16, 1.6)$ million individuals. While the large search sets S_{nb} were used used, with number of searches in the hundreds of thousands, the number of observed scores in the far tails is small: To get reduced uncertainty more searches would be necessary. Missing plots indicate the run is not yet complete.

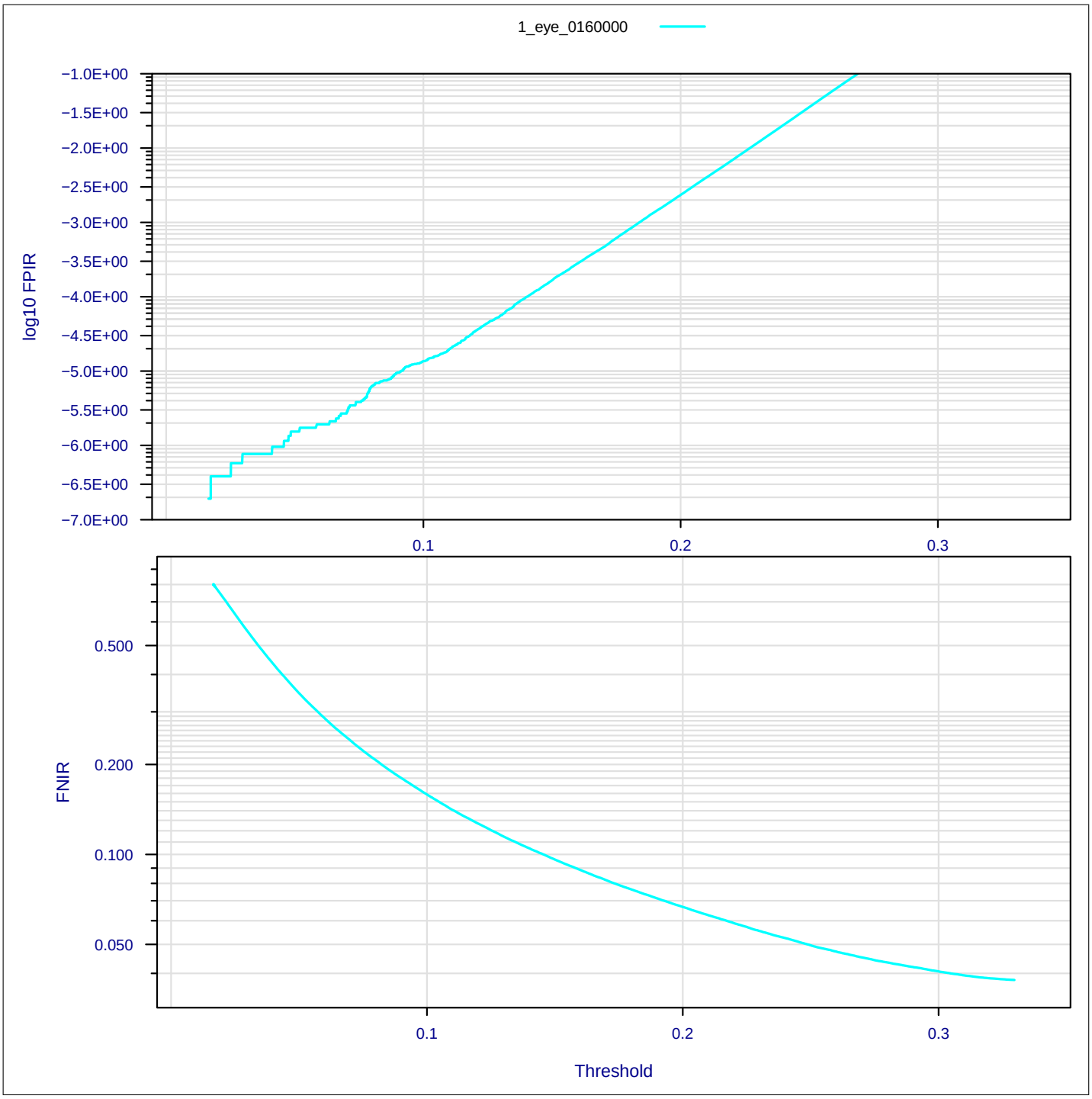

Figure 32: **Threshold calibration curves** for implementation S01B executing searches for single-eye enrolled populations $N = (0.16, 1.6, 4)$ million, and two-eye populations of $N = (0.16, 1.6)$ million individuals. While the large search sets S_{nb} were used used, with number of searches in the hundreds of thousands, the number of observed scores in the far tails is small: To get reduced uncertainty more searches would be necessary. Missing plots indicate the run is not yet complete.

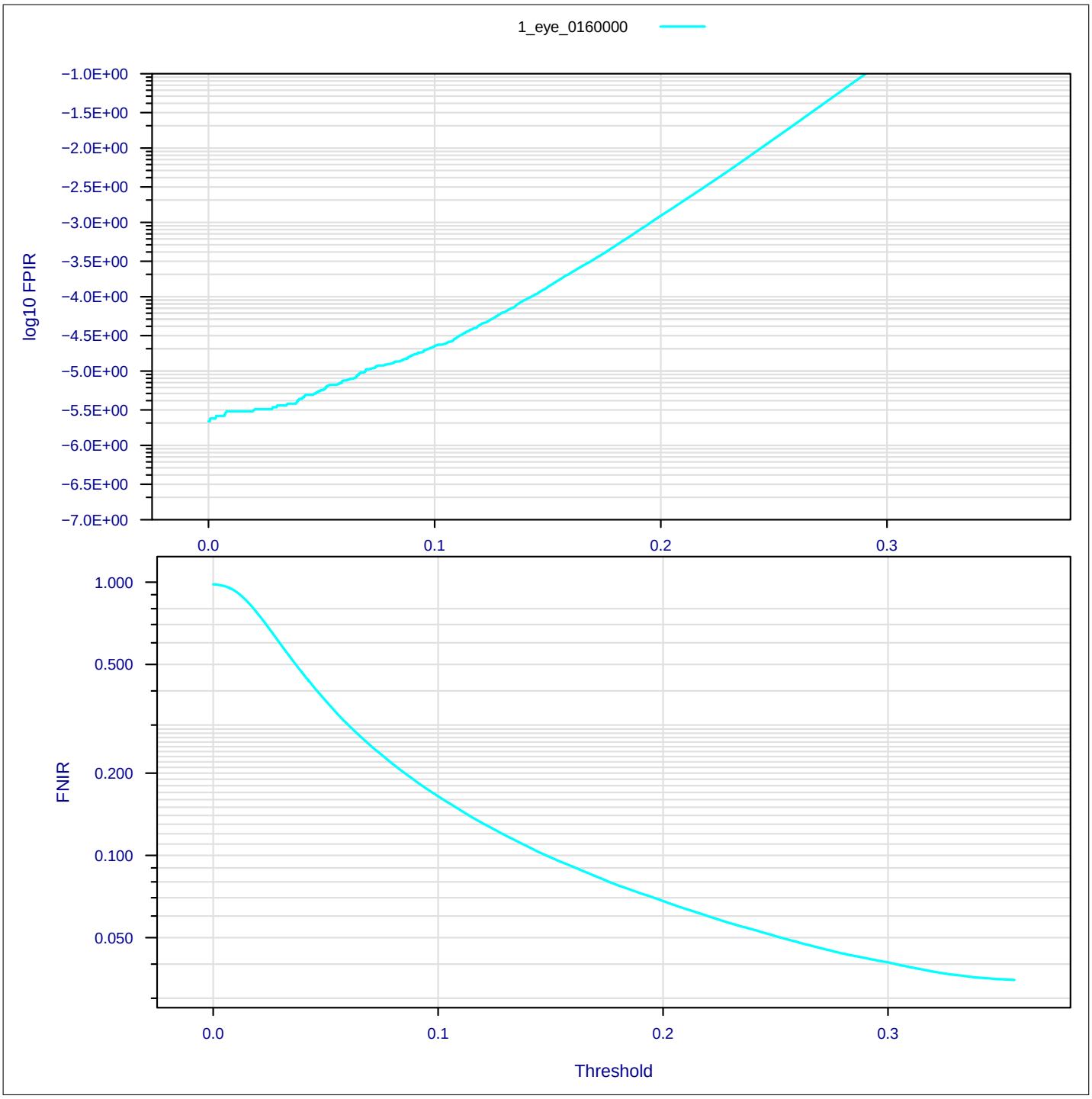

Figure 33: **Threshold calibration curves** for implementation S02B executing searches for single-eye enrolled populations $N = (0.16, 1.6, 4)$ million, and two-eye populations of $N = (0.16, 1.6)$ million individuals. While the large search sets S_{nb} were used used, with number of searches in the hundreds of thousands, the number of observed scores in the far tails is small: To get reduced uncertainty more searches would be necessary. Missing plots indicate the run is not yet complete.

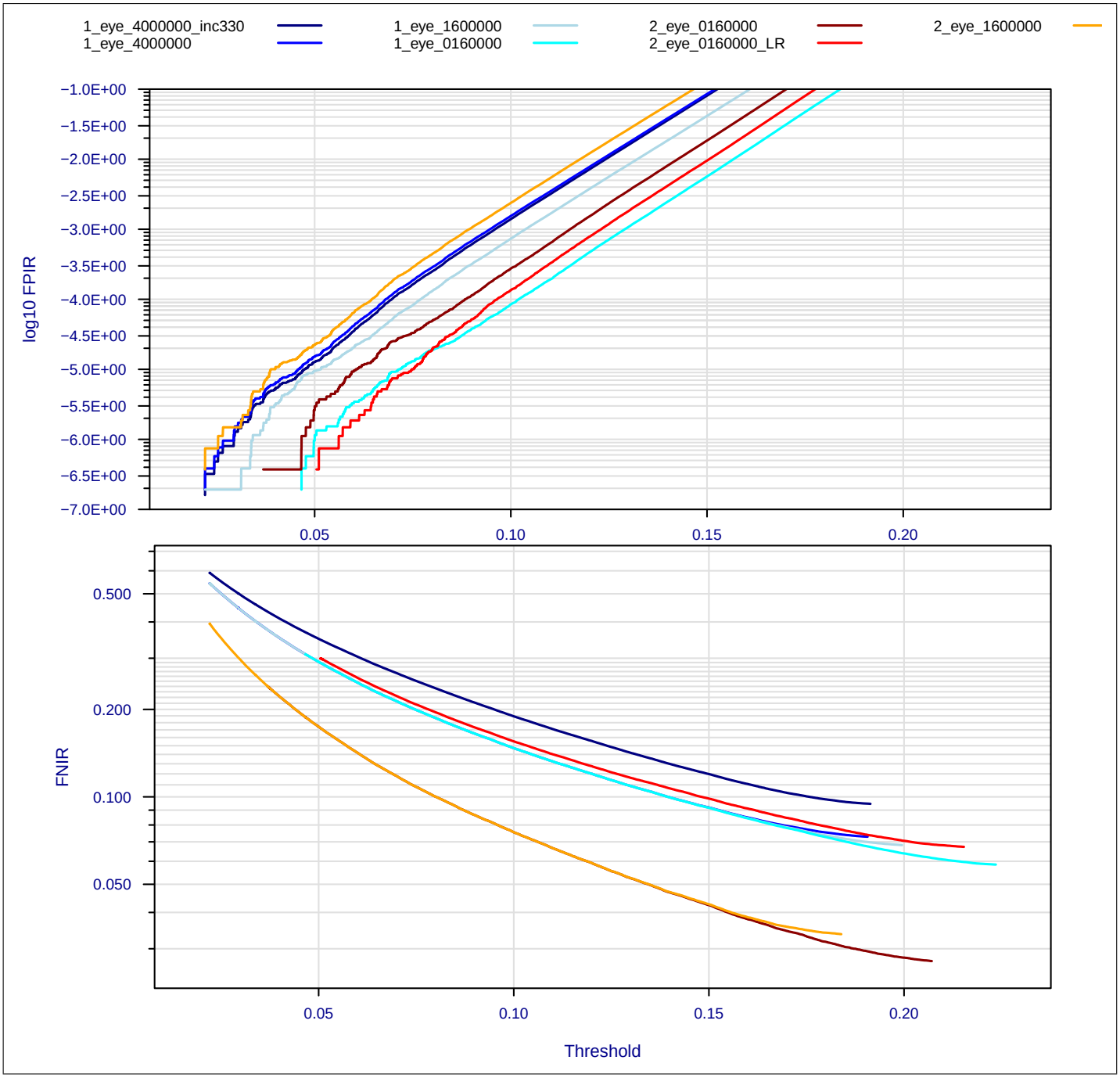

Figure 34: **Threshold calibration curves** for implementation S03A executing searches for single-eye enrolled populations $N = (0.16, 1.6, 4)$ million, and two-eye populations of $N = (0.16, 1.6)$ million individuals. While the large search sets S_{nb} were used used, with number of searches in the hundreds of thousands, the number of observed scores in the far tails is small: To get reduced uncertainty more searches would be necessary. Missing plots indicate the run is not yet complete.

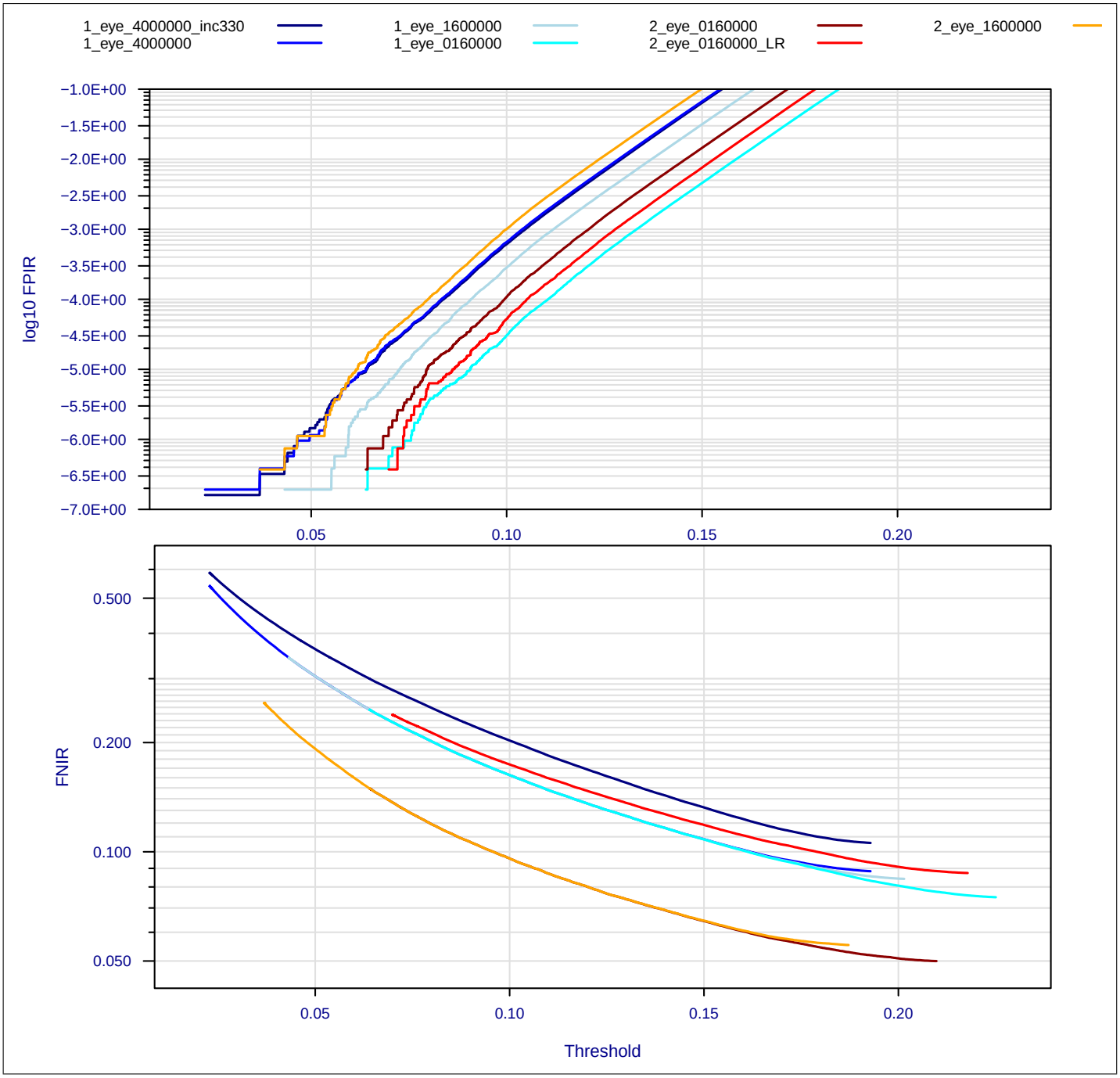

Figure 35: **Threshold calibration curves** for implementation S04A executing searches for single-eye enrolled populations $N = (0.16, 1.6, 4)$ million, and two-eye populations of $N = (0.16, 1.6)$ million individuals. While the large search sets S_{nb} were used used, with number of searches in the hundreds of thousands, the number of observed scores in the far tails is small: To get reduced uncertainty more searches would be necessary. Missing plots indicate the run is not yet complete.

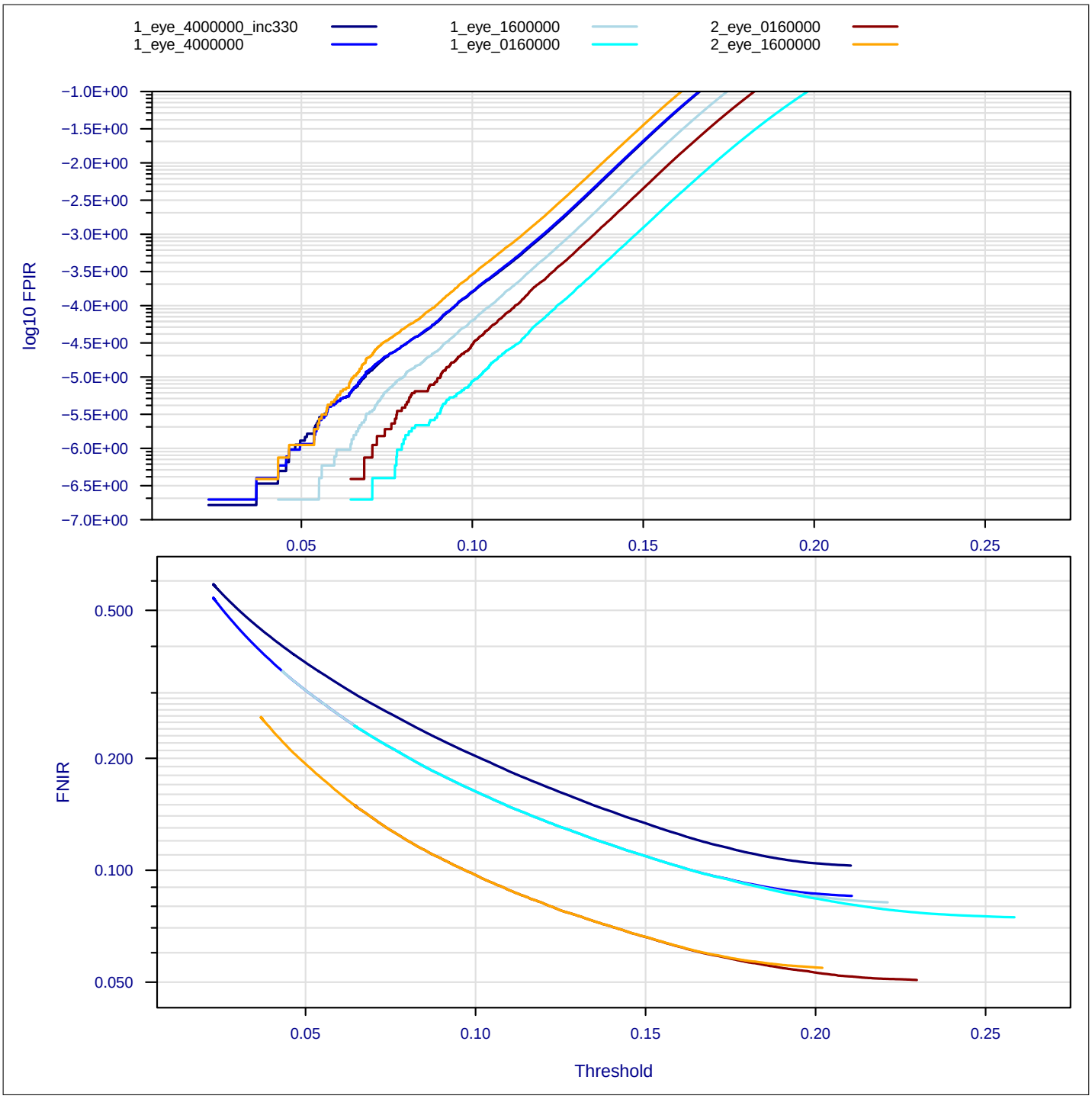

Figure 36: **Threshold calibration curves** for implementation S05A executing searches for single-eye enrolled populations $N = (0.16, 1.6, 4)$ million, and two-eye populations of $N = (0.16, 1.6)$ million individuals. While the large search sets S_{nb} were used used, with number of searches in the hundreds of thousands, the number of observed scores in the far tails is small: To get reduced uncertainty more searches would be necessary. Missing plots indicate the run is not yet complete.

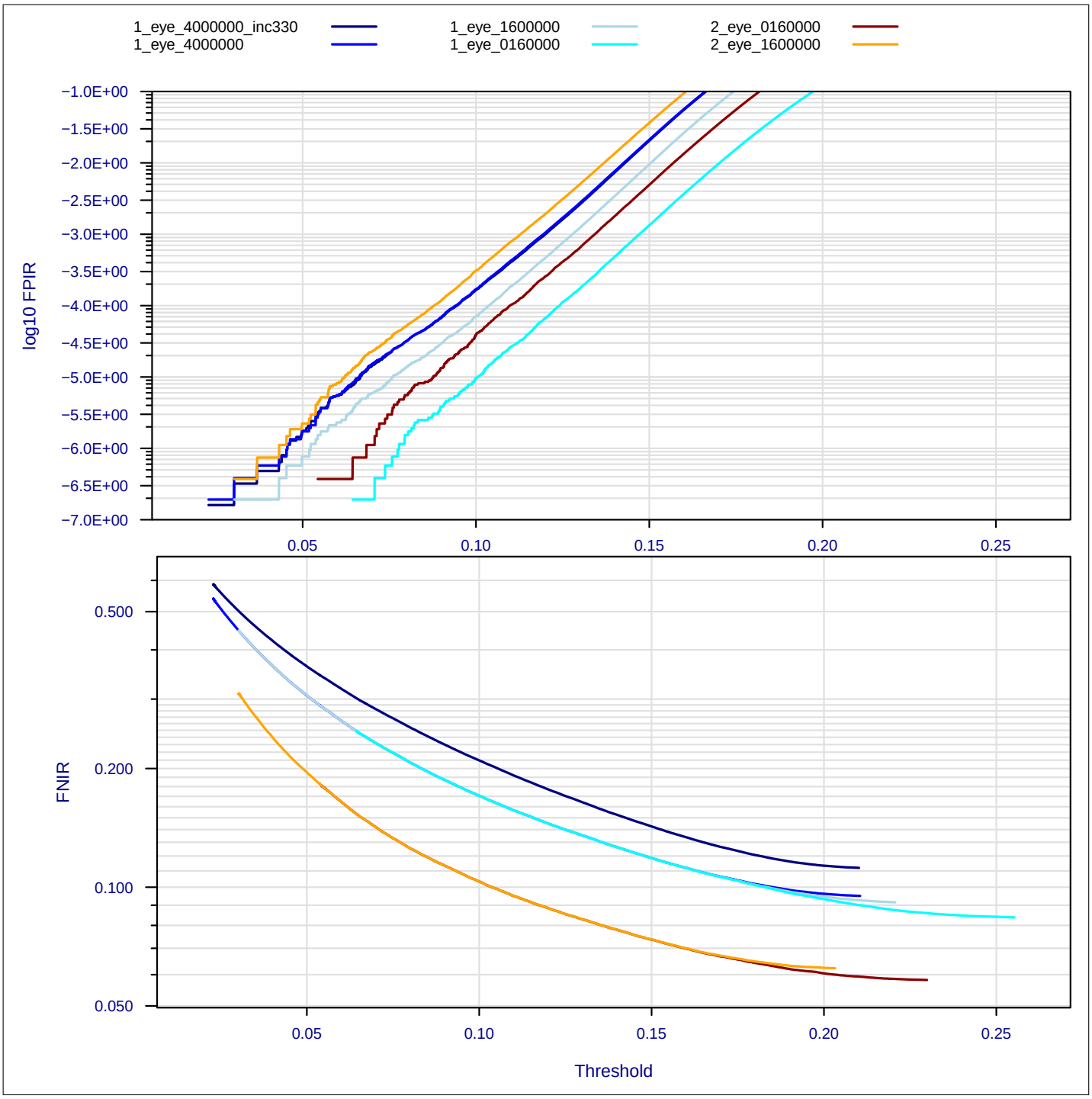

Figure 37: **Threshold calibration curves** for implementation S11A executing searches for single-eye enrolled populations $N = (0.16, 1.6, 4)$ million, and two-eye populations of $N = (0.16, 1.6)$ million individuals. While the large search sets S_{nb} were used used, with number of searches in the hundreds of thousands, the number of observed scores in the far tails is small: To get reduced uncertainty more searches would be necessary. Missing plots indicate the run is not yet complete.

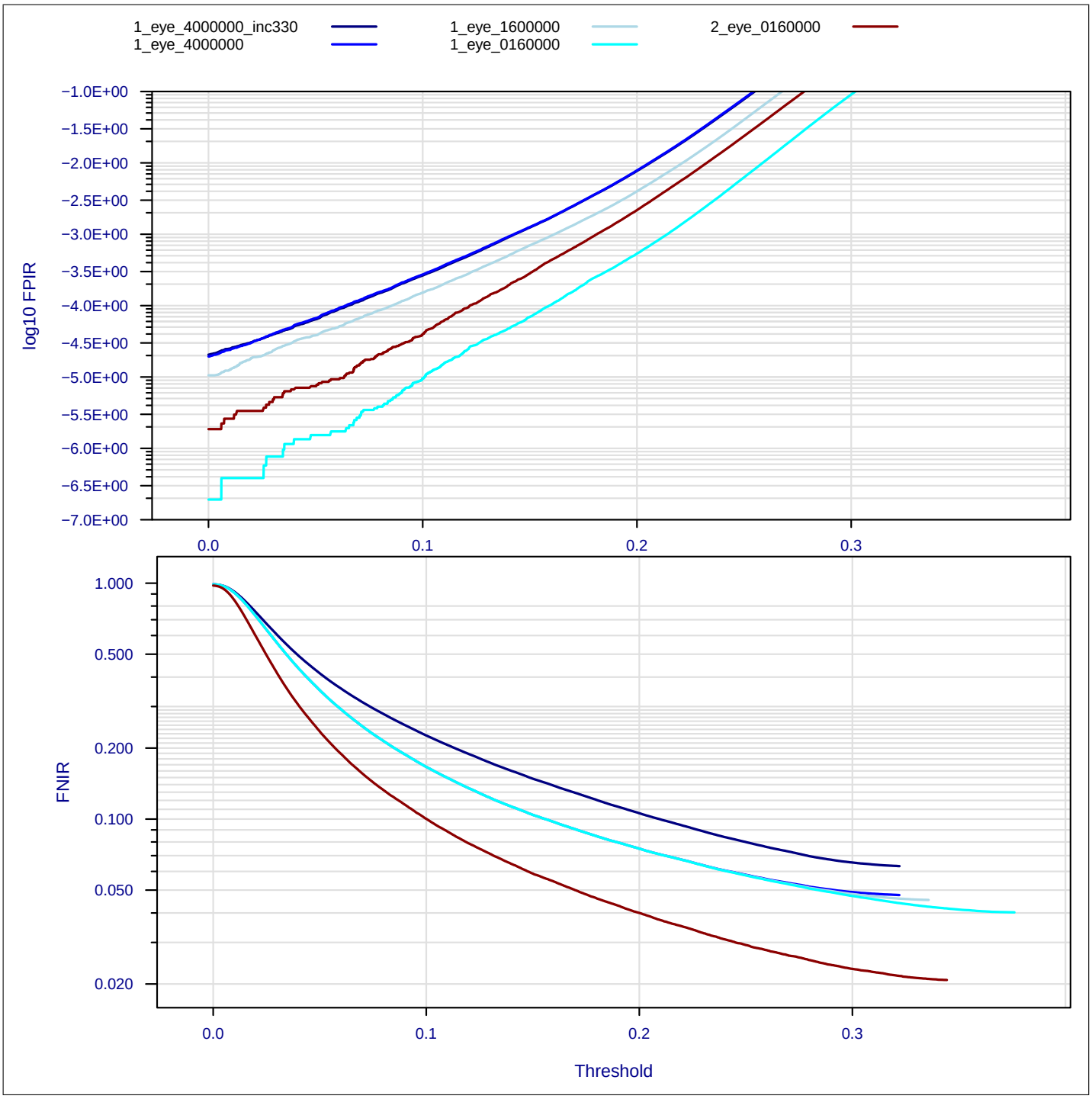

Figure 38: **Threshold calibration curves** for implementation S11B executing searches for single-eye enrolled populations $N = (0.16, 1.6, 4)$ million, and two-eye populations of $N = (0.16, 1.6)$ million individuals. While the large search sets S_{nb} were used used, with number of searches in the hundreds of thousands, the number of observed scores in the far tails is small: To get reduced uncertainty more searches would be necessary. Missing plots indicate the run is not yet complete.

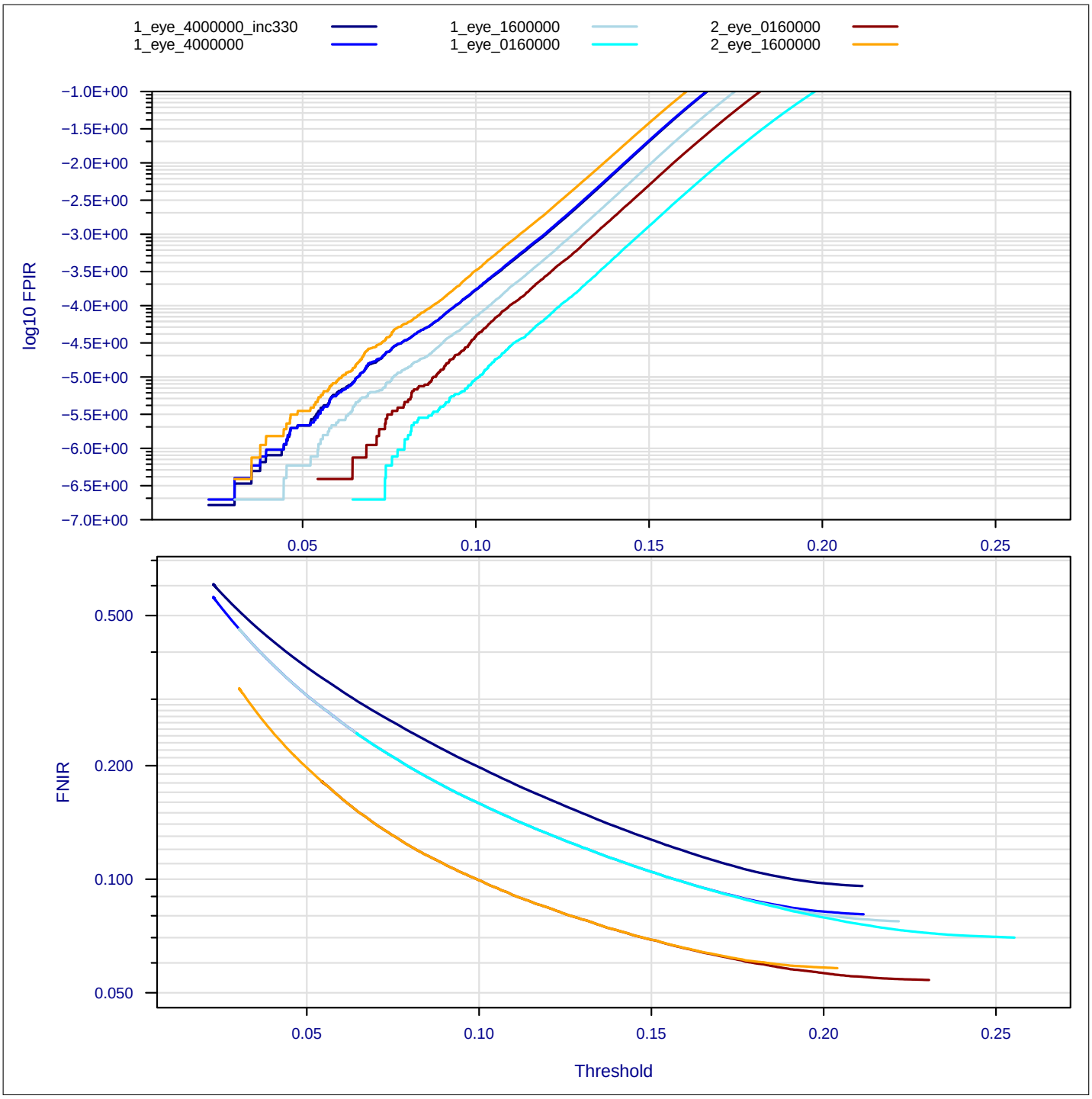

Figure 39: **Threshold calibration curves** for implementation S12A executing searches for single-eye enrolled populations $N = (0.16, 1.6, 4)$ million, and two-eye populations of $N = (0.16, 1.6)$ million individuals. While the large search sets S_{nb} were used used, with number of searches in the hundreds of thousands, the number of observed scores in the far tails is small: To get reduced uncertainty more searches would be necessary. Missing plots indicate the run is not yet complete.

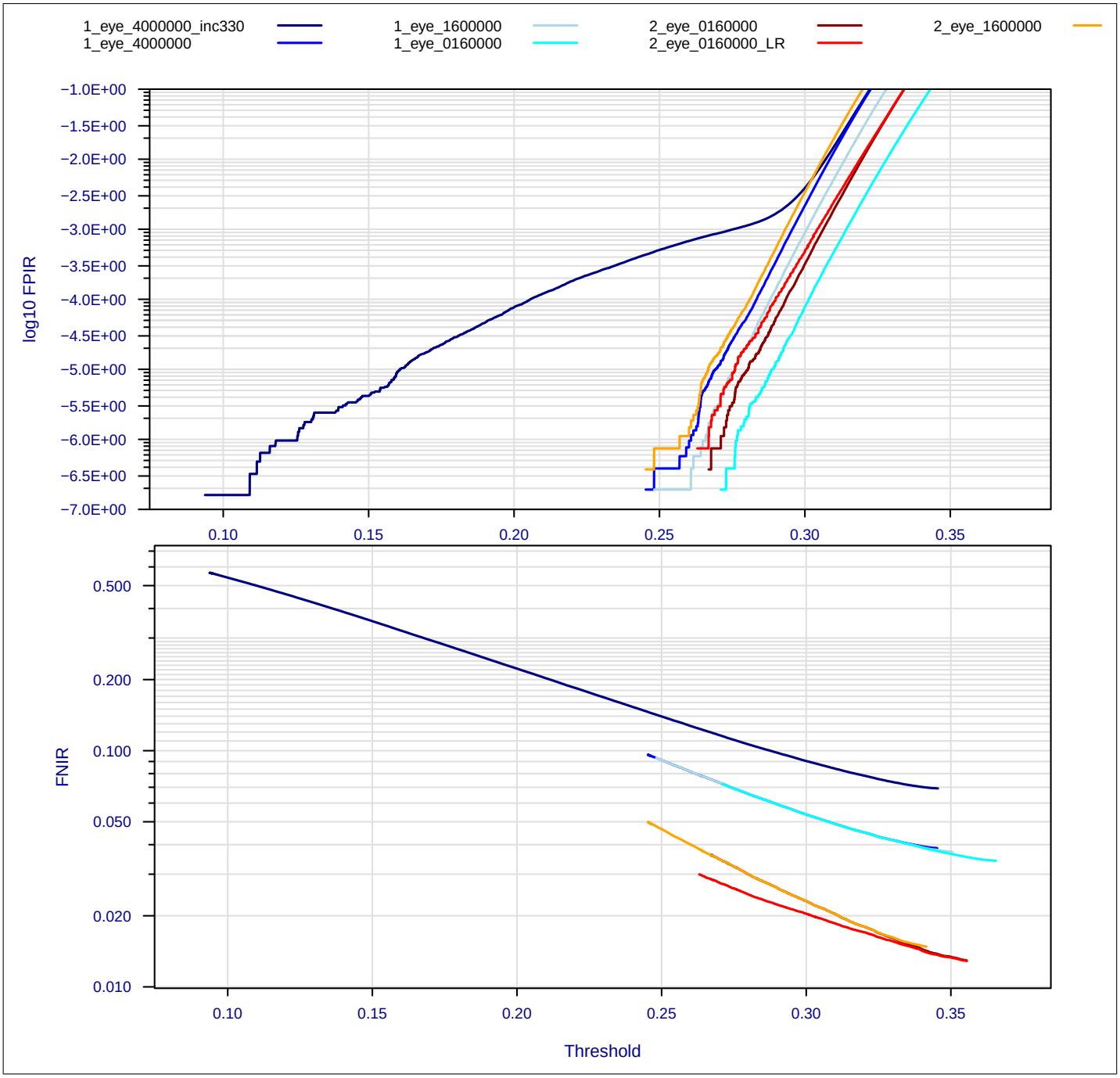

Figure 40: **Threshold calibration curves** for implementation T01A executing searches for single-eye enrolled populations $N = (0.16, 1.6, 4)$ million, and two-eye populations of $N = (0.16, 1.6)$ million individuals. While the large search sets S_{nb} were used used, with number of searches in the hundreds of thousands, the number of observed scores in the far tails is small: To get reduced uncertainty more searches would be necessary. Missing plots indicate the run is not yet complete.

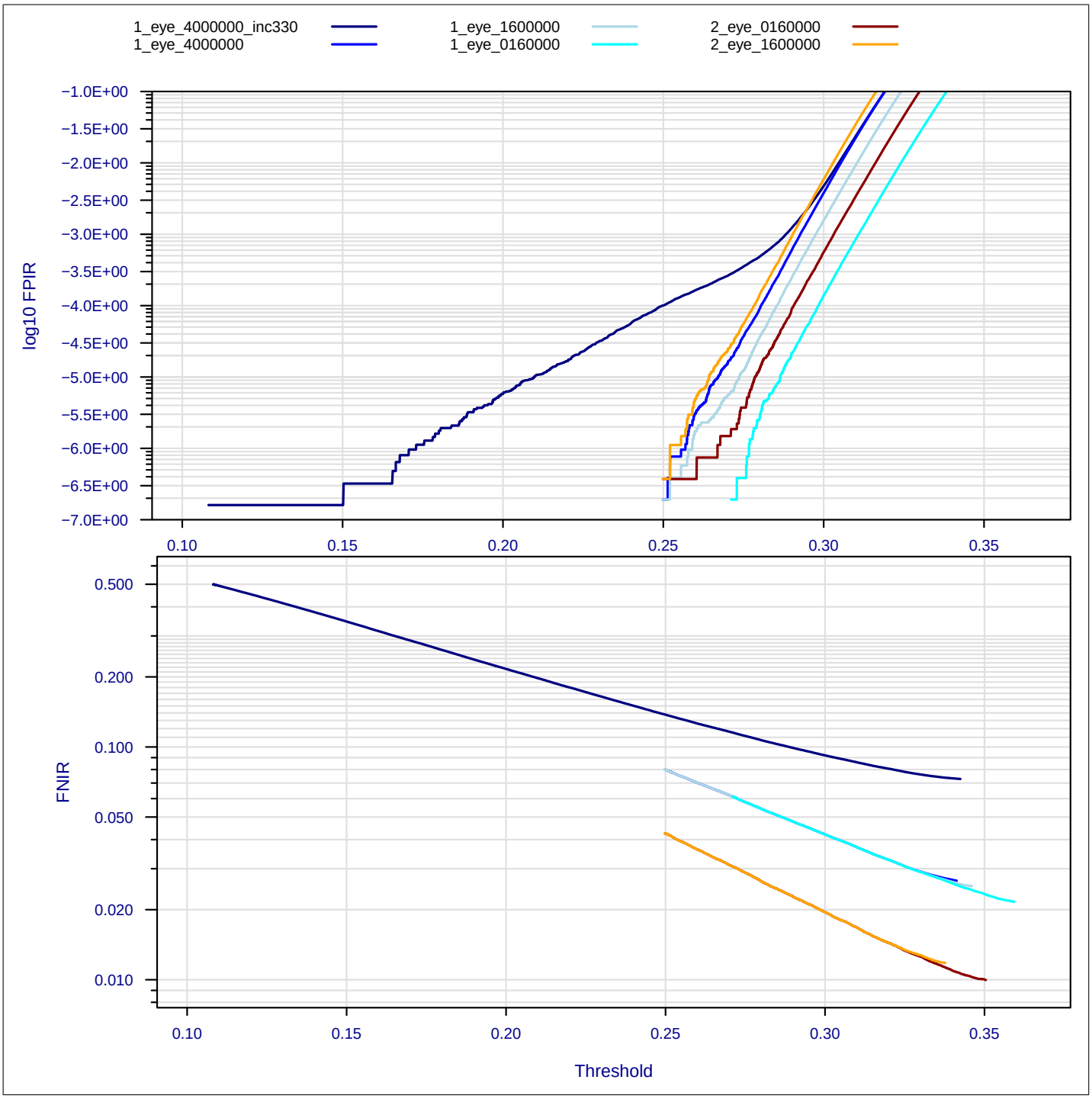

Figure 41: **Threshold calibration curves** for implementation T01B executing searches for single-eye enrolled populations $N = (0.16, 1.6, 4)$ million, and two-eye populations of $N = (0.16, 1.6)$ million individuals. While the large search sets S_{nb} were used used, with number of searches in the hundreds of thousands, the number of observed scores in the far tails is small: To get reduced uncertainty more searches would be necessary. Missing plots indicate the run is not yet complete.

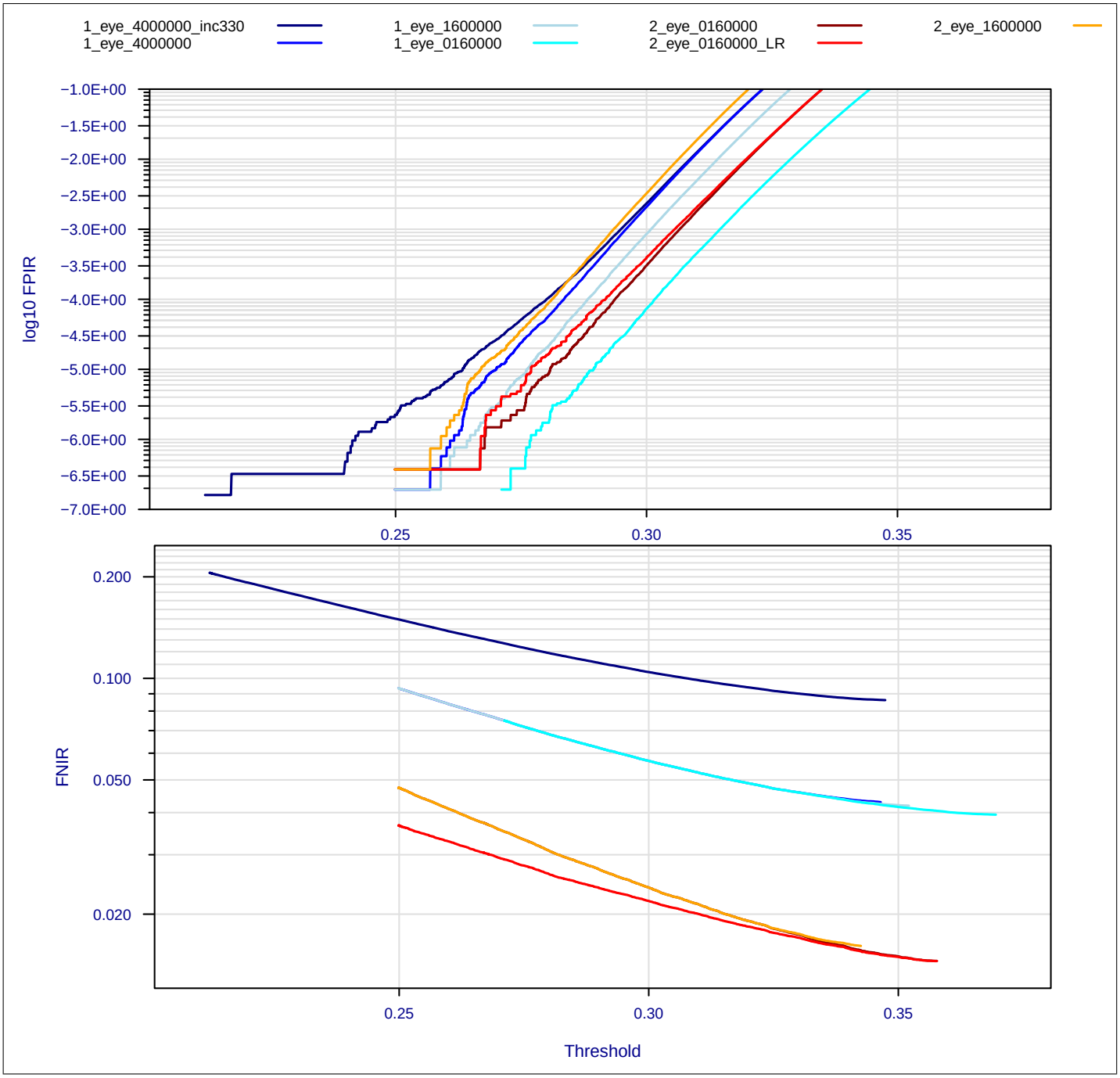

Figure 42: **Threshold calibration curves** for implementation T02A executing searches for single-eye enrolled populations $N = (0.16, 1.6, 4)$ million, and two-eye populations of $N = (0.16, 1.6)$ million individuals. While the large search sets S_{nb} were used used, with number of searches in the hundreds of thousands, the number of observed scores in the far tails is small: To get reduced uncertainty more searches would be necessary. Missing plots indicate the run is not yet complete.

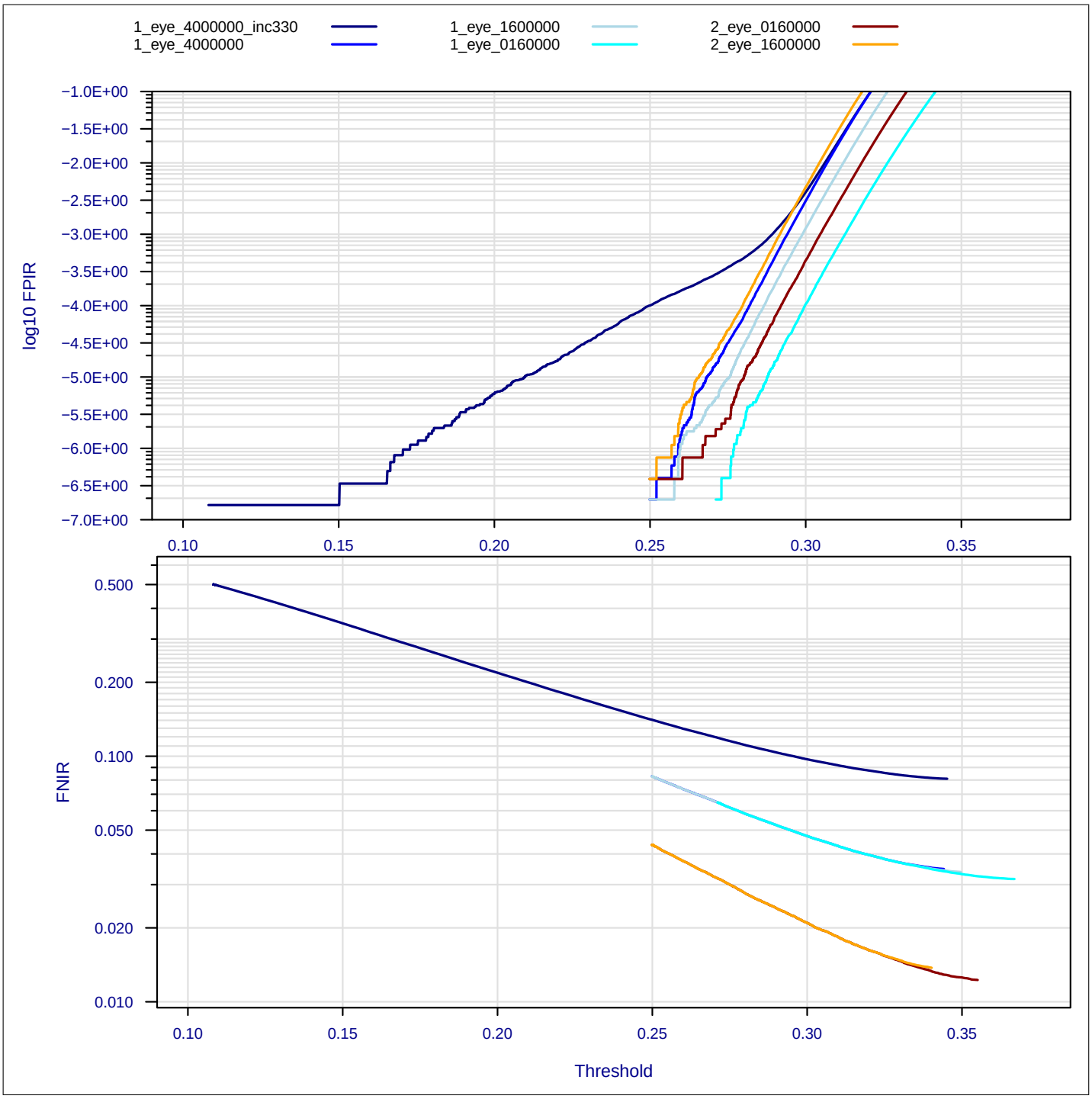

Figure 43: **Threshold calibration curves** for implementation T02B executing searches for single-eye enrolled populations $N = (0.16, 1.6, 4)$ million, and two-eye populations of $N = (0.16, 1.6)$ million individuals. While the large search sets S_{nb} were used used, with number of searches in the hundreds of thousands, the number of observed scores in the far tails is small: To get reduced uncertainty more searches would be necessary. Missing plots indicate the run is not yet complete.

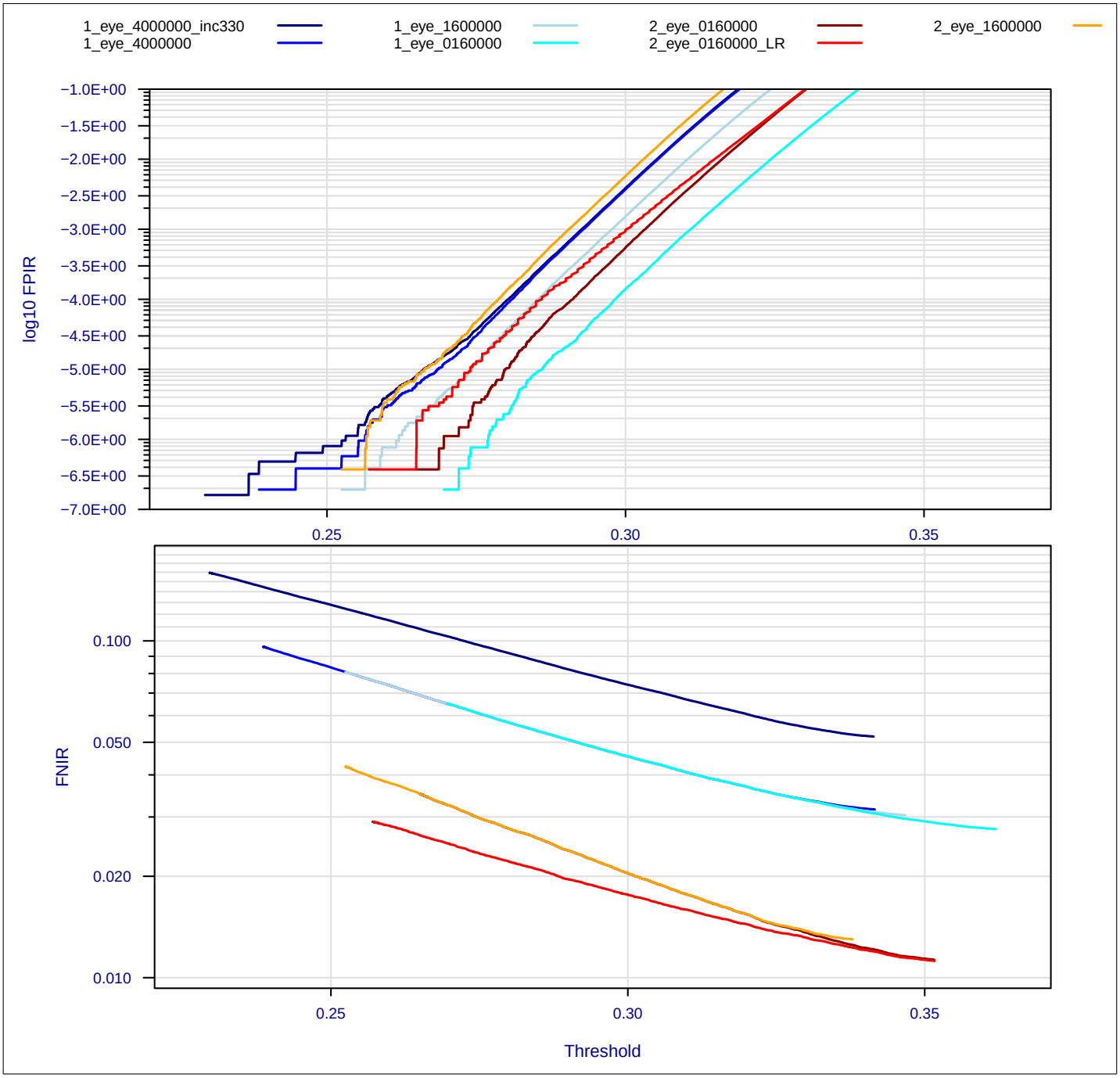

Figure 44: **Threshold calibration curves** for implementation T03A executing searches for single-eye enrolled populations $N = (0.16, 1.6, 4)$ million, and two-eye populations of $N = (0.16, 1.6)$ million individuals. While the large search sets S_{nb} were used used, with number of searches in the hundreds of thousands, the number of observed scores in the far tails is small: To get reduced uncertainty more searches would be necessary. Missing plots indicate the run is not yet complete.

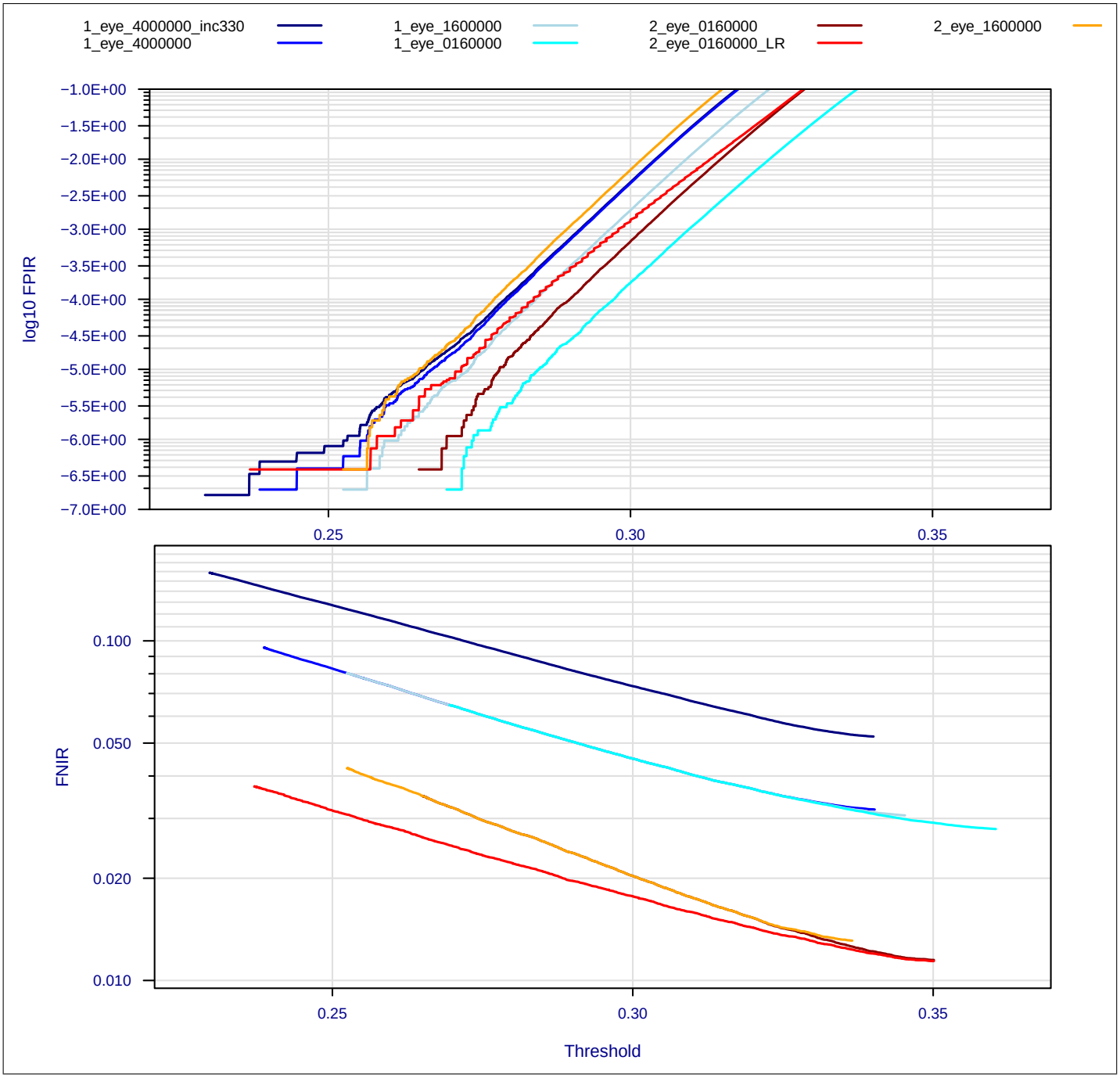

Figure 45: **Threshold calibration curves** for implementation T03B executing searches for single-eye enrolled populations $N = (0.16, 1.6, 4)$ million, and two-eye populations of $N = (0.16, 1.6)$ million individuals. While the large search sets S_{nb} were used used, with number of searches in the hundreds of thousands, the number of observed scores in the far tails is small: To get reduced uncertainty more searches would be necessary. Missing plots indicate the run is not yet complete.

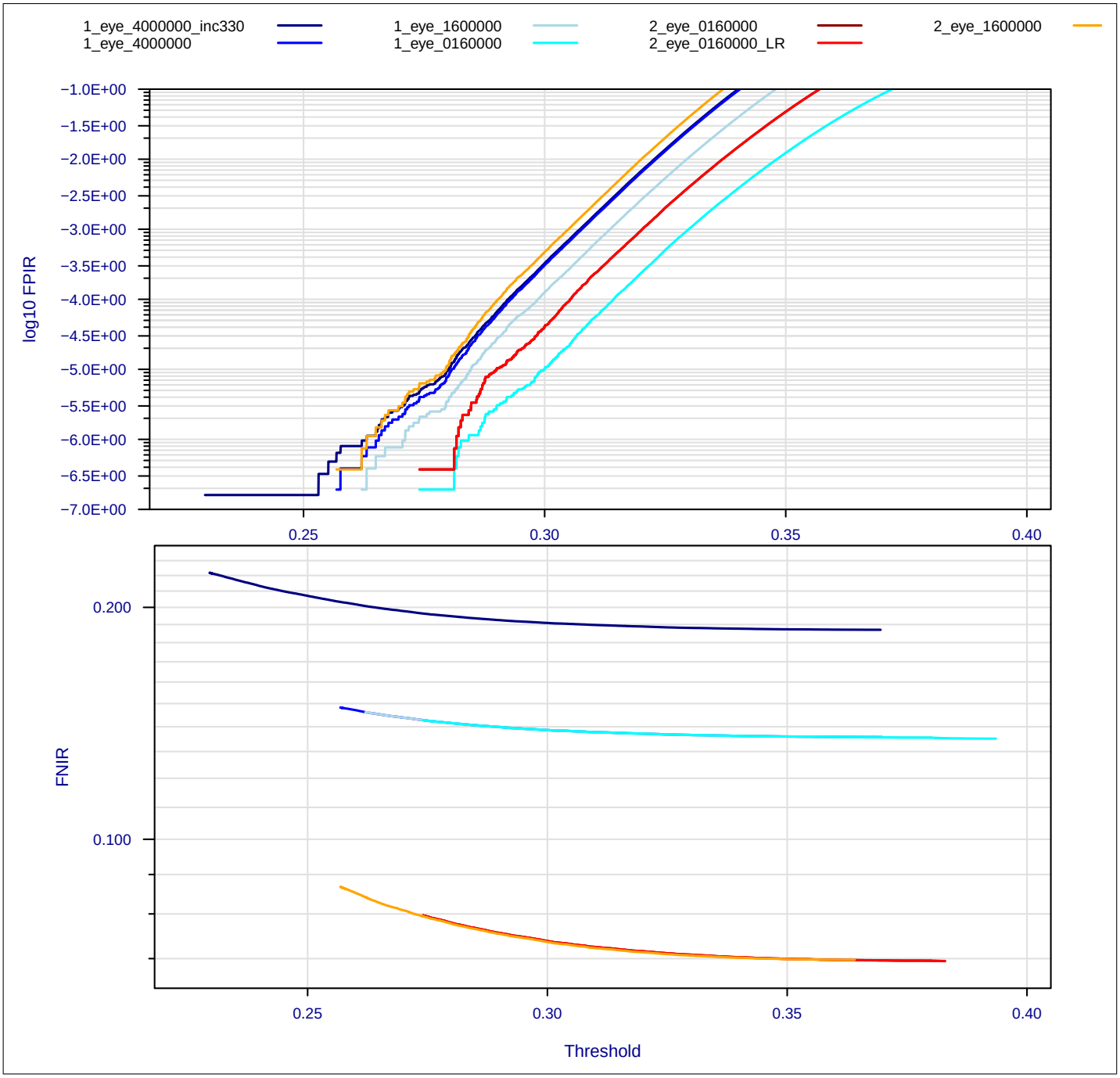

Figure 46: **Threshold calibration curves** for implementation T04A executing searches for single-eye enrolled populations $N = (0.16, 1.6, 4)$ million, and two-eye populations of $N = (0.16, 1.6)$ million individuals. While the large search sets S_{nb} were used used, with number of searches in the hundreds of thousands, the number of observed scores in the far tails is small: To get reduced uncertainty more searches would be necessary. Missing plots indicate the run is not yet complete.

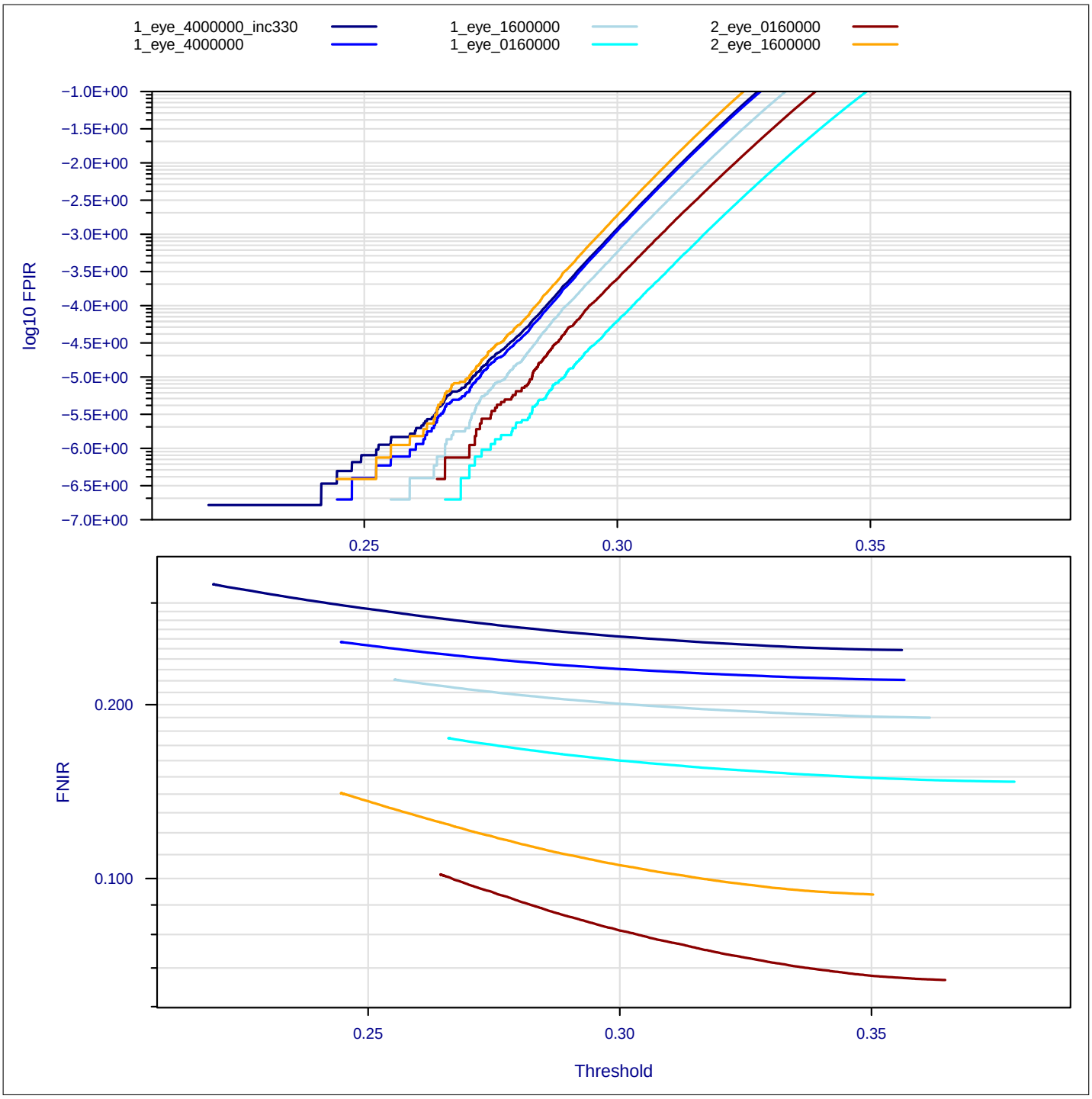

Figure 47: **Threshold calibration curves** for implementation T11A executing searches for single-eye enrolled populations $N = (0.16, 1.6, 4)$ million, and two-eye populations of $N = (0.16, 1.6)$ million individuals. While the large search sets S_{nb} were used used, with number of searches in the hundreds of thousands, the number of observed scores in the far tails is small: To get reduced uncertainty more searches would be necessary. Missing plots indicate the run is not yet complete.

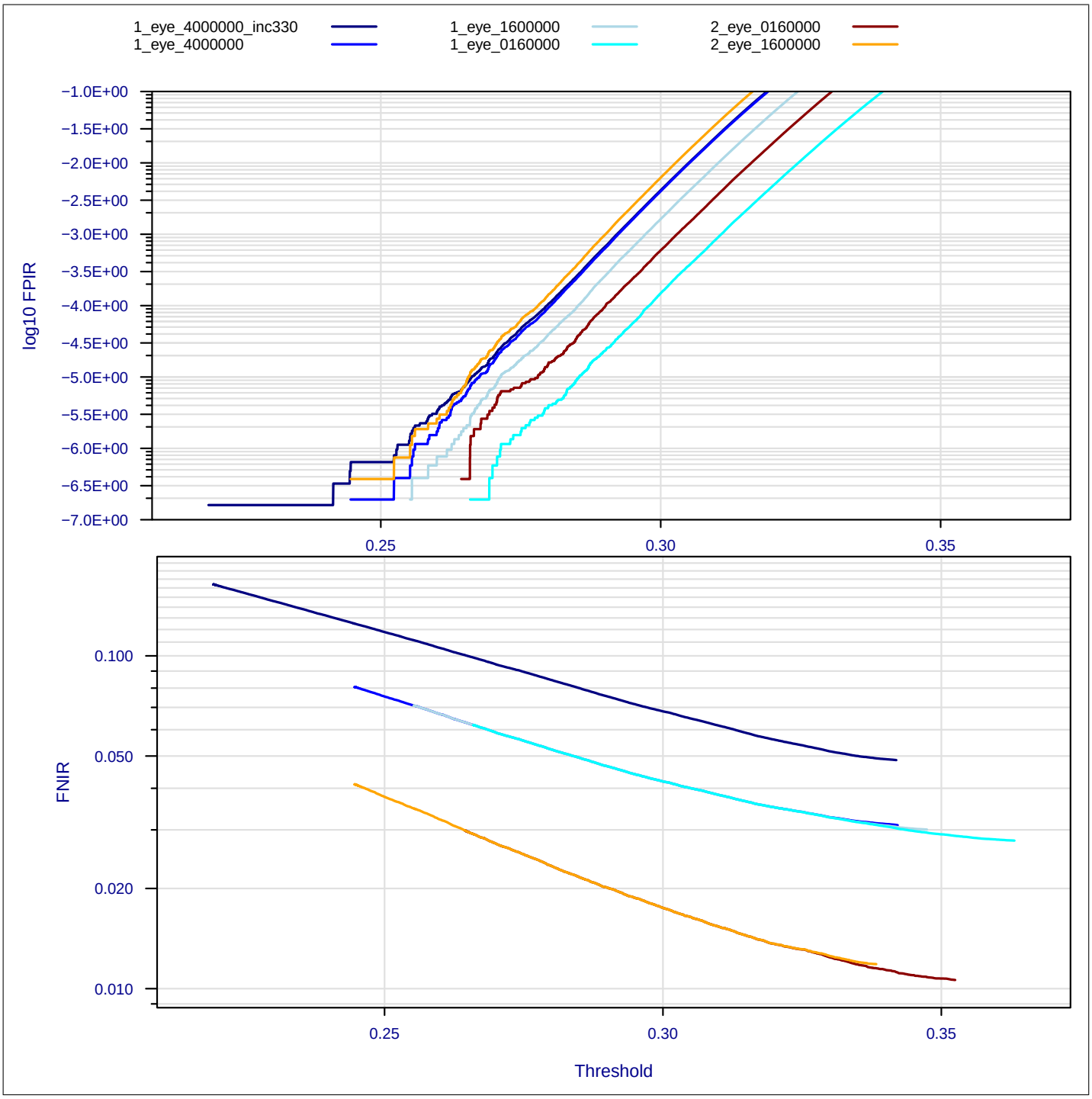

Figure 48: **Threshold calibration curves** for implementation T11B executing searches for single-eye enrolled populations $N = (0.16, 1.6, 4)$ million, and two-eye populations of $N = (0.16, 1.6)$ million individuals. While the large search sets S_{nb} were used used, with number of searches in the hundreds of thousands, the number of observed scores in the far tails is small: To get reduced uncertainty more searches would be necessary. Missing plots indicate the run is not yet complete.

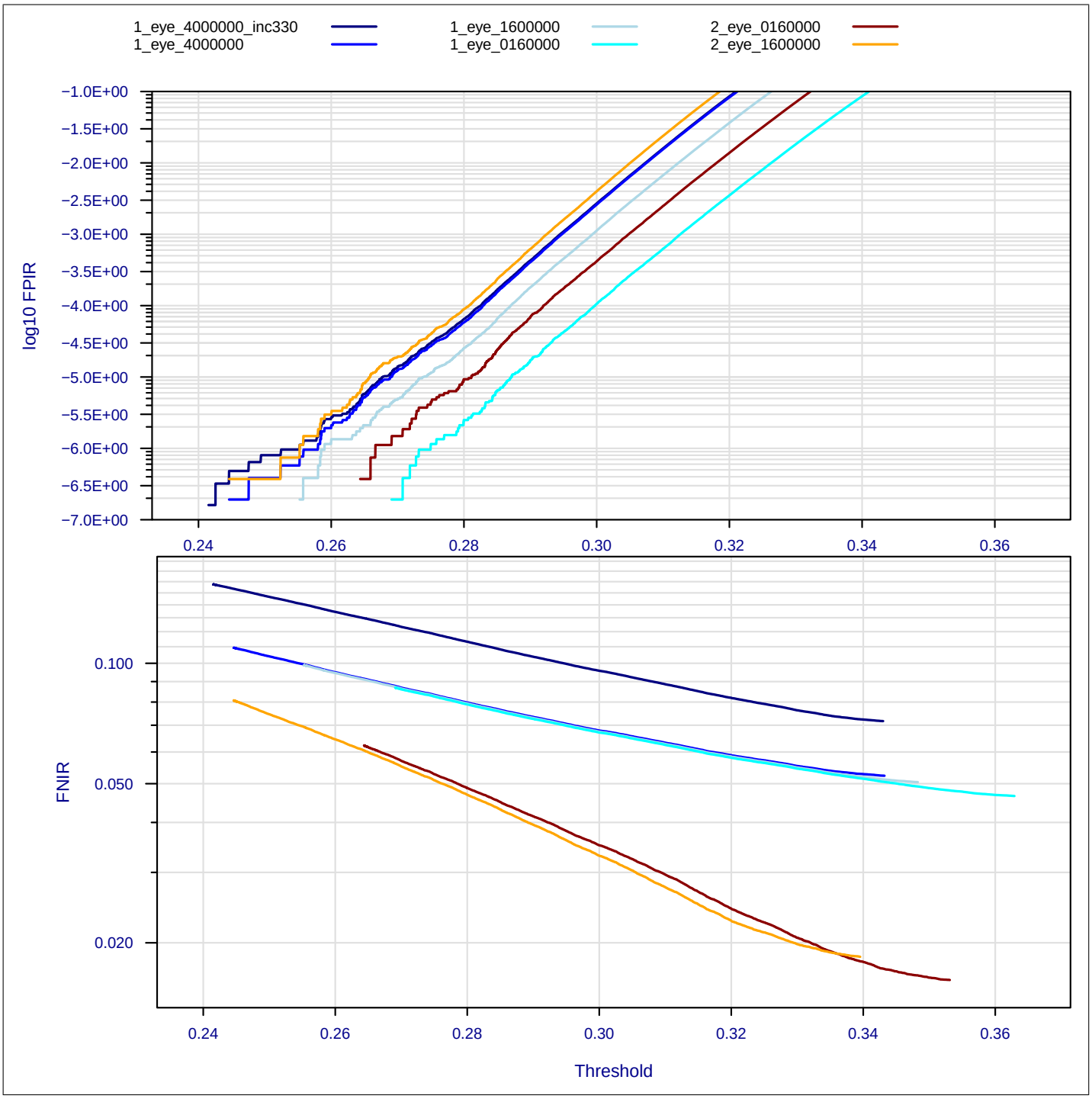

Figure 49: **Threshold calibration curves** for implementation T12B executing searches for single-eye enrolled populations $N = (0.16, 1.6, 4)$ million, and two-eye populations of $N = (0.16, 1.6)$ million individuals. While the large search sets S_{nb} were used used, with number of searches in the hundreds of thousands, the number of observed scores in the far tails is small: To get reduced uncertainty more searches would be necessary. Missing plots indicate the run is not yet complete.

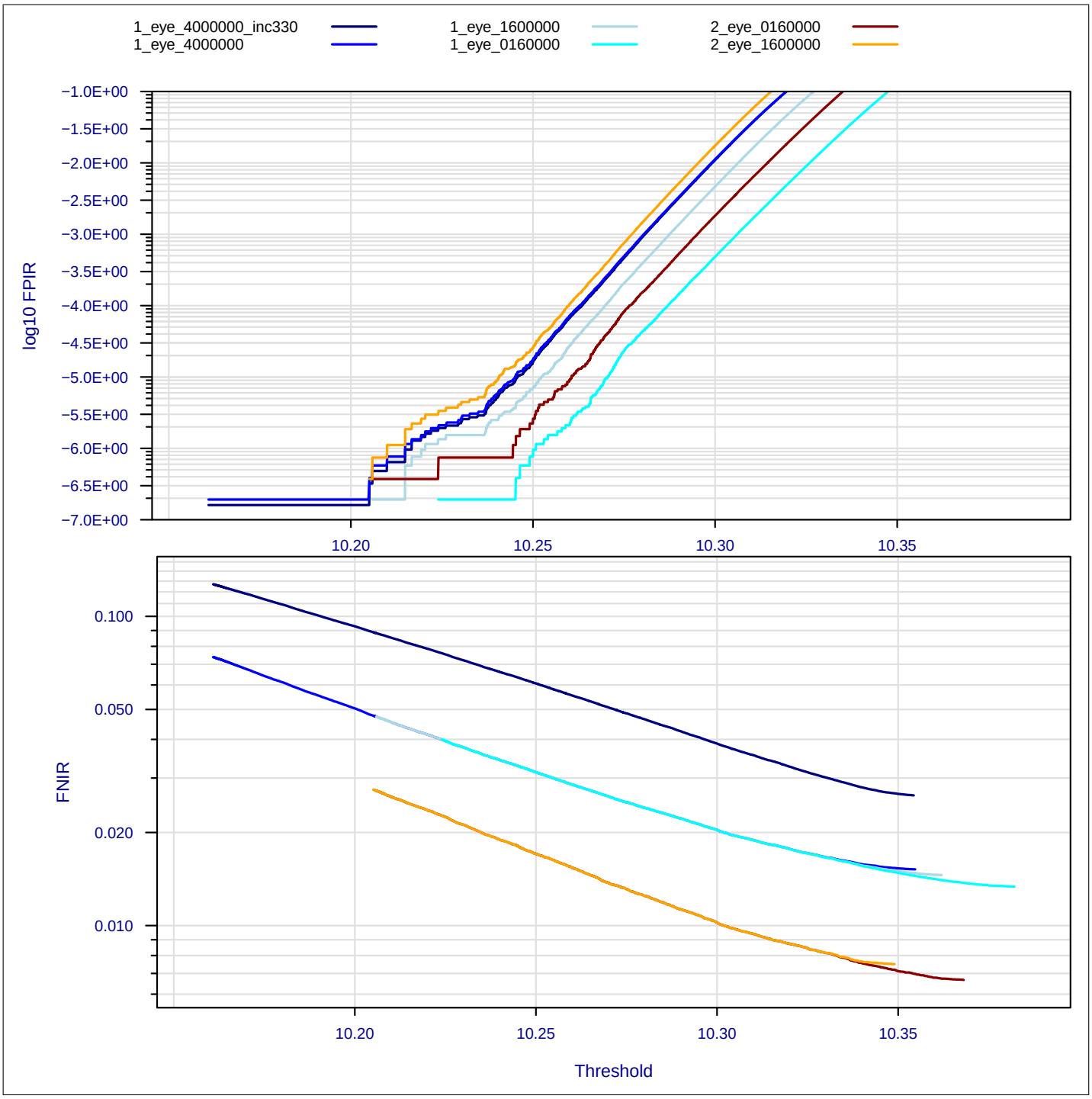

Figure 50: **Threshold calibration curves** for implementation U01A executing searches for single-eye enrolled populations $N = (0.16, 1.6, 4)$ million, and two-eye populations of $N = (0.16, 1.6)$ million individuals. While the large search sets S_{nb} were used used, with number of searches in the hundreds of thousands, the number of observed scores in the far tails is small: To get reduced uncertainty more searches would be necessary. Missing plots indicate the run is not yet complete.

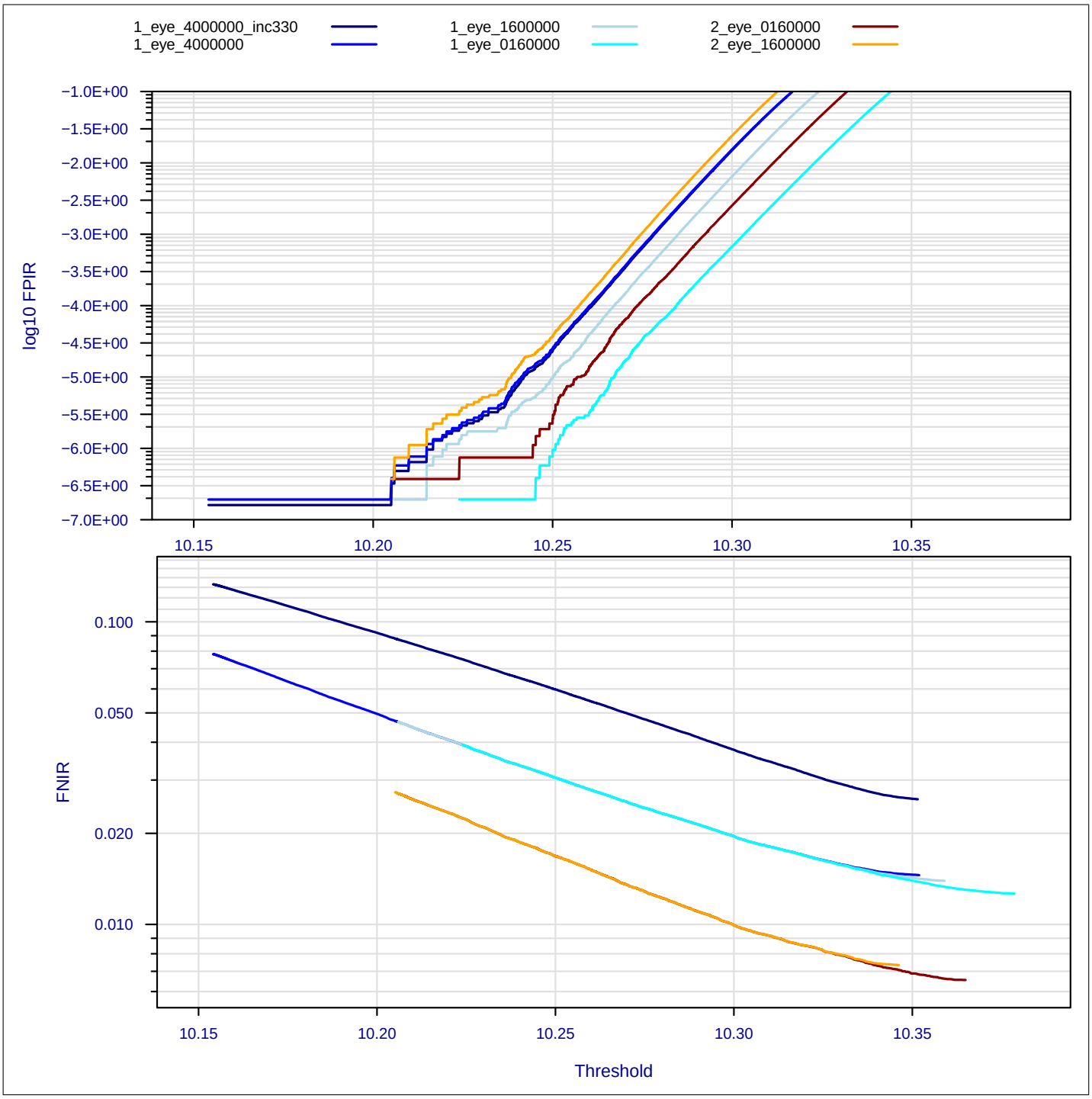

Figure 51: **Threshold calibration curves** for implementation U01B executing searches for single-eye enrolled populations $N = (0.16, 1.6, 4)$ million, and two-eye populations of $N = (0.16, 1.6)$ million individuals. While the large search sets S_{nb} were used used, with number of searches in the hundreds of thousands, the number of observed scores in the far tails is small: To get reduced uncertainty more searches would be necessary. Missing plots indicate the run is not yet complete.

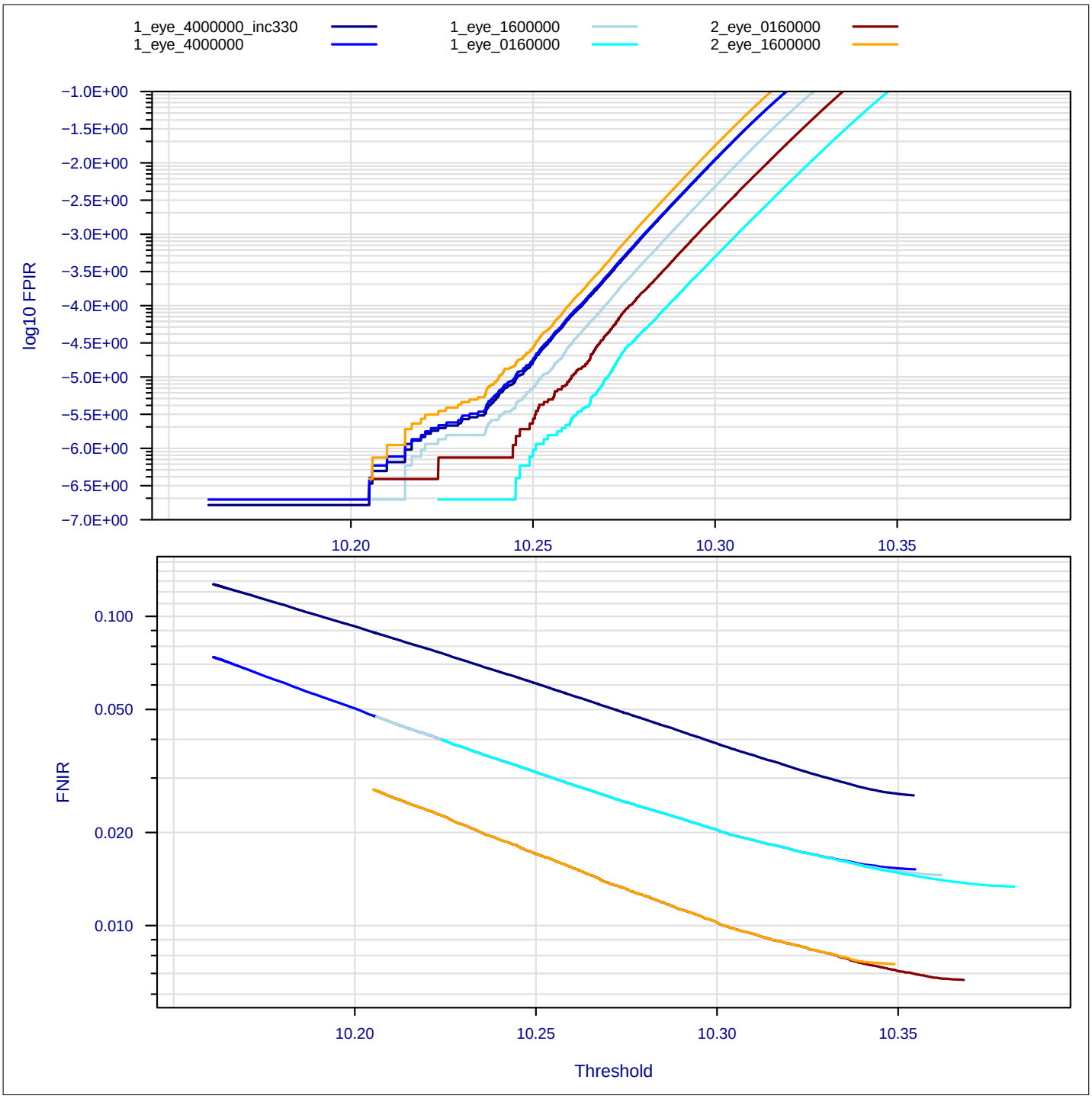

Figure 52: **Threshold calibration curves** for implementation U02A executing searches for single-eye enrolled populations $N = (0.16, 1.6, 4)$ million, and two-eye populations of $N = (0.16, 1.6)$ million individuals. While the large search sets S_{nb} were used used, with number of searches in the hundreds of thousands, the number of observed scores in the far tails is small: To get reduced uncertainty more searches would be necessary. Missing plots indicate the run is not yet complete.

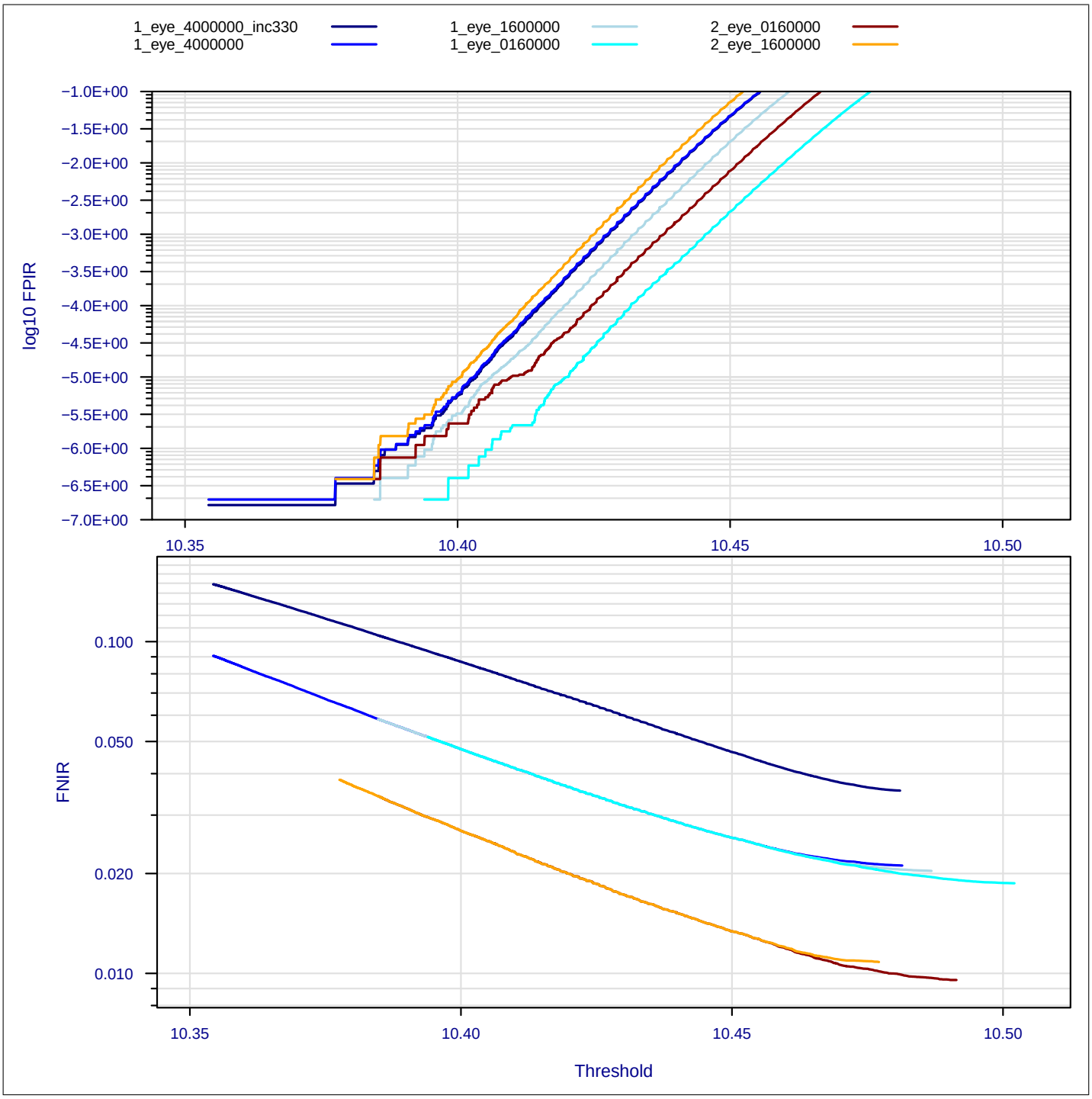

Figure 53: **Threshold calibration curves** for implementation U03A executing searches for single-eye enrolled populations $N = (0.16, 1.6, 4)$ million, and two-eye populations of $N = (0.16, 1.6)$ million individuals. While the large search sets S_{nb} were used used, with number of searches in the hundreds of thousands, the number of observed scores in the far tails is small: To get reduced uncertainty more searches would be necessary. Missing plots indicate the run is not yet complete.

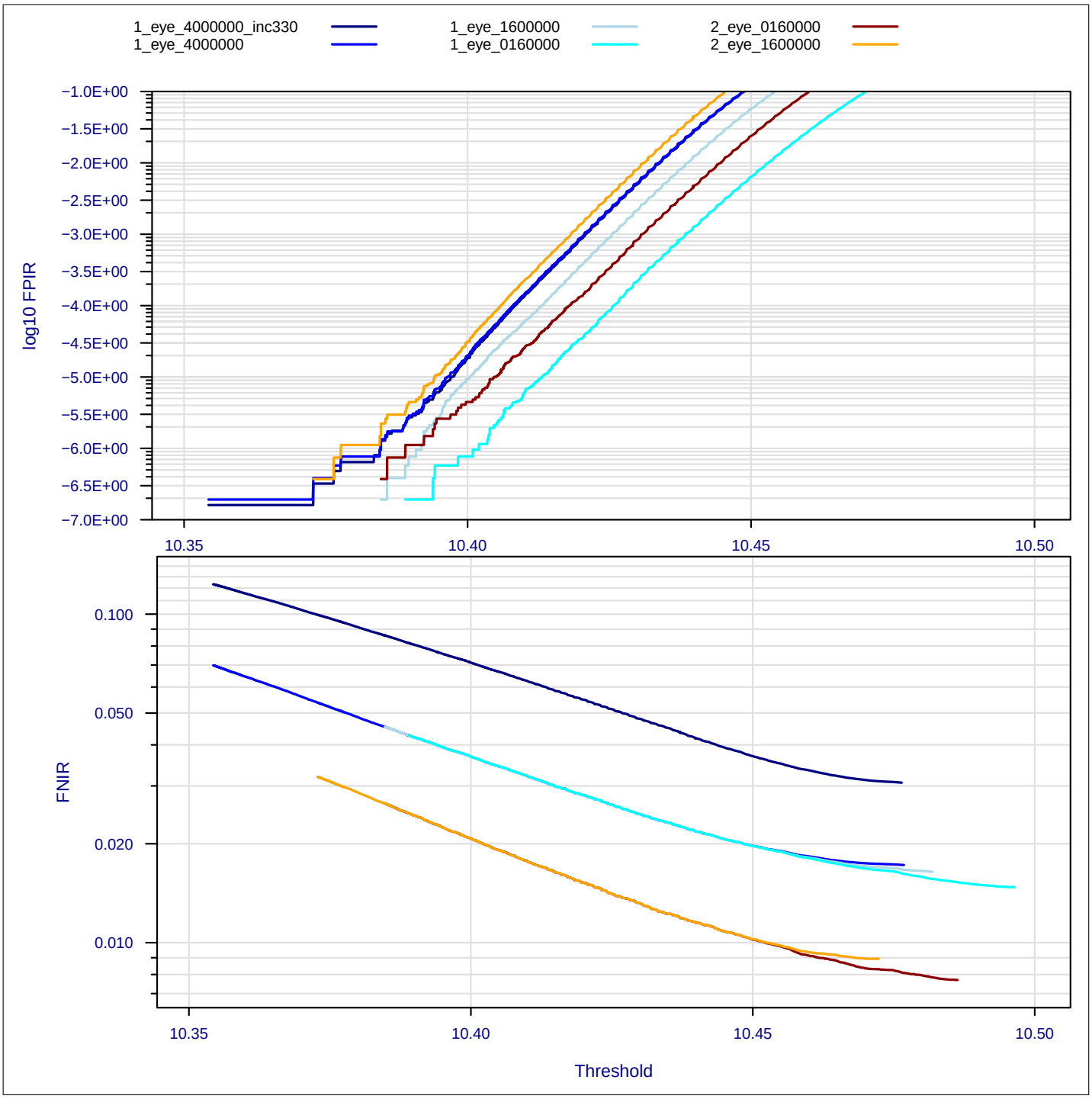

Figure 54: **Threshold calibration curves** for implementation U03B executing searches for single-eye enrolled populations $N = (0.16, 1.6, 4)$ million, and two-eye populations of $N = (0.16, 1.6)$ million individuals. While the large search sets S_{nb} were used used, with number of searches in the hundreds of thousands, the number of observed scores in the far tails is small: To get reduced uncertainty more searches would be necessary. Missing plots indicate the run is not yet complete.

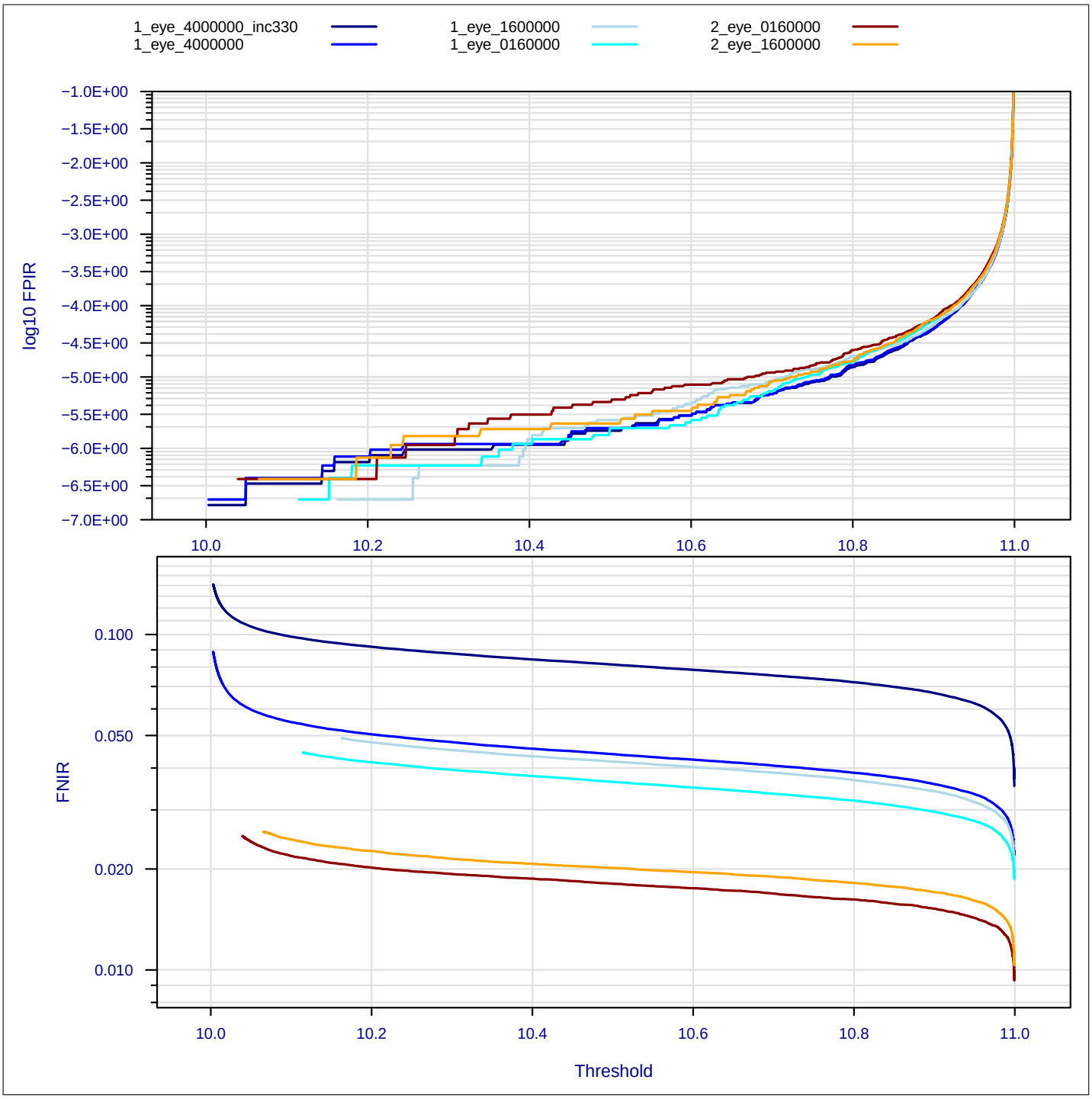

Figure 55: **Threshold calibration curves** for implementation U04A executing searches for single-eye enrolled populations $N = (0.16, 1.6, 4)$ million, and two-eye populations of $N = (0.16, 1.6)$ million individuals. While the large search sets S_{nb} were used used, with number of searches in the hundreds of thousands, the number of observed scores in the far tails is small: To get reduced uncertainty more searches would be necessary. Missing plots indicate the run is not yet complete.

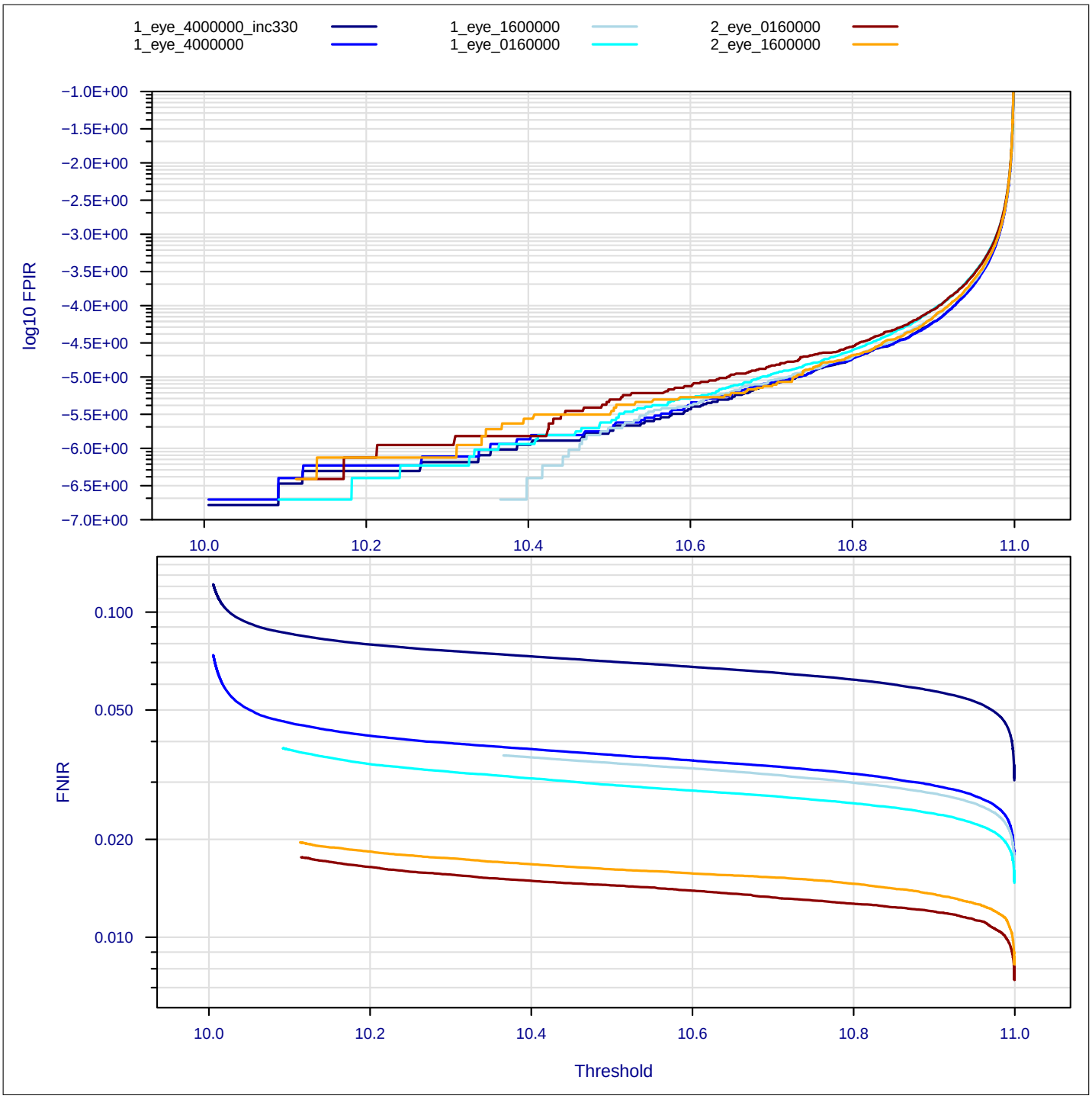

Figure 56: **Threshold calibration curves** for implementation U04B executing searches for single-eye enrolled populations $N = (0.16, 1.6, 4)$ million, and two-eye populations of $N = (0.16, 1.6)$ million individuals. While the large search sets S_{nb} were used used, with number of searches in the hundreds of thousands, the number of observed scores in the far tails is small: To get reduced uncertainty more searches would be necessary. Missing plots indicate the run is not yet complete.

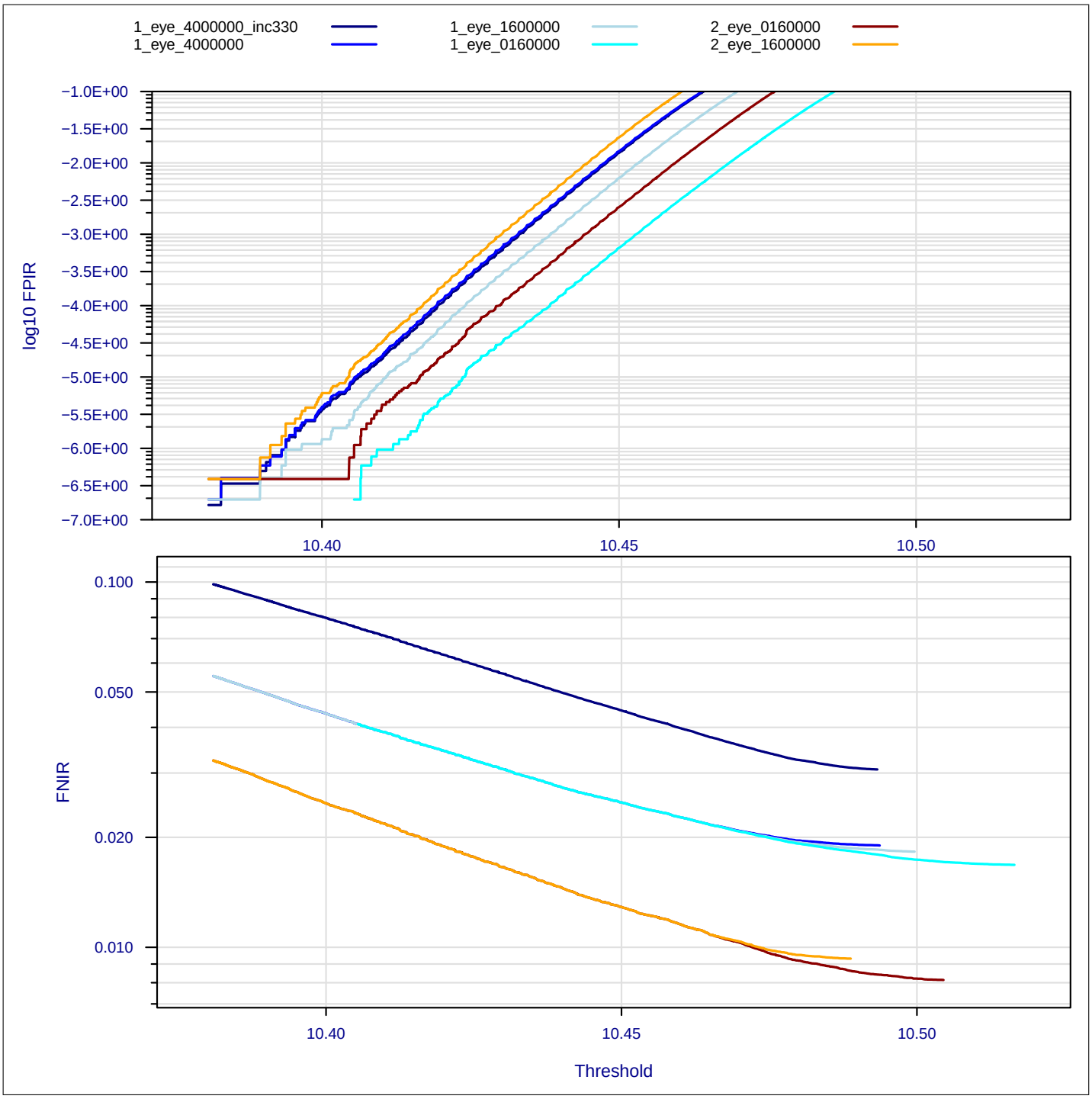

Figure 57: **Threshold calibration curves** for implementation U11A executing searches for single-eye enrolled populations $N = (0.16, 1.6, 4)$ million, and two-eye populations of $N = (0.16, 1.6)$ million individuals. While the large search sets S_{nb} were used used, with number of searches in the hundreds of thousands, the number of observed scores in the far tails is small: To get reduced uncertainty more searches would be necessary. Missing plots indicate the run is not yet complete.

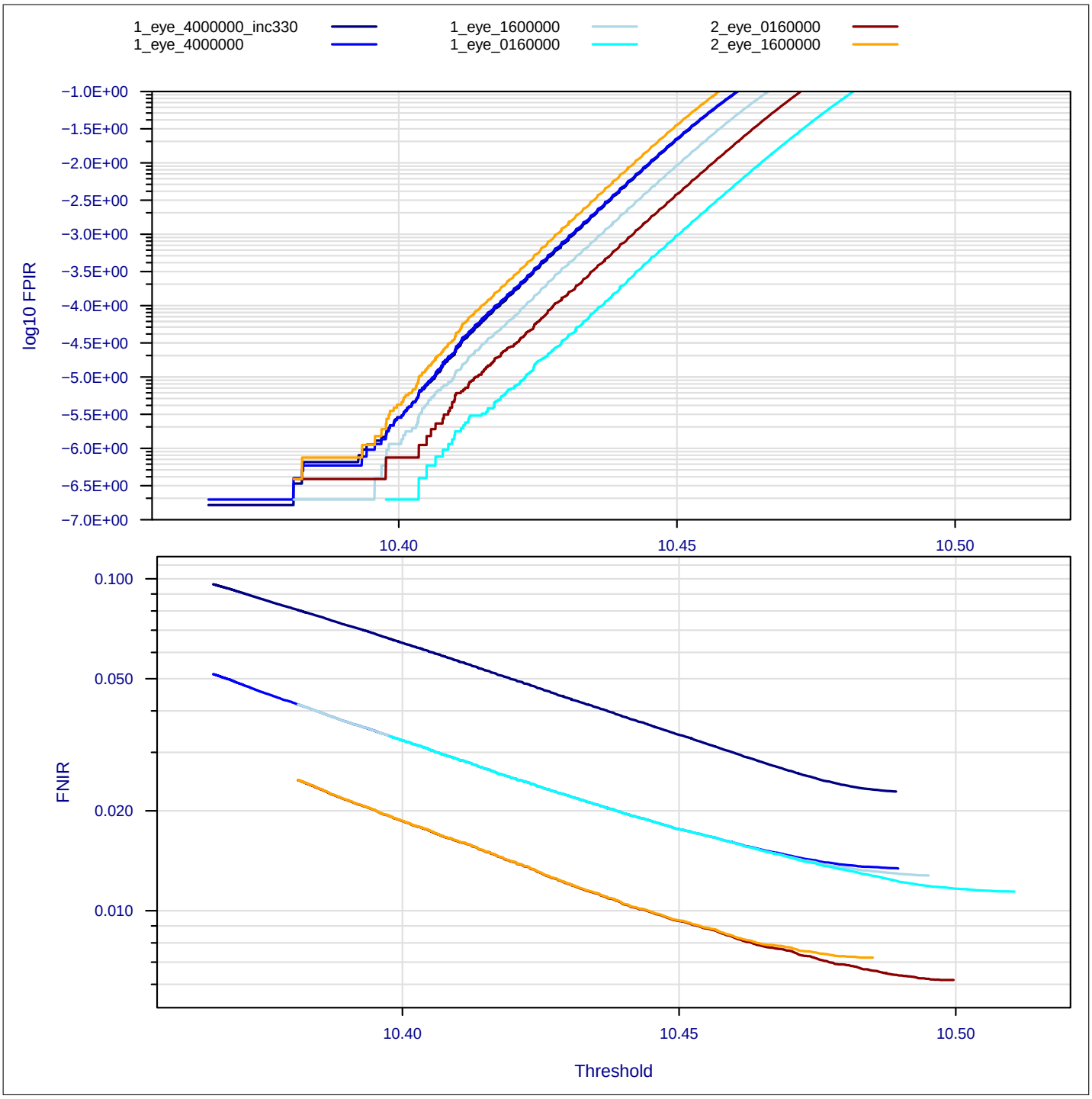

Figure 58: **Threshold calibration curves** for implementation U11B executing searches for single-eye enrolled populations $N = (0.16, 1.6, 4)$ million, and two-eye populations of $N = (0.16, 1.6)$ million individuals. While the large search sets S_{nb} were used used, with number of searches in the hundreds of thousands, the number of observed scores in the far tails is small: To get reduced uncertainty more searches would be necessary. Missing plots indicate the run is not yet complete.

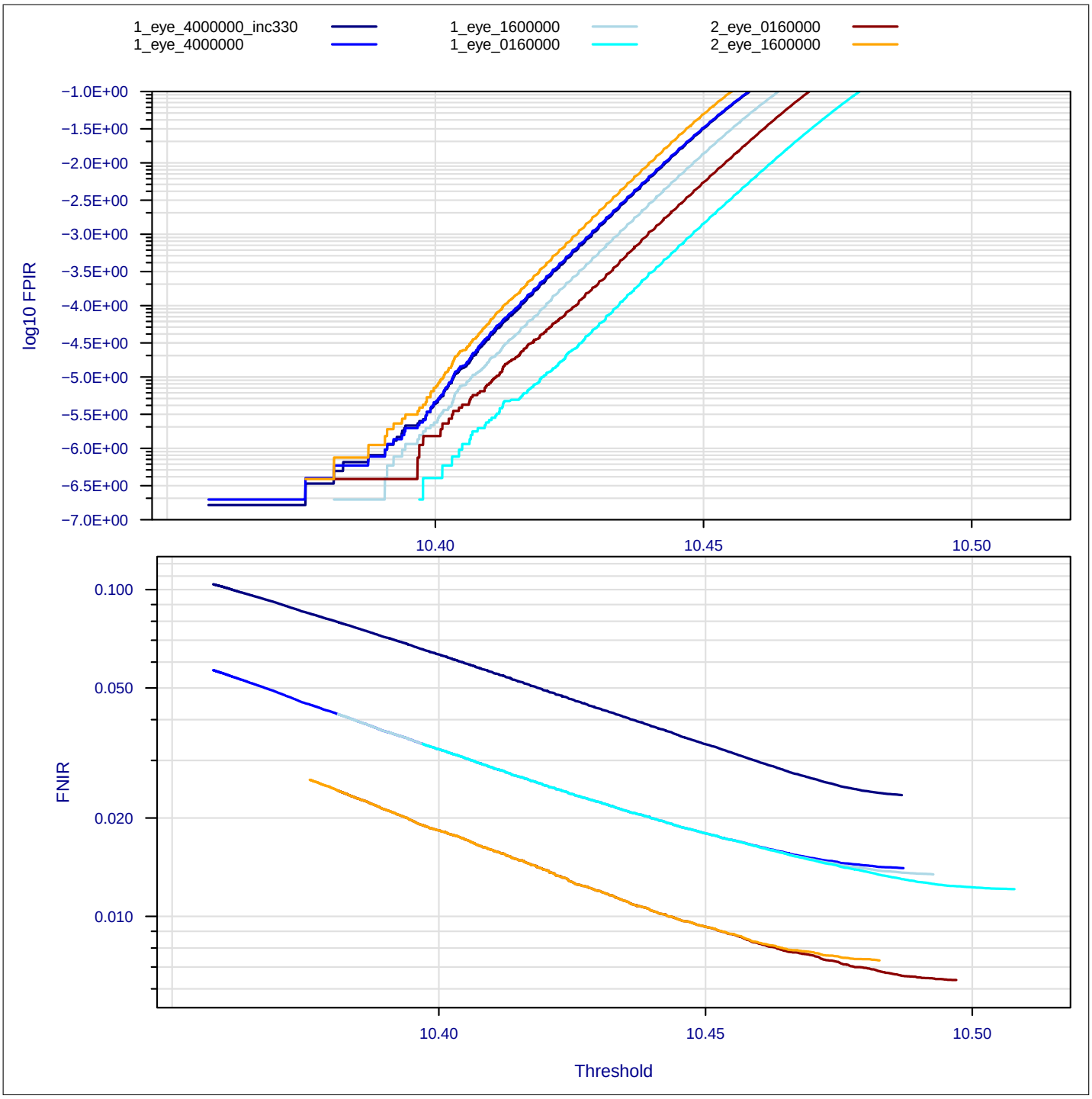

Figure 59: **Threshold calibration curves** for implementation U12A executing searches for single-eye enrolled populations $N = (0.16, 1.6, 4)$ million, and two-eye populations of $N = (0.16, 1.6)$ million individuals. While the large search sets S_{nb} were used used, with number of searches in the hundreds of thousands, the number of observed scores in the far tails is small: To get reduced uncertainty more searches would be necessary. Missing plots indicate the run is not yet complete.

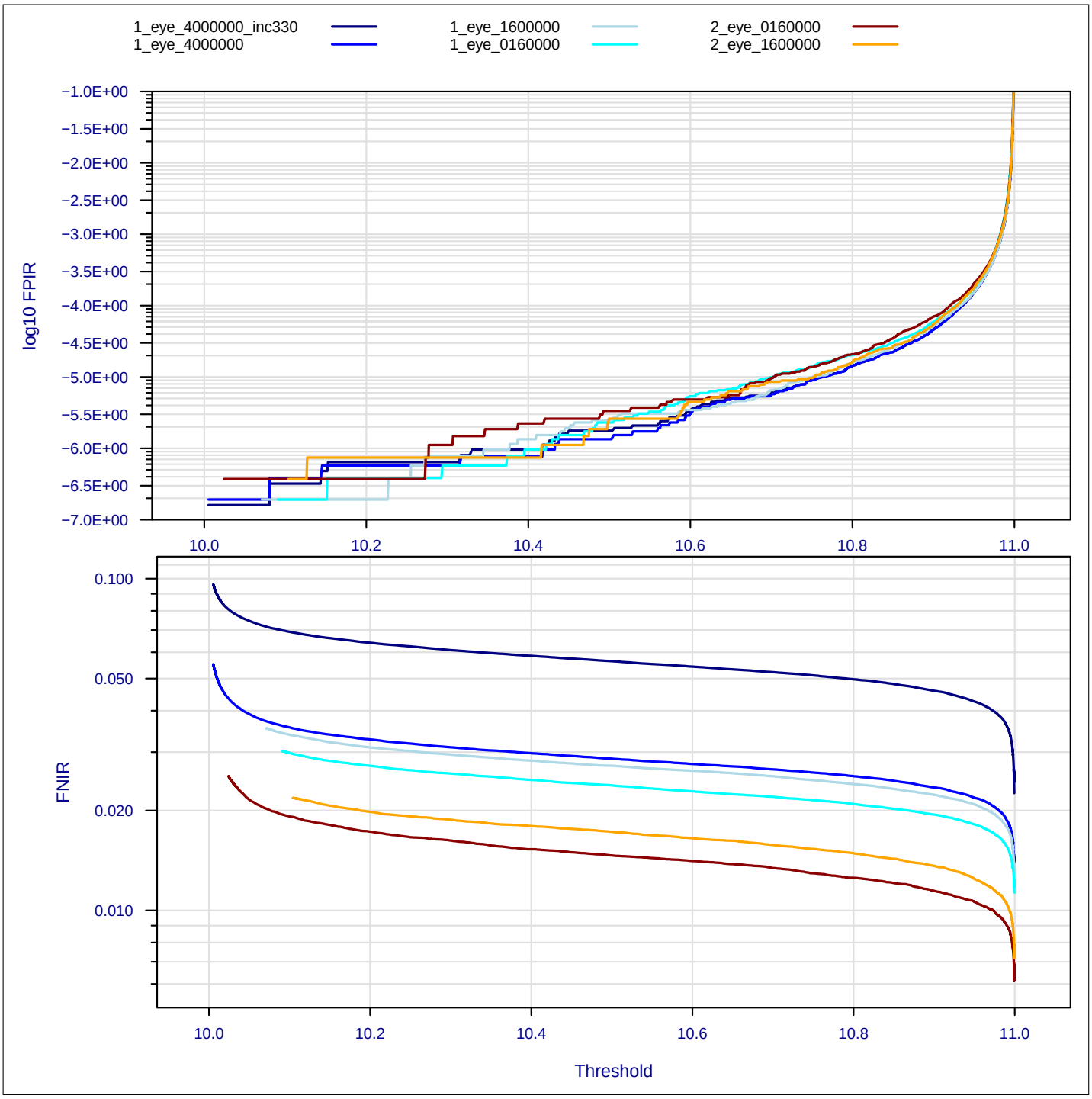

Figure 60: **Threshold calibration curves** for implementation U12B executing searches for single-eye enrolled populations $N = (0.16, 1.6, 4)$ million, and two-eye populations of $N = (0.16, 1.6)$ million individuals. While the large search sets S_{nb} were used used, with number of searches in the hundreds of thousands, the number of observed scores in the far tails is small: To get reduced uncertainty more searches would be necessary. Missing plots indicate the run is not yet complete.

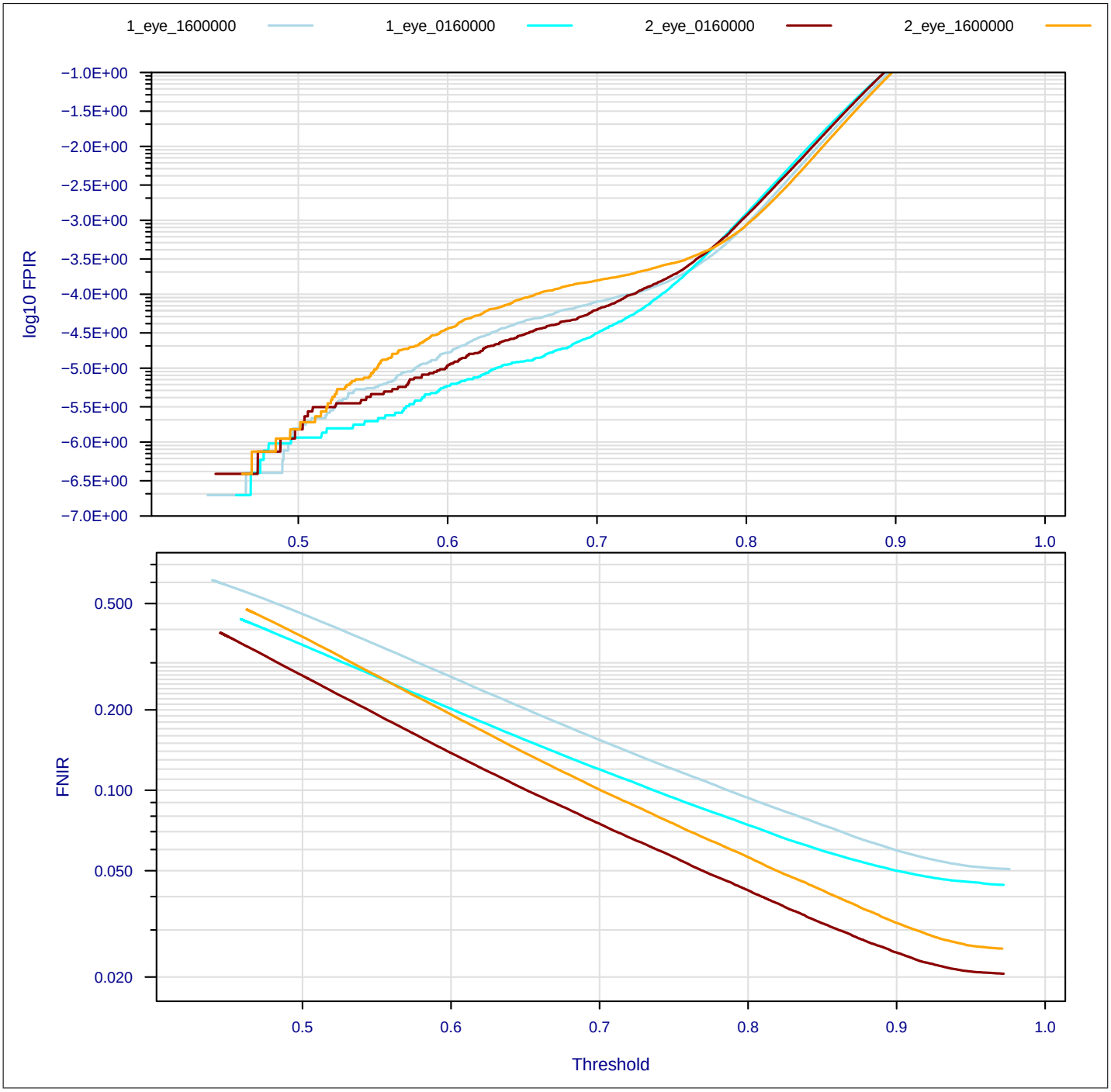

Figure 61: **Threshold calibration curves** for implementation V01A executing searches for single-eye enrolled populations $N = (0.16, 1.6, 4)$ million, and two-eye populations of $N = (0.16, 1.6)$ million individuals. While the large search sets S_{nb} were used used, with number of searches in the hundreds of thousands, the number of observed scores in the far tails is small: To get reduced uncertainty more searches would be necessary. Missing plots indicate the run is not yet complete.

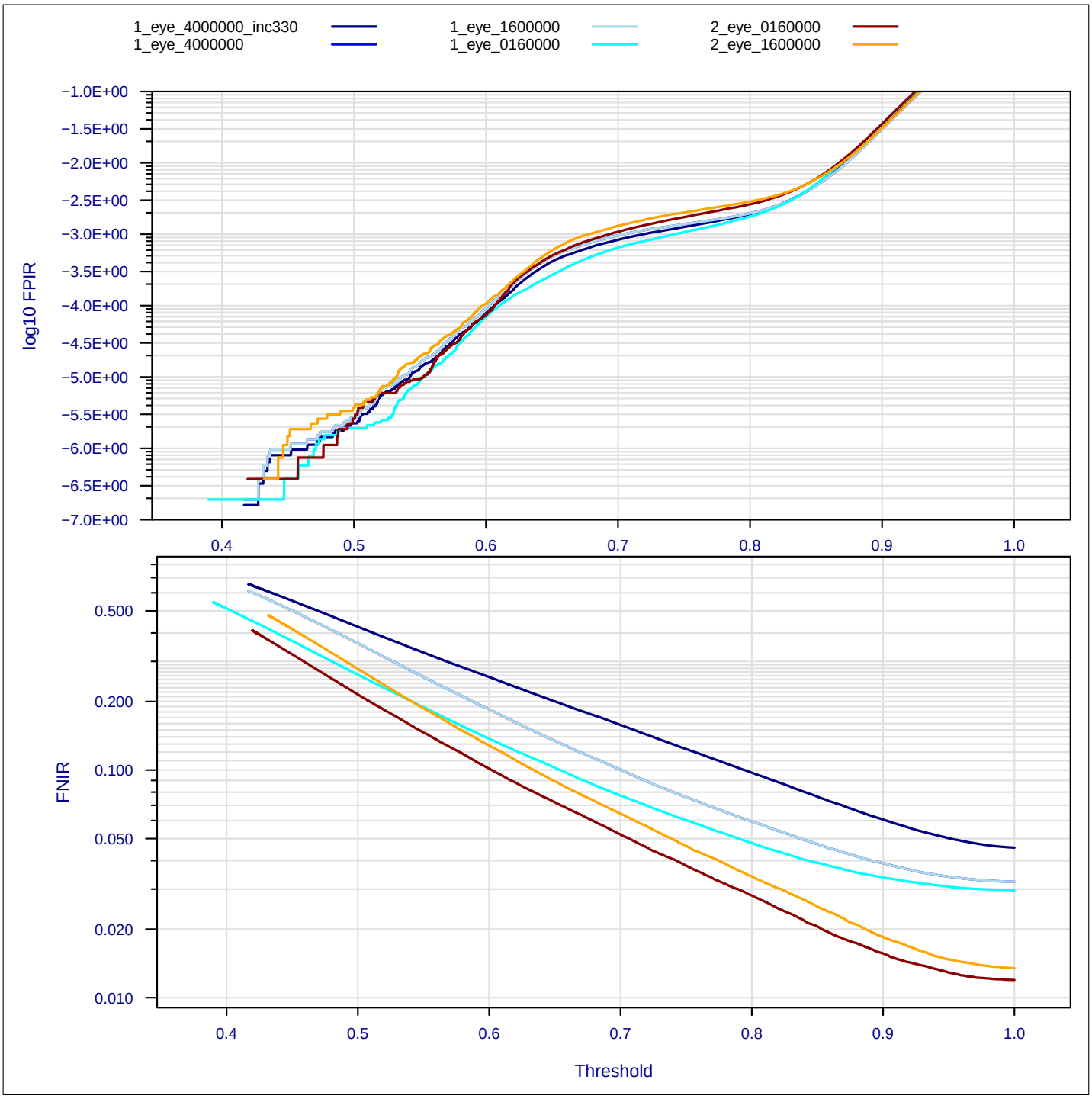

Figure 62: **Threshold calibration curves** for implementation V02A executing searches for single-eye enrolled populations $N = (0.16, 1.6, 4)$ million, and two-eye populations of $N = (0.16, 1.6)$ million individuals. While the large search sets S_{nb} were used used, with number of searches in the hundreds of thousands, the number of observed scores in the far tails is small: To get reduced uncertainty more searches would be necessary. Missing plots indicate the run is not yet complete.

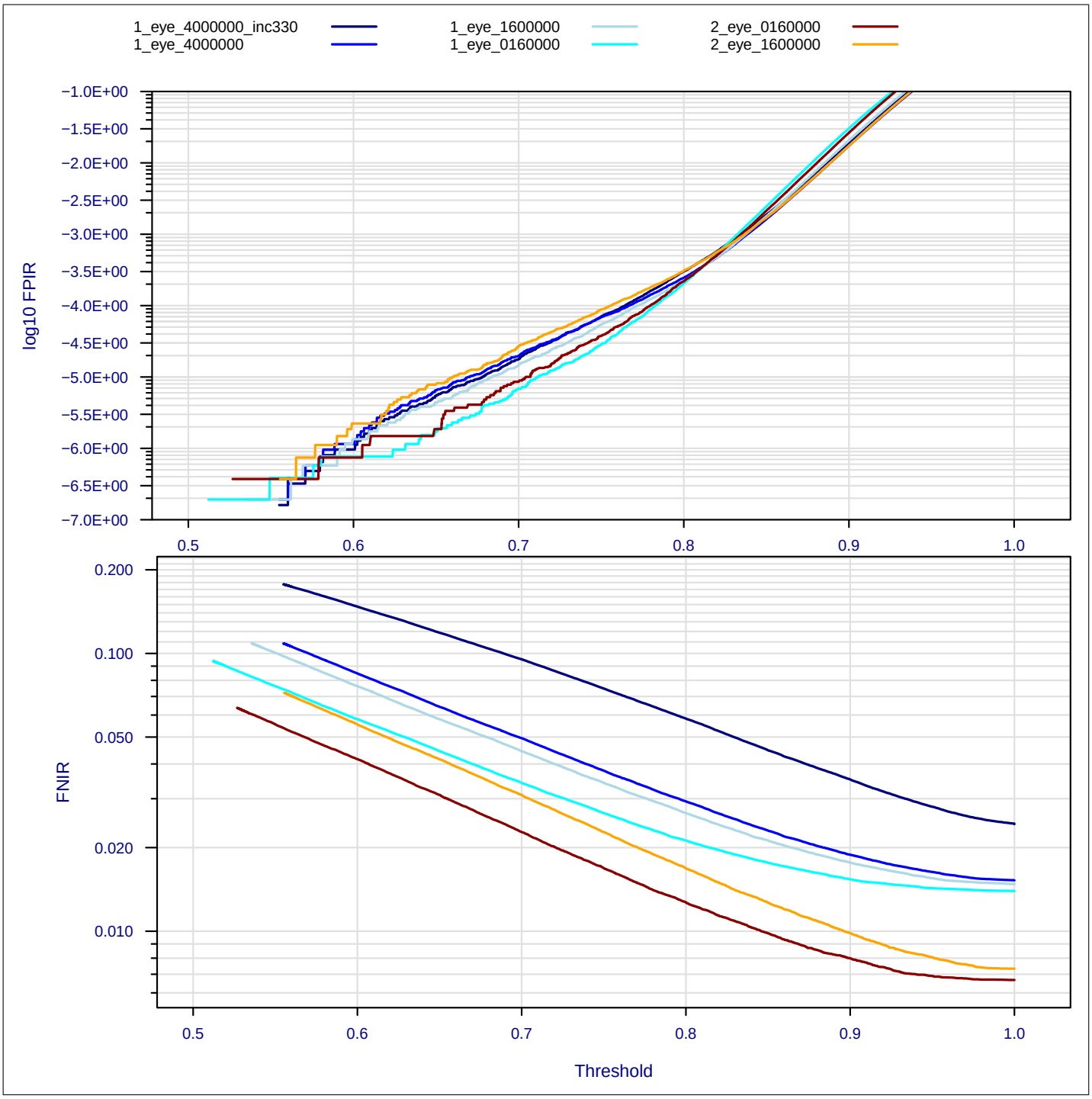

Figure 63: **Threshold calibration curves** for implementation V03A executing searches for single-eye enrolled populations $N = (0.16, 1.6, 4)$ million, and two-eye populations of $N = (0.16, 1.6)$ million individuals. While the large search sets S_{nb} were used used, with number of searches in the hundreds of thousands, the number of observed scores in the far tails is small: To get reduced uncertainty more searches would be necessary. Missing plots indicate the run is not yet complete.

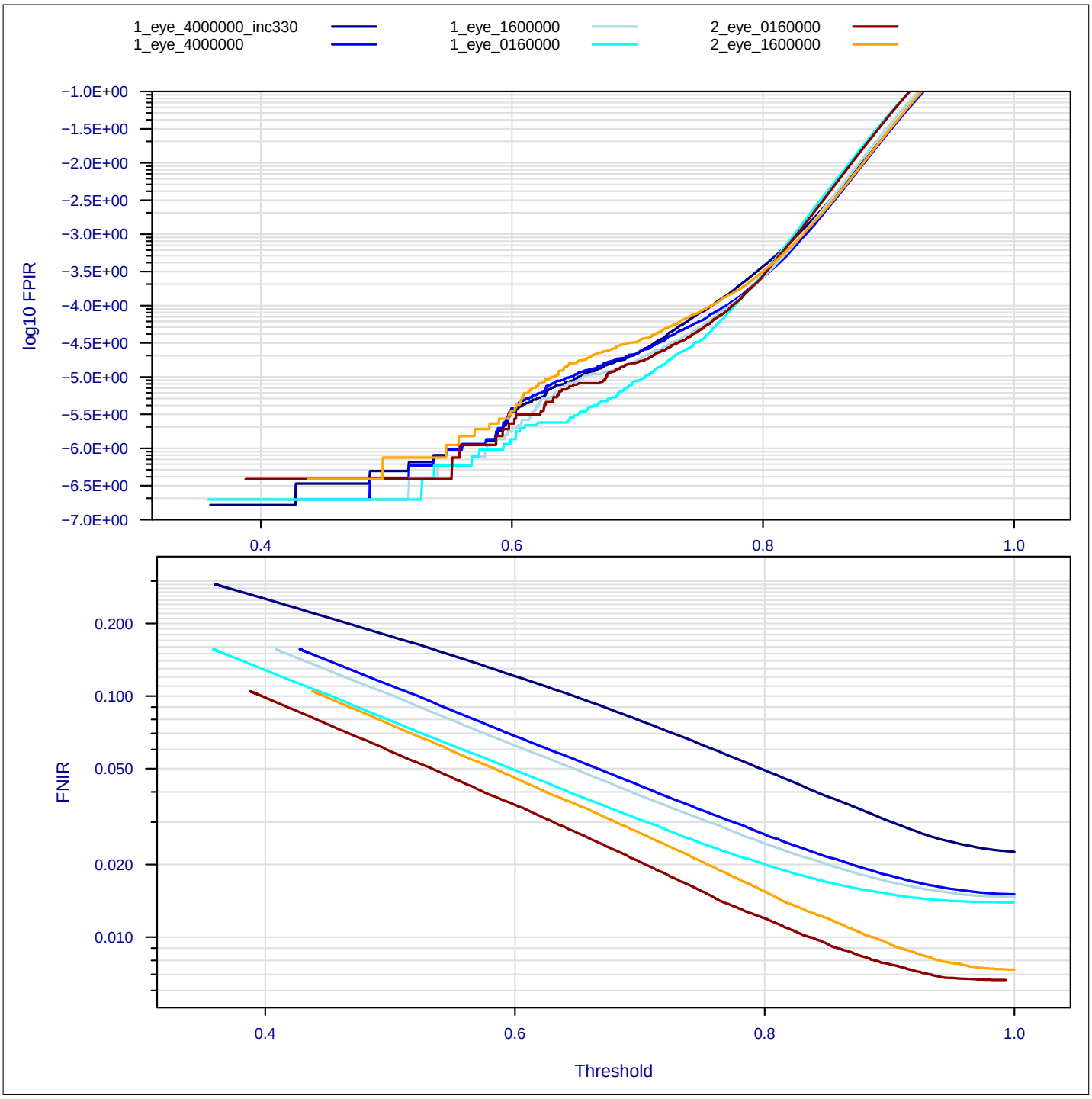

Figure 64: **Threshold calibration curves** for implementation V03B executing searches for single-eye enrolled populations $N = (0.16, 1.6, 4)$ million, and two-eye populations of $N = (0.16, 1.6)$ million individuals. While the large search sets S_{nb} were used used, with number of searches in the hundreds of thousands, the number of observed scores in the far tails is small: To get reduced uncertainty more searches would be necessary. Missing plots indicate the run is not yet complete.

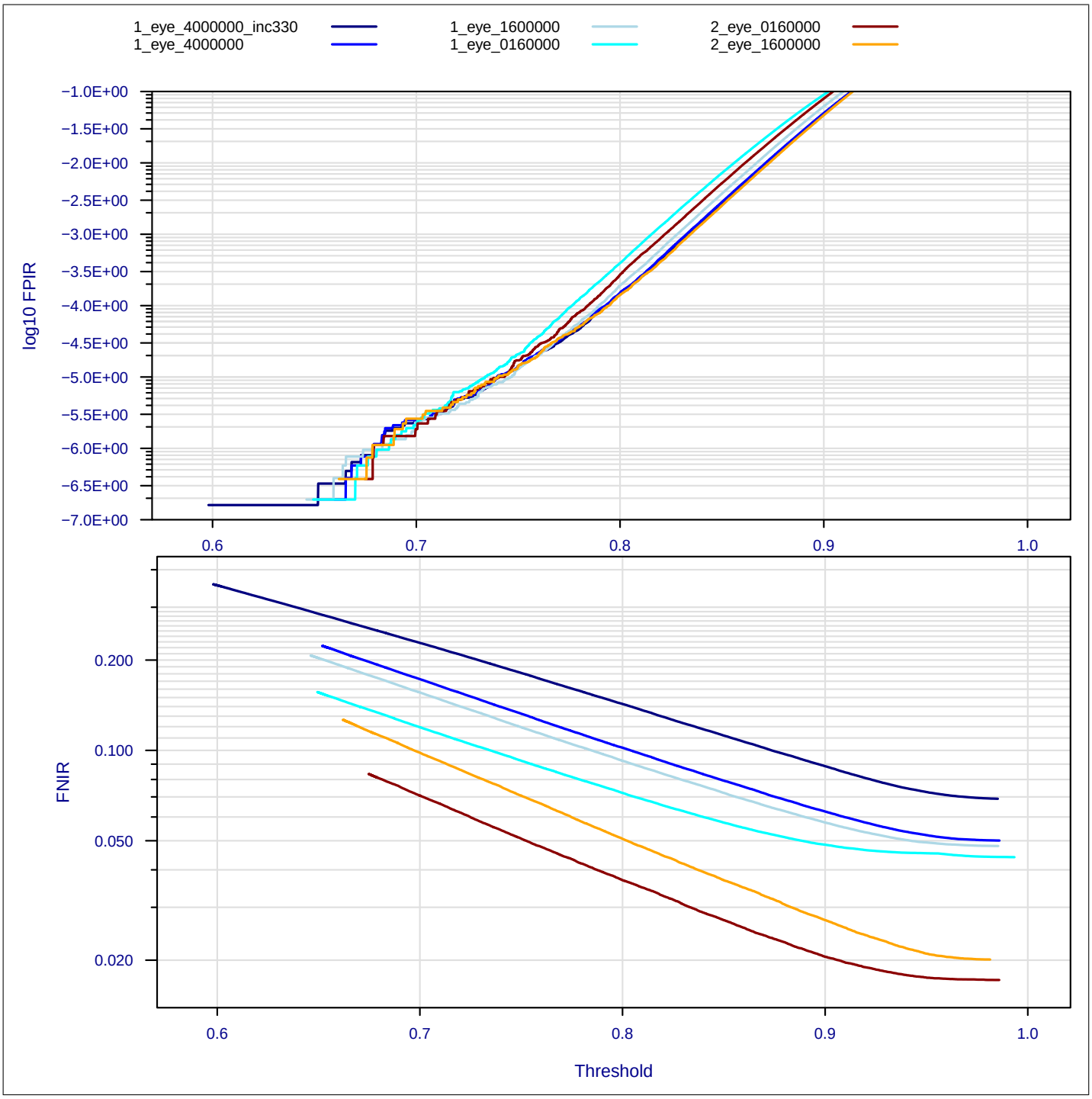

Figure 65: **Threshold calibration curves** for implementation V04A executing searches for single-eye enrolled populations $N = (0.16, 1.6, 4)$ million, and two-eye populations of $N = (0.16, 1.6)$ million individuals. While the large search sets S_{nb} were used used, with number of searches in the hundreds of thousands, the number of observed scores in the far tails is small: To get reduced uncertainty more searches would be necessary. Missing plots indicate the run is not yet complete.

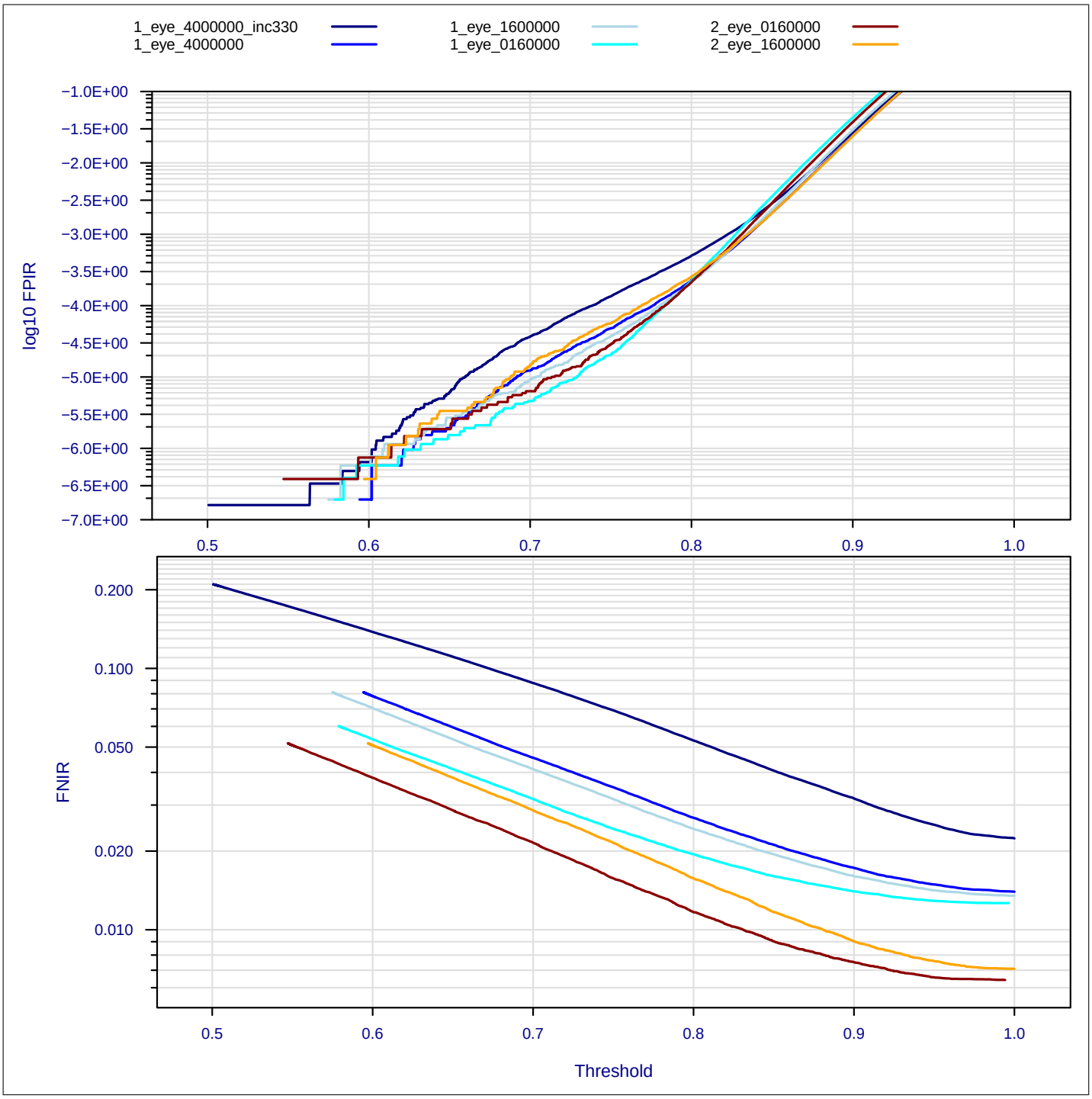

Figure 66: **Threshold calibration curves** for implementation V11A executing searches for single-eye enrolled populations $N = (0.16, 1.6, 4)$ million, and two-eye populations of $N = (0.16, 1.6)$ million individuals. While the large search sets S_{nb} were used used, with number of searches in the hundreds of thousands, the number of observed scores in the far tails is small: To get reduced uncertainty more searches would be necessary. Missing plots indicate the run is not yet complete.

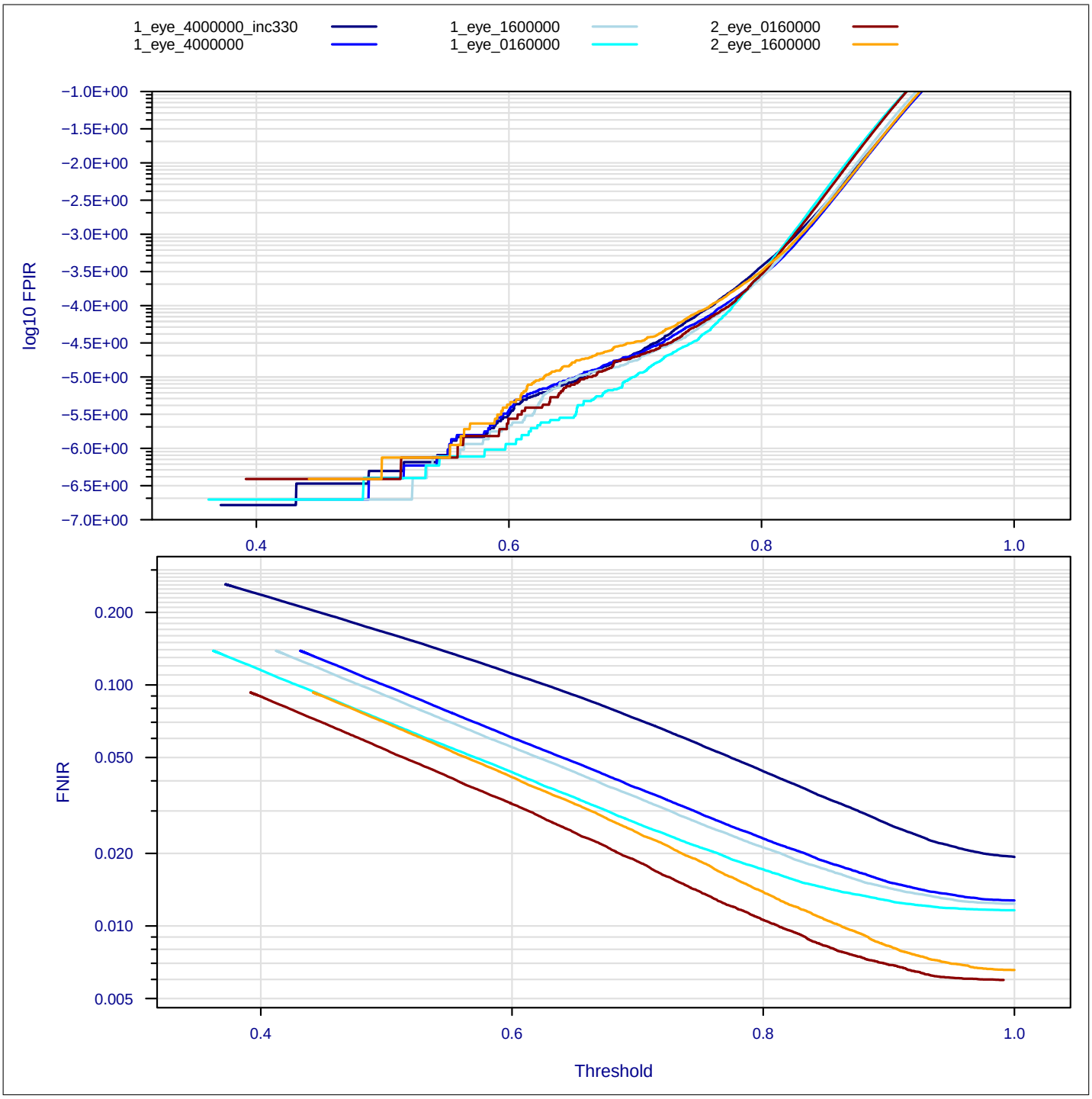

Figure 67: **Threshold calibration curves** for implementation V11B executing searches for single-eye enrolled populations $N = (0.16, 1.6, 4)$ million, and two-eye populations of $N = (0.16, 1.6)$ million individuals. While the large search sets S_{nb} were used used, with number of searches in the hundreds of thousands, the number of observed scores in the far tails is small: To get reduced uncertainty more searches would be necessary. Missing plots indicate the run is not yet complete.

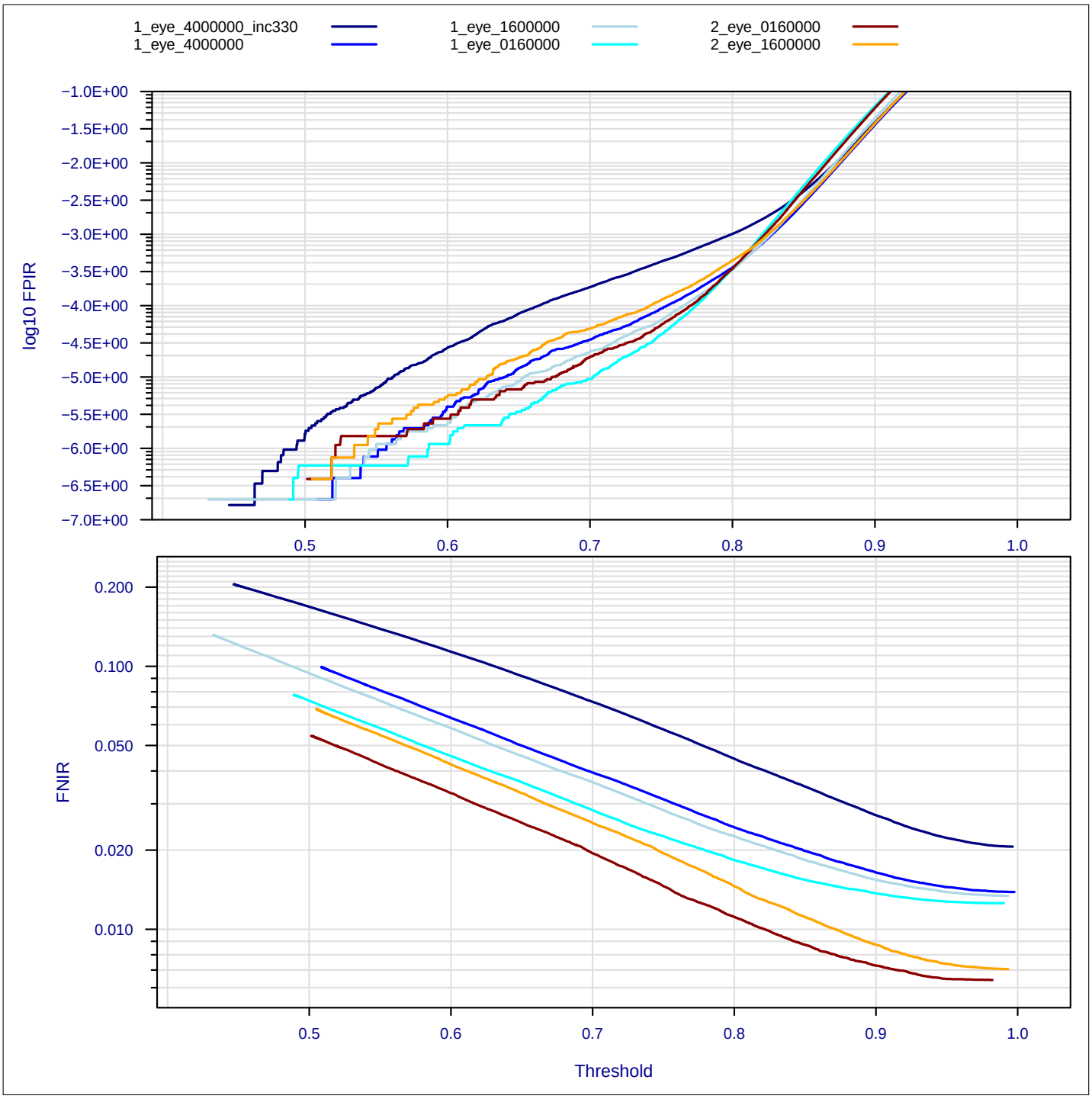

Figure 68: **Threshold calibration curves** for implementation V12A executing searches for single-eye enrolled populations $N = (0.16, 1.6, 4)$ million, and two-eye populations of $N = (0.16, 1.6)$ million individuals. While the large search sets S_{nb} were used used, with number of searches in the hundreds of thousands, the number of observed scores in the far tails is small: To get reduced uncertainty more searches would be necessary. Missing plots indicate the run is not yet complete.

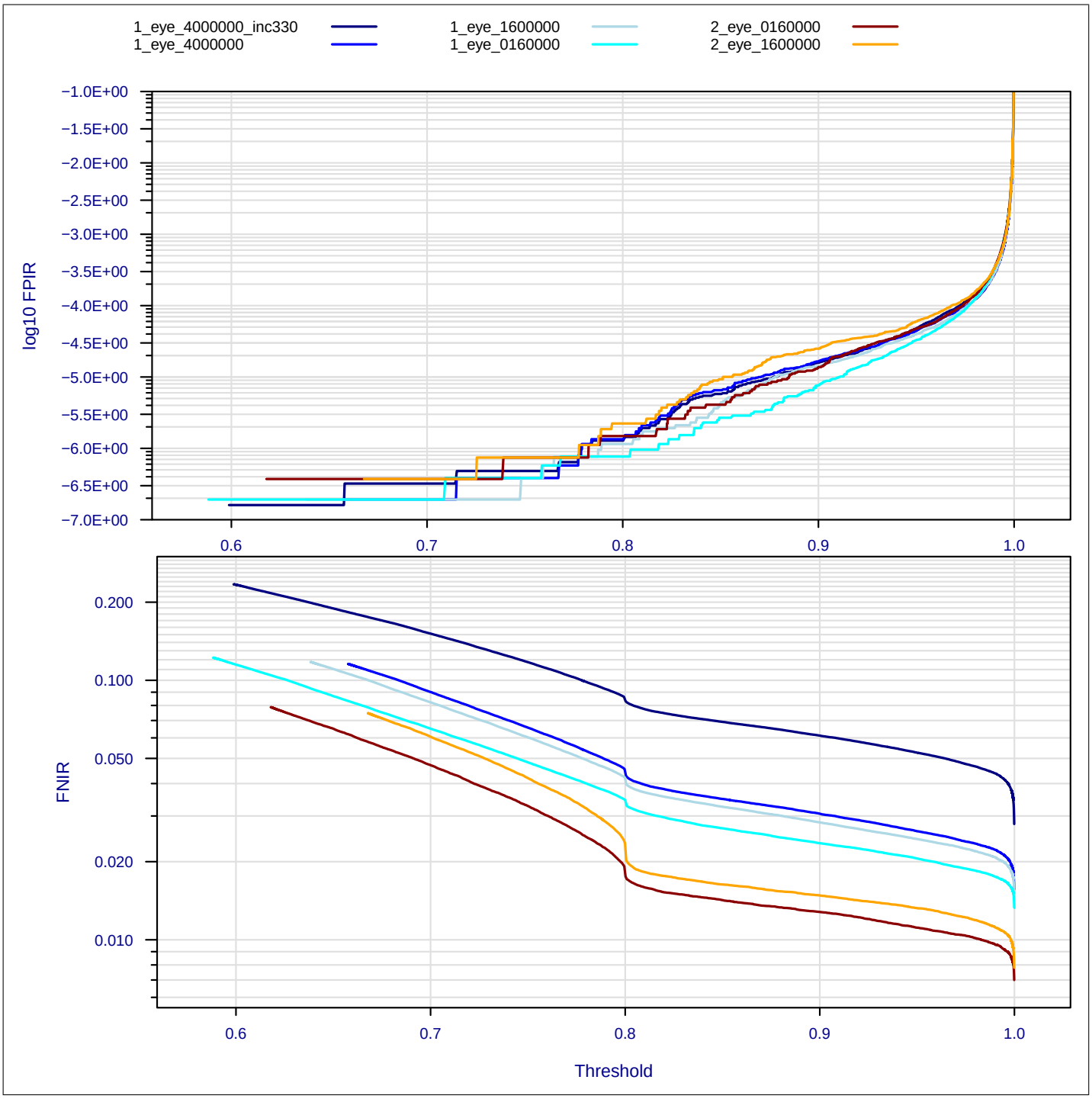

Figure 69: **Threshold calibration curves** for implementation V12B executing searches for single-eye enrolled populations $N = (0.16, 1.6, 4)$ million, and two-eye populations of $N = (0.16, 1.6)$ million individuals. While the large search sets S_{nb} were used used, with number of searches in the hundreds of thousands, the number of observed scores in the far tails is small: To get reduced uncertainty more searches would be necessary. Missing plots indicate the run is not yet complete.

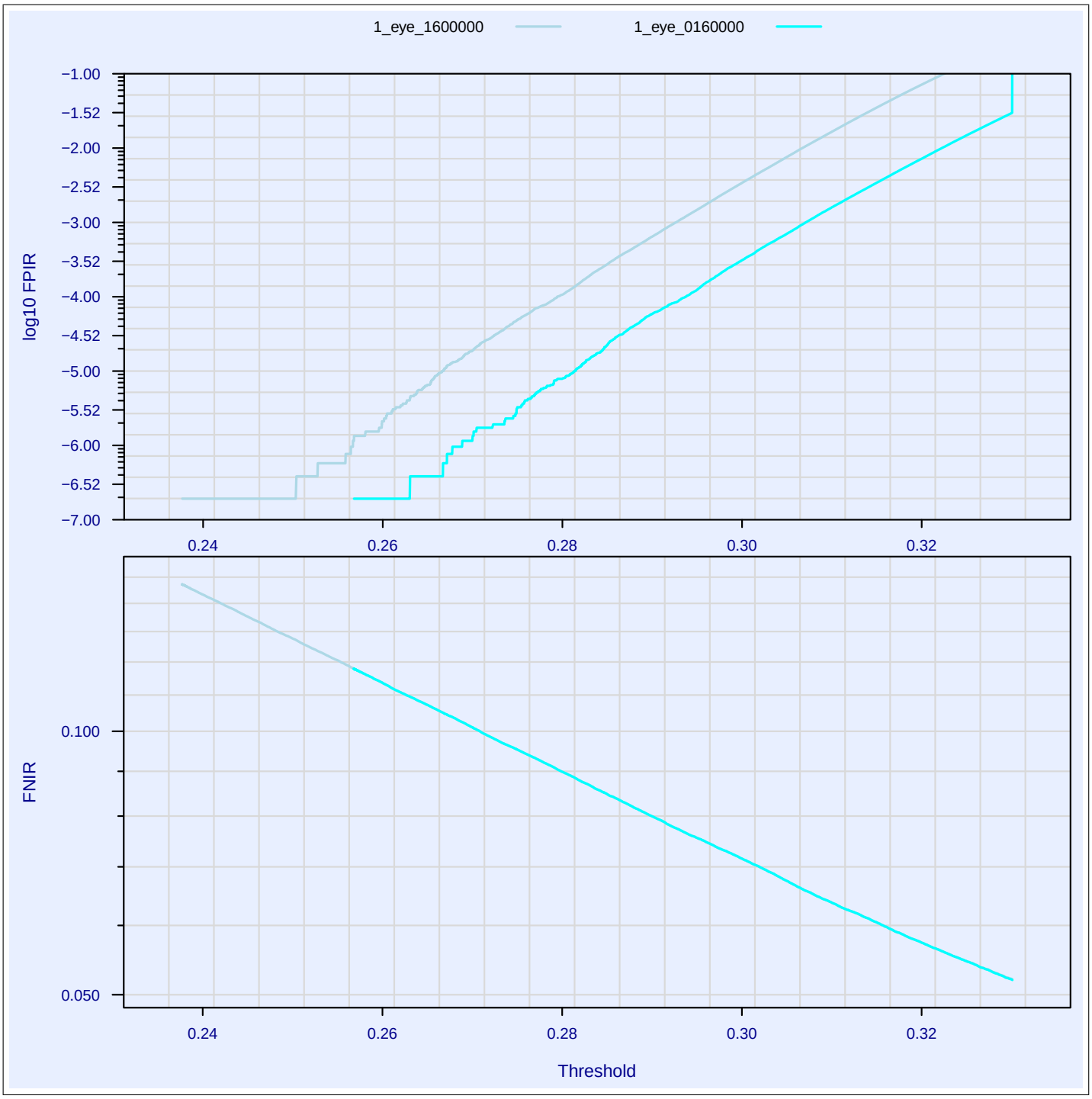

Figure 70: **Threshold calibration curves** for implementation W01A executing searches for single-eye enrolled populations $N = (0.16, 1.6, 4)$ million, and two-eye populations of $N = (0.16, 1.6)$ million individuals. While the large search sets S_{nb} were used used, with number of searches in the hundreds of thousands, the number of observed scores in the far tails is small: To get reduced uncertainty more searches would be necessary. Missing plots indicate the run is not yet complete.

Figure 71: **Threshold calibration curves** for implementation W01B executing searches for single-eye enrolled populations $N = (0.16, 1.6, 4)$ million, and two-eye populations of $N = (0.16, 1.6)$ million individuals. While the large search sets S_{nb} were used used, with number of searches in the hundreds of thousands, the number of observed scores in the far tails is small: To get reduced uncertainty more searches would be necessary. Missing plots indicate the run is not yet complete.

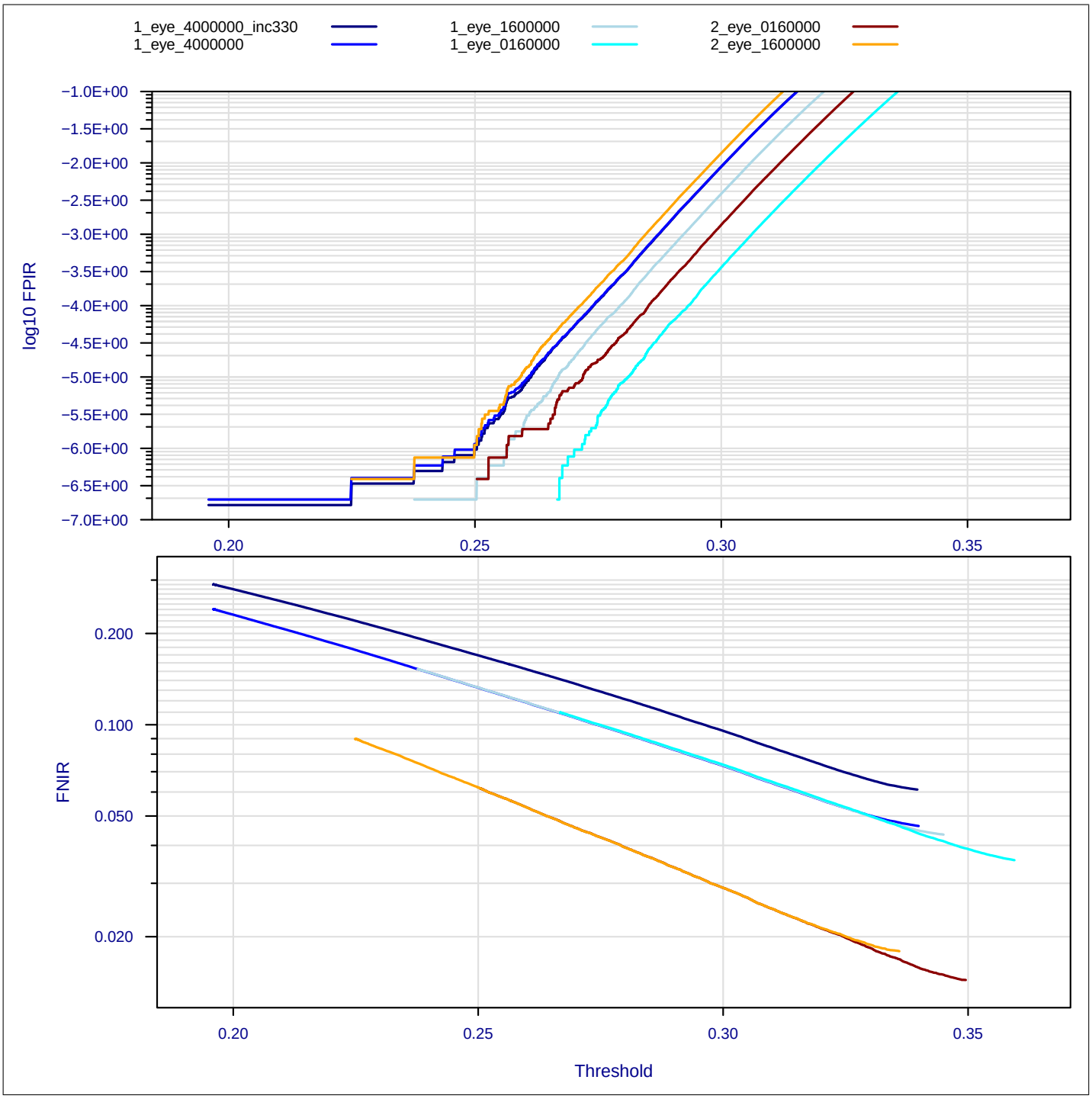

Figure 72: **Threshold calibration curves** for implementation W02A executing searches for single-eye enrolled populations $N = (0.16, 1.6, 4)$ million, and two-eye populations of $N = (0.16, 1.6)$ million individuals. While the large search sets S_{nb} were used used, with number of searches in the hundreds of thousands, the number of observed scores in the far tails is small: To get reduced uncertainty more searches would be necessary. Missing plots indicate the run is not yet complete.

Figure 73: **Threshold calibration curves** for implementation W02B executing searches for single-eye enrolled populations $N = (0.16, 1.6, 4)$ million, and two-eye populations of $N = (0.16, 1.6)$ million individuals. While the large search sets S_{nb} were used used, with number of searches in the hundreds of thousands, the number of observed scores in the far tails is small: To get reduced uncertainty more searches would be necessary. Missing plots indicate the run is not yet complete.

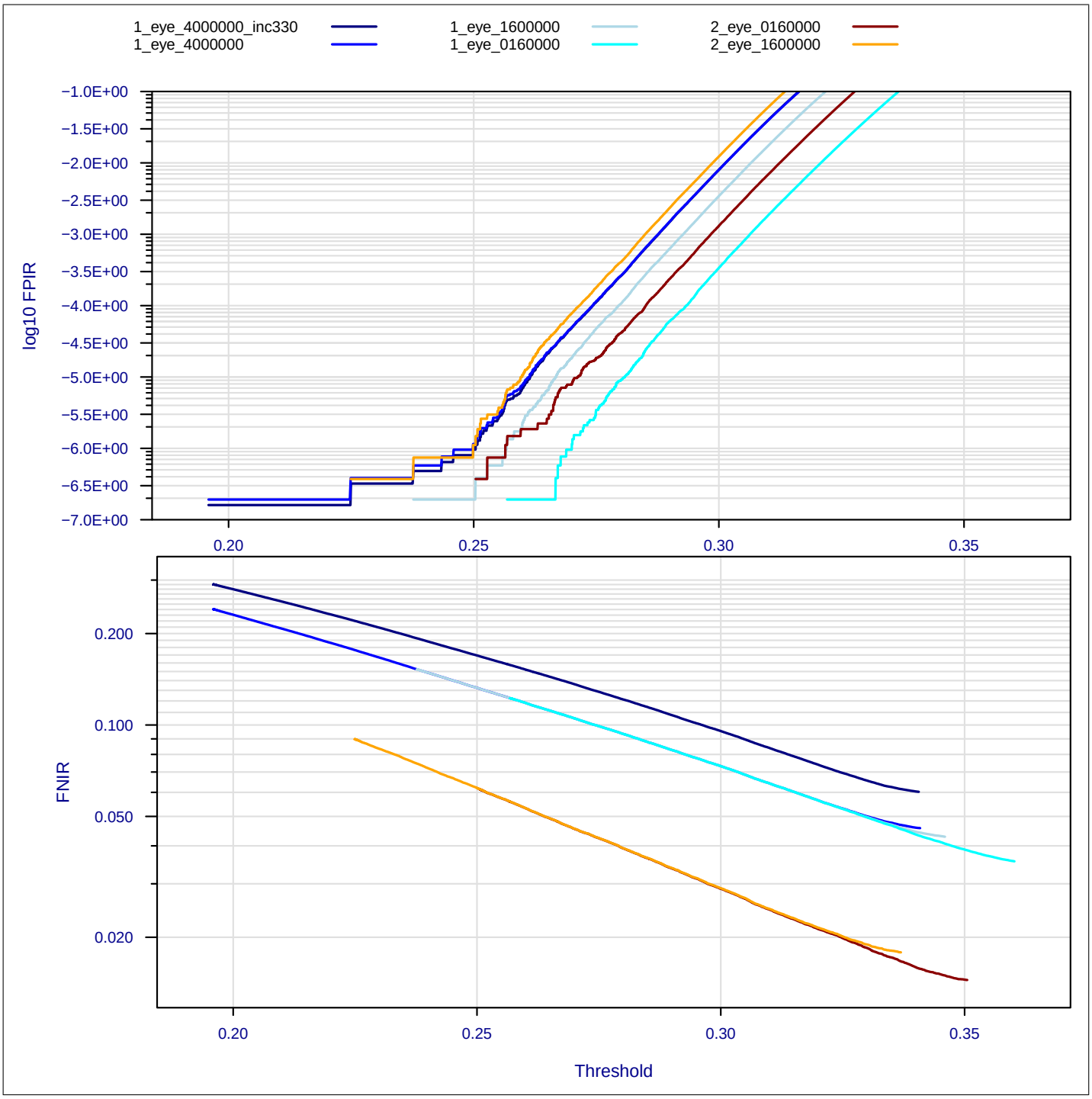

Figure 74: **Threshold calibration curves** for implementation W03A executing searches for single-eye enrolled populations $N = (0.16, 1.6, 4)$ million, and two-eye populations of $N = (0.16, 1.6)$ million individuals. While the large search sets S_{nb} were used used, with number of searches in the hundreds of thousands, the number of observed scores in the far tails is small: To get reduced uncertainty more searches would be necessary. Missing plots indicate the run is not yet complete.

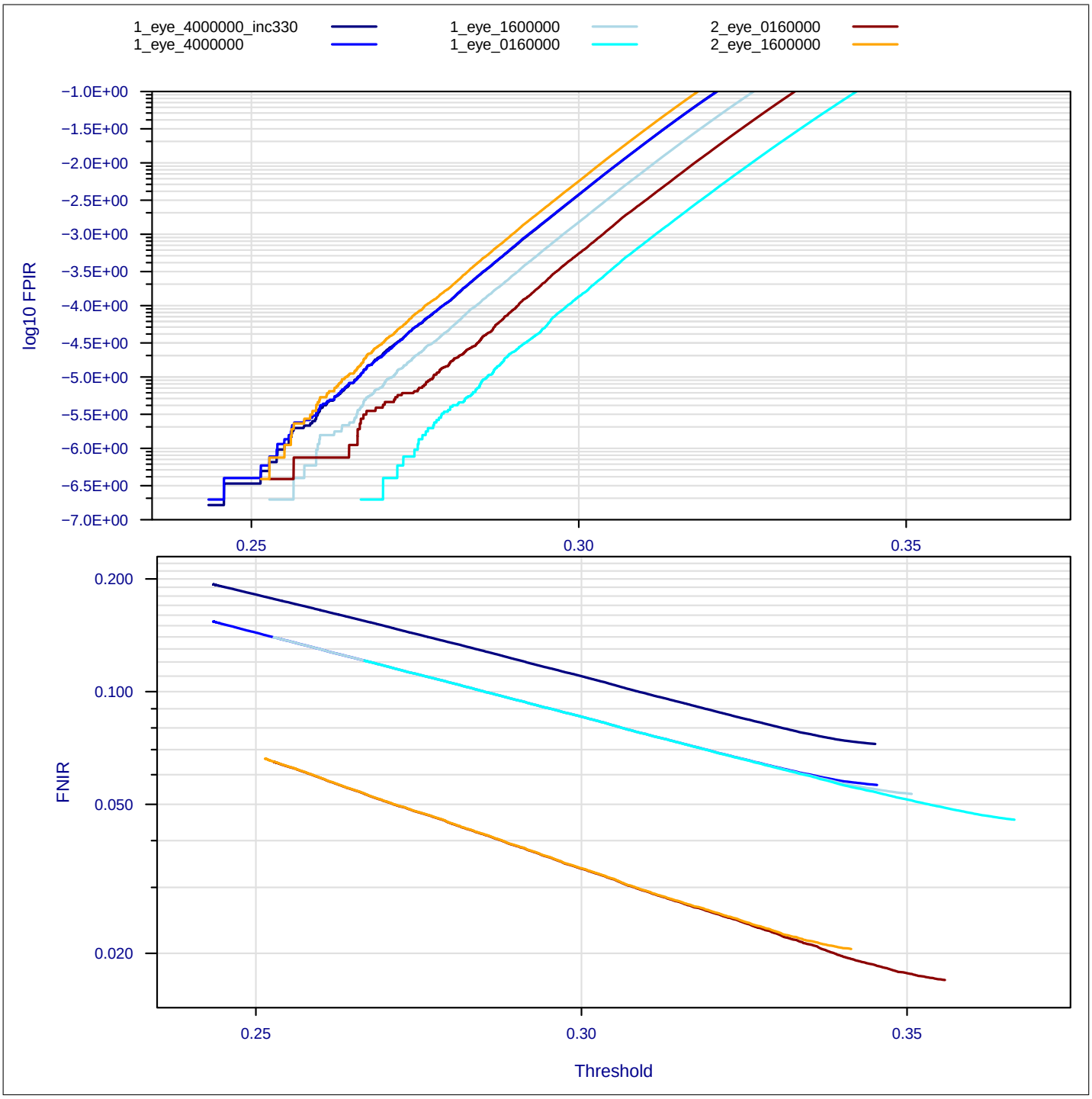

Figure 75: **Threshold calibration curves** for implementation W04A executing searches for single-eye enrolled populations $N = (0.16, 1.6, 4)$ million, and two-eye populations of $N = (0.16, 1.6)$ million individuals. While the large search sets S_{nb} were used used, with number of searches in the hundreds of thousands, the number of observed scores in the far tails is small: To get reduced uncertainty more searches would be necessary. Missing plots indicate the run is not yet complete.

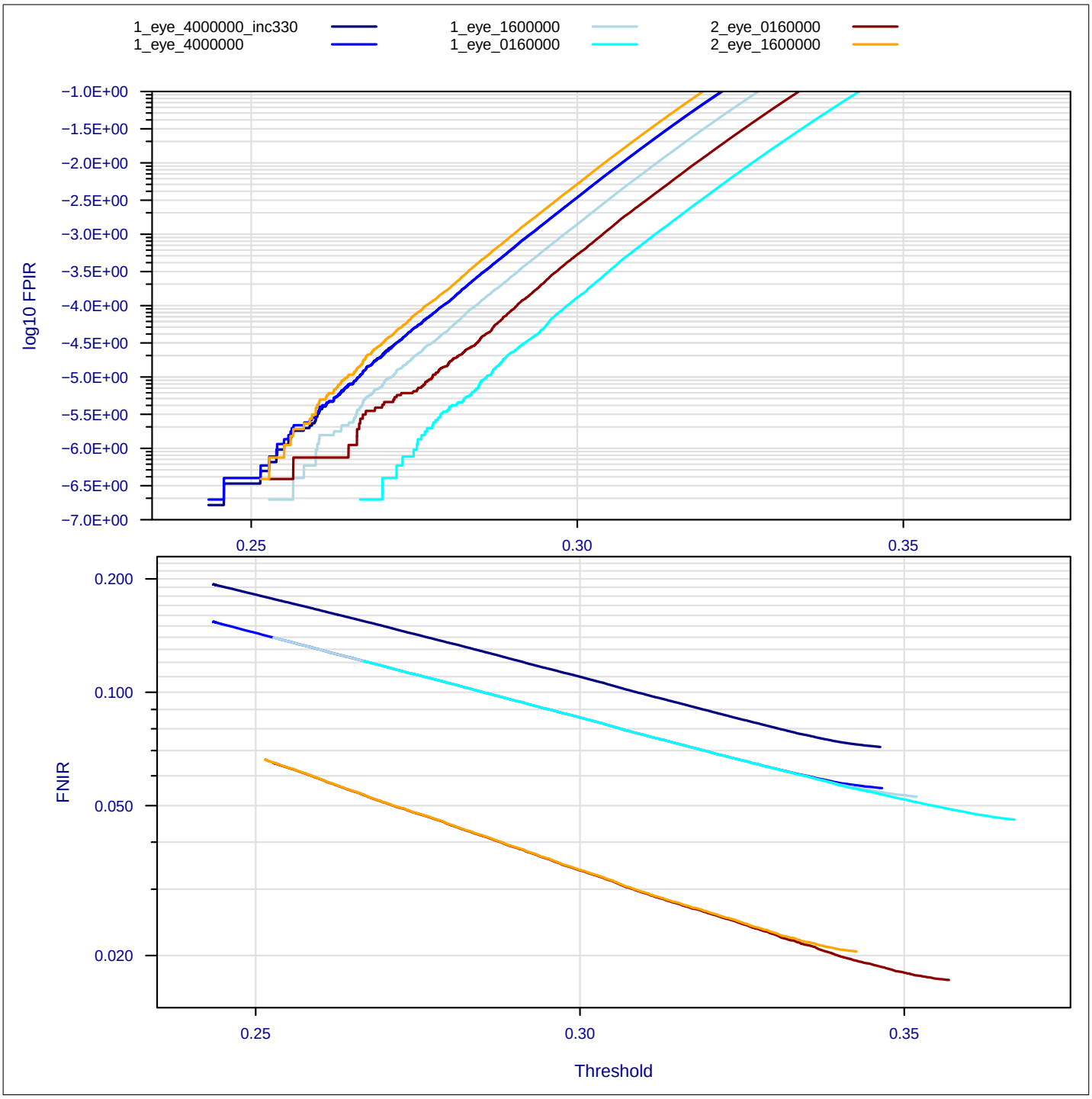

Figure 76: **Threshold calibration curves** for implementation W05A executing searches for single-eye enrolled populations $N = (0.16, 1.6, 4)$ million, and two-eye populations of $N = (0.16, 1.6)$ million individuals. While the large search sets S_{nb} were used used, with number of searches in the hundreds of thousands, the number of observed scores in the far tails is small: To get reduced uncertainty more searches would be necessary. Missing plots indicate the run is not yet complete.

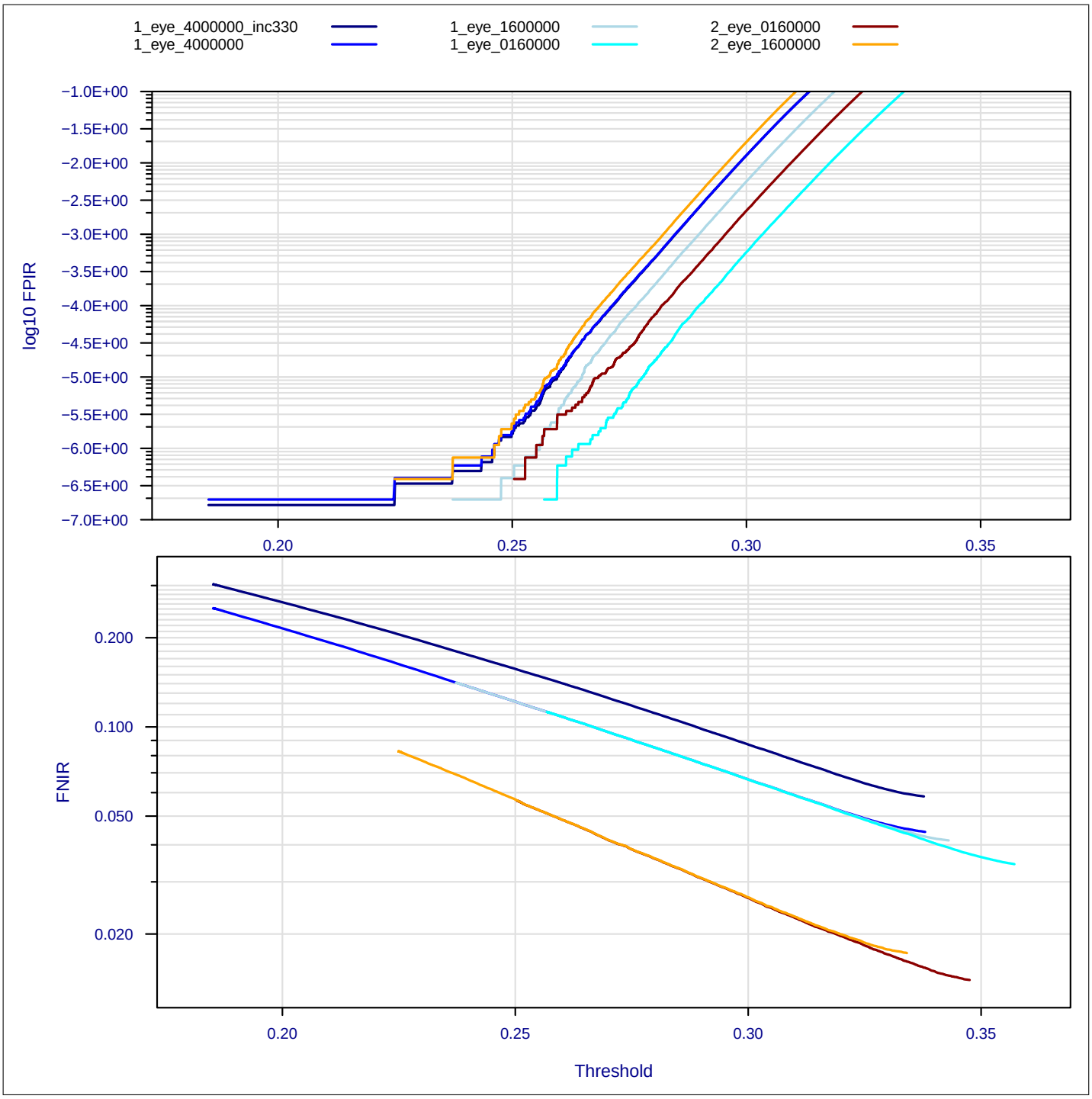

Figure 77: **Threshold calibration curves** for implementation W11A executing searches for single-eye enrolled populations $N = (0.16, 1.6, 4)$ million, and two-eye populations of $N = (0.16, 1.6)$ million individuals. While the large search sets S_{nb} were used used, with number of searches in the hundreds of thousands, the number of observed scores in the far tails is small: To get reduced uncertainty more searches would be necessary. Missing plots indicate the run is not yet complete.

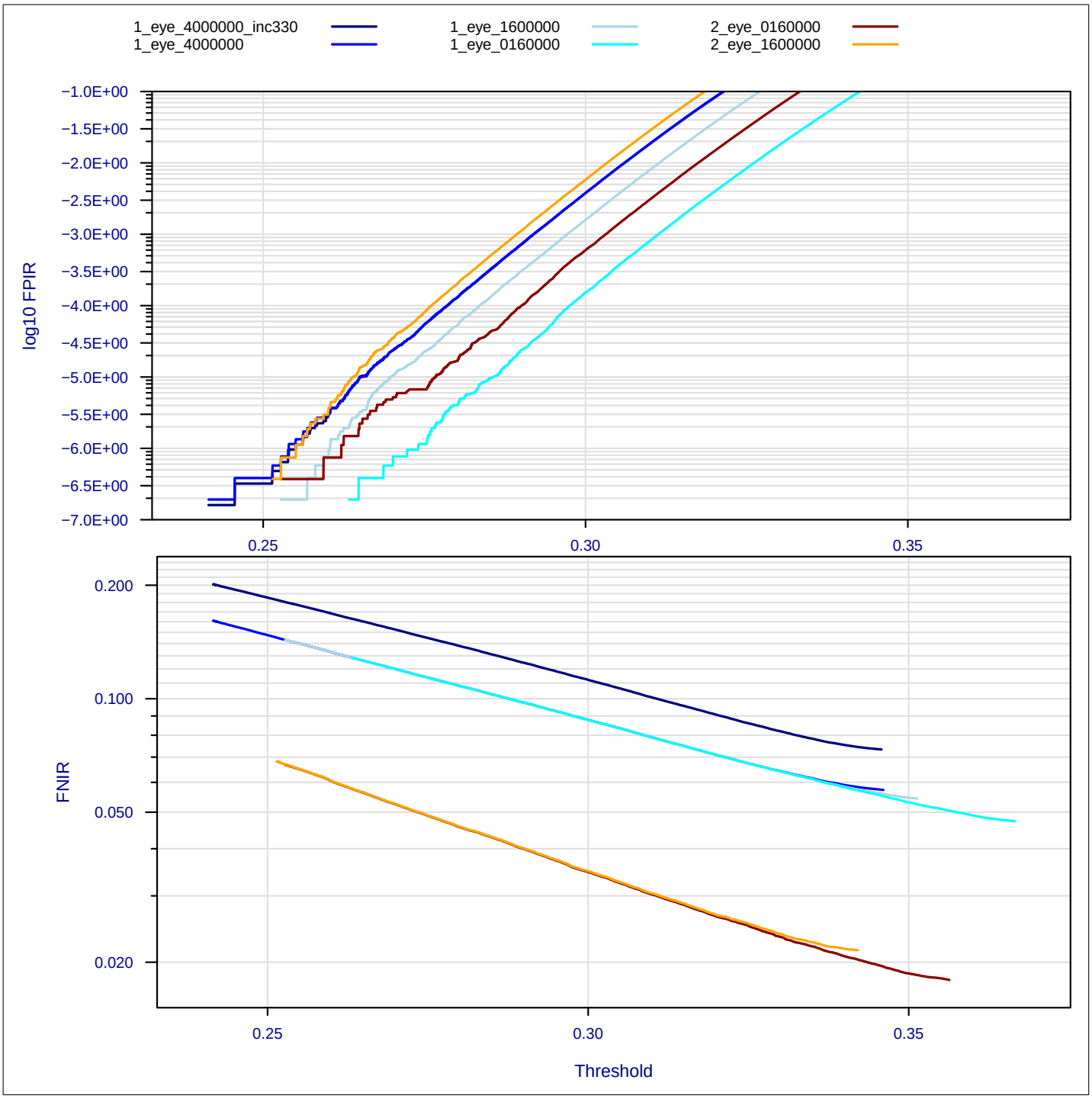

Figure 78: **Threshold calibration curves** for implementation W11B executing searches for single-eye enrolled populations $N = (0.16, 1.6, 4)$ million, and two-eye populations of $N = (0.16, 1.6)$ million individuals. While the large search sets S_{nb} were used used, with number of searches in the hundreds of thousands, the number of observed scores in the far tails is small: To get reduced uncertainty more searches would be necessary. Missing plots indicate the run is not yet complete.

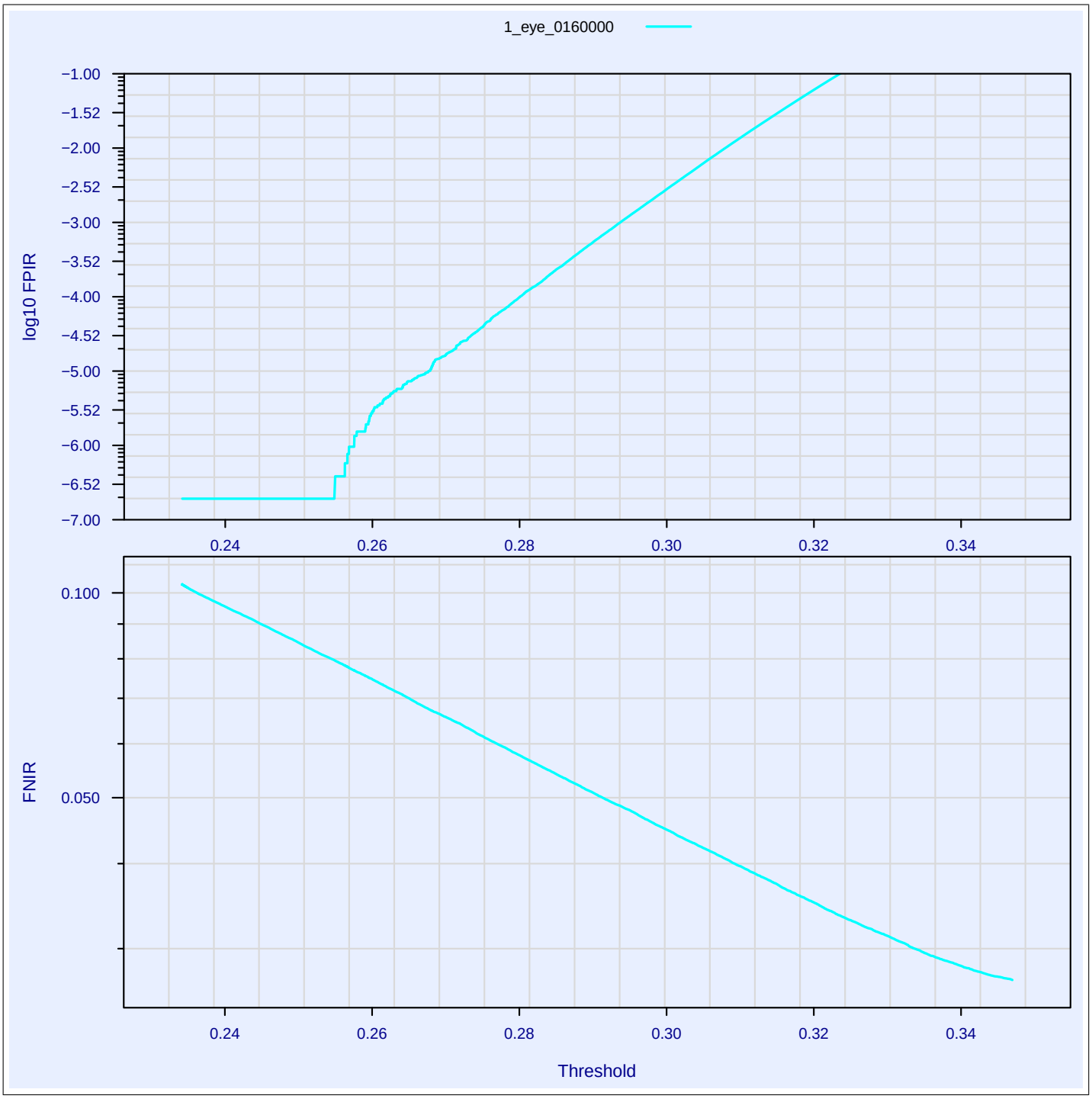

Figure 79: **Threshold calibration curves** for implementation W12A executing searches for single-eye enrolled populations $N = (0.16, 1.6, 4)$ million, and two-eye populations of $N = (0.16, 1.6)$ million individuals. While the large search sets S_{nb} were used used, with number of searches in the hundreds of thousands, the number of observed scores in the far tails is small: To get reduced uncertainty more searches would be necessary. Missing plots indicate the run is not yet complete.

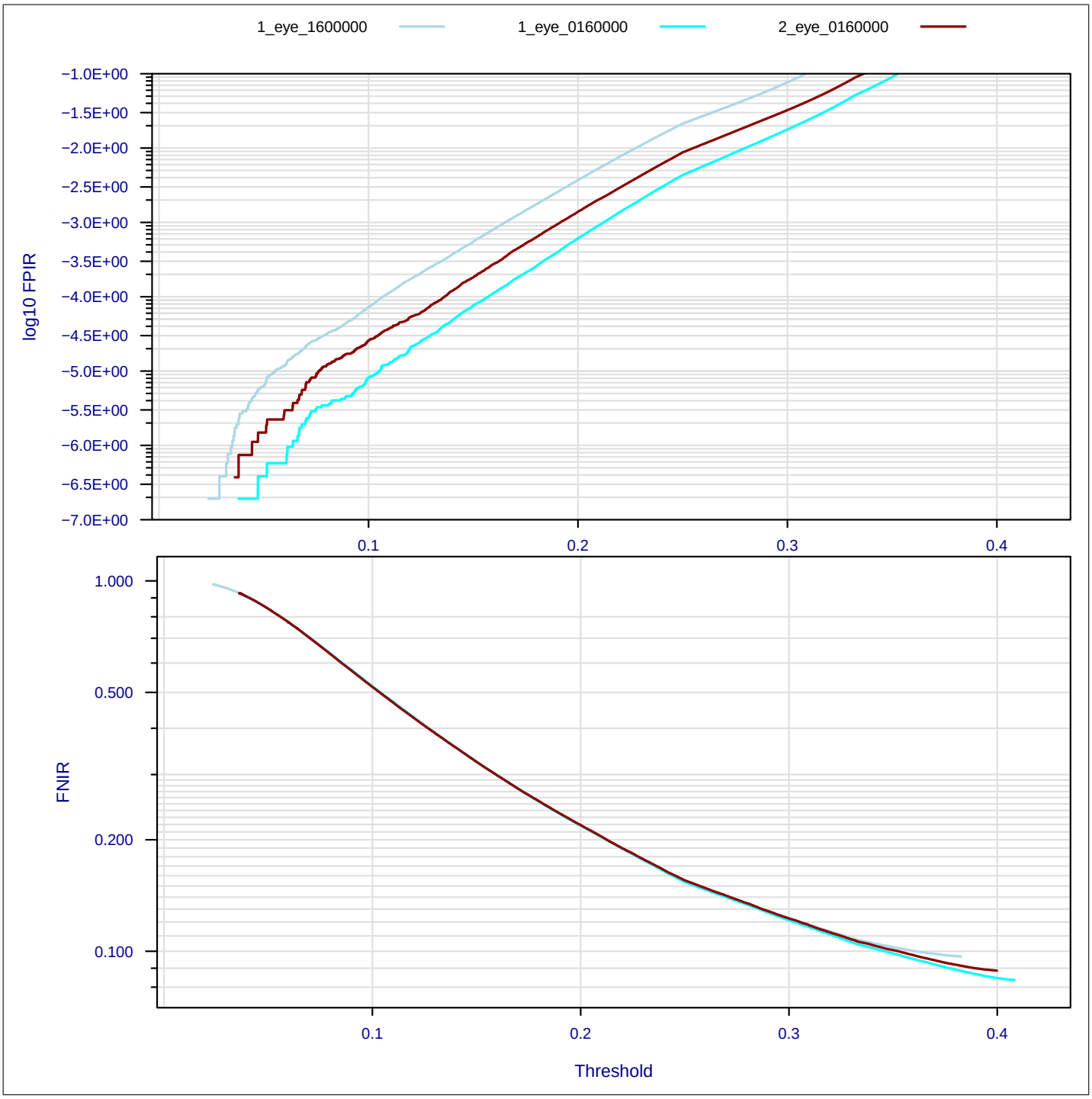

Figure 80: **Threshold calibration curves** for implementation X02A executing searches for single-eye enrolled populations $N = (0.16, 1.6, 4)$ million, and two-eye populations of $N = (0.16, 1.6)$ million individuals. While the large search sets S_{nb} were used used, with number of searches in the hundreds of thousands, the number of observed scores in the far tails is small: To get reduced uncertainty more searches would be necessary. Missing plots indicate the run is not yet complete.

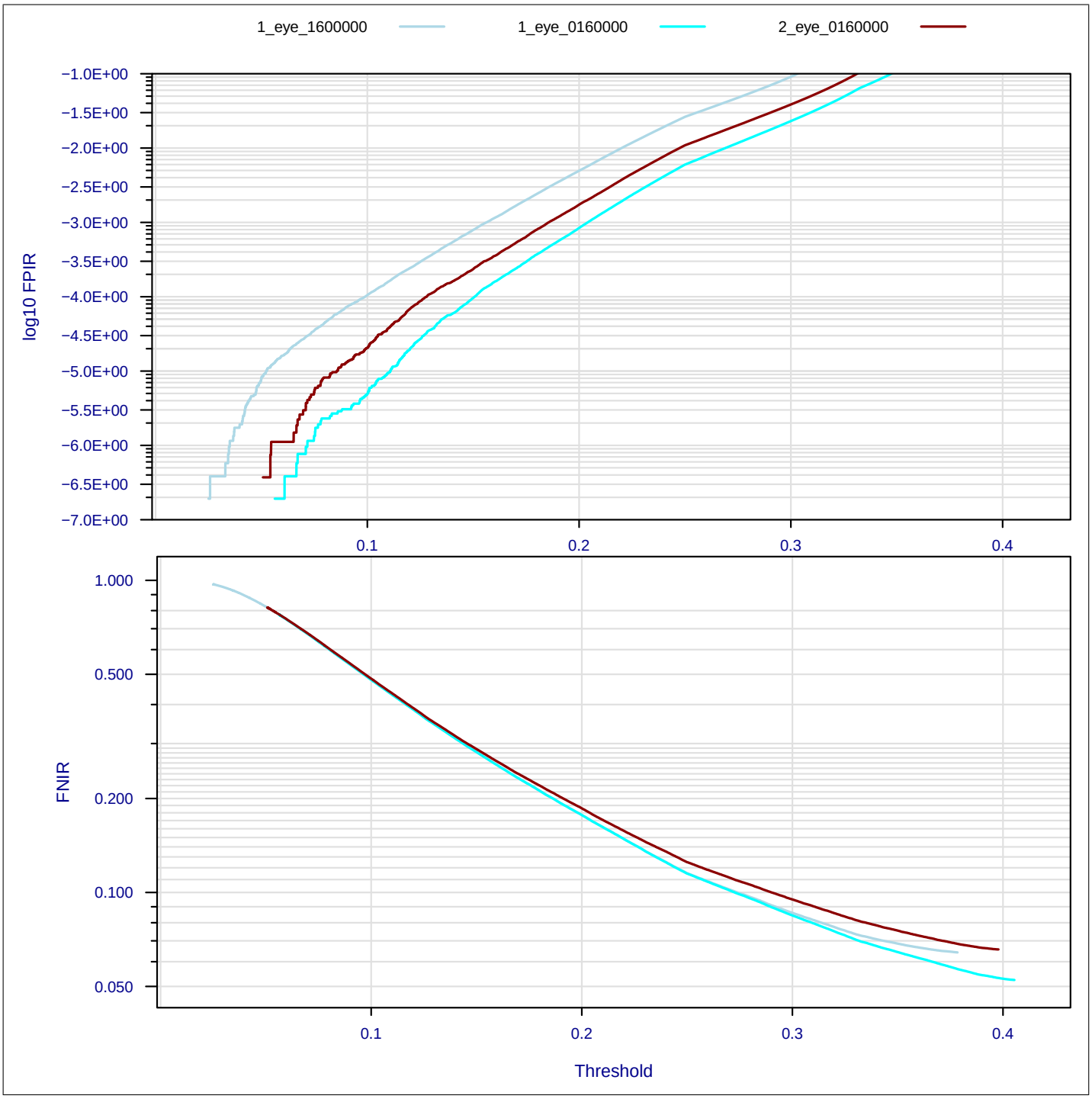

Figure 81: **Threshold calibration curves** for implementation X03A executing searches for single-eye enrolled populations $N = (0.16, 1.6, 4)$ million, and two-eye populations of $N = (0.16, 1.6)$ million individuals. While the large search sets S_{nb} were used used, with number of searches in the hundreds of thousands, the number of observed scores in the far tails is small: To get reduced uncertainty more searches would be necessary. Missing plots indicate the run is not yet complete.

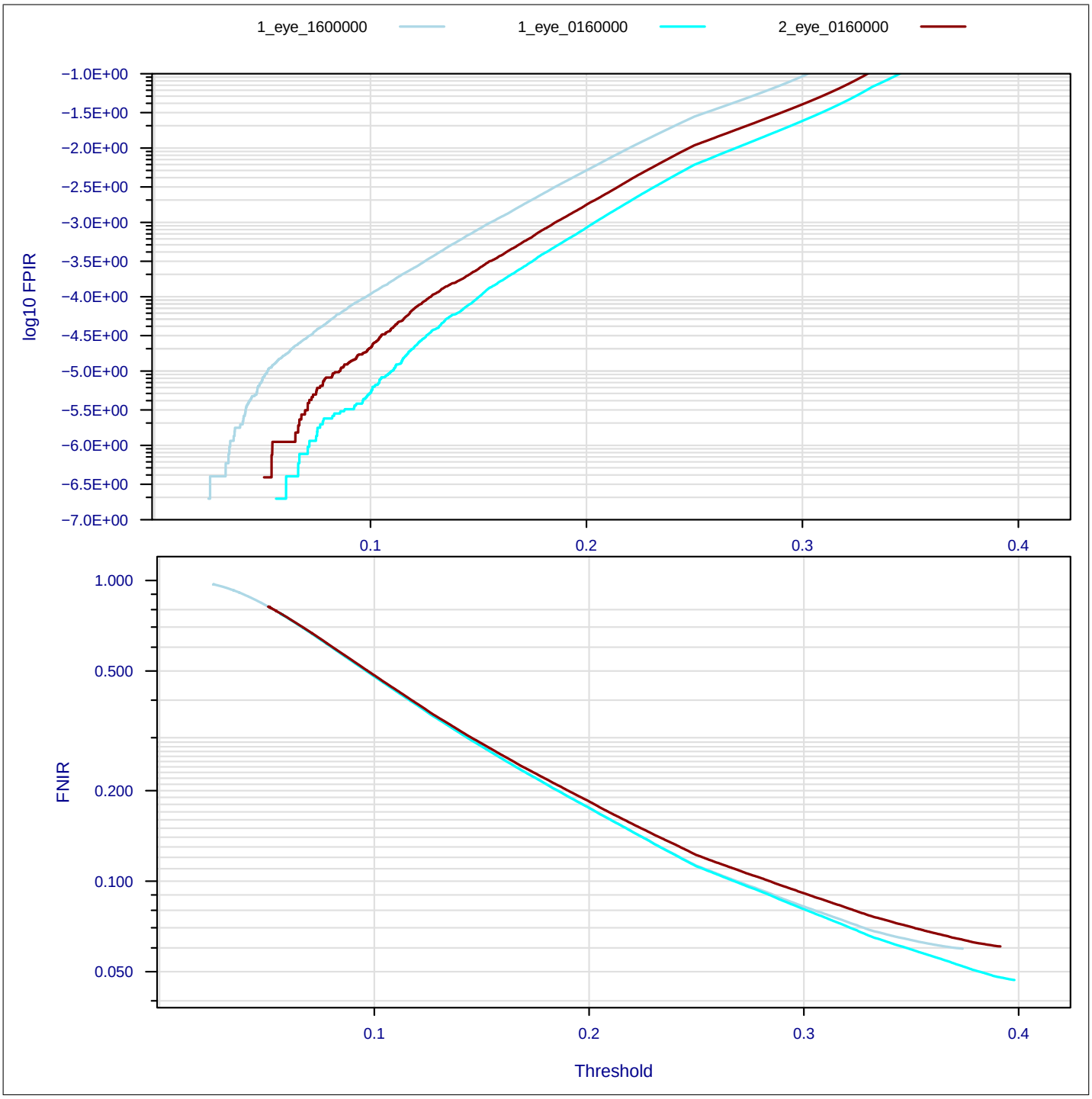

Figure 82: **Threshold calibration curves** for implementation X04A executing searches for single-eye enrolled populations $N = (0.16, 1.6, 4)$ million, and two-eye populations of $N = (0.16, 1.6)$ million individuals. While the large search sets S_{nb} were used used, with number of searches in the hundreds of thousands, the number of observed scores in the far tails is small: To get reduced uncertainty more searches would be necessary. Missing plots indicate the run is not yet complete.

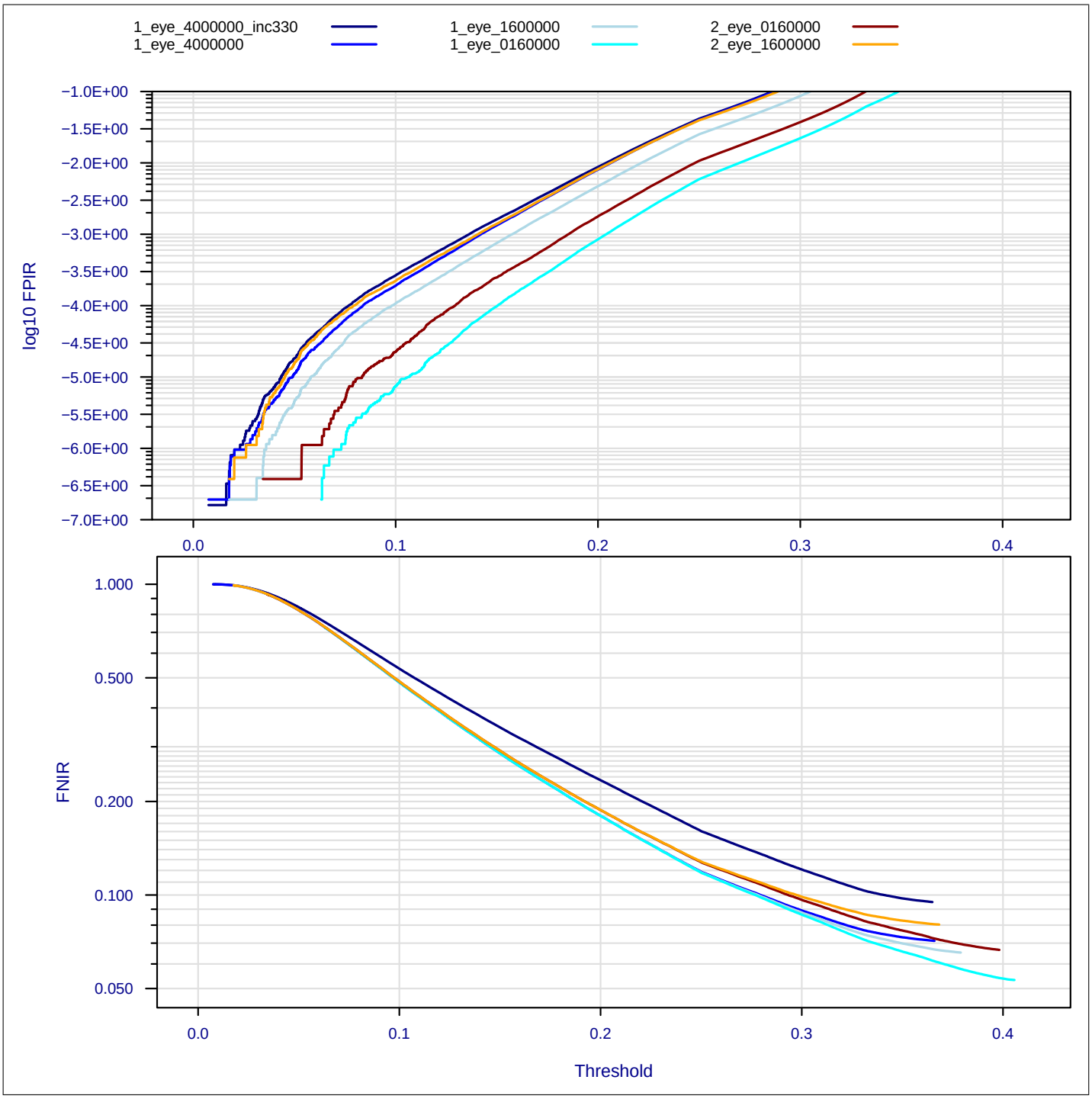

Figure 83: **Threshold calibration curves** for implementation X11A executing searches for single-eye enrolled populations $N = (0.16, 1.6, 4)$ million, and two-eye populations of $N = (0.16, 1.6)$ million individuals. While the large search sets S_{nb} were used used, with number of searches in the hundreds of thousands, the number of observed scores in the far tails is small: To get reduced uncertainty more searches would be necessary. Missing plots indicate the run is not yet complete.

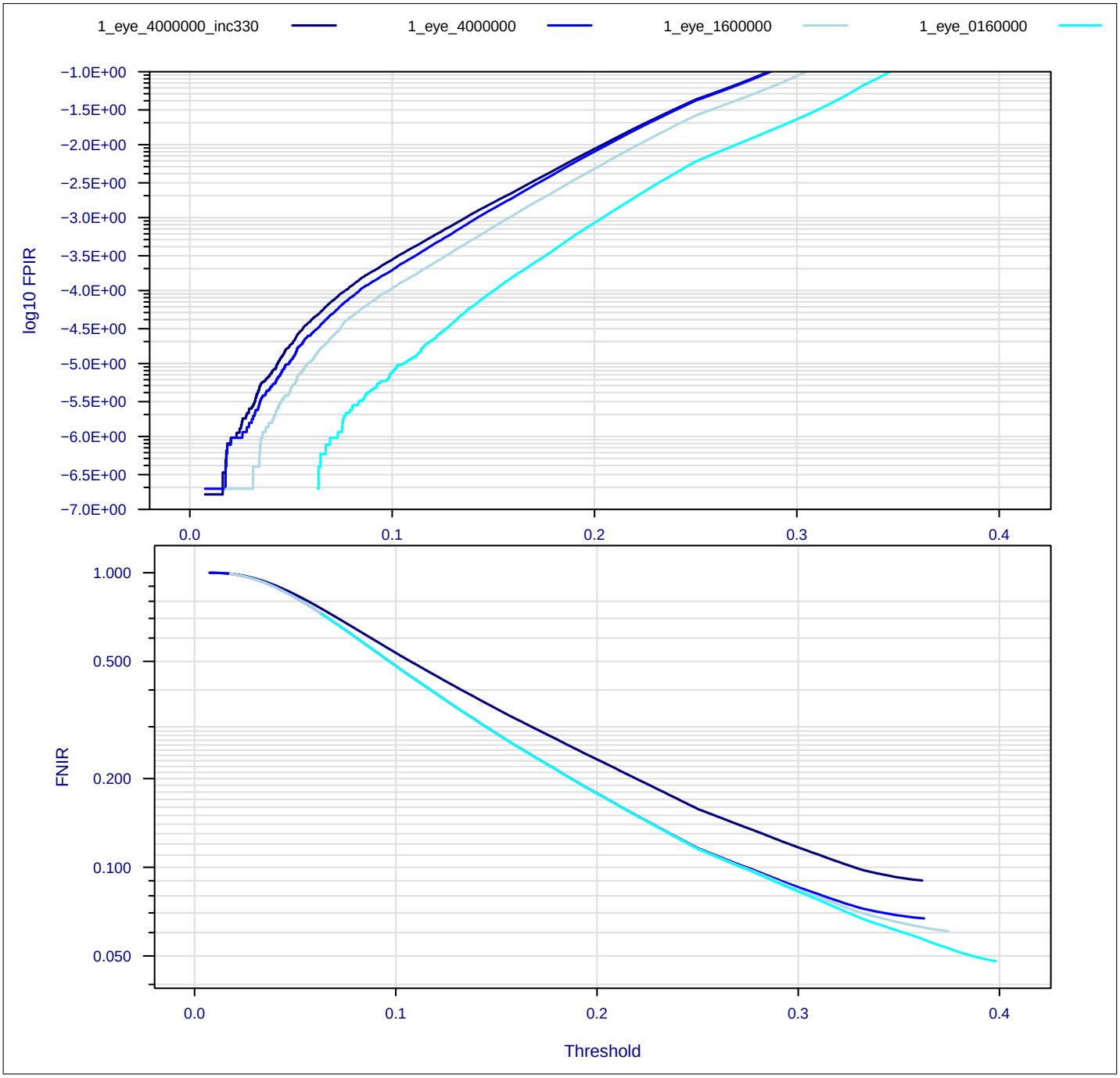

Figure 84: **Threshold calibration curves** for implementation X11B executing searches for single-eye enrolled populations $N = (0.16, 1.6, 4)$ million, and two-eye populations of $N = (0.16, 1.6)$ million individuals. While the large search sets S_{nb} were used used, with number of searches in the hundreds of thousands, the number of observed scores in the far tails is small: To get reduced uncertainty more searches would be necessary. Missing plots indicate the run is not yet complete.

Figure 85: **Threshold calibration curves** for implementation Y02A executing searches for single-eye enrolled populations $N = (0.16, 1.6, 4)$ million, and two-eye populations of $N = (0.16, 1.6)$ million individuals. While the large search sets S_{nb} were used used, with number of searches in the hundreds of thousands, the number of observed scores in the far tails is small: To get reduced uncertainty more searches would be necessary. Missing plots indicate the run is not yet complete.

Figure 86: **Threshold calibration curves** for implementation Y02B executing searches for single-eye enrolled populations $N = (0.16, 1.6, 4)$ million, and two-eye populations of $N = (0.16, 1.6)$ million individuals. While the large search sets S_{nb} were used used, with number of searches in the hundreds of thousands, the number of observed scores in the far tails is small: To get reduced uncertainty more searches would be necessary. Missing plots indicate the run is not yet complete.

Figure 87: **Threshold calibration curves** for implementation Y03A executing searches for single-eye enrolled populations $N = (0.16, 1.6, 4)$ million, and two-eye populations of $N = (0.16, 1.6)$ million individuals. While the large search sets S_{nb} were used used, with number of searches in the hundreds of thousands, the number of observed scores in the far tails is small: To get reduced uncertainty more searches would be necessary. Missing plots indicate the run is not yet complete.

Figure 88: **Threshold calibration curves** for implementation Y03B executing searches for single-eye enrolled populations $N = (0.16, 1.6, 4)$ million, and two-eye populations of $N = (0.16, 1.6)$ million individuals. While the large search sets S_{nb} were used used, with number of searches in the hundreds of thousands, the number of observed scores in the far tails is small: To get reduced uncertainty more searches would be necessary. Missing plots indicate the run is not yet complete.

Appendix D: Effect of Population Size on DET

Figure 89: **Effect of population size** onDETs for implementation I01A executing searches for single-eye enrolled populations $N = (0.16, 1.6, 4)$ million, and two-eye populations of $N = (0.16, 1.6)$ million individuals. The straight lines, which link points of constant threshold, show how the two error rates would vary if a fixed threshold were adopted operationally. Horizontal lines indicate that enrolled population N is influential only on FPIR, via $\text{FPIR}(N_2) = (N_2/N_1)\text{FPIR}(N_1)$. When this relationship is not evident, the implementation may be adjusting scores as a function of N (e.g. as described in [cite Daugman]). The large search sets S_{nb} are used. Missing plots indicate the run is not yet complete.

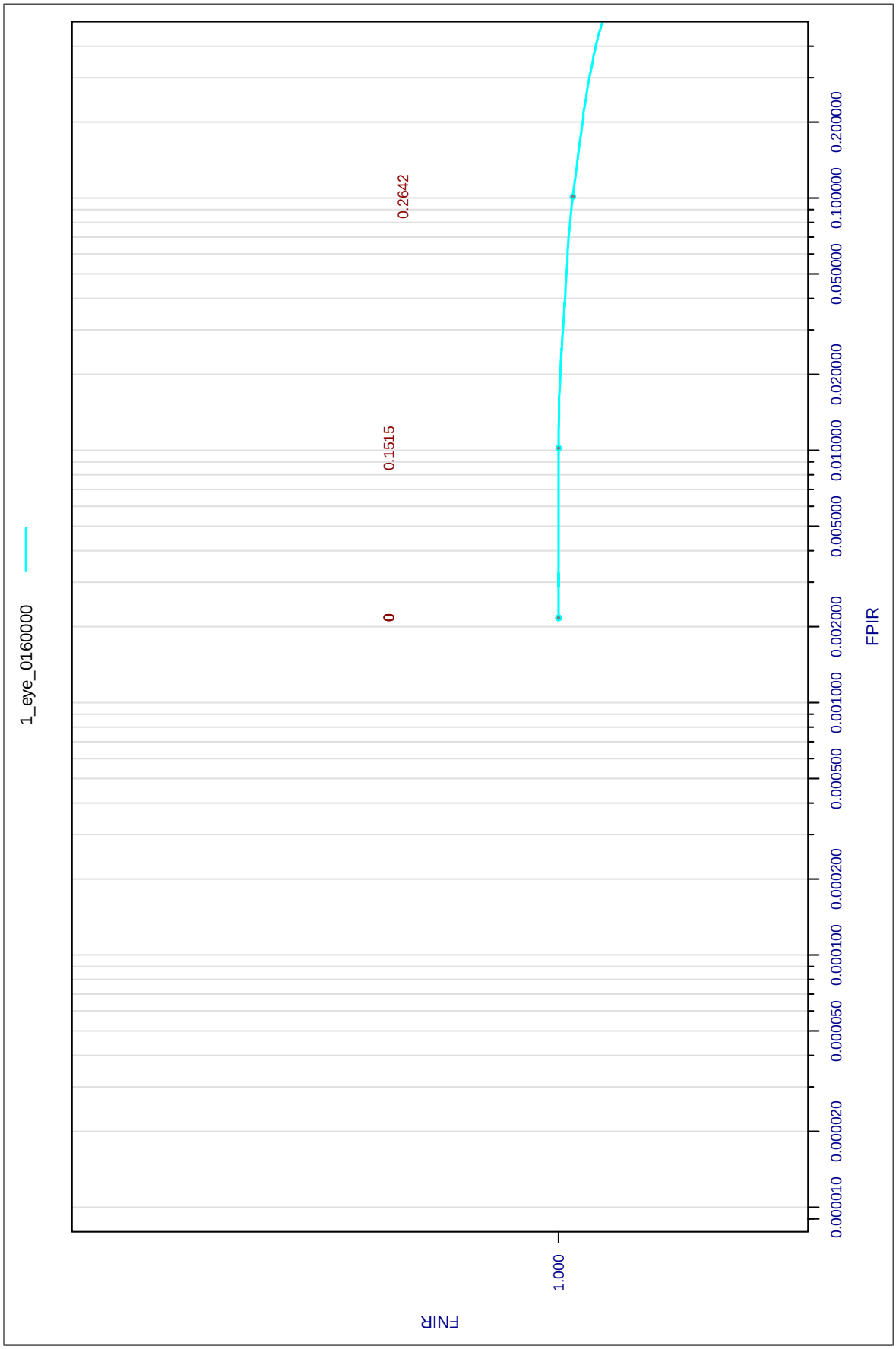

Figure 90: **Effect of population size** onDETs for implementation I02A executing searches for single-eye enrolled populations $N = (0.16, 1.6, 4)$ million, and two-eye populations of $N = (0.16, 1.6)$ million individuals. The straight lines, which link points of constant threshold, show how the two error rates would vary if a fixed threshold were adopted operationally. Horizontal lines indicate that enrolled population N is influential only on FPIR, via $\text{FPIR}(N_2) = (N_2/N_1)\text{FPIR}(N_1)$. When this relationship is not evident, the implementation may be adjusting scores as a function of N (e.g. as described in [cite Daugman]). The large search sets $S_{n,b}$ are used. Missing plots indicate the run is not yet complete.

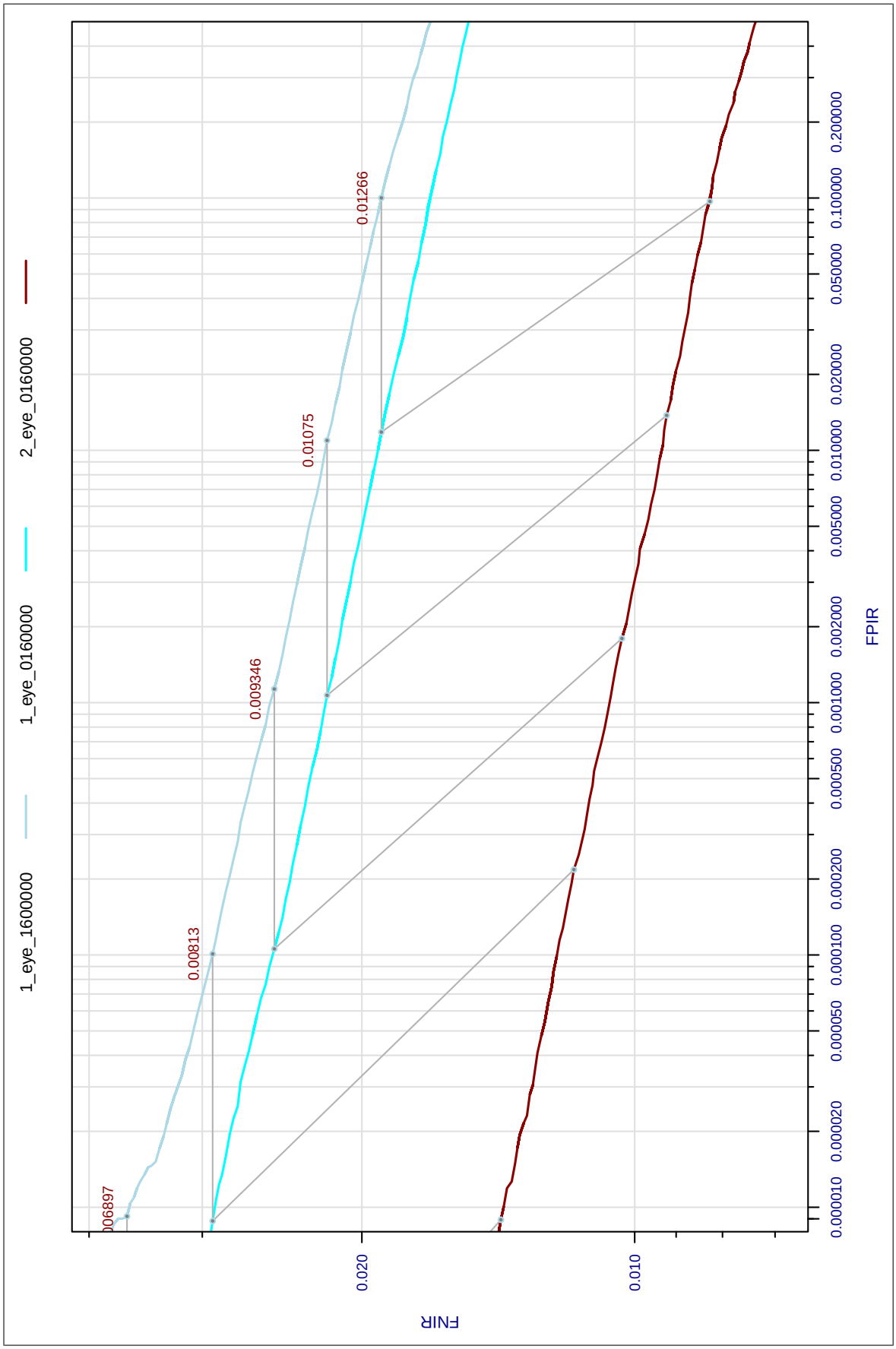

Figure 91: **Effect of population size** onDETs for implementation N02A executing searches for single-eye enrolled populations $N = (0.16, 1.6, 4)$ million, and two-eye populations of $N = (0.16, 1.6)$ million individuals. The straight lines, which link points of constant threshold, show how the two error rates would vary if a fixed threshold were adopted operationally. Horizontal lines indicate that enrolled population N is influential only on FPIR, via $\text{FPIR}(N_2) = (N_2/N_1)\text{FPIR}(N_1)$. When this relationship is not evident, the implementation may be adjusting scores as a function of N (e.g. as described in [cite Daugman]). The large search sets $S_{n,b}$ are used. Missing plots indicate the run is not yet complete.

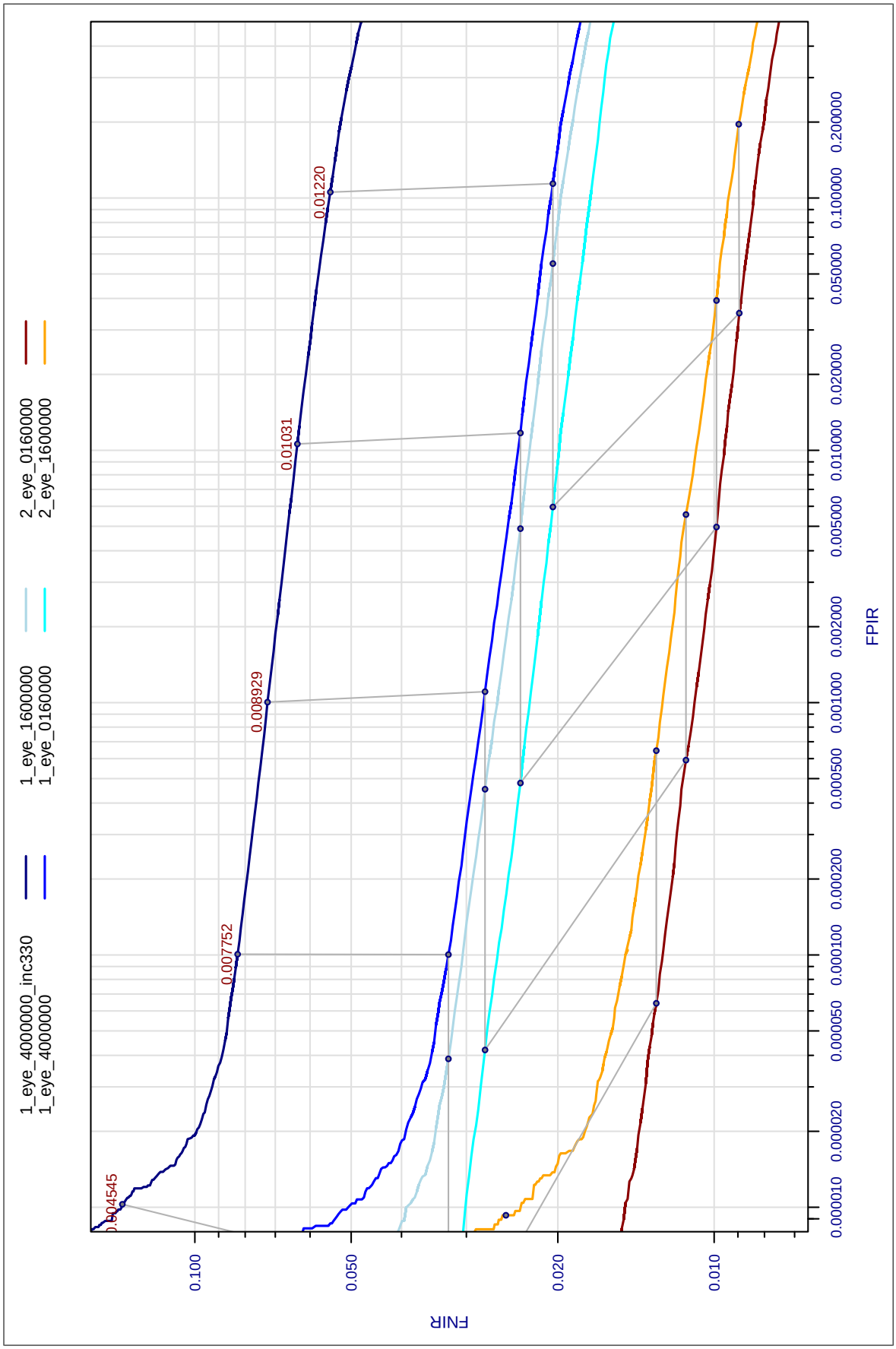

Figure 92: **Effect of population size** onDETs for implementation N02B executing searches for single-eye enrolled populations $N = (0.16, 1.6, 4)$ million, and two-eye populations of $N = (0.16, 1.6)$ million individuals. The straight lines, which link points of constant threshold, show how the two error rates would vary if a fixed threshold were adopted operationally. Horizontal lines indicate that enrolled population N is influential only on FPIR, via $\text{FPIR}(N_2) = (N_2/N_1)\text{FPIR}(N_1)$. When this relationship is not evident, the implementation may be adjusting scores as a function of N (e.g. as described in [cite Daugman]). The large search sets S_{nb} are used. Missing plots indicate the run is not yet complete.

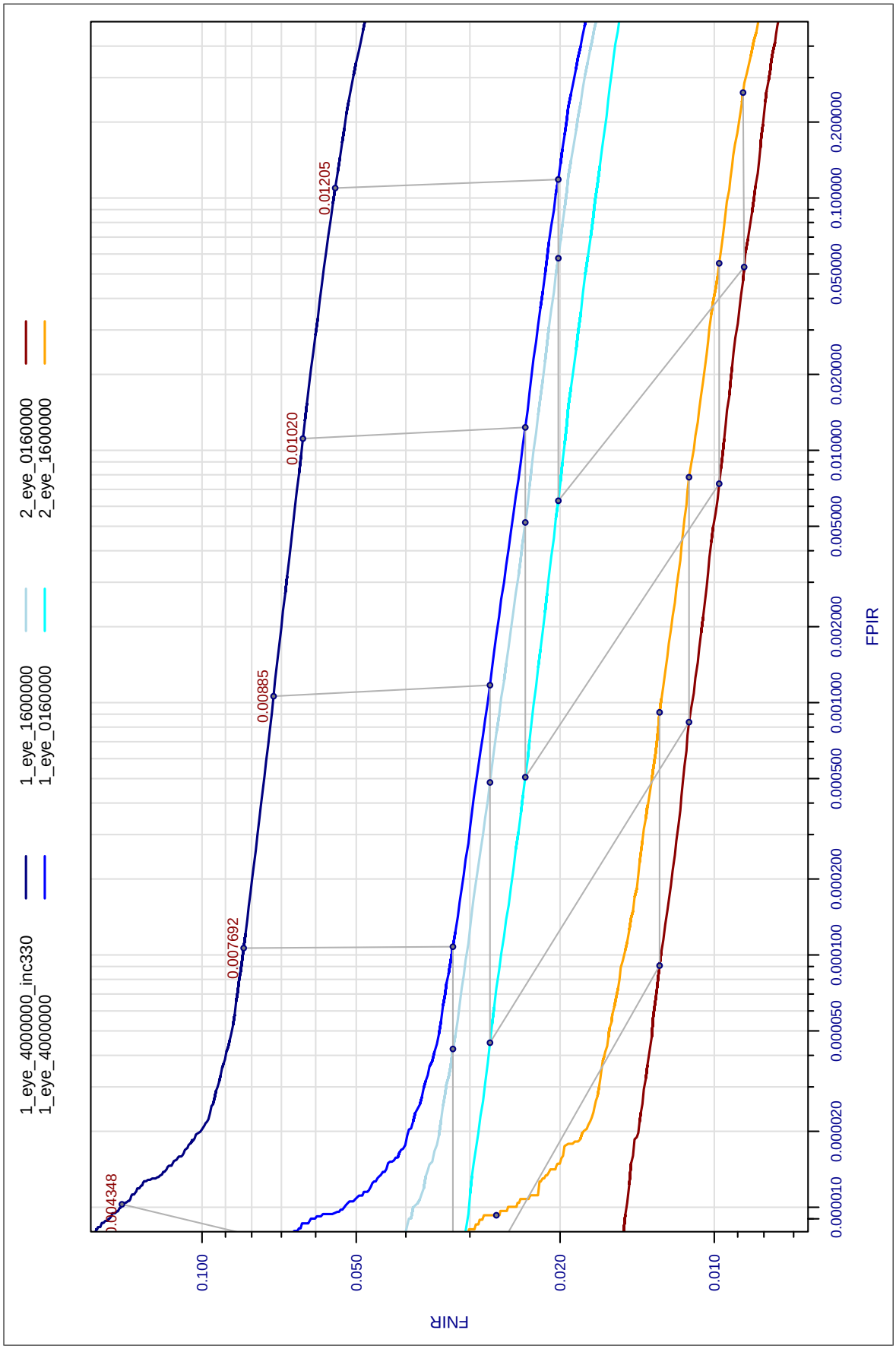

Figure 93: **Effect of population size** onDETs for implementation N03A executing searches for single-eye enrolled populations $N = (0.16, 1.6, 4)$ million, and two-eye populations of $N = (0.16, 1.6)$ million individuals. The straight lines, which link points of constant threshold, show how the two error rates would vary if a fixed threshold were adopted operationally. Horizontal lines indicate that enrolled population N is influential only on FPIR, via $\text{FPIR}(N_2) = (N_2/N_1)\text{FPIR}(N_1)$. When this relationship is not evident, the implementation may be adjusting scores as a function of N (e.g. as described in [cite Daugman]). The large search sets S_{nb} are used. Missing plots indicate the run is not yet complete.

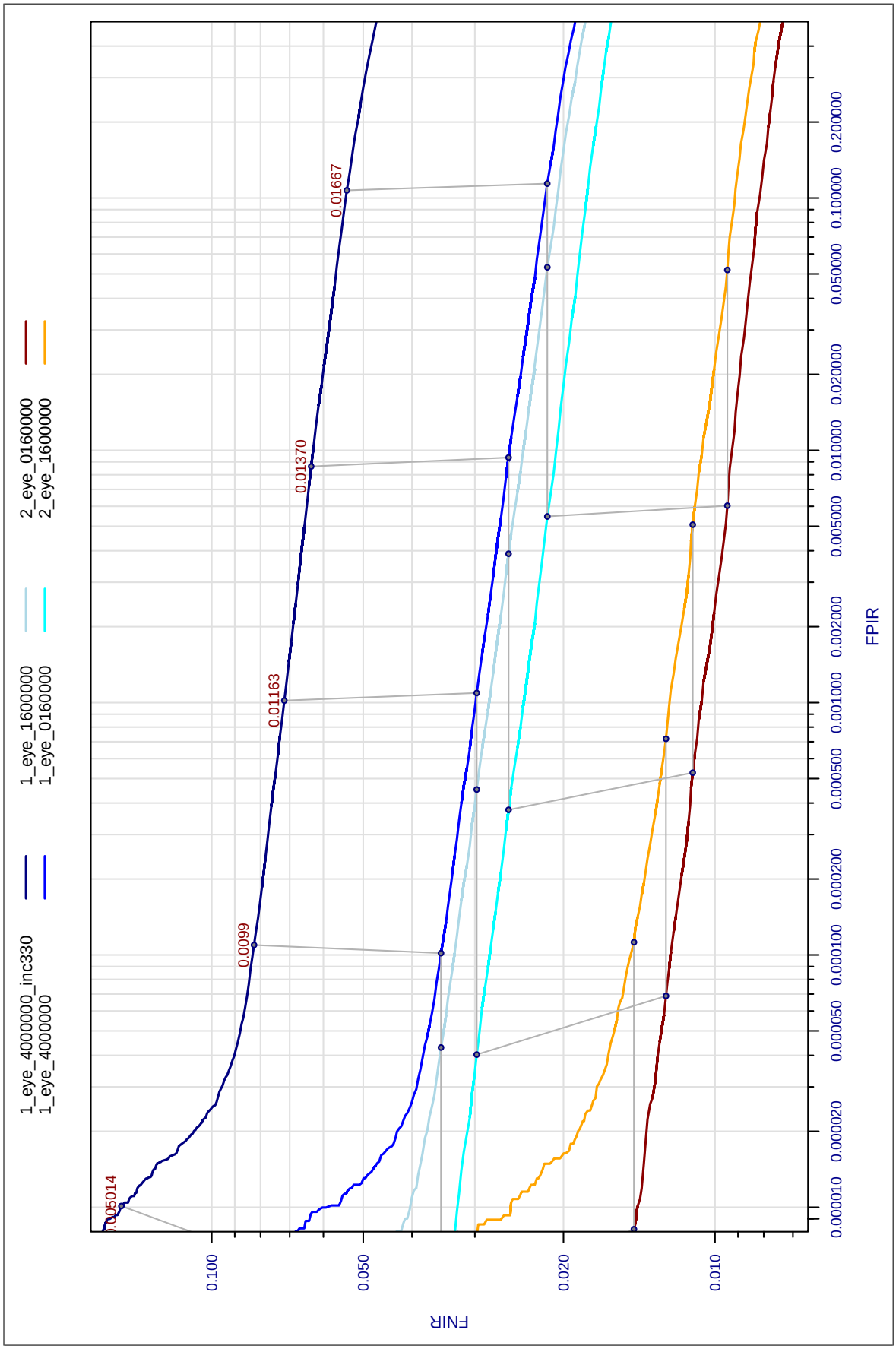

Figure 94: Effect of population size onDETs for implementation N03B executing searches for single-eye enrolled populations $N = (0.16, 1.6, 4)$ million, and two-eye populations of $N = (0.16, 1.6)$ million individuals. The straight lines, which link points of constant threshold, show how the two error rates would vary if a fixed threshold were adopted operationally. Horizontal lines indicate that enrolled population N is influential only on FPIR, via $\text{FPIR}(N_2) = (N_2/N_1)\text{FPIR}(N_1)$. When this relationship is not evident, the implementation may be adjusting scores as a function of N (e.g. as described in [cite Daugman]). The large search sets S_{nb} are used. Missing plots indicate the run is not yet complete.

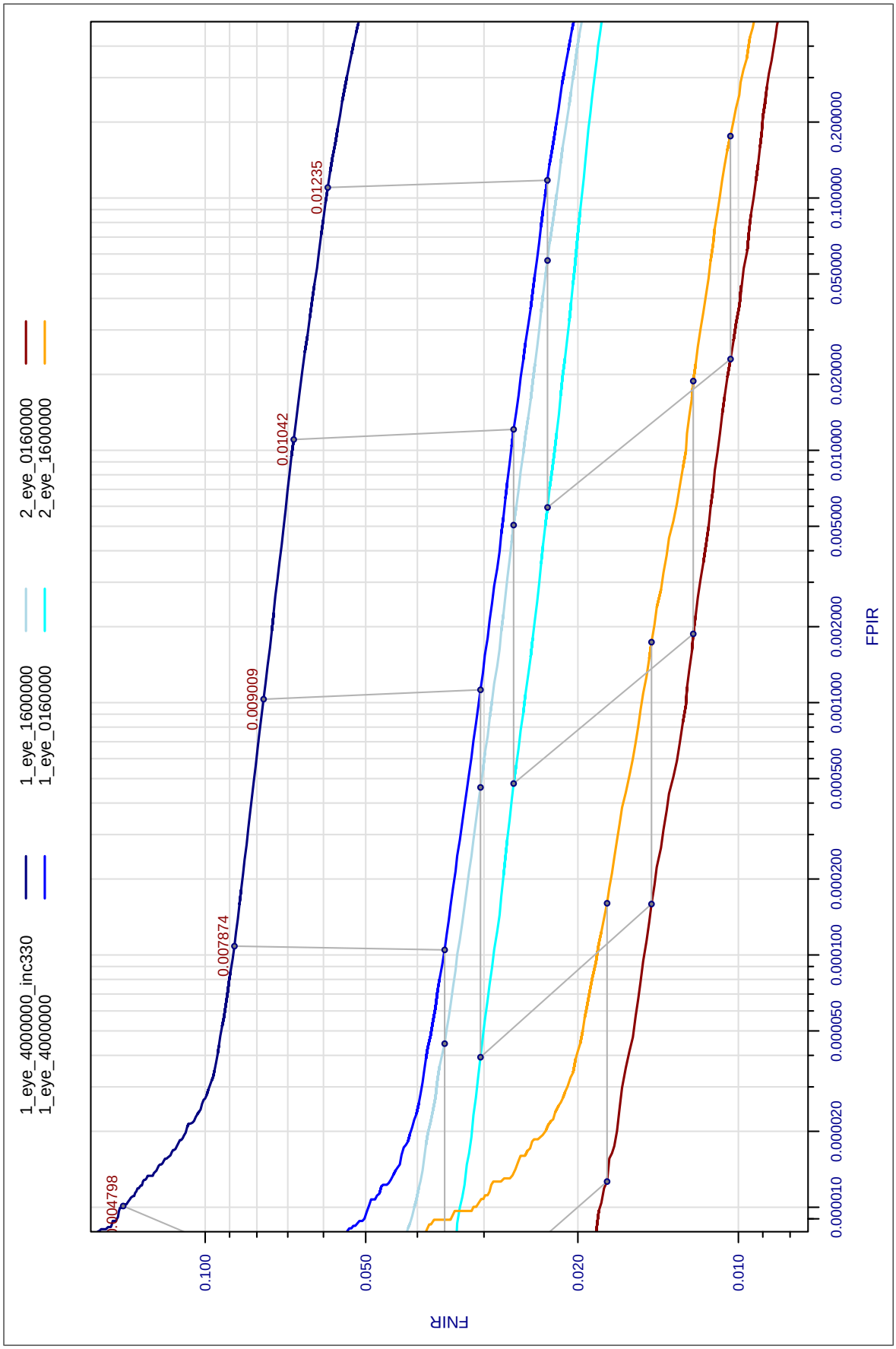

Figure 95: Effect of population size onDETs for implementation N04A executing searches for single-eye enrolled populations $N = (0.16, 1.6, 4)$ million, and two-eye populations of $N = (0.16, 1.6)$ million individuals. The straight lines, which link points of constant threshold, show how the two error rates would vary if a fixed threshold were adopted operationally. Horizontal lines indicate that enrolled population N is influential only on FPIR, via $\text{FPIR}(N_2) = (N_2/N_1)\text{FPIR}(N_1)$. When this relationship is not evident, the implementation may be adjusting scores as a function of N (e.g. as described in [cite Daugman]). The large search sets S_{nb} are used. Missing plots indicate the run is not yet complete.

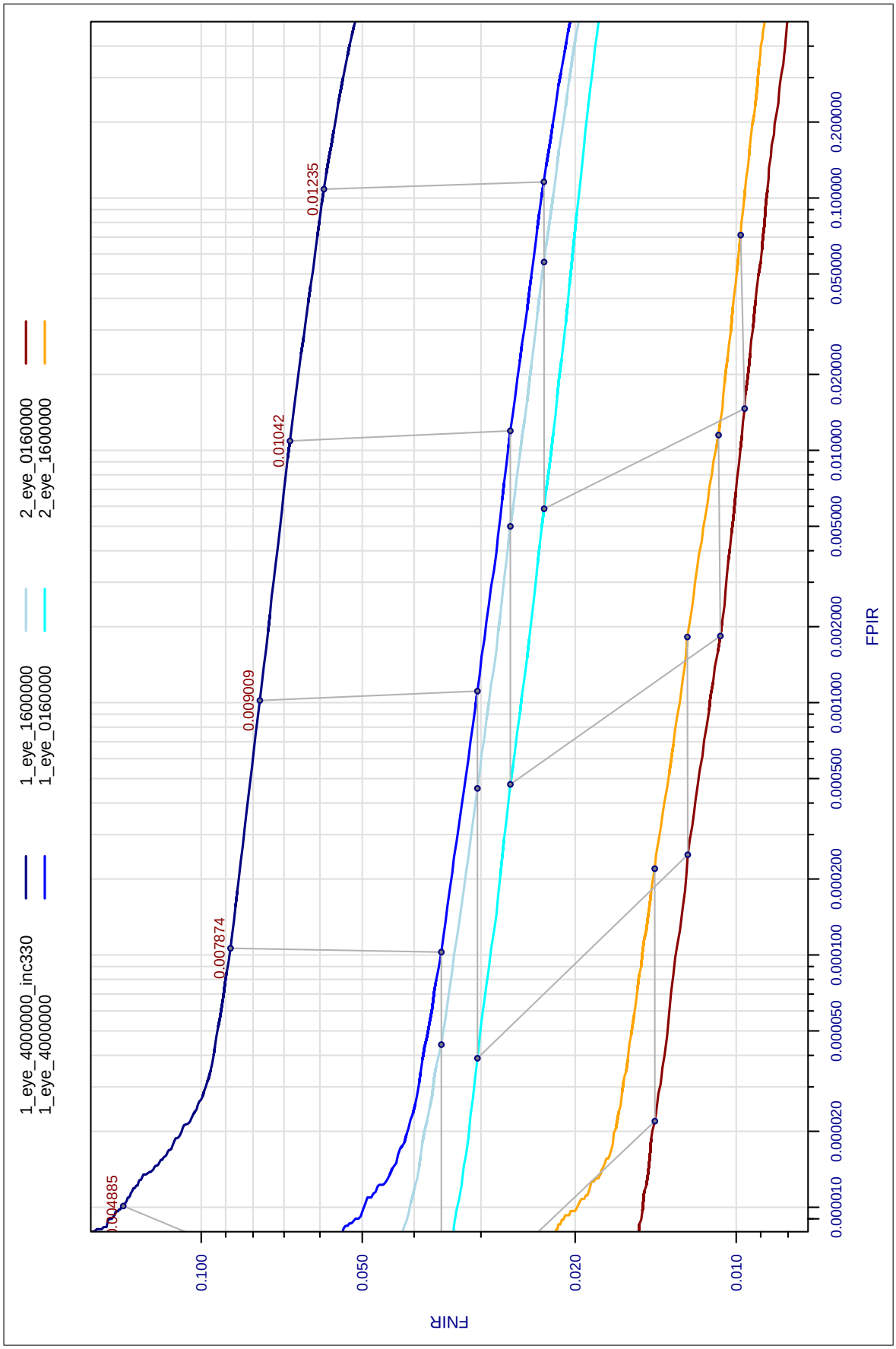

Figure 96: **Effect of population size** onDETs for implementation N11A executing searches for single-eye enrolled populations $N = (0.16, 1.6, 4)$ million, and two-eye populations of $N = (0.16, 1.6)$ million individuals. The straight lines, which link points of constant threshold, show how the two error rates would vary if a fixed threshold were adopted operationally. Horizontal lines indicate that enrolled population N is influential only on FPIR, via $\text{FPIR}(N_2) = (N_2/N_1)\text{FPIR}(N_1)$. When this relationship is not evident, the implementation may be adjusting scores as a function of N (e.g. as described in [cite Daugman]). The large search sets S_{nb} are used. Missing plots indicate the run is not yet complete.

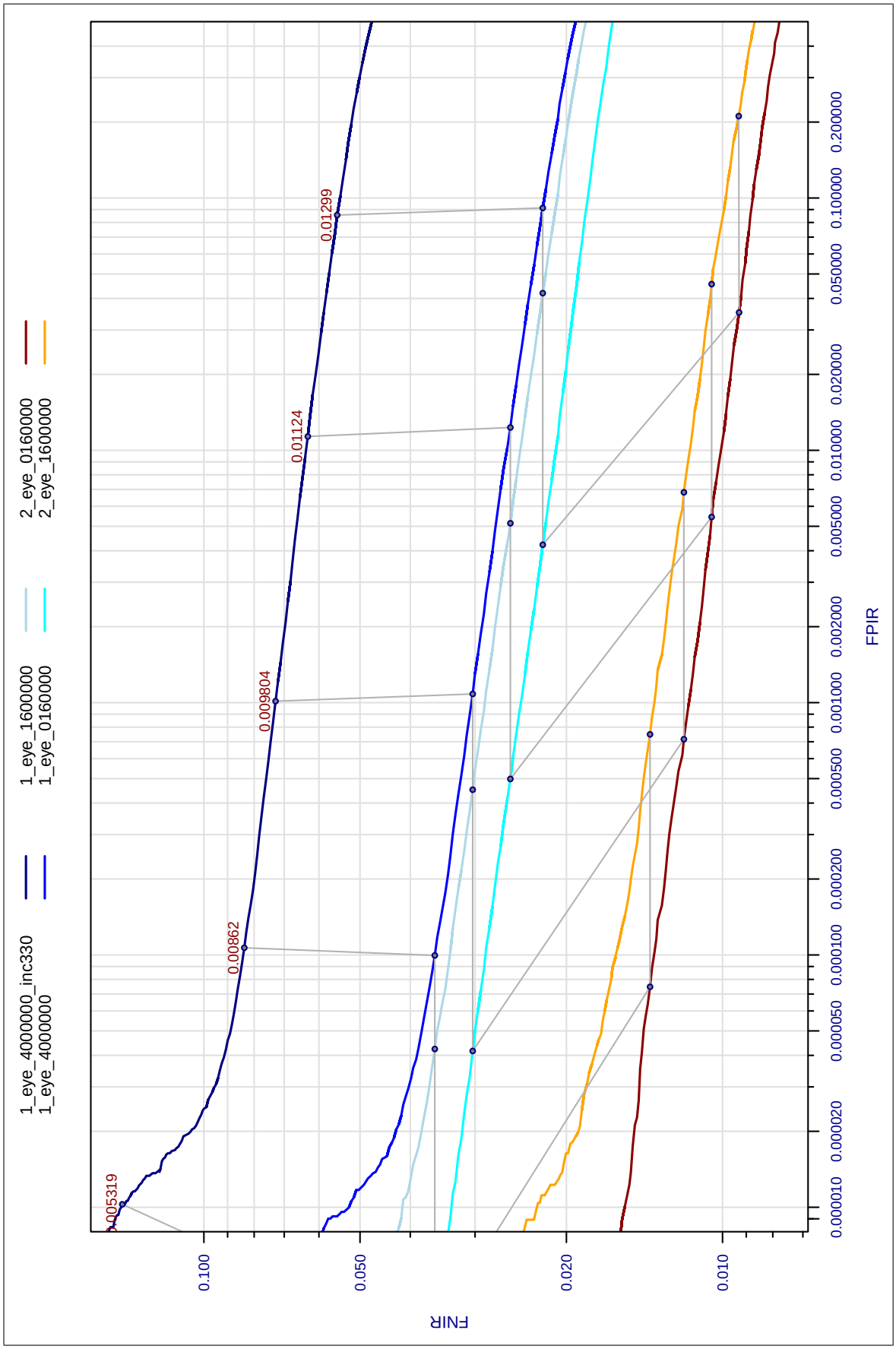

Figure 97: **Effect of population size** onDETs for implementation N11B executing searches for single-eye enrolled populations $N = (0.16, 1.6, 4)$ million, and two-eye populations of $N = (0.16, 1.6)$ million individuals. The straight lines, which link points of constant threshold, show how the two error rates would vary if a fixed threshold were adopted operationally. Horizontal lines indicate that enrolled population N is influential only on FPIR, via $\text{FPIR}(N_2) = (N_2/N_1)\text{FPIR}(N_1)$. When this relationship is not evident, the implementation may be adjusting scores as a function of N (e.g. as described in [cite Daugman]). The large search sets S_{nb} are used. Missing plots indicate the run is not yet complete.

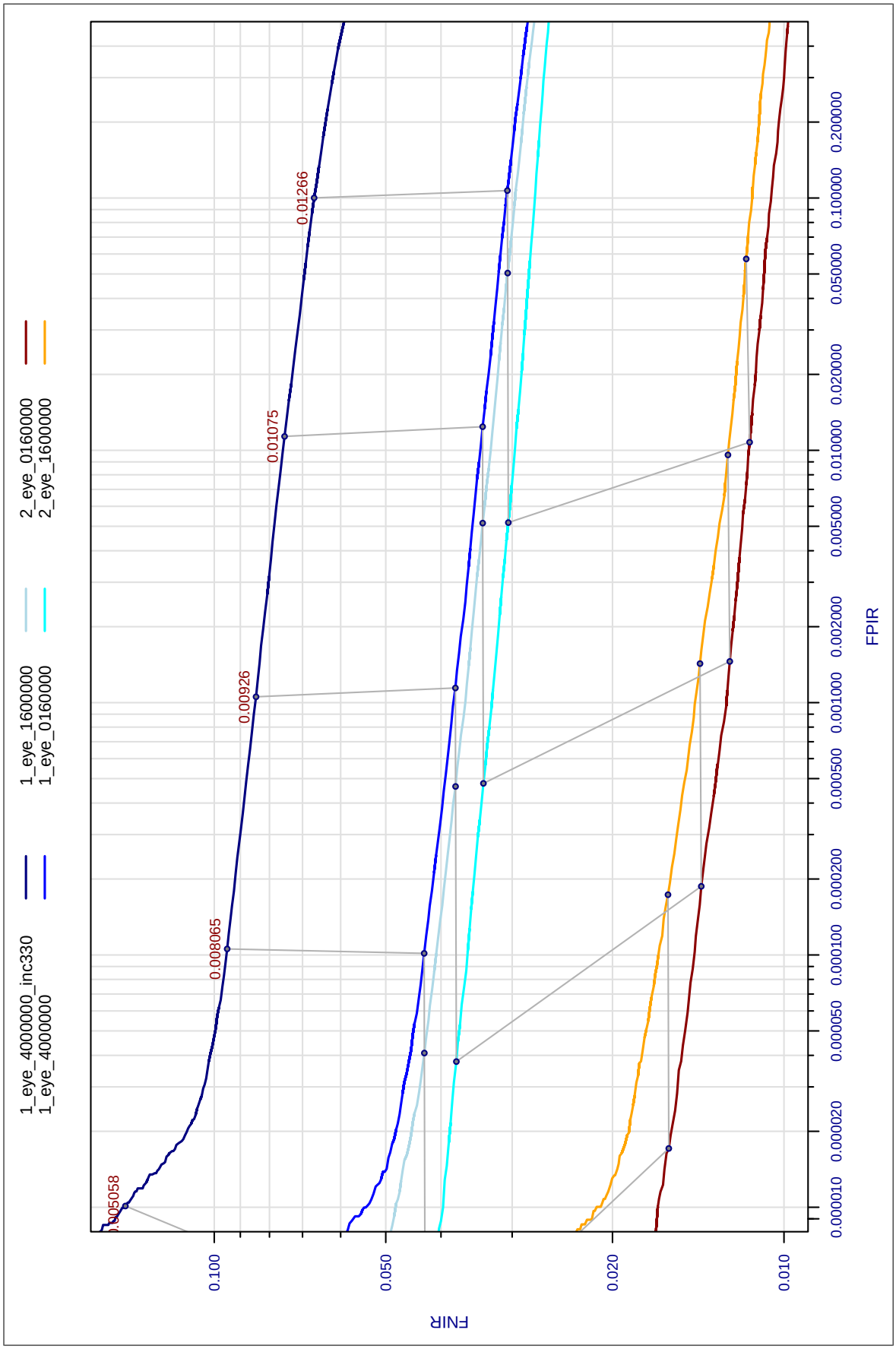

Figure 98: **Effect of population size** onDETs for implementation N12A executing searches for single-eye enrolled populations $N = (0.16, 1.6, 4)$ million, and two-eye populations of $N = (0.16, 1.6)$ million individuals. The straight lines, which link points of constant threshold, show how the two error rates would vary if a fixed threshold were adopted operationally. Horizontal lines indicate that enrolled population N is influential only on FPIR, via $\text{FPIR}(N_2) = (N_2/N_1)\text{FPIR}(N_1)$. When this relationship is not evident, the implementation may be adjusting scores as a function of N (e.g. as described in [cite Daugman]). The large search sets $S_{n,b}$ are used. Missing plots indicate the run is not yet complete.

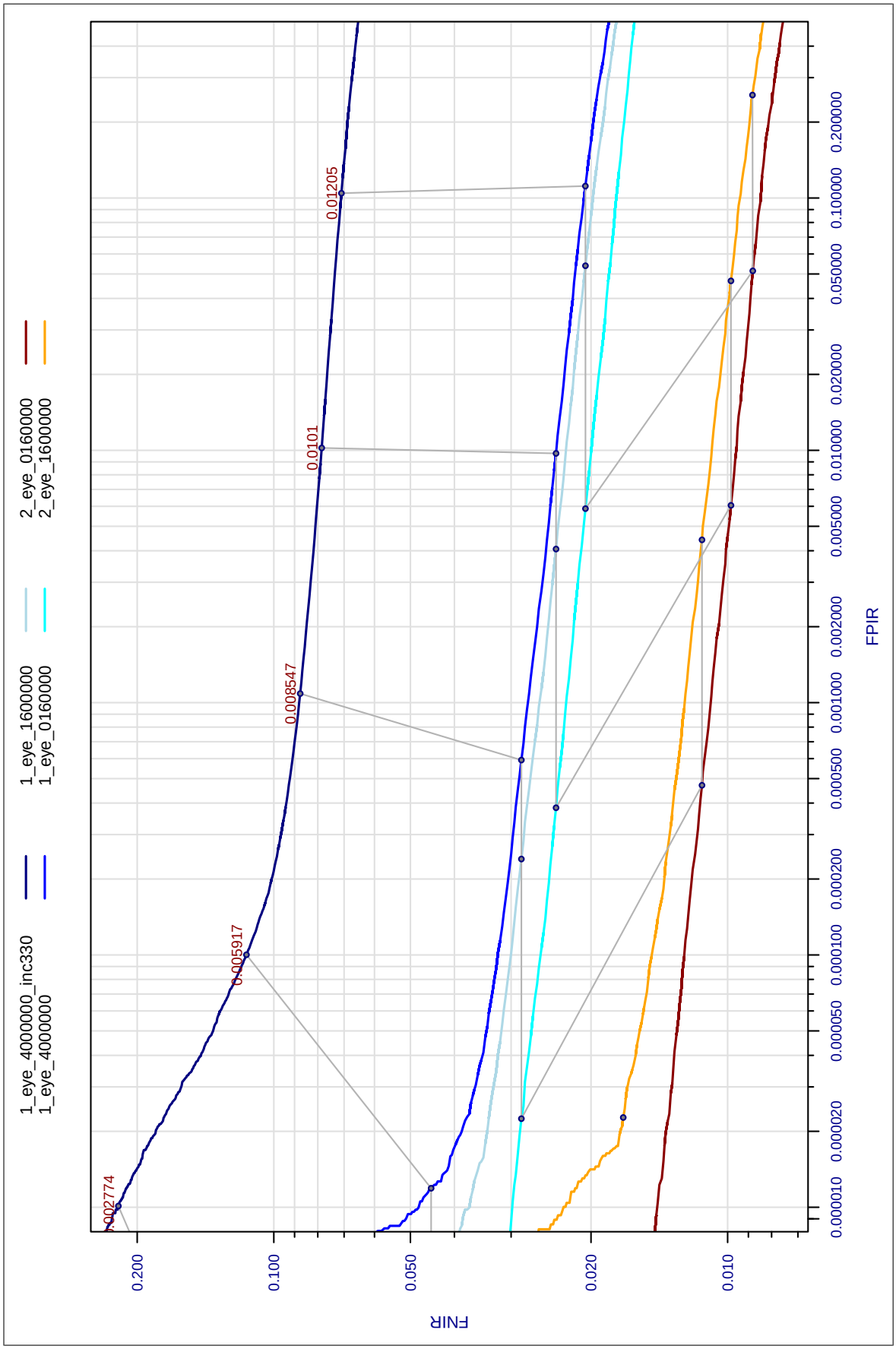

Figure 99: Effect of population size onDETs for implementation N12B executing searches for single-eye enrolled populations $N = (0.16, 1.6, 4)$ million, and two-eye populations of $N = (0.16, 1.6)$ million individuals. The straight lines, which link points of constant threshold, show how the two error rates would vary if a fixed threshold were adopted operationally. Horizontal lines indicate that enrolled population N is influential only on FPIR, via $\text{FPIR}(N_2) = (N_2/N_1)\text{FPIR}(N_1)$. When this relationship is not evident, the implementation may be adjusting scores as a function of N (e.g. as described in [cite Daugman]). The large search sets $S_{n,b}$ are used. Missing plots indicate the run is not yet complete.

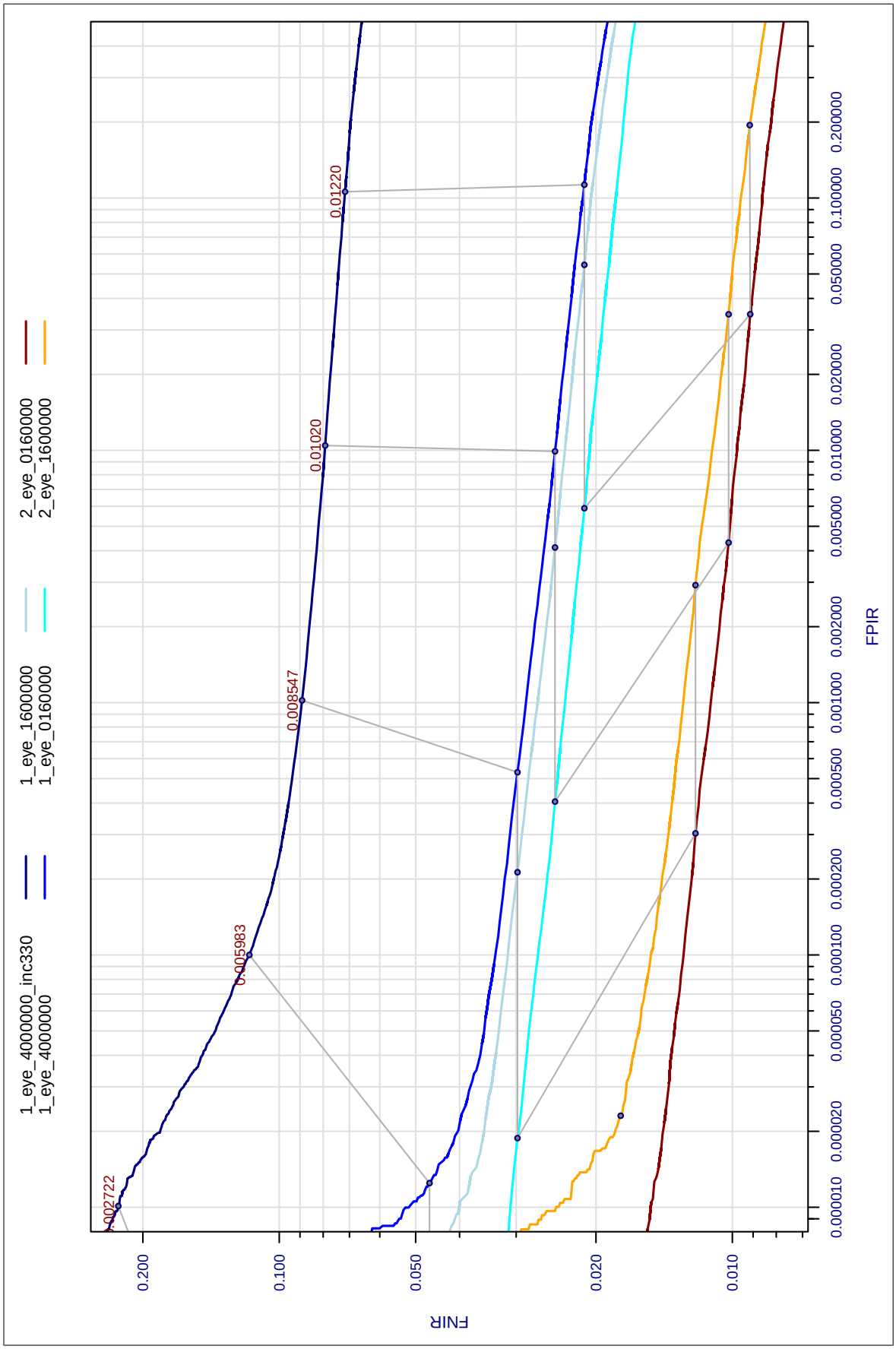

Figure 100: **Effect of population size** ONDETS for implementation N13B executing searches for single-eye enrolled populations $N = (0.16, 1.6, 4)$ million, and two-eye populations of $N = (0.16, 1.6)$ million individuals. The straight lines, which link points of constant threshold, show how the two error rates would vary if a fixed threshold were adopted operationally. Horizontal lines indicate that enrolled population N is influential only on FPIR, via $\text{FPIR}(N_2) = (N_2/N_1)\text{FPIR}(N_1)$. When this relationship is not evident, the implementation may be adjusting scores as a function of N (e.g. as described in [cite Daugman]). The large search sets S_{nb} are used. Missing plots indicate the run is not yet complete.

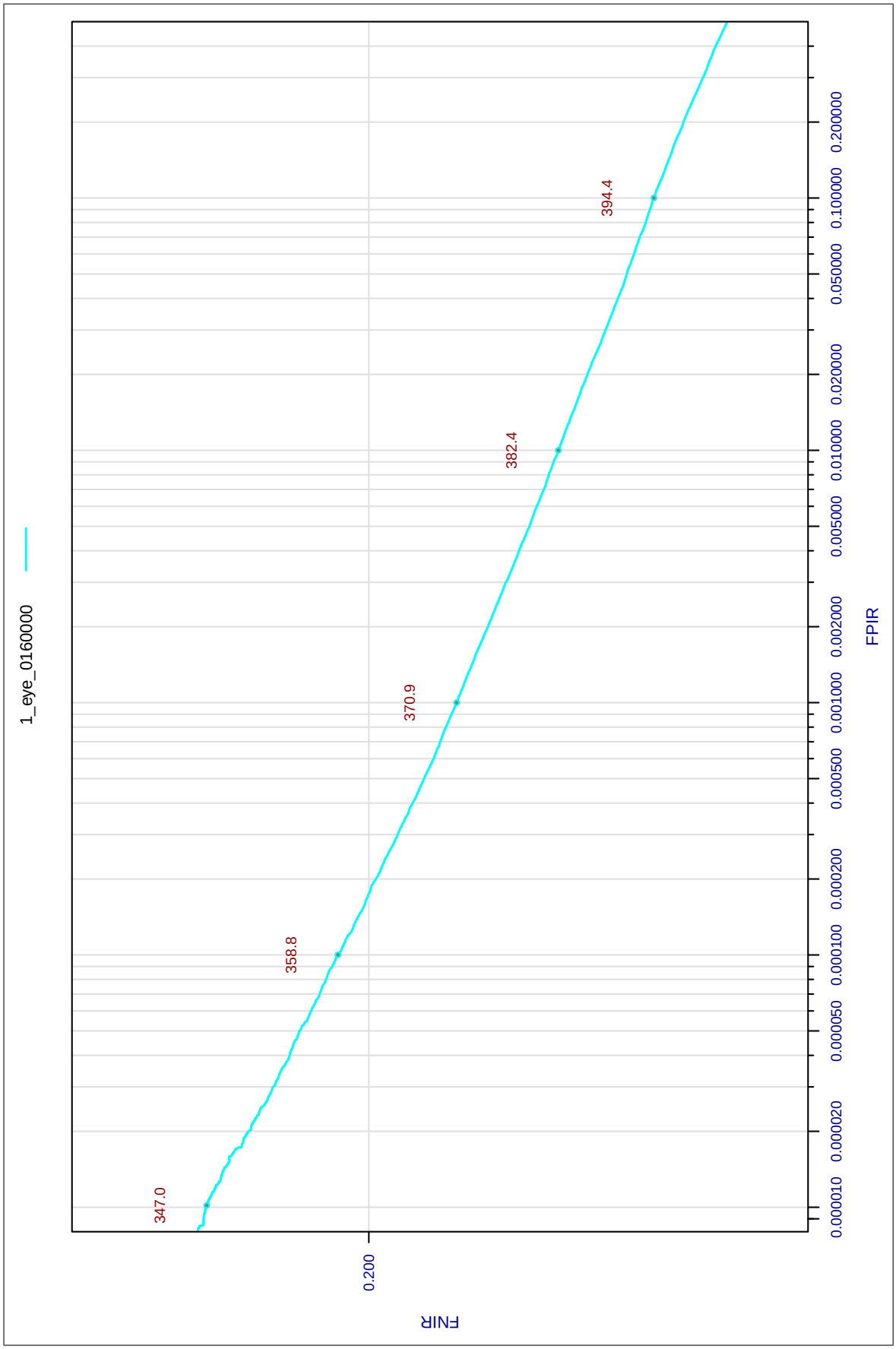

Figure 101: **Effect of population size** ONDETS for implementation P02A executing searches for single-eye enrolled populations $N = (0.16, 1.6, 4)$ million, and two-eye populations of $N = (0.16, 1.6)$ million individuals. The straight lines, which link points of constant threshold, show how the two error rates would vary if a fixed threshold were adopted operationally. Horizontal lines indicate that enrolled population N is influential only on FPIR, via $\text{FPIR}(N_2) = (N_2/N_1)\text{FPIR}(N_1)$. When this relationship is not evident, the implementation may be adjusting scores as a function of N (e.g. as described in [cite Daugman]). The large search sets $S_{n,b}$ are used. Missing plots indicate the run is not yet complete.

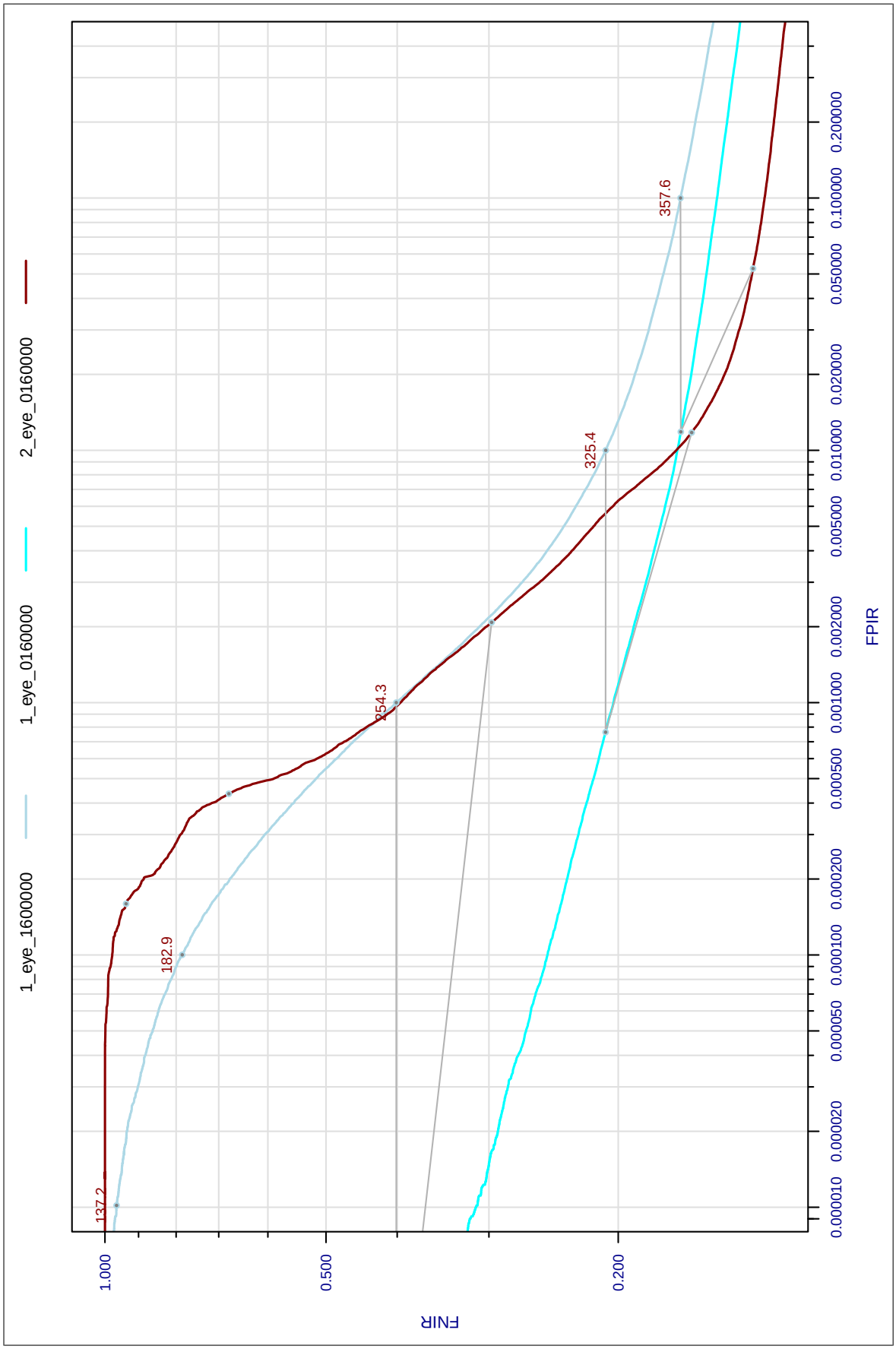

Figure 102: **Effect of population size** onDETs for implementation P11A executing searches for single-eye enrolled populations $N = (0.16, 1.6, 4)$ million, and two-eye populations of $N = (0.16, 1.6)$ million individuals. The straight lines, which link points of constant threshold, show how the two error rates would vary if a fixed threshold were adopted operationally. Horizontal lines indicate that enrolled population N is influential only on FPIR, via $\text{FPIR}(N_2) = (N_2/N_1)\text{FPIR}(N_1)$. When this relationship is not evident, the implementation may be adjusting scores as a function of N (e.g. as described in [cite Daugman]). The large search sets S_{nb} are used. Missing plots indicate the run is not yet complete.

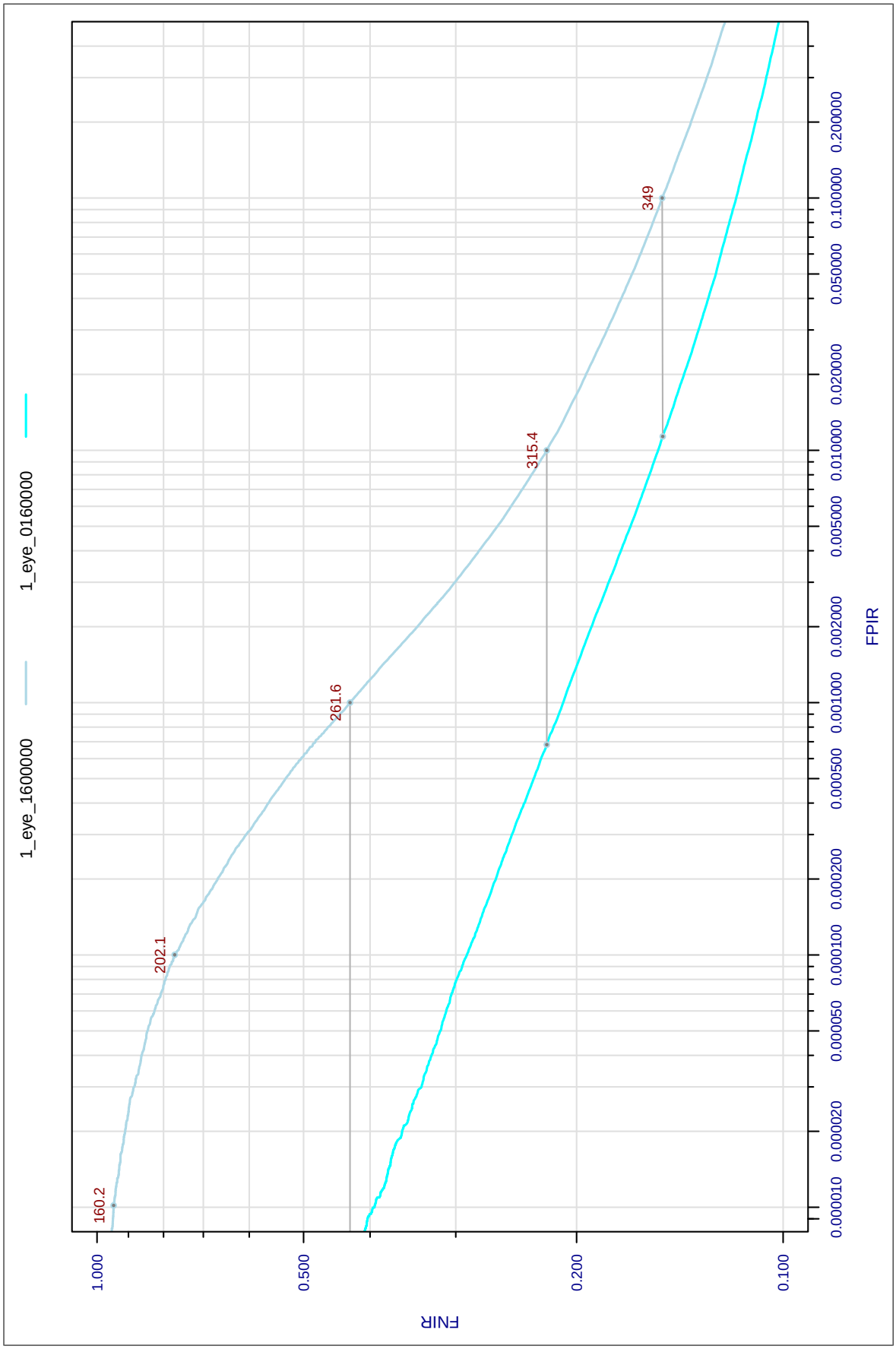

Figure 103: **Effect of population size** onDETs for implementation P11B executing searches for single-eye enrolled populations $N = (0.16, 1.6, 4)$ million, and two-eye populations of $N = (0.16, 1.6)$ million individuals. The straight lines, which link points of constant threshold, show how the two error rates would vary if a fixed threshold were adopted operationally. Horizontal lines indicate that enrolled population N is influential only on FPIR, via $\text{FPIR}(N_2) = (N_2/N_1)\text{FPIR}(N_1)$. When this relationship is not evident, the implementation may be adjusting scores as a function of N (e.g. as described in [cite Daugman]). The large search sets $S_{n,b}$ are used. Missing plots indicate the run is not yet complete.

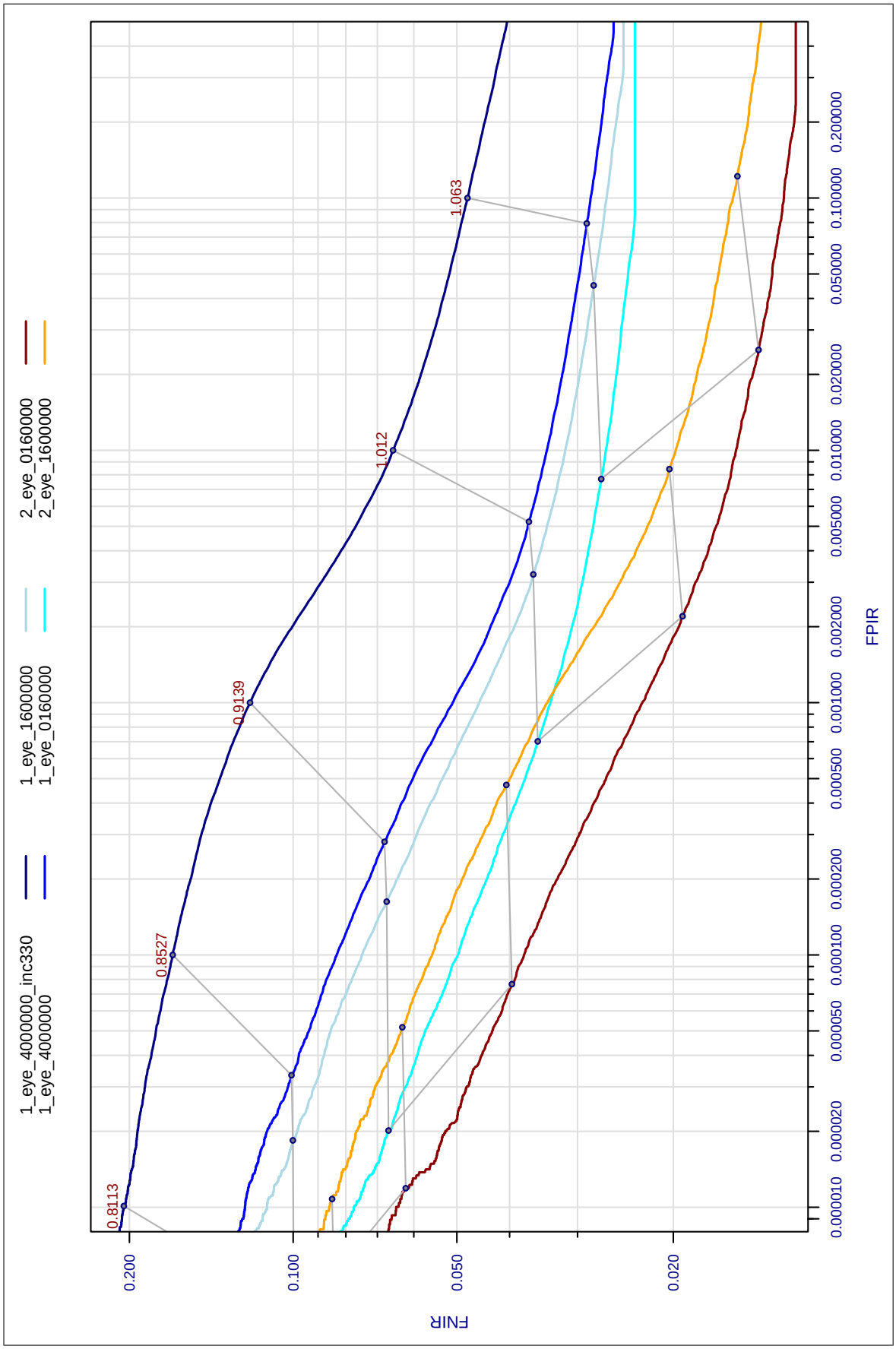

Figure 104: **Effect of population size** on DETs for implementation Q02A executing searches for single-eye enrolled populations $N = (0.16, 1.6, 4)$ million, and two-eye populations of $N = (0.16, 1.6)$ million individuals. The straight lines, which link points of constant threshold, show how the two error rates would vary if a fixed threshold were adopted operationally. Horizontal lines indicate that enrolled population N is influential only on FPIR, via $\text{FPIR}(N_2) = (N_2/N_1)\text{FPIR}(N_1)$. When this relationship is not evident, the implementation may be adjusting scores as a function of N (e.g. as described in [cite Daugman]). The large search sets S_{nb} are used. Missing plots indicate the run is not yet complete.

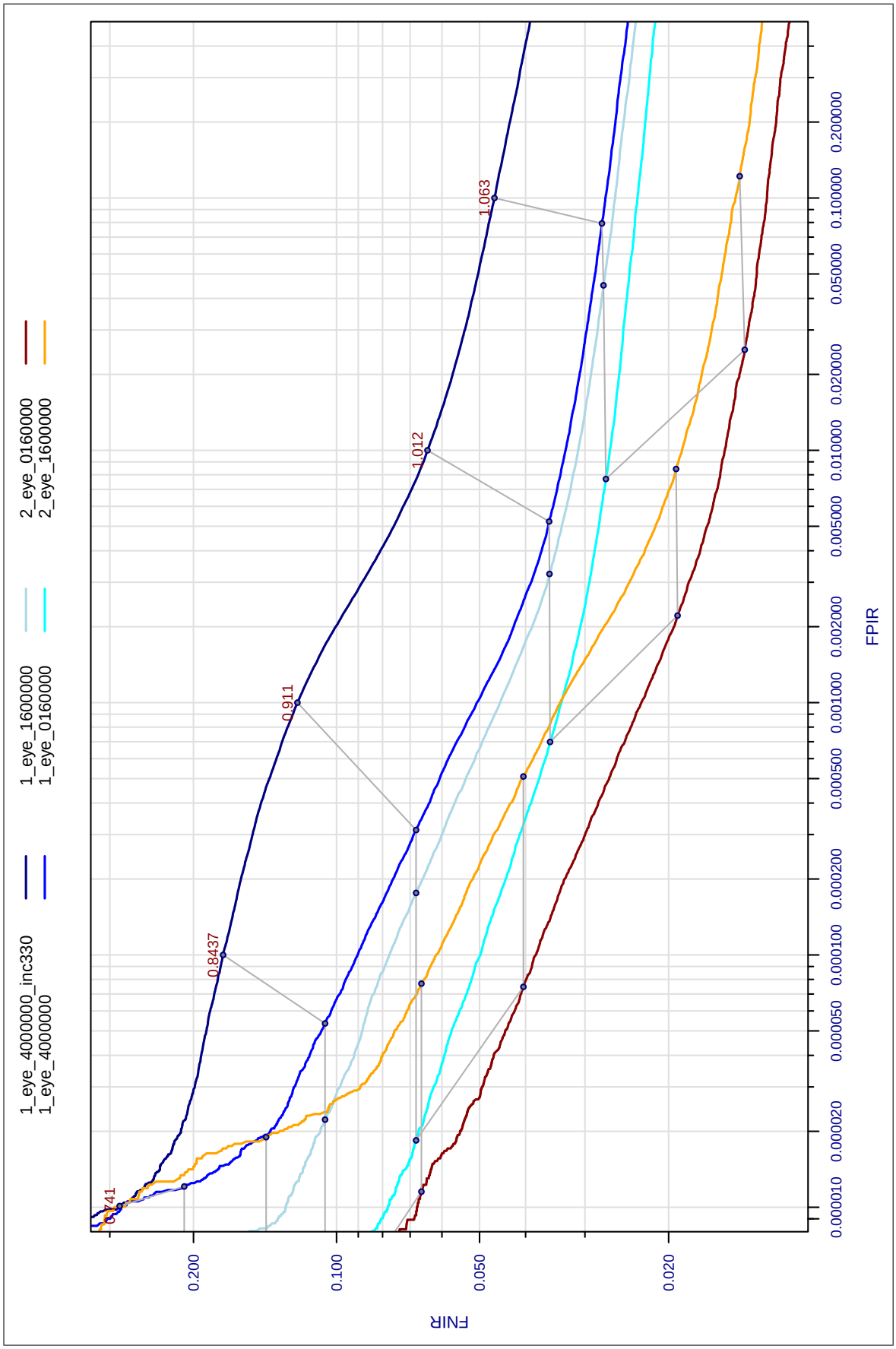

Figure 105: **Effect of population size** onDETs for implementation Q02B executing searches for single-eye enrolled populations $N = (0.16, 1.6, 4)$ million, and two-eye populations of $N = (0.16, 1.6)$ million individuals. The straight lines, which link points of constant threshold, show how the two error rates would vary if a fixed threshold were adopted operationally. Horizontal lines indicate that enrolled population N is influential only on FPIR, via $\text{FPIR}(N_2) = (N_2/N_1)\text{FPIR}(N_1)$. When this relationship is not evident, the implementation may be adjusting scores as a function of N (e.g. as described in [cite Daugman]). The large search sets S_{nb} are used. Missing plots indicate the run is not yet complete.

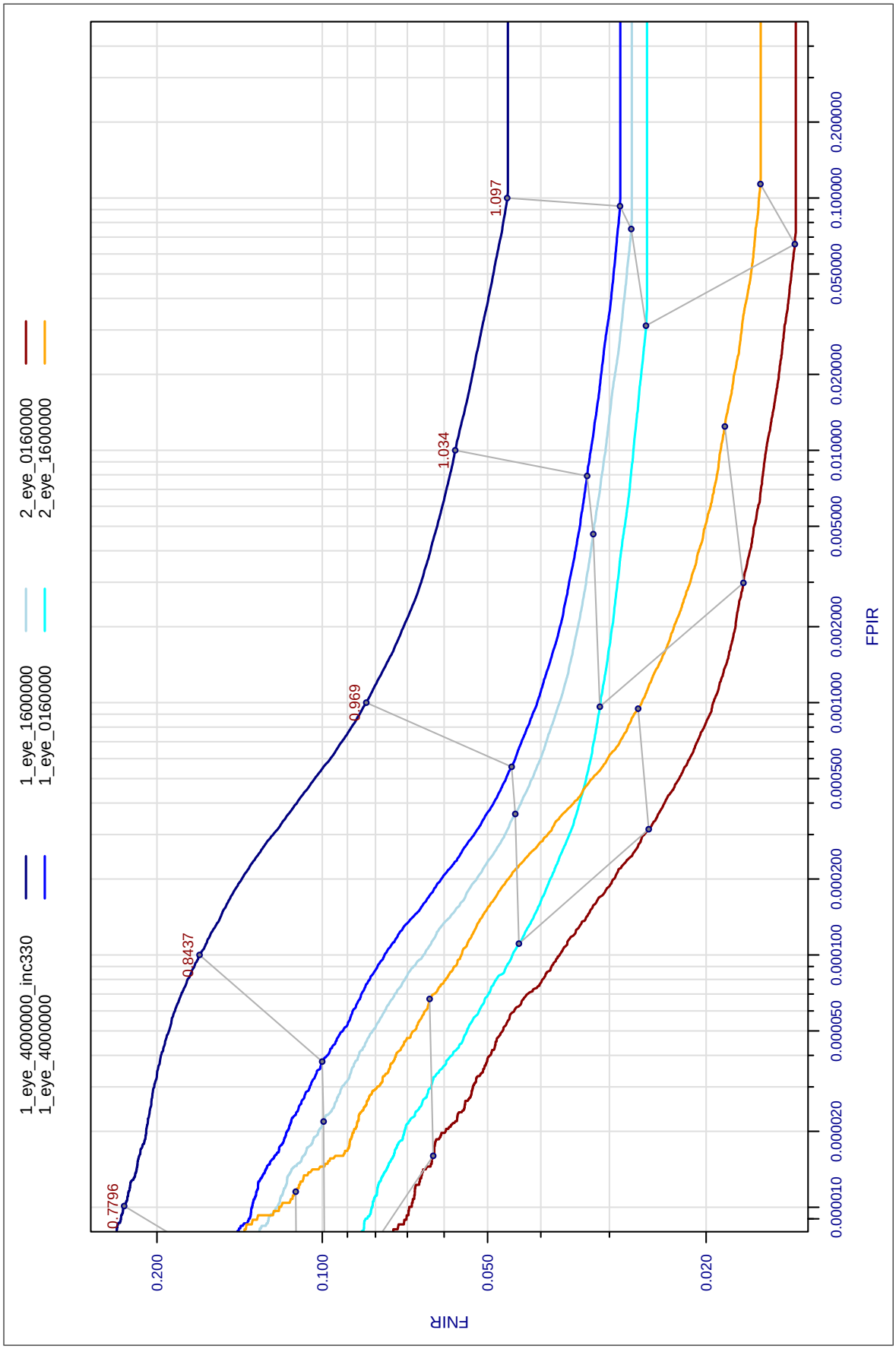

Figure 106: **Effect of population size** onDETs for implementation Q03A executing searches for single-eye enrolled populations $N = (0.16, 1.6, 4)$ million, and two-eye populations of $N = (0.16, 1.6)$ million individuals. The straight lines, which link points of constant threshold, show how the two error rates would vary if a fixed threshold were adopted operationally. Horizontal lines indicate that enrolled population N is influential only on FPIR, via $\text{FPIR}(N_2) = (N_2/N_1)\text{FPIR}(N_1)$. When this relationship is not evident, the implementation may be adjusting scores as a function of N (e.g. as described in [cite Daugman]). The large search sets S_{nb} are used. Missing plots indicate the run is not yet complete.

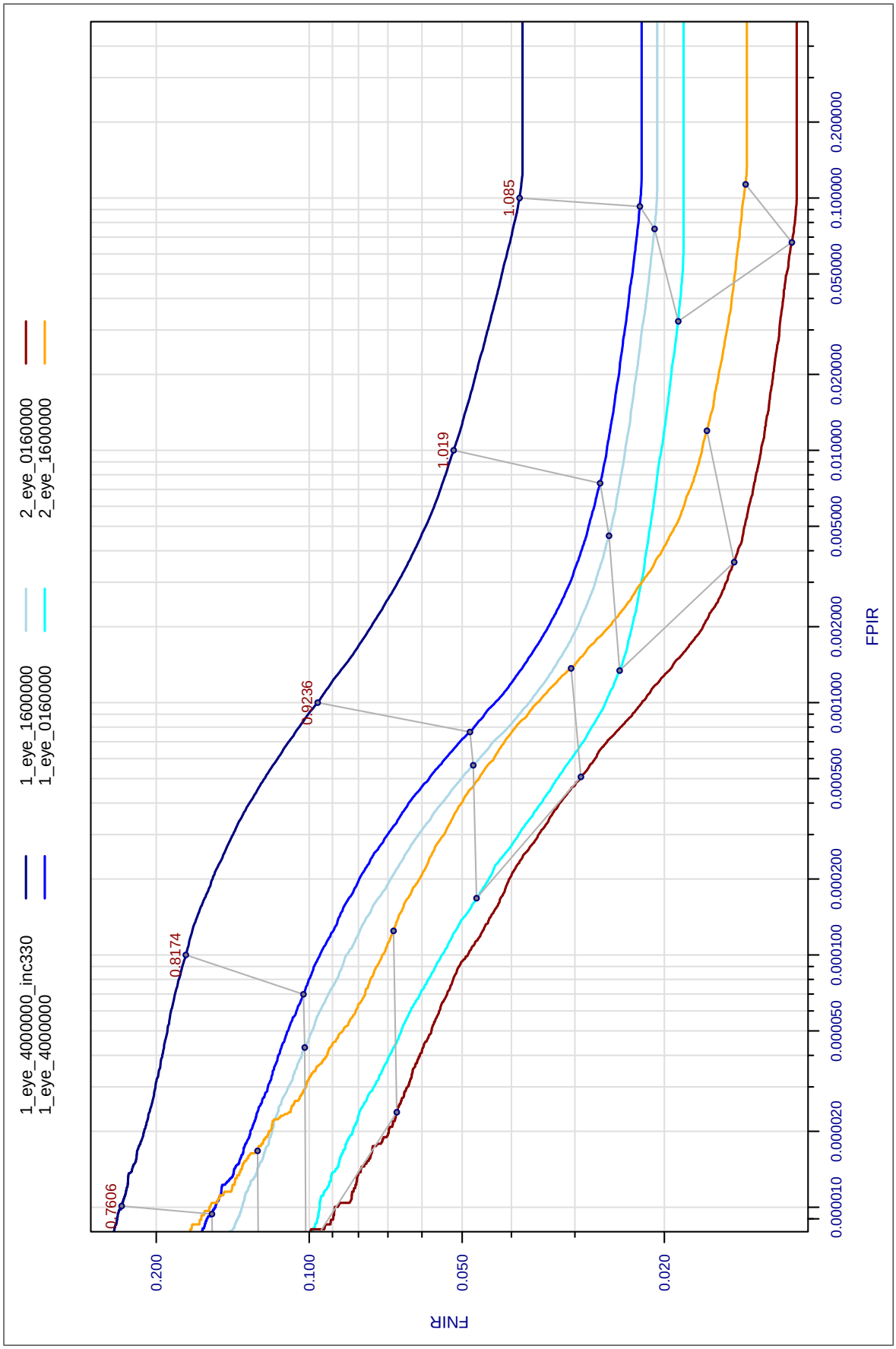

Figure 107: **Effect of population size** ONDETS for implementation Q03B executing searches for single-eye enrolled populations $N = (0.16, 1.6, 4)$ million, and two-eye populations of $N = (0.16, 1.6)$ million individuals. The straight lines, which link points of constant threshold, show how the two error rates would vary if a fixed threshold were adopted operationally. Horizontal lines indicate that enrolled population N is influential only on FPIR, via $\text{FPIR}(N_2) = (N_2/N_1)\text{FPIR}(N_1)$. When this relationship is not evident, the implementation may be adjusting scores as a function of N (e.g. as described in [cite Daugman]). The large search sets S_{nb} are used. Missing plots indicate the run is not yet complete.

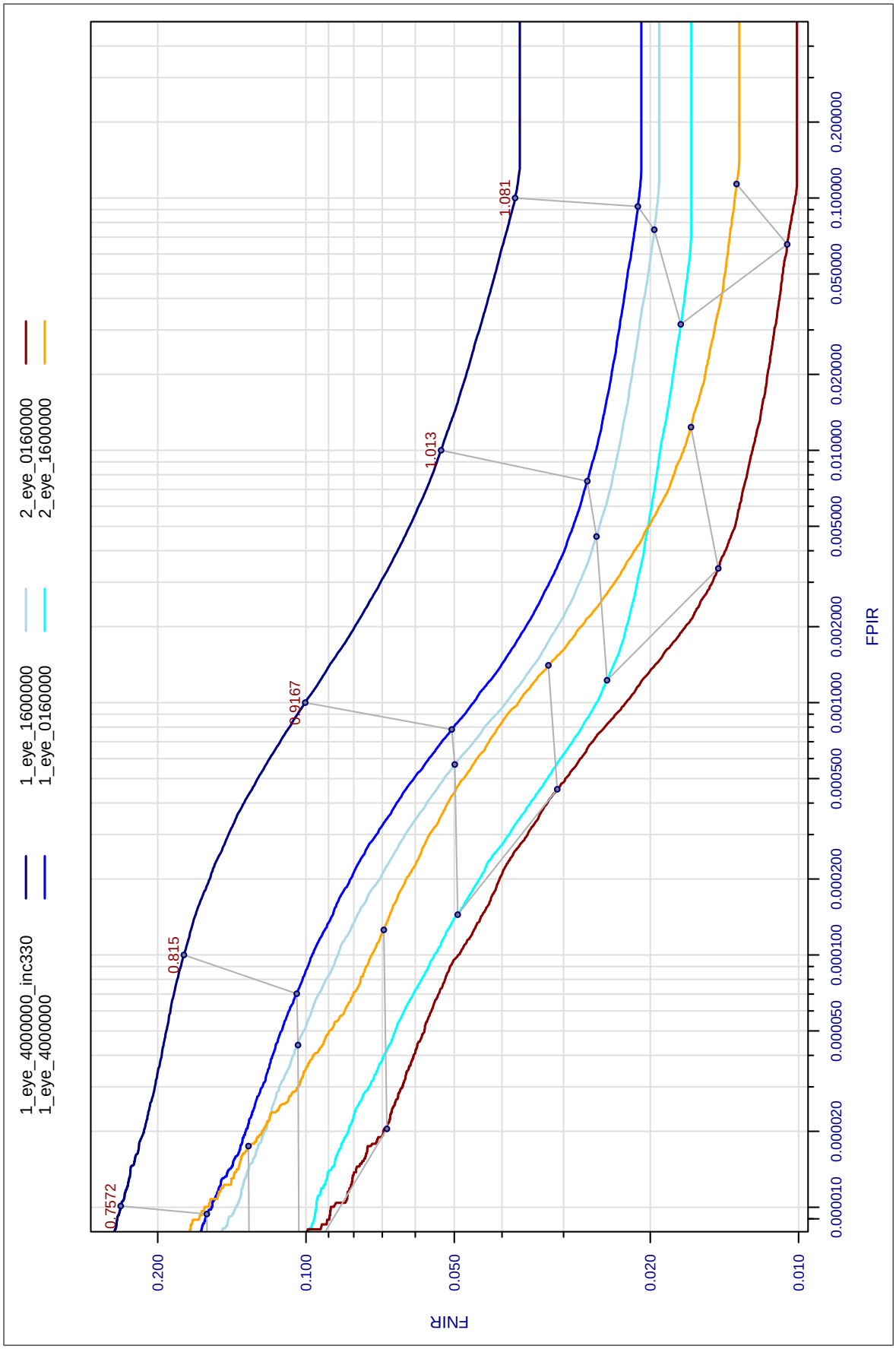

Figure 108: **Effect of population size** onDETs for implementation Q04B executing searches for single-eye enrolled populations $N = (0.16, 1.6, 4)$ million, and two-eye populations of $N = (0.16, 1.6)$ million individuals. The straight lines, which link points of constant threshold, show how the two error rates would vary if a fixed threshold were adopted operationally. Horizontal lines indicate that enrolled population N is influential only on FPIR, via $\text{FPIR}(N_2) = (N_2/N_1)\text{FPIR}(N_1)$. When this relationship is not evident, the implementation may be adjusting scores as a function of N (e.g. as described in [cite Daugman]). The large search sets S_{nb} are used. Missing plots indicate the run is not yet complete.

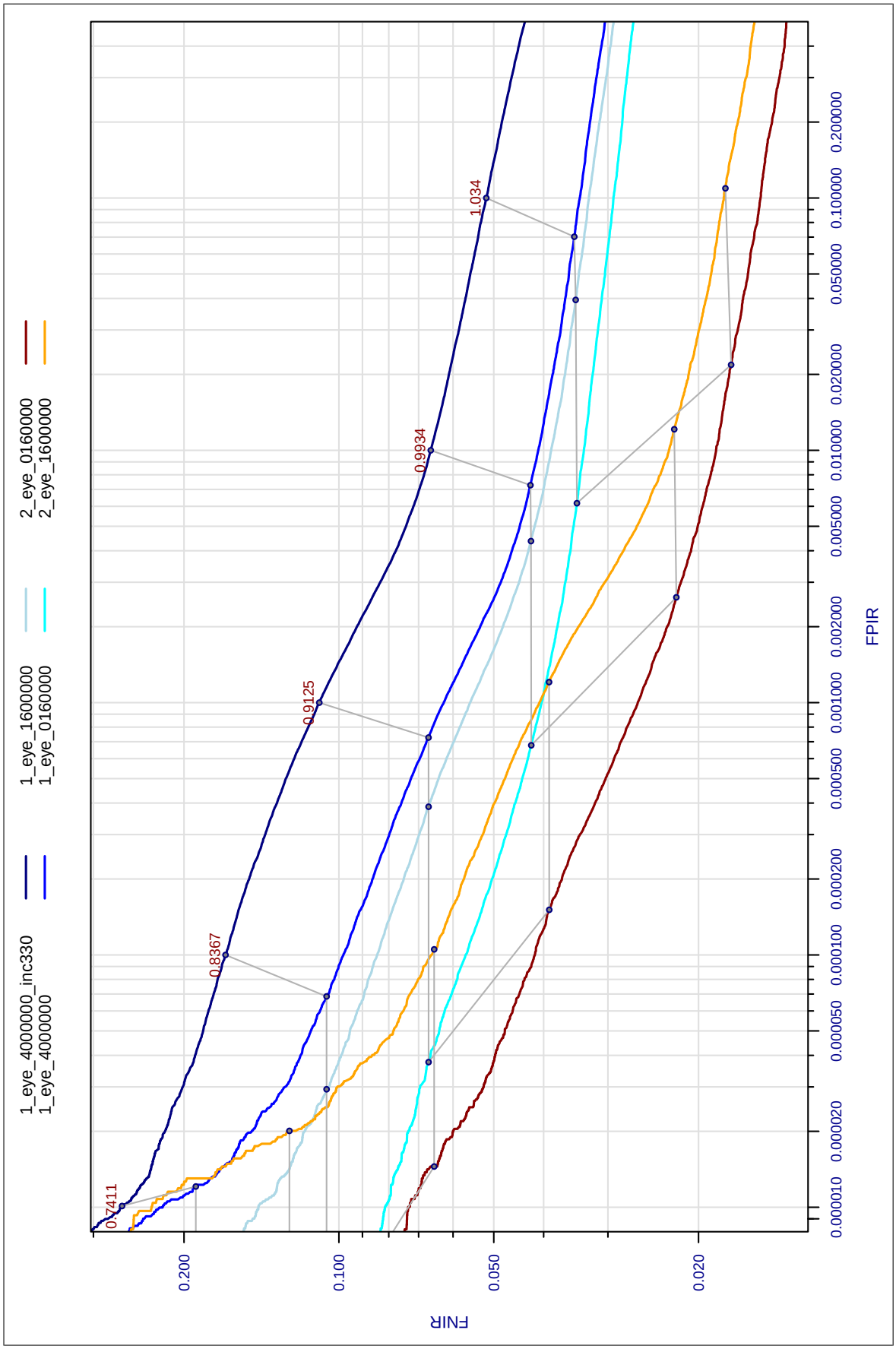

Figure 109: **Effect of population size** onDETs for implementation Q11B executing searches for single-eye enrolled populations $N = (0.16, 1.6, 4)$ million, and two-eye populations of $N = (0.16, 1.6)$ million individuals. The straight lines, which link points of constant threshold, show how the two error rates would vary if a fixed threshold were adopted operationally. Horizontal lines indicate that enrolled population N is influential only on FPIR, via $\text{FPIR}(N_2) = (N_2/N_1)\text{FPIR}(N_1)$. When this relationship is not evident, the implementation may be adjusting scores as a function of N (e.g. as described in [cite Daugman]). The large search sets $S_{n,b}$ are used. Missing plots indicate the run is not yet complete.

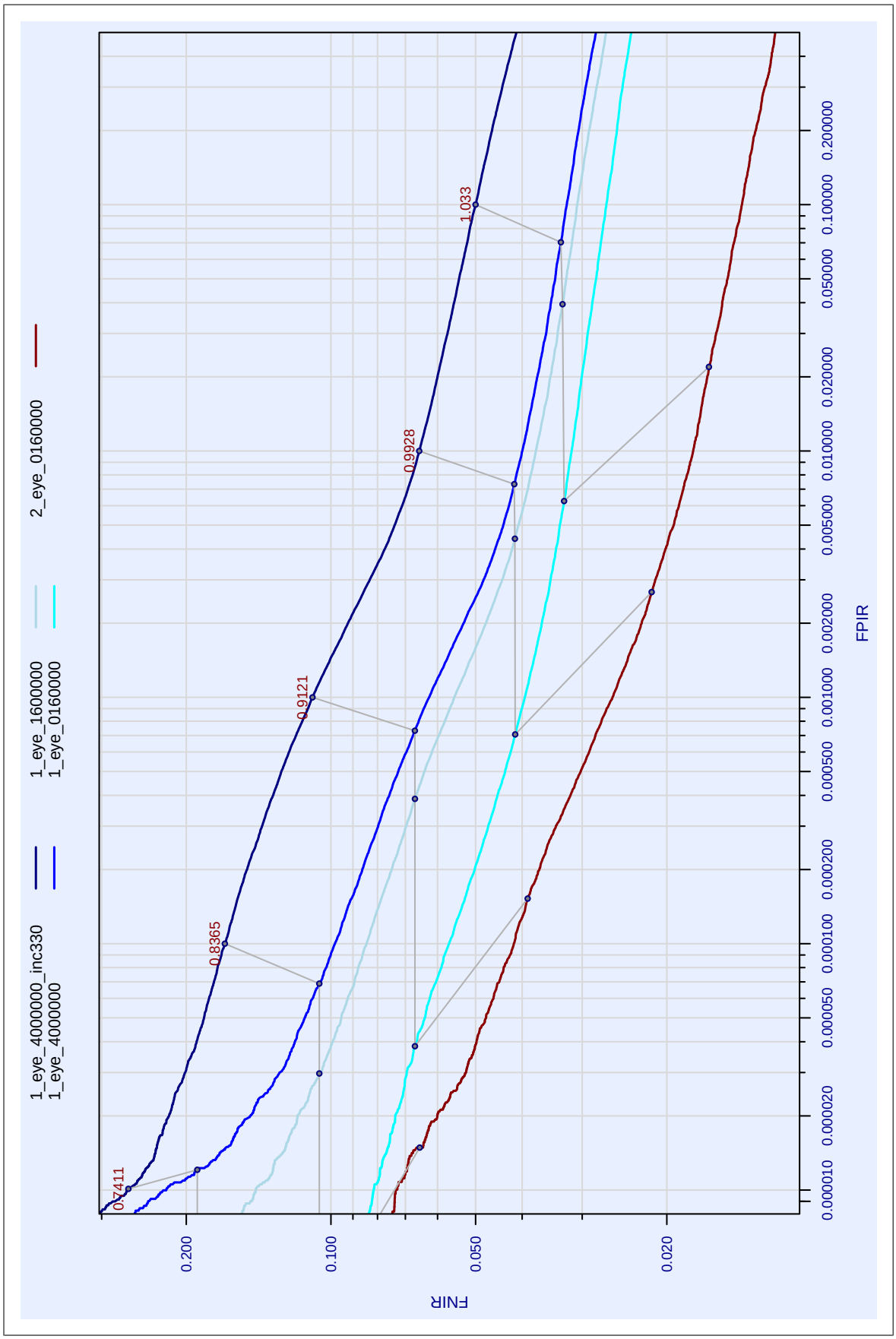

Figure 110: **Effect of population size** onDETs for implementation Q12B executing searches for single-eye enrolled populations $N = (0.16, 1.6, 4)$ million, and two-eye populations of $N = (0.16, 1.6)$ million individuals. The straight lines, which link points of constant threshold, show how the two error rates would vary if a fixed threshold were adopted operationally. Horizontal lines indicate that enrolled population N is influential only on FPIR, via $\text{FPIR}(N_2) = (N_2/N_1)\text{FPIR}(N_1)$. When this relationship is not evident, the implementation may be adjusting scores as a function of N (e.g. as described in [cite Daugman]). The large search sets S_{nb} are used. Missing plots indicate the run is not yet complete.

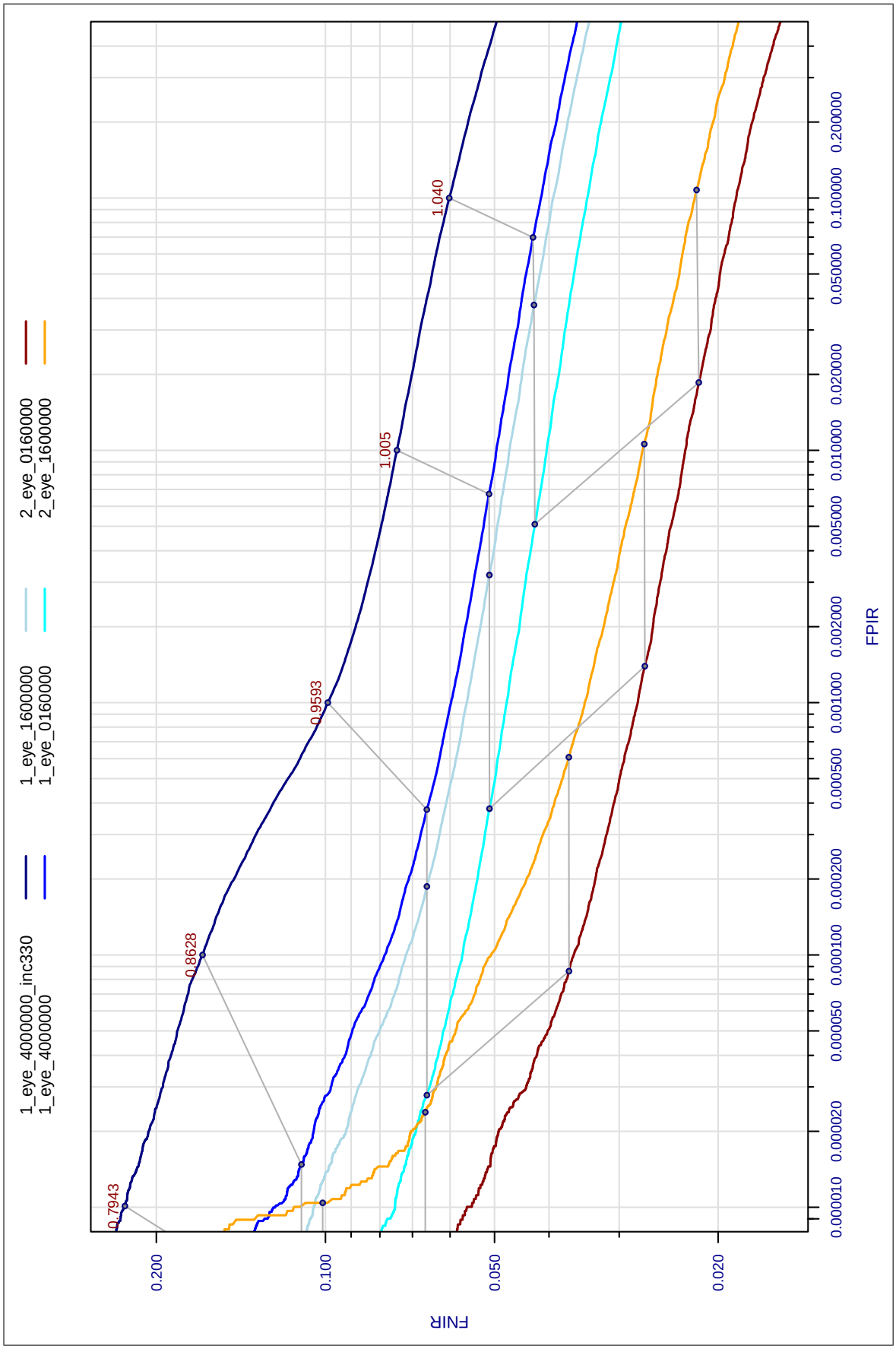

Figure 111: **Effect of population size** ONDETS for implementation Q13B executing searches for single-eye enrolled populations $N = (0.16, 1.6, 4)$ million, and two-eye populations of $N = (0.16, 1.6)$ million individuals. The straight lines, which link points of constant threshold, show how the two error rates would vary if a fixed threshold were adopted operationally. Horizontal lines indicate that enrolled population N is influential only on FPIR, via $\text{FPIR}(N_2) = (N_2/N_1)\text{FPIR}(N_1)$. When this relationship is not evident, the implementation may be adjusting scores as a function of N (e.g. as described in [cite Daugman]). The large search sets S_{nb} are used. Missing plots indicate the run is not yet complete.

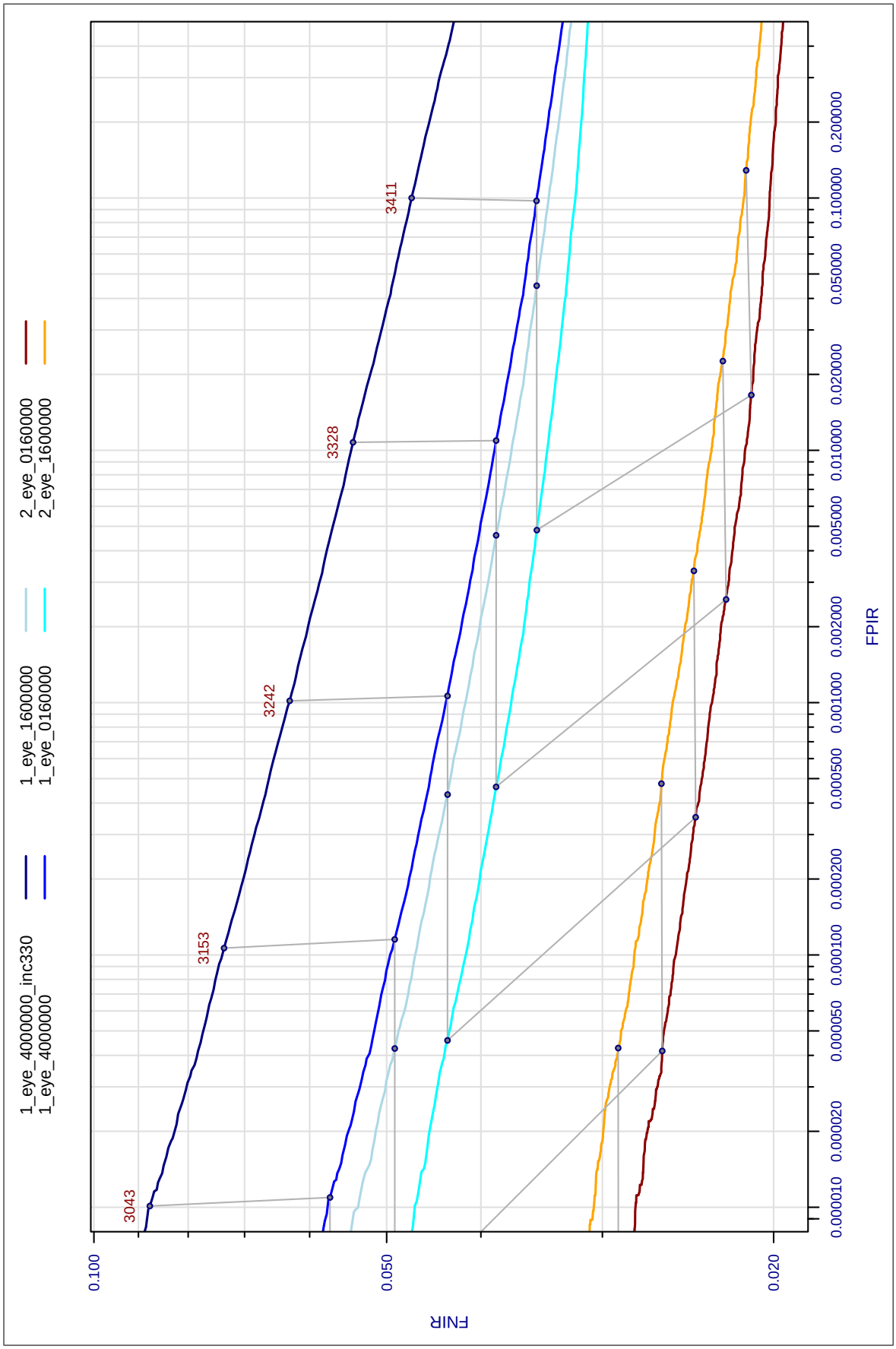

Figure 112: **Effect of population size** onDETs for implementation R02A executing searches for single-eye enrolled populations $N = (0.16, 1.6, 4)$ million, and two-eye populations of $N = (0.16, 1.6)$ million individuals. The straight lines, which link points of constant threshold, show how the two error rates would vary if a fixed threshold were adopted operationally. Horizontal lines indicate that enrolled population N is influential only on FPIR, via $\text{FPIR}(N_2) = (N_2/N_1)\text{FPIR}(N_1)$. When this relationship is not evident, the implementation may be adjusting scores as a function of N (e.g. as described in [cite Daugman]). The large search sets $S_{n,b}$ are used. Missing plots indicate the run is not yet complete.

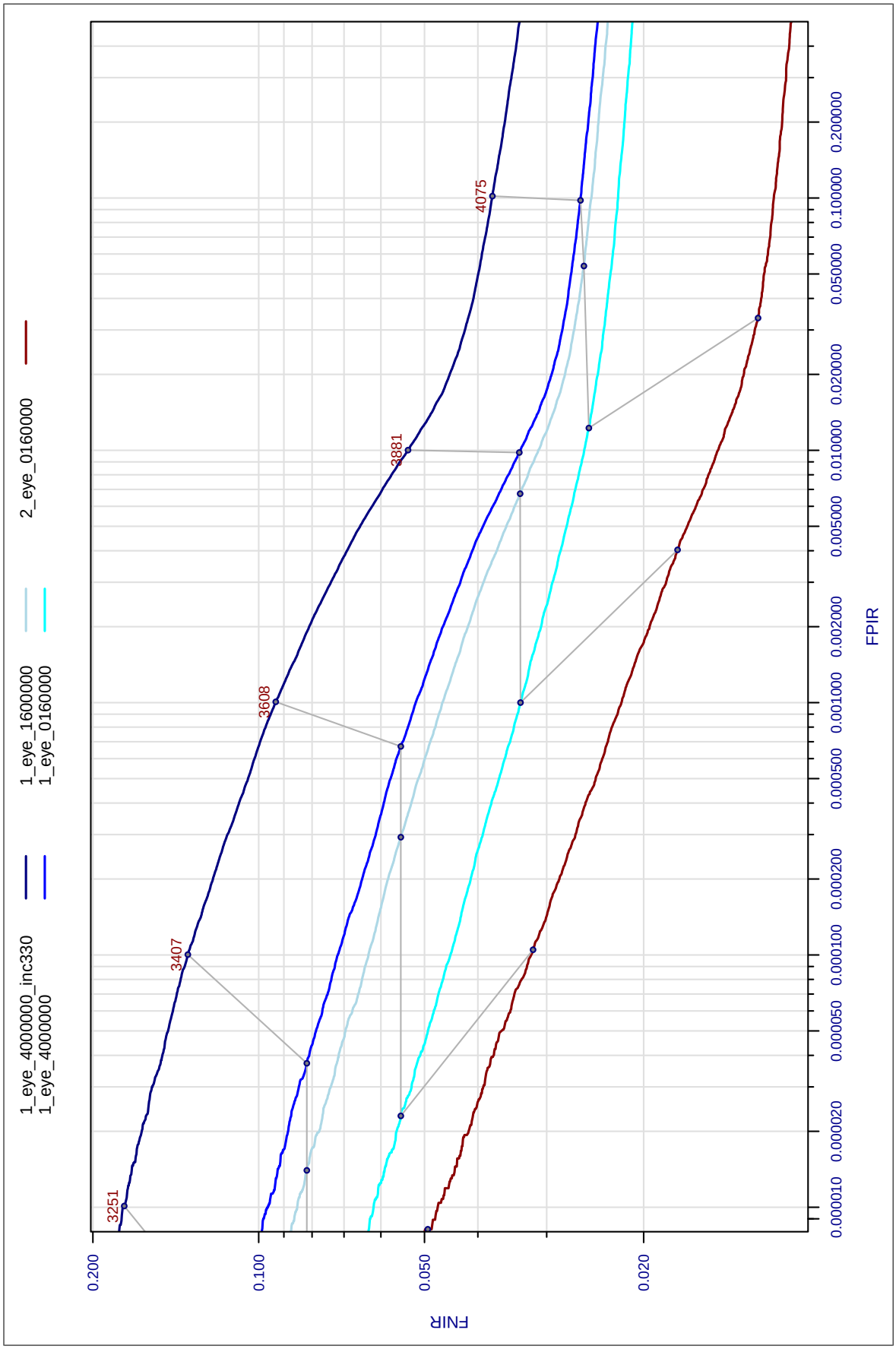

Figure 113: **Effect of population size** onDETs for implementation R02B executing searches for single-eye enrolled populations $N = (0.16, 1.6, 4)$ million, and two-eye populations of $N = (0.16, 1.6)$ million individuals. The straight lines, which link points of constant threshold, show how the two error rates would vary if a fixed threshold were adopted operationally. Horizontal lines indicate that enrolled population N is influential only on FPIR, via $\text{FPIR}(N_2) = (N_2/N_1)\text{FPIR}(N_1)$. When this relationship is not evident, the implementation may be adjusting scores as a function of N (e.g. as described in [cite Daugman]). The large search sets S_{nb} are used. Missing plots indicate the run is not yet complete.

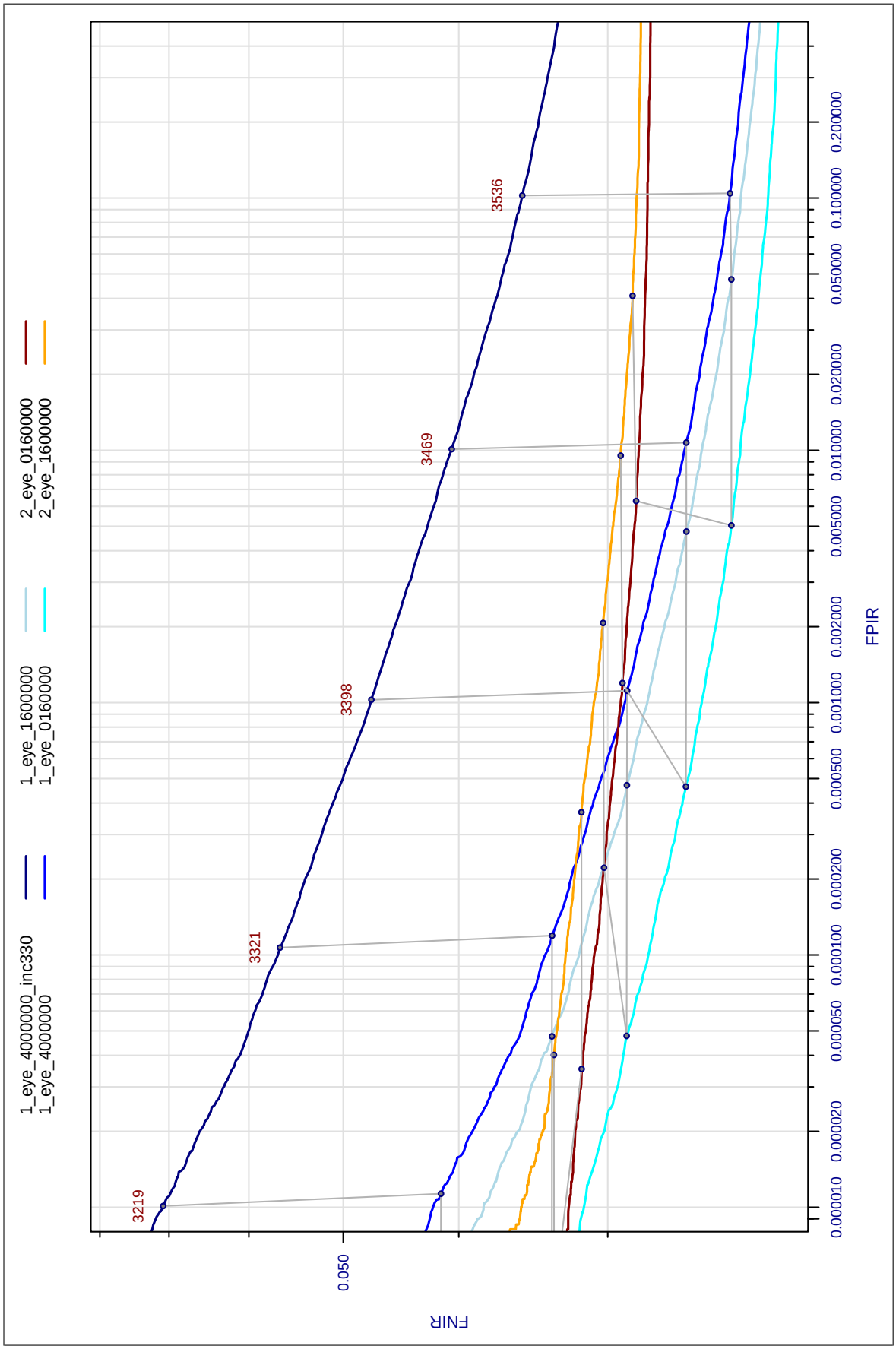

Figure 114: **Effect of population size** ONDETS for implementation R03A executing searches for single-eye enrolled populations $N = (0.16, 1.6, 4)$ million, and two-eye populations of $N = (0.16, 1.6)$ million individuals. The straight lines, which link points of constant threshold, show how the two error rates would vary if a fixed threshold were adopted operationally. Horizontal lines indicate that enrolled population N is influential only on FPIR, via $\text{FPIR}(N_2) = (N_2/N_1)\text{FPIR}(N_1)$. When this relationship is not evident, the implementation may be adjusting scores as a function of N (e.g. as described in [cite Daugman]). The large search sets $S_{n,b}$ are used. Missing plots indicate the run is not yet complete.

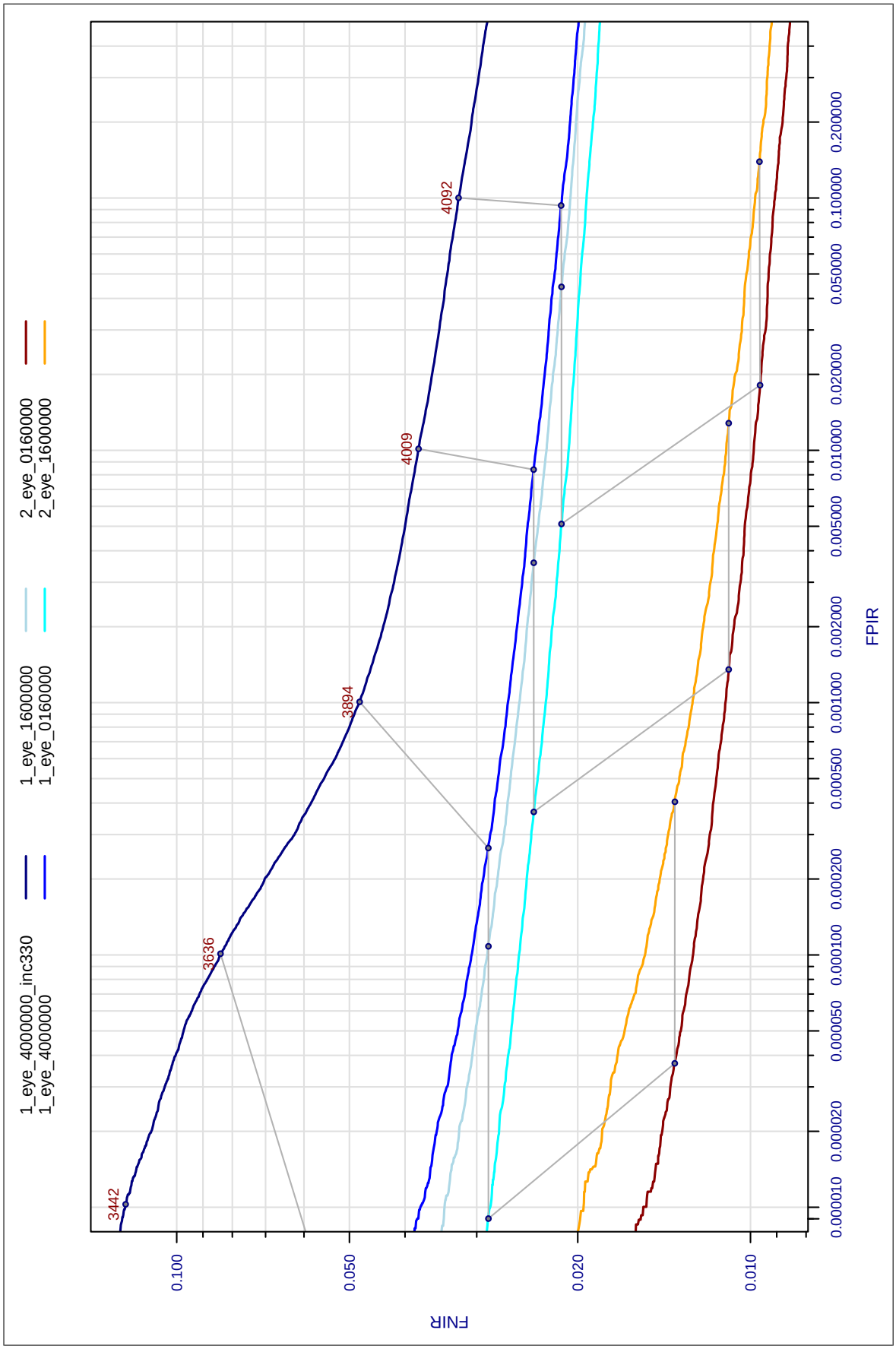

Figure 115: **Effect of population size** onDETs for implementation R03B executing searches for single-eye enrolled populations $N = (0.16, 1.6, 4)$ million, and two-eye populations of $N = (0.16, 1.6)$ million individuals. The straight lines, which link points of constant threshold, show how the two error rates would vary if a fixed threshold were adopted operationally. Horizontal lines indicate that enrolled population N is influential only on FPIR, via $\text{FPIR}(N_2) = (N_2/N_1)\text{FPIR}(N_1)$. When this relationship is not evident, the implementation may be adjusting scores as a function of N (e.g. as described in [cite Daugman]). The large search sets $S_{n,b}$ are used. Missing plots indicate the run is not yet complete.

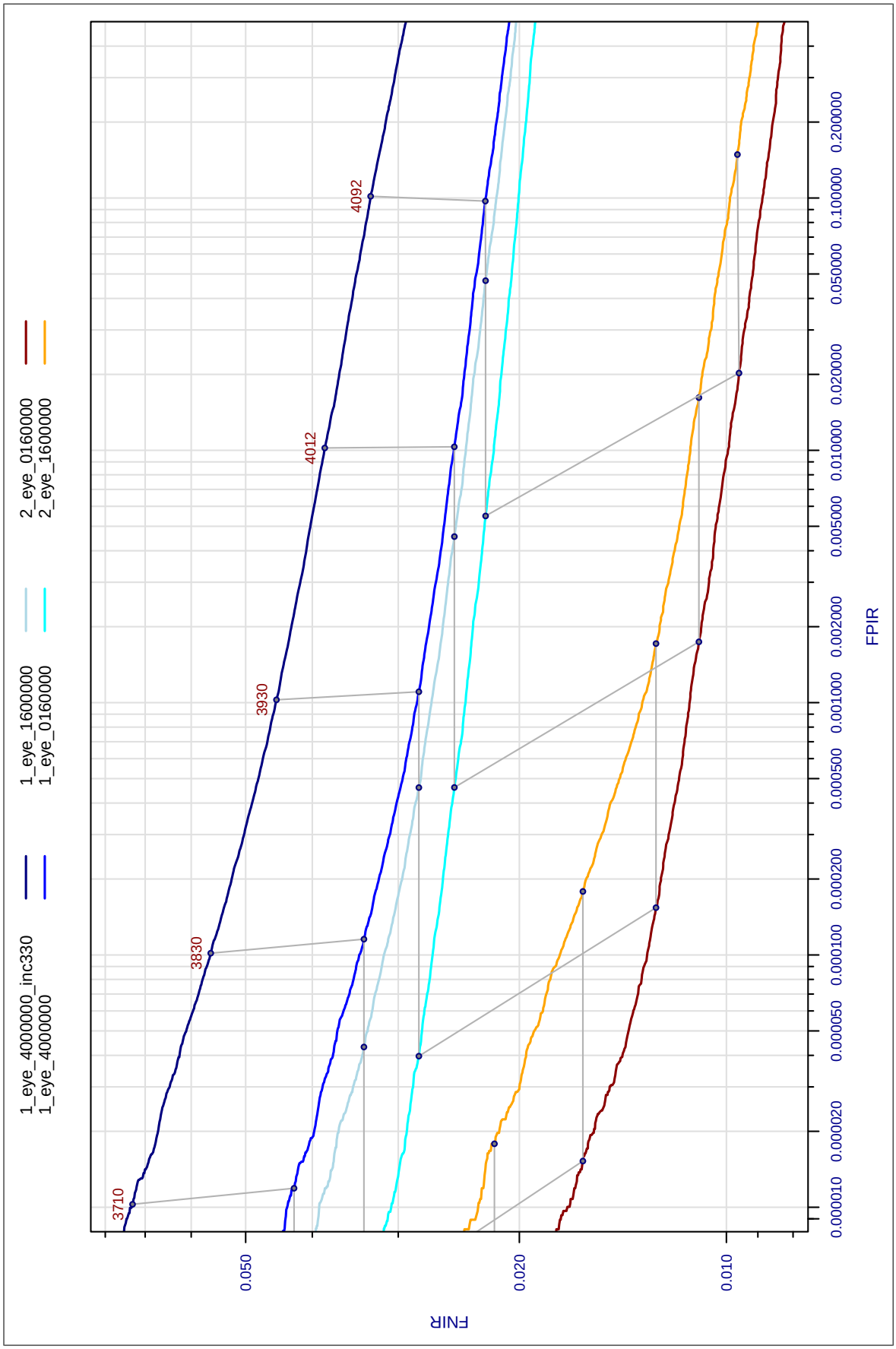

Figure 116: **Effect of population size** onDETs for implementation R04B executing searches for single-eye enrolled populations $N = (0.16, 1.6, 4)$ million, and two-eye populations of $N = (0.16, 1.6)$ million individuals. The straight lines, which link points of constant threshold, show how the two error rates would vary if a fixed threshold were adopted operationally. Horizontal lines indicate that enrolled population N is influential only on FPIR, via $\text{FPIR}(N_2) = (N_2/N_1)\text{FPIR}(N_1)$. When this relationship is not evident, the implementation may be adjusting scores as a function of N (e.g. as described in [cite Daugman]). The large search sets $S_{n,b}$ are used. Missing plots indicate the run is not yet complete.

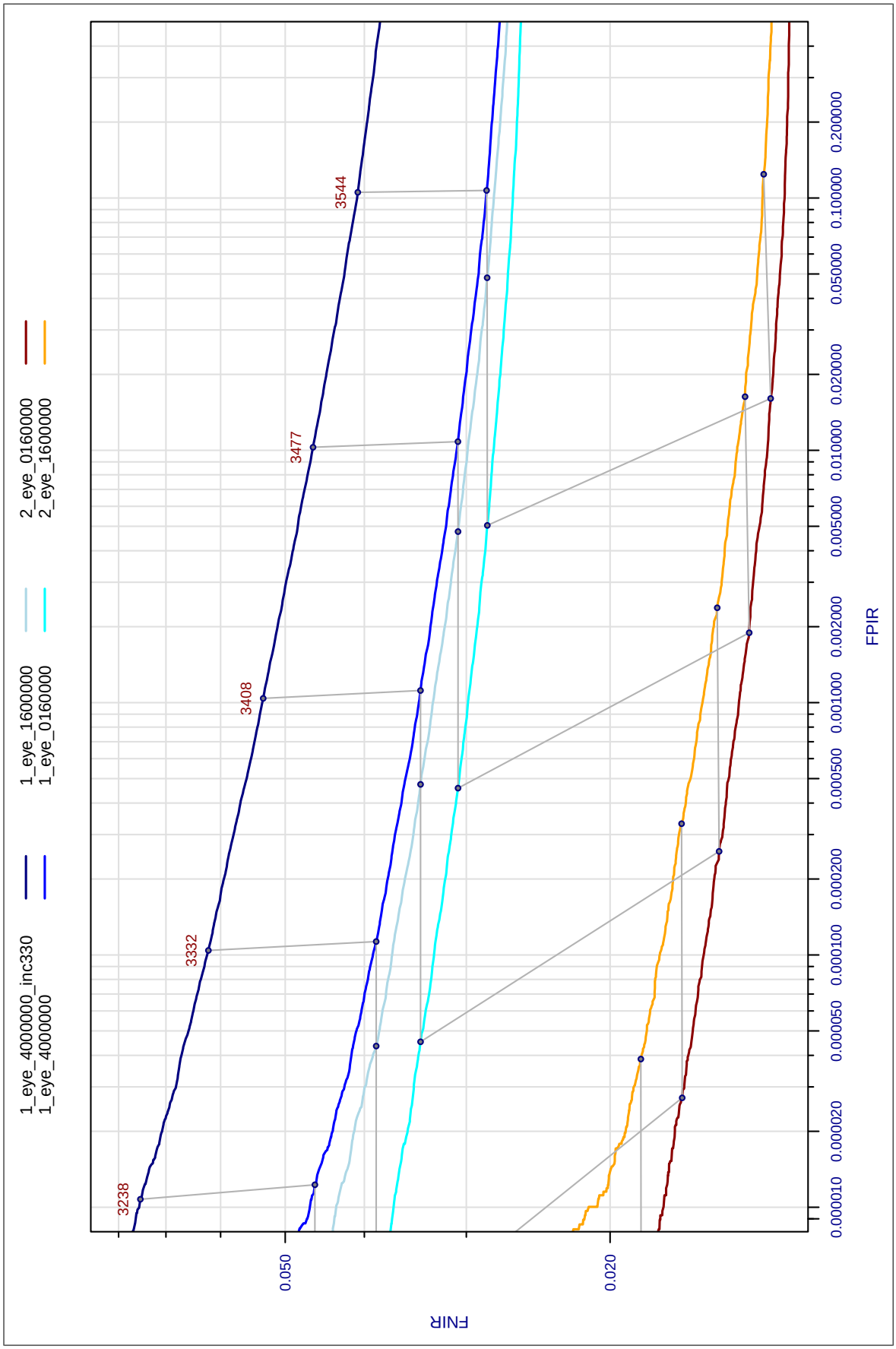

Figure 117: **Effect of population size** onDETs for implementation R11A executing searches for single-eye enrolled populations $N = (0.16, 1.6, 4)$ million, and two-eye populations of $N = (0.16, 1.6)$ million individuals. The straight lines, which link points of constant threshold, show how the two error rates would vary if a fixed threshold were adopted operationally. Horizontal lines indicate that enrolled population N is influential only on FPIR, via $\text{FPIR}(N_2) = (N_2/N_1)\text{FPIR}(N_1)$. When this relationship is not evident, the implementation may be adjusting scores as a function of N (e.g. as described in [cite Daugman]). The large search sets S_{nb} are used. Missing plots indicate the run is not yet complete.

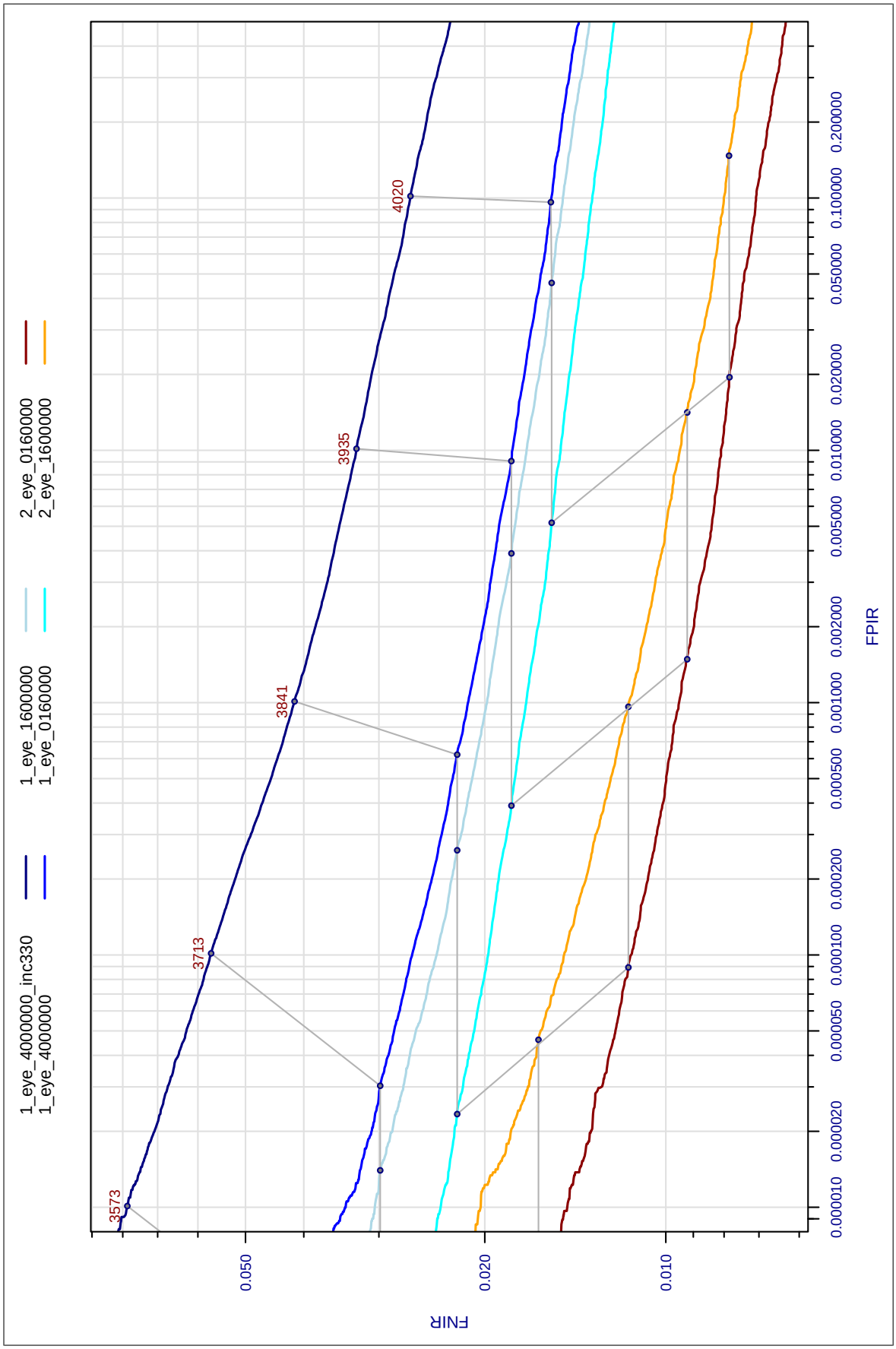

Figure 118: **Effect of population size** onDETs for implementation R11B executing searches for single-eye enrolled populations $N = (0.16, 1.6, 4)$ million, and two-eye populations of $N = (0.16, 1.6)$ million individuals. The straight lines, which link points of constant threshold, show how the two error rates would vary if a fixed threshold were adopted operationally. Horizontal lines indicate that enrolled population N is influential only on FPIR, via $\text{FPIR}(N_2) = (N_2/N_1)\text{FPIR}(N_1)$. When this relationship is not evident, the implementation may be adjusting scores as a function of N (e.g. as described in [cite Daugman]). The large search sets S_{nb} are used. Missing plots indicate the run is not yet complete.

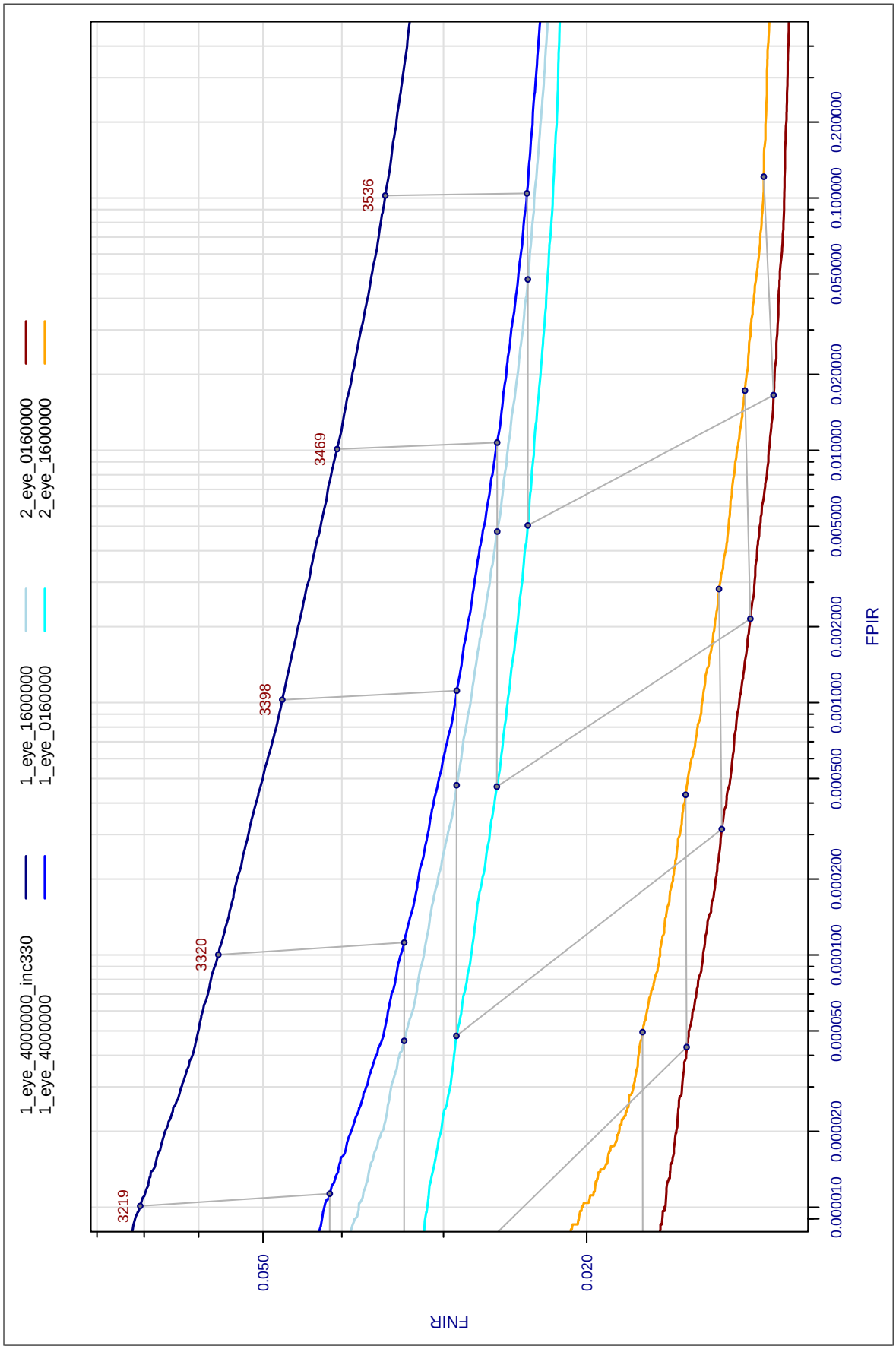

Figure 119: **Effect of population size** onDETs for implementation R12A executing searches for single-eye enrolled populations $N = (0.16, 1.6, 4)$ million, and two-eye populations of $N = (0.16, 1.6)$ million individuals. The straight lines, which link points of constant threshold, show how the two error rates would vary if a fixed threshold were adopted operationally. Horizontal lines indicate that enrolled population N is influential only on FPIR, via $\text{FPIR}(N_2) = (N_2/N_1)\text{FPIR}(N_1)$. When this relationship is not evident, the implementation may be adjusting scores as a function of N (e.g. as described in [cite Daugman]). The large search sets S_{nb} are used. Missing plots indicate the run is not yet complete.

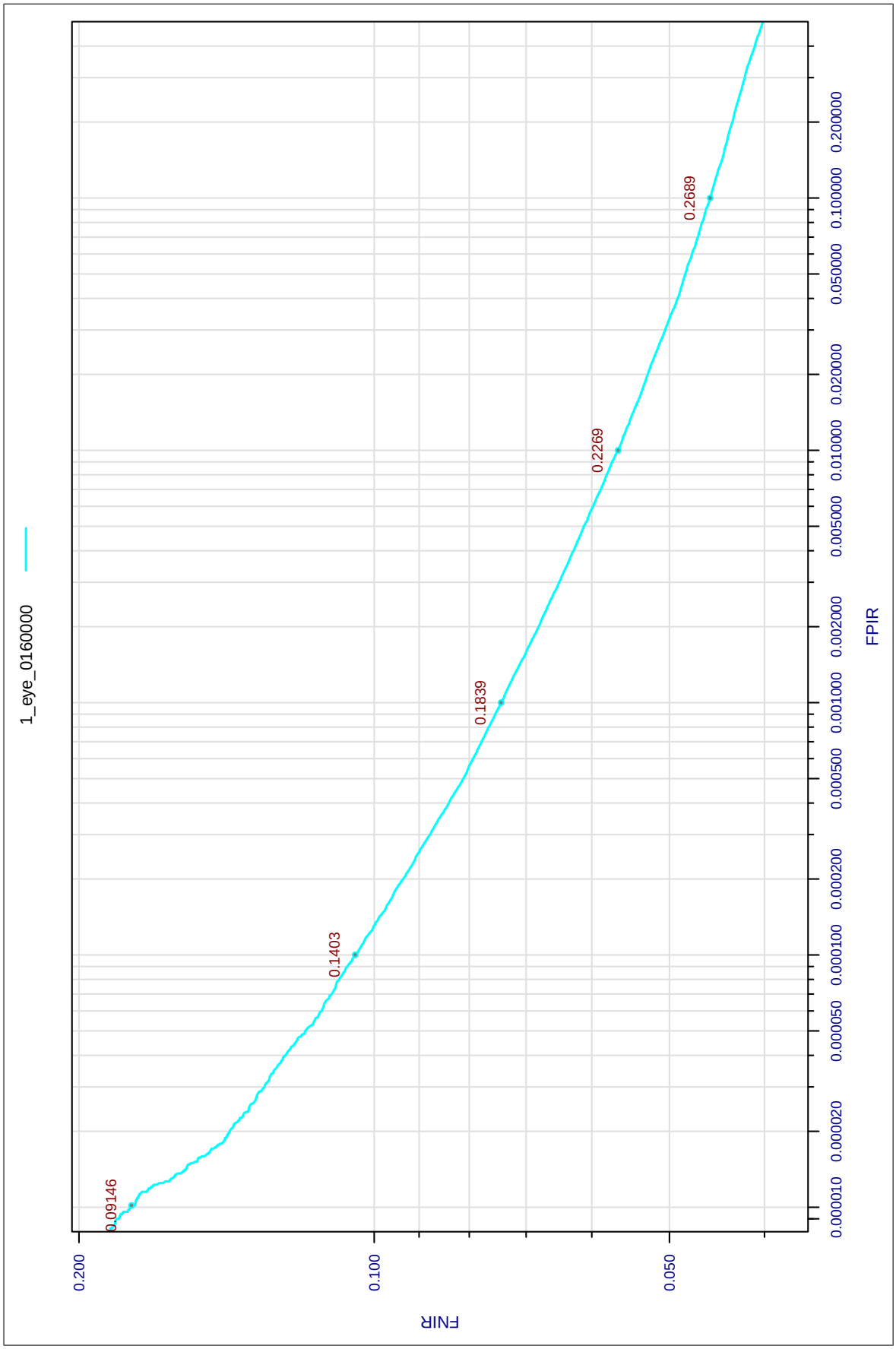

Figure 120: **Effect of population size** onDETs for implementation S01B executing searches for single-eye enrolled populations $N = (0.16, 1.6, 4)$ million, and two-eye populations of $N = (0.16, 1.6)$ million individuals. The straight lines, which link points of constant threshold, show how the two error rates would vary if a fixed threshold were adopted operationally. Horizontal lines indicate that enrolled population N is influential only on FPIR, via $\text{FPIR}(N_2) = (N_2/N_1)\text{FPIR}(N_1)$. When this relationship is not evident, the implementation may be adjusting scores as a function of N (e.g. as described in [cite Daugman]). The large search sets $S_{n,b}$ are used. Missing plots indicate the run is not yet complete.

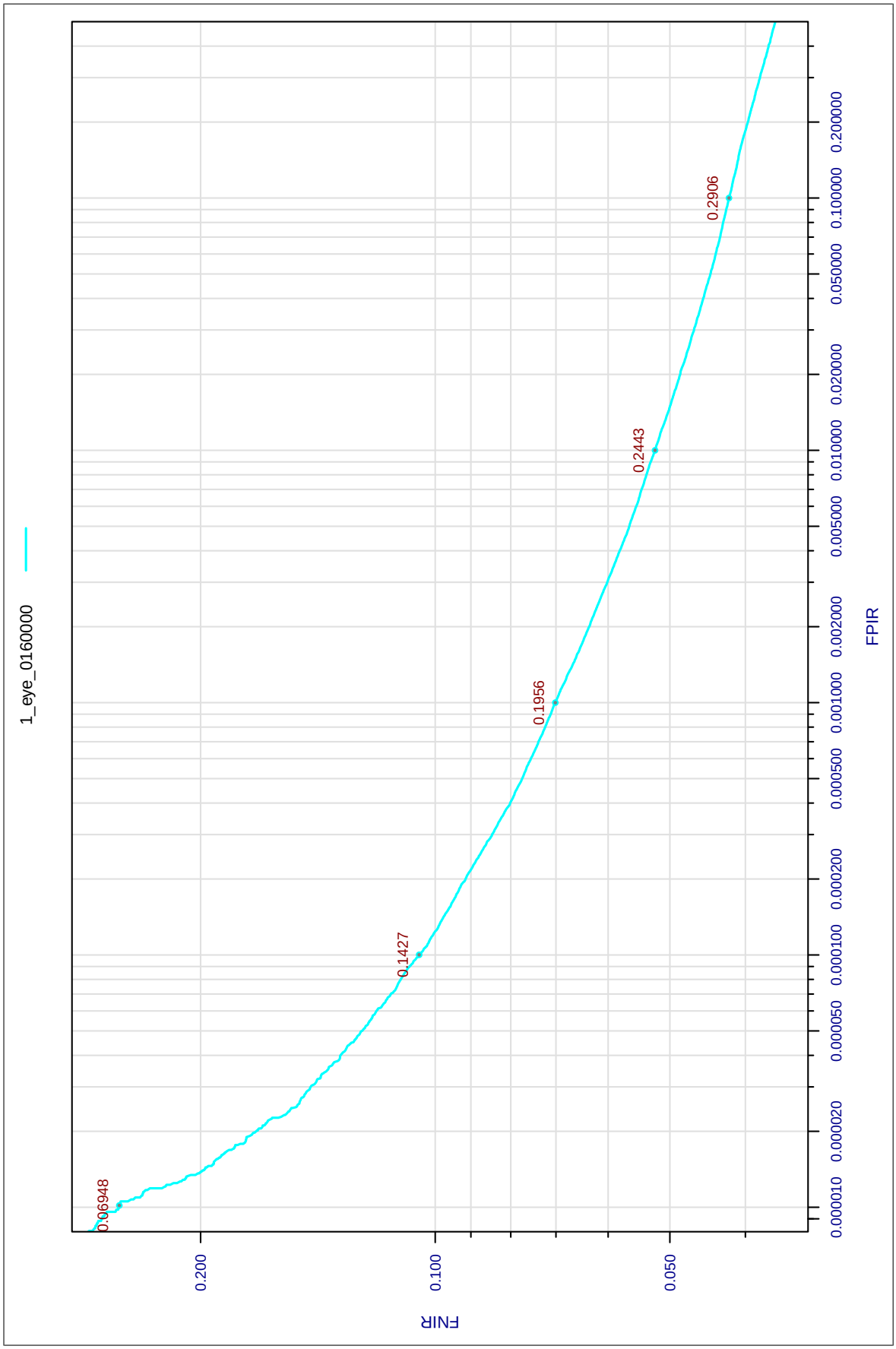

Figure 121: **Effect of population size** onDETs for implementation S02B executing searches for single-eye enrolled populations $N = (0.16, 1.6, 4)$ million, and two-eye populations of $N = (0.16, 1.6)$ million individuals. The straight lines, which link points of constant threshold, show how the two error rates would vary if a fixed threshold were adopted operationally. Horizontal lines indicate that enrolled population N is influential only on FPIR, via $\text{FPIR}(N_2) = (N_2/N_1)\text{FPIR}(N_1)$. When this relationship is not evident, the implementation may be adjusting scores as a function of N (e.g. as described in [cite Daugman]). The large search sets $S_{n,b}$ are used. Missing plots indicate the run is not yet complete.

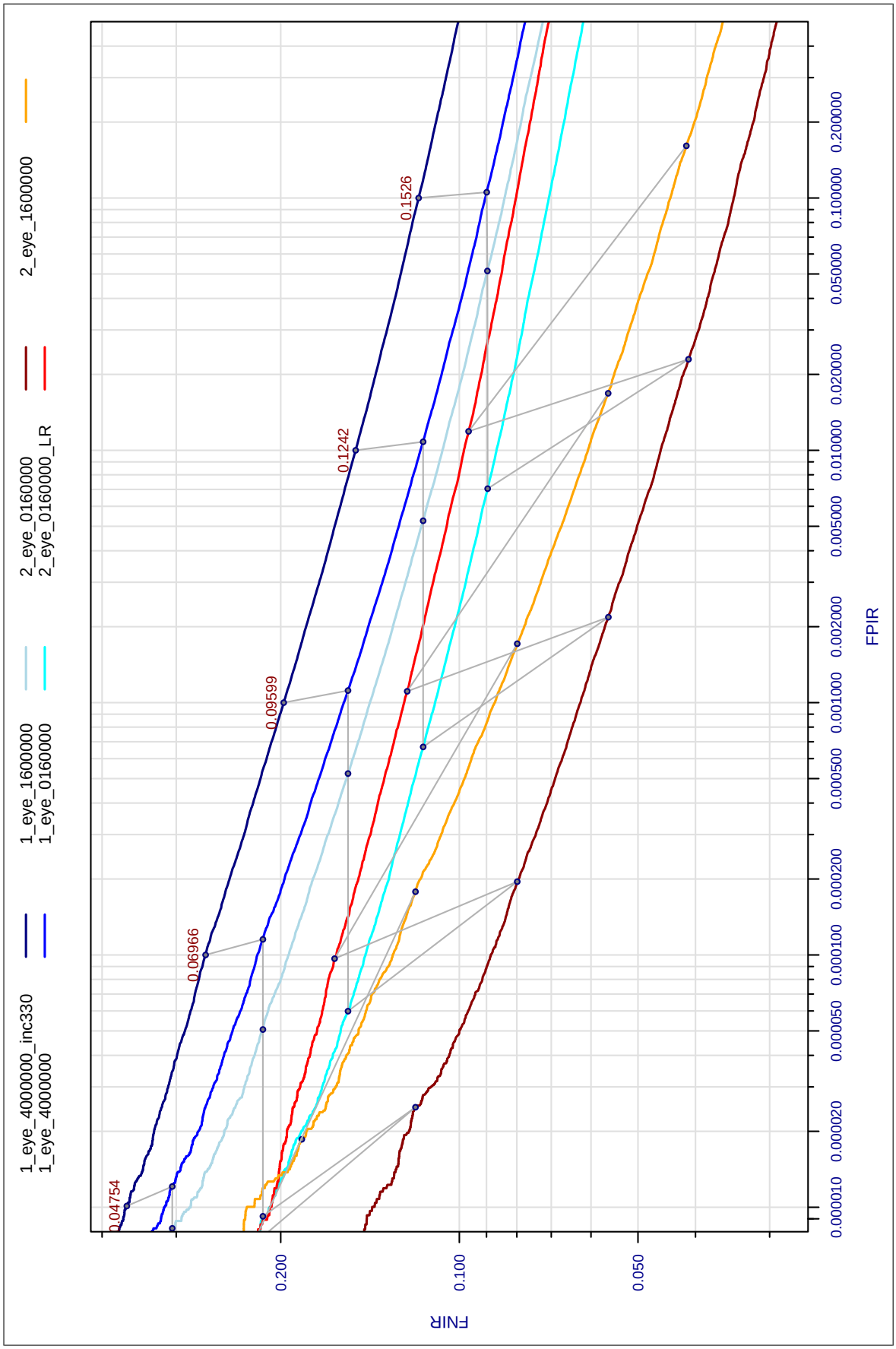

Figure 122: **Effect of population size** onDETs for implementation S03A executing searches for single-eye enrolled populations $N = (0.16, 1.6, 4)$ million, and two-eye populations of $N = (0.16, 1.6)$ million individuals. The straight lines, which link points of constant threshold, show how the two error rates would vary if a fixed threshold were adopted operationally. Horizontal lines indicate that enrolled population N is influential only on FPIR, via $\text{FPIR}(N_2) = (N_2/N_1)\text{FPIR}(N_1)$. When this relationship is not evident, the implementation may be adjusting scores as a function of N (e.g. as described in [cite Daugman]). The large search sets $S_{n,b}$ are used. Missing plots indicate the run is not yet complete.

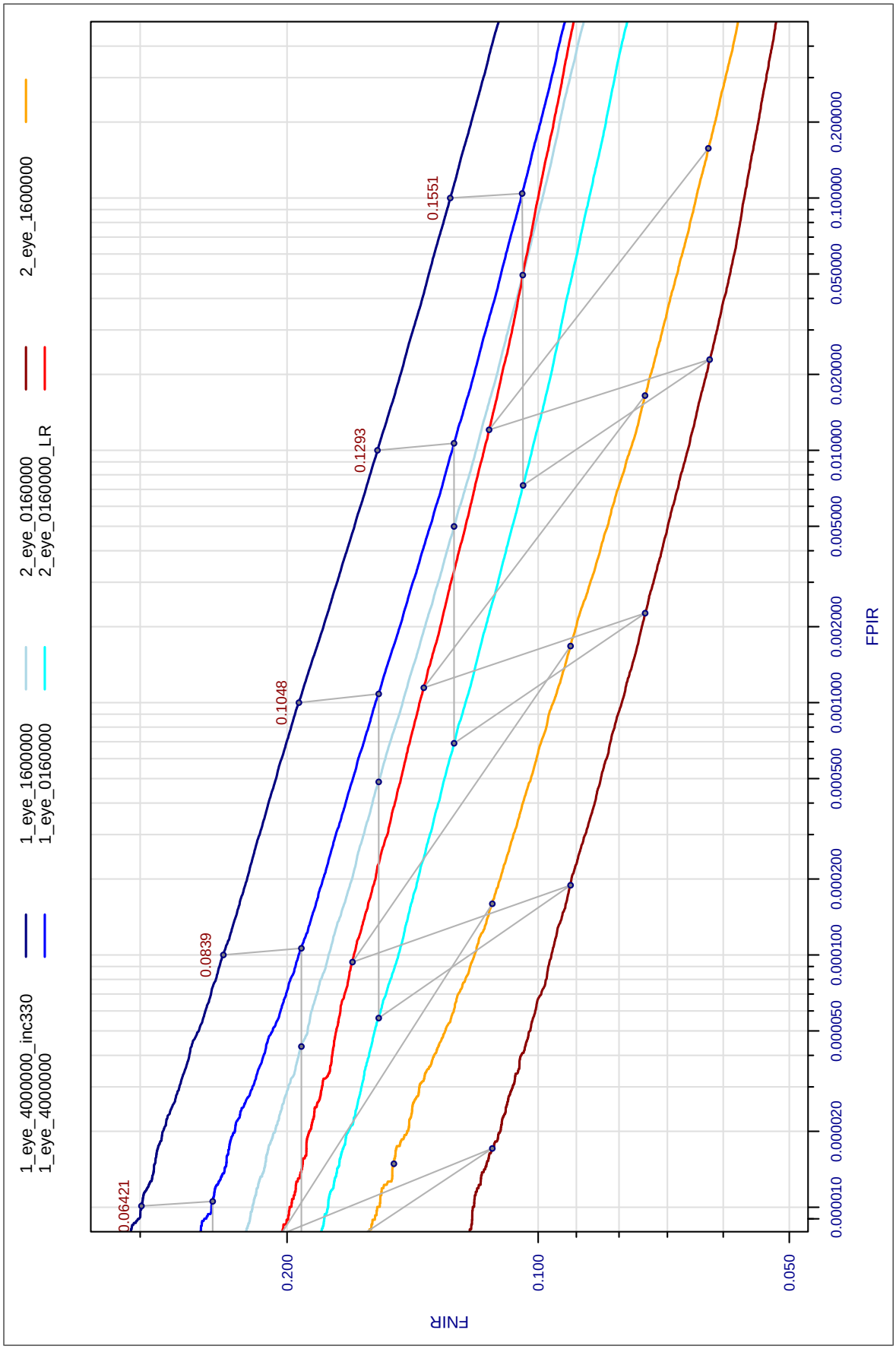

Figure 123: **Effect of population size** onDETs for implementation S04A executing searches for single-eye enrolled populations $N = (0.16, 1.6, 4)$ million, and two-eye populations of $N = (0.16, 1.6)$ million individuals. The straight lines, which link points of constant threshold, show how the two error rates would vary if a fixed threshold were adopted operationally. Horizontal lines indicate that enrolled population N is influential only on FPIR, via $\text{FPIR}(N_2) = (N_2/N_1)\text{FPIR}(N_1)$. When this relationship is not evident, the implementation may be adjusting scores as a function of N (e.g. as described in [cite Daugman]). The large search sets S_{nb} are used. Missing plots indicate the run is not yet complete.

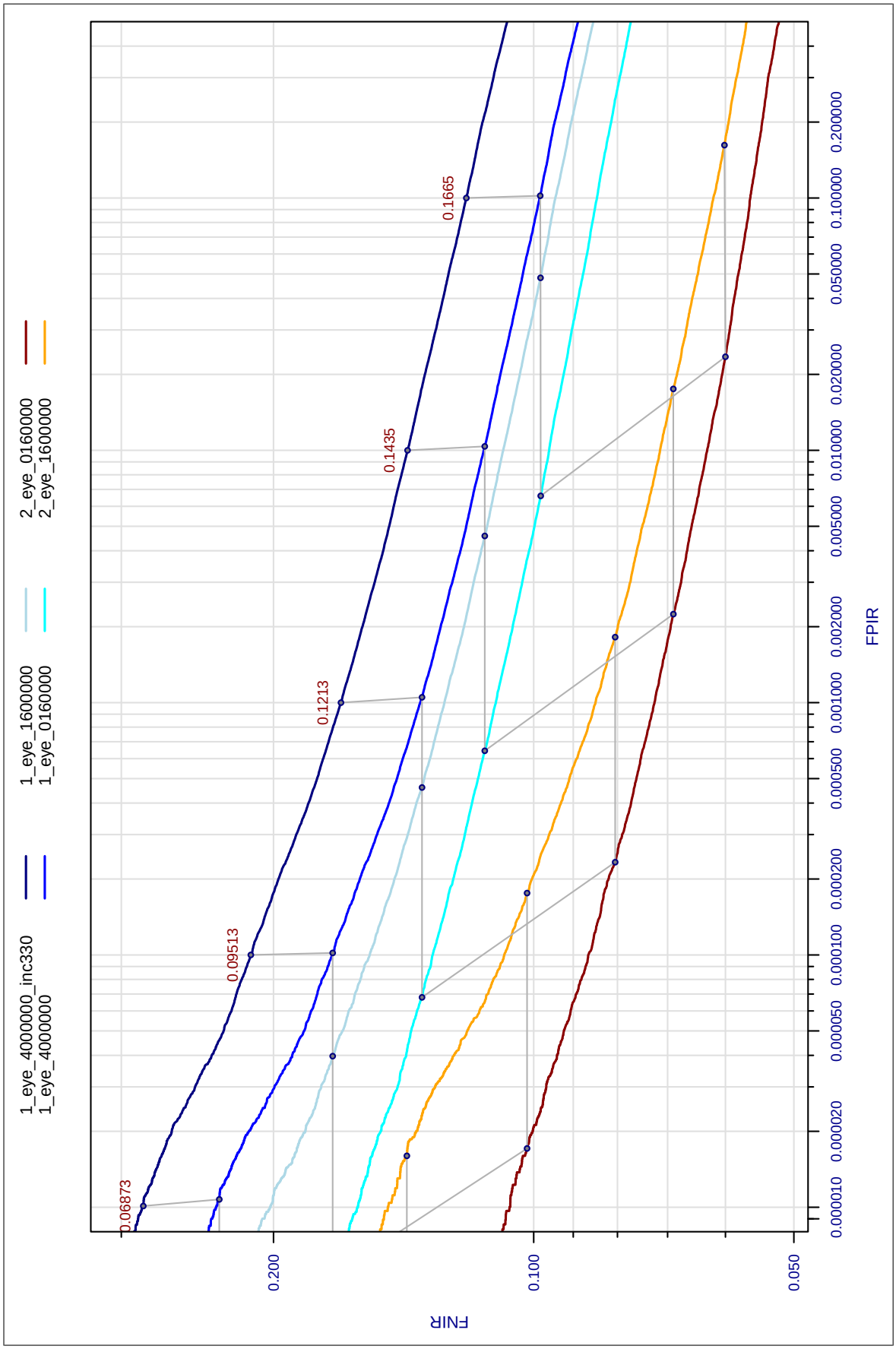

Figure 124: **Effect of population size** onDETs for implementation S05A executing searches for single-eye enrolled populations $N = (0.16, 1.6, 4)$ million, and two-eye populations of $N = (0.16, 1.6)$ million individuals. The straight lines, which link points of constant threshold, show how the two error rates would vary if a fixed threshold were adopted operationally. Horizontal lines indicate that enrolled population N is influential only on FPIR, via $\text{FPIR}(N_2) = (N_2/N_1)\text{FPIR}(N_1)$. When this relationship is not evident, the implementation may be adjusting scores as a function of N (e.g. as described in [cite Daugman]). The large search sets S_{nb} are used. Missing plots indicate the run is not yet complete.

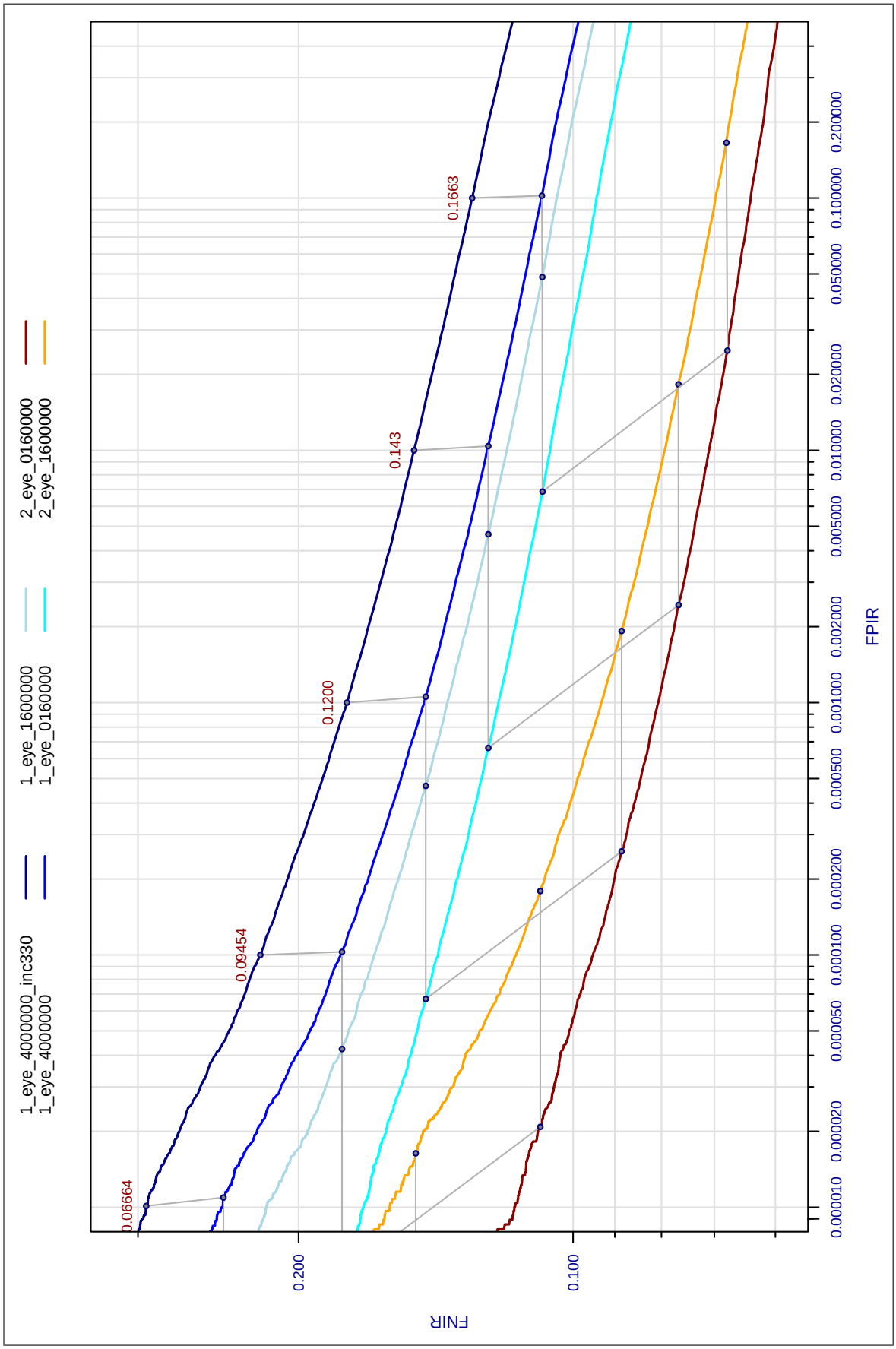

Figure 125: **Effect of population size** onDETs for implementation S11A executing searches for single-eye enrolled populations $N = (0.16, 1.6, 4)$ million, and two-eye populations of $N = (0.16, 1.6)$ million individuals. The straight lines, which link points of constant threshold, show how the two error rates would vary if a fixed threshold were adopted operationally. Horizontal lines indicate that enrolled population N is influential only on FPIR, via $\text{FPIR}(N_2) = (N_2/N_1)\text{FPIR}(N_1)$. When this relationship is not evident, the implementation may be adjusting scores as a function of N (e.g. as described in [cite Daugman]). The large search sets S_{nb} are used. Missing plots indicate the run is not yet complete.

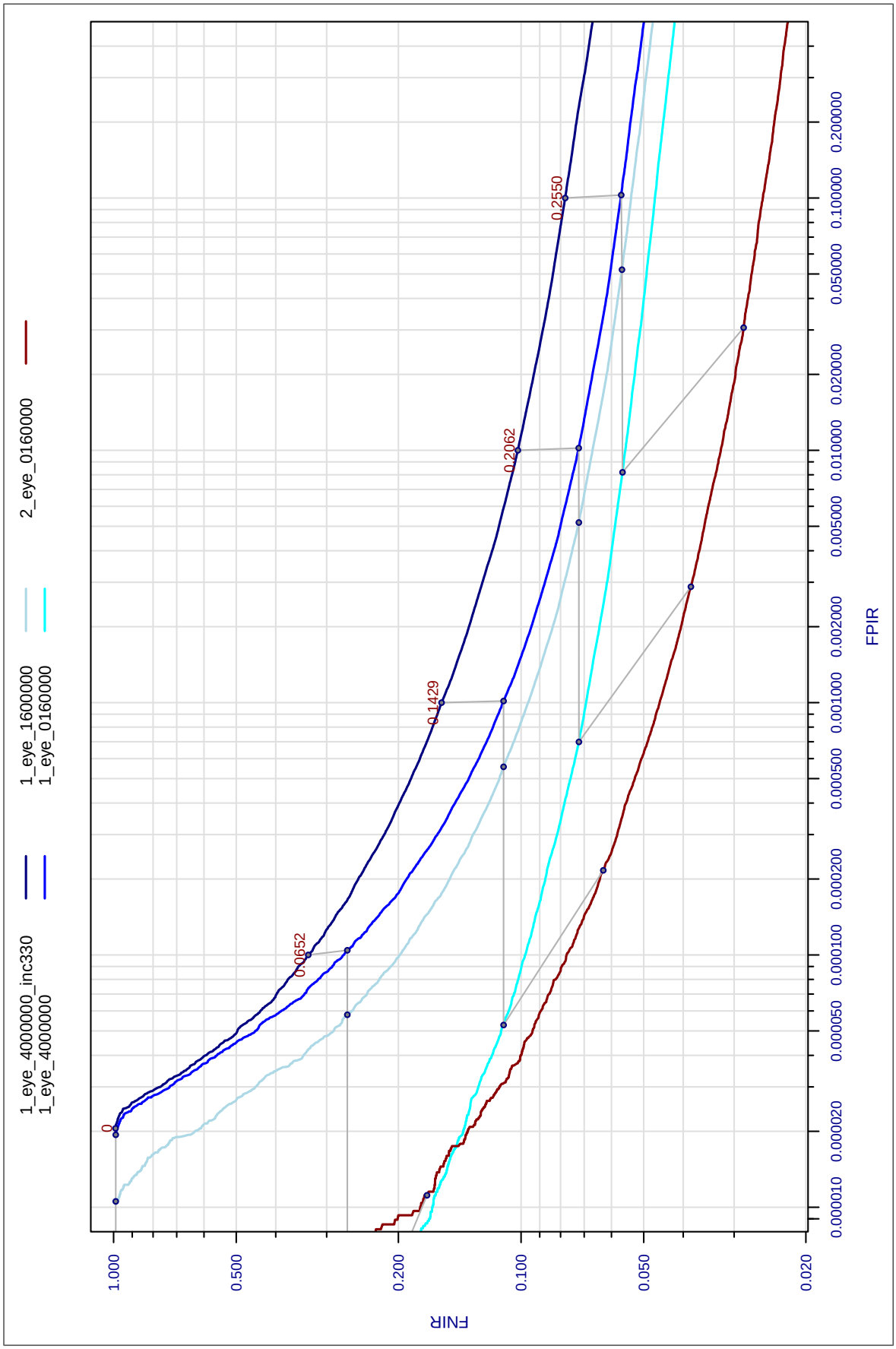

Figure 126: **Effect of population size** onDETs for implementation S11B executing searches for single-eye enrolled populations $N = (0.16, 1.6, 4)$ million, and two-eye populations of $N = (0.16, 1.6)$ million individuals. The straight lines, which link points of constant threshold, show how the two error rates would vary if a fixed threshold were adopted operationally. Horizontal lines indicate that enrolled population N is influential only on FPIR, via $\text{FPIR}(N_2) = (N_2/N_1)\text{FPIR}(N_1)$. When this relationship is not evident, the implementation may be adjusting scores as a function of N (e.g. as described in [cite Daugman]). The large search sets S_{nb} are used. Missing plots indicate the run is not yet complete.

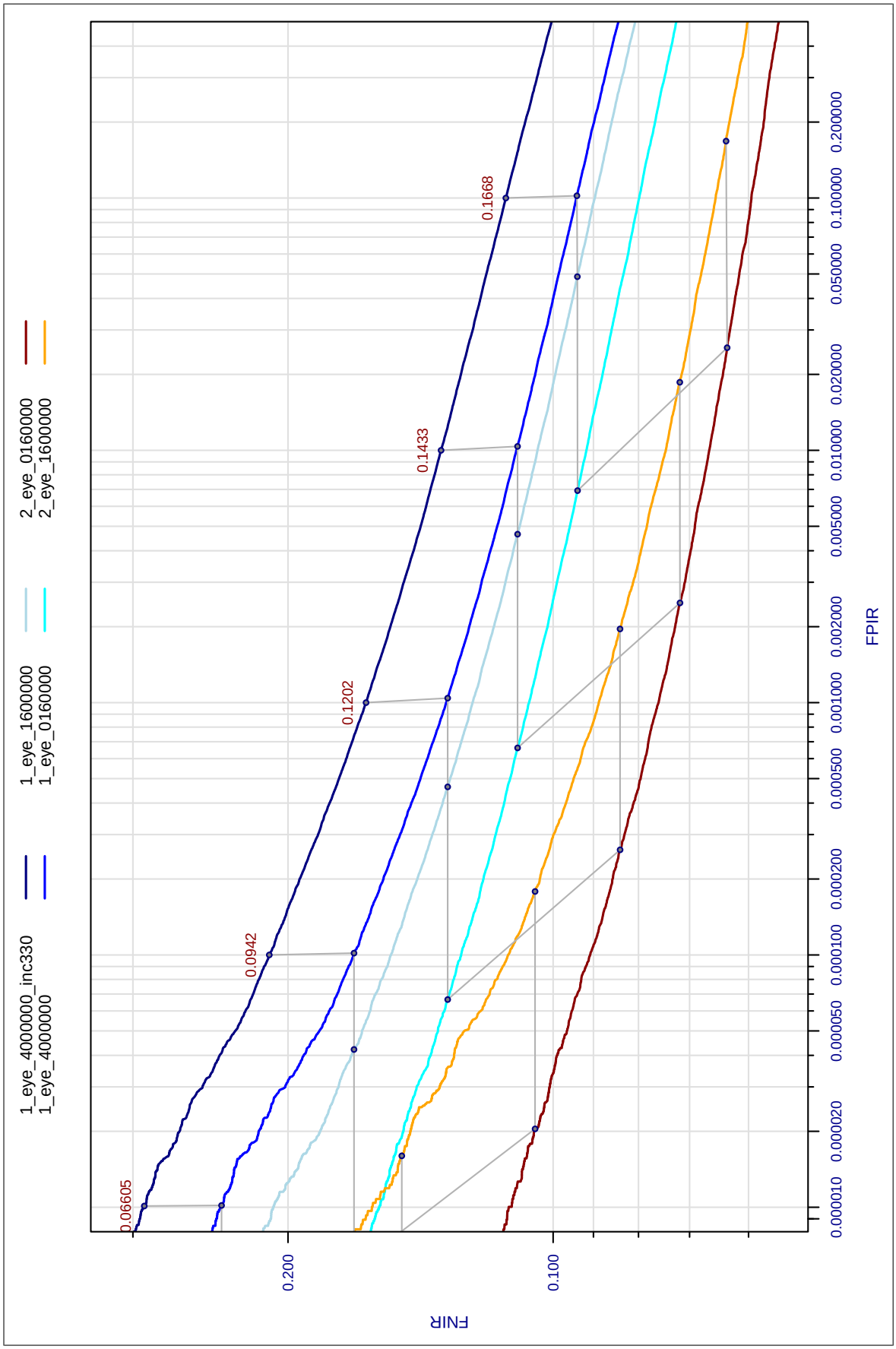

Figure 127: **Effect of population size** onDETs for implementation S12A executing searches for single-eye enrolled populations $N = (0.16, 1.6, 4)$ million, and two-eye populations of $N = (0.16, 1.6)$ million individuals. The straight lines, which link points of constant threshold, show how the two error rates would vary if a fixed threshold were adopted operationally. Horizontal lines indicate that enrolled population N is influential only on FPIR, via $\text{FPIR}(N_2) = (N_2/N_1)\text{FPIR}(N_1)$. When this relationship is not evident, the implementation may be adjusting scores as a function of N (e.g. as described in [cite Daugman]). The large search sets S_{nb} are used. Missing plots indicate the run is not yet complete.

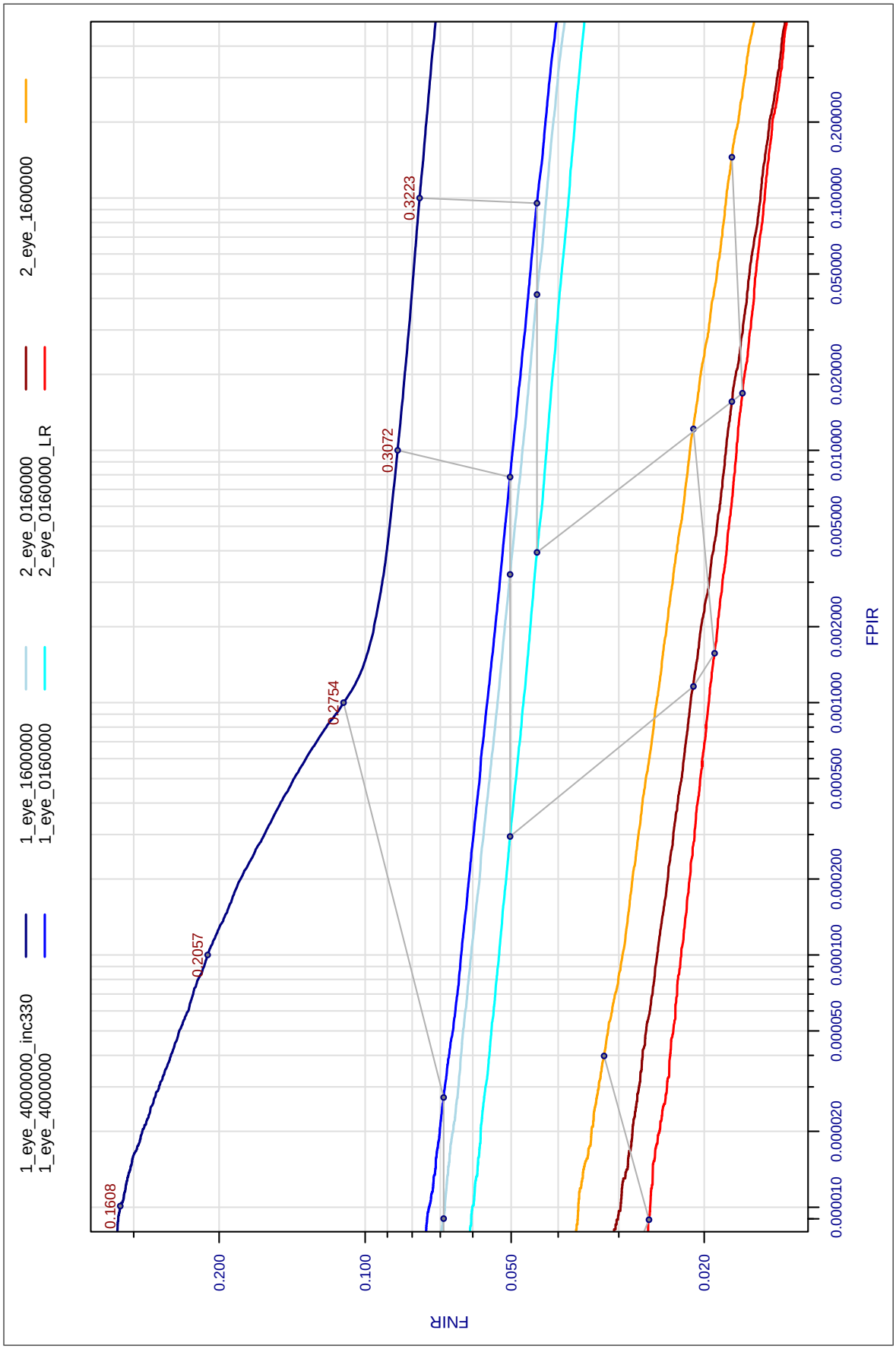

Figure 128: **Effect of population size** onDETs for implementation T01A executing searches for single-eye enrolled populations $N = (0.16, 1.6, 4)$ million, and two-eye populations of $N = (0.16, 1.6)$ million individuals. The straight lines, which link points of constant threshold, show how the two error rates would vary if a fixed threshold were adopted operationally. Horizontal lines indicate that enrolled population N is influential only on FPIR, via $\text{FPIR}(N_2) = (N_2/N_1)\text{FPIR}(N_1)$. When this relationship is not evident, the implementation may be adjusting scores as a function of N (e.g. as described in [cite Daugman]). The large search sets S_{nb} are used. Missing plots indicate the run is not yet complete.

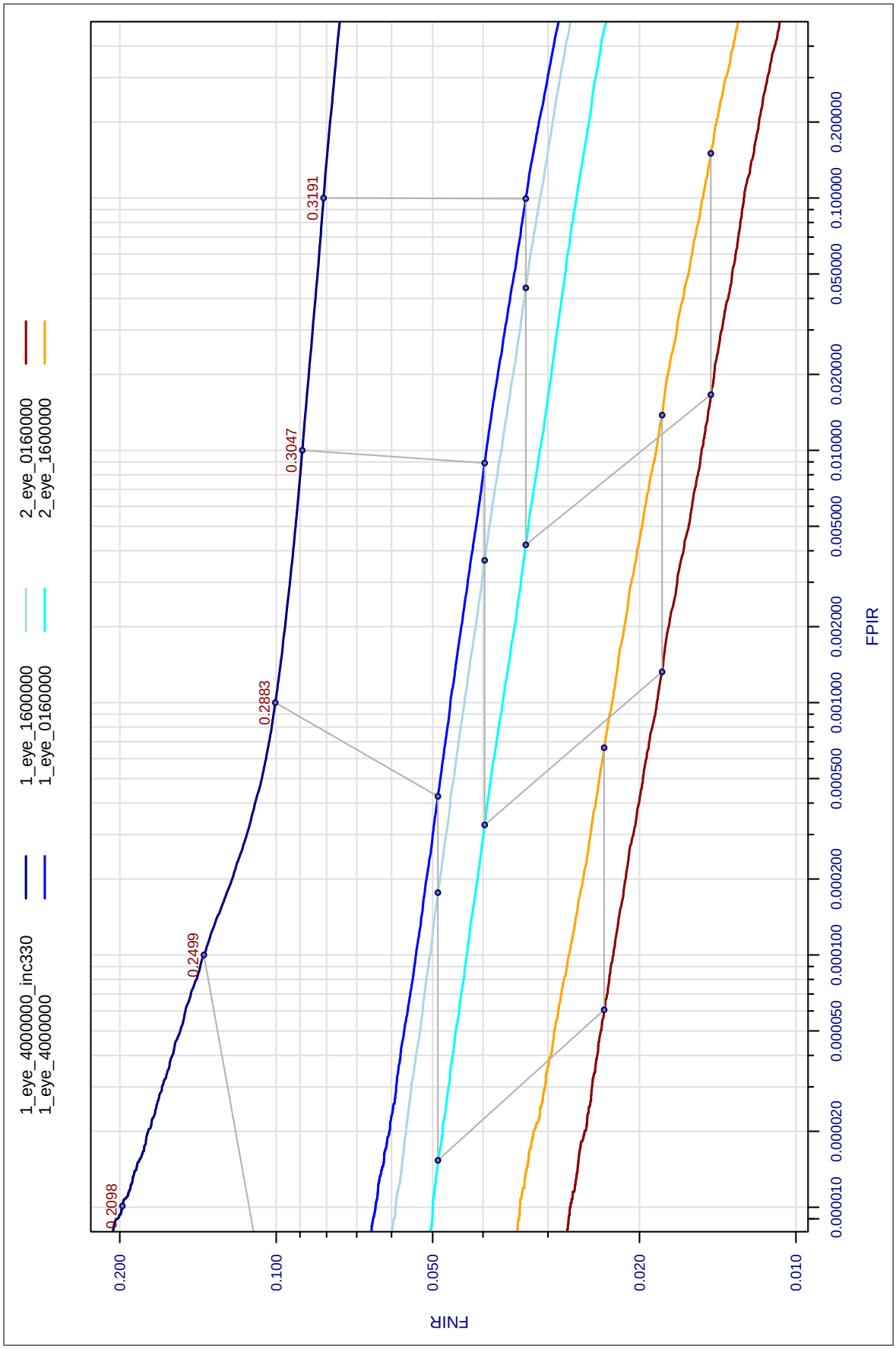

Figure 129: **Effect of population size** onDETs for implementation T01B executing searches for single-eye enrolled populations $N = (0.16, 1.6, 4)$ million, and two-eye populations of $N = (0.16, 1.6)$ million individuals. The straight lines, which link points of constant threshold, show how the two error rates would vary if a fixed threshold were adopted operationally. Horizontal lines indicate that enrolled population N is influential only on FPIR, via $\text{FPIR}(N_2) = (N_2/N_1)\text{FPIR}(N_1)$. When this relationship is not evident, the implementation may be adjusting scores as a function of N (e.g. as described in [cite Daugman]). The large search sets S_{nb} are used. Missing plots indicate the run is not yet complete.

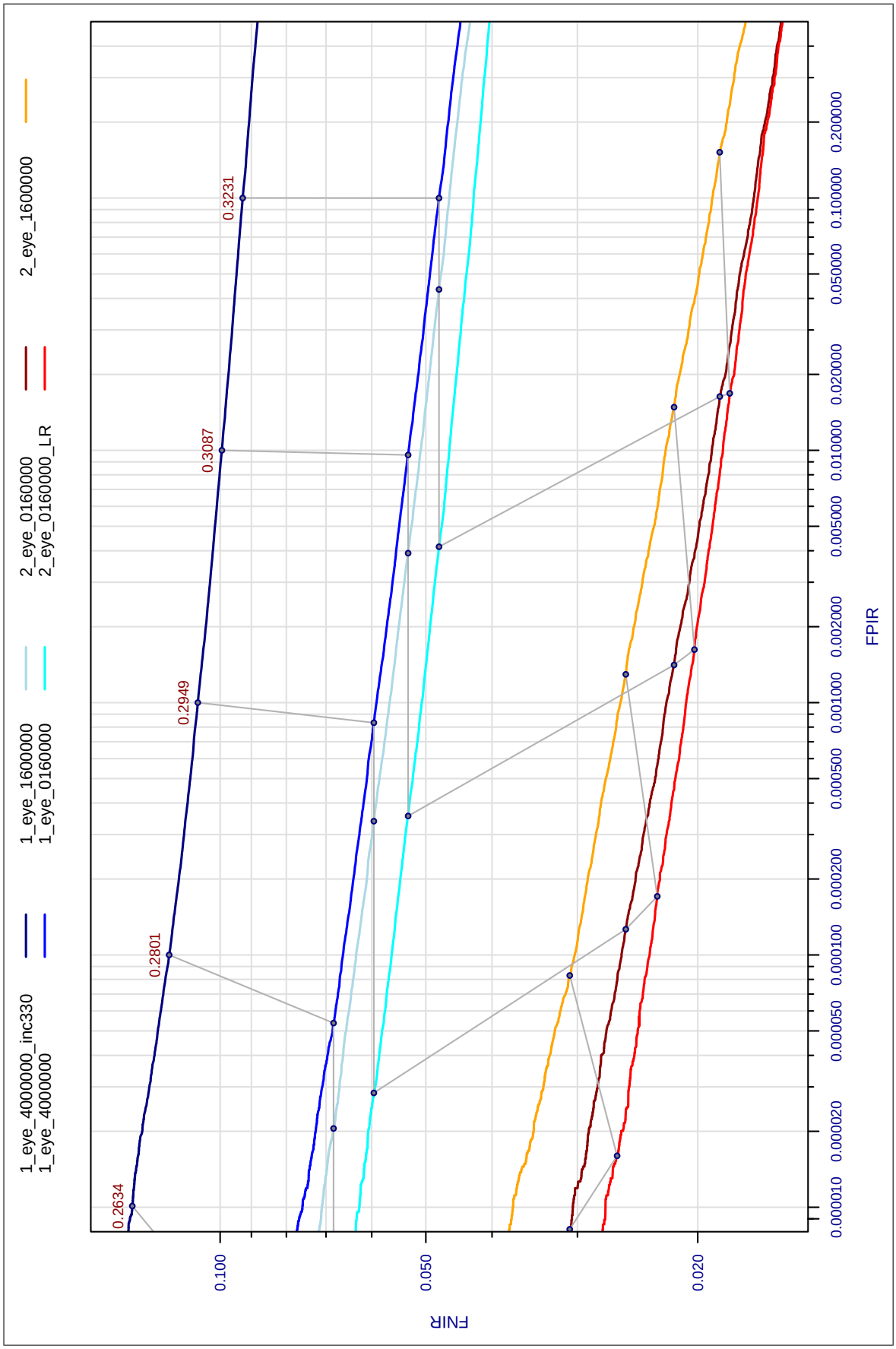

Figure 130: **Effect of population size** onDETs for implementation T02A executing searches for single-eye enrolled populations $N = (0.16, 1.6, 4)$ million, and two-eye populations of $N = (0.16, 1.6)$ million individuals. The straight lines, which link points of constant threshold, show how the two error rates would vary if a fixed threshold were adopted operationally. Horizontal lines indicate that enrolled population N is influential only on FPIR, via $\text{FPIR}(N_2) = (N_2/N_1)\text{FPIR}(N_1)$. When this relationship is not evident, the implementation may be adjusting scores as a function of N (e.g. as described in [cite Daugman]). The large search sets $S_{n,b}$ are used. Missing plots indicate the run is not yet complete.

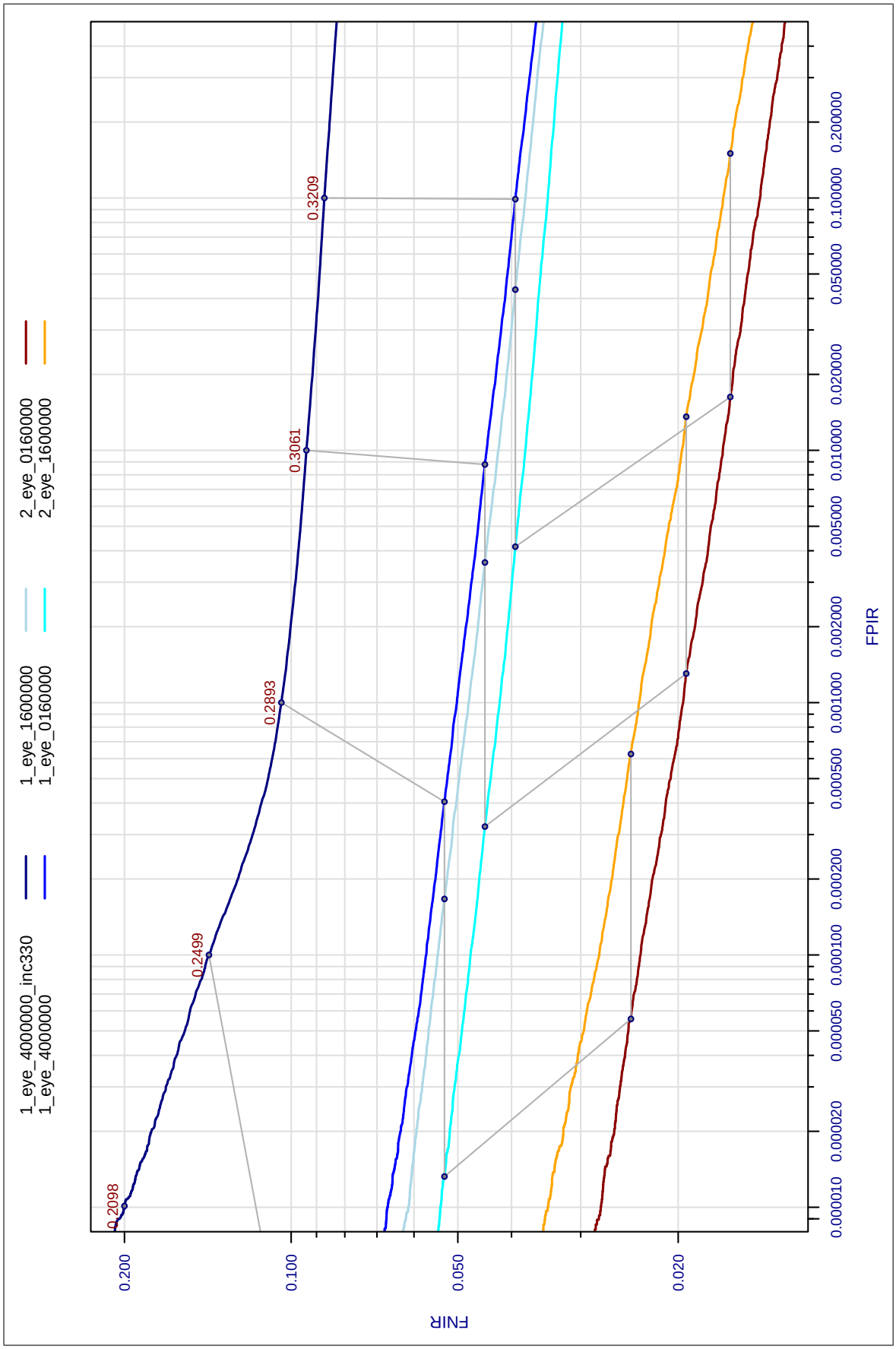

Figure 131: **Effect of population size** onDETs for implementation T02B executing searches for single-eye enrolled populations $N = (0.16, 1.6, 4)$ million, and two-eye populations of $N = (0.16, 1.6)$ million individuals. The straight lines, which link points of constant threshold, show how the two error rates would vary if a fixed threshold were adopted operationally. Horizontal lines indicate that enrolled population N is influential only on FPIR, via $\text{FPIR}(N_2) = (N_2/N_1)\text{FPIR}(N_1)$. When this relationship is not evident, the implementation may be adjusting scores as a function of N (e.g. as described in [cite Daugman]). The large search sets $S_{n,b}$ are used. Missing plots indicate the run is not yet complete.

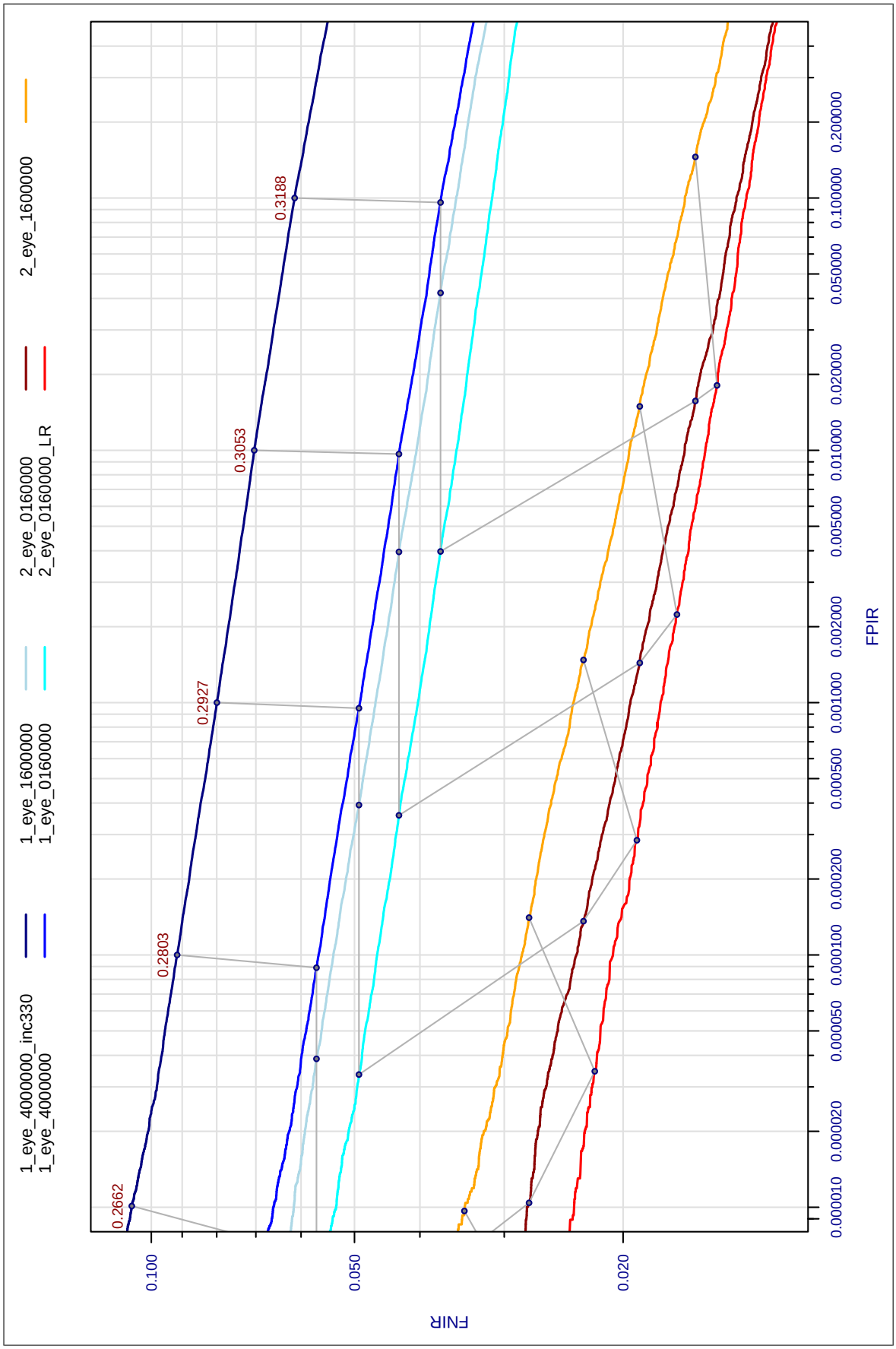

Figure 132: **Effect of population size** onDETs for implementation T03A executing searches for single-eye enrolled populations $N = (0.16, 1.6, 4)$ million, and two-eye populations of $N = (0.16, 1.6)$ million individuals. The straight lines, which link points of constant threshold, show how the two error rates would vary if a fixed threshold were adopted operationally. Horizontal lines indicate that enrolled population N is influential only on FPIR, via $\text{FPIR}(N_2) = (N_2/N_1)\text{FPIR}(N_1)$. When this relationship is not evident, the implementation may be adjusting scores as a function of N (e.g. as described in [cite Daugman]). The large search sets S_{nb} are used. Missing plots indicate the run is not yet complete.

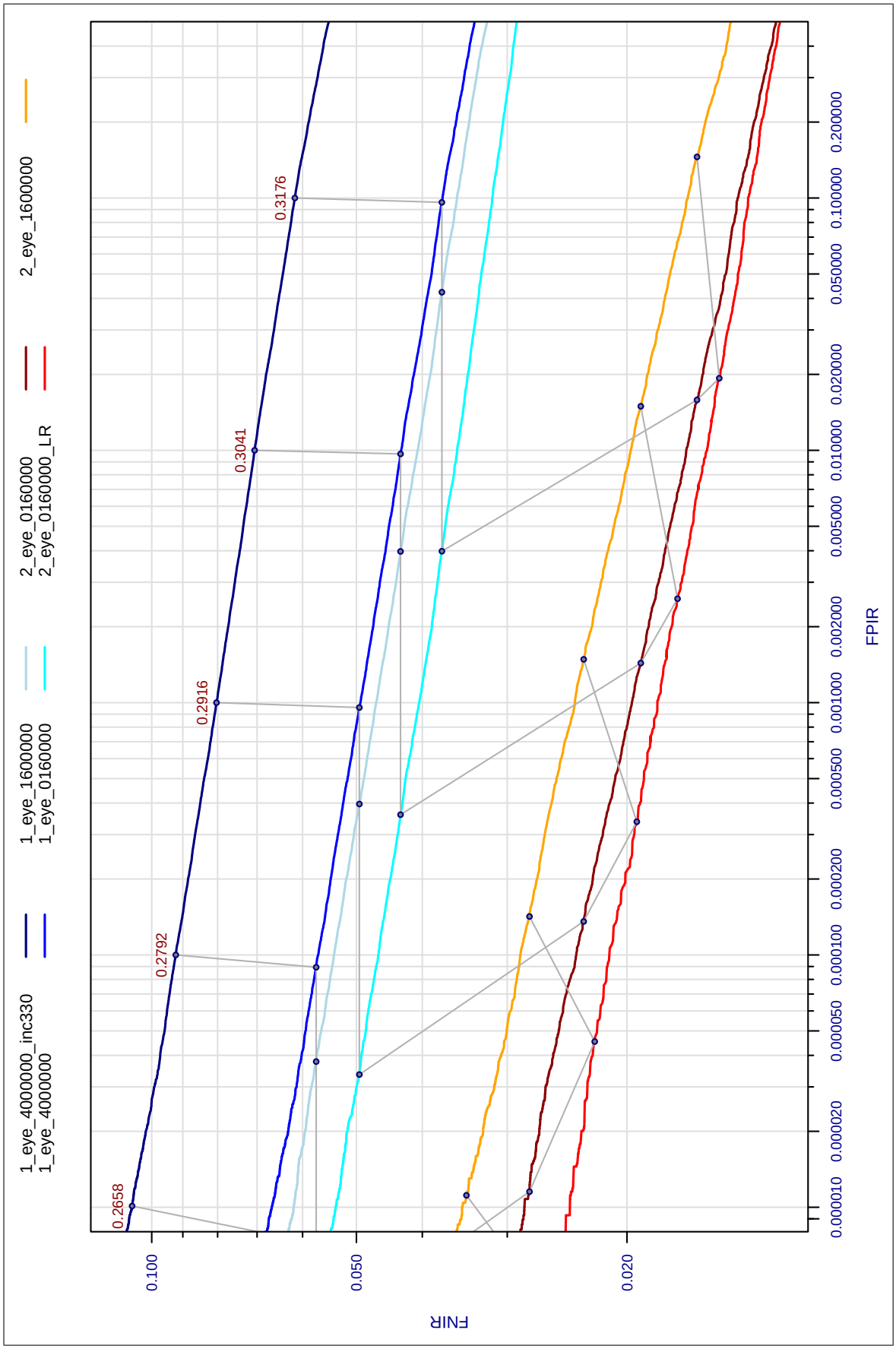

Figure 133: **Effect of population size** onDETs for implementation T03B executing searches for single-eye enrolled populations $N = (0.16, 1.6, 4)$ million, and two-eye populations of $N = (0.16, 1.6)$ million individuals. The straight lines, which link points of constant threshold, show how the two error rates would vary if a fixed threshold were adopted operationally. Horizontal lines indicate that enrolled population N is influential only on FPIR, via $\text{FPIR}(N_2) = (N_2/N_1)\text{FPIR}(N_1)$. When this relationship is not evident, the implementation may be adjusting scores as a function of N (e.g. as described in [cite Daugman]). The large search sets S_{nb} are used. Missing plots indicate the run is not yet complete.

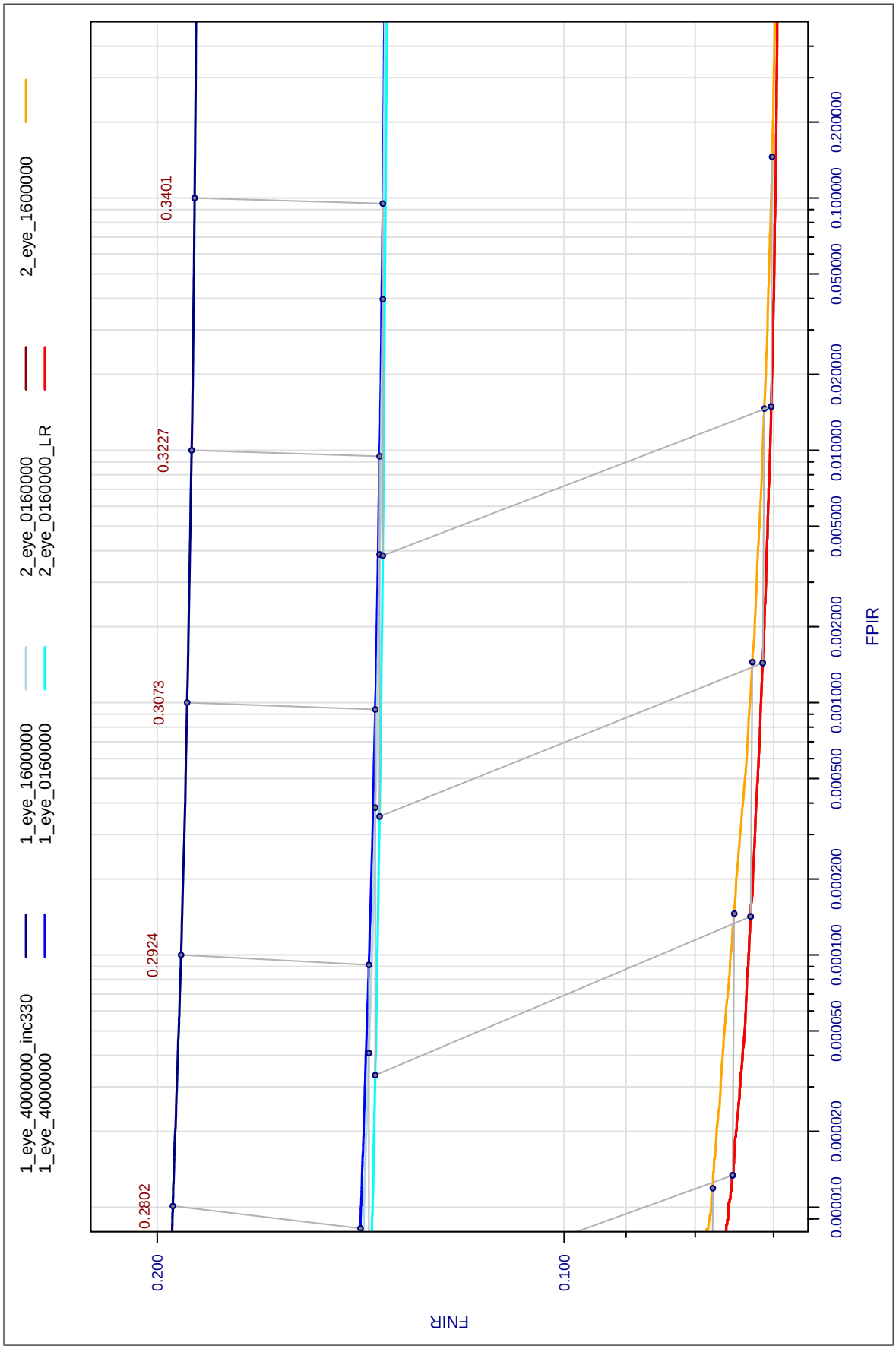

Figure 134: **Effect of population size** onDETs for implementation T04A executing searches for single-eye enrolled populations $N = (0.16, 1.6, 4)$ million, and two-eye populations of $N = (0.16, 1.6)$ million individuals. The straight lines, which link points of constant threshold, show how the two error rates would vary if a fixed threshold were adopted operationally. Horizontal lines indicate that enrolled population N is influential only on FPIR, via $\text{FPIR}(N_2) = (N_2/N_1)\text{FPIR}(N_1)$. When this relationship is not evident, the implementation may be adjusting scores as a function of N (e.g. as described in [cite Daugman]). The large search sets $S_{n,b}$ are used. Missing plots indicate the run is not yet complete.

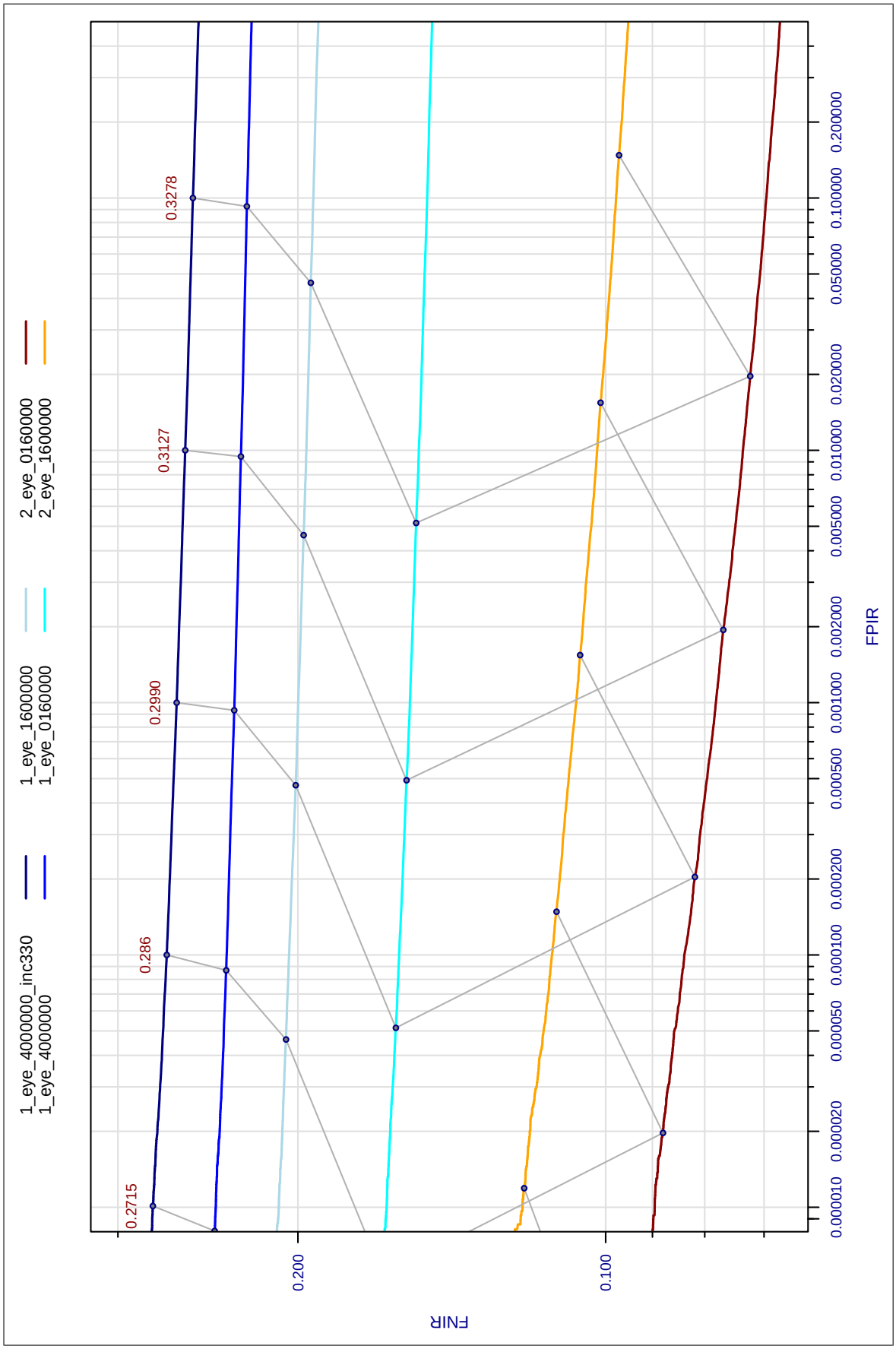

Figure 135: **Effect of population size** onDETs for implementation T11A executing searches for single-eye enrolled populations $N = (0.16, 1.6, 4)$ million, and two-eye populations of $N = (0.16, 1.6)$ million individuals. The straight lines, which link points of constant threshold, show how the two error rates would vary if a fixed threshold were adopted operationally. Horizontal lines indicate that enrolled population N is influential only on FPIR, via $\text{FPIR}(N_2) = (N_2/N_1)\text{FPIR}(N_1)$. When this relationship is not evident, the implementation may be adjusting scores as a function of N (e.g. as described in [cite Daugman]). The large search sets $S_{n,b}$ are used. Missing plots indicate the run is not yet complete.

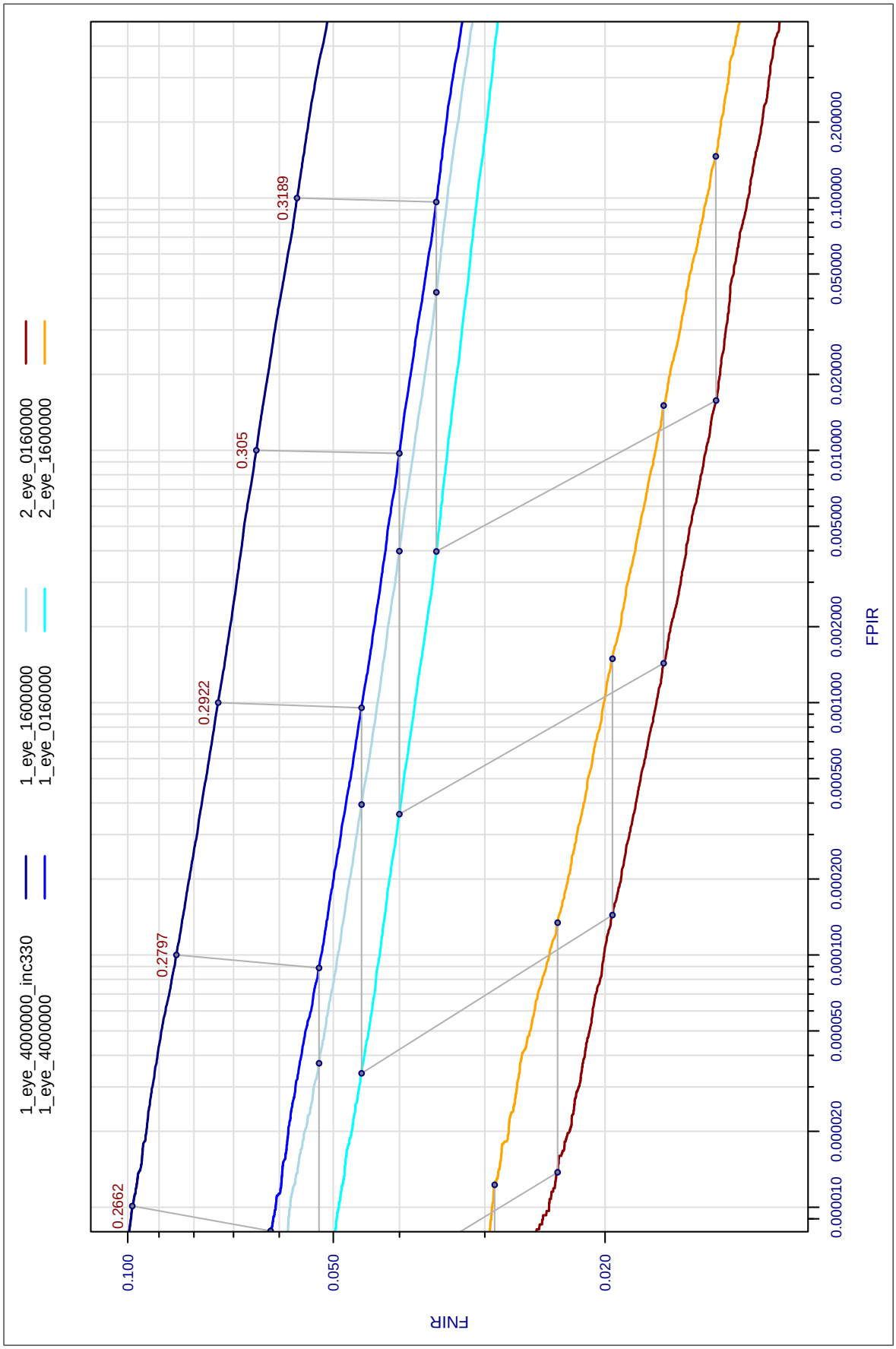

Figure 136: **Effect of population size** onDETs for implementation T11B executing searches for single-eye enrolled populations $N = (0.16, 1.6, 4)$ million, and two-eye populations of $N = (0.16, 1.6)$ million individuals. The straight lines, which link points of constant threshold, show how the two error rates would vary if a fixed threshold were adopted operationally. Horizontal lines indicate that enrolled population N is influential only on FPIR, via $\text{FPIR}(N_2) = (N_2/N_1)\text{FPIR}(N_1)$. When this relationship is not evident, the implementation may be adjusting scores as a function of N (e.g. as described in [cite Daugman]). The large search sets S_{nb} are used. Missing plots indicate the run is not yet complete.

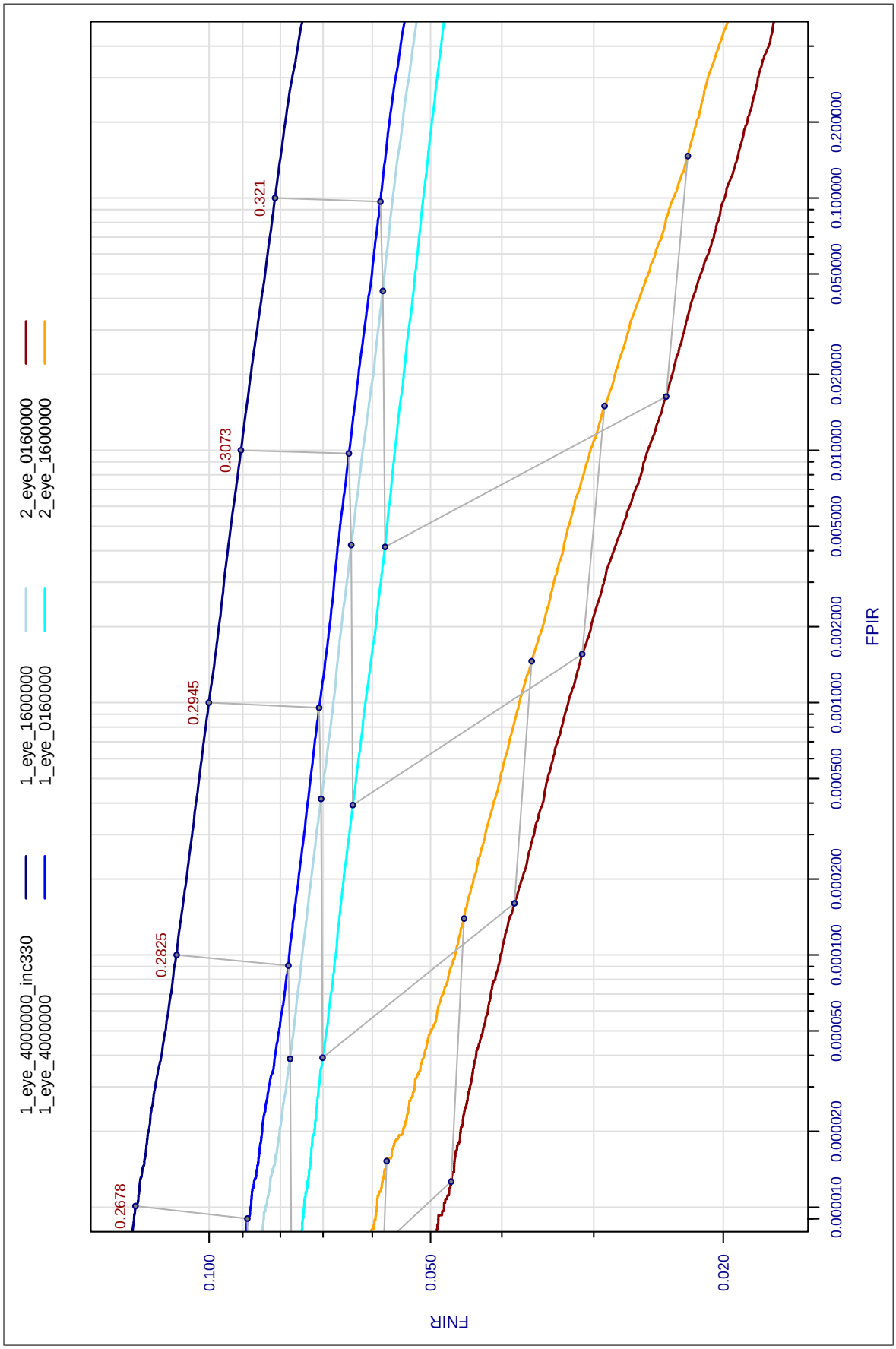

Figure 137: **Effect of population size** onDETs for implementation T12B executing searches for single-eye enrolled populations $N = (0.16, 1.6, 4)$ million, and two-eye populations of $N = (0.16, 1.6)$ million individuals. The straight lines, which link points of constant threshold, show how the two error rates would vary if a fixed threshold were adopted operationally. Horizontal lines indicate that enrolled population N is influential only on FPIR, via $\text{FPIR}(N_2) = (N_2/N_1)\text{FPIR}(N_1)$. When this relationship is not evident, the implementation may be adjusting scores as a function of N (e.g. as described in [cite Daugman]). The large search sets $S_{n,b}$ are used. Missing plots indicate the run is not yet complete.

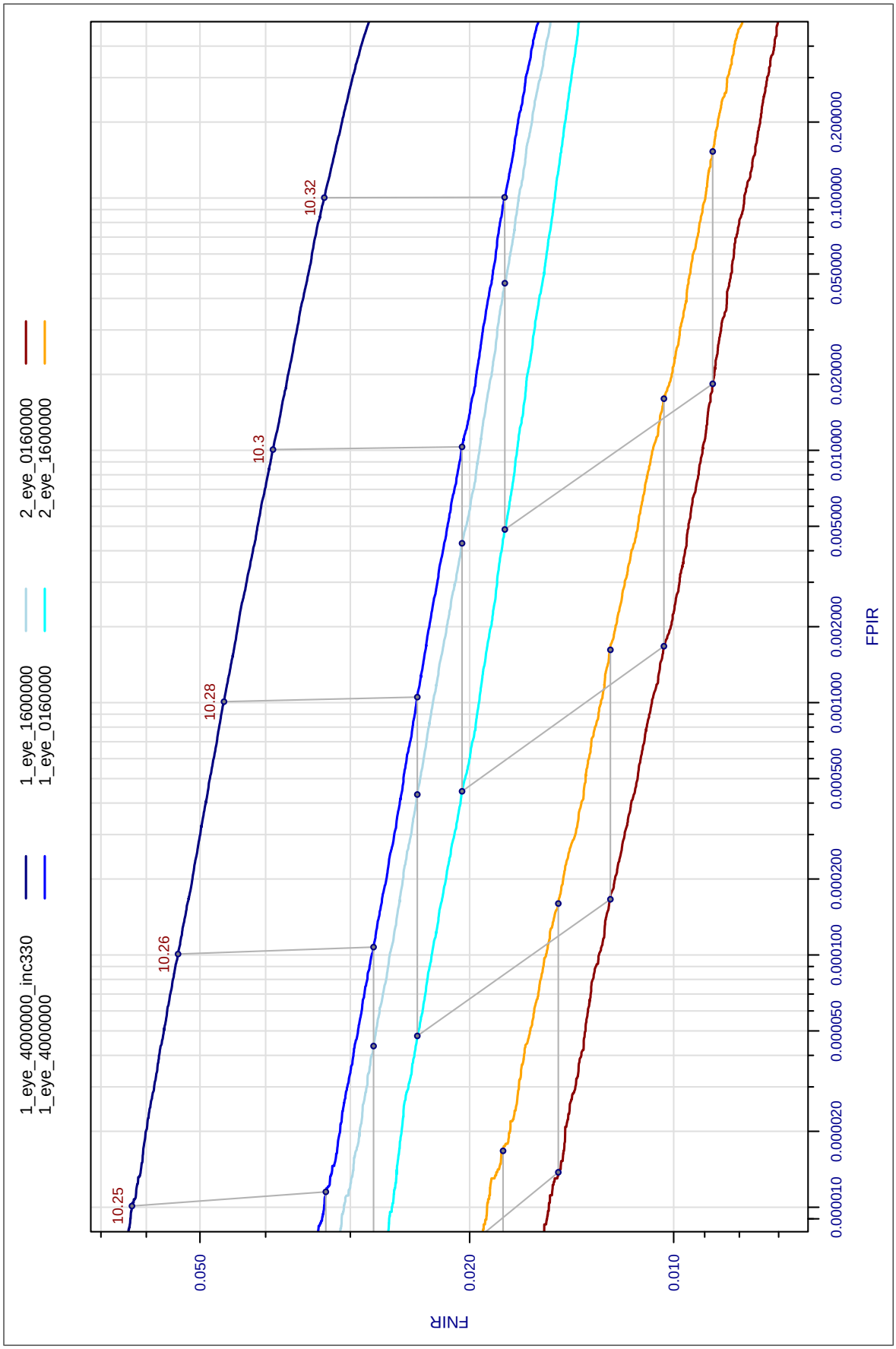

Figure 138: **Effect of population size** onDETs for implementation U01A executing searches for single-eye enrolled populations $N = (0.16, 1.6, 4)$ million, and two-eye populations of $N = (0.16, 1.6)$ million individuals. The straight lines, which link points of constant threshold, show how the two error rates would vary if a fixed threshold were adopted operationally. Horizontal lines indicate that enrolled population N is influential only on FPIR, via $\text{FPIR}(N_2) = (N_2/N_1)\text{FPIR}(N_1)$. When this relationship is not evident, the implementation may be adjusting scores as a function of N (e.g. as described in [cite Daugman]). The large search sets S_{nb} are used. Missing plots indicate the run is not yet complete.

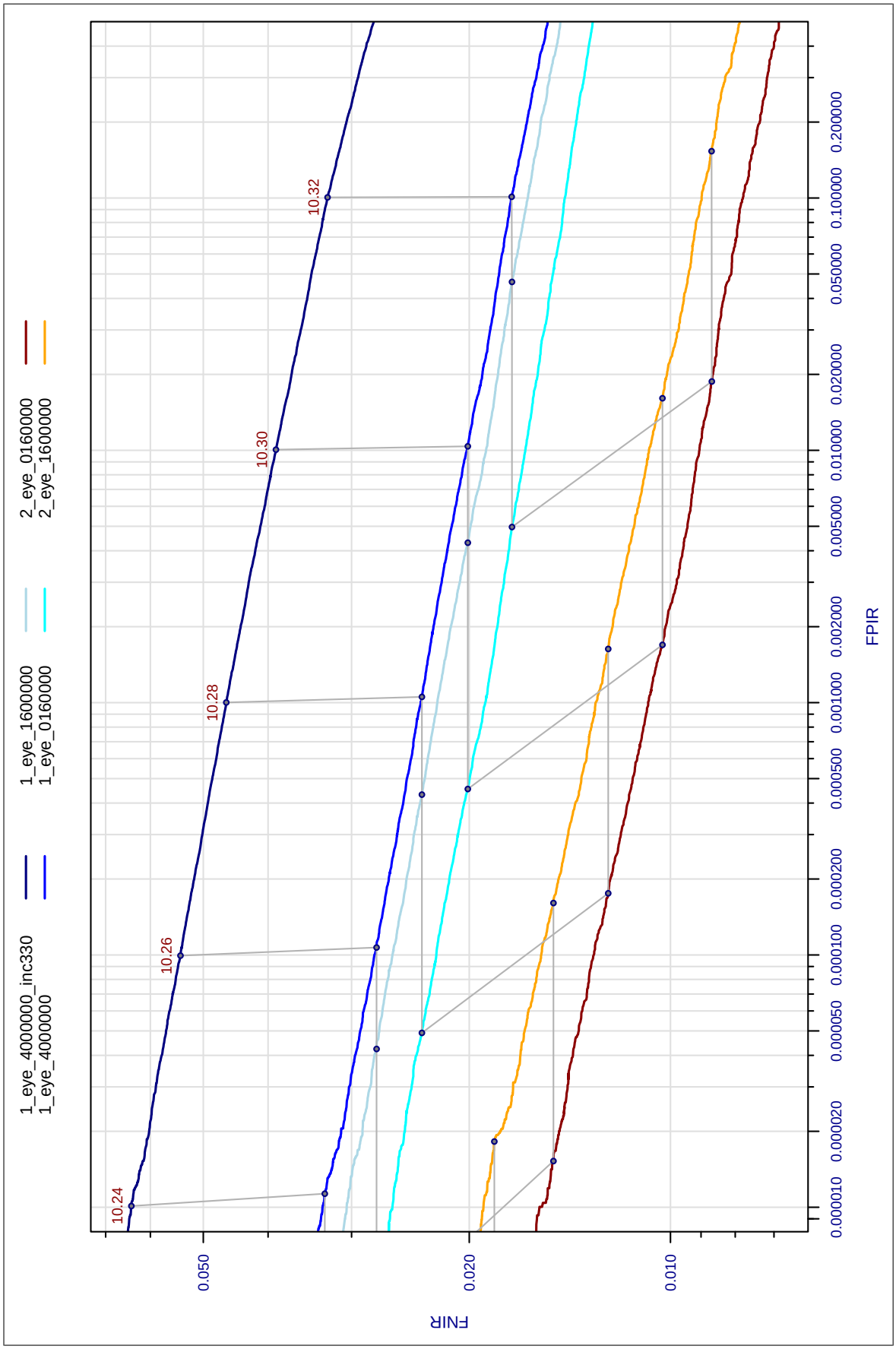

Figure 139: **Effect of population size** onDETs for implementation U01B executing searches for single-eye enrolled populations $N = (0.16, 1.6, 4)$ million, and two-eye populations of $N = (0.16, 1.6)$ million individuals. The straight lines, which link points of constant threshold, show how the two error rates would vary if a fixed threshold were adopted operationally. Horizontal lines indicate that enrolled population N is influential only on FPIR, via $\text{FPIR}(N_2) = (N_2/N_1)\text{FPIR}(N_1)$. When this relationship is not evident, the implementation may be adjusting scores as a function of N (e.g. as described in [cite Daugman]). The large search sets S_{nb} are used. Missing plots indicate the run is not yet complete.

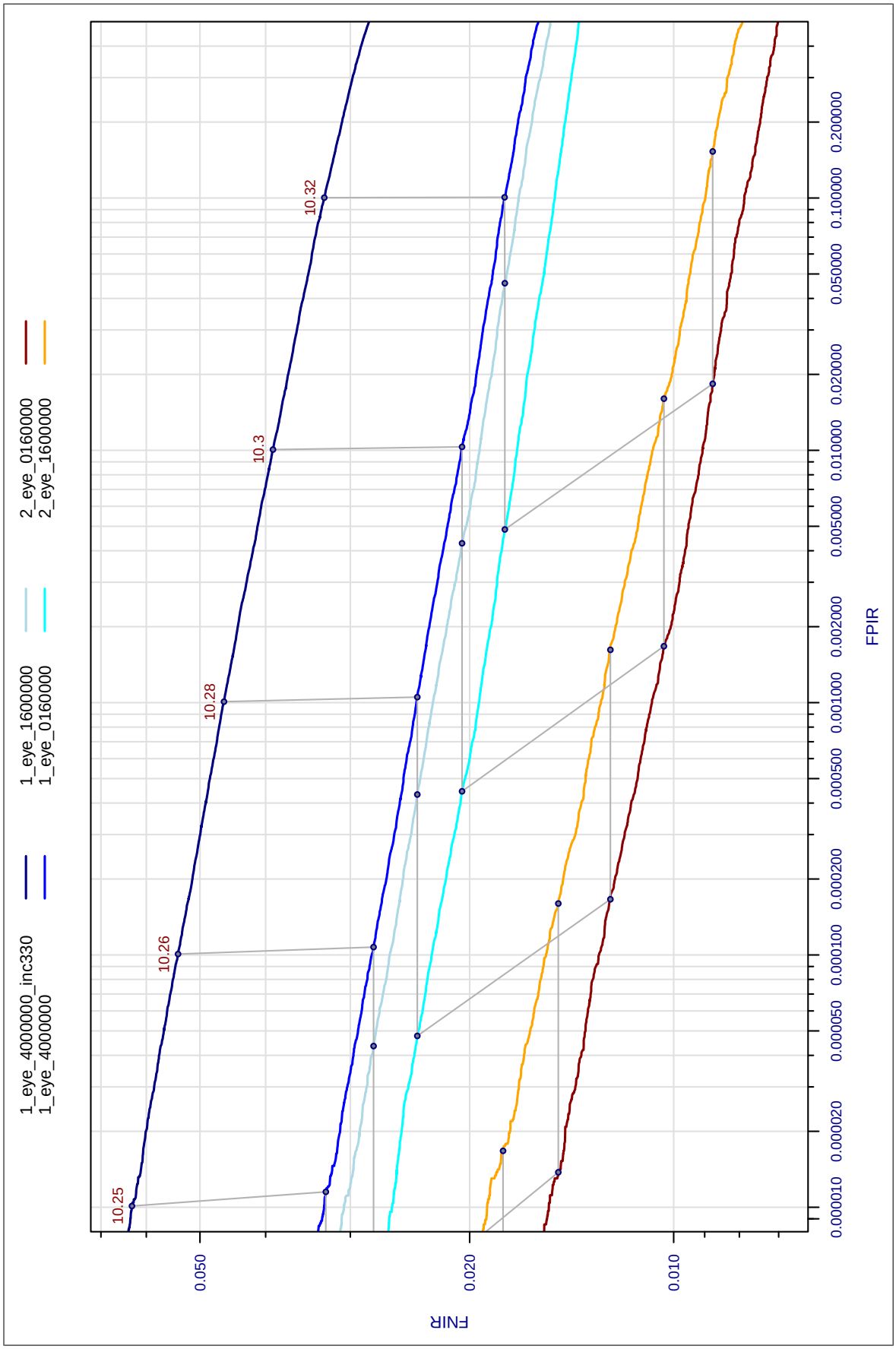

Figure 140: **Effect of population size** onDETs for implementation U02A executing searches for single-eye enrolled populations $N = (0.16, 1.6, 4)$ million, and two-eye populations of $N = (0.16, 1.6)$ million individuals. The straight lines, which link points of constant threshold, show how the two error rates would vary if a fixed threshold were adopted operationally. Horizontal lines indicate that enrolled population N is influential only on FPIR, via $\text{FPIR}(N_2) = (N_2/N_1)\text{FPIR}(N_1)$. When this relationship is not evident, the implementation may be adjusting scores as a function of N (e.g. as described in [cite Daugman]). The large search sets S_{nb} are used. Missing plots indicate the run is not yet complete.

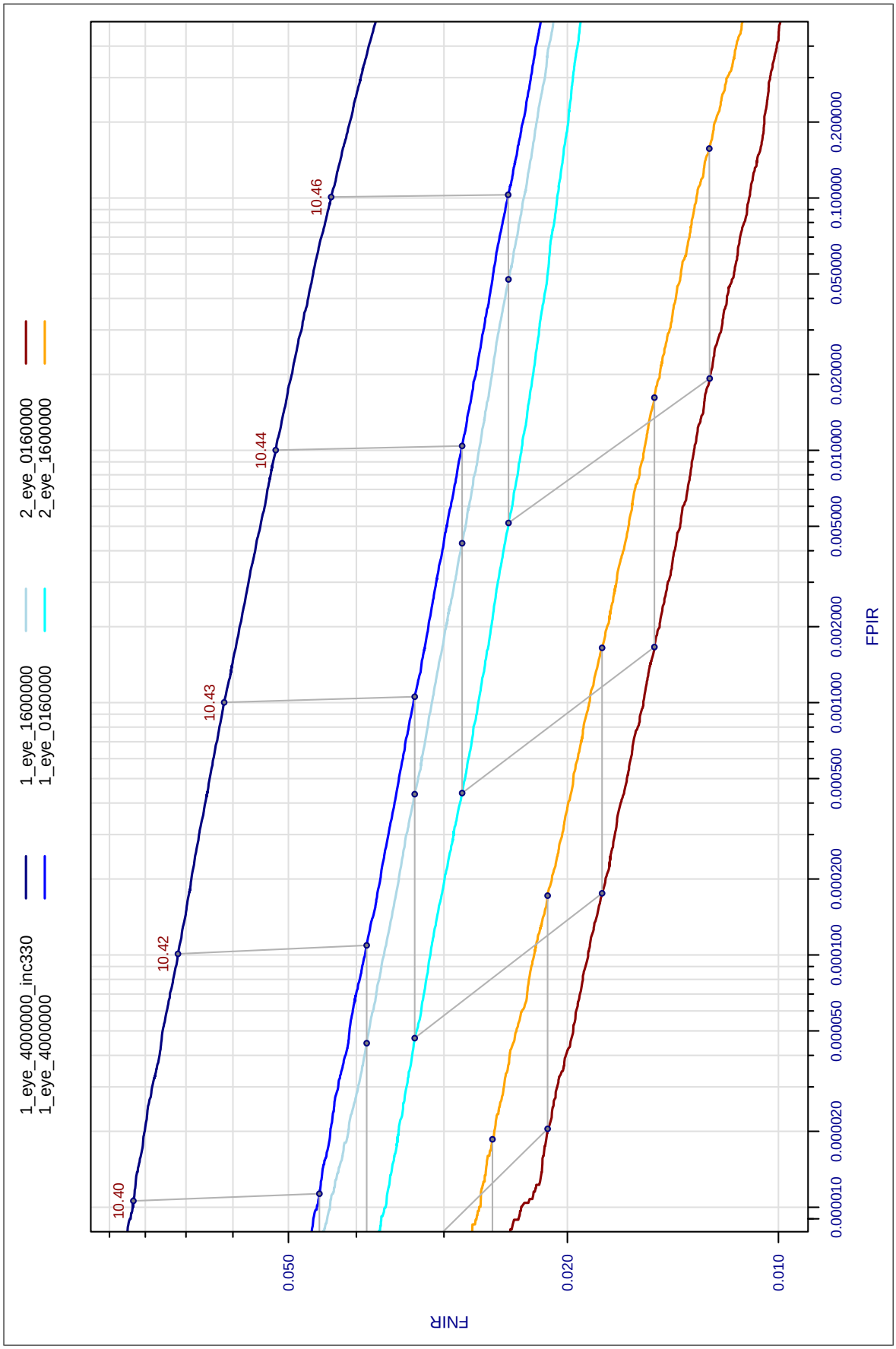

Figure 141: **Effect of population size** onDETs for implementation U03A executing searches for single-eye enrolled populations $N = (0.16, 1.6, 4)$ million, and two-eye populations of $N = (0.16, 1.6)$ million individuals. The straight lines, which link points of constant threshold, show how the two error rates would vary if a fixed threshold were adopted operationally. Horizontal lines indicate that enrolled population N is influential only on FPIR, via $\text{FPIR}(N_2) = (N_2/N_1)\text{FPIR}(N_1)$. When this relationship is not evident, the implementation may be adjusting scores as a function of N (e.g. as described in [cite Daugman]). The large search sets S_{nb} are used. Missing plots indicate the run is not yet complete.

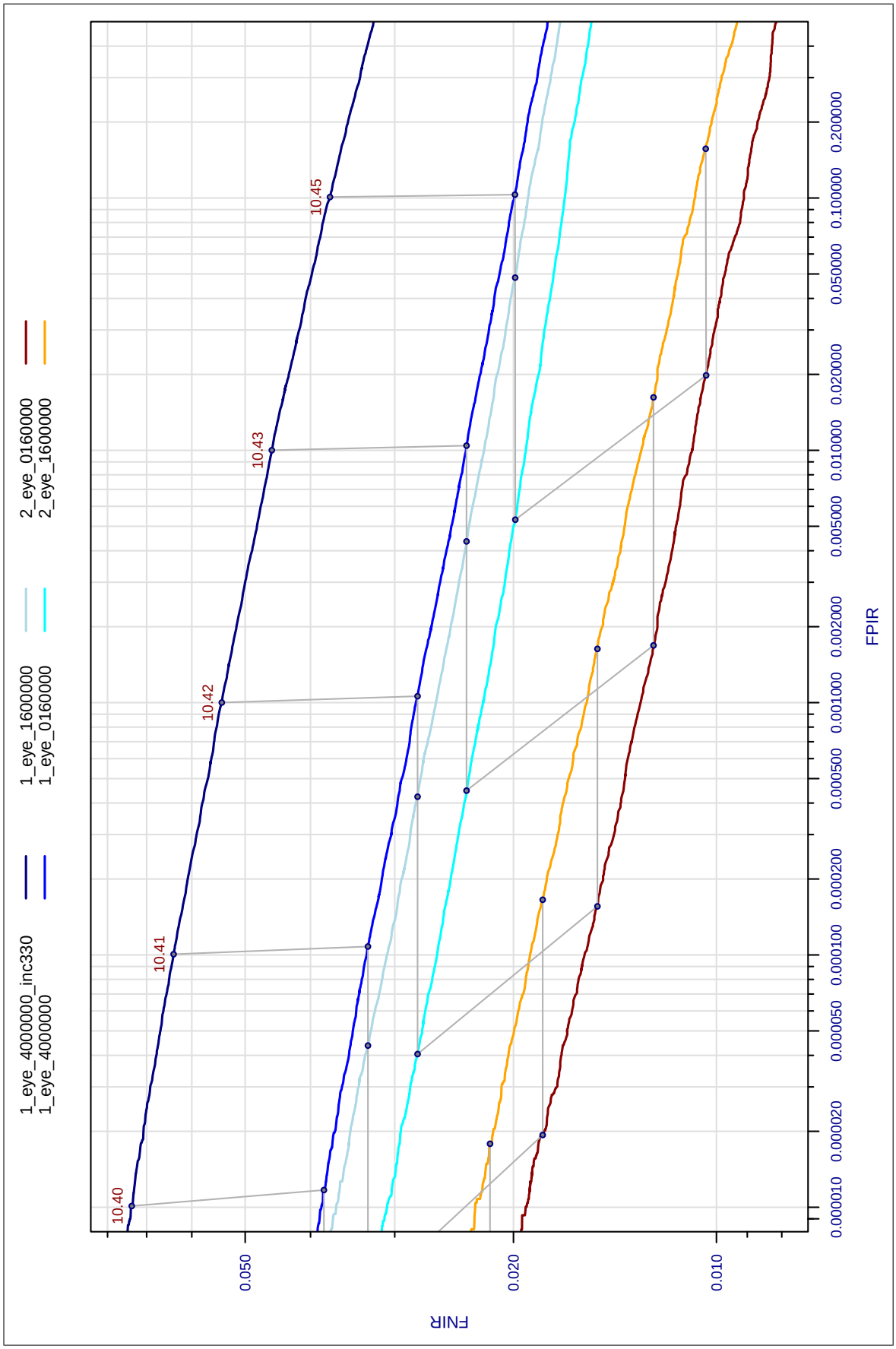

Figure 142: **Effect of population size** onDETs for implementation U03B executing searches for single-eye enrolled populations $N = (0.16, 1.6, 4)$ million, and two-eye populations of $N = (0.16, 1.6)$ million individuals. The straight lines, which link points of constant threshold, show how the two error rates would vary if a fixed threshold were adopted operationally. Horizontal lines indicate that enrolled population N is influential only on FPIR, via $\text{FPIR}(N_2) = (N_2/N_1)\text{FPIR}(N_1)$. When this relationship is not evident, the implementation may be adjusting scores as a function of N (e.g. as described in [cite Daugman]). The large search sets S_{nb} are used. Missing plots indicate the run is not yet complete.

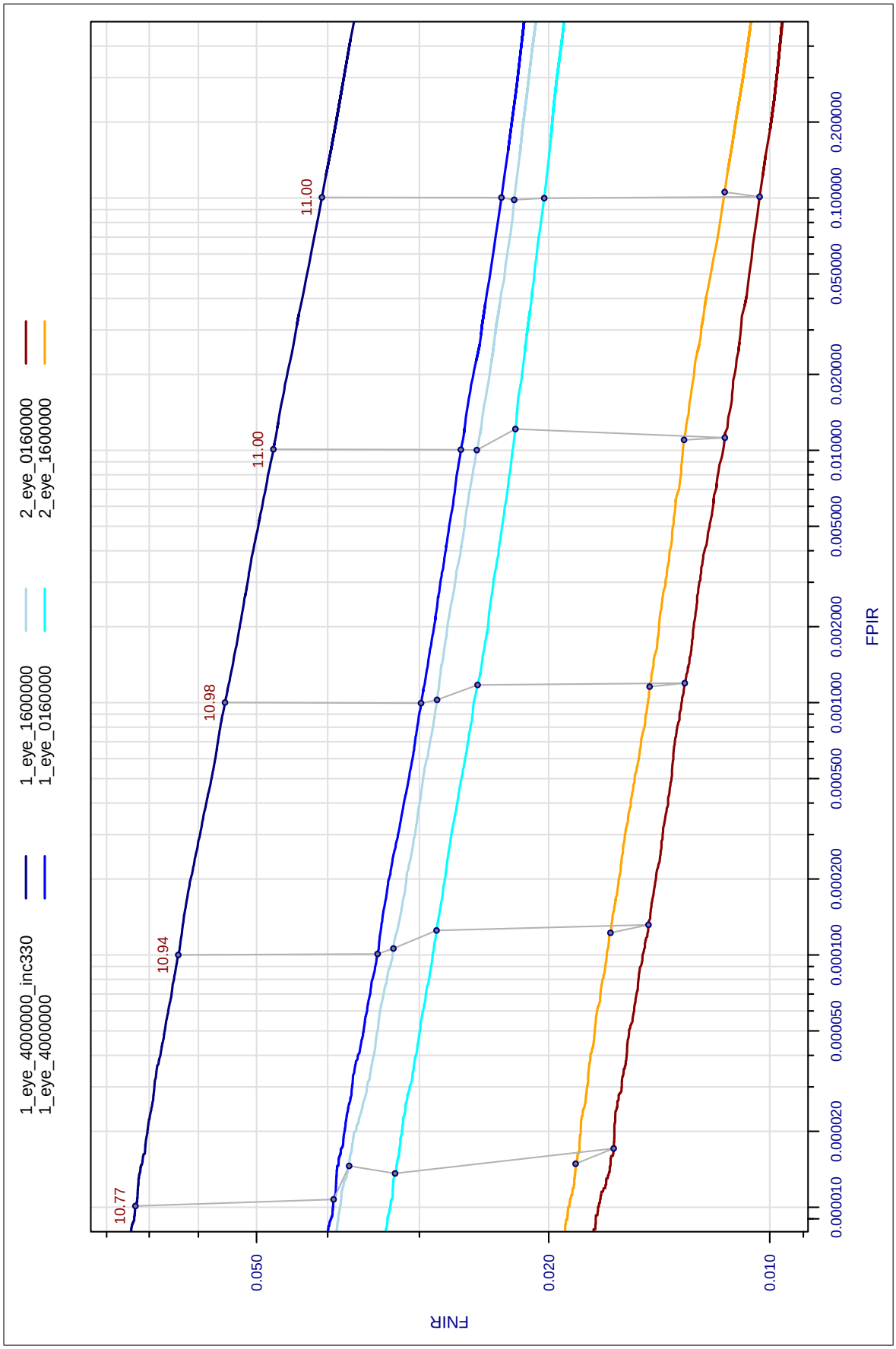

Figure 143: **Effect of population size** onDETs for implementation U04A executing searches for single-eye enrolled populations $N = (0.16, 1.6, 4)$ million, and two-eye populations of $N = (0.16, 1.6)$ million individuals. The straight lines, which link points of constant threshold, show how the two error rates would vary if a fixed threshold were adopted operationally. Horizontal lines indicate that enrolled population N is influential only on FPIR, via $\text{FPIR}(N_2) = (N_2/N_1)\text{FPIR}(N_1)$. When this relationship is not evident, the implementation may be adjusting scores as a function of N (e.g. as described in [cite Daugman]). The large search sets $S_{n,b}$ are used. Missing plots indicate the run is not yet complete.

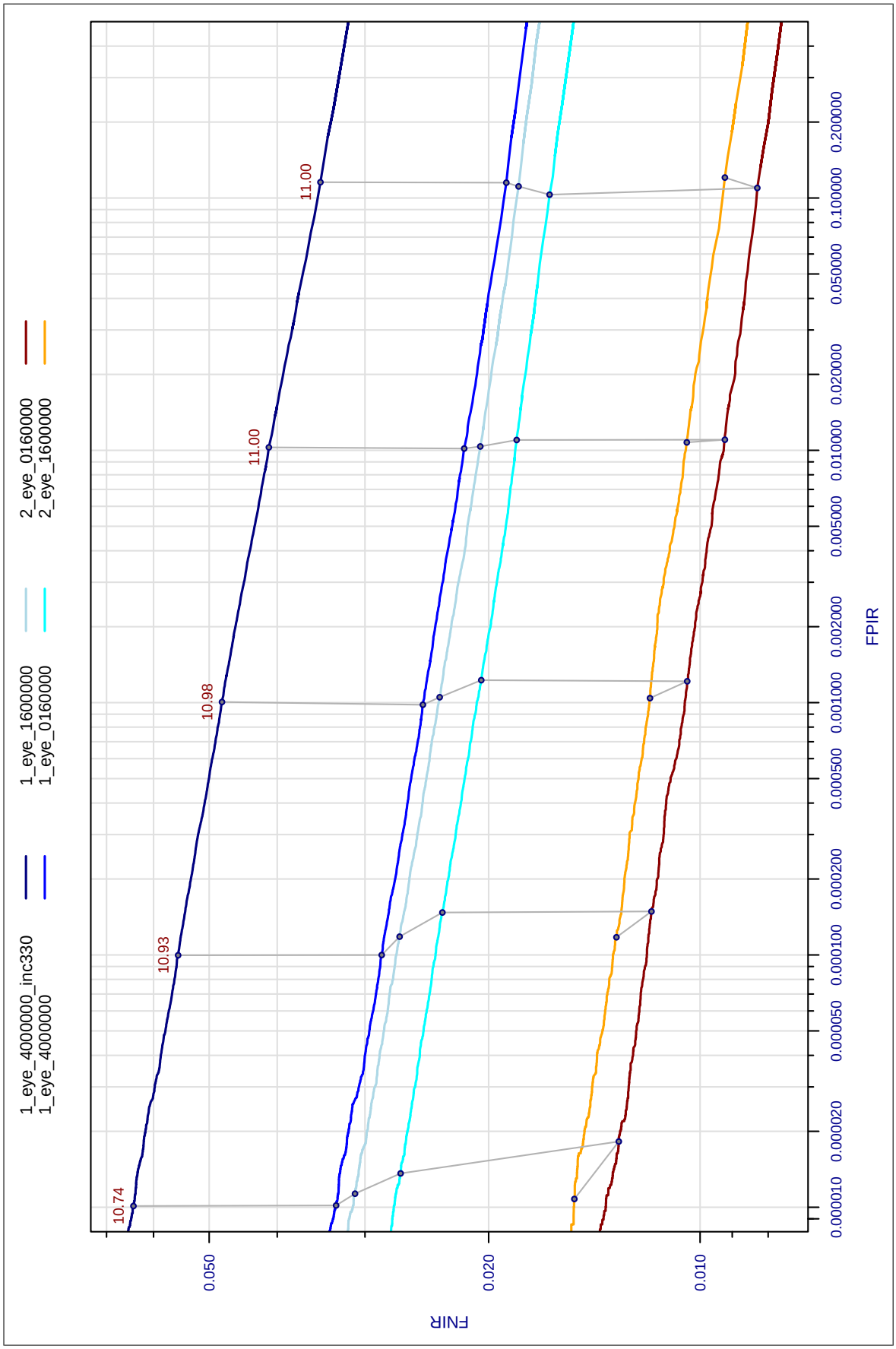

Figure 144: **Effect of population size** onDETs for implementation U04B executing searches for single-eye enrolled populations $N = (0.16, 1.6, 4)$ million, and two-eye populations of $N = (0.16, 1.6)$ million individuals. The straight lines, which link points of constant threshold, show how the two error rates would vary if a fixed threshold were adopted operationally. Horizontal lines indicate that enrolled population N is influential only on FPIR, via $\text{FPIR}(N_2) = (N_2/N_1)\text{FPIR}(N_1)$. When this relationship is not evident, the implementation may be adjusting scores as a function of N (e.g. as described in [cite Daugman]). The large search sets $S_{n,b}$ are used. Missing plots indicate the run is not yet complete.

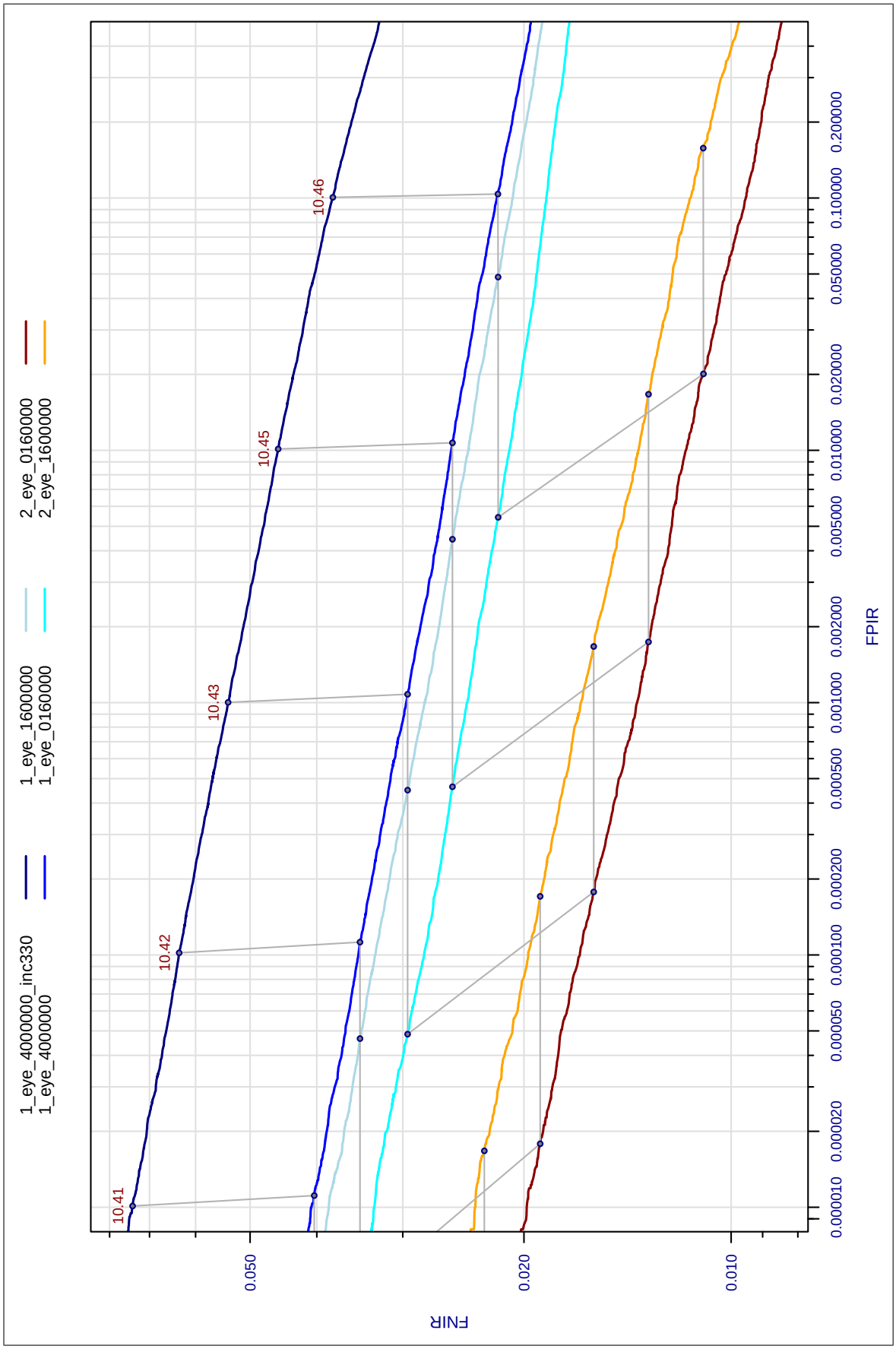

Figure 145: **Effect of population size** onDETs for implementation U11A executing searches for single-eye enrolled populations $N = (0.16, 1.6, 4)$ million, and two-eye populations of $N = (0.16, 1.6)$ million individuals. The straight lines, which link points of constant threshold, show how the two error rates would vary if a fixed threshold were adopted operationally. Horizontal lines indicate that enrolled population N is influential only on FPIR, via $\text{FPIR}(N_2) = (N_2/N_1)\text{FPIR}(N_1)$. When this relationship is not evident, the implementation may be adjusting scores as a function of N (e.g. as described in [cite Daugman]). The large search sets S_{nb} are used. Missing plots indicate the run is not yet complete.

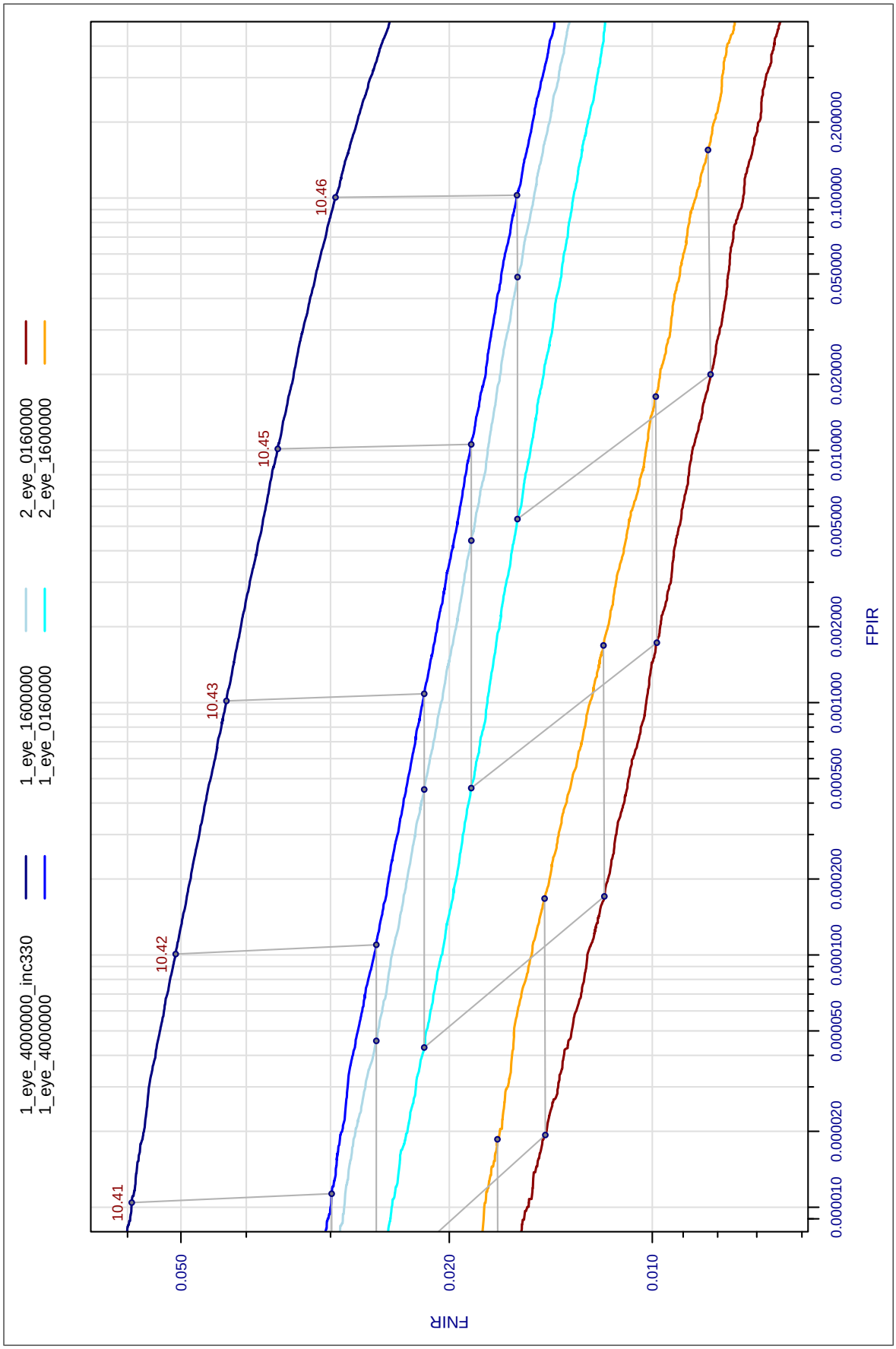

Figure 146: **Effect of population size** onDETs for implementation U11B executing searches for single-eye enrolled populations $N = (0.16, 1.6, 4)$ million, and two-eye populations of $N = (0.16, 1.6)$ million individuals. The straight lines, which link points of constant threshold, show how the two error rates would vary if a fixed threshold were adopted operationally. Horizontal lines indicate that enrolled population N is influential only on FPIR, via $\text{FPIR}(N_2) = (N_2/N_1)\text{FPIR}(N_1)$. When this relationship is not evident, the implementation may be adjusting scores as a function of N (e.g. as described in [cite Daugman]). The large search sets S_{nb} are used. Missing plots indicate the run is not yet complete.

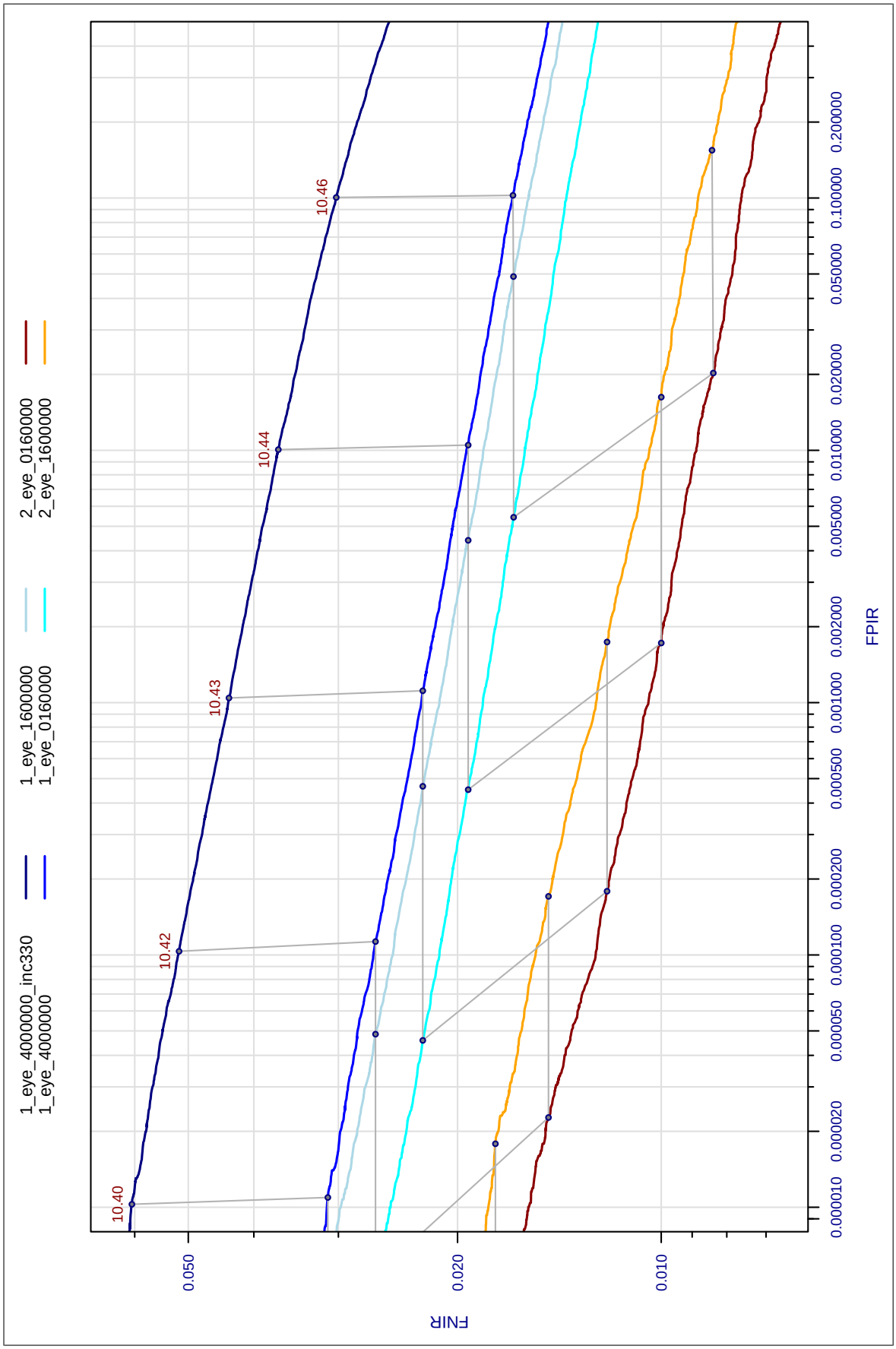

Figure 147: **Effect of population size** onDETs for implementation U12A executing searches for single-eye enrolled populations $N = (0.16, 1.6, 4)$ million, and two-eye populations of $N = (0.16, 1.6)$ million individuals. The straight lines, which link points of constant threshold, show how the two error rates would vary if a fixed threshold were adopted operationally. Horizontal lines indicate that enrolled population N is influential only on FPIR, via $\text{FPIR}(N_2) = (N_2/N_1)\text{FPIR}(N_1)$. When this relationship is not evident, the implementation may be adjusting scores as a function of N (e.g. as described in [cite Daugman]). The large search sets S_{nb} are used. Missing plots indicate the run is not yet complete.

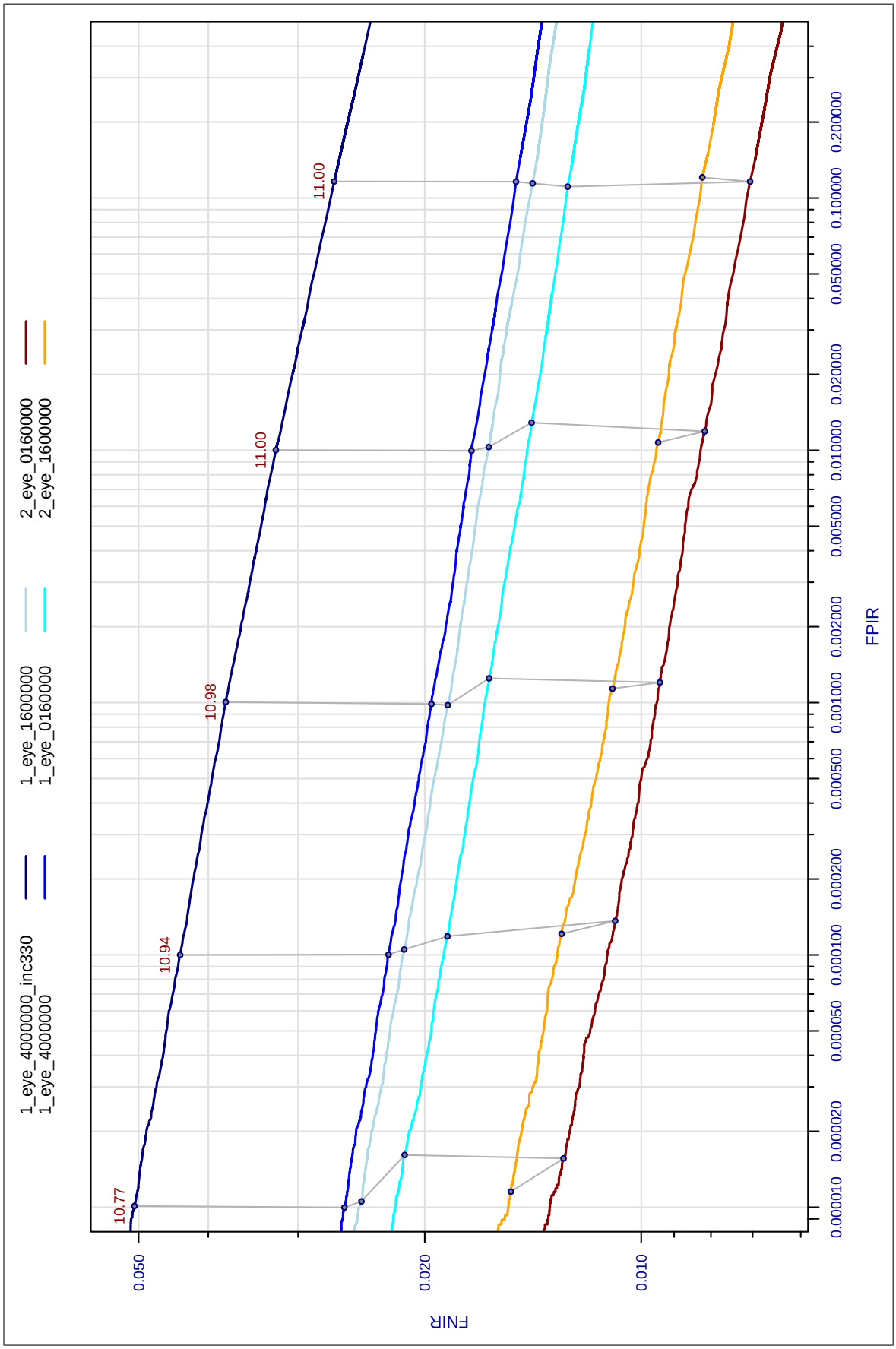

Figure 148: **Effect of population size** onDETs for implementation U12B executing searches for single-eye enrolled populations $N = (0.16, 1.6, 4)$ million, and two-eye populations of $N = (0.16, 1.6)$ million individuals. The straight lines, which link points of constant threshold, show how the two error rates would vary if a fixed threshold were adopted operationally. Horizontal lines indicate that enrolled population N is influential only on FPIR, via $\text{FPIR}(N_2) = (N_2/N_1)\text{FPIR}(N_1)$. When this relationship is not evident, the implementation may be adjusting scores as a function of N (e.g. as described in [cite Daugman]). The large search sets S_{nb} are used. Missing plots indicate the run is not yet complete.

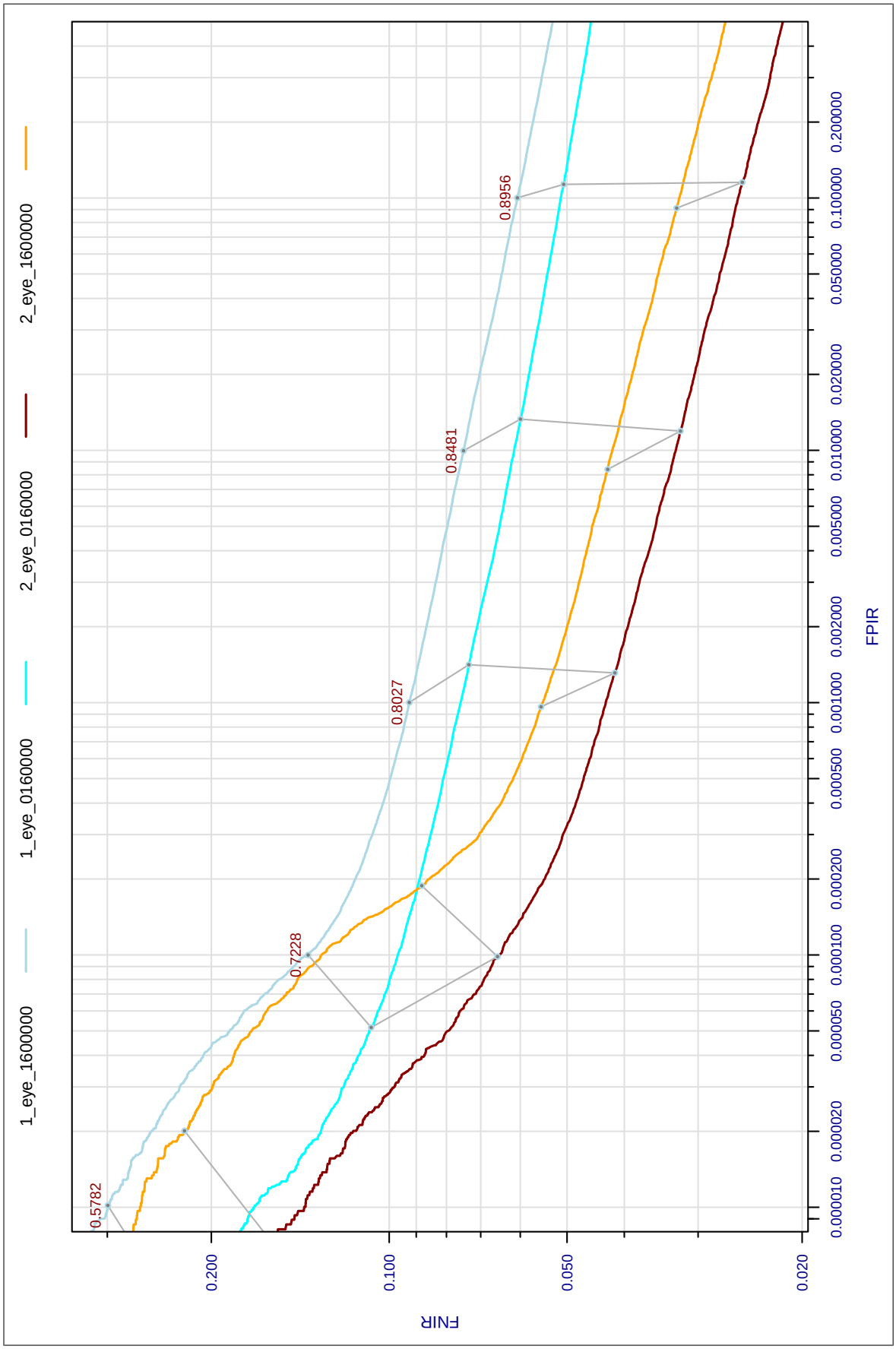

Figure 149: **Effect of population size** onDETs for implementation V01A executing searches for single-eye enrolled populations $N = (0.16, 1.6, 4)$ million, and two-eye populations of $N = (0.16, 1.6)$ million individuals. The straight lines, which link points of constant threshold, show how the two error rates would vary if a fixed threshold were adopted operationally. Horizontal lines indicate that enrolled population N is influential only on FPIR, via $\text{FPIR}(N_2) = (N_2/N_1)\text{FPIR}(N_1)$. When this relationship is not evident, the implementation may be adjusting scores as a function of N (e.g. as described in [cite Daugman]). The large search sets S_{nb} are used. Missing plots indicate the run is not yet complete.

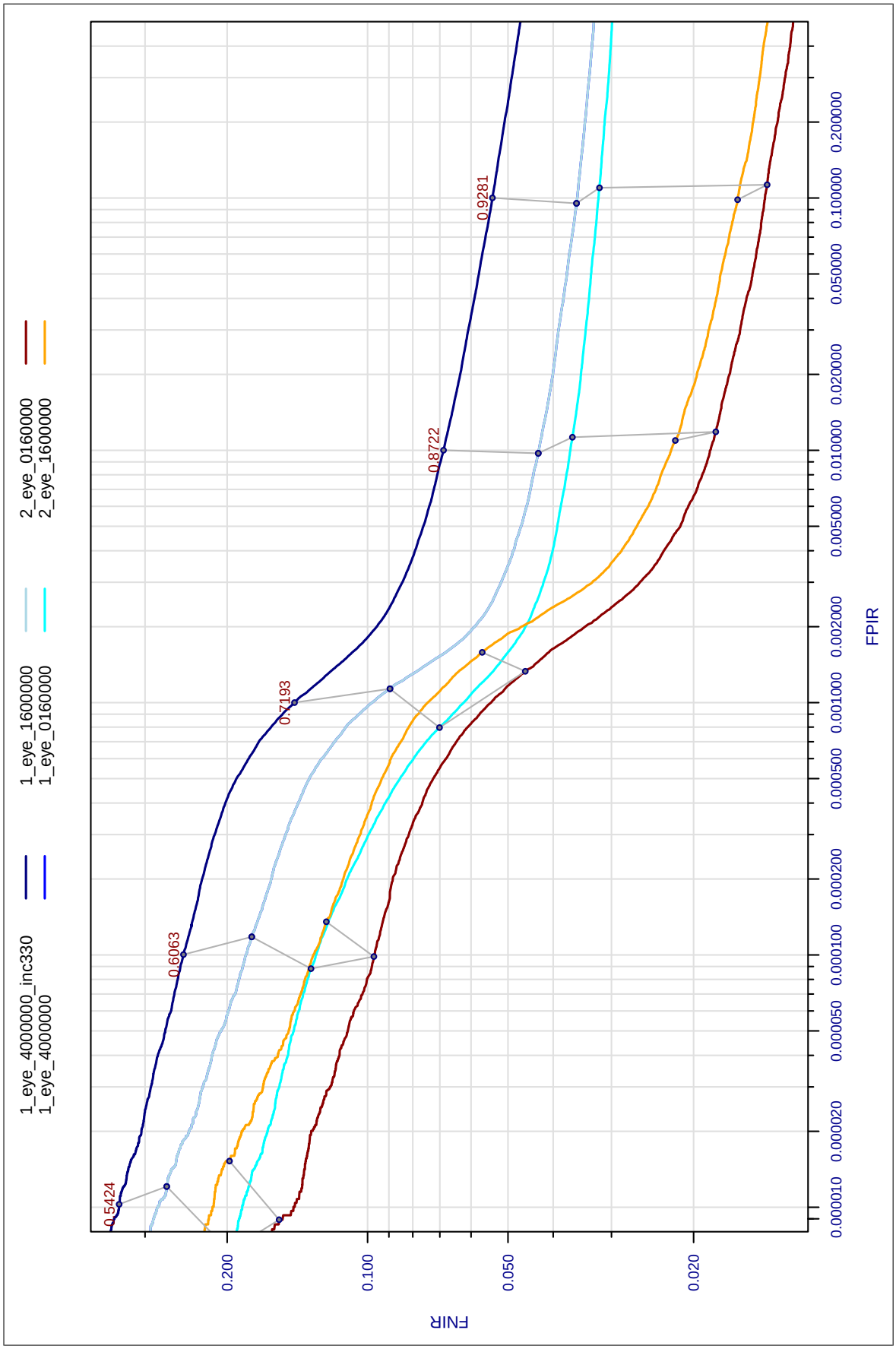

Figure 150: **Effect of population size** onDETs for implementation V02A executing searches for single-eye enrolled populations $N = (0.16, 1.6, 4)$ million, and two-eye populations of $N = (0.16, 1.6)$ million individuals. The straight lines, which link points of constant threshold, show how the two error rates would vary if a fixed threshold were adopted operationally. Horizontal lines indicate that enrolled population N is influential only on FPIR, via $\text{FPIR}(N_2) = (N_2/N_1)\text{FPIR}(N_1)$. When this relationship is not evident, the implementation may be adjusting scores as a function of N (e.g. as described in [cite Daugman]). The large search sets $S_{n,b}$ are used. Missing plots indicate the run is not yet complete.

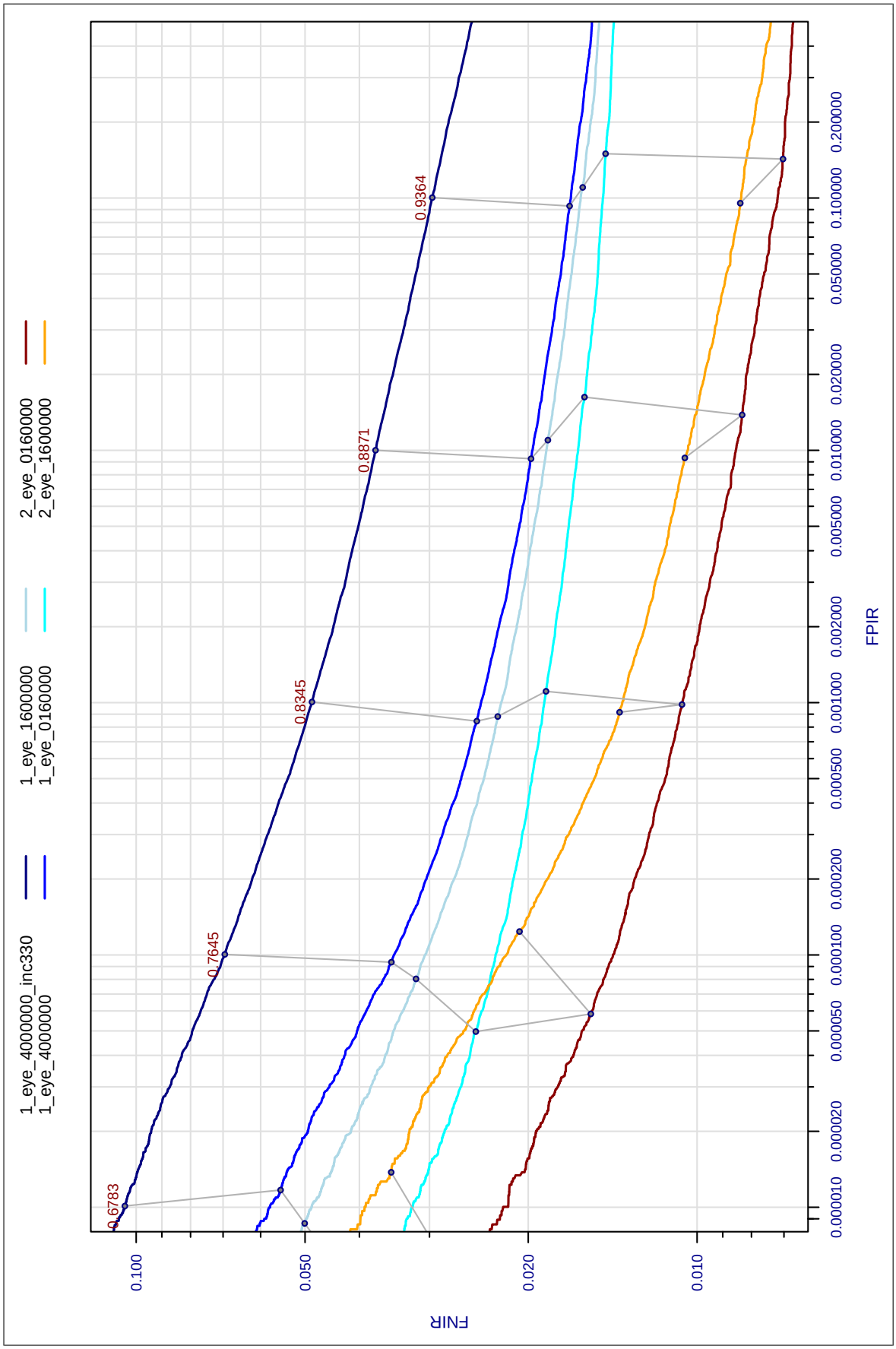

Figure 151: **Effect of population size** onDETs for implementation V03A executing searches for single-eye enrolled populations $N = (0.16, 1.6, 4)$ million, and two-eye populations of $N = (0.16, 1.6)$ million individuals. The straight lines, which link points of constant threshold, show how the two error rates would vary if a fixed threshold were adopted operationally. Horizontal lines indicate that enrolled population N is influential only on FPIR, via $\text{FPIR}(N_2) = (N_2/N_1)\text{FPIR}(N_1)$. When this relationship is not evident, the implementation may be adjusting scores as a function of N (e.g. as described in [cite Daugman]). The large search sets S_{nb} are used. Missing plots indicate the run is not yet complete.

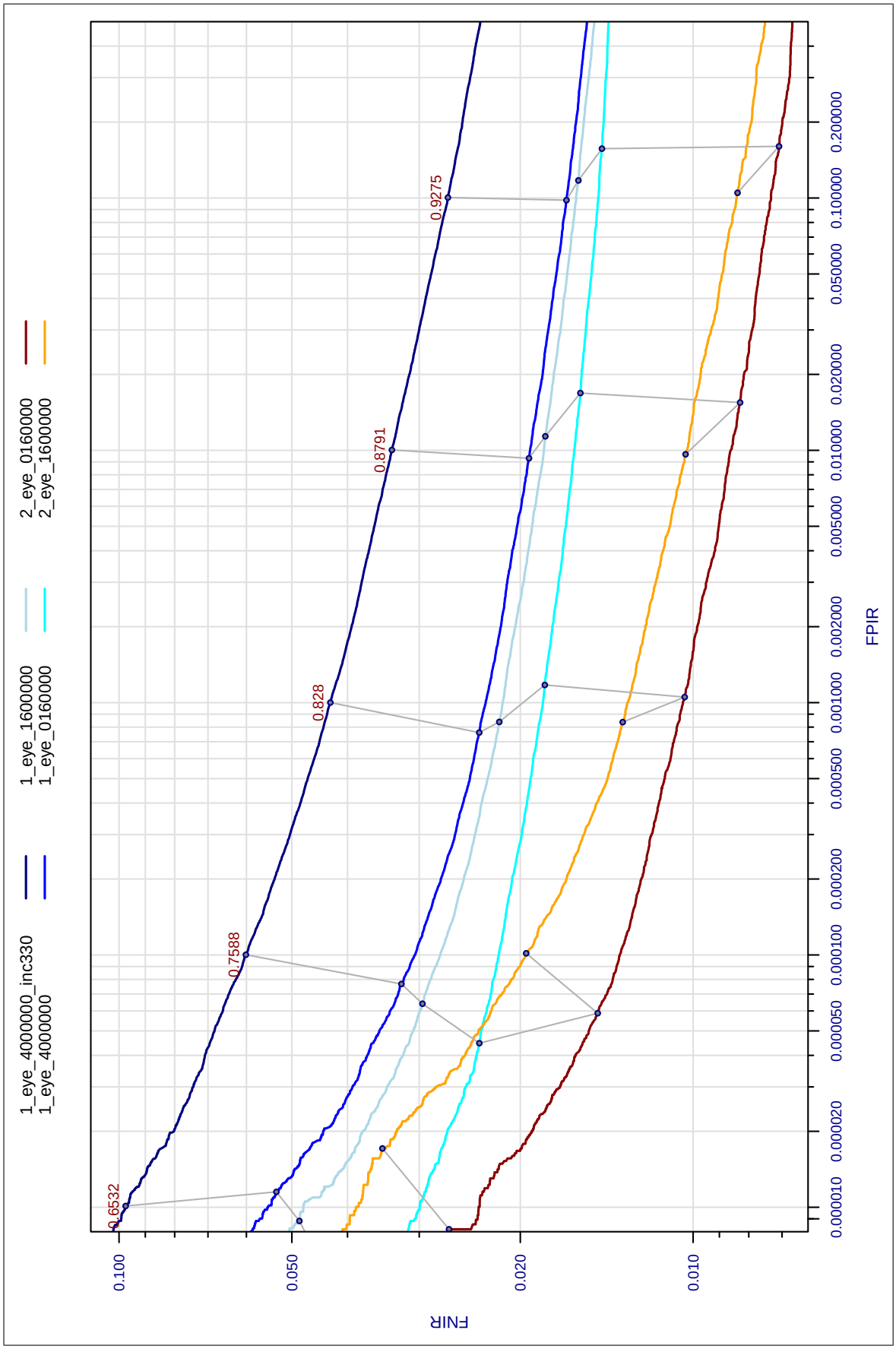

Figure 152: **Effect of population size** onDETs for implementation V03B executing searches for single-eye enrolled populations $N = (0.16, 1.6, 4)$ million, and two-eye populations of $N = (0.16, 1.6)$ million individuals. The straight lines, which link points of constant threshold, show how the two error rates would vary if a fixed threshold were adopted operationally. Horizontal lines indicate that enrolled population N is influential only on FPIR, via $\text{FPIR}(N_2) = (N_2/N_1)\text{FPIR}(N_1)$. When this relationship is not evident, the implementation may be adjusting scores as a function of N (e.g. as described in [cite Daugman]). The large search sets S_{nb} are used. Missing plots indicate the run is not yet complete.

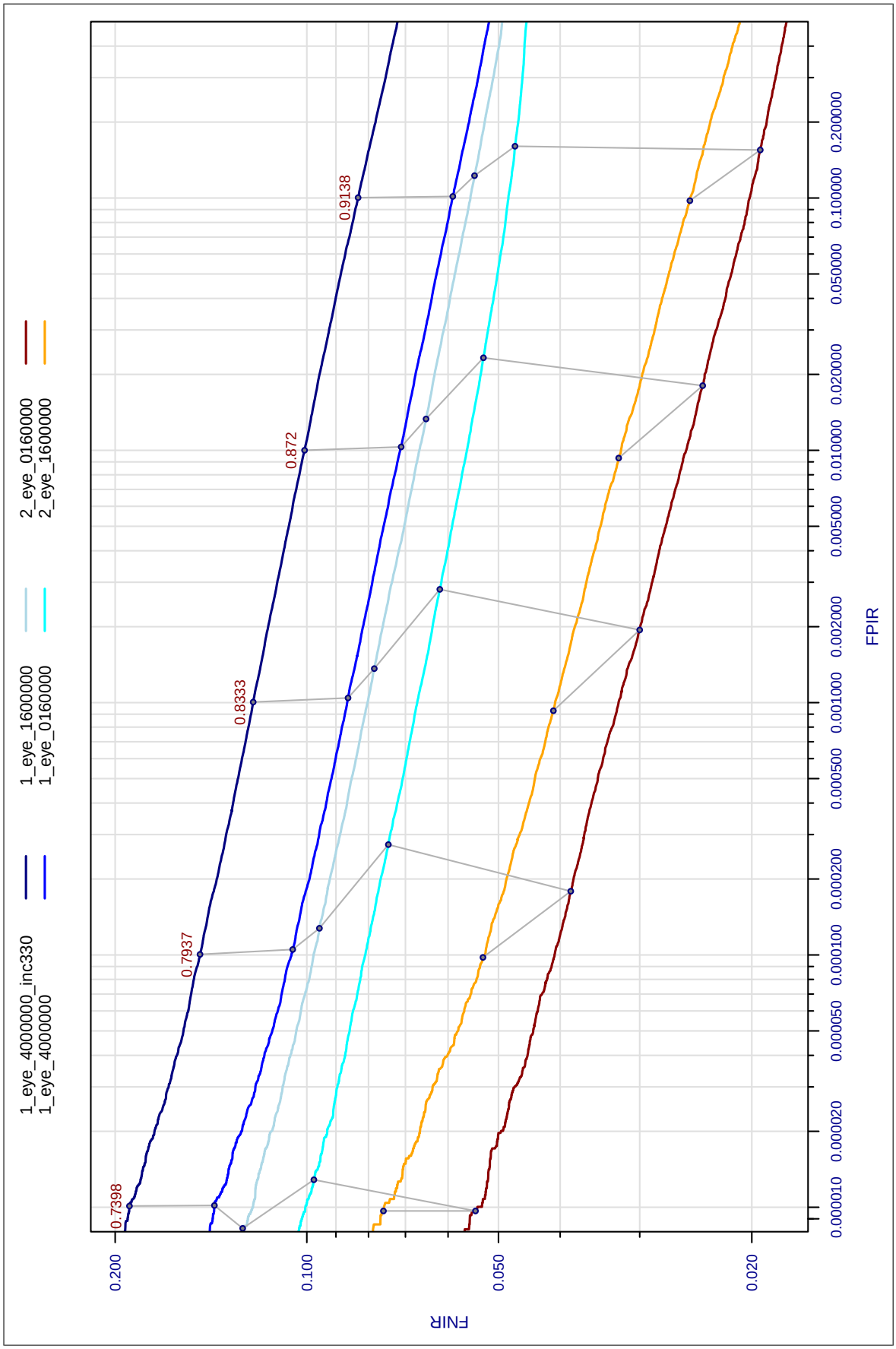

Figure 153: **Effect of population size** onDETs for implementation V04A executing searches for single-eye enrolled populations $N = (0.16, 1.6, 4)$ million, and two-eye populations of $N = (0.16, 1.6)$ million individuals. The straight lines, which link points of constant threshold, show how the two error rates would vary if a fixed threshold were adopted operationally. Horizontal lines indicate that enrolled population N is influential only on FPIR, via $\text{FPIR}(N_2) = (N_2/N_1)\text{FPIR}(N_1)$. When this relationship is not evident, the implementation may be adjusting scores as a function of N (e.g. as described in [cite Daugman]). The large search sets $S_{n,b}$ are used. Missing plots indicate the run is not yet complete.

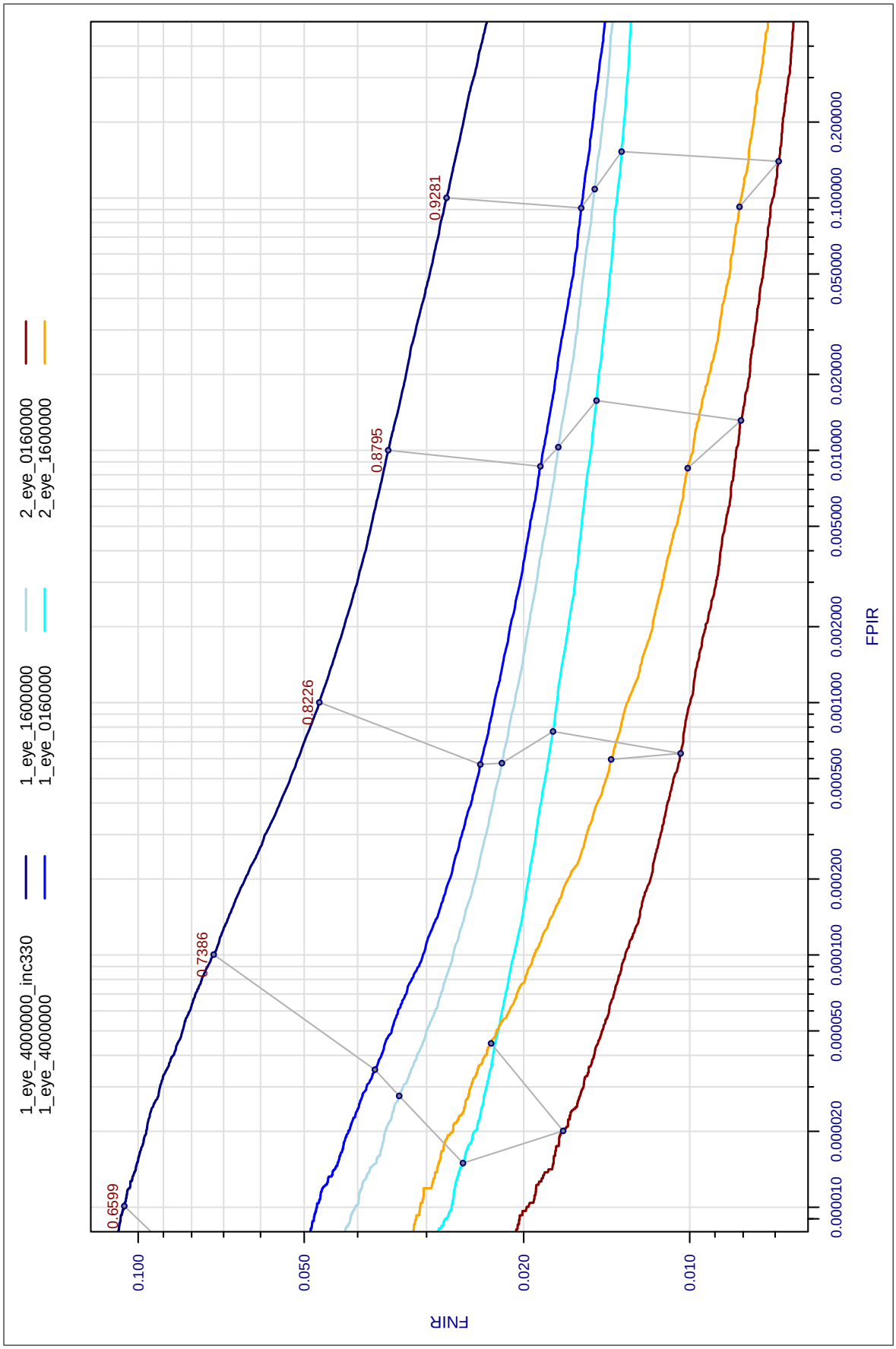

Figure 154: **Effect of population size** onDETs for implementation V11A executing searches for single-eye enrolled populations $N = (0.16, 1.6, 4)$ million, and two-eye populations of $N = (0.16, 1.6)$ million individuals. The straight lines, which link points of constant threshold, show how the two error rates would vary if a fixed threshold were adopted operationally. Horizontal lines indicate that enrolled population N is influential only on FPIR, via $\text{FPIR}(N_2) = (N_2/N_1)\text{FPIR}(N_1)$. When this relationship is not evident, the implementation may be adjusting scores as a function of N (e.g. as described in [cite Daugman]). The large search sets S_{nb} are used. Missing plots indicate the run is not yet complete.

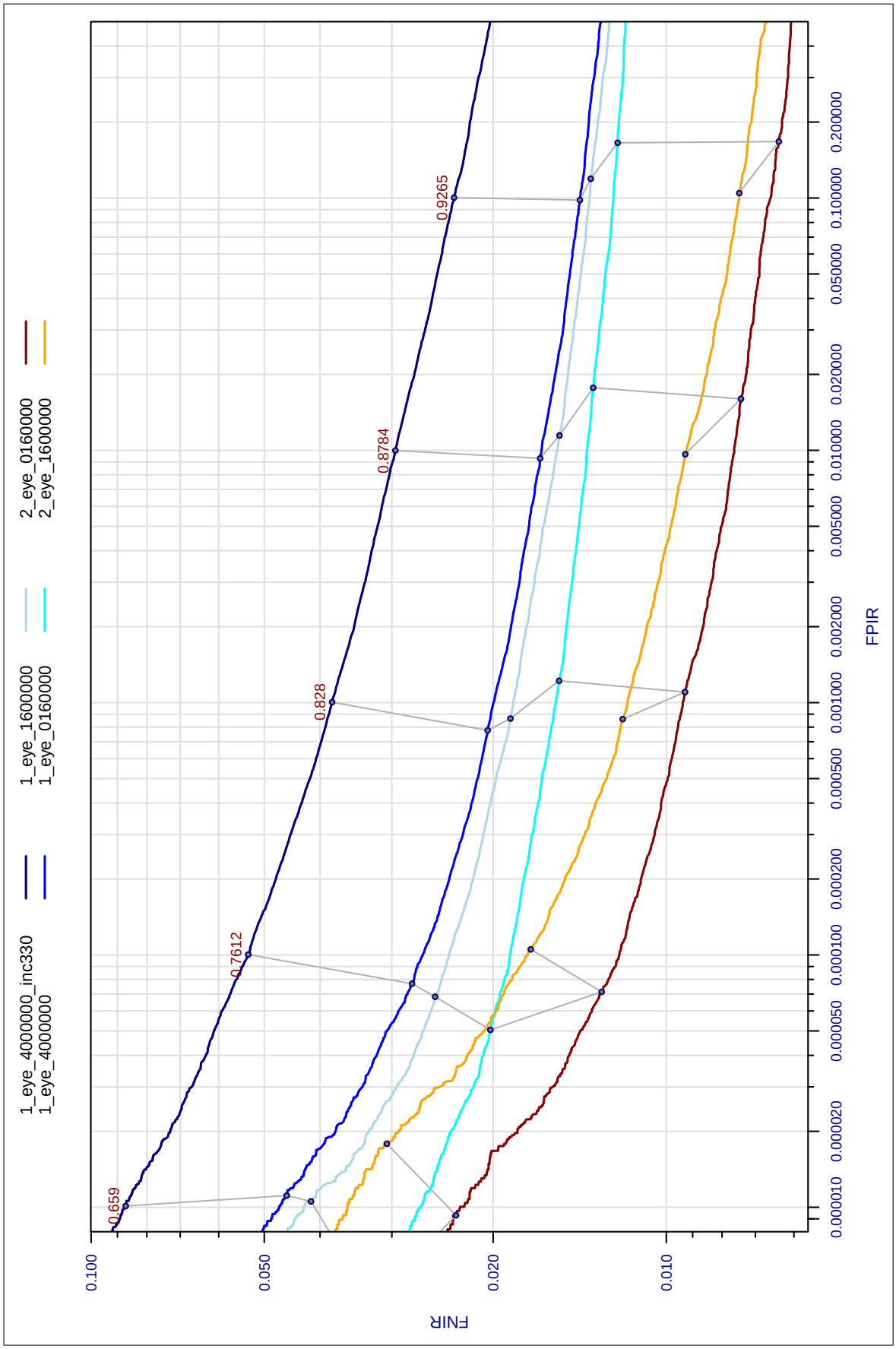

Figure 155: **Effect of population size** onDETs for implementation V11B executing searches for single-eye enrolled populations $N = (0.16, 1.6, 4)$ million, and two-eye populations of $N = (0.16, 1.6)$ million individuals. The straight lines, which link points of constant threshold, show how the two error rates would vary if a fixed threshold were adopted operationally. Horizontal lines indicate that enrolled population N is influential only on FPIR, via $\text{FPIR}(N_2) = (N_2/N_1)\text{FPIR}(N_1)$. When this relationship is not evident, the implementation may be adjusting scores as a function of N (e.g. as described in [cite Daugman]). The large search sets S_{nb} are used. Missing plots indicate the run is not yet complete.

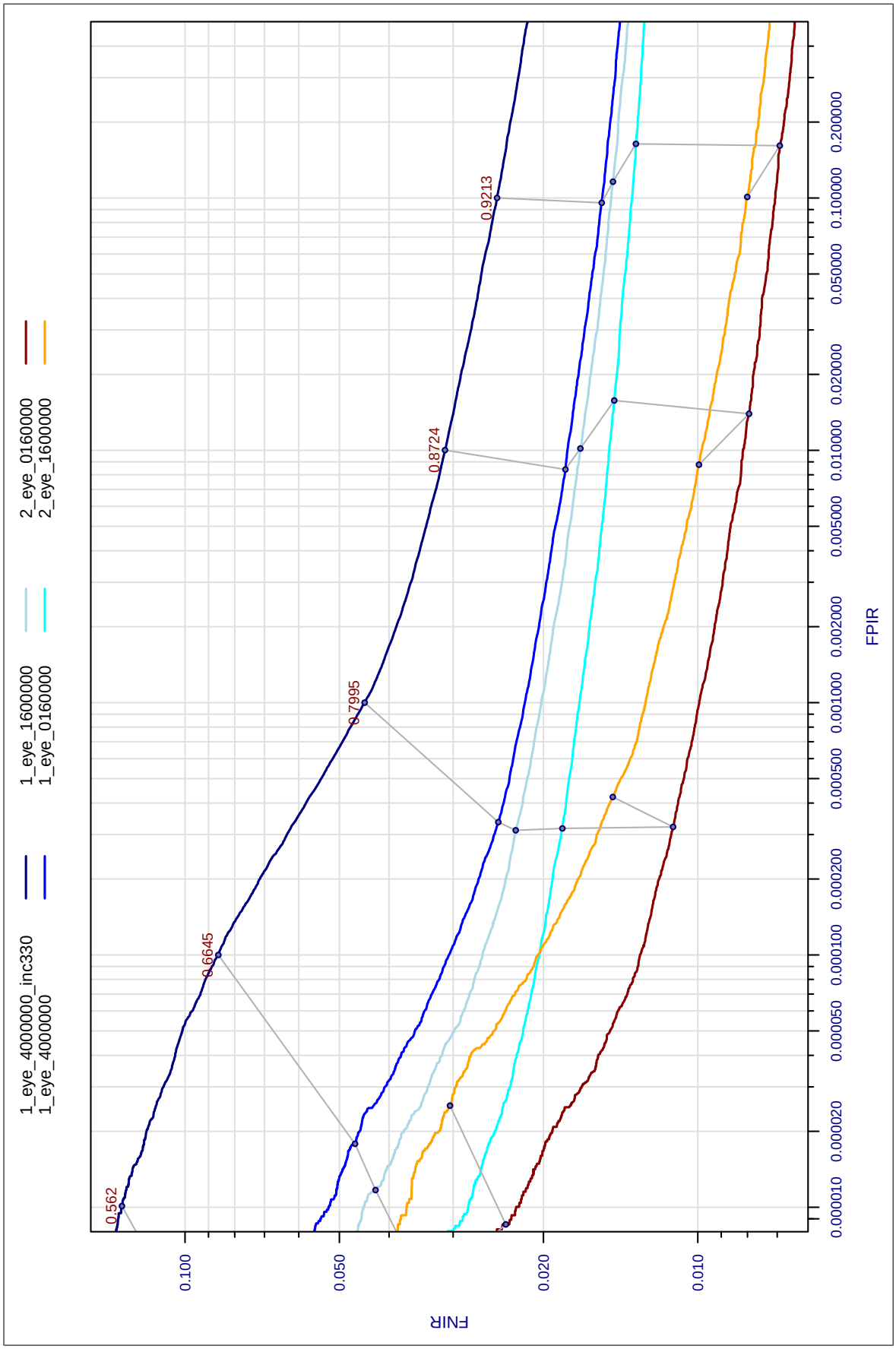

Figure 156: **Effect of population size** onDETs for implementation V12A executing searches for single-eye enrolled populations $N = (0.16, 1.6, 4)$ million, and two-eye populations of $N = (0.16, 1.6)$ million individuals. The straight lines, which link points of constant threshold, show how the two error rates would vary if a fixed threshold were adopted operationally. Horizontal lines indicate that enrolled population N is influential only on FPIR, via $\text{FPIR}(N_2) = (N_2/N_1)\text{FPIR}(N_1)$. When this relationship is not evident, the implementation may be adjusting scores as a function of N (e.g. as described in [cite Daugman]). The large search sets $S_{n,b}$ are used. Missing plots indicate the run is not yet complete.

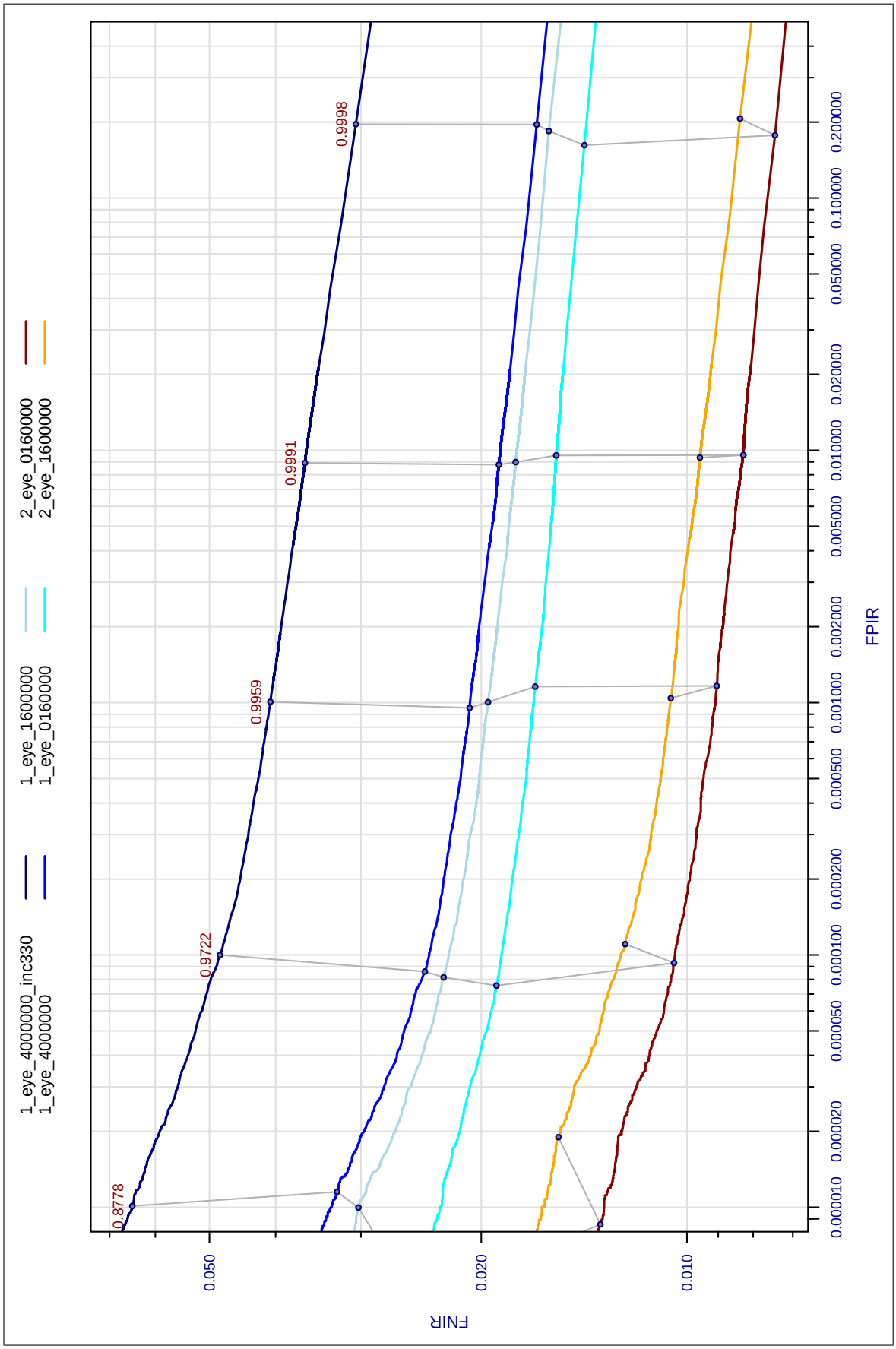

Figure 157: **Effect of population size** onDETs for implementation V12B executing searches for single-eye enrolled populations $N = (0.16, 1.6, 4)$ million, and two-eye populations of $N = (0.16, 1.6)$ million individuals. The straight lines, which link points of constant threshold, show how the two error rates would vary if a fixed threshold were adopted operationally. Horizontal lines indicate that enrolled population N is influential only on FPIR, via $\text{FPIR}(N_2) = (N_2/N_1)\text{FPIR}(N_1)$. When this relationship is not evident, the implementation may be adjusting scores as a function of N (e.g. as described in [cite Daugman]). The large search sets S_{nb} are used. Missing plots indicate the run is not yet complete.

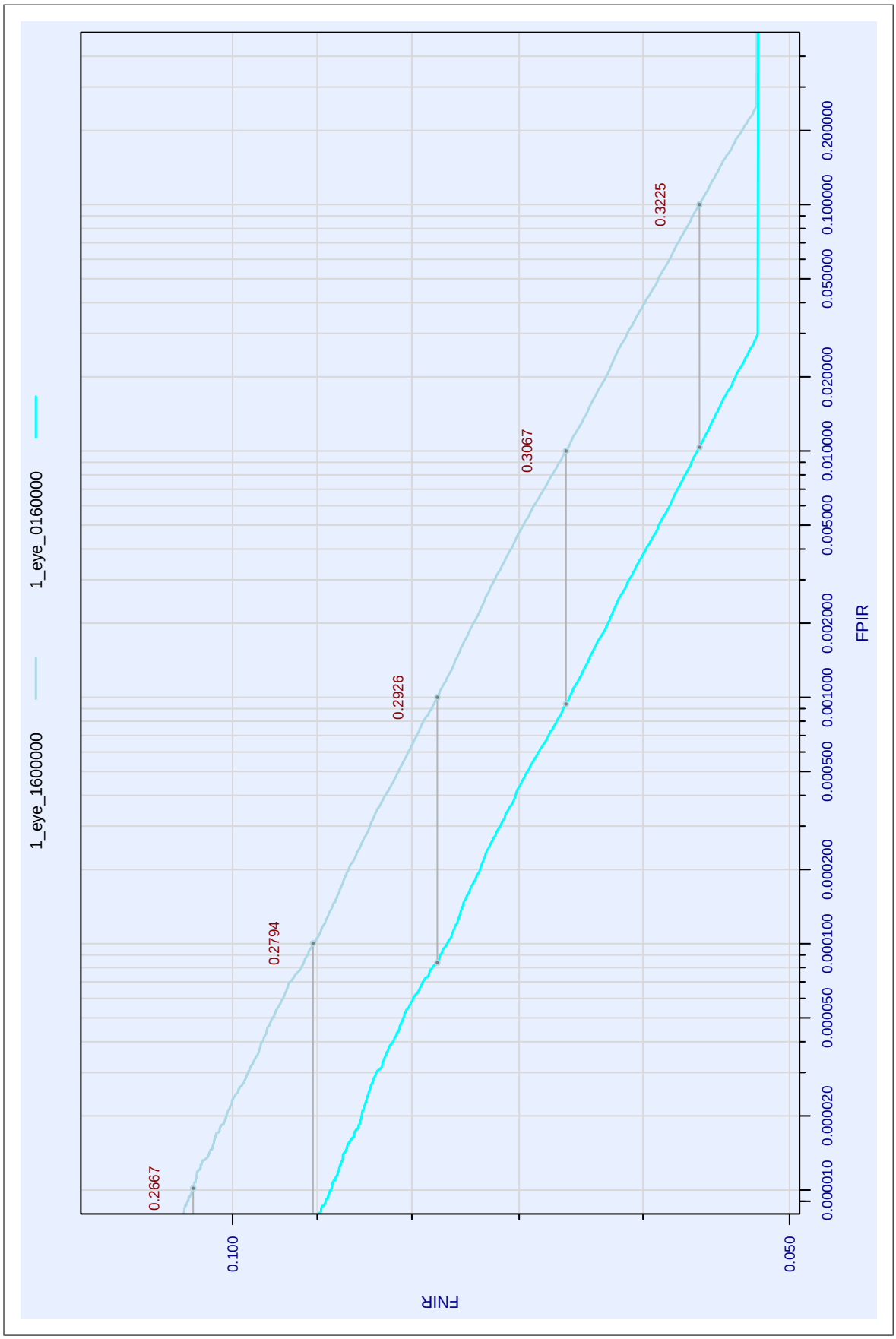

Figure 158: **Effect of population size** onDETs for implementation W01A executing searches for single-eye enrolled populations $N = (0.16, 1.6, 4)$ million, and two-eye populations of $N = (0.16, 1.6)$ million individuals. The straight lines, which link points of constant threshold, show how the two error rates would vary if a fixed threshold were adopted operationally. Horizontal lines indicate that enrolled population N is influential only on FPIR, via $\text{FPIR}(N_2) = (N_2/N_1)\text{FPIR}(N_1)$. When this relationship is not evident, the implementation may be adjusting scores as a function of N (e.g. as described in [cite Daugman]). The large search sets $S_{n,b}$ are used. Missing plots indicate the run is not yet complete.

Figure 159: **Effect of population size** onDETs for implementation W01B executing searches for single-eye enrolled populations $N = (0.16, 1.6, 4)$ million, and two-eye populations of $N = (0.16, 1.6)$ million individuals. The straight lines, which link points of constant threshold, show how the two error rates would vary if a fixed threshold were adopted operationally. Horizontal lines indicate that enrolled population N is influential only on FPIR, via $\text{FPIR}(N_2) = (N_2/N_1)\text{FPIR}(N_1)$. When this relationship is not evident, the implementation may be adjusting scores as a function of N (e.g. as described in [cite Daugman]). The large search sets S_{nb} are used. Missing plots indicate the run is not yet complete.

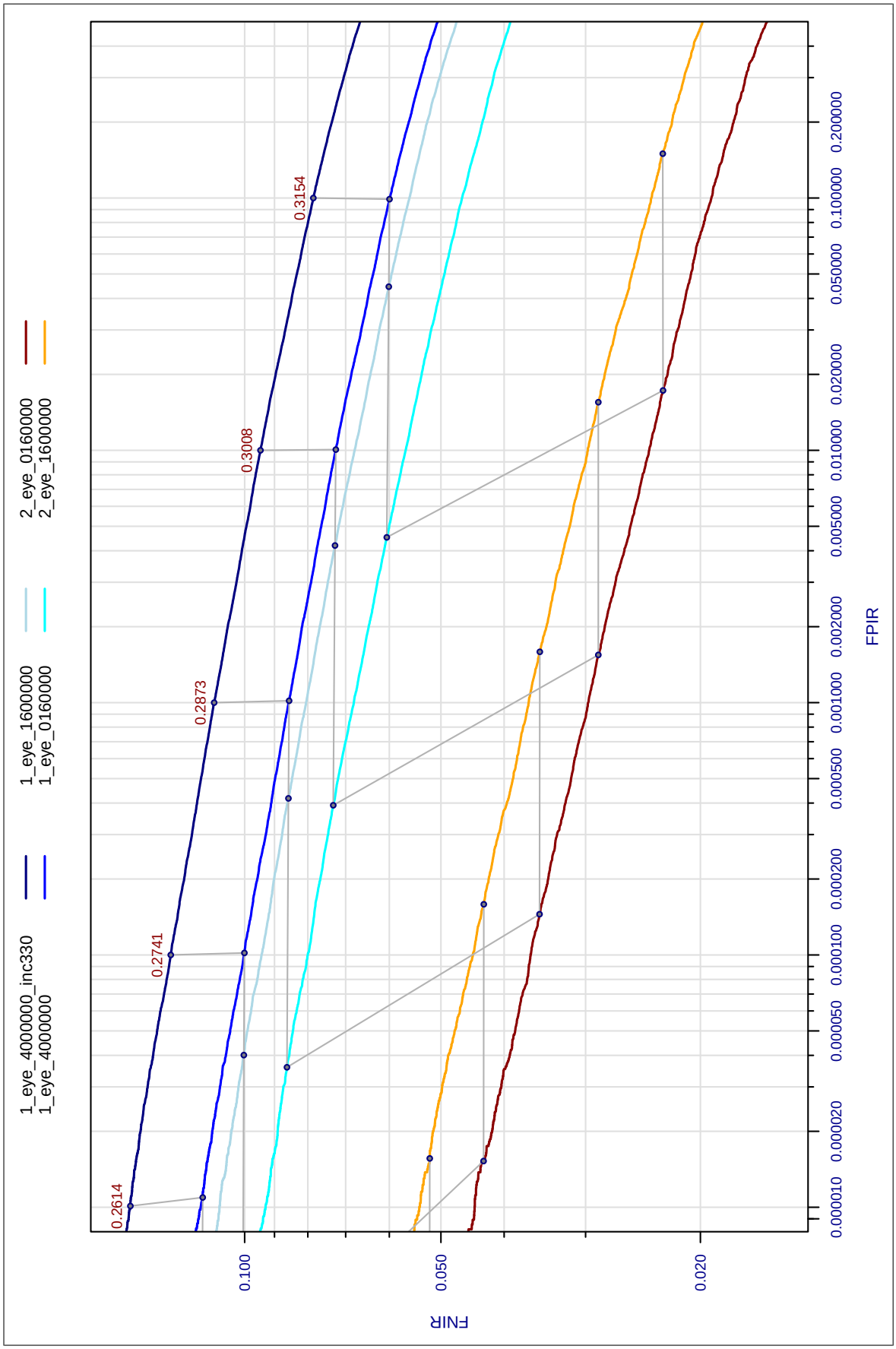

Figure 160: **Effect of population size** onDETs for implementation W02A executing searches for single-eye enrolled populations $N = (0.16, 1.6, 4)$ million, and two-eye populations of $N = (0.16, 1.6)$ million individuals. The straight lines, which link points of constant threshold, show how the two error rates would vary if a fixed threshold were adopted operationally. Horizontal lines indicate that enrolled population N is influential only on FPIR, via $\text{FPIR}(N_2) = (N_2/N_1)\text{FPIR}(N_1)$. When this relationship is not evident, the implementation may be adjusting scores as a function of N (e.g. as described in [cite Daugman]). The large search sets $S_{n,b}$ are used. Missing plots indicate the run is not yet complete.

Figure 161: **Effect of population size** onDETs for implementation W02B executing searches for single-eye enrolled populations $N = (0.16, 1.6, 4)$ million, and two-eye populations of $N = (0.16, 1.6)$ million individuals. The straight lines, which link points of constant threshold, show how the two error rates would vary if a fixed threshold were adopted operationally. Horizontal lines indicate that enrolled population N is influential only on FPIR, via $\text{FPIR}(N_2) = (N_2/N_1)\text{FPIR}(N_1)$. When this relationship is not evident, the implementation may be adjusting scores as a function of N (e.g. as described in [cite Daugman]). The large search sets S_{nb} are used. Missing plots indicate the run is not yet complete.

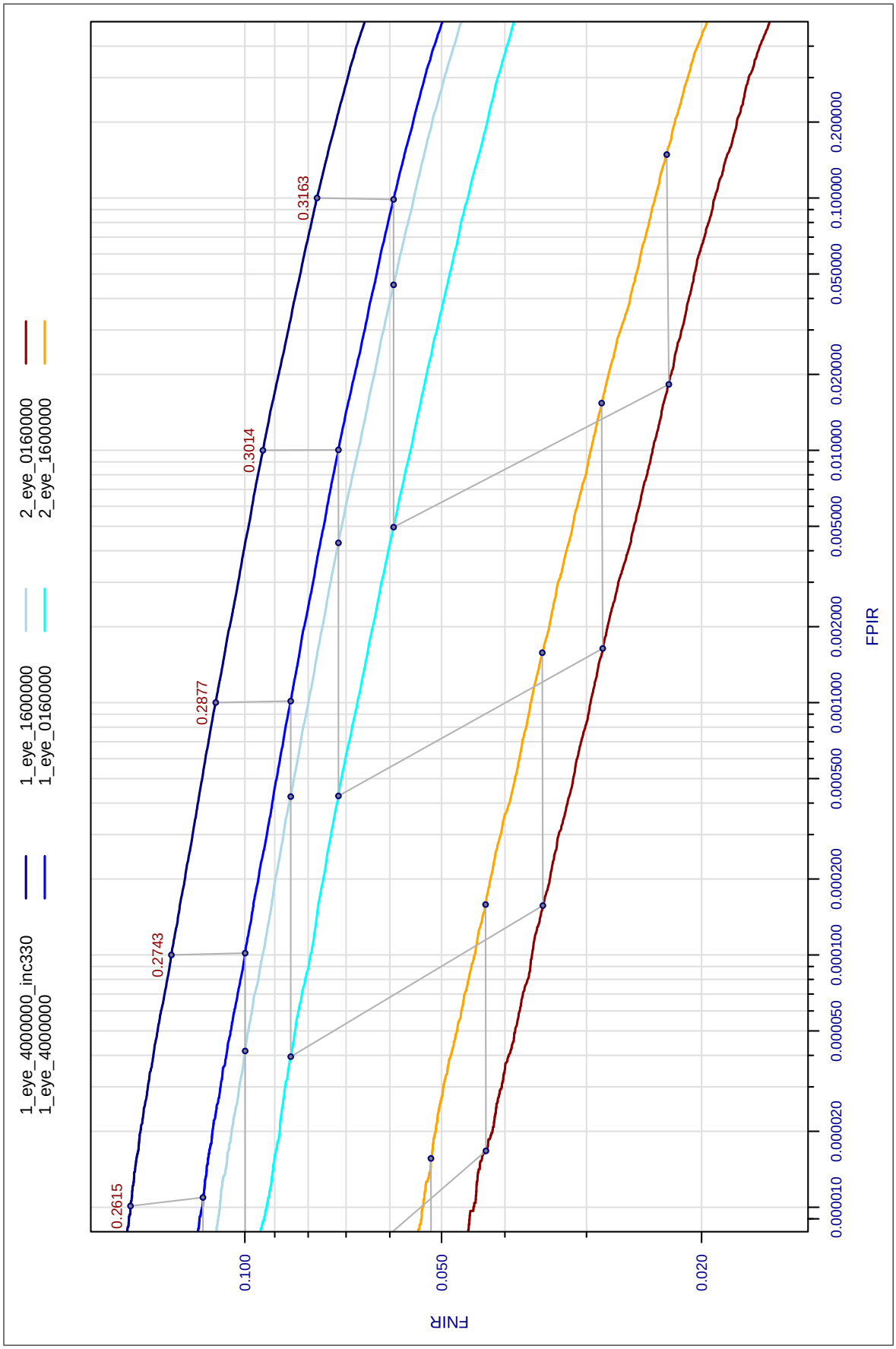

Figure 162: **Effect of population size** onDETs for implementation W03A executing searches for single-eye enrolled populations $N = (0.16, 1.6, 4)$ million, and two-eye populations of $N = (0.16, 1.6)$ million individuals. The straight lines, which link points of constant threshold, show how the two error rates would vary if a fixed threshold were adopted operationally. Horizontal lines indicate that enrolled population N is influential only on FPIR, via $\text{FPIR}(N_2) = (N_2/N_1)\text{FPIR}(N_1)$. When this relationship is not evident, the implementation may be adjusting scores as a function of N (e.g. as described in [cite Daugman]). The large search sets S_{nb} are used. Missing plots indicate the run is not yet complete.

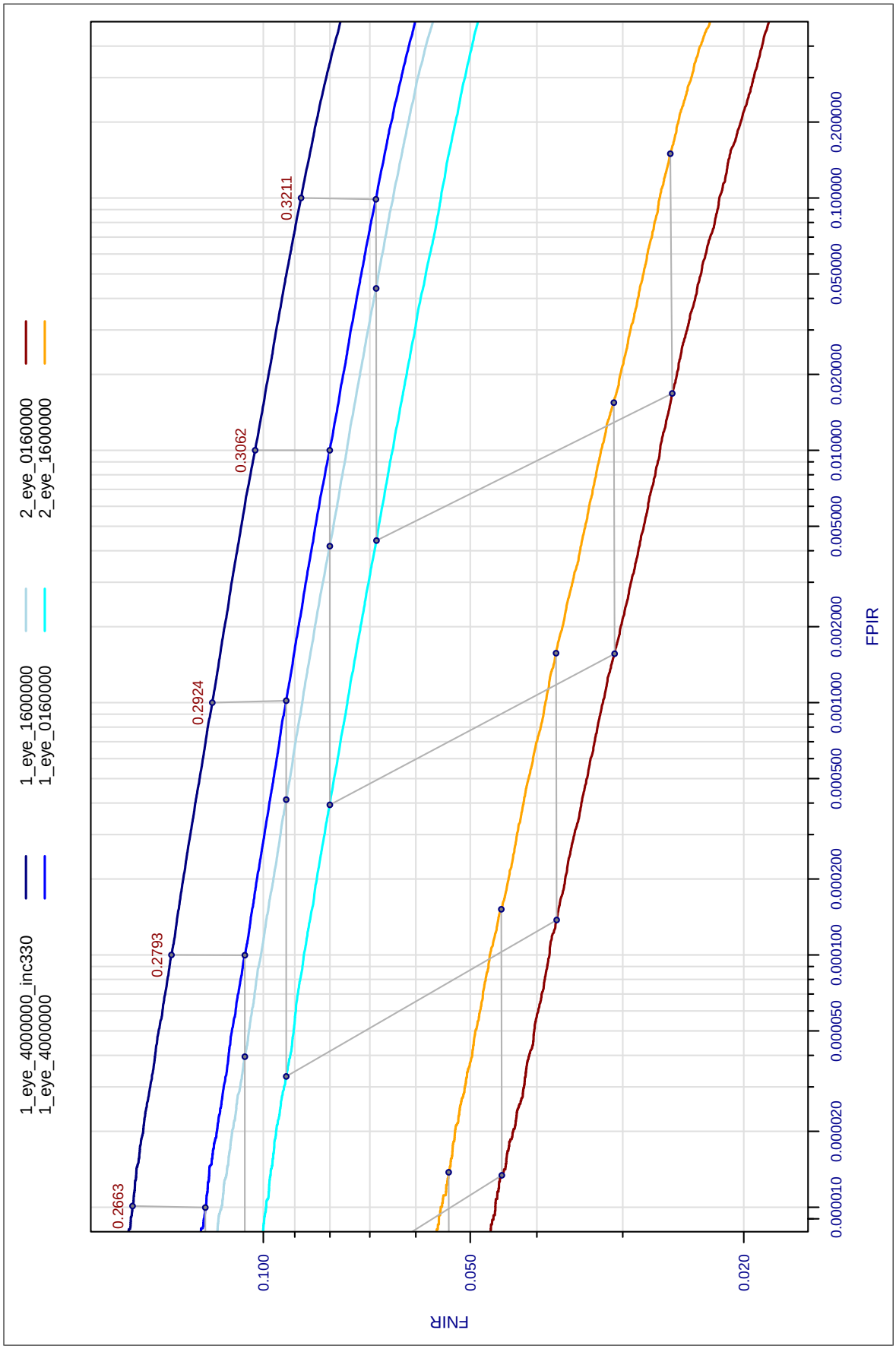

Figure 163: **Effect of population size** onDETs for implementation W04A executing searches for single-eye enrolled populations $N = (0.16, 1.6, 4)$ million, and two-eye populations of $N = (0.16, 1.6)$ million individuals. The straight lines, which link points of constant threshold, show how the two error rates would vary if a fixed threshold were adopted operationally. Horizontal lines indicate that enrolled population N is influential only on FPIR, via $\text{FPIR}(N_2) = (N_2/N_1)\text{FPIR}(N_1)$. When this relationship is not evident, the implementation may be adjusting scores as a function of N (e.g. as described in [cite Daugman]). The large search sets $S_{n,b}$ are used. Missing plots indicate the run is not yet complete.

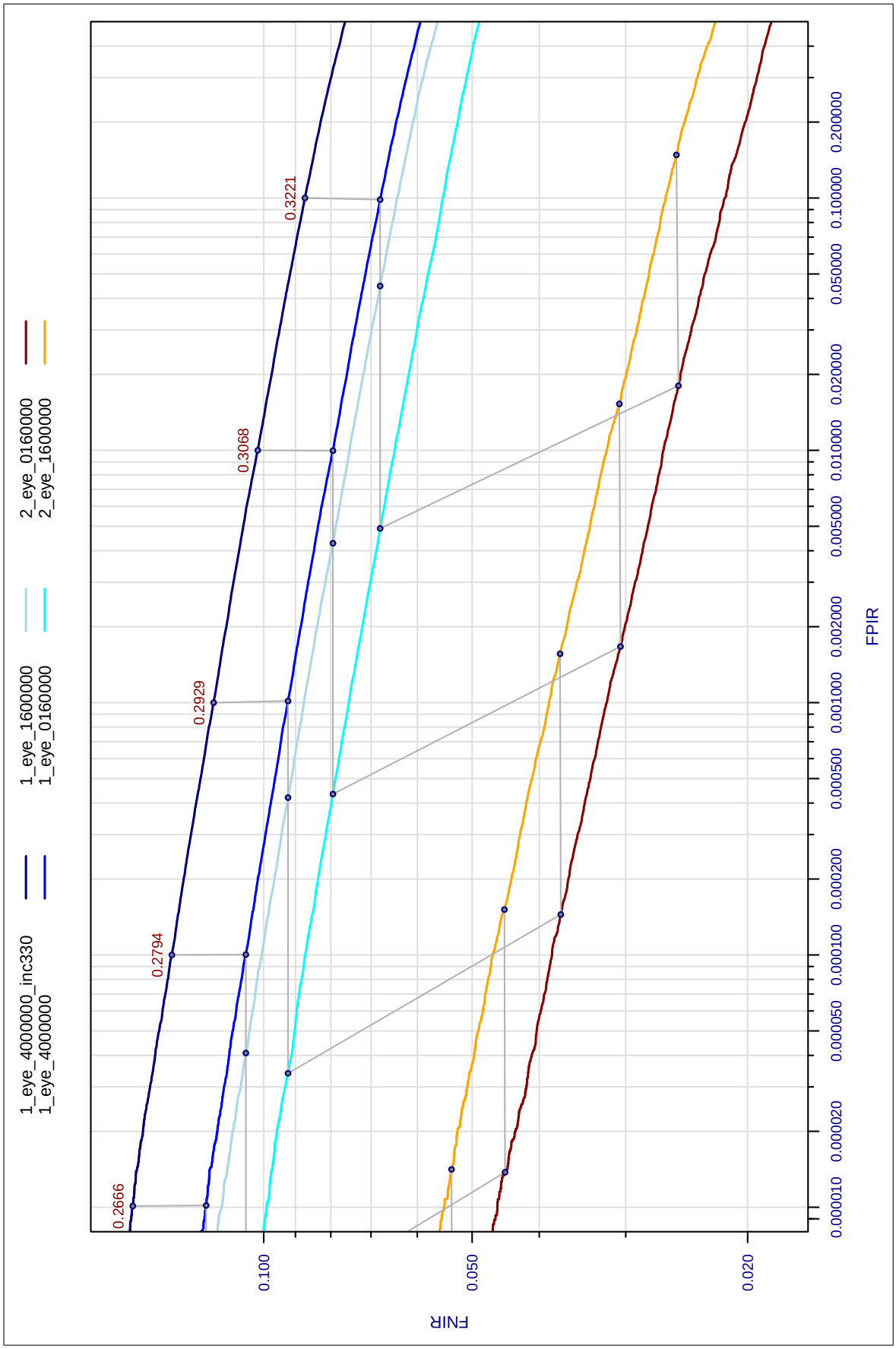

Figure 164: **Effect of population size** onDETs for implementation W05A executing searches for single-eye enrolled populations $N = (0.16, 1.6, 4)$ million, and two-eye populations of $N = (0.16, 1.6)$ million individuals. The straight lines, which link points of constant threshold, show how the two error rates would vary if a fixed threshold were adopted operationally. Horizontal lines indicate that enrolled population N is influential only on FPIR, via $\text{FPIR}(N_2) = (N_2/N_1)\text{FPIR}(N_1)$. When this relationship is not evident, the implementation may be adjusting scores as a function of N (e.g. as described in [cite Daugman]). The large search sets $S_{n,b}$ are used. Missing plots indicate the run is not yet complete.

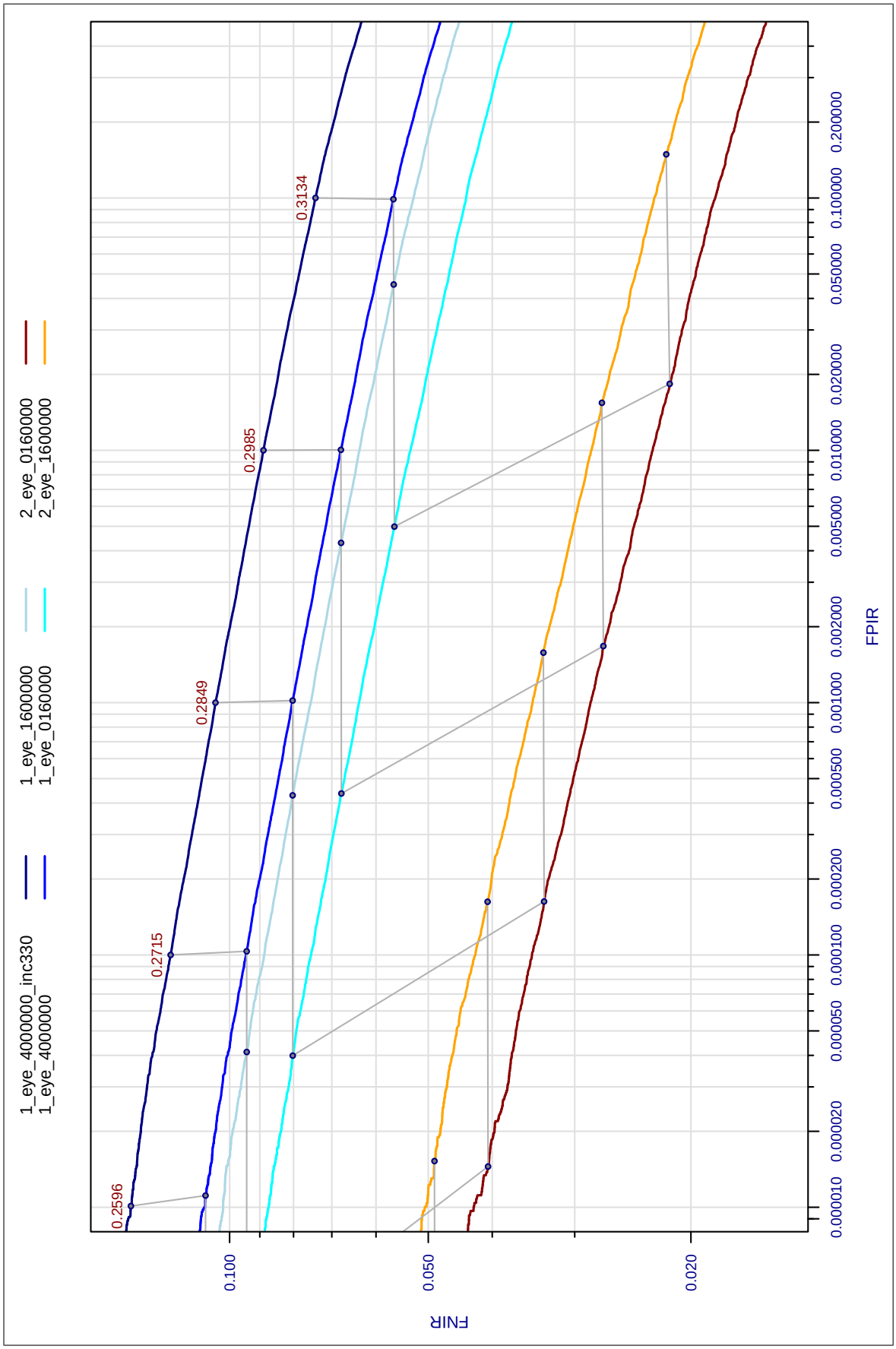

Figure 165: **Effect of population size** onDETs for implementation W11A executing searches for single-eye enrolled populations $N = (0.16, 1.6, 4)$ million, and two-eye populations of $N = (0.16, 1.6)$ million individuals. The straight lines, which link points of constant threshold, show how the two error rates would vary if a fixed threshold were adopted operationally. Horizontal lines indicate that enrolled population N is influential only on FPIR, via $\text{FPIR}(N_2) = (N_2/N_1)\text{FPIR}(N_1)$. When this relationship is not evident, the implementation may be adjusting scores as a function of N (e.g. as described in [cite Daugman]). The large search sets $S_{n,b}$ are used. Missing plots indicate the run is not yet complete.

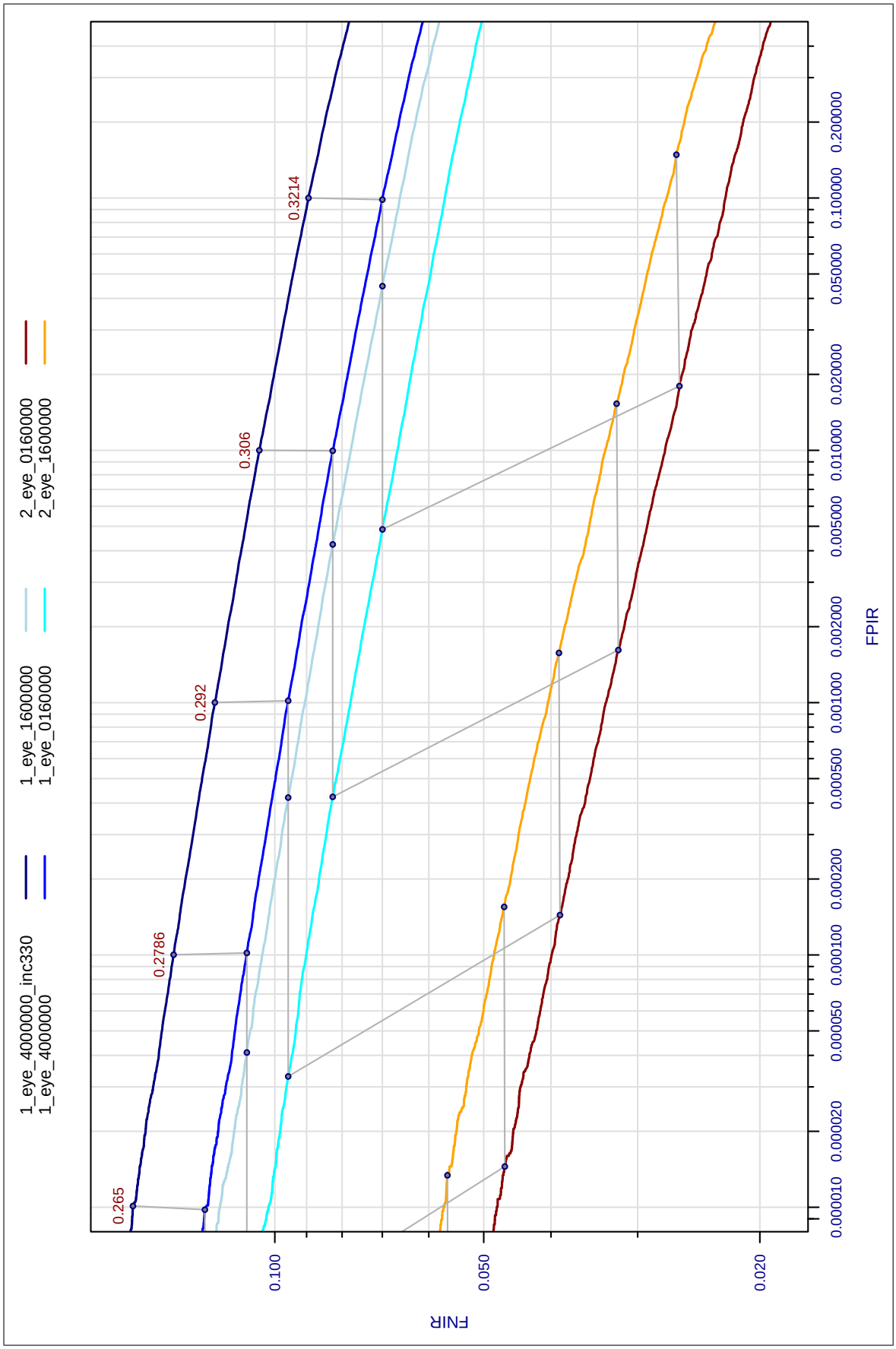

Figure 166: **Effect of population size** onDETs for implementation W11B executing searches for single-eye enrolled populations $N = (0.16, 1.6, 4)$ million, and two-eye populations of $N = (0.16, 1.6)$ million individuals. The straight lines, which link points of constant threshold, show how the two error rates would vary if a fixed threshold were adopted operationally. Horizontal lines indicate that enrolled population N is influential only on FPIR, via $\text{FPIR}(N_2) = (N_2/N_1)\text{FPIR}(N_1)$. When this relationship is not evident, the implementation may be adjusting scores as a function of N (e.g. as described in [cite Daugman]). The large search sets $S_{n,b}$ are used. Missing plots indicate the run is not yet complete.

Figure 167: **Effect of population size** onDETs for implementation W12A executing searches for single-eye enrolled populations $N = (0.16, 1.6, 4)$ million, and two-eye populations of $N = (0.16, 1.6)$ million individuals. The straight lines, which link points of constant threshold, show how the two error rates would vary if a fixed threshold were adopted operationally. Horizontal lines indicate that enrolled population N is influential only on FPIR, via $\text{FPIR}(N_2) = (N_2/N_1)\text{FPIR}(N_1)$. When this relationship is not evident, the implementation may be adjusting scores as a function of N (e.g. as described in [cite Daugman]). The large search sets S_{nb} are used. Missing plots indicate the run is not yet complete.

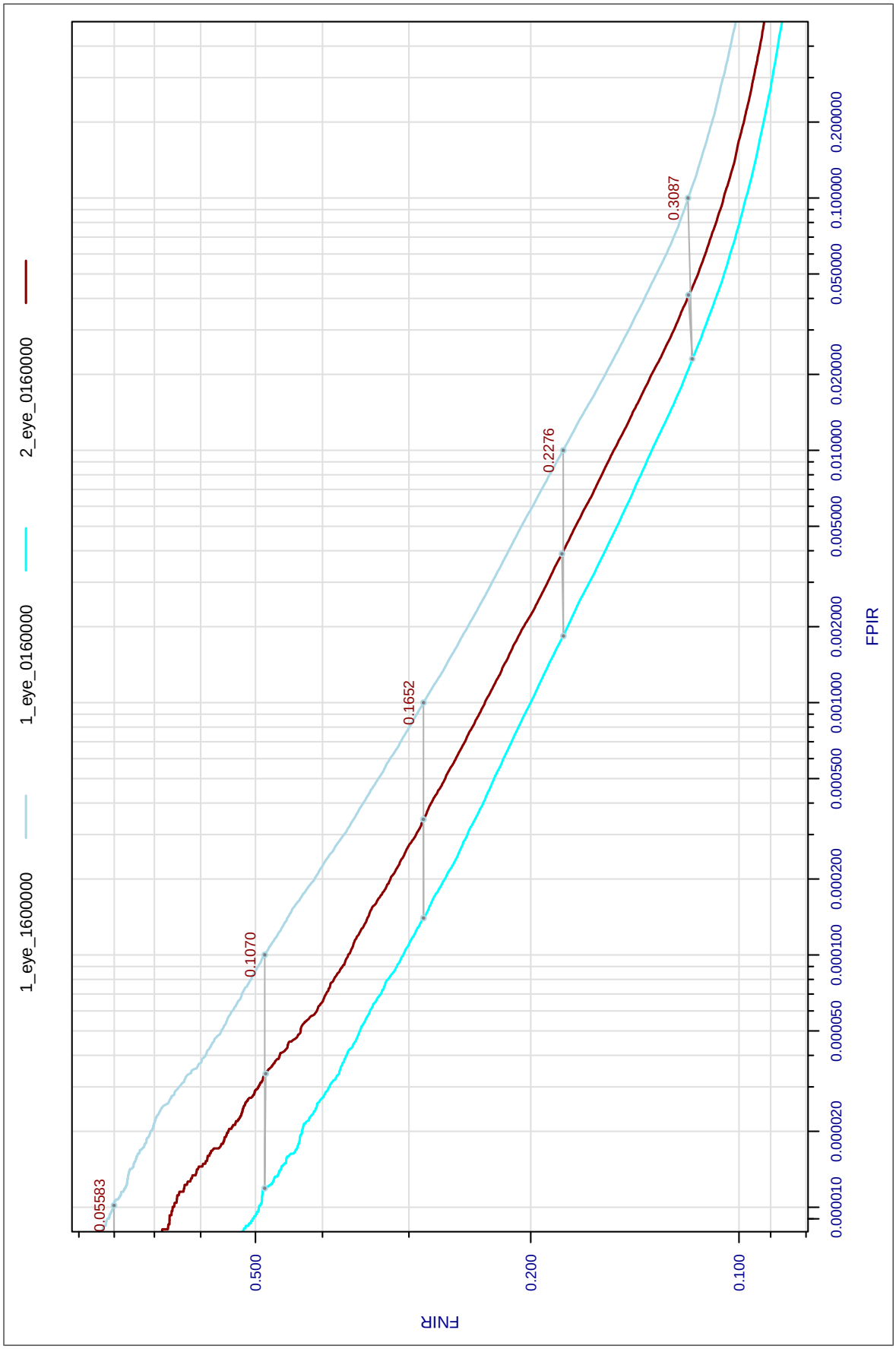

Figure 168: **Effect of population size** onDETs for implementation X02A executing searches for single-eye enrolled populations $N = (0.16, 1.6, 4)$ million, and two-eye populations of $N = (0.16, 1.6)$ million individuals. The straight lines, which link points of constant threshold, show how the two error rates would vary if a fixed threshold were adopted operationally. Horizontal lines indicate that enrolled population N is influential only on FPIR, via $\text{FPIR}(N_2) = (N_2/N_1)\text{FPIR}(N_1)$. When this relationship is not evident, the implementation may be adjusting scores as a function of N (e.g. as described in [cite Daugman]). The large search sets S_{nb} are used. Missing plots indicate the run is not yet complete.

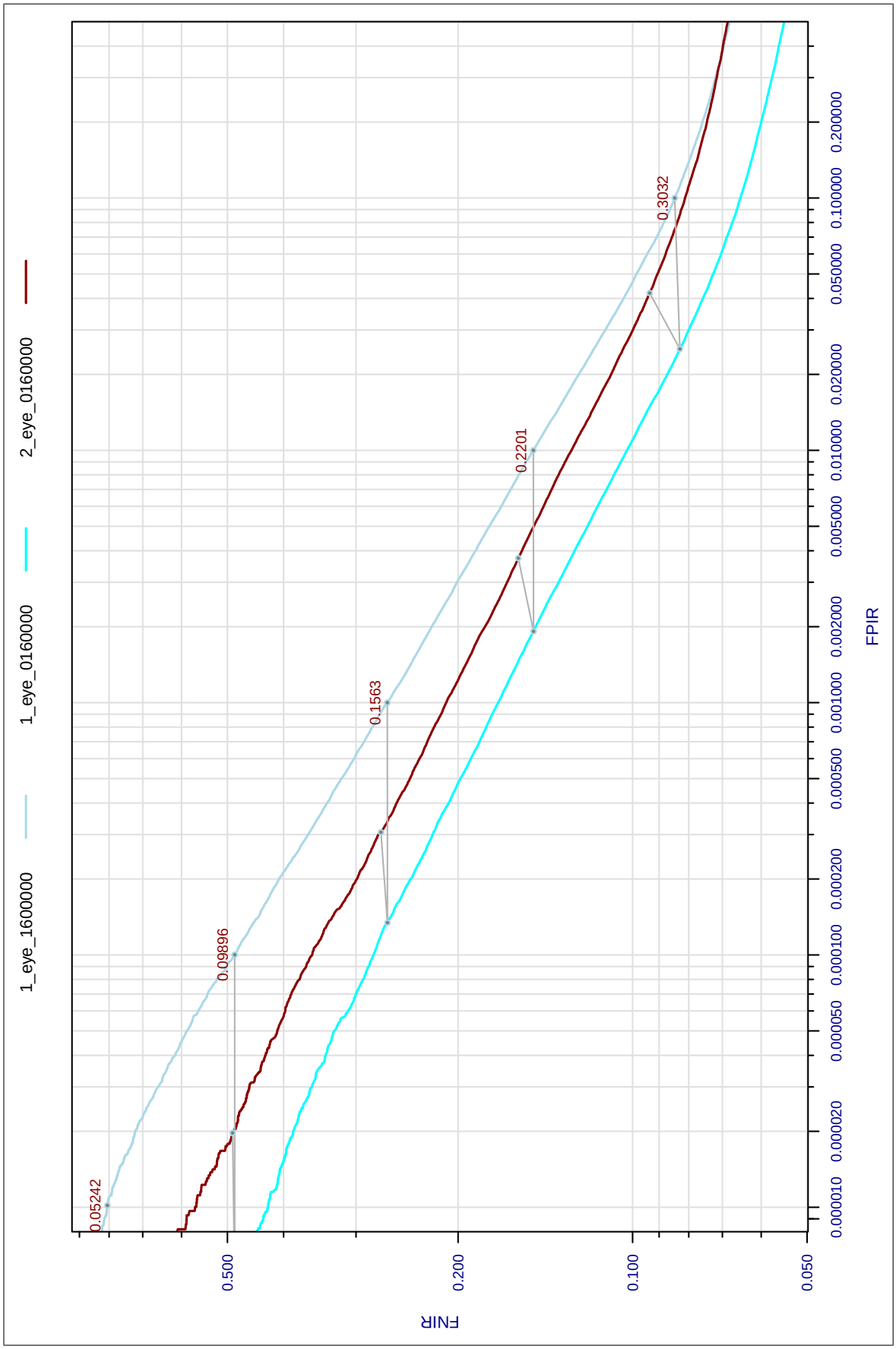

Figure 169: **Effect of population size** onDETs for implementation X03A executing searches for single-eye enrolled populations $N = (0.16, 1.6, 4)$ million, and two-eye populations of $N = (0.16, 1.6)$ million individuals. The straight lines, which link points of constant threshold, show how the two error rates would vary if a fixed threshold were adopted operationally. Horizontal lines indicate that enrolled population N is influential only on FPIR, via $\text{FPIR}(N_2) = (N_2/N_1)\text{FPIR}(N_1)$. When this relationship is not evident, the implementation may be adjusting scores as a function of N (e.g. as described in [cite Daugman]). The large search sets S_{nb} are used. Missing plots indicate the run is not yet complete.

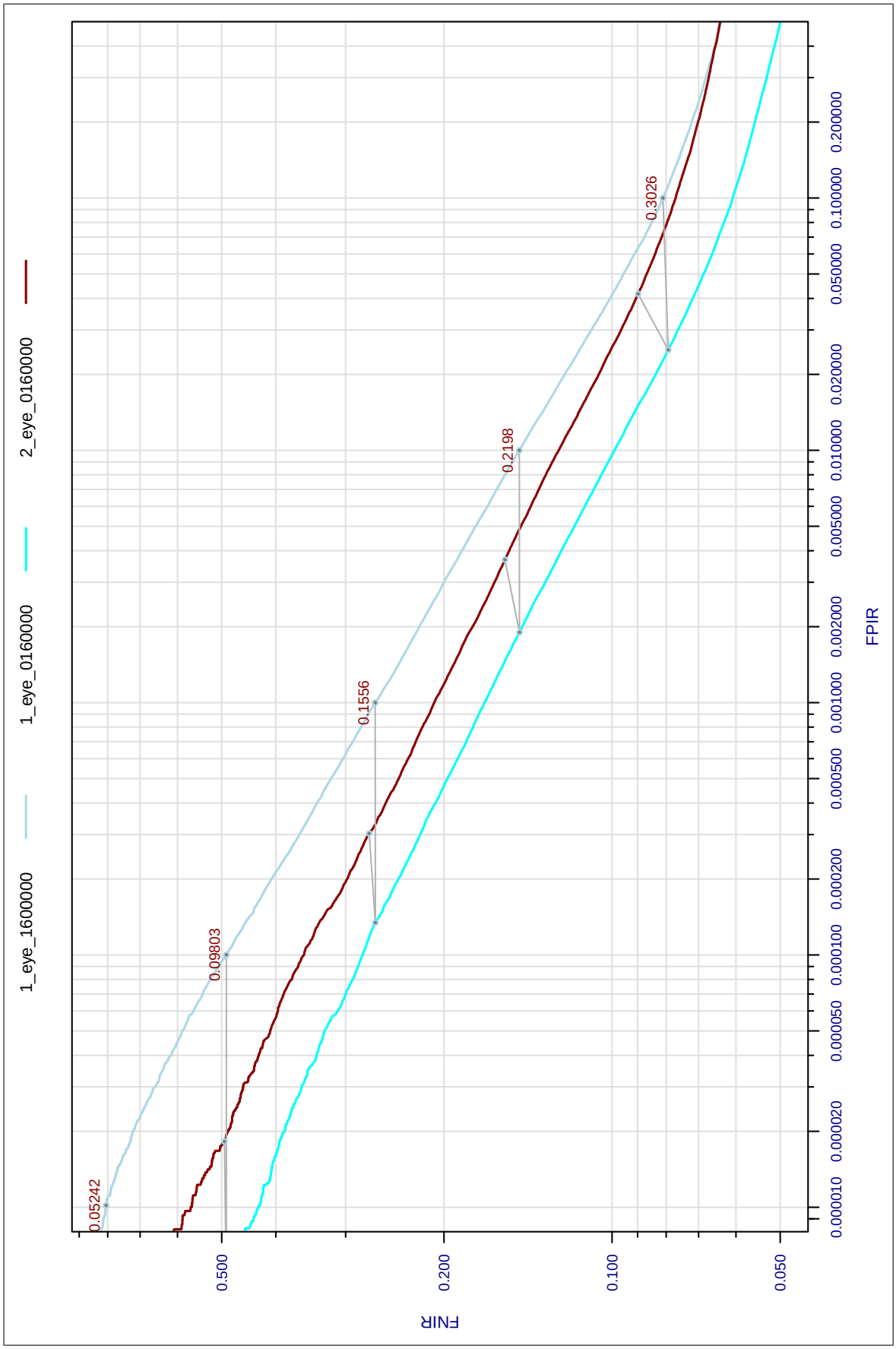

Figure 170: **Effect of population size** onDETs for implementation X04A executing searches for single-eye enrolled populations $N = (0.16, 1.6, 4)$ million, and two-eye populations of $N = (0.16, 1.6)$ million individuals. The straight lines, which link points of constant threshold, show how the two error rates would vary if a fixed threshold were adopted operationally. Horizontal lines indicate that enrolled population N is influential only on FPIR, via $\text{FPIR}(N_2) = (N_2/N_1)\text{FPIR}(N_1)$. When this relationship is not evident, the implementation may be adjusting scores as a function of N (e.g. as described in [cite Daugman]). The large search sets S_{nb} are used. Missing plots indicate the run is not yet complete.

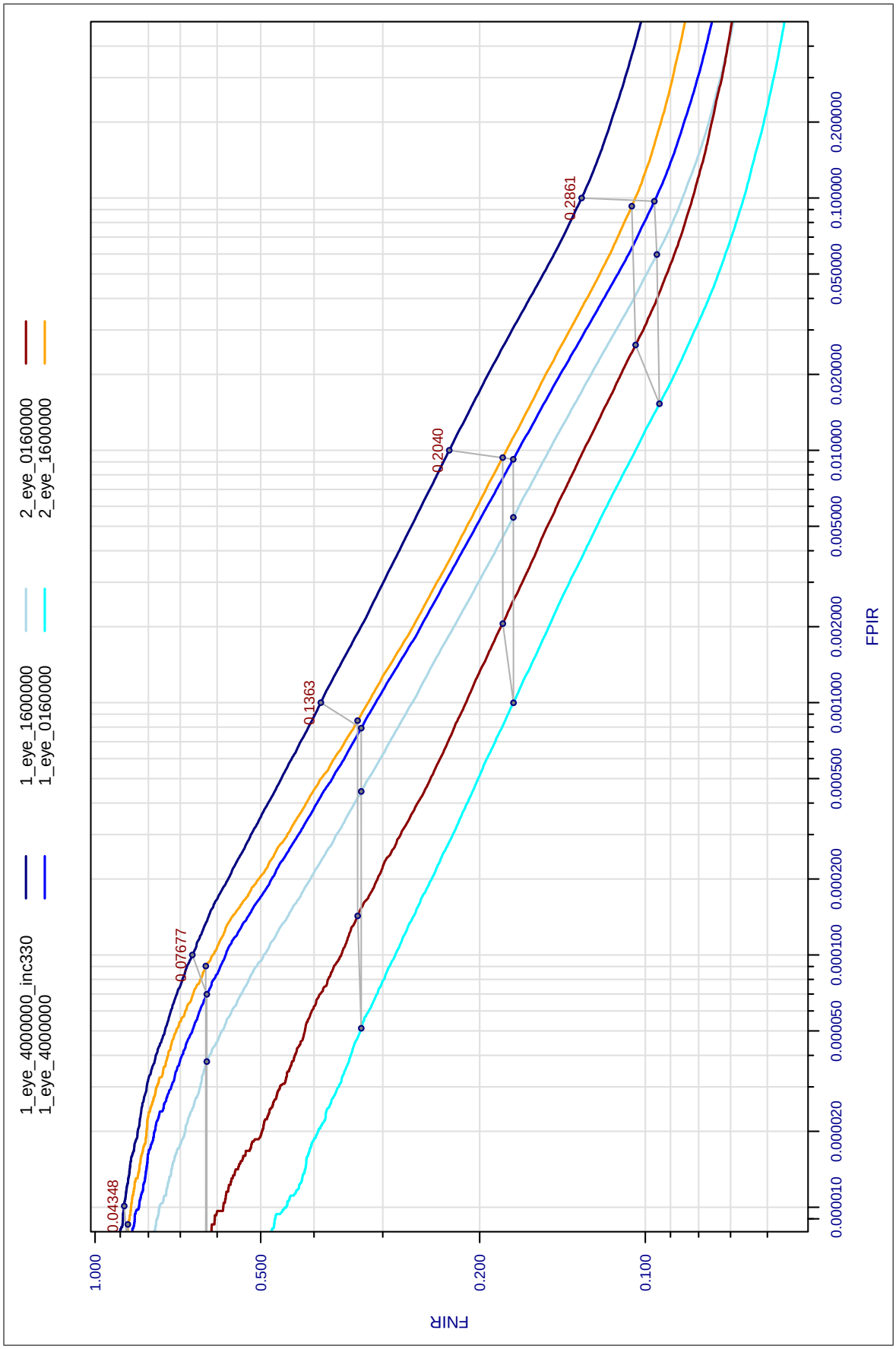

Figure 171: **Effect of population size** onDETs for implementation X11A executing searches for single-eye enrolled populations $N = (0.16, 1.6, 4)$ million, and two-eye populations of $N = (0.16, 1.6)$ million individuals. The straight lines, which link points of constant threshold, show how the two error rates would vary if a fixed threshold were adopted operationally. Horizontal lines indicate that enrolled population N is influential only on FPIR, via $\text{FPIR}(N_2) = (N_2/N_1)\text{FPIR}(N_1)$. When this relationship is not evident, the implementation may be adjusting scores as a function of N (e.g. as described in [cite Daugman]). The large search sets S_{nb} are used. Missing plots indicate the run is not yet complete.

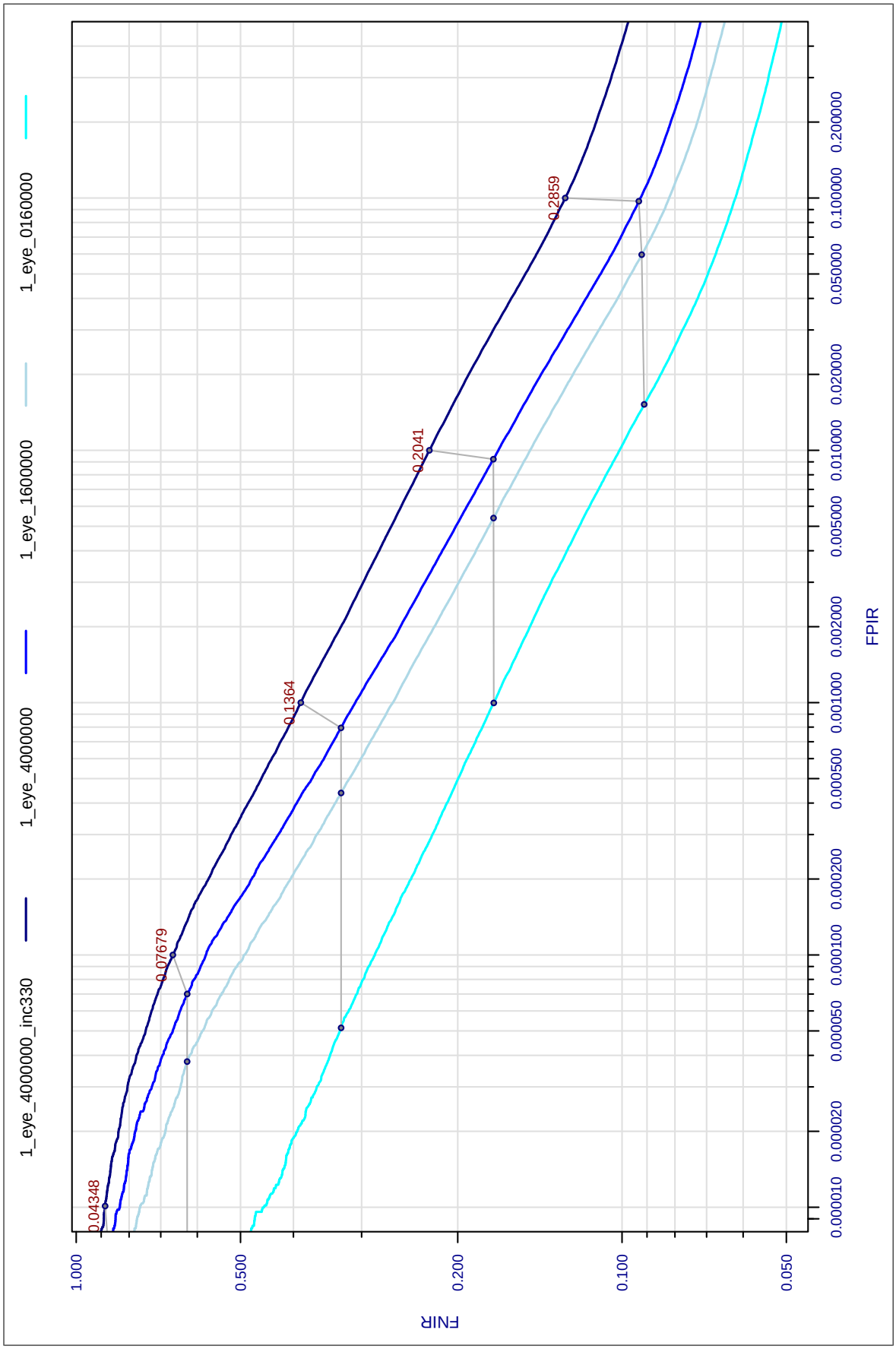

Figure 172: **Effect of population size** onDETs for implementation X11B executing searches for single-eye enrolled populations $N = (0.16, 1.6, 4)$ million, and two-eye populations of $N = (0.16, 1.6)$ million individuals. The straight lines, which link points of constant threshold, show how the two error rates would vary if a fixed threshold were adopted operationally. Horizontal lines indicate that enrolled population N is influential only on FPIR, via $\text{FPIR}(N_2) = (N_2/N_1)\text{FPIR}(N_1)$. When this relationship is not evident, the implementation may be adjusting scores as a function of N (e.g. as described in [cite Daugman]). The large search sets S_{nb} are used. Missing plots indicate the run is not yet complete.

Figure 173: **Effect of population size** onDETs for implementation Y02A executing searches for single-eye enrolled populations $N = (0.16, 1.6, 4)$ million, and two-eye populations of $N = (0.16, 1.6)$ million individuals. The straight lines, which link points of constant threshold, show how the two error rates would vary if a fixed threshold were adopted operationally. Horizontal lines indicate that enrolled population N is influential only on FPIR, via $\text{FPIR}(N_2) = (N_2/N_1)\text{FPIR}(N_1)$. When this relationship is not evident, the implementation may be adjusting scores as a function of N (e.g. as described in [cite Daugman]). The large search sets S_{nb} are used. Missing plots indicate the run is not yet complete.

Figure 174: **Effect of population size** onDETs for implementation Y02B executing searches for single-eye enrolled populations $N = (0.16, 1.6, 4)$ million, and two-eye populations of $N = (0.16, 1.6)$ million individuals. The straight lines, which link points of constant threshold, show how the two error rates would vary if a fixed threshold were adopted operationally. Horizontal lines indicate that enrolled population N is influential only on FPIR, via $\text{FPIR}(N_2) = (N_2/N_1)\text{FPIR}(N_1)$. When this relationship is not evident, the implementation may be adjusting scores as a function of N (e.g. as described in [cite Daugman]). The large search sets S_{nb} are used. Missing plots indicate the run is not yet complete.

Figure 175: **Effect of population size** onDETs for implementation Y03A executing searches for single-eye enrolled populations $N = (0.16, 1.6, 4)$ million, and two-eye populations of $N = (0.16, 1.6)$ million individuals. The straight lines, which link points of constant threshold, show how the two error rates would vary if a fixed threshold were adopted operationally. Horizontal lines indicate that enrolled population N is influential only on FPIR, via $\text{FPIR}(N_2) = (N_2/N_1)\text{FPIR}(N_1)$. When this relationship is not evident, the implementation may be adjusting scores as a function of N (e.g. as described in [cite Daugman]). The large search sets S_{nb} are used. Missing plots indicate the run is not yet complete.

Figure 176: **Effect of population size** onDETs for implementation Y03B executing searches for single-eye enrolled populations $N = (0.16, 1.6, 4)$ million, and two-eye populations of $N = (0.16, 1.6)$ million individuals. The straight lines, which link points of constant threshold, show how the two error rates would vary if a fixed threshold were adopted operationally. Horizontal lines indicate that enrolled population N is influential only on FPIR, via $\text{FPIR}(N_2) = (N_2/N_1)\text{FPIR}(N_1)$. When this relationship is not evident, the implementation may be adjusting scores as a function of N (e.g. as described in [cite Daugman]). The large search sets S_{nb} are used. Missing plots indicate the run is not yet complete.

Appendix E: Effect of Compression

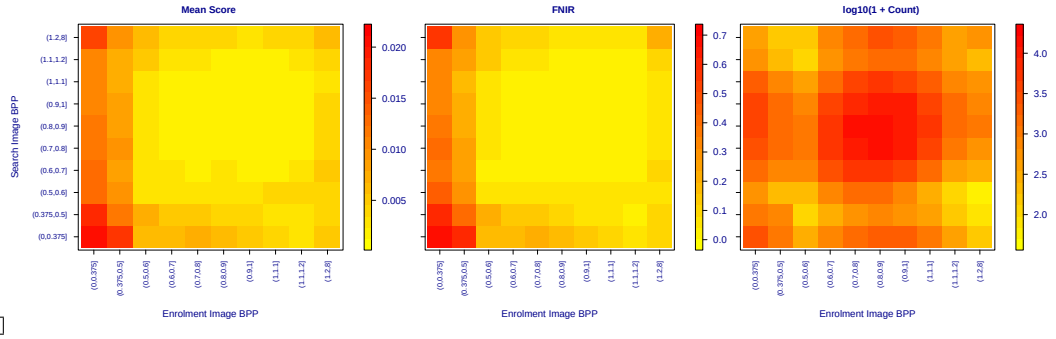

(a) Paired CRs, mate searches

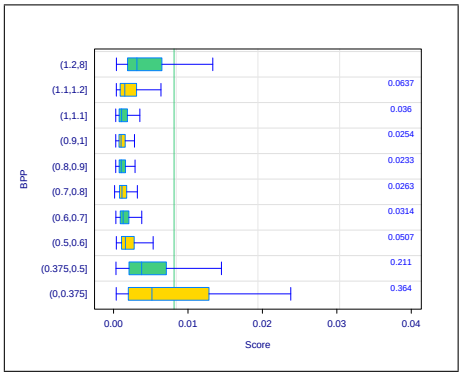

(b) Minimum CR, mate searches

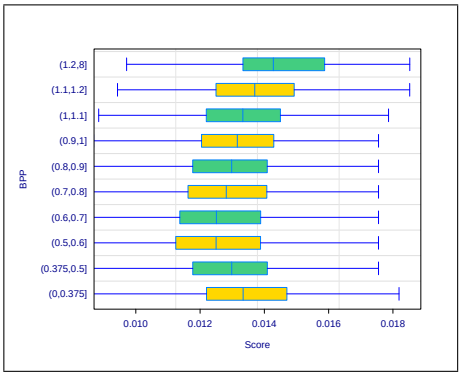

(c) Minimum CR, top nonmate

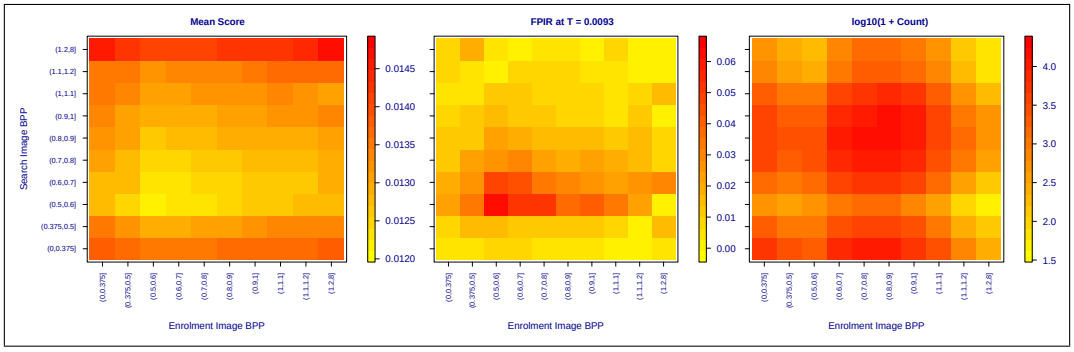

(d) Paired CRs, top nonmate

Figure 177: Effect of compression on accuracy for implementation N02A executing searches in an enrolled population of N = 1.6 million. The axes are labelled by binned values of the number of bits per pixel (BPP) implied by the JPEG filesize and the image dimensions. The lowest BPP bin is populated largely by the overly compressed 330x330 images. For mate searches, the three heatmaps give, respectively, the score, FNIR at FPIR = 0.0001, and the log of the count of images in each bin (3 corresponds to 1000). For nonmate searches, the threshold is set to give FPIR = 0.001 globally. The boxplots show the effect on the score, with the FNIR value annotated at right.

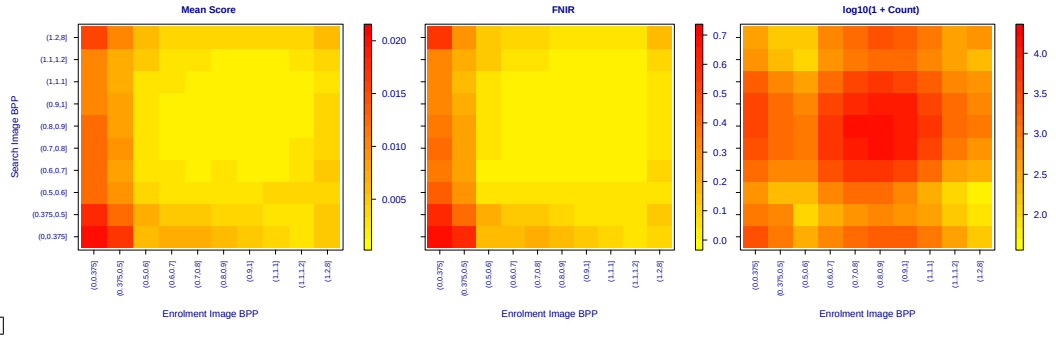

(a) Paired CRs, mate searches

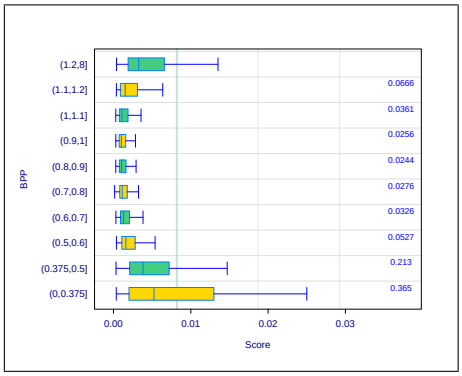

(b) Minimum CR, mate searches

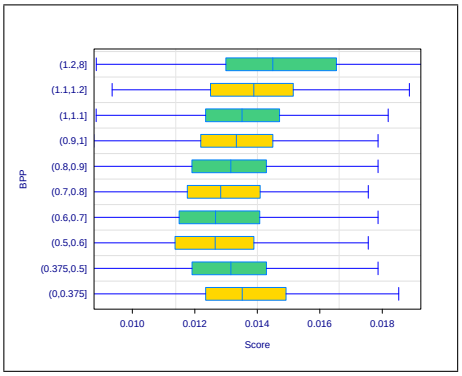

(c) Minimum CR, top nonmate

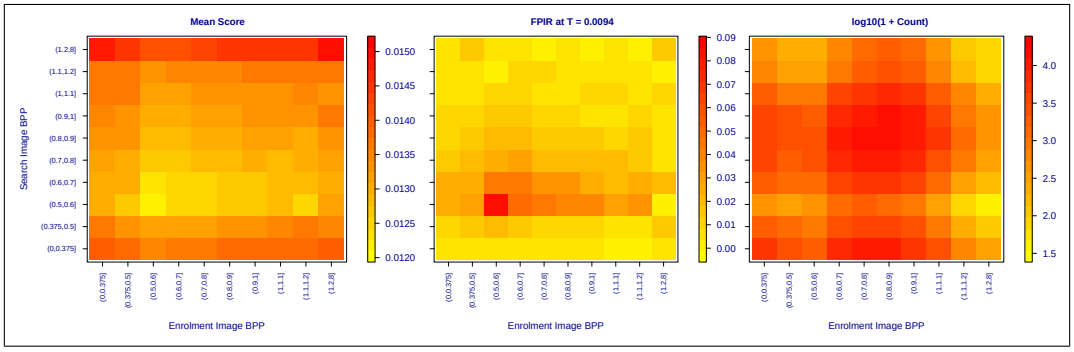

(d) Paired CRs, top nonmate

Figure 178: Effect of compression on accuracy for implementation N02B executing searches in an enrolled population of N = 1.6 million. The axes are labelled by binned values of the number of bits per pixel (BPP) implied by the JPEG filesize and the image dimensions. The lowest BPP bin is populated largely by the overly compressed 330x330 images. For mate searches, the three heatmaps give, respectively, the score, FNIR at FPIR = 0.0001, and the log of the count of images in each bin (3 corresponds to 1000). For nonmate searches, the threshold is set to give FPIR = 0.001 globally. The boxplots show the effect on the score, with the FNIR value annotated at right.

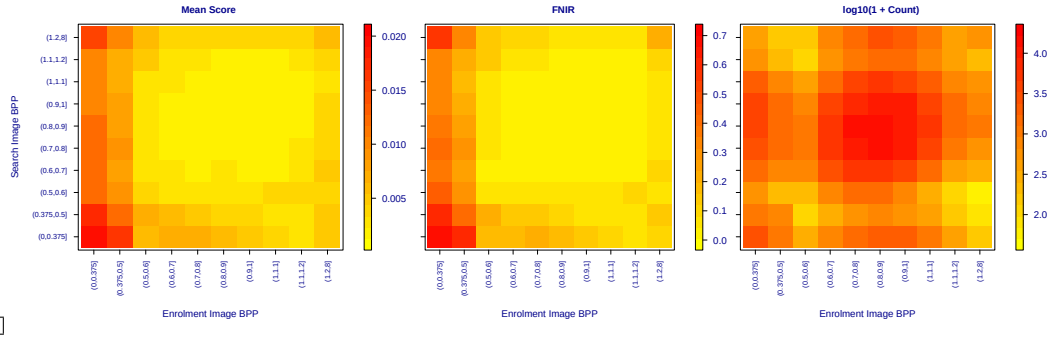

(a) Paired CRs, mate searches

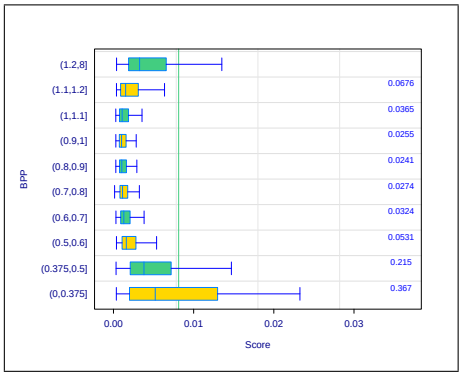

(b) Minimum CR, mate searches

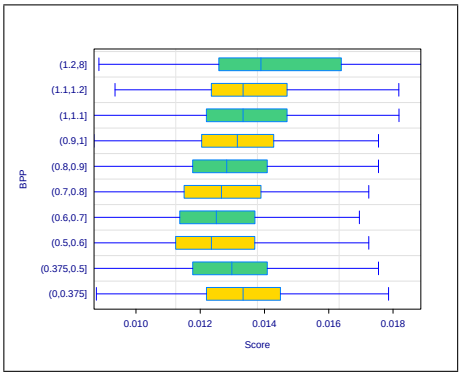

(c) Minimum CR, top nonmate

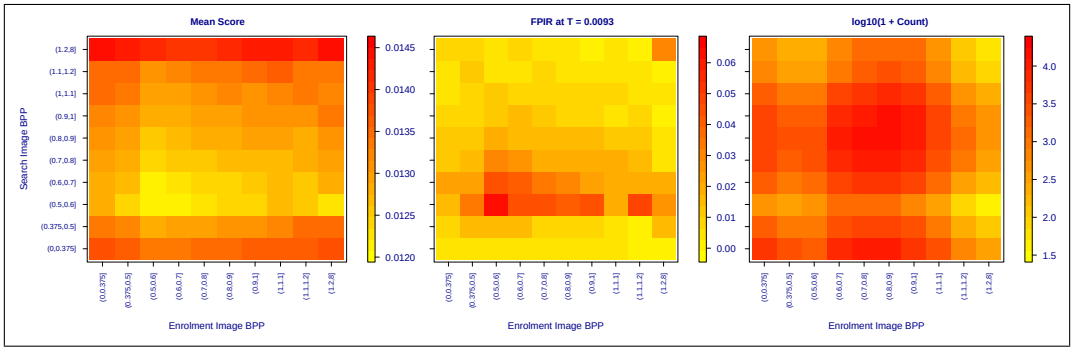

(d) Paired CRs, top nonmate

Figure 179: Effect of compression on accuracy for implementation N03A executing searches in an enrolled population of N = 1.6 million. The axes are labelled by binned values of the number of bits per pixel (BPP) implied by the JPEG filesize and the image dimensions. The lowest BPP bin is populated largely by the overly compressed 330x330 images. For mate searches, the three heatmaps give, respectively, the score, FNIR at FPIR = 0.0001, and the log of the count of images in each bin (3 corresponds to 1000). For nonmate searches, the threshold is set to give FPIR = 0.001 globally. The boxplots show the effect on the score, with the FNIR value annotated at right.

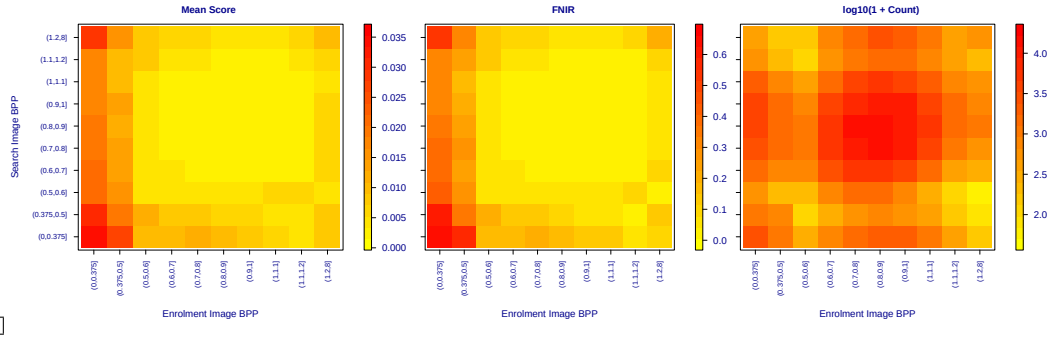

(a) Paired CRs, mate searches

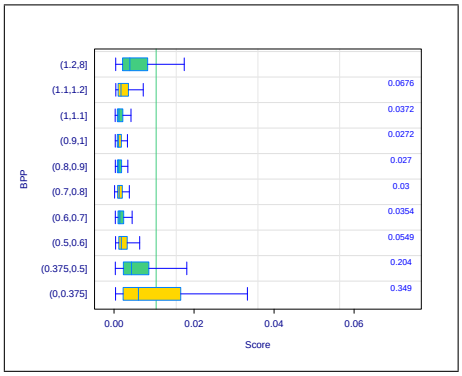

(b) Minimum CR, mate searches

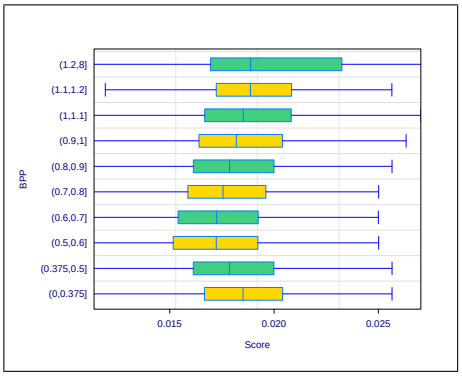

(c) Minimum CR, top nonmate

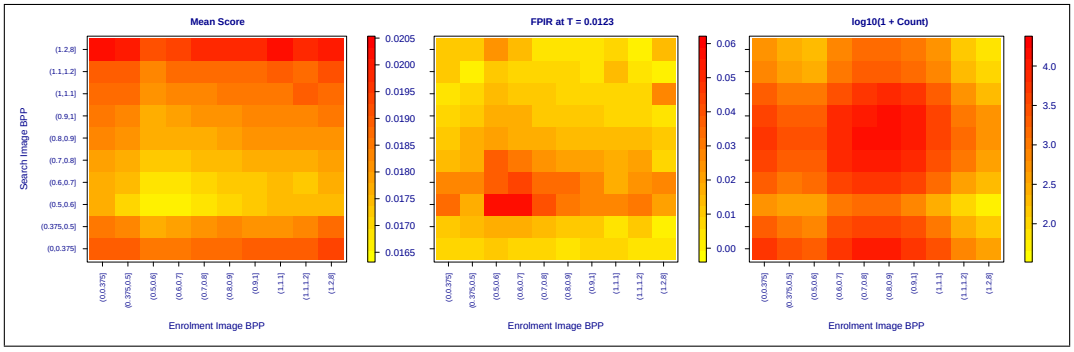

(d) Paired CRs, top nonmate

Figure 180: Effect of compression on accuracy for implementation N03B executing searches in an enrolled population of N = 1.6 million. The axes are labelled by binned values of the number of bits per pixel (BPP) implied by the JPEG filesize and the image dimensions. The lowest BPP bin is populated largely by the overly compressed 330x330 images. For mate searches, the three heatmaps give, respectively, the score, FNIR at FPIR = 0.0001, and the log of the count of images in each bin (3 corresponds to 1000). For nonmate searches, the threshold is set to give FPIR = 0.001 globally. The boxplots show the effect on the score, with the FNIR value annotated at right.

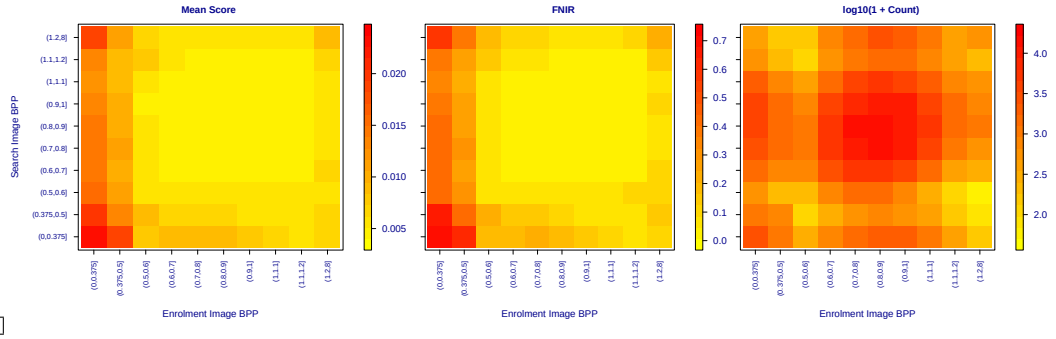

(a) Paired CRs, mate searches

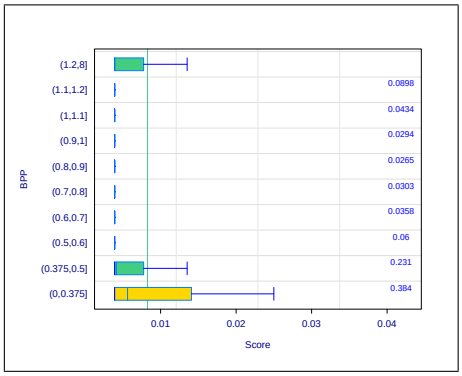

(b) Minimum CR, mate searches

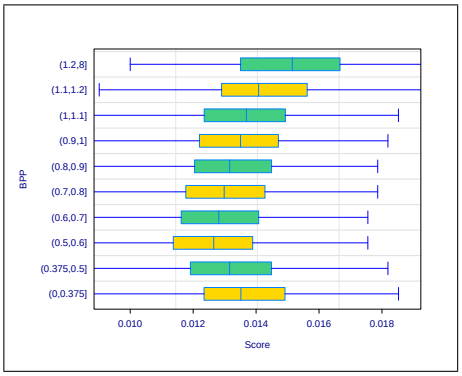

(c) Minimum CR, top nonmate

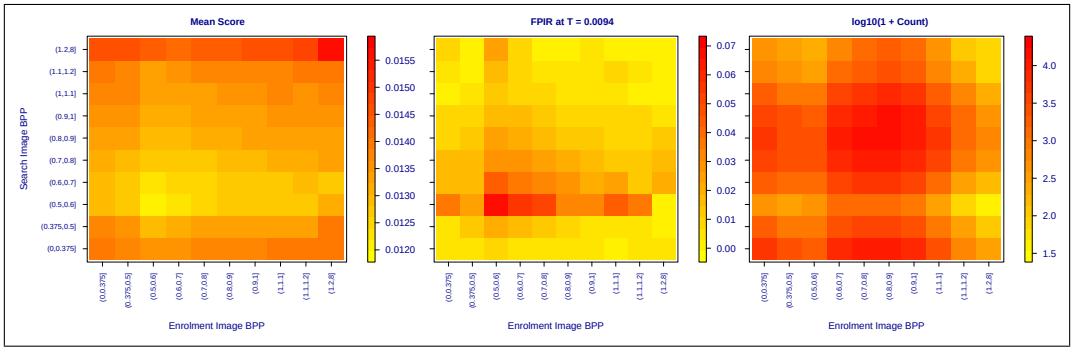

(d) Paired CRs, top nonmate

Figure 181: Effect of compression on accuracy for implementation N04A executing searches in an enrolled population of N = 1.6 million. The axes are labelled by binned values of the number of bits per pixel (BPP) implied by the JPEG filesize and the image dimensions. The lowest BPP bin is populated largely by the overly compressed 330x330 images. For mate searches, the three heatmaps give, respectively, the score, FNIR at FPIR = 0.0001, and the log of the count of images in each bin (3 corresponds to 1000). For nonmate searches, the threshold is set to give FPIR = 0.001 globally. The boxplots show the effect on the score, with the FNIR value annotated at right.

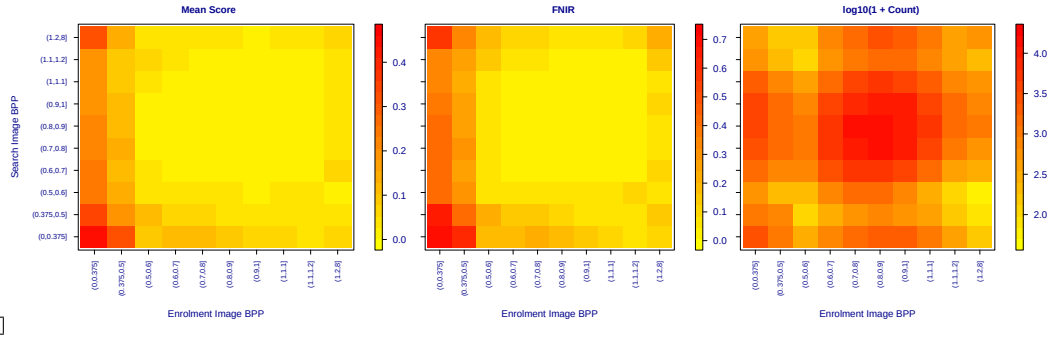

(a) Paired CRs, mate searches

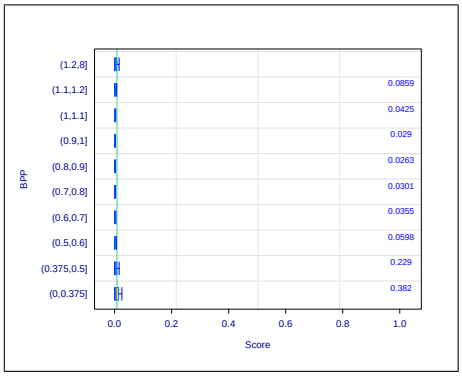

(b) Minimum CR, mate searches

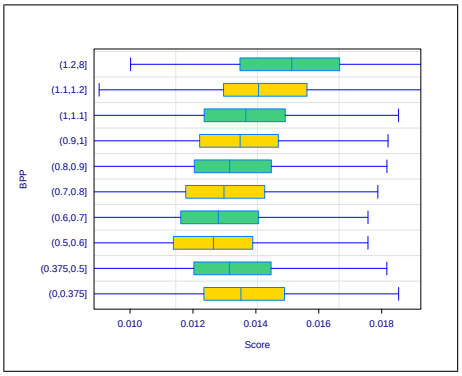

(c) Minimum CR, top nonmate

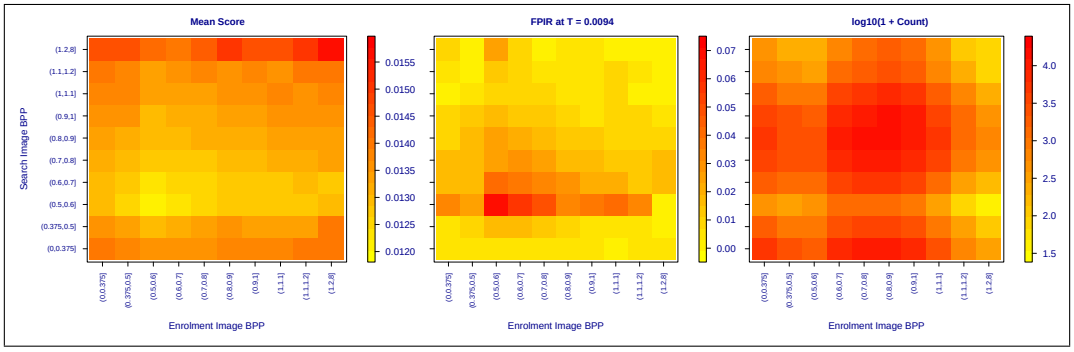

(d) Paired CRs, top nonmate

Figure 182: Effect of compression on accuracy for implementation N11A executing searches in an enrolled population of N = 1.6 million. The axes are labelled by binned values of the number of bits per pixel (BPP) implied by the JPEG filesize and the image dimensions. The lowest BPP bin is populated largely by the overly compressed 330x330 images. For mate searches, the three heatmaps give, respectively, the score, FNIR at FPIR = 0.0001, and the log of the count of images in each bin (3 corresponds to 1000). For nonmate searches, the threshold is set to give FPIR = 0.001 globally. The boxplots show the effect on the score, with the FNIR value annotated at right.

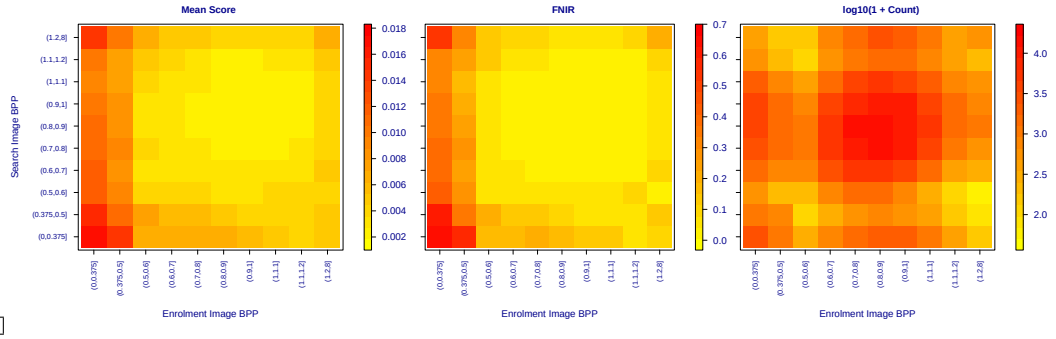

(a) Paired CRs, mate searches

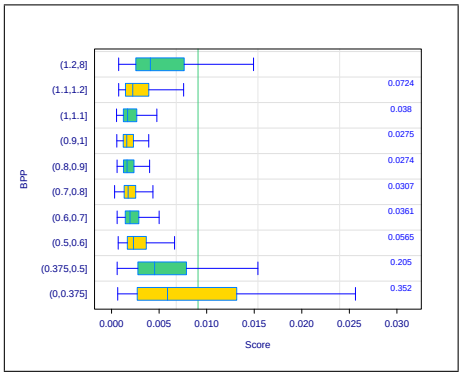

(b) Minimum CR, mate searches

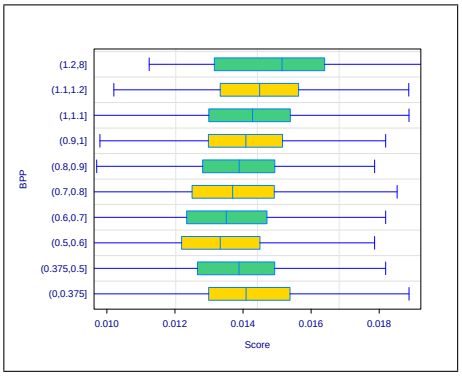

(c) Minimum CR, top nonmate

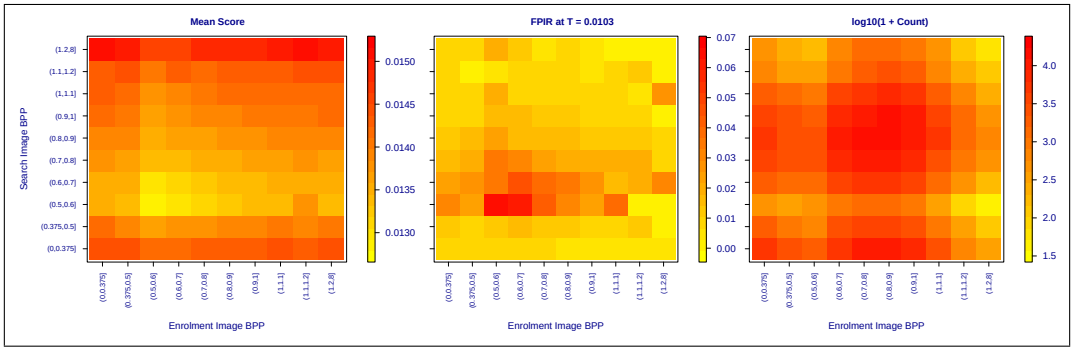

(d) Paired CRs, top nonmate

Figure 183: Effect of compression on accuracy for implementation N11B executing searches in an enrolled population of N = 1.6 million. The axes are labelled by binned values of the number of bits per pixel (BPP) implied by the JPEG filesize and the image dimensions. The lowest BPP bin is populated largely by the overly compressed 330x330 images. For mate searches, the three heatmaps give, respectively, the score, FNIR at FPIR = 0.0001, and the log of the count of images in each bin (3 corresponds to 1000). For nonmate searches, the threshold is set to give FPIR = 0.001 globally. The boxplots show the effect on the score, with the FNIR value annotated at right.

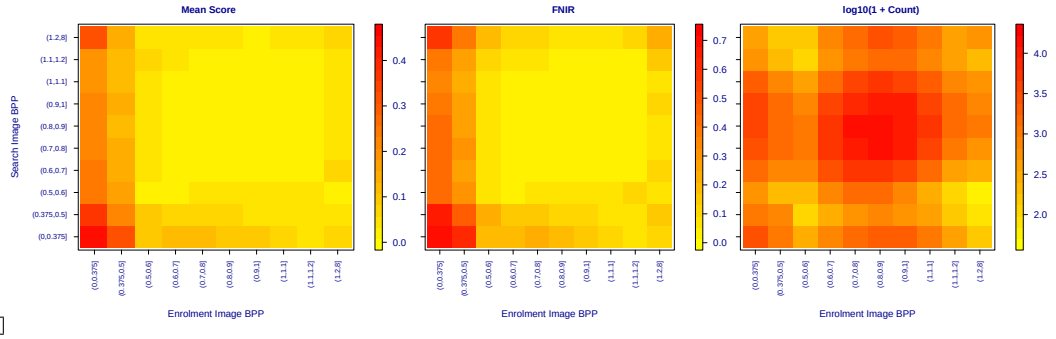

(a) Paired CRs, mate searches

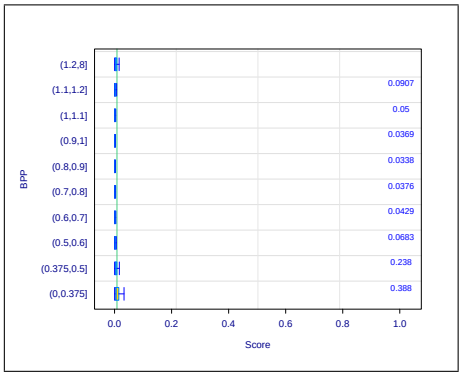

(b) Minimum CR, mate searches

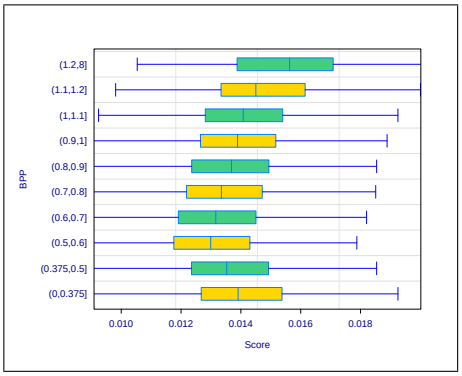

(c) Minimum CR, top nonmate

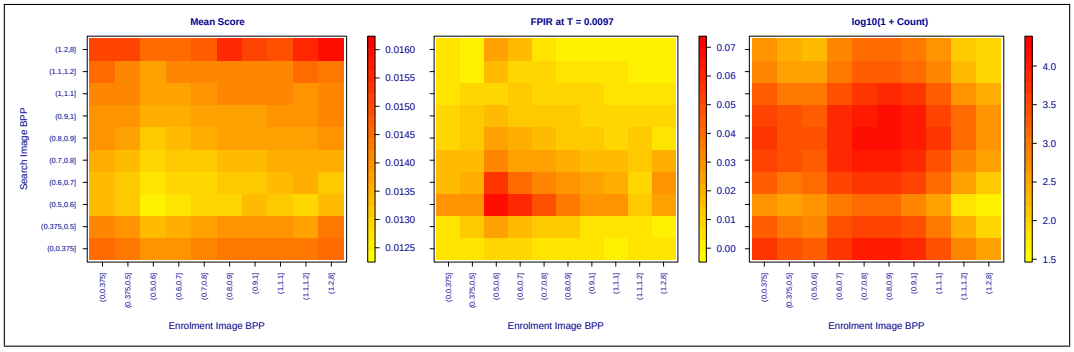

(d) Paired CRs, top nonmate

Figure 184: Effect of compression on accuracy for implementation N12A executing searches in an enrolled population of N = 1.6 million. The axes are labelled by binned values of the number of bits per pixel (BPP) implied by the JPEG filesize and the image dimensions. The lowest BPP bin is populated largely by the overly compressed 330x330 images. For mate searches, the three heatmaps give, respectively, the score, FNIR at FPIR = 0.0001, and the log of the count of images in each bin (3 corresponds to 1000). For nonmate searches, the threshold is set to give FPIR = 0.001 globally. The boxplots show the effect on the score, with the FNIR value annotated at right.

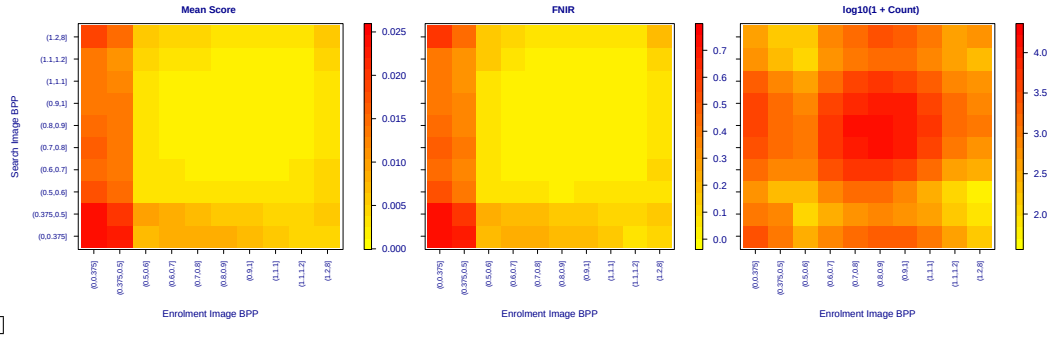

(a) Paired CRs, mate searches

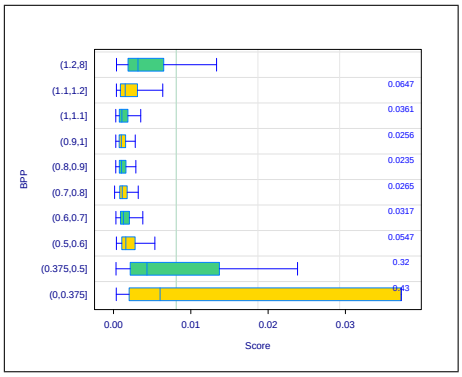

(b) Minimum CR, mate searches

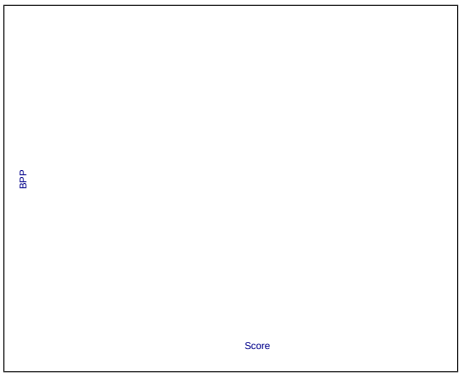

(c) Minimum CR, top nonmate

Figure 185: Effect of compression on accuracy for implementation N12B executing searches in an enrolled population of N = 1.6 million. The axes are labelled by binned values of the number of bits per pixel (BPP) implied by the JPEG filesize and the image dimensions. The lowest BPP bin is populated largely by the overly compressed 330x330 images. For mate searches, the three heatmaps give, respectively, the score, FNIR at FPIR = 0.0001, and the log of the count of images in each bin (3 corresponds to 1000). For nonmate searches, the threshold is set to give FPIR = 0.001 globally. The boxplots show the effect on the score, with the FNIR value annotated at right.

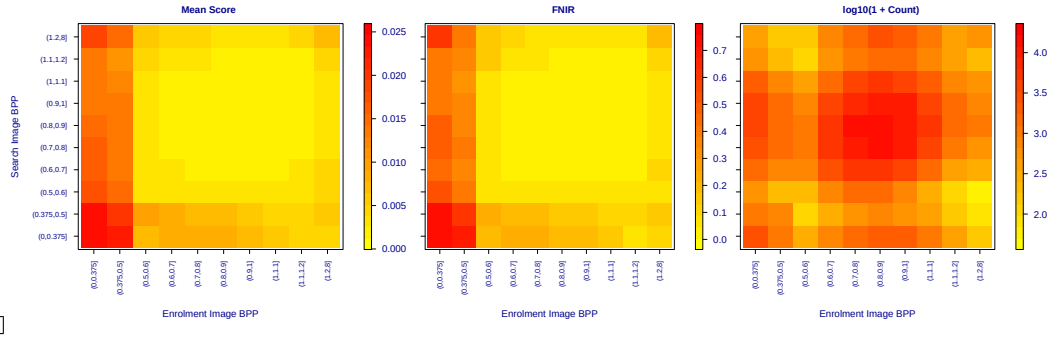

(a) Paired CRs, mate searches

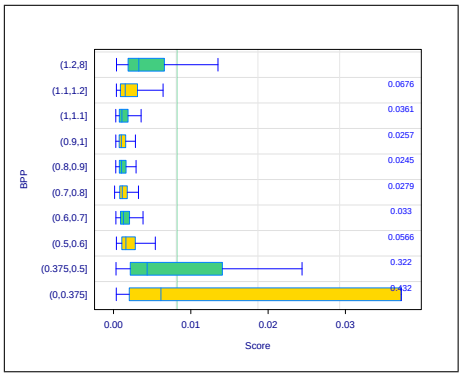

(b) Minimum CR, mate searches

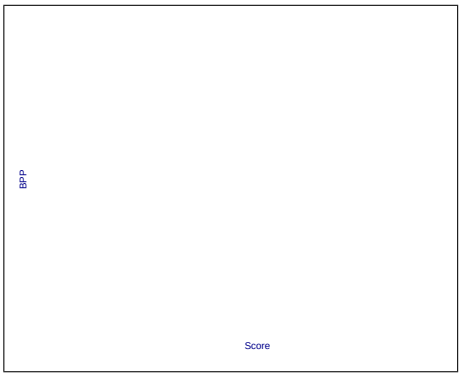

(c) Minimum CR, top nonmate

Figure 186: Effect of compression on accuracy for implementation N13B executing searches in an enrolled population of N = 1.6 million. The axes are labelled by binned values of the number of bits per pixel (BPP) implied by the JPEG filesize and the image dimensions. The lowest BPP bin is populated largely by the overly compressed 330x330 images. For mate searches, the three heatmaps give, respectively, the score, FNIR at FPIR = 0.0001, and the log of the count of images in each bin (3 corresponds to 1000). For nonmate searches, the threshold is set to give FPIR = 0.001 globally. The boxplots show the effect on the score, with the FNIR value annotated at right.

Figure 187: Effect of compression on accuracy for implementation P02A executing searches in an enrolled population of N = 1.6 million. The axes are labelled by binned values of the number of bits per pixel (BPP) implied by the JPEG filesize and the image dimensions. The lowest BPP bin is populated largely by the overly compressed 330x330 images. For mate searches, the three heatmaps give, respectively, the score, FNIR at FPIR = 0.0001, and the log of the count of images in each bin (3 corresponds to 1000). For nonmate searches, the threshold is set to give FPIR = 0.001 globally. The boxplots show the effect on the score, with the FNIR value annotated at right.

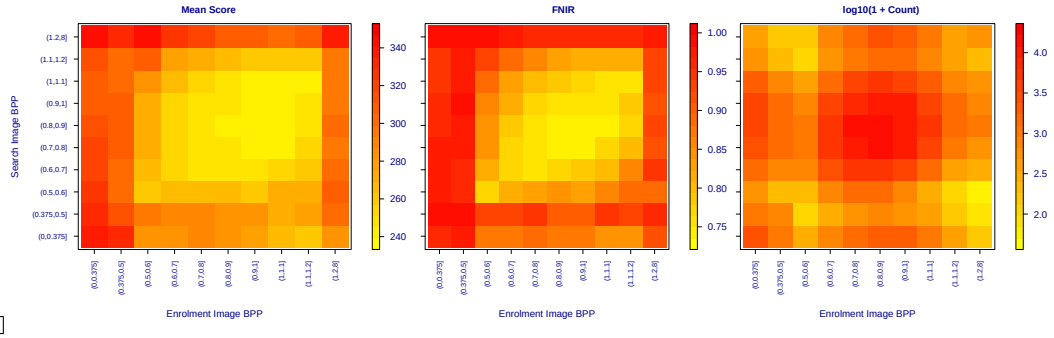

(a) Paired CRs, mate searches

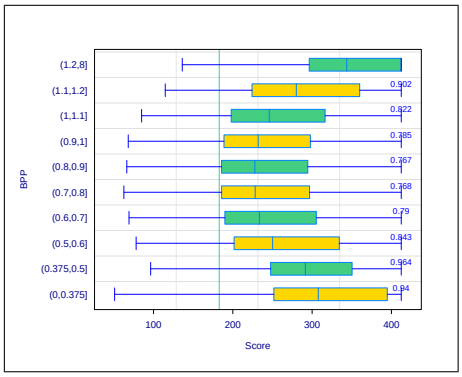

(b) Minimum CR, mate searches

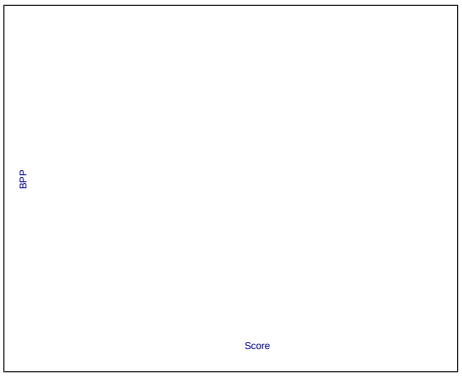

(c) Minimum CR, top nonmate

Figure 188: Effect of compression on accuracy for implementation P11A executing searches in an enrolled population of N = 1.6 million. The axes are labelled by binned values of the number of bits per pixel (BPP) implied by the JPEG filesize and the image dimensions. The lowest BPP bin is populated largely by the overly compressed 330x330 images. For mate searches, the three heatmaps give, respectively, the score, FNIR at FPIR = 0.0001, and the log of the count of images in each bin (3 corresponds to 1000). For nonmate searches, the threshold is set to give FPIR = 0.001 globally. The boxplots show the effect on the score, with the FNIR value annotated at right.

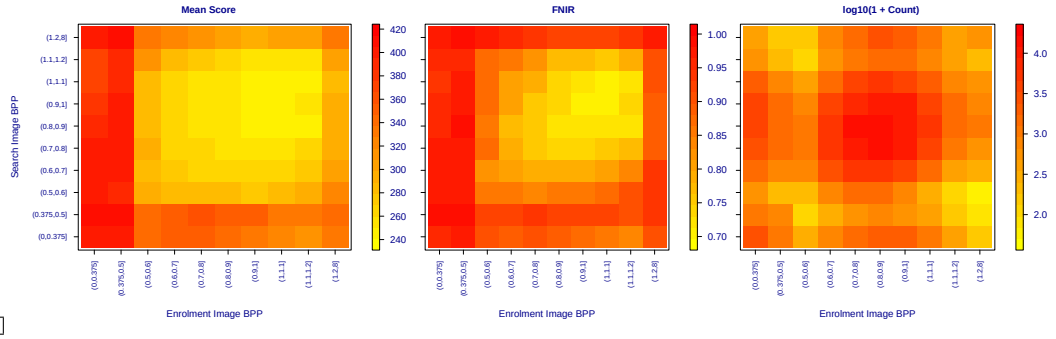

(a) Paired CRs, mate searches

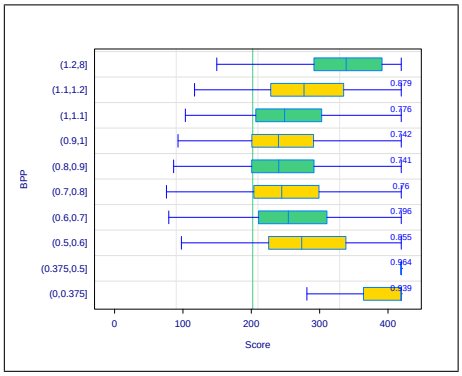

(b) Minimum CR, mate searches

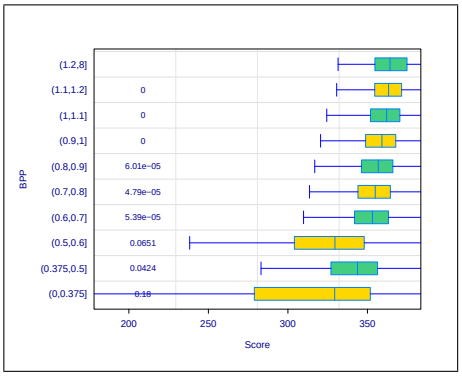

(c) Minimum CR, top nonmate

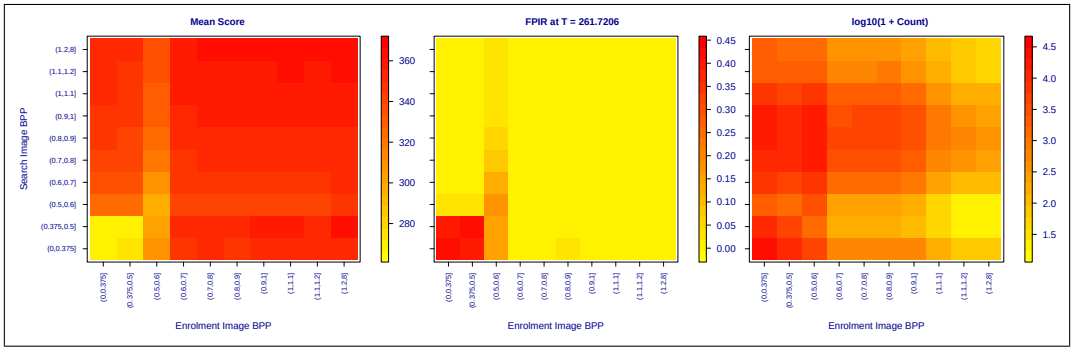

(d) Paired CRs, top nonmate

Figure 189: Effect of compression on accuracy for implementation P11B executing searches in an enrolled population of N = 1.6 million. The axes are labelled by binned values of the number of bits per pixel (BPP) implied by the JPEG filesize and the image dimensions. The lowest BPP bin is populated largely by the overly compressed 330x330 images. For mate searches, the three heatmaps give, respectively, the score, FNIR at FPIR = 0.0001, and the log of the count of images in each bin (3 corresponds to 1000). For nonmate searches, the threshold is set to give FPIR = 0.001 globally. The boxplots show the effect on the score, with the FNIR value annotated at right.

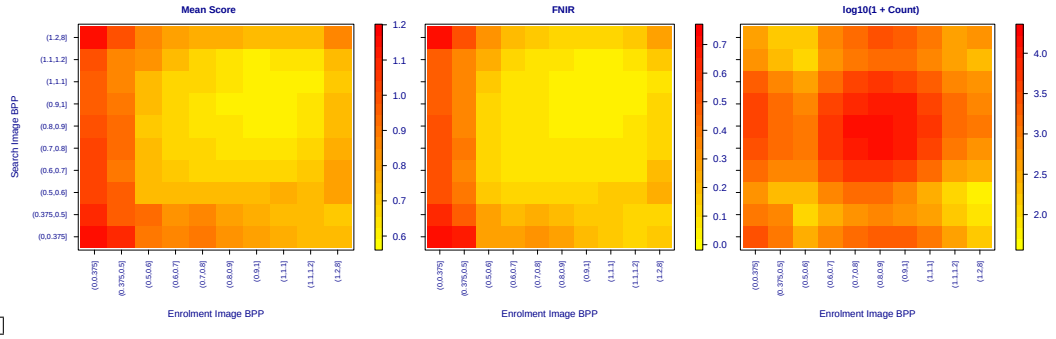

(a) Paired CRs, mate searches

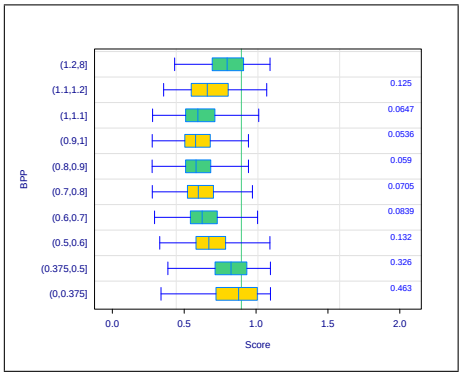

(b) Minimum CR, mate searches

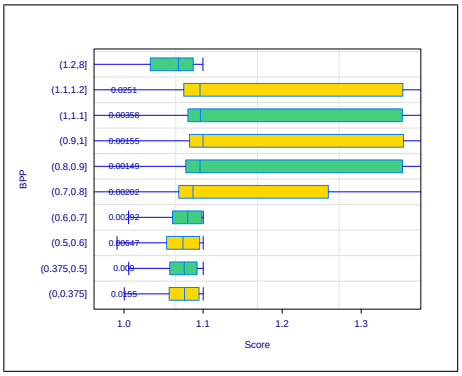

(c) Minimum CR, top nonmate

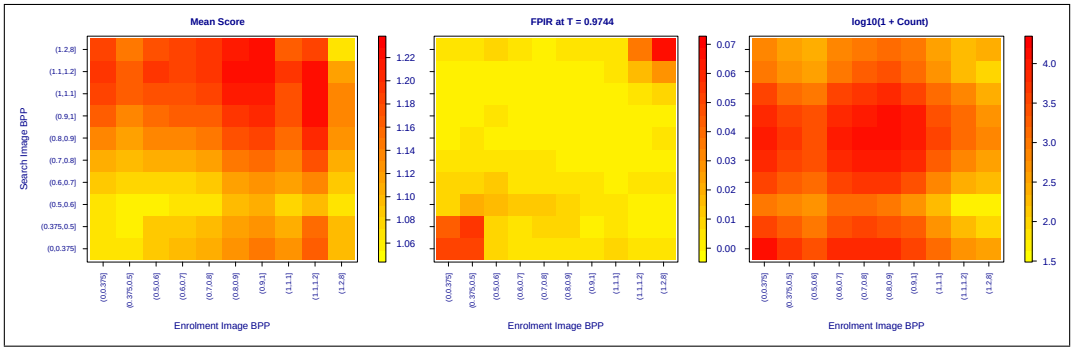

(d) Paired CRs, top nonmate

Figure 190: Effect of compression on accuracy for implementation Q02A executing searches in an enrolled population of N = 1.6 million. The axes are labelled by binned values of the number of bits per pixel (BPP) implied by the JPEG filesize and the image dimensions. The lowest BPP bin is populated largely by the overly compressed 330x330 images. For mate searches, the three heatmaps give, respectively, the score, FNIR at FPIR = 0.0001, and the log of the count of images in each bin (3 corresponds to 1000). For nonmate searches, the threshold is set to give FPIR = 0.001 globally. The boxplots show the effect on the score, with the FNIR value annotated at right.

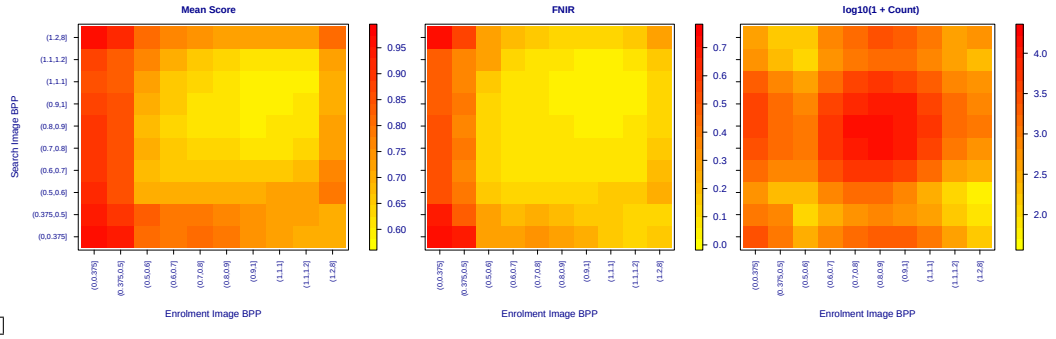

(a) Paired CRs, mate searches

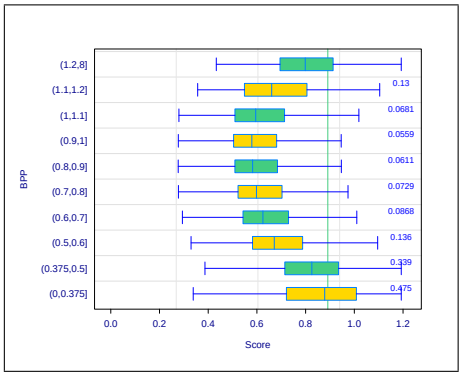

(b) Minimum CR, mate searches

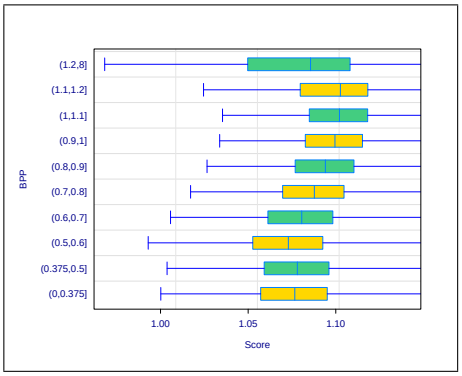

(c) Minimum CR, top nonmate

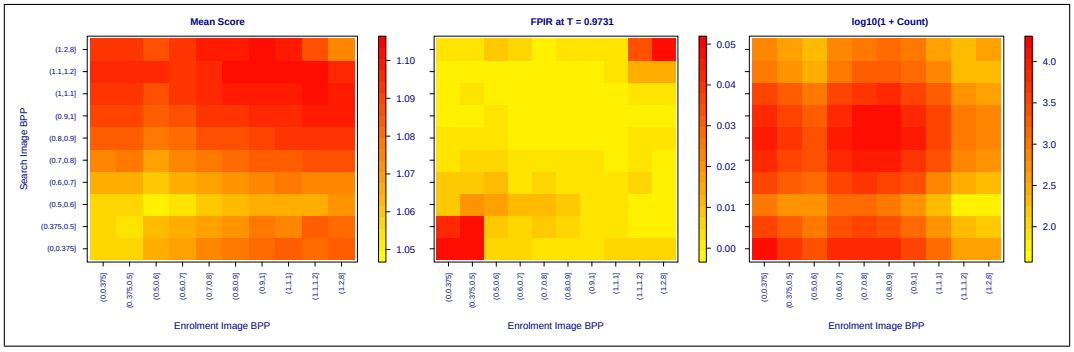

(d) Paired CRs, top nonmate

Figure 191: Effect of compression on accuracy for implementation Q02B executing searches in an enrolled population of N = 1.6 million. The axes are labelled by binned values of the number of bits per pixel (BPP) implied by the JPEG filesize and the image dimensions. The lowest BPP bin is populated largely by the overly compressed 330x330 images. For mate searches, the three heatmaps give, respectively, the score, FNIR at FPIR = 0.0001, and the log of the count of images in each bin (3 corresponds to 1000). For nonmate searches, the threshold is set to give FPIR = 0.001 globally. The boxplots show the effect on the score, with the FNIR value annotated at right.

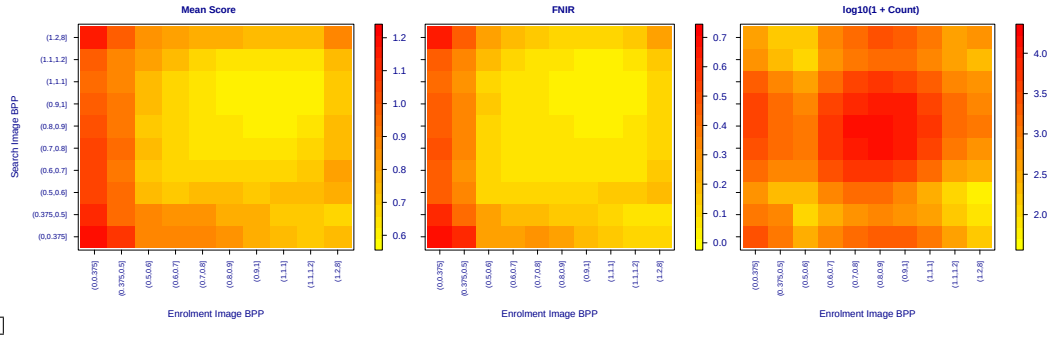

(a) Paired CRs, mate searches

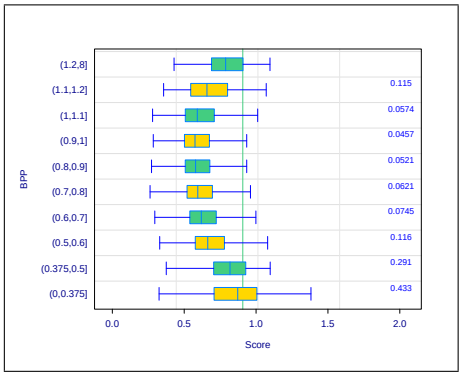

(b) Minimum CR, mate searches

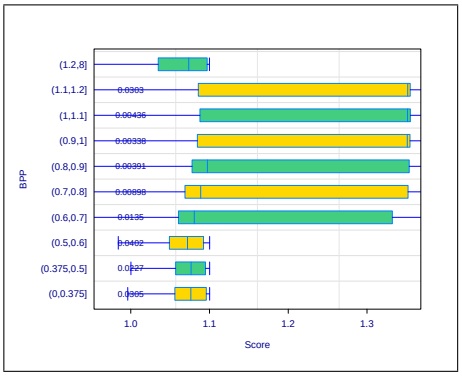

(c) Minimum CR, top nonmate

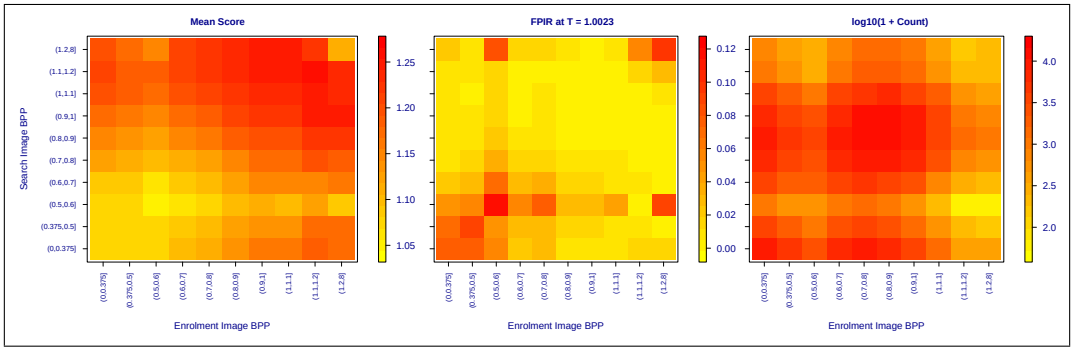

(d) Paired CRs, top nonmate

Figure 192: Effect of compression on accuracy for implementation Q03A executing searches in an enrolled population of N = 1.6 million. The axes are labelled by binned values of the number of bits per pixel (BPP) implied by the JPEG filesize and the image dimensions. The lowest BPP bin is populated largely by the overly compressed 330x330 images. For mate searches, the three heatmaps give, respectively, the score, FNIR at FPIR = 0.0001, and the log of the count of images in each bin (3 corresponds to 1000). For nonmate searches, the threshold is set to give FPIR = 0.001 globally. The boxplots show the effect on the score, with the FNIR value annotated at right.

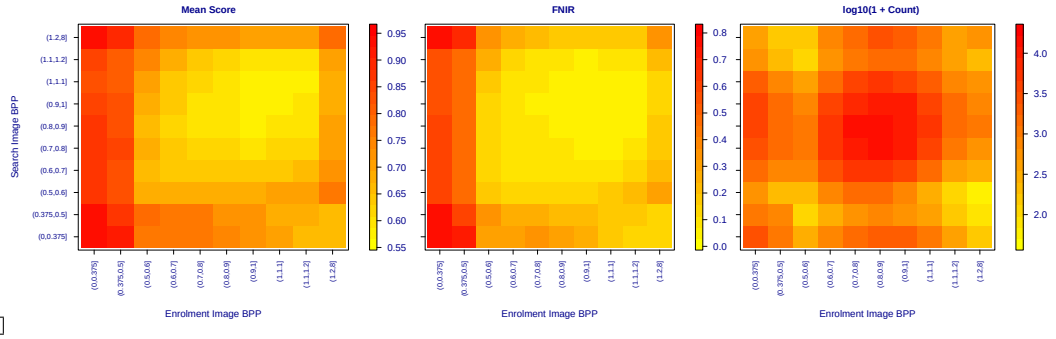

(a) Paired CRs, mate searches

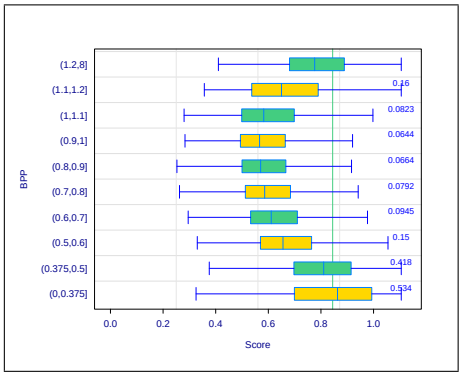

(b) Minimum CR, mate searches

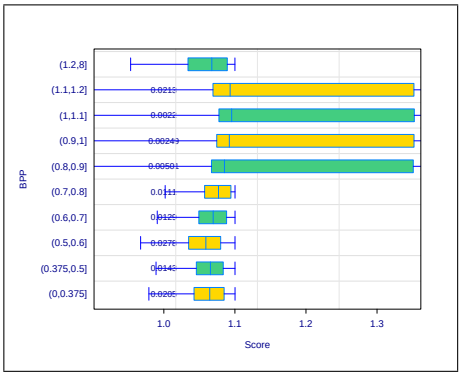

(c) Minimum CR, top nonmate

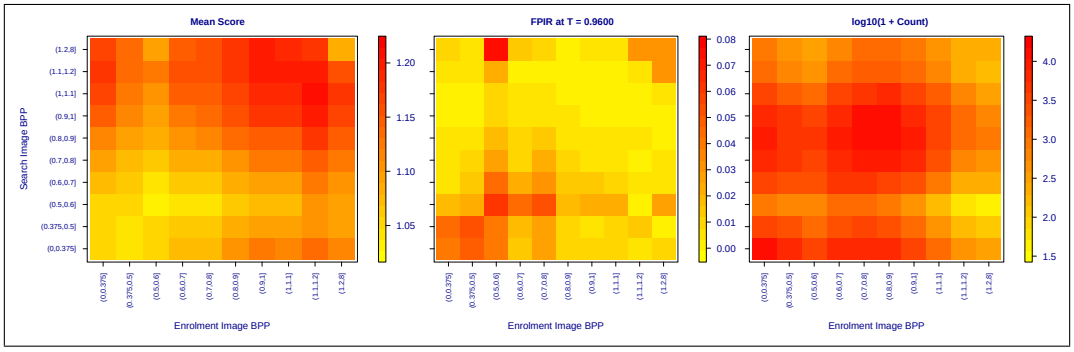

(d) Paired CRs, top nonmate

Figure 193: Effect of compression on accuracy for implementation Q03B executing searches in an enrolled population of N = 1.6 million. The axes are labelled by binned values of the number of bits per pixel (BPP) implied by the JPEG filesize and the image dimensions. The lowest BPP bin is populated largely by the overly compressed 330x330 images. For mate searches, the three heatmaps give, respectively, the score, FNIR at FPIR = 0.0001, and the log of the count of images in each bin (3 corresponds to 1000). For nonmate searches, the threshold is set to give FPIR = 0.001 globally. The boxplots show the effect on the score, with the FNIR value annotated at right.

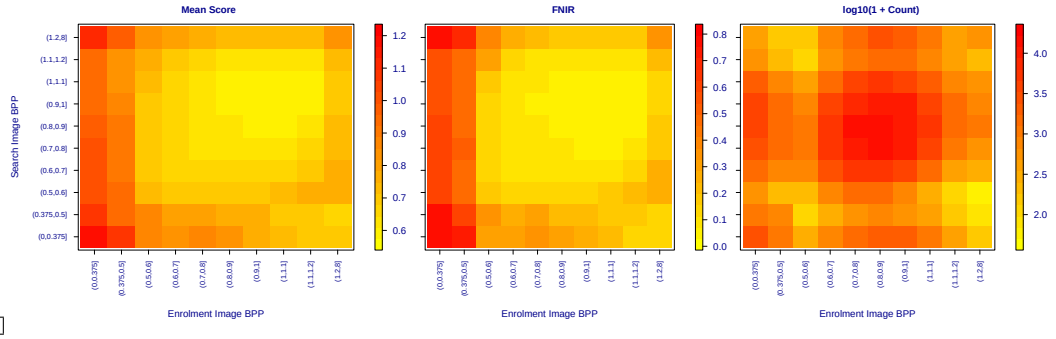

(a) Paired CRs, mate searches

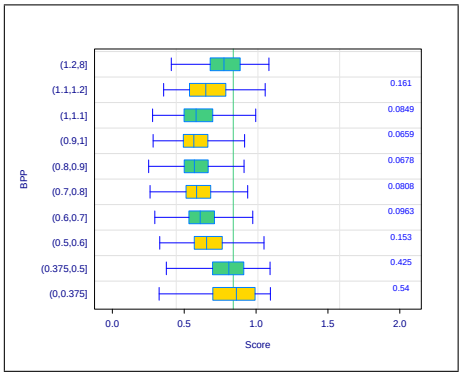

(b) Minimum CR, mate searches

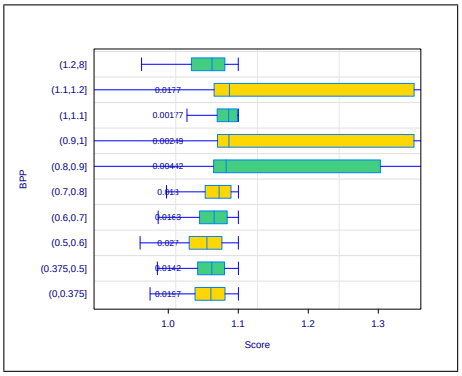

(c) Minimum CR, top nonmate

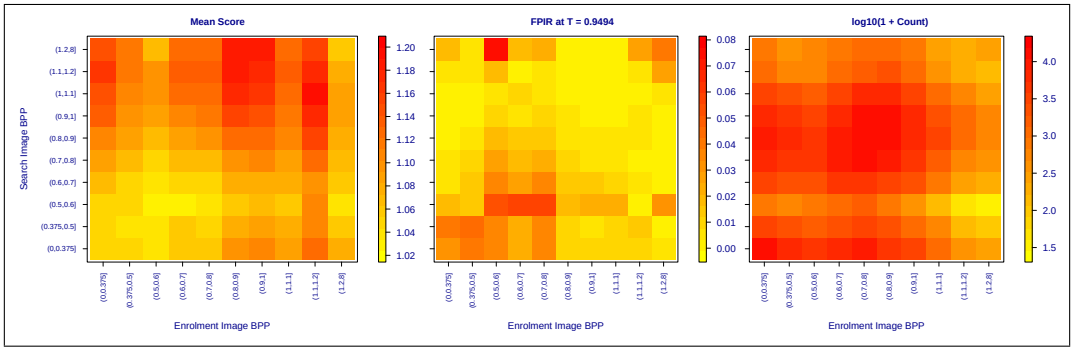

(d) Paired CRs, top nonmate

Figure 194: Effect of compression on accuracy for implementation Q04B executing searches in an enrolled population of N = 1.6 million. The axes are labelled by binned values of the number of bits per pixel (BPP) implied by the JPEG filesize and the image dimensions. The lowest BPP bin is populated largely by the overly compressed 330x330 images. For mate searches, the three heatmaps give, respectively, the score, FNIR at FPIR = 0.0001, and the log of the count of images in each bin (3 corresponds to 1000). For nonmate searches, the threshold is set to give FPIR = 0.001 globally. The boxplots show the effect on the score, with the FNIR value annotated at right.

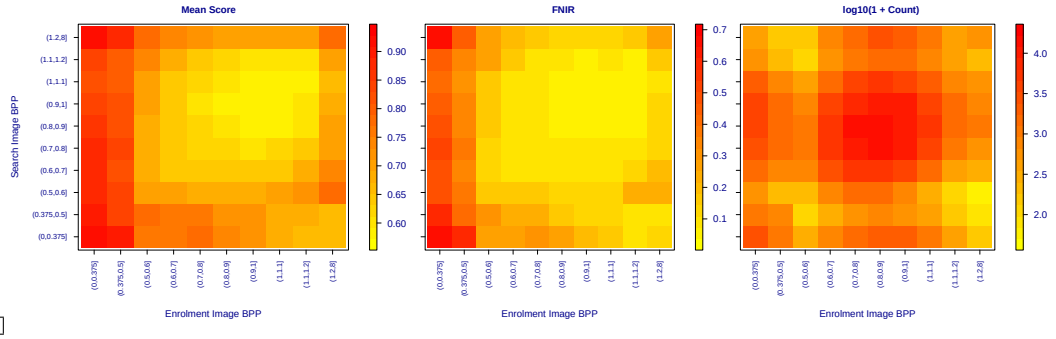

(a) Paired CRs, mate searches

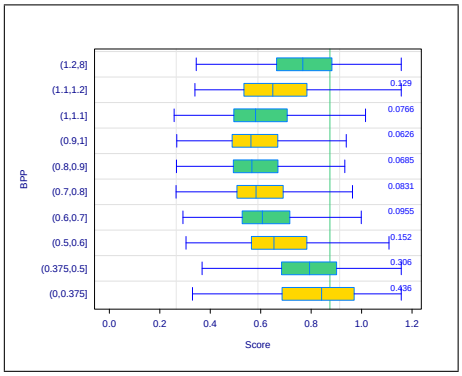

(b) Minimum CR, mate searches

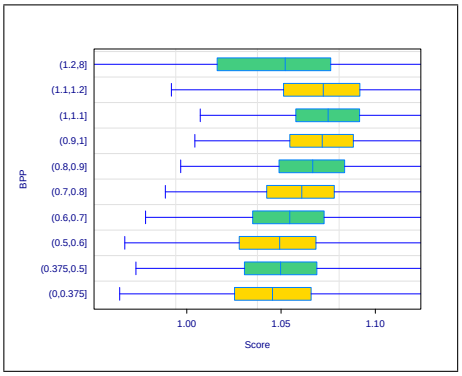

(c) Minimum CR, top nonmate

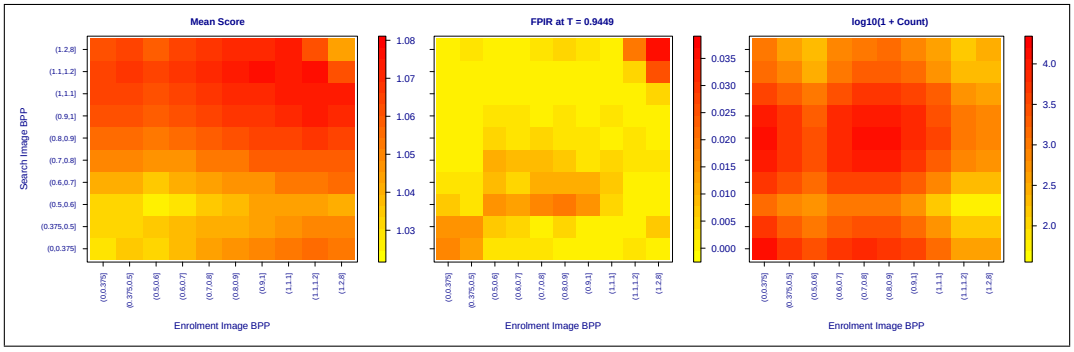

(d) Paired CRs, top nonmate

Figure 195: Effect of compression on accuracy for implementation Q11B executing searches in an enrolled population of N = 1.6 million. The axes are labelled by binned values of the number of bits per pixel (BPP) implied by the JPEG filesize and the image dimensions. The lowest BPP bin is populated largely by the overly compressed 330x330 images. For mate searches, the three heatmaps give, respectively, the score, FNIR at FPIR = 0.0001, and the log of the count of images in each bin (3 corresponds to 1000). For nonmate searches, the threshold is set to give FPIR = 0.001 globally. The boxplots show the effect on the score, with the FNIR value annotated at right.

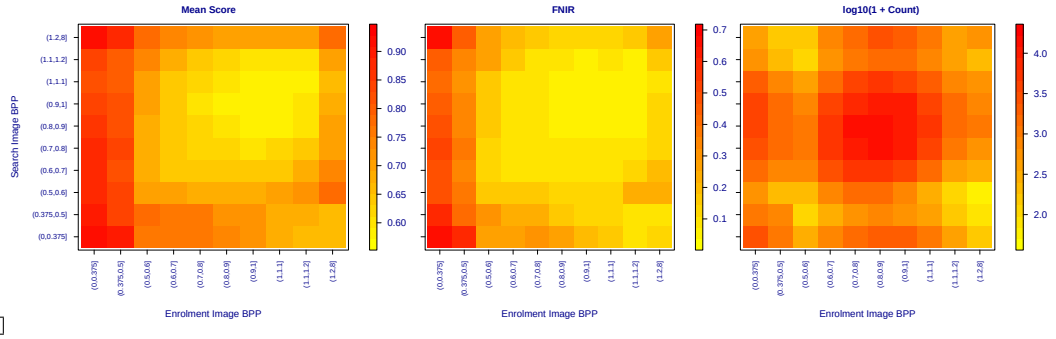

(a) Paired CRs, mate searches

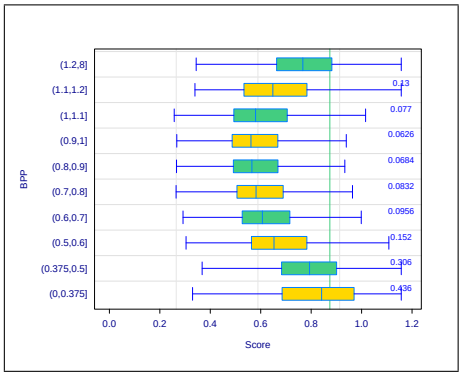

(b) Minimum CR, mate searches

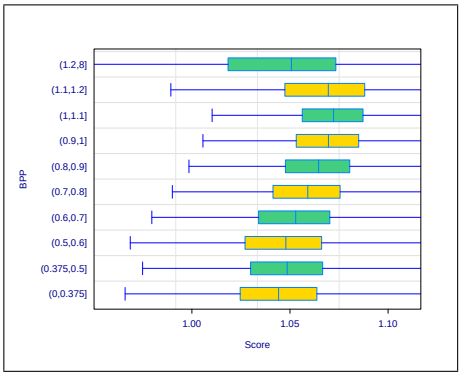

(c) Minimum CR, top nonmate

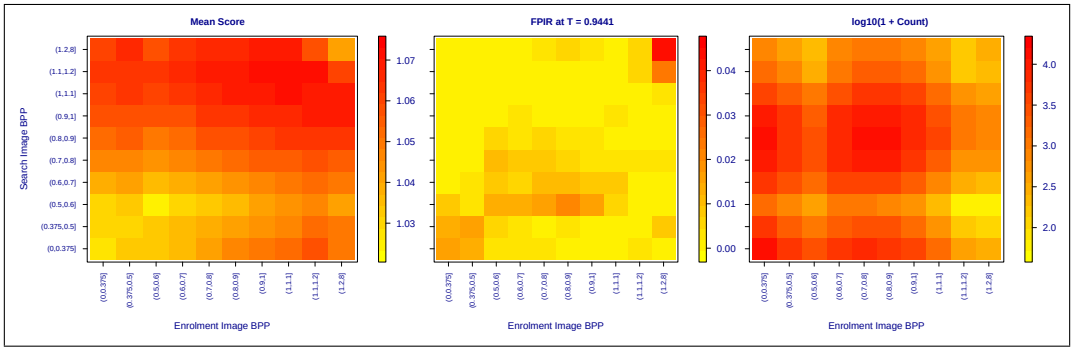

(d) Paired CRs, top nonmate

Figure 196: Effect of compression on accuracy for implementation Q12B executing searches in an enrolled population of N = 1.6 million. The axes are labelled by binned values of the number of bits per pixel (BPP) implied by the JPEG filesize and the image dimensions. The lowest BPP bin is populated largely by the overly compressed 330x330 images. For mate searches, the three heatmaps give, respectively, the score, FNIR at FPIR = 0.0001, and the log of the count of images in each bin (3 corresponds to 1000). For nonmate searches, the threshold is set to give FPIR = 0.001 globally. The boxplots show the effect on the score, with the FNIR value annotated at right.

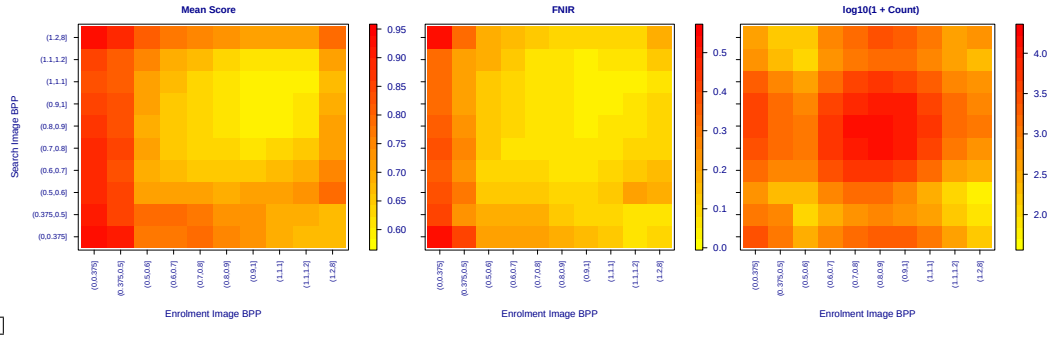

(a) Paired CRs, mate searches

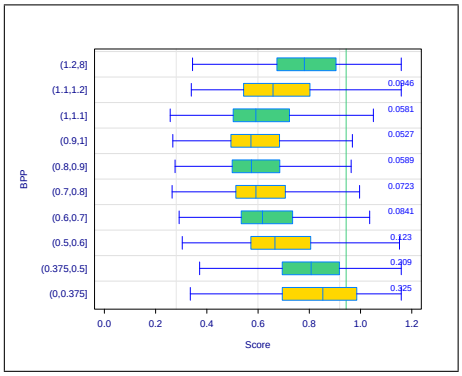

(b) Minimum CR, mate searches

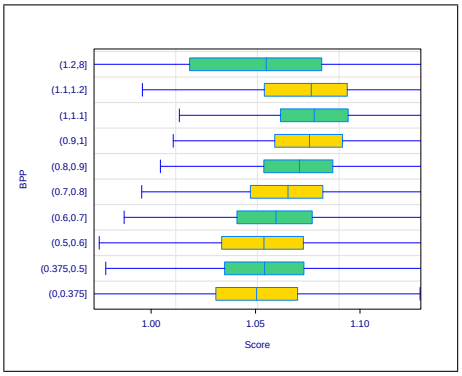

(c) Minimum CR, top nonmate

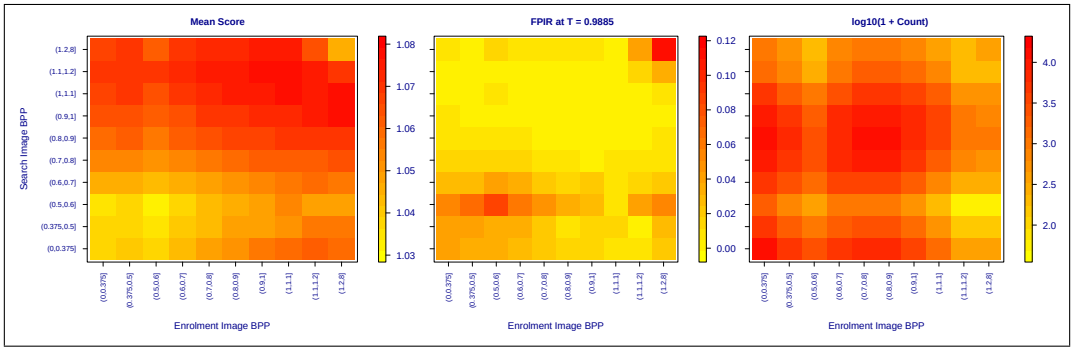

(d) Paired CRs, top nonmate

Figure 197: Effect of compression on accuracy for implementation Q13B executing searches in an enrolled population of N = 1.6 million. The axes are labelled by binned values of the number of bits per pixel (BPP) implied by the JPEG filesize and the image dimensions. The lowest BPP bin is populated largely by the overly compressed 330x330 images. For mate searches, the three heatmaps give, respectively, the score, FNIR at FPIR = 0.0001, and the log of the count of images in each bin (3 corresponds to 1000). For nonmate searches, the threshold is set to give FPIR = 0.001 globally. The boxplots show the effect on the score, with the FNIR value annotated at right.

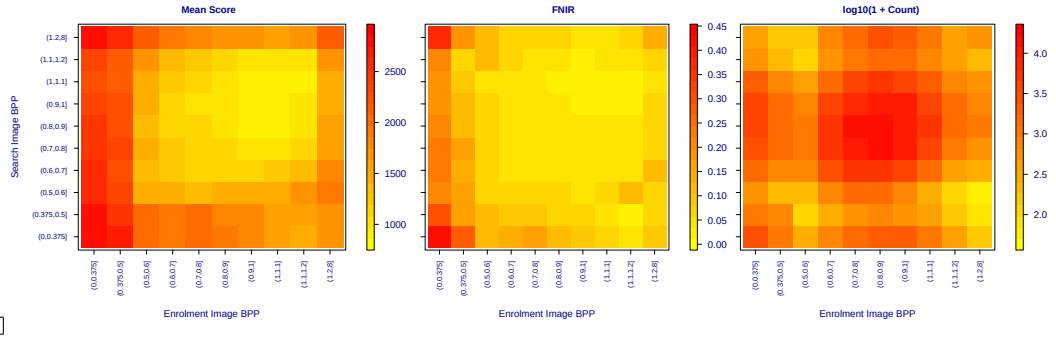

(a) Paired CRs, mate searches

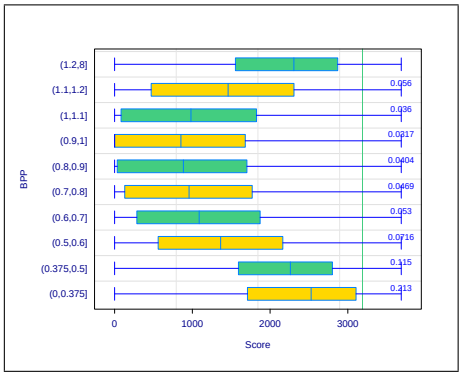

(b) Minimum CR, mate searches

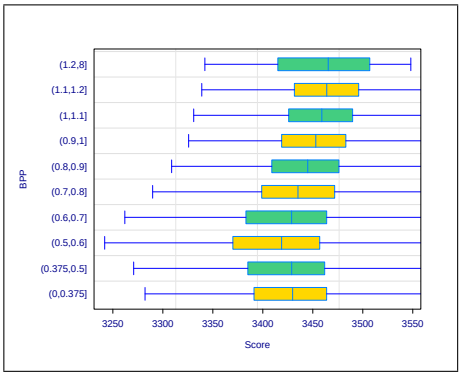

(c) Minimum CR, top nonmate

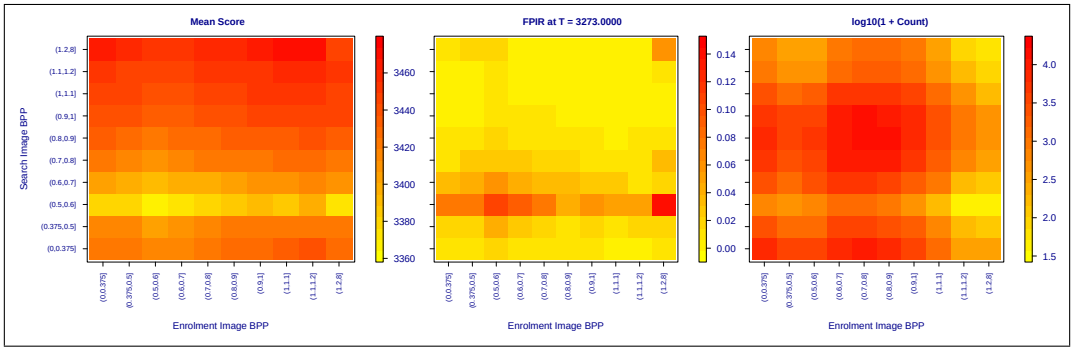

(d) Paired CRs, top nonmate

Figure 198: Effect of compression on accuracy for implementation R02A executing searches in an enrolled population of N = 1.6 million. The axes are labelled by binned values of the number of bits per pixel (BPP) implied by the JPEG filesize and the image dimensions. The lowest BPP bin is populated largely by the overly compressed 330x330 images. For mate searches, the three heatmaps give, respectively, the score, FNIR at FPIR = 0.0001, and the log of the count of images in each bin (3 corresponds to 1000). For nonmate searches, the threshold is set to give FPIR = 0.001 globally. The boxplots show the effect on the score, with the FNIR value annotated at right.

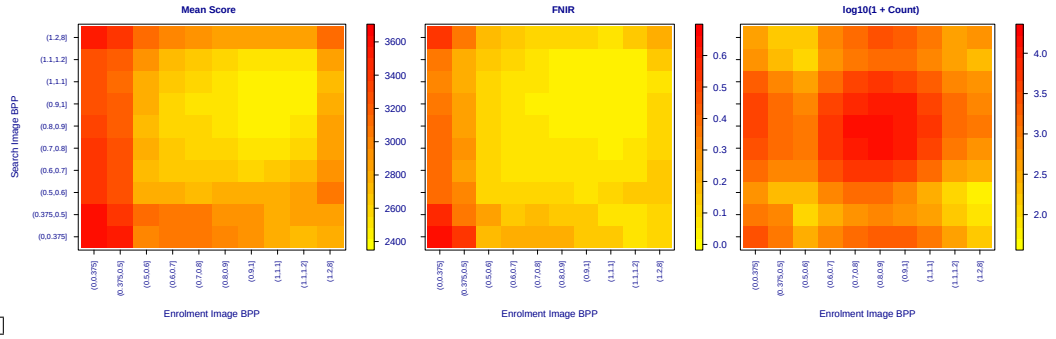

(a) Paired CRs, mate searches

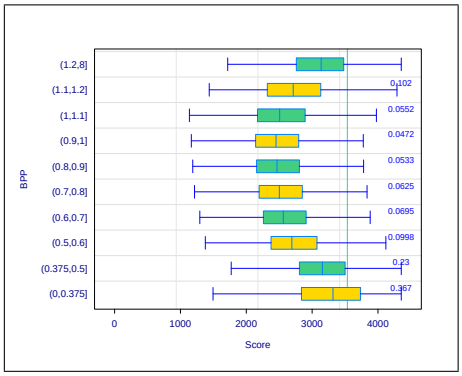

(b) Minimum CR, mate searches

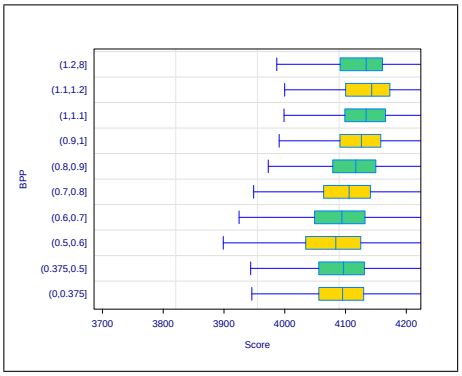

(c) Minimum CR, top nonmate

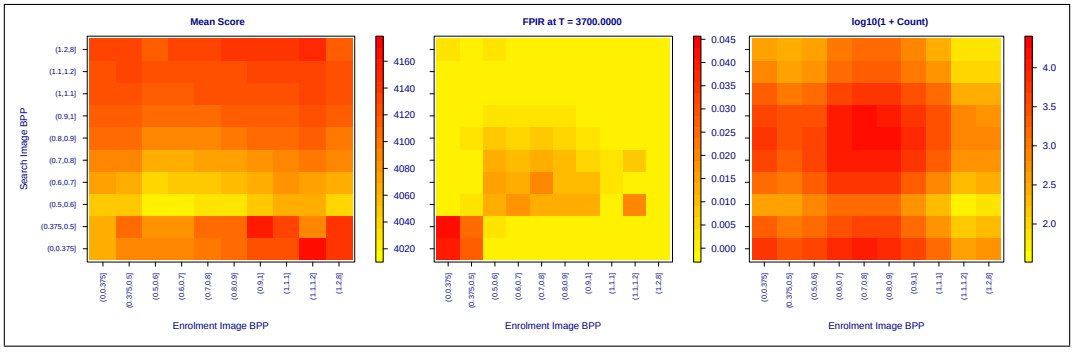

(d) Paired CRs, top nonmate

Figure 199: Effect of compression on accuracy for implementation R02B executing searches in an enrolled population of N = 1.6 million. The axes are labelled by binned values of the number of bits per pixel (BPP) implied by the JPEG filesize and the image dimensions. The lowest BPP bin is populated largely by the overly compressed 330x330 images. For mate searches, the three heatmaps give, respectively, the score, FNIR at FPIR = 0.0001, and the log of the count of images in each bin (3 corresponds to 1000). For nonmate searches, the threshold is set to give FPIR = 0.001 globally. The boxplots show the effect on the score, with the FNIR value annotated at right.

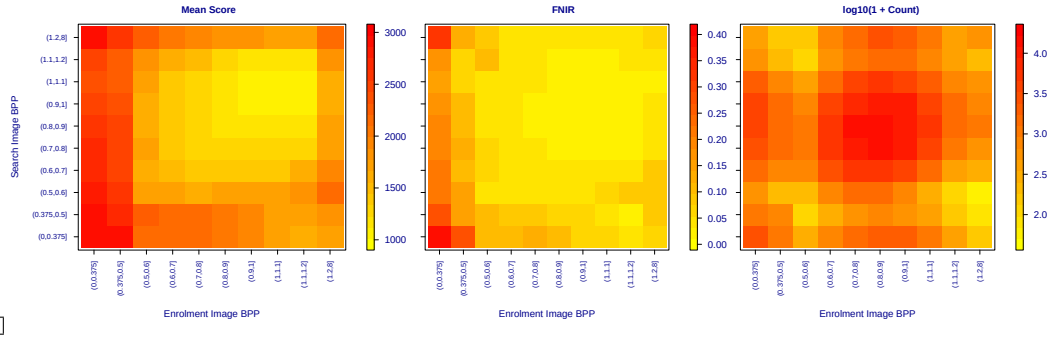

(a) Paired CRs, mate searches

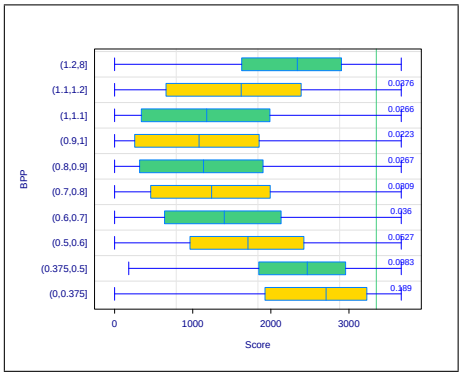

(b) Minimum CR, mate searches

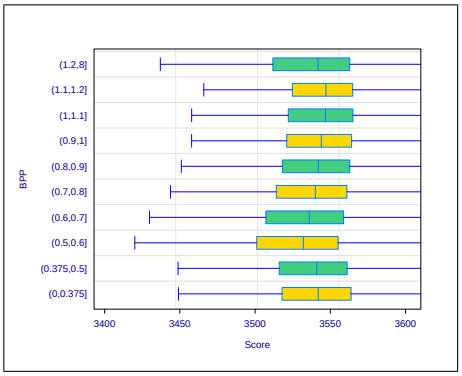

(c) Minimum CR, top nonmate

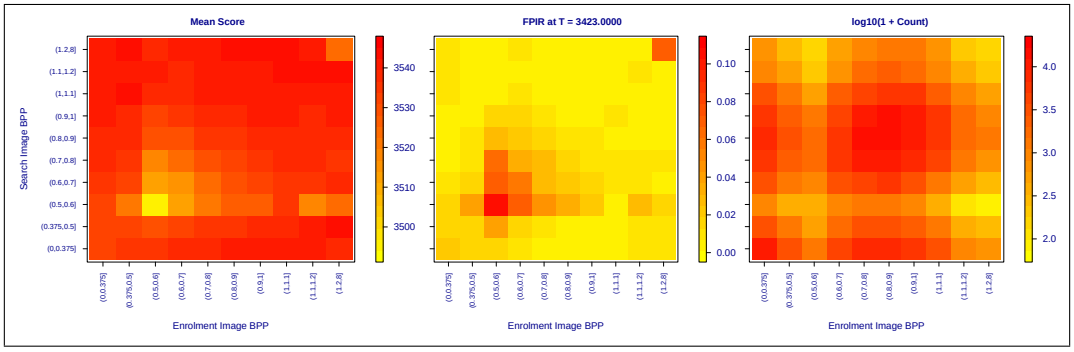

(d) Paired CRs, top nonmate

Figure 200: Effect of compression on accuracy for implementation R03A executing searches in an enrolled population of N = 1.6 million. The axes are labelled by binned values of the number of bits per pixel (BPP) implied by the JPEG filesize and the image dimensions. The lowest BPP bin is populated largely by the overly compressed 330x330 images. For mate searches, the three heatmaps give, respectively, the score, FNIR at FPIR = 0.0001, and the log of the count of images in each bin (3 corresponds to 1000). For nonmate searches, the threshold is set to give FPIR = 0.001 globally. The boxplots show the effect on the score, with the FNIR value annotated at right.

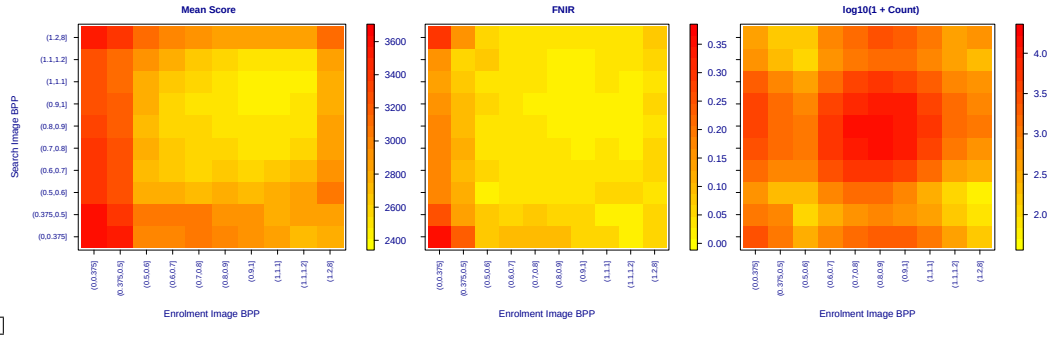

(a) Paired CRs, mate searches

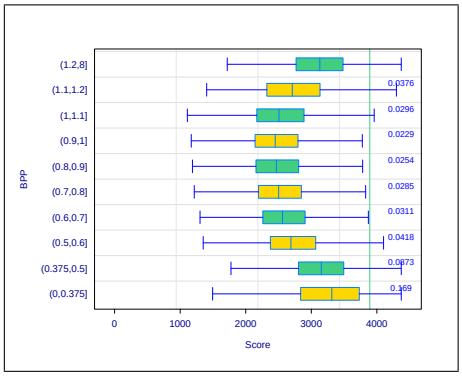

(b) Minimum CR, mate searches

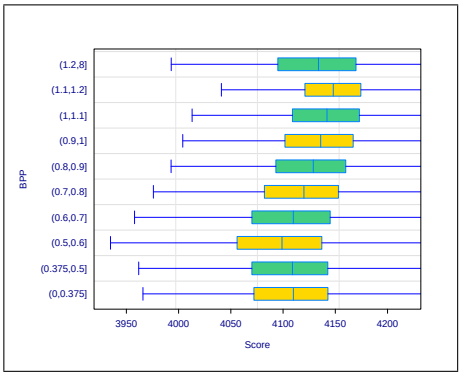

(c) Minimum CR, top nonmate

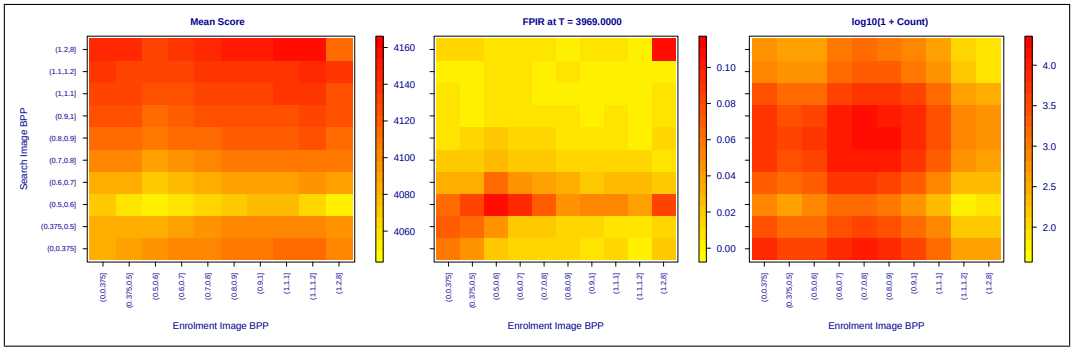

(d) Paired CRs, top nonmate

Figure 201: Effect of compression on accuracy for implementation R03B executing searches in an enrolled population of N = 1.6 million. The axes are labelled by binned values of the number of bits per pixel (BPP) implied by the JPEG filesize and the image dimensions. The lowest BPP bin is populated largely by the overly compressed 330x330 images. For mate searches, the three heatmaps give, respectively, the score, FNIR at FPIR = 0.0001, and the log of the count of images in each bin (3 corresponds to 1000). For nonmate searches, the threshold is set to give FPIR = 0.001 globally. The boxplots show the effect on the score, with the FNIR value annotated at right.

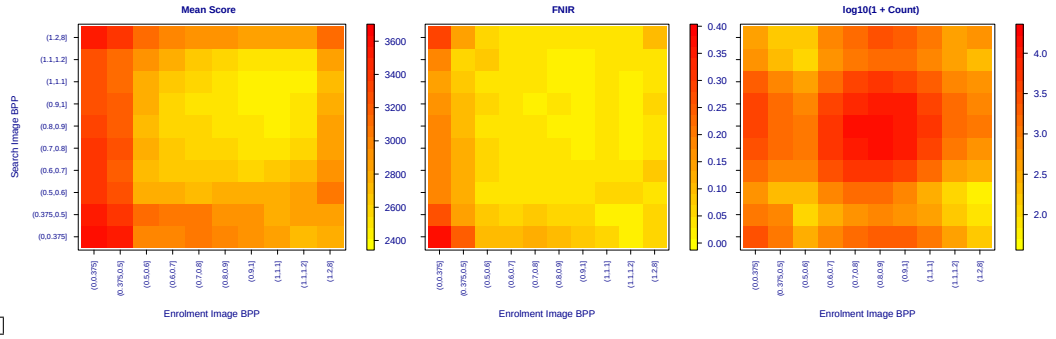

(a) Paired CRs, mate searches

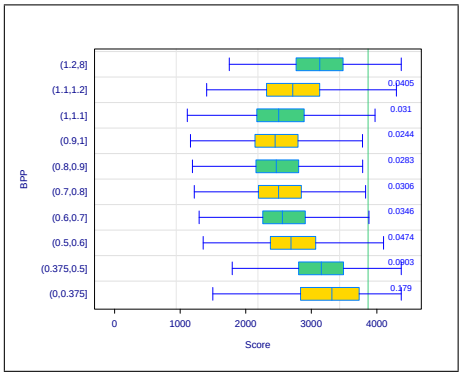

(b) Minimum CR, mate searches

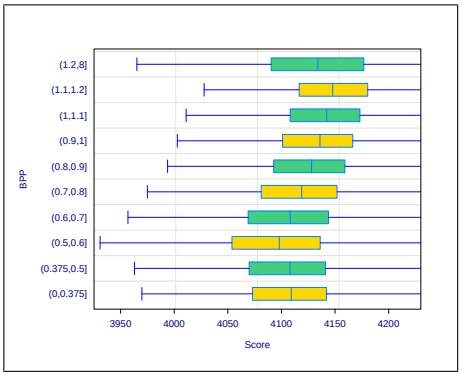

(c) Minimum CR, top nonmate

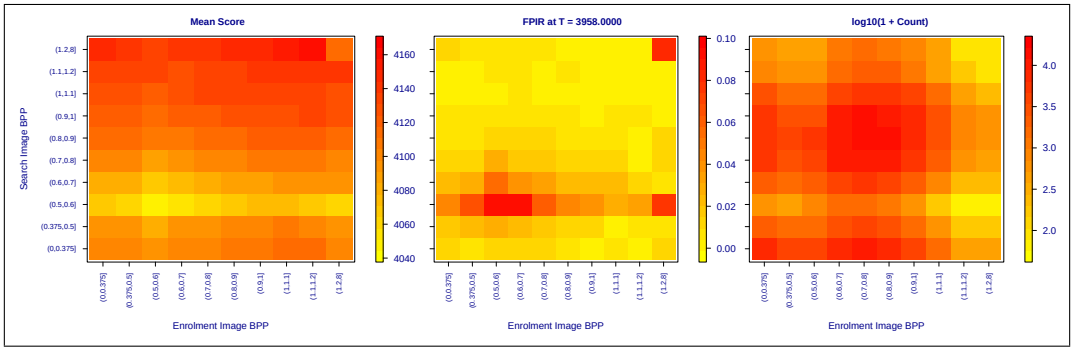

(d) Paired CRs, top nonmate

Figure 202: Effect of compression on accuracy for implementation R04B executing searches in an enrolled population of N = 1.6 million. The axes are labelled by binned values of the number of bits per pixel (BPP) implied by the JPEG filesize and the image dimensions. The lowest BPP bin is populated largely by the overly compressed 330x330 images. For mate searches, the three heatmaps give, respectively, the score, FNIR at FPIR = 0.0001, and the log of the count of images in each bin (3 corresponds to 1000). For nonmate searches, the threshold is set to give FPIR = 0.001 globally. The boxplots show the effect on the score, with the FNIR value annotated at right.

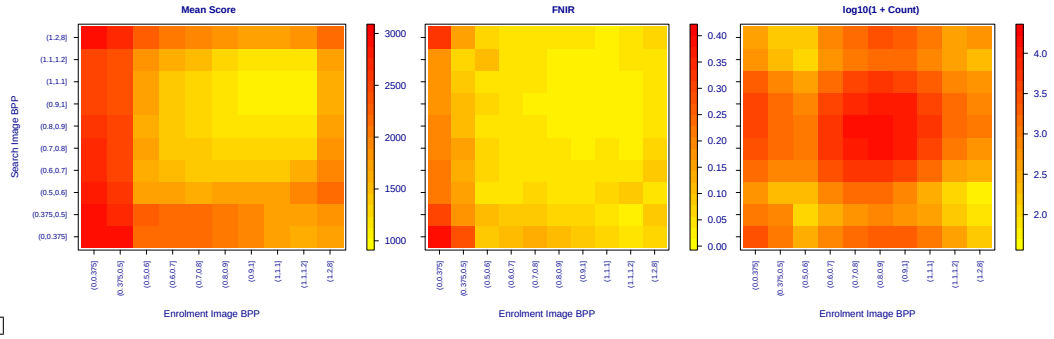

(a) Paired CRs, mate searches

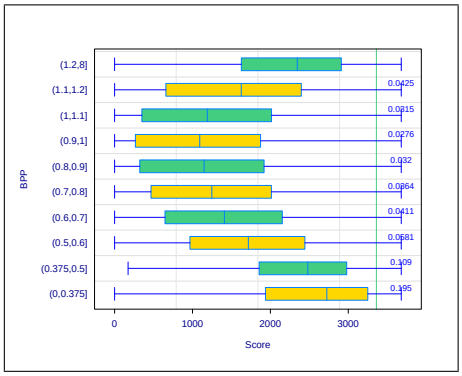

(b) Minimum CR, mate searches

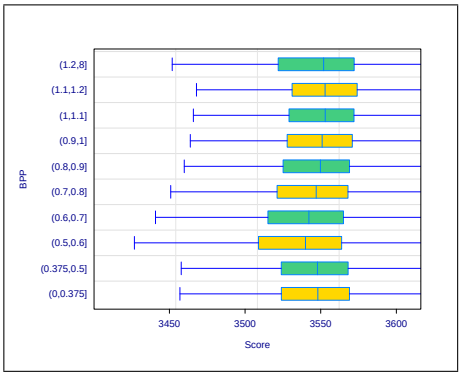

(c) Minimum CR, top nonmate

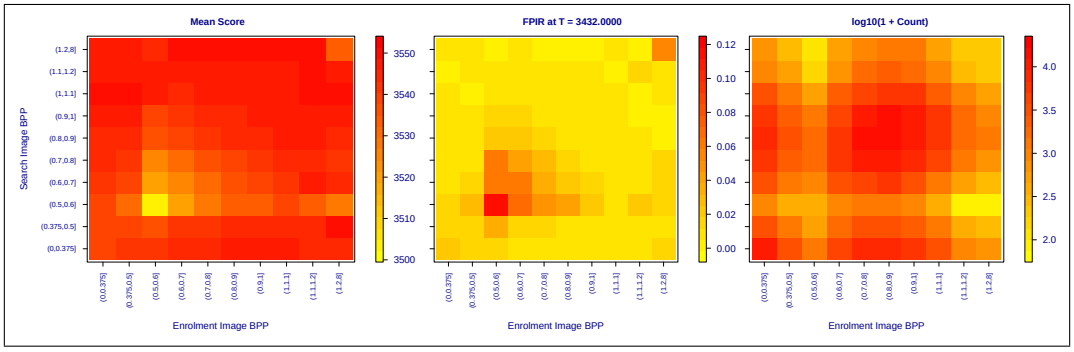

(d) Paired CRs, top nonmate

Figure 203: Effect of compression on accuracy for implementation R11A executing searches in an enrolled population of N = 1.6 million. The axes are labelled by binned values of the number of bits per pixel (BPP) implied by the JPEG filesize and the image dimensions. The lowest BPP bin is populated largely by the overly compressed 330x330 images. For mate searches, the three heatmaps give, respectively, the score, FNIR at FPIR = 0.0001, and the log of the count of images in each bin (3 corresponds to 1000). For nonmate searches, the threshold is set to give FPIR = 0.001 globally. The boxplots show the effect on the score, with the FNIR value annotated at right.

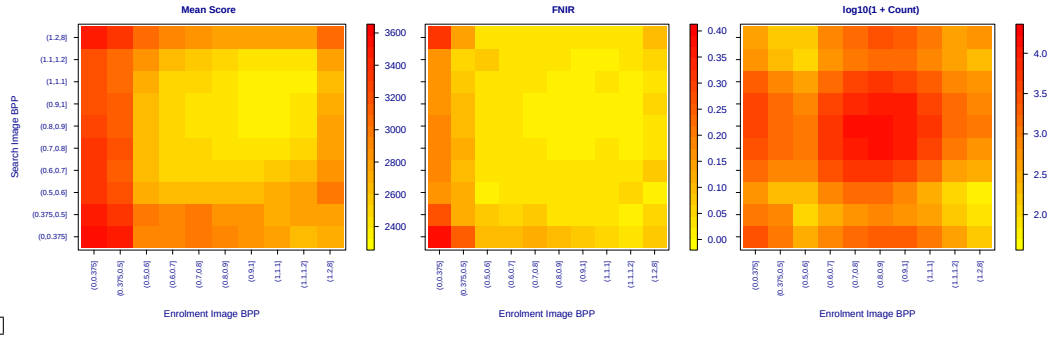

(a) Paired CRs, mate searches

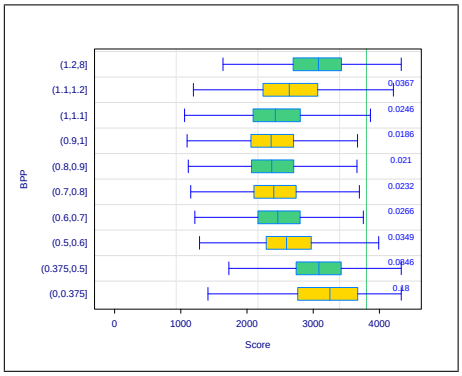

(b) Minimum CR, mate searches

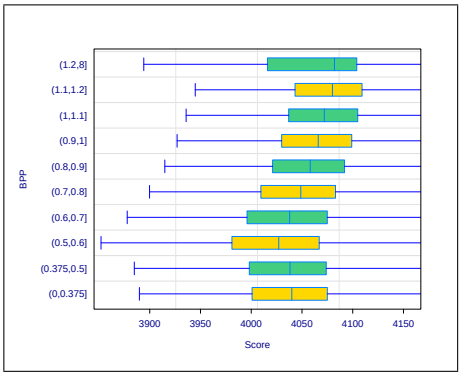

(c) Minimum CR, top nonmate

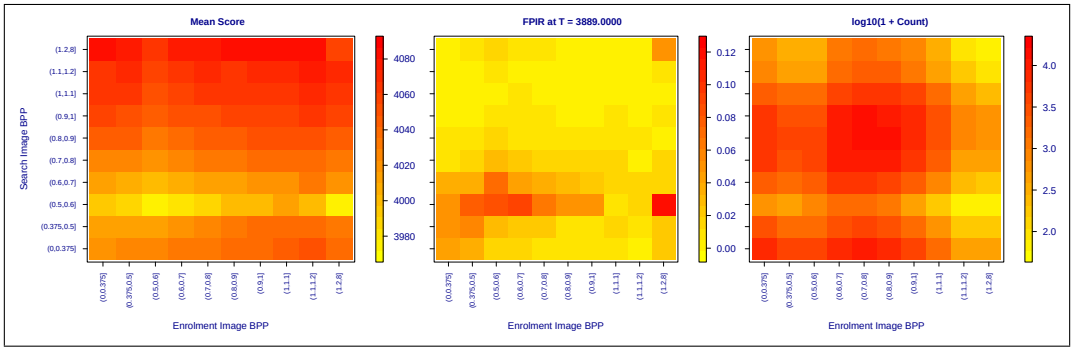

(d) Paired CRs, top nonmate

Figure 204: Effect of compression on accuracy for implementation R11B executing searches in an enrolled population of N = 1.6 million. The axes are labelled by binned values of the number of bits per pixel (BPP) implied by the JPEG filesize and the image dimensions. The lowest BPP bin is populated largely by the overly compressed 330x330 images. For mate searches, the three heatmaps give, respectively, the score, FNIR at FPIR = 0.0001, and the log of the count of images in each bin (3 corresponds to 1000). For nonmate searches, the threshold is set to give FPIR = 0.001 globally. The boxplots show the effect on the score, with the FNIR value annotated at right.

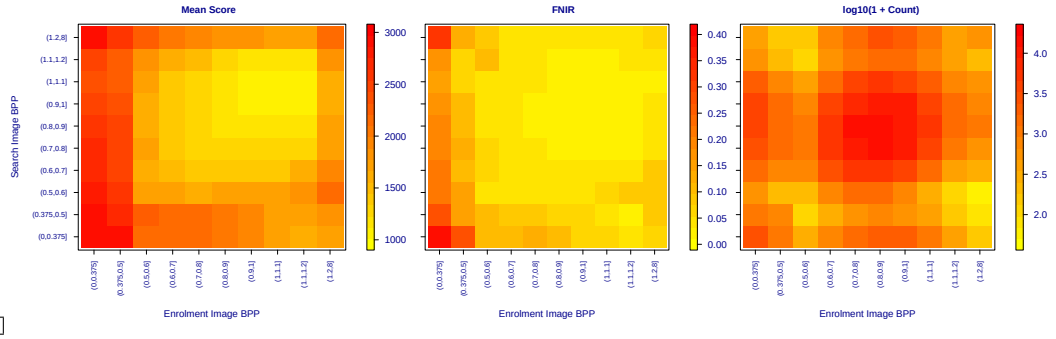

(a) Paired CRs, mate searches

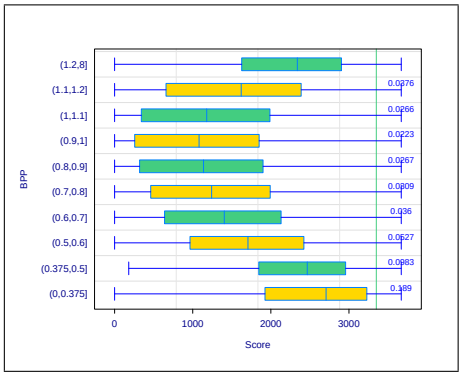

(b) Minimum CR, mate searches

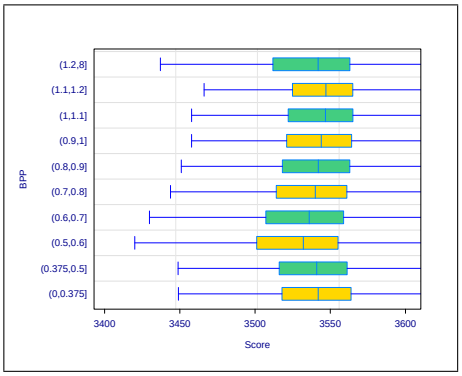

(c) Minimum CR, top nonmate

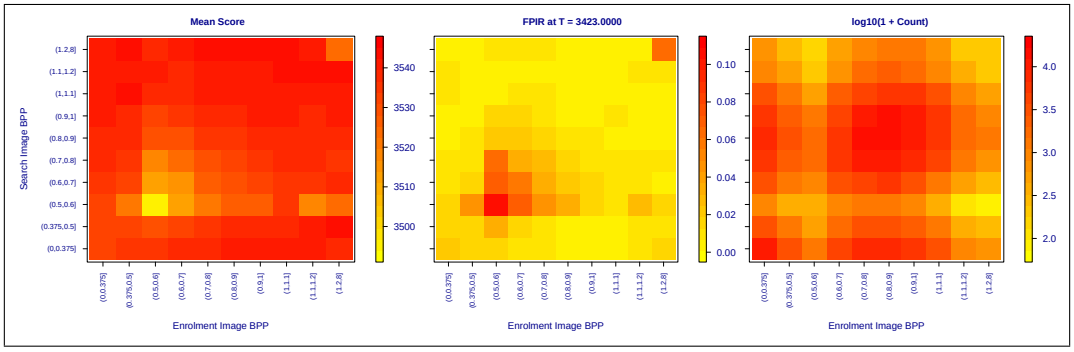

(d) Paired CRs, top nonmate

Figure 205: Effect of compression on accuracy for implementation R12A executing searches in an enrolled population of N = 1.6 million. The axes are labelled by binned values of the number of bits per pixel (BPP) implied by the JPEG filesize and the image dimensions. The lowest BPP bin is populated largely by the overly compressed 330x330 images. For mate searches, the three heatmaps give, respectively, the score, FNIR at FPIR = 0.0001, and the log of the count of images in each bin (3 corresponds to 1000). For nonmate searches, the threshold is set to give FPIR = 0.001 globally. The boxplots show the effect on the score, with the FNIR value annotated at right.

Figure 206: Effect of compression on accuracy for implementation S01B executing searches in an enrolled population of N = 1.6 million. The axes are labelled by binned values of the number of bits per pixel (BPP) implied by the JPEG filesize and the image dimensions. The lowest BPP bin is populated largely by the overly compressed 330x330 images. For mate searches, the three heatmaps give, respectively, the score, FNIR at FPIR = 0.0001, and the log of the count of images in each bin (3 corresponds to 1000). For nonmate searches, the threshold is set to give FPIR = 0.001 globally. The boxplots show the effect on the score, with the FNIR value annotated at right.

Figure 207: Effect of compression on accuracy for implementation S02B executing searches in an enrolled population of N = 1.6 million. The axes are labelled by binned values of the number of bits per pixel (BPP) implied by the JPEG filesize and the image dimensions. The lowest BPP bin is populated largely by the overly compressed 330x330 images. For mate searches, the three heatmaps give, respectively, the score, FNIR at FPIR = 0.0001, and the log of the count of images in each bin (3 corresponds to 1000). For nonmate searches, the threshold is set to give FPIR = 0.001 globally. The boxplots show the effect on the score, with the FNIR value annotated at right.

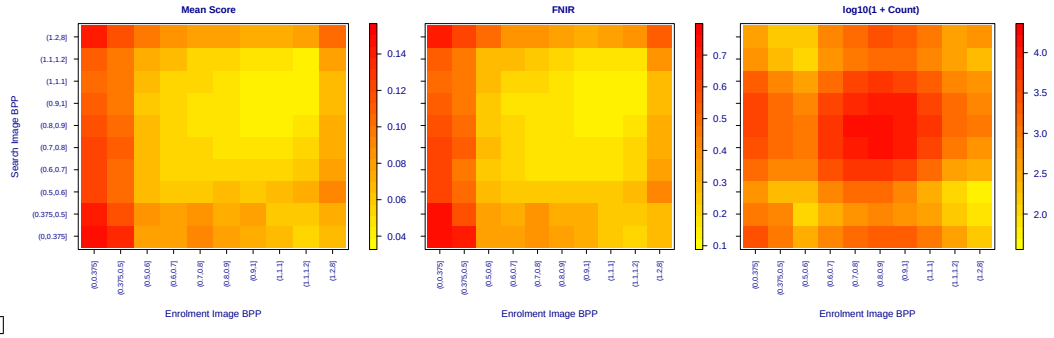

(a) Paired CRs, mate searches

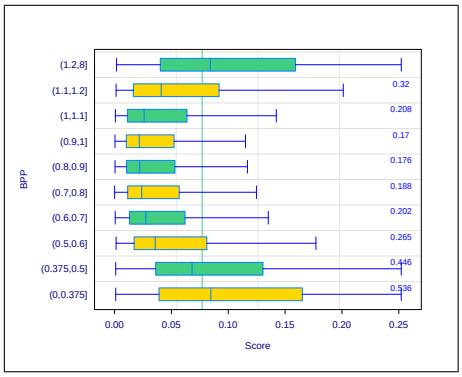

(b) Minimum CR, mate searches

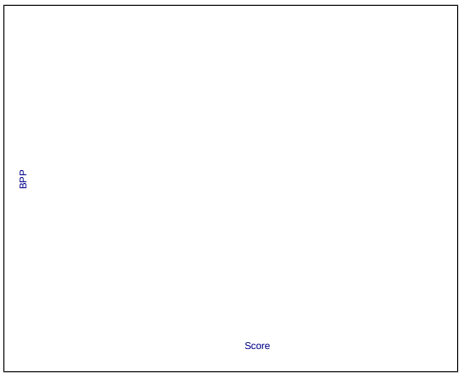

(c) Minimum CR, top nonmate

Figure 208: Effect of compression on accuracy for implementation S03A executing searches in an enrolled population of N = 1.6 million. The axes are labelled by binned values of the number of bits per pixel (BPP) implied by the JPEG filesize and the image dimensions. The lowest BPP bin is populated largely by the overly compressed 330x330 images. For mate searches, the three heatmaps give, respectively, the score, FNIR at FPIR = 0.0001, and the log of the count of images in each bin (3 corresponds to 1000). For nonmate searches, the threshold is set to give FPIR = 0.001 globally. The boxplots show the effect on the score, with the FNIR value annotated at right.

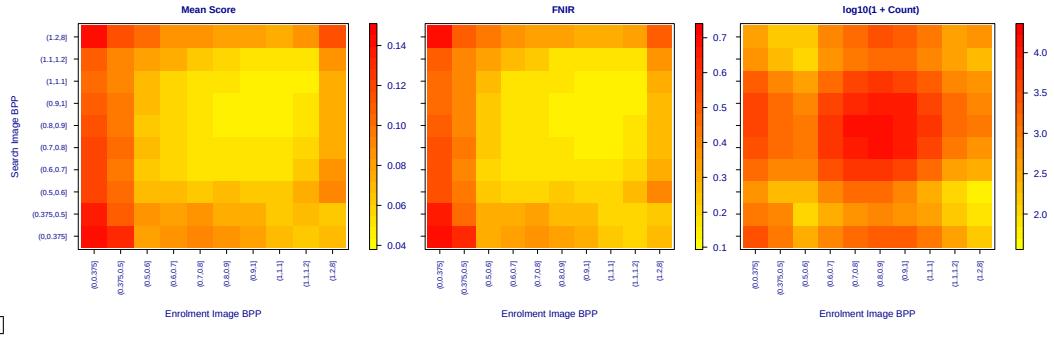

(a) Paired CRs, mate searches

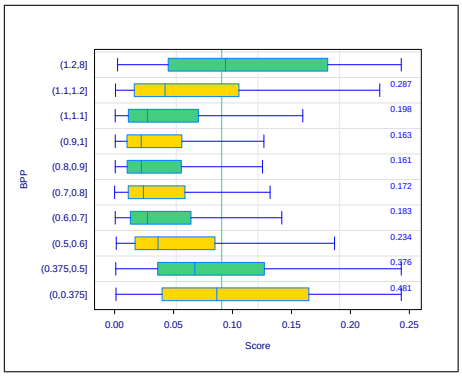

(b) Minimum CR, mate searches

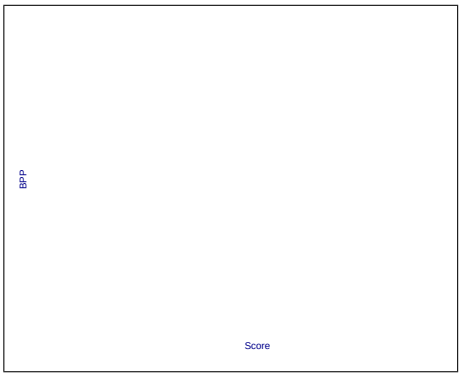

(c) Minimum CR, top nonmate

Figure 209: Effect of compression on accuracy for implementation S04A executing searches in an enrolled population of N = 1.6 million. The axes are labelled by binned values of the number of bits per pixel (BPP) implied by the JPEG filesize and the image dimensions. The lowest BPP bin is populated largely by the overly compressed 330x330 images. For mate searches, the three heatmaps give, respectively, the score, FNIR at FPIR = 0.0001, and the log of the count of images in each bin (3 corresponds to 1000). For nonmate searches, the threshold is set to give FPIR = 0.001 globally. The boxplots show the effect on the score, with the FNIR value annotated at right.

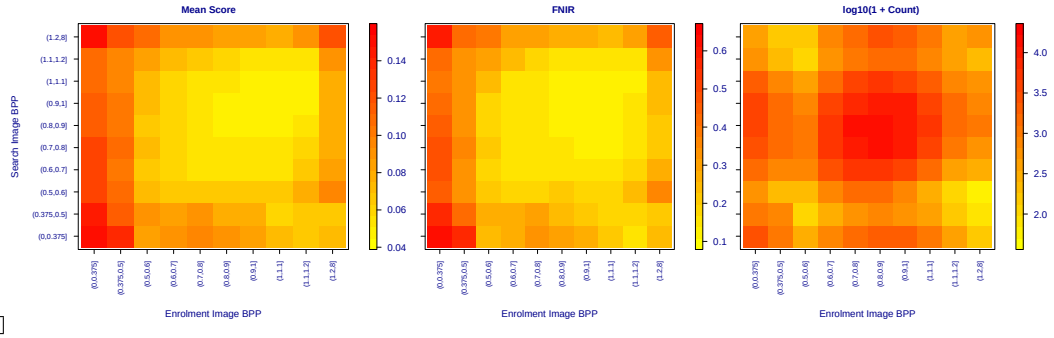

(a) Paired CRs, mate searches

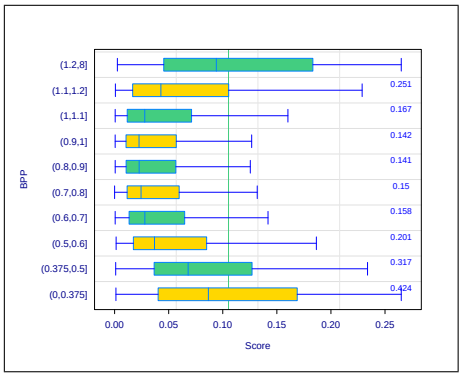

(b) Minimum CR, mate searches

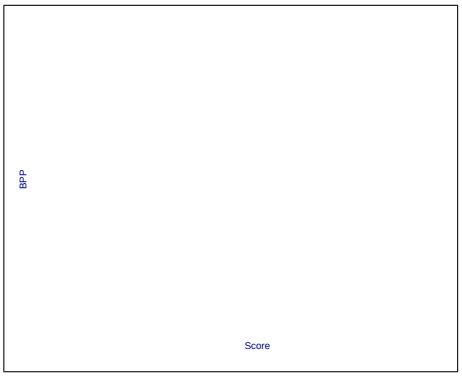

(c) Minimum CR, top nonmate

Figure 210: Effect of compression on accuracy for implementation S05A executing searches in an enrolled population of N = 1.6 million. The axes are labelled by binned values of the number of bits per pixel (BPP) implied by the JPEG filesize and the image dimensions. The lowest BPP bin is populated largely by the overly compressed 330x330 images. For mate searches, the three heatmaps give, respectively, the score, FNIR at FPIR = 0.0001, and the log of the count of images in each bin (3 corresponds to 1000). For nonmate searches, the threshold is set to give FPIR = 0.001 globally. The boxplots show the effect on the score, with the FNIR value annotated at right.

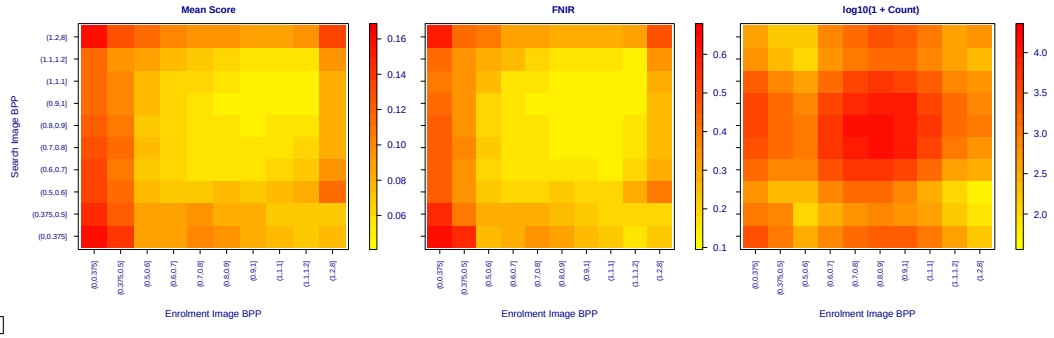

(a) Paired CRs, mate searches

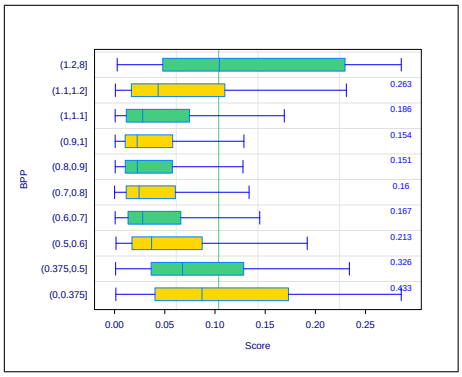

(b) Minimum CR, mate searches

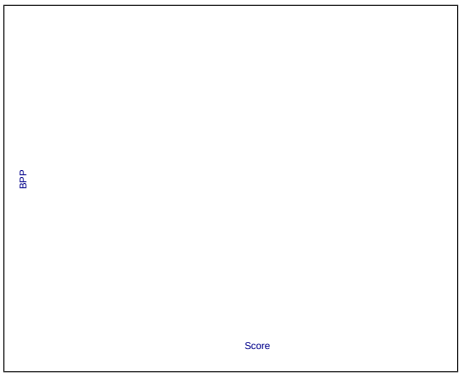

(c) Minimum CR, top nonmate

Figure 211: Effect of compression on accuracy for implementation S11A executing searches in an enrolled population of N = 1.6 million. The axes are labelled by binned values of the number of bits per pixel (BPP) implied by the JPEG filesize and the image dimensions. The lowest BPP bin is populated largely by the overly compressed 330x330 images. For mate searches, the three heatmaps give, respectively, the score, FNIR at FPIR = 0.0001, and the log of the count of images in each bin (3 corresponds to 1000). For nonmate searches, the threshold is set to give FPIR = 0.001 globally. The boxplots show the effect on the score, with the FNIR value annotated at right.

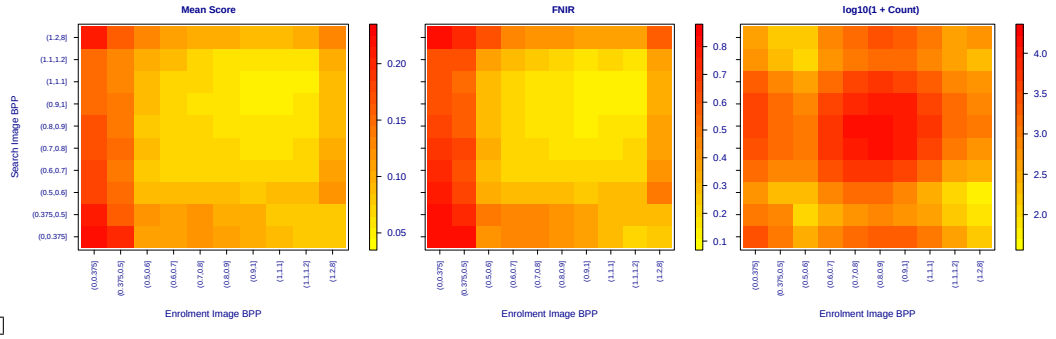

(a) Paired CRs, mate searches

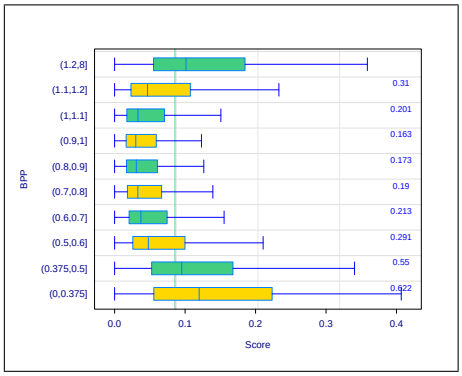

(b) Minimum CR, mate searches

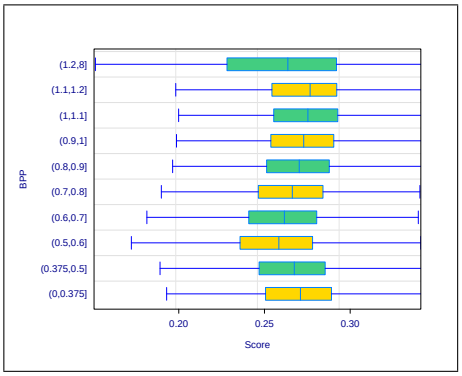

(c) Minimum CR, top nonmate

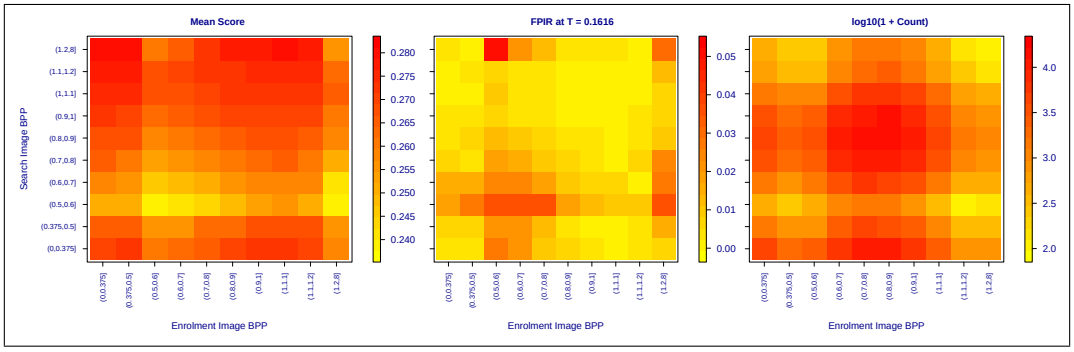

(d) Paired CRs, top nonmate

Figure 212: Effect of compression on accuracy for implementation S11B executing searches in an enrolled population of N = 1.6 million. The axes are labelled by binned values of the number of bits per pixel (BPP) implied by the JPEG filesize and the image dimensions. The lowest BPP bin is populated largely by the overly compressed 330x330 images. For mate searches, the three heatmaps give, respectively, the score, FNIR at FPIR = 0.0001, and the log of the count of images in each bin (3 corresponds to 1000). For nonmate searches, the threshold is set to give FPIR = 0.001 globally. The boxplots show the effect on the score, with the FNIR value annotated at right.

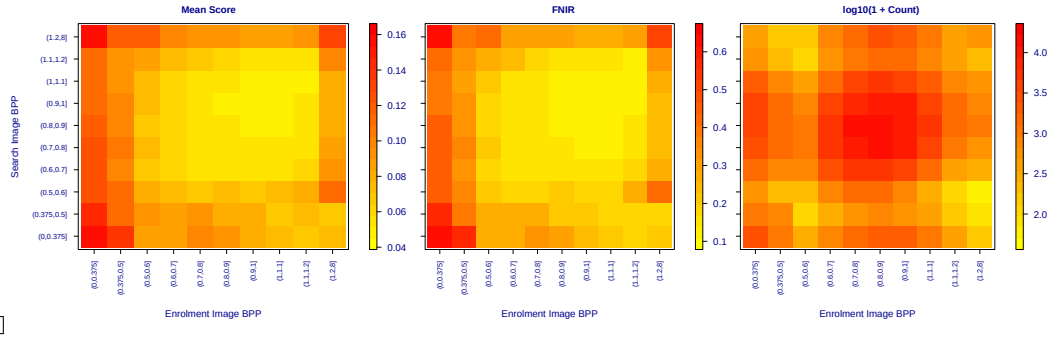

(a) Paired CRs, mate searches

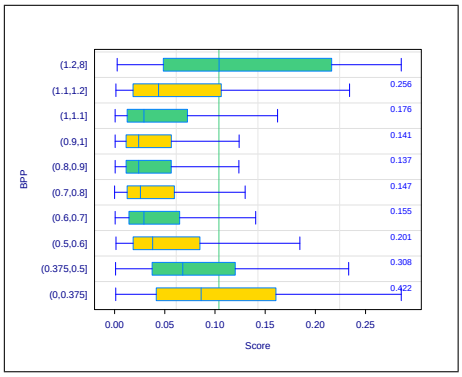

(b) Minimum CR, mate searches

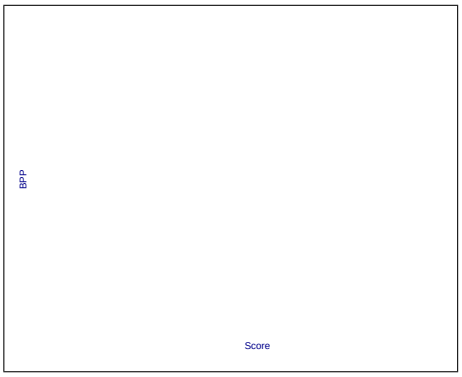

(c) Minimum CR, top nonmate

Figure 213: Effect of compression on accuracy for implementation S12A executing searches in an enrolled population of N = 1.6 million. The axes are labelled by binned values of the number of bits per pixel (BPP) implied by the JPEG filesize and the image dimensions. The lowest BPP bin is populated largely by the overly compressed 330x330 images. For mate searches, the three heatmaps give, respectively, the score, FNIR at FPIR = 0.0001, and the log of the count of images in each bin (3 corresponds to 1000). For nonmate searches, the threshold is set to give FPIR = 0.001 globally. The boxplots show the effect on the score, with the FNIR value annotated at right.

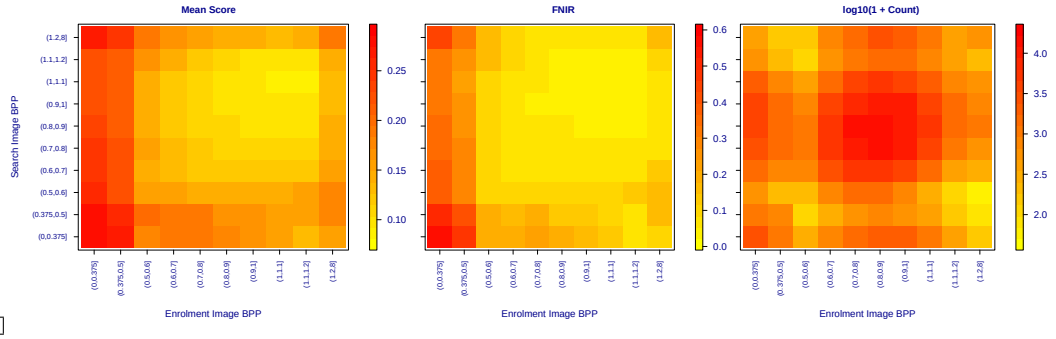

(a) Paired CRs, mate searches

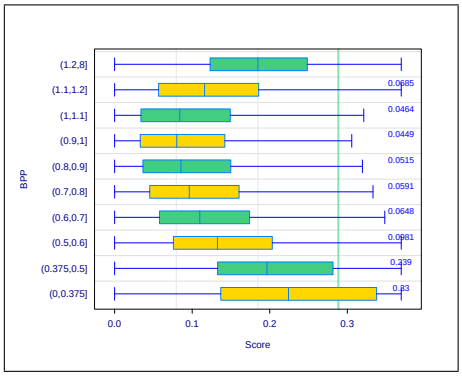

(b) Minimum CR, mate searches

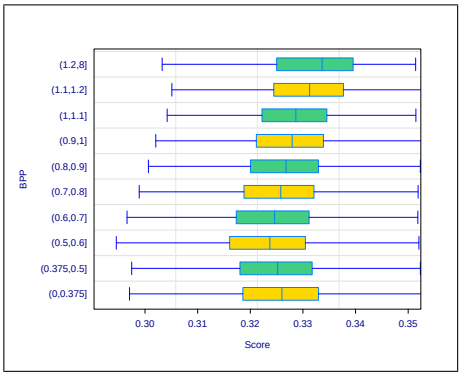

(c) Minimum CR, top nonmate

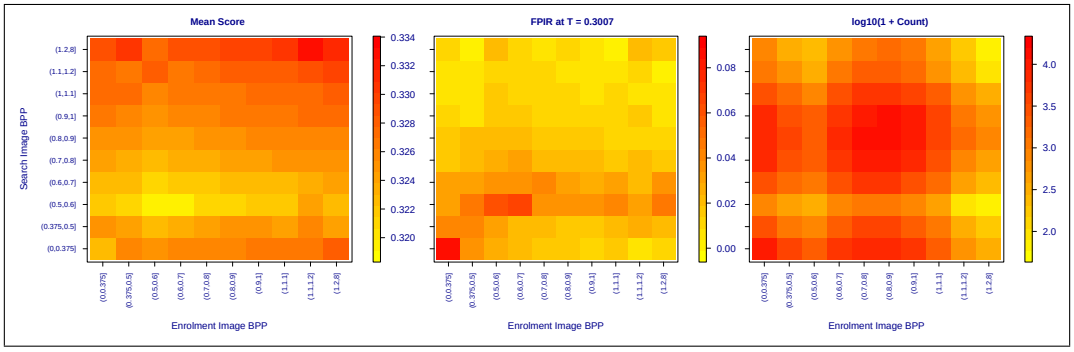

(d) Paired CRs, top nonmate

Figure 214: Effect of compression on accuracy for implementation T01A executing searches in an enrolled population of N = 1.6 million. The axes are labelled by binned values of the number of bits per pixel (BPP) implied by the JPEG filesize and the image dimensions. The lowest BPP bin is populated largely by the overly compressed 330x330 images. For mate searches, the three heatmaps give, respectively, the score, FNIR at FPIR = 0.0001, and the log of the count of images in each bin (3 corresponds to 1000). For nonmate searches, the threshold is set to give FPIR = 0.001 globally. The boxplots show the effect on the score, with the FNIR value annotated at right.

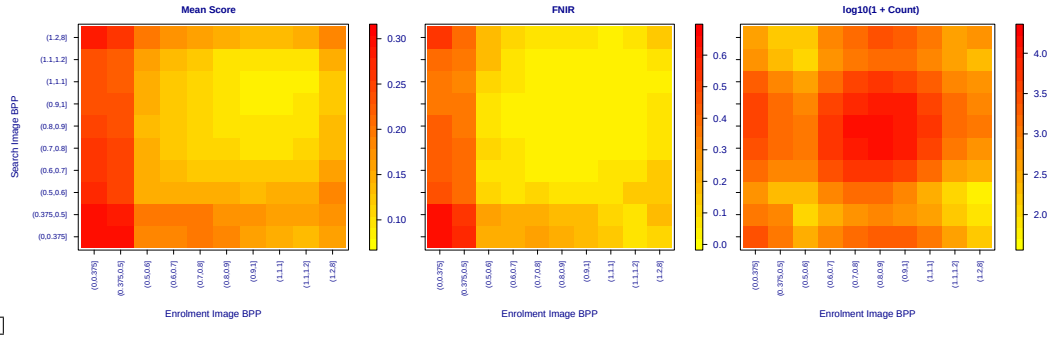

(a) Paired CRs, mate searches

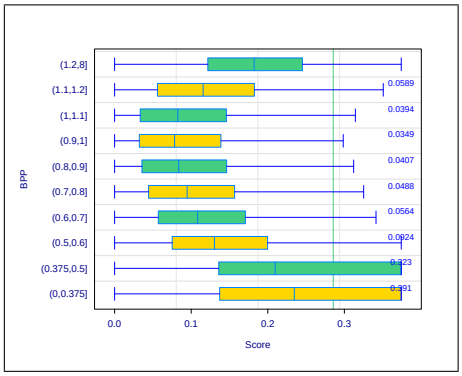

(b) Minimum CR, mate searches

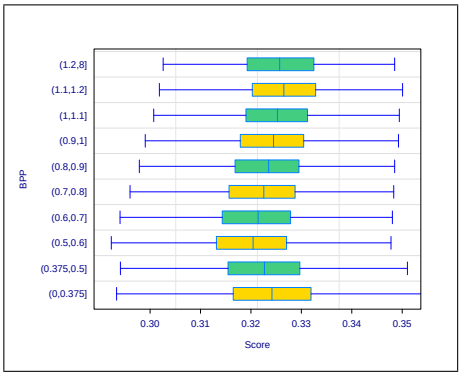

(c) Minimum CR, top nonmate

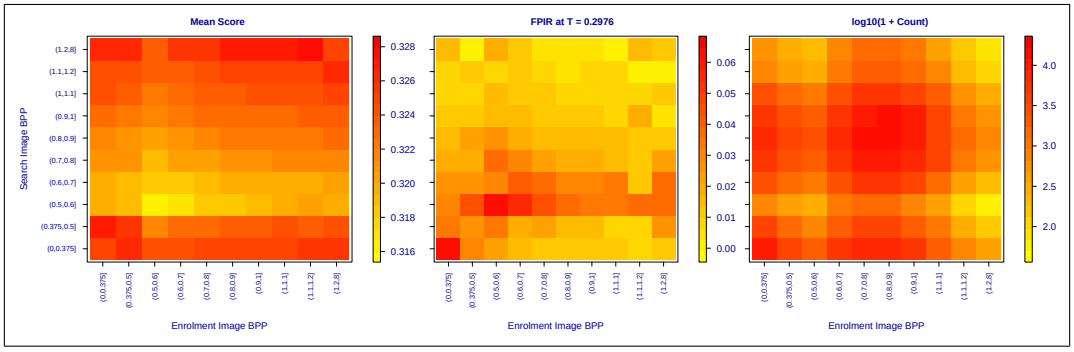

(d) Paired CRs, top nonmate

Figure 215: Effect of compression on accuracy for implementation T01B executing searches in an enrolled population of N = 1.6 million. The axes are labelled by binned values of the number of bits per pixel (BPP) implied by the JPEG filesize and the image dimensions. The lowest BPP bin is populated largely by the overly compressed 330x330 images. For mate searches, the three heatmaps give, respectively, the score, FNIR at FPIR = 0.0001, and the log of the count of images in each bin (3 corresponds to 1000). For nonmate searches, the threshold is set to give FPIR = 0.001 globally. The boxplots show the effect on the score, with the FNIR value annotated at right.

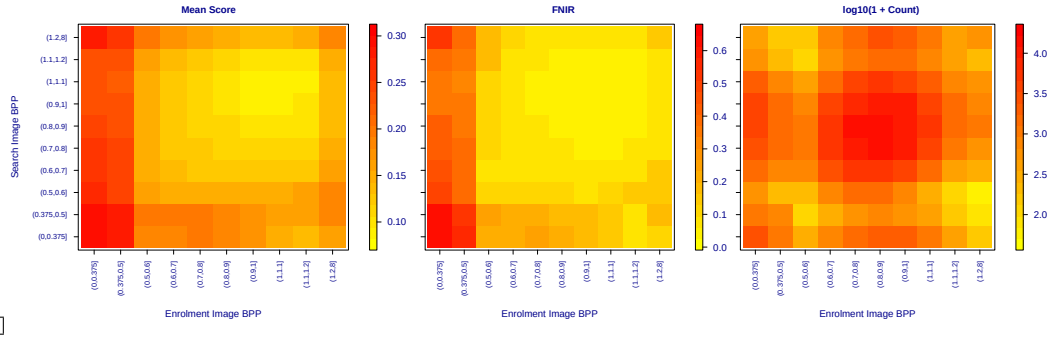

(a) Paired CRs, mate searches

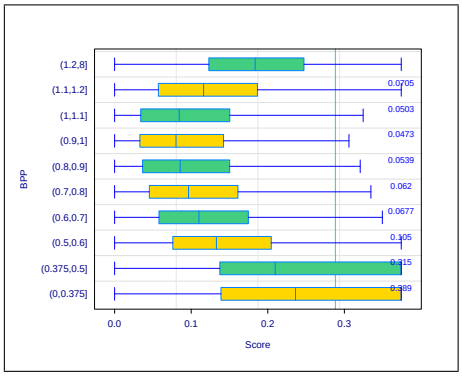

(b) Minimum CR, mate searches

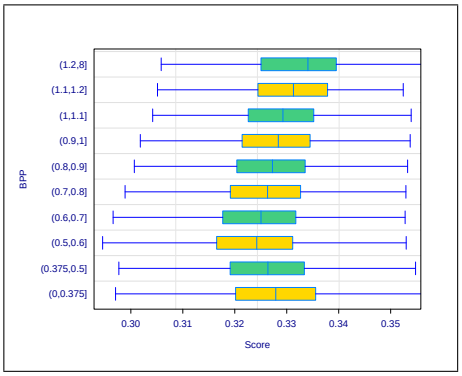

(c) Minimum CR, top nonmate

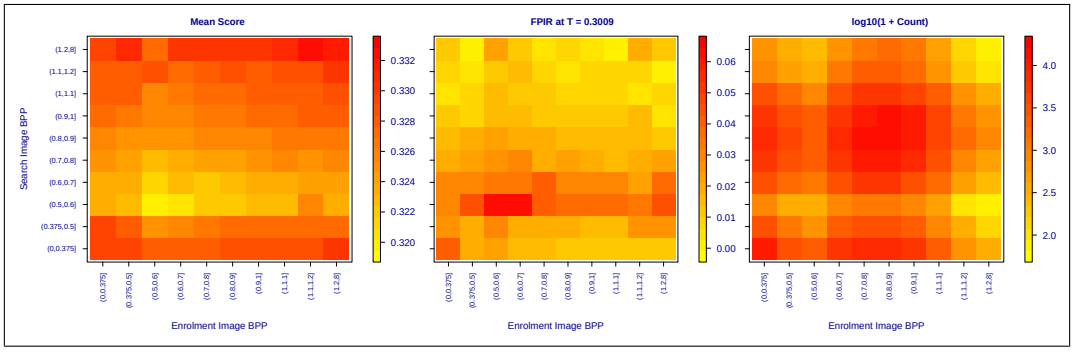

(d) Paired CRs, top nonmate

Figure 216: Effect of compression on accuracy for implementation T02A executing searches in an enrolled population of N = 1.6 million. The axes are labelled by binned values of the number of bits per pixel (BPP) implied by the JPEG filesize and the image dimensions. The lowest BPP bin is populated largely by the overly compressed 330x330 images. For mate searches, the three heatmaps give, respectively, the score, FNIR at FPIR = 0.0001, and the log of the count of images in each bin (3 corresponds to 1000). For nonmate searches, the threshold is set to give FPIR = 0.001 globally. The boxplots show the effect on the score, with the FNIR value annotated at right.

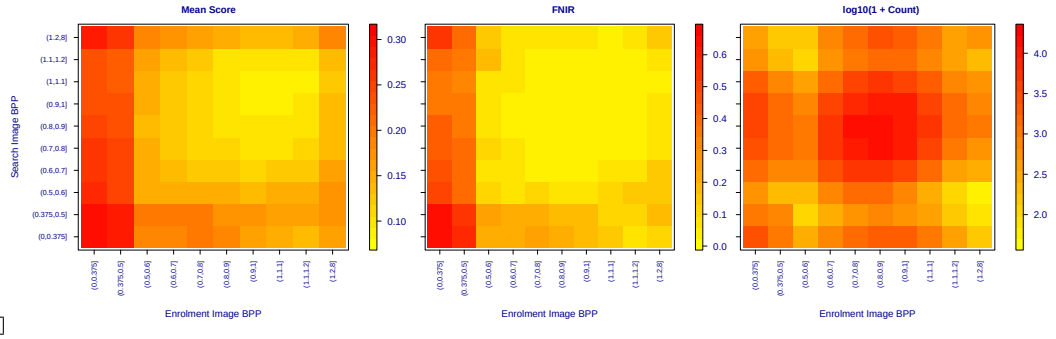

(a) Paired CRs, mate searches

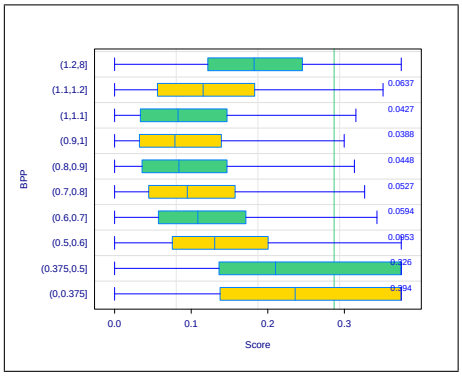

(b) Minimum CR, mate searches

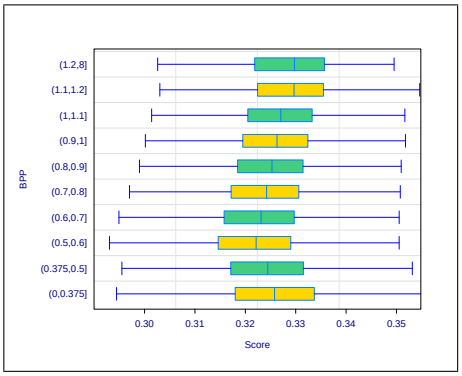

(c) Minimum CR, top nonmate

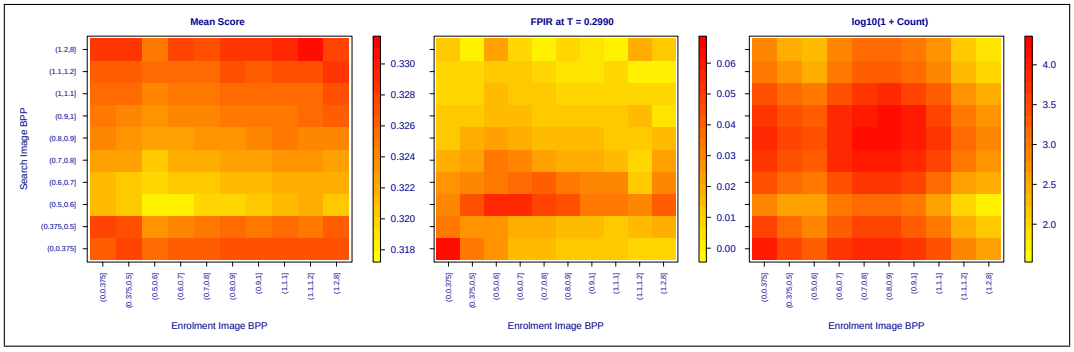

(d) Paired CRs, top nonmate

Figure 217: Effect of compression on accuracy for implementation T02B executing searches in an enrolled population of N = 1.6 million. The axes are labelled by binned values of the number of bits per pixel (BPP) implied by the JPEG filesize and the image dimensions. The lowest BPP bin is populated largely by the overly compressed 330x330 images. For mate searches, the three heatmaps give, respectively, the score, FNIR at FPIR = 0.0001, and the log of the count of images in each bin (3 corresponds to 1000). For nonmate searches, the threshold is set to give FPIR = 0.001 globally. The boxplots show the effect on the score, with the FNIR value annotated at right.

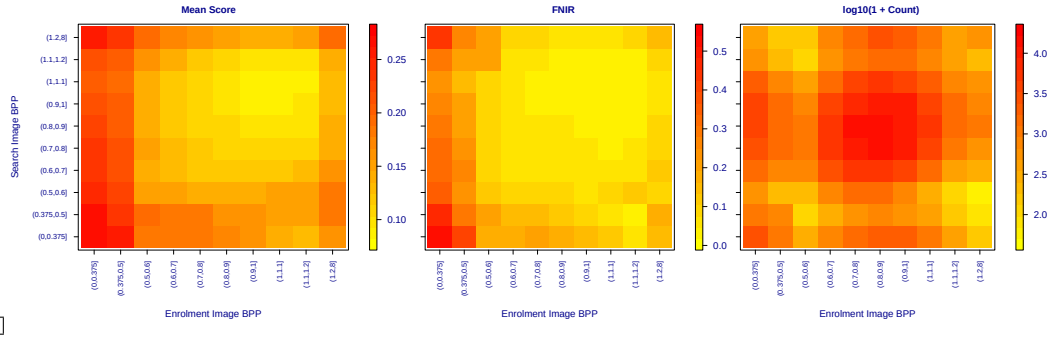

(a) Paired CRs, mate searches

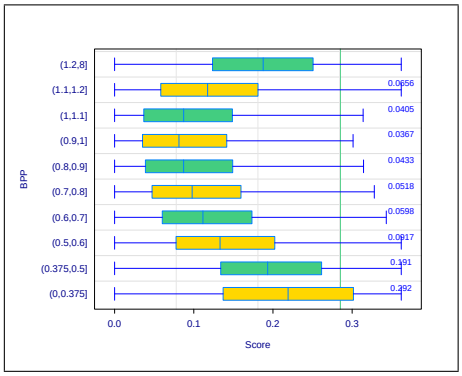

(b) Minimum CR, mate searches

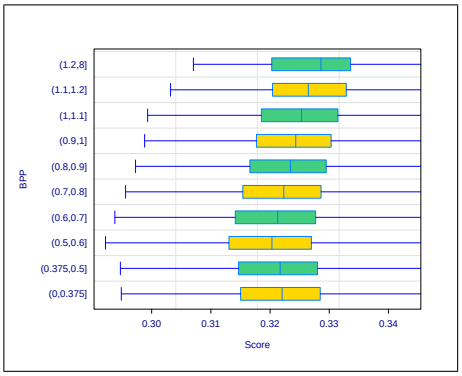

(c) Minimum CR, top nonmate

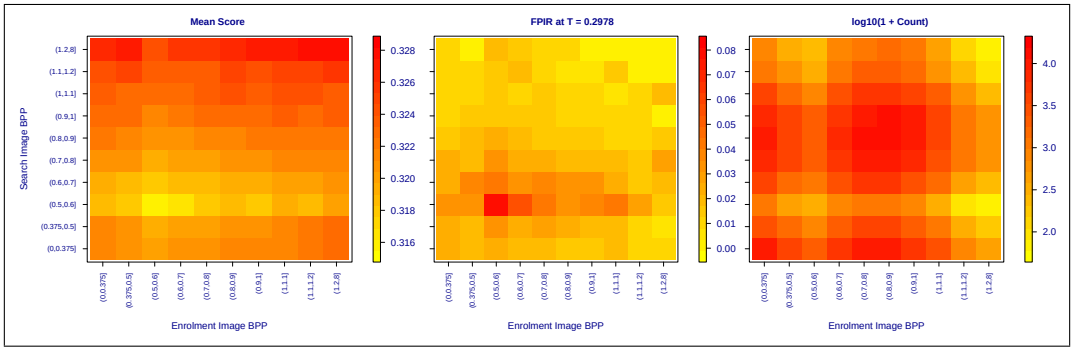

(d) Paired CRs, top nonmate

Figure 218: Effect of compression on accuracy for implementation T03A executing searches in an enrolled population of N = 1.6 million. The axes are labelled by binned values of the number of bits per pixel (BPP) implied by the JPEG filesize and the image dimensions. The lowest BPP bin is populated largely by the overly compressed 330x330 images. For mate searches, the three heatmaps give, respectively, the score, FNIR at FPIR = 0.0001, and the log of the count of images in each bin (3 corresponds to 1000). For nonmate searches, the threshold is set to give FPIR = 0.001 globally. The boxplots show the effect on the score, with the FNIR value annotated at right.

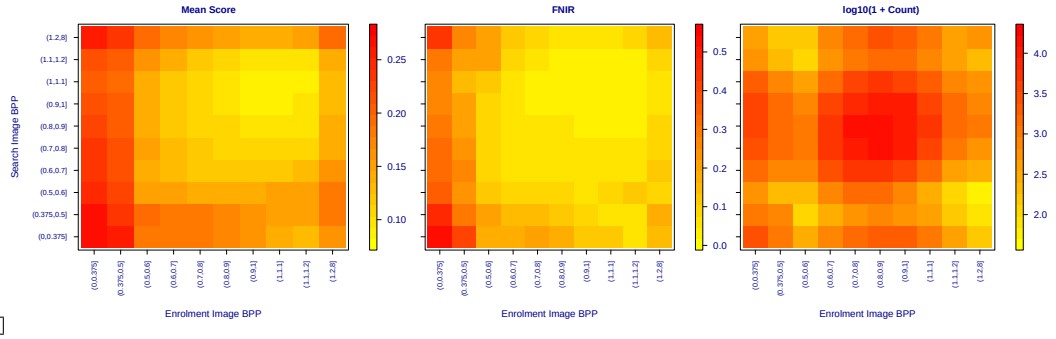

(a) Paired CRs, mate searches

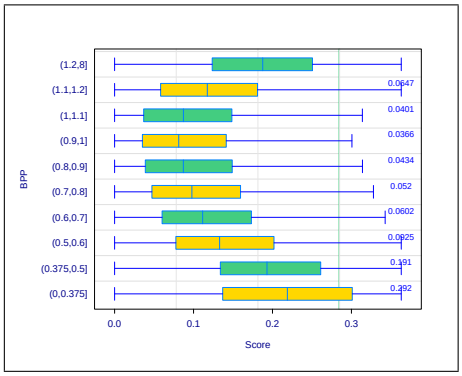

(b) Minimum CR, mate searches

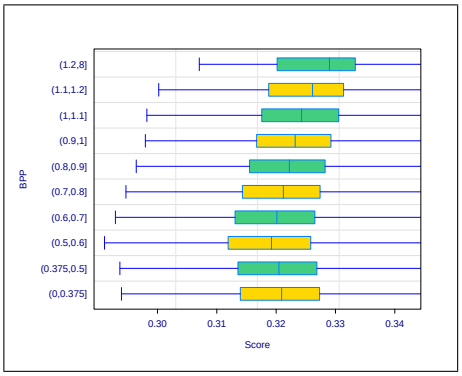

(c) Minimum CR, top nonmate

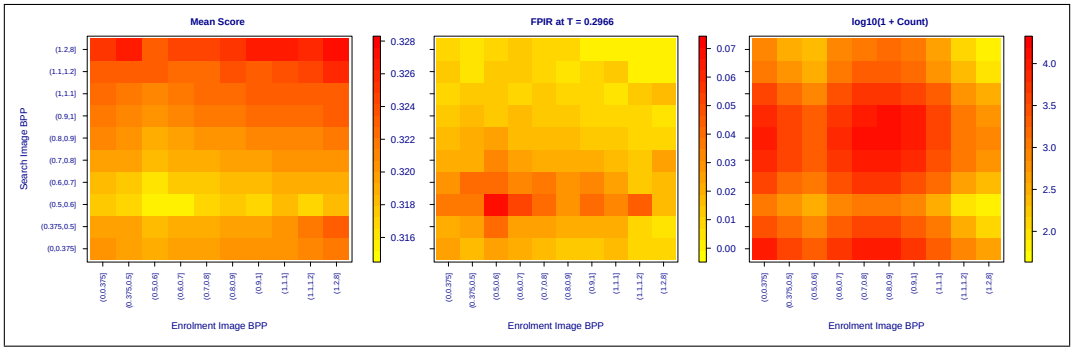

(d) Paired CRs, top nonmate

Figure 219: Effect of compression on accuracy for implementation T03B executing searches in an enrolled population of N = 1.6 million. The axes are labelled by binned values of the number of bits per pixel (BPP) implied by the JPEG filesize and the image dimensions. The lowest BPP bin is populated largely by the overly compressed 330x330 images. For mate searches, the three heatmaps give, respectively, the score, FNIR at FPIR = 0.0001, and the log of the count of images in each bin (3 corresponds to 1000). For nonmate searches, the threshold is set to give FPIR = 0.001 globally. The boxplots show the effect on the score, with the FNIR value annotated at right.

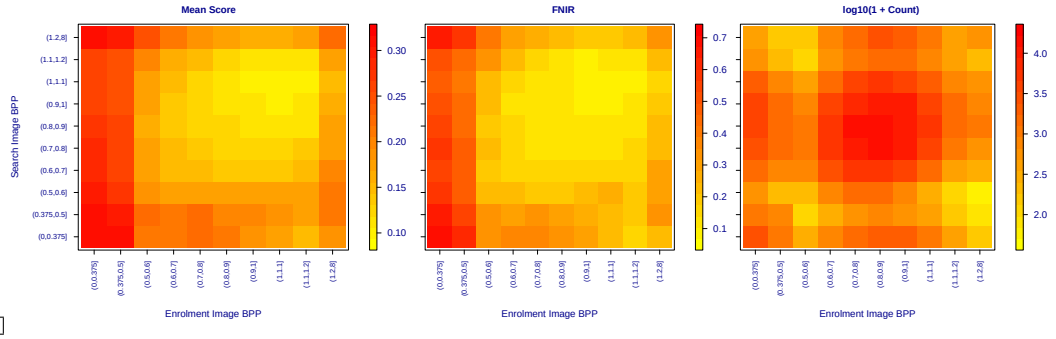

(a) Paired CRs, mate searches

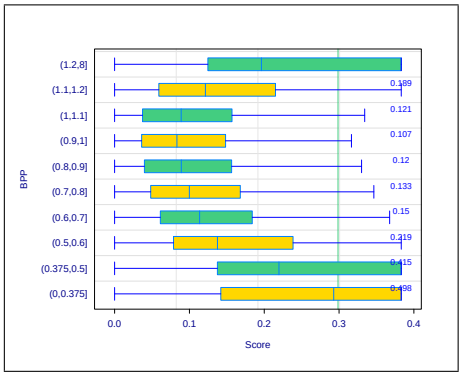

(b) Minimum CR, mate searches

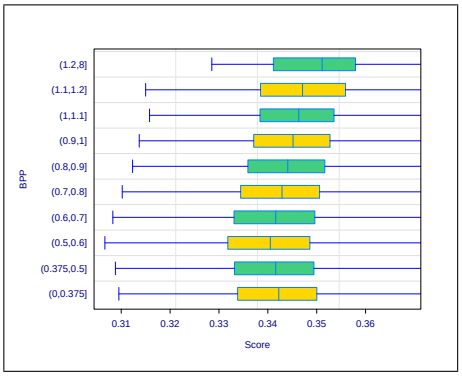

(c) Minimum CR, top nonmate

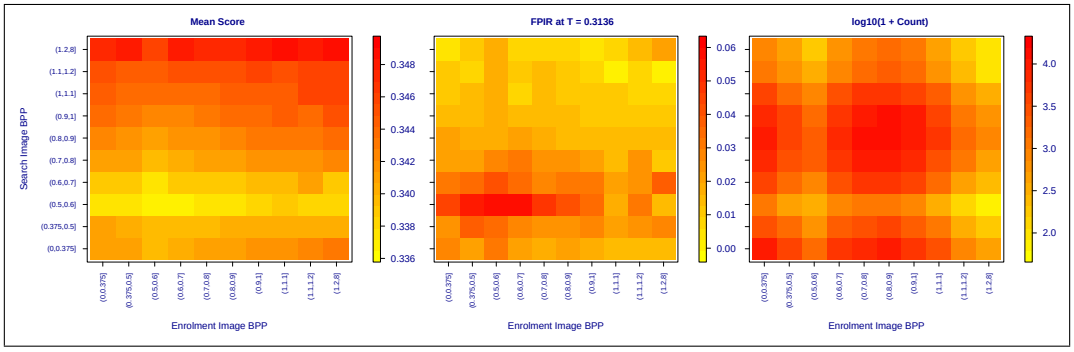

(d) Paired CRs, top nonmate

Figure 220: Effect of compression on accuracy for implementation T04A executing searches in an enrolled population of N = 1.6 million. The axes are labelled by binned values of the number of bits per pixel (BPP) implied by the JPEG filesize and the image dimensions. The lowest BPP bin is populated largely by the overly compressed 330x330 images. For mate searches, the three heatmaps give, respectively, the score, FNIR at FPIR = 0.0001, and the log of the count of images in each bin (3 corresponds to 1000). For nonmate searches, the threshold is set to give FPIR = 0.001 globally. The boxplots show the effect on the score, with the FNIR value annotated at right.

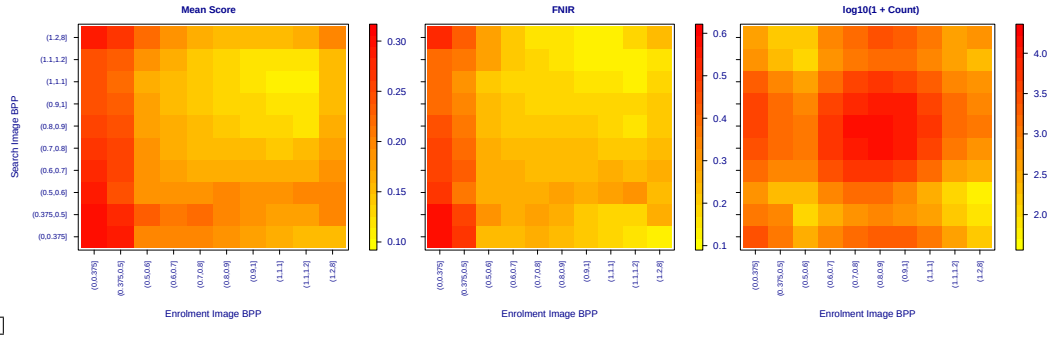

(a) Paired CRs, mate searches

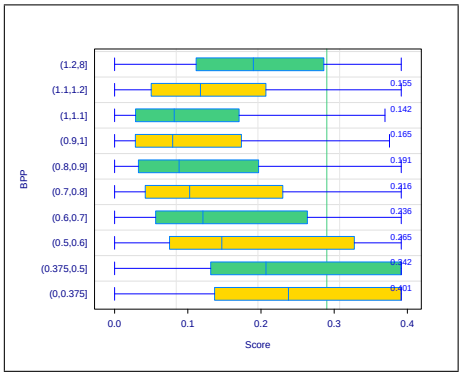

(b) Minimum CR, mate searches

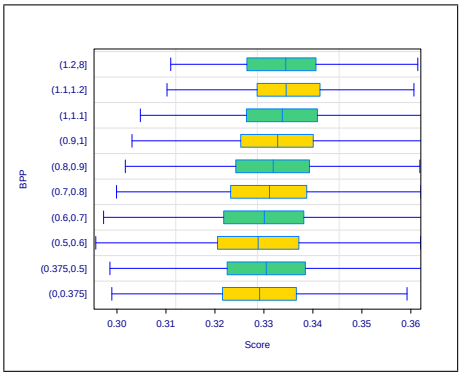

(c) Minimum CR, top nonmate

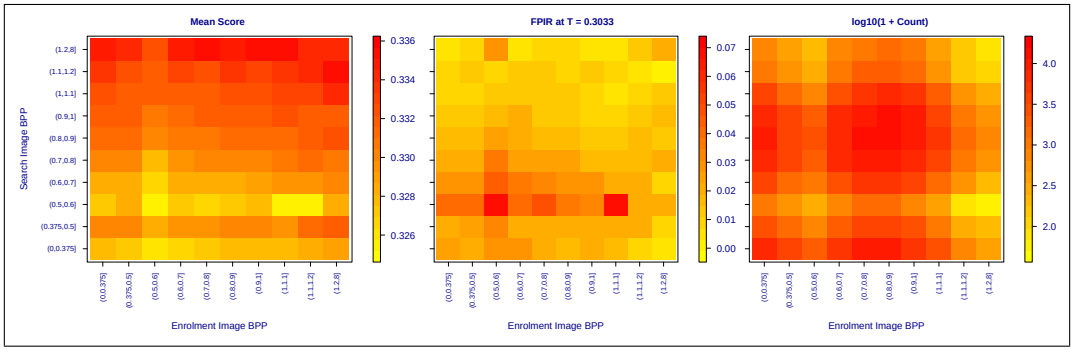

(d) Paired CRs, top nonmate

Figure 221: Effect of compression on accuracy for implementation T11A executing searches in an enrolled population of N = 1.6 million. The axes are labelled by binned values of the number of bits per pixel (BPP) implied by the JPEG filesize and the image dimensions. The lowest BPP bin is populated largely by the overly compressed 330x330 images. For mate searches, the three heatmaps give, respectively, the score, FNIR at FPIR = 0.0001, and the log of the count of images in each bin (3 corresponds to 1000). For nonmate searches, the threshold is set to give FPIR = 0.001 globally. The boxplots show the effect on the score, with the FNIR value annotated at right.

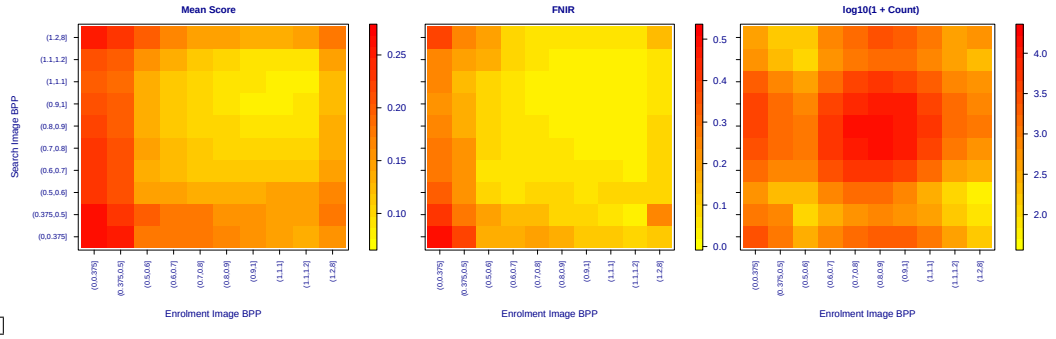

(a) Paired CRs, mate searches

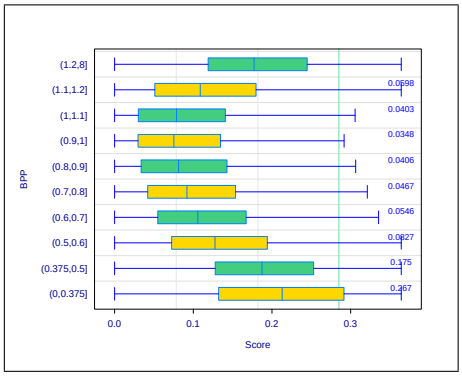

(b) Minimum CR, mate searches

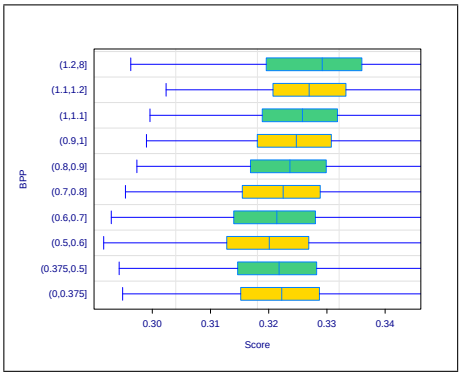

(c) Minimum CR, top nonmate

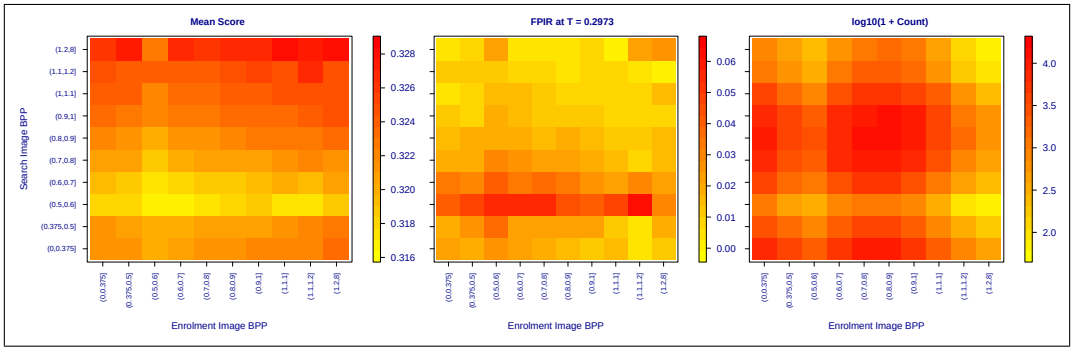

(d) Paired CRs, top nonmate

Figure 222: Effect of compression on accuracy for implementation T11B executing searches in an enrolled population of N = 1.6 million. The axes are labelled by binned values of the number of bits per pixel (BPP) implied by the JPEG filesize and the image dimensions. The lowest BPP bin is populated largely by the overly compressed 330x330 images. For mate searches, the three heatmaps give, respectively, the score, FNIR at FPIR = 0.0001, and the log of the count of images in each bin (3 corresponds to 1000). For nonmate searches, the threshold is set to give FPIR = 0.001 globally. The boxplots show the effect on the score, with the FNIR value annotated at right.

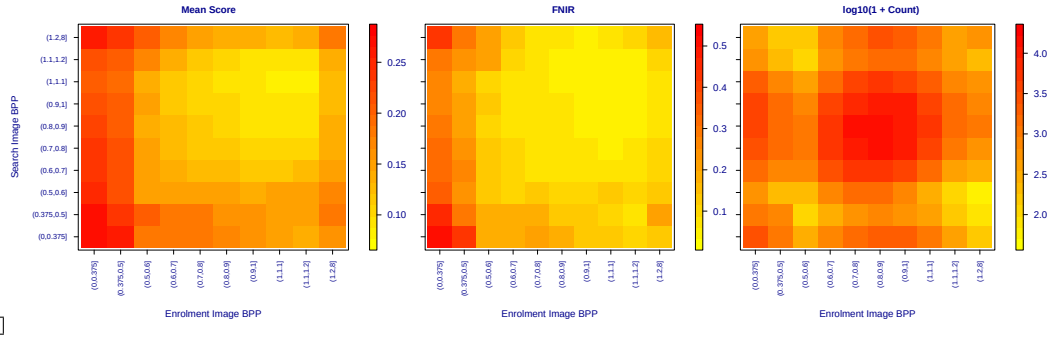

(a) Paired CRs, mate searches

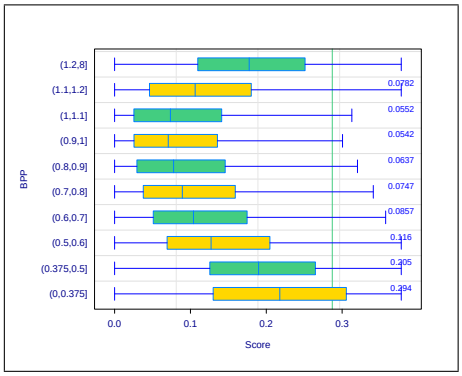

(b) Minimum CR, mate searches

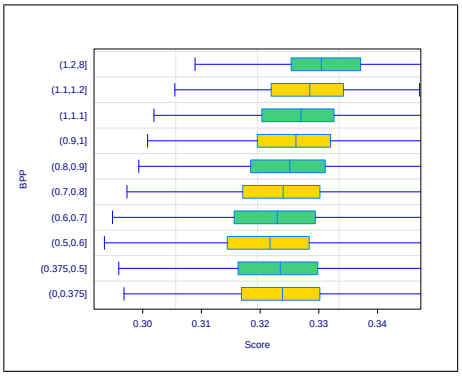

(c) Minimum CR, top nonmate

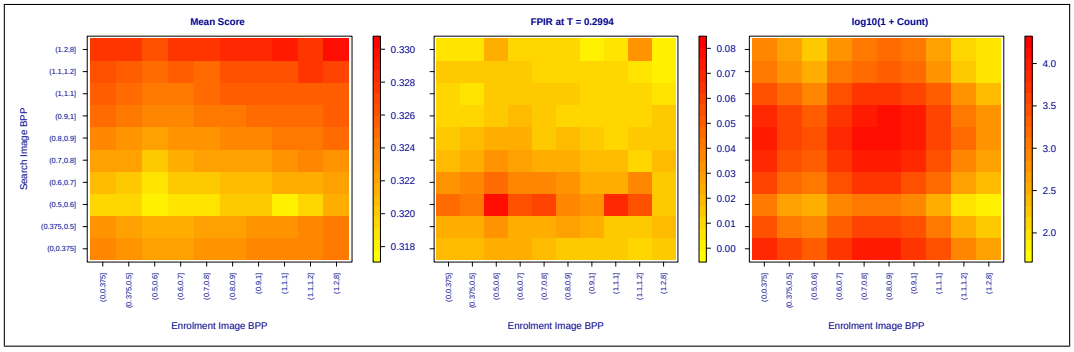

(d) Paired CRs, top nonmate

Figure 223: Effect of compression on accuracy for implementation T12B executing searches in an enrolled population of N = 1.6 million. The axes are labelled by binned values of the number of bits per pixel (BPP) implied by the JPEG filesize and the image dimensions. The lowest BPP bin is populated largely by the overly compressed 330x330 images. For mate searches, the three heatmaps give, respectively, the score, FNIR at FPIR = 0.0001, and the log of the count of images in each bin (3 corresponds to 1000). For nonmate searches, the threshold is set to give FPIR = 0.001 globally. The boxplots show the effect on the score, with the FNIR value annotated at right.

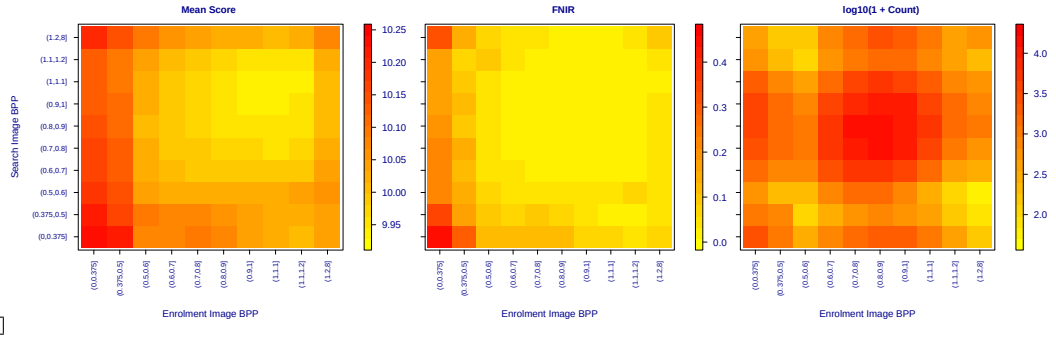

(a) Paired CRs, mate searches

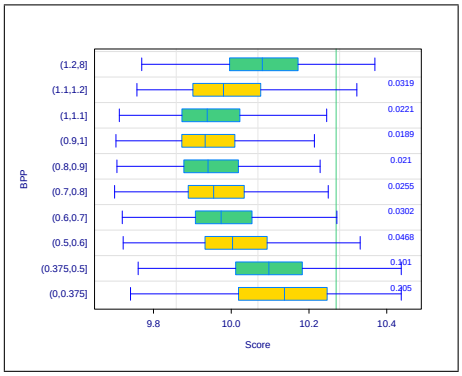

(b) Minimum CR, mate searches

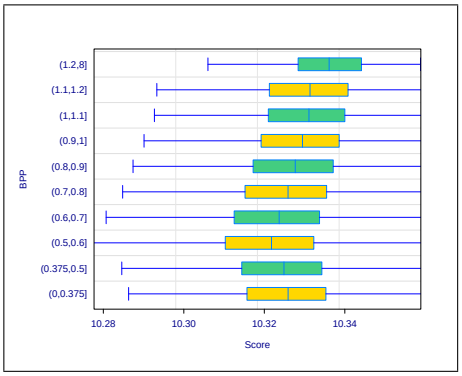

(c) Minimum CR, top nonmate

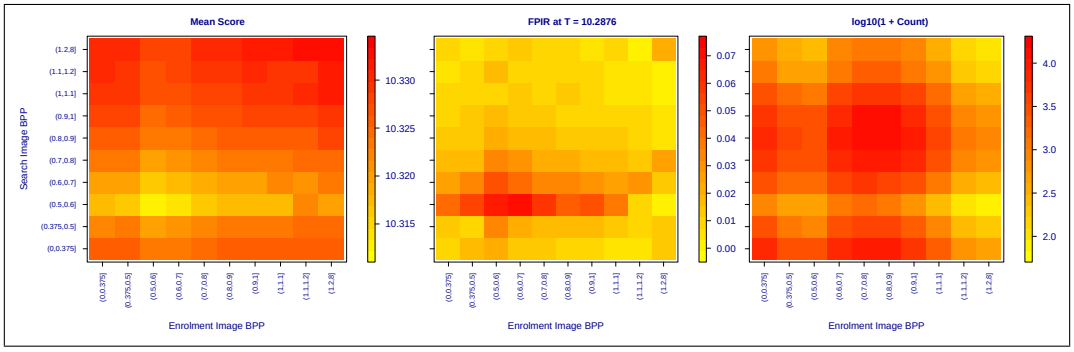

(d) Paired CRs, top nonmate

Figure 224: Effect of compression on accuracy for implementation U01A executing searches in an enrolled population of N = 1.6 million. The axes are labelled by binned values of the number of bits per pixel (BPP) implied by the JPEG filesize and the image dimensions. The lowest BPP bin is populated largely by the overly compressed 330x330 images. For mate searches, the three heatmaps give, respectively, the score, FNIR at FPIR = 0.0001, and the log of the count of images in each bin (3 corresponds to 1000). For nonmate searches, the threshold is set to give FPIR = 0.001 globally. The boxplots show the effect on the score, with the FNIR value annotated at right.

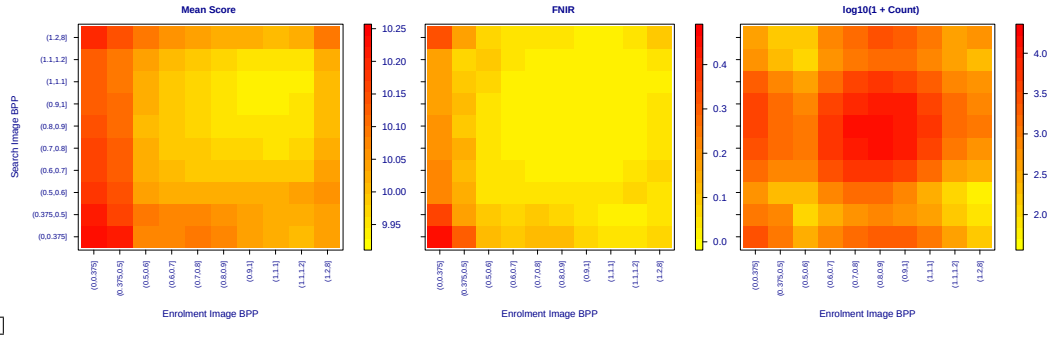

(a) Paired CRs, mate searches

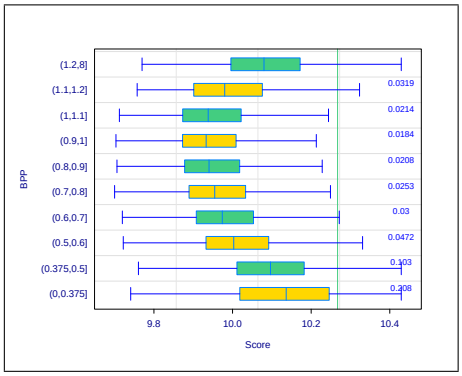

(b) Minimum CR, mate searches

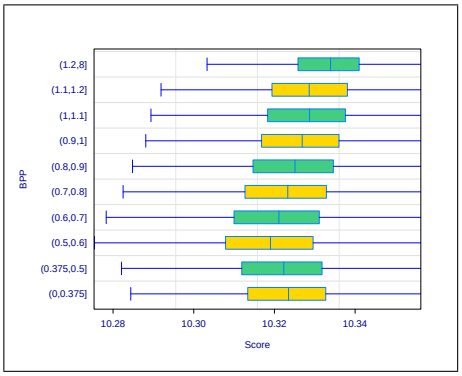

(c) Minimum CR, top nonmate

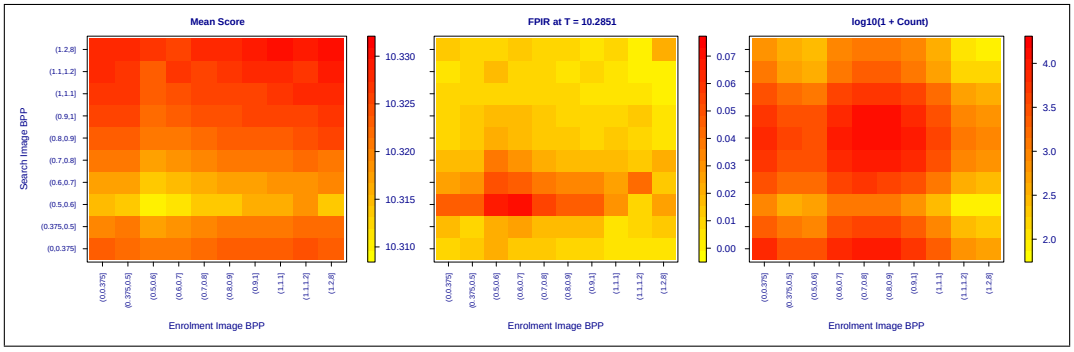

(d) Paired CRs, top nonmate

Figure 225: Effect of compression on accuracy for implementation U01B executing searches in an enrolled population of N = 1.6 million. The axes are labelled by binned values of the number of bits per pixel (BPP) implied by the JPEG filesize and the image dimensions. The lowest BPP bin is populated largely by the overly compressed 330x330 images. For mate searches, the three heatmaps give, respectively, the score, FNIR at FPIR = 0.0001, and the log of the count of images in each bin (3 corresponds to 1000). For nonmate searches, the threshold is set to give FPIR = 0.001 globally. The boxplots show the effect on the score, with the FNIR value annotated at right.

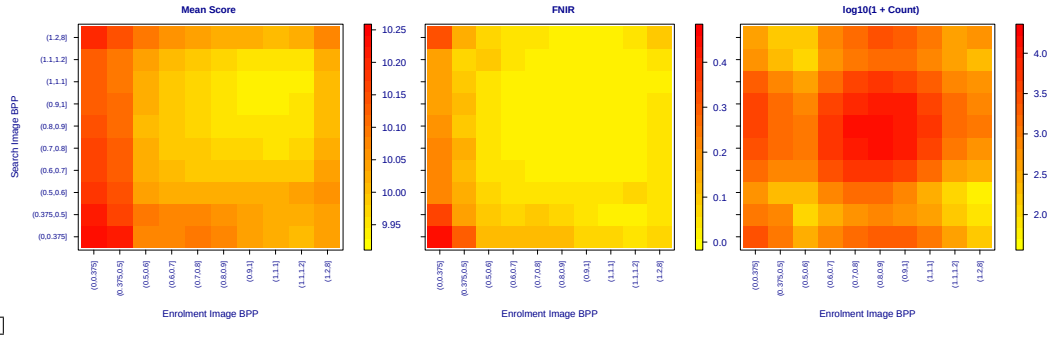

(a) Paired CRs, mate searches

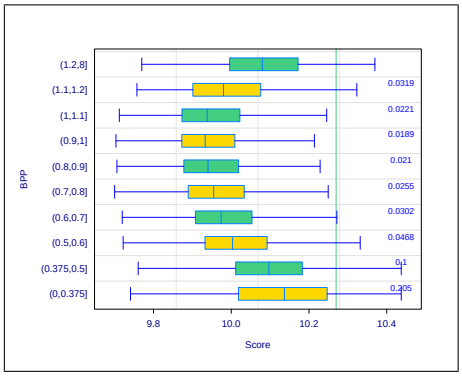

(b) Minimum CR, mate searches

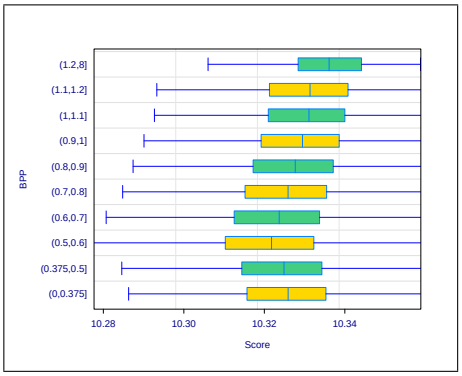

(c) Minimum CR, top nonmate

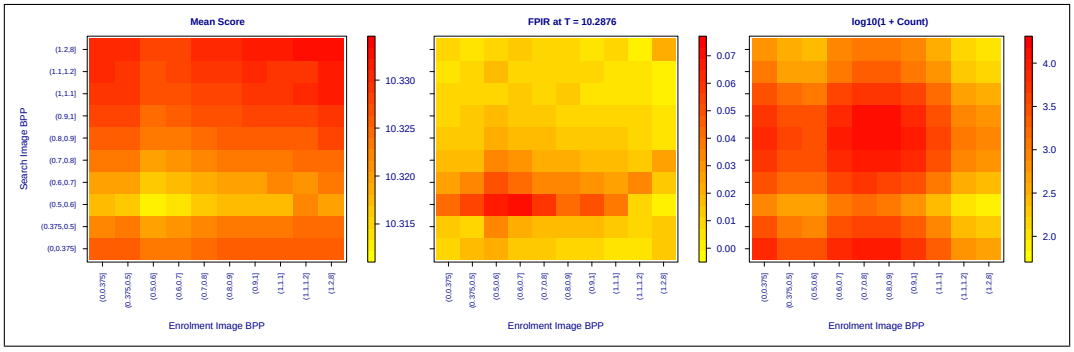

(d) Paired CRs, top nonmate

Figure 226: Effect of compression on accuracy for implementation U02A executing searches in an enrolled population of N = 1.6 million. The axes are labelled by binned values of the number of bits per pixel (BPP) implied by the JPEG filesize and the image dimensions. The lowest BPP bin is populated largely by the overly compressed 330x330 images. For mate searches, the three heatmaps give, respectively, the score, FNIR at FPIR = 0.0001, and the log of the count of images in each bin (3 corresponds to 1000). For nonmate searches, the threshold is set to give FPIR = 0.001 globally. The boxplots show the effect on the score, with the FNIR value annotated at right.

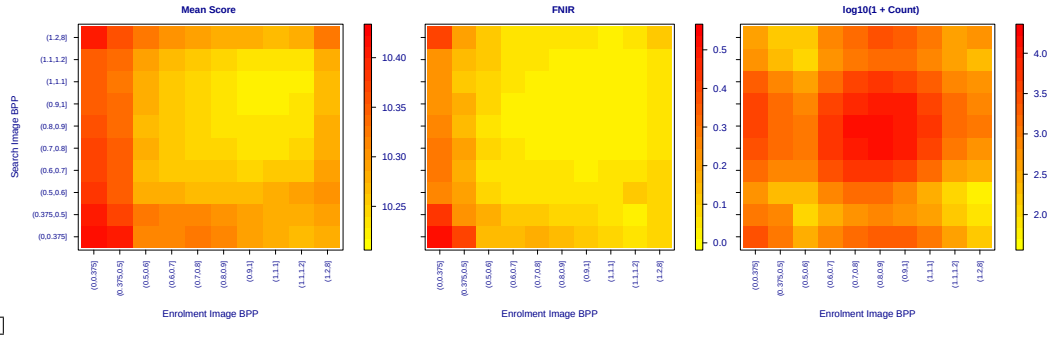

(a) Paired CRs, mate searches

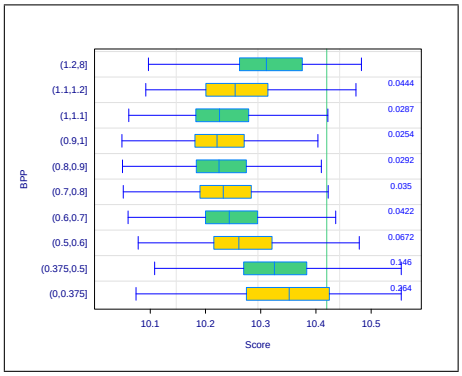

(b) Minimum CR, mate searches

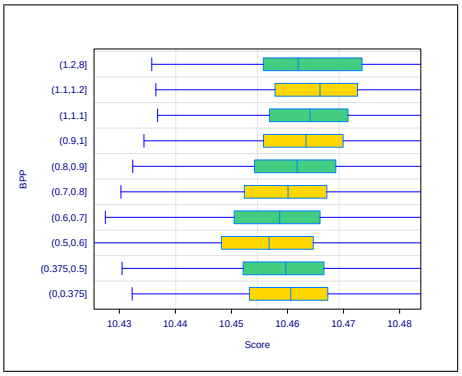

(c) Minimum CR, top nonmate

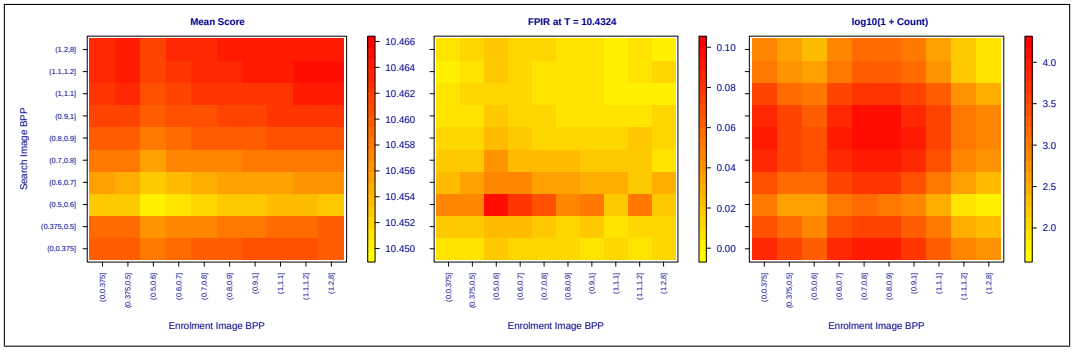

(d) Paired CRs, top nonmate

Figure 227: Effect of compression on accuracy for implementation U03A executing searches in an enrolled population of N = 1.6 million. The axes are labelled by binned values of the number of bits per pixel (BPP) implied by the JPEG filesize and the image dimensions. The lowest BPP bin is populated largely by the overly compressed 330x330 images. For mate searches, the three heatmaps give, respectively, the score, FNIR at FPIR = 0.0001, and the log of the count of images in each bin (3 corresponds to 1000). For nonmate searches, the threshold is set to give FPIR = 0.001 globally. The boxplots show the effect on the score, with the FNIR value annotated at right.

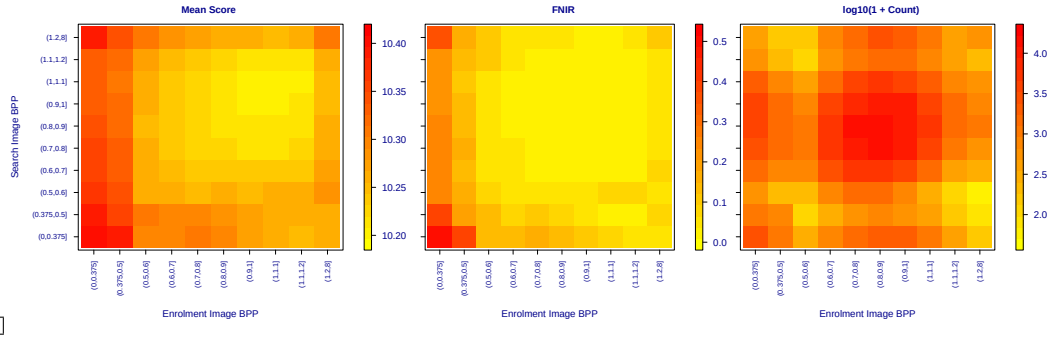

(a) Paired CRs, mate searches

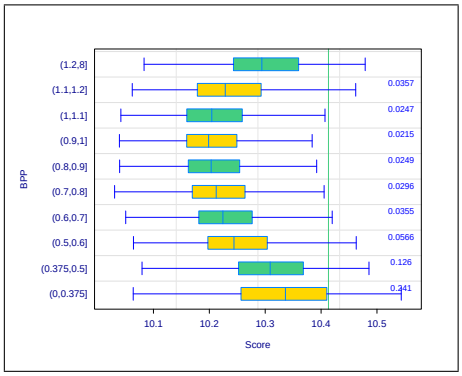

(b) Minimum CR, mate searches

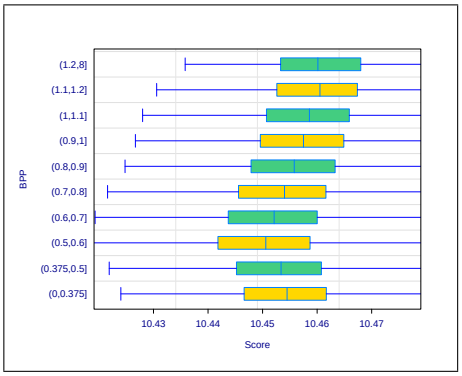

(c) Minimum CR, top nonmate

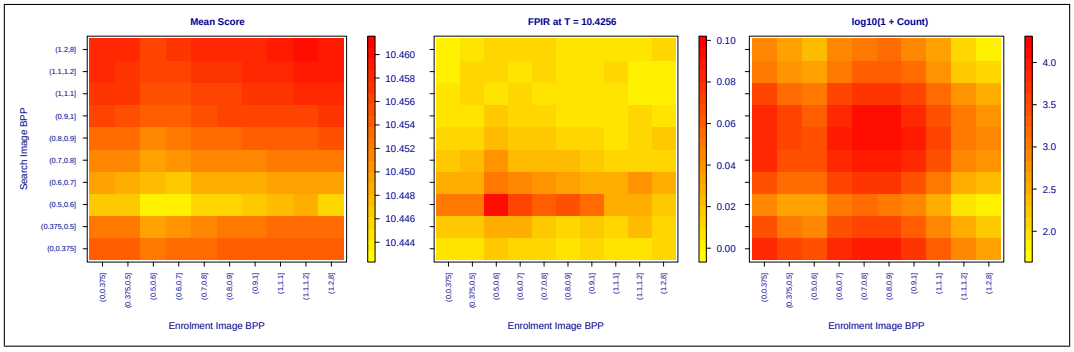

(d) Paired CRs, top nonmate

Figure 228: Effect of compression on accuracy for implementation U03B executing searches in an enrolled population of N = 1.6 million. The axes are labelled by binned values of the number of bits per pixel (BPP) implied by the JPEG filesize and the image dimensions. The lowest BPP bin is populated largely by the overly compressed 330x330 images. For mate searches, the three heatmaps give, respectively, the score, FNIR at FPIR = 0.0001, and the log of the count of images in each bin (3 corresponds to 1000). For nonmate searches, the threshold is set to give FPIR = 0.001 globally. The boxplots show the effect on the score, with the FNIR value annotated at right.

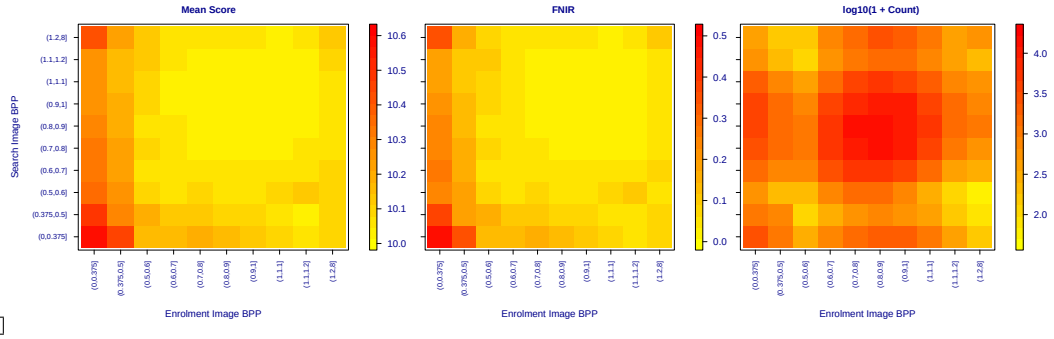

(a) Paired CRs, mate searches

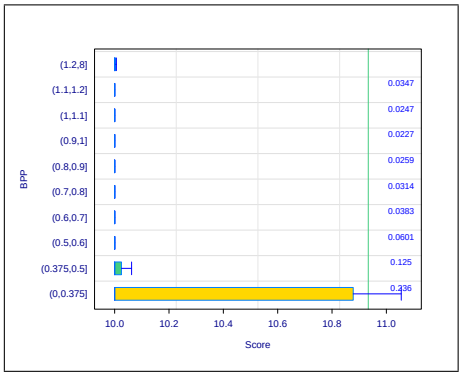

(b) Minimum CR, mate searches

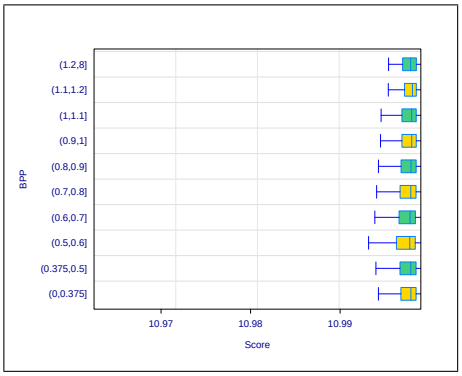

(c) Minimum CR, top nonmate

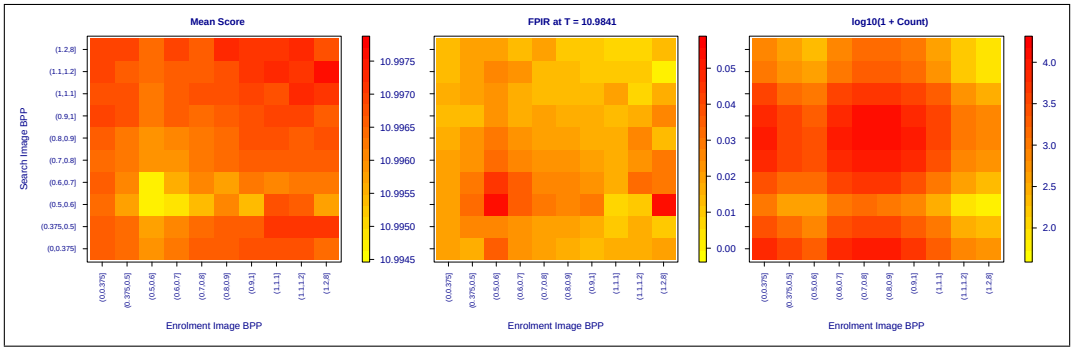

(d) Paired CRs, top nonmate

Figure 229: Effect of compression on accuracy for implementation U04A executing searches in an enrolled population of N = 1.6 million. The axes are labelled by binned values of the number of bits per pixel (BPP) implied by the JPEG filesize and the image dimensions. The lowest BPP bin is populated largely by the overly compressed 330x330 images. For mate searches, the three heatmaps give, respectively, the score, FNIR at FPIR = 0.0001, and the log of the count of images in each bin (3 corresponds to 1000). For nonmate searches, the threshold is set to give FPIR = 0.001 globally. The boxplots show the effect on the score, with the FNIR value annotated at right.

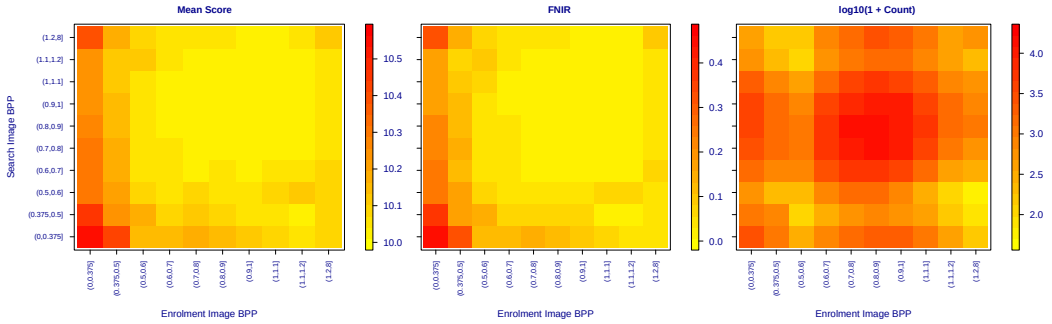

(a) Paired CRs, mate searches

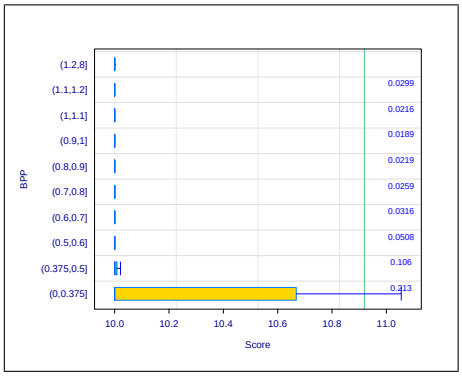

(b) Minimum CR, mate searches

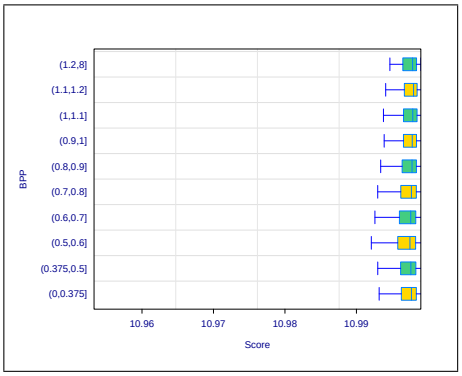

(c) Minimum CR, top nonmate

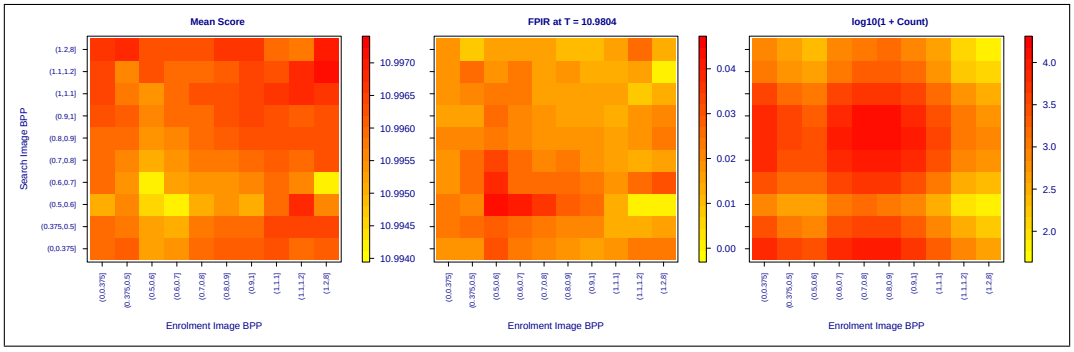

(d) Paired CRs, top nonmate

Figure 230: Effect of compression on accuracy for implementation U04B executing searches in an enrolled population of N = 1.6 million. The axes are labelled by binned values of the number of bits per pixel (BPP) implied by the JPEG filesize and the image dimensions. The lowest BPP bin is populated largely by the overly compressed 330x330 images. For mate searches, the three heatmaps give, respectively, the score, FNIR at FPIR = 0.0001, and the log of the count of images in each bin (3 corresponds to 1000). For nonmate searches, the threshold is set to give FPIR = 0.001 globally. The boxplots show the effect on the score, with the FNIR value annotated at right.

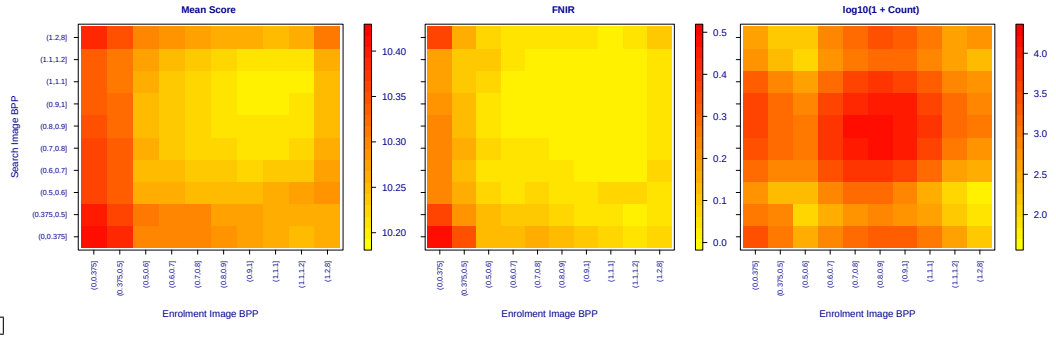

(a) Paired CRs, mate searches

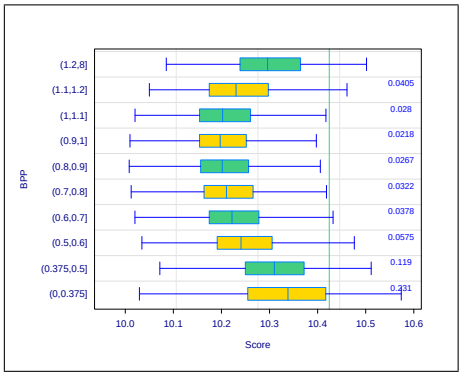

(b) Minimum CR, mate searches

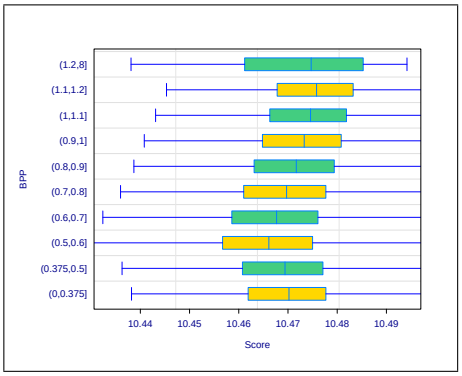

(c) Minimum CR, top nonmate

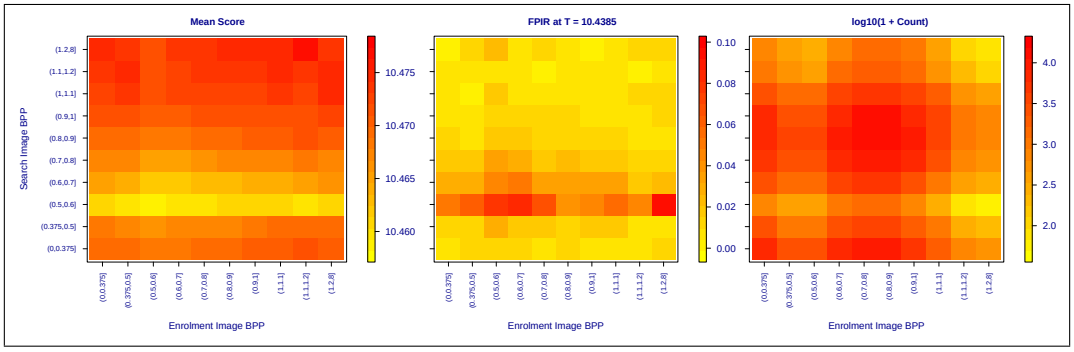

(d) Paired CRs, top nonmate

Figure 231: Effect of compression on accuracy for implementation U11A executing searches in an enrolled population of N = 1.6 million. The axes are labelled by binned values of the number of bits per pixel (BPP) implied by the JPEG filesize and the image dimensions. The lowest BPP bin is populated largely by the overly compressed 330x330 images. For mate searches, the three heatmaps give, respectively, the score, FNIR at FPIR = 0.0001, and the log of the count of images in each bin (3 corresponds to 1000). For nonmate searches, the threshold is set to give FPIR = 0.001 globally. The boxplots show the effect on the score, with the FNIR value annotated at right.

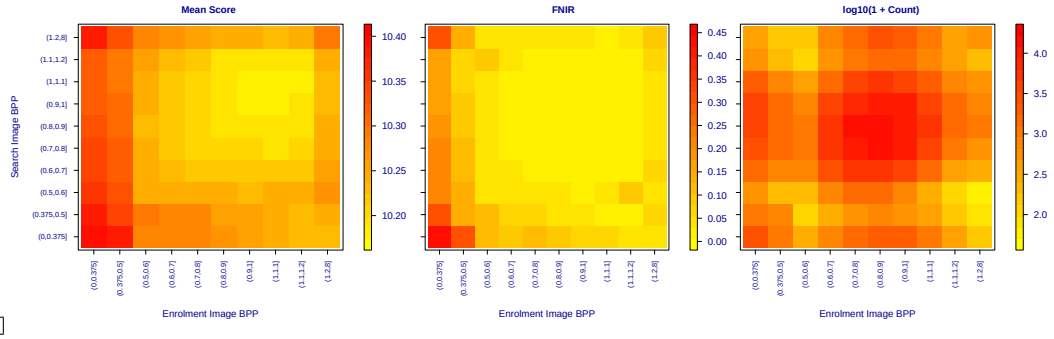

(a) Paired CRs, mate searches

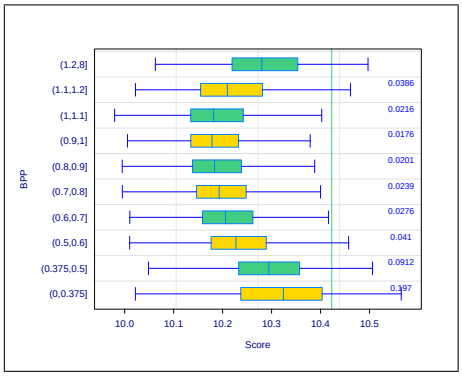

(b) Minimum CR, mate searches

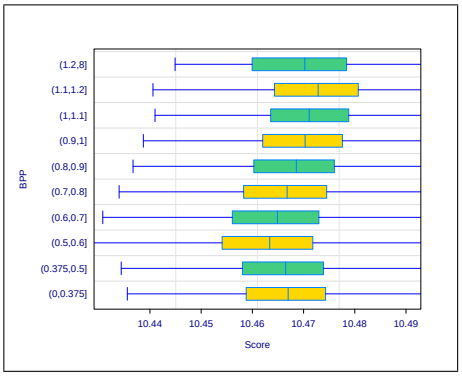

(c) Minimum CR, top nonmate

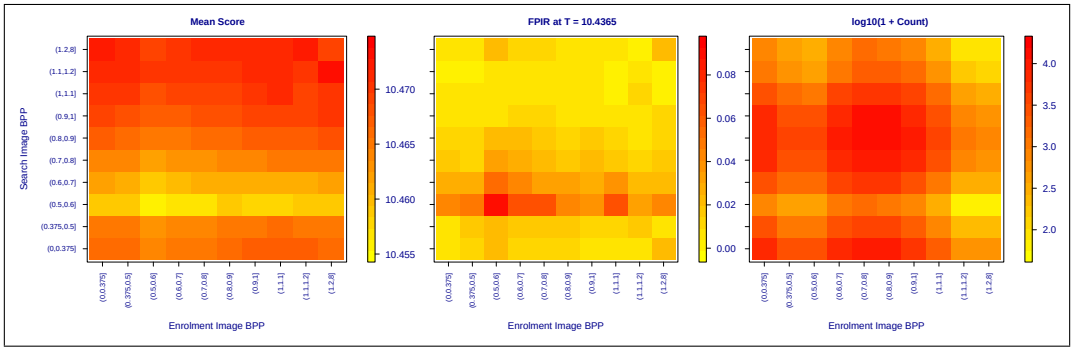

(d) Paired CRs, top nonmate

Figure 232: Effect of compression on accuracy for implementation U11B executing searches in an enrolled population of N = 1.6 million. The axes are labelled by binned values of the number of bits per pixel (BPP) implied by the JPEG filesize and the image dimensions. The lowest BPP bin is populated largely by the overly compressed 330x330 images. For mate searches, the three heatmaps give, respectively, the score, FNIR at FPIR = 0.0001, and the log of the count of images in each bin (3 corresponds to 1000). For nonmate searches, the threshold is set to give FPIR = 0.001 globally. The boxplots show the effect on the score, with the FNIR value annotated at right.

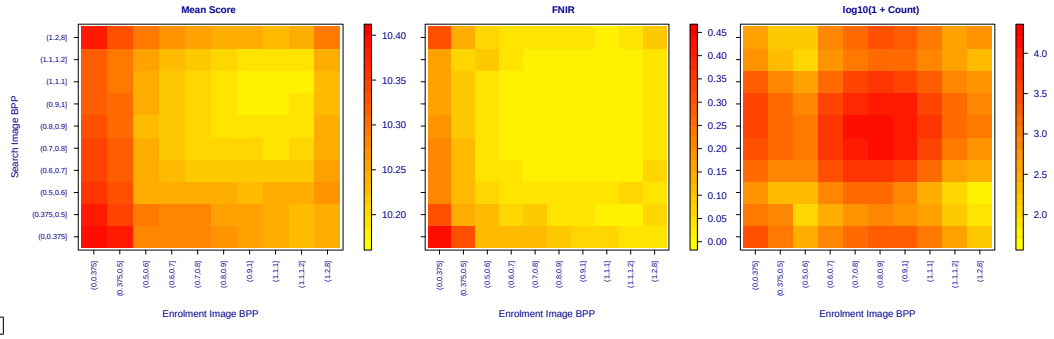

(a) Paired CRs, mate searches

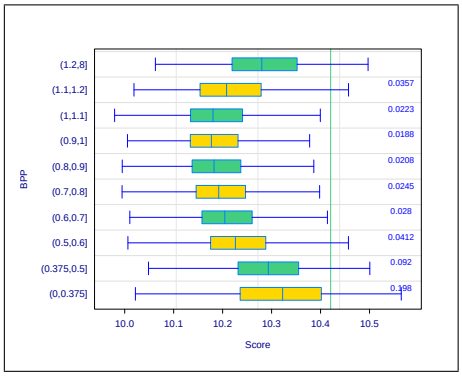

(b) Minimum CR, mate searches

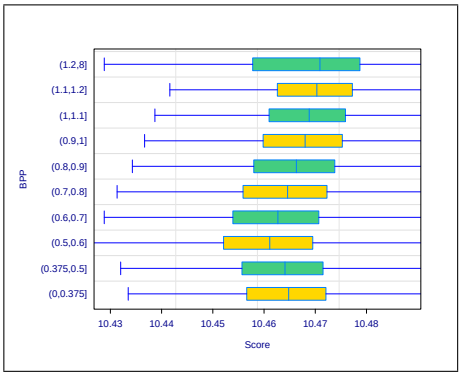

(c) Minimum CR, top nonmate

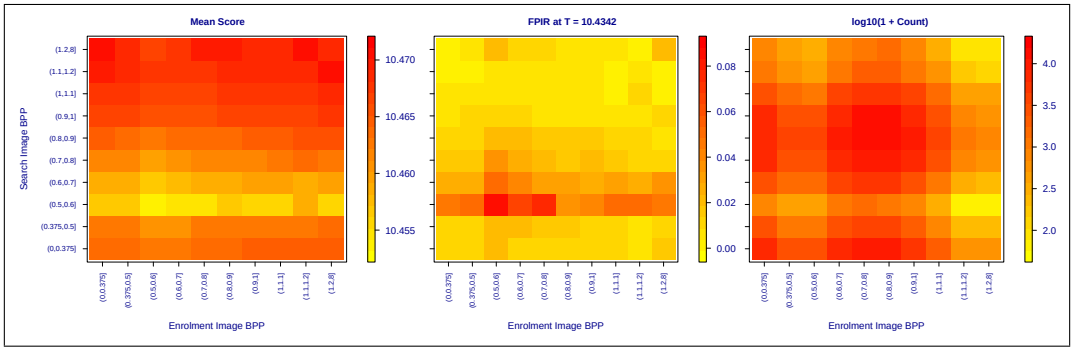

(d) Paired CRs, top nonmate

Figure 233: Effect of compression on accuracy for implementation U12A executing searches in an enrolled population of N = 1.6 million. The axes are labelled by binned values of the number of bits per pixel (BPP) implied by the JPEG filesize and the image dimensions. The lowest BPP bin is populated largely by the overly compressed 330x330 images. For mate searches, the three heatmaps give, respectively, the score, FNIR at FPIR = 0.0001, and the log of the count of images in each bin (3 corresponds to 1000). For nonmate searches, the threshold is set to give FPIR = 0.001 globally. The boxplots show the effect on the score, with the FNIR value annotated at right.

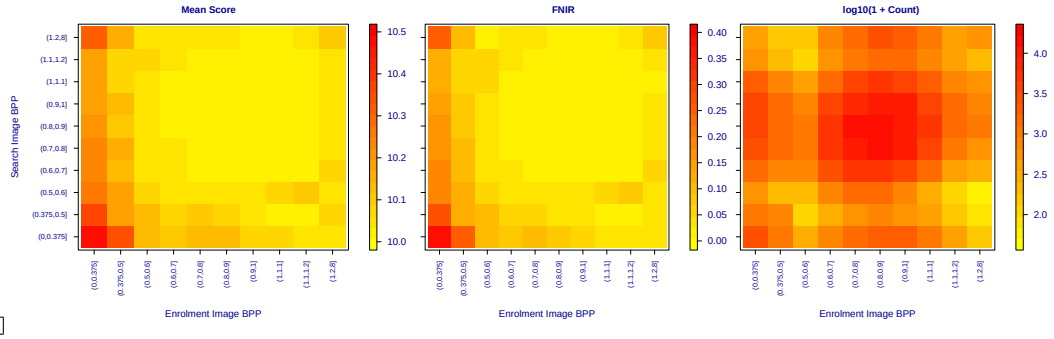

(a) Paired CRs, mate searches

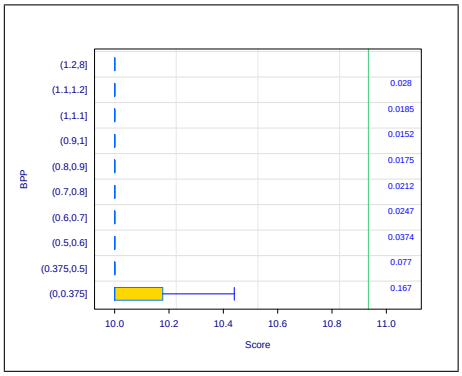

(b) Minimum CR, mate searches

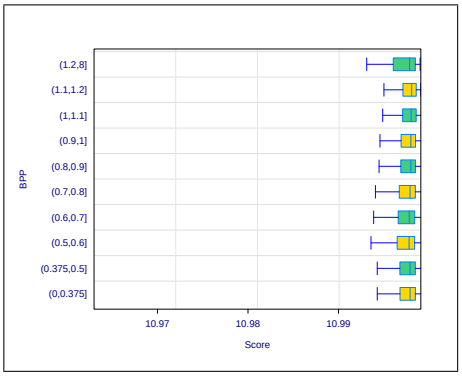

(c) Minimum CR, top nonmate

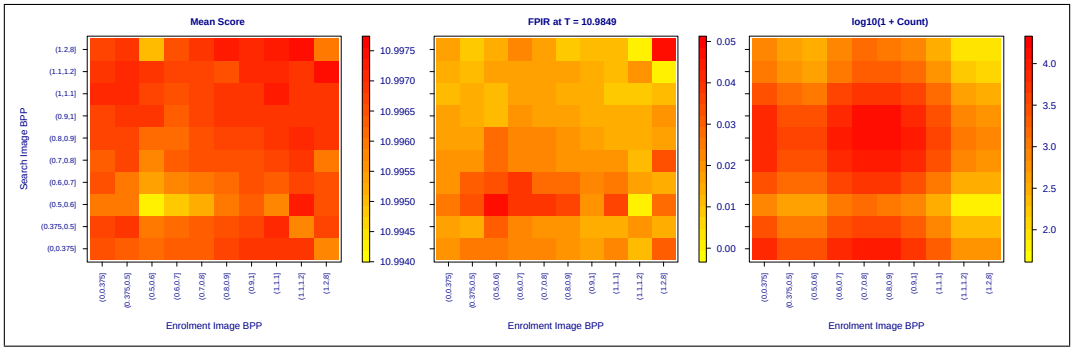

(d) Paired CRs, top nonmate

Figure 234: Effect of compression on accuracy for implementation U12B executing searches in an enrolled population of N = 1.6 million. The axes are labelled by binned values of the number of bits per pixel (BPP) implied by the JPEG filesize and the image dimensions. The lowest BPP bin is populated largely by the overly compressed 330x330 images. For mate searches, the three heatmaps give, respectively, the score, FNIR at FPIR = 0.0001, and the log of the count of images in each bin (3 corresponds to 1000). For nonmate searches, the threshold is set to give FPIR = 0.001 globally. The boxplots show the effect on the score, with the FNIR value annotated at right.

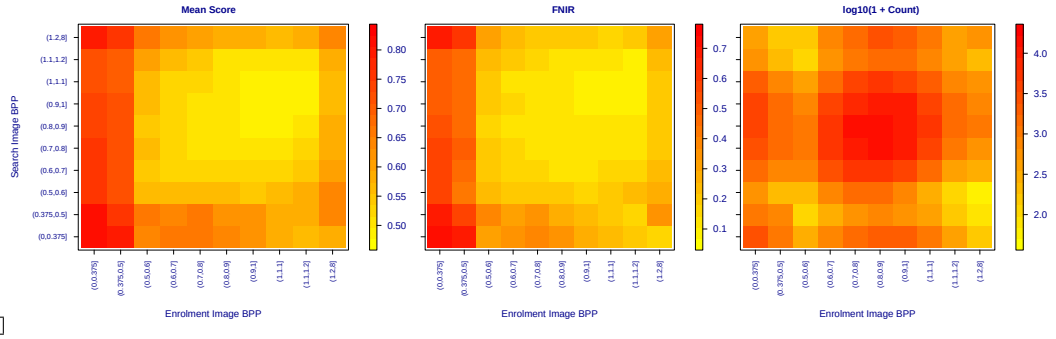

(a) Paired CRs, mate searches

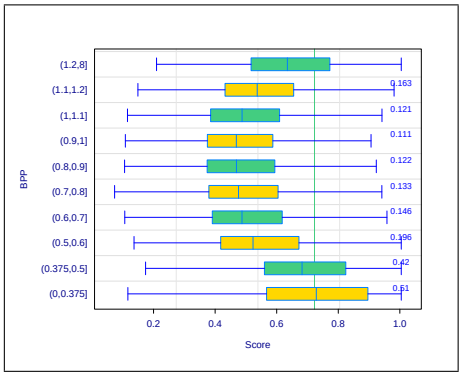

(b) Minimum CR, mate searches

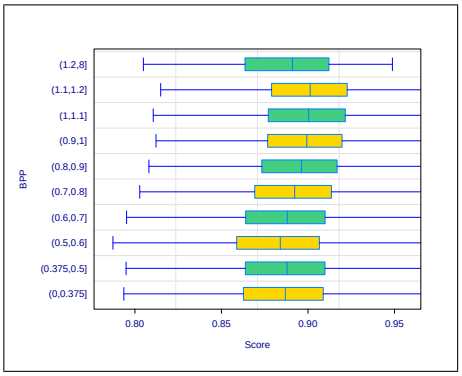

(c) Minimum CR, top nonmate

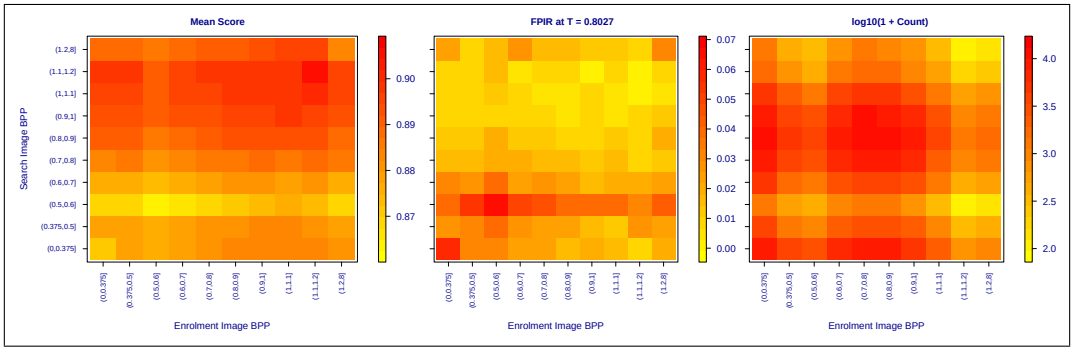

(d) Paired CRs, top nonmate

Figure 235: Effect of compression on accuracy for implementation V01A executing searches in an enrolled population of N = 1.6 million. The axes are labelled by binned values of the number of bits per pixel (BPP) implied by the JPEG filesize and the image dimensions. The lowest BPP bin is populated largely by the overly compressed 330x330 images. For mate searches, the three heatmaps give, respectively, the score, FNIR at FPIR = 0.0001, and the log of the count of images in each bin (3 corresponds to 1000). For nonmate searches, the threshold is set to give FPIR = 0.001 globally. The boxplots show the effect on the score, with the FNIR value annotated at right.

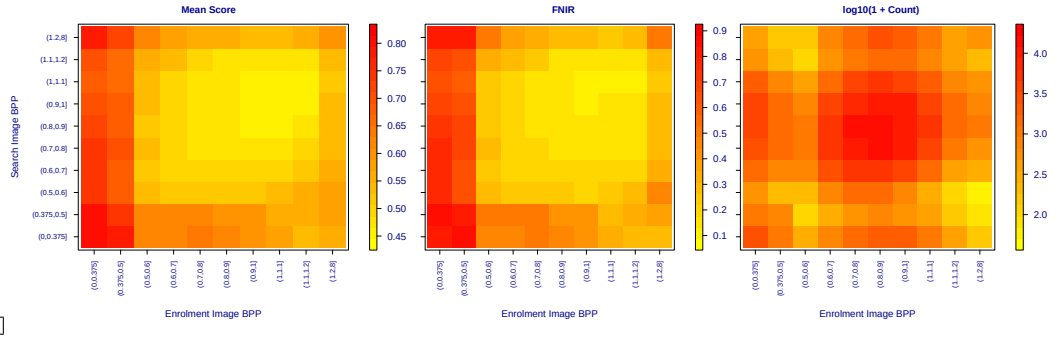

(a) Paired CRs, mate searches

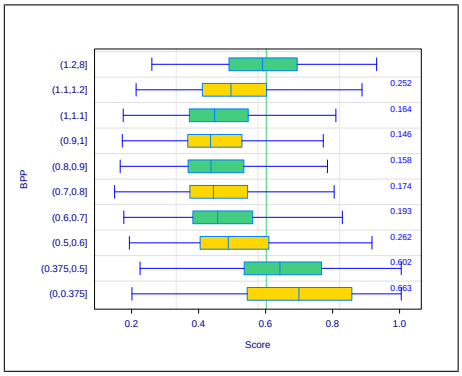

(b) Minimum CR, mate searches

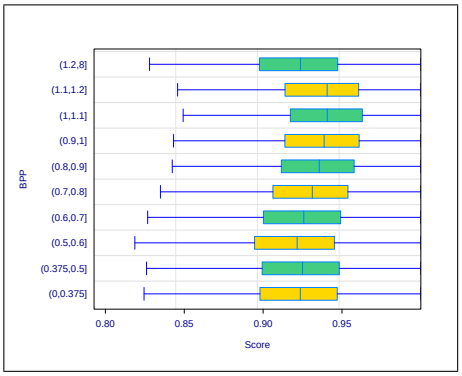

(c) Minimum CR, top nonmate

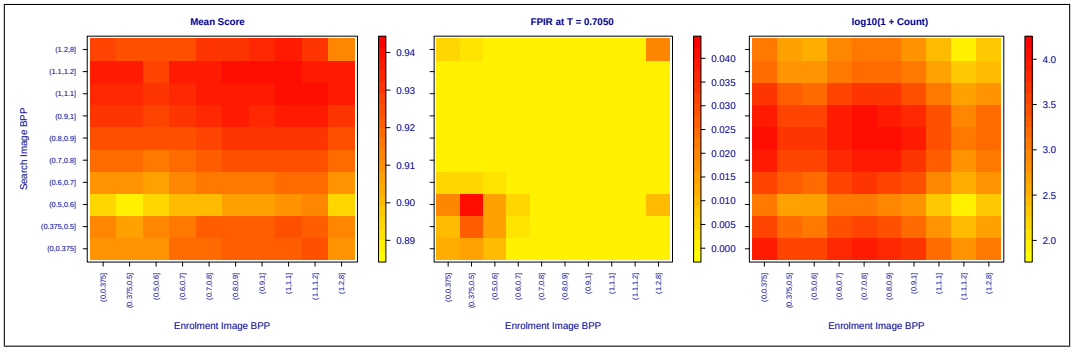

(d) Paired CRs, top nonmate

Figure 236: Effect of compression on accuracy for implementation V02A executing searches in an enrolled population of N = 1.6 million. The axes are labelled by binned values of the number of bits per pixel (BPP) implied by the JPEG filesize and the image dimensions. The lowest BPP bin is populated largely by the overly compressed 330x330 images. For mate searches, the three heatmaps give, respectively, the score, FNIR at FPIR = 0.0001, and the log of the count of images in each bin (3 corresponds to 1000). For nonmate searches, the threshold is set to give FPIR = 0.001 globally. The boxplots show the effect on the score, with the FNIR value annotated at right.

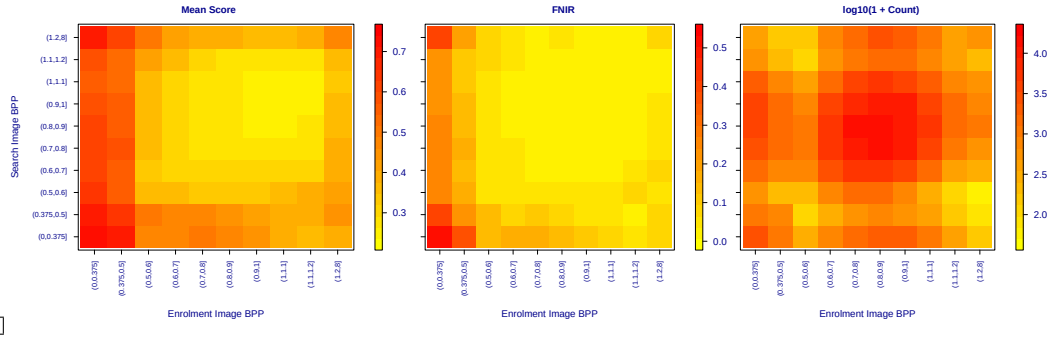

(a) Paired CRs, mate searches

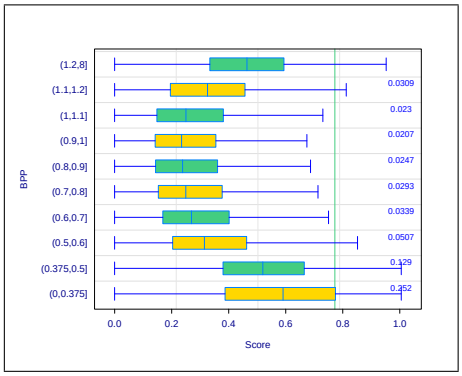

(b) Minimum CR, mate searches

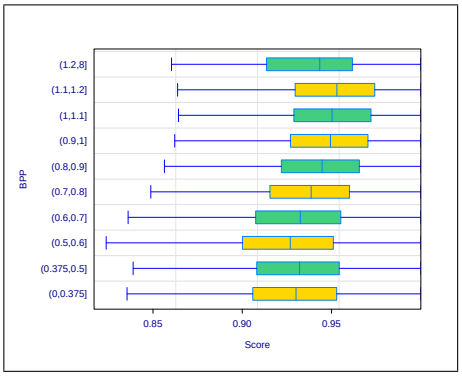

(c) Minimum CR, top nonmate

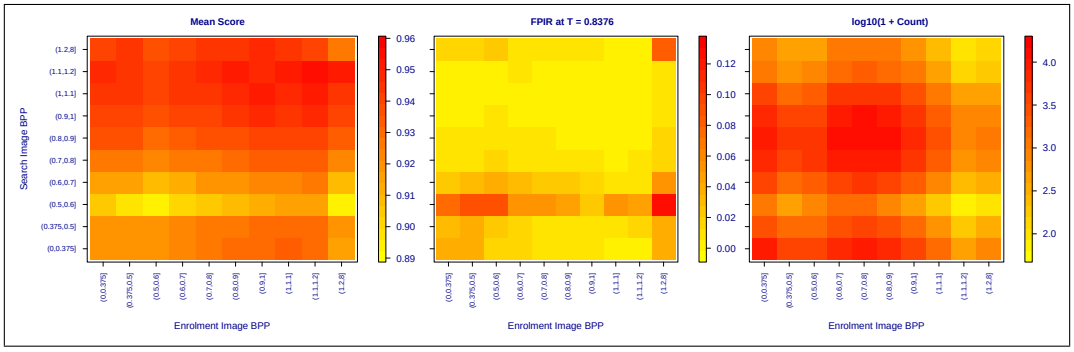

(d) Paired CRs, top nonmate

Figure 237: Effect of compression on accuracy for implementation V03A executing searches in an enrolled population of N = 1.6 million. The axes are labelled by binned values of the number of bits per pixel (BPP) implied by the JPEG filesize and the image dimensions. The lowest BPP bin is populated largely by the overly compressed 330x330 images. For mate searches, the three heatmaps give, respectively, the score, FNIR at FPIR = 0.0001, and the log of the count of images in each bin (3 corresponds to 1000). For nonmate searches, the threshold is set to give FPIR = 0.001 globally. The boxplots show the effect on the score, with the FNIR value annotated at right.

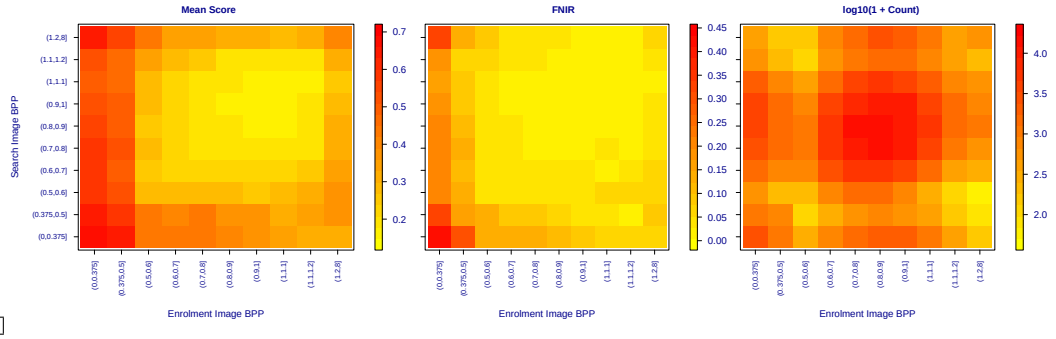

(a) Paired CRs, mate searches

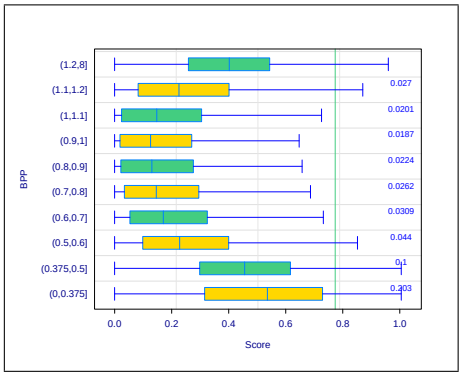

(b) Minimum CR, mate searches

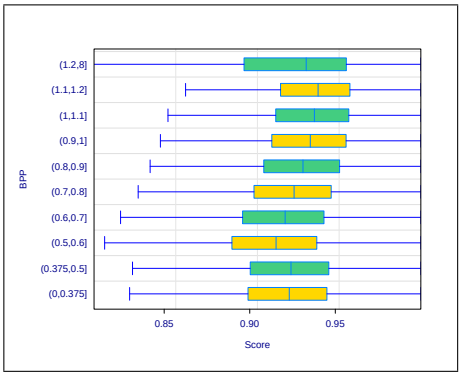

(c) Minimum CR, top nonmate

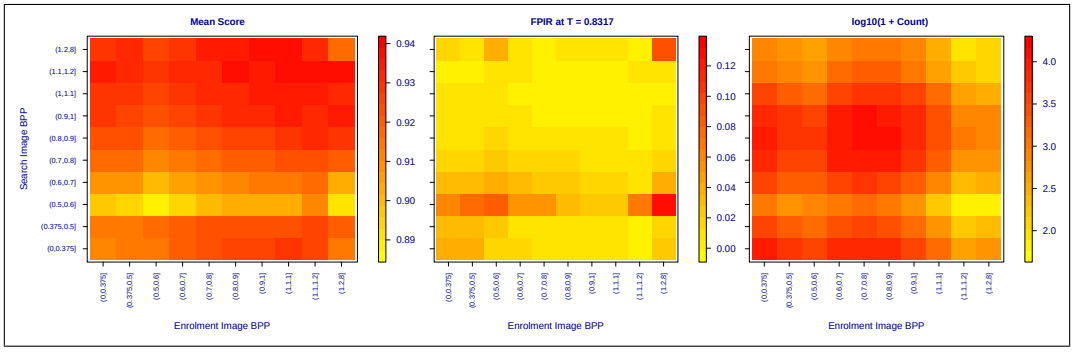

(d) Paired CRs, top nonmate

Figure 238: Effect of compression on accuracy for implementation V03B executing searches in an enrolled population of N = 1.6 million. The axes are labelled by binned values of the number of bits per pixel (BPP) implied by the JPEG filesize and the image dimensions. The lowest BPP bin is populated largely by the overly compressed 330x330 images. For mate searches, the three heatmaps give, respectively, the score, FNIR at FPIR = 0.0001, and the log of the count of images in each bin (3 corresponds to 1000). For nonmate searches, the threshold is set to give FPIR = 0.001 globally. The boxplots show the effect on the score, with the FNIR value annotated at right.

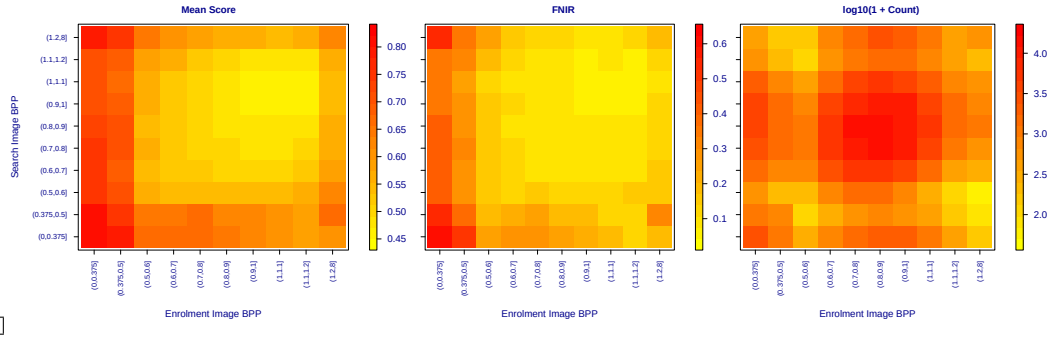

(a) Paired CRs, mate searches

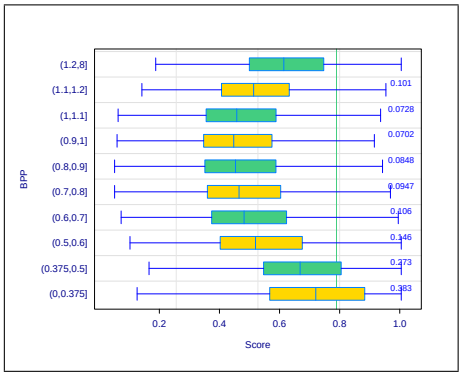

(b) Minimum CR, mate searches

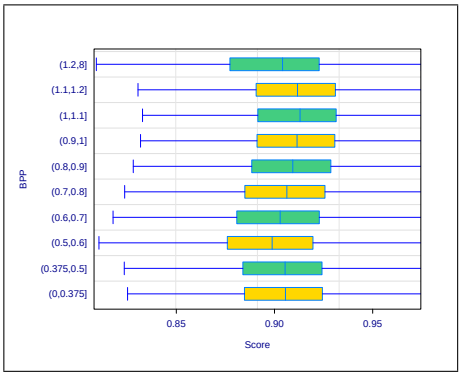

(c) Minimum CR, top nonmate

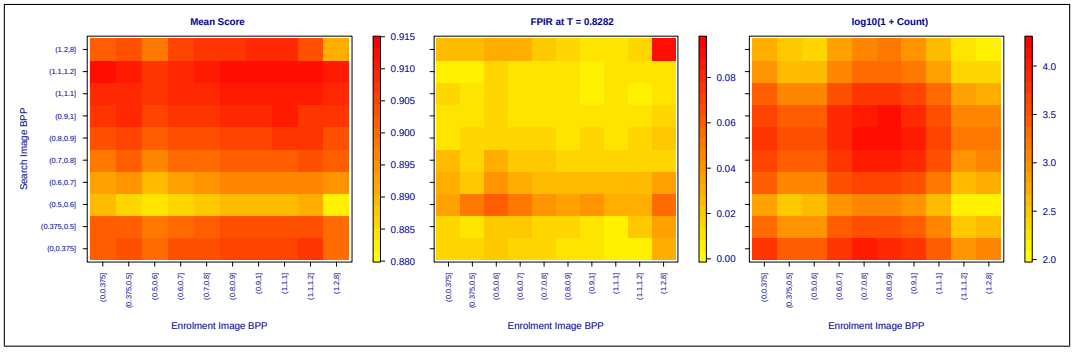

(d) Paired CRs, top nonmate

Figure 239: Effect of compression on accuracy for implementation V04A executing searches in an enrolled population of N = 1.6 million. The axes are labelled by binned values of the number of bits per pixel (BPP) implied by the JPEG filesize and the image dimensions. The lowest BPP bin is populated largely by the overly compressed 330x330 images. For mate searches, the three heatmaps give, respectively, the score, FNIR at FPIR = 0.0001, and the log of the count of images in each bin (3 corresponds to 1000). For nonmate searches, the threshold is set to give FPIR = 0.001 globally. The boxplots show the effect on the score, with the FNIR value annotated at right.

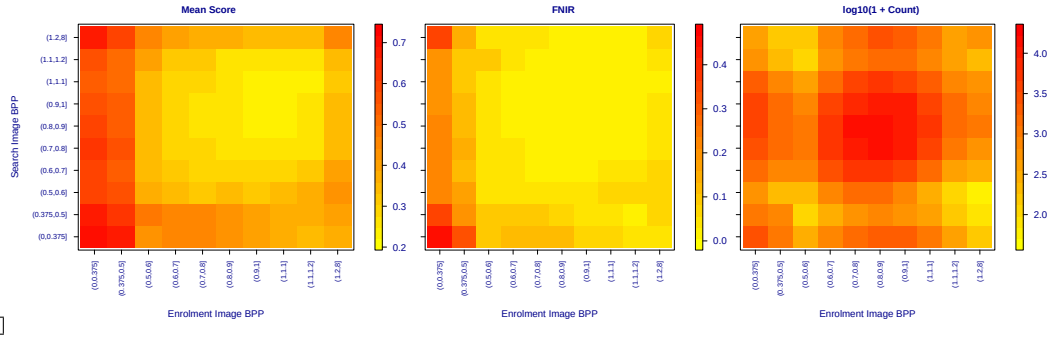

(a) Paired CRs, mate searches

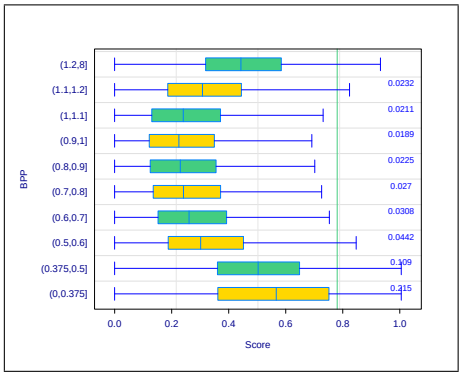

(b) Minimum CR, mate searches

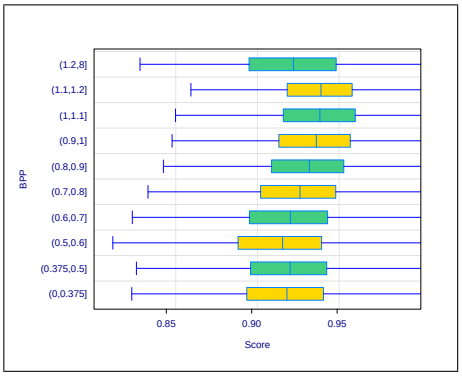

(c) Minimum CR, top nonmate

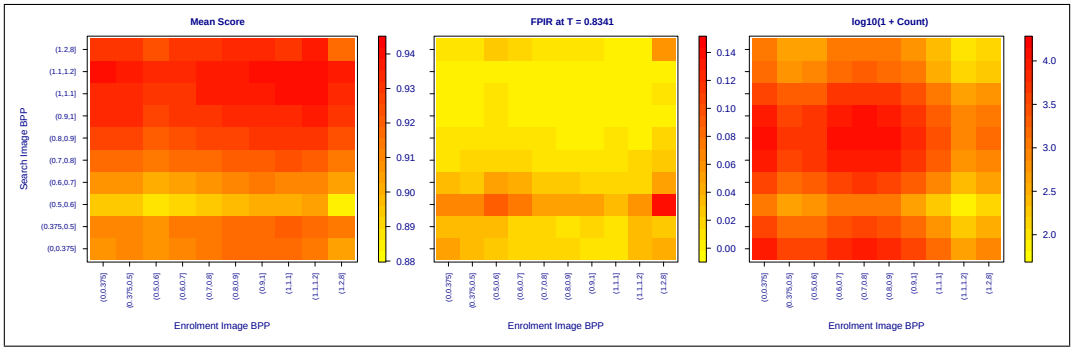

(d) Paired CRs, top nonmate

Figure 240: Effect of compression on accuracy for implementation V11A executing searches in an enrolled population of N = 1.6 million. The axes are labelled by binned values of the number of bits per pixel (BPP) implied by the JPEG filesize and the image dimensions. The lowest BPP bin is populated largely by the overly compressed 330x330 images. For mate searches, the three heatmaps give, respectively, the score, FNIR at FPIR = 0.0001, and the log of the count of images in each bin (3 corresponds to 1000). For nonmate searches, the threshold is set to give FPIR = 0.001 globally. The boxplots show the effect on the score, with the FNIR value annotated at right.

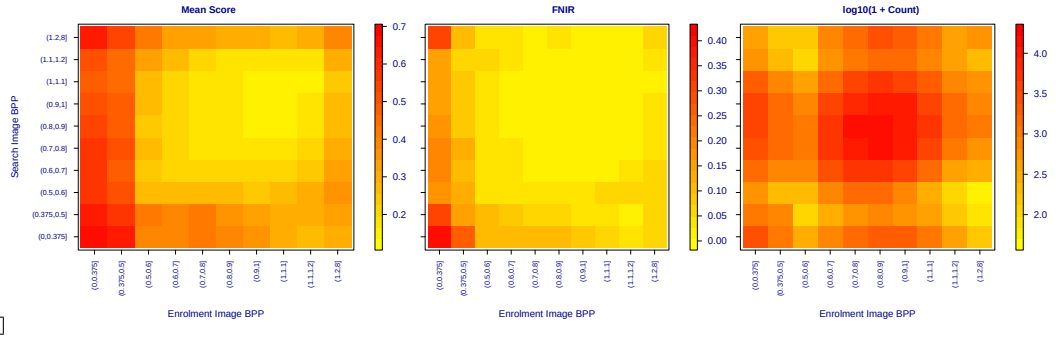

(a) Paired CRs, mate searches

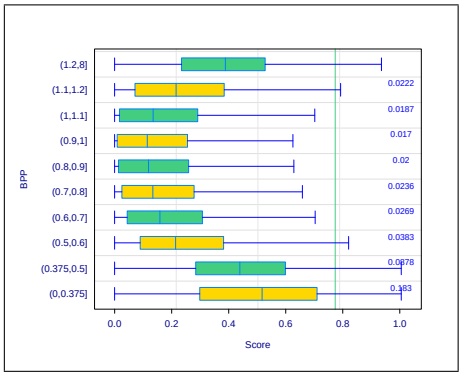

(b) Minimum CR, mate searches

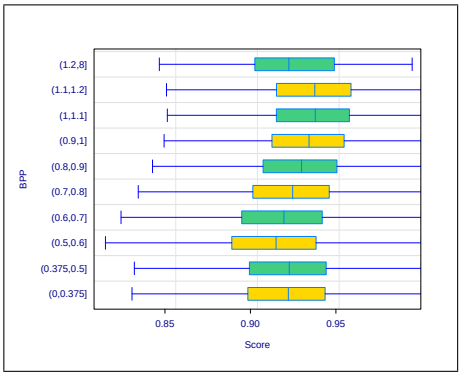

(c) Minimum CR, top nonmate

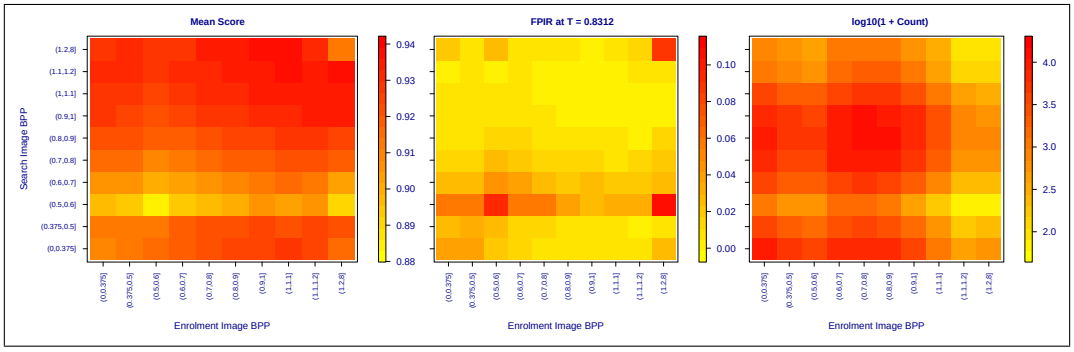

(d) Paired CRs, top nonmate

Figure 241: Effect of compression on accuracy for implementation V11B executing searches in an enrolled population of N = 1.6 million. The axes are labelled by binned values of the number of bits per pixel (BPP) implied by the JPEG filesize and the image dimensions. The lowest BPP bin is populated largely by the overly compressed 330x330 images. For mate searches, the three heatmaps give, respectively, the score, FNIR at FPIR = 0.0001, and the log of the count of images in each bin (3 corresponds to 1000). For nonmate searches, the threshold is set to give FPIR = 0.001 globally. The boxplots show the effect on the score, with the FNIR value annotated at right.

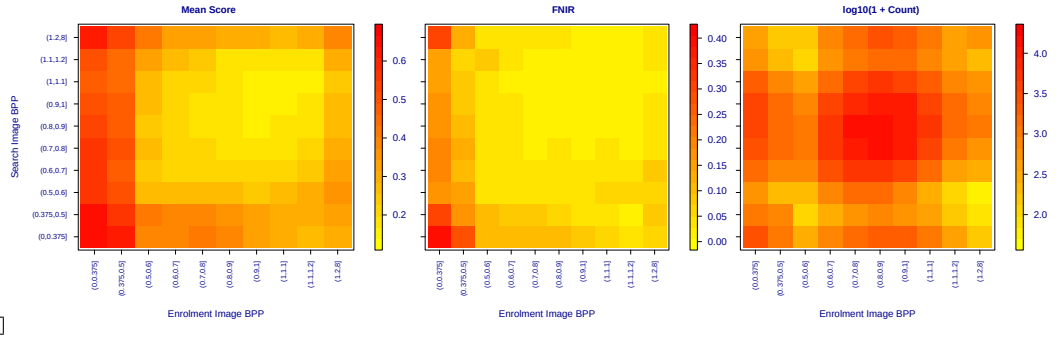

(a) Paired CRs, mate searches

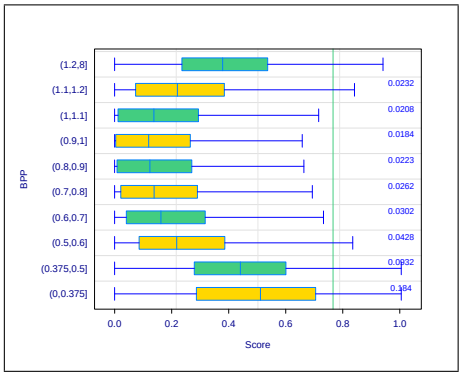

(b) Minimum CR, mate searches

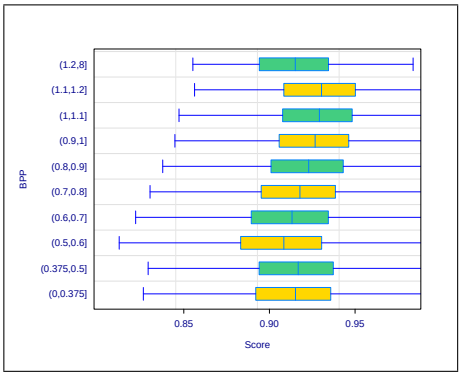

(c) Minimum CR, top nonmate

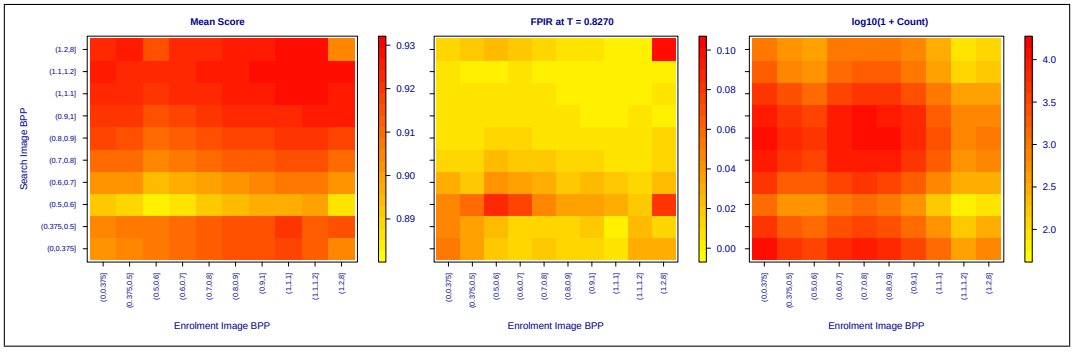

(d) Paired CRs, top nonmate

Figure 242: Effect of compression on accuracy for implementation V12A executing searches in an enrolled population of N = 1.6 million. The axes are labelled by binned values of the number of bits per pixel (BPP) implied by the JPEG filesize and the image dimensions. The lowest BPP bin is populated largely by the overly compressed 330x330 images. For mate searches, the three heatmaps give, respectively, the score, FNIR at FPIR = 0.0001, and the log of the count of images in each bin (3 corresponds to 1000). For nonmate searches, the threshold is set to give FPIR = 0.001 globally. The boxplots show the effect on the score, with the FNIR value annotated at right.

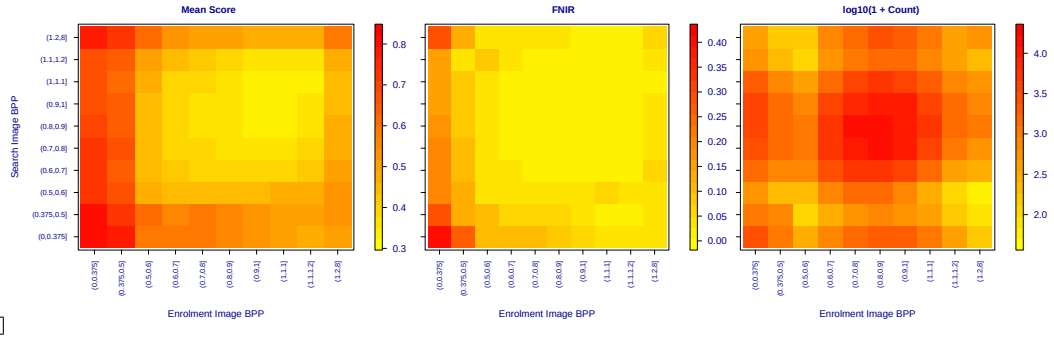

(a) Paired CRs, mate searches

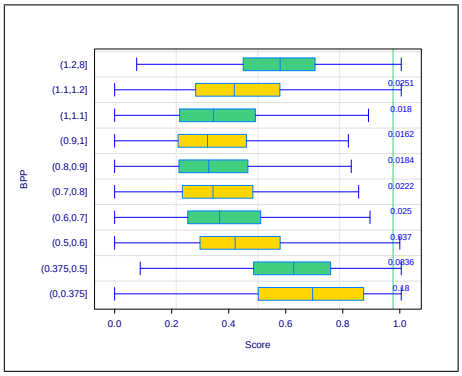

(b) Minimum CR, mate searches

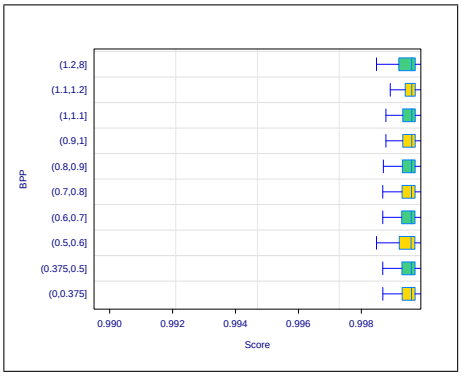

(c) Minimum CR, top nonmate

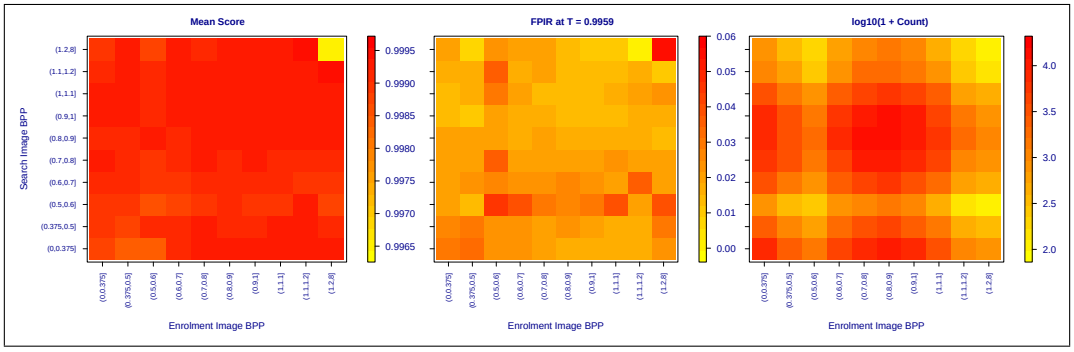

(d) Paired CRs, top nonmate

Figure 243: Effect of compression on accuracy for implementation V12B executing searches in an enrolled population of N = 1.6 million. The axes are labelled by binned values of the number of bits per pixel (BPP) implied by the JPEG filesize and the image dimensions. The lowest BPP bin is populated largely by the overly compressed 330x330 images. For mate searches, the three heatmaps give, respectively, the score, FNIR at FPIR = 0.0001, and the log of the count of images in each bin (3 corresponds to 1000). For nonmate searches, the threshold is set to give FPIR = 0.001 globally. The boxplots show the effect on the score, with the FNIR value annotated at right.

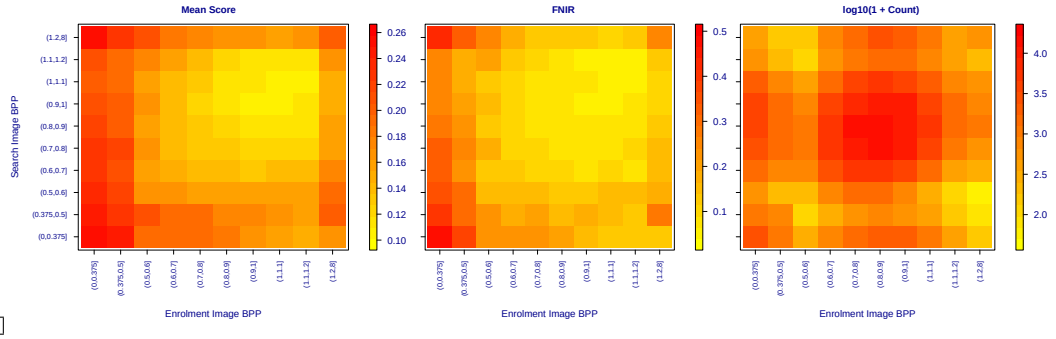

(a) Paired CRs, mate searches

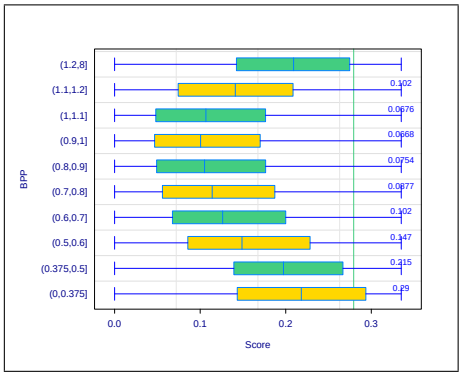

(b) Minimum CR, mate searches

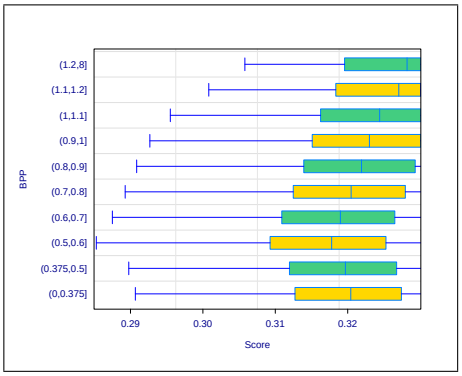

(c) Minimum CR, top nonmate

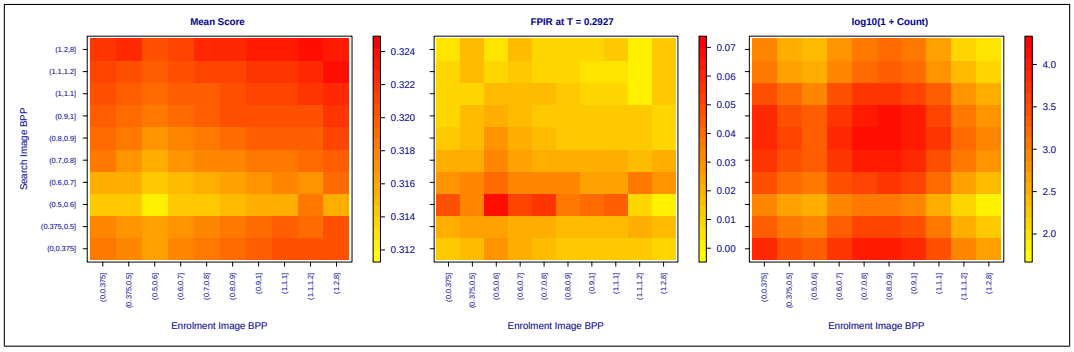

(d) Paired CRs, top nonmate

Figure 244: Effect of compression on accuracy for implementation W01A executing searches in an enrolled population of N = 1.6 million. The axes are labelled by binned values of the number of bits per pixel (BPP) implied by the JPEG filesize and the image dimensions. The lowest BPP bin is populated largely by the overly compressed 330x330 images. For mate searches, the three heatmaps give, respectively, the score, FNIR at FPIR = 0.0001, and the log of the count of images in each bin (3 corresponds to 1000). For nonmate searches, the threshold is set to give FPIR = 0.001 globally. The boxplots show the effect on the score, with the FNIR value annotated at right.

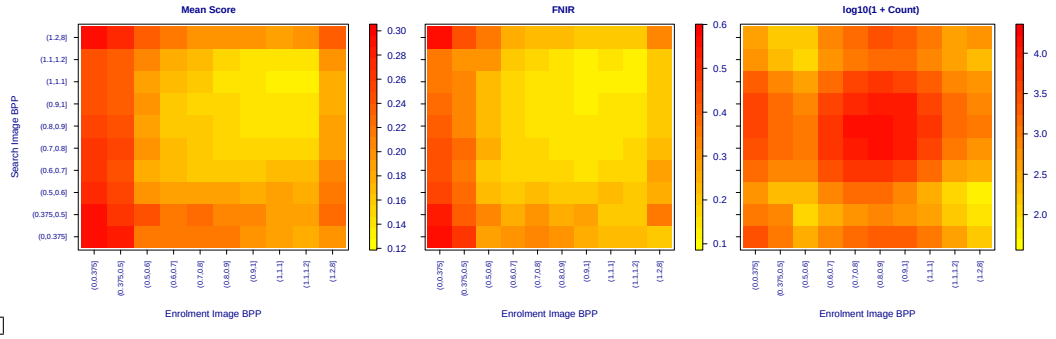

(a) Paired CRs, mate searches

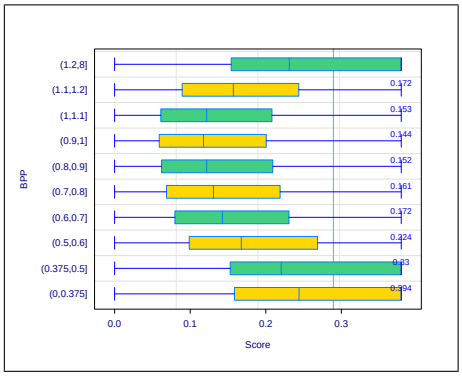

(b) Minimum CR, mate searches

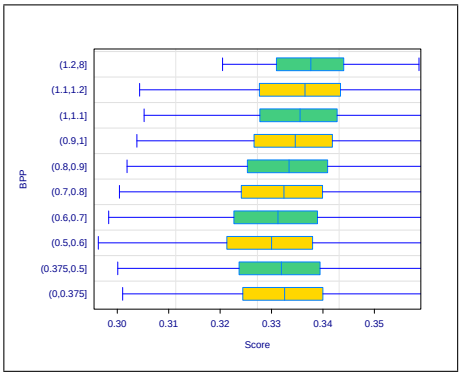

(c) Minimum CR, top nonmate

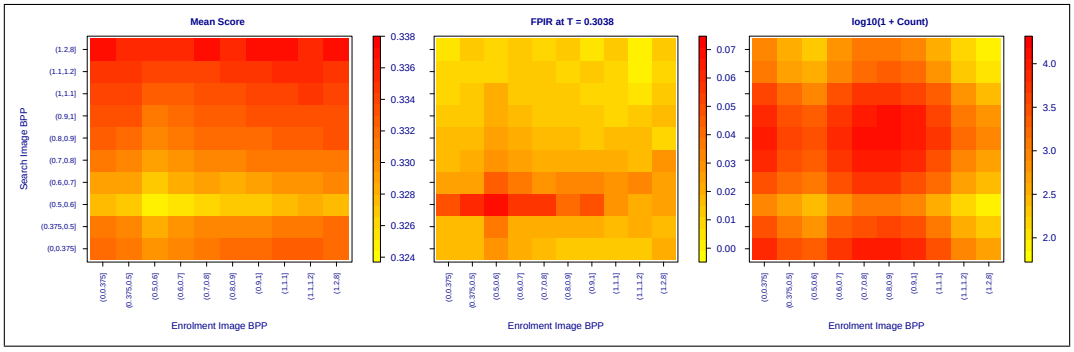

(d) Paired CRs, top nonmate

Figure 245: Effect of compression on accuracy for implementation W01B executing searches in an enrolled population of N = 1.6 million. The axes are labelled by binned values of the number of bits per pixel (BPP) implied by the JPEG filesize and the image dimensions. The lowest BPP bin is populated largely by the overly compressed 330x330 images. For mate searches, the three heatmaps give, respectively, the score, FNIR at FPIR = 0.0001, and the log of the count of images in each bin (3 corresponds to 1000). For nonmate searches, the threshold is set to give FPIR = 0.001 globally. The boxplots show the effect on the score, with the FNIR value annotated at right.

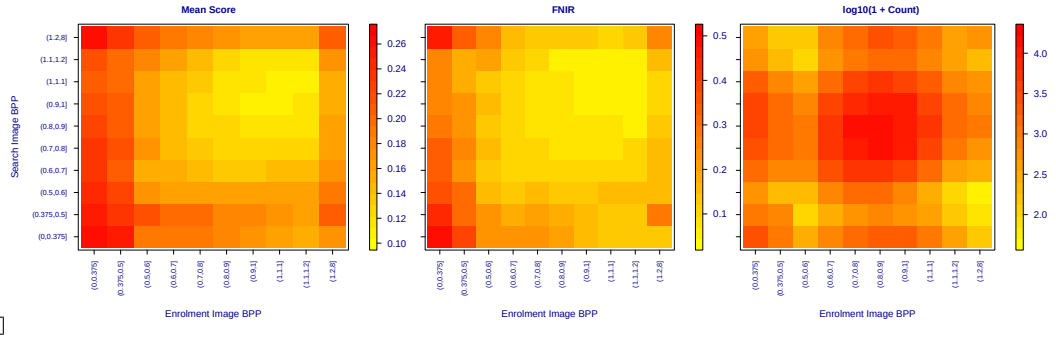

(a) Paired CRs, mate searches

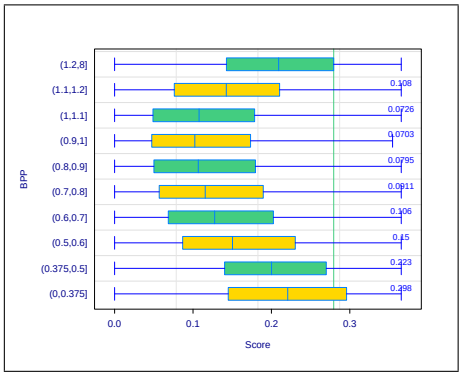

(b) Minimum CR, mate searches

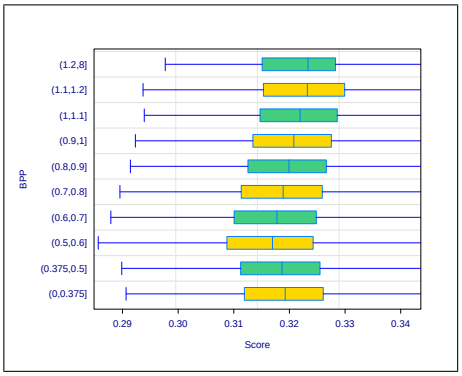

(c) Minimum CR, top nonmate

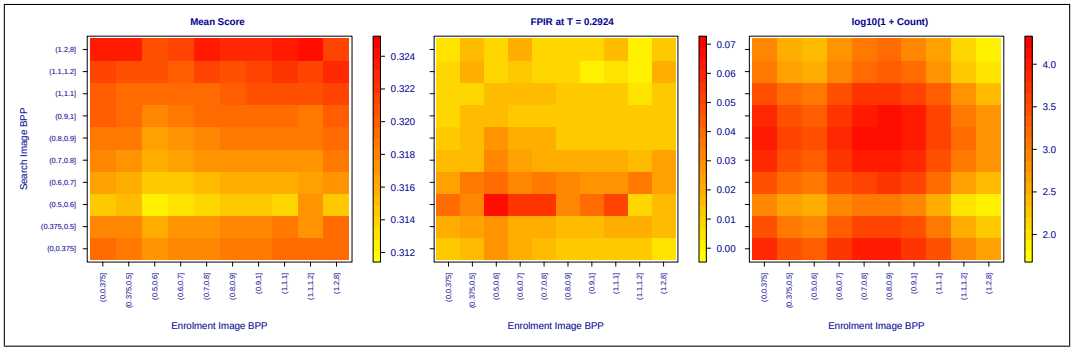

(d) Paired CRs, top nonmate

Figure 246: Effect of compression on accuracy for implementation W02A executing searches in an enrolled population of N = 1.6 million. The axes are labelled by binned values of the number of bits per pixel (BPP) implied by the JPEG filesize and the image dimensions. The lowest BPP bin is populated largely by the overly compressed 330x330 images. For mate searches, the three heatmaps give, respectively, the score, FNIR at FPIR = 0.0001, and the log of the count of images in each bin (3 corresponds to 1000). For nonmate searches, the threshold is set to give FPIR = 0.001 globally. The boxplots show the effect on the score, with the FNIR value annotated at right.

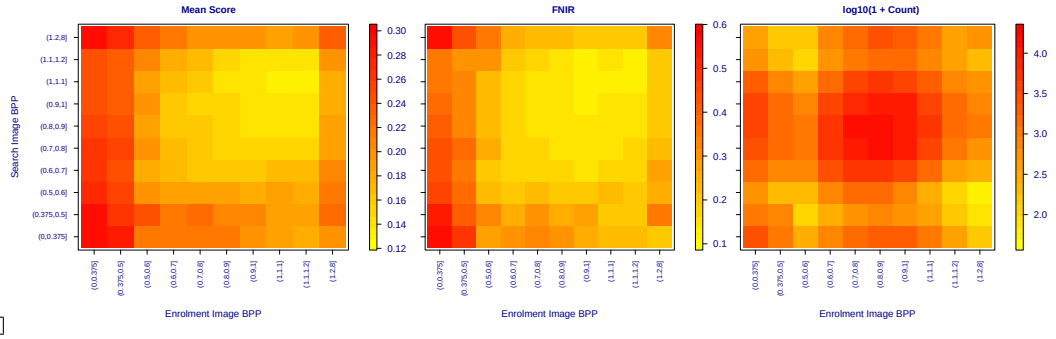

(a) Paired CRs, mate searches

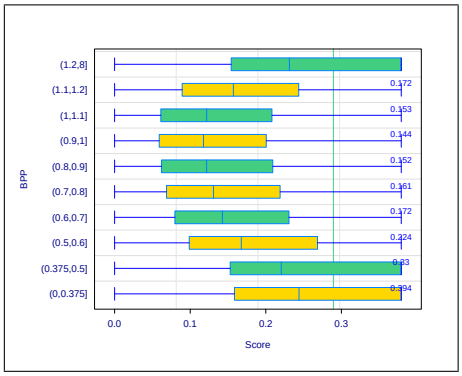

(b) Minimum CR, mate searches

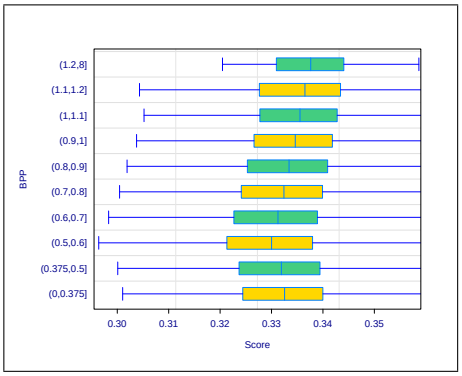

(c) Minimum CR, top nonmate

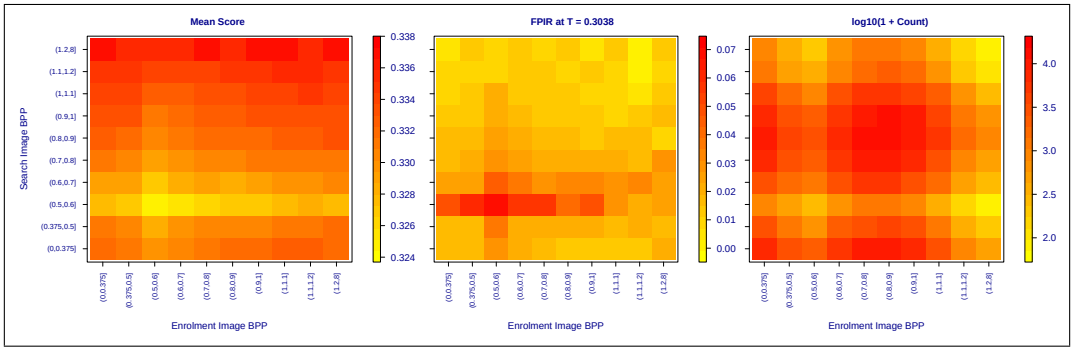

(d) Paired CRs, top nonmate

Figure 247: Effect of compression on accuracy for implementation W02B executing searches in an enrolled population of N = 1.6 million. The axes are labelled by binned values of the number of bits per pixel (BPP) implied by the JPEG filesize and the image dimensions. The lowest BPP bin is populated largely by the overly compressed 330x330 images. For mate searches, the three heatmaps give, respectively, the score, FNIR at FPIR = 0.0001, and the log of the count of images in each bin (3 corresponds to 1000). For nonmate searches, the threshold is set to give FPIR = 0.001 globally. The boxplots show the effect on the score, with the FNIR value annotated at right.

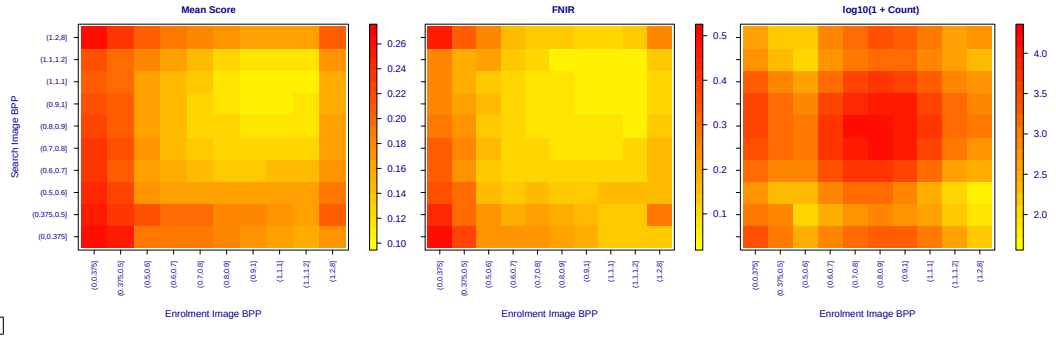

(a) Paired CRs, mate searches

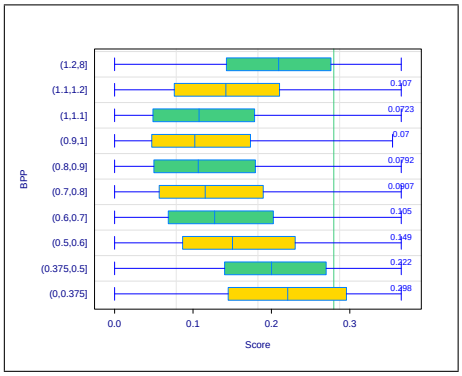

(b) Minimum CR, mate searches

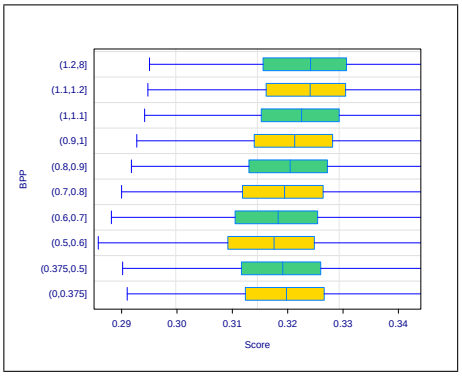

(c) Minimum CR, top nonmate

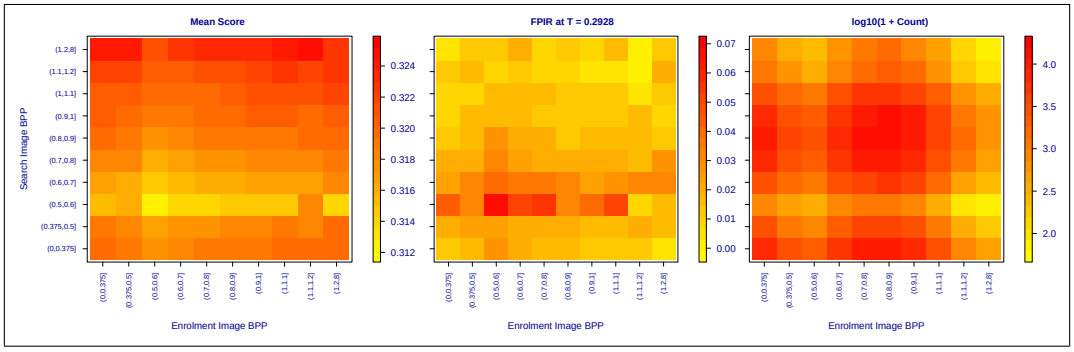

(d) Paired CRs, top nonmate

Figure 248: Effect of compression on accuracy for implementation W03A executing searches in an enrolled population of N = 1.6 million. The axes are labelled by binned values of the number of bits per pixel (BPP) implied by the JPEG filesize and the image dimensions. The lowest BPP bin is populated largely by the overly compressed 330x330 images. For mate searches, the three heatmaps give, respectively, the score, FNIR at FPIR = 0.0001, and the log of the count of images in each bin (3 corresponds to 1000). For nonmate searches, the threshold is set to give FPIR = 0.001 globally. The boxplots show the effect on the score, with the FNIR value annotated at right.

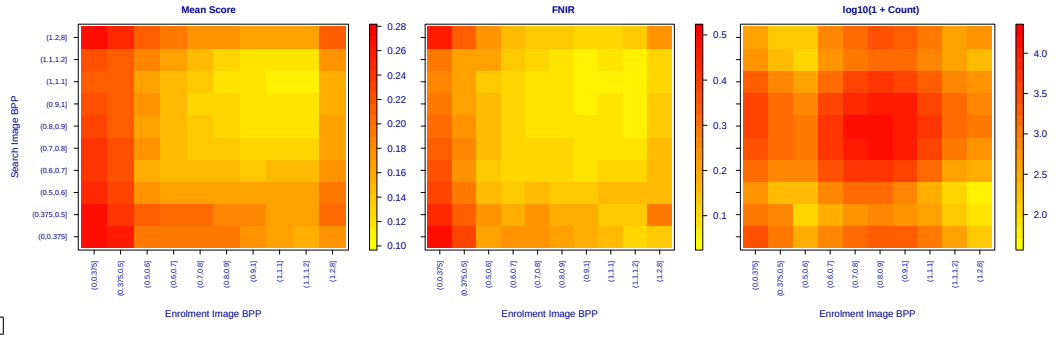

(a) Paired CRs, mate searches

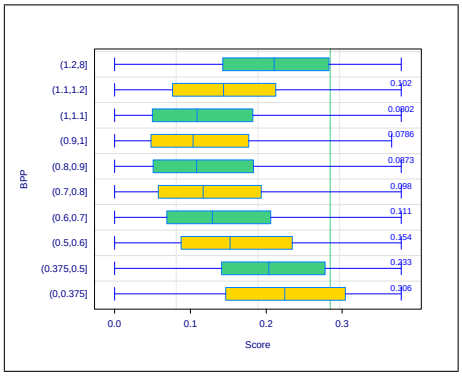

(b) Minimum CR, mate searches

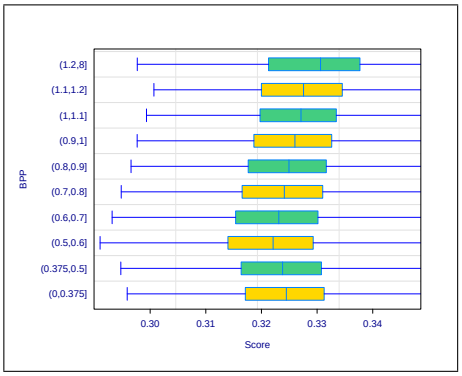

(c) Minimum CR, top nonmate

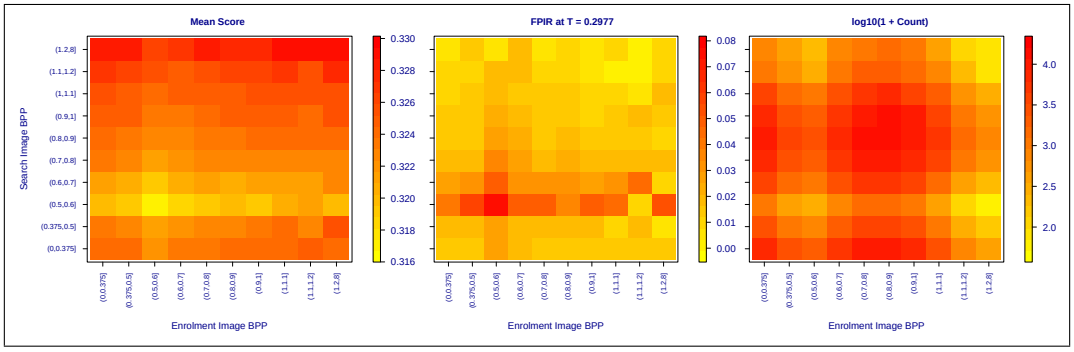

(d) Paired CRs, top nonmate

Figure 249: Effect of compression on accuracy for implementation W04A executing searches in an enrolled population of N = 1.6 million. The axes are labelled by binned values of the number of bits per pixel (BPP) implied by the JPEG filesize and the image dimensions. The lowest BPP bin is populated largely by the overly compressed 330x330 images. For mate searches, the three heatmaps give, respectively, the score, FNIR at FPIR = 0.0001, and the log of the count of images in each bin (3 corresponds to 1000). For nonmate searches, the threshold is set to give FPIR = 0.001 globally. The boxplots show the effect on the score, with the FNIR value annotated at right.

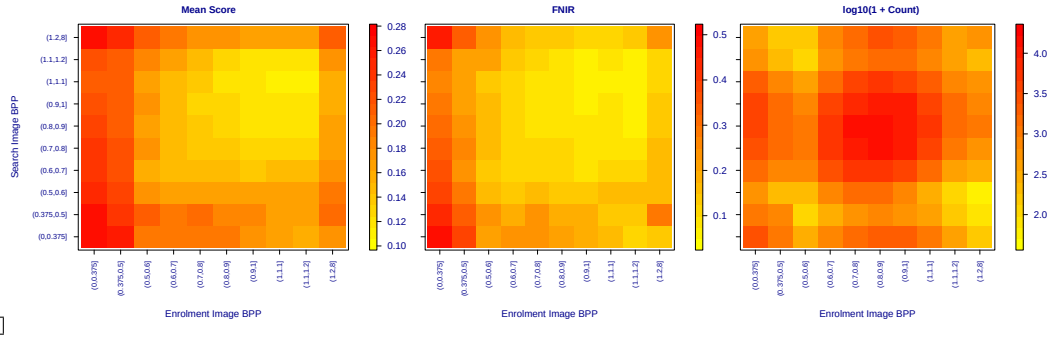

(a) Paired CRs, mate searches

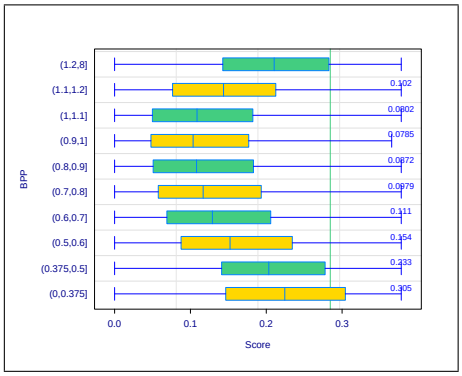

(b) Minimum CR, mate searches

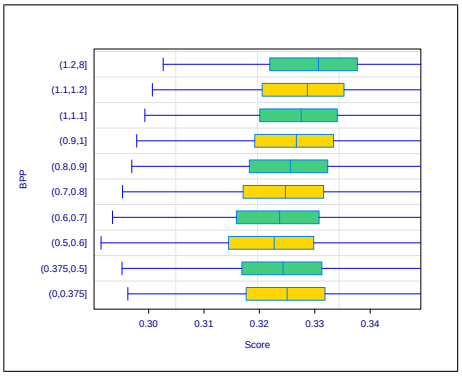

(c) Minimum CR, top nonmate

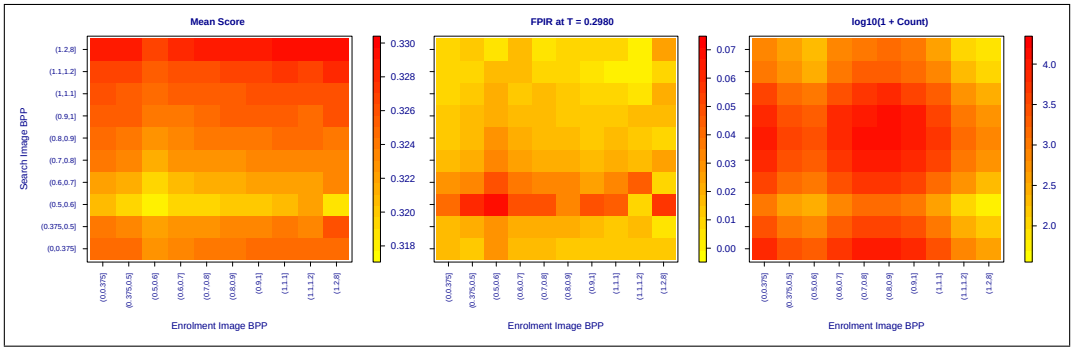

(d) Paired CRs, top nonmate

Figure 250: Effect of compression on accuracy for implementation W05A executing searches in an enrolled population of N = 1.6 million. The axes are labelled by binned values of the number of bits per pixel (BPP) implied by the JPEG filesize and the image dimensions. The lowest BPP bin is populated largely by the overly compressed 330x330 images. For mate searches, the three heatmaps give, respectively, the score, FNIR at FPIR = 0.0001, and the log of the count of images in each bin (3 corresponds to 1000). For nonmate searches, the threshold is set to give FPIR = 0.001 globally. The boxplots show the effect on the score, with the FNIR value annotated at right.

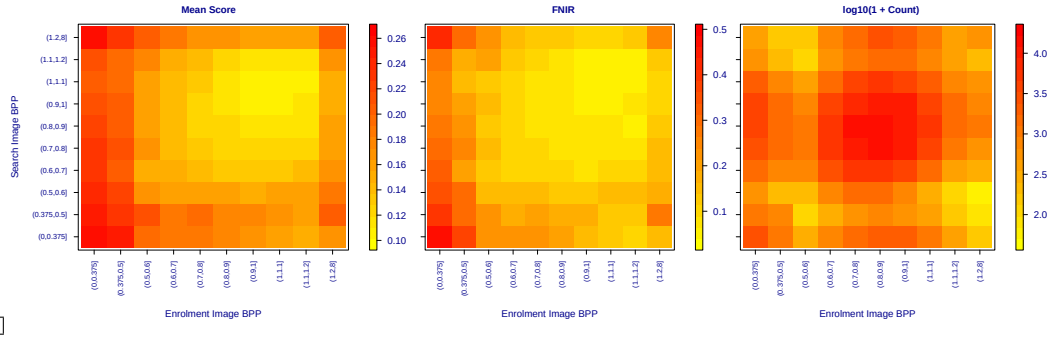

(a) Paired CRs, mate searches

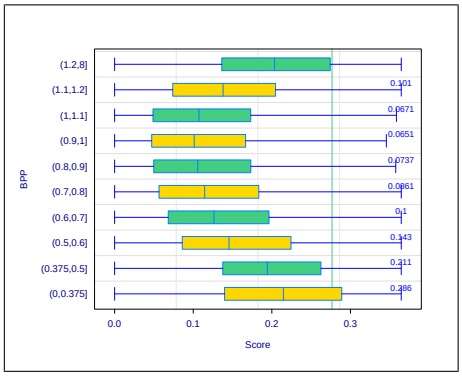

(b) Minimum CR, mate searches

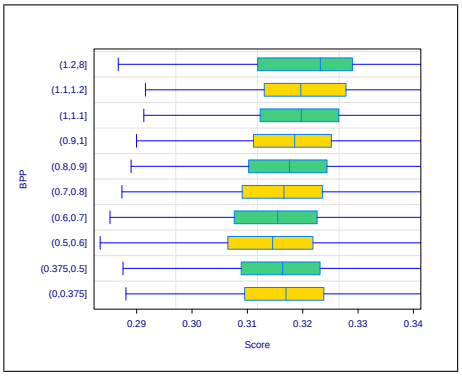

(c) Minimum CR, top nonmate

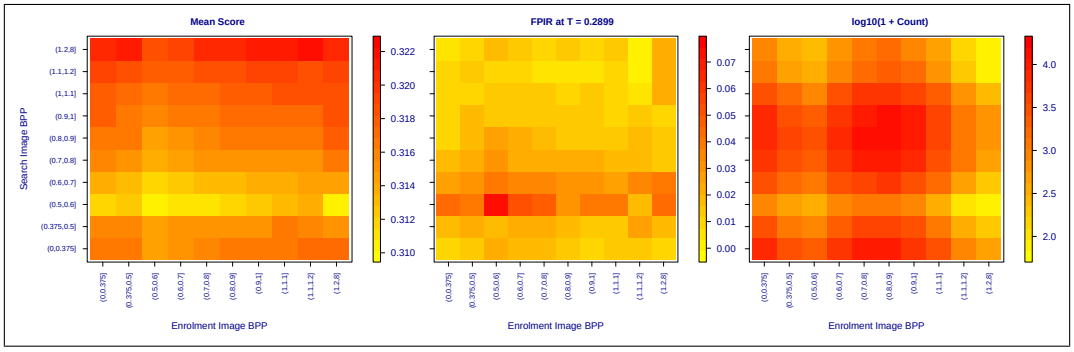

(d) Paired CRs, top nonmate

Figure 251: Effect of compression on accuracy for implementation W11A executing searches in an enrolled population of N = 1.6 million. The axes are labelled by binned values of the number of bits per pixel (BPP) implied by the JPEG filesize and the image dimensions. The lowest BPP bin is populated largely by the overly compressed 330x330 images. For mate searches, the three heatmaps give, respectively, the score, FNIR at FPIR = 0.0001, and the log of the count of images in each bin (3 corresponds to 1000). For nonmate searches, the threshold is set to give FPIR = 0.001 globally. The boxplots show the effect on the score, with the FNIR value annotated at right.

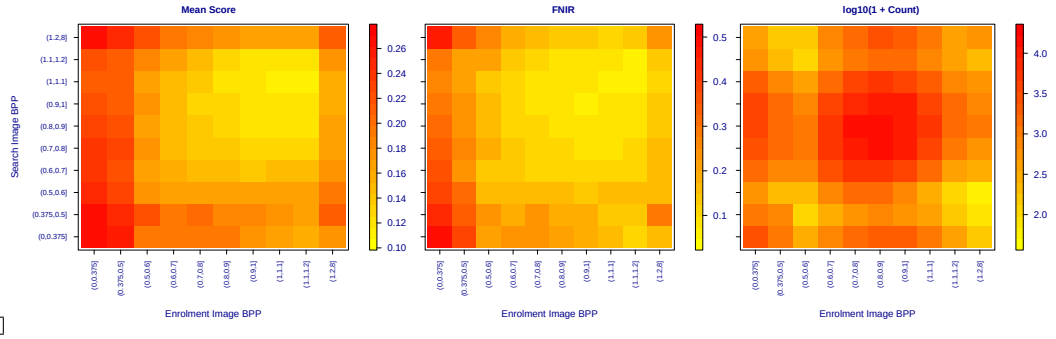

(a) Paired CRs, mate searches

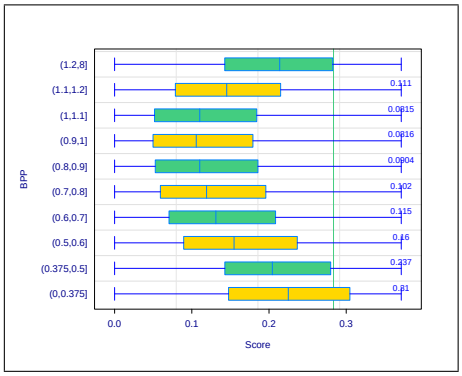

(b) Minimum CR, mate searches

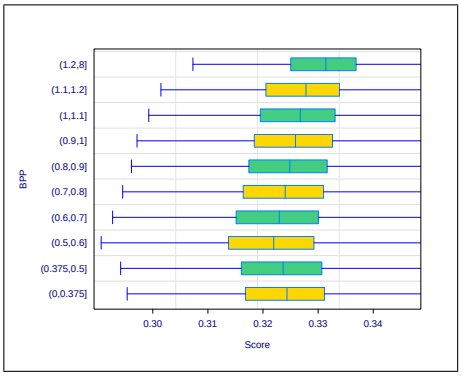

(c) Minimum CR, top nonmate

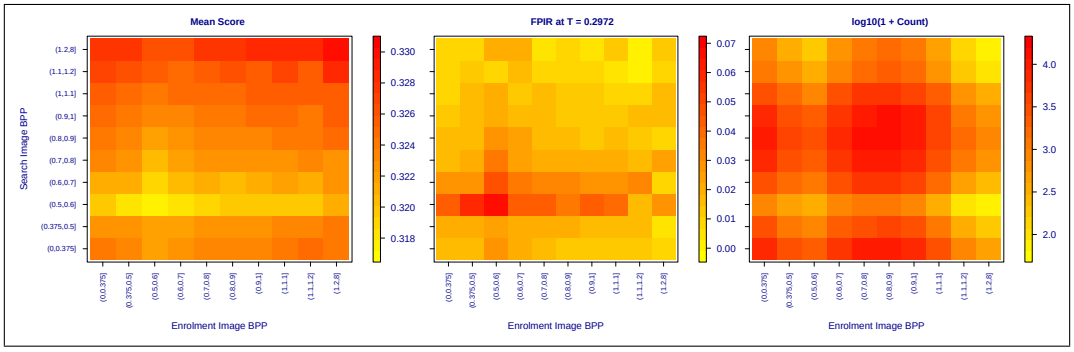

(d) Paired CRs, top nonmate

Figure 252: Effect of compression on accuracy for implementation W11B executing searches in an enrolled population of N = 1.6 million. The axes are labelled by binned values of the number of bits per pixel (BPP) implied by the JPEG filesize and the image dimensions. The lowest BPP bin is populated largely by the overly compressed 330x330 images. For mate searches, the three heatmaps give, respectively, the score, FNIR at FPIR = 0.0001, and the log of the count of images in each bin (3 corresponds to 1000). For nonmate searches, the threshold is set to give FPIR = 0.001 globally. The boxplots show the effect on the score, with the FNIR value annotated at right.

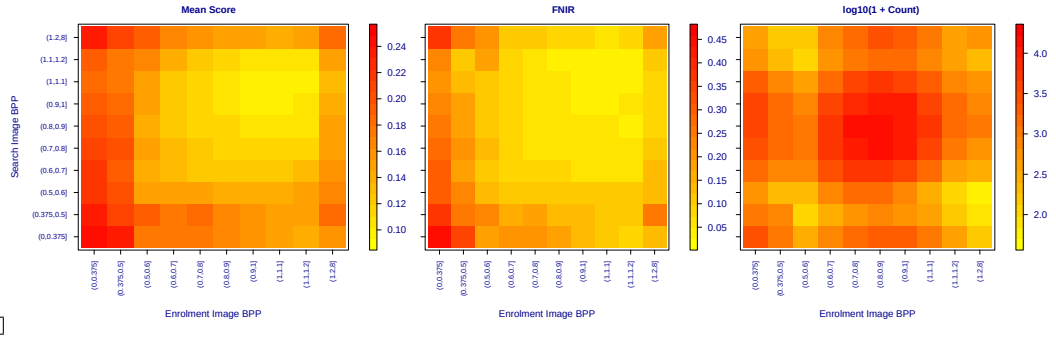

(a) Paired CRs, mate searches

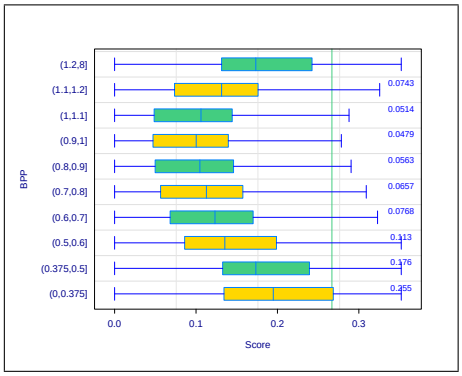

(b) Minimum CR, mate searches

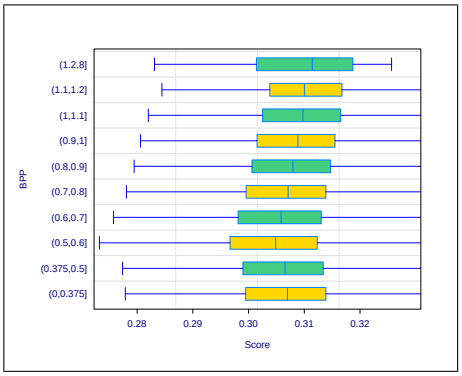

(c) Minimum CR, top nonmate

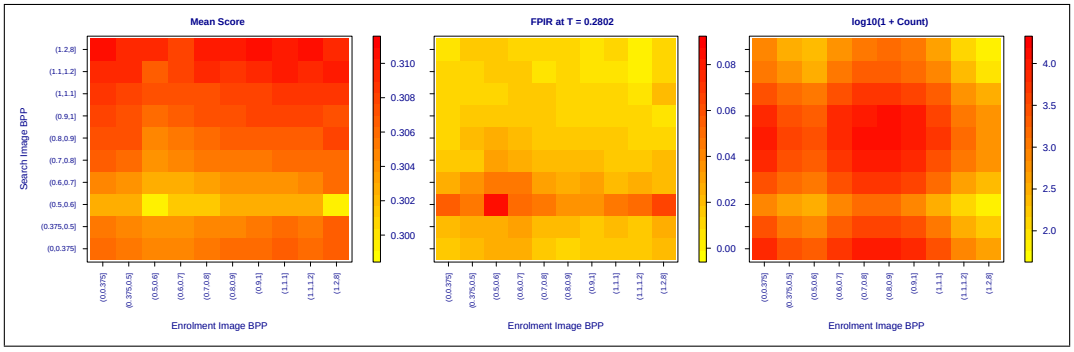

(d) Paired CRs, top nonmate

Figure 253: Effect of compression on accuracy for implementation W12A executing searches in an enrolled population of N = 1.6 million. The axes are labelled by binned values of the number of bits per pixel (BPP) implied by the JPEG filesize and the image dimensions. The lowest BPP bin is populated largely by the overly compressed 330x330 images. For mate searches, the three heatmaps give, respectively, the score, FNIR at FPIR = 0.0001, and the log of the count of images in each bin (3 corresponds to 1000). For nonmate searches, the threshold is set to give FPIR = 0.001 globally. The boxplots show the effect on the score, with the FNIR value annotated at right.

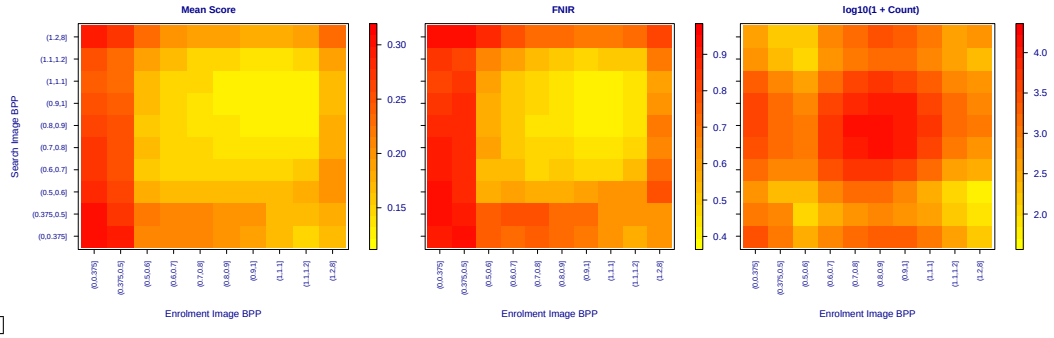

(a) Paired CRs, mate searches

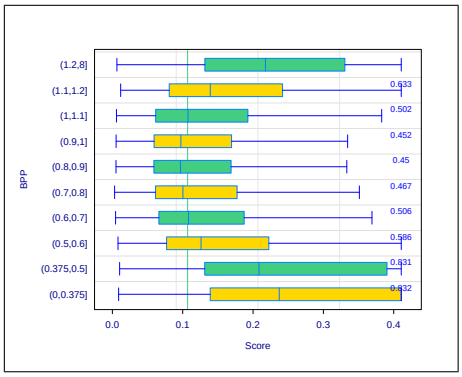

(b) Minimum CR, mate searches

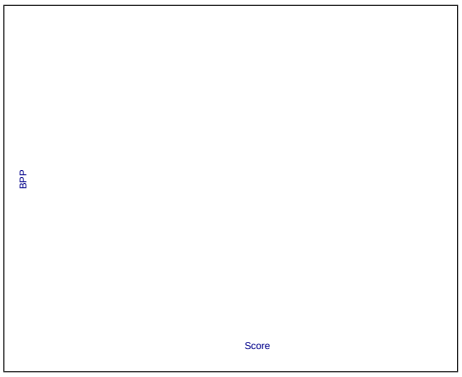

(c) Minimum CR, top nonmate

Figure 254: Effect of compression on accuracy for implementation X02A executing searches in an enrolled population of N = 1.6 million. The axes are labelled by binned values of the number of bits per pixel (BPP) implied by the JPEG filesize and the image dimensions. The lowest BPP bin is populated largely by the overly compressed 330x330 images. For mate searches, the three heatmaps give, respectively, the score, FNIR at FPIR = 0.0001, and the log of the count of images in each bin (3 corresponds to 1000). For nonmate searches, the threshold is set to give FPIR = 0.001 globally. The boxplots show the effect on the score, with the FNIR value annotated at right.

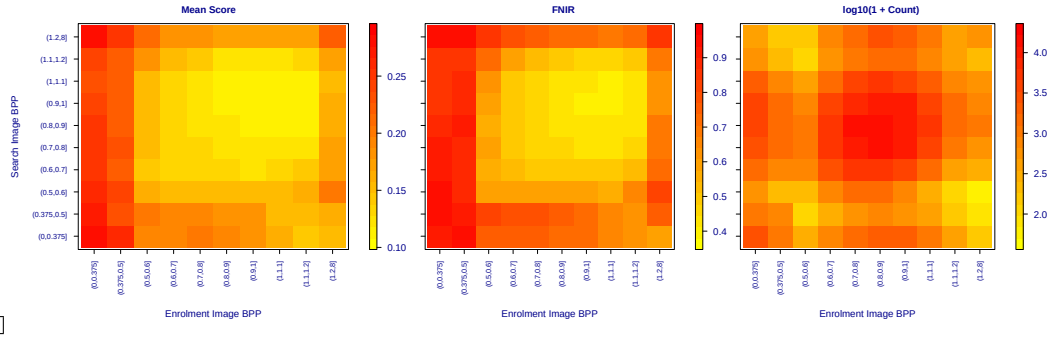

(a) Paired CRs, mate searches

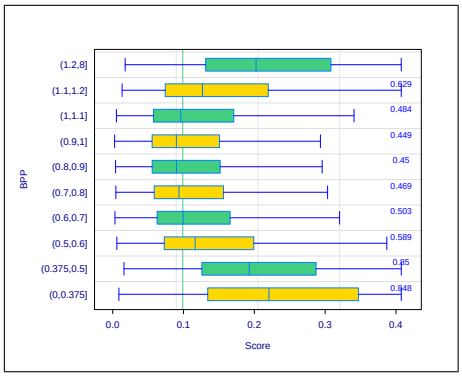

(b) Minimum CR, mate searches

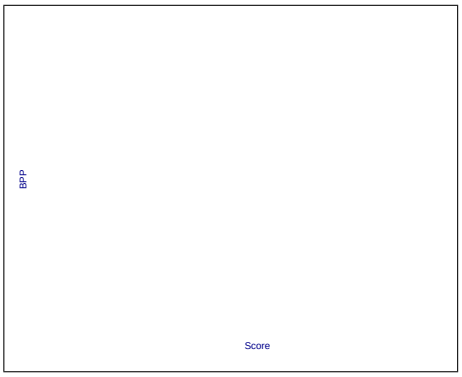

(c) Minimum CR, top nonmate

Figure 255: Effect of compression on accuracy for implementation X03A executing searches in an enrolled population of N = 1.6 million. The axes are labelled by binned values of the number of bits per pixel (BPP) implied by the JPEG filesize and the image dimensions. The lowest BPP bin is populated largely by the overly compressed 330x330 images. For mate searches, the three heatmaps give, respectively, the score, FNIR at FPIR = 0.0001, and the log of the count of images in each bin (3 corresponds to 1000). For nonmate searches, the threshold is set to give FPIR = 0.001 globally. The boxplots show the effect on the score, with the FNIR value annotated at right.

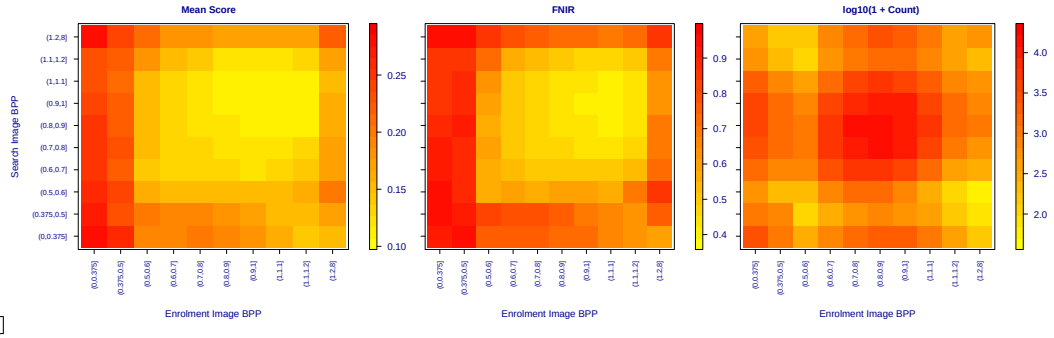

(a) Paired CRs, mate searches

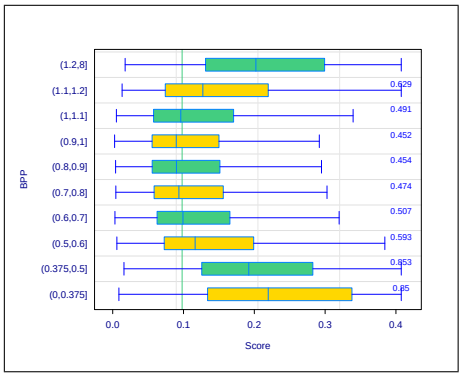

(b) Minimum CR, mate searches

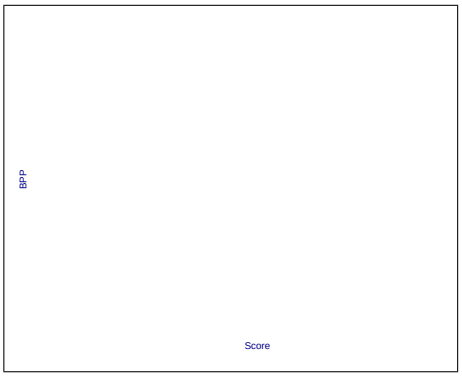

(c) Minimum CR, top nonmate

Figure 256: Effect of compression on accuracy for implementation X04A executing searches in an enrolled population of N = 1.6 million. The axes are labelled by binned values of the number of bits per pixel (BPP) implied by the JPEG filesize and the image dimensions. The lowest BPP bin is populated largely by the overly compressed 330x330 images. For mate searches, the three heatmaps give, respectively, the score, FNIR at FPIR = 0.0001, and the log of the count of images in each bin (3 corresponds to 1000). For nonmate searches, the threshold is set to give FPIR = 0.001 globally. The boxplots show the effect on the score, with the FNIR value annotated at right.

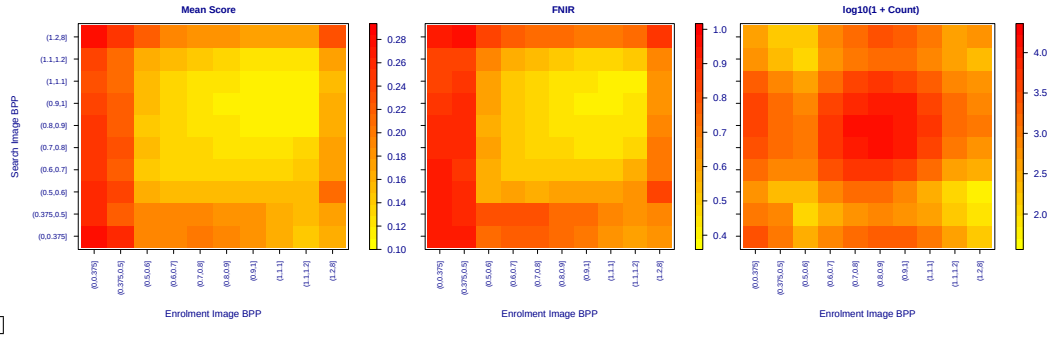

(a) Paired CRs, mate searches

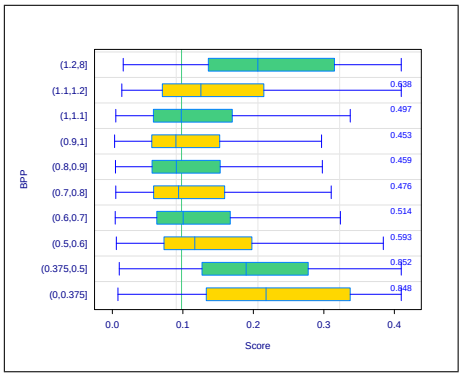

(b) Minimum CR, mate searches

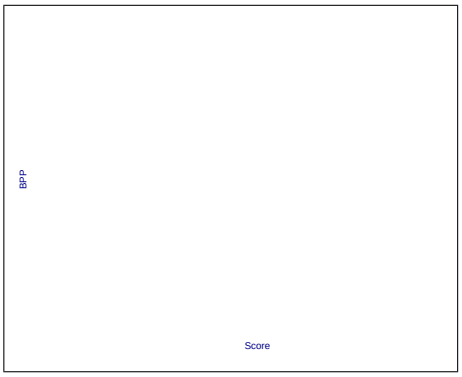

(c) Minimum CR, top nonmate

Figure 257: Effect of compression on accuracy for implementation X11A executing searches in an enrolled population of N = 1.6 million. The axes are labelled by binned values of the number of bits per pixel (BPP) implied by the JPEG filesize and the image dimensions. The lowest BPP bin is populated largely by the overly compressed 330x330 images. For mate searches, the three heatmaps give, respectively, the score, FNIR at FPIR = 0.0001, and the log of the count of images in each bin (3 corresponds to 1000). For nonmate searches, the threshold is set to give FPIR = 0.001 globally. The boxplots show the effect on the score, with the FNIR value annotated at right.

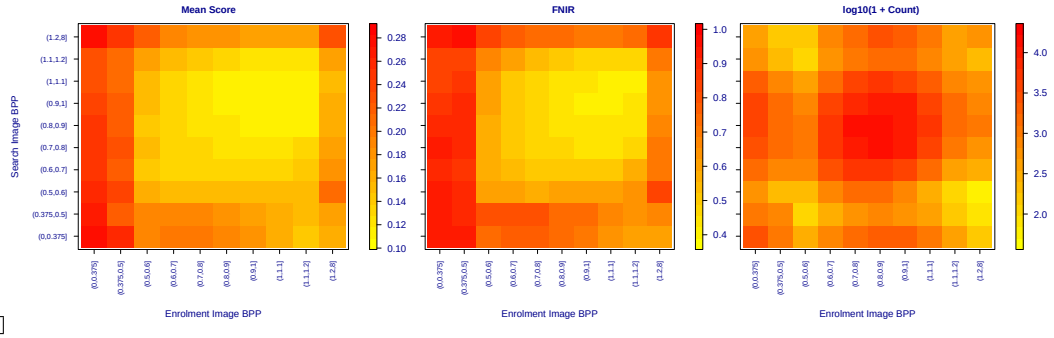

(a) Paired CRs, mate searches

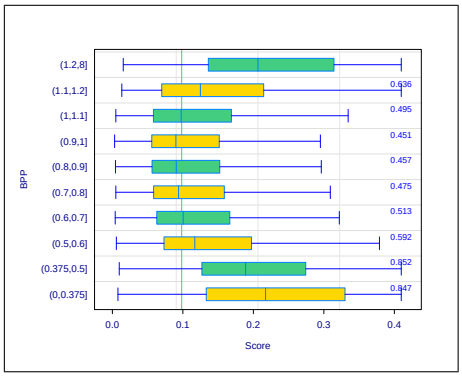

(b) Minimum CR, mate searches

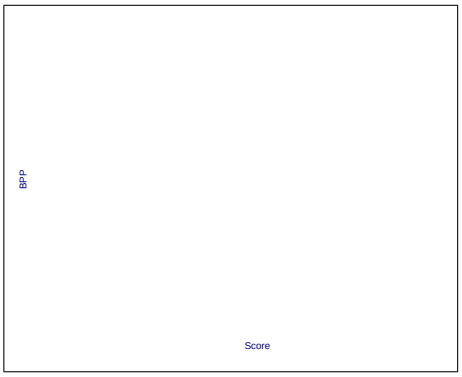

(c) Minimum CR, top nonmate

Figure 258: Effect of compression on accuracy for implementation X11B executing searches in an enrolled population of N = 1.6 million. The axes are labelled by binned values of the number of bits per pixel (BPP) implied by the JPEG filesize and the image dimensions. The lowest BPP bin is populated largely by the overly compressed 330x330 images. For mate searches, the three heatmaps give, respectively, the score, FNIR at FPIR = 0.0001, and the log of the count of images in each bin (3 corresponds to 1000). For nonmate searches, the threshold is set to give FPIR = 0.001 globally. The boxplots show the effect on the score, with the FNIR value annotated at right.

Figure 259: Effect of compression on accuracy for implementation Y02A executing searches in an enrolled population of N = 1.6 million. The axes are labelled by binned values of the number of bits per pixel (BPP) implied by the JPEG filesize and the image dimensions. The lowest BPP bin is populated largely by the overly compressed 330x330 images. For mate searches, the three heatmaps give, respectively, the score, FNIR at FPIR = 0.0001, and the log of the count of images in each bin (3 corresponds to 1000). For nonmate searches, the threshold is set to give FPIR = 0.001 globally. The boxplots show the effect on the score, with the FNIR value annotated at right.

Figure 260: Effect of compression on accuracy for implementation Y02B executing searches in an enrolled population of N = 1.6 million. The axes are labelled by binned values of the number of bits per pixel (BPP) implied by the JPEG filesize and the image dimensions. The lowest BPP bin is populated largely by the overly compressed 330x330 images. For mate searches, the three heatmaps give, respectively, the score, FNIR at FPIR = 0.0001, and the log of the count of images in each bin (3 corresponds to 1000). For nonmate searches, the threshold is set to give FPIR = 0.001 globally. The boxplots show the effect on the score, with the FNIR value annotated at right.

Figure 261: Effect of compression on accuracy for implementation Y03A executing searches in an enrolled population of N = 1.6 million. The axes are labelled by binned values of the number of bits per pixel (BPP) implied by the JPEG filesize and the image dimensions. The lowest BPP bin is populated largely by the overly compressed 330x330 images. For mate searches, the three heatmaps give, respectively, the score, FNIR at FPIR = 0.0001, and the log of the count of images in each bin (3 corresponds to 1000). For nonmate searches, the threshold is set to give FPIR = 0.001 globally. The boxplots show the effect on the score, with the FNIR value annotated at right.

Figure 262: Effect of compression on accuracy for implementation Y03B executing searches in an enrolled population of N = 1.6 million. The axes are labelled by binned values of the number of bits per pixel (BPP) implied by the JPEG filesize and the image dimensions. The lowest BPP bin is populated largely by the overly compressed 330x330 images. For mate searches, the three heatmaps give, respectively, the score, FNIR at FPIR = 0.0001, and the log of the count of images in each bin (3 corresponds to 1000). For nonmate searches, the threshold is set to give FPIR = 0.001 globally. The boxplots show the effect on the score, with the FNIR value annotated at right.

Figure 263: Heatmaps for implementation I01A executing mate searches in an enrolled population of N = 1.6 million. The radius images are binned by into twelve quantiles spanning $[0, 1]$. The dilation values are cut into ranges bounded by: $(0, 0.2, 0.28, 0.34, 0.40, 0.46, 0.52, 0.58, 1)$. The pathologically compressed 330x330 images are excluded from this analysis.

Appendix F: Effect of Pupil Dilation and Constriction

Figure 264: Miss rate statistics for implementation I01A executing mate searches in an enrolled population of N = 1.6 million. The figures plots FNIR at FPIR = 0.0001 versus the IREX I metric for dilation consistency $(1 - \max(D_1, D_2))/(1 - \min(D_1, D_2))$ where D_i is pupil-iris radius ratio, and the subscripts refer to the mated enrollment and search image. The pathologically compressed 330x330 images are excluded from this analysis. The second figure breaks out dilation effects for interoperating camera pairs, CM and L1.

Figure 265: Heatmaps for implementation I02A executing mate searches in an enrolled population of N = 1.6 million. The radius images are binned by into twelve quantiles spanning $[0, 1]$. The dilation values are cut into ranges bounded by: $(0, 0.2, 0.28, 0.34, 0.40, 0.46, 0.52, 0.58, 1)$. The pathologically compressed 330x330 images are excluded from this analysis.

Heatmaps for implementation I01A executing mate searches in an enrolled population of N = 1.6 million.

Figure 266: Miss rate statistics for implementation I02A executing mate searches in an enrolled population of N = 1.6 million. The figures plots FNIR at FPIR = 0.0001 versus the IREX I metric for dilation consistency $(1 - \max(D_1, D_2))/(1 - \min(D_1, D_2))$ where D_i is pupil-iris radius ratio, and the subscripts refer to the mated enrollment and search image. The pathologically compressed 330x330 images are excluded from this analysis. The second figure breaks out dilation effects for interoperating camera pairs, CM and L1.

Figure 267: Heatmaps for implementation J01A executing mate searches in an enrolled population of N = 1.6 million. The radius images are binned by into twelve quantiles spanning $[0, 1]$. The dilation values are cut into ranges bounded by: $(0, 0.2, 0.28, 0.34, 0.40, 0.46, 0.52, 0.58, 1)$. The pathologically compressed 330x330 images are excluded from this analysis.

Heatmaps for implementation I02A executing mate searches in an enrolled population of N = 1.6 million.

Figure 268: Miss rate statistics for implementation J01A executing mate searches in an enrolled population of N = 1.6 million. The figures plots FNIR at FPIR = 0.0001 versus the IREX I metric for dilation consistency $(1 - \max(D_1, D_2))/(1 - \min(D_1, D_2))$ where D_i is pupil-iris radius ratio, and the subscripts refer to the mated enrollment and search image. The pathologically compressed 330x330 images are excluded from this analysis. The second figure breaks out dilation effects for interoperating camera pairs, CM and L1.

Figure 269: Heatmaps for implementation J02A executing mate searches in an enrolled population of N = 1.6 million. The radius images are binned by into twelve quantiles spanning $[0, 1]$. The dilation values are cut into ranges bounded by: $(0, 0.2, 0.28, 0.34, 0.40, 0.46, 0.52, 0.58, 1)$. The pathologically compressed 330x330 images are excluded from this analysis.

Heatmaps for implementation J01A executing mate searches in an enrolled population of N = 1.6 million.

Figure 270: Miss rate statistics for implementation J02A executing mate searches in an enrolled population of N = 1.6 million. The figures plots FNIR at FPIR = 0.0001 versus the IREX I metric for dilation consistency $(1 - \max(D_1, D_2))/(1 - \min(D_1, D_2))$ where D_i is pupil-iris radius ratio, and the subscripts refer to the mated enrollment and search image. The pathologically compressed 330x330 images are excluded from this analysis. The second figure breaks out dilation effects for interoperating camera pairs, CM and L1.

Heatmaps for implementation J02A executing mate searches in an enrolled population of N = 1.6 million.

(a) Iris radius: Dis-similarity Score, Miss Rate, $\log_{10}(1+\text{Count})$

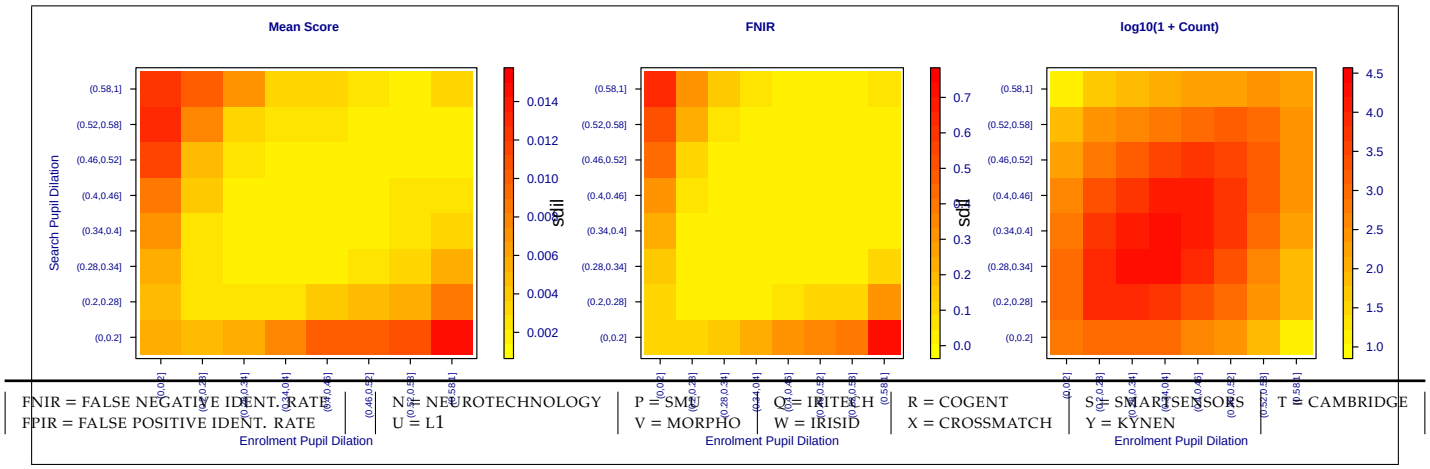

(b) Mate Dilation: Dis-similarity Score, Miss Rate, $\log_{10}(1+\text{Count})$

Heatmaps for implementation N02A executing mate searches in an enrolled population of N = 1.6 million.

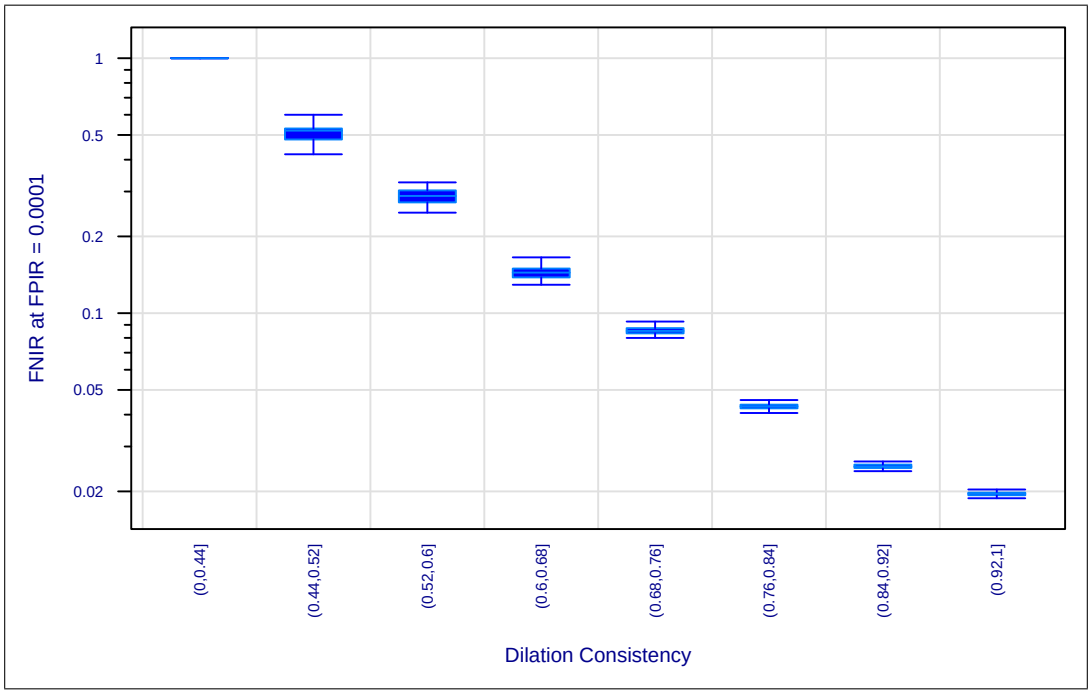

(a) Boxplot, all images

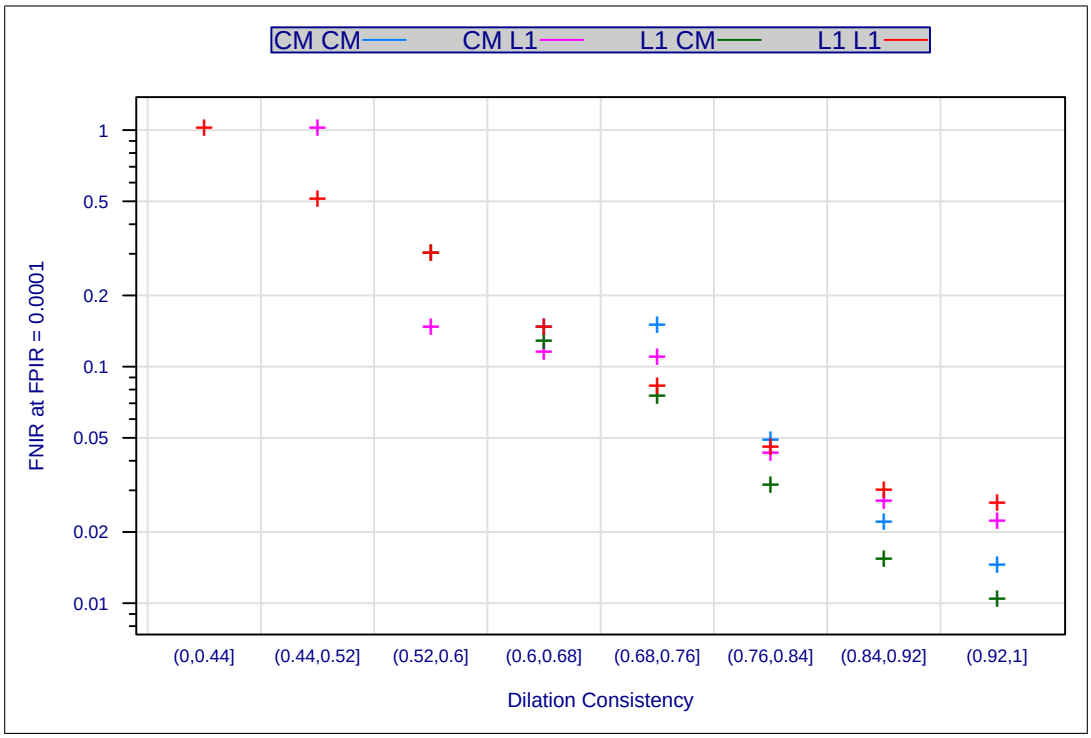

(b) Mean, L1 and CM images

Figure 272: Miss rate statistics for implementation N02A executing mate searches in an enrolled population of N = 1.6 million. The figures plots FNIR at FPIR = 0.0001 versus the IREX I metric for dilation consistency $(1 - \max(D_1, D_2))/(1 - \min(D_1, D_2))$ where D_i is pupil-iris radius ratio, and the subscripts refer to the mated enrollment and search image. The pathologically compressed 330x330 images are excluded from this analysis. The second figure breaks out dilation effects for interoperating camera pairs, CM and L1.

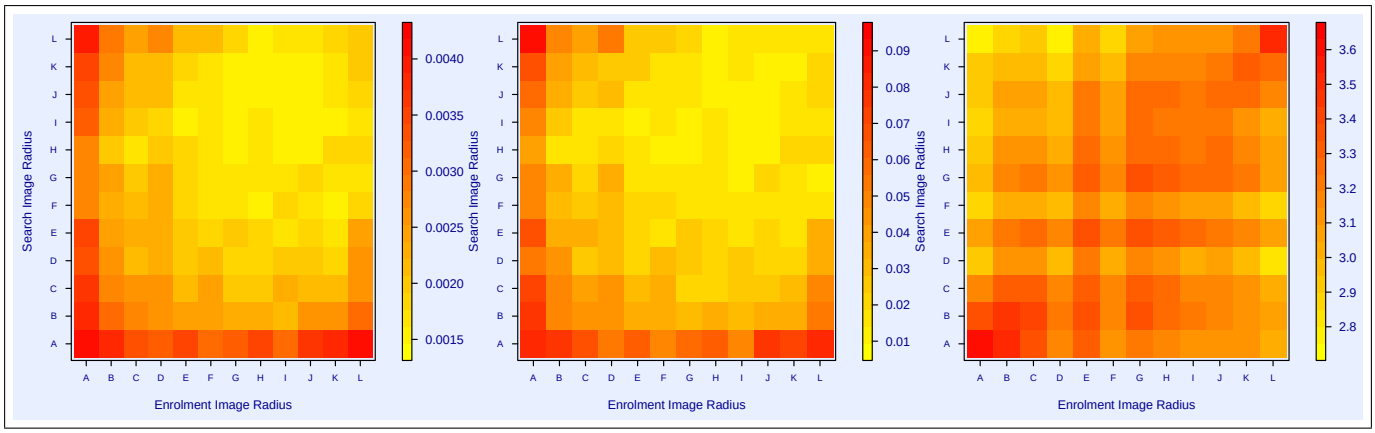

(a) Iris radius: Dis-similarity Score, Miss Rate, $\log_{10}(1+\text{Count})$

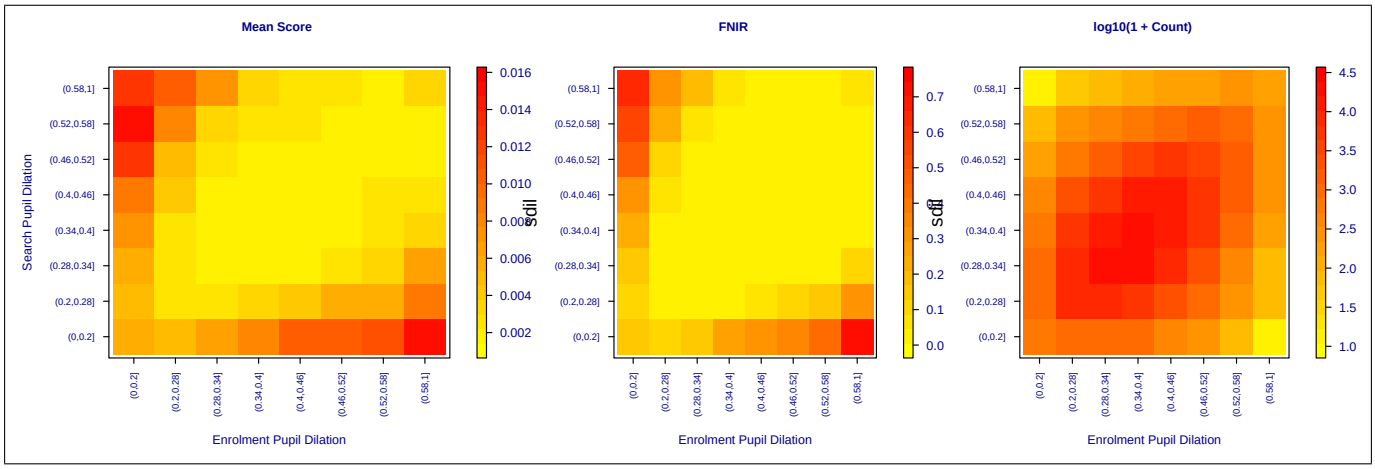

(b) Mate Dilation: Dis-similarity Score, Miss Rate, $\log_{10}(1+\text{Count})$

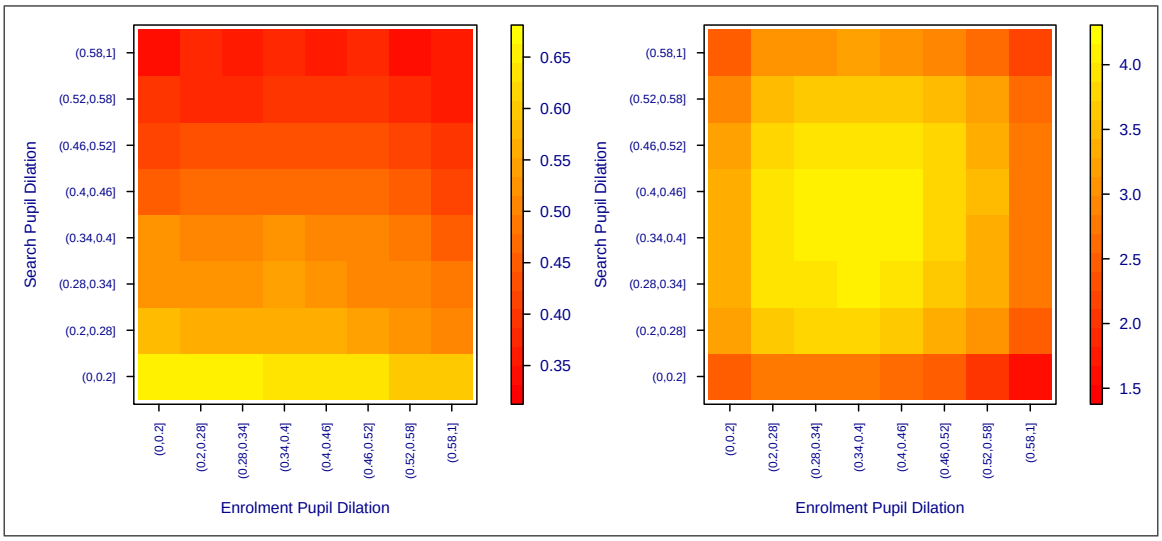

(c) Nonmate Dilation, Dis-similarity Score, Miss Rate, $\log_{10}(1+\text{Count})$

Figure 273: Heatmaps for implementation N02B executing mate searches in an enrolled population of N = 1.6 million. The radius images are binned by into twelve quantiles spanning $[0, 1]$. The dilation values are cut into ranges bounded by: $(0, 0.2, 0.28, 0.34, 0.40, 0.46, 0.52, 0.58, 1)$. The pathologically compressed 330x330 images are excluded from this analysis.

Heatmaps for implementation N02B executing mate searches in an enrolled population of N = 1.6 million.

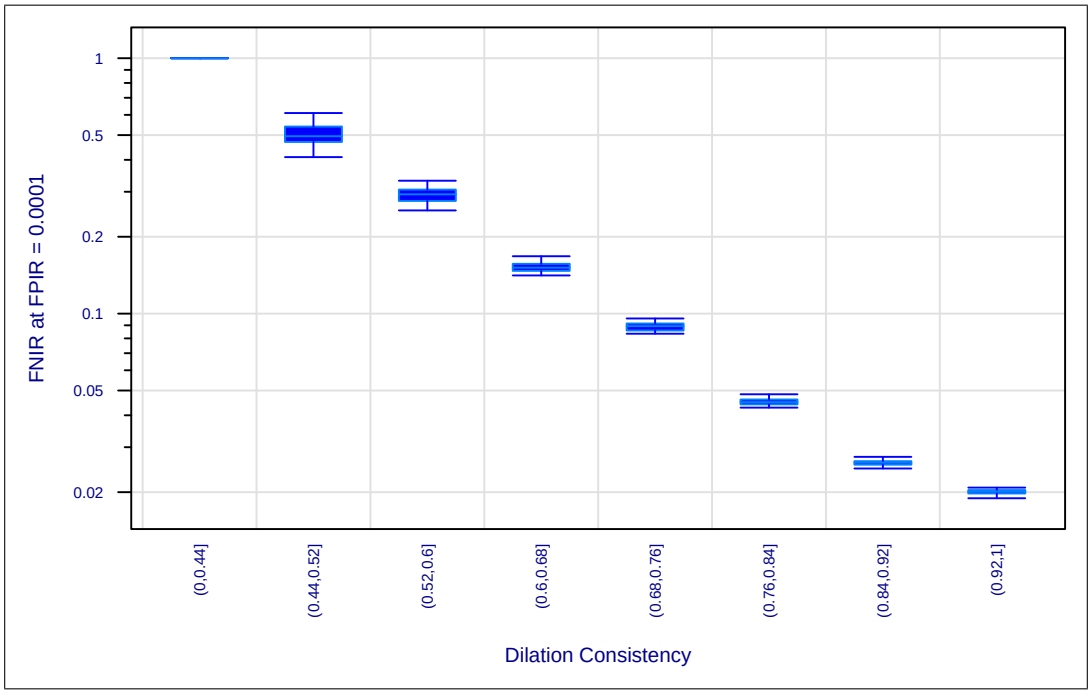

(a) Boxplot, all images

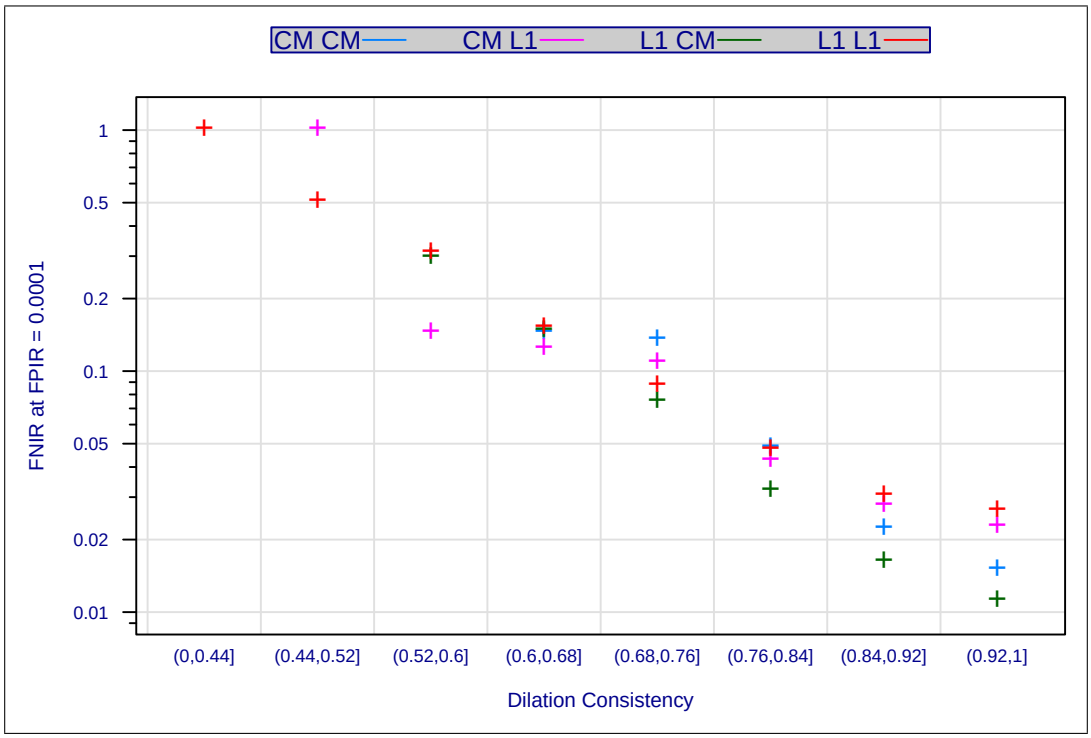

(b) Mean, L1 and CM images

Figure 274: Miss rate statistics for implementation N02B executing mate searches in an enrolled population of N = 1.6 million. The figures plots FNIR at FPIR = 0.0001 versus the IREX I metric for dilation consistency $(1 - \max(D_1, D_2))/(1 - \min(D_1, D_2))$ where D_i is pupil-iris radius ratio, and the subscripts refer to the mated enrollment and search image. The pathologically compressed 330x330 images are excluded from this analysis. The second figure breaks out dilation effects for interoperating camera pairs, CM and L1.

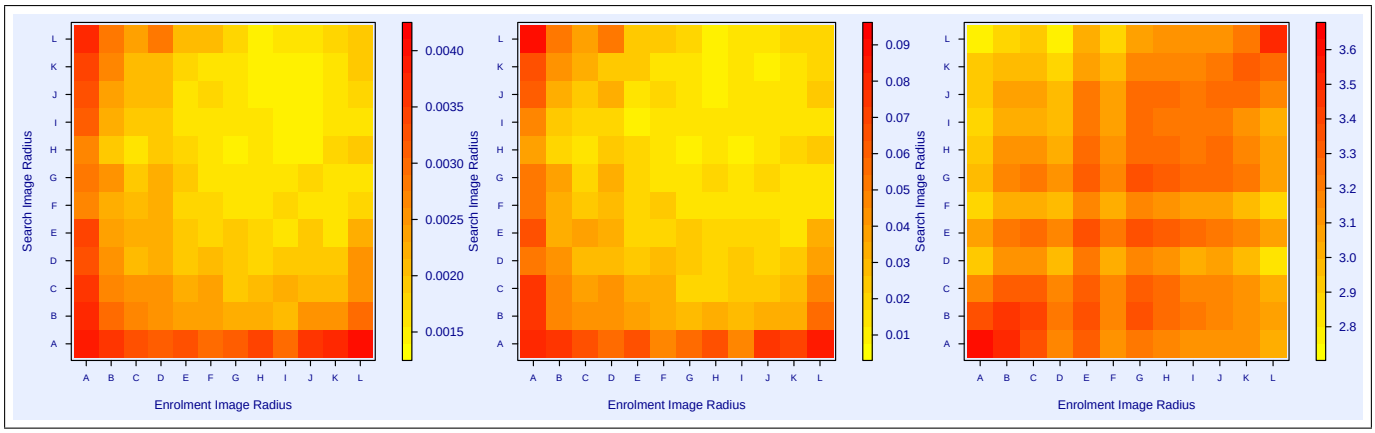

(a) Iris radius: Dis-similarity Score, Miss Rate, $\log_{10}(1+\text{Count})$

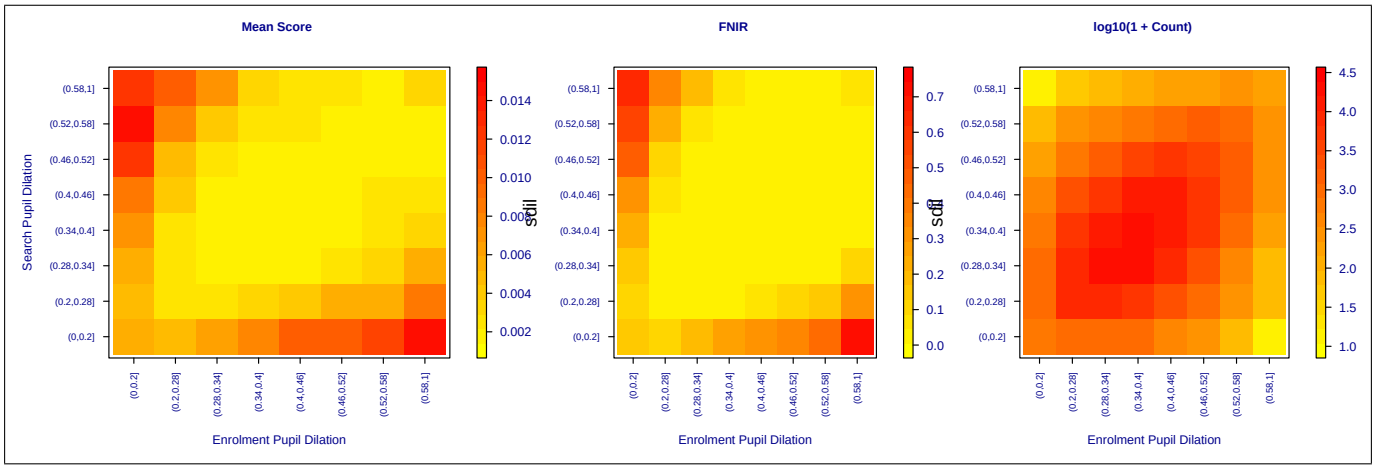

(b) Mate Dilation: Dis-similarity Score, Miss Rate, $\log_{10}(1+\text{Count})$

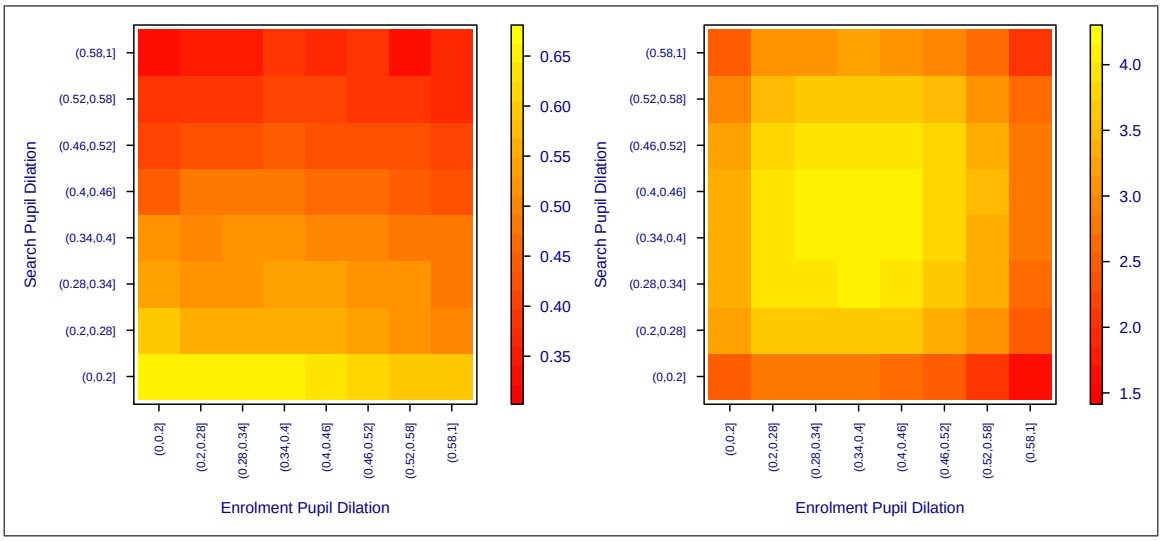

(c) Nonmate Dilation, Dis-similarity Score, Miss Rate, $\log_{10}(1+\text{Count})$

Figure 275: Heatmaps for implementation N03A executing mate searches in an enrolled population of N = 1.6 million. The radius images are binned by into twelve quantiles spanning $[0, 1]$. The dilation values are cut into ranges bounded by: $(0, 0.2, 0.28, 0.34, 0.40, 0.46, 0.52, 0.58, 1)$. The pathologically compressed 330x330 images are excluded from this analysis.

Heatmaps for implementation N03A executing mate searches in an enrolled population of N = 1.6 million.

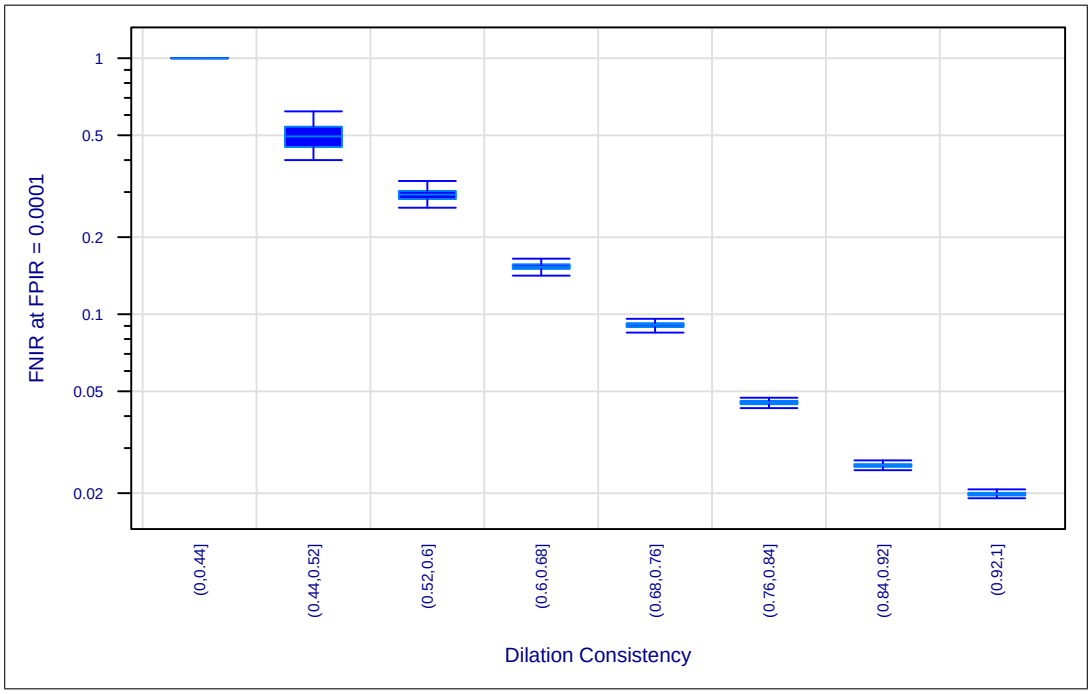

(a) Boxplot, all images

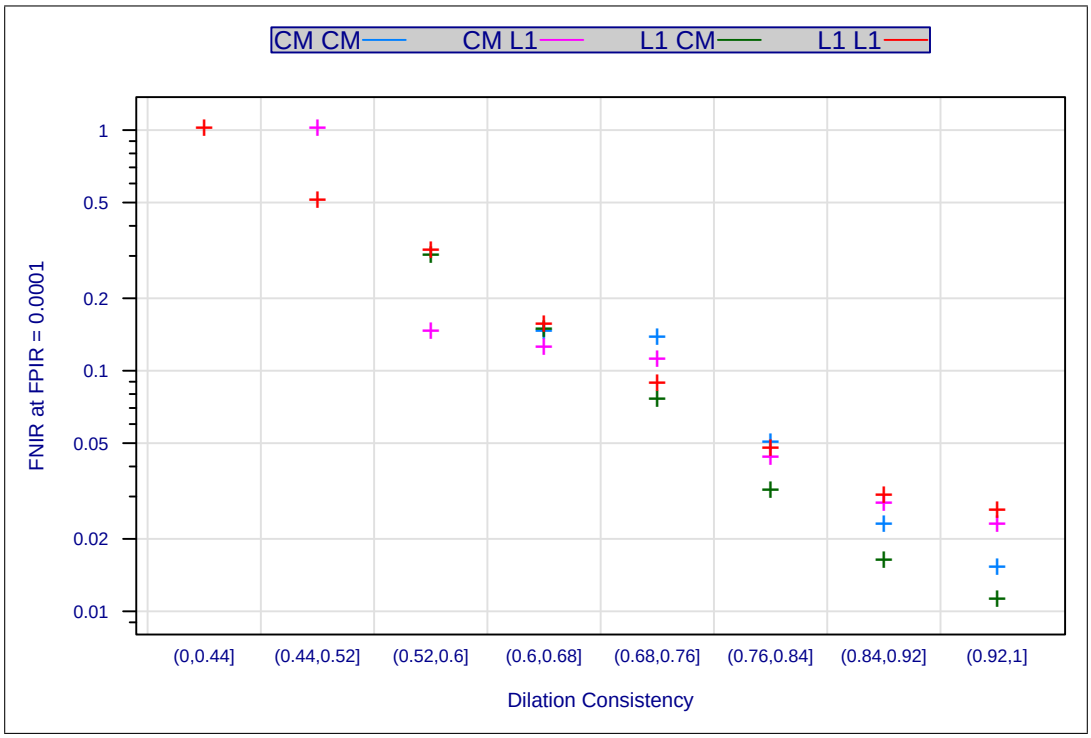

(b) Mean, L1 and CM images

Figure 276: Miss rate statistics for implementation N03A executing mate searches in an enrolled population of N = 1.6 million. The figures plots FNIR at FPIR = 0.0001 versus the IREX I metric for dilation consistency $(1 - \max(D_1, D_2))/(1 - \min(D_1, D_2))$ where D_i is pupil-iris radius ratio, and the subscripts refer to the mated enrollment and search image. The pathologically compressed 330x330 images are excluded from this analysis. The second figure breaks out dilation effects for interoperating camera pairs, CM and L1.

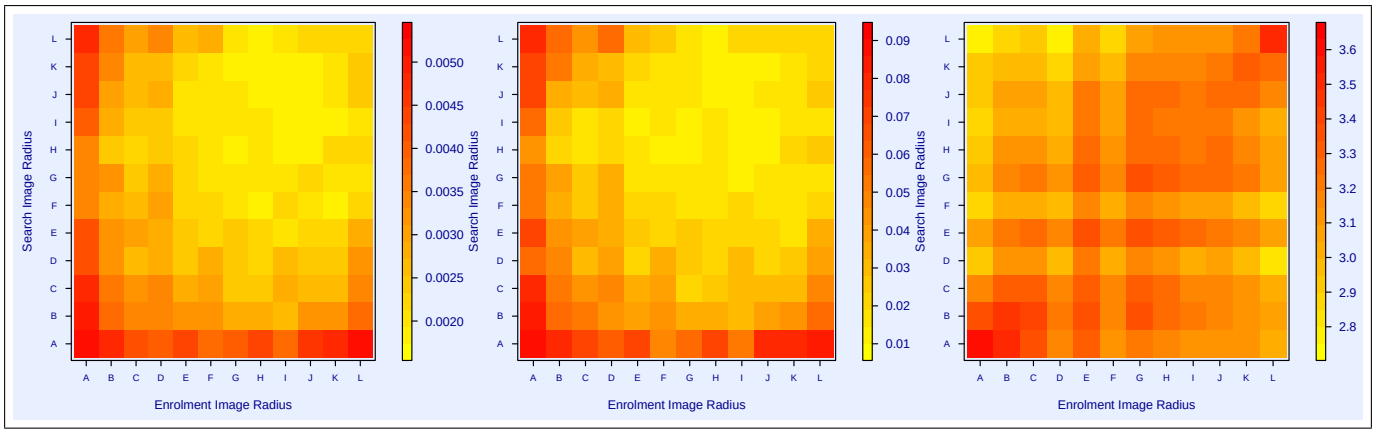

(a) Iris radius: Dis-similarity Score, Miss Rate, $\log_{10}(1+\text{Count})$

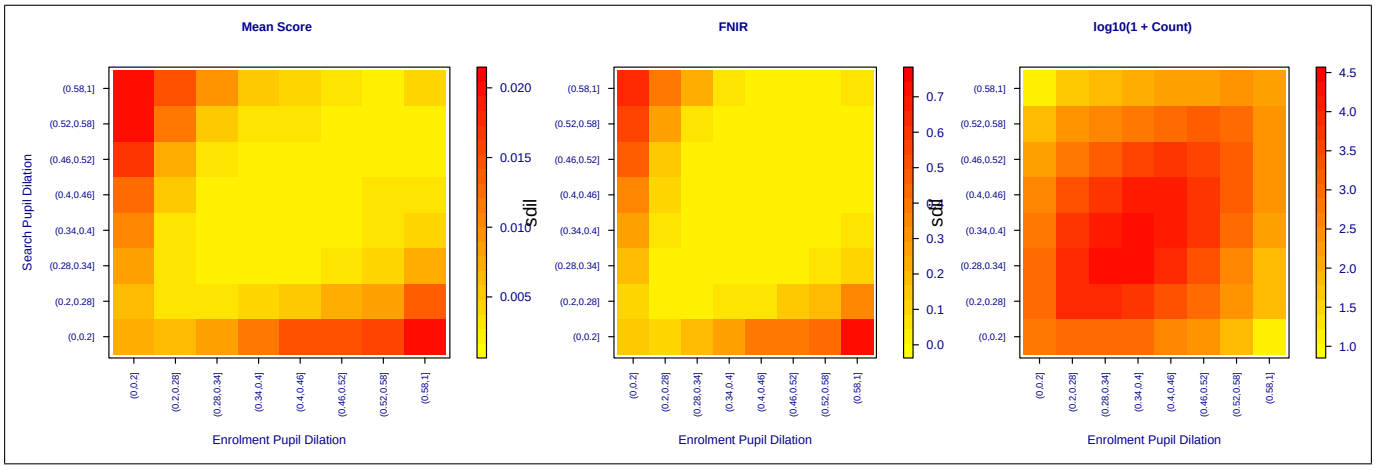

(b) Mate Dilation: Dis-similarity Score, Miss Rate, $\log_{10}(1+\text{Count})$

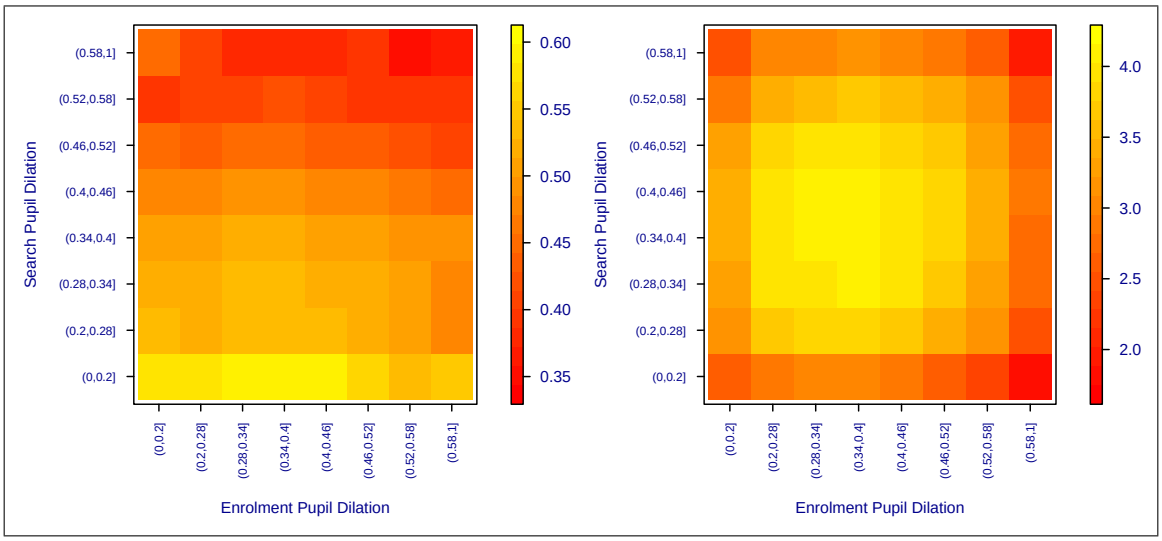

(c) Nonmate Dilation, Dis-similarity Score, Miss Rate, $\log_{10}(1+\text{Count})$

Figure 277: Heatmaps for implementation N03B executing mate searches in an enrolled population of N = 1.6 million. The radius images are binned by into twelve quantiles spanning $[0, 1]$. The dilation values are cut into ranges bounded by: $(0, 0.2, 0.28, 0.34, 0.40, 0.46, 0.52, 0.58, 1)$. The pathologically compressed 330x330 images are excluded from this analysis.

Heatmaps for implementation N03B executing mate searches in an enrolled population of N = 1.6 million.

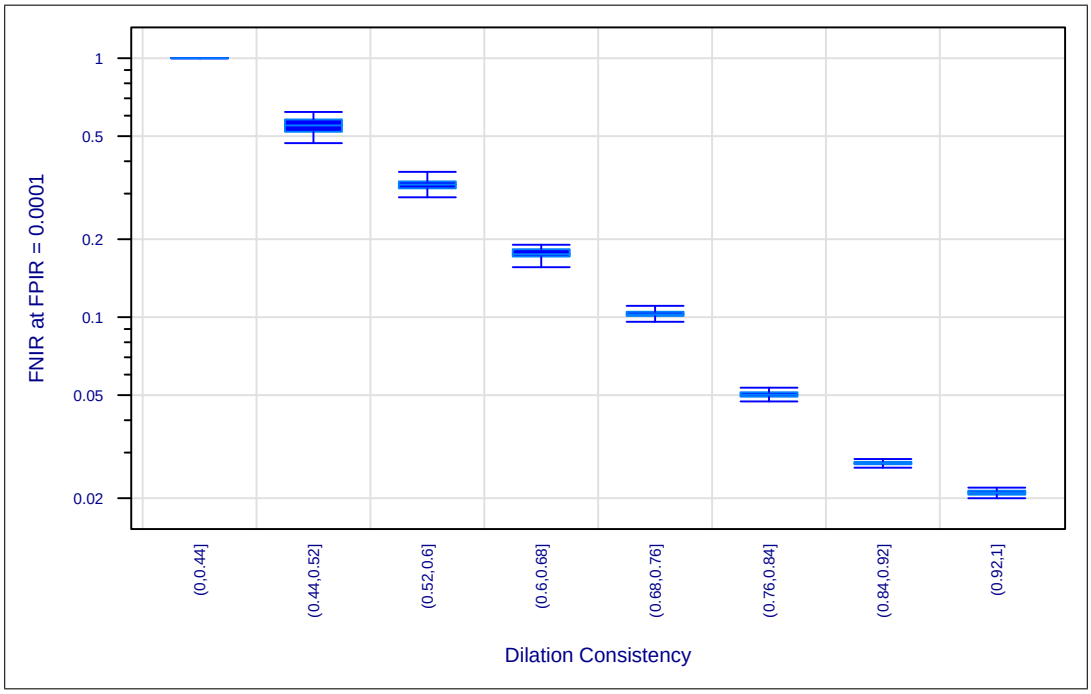

(a) Boxplot, all images

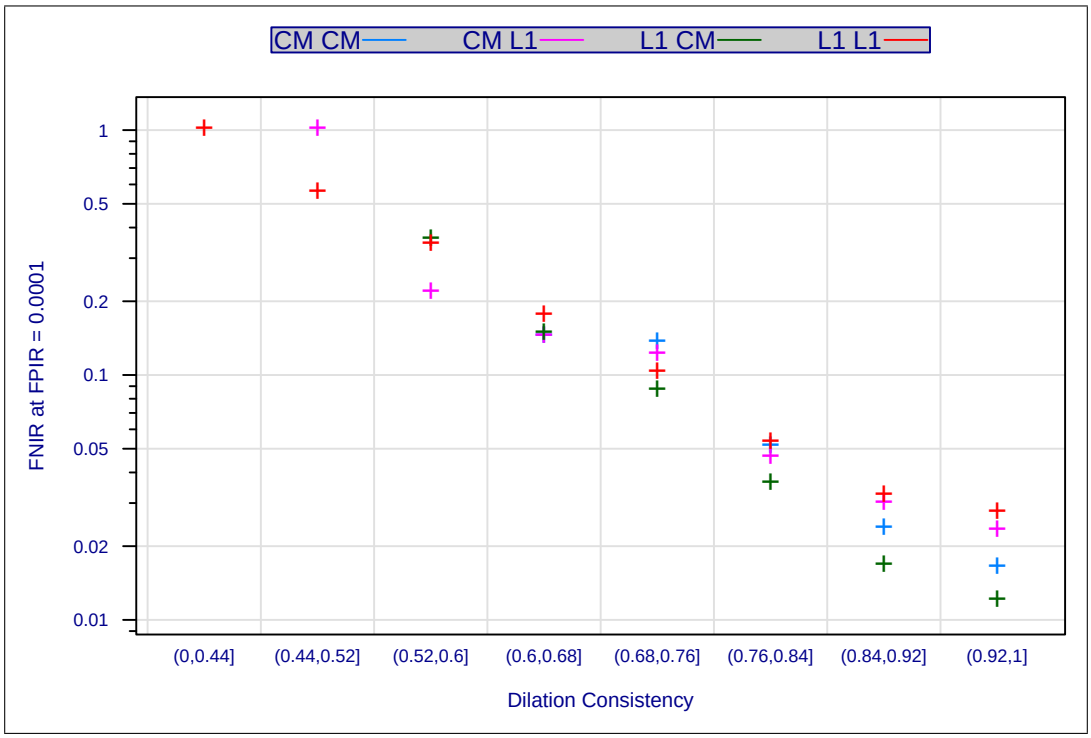

(b) Mean, L1 and CM images

Figure 278: Miss rate statistics for implementation N03B executing mate searches in an enrolled population of N = 1.6 million. The figures plots FNIR at FPIR = 0.0001 versus the IREX I metric for dilation consistency $(1 - \max(D_1, D_2))/(1 - \min(D_1, D_2))$ where D_i is pupil-iris radius ratio, and the subscripts refer to the mated enrollment and search image. The pathologically compressed 330x330 images are excluded from this analysis. The second figure breaks out dilation effects for interoperating camera pairs, CM and L1.

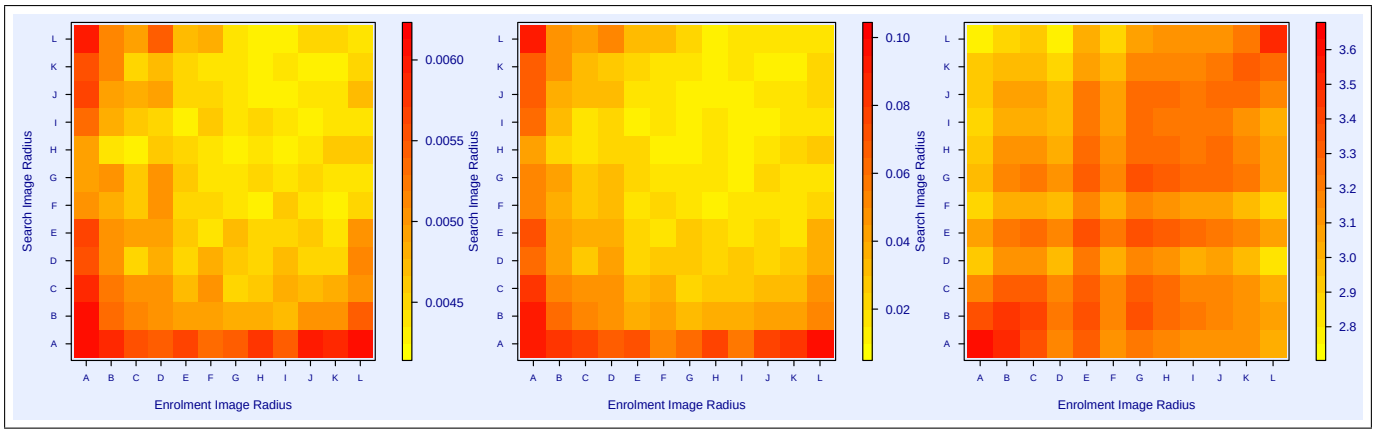

(a) Iris radius: Dis-similarity Score, Miss Rate, $\log_{10}(1+\text{Count})$

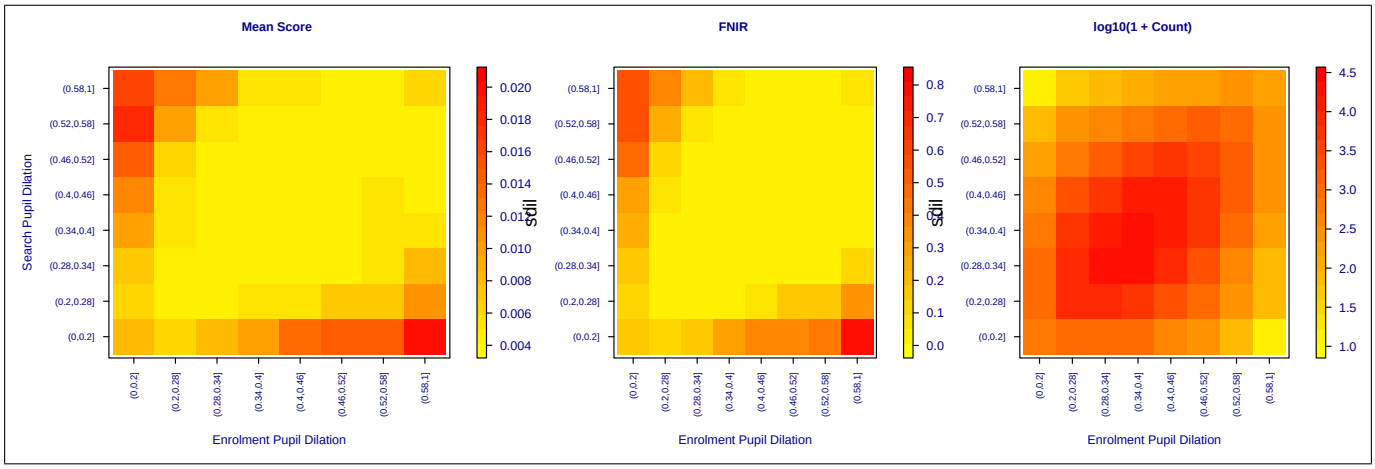

(b) Mate Dilation: Dis-similarity Score, Miss Rate, $\log_{10}(1+\text{Count})$

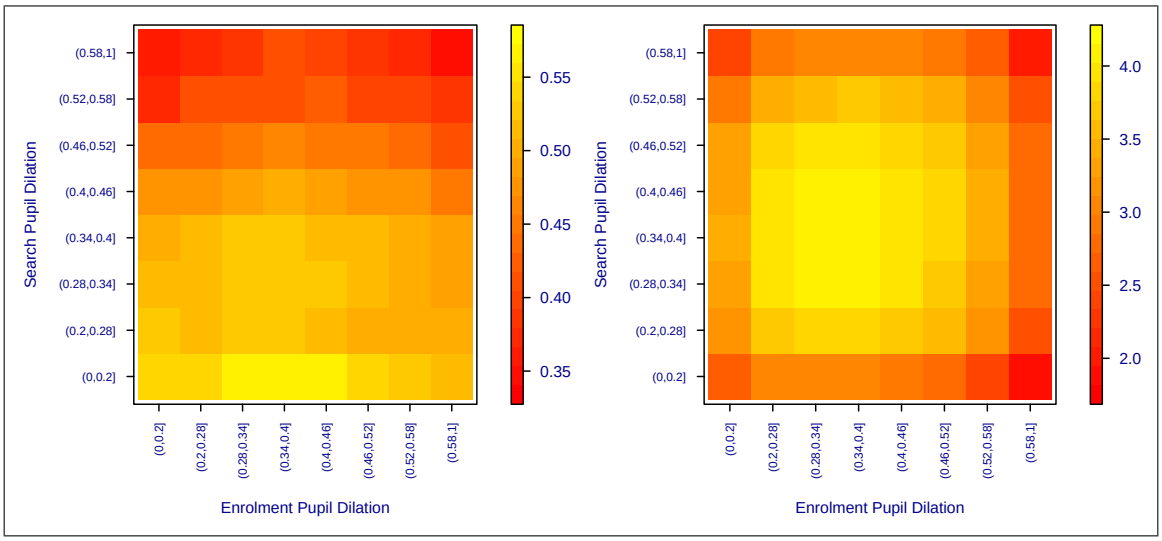

(c) Nonmate Dilation, Dis-similarity Score, Miss Rate, $\log_{10}(1+\text{Count})$

Figure 279: Heatmaps for implementation N04A executing mate searches in an enrolled population of N = 1.6 million. The radius images are binned by into twelve quantiles spanning $[0, 1]$. The dilation values are cut into ranges bounded by: $(0, 0.2, 0.28, 0.34, 0.40, 0.46, 0.52, 0.58, 1)$. The pathologically compressed 330x330 images are excluded from this analysis.

Heatmaps for implementation N04A executing mate searches in an enrolled population of N = 1.6 million.

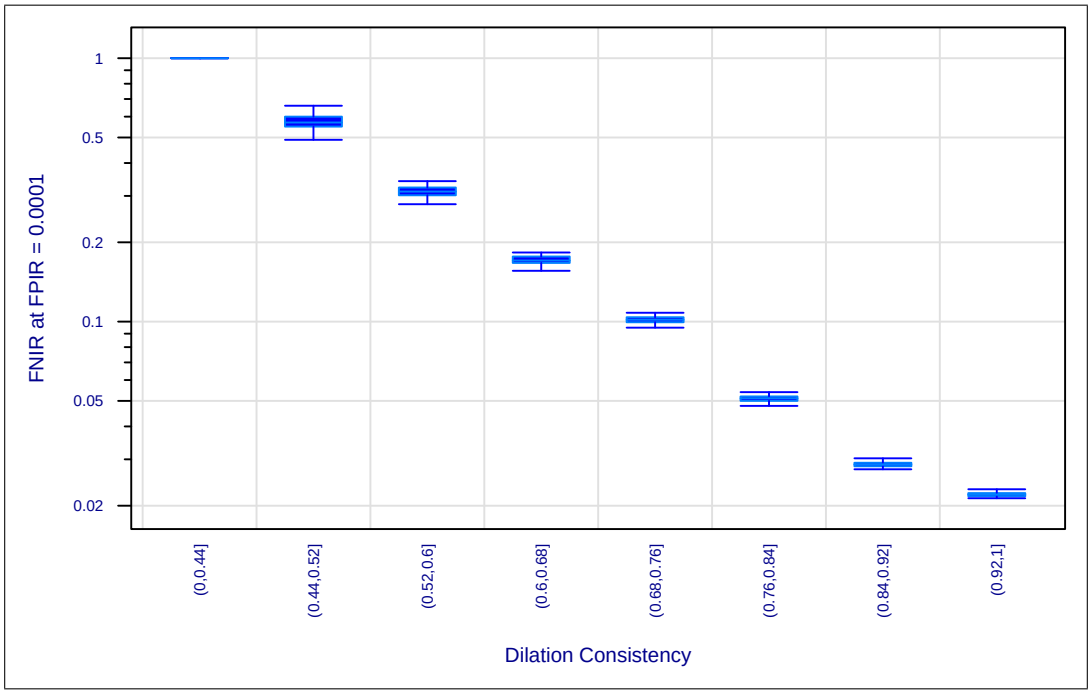

(a) Boxplot, all images

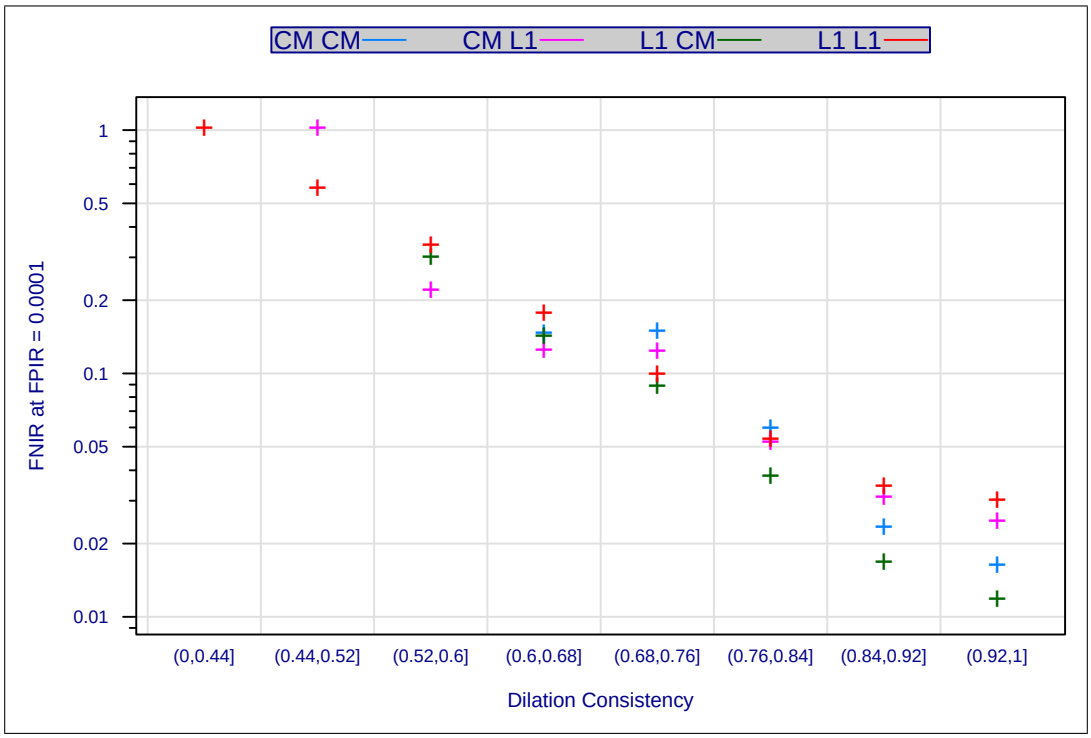

(b) Mean, L1 and CM images

Figure 280: Miss rate statistics for implementation N04A executing mate searches in an enrolled population of N = 1.6 million. The figures plots FNIR at FPIR = 0.0001 versus the IREX I metric for dilation consistency $(1 - \max(D_1, D_2))/(1 - \min(D_1, D_2))$ where D_i is pupil-iris radius ratio, and the subscripts refer to the mated enrollment and search image. The pathologically compressed 330x330 images are excluded from this analysis. The second figure breaks out dilation effects for interoperating camera pairs, CM and L1.

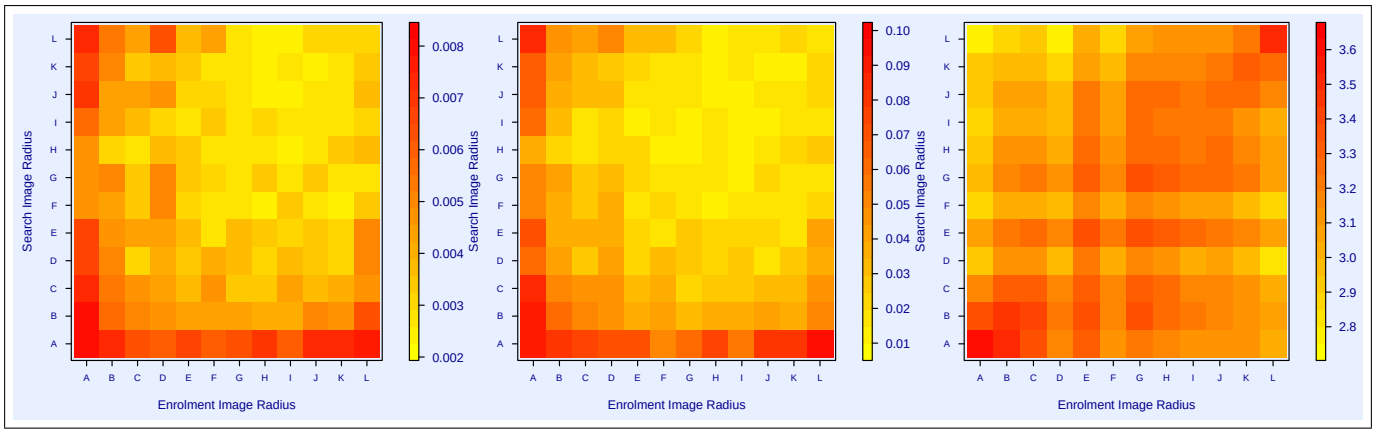

(a) Iris radius: Dis-similarity Score, Miss Rate, $\log_{10}(1+\text{Count})$

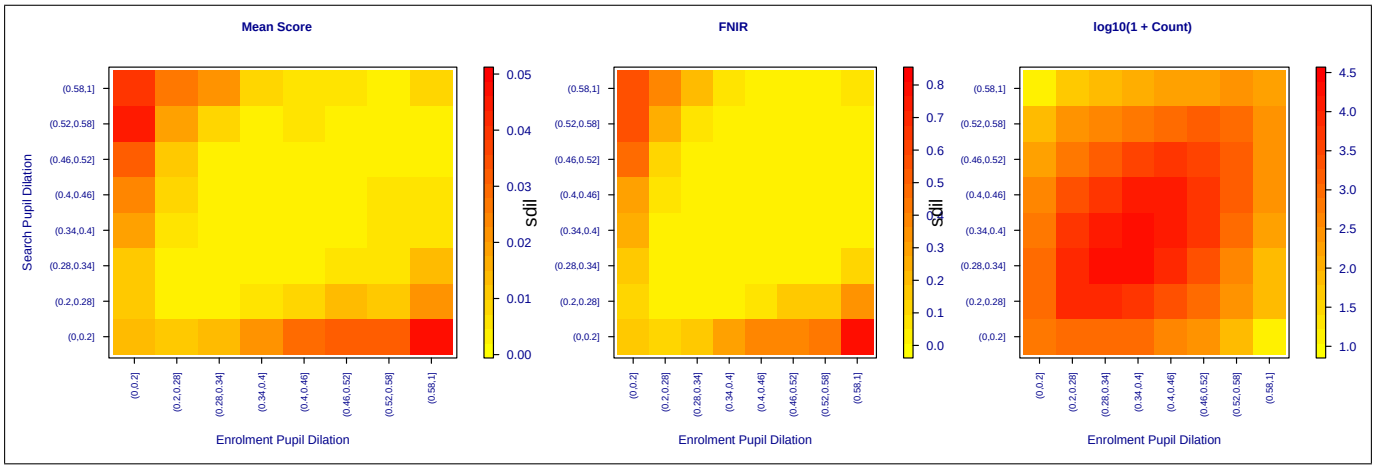

(b) Mate Dilation: Dis-similarity Score, Miss Rate, $\log_{10}(1+\text{Count})$

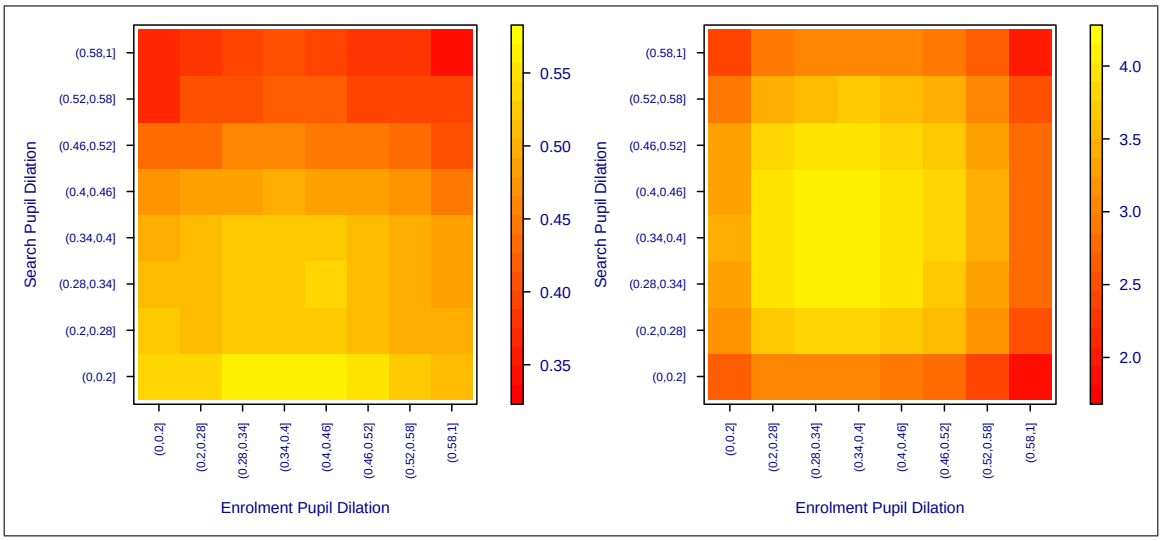

(c) Nonmate Dilation, Dis-similarity Score, Miss Rate, $\log_{10}(1+\text{Count})$

Figure 281: Heatmaps for implementation N11A executing mate searches in an enrolled population of N = 1.6 million. The radius images are binned by into twelve quantiles spanning $[0, 1]$. The dilation values are cut into ranges bounded by: $(0, 0.2, 0.28, 0.34, 0.40, 0.46, 0.52, 0.58, 1)$. The pathologically compressed 330x330 images are excluded from this analysis.

Heatmaps for implementation N11A executing mate searches in an enrolled population of N = 1.6 million.

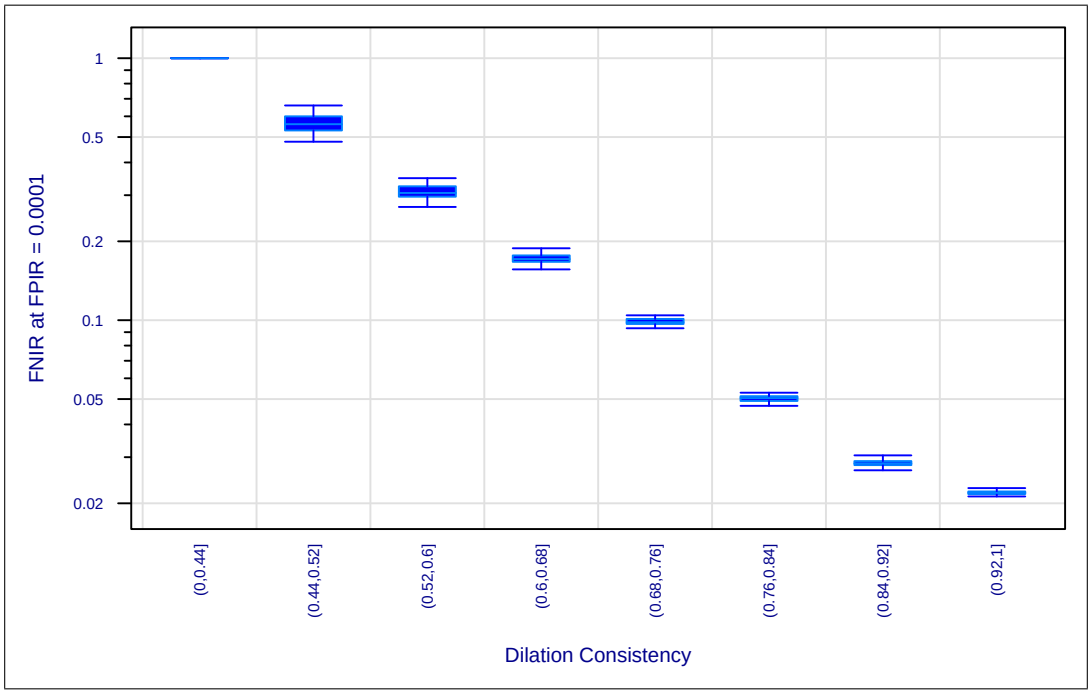

(a) Boxplot, all images

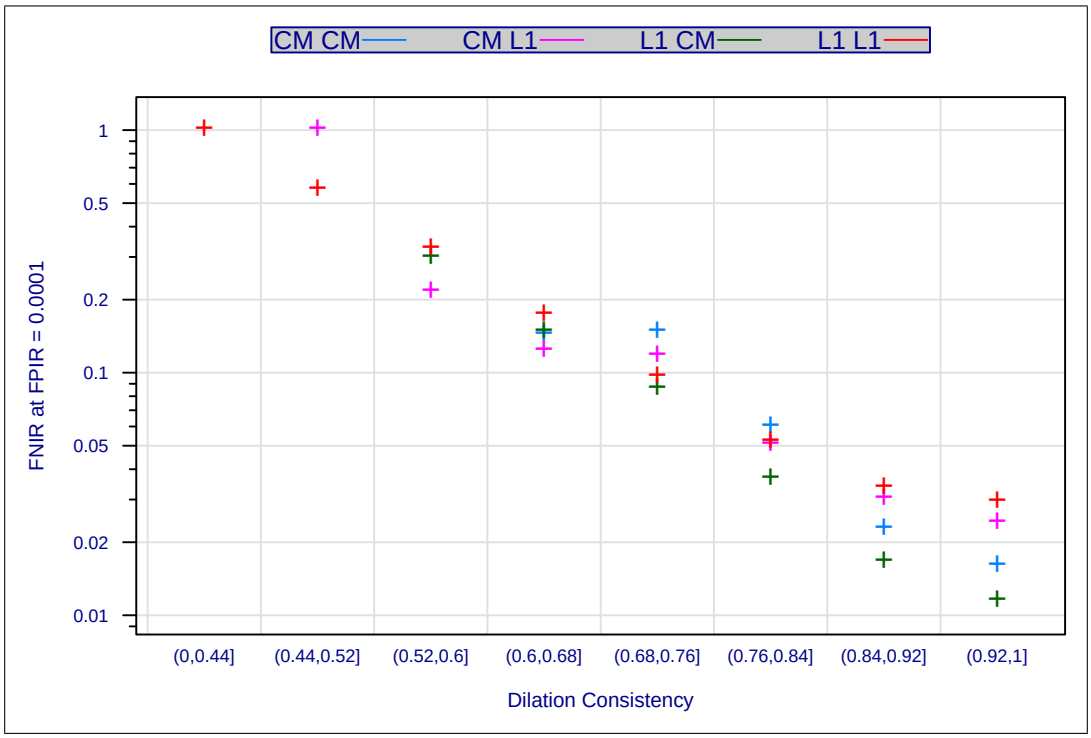

(b) Mean, L1 and CM images

Figure 282: Miss rate statistics for implementation N11A executing mate searches in an enrolled population of N = 1.6 million. The figures plots FNIR at FPIR = 0.0001 versus the IREX I metric for dilation consistency $(1 - \max(D_1, D_2))/(1 - \min(D_1, D_2))$ where D_i is pupil-iris radius ratio, and the subscripts refer to the mated enrollment and search image. The pathologically compressed 330x330 images are excluded from this analysis. The second figure breaks out dilation effects for interoperating camera pairs, CM and L1.

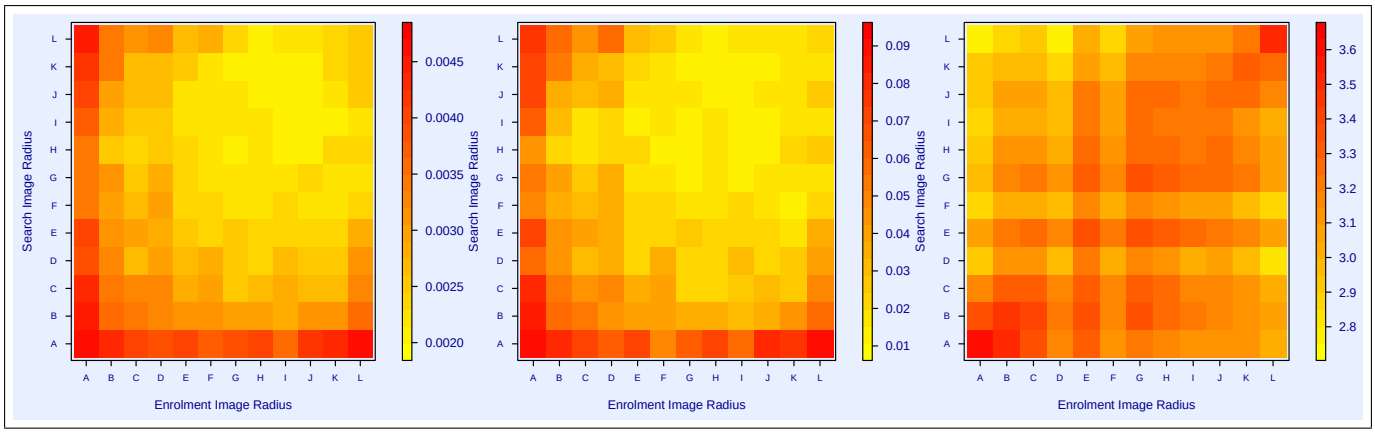

(a) Iris radius: Dis-similarity Score, Miss Rate, $\log_{10}(1+\text{Count})$

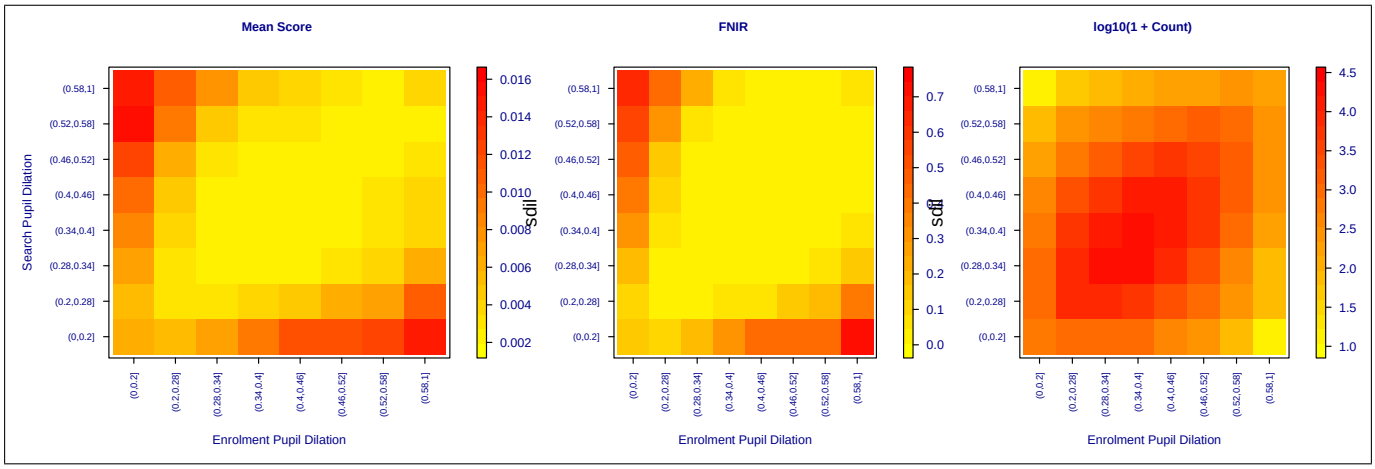

(b) Mate Dilation: Dis-similarity Score, Miss Rate, $\log_{10}(1+\text{Count})$

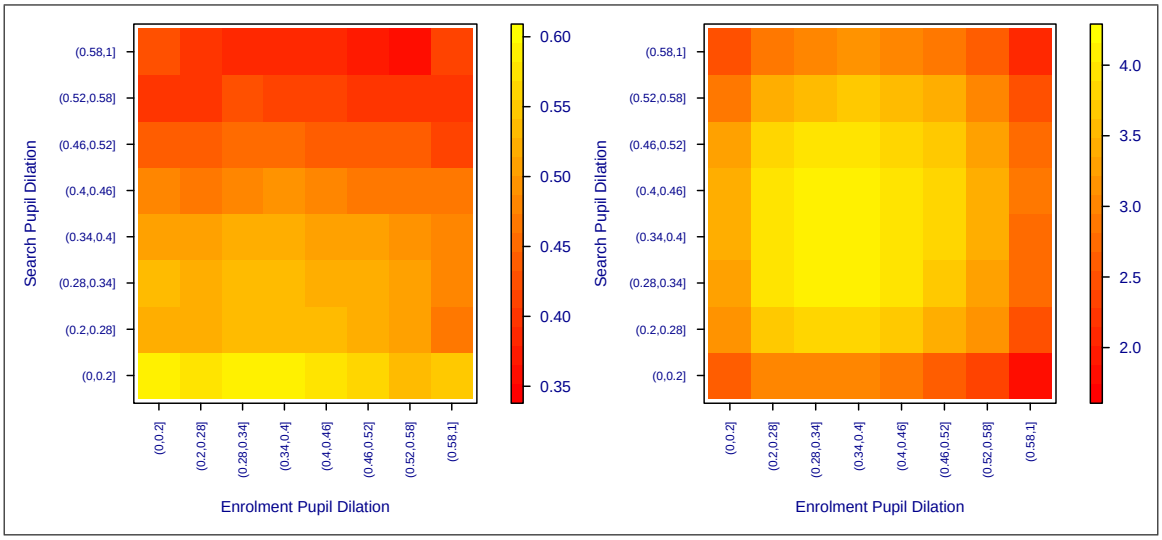

(c) Nonmate Dilation, Dis-similarity Score, Miss Rate, $\log_{10}(1+\text{Count})$

Figure 283: Heatmaps for implementation N11B executing mate searches in an enrolled population of N = 1.6 million. The radius images are binned by into twelve quantiles spanning $[0, 1]$. The dilation values are cut into ranges bounded by: $(0, 0.2, 0.28, 0.34, 0.40, 0.46, 0.52, 0.58, 1)$. The pathologically compressed 330x330 images are excluded from this analysis.

Heatmaps for implementation N11B executing mate searches in an enrolled population of N = 1.6 million.

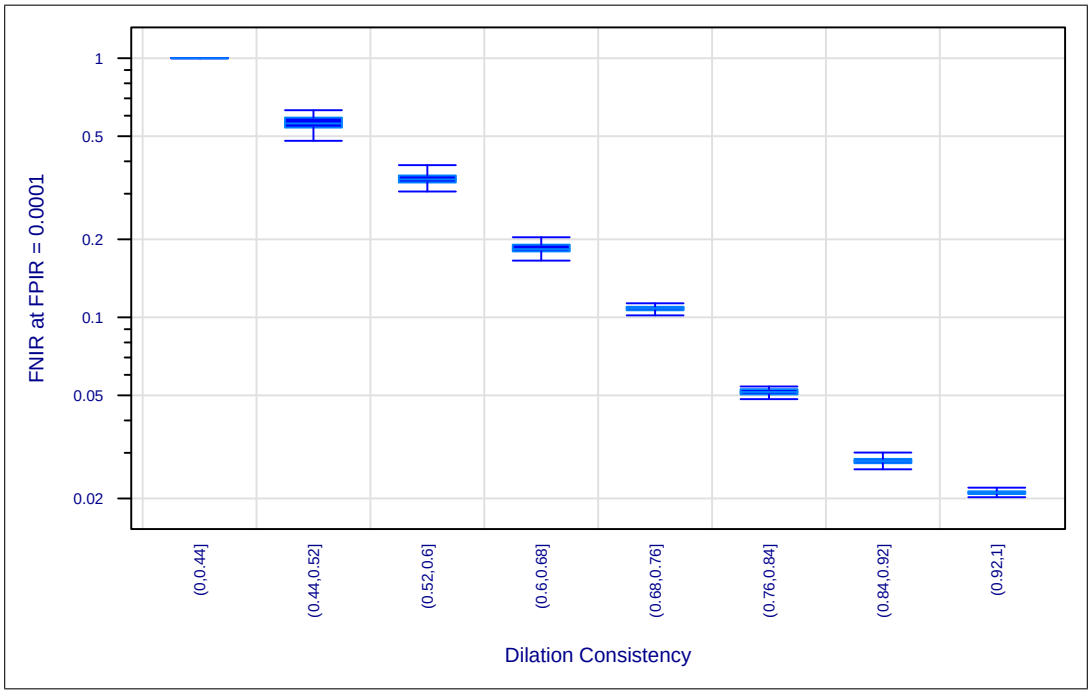

(a) Boxplot, all images

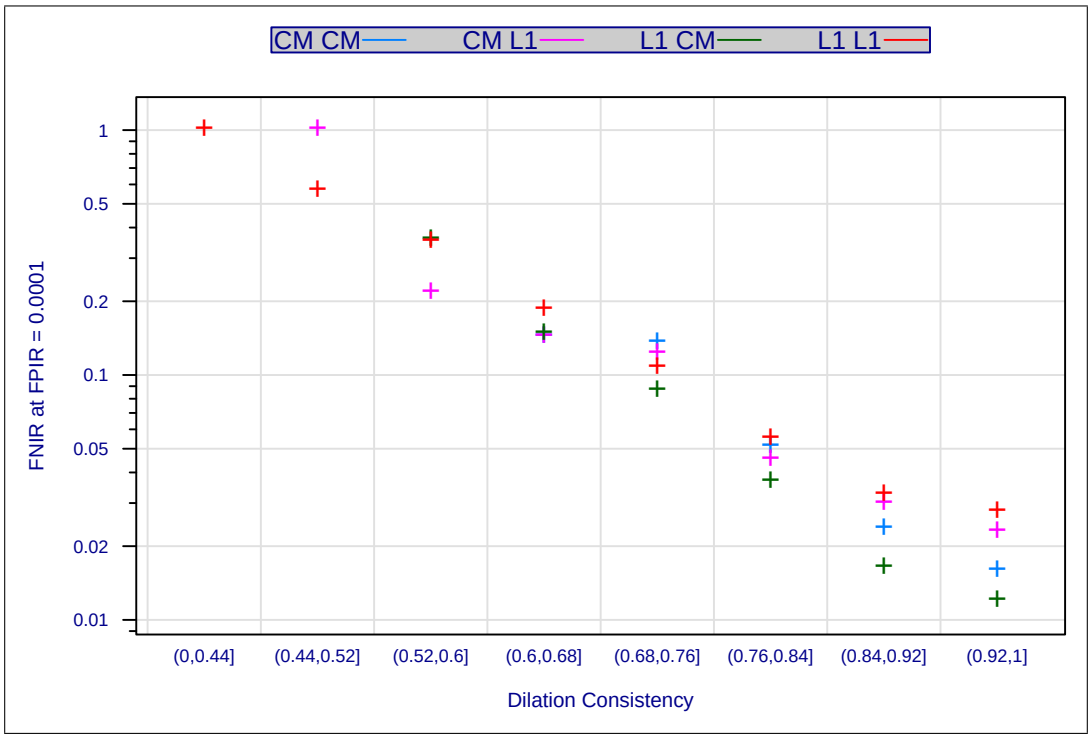

(b) Mean, L1 and CM images

Figure 284: Miss rate statistics for implementation N11B executing mate searches in an enrolled population of N = 1.6 million. The figures plots FNIR at FPIR = 0.0001 versus the IREX I metric for dilation consistency $(1 - \max(D_1, D_2))/(1 - \min(D_1, D_2))$ where D_i is pupil-iris radius ratio, and the subscripts refer to the mated enrollment and search image. The pathologically compressed 330x330 images are excluded from this analysis. The second figure breaks out dilation effects for interoperating camera pairs, CM and L1.

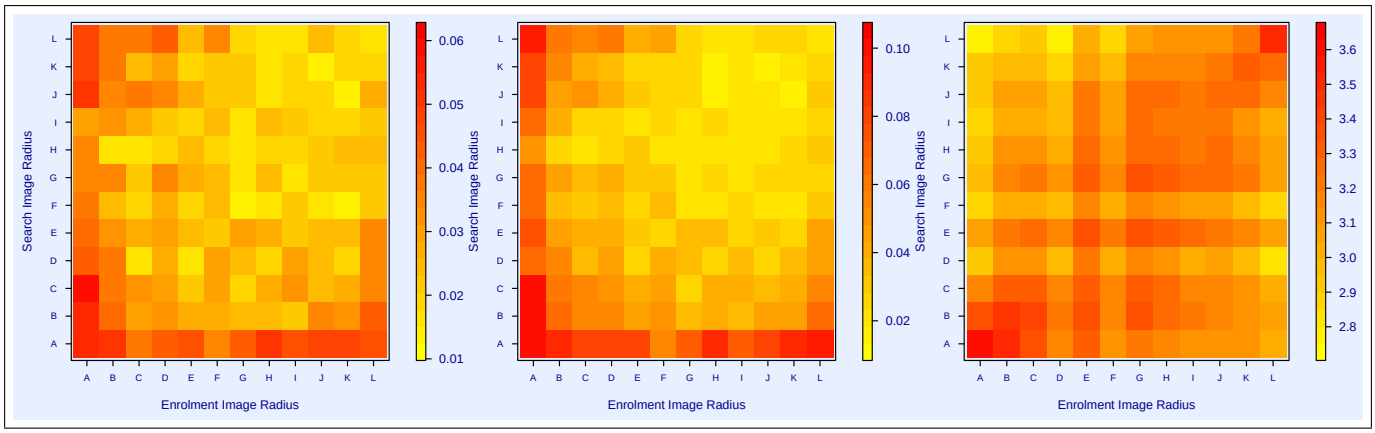

(a) Iris radius: Dis-similarity Score, Miss Rate, $\log_{10}(1+\text{Count})$

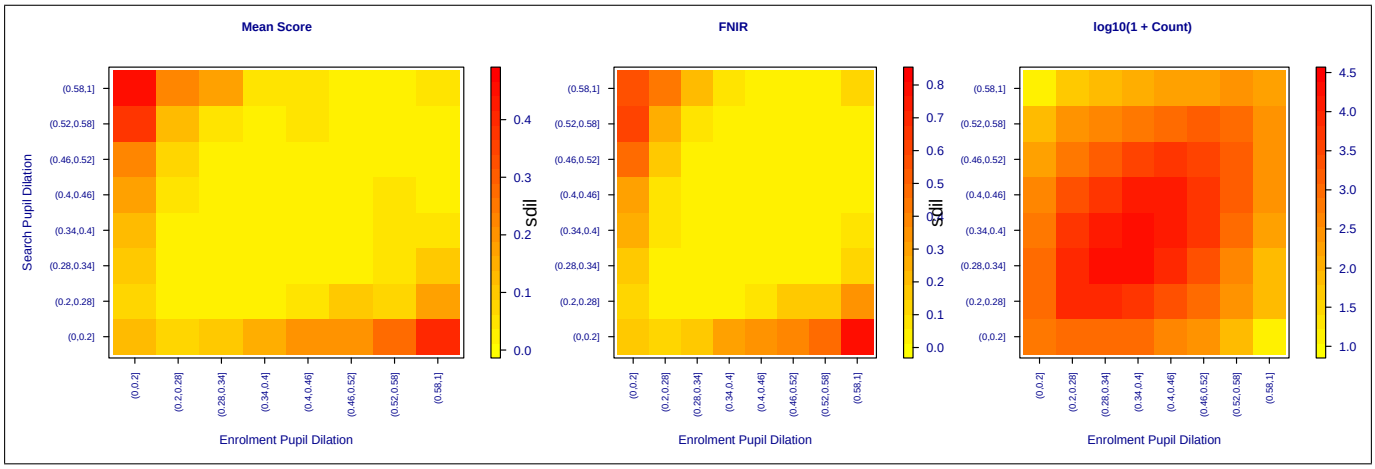

(b) Mate Dilation: Dis-similarity Score, Miss Rate, $\log_{10}(1+\text{Count})$

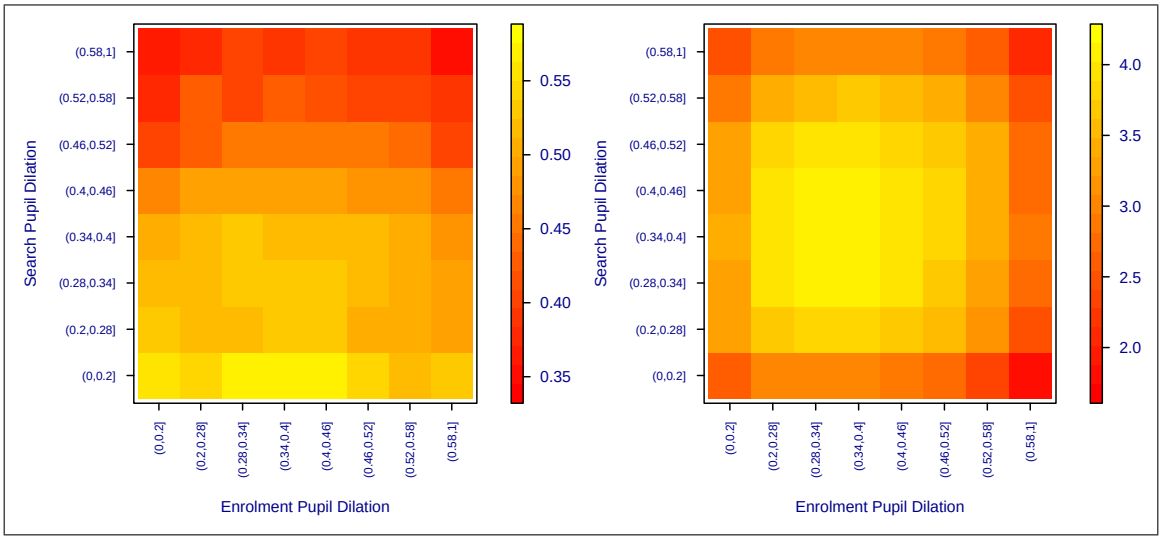

(c) Nonmate Dilation, Dis-similarity Score, Miss Rate, $\log_{10}(1+\text{Count})$

Figure 285: Heatmaps for implementation N12A executing mate searches in an enrolled population of N = 1.6 million. The radius images are binned by into twelve quantiles spanning $[0, 1]$. The dilation values are cut into ranges bounded by: $(0, 0.2, 0.28, 0.34, 0.40, 0.46, 0.52, 0.58, 1)$. The pathologically compressed 330x330 images are excluded from this analysis.

Heatmaps for implementation N12A executing mate searches in an enrolled population of N = 1.6 million.

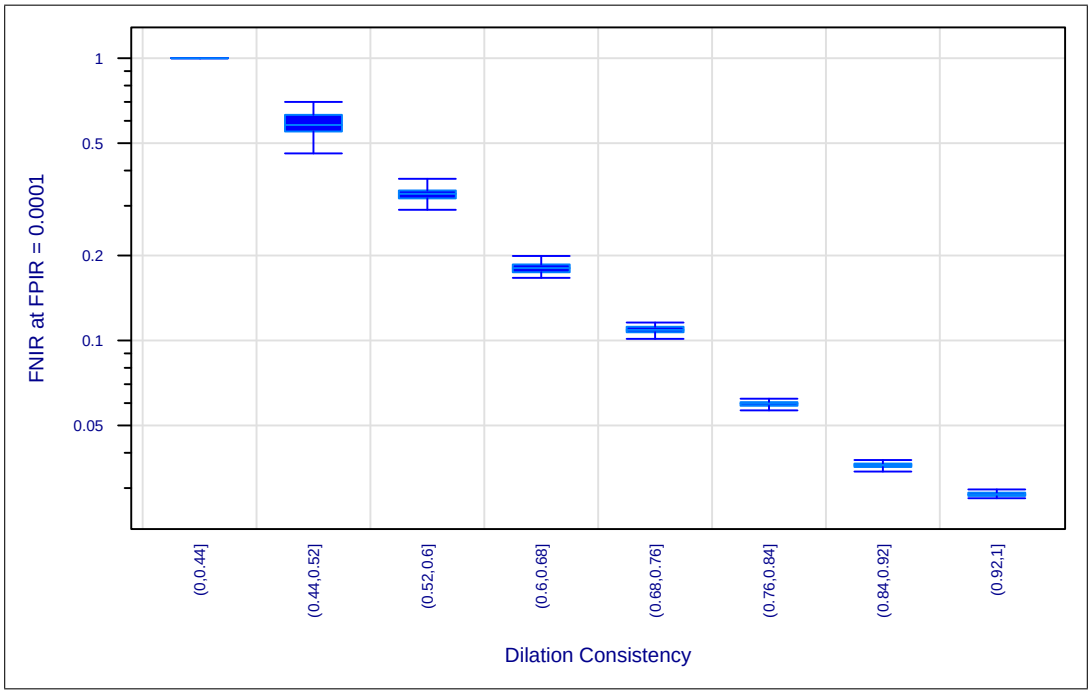

(a) Boxplot, all images

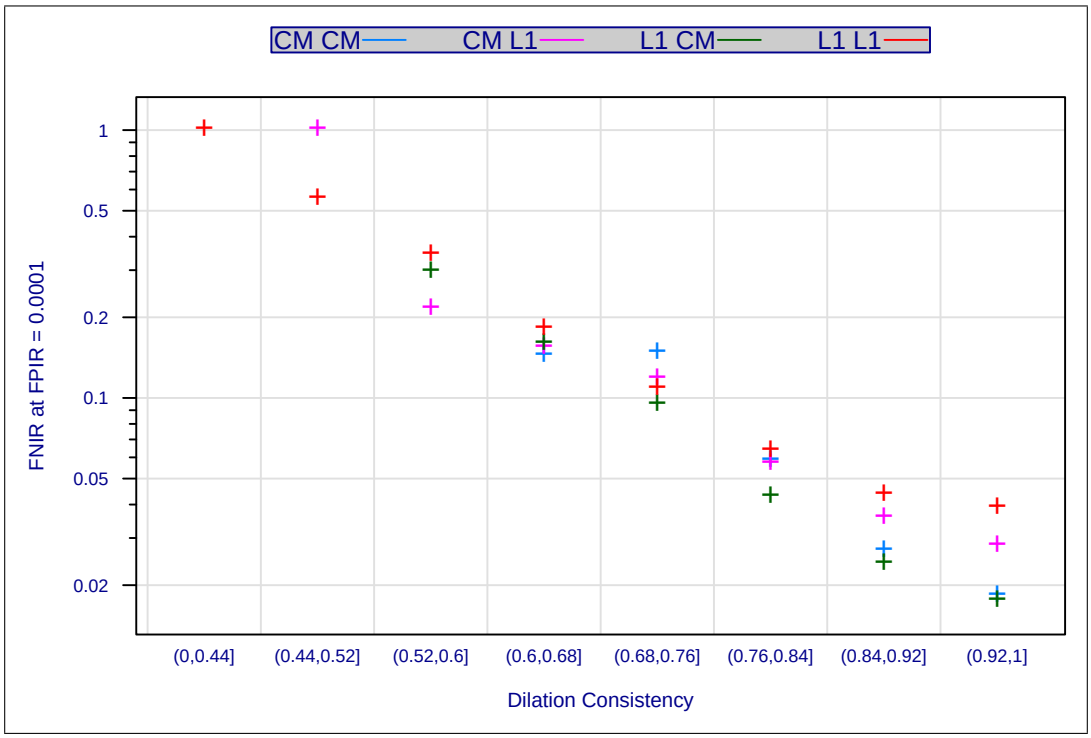

(b) Mean, L1 and CM images

Figure 286: Miss rate statistics for implementation N12A executing mate searches in an enrolled population of N = 1.6 million. The figures plots FNIR at FPIR = 0.0001 versus the IREX I metric for dilation consistency $(1 - \max(D_1, D_2))/(1 - \min(D_1, D_2))$ where D_i is pupil-iris radius ratio, and the subscripts refer to the mated enrollment and search image. The pathologically compressed 330x330 images are excluded from this analysis. The second figure breaks out dilation effects for interoperating camera pairs, CM and L1.

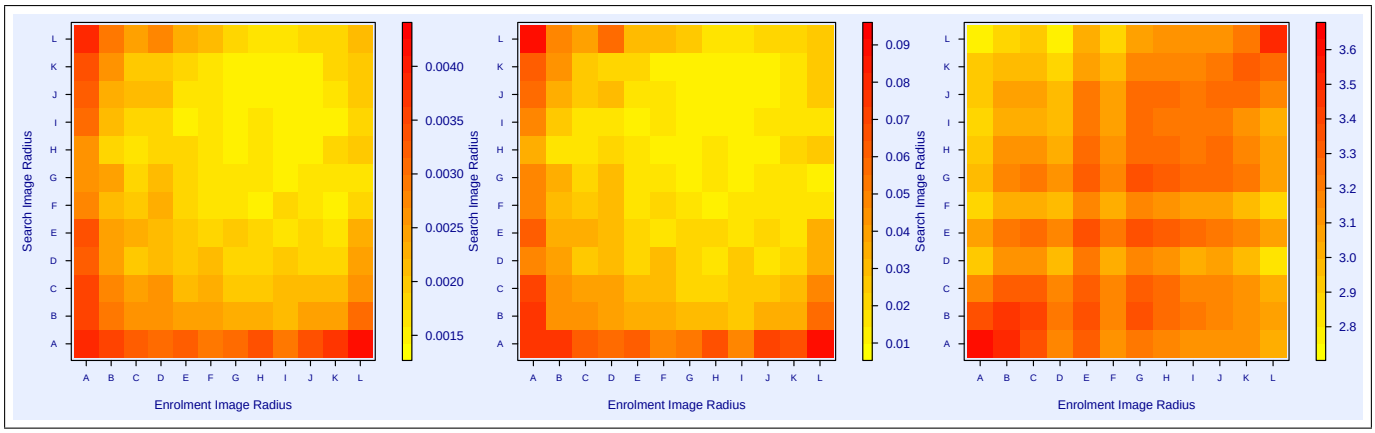

(a) Iris radius: Dis-similarity Score, Miss Rate, $\log_{10}(1+\text{Count})$

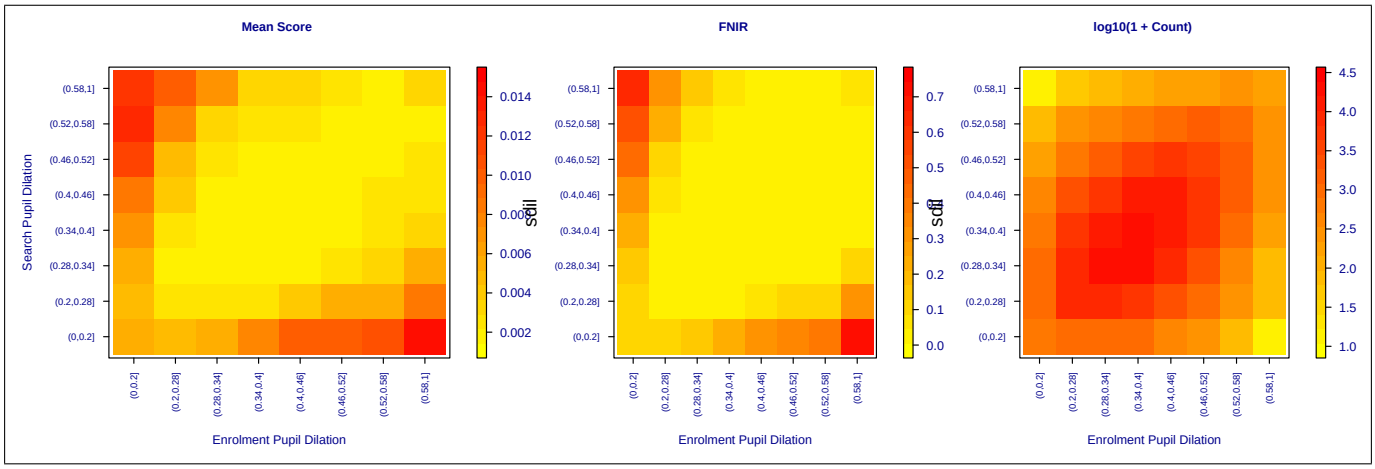

(b) Mate Dilation: Dis-similarity Score, Miss Rate, $\log_{10}(1+\text{Count})$

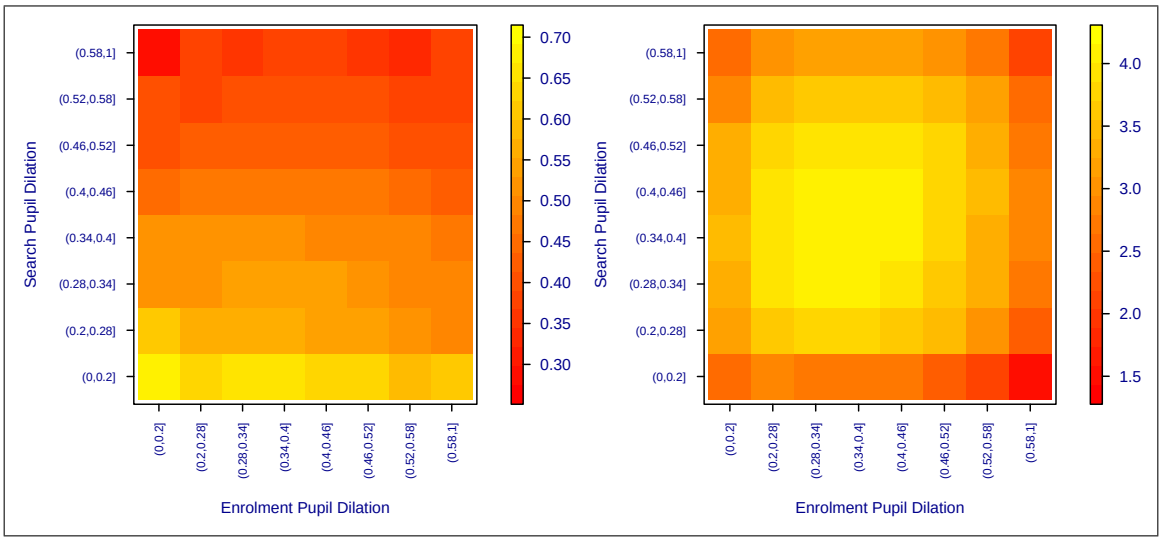

(c) Nonmate Dilation, Dis-similarity Score, Miss Rate, $\log_{10}(1+\text{Count})$

Figure 287: Heatmaps for implementation N12B executing mate searches in an enrolled population of N = 1.6 million. The radius images are binned by into twelve quantiles spanning $[0, 1]$. The dilation values are cut into ranges bounded by: $(0, 0.2, 0.28, 0.34, 0.40, 0.46, 0.52, 0.58, 1)$. The pathologically compressed 330x330 images are excluded from this analysis.

Heatmaps for implementation N12B executing mate searches in an enrolled population of N = 1.6 million.

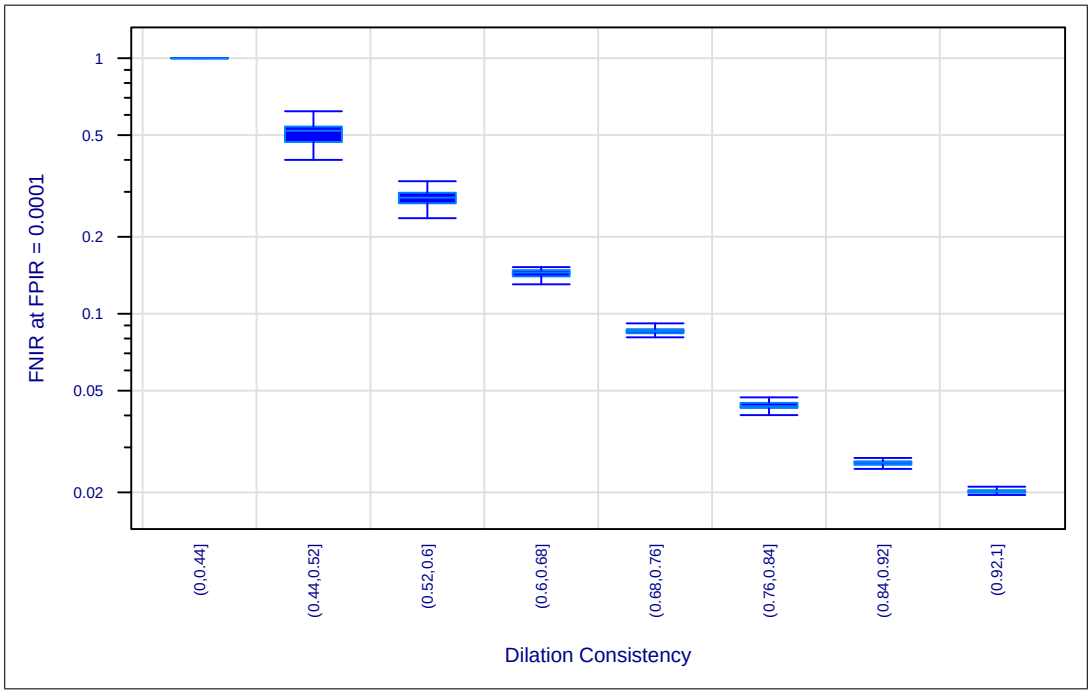

(a) Boxplot, all images

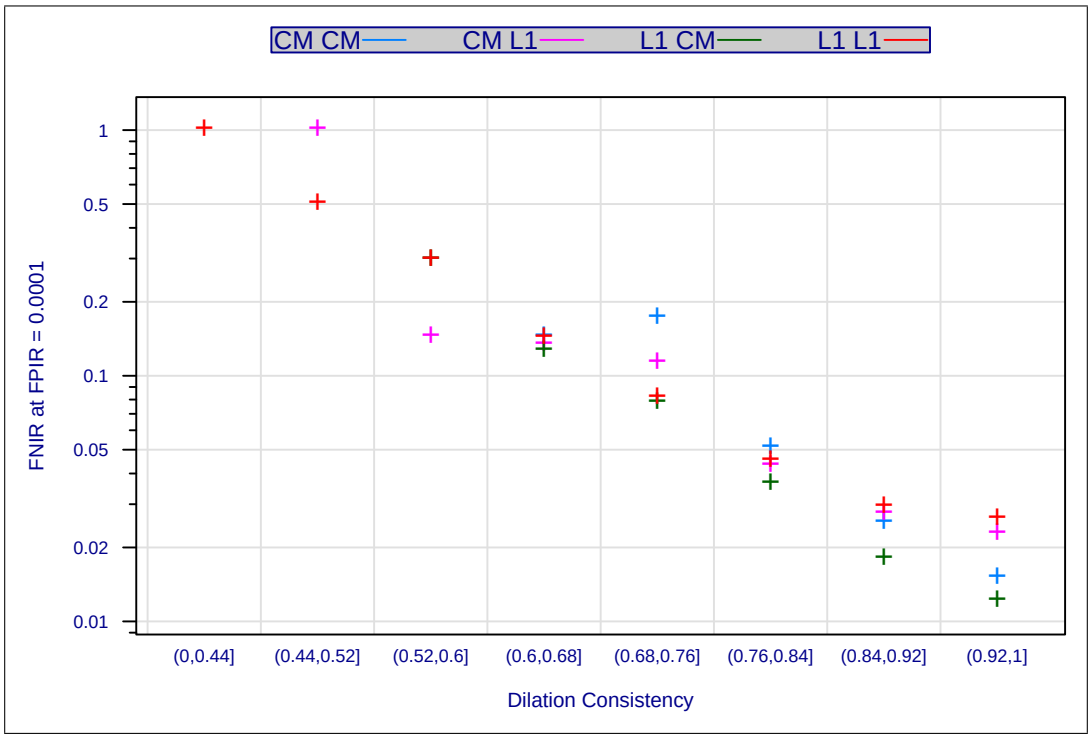

(b) Mean, L1 and CM images

Figure 288: Miss rate statistics for implementation N12B executing mate searches in an enrolled population of N = 1.6 million. The figures plots FNIR at FPIR = 0.0001 versus the IREX I metric for dilation consistency $(1 - \max(D_1, D_2))/(1 - \min(D_1, D_2))$ where D_i is pupil-iris radius ratio, and the subscripts refer to the mated enrollment and search image. The pathologically compressed 330x330 images are excluded from this analysis. The second figure breaks out dilation effects for interoperating camera pairs, CM and L1.

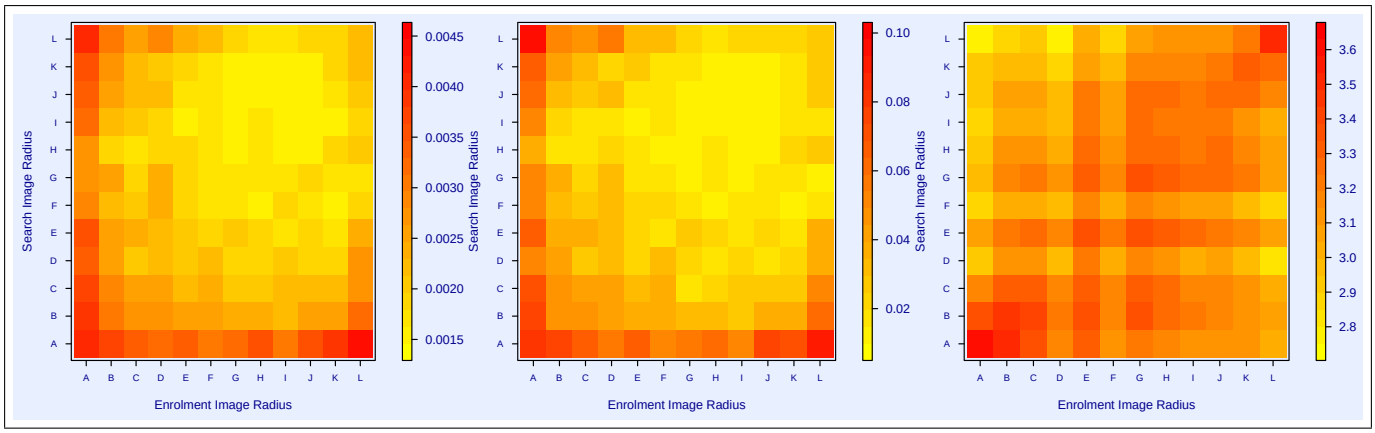

(a) Iris radius: Dis-similarity Score, Miss Rate, $\log_{10}(1+\text{Count})$

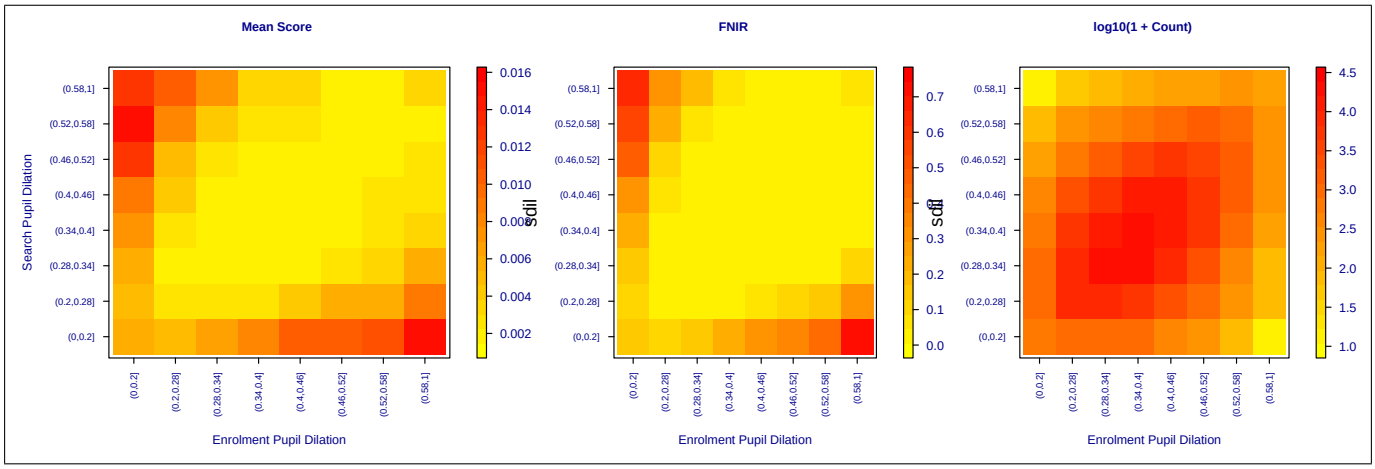

(b) Mate Dilation: Dis-similarity Score, Miss Rate, $\log_{10}(1+\text{Count})$

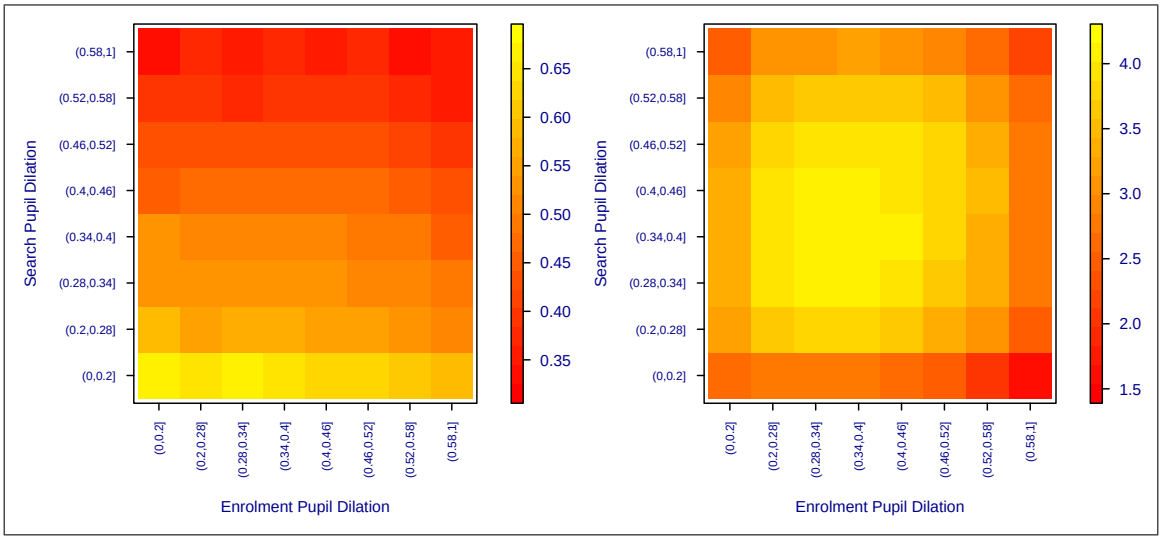

(c) Nonmate Dilation, Dis-similarity Score, Miss Rate, $\log_{10}(1+\text{Count})$

Figure 289: Heatmaps for implementation N13B executing mate searches in an enrolled population of N = 1.6 million. The radius images are binned by into twelve quantiles spanning $[0, 1]$. The dilation values are cut into ranges bounded by: $(0, 0.2, 0.28, 0.34, 0.40, 0.46, 0.52, 0.58, 1)$. The pathologically compressed 330x330 images are excluded from this analysis.

Heatmaps for implementation N13B executing mate searches in an enrolled population of N = 1.6 million.

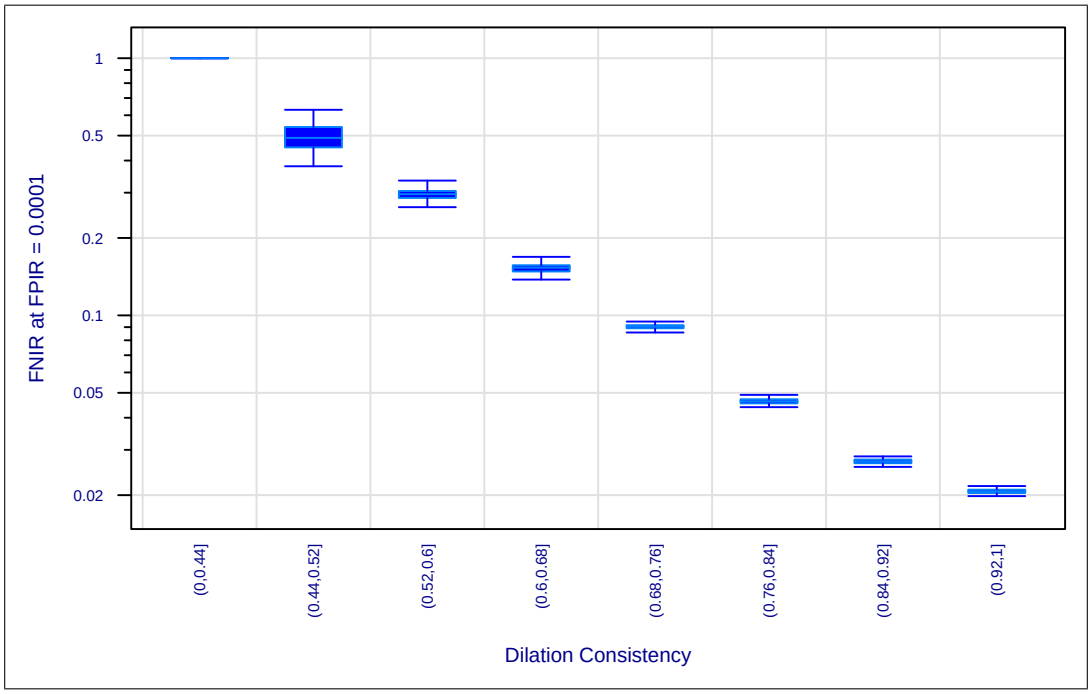

(a) Boxplot, all images

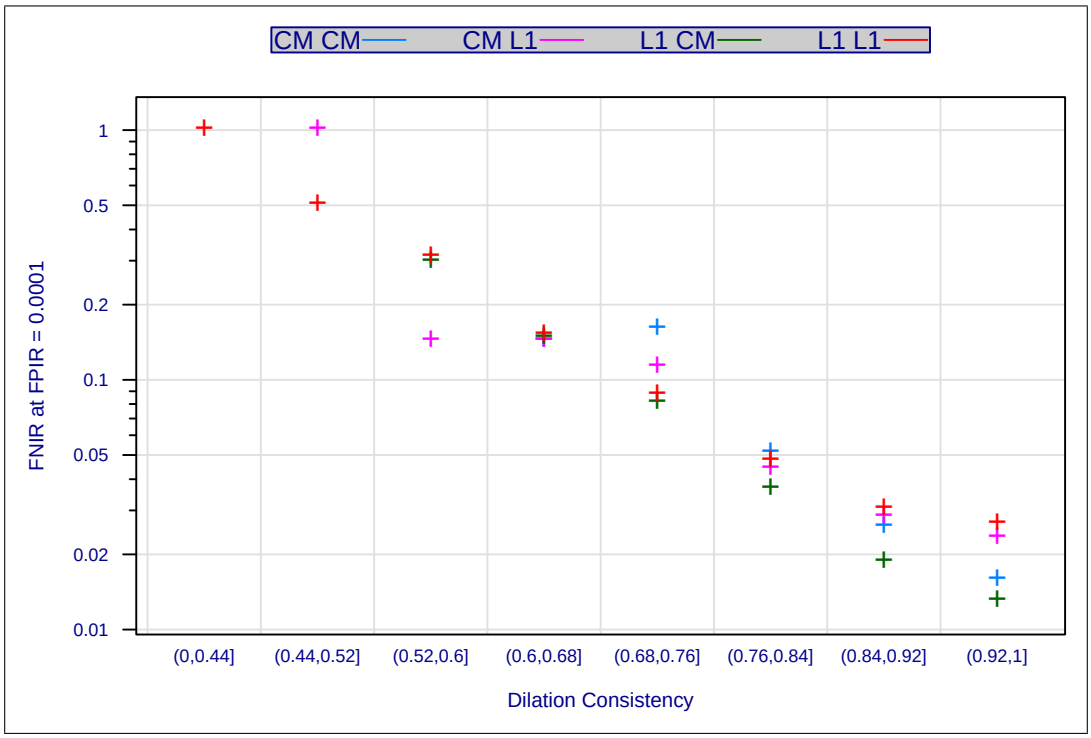

(b) Mean, L1 and CM images

Figure 290: Miss rate statistics for implementation N13B executing mate searches in an enrolled population of N = 1.6 million. The figures plots FNIR at FPIR = 0.0001 versus the IREX I metric for dilation consistency $(1 - \max(D_1, D_2))/(1 - \min(D_1, D_2))$ where D_i is pupil-iris radius ratio, and the subscripts refer to the mated enrollment and search image. The pathologically compressed 330x330 images are excluded from this analysis. The second figure breaks out dilation effects for interoperating camera pairs, CM and L1.

Figure 291: Heatmaps for implementation P02A executing mate searches in an enrolled population of N = 1.6 million. The radius images are binned by into twelve quantiles spanning $[0, 1]$. The dilation values are cut into ranges bounded by: $(0, 0.2, 0.28, 0.34, 0.40, 0.46, 0.52, 0.58, 1)$. The pathologically compressed 330x330 images are excluded from this analysis.

Figure 292: Miss rate statistics for implementation P02A executing mate searches in an enrolled population of N = 1.6 million. The figures plots FNIR at FPIR = 0.0001 versus the IREX I metric for dilation consistency $(1 - \max(D_1, D_2))/(1 - \min(D_1, D_2))$ where D_i is pupil-iris radius ratio, and the subscripts refer to the mated enrollment and search image. The pathologically compressed 330x330 images are excluded from this analysis. The second figure breaks out dilation effects for interoperating camera pairs, CM and L1.

Heatmaps for implementation P02A executing mate searches in an enrolled population of N = 1.6 million.

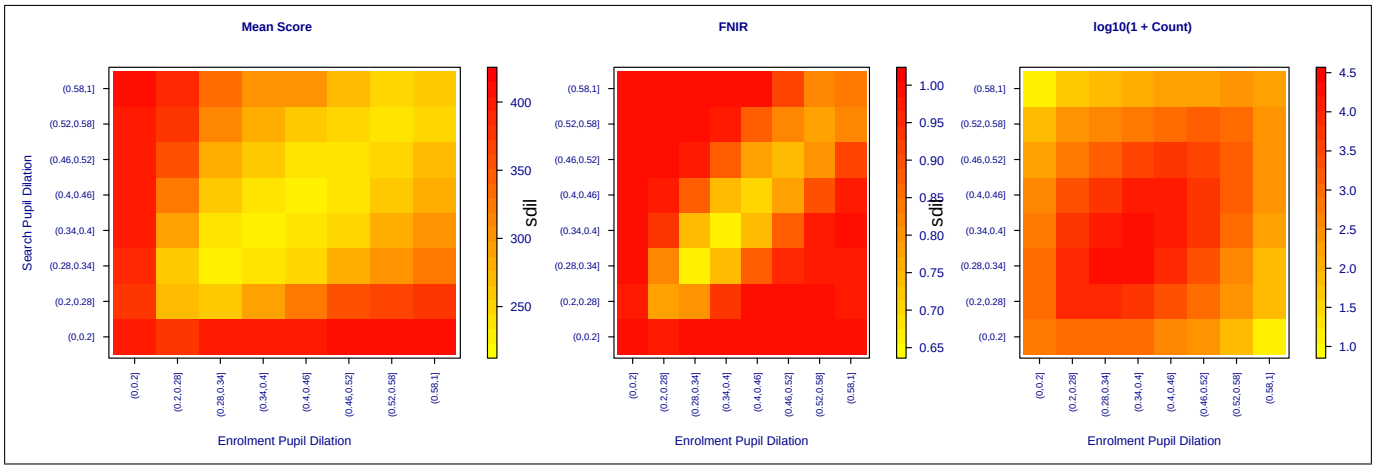

(a) Mate Dilation: Dis-similarity Score, Miss Rate, $\log_{10}(1+\text{Count})$

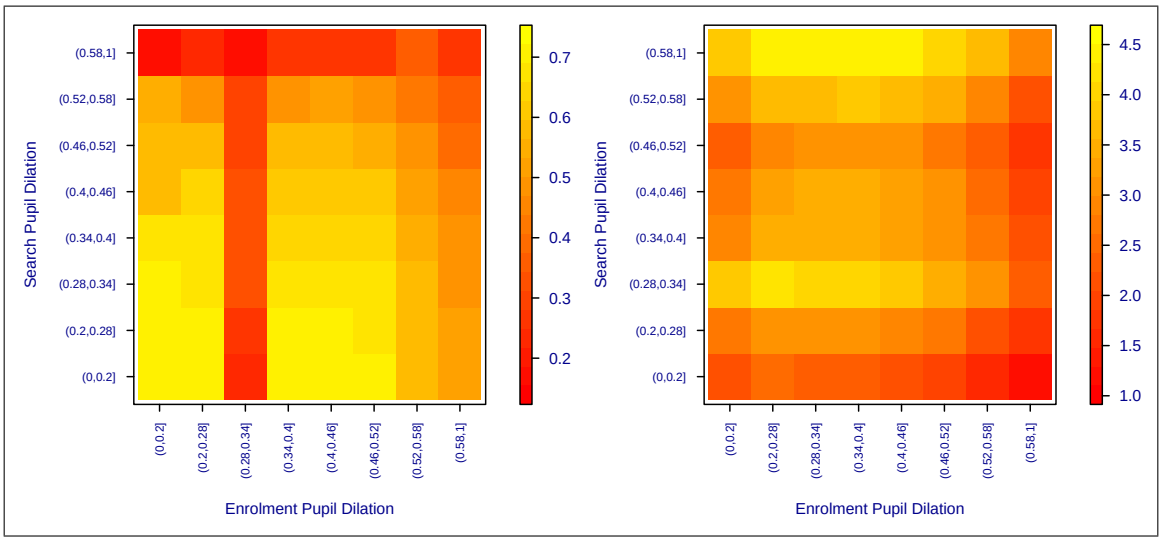

(b) Nonmate Dilation, Dis-similarity Score, Miss Rate, $\log_{10}(1+\text{Count})$

Figure 293: Heatmaps for implementation P11A executing mate searches in an enrolled population of N = 1.6 million. The radius images are binned by into twelve quantiles spanning $[0, 1]$. The dilation values are cut into ranges bounded by: $(0, 0.2, 0.28, 0.34, 0.40, 0.46, 0.52, 0.58, 1)$. The pathologically compressed 330x330 images are excluded from this analysis.

Heatmaps for implementation P11A executing mate searches in an enrolled population of N = 1.6 million.

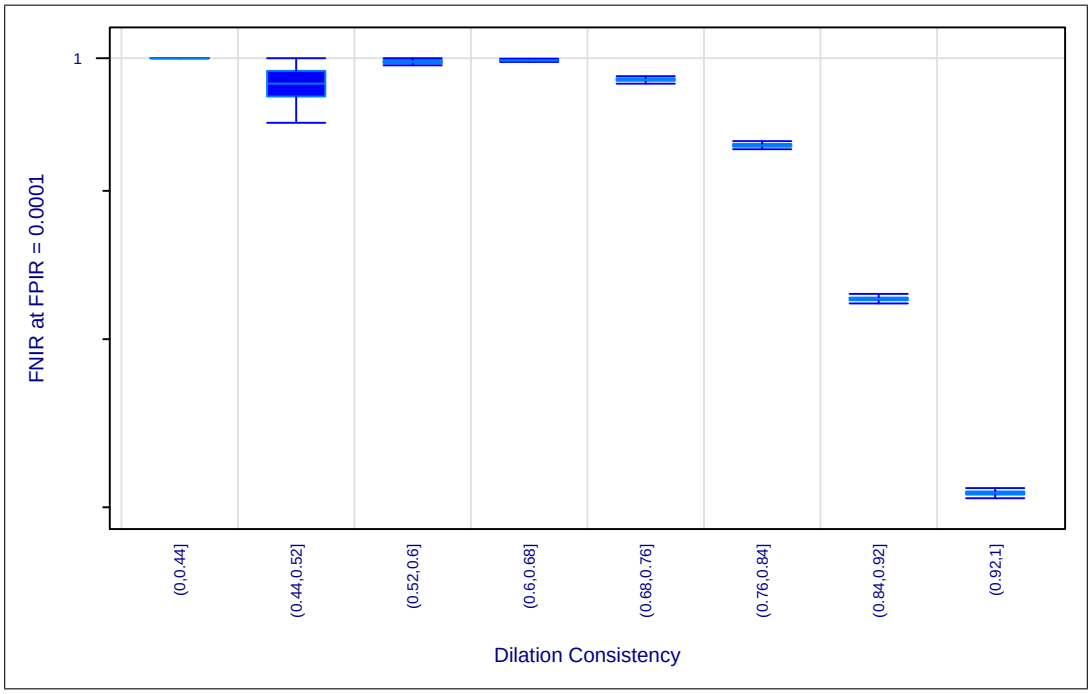

(a) Boxplot, all images

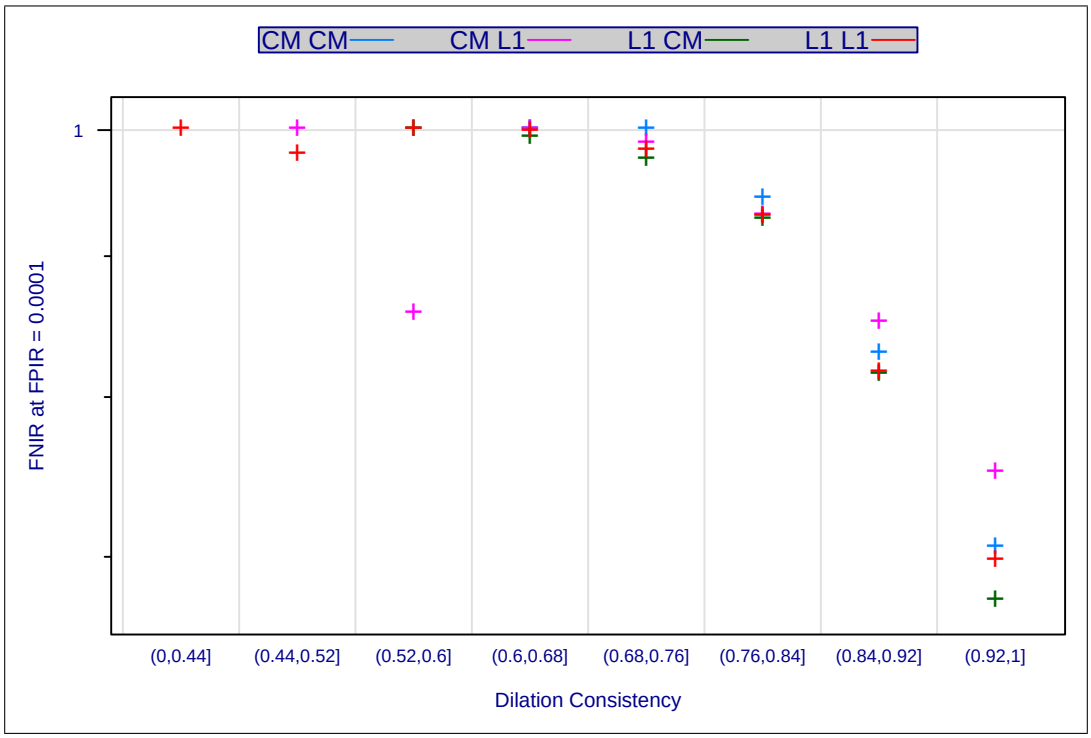

(b) Mean, L1 and CM images

Figure 294: Miss rate statistics for implementation P11A executing mate searches in an enrolled population of N = 1.6 million. The figures plots FNIR at FPIR = 0.0001 versus the IREX I metric for dilation consistency $(1 - \max(D_1, D_2))/(1 - \min(D_1, D_2))$ where D_i is pupil-iris radius ratio, and the subscripts refer to the mated enrollment and search image. The pathologically compressed 330x330 images are excluded from this analysis. The second figure breaks out dilation effects for interoperating camera pairs, CM and L1.

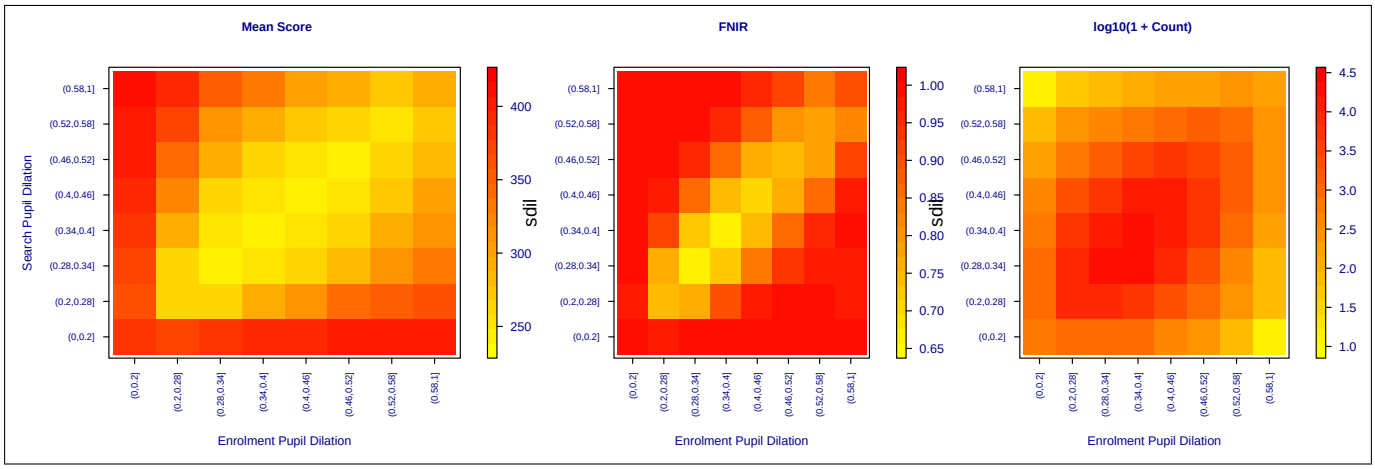

(a) Mate Dilation: Dis-similarity Score, Miss Rate, $\log_{10}(1+\text{Count})$

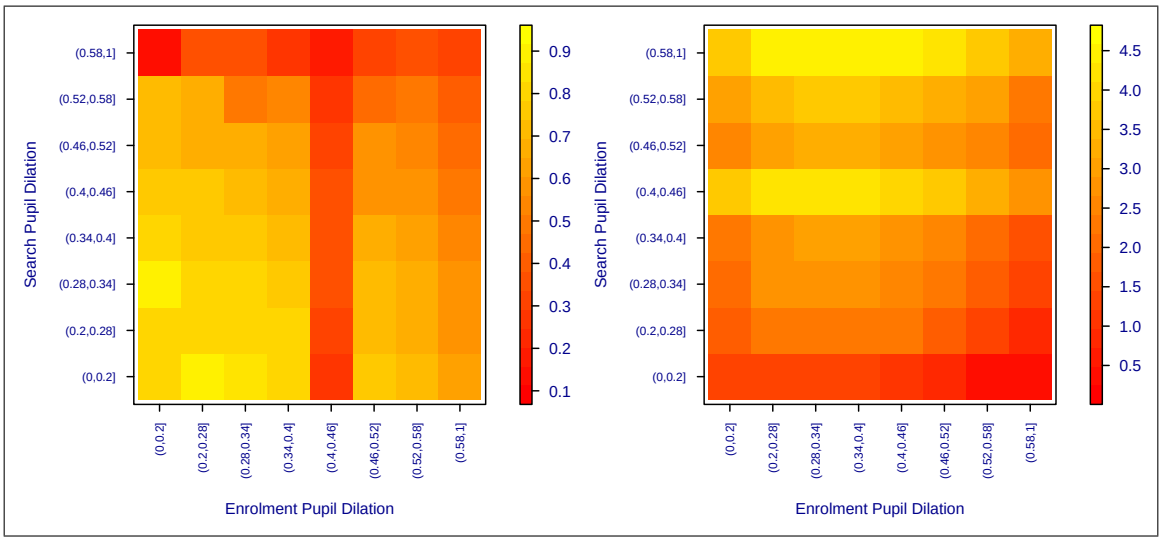

(b) Nonmate Dilation, Dis-similarity Score, Miss Rate, $\log_{10}(1+\text{Count})$

Figure 295: Heatmaps for implementation P11B executing mate searches in an enrolled population of N = 1.6 million. The radius images are binned by into twelve quantiles spanning $[0, 1]$. The dilation values are cut into ranges bounded by: $(0, 0.2, 0.28, 0.34, 0.40, 0.46, 0.52, 0.58, 1)$. The pathologically compressed 330x330 images are excluded from this analysis.

Heatmaps for implementation P11B executing mate searches in an enrolled population of N = 1.6 million.

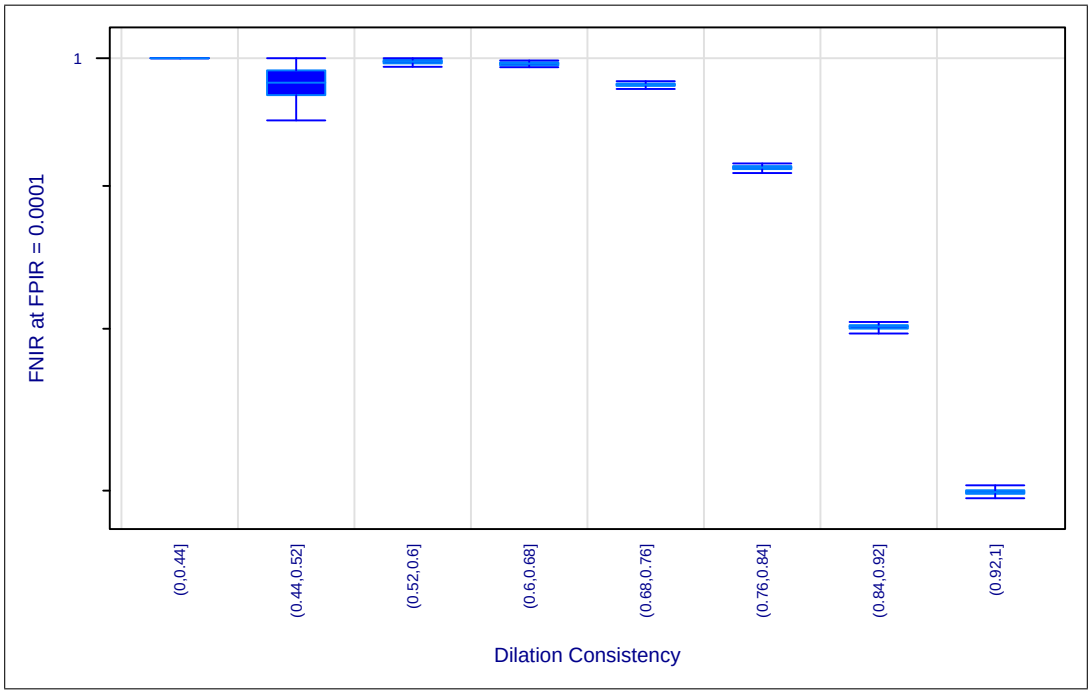

(a) Boxplot, all images

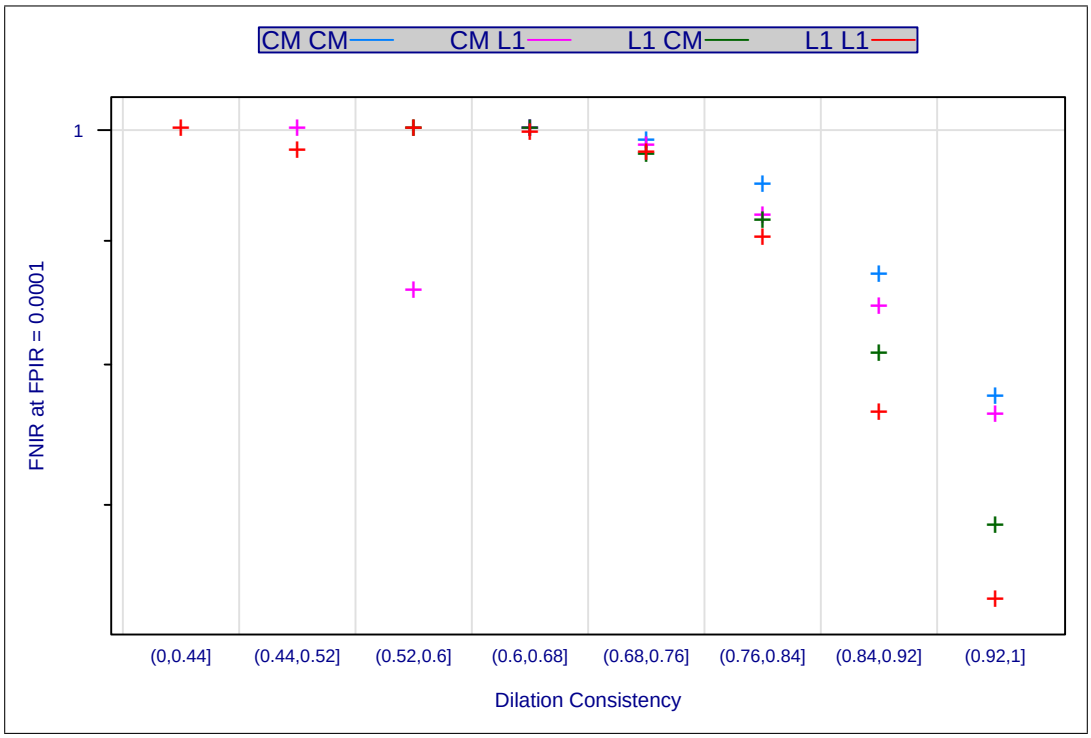

(b) Mean, L1 and CM images

Figure 296: Miss rate statistics for implementation P11B executing mate searches in an enrolled population of N = 1.6 million. The figures plots FNIR at FPIR = 0.0001 versus the IREX I metric for dilation consistency $(1 - \max(D_1, D_2))/(1 - \min(D_1, D_2))$ where D_i is pupil-iris radius ratio, and the subscripts refer to the mated enrollment and search image. The pathologically compressed 330x330 images are excluded from this analysis. The second figure breaks out dilation effects for interoperating camera pairs, CM and L1.

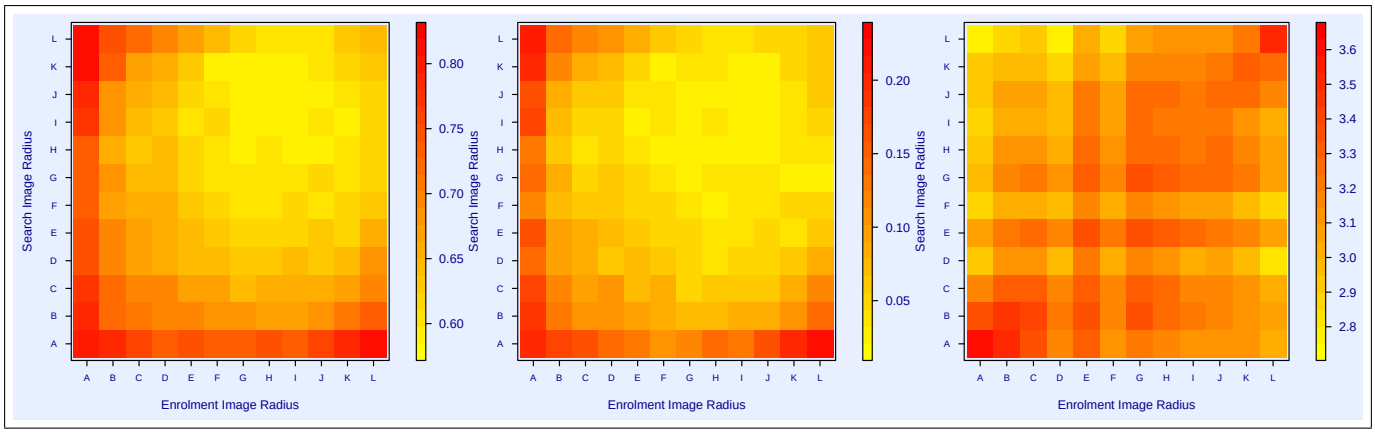

(a) Iris radius: Dis-similarity Score, Miss Rate, $\log_{10}(1+\text{Count})$

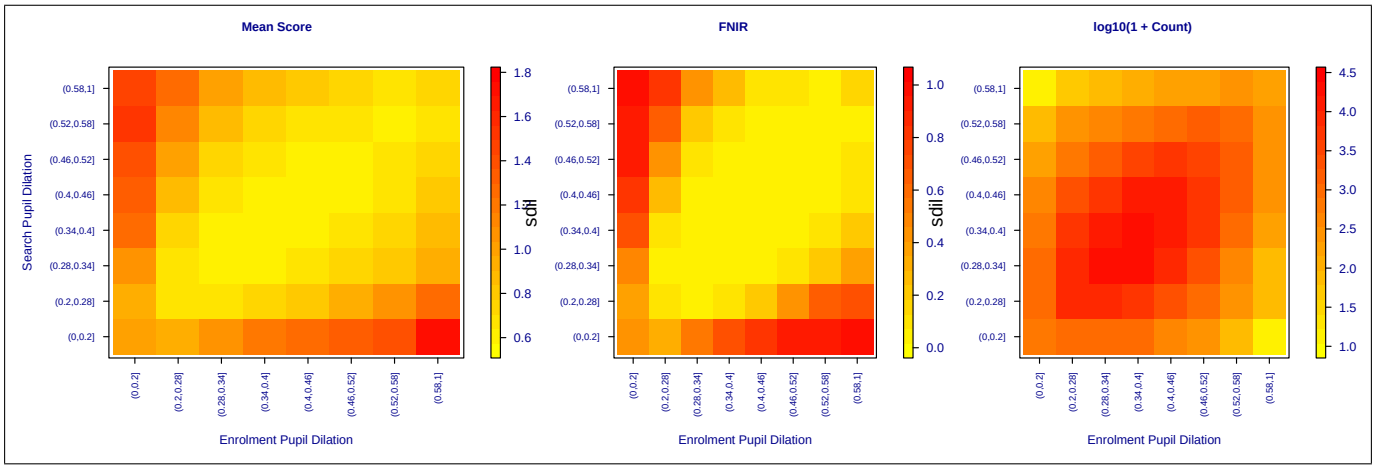

(b) Mate Dilation: Dis-similarity Score, Miss Rate, $\log_{10}(1+\text{Count})$

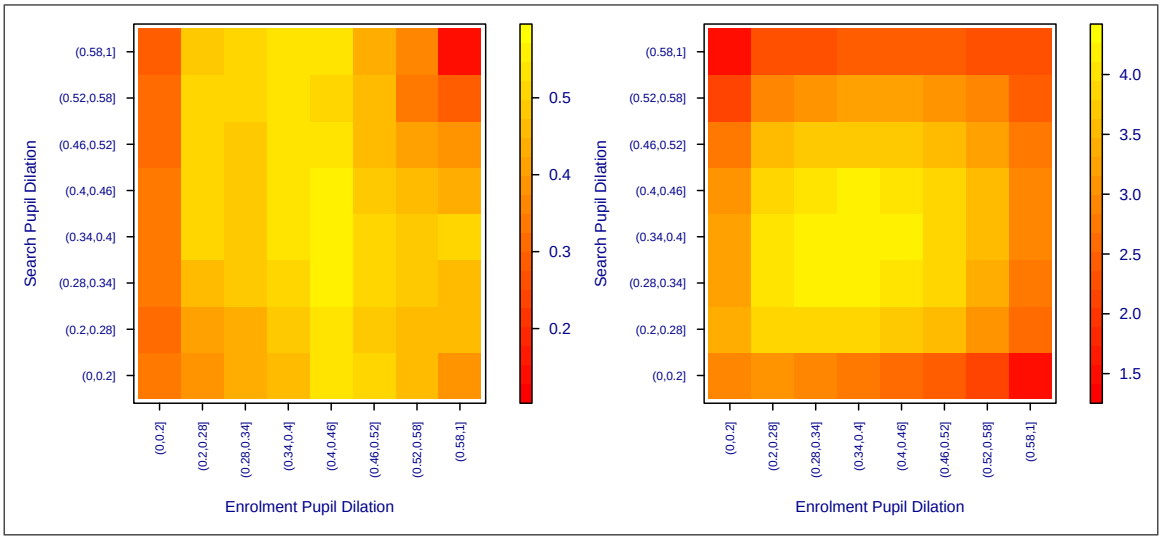

(c) Nonmate Dilation, Dis-similarity Score, Miss Rate, $\log_{10}(1+\text{Count})$

Figure 297: Heatmaps for implementation Q02A executing mate searches in an enrolled population of N = 1.6 million. The radius images are binned by into twelve quantiles spanning $[0, 1]$. The dilation values are cut into ranges bounded by: $(0, 0.2, 0.28, 0.34, 0.40, 0.46, 0.52, 0.58, 1)$. The pathologically compressed 330x330 images are excluded from this analysis.

Heatmaps for implementation Q02A executing mate searches in an enrolled population of N = 1.6 million.

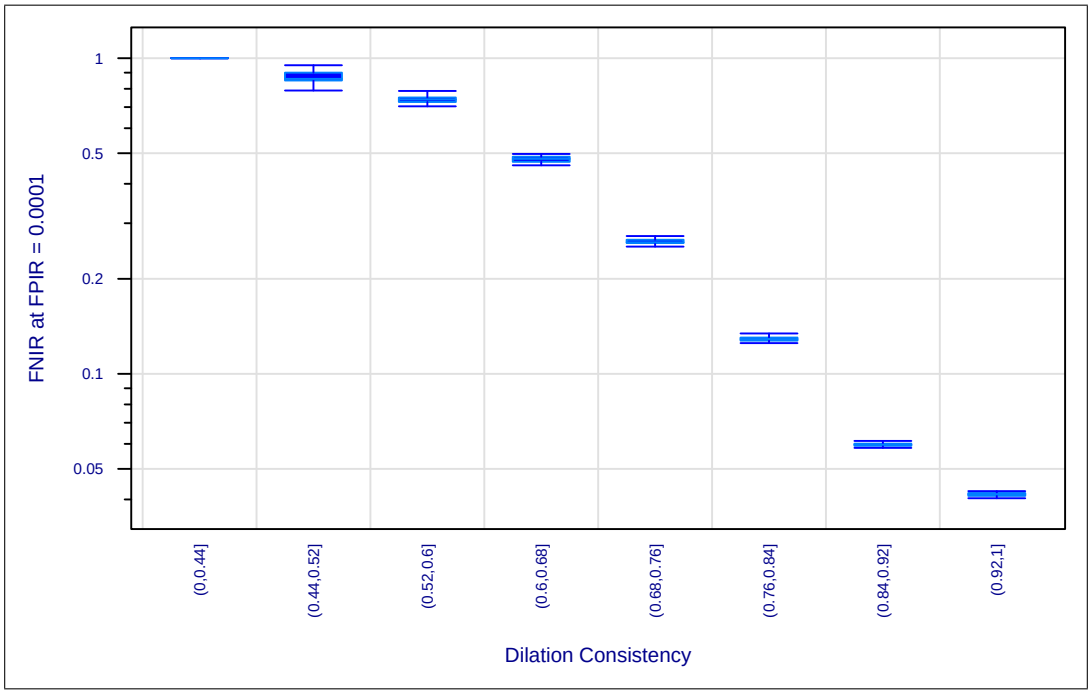

(a) Boxplot, all images

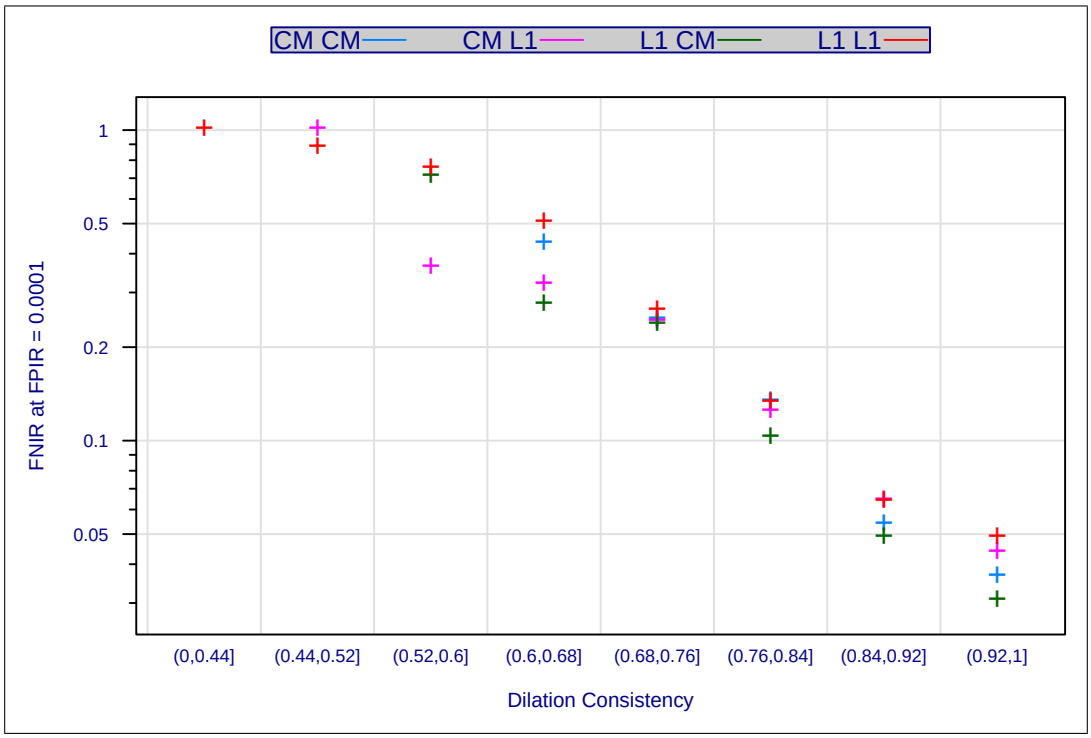

(b) Mean, L1 and CM images

Figure 298: Miss rate statistics for implementation Q02A executing mate searches in an enrolled population of N = 1.6 million. The figures plots FNIR at FPIR = 0.0001 versus the IREX I metric for dilation consistency $(1 - \max(D_1, D_2))/(1 - \min(D_1, D_2))$ where D_i is pupil-iris radius ratio, and the subscripts refer to the mated enrollment and search image. The pathologically compressed 330x330 images are excluded from this analysis. The second figure breaks out dilation effects for interoperating camera pairs, CM and L1.

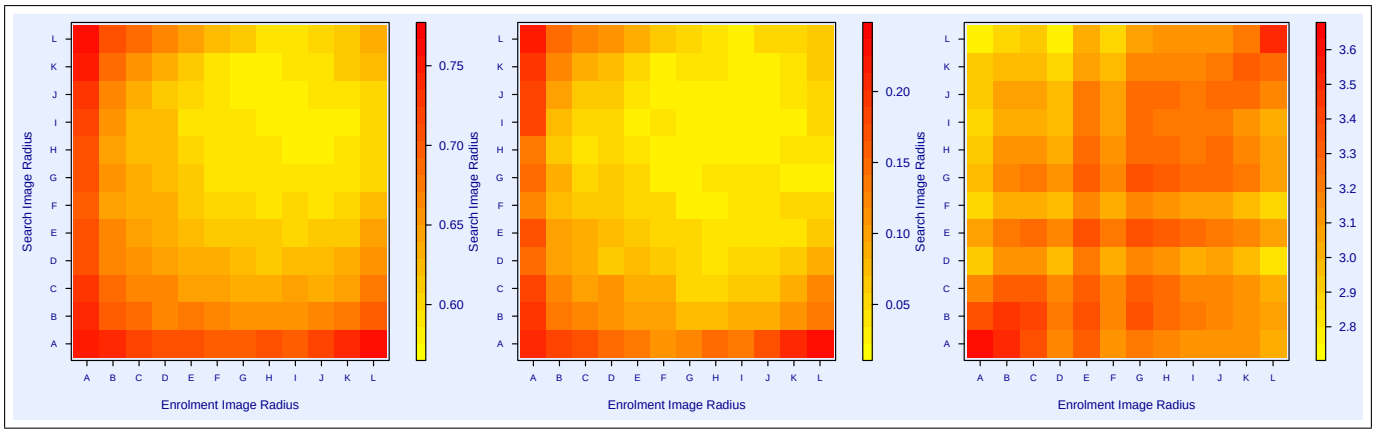

(a) Iris radius: Dis-similarity Score, Miss Rate, $\log_{10}(1+\text{Count})$

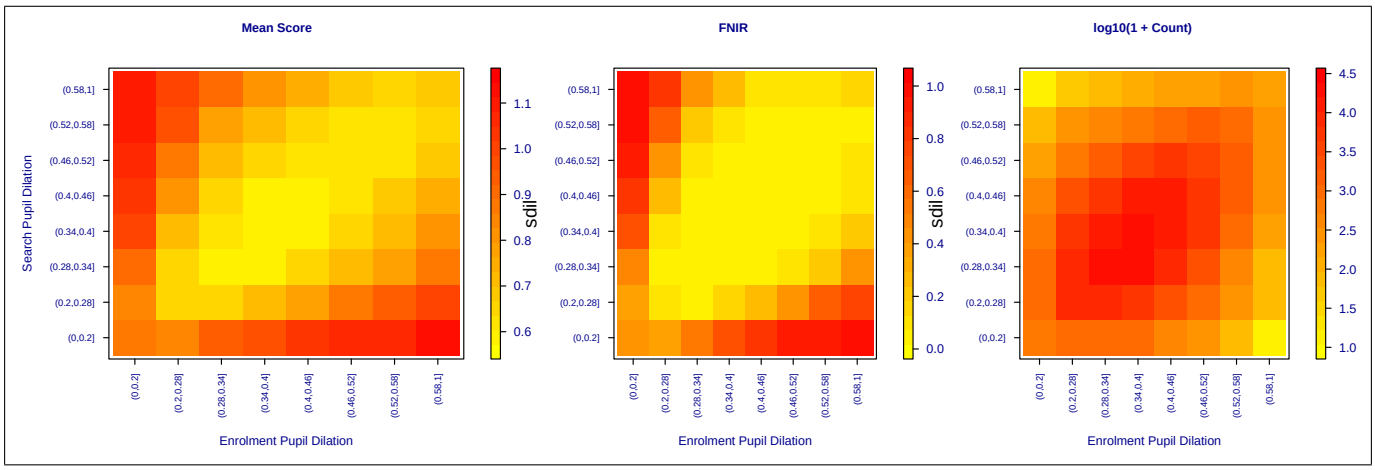

(b) Mate Dilation: Dis-similarity Score, Miss Rate, $\log_{10}(1+\text{Count})$

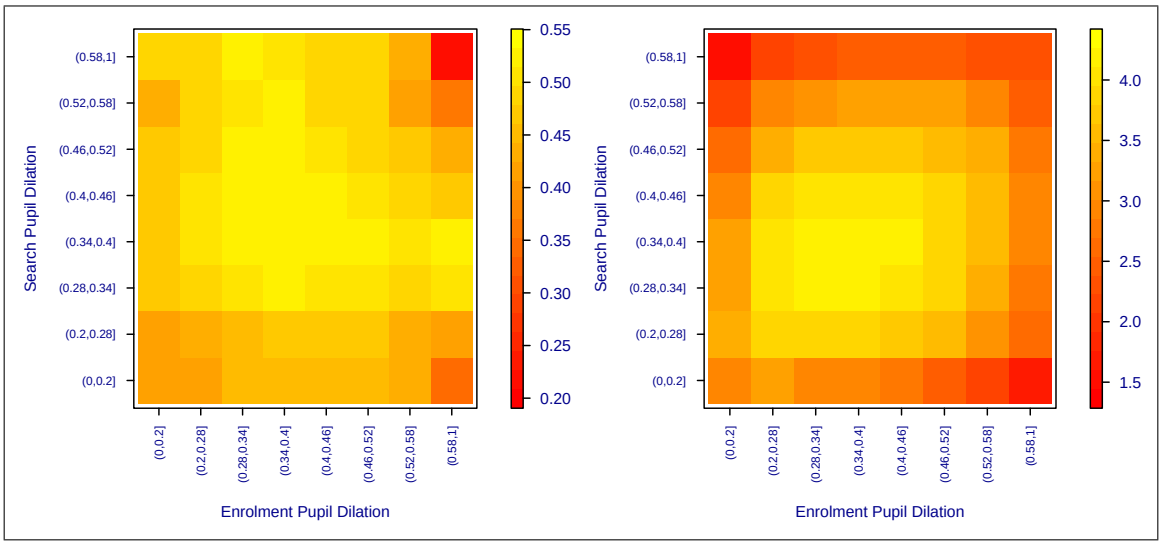

(c) Nonmate Dilation, Dis-similarity Score, Miss Rate, $\log_{10}(1+\text{Count})$

Figure 299: Heatmaps for implementation Q02B executing mate searches in an enrolled population of N = 1.6 million. The radius images are binned by into twelve quantiles spanning $[0, 1]$. The dilation values are cut into ranges bounded by: $(0, 0.2, 0.28, 0.34, 0.40, 0.46, 0.52, 0.58, 1)$. The pathologically compressed 330x330 images are excluded from this analysis.

Heatmaps for implementation Q02B executing mate searches in an enrolled population of N = 1.6 million.

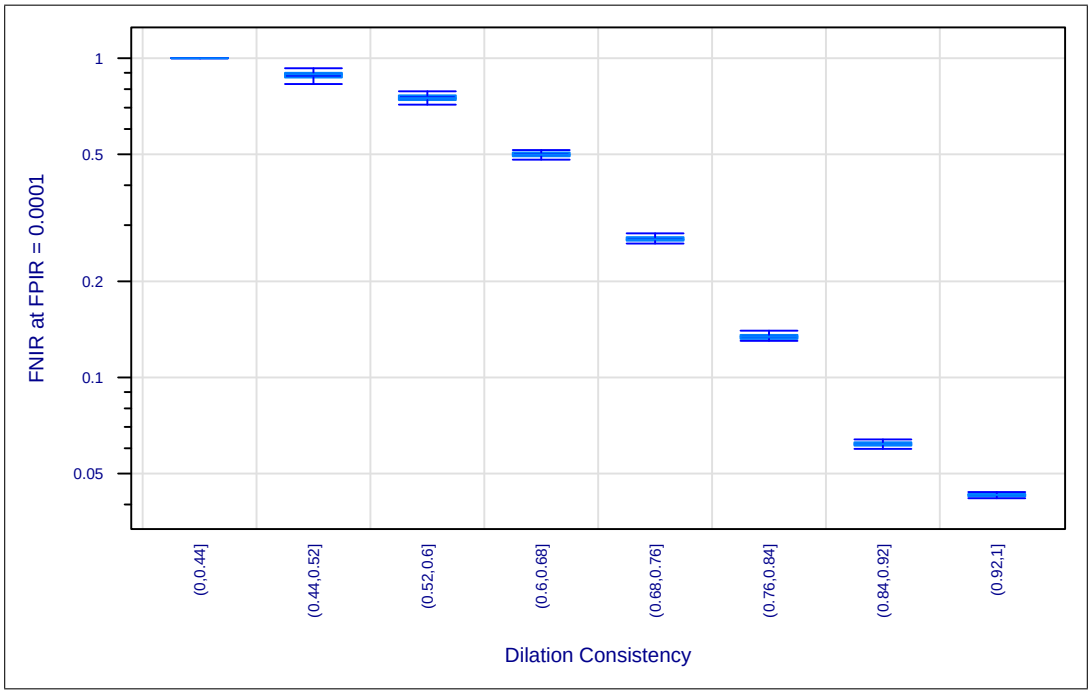

(a) Boxplot, all images

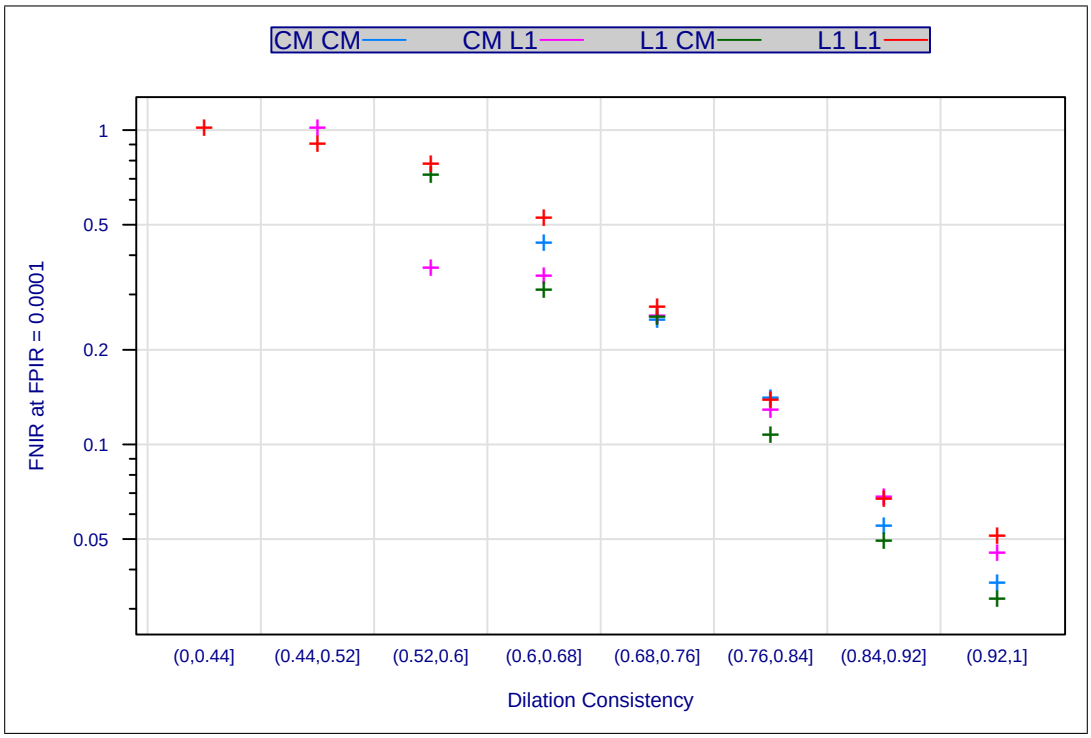

(b) Mean, L1 and CM images

Figure 300: Miss rate statistics for implementation Q02B executing mate searches in an enrolled population of N = 1.6 million. The figures plots FNIR at FPIR = 0.0001 versus the IREX I metric for dilation consistency $(1 - \max(D_1, D_2))/(1 - \min(D_1, D_2))$ where D_i is pupil-iris radius ratio, and the subscripts refer to the mated enrollment and search image. The pathologically compressed 330x330 images are excluded from this analysis. The second figure breaks out dilation effects for interoperating camera pairs, CM and L1.

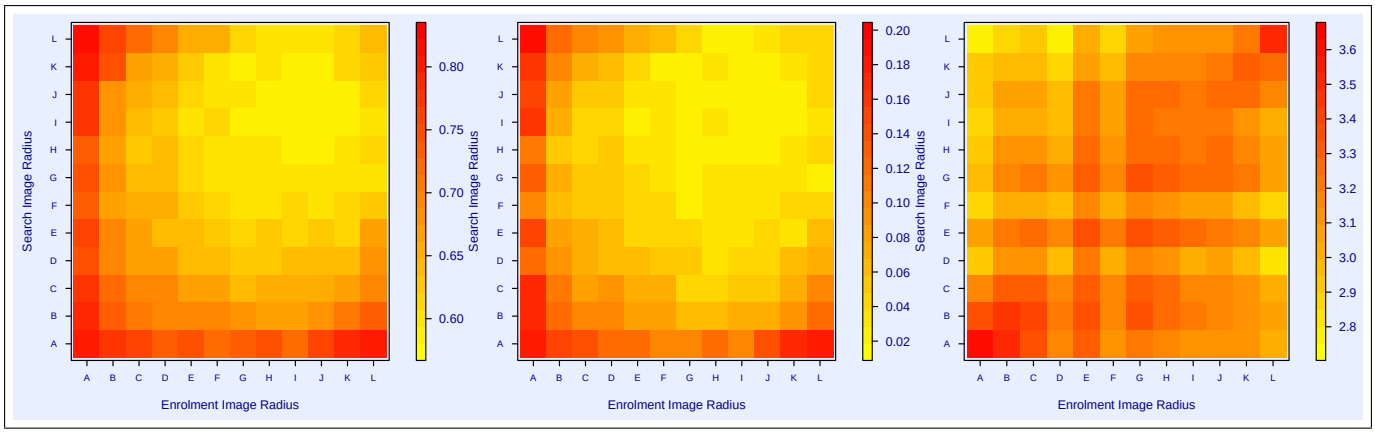

(a) Iris radius: Dis-similarity Score, Miss Rate, $\log_{10}(1+\text{Count})$

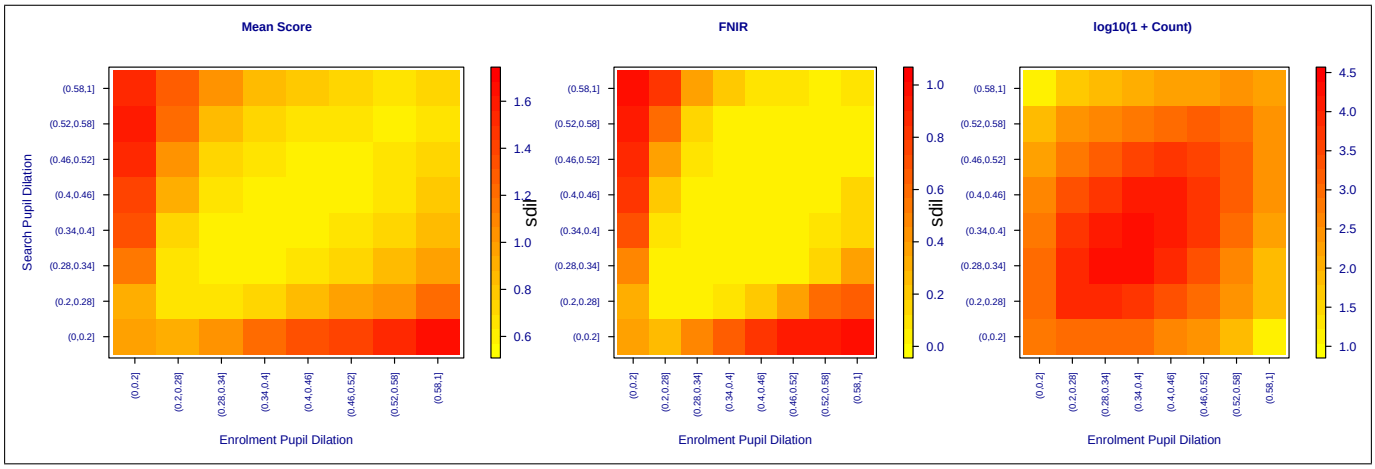

(b) Mate Dilation: Dis-similarity Score, Miss Rate, $\log_{10}(1+\text{Count})$

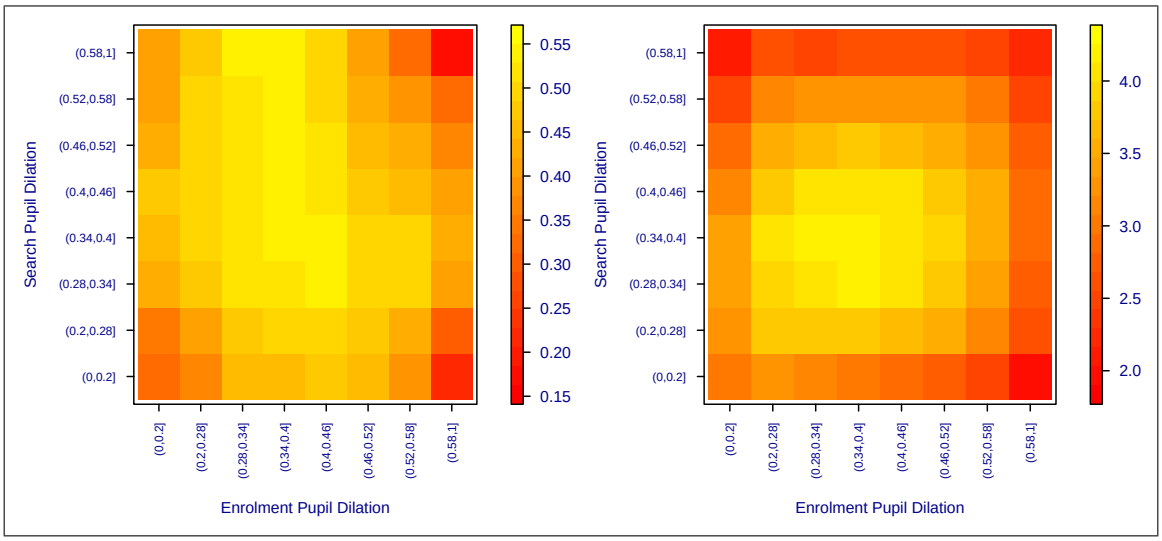

(c) Nonmate Dilation, Dis-similarity Score, Miss Rate, $\log_{10}(1+\text{Count})$

Figure 301: Heatmaps for implementation Q03A executing mate searches in an enrolled population of N = 1.6 million. The radius images are binned by into twelve quantiles spanning $[0, 1]$. The dilation values are cut into ranges bounded by: $(0, 0.2, 0.28, 0.34, 0.40, 0.46, 0.52, 0.58, 1)$. The pathologically compressed 330x330 images are excluded from this analysis.

Heatmaps for implementation Q03A executing mate searches in an enrolled population of N = 1.6 million.

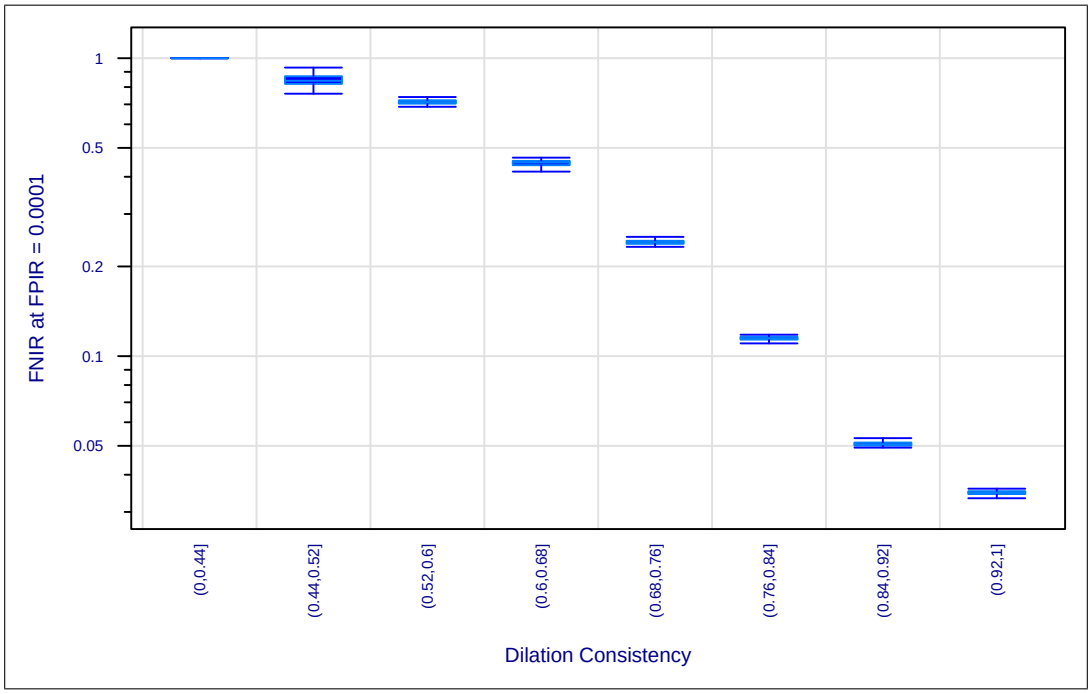

(a) Boxplot, all images

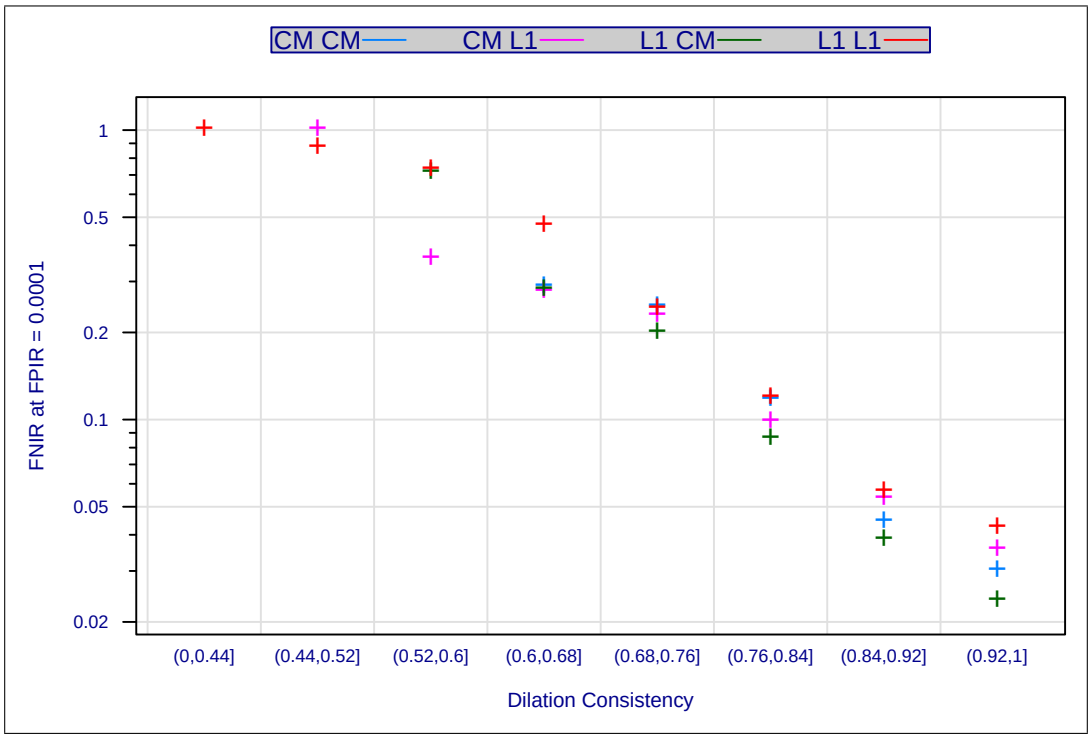

(b) Mean, L1 and CM images

Figure 302: Miss rate statistics for implementation Q03A executing mate searches in an enrolled population of N = 1.6 million. The figures plots FNIR at FPIR = 0.0001 versus the IREX I metric for dilation consistency $(1 - \max(D_1, D_2))/(1 - \min(D_1, D_2))$ where D_i is pupil-iris radius ratio, and the subscripts refer to the mated enrollment and search image. The pathologically compressed 330x330 images are excluded from this analysis. The second figure breaks out dilation effects for interoperating camera pairs, CM and L1.

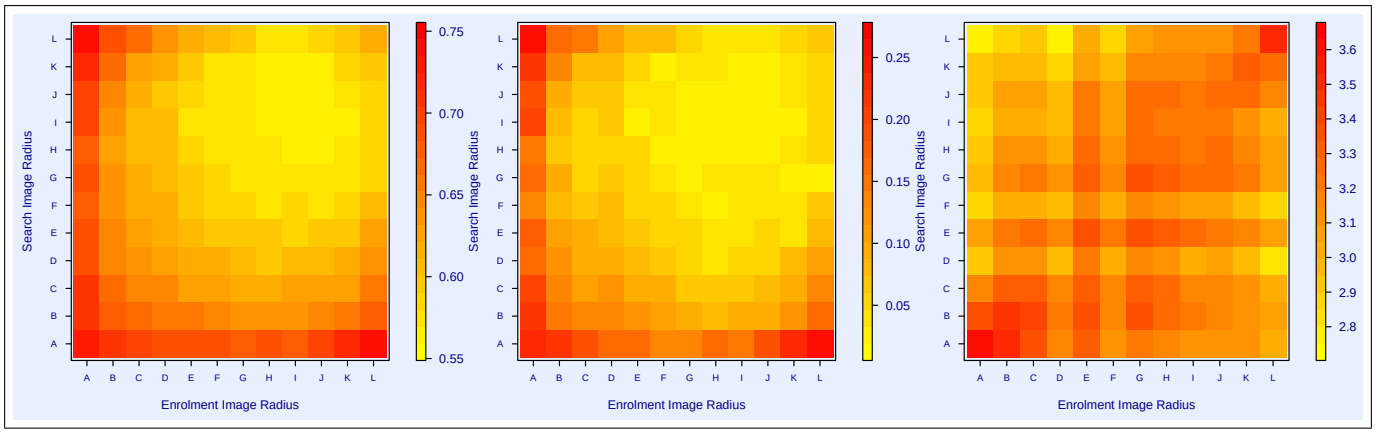

(a) Iris radius: Dis-similarity Score, Miss Rate, $\log_{10}(1+\text{Count})$

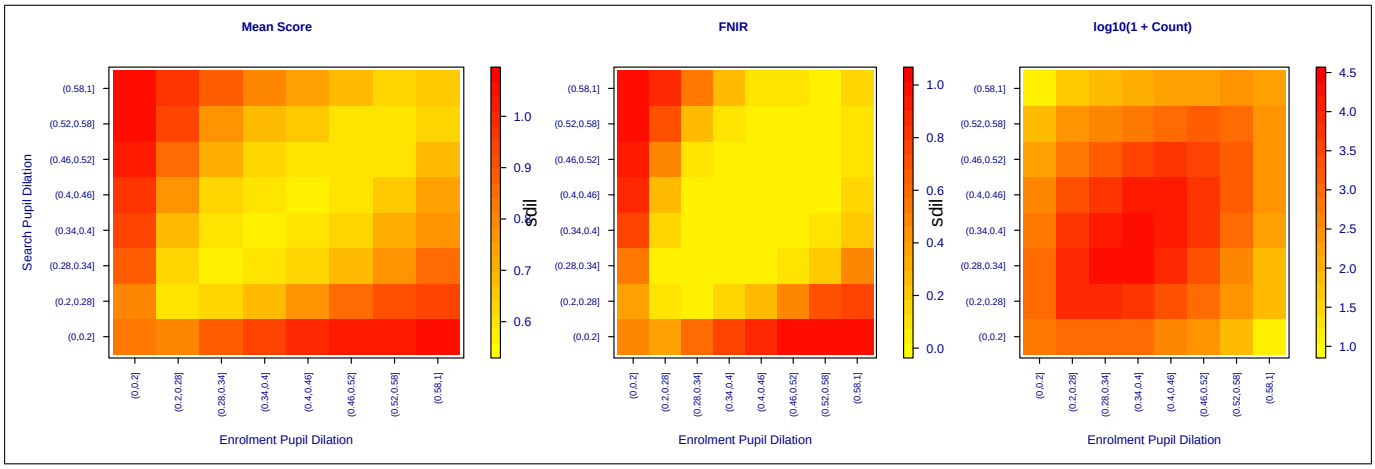

(b) Mate Dilation: Dis-similarity Score, Miss Rate, $\log_{10}(1+\text{Count})$

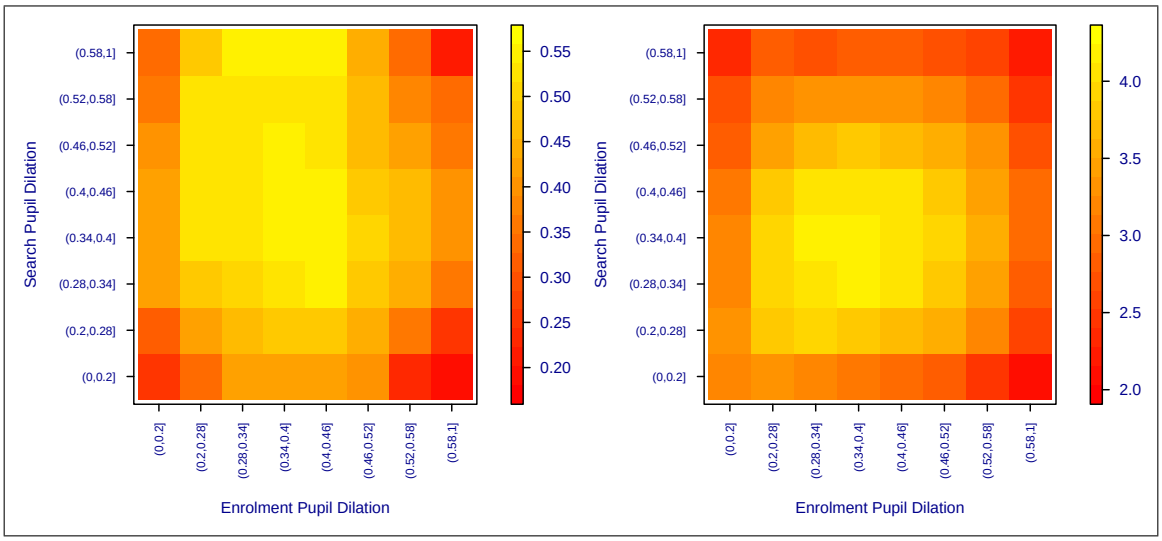

(c) Nonmate Dilation, Dis-similarity Score, Miss Rate, $\log_{10}(1+\text{Count})$

Figure 303: Heatmaps for implementation Q03B executing mate searches in an enrolled population of N = 1.6 million. The radius images are binned by into twelve quantiles spanning $[0, 1]$. The dilation values are cut into ranges bounded by: $(0, 0.2, 0.28, 0.34, 0.40, 0.46, 0.52, 0.58, 1)$. The pathologically compressed 330x330 images are excluded from this analysis.

Heatmaps for implementation Q03B executing mate searches in an enrolled population of N = 1.6 million.

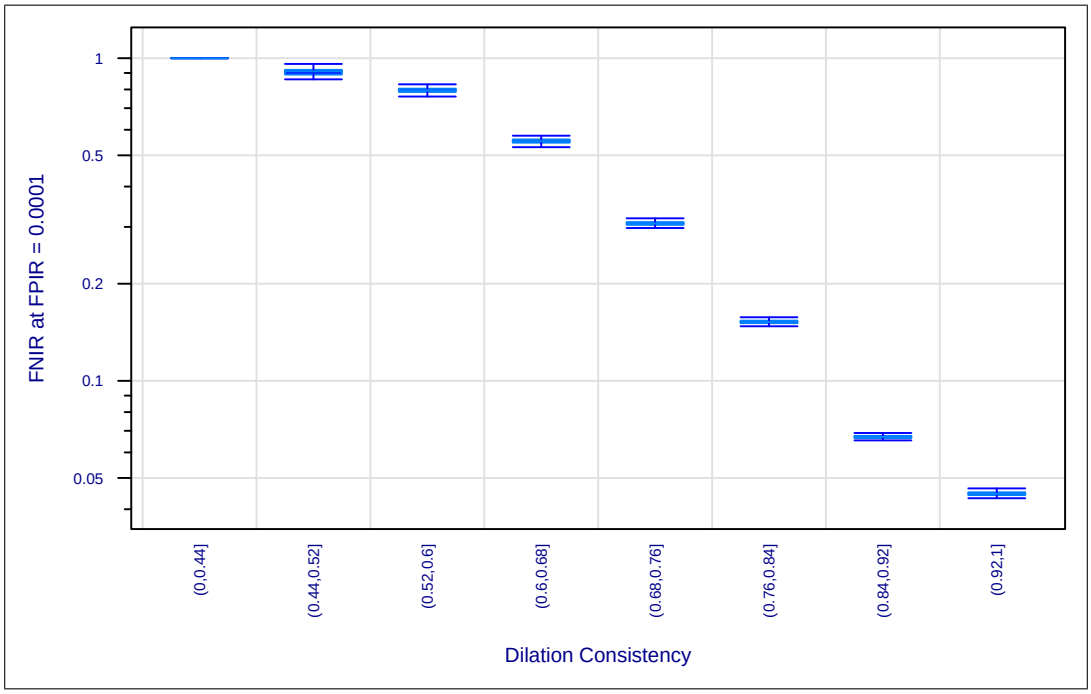

(a) Boxplot, all images

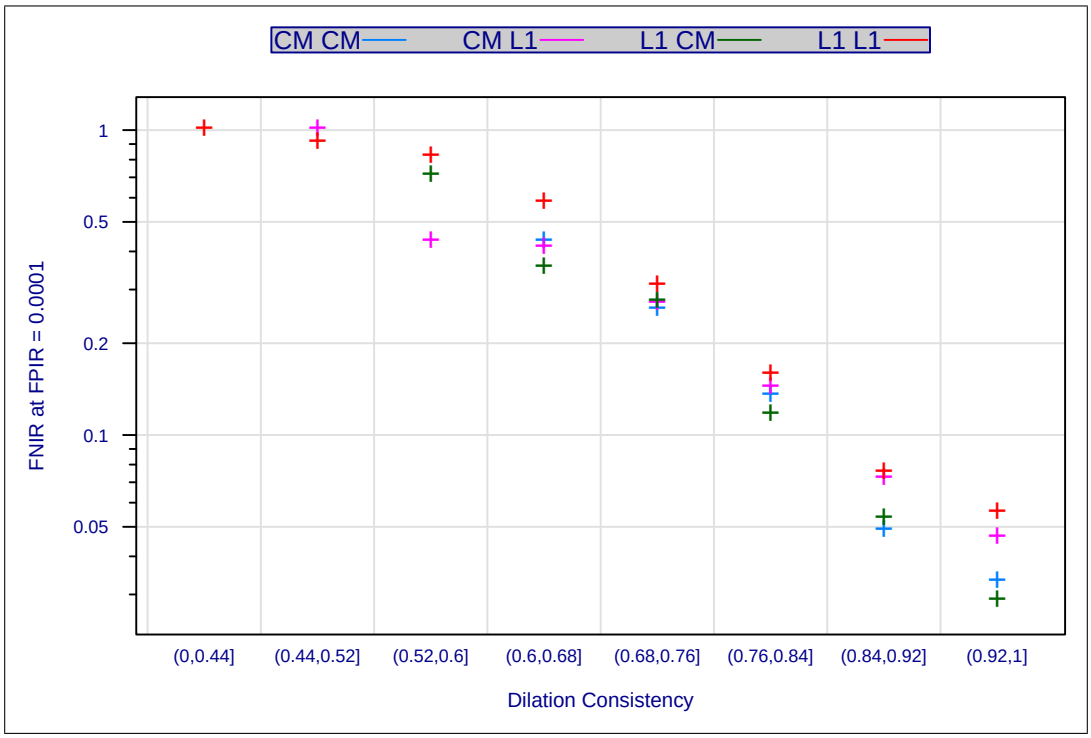

(b) Mean, L1 and CM images

Figure 304: Miss rate statistics for implementation Q03B executing mate searches in an enrolled population of N = 1.6 million. The figures plots FNIR at FPIR = 0.0001 versus the IREX I metric for dilation consistency $(1 - \max(D_1, D_2))/(1 - \min(D_1, D_2))$ where D_i is pupil-iris radius ratio, and the subscripts refer to the mated enrollment and search image. The pathologically compressed 330x330 images are excluded from this analysis. The second figure breaks out dilation effects for interoperating camera pairs, CM and L1.

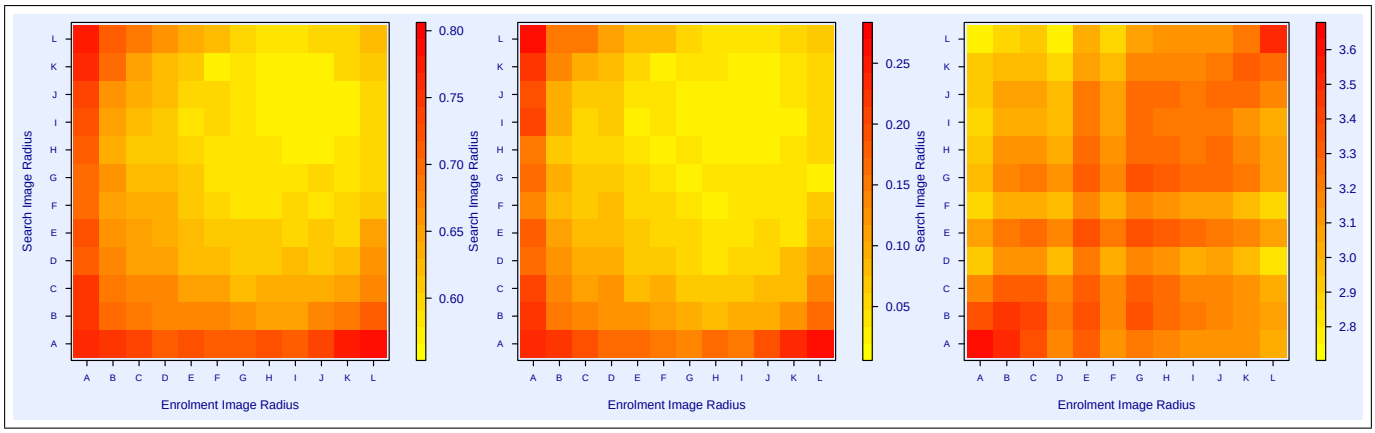

(a) Iris radius: Dis-similarity Score, Miss Rate, $\log_{10}(1+\text{Count})$

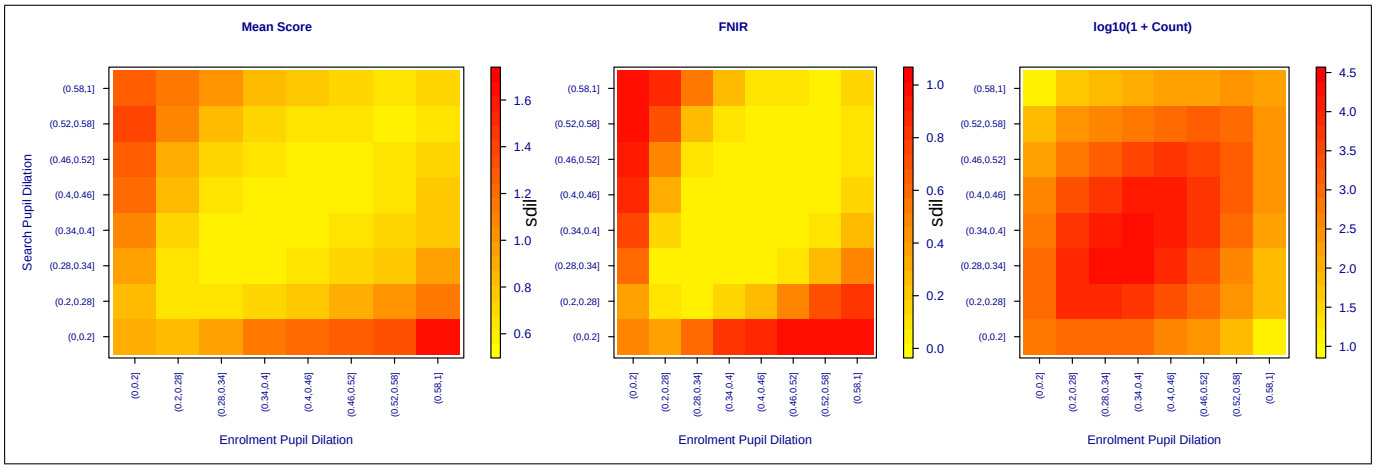

(b) Mate Dilation: Dis-similarity Score, Miss Rate, $\log_{10}(1+\text{Count})$

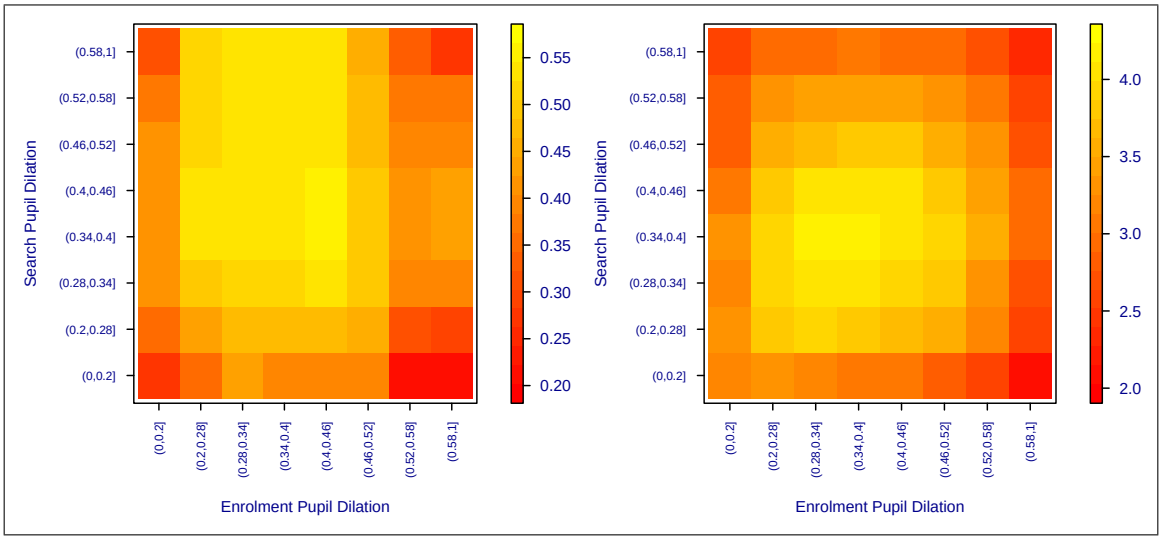

(c) Nonmate Dilation, Dis-similarity Score, Miss Rate, $\log_{10}(1+\text{Count})$

Figure 305: Heatmaps for implementation Q04B executing mate searches in an enrolled population of N = 1.6 million. The radius images are binned by into twelve quantiles spanning $[0, 1]$. The dilation values are cut into ranges bounded by: $(0, 0.2, 0.28, 0.34, 0.40, 0.46, 0.52, 0.58, 1)$. The pathologically compressed 330x330 images are excluded from this analysis.

Heatmaps for implementation Q04B executing mate searches in an enrolled population of N = 1.6 million.

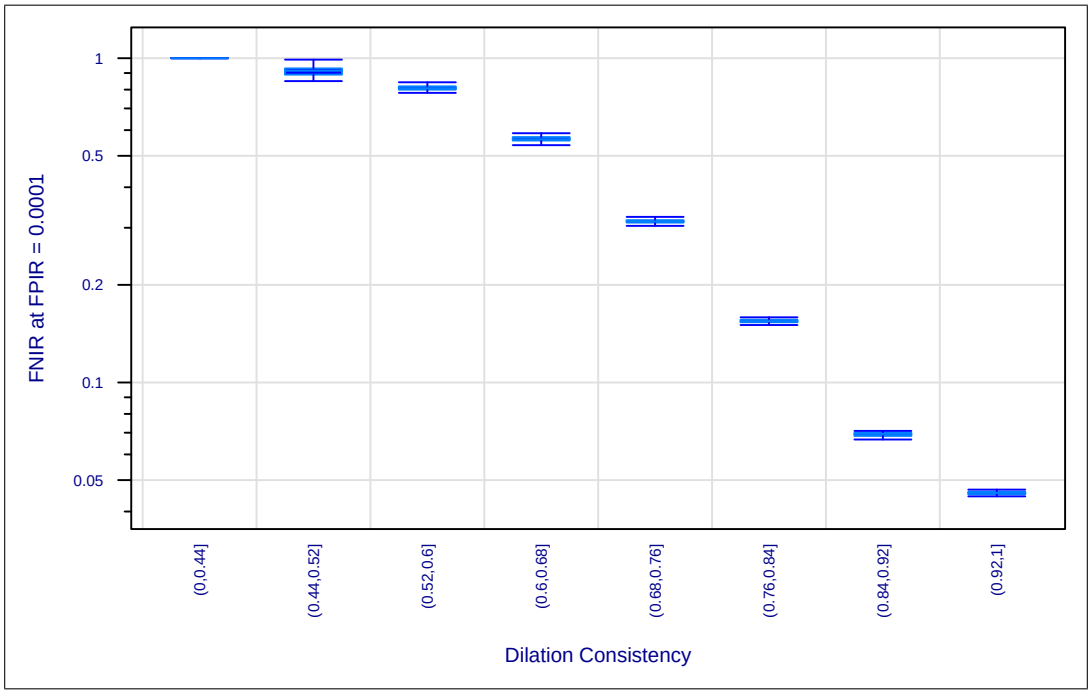

(a) Boxplot, all images

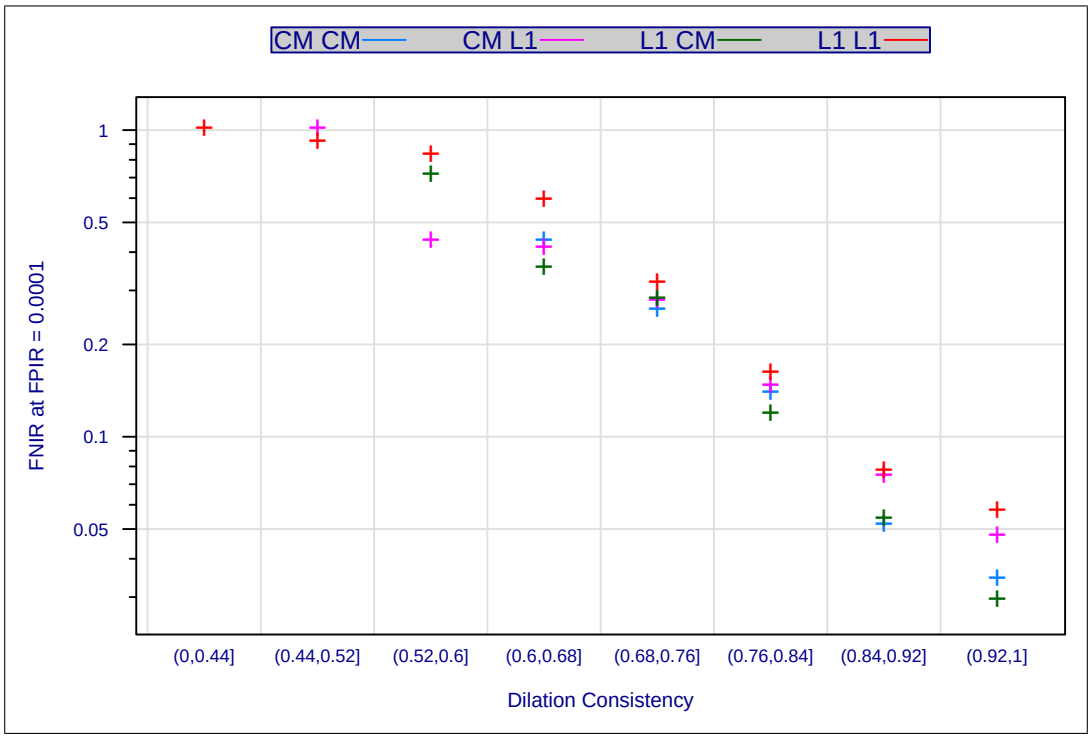

(b) Mean, L1 and CM images

Figure 306: Miss rate statistics for implementation Q04B executing mate searches in an enrolled population of N = 1.6 million. The figures plots FNIR at FPIR = 0.0001 versus the IREX I metric for dilation consistency $(1 - \max(D_1, D_2))/(1 - \min(D_1, D_2))$ where D_i is pupil-iris radius ratio, and the subscripts refer to the mated enrollment and search image. The pathologically compressed 330x330 images are excluded from this analysis. The second figure breaks out dilation effects for interoperating camera pairs, CM and L1.

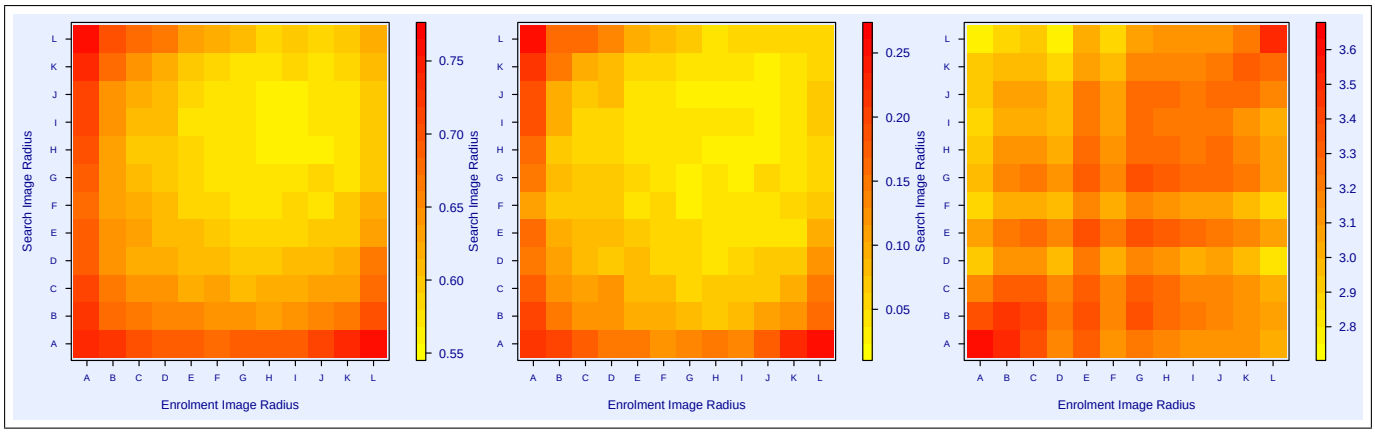

(a) Iris radius: Dis-similarity Score, Miss Rate, $\log_{10}(1+\text{Count})$

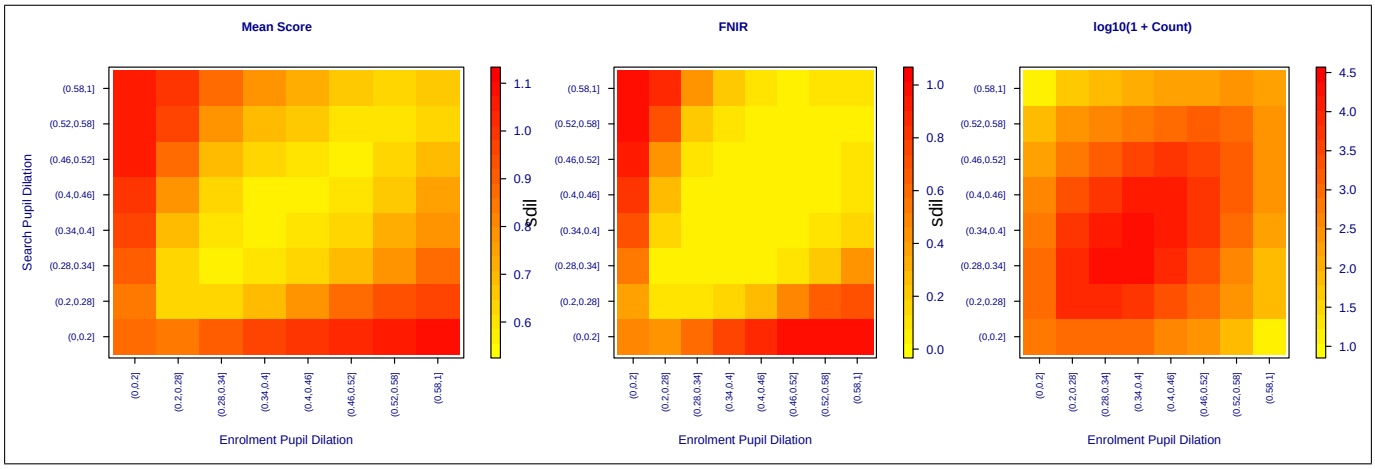

(b) Mate Dilation: Dis-similarity Score, Miss Rate, $\log_{10}(1+\text{Count})$

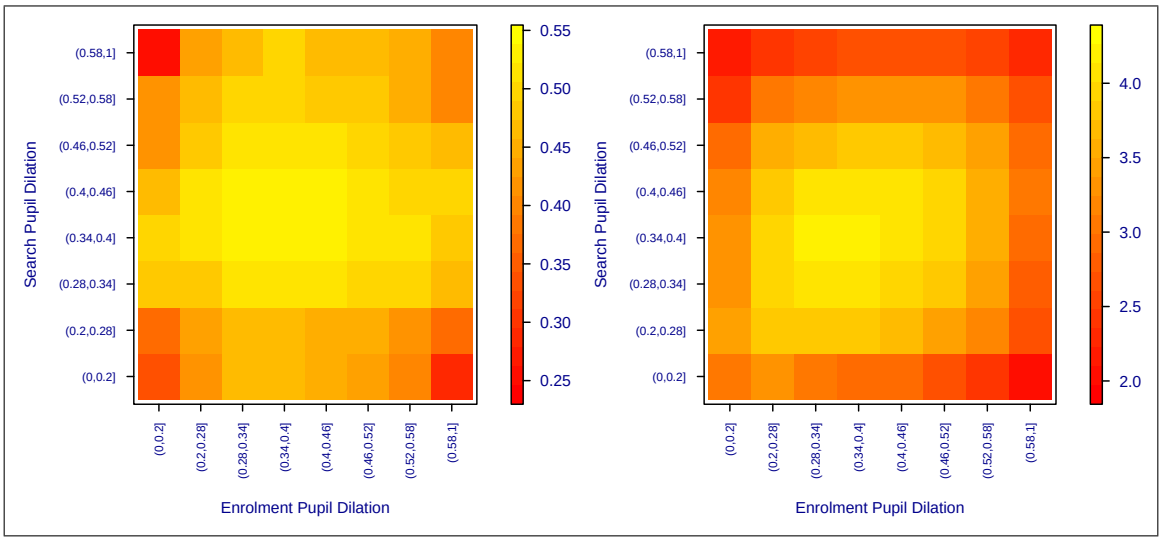

(c) Nonmate Dilation, Dis-similarity Score, Miss Rate, $\log_{10}(1+\text{Count})$

Figure 307: Heatmaps for implementation Q11B executing mate searches in an enrolled population of N = 1.6 million. The radius images are binned by into twelve quantiles spanning $[0, 1]$. The dilation values are cut into ranges bounded by: $(0, 0.2, 0.28, 0.34, 0.40, 0.46, 0.52, 0.58, 1)$. The pathologically compressed 330x330 images are excluded from this analysis.

Heatmaps for implementation Q11B executing mate searches in an enrolled population of N = 1.6 million.

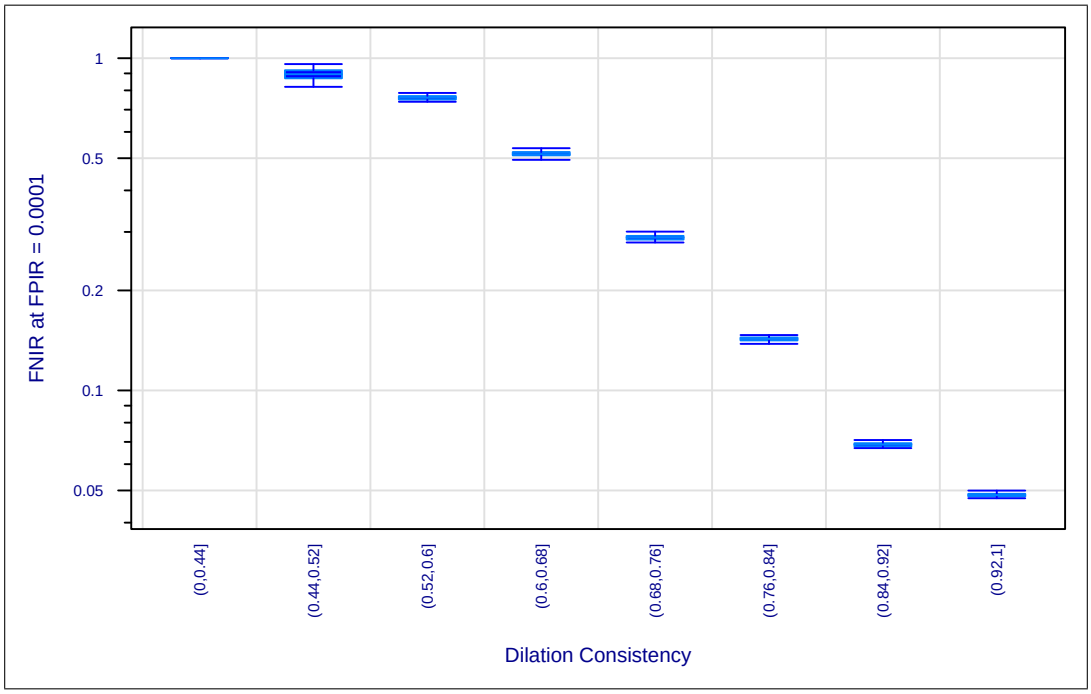

(a) Boxplot, all images

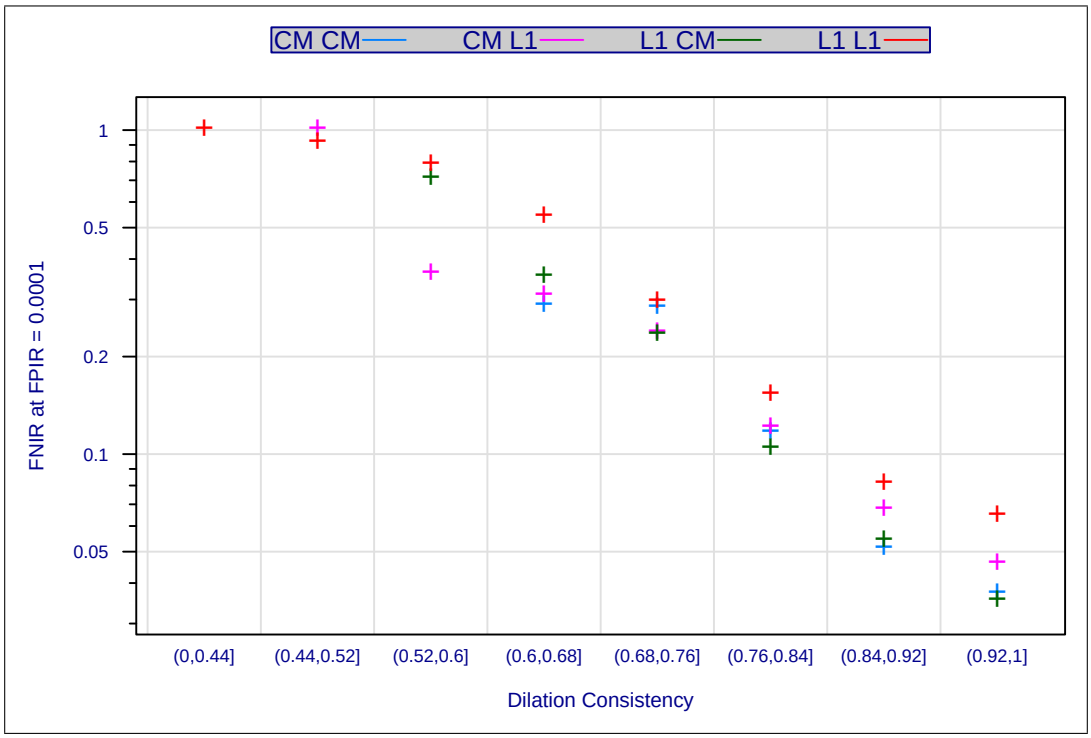

(b) Mean, L1 and CM images

Figure 308: Miss rate statistics for implementation Q11B executing mate searches in an enrolled population of N = 1.6 million. The figures plots FNIR at FPIR = 0.0001 versus the IREX I metric for dilation consistency $(1 - \max(D_1, D_2))/(1 - \min(D_1, D_2))$ where D_i is pupil-iris radius ratio, and the subscripts refer to the mated enrollment and search image. The pathologically compressed 330x330 images are excluded from this analysis. The second figure breaks out dilation effects for interoperating camera pairs, CM and L1.

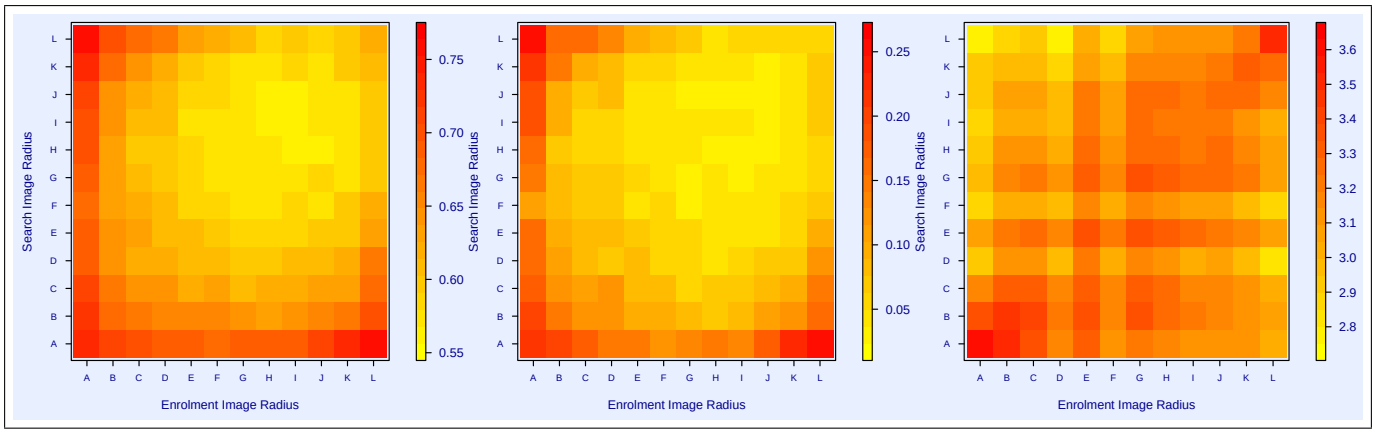

(a) Iris radius: Dis-similarity Score, Miss Rate, $\log_{10}(1+\text{Count})$

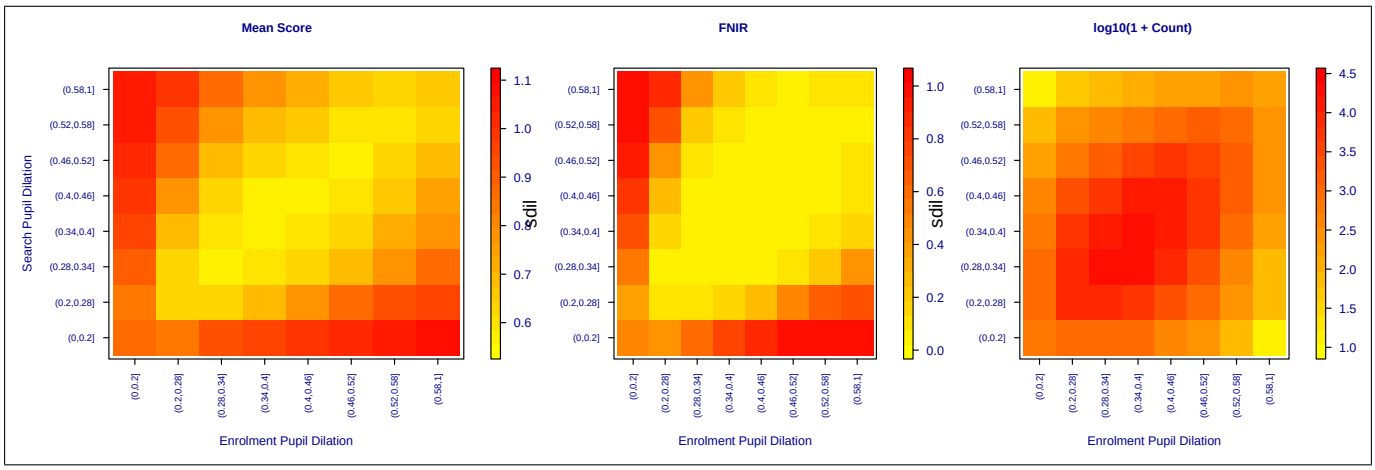

(b) Mate Dilation: Dis-similarity Score, Miss Rate, $\log_{10}(1+\text{Count})$

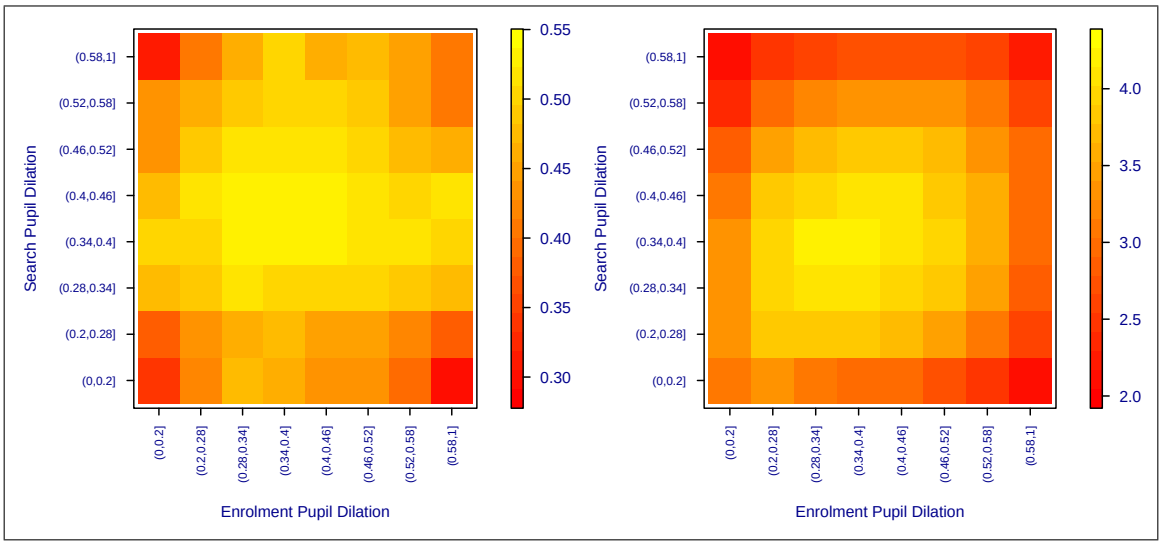

(c) Nonmate Dilation, Dis-similarity Score, Miss Rate, $\log_{10}(1+\text{Count})$

Figure 309: Heatmaps for implementation Q12B executing mate searches in an enrolled population of N = 1.6 million. The radius images are binned by into twelve quantiles spanning $[0, 1]$. The dilation values are cut into ranges bounded by: $(0, 0.2, 0.28, 0.34, 0.40, 0.46, 0.52, 0.58, 1)$. The pathologically compressed 330x330 images are excluded from this analysis.

Heatmaps for implementation Q12B executing mate searches in an enrolled population of N = 1.6 million.

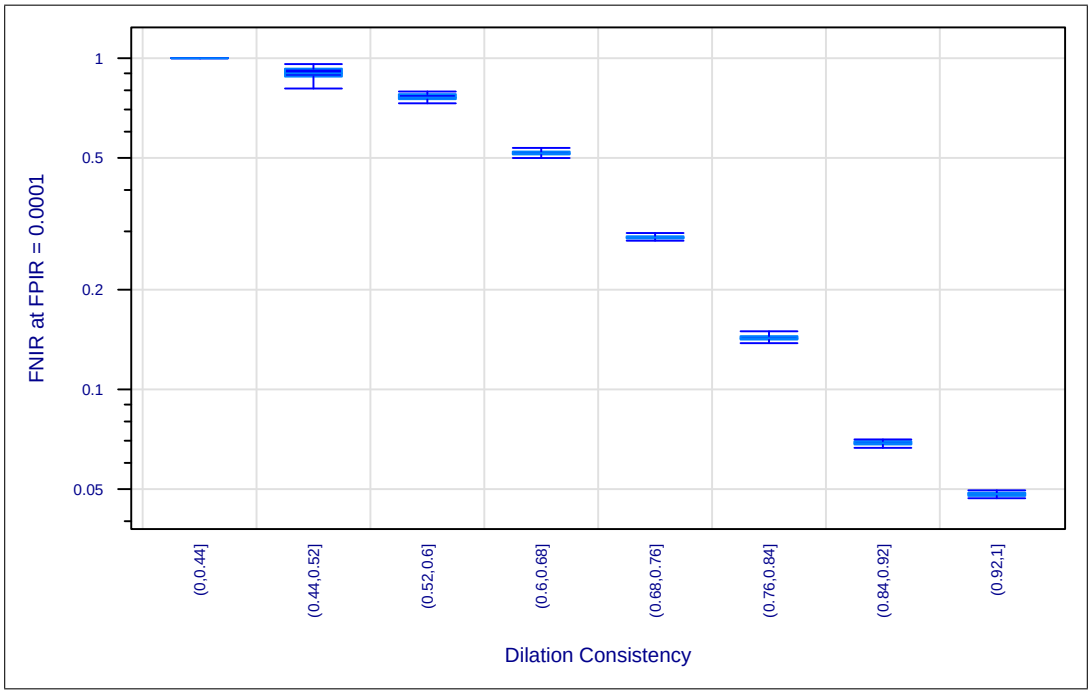

(a) Boxplot, all images

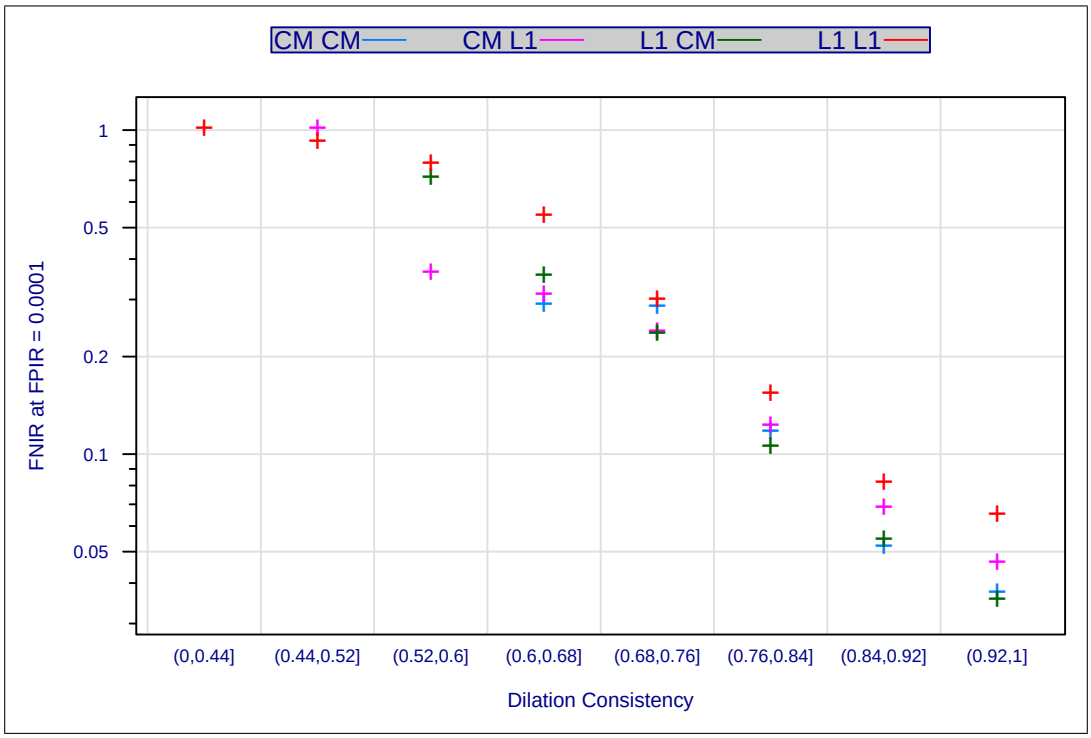

(b) Mean, L1 and CM images

Figure 310: Miss rate statistics for implementation Q12B executing mate searches in an enrolled population of N = 1.6 million. The figures plots FNIR at FPIR = 0.0001 versus the IREX I metric for dilation consistency $(1 - \max(D_1, D_2))/(1 - \min(D_1, D_2))$ where D_i is pupil-iris radius ratio, and the subscripts refer to the mated enrollment and search image. The pathologically compressed 330x330 images are excluded from this analysis. The second figure breaks out dilation effects for interoperating camera pairs, CM and L1.

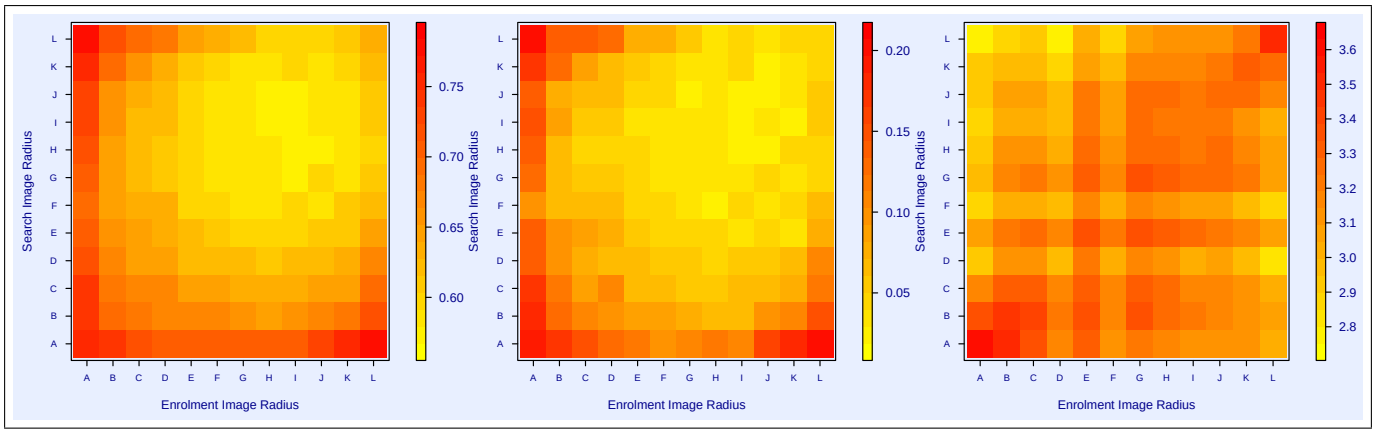

(a) Iris radius: Dis-similarity Score, Miss Rate, $\log_{10}(1+\text{Count})$

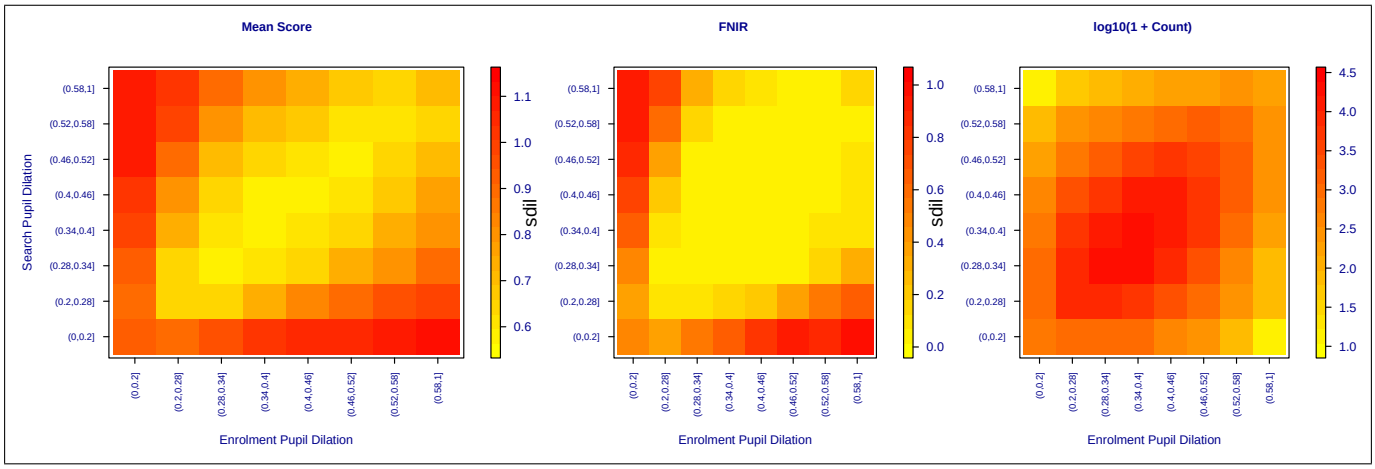

(b) Mate Dilation: Dis-similarity Score, Miss Rate, $\log_{10}(1+\text{Count})$

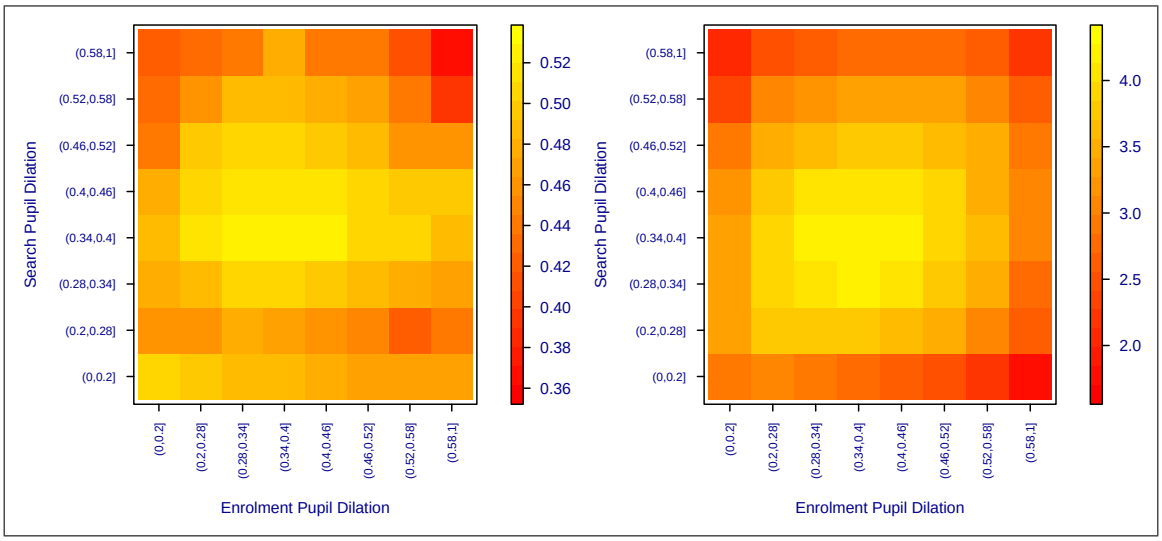

(c) Nonmate Dilation, Dis-similarity Score, Miss Rate, $\log_{10}(1+\text{Count})$

Figure 311: Heatmaps for implementation Q13B executing mate searches in an enrolled population of N = 1.6 million. The radius images are binned by into twelve quantiles spanning $[0, 1]$. The dilation values are cut into ranges bounded by: $(0, 0.2, 0.28, 0.34, 0.40, 0.46, 0.52, 0.58, 1)$. The pathologically compressed 330x330 images are excluded from this analysis.

Heatmaps for implementation Q13B executing mate searches in an enrolled population of N = 1.6 million.

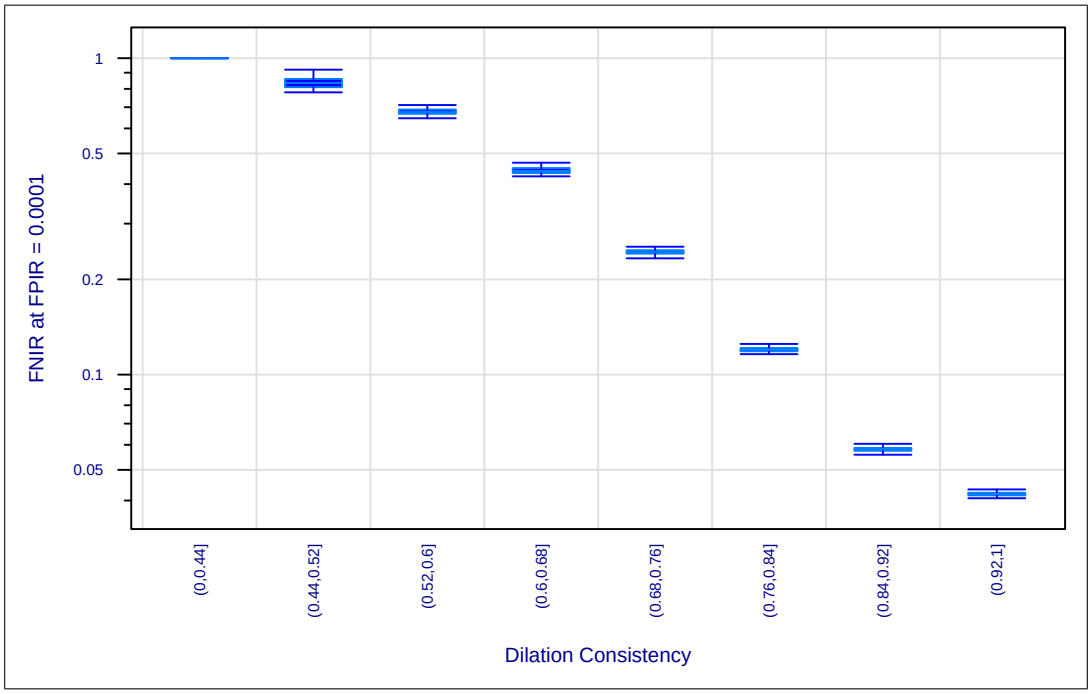

(a) Boxplot, all images

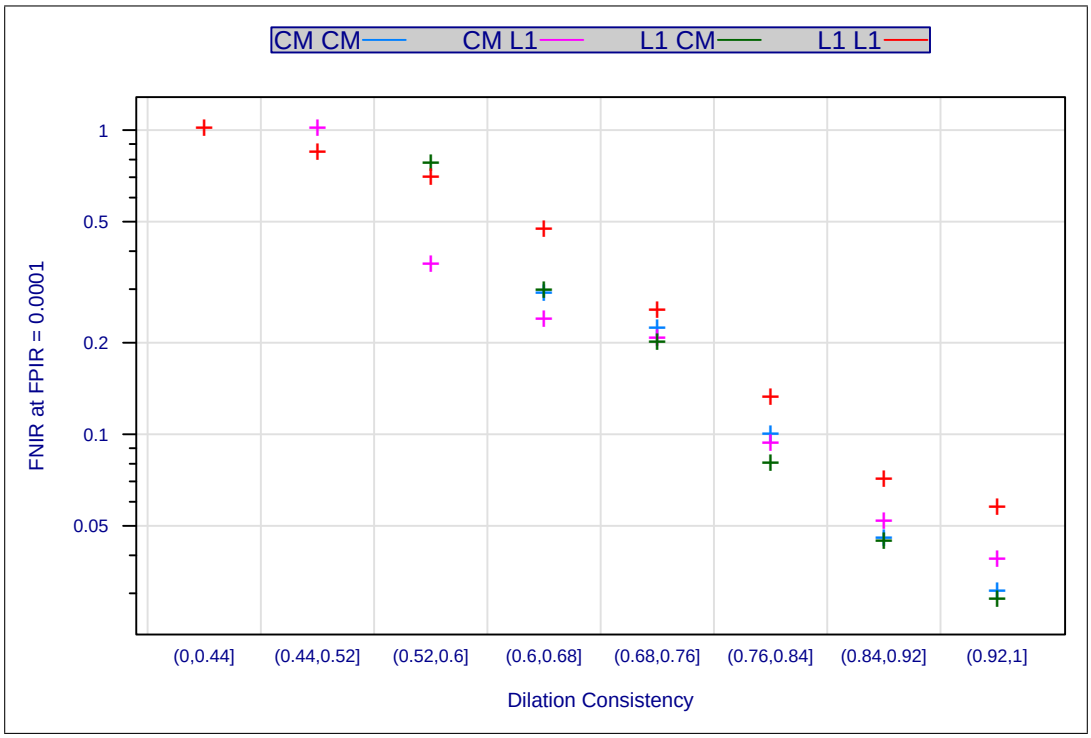

(b) Mean, L1 and CM images

Figure 312: Miss rate statistics for implementation Q13B executing mate searches in an enrolled population of N = 1.6 million. The figures plots FNIR at FPIR = 0.0001 versus the IREX I metric for dilation consistency $(1 - \max(D_1, D_2))/(1 - \min(D_1, D_2))$ where D_i is pupil-iris radius ratio, and the subscripts refer to the mated enrollment and search image. The pathologically compressed 330x330 images are excluded from this analysis. The second figure breaks out dilation effects for interoperating camera pairs, CM and L1.

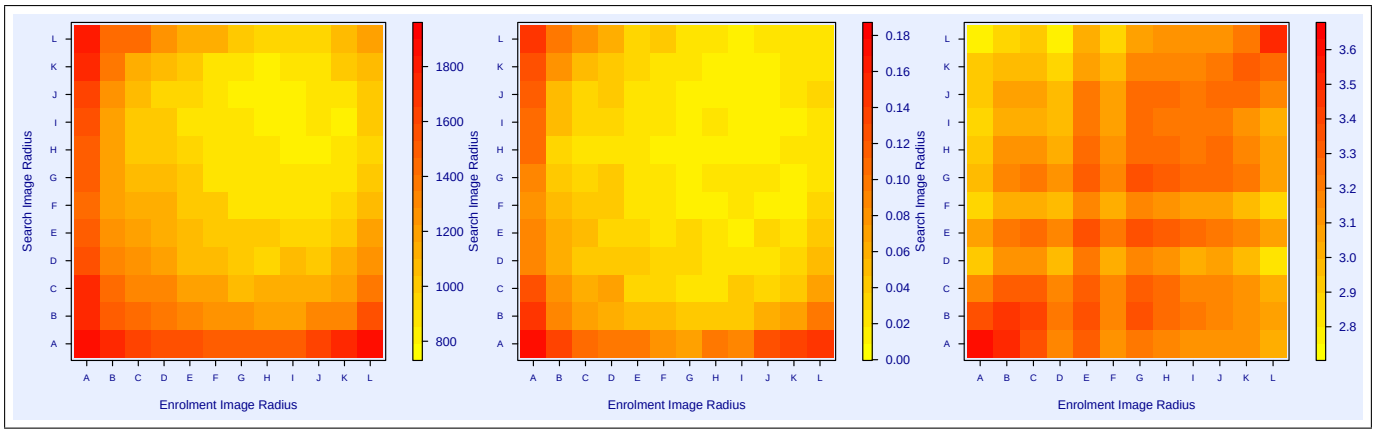

(a) Iris radius: Dis-similarity Score, Miss Rate, $\log_{10}(1+\text{Count})$

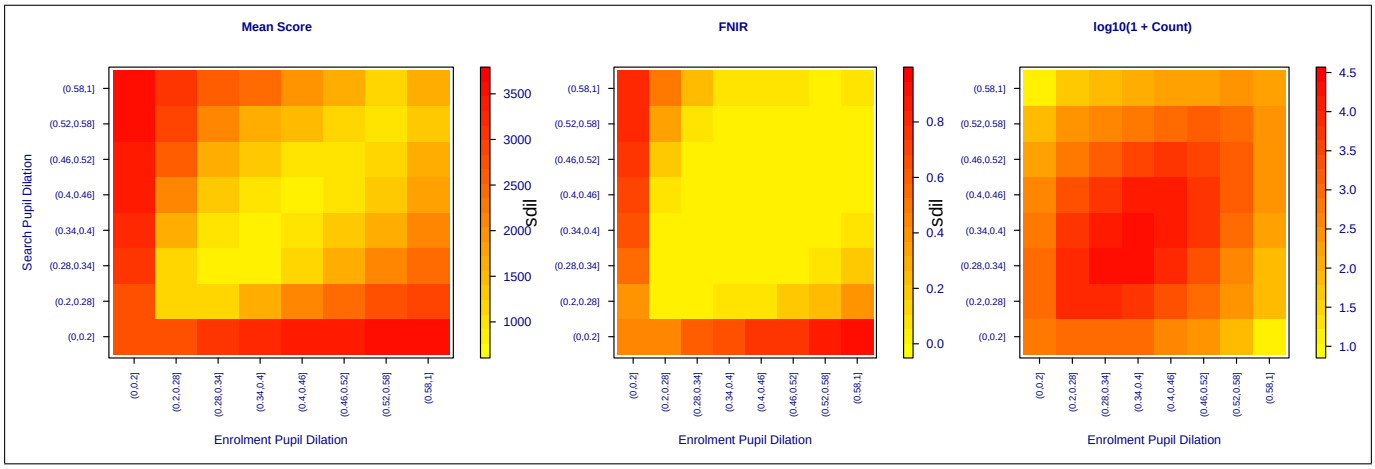

(b) Mate Dilation: Dis-similarity Score, Miss Rate, $\log_{10}(1+\text{Count})$

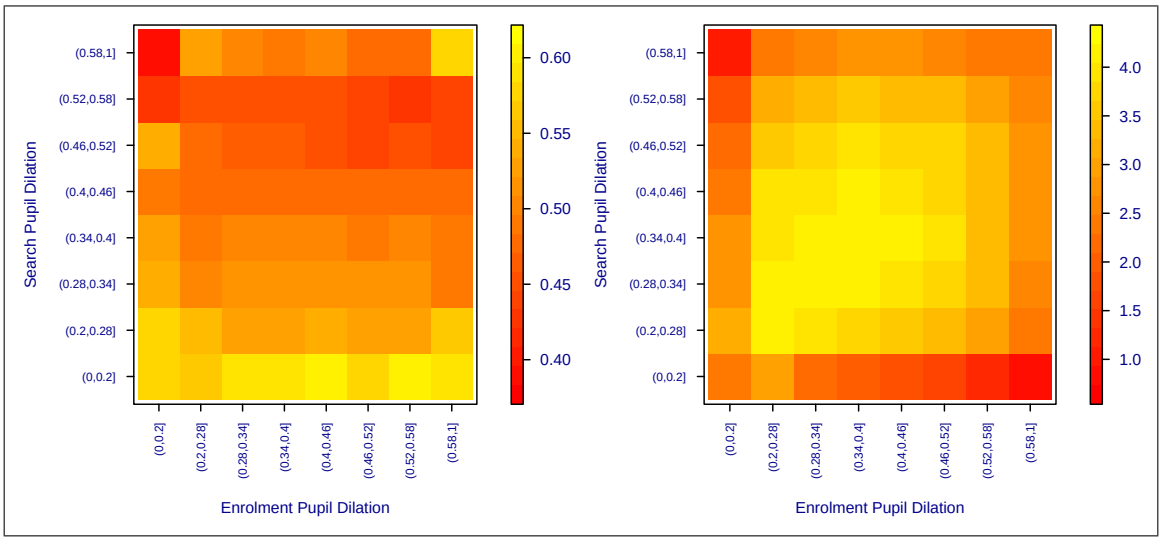

(c) Nonmate Dilation, Dis-similarity Score, Miss Rate, $\log_{10}(1+\text{Count})$

Figure 313: Heatmaps for implementation R02A executing mate searches in an enrolled population of N = 1.6 million. The radius images are binned by into twelve quantiles spanning $[0, 1]$. The dilation values are cut into ranges bounded by: $(0, 0.2, 0.28, 0.34, 0.40, 0.46, 0.52, 0.58, 1)$. The pathologically compressed 330x330 images are excluded from this analysis.

Heatmaps for implementation R02A executing mate searches in an enrolled population of N = 1.6 million.

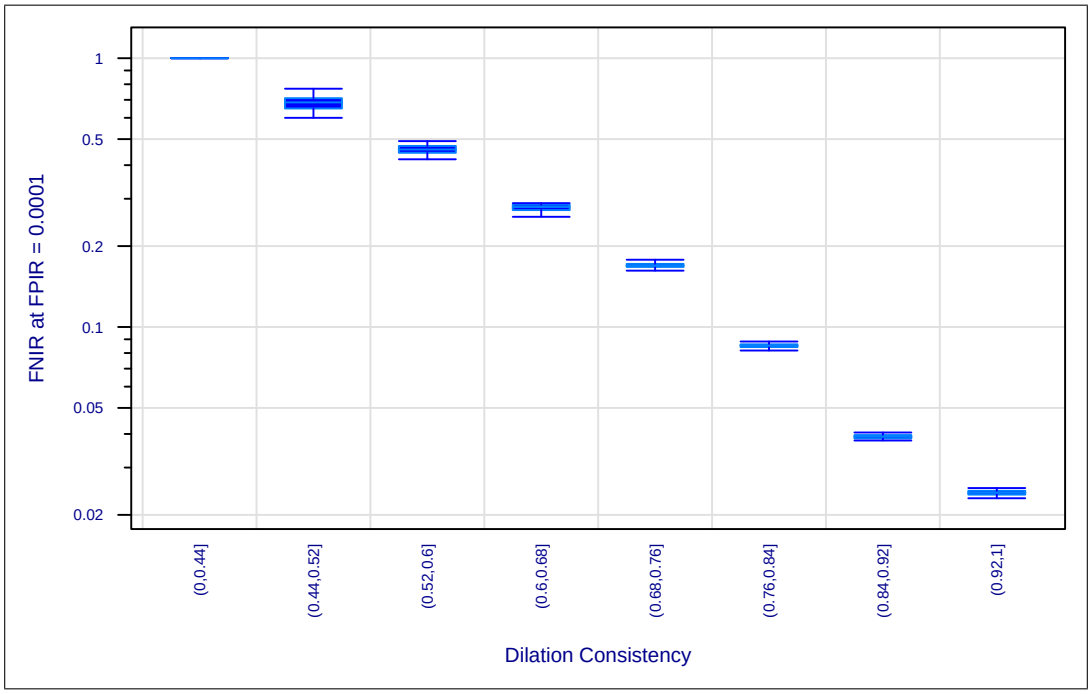

(a) Boxplot, all images

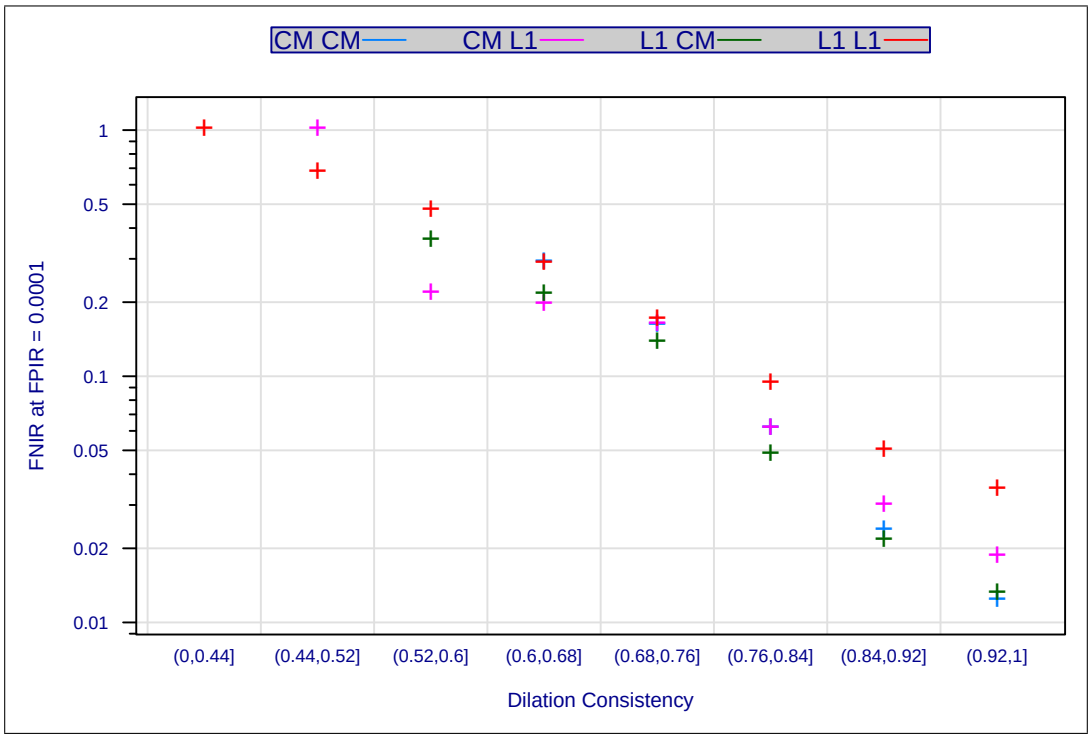

(b) Mean, L1 and CM images

Figure 314: Miss rate statistics for implementation R02A executing mate searches in an enrolled population of N = 1.6 million. The figures plots FNIR at FPIR = 0.0001 versus the IREX I metric for dilation consistency $(1 - \max(D_1, D_2))/(1 - \min(D_1, D_2))$ where D_i is pupil-iris radius ratio, and the subscripts refer to the mated enrollment and search image. The pathologically compressed 330x330 images are excluded from this analysis. The second figure breaks out dilation effects for interoperating camera pairs, CM and L1.

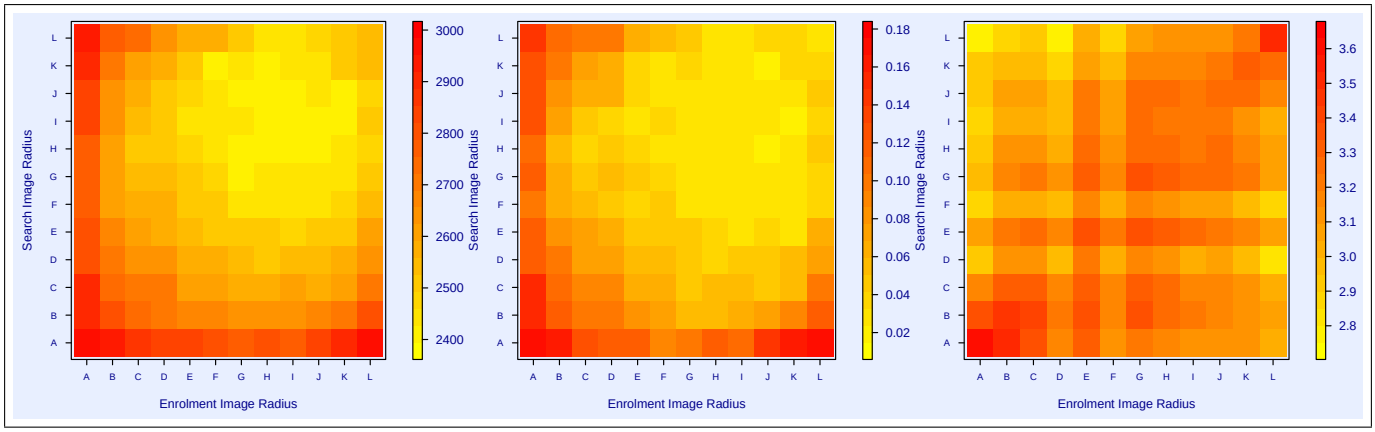

(a) Iris radius: Dis-similarity Score, Miss Rate, $\log_{10}(1+\text{Count})$

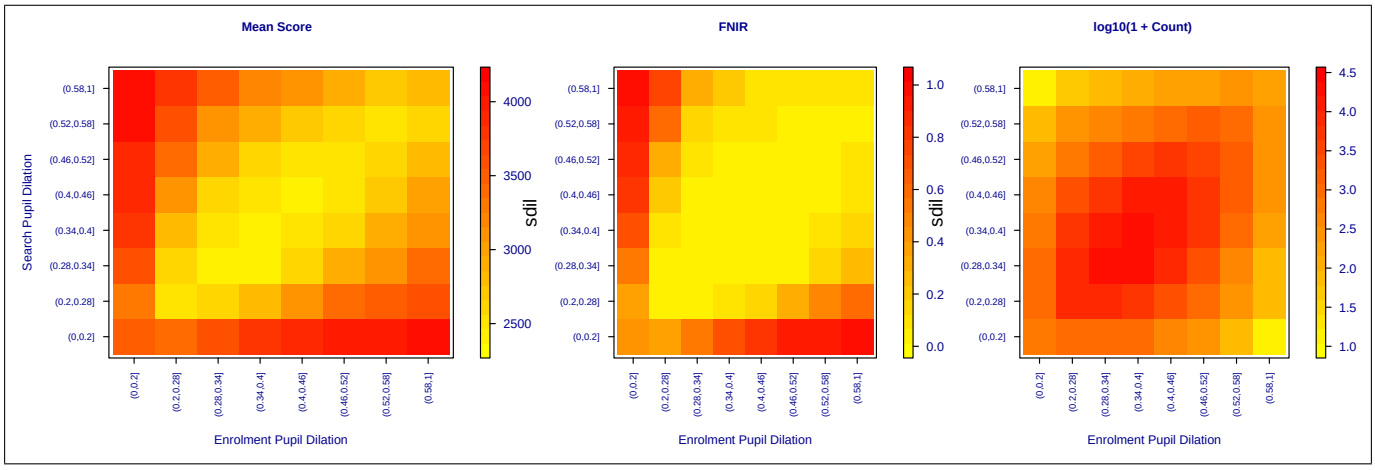

(b) Mate Dilation: Dis-similarity Score, Miss Rate, $\log_{10}(1+\text{Count})$

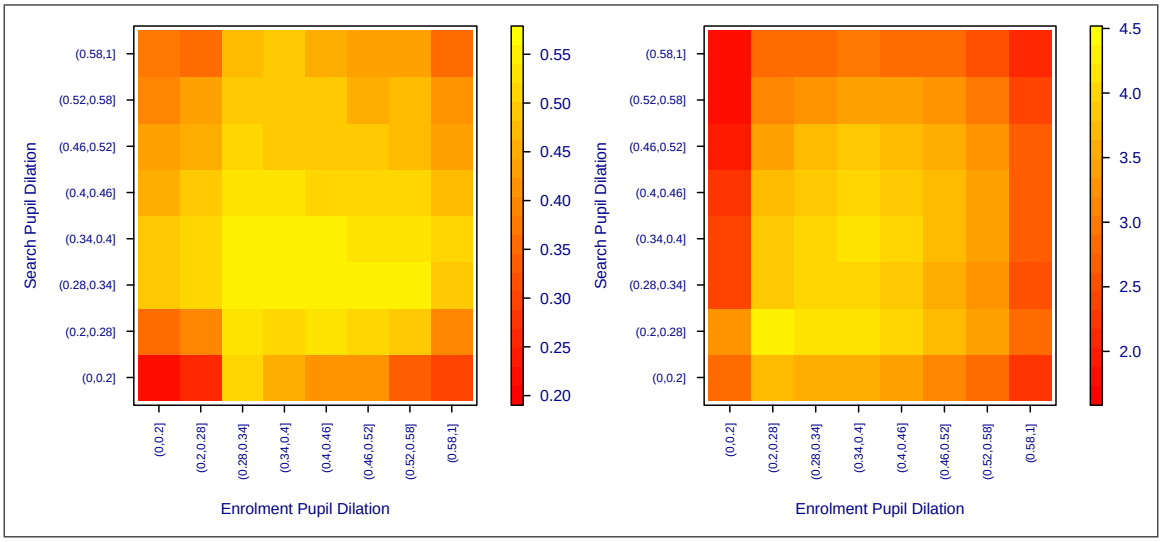

(c) Nonmate Dilation, Dis-similarity Score, Miss Rate, $\log_{10}(1+\text{Count})$

Figure 315: Heatmaps for implementation R02B executing mate searches in an enrolled population of N = 1.6 million. The radius images are binned by into twelve quantiles spanning $[0, 1]$. The dilation values are cut into ranges bounded by: $(0, 0.2, 0.28, 0.34, 0.40, 0.46, 0.52, 0.58, 1)$. The pathologically compressed 330x330 images are excluded from this analysis.

Heatmaps for implementation R02B executing mate searches in an enrolled population of N = 1.6 million.

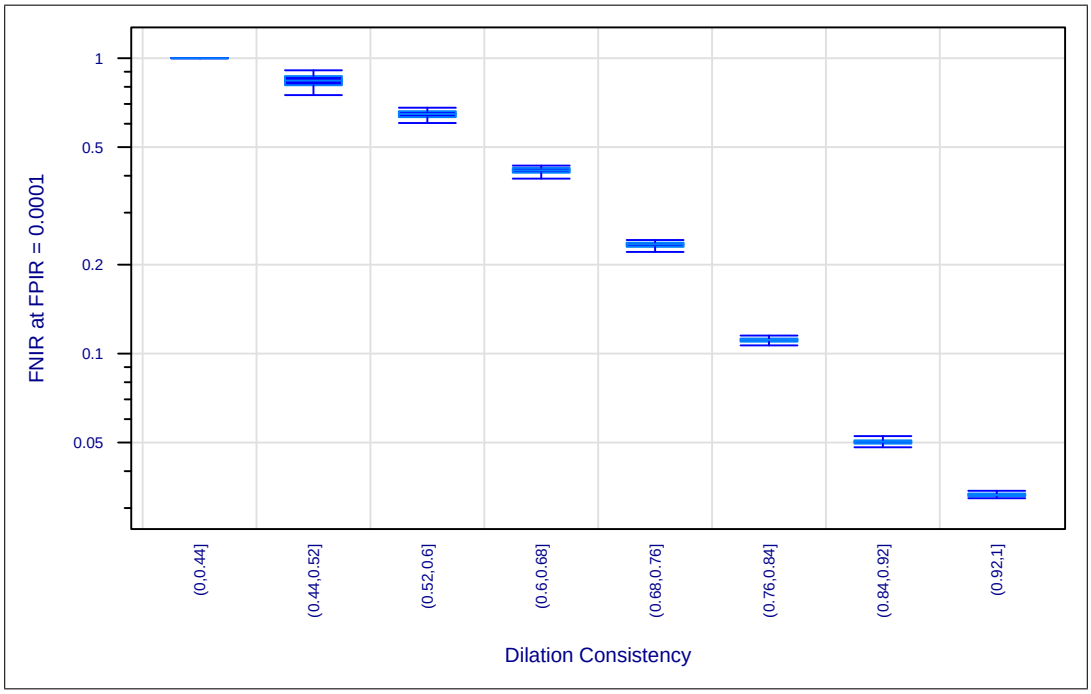

(a) Boxplot, all images

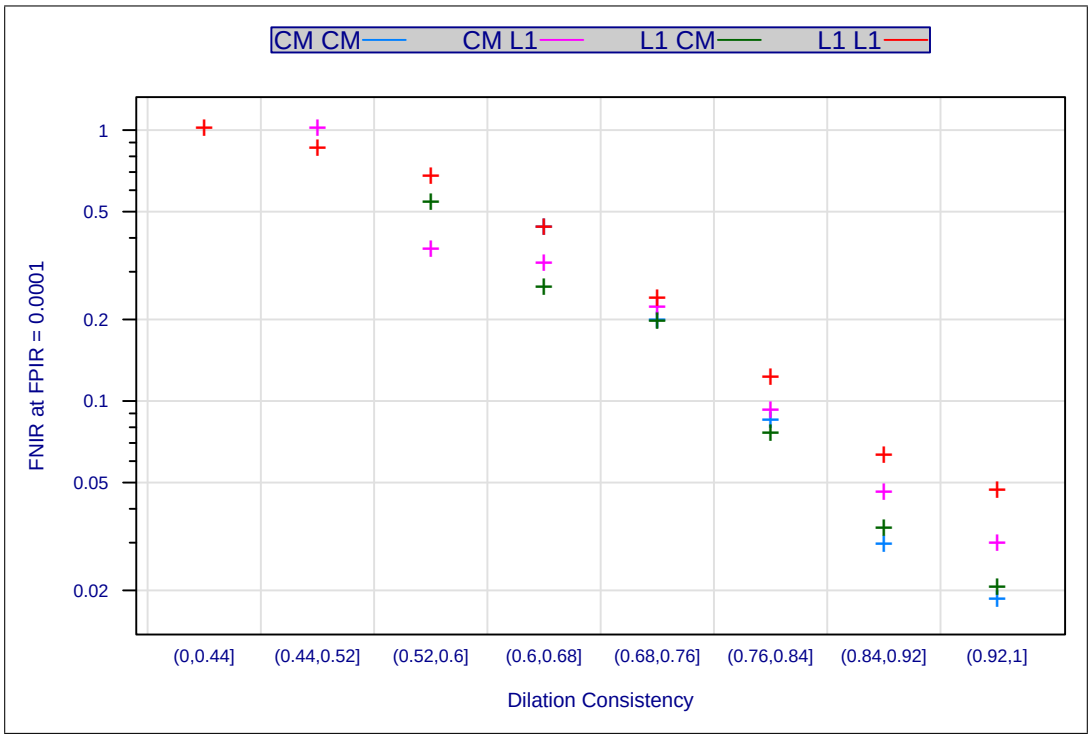

(b) Mean, L1 and CM images

Figure 316: Miss rate statistics for implementation R02B executing mate searches in an enrolled population of N = 1.6 million. The figures plots FNIR at FPIR = 0.0001 versus the IREX I metric for dilation consistency $(1 - \max(D_1, D_2))/(1 - \min(D_1, D_2))$ where D_i is pupil-iris radius ratio, and the subscripts refer to the mated enrollment and search image. The pathologically compressed 330x330 images are excluded from this analysis. The second figure breaks out dilation effects for interoperating camera pairs, CM and L1.

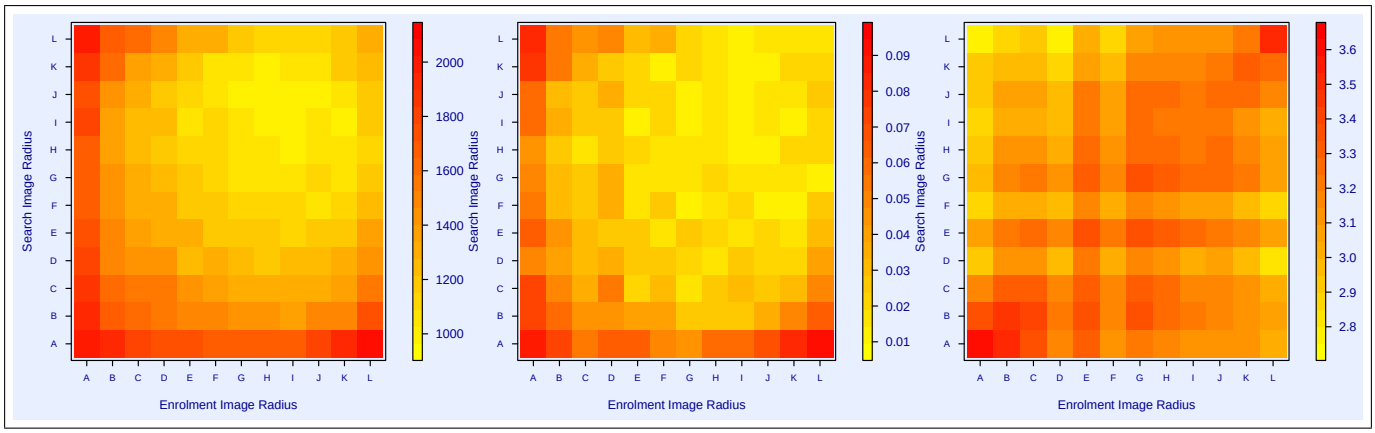

(a) Iris radius: Dis-similarity Score, Miss Rate, $\log_{10}(1+\text{Count})$

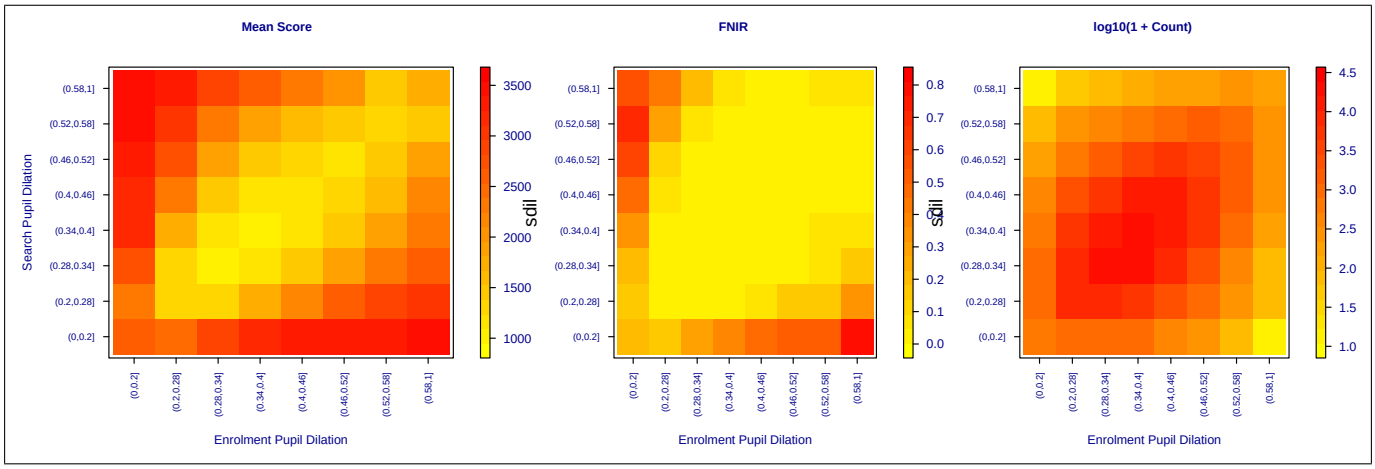

(b) Mate Dilation: Dis-similarity Score, Miss Rate, $\log_{10}(1+\text{Count})$

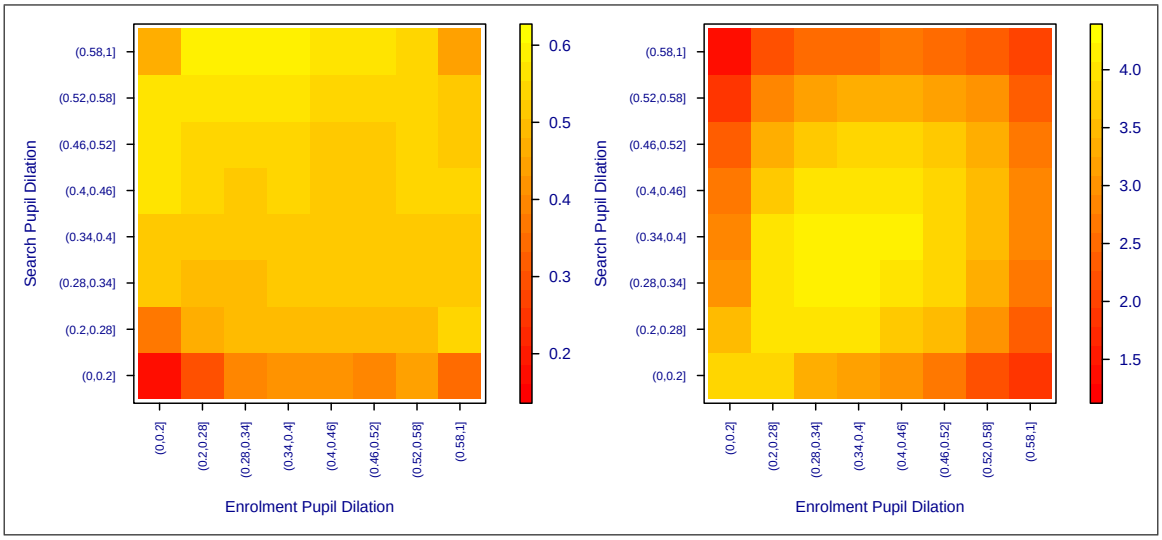

(c) Nonmate Dilation, Dis-similarity Score, Miss Rate, $\log_{10}(1+\text{Count})$

Figure 317: Heatmaps for implementation R03A executing mate searches in an enrolled population of N = 1.6 million. The radius images are binned by into twelve quantiles spanning $[0, 1]$. The dilation values are cut into ranges bounded by: $(0, 0.2, 0.28, 0.34, 0.40, 0.46, 0.52, 0.58, 1)$. The pathologically compressed 330x330 images are excluded from this analysis.

Heatmaps for implementation R03A executing mate searches in an enrolled population of N = 1.6 million.

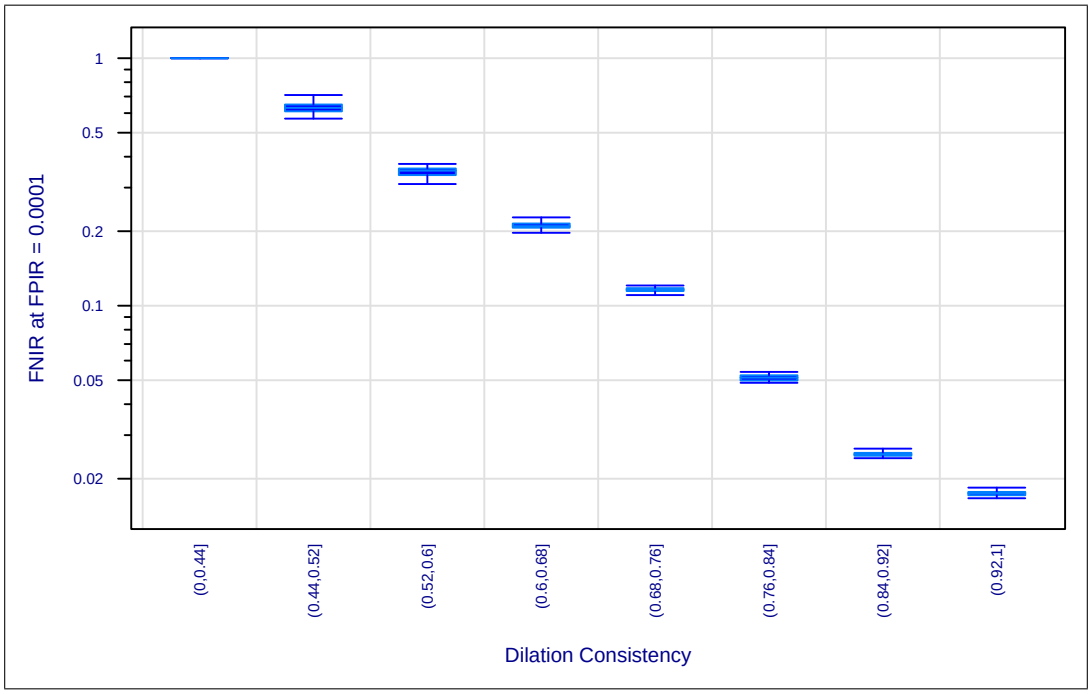

(a) Boxplot, all images

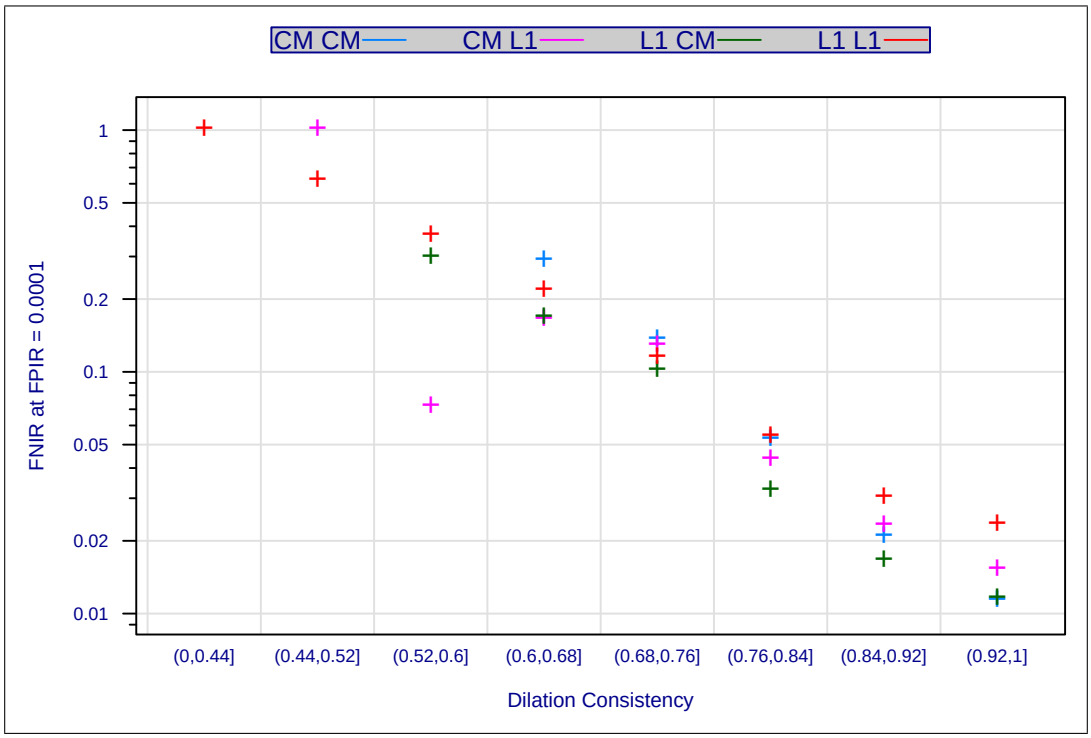

(b) Mean, L1 and CM images

Figure 318: Miss rate statistics for implementation R03A executing mate searches in an enrolled population of N = 1.6 million. The figures plots FNIR at FPIR = 0.0001 versus the IREX I metric for dilation consistency $(1 - \max(D_1, D_2))/(1 - \min(D_1, D_2))$ where D_i is pupil-iris radius ratio, and the subscripts refer to the mated enrollment and search image. The pathologically compressed 330x330 images are excluded from this analysis. The second figure breaks out dilation effects for interoperating camera pairs, CM and L1.

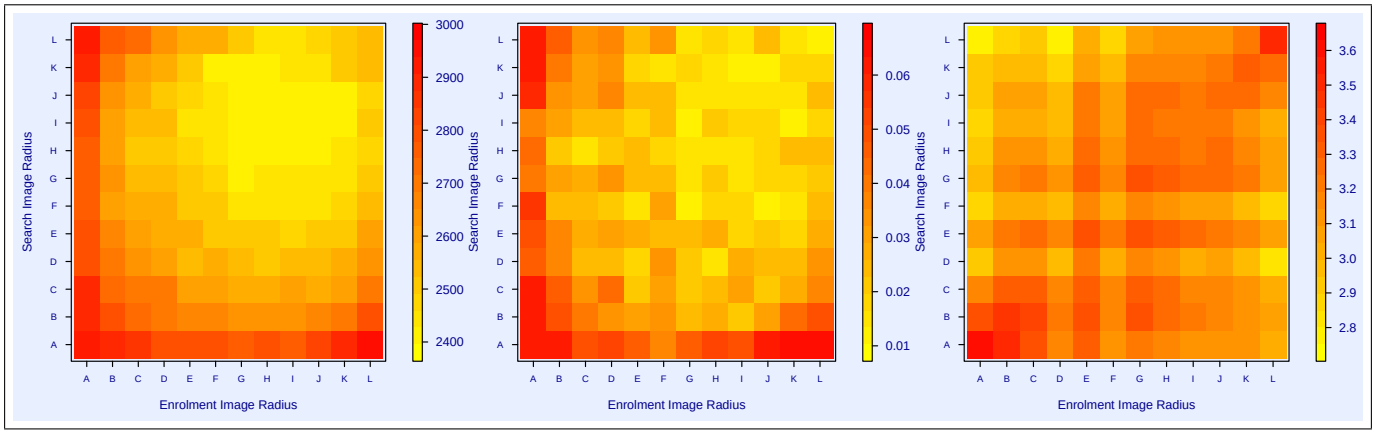

(a) Iris radius: Dis-similarity Score, Miss Rate, $\log_{10}(1+\text{Count})$

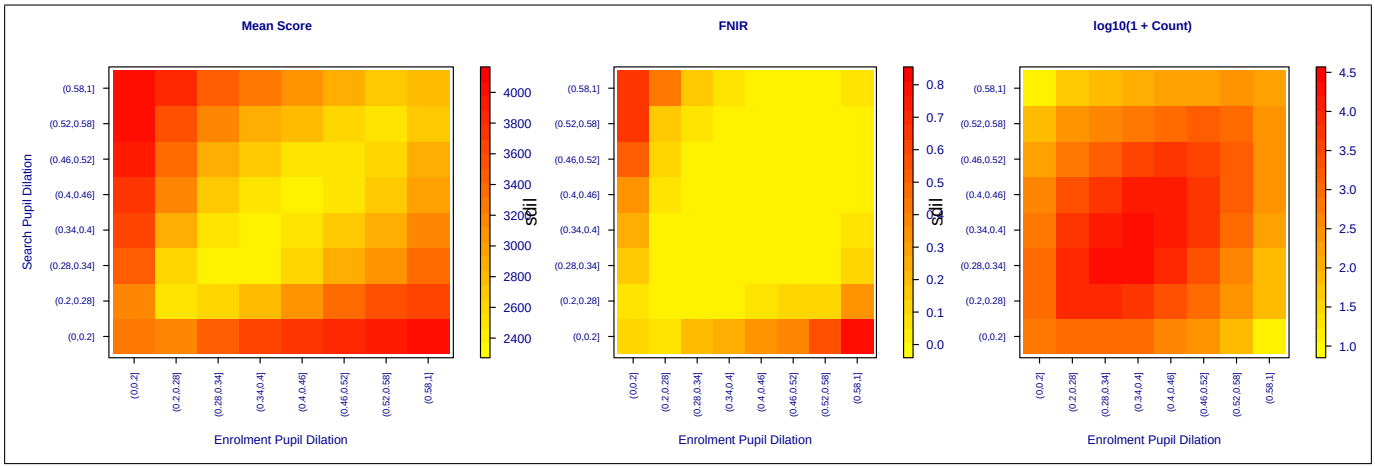

(b) Mate Dilation: Dis-similarity Score, Miss Rate, $\log_{10}(1+\text{Count})$

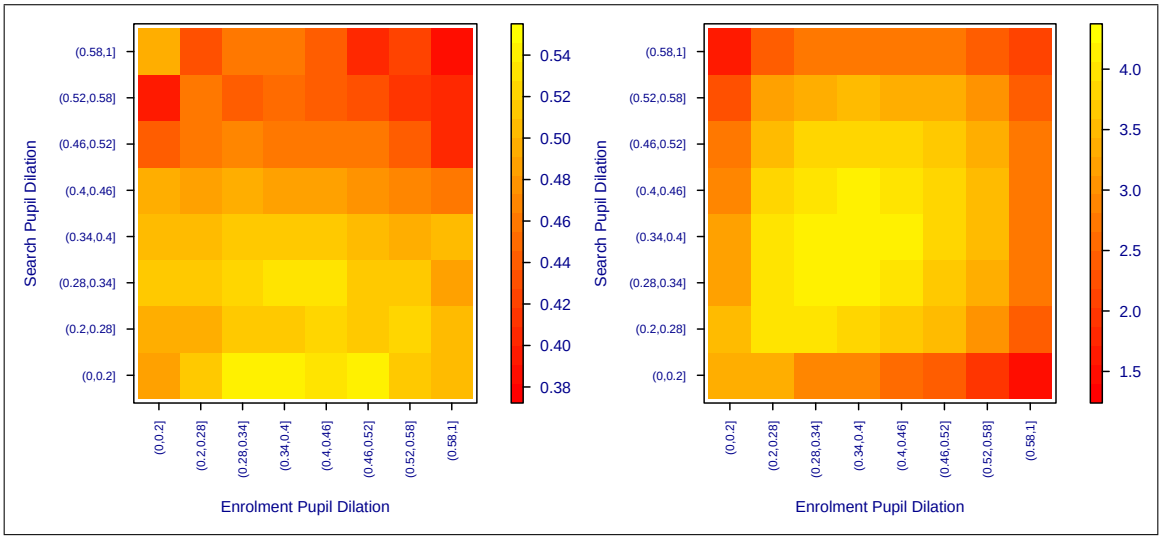

(c) Nonmate Dilation, Dis-similarity Score, Miss Rate, $\log_{10}(1+\text{Count})$

Figure 319: Heatmaps for implementation R03B executing mate searches in an enrolled population of N = 1.6 million. The radius images are binned by into twelve quantiles spanning $[0, 1]$. The dilation values are cut into ranges bounded by: $(0, 0.2, 0.28, 0.34, 0.40, 0.46, 0.52, 0.58, 1)$. The pathologically compressed 330x330 images are excluded from this analysis.

Heatmaps for implementation R03B executing mate searches in an enrolled population of N = 1.6 million.

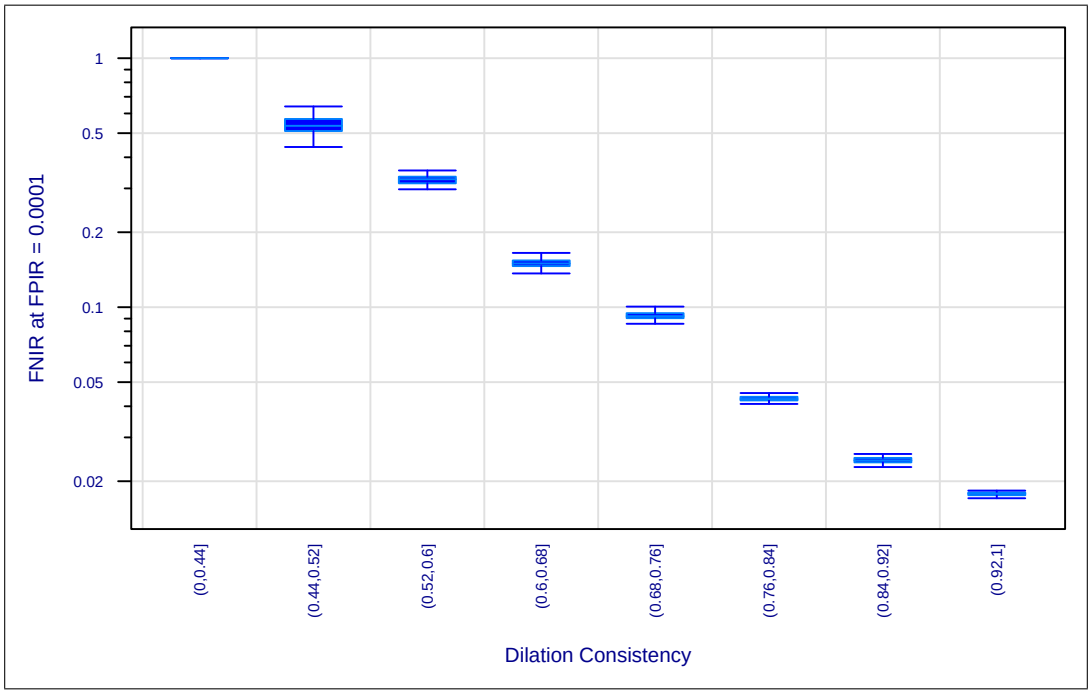

(a) Boxplot, all images

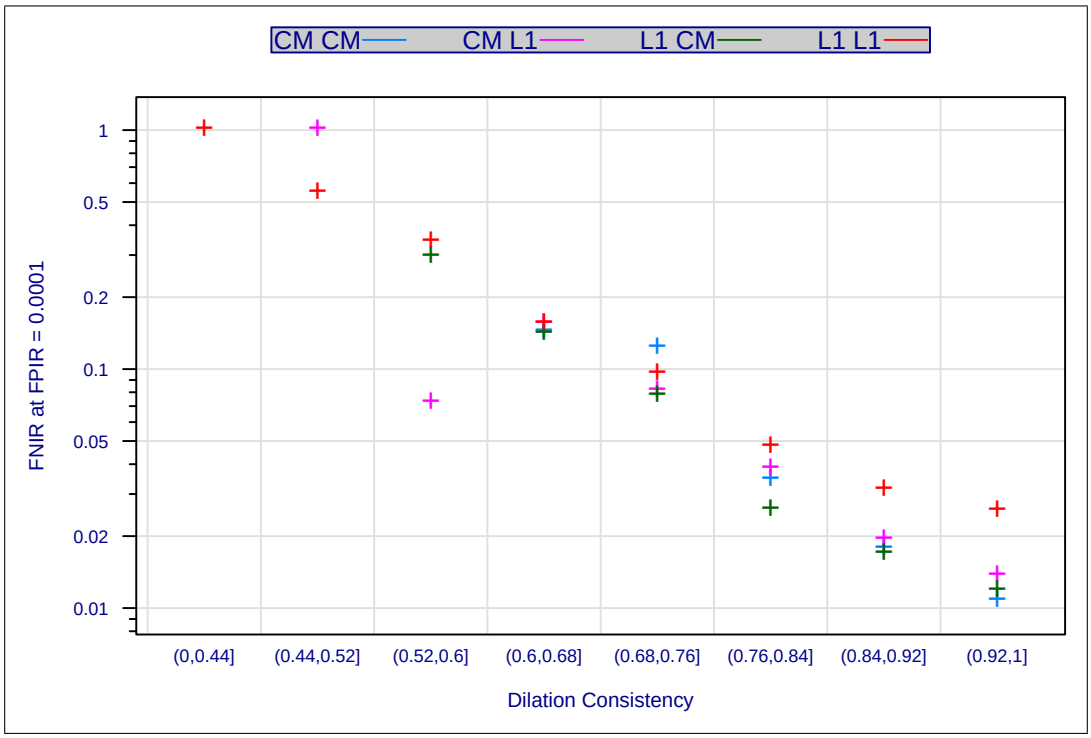

(b) Mean, L1 and CM images

Figure 320: Miss rate statistics for implementation R03B executing mate searches in an enrolled population of N = 1.6 million. The figures plots FNIR at FPIR = 0.0001 versus the IREX I metric for dilation consistency $(1 - \max(D_1, D_2))/(1 - \min(D_1, D_2))$ where D_i is pupil-iris radius ratio, and the subscripts refer to the mated enrollment and search image. The pathologically compressed 330x330 images are excluded from this analysis. The second figure breaks out dilation effects for interoperating camera pairs, CM and L1.

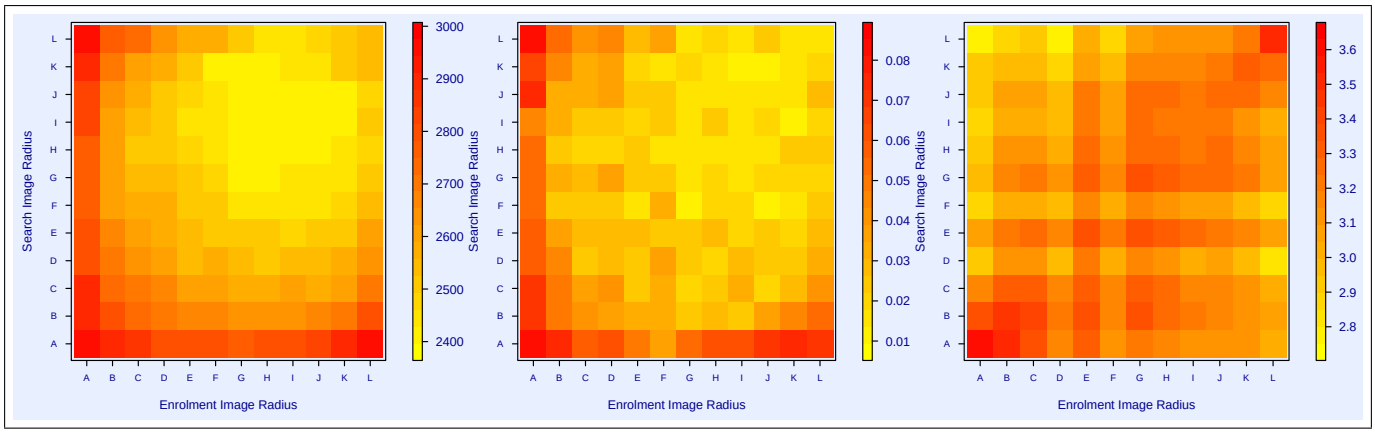

(a) Iris radius: Dis-similarity Score, Miss Rate, $\log_{10}(1+\text{Count})$

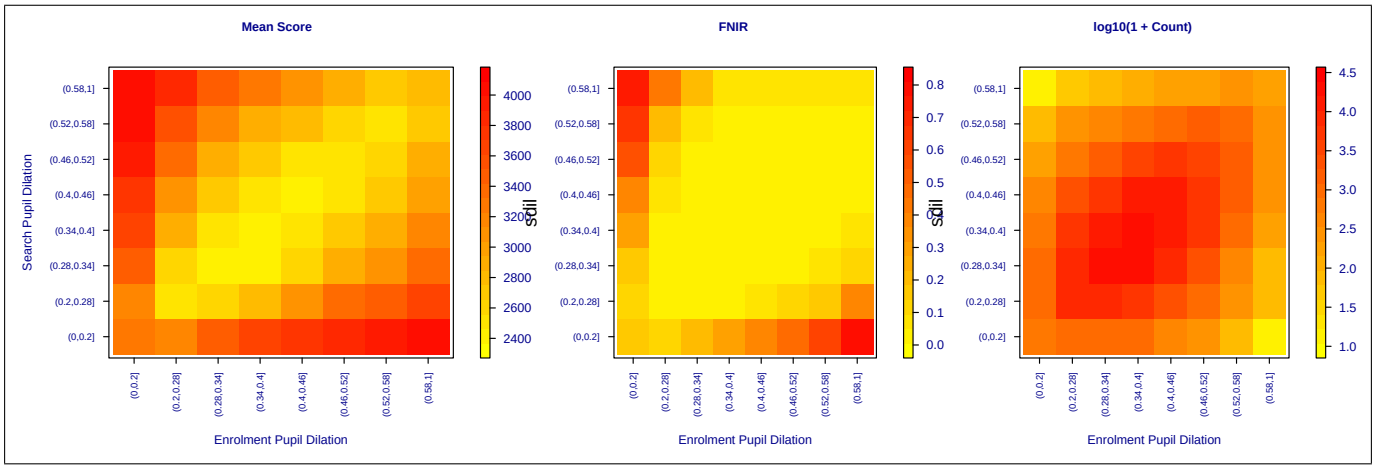

(b) Mate Dilation: Dis-similarity Score, Miss Rate, $\log_{10}(1+\text{Count})$

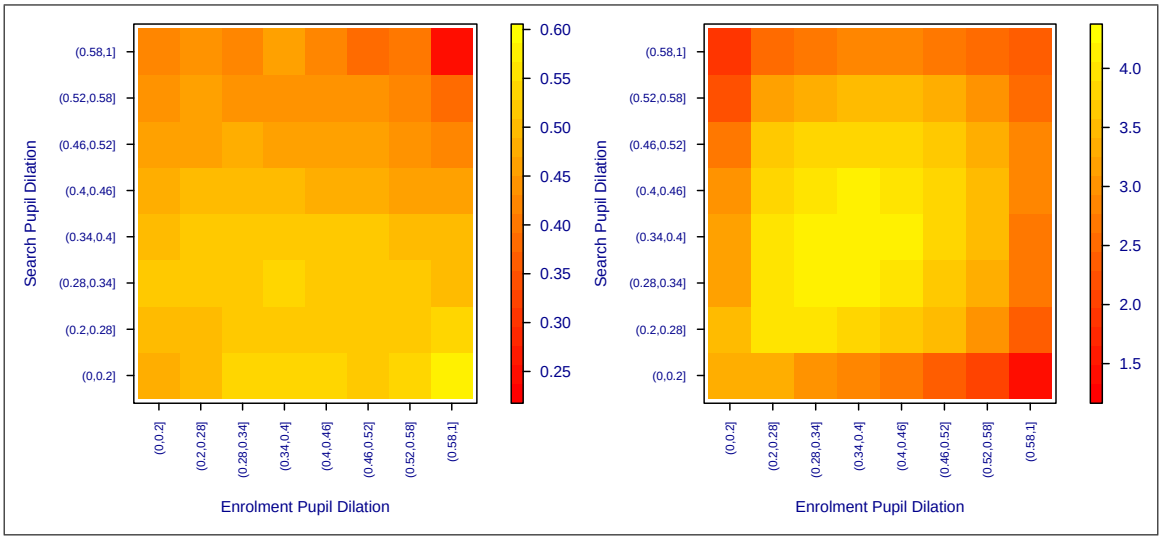

(c) Nonmate Dilation, Dis-similarity Score, Miss Rate, $\log_{10}(1+\text{Count})$

Figure 321: Heatmaps for implementation R04B executing mate searches in an enrolled population of N = 1.6 million. The radius images are binned by into twelve quantiles spanning $[0, 1]$. The dilation values are cut into ranges bounded by: $(0, 0.2, 0.28, 0.34, 0.40, 0.46, 0.52, 0.58, 1)$. The pathologically compressed 330x330 images are excluded from this analysis.

Heatmaps for implementation R04B executing mate searches in an enrolled population of N = 1.6 million.

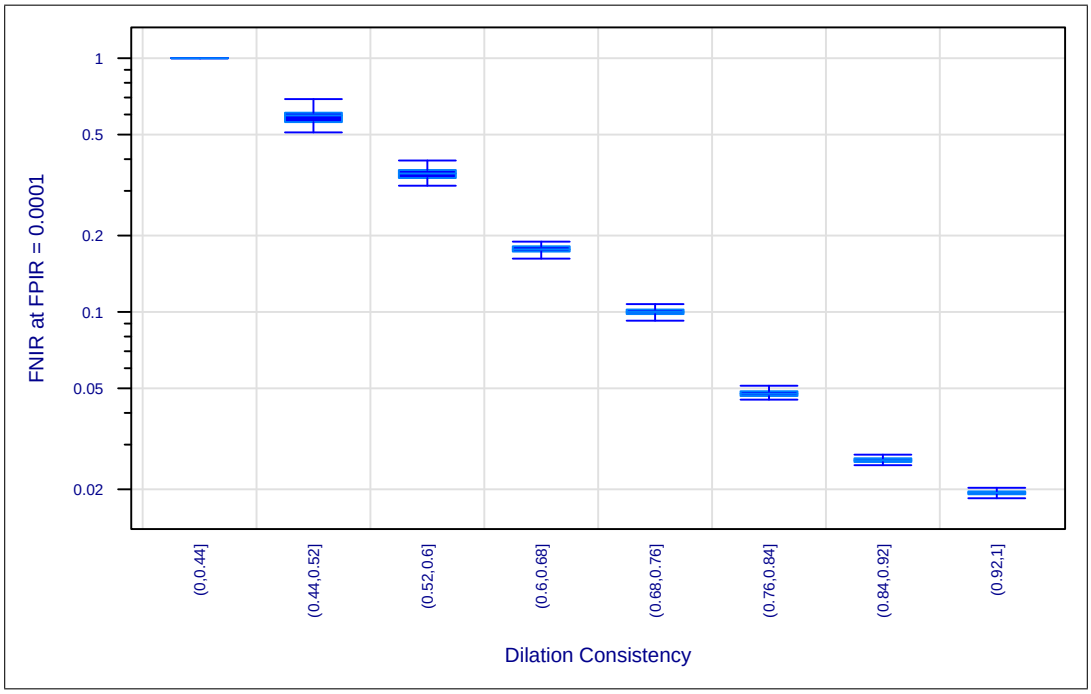

(a) Boxplot, all images

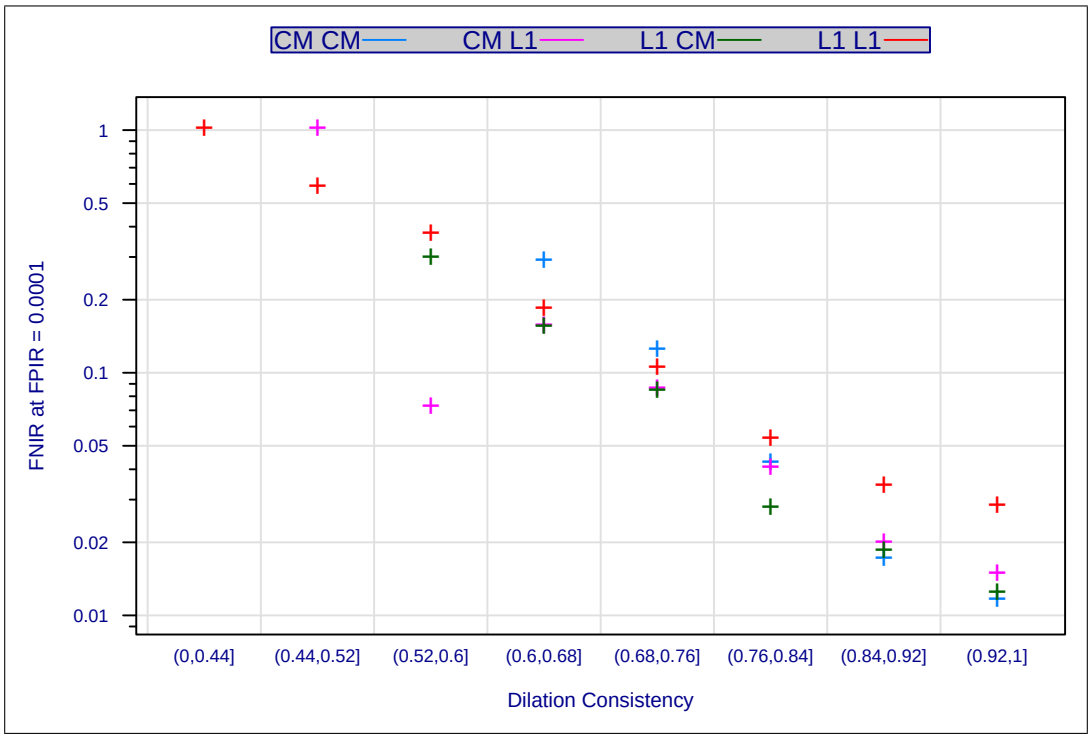

(b) Mean, L1 and CM images

Figure 322: Miss rate statistics for implementation R04B executing mate searches in an enrolled population of N = 1.6 million. The figures plots FNIR at FPIR = 0.0001 versus the IREX I metric for dilation consistency $(1 - \max(D_1, D_2))/(1 - \min(D_1, D_2))$ where D_i is pupil-iris radius ratio, and the subscripts refer to the mated enrollment and search image. The pathologically compressed 330x330 images are excluded from this analysis. The second figure breaks out dilation effects for interoperating camera pairs, CM and L1.

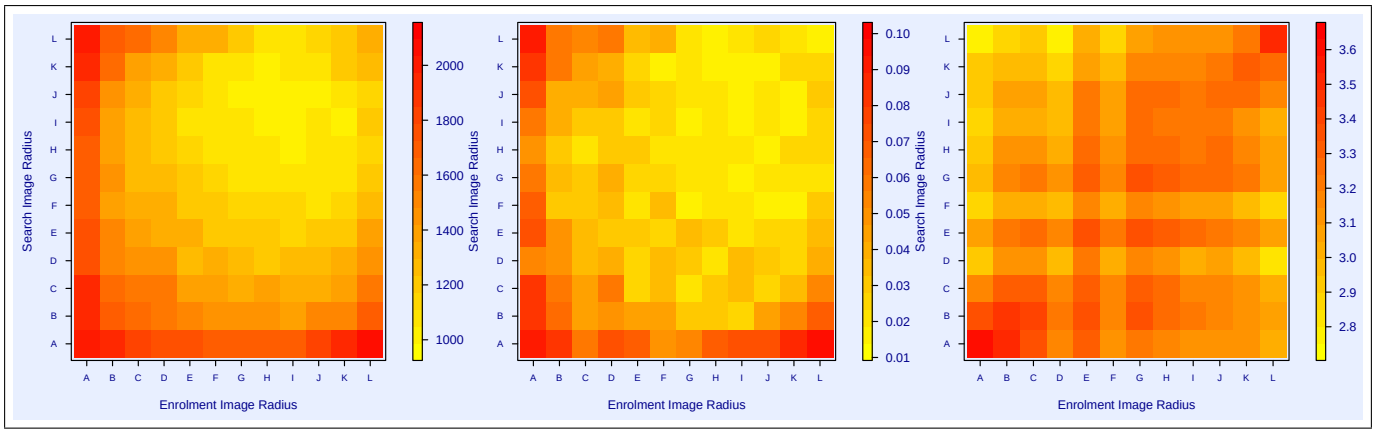

(a) Iris radius: Dis-similarity Score, Miss Rate, $\log_{10}(1+\text{Count})$

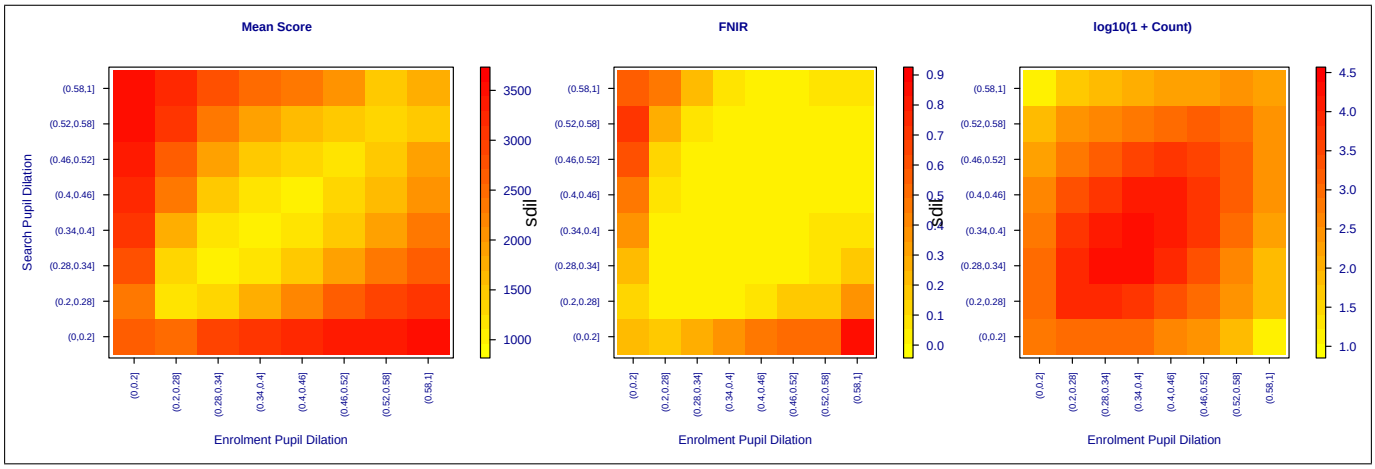

(b) Mate Dilation: Dis-similarity Score, Miss Rate, $\log_{10}(1+\text{Count})$

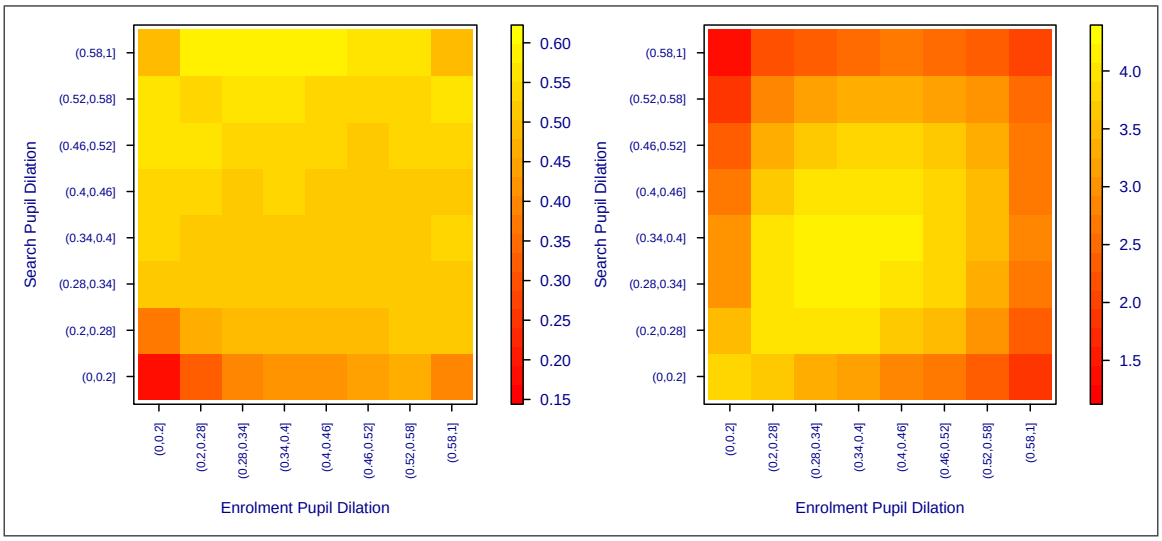

(c) Nonmate Dilation, Dis-similarity Score, Miss Rate, $\log_{10}(1+\text{Count})$

Figure 323: Heatmaps for implementation R11A executing mate searches in an enrolled population of N = 1.6 million. The radius images are binned by into twelve quantiles spanning $[0, 1]$. The dilation values are cut into ranges bounded by: $(0, 0.2, 0.28, 0.34, 0.40, 0.46, 0.52, 0.58, 1)$. The pathologically compressed 330x330 images are excluded from this analysis.

Heatmaps for implementation R11A executing mate searches in an enrolled population of N = 1.6 million.

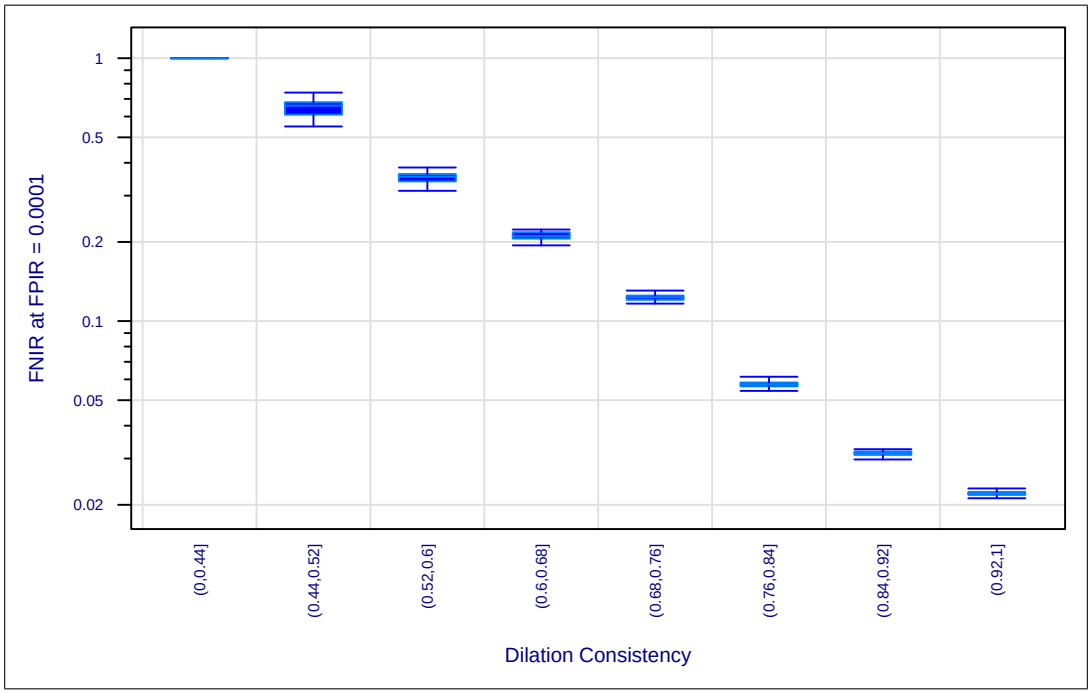

(a) Boxplot, all images

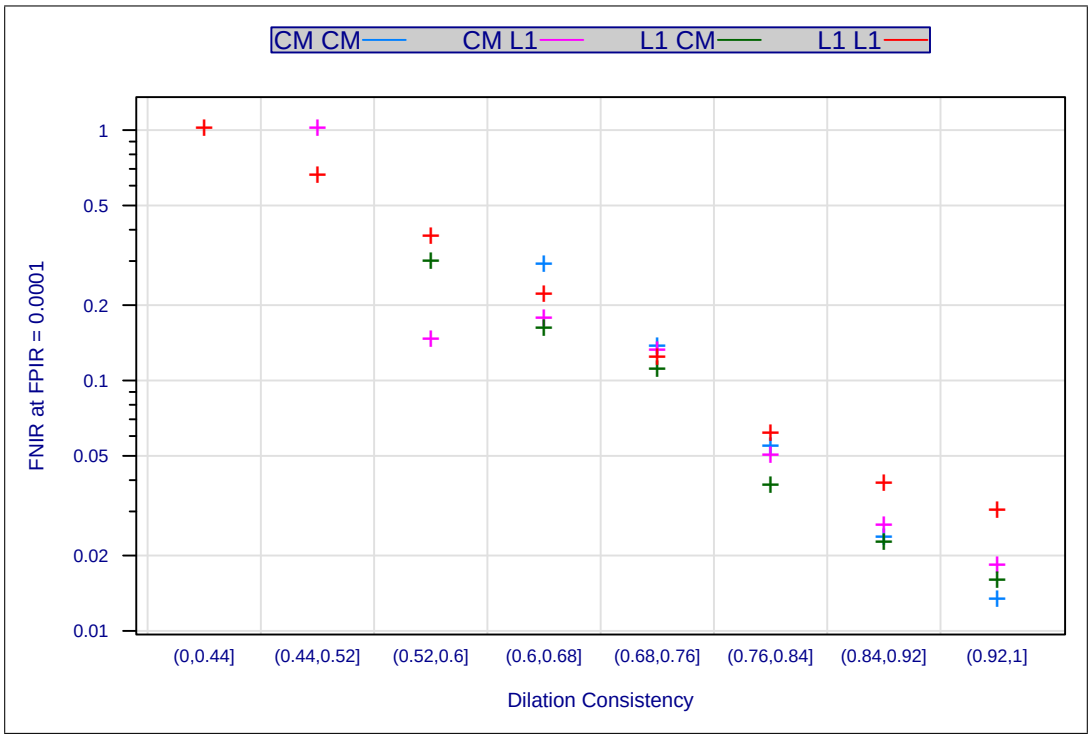

(b) Mean, L1 and CM images

Figure 324: Miss rate statistics for implementation R11A executing mate searches in an enrolled population of N = 1.6 million. The figures plots FNIR at FPIR = 0.0001 versus the IREX I metric for dilation consistency $(1 - \max(D_1, D_2))/(1 - \min(D_1, D_2))$ where D_i is pupil-iris radius ratio, and the subscripts refer to the mated enrollment and search image. The pathologically compressed 330x330 images are excluded from this analysis. The second figure breaks out dilation effects for interoperating camera pairs, CM and L1.

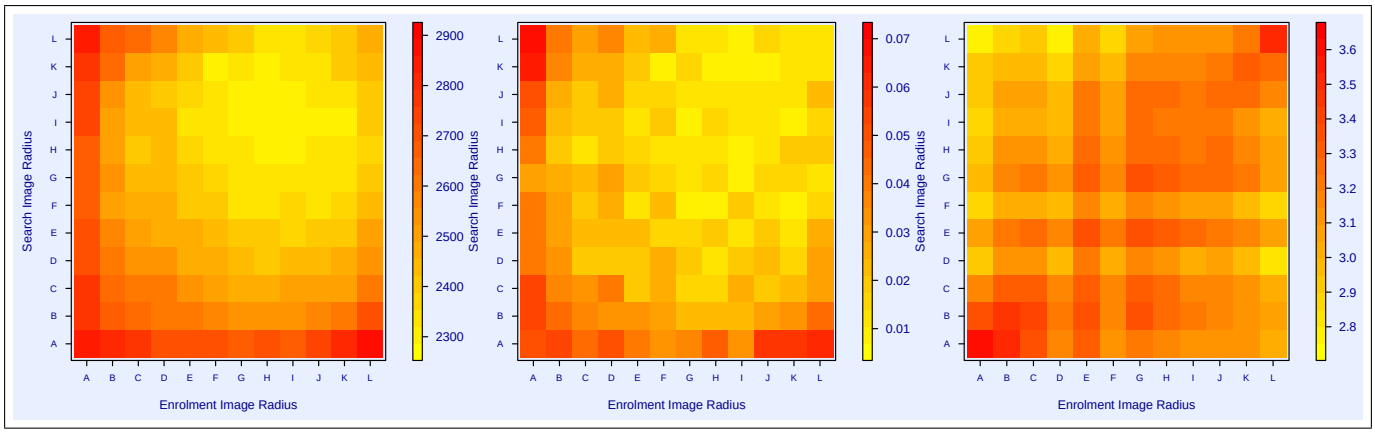

(a) Iris radius: Dis-similarity Score, Miss Rate, $\log_{10}(1+\text{Count})$

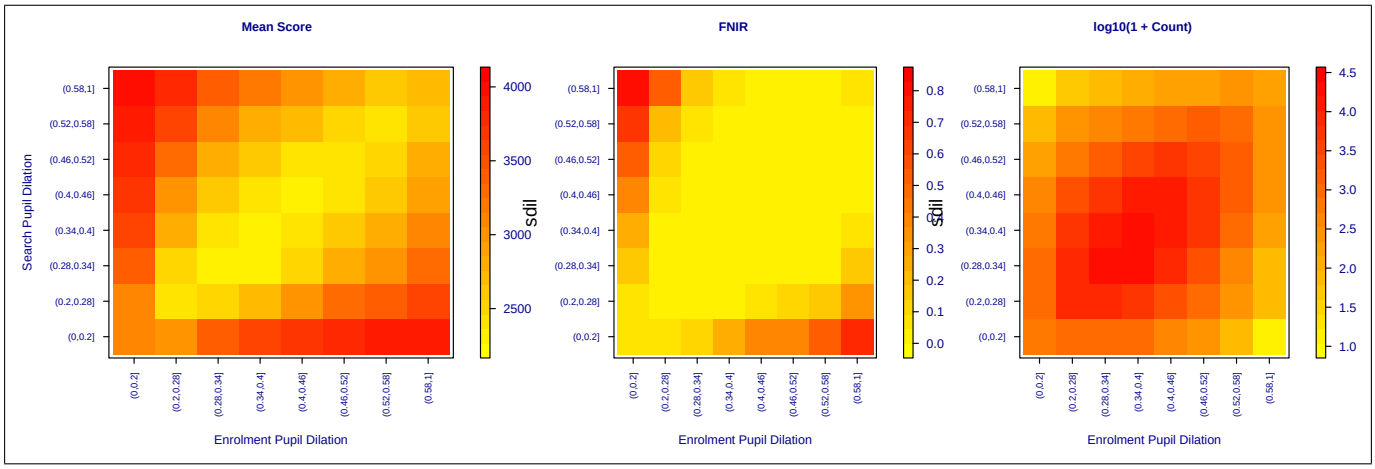

(b) Mate Dilation: Dis-similarity Score, Miss Rate, $\log_{10}(1+\text{Count})$

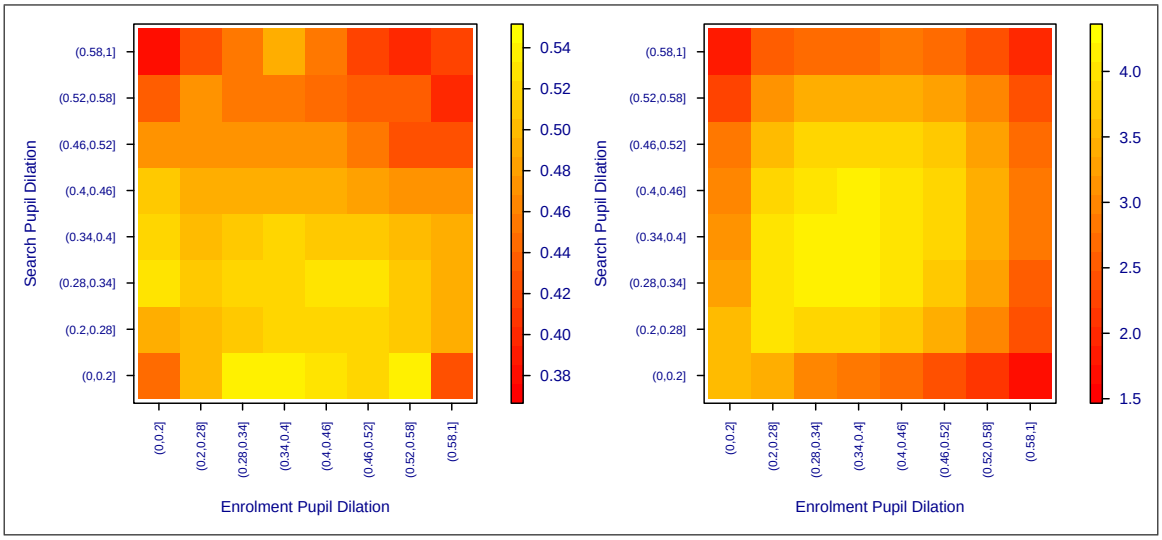

(c) Nonmate Dilation, Dis-similarity Score, Miss Rate, $\log_{10}(1+\text{Count})$

Figure 325: Heatmaps for implementation R11B executing mate searches in an enrolled population of N = 1.6 million. The radius images are binned by into twelve quantiles spanning $[0, 1]$. The dilation values are cut into ranges bounded by: $(0, 0.2, 0.28, 0.34, 0.40, 0.46, 0.52, 0.58, 1)$. The pathologically compressed 330x330 images are excluded from this analysis.

Heatmaps for implementation R11B executing mate searches in an enrolled population of N = 1.6 million.

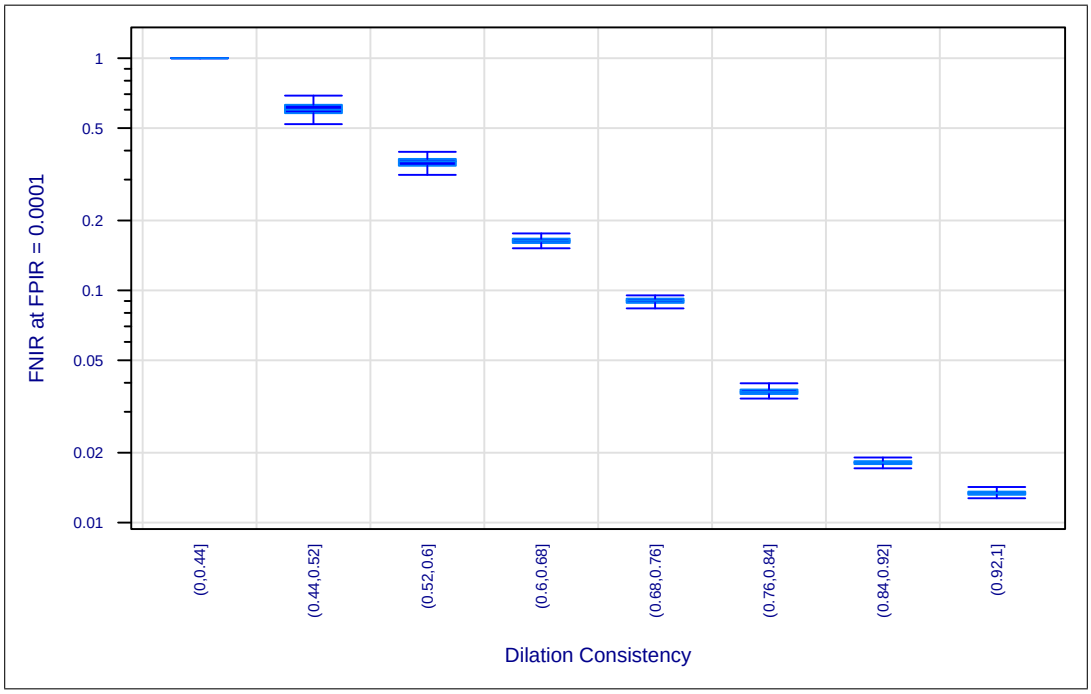

(a) Boxplot, all images

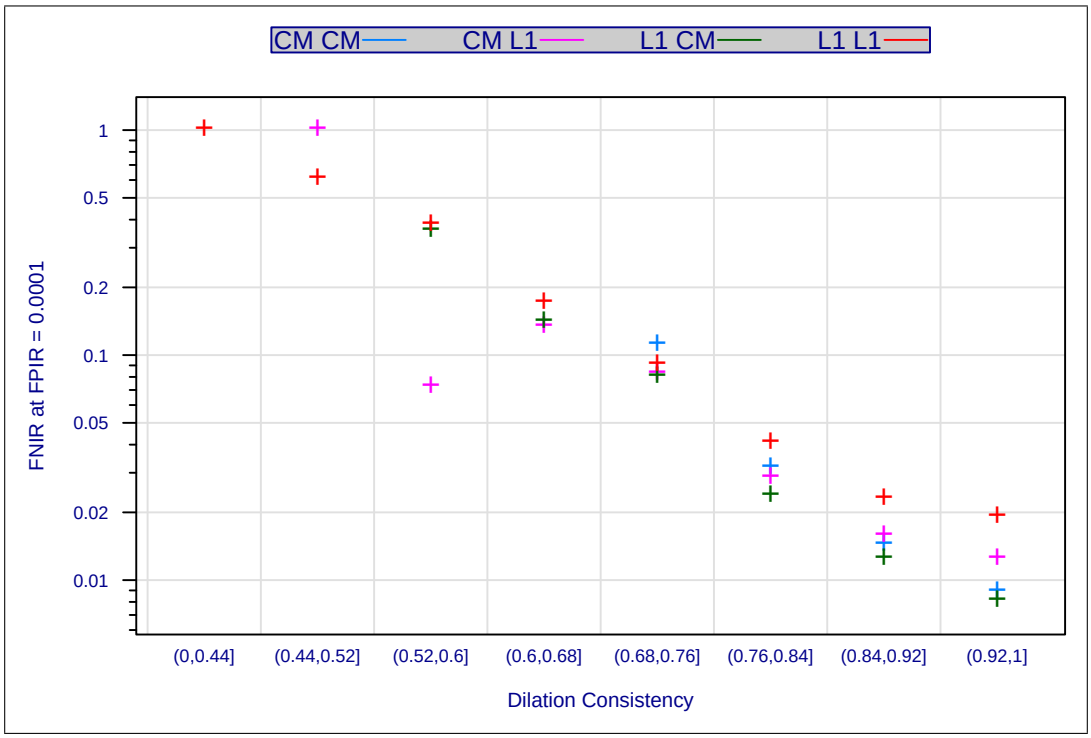

(b) Mean, L1 and CM images

Figure 326: Miss rate statistics for implementation R11B executing mate searches in an enrolled population of N = 1.6 million. The figures plots FNIR at FPIR = 0.0001 versus the IREX I metric for dilation consistency $(1 - \max(D_1, D_2))/(1 - \min(D_1, D_2))$ where D_i is pupil-iris radius ratio, and the subscripts refer to the mated enrollment and search image. The pathologically compressed 330x330 images are excluded from this analysis. The second figure breaks out dilation effects for interoperating camera pairs, CM and L1.

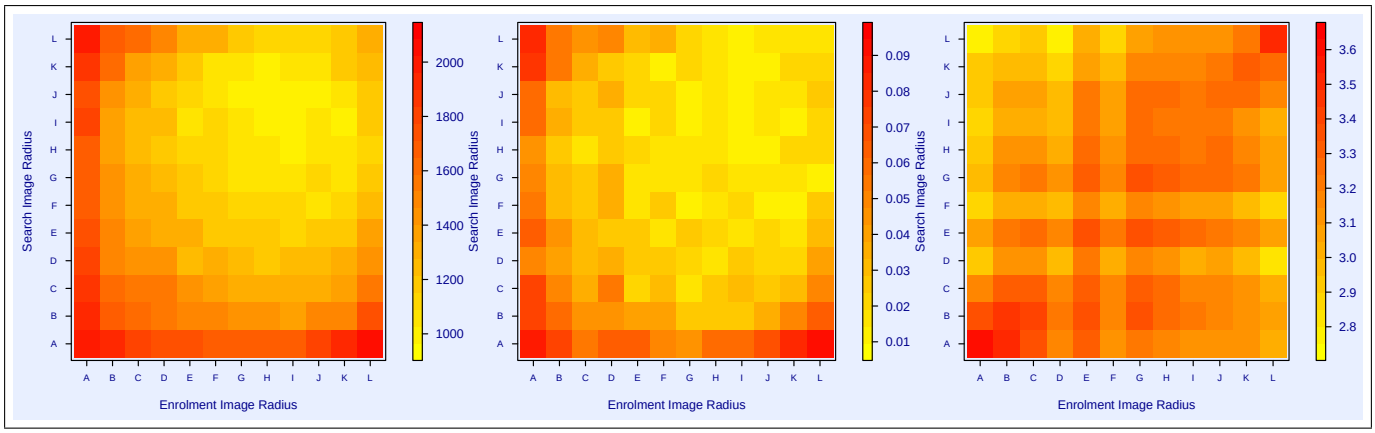

(a) Iris radius: Dis-similarity Score, Miss Rate, $\log_{10}(1+\text{Count})$

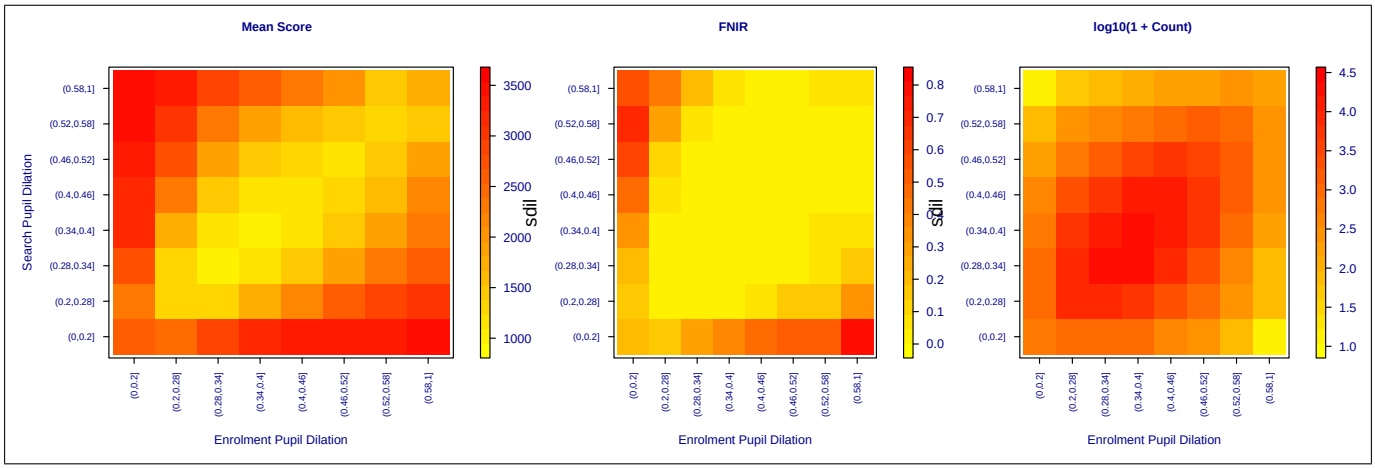

(b) Mate Dilation: Dis-similarity Score, Miss Rate, $\log_{10}(1+\text{Count})$

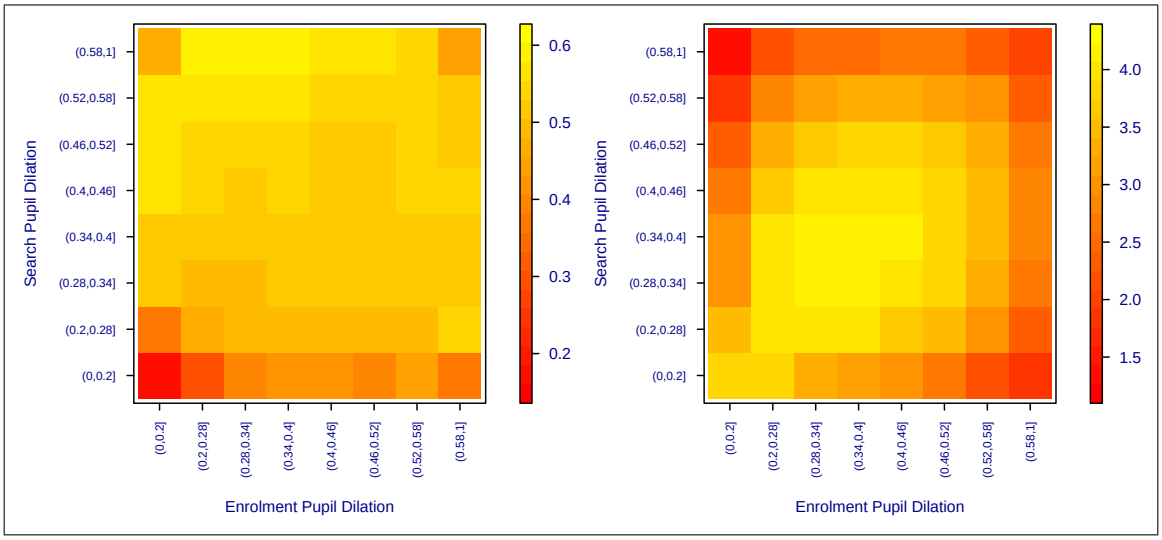

(c) Nonmate Dilation, Dis-similarity Score, Miss Rate, $\log_{10}(1+\text{Count})$

Figure 327: Heatmaps for implementation R12A executing mate searches in an enrolled population of N = 1.6 million. The radius images are binned by into twelve quantiles spanning $[0, 1]$. The dilation values are cut into ranges bounded by: $(0, 0.2, 0.28, 0.34, 0.40, 0.46, 0.52, 0.58, 1)$. The pathologically compressed 330x330 images are excluded from this analysis.

Heatmaps for implementation R12A executing mate searches in an enrolled population of N = 1.6 million.

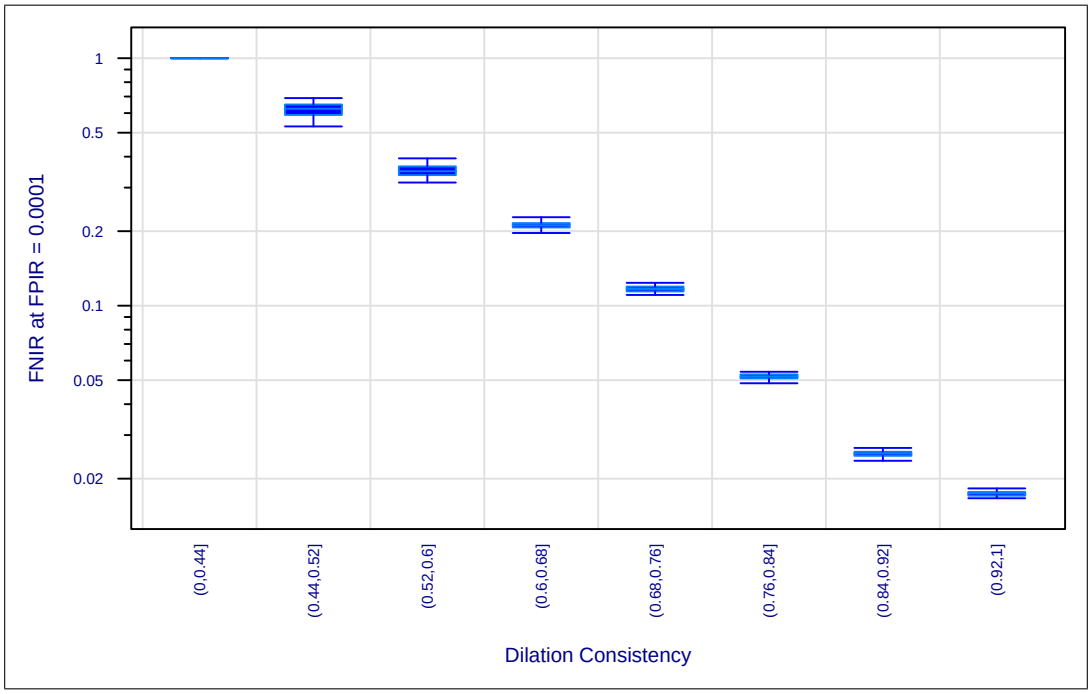

(a) Boxplot, all images

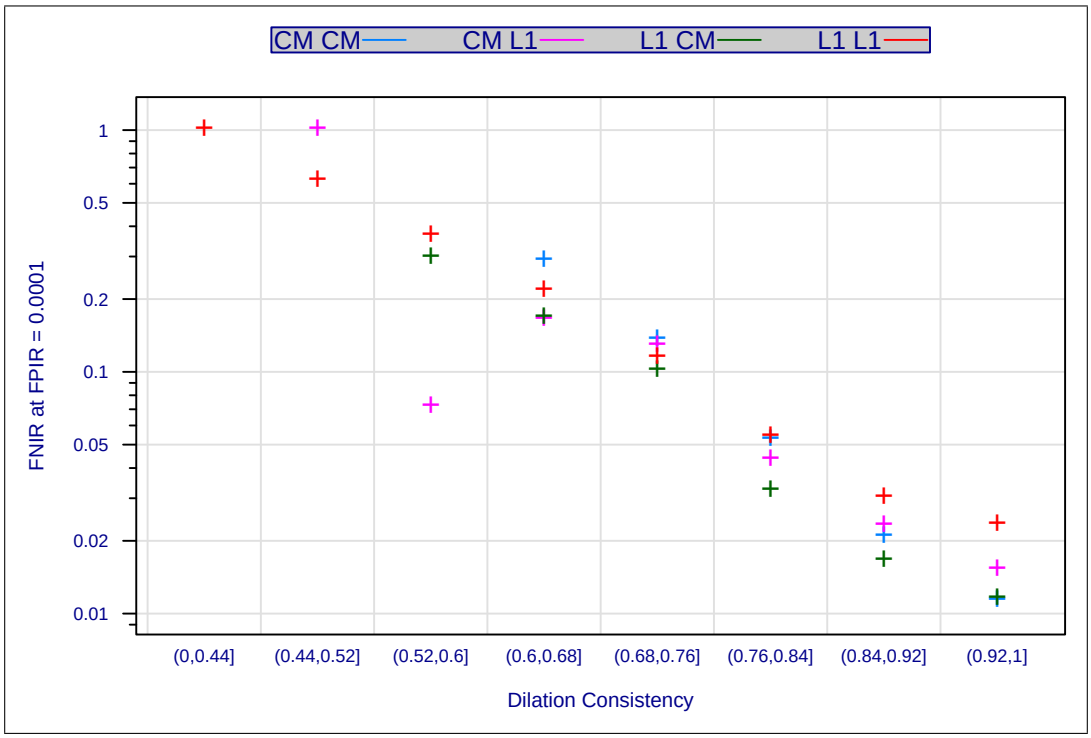

(b) Mean, L1 and CM images

Figure 328: Miss rate statistics for implementation R12A executing mate searches in an enrolled population of N = 1.6 million. The figures plots FNIR at FPIR = 0.0001 versus the IREX I metric for dilation consistency $(1 - \max(D_1, D_2))/(1 - \min(D_1, D_2))$ where D_i is pupil-iris radius ratio, and the subscripts refer to the mated enrollment and search image. The pathologically compressed 330x330 images are excluded from this analysis. The second figure breaks out dilation effects for interoperating camera pairs, CM and L1.

Figure 329: Heatmaps for implementation S01B executing mate searches in an enrolled population of N = 1.6 million. The radius images are binned by into twelve quantiles spanning $[0, 1]$. The dilation values are cut into ranges bounded by: $(0, 0.2, 0.28, 0.34, 0.40, 0.46, 0.52, 0.58, 1)$. The pathologically compressed 330x330 images are excluded from this analysis.

Figure 330: Miss rate statistics for implementation S01B executing mate searches in an enrolled population of N = 1.6 million. The figures plots FNIR at FPIR = 0.0001 versus the IREX I metric for dilation consistency $(1 - \max(D_1, D_2))/(1 - \min(D_1, D_2))$ where D_i is pupil-iris radius ratio, and the subscripts refer to the mated enrollment and search image. The pathologically compressed 330x330 images are excluded from this analysis. The second figure breaks out dilation effects for interoperating camera pairs, CM and L1.

Figure 331: Heatmaps for implementation S02B executing mate searches in an enrolled population of N = 1.6 million. The radius images are binned by into twelve quantiles spanning $[0, 1]$. The dilation values are cut into ranges bounded by: $(0, 0.2, 0.28, 0.34, 0.40, 0.46, 0.52, 0.58, 1)$. The pathologically compressed 330x330 images are excluded from this analysis.

Heatmaps for implementation S01B executing mate searches in an enrolled population of N = 1.6 million.

Figure 332: Miss rate statistics for implementation S02B executing mate searches in an enrolled population of N = 1.6 million. The figures plots FNIR at FPIR = 0.0001 versus the IREX I metric for dilation consistency $(1 - \max(D_1, D_2))/(1 - \min(D_1, D_2))$ where D_i is pupil-iris radius ratio, and the subscripts refer to the mated enrollment and search image. The pathologically compressed 330x330 images are excluded from this analysis. The second figure breaks out dilation effects for interoperating camera pairs, CM and L1.

Heatmaps for implementation S02B executing mate searches in an enrolled population of N = 1.6 million.

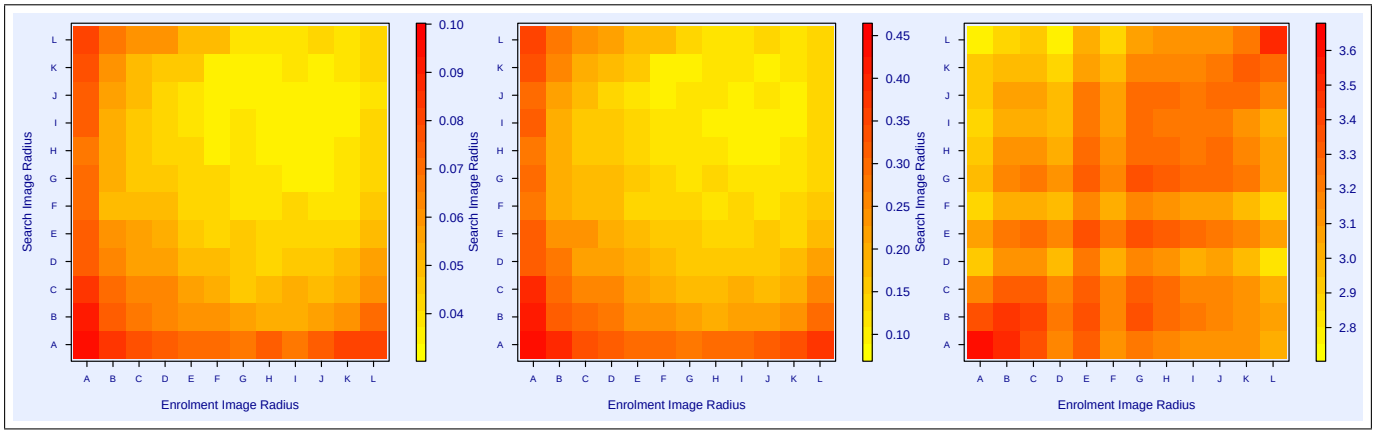

(a) Iris radius: Dis-similarity Score, Miss Rate, $\log_{10}(1+\text{Count})$

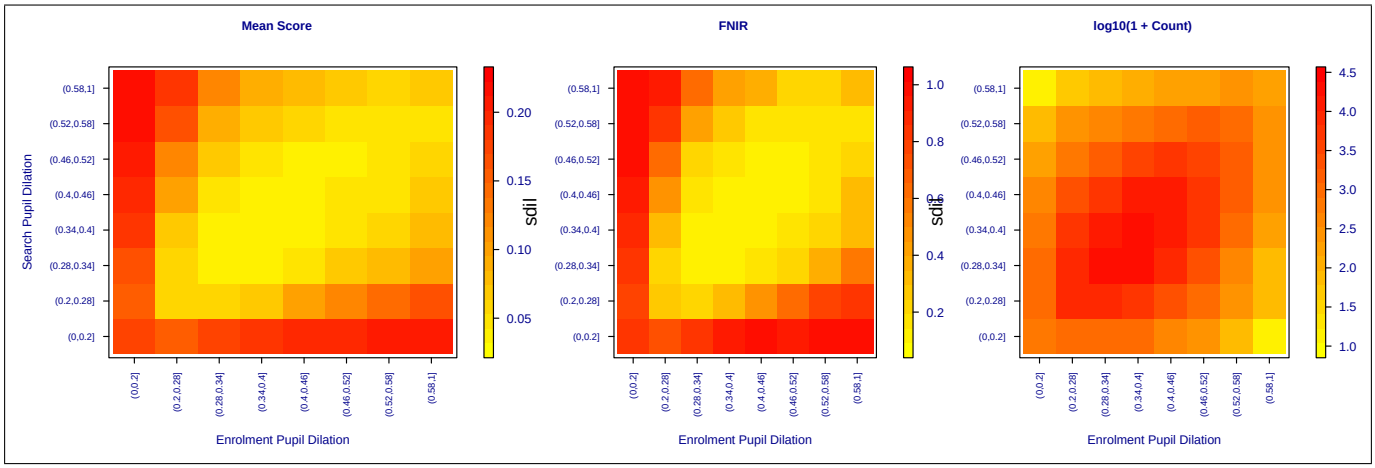

(b) Mate Dilation: Dis-similarity Score, Miss Rate, $\log_{10}(1+\text{Count})$

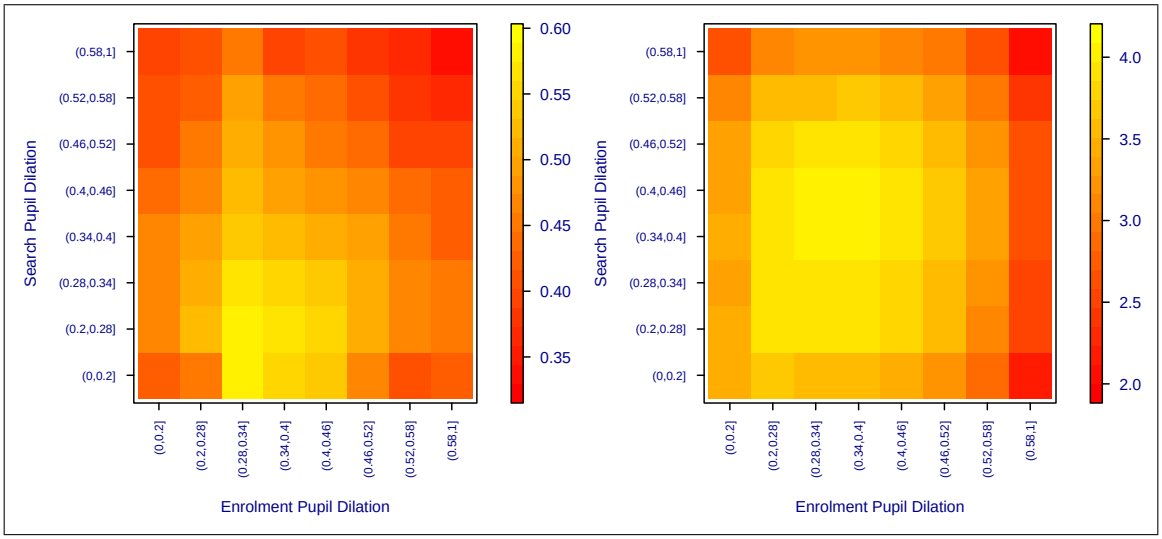

(c) Nonmate Dilation, Dis-similarity Score, Miss Rate, $\log_{10}(1+\text{Count})$

Figure 333: Heatmaps for implementation S03A executing mate searches in an enrolled population of N = 1.6 million. The radius images are binned by into twelve quantiles spanning $[0, 1]$. The dilation values are cut into ranges bounded by: $(0, 0.2, 0.28, 0.34, 0.40, 0.46, 0.52, 0.58, 1)$. The pathologically compressed 330x330 images are excluded from this analysis.

Heatmaps for implementation S03A executing mate searches in an enrolled population of N = 1.6 million.

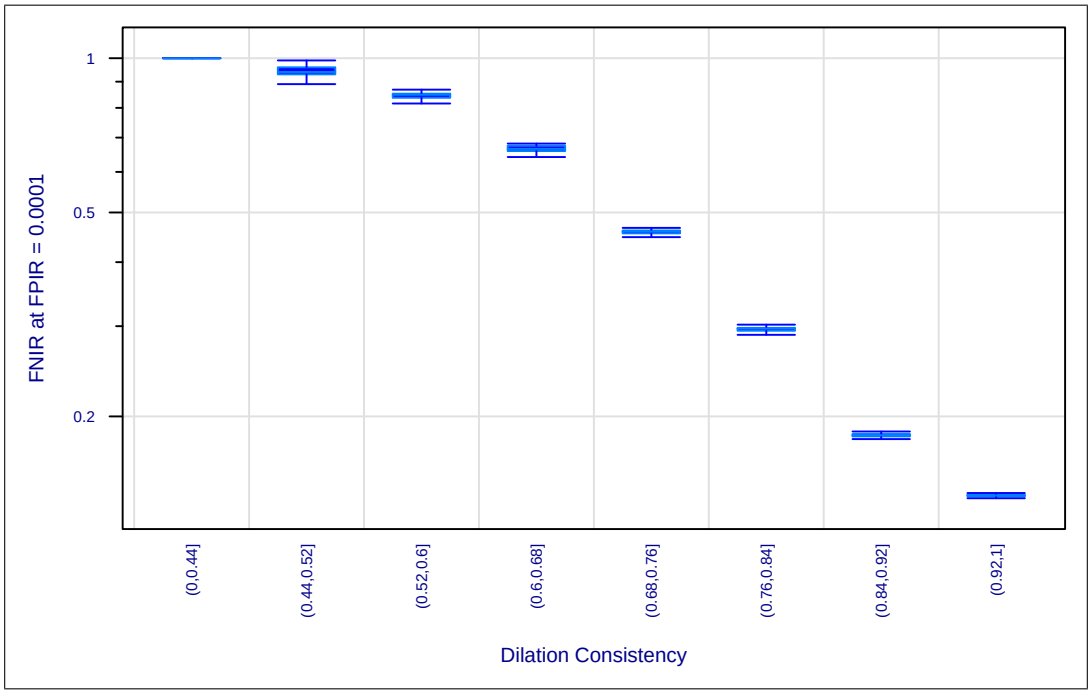

(a) Boxplot, all images

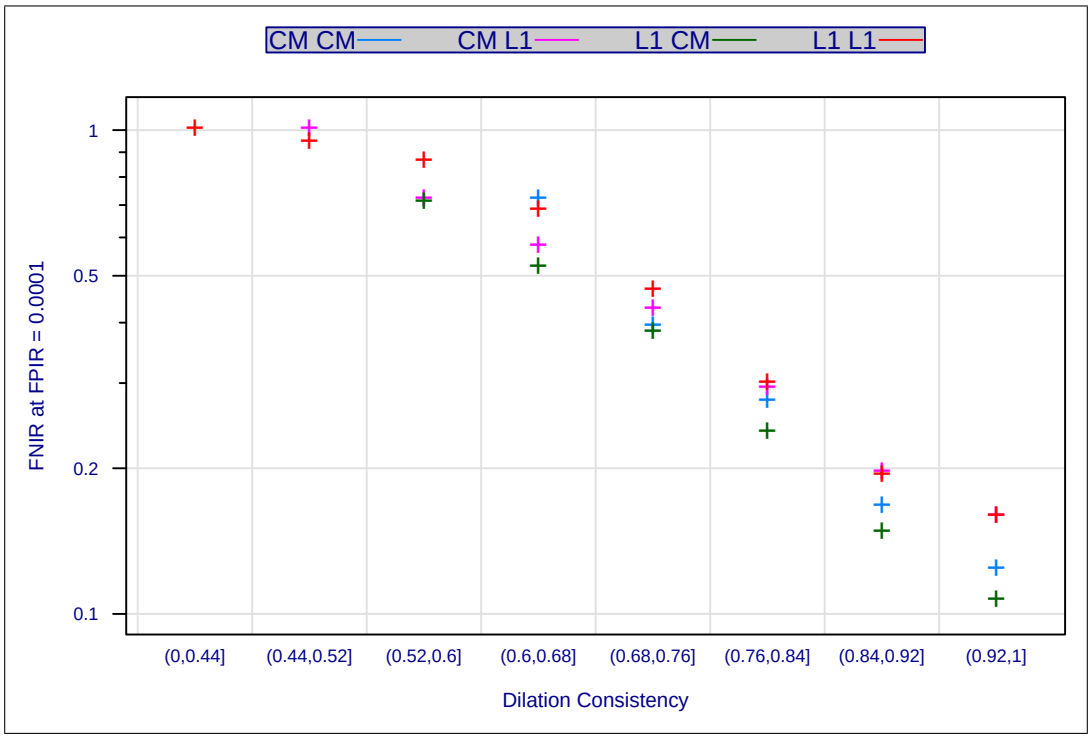

(b) Mean, L1 and CM images

Figure 334: Miss rate statistics for implementation S03A executing mate searches in an enrolled population of N = 1.6 million. The figures plots FNIR at FPIR = 0.0001 versus the IREX I metric for dilation consistency $(1 - \max(D_1, D_2))/(1 - \min(D_1, D_2))$ where D_i is pupil-iris radius ratio, and the subscripts refer to the mated enrollment and search image. The pathologically compressed 330x330 images are excluded from this analysis. The second figure breaks out dilation effects for interoperating camera pairs, CM and L1.

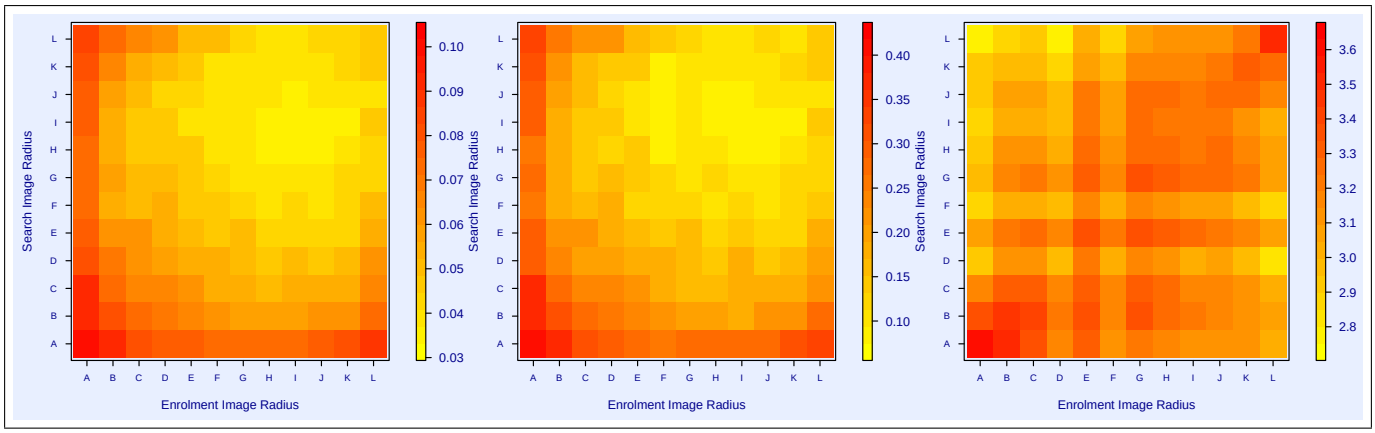

(a) Iris radius: Dis-similarity Score, Miss Rate, $\log_{10}(1+\text{Count})$

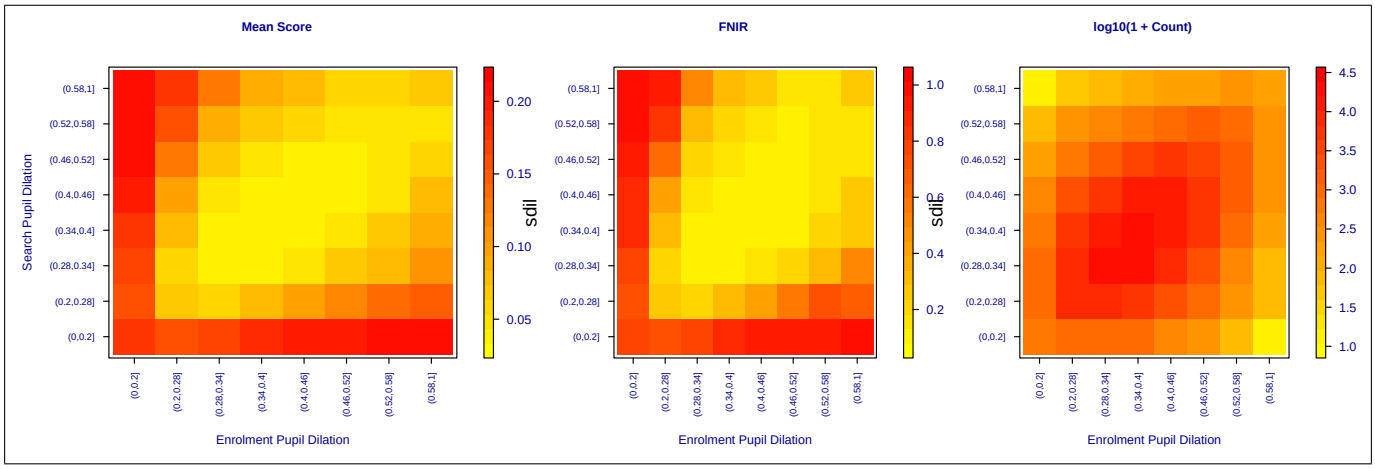

(b) Mate Dilation: Dis-similarity Score, Miss Rate, $\log_{10}(1+\text{Count})$

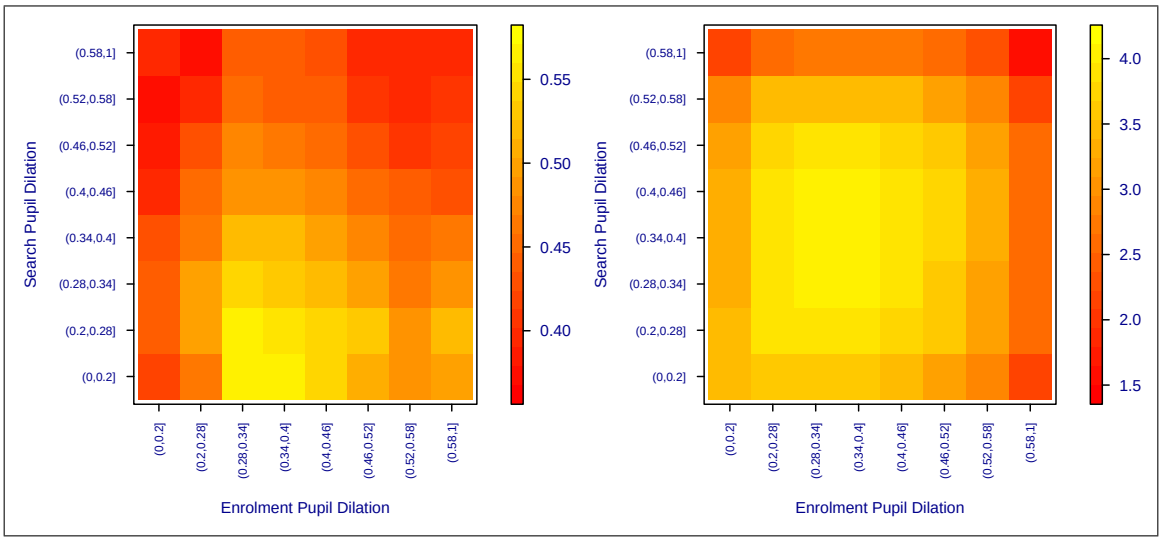

(c) Nonmate Dilation, Dis-similarity Score, Miss Rate, $\log_{10}(1+\text{Count})$

Figure 335: Heatmaps for implementation S04A executing mate searches in an enrolled population of N = 1.6 million. The radius images are binned by into twelve quantiles spanning $[0, 1]$. The dilation values are cut into ranges bounded by: $(0, 0.2, 0.28, 0.34, 0.40, 0.46, 0.52, 0.58, 1)$. The pathologically compressed 330x330 images are excluded from this analysis.

Heatmaps for implementation S04A executing mate searches in an enrolled population of N = 1.6 million.

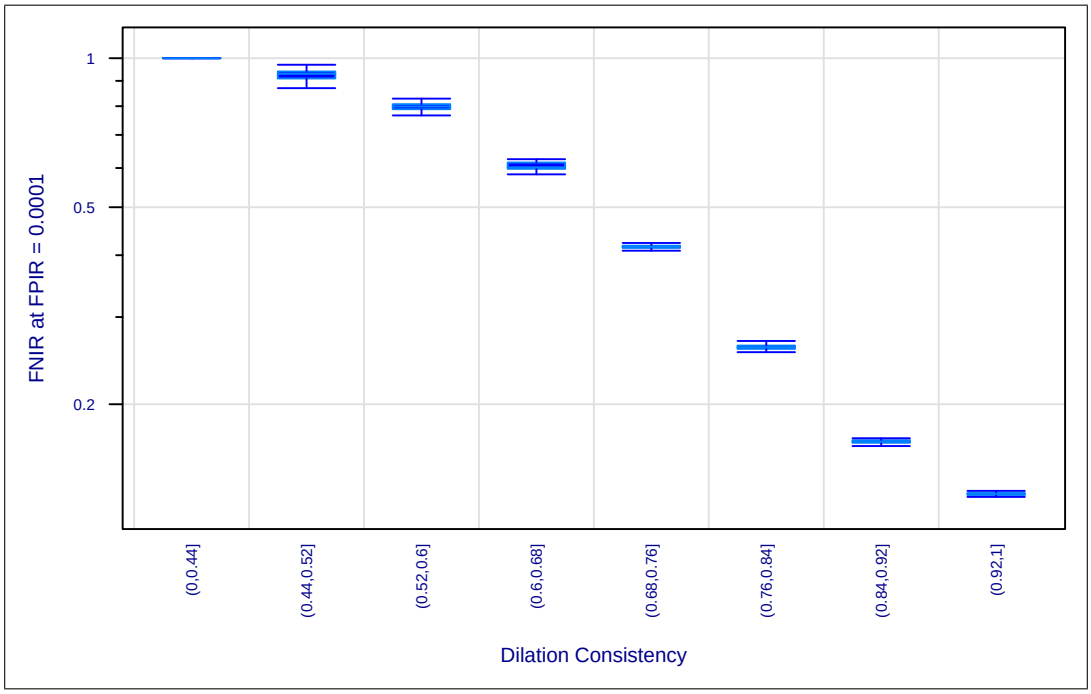

(a) Boxplot, all images

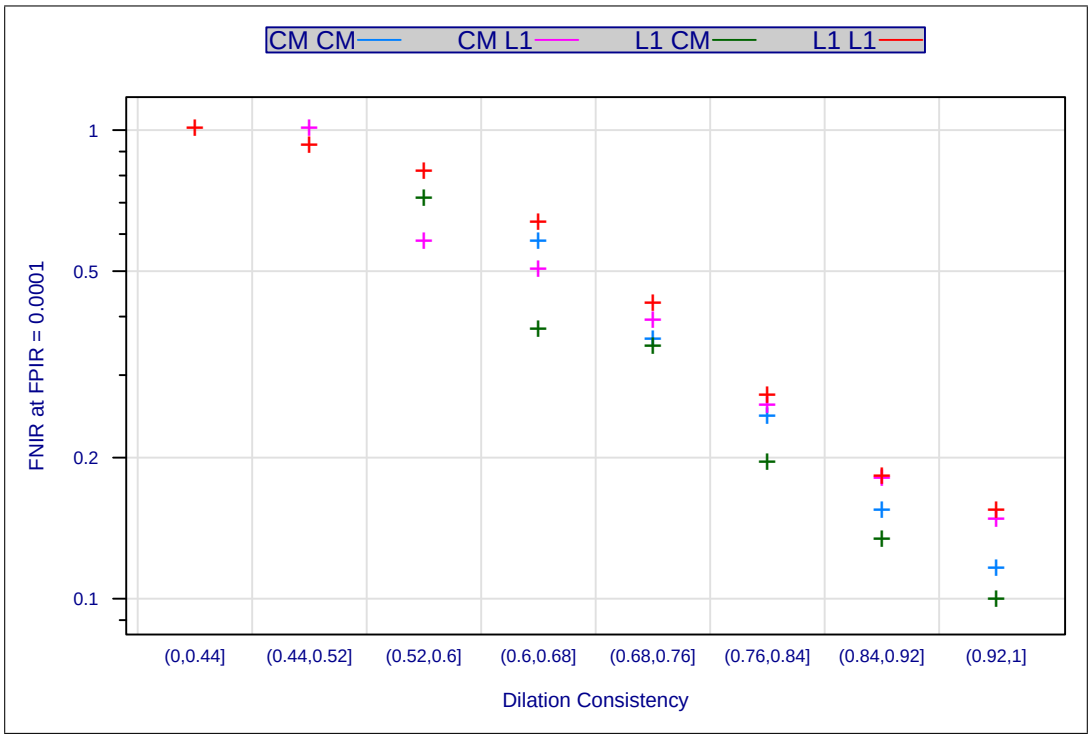

(b) Mean, L1 and CM images

Figure 336: Miss rate statistics for implementation S04A executing mate searches in an enrolled population of N = 1.6 million. The figures plots FNIR at FPIR = 0.0001 versus the IREX I metric for dilation consistency $(1 - \max(D_1, D_2))/(1 - \min(D_1, D_2))$ where D_i is pupil-iris radius ratio, and the subscripts refer to the mated enrollment and search image. The pathologically compressed 330x330 images are excluded from this analysis. The second figure breaks out dilation effects for interoperating camera pairs, CM and L1.

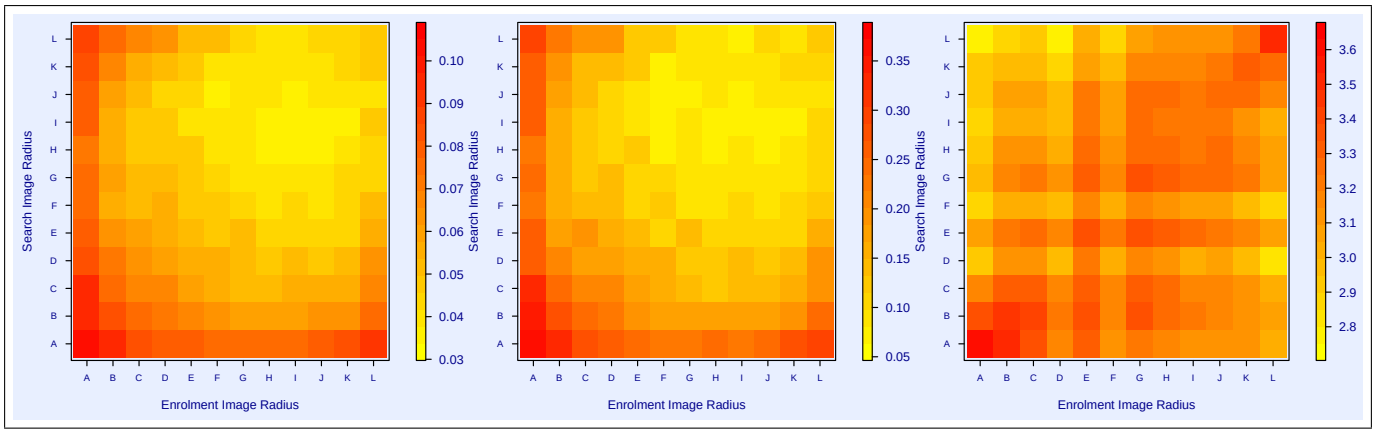

(a) Iris radius: Dis-similarity Score, Miss Rate, $\log_{10}(1+\text{Count})$

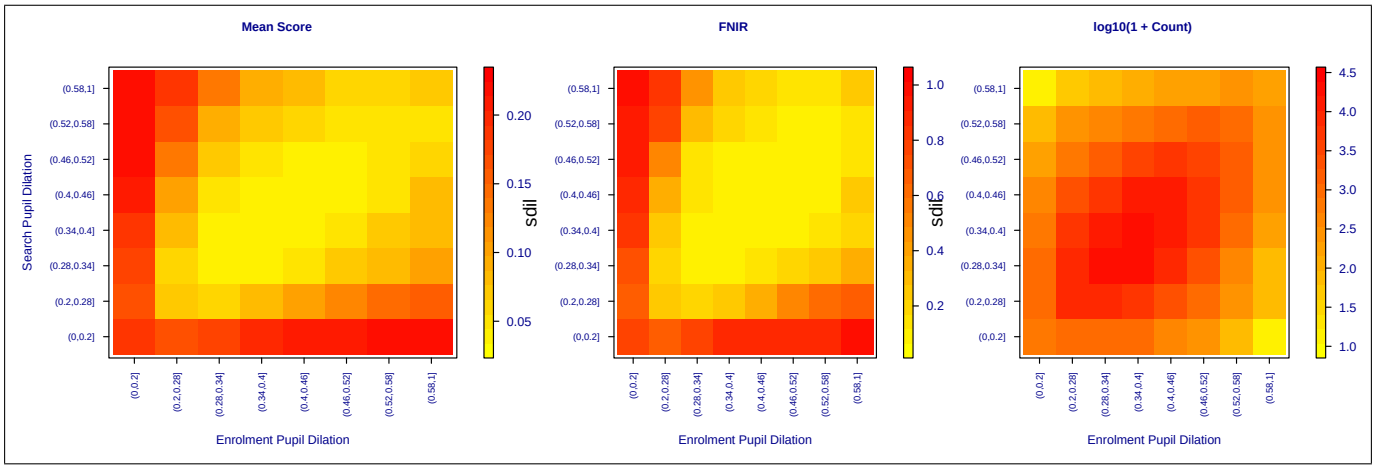

(b) Mate Dilation: Dis-similarity Score, Miss Rate, $\log_{10}(1+\text{Count})$

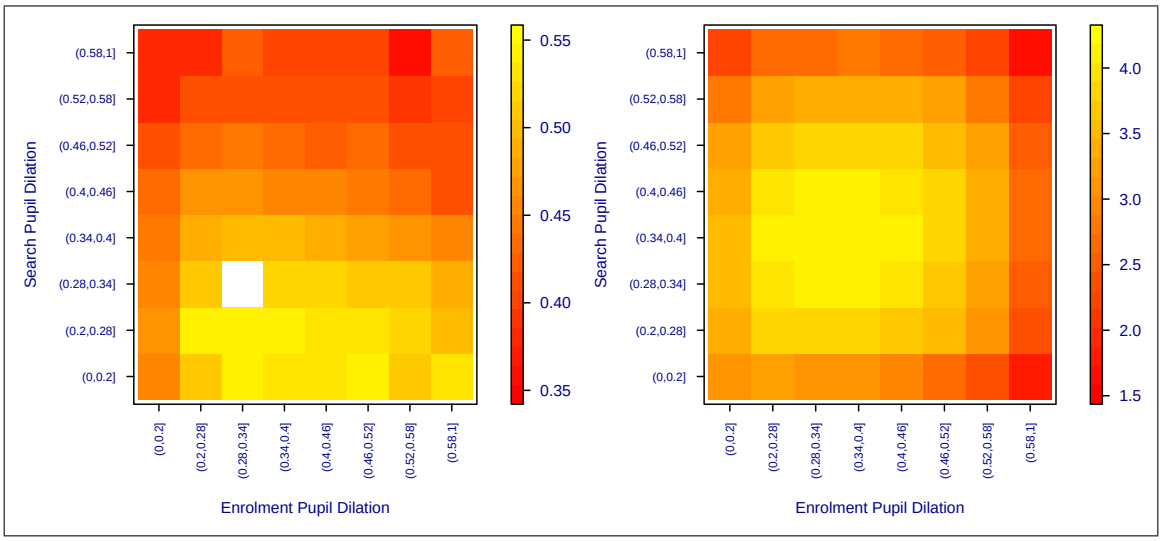

(c) Nonmate Dilation, Dis-similarity Score, Miss Rate, $\log_{10}(1+\text{Count})$

Figure 337: Heatmaps for implementation S05A executing mate searches in an enrolled population of N = 1.6 million. The radius images are binned by into twelve quantiles spanning $[0, 1]$. The dilation values are cut into ranges bounded by: $(0, 0.2, 0.28, 0.34, 0.40, 0.46, 0.52, 0.58, 1)$. The pathologically compressed 330x330 images are excluded from this analysis.

Heatmaps for implementation S05A executing mate searches in an enrolled population of N = 1.6 million.

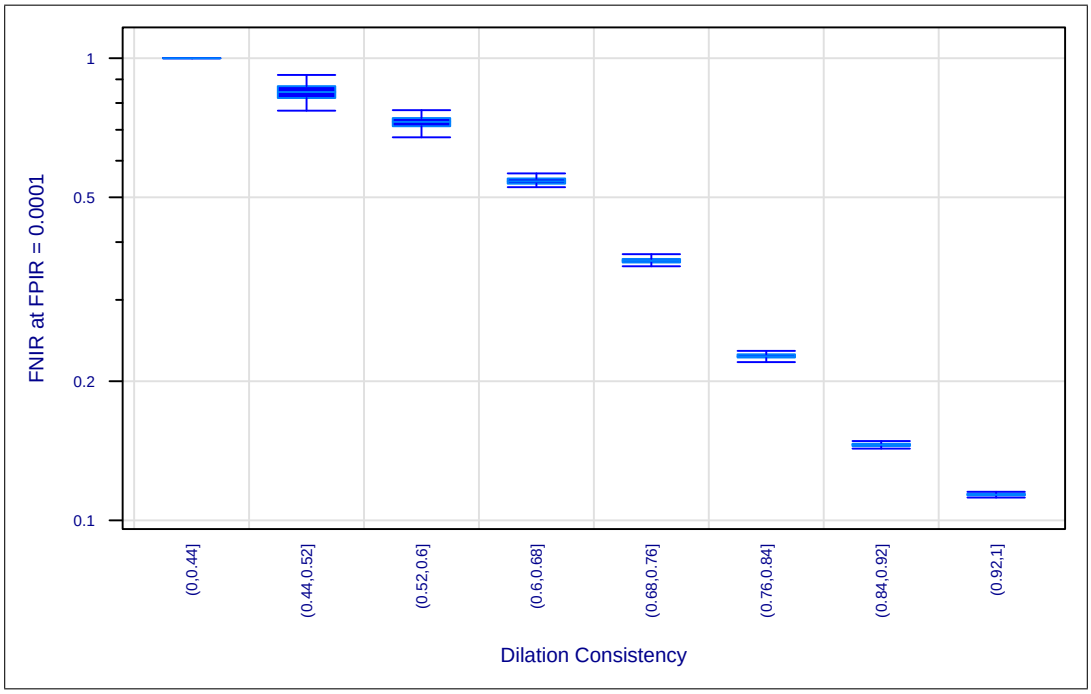

(a) Boxplot, all images

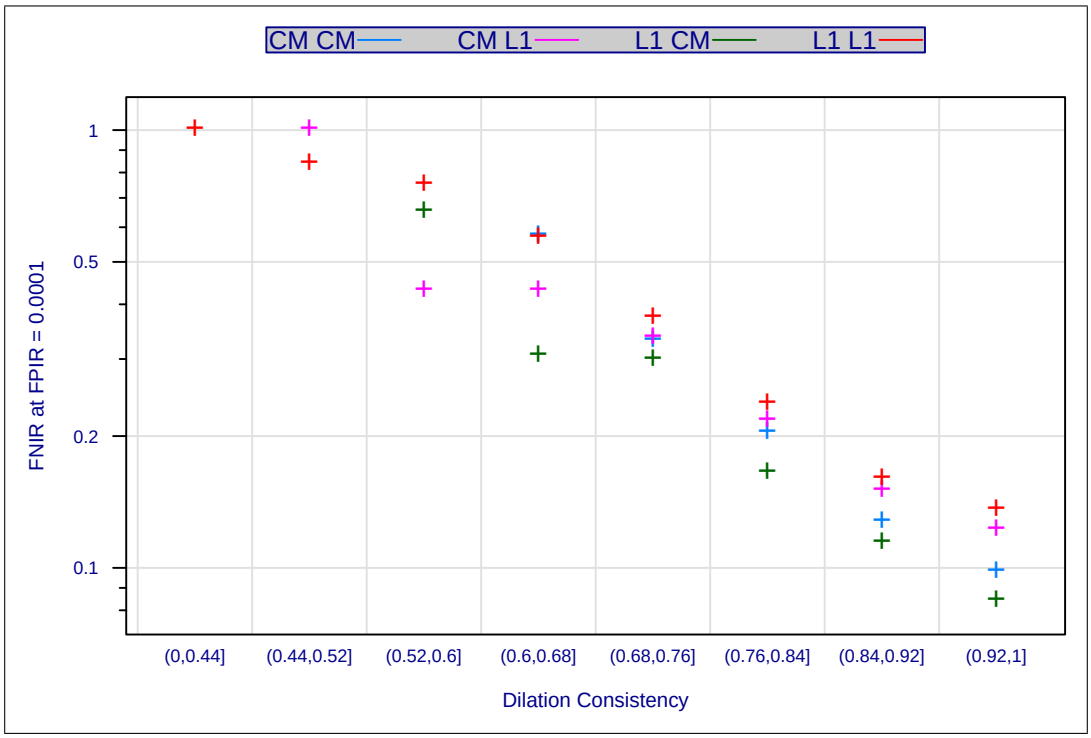

(b) Mean, L1 and CM images

Figure 338: Miss rate statistics for implementation S05A executing mate searches in an enrolled population of N = 1.6 million. The figures plots FNIR at FPIR = 0.0001 versus the IREX I metric for dilation consistency $(1 - \max(D_1, D_2))/(1 - \min(D_1, D_2))$ where D_i is pupil-iris radius ratio, and the subscripts refer to the mated enrollment and search image. The pathologically compressed 330x330 images are excluded from this analysis. The second figure breaks out dilation effects for interoperating camera pairs, CM and L1.

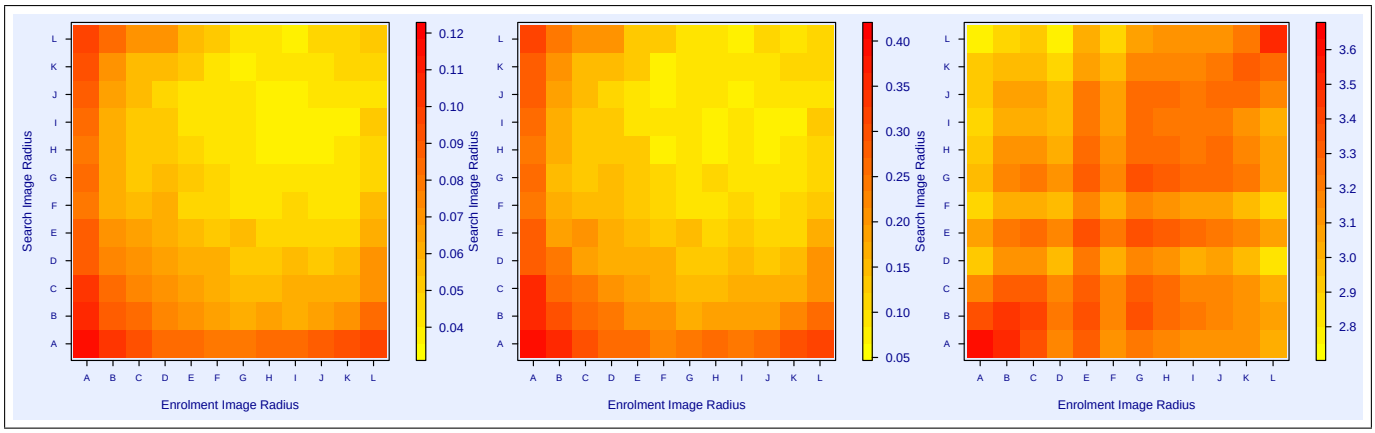

(a) Iris radius: Dis-similarity Score, Miss Rate, $\log_{10}(1+\text{Count})$

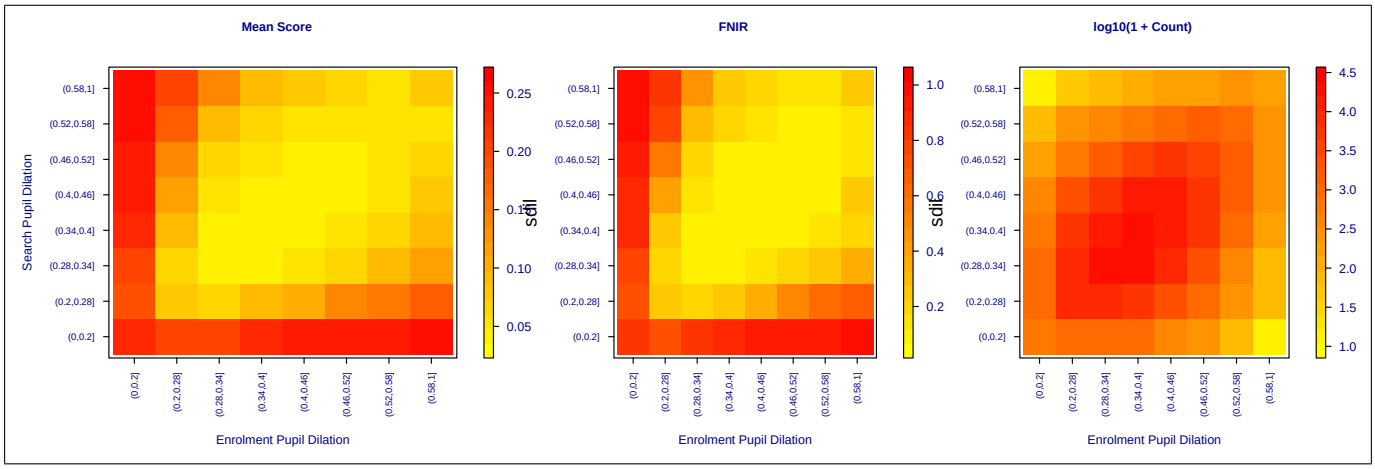

(b) Mate Dilation: Dis-similarity Score, Miss Rate, $\log_{10}(1+\text{Count})$

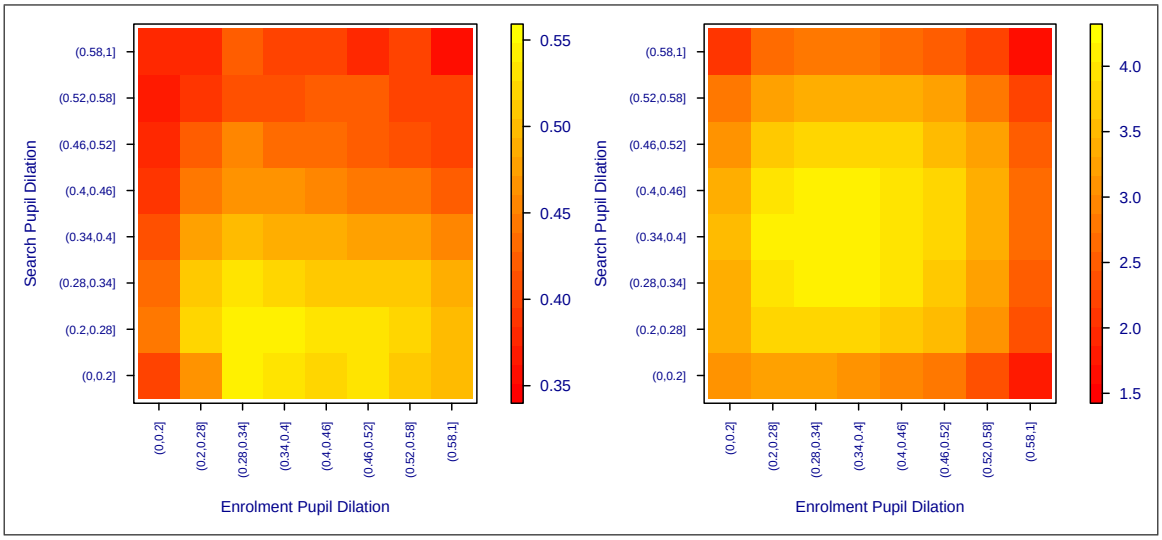

(c) Nonmate Dilation, Dis-similarity Score, Miss Rate, $\log_{10}(1+\text{Count})$

Figure 339: Heatmaps for implementation S11A executing mate searches in an enrolled population of N = 1.6 million. The radius images are binned by into twelve quantiles spanning $[0, 1]$. The dilation values are cut into ranges bounded by: $(0, 0.2, 0.28, 0.34, 0.40, 0.46, 0.52, 0.58, 1)$. The pathologically compressed 330x330 images are excluded from this analysis.

Heatmaps for implementation S11A executing mate searches in an enrolled population of N = 1.6 million.

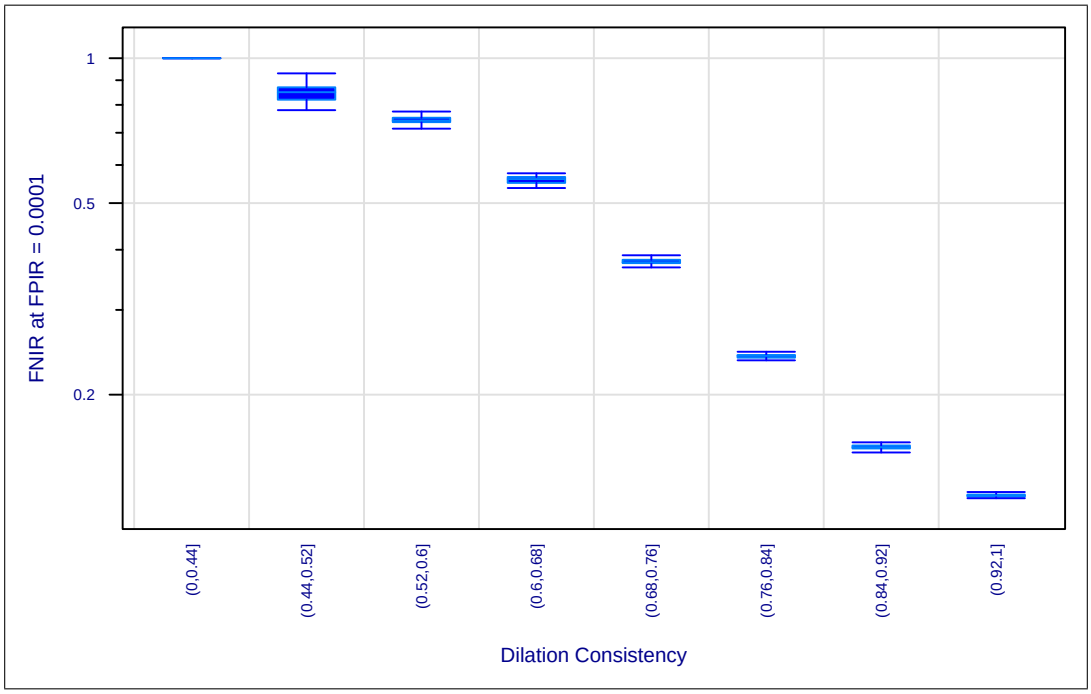

(a) Boxplot, all images

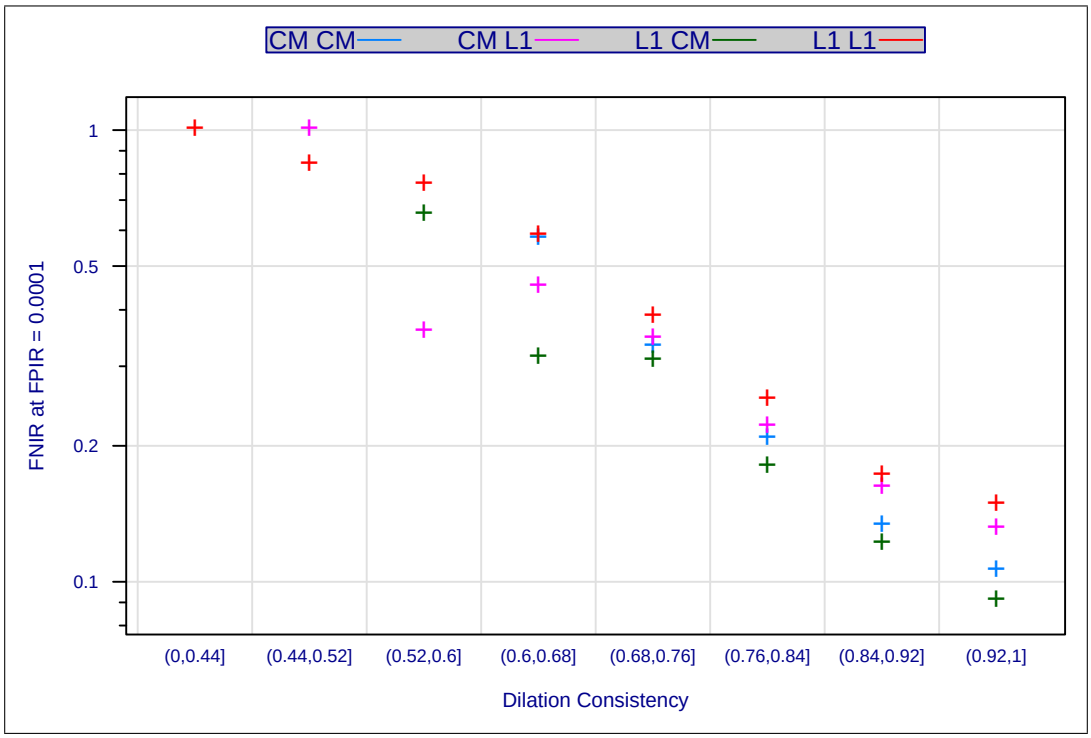

(b) Mean, L1 and CM images

Figure 340: Miss rate statistics for implementation S11A executing mate searches in an enrolled population of N = 1.6 million. The figures plots FNIR at FPIR = 0.0001 versus the IREX I metric for dilation consistency $(1 - \max(D_1, D_2))/(1 - \min(D_1, D_2))$ where D_i is pupil-iris radius ratio, and the subscripts refer to the mated enrollment and search image. The pathologically compressed 330x330 images are excluded from this analysis. The second figure breaks out dilation effects for interoperating camera pairs, CM and L1.

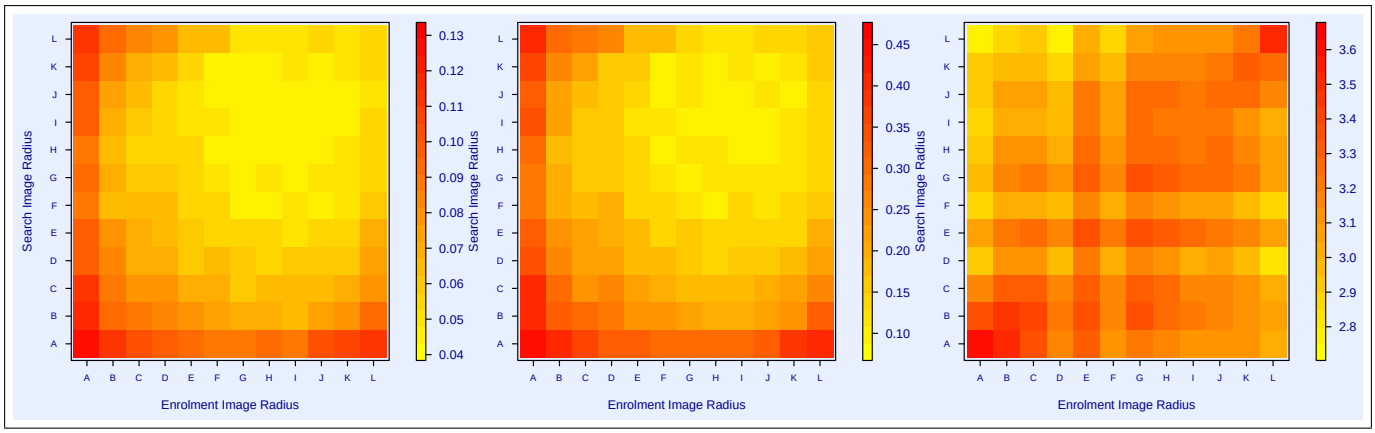

(a) Iris radius: Dis-similarity Score, Miss Rate, $\log_{10}(1+\text{Count})$

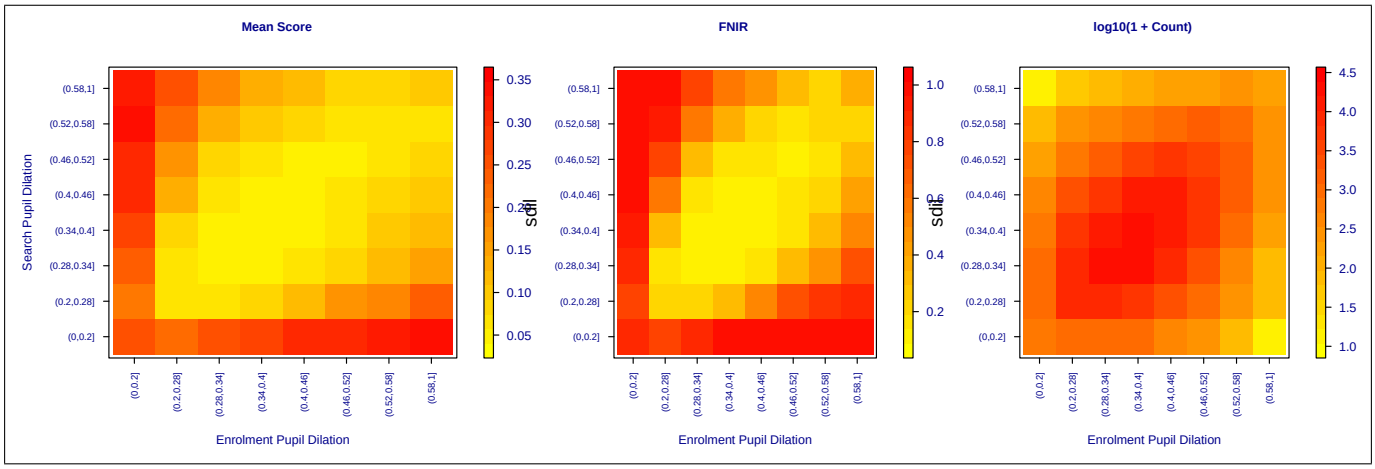

(b) Mate Dilation: Dis-similarity Score, Miss Rate, $\log_{10}(1+\text{Count})$

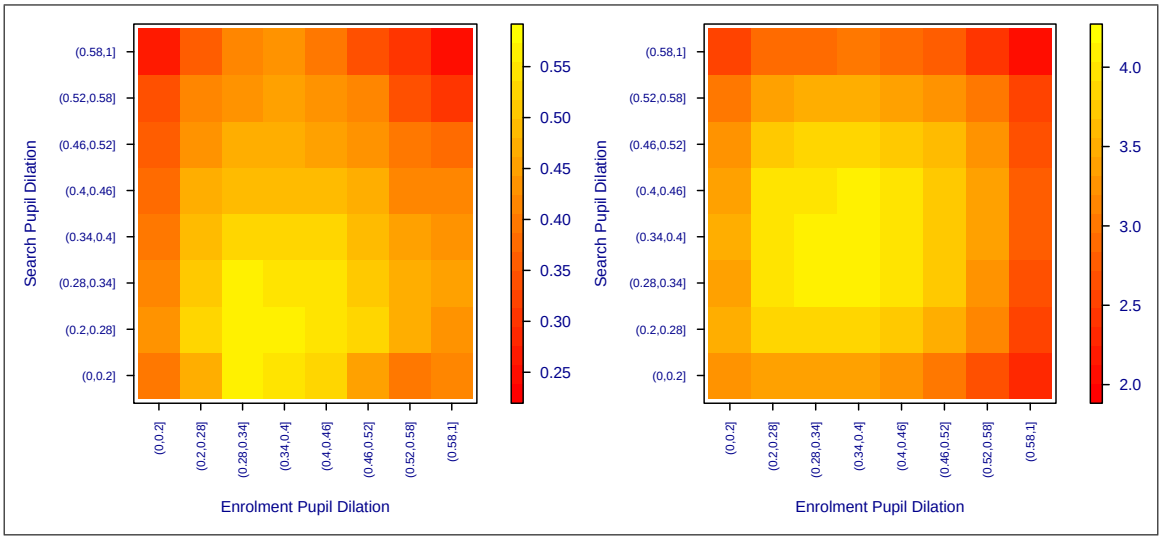

(c) Nonmate Dilation, Dis-similarity Score, Miss Rate, $\log_{10}(1+\text{Count})$

Figure 341: Heatmaps for implementation S11B executing mate searches in an enrolled population of N = 1.6 million. The radius images are binned by into twelve quantiles spanning $[0, 1]$. The dilation values are cut into ranges bounded by: $(0, 0.2, 0.28, 0.34, 0.40, 0.46, 0.52, 0.58, 1)$. The pathologically compressed 330x330 images are excluded from this analysis.

Heatmaps for implementation S11B executing mate searches in an enrolled population of N = 1.6 million.

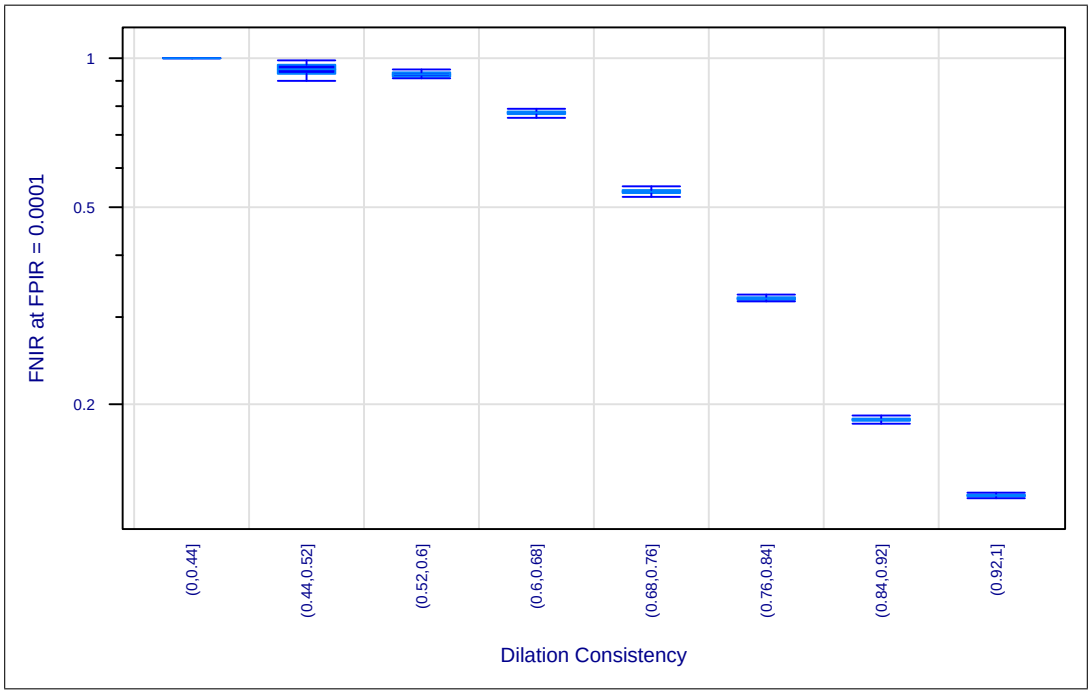

(a) Boxplot, all images

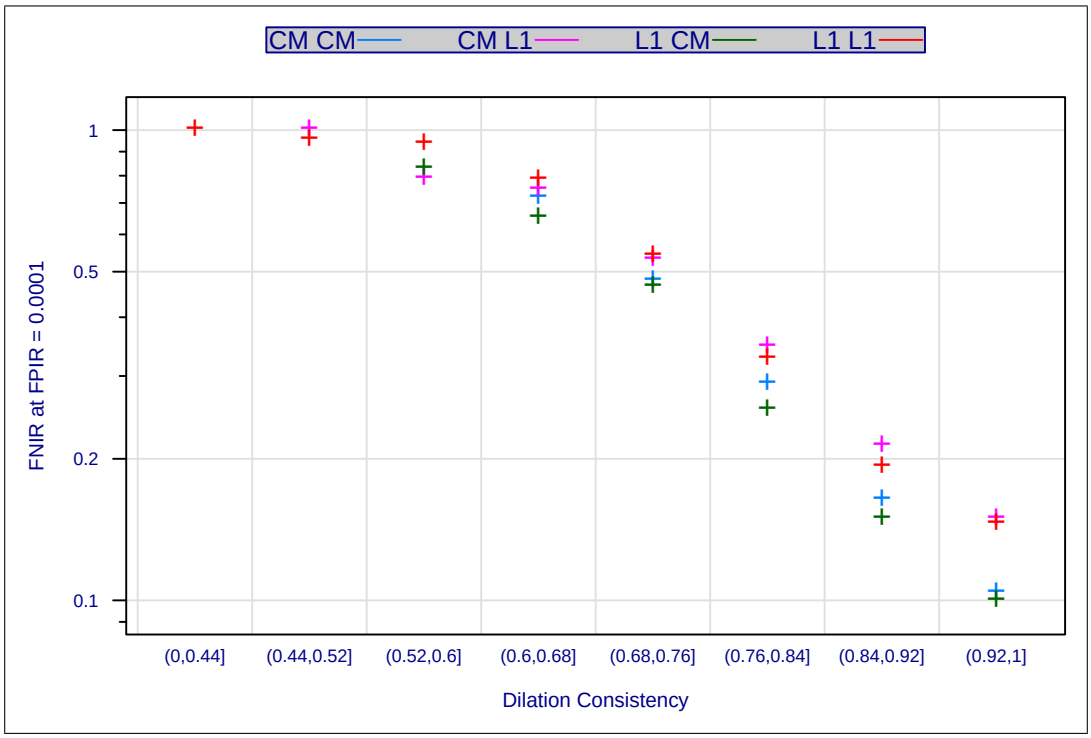

(b) Mean, L1 and CM images

Figure 342: Miss rate statistics for implementation S11B executing mate searches in an enrolled population of N = 1.6 million. The figures plots FNIR at FPIR = 0.0001 versus the IREX I metric for dilation consistency $(1 - \max(D_1, D_2))/(1 - \min(D_1, D_2))$ where D_i is pupil-iris radius ratio, and the subscripts refer to the mated enrollment and search image. The pathologically compressed 330x330 images are excluded from this analysis. The second figure breaks out dilation effects for interoperating camera pairs, CM and L1.

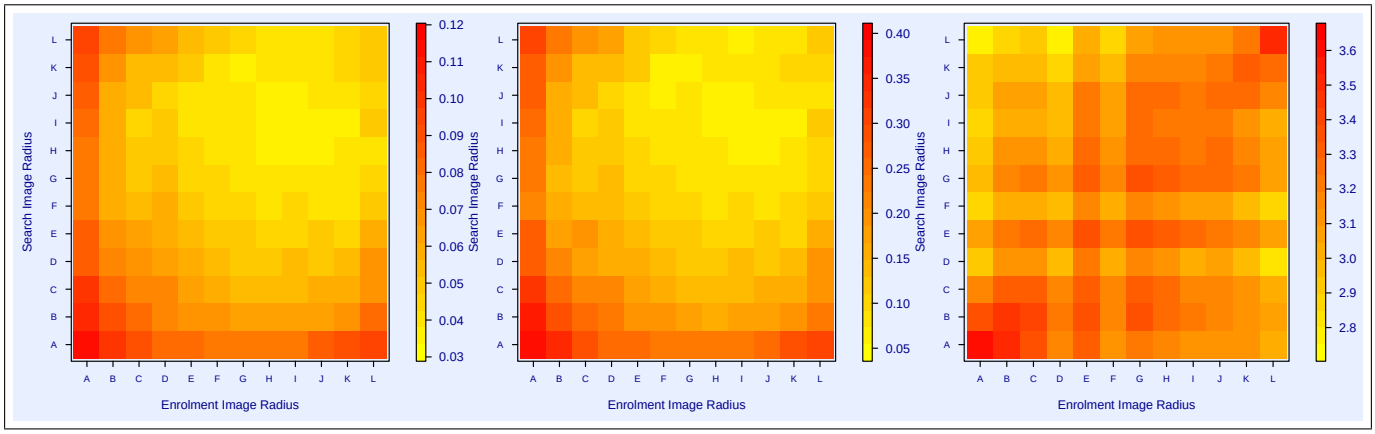

(a) Iris radius: Dis-similarity Score, Miss Rate, $\log_{10}(1+\text{Count})$

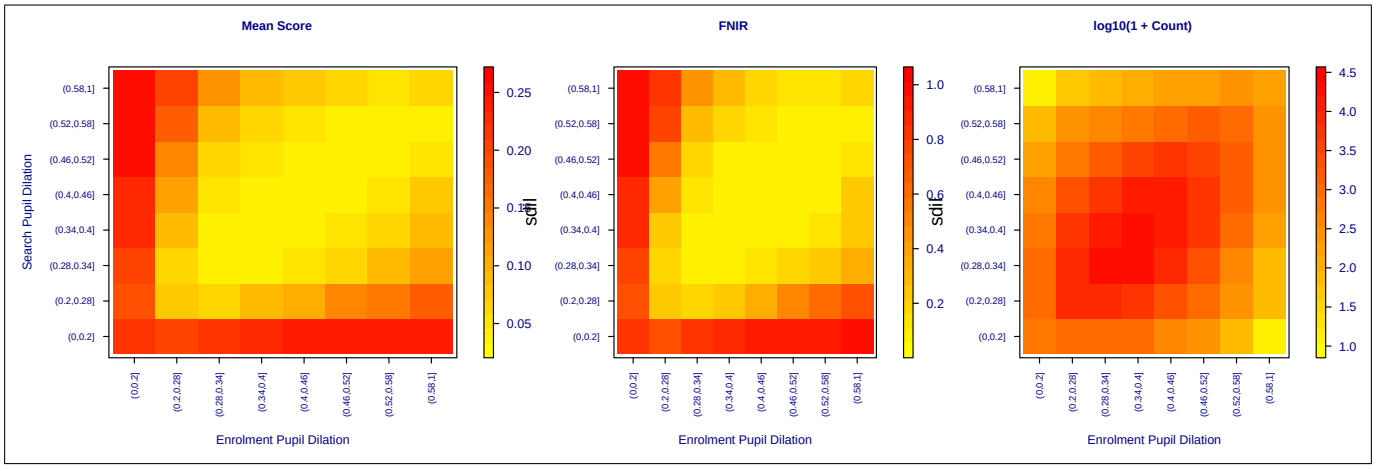

(b) Mate Dilation: Dis-similarity Score, Miss Rate, $\log_{10}(1+\text{Count})$

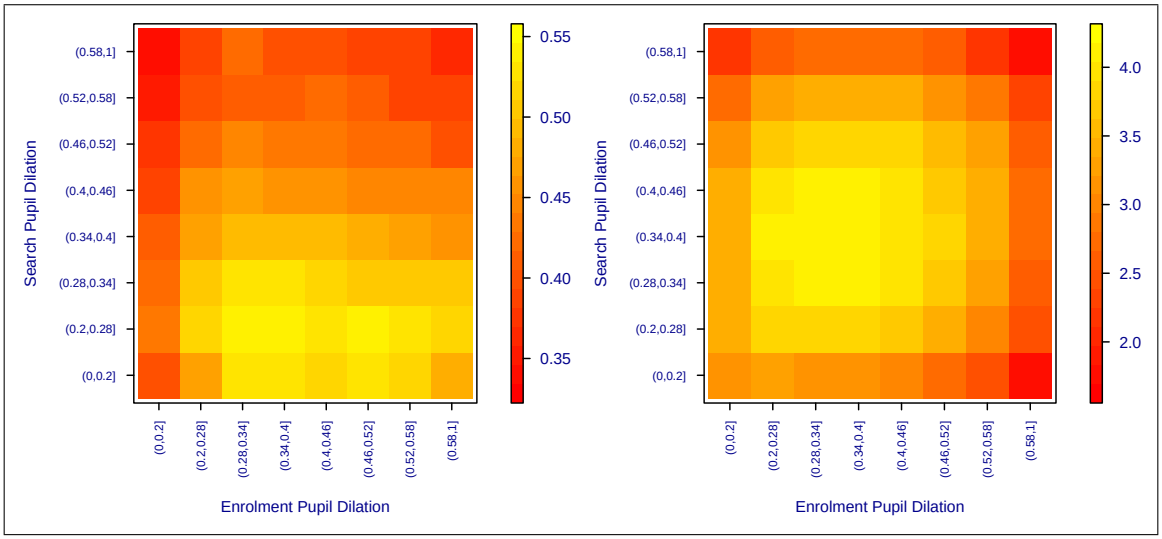

(c) Nonmate Dilation, Dis-similarity Score, Miss Rate, $\log_{10}(1+\text{Count})$

Figure 343: Heatmaps for implementation S12A executing mate searches in an enrolled population of N = 1.6 million. The radius images are binned by into twelve quantiles spanning $[0, 1]$. The dilation values are cut into ranges bounded by: $(0, 0.2, 0.28, 0.34, 0.40, 0.46, 0.52, 0.58, 1)$. The pathologically compressed 330x330 images are excluded from this analysis.

Heatmaps for implementation S12A executing mate searches in an enrolled population of N = 1.6 million.

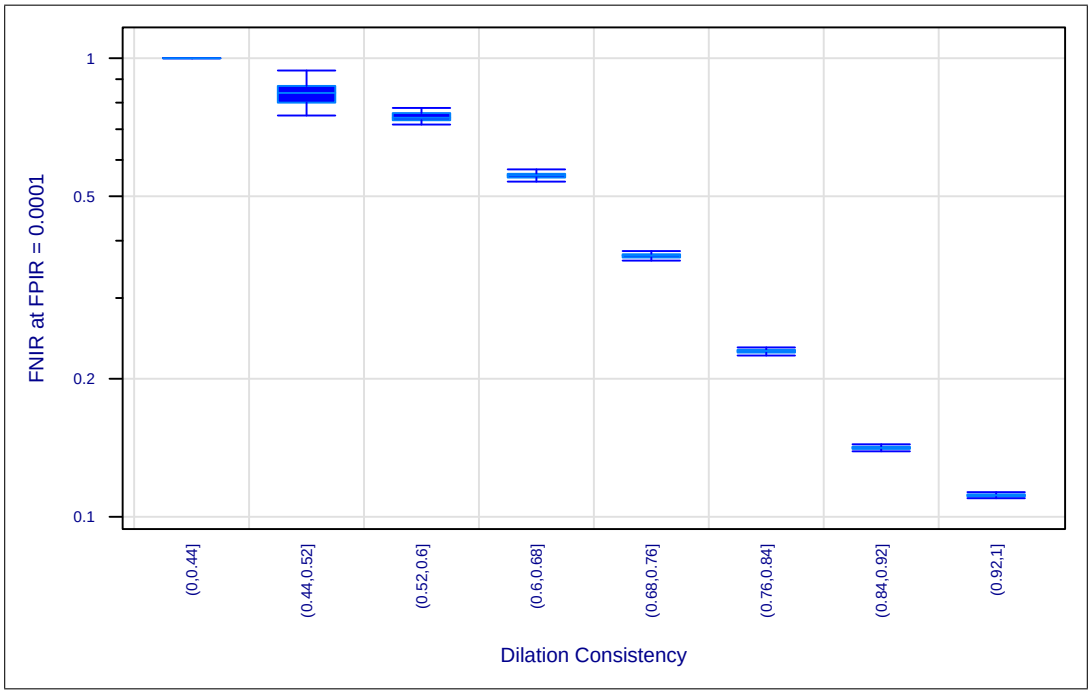

(a) Boxplot, all images

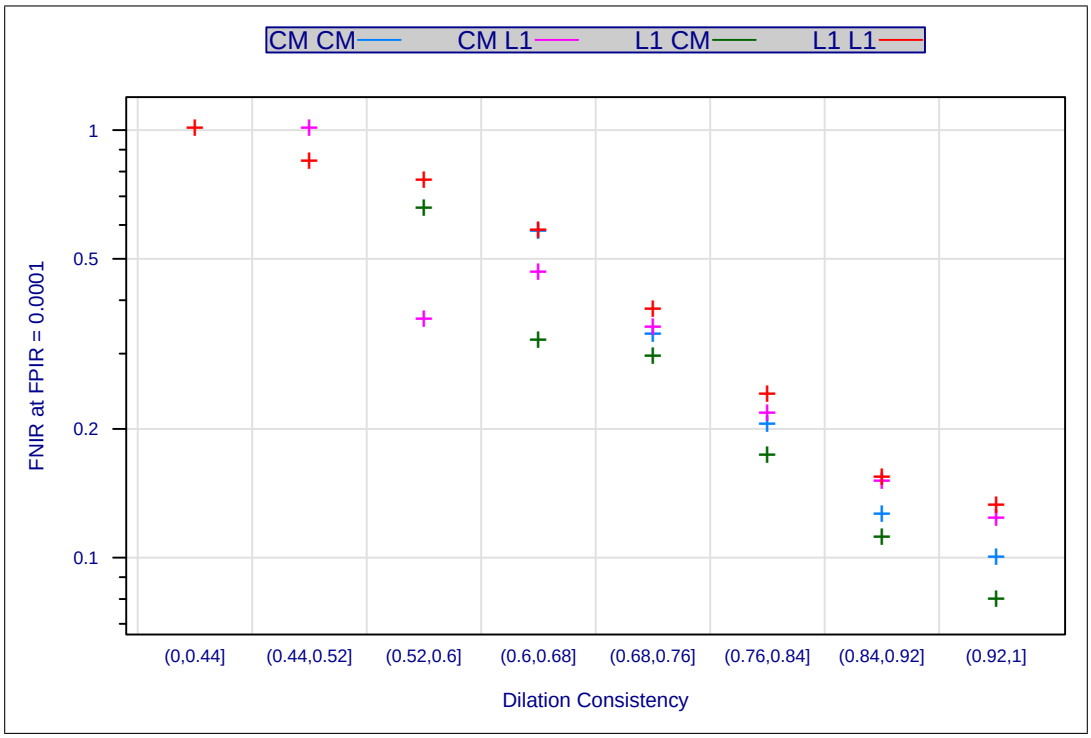

(b) Mean, L1 and CM images

Figure 344: Miss rate statistics for implementation S12A executing mate searches in an enrolled population of N = 1.6 million. The figures plots FNIR at FPIR = 0.0001 versus the IREX I metric for dilation consistency $(1 - \max(D_1, D_2))/(1 - \min(D_1, D_2))$ where D_i is pupil-iris radius ratio, and the subscripts refer to the mated enrollment and search image. The pathologically compressed 330x330 images are excluded from this analysis. The second figure breaks out dilation effects for interoperating camera pairs, CM and L1.

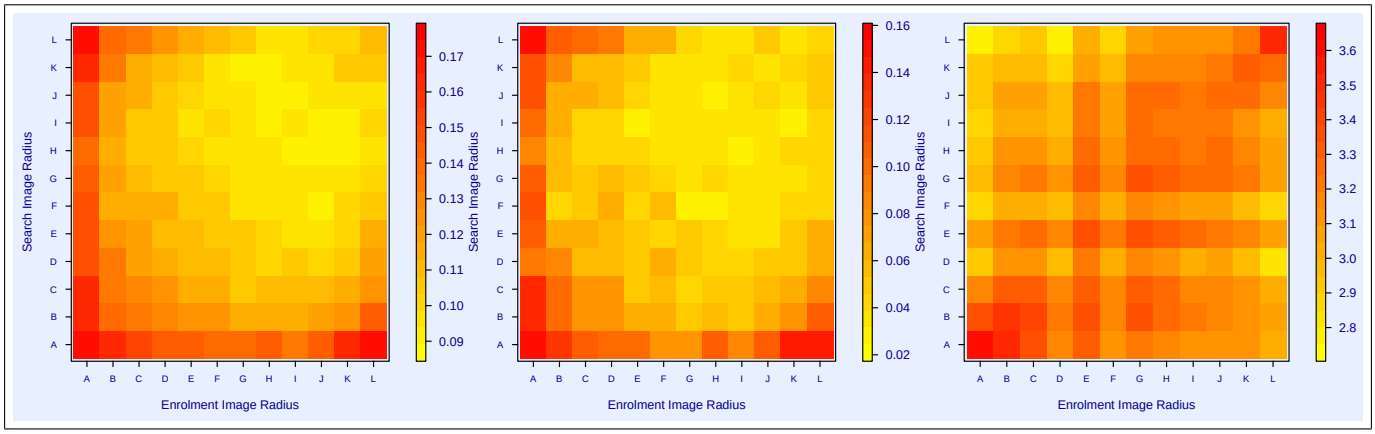

(a) Iris radius: Dis-similarity Score, Miss Rate, $\log_{10}(1+\text{Count})$

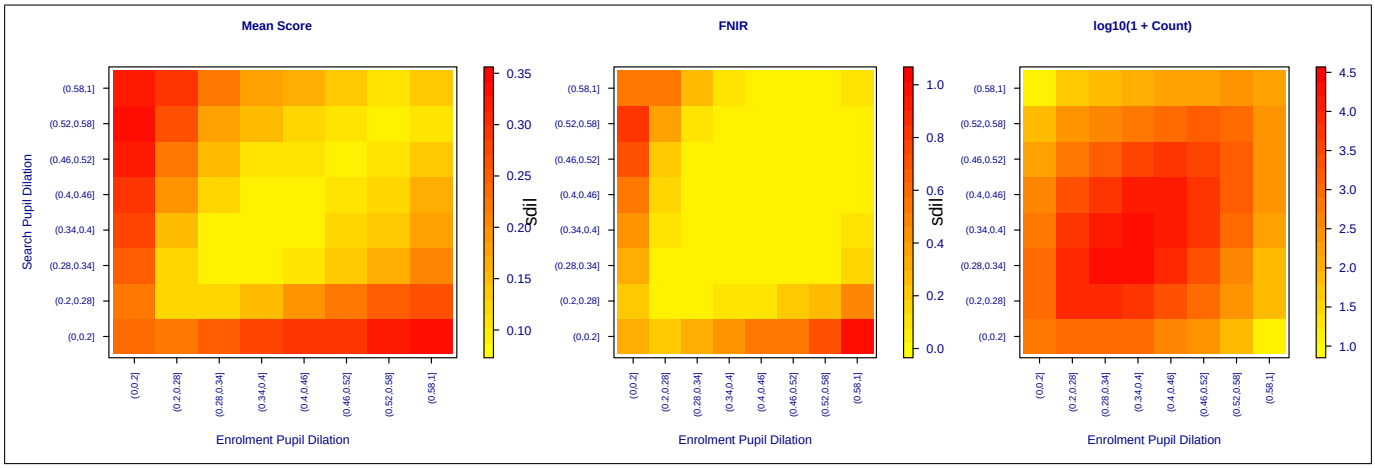

(b) Mate Dilation: Dis-similarity Score, Miss Rate, $\log_{10}(1+\text{Count})$

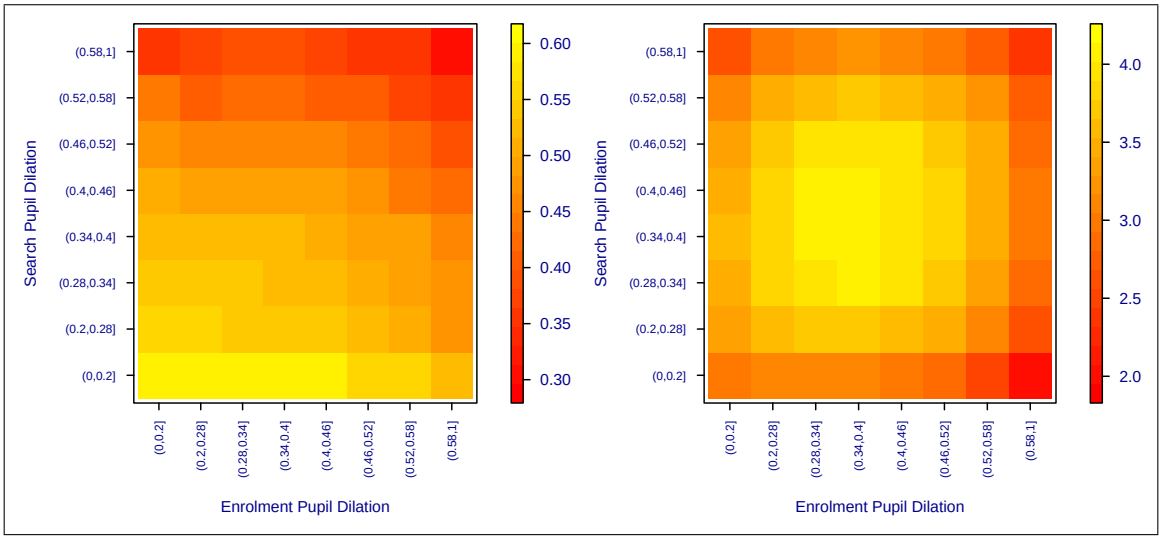

(c) Nonmate Dilation, Dis-similarity Score, Miss Rate, $\log_{10}(1+\text{Count})$

Figure 345: Heatmaps for implementation T01A executing mate searches in an enrolled population of N = 1.6 million. The radius images are binned by into twelve quantiles spanning $[0, 1]$. The dilation values are cut into ranges bounded by: $(0, 0.2, 0.28, 0.34, 0.40, 0.46, 0.52, 0.58, 1)$. The pathologically compressed 330x330 images are excluded from this analysis.

Heatmaps for implementation T01A executing mate searches in an enrolled population of N = 1.6 million.

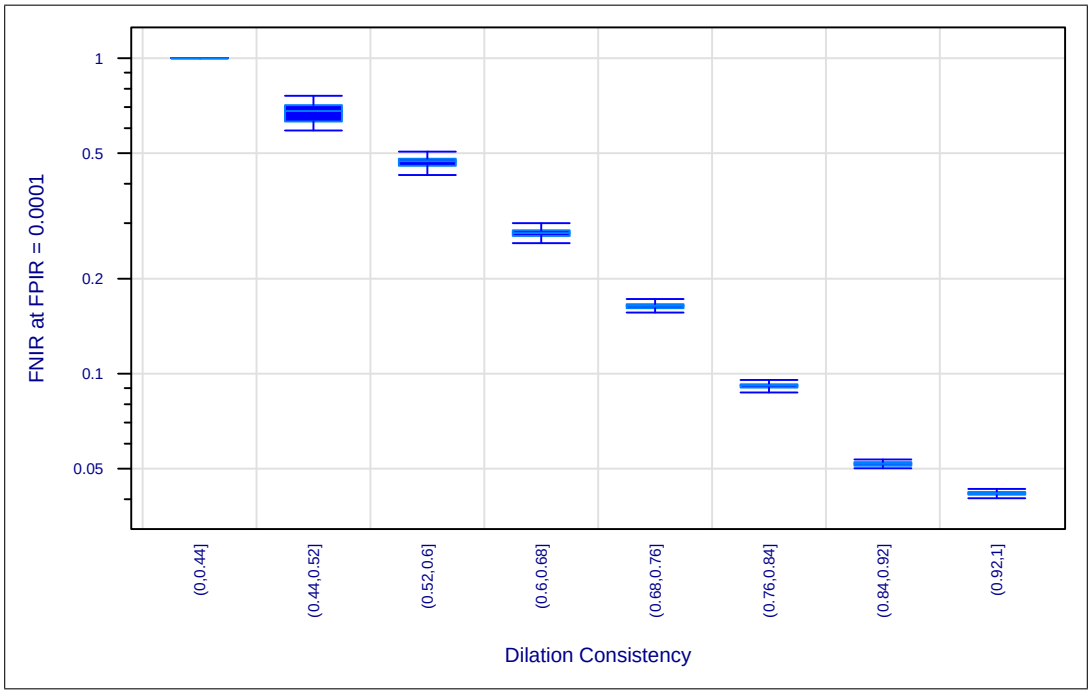

(a) Boxplot, all images

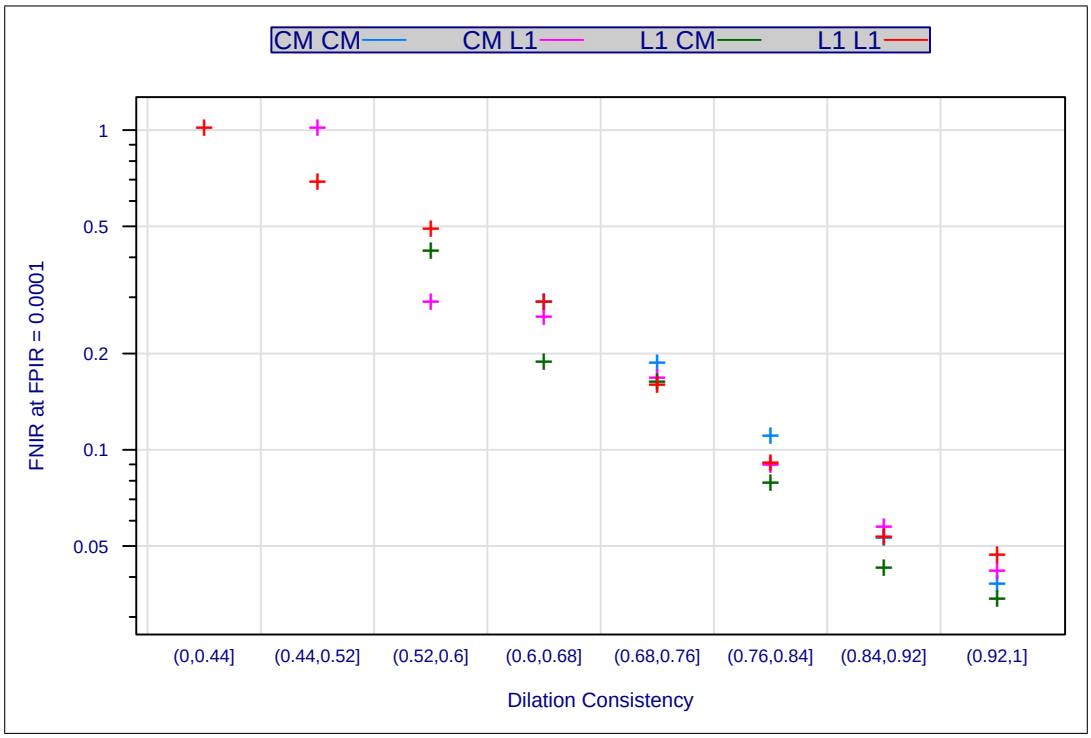

(b) Mean, L1 and CM images

Figure 346: Miss rate statistics for implementation T01A executing mate searches in an enrolled population of N = 1.6 million. The figures plots FNIR at FPIR = 0.0001 versus the IREX I metric for dilation consistency $(1 - \max(D_1, D_2))/(1 - \min(D_1, D_2))$ where D_i is pupil-iris radius ratio, and the subscripts refer to the mated enrollment and search image. The pathologically compressed 330x330 images are excluded from this analysis. The second figure breaks out dilation effects for interoperating camera pairs, CM and L1.

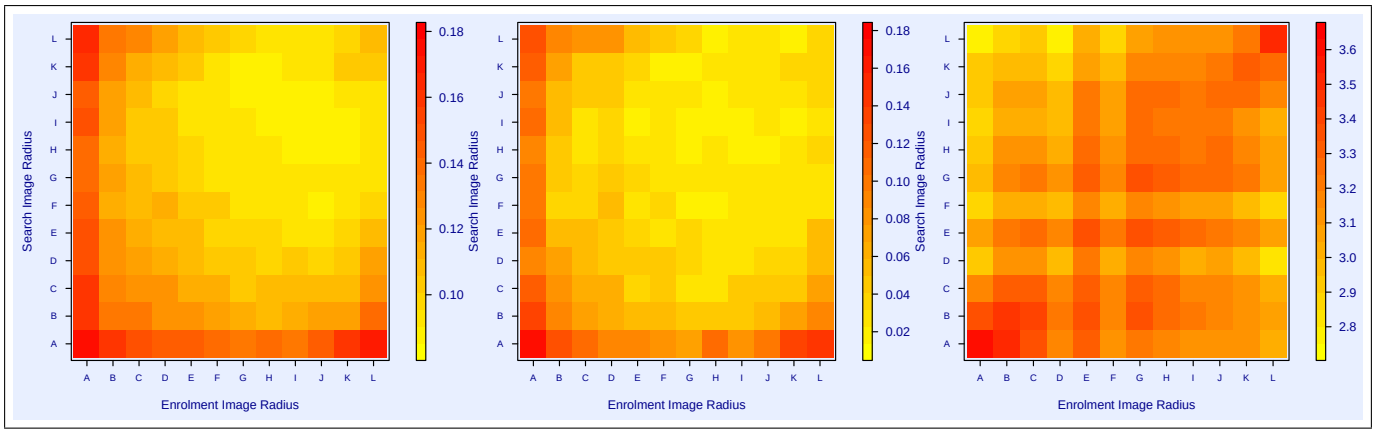

(a) Iris radius: Dis-similarity Score, Miss Rate, $\log_{10}(1+\text{Count})$

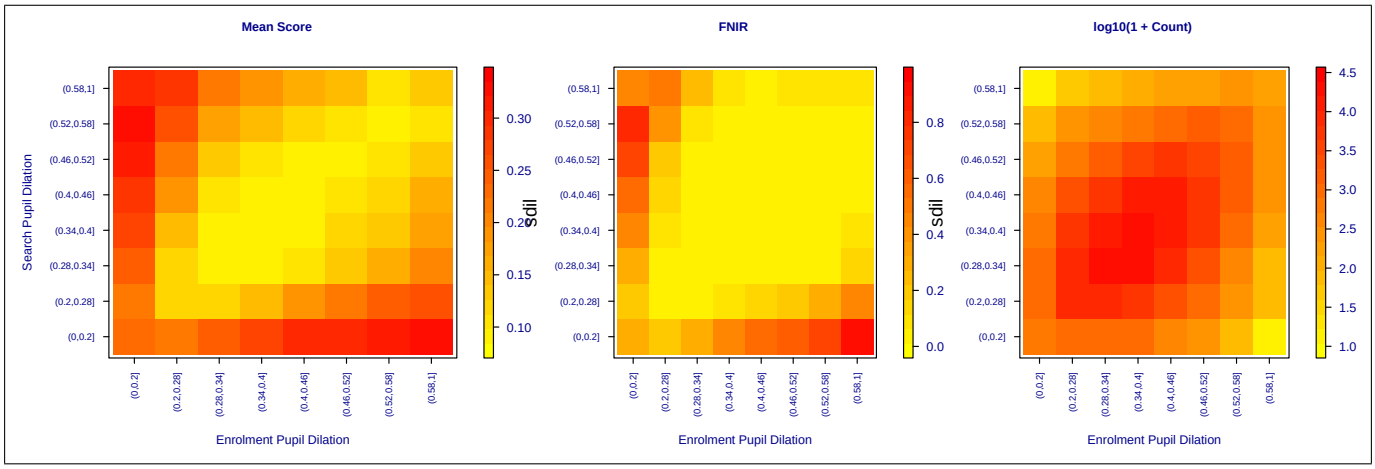

(b) Mate Dilation: Dis-similarity Score, Miss Rate, $\log_{10}(1+\text{Count})$

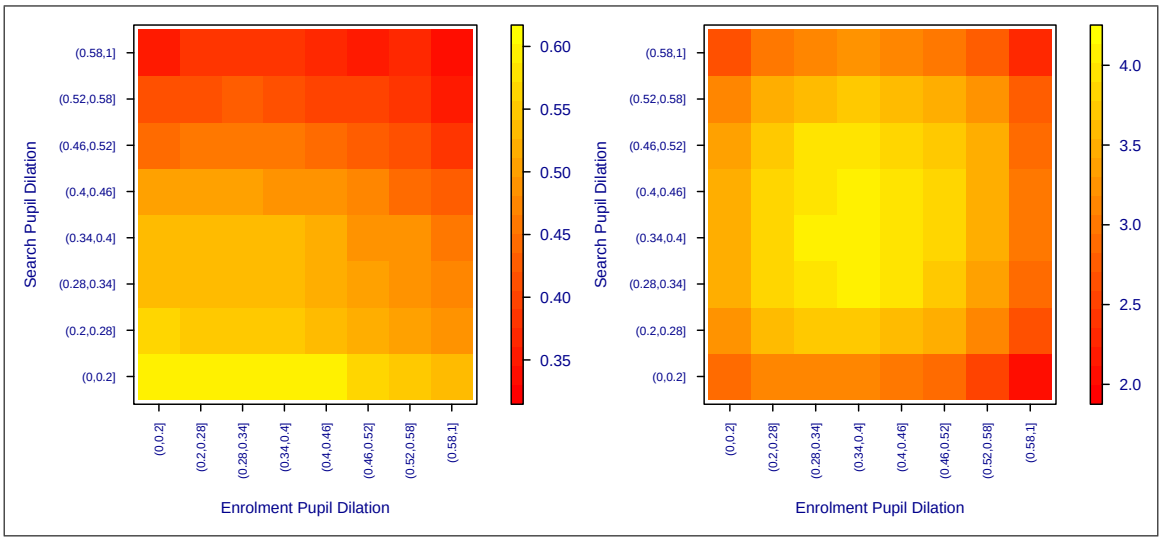

(c) Nonmate Dilation, Dis-similarity Score, Miss Rate, $\log_{10}(1+\text{Count})$

Figure 347: Heatmaps for implementation T01B executing mate searches in an enrolled population of N = 1.6 million. The radius images are binned by into twelve quantiles spanning $[0, 1]$. The dilation values are cut into ranges bounded by: $(0, 0.2, 0.28, 0.34, 0.40, 0.46, 0.52, 0.58, 1)$. The pathologically compressed 330x330 images are excluded from this analysis.

Heatmaps for implementation T01B executing mate searches in an enrolled population of N = 1.6 million.

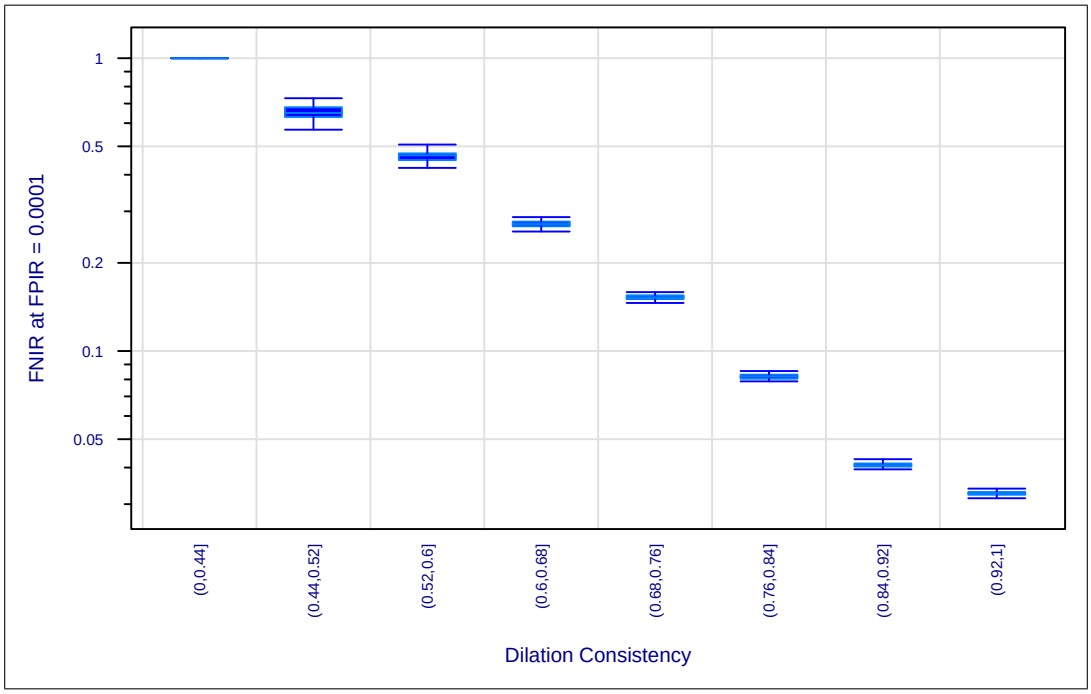

(a) Boxplot, all images

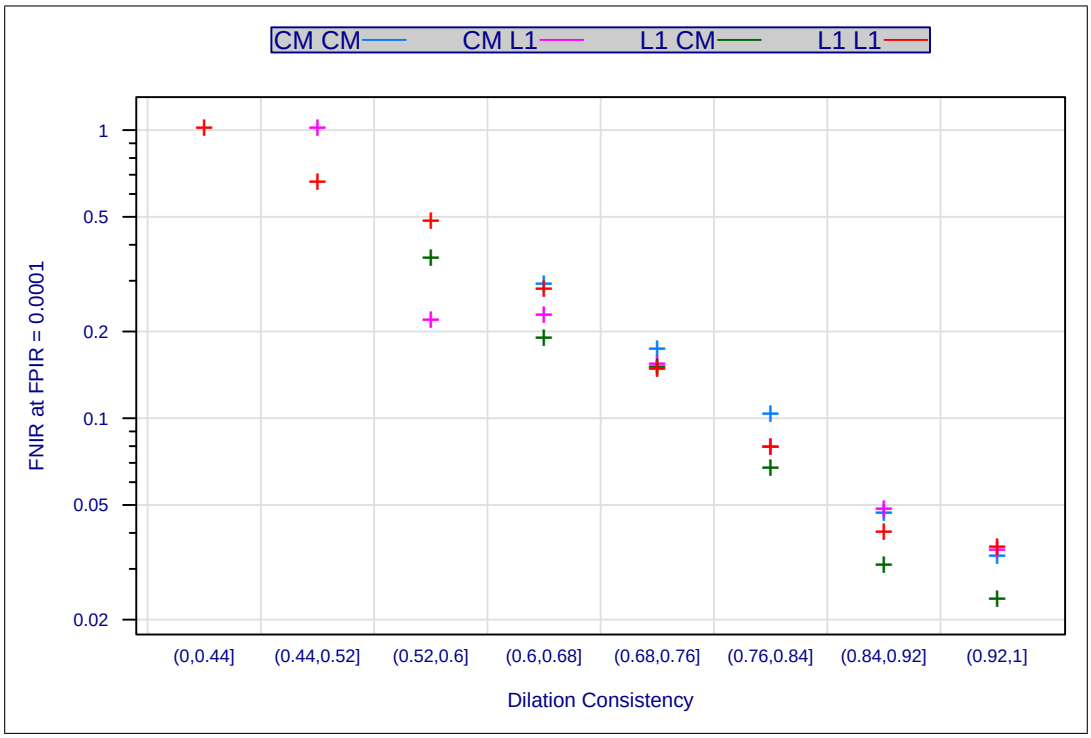

(b) Mean, L1 and CM images

Figure 348: Miss rate statistics for implementation T01B executing mate searches in an enrolled population of N = 1.6 million. The figures plots FNIR at FPIR = 0.0001 versus the IREX I metric for dilation consistency $(1 - \max(D_1, D_2))/(1 - \min(D_1, D_2))$ where D_i is pupil-iris radius ratio, and the subscripts refer to the mated enrollment and search image. The pathologically compressed 330x330 images are excluded from this analysis. The second figure breaks out dilation effects for interoperating camera pairs, CM and L1.

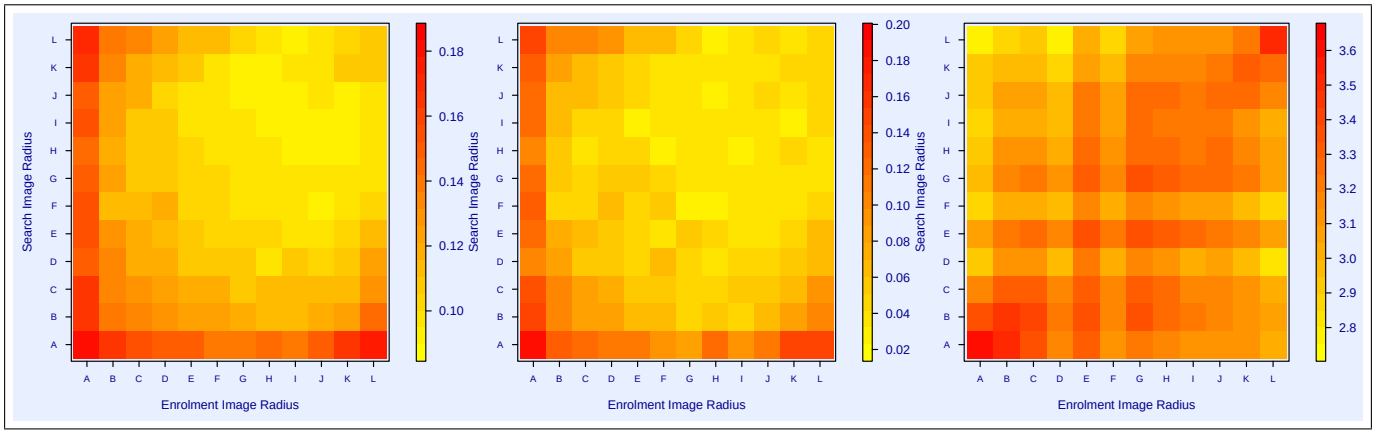

(a) Iris radius: Dis-similarity Score, Miss Rate, $\log_{10}(1+\text{Count})$

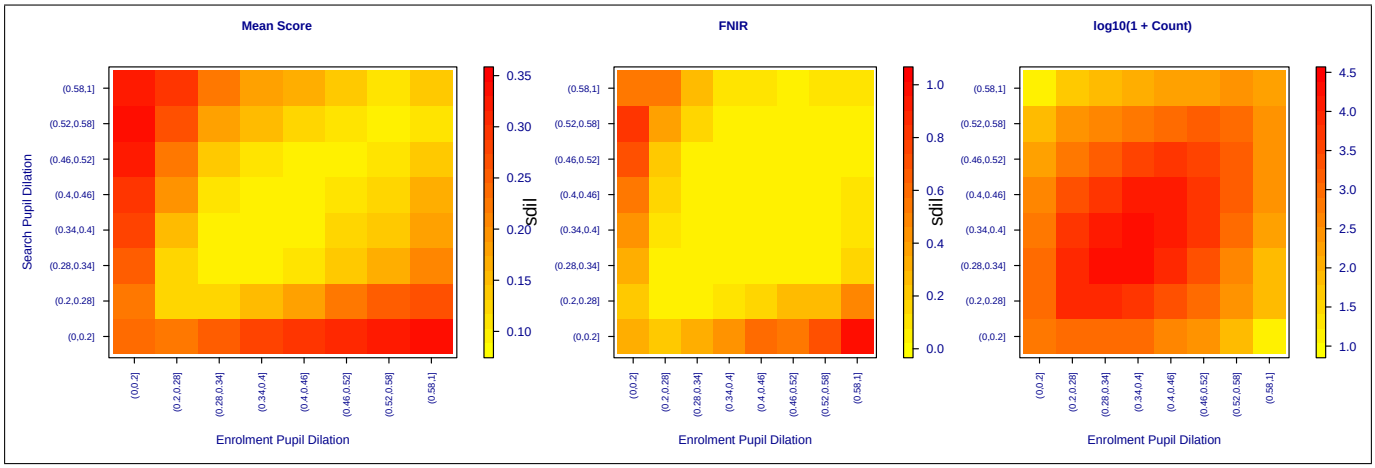

(b) Mate Dilation: Dis-similarity Score, Miss Rate, $\log_{10}(1+\text{Count})$

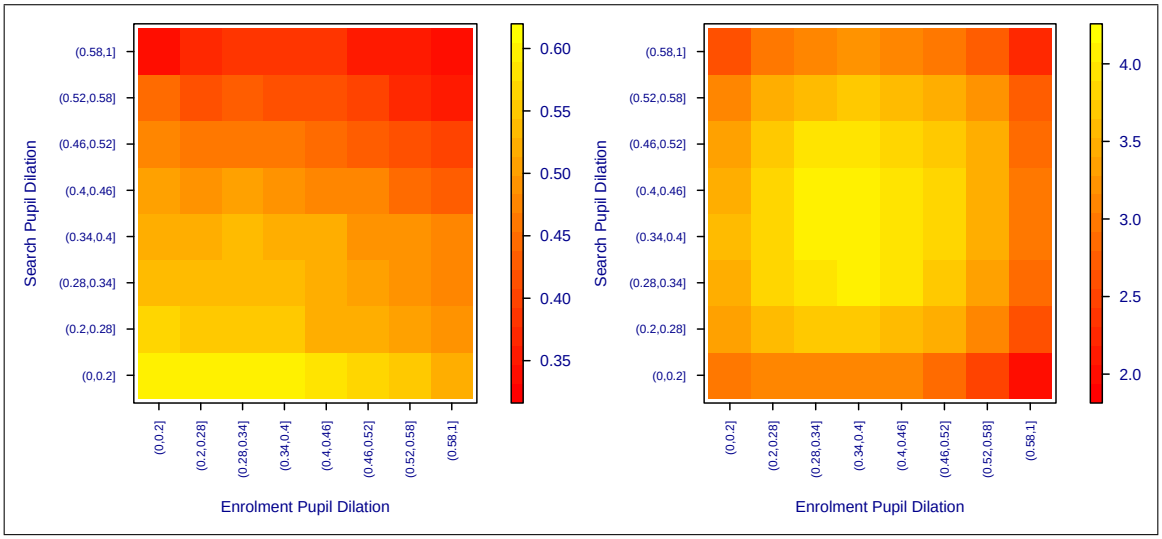

(c) Nonmate Dilation, Dis-similarity Score, Miss Rate, $\log_{10}(1+\text{Count})$

Figure 349: Heatmaps for implementation T02A executing mate searches in an enrolled population of N = 1.6 million. The radius images are binned by into twelve quantiles spanning $[0, 1]$. The dilation values are cut into ranges bounded by: $(0, 0.2, 0.28, 0.34, 0.40, 0.46, 0.52, 0.58, 1)$. The pathologically compressed 330x330 images are excluded from this analysis.

Heatmaps for implementation T02A executing mate searches in an enrolled population of N = 1.6 million.

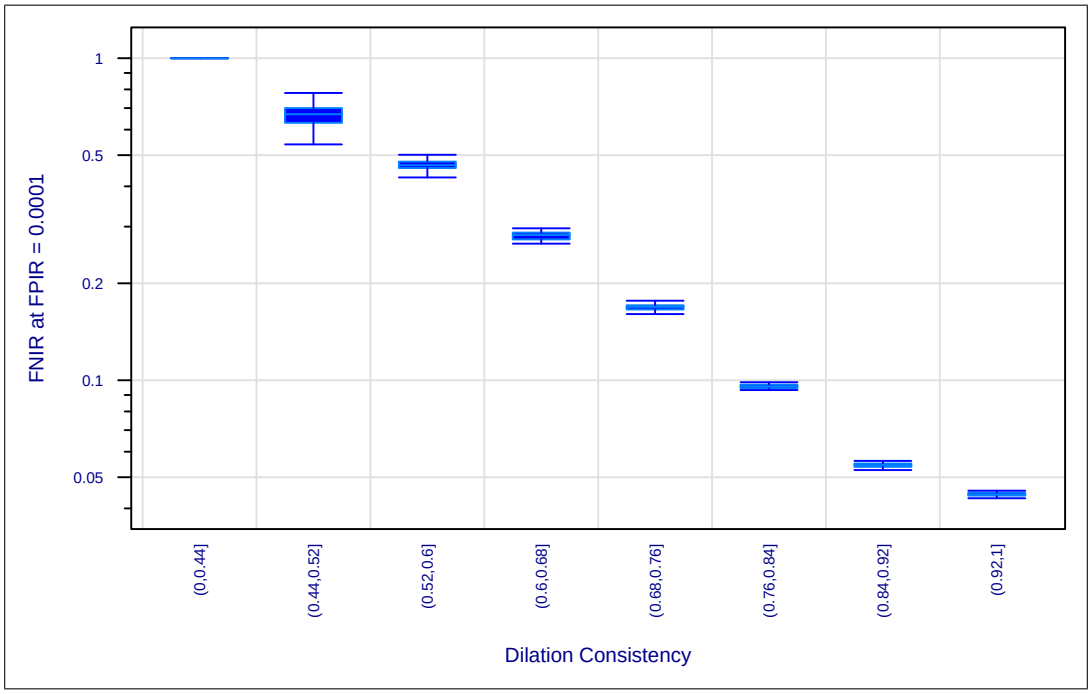

(a) Boxplot, all images

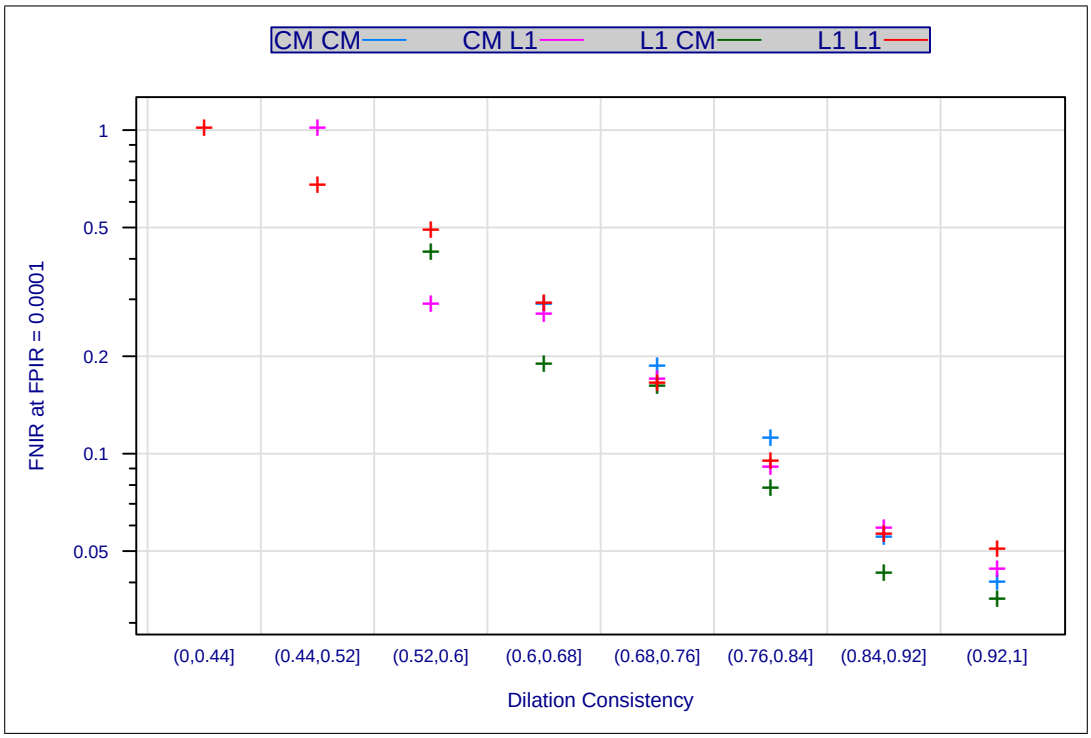

(b) Mean, L1 and CM images

Figure 350: Miss rate statistics for implementation T02A executing mate searches in an enrolled population of N = 1.6 million. The figures plots FNIR at FPIR = 0.0001 versus the IREX I metric for dilation consistency $(1 - \max(D_1, D_2))/(1 - \min(D_1, D_2))$ where D_i is pupil-iris radius ratio, and the subscripts refer to the mated enrollment and search image. The pathologically compressed 330x330 images are excluded from this analysis. The second figure breaks out dilation effects for interoperating camera pairs, CM and L1.

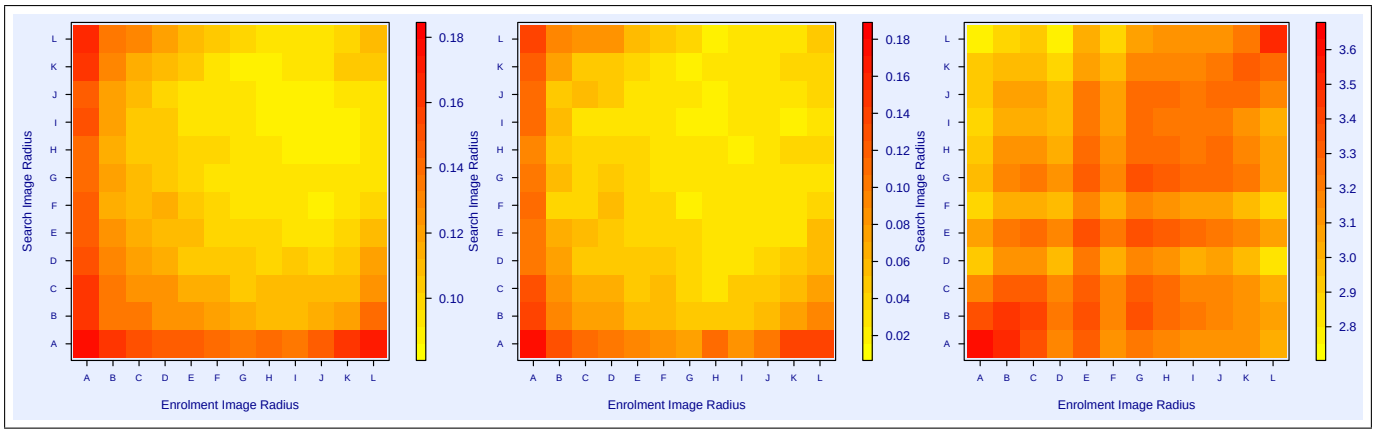

(a) Iris radius: Dis-similarity Score, Miss Rate, $\log_{10}(1+\text{Count})$

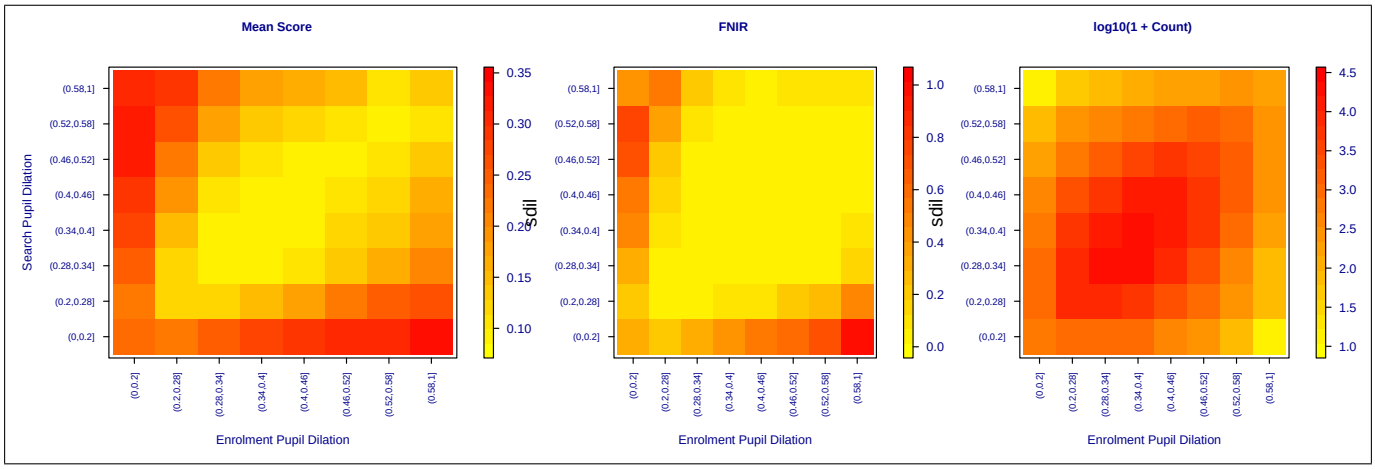

(b) Mate Dilation: Dis-similarity Score, Miss Rate, $\log_{10}(1+\text{Count})$

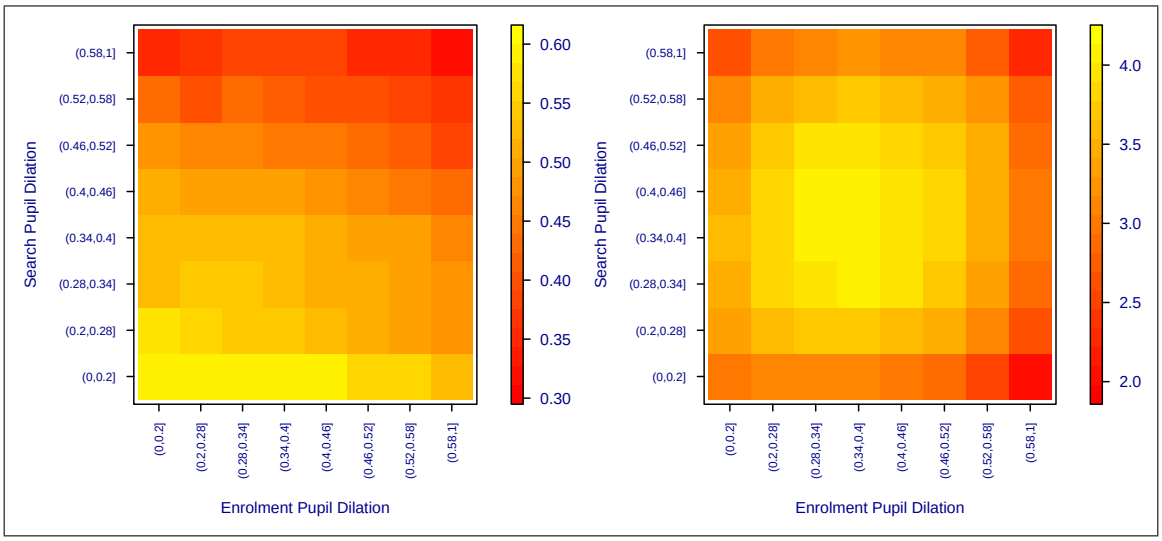

(c) Nonmate Dilation, Dis-similarity Score, Miss Rate, $\log_{10}(1+\text{Count})$

Figure 351: Heatmaps for implementation T02B executing mate searches in an enrolled population of N = 1.6 million. The radius images are binned by into twelve quantiles spanning $[0, 1]$. The dilation values are cut into ranges bounded by: $(0, 0.2, 0.28, 0.34, 0.40, 0.46, 0.52, 0.58, 1)$. The pathologically compressed 330x330 images are excluded from this analysis.

Heatmaps for implementation T02B executing mate searches in an enrolled population of N = 1.6 million.

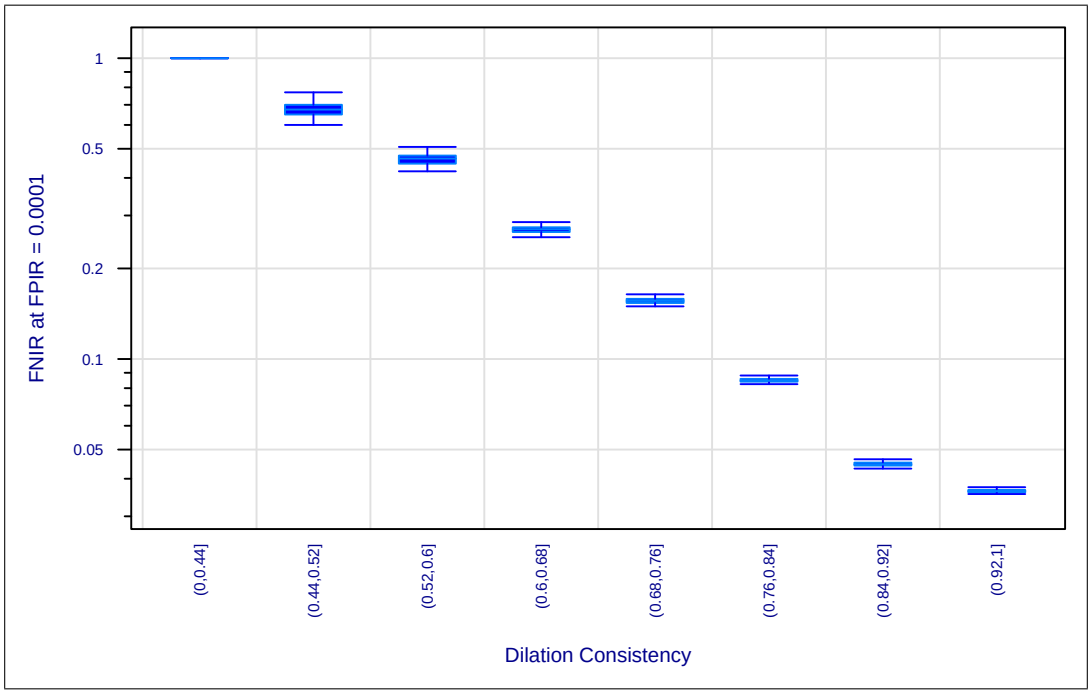

(a) Boxplot, all images

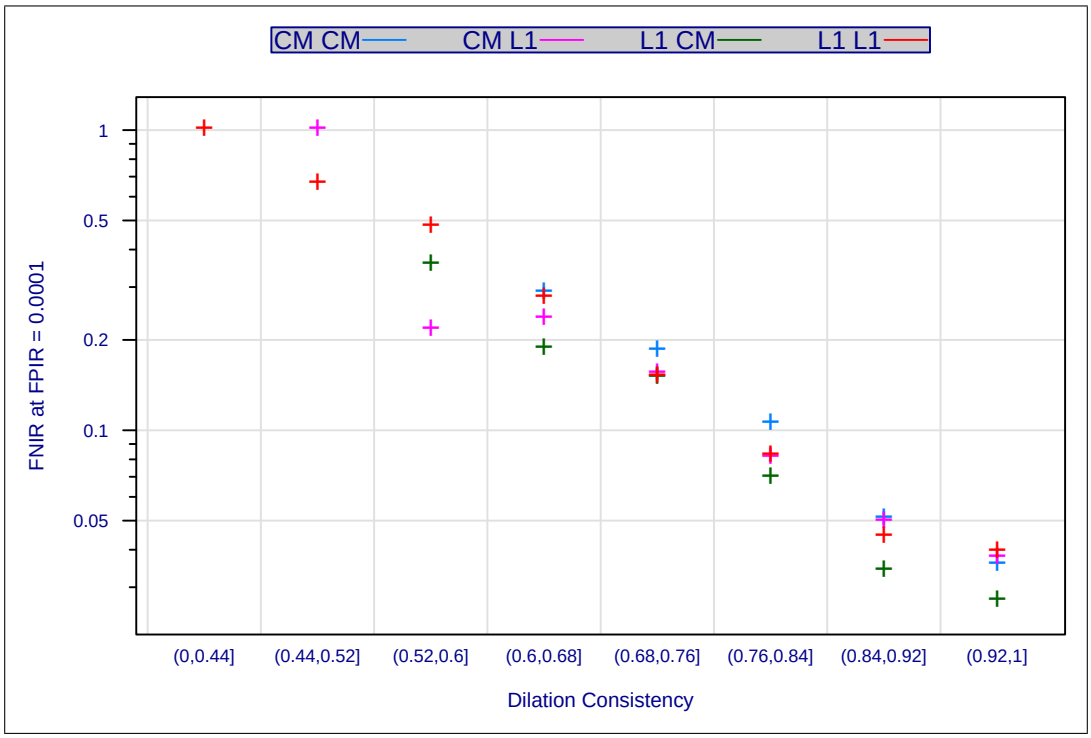

(b) Mean, L1 and CM images

Figure 352: Miss rate statistics for implementation T02B executing mate searches in an enrolled population of N = 1.6 million. The figures plots FNIR at FPIR = 0.0001 versus the IREX I metric for dilation consistency $(1 - \max(D_1, D_2))/(1 - \min(D_1, D_2))$ where D_i is pupil-iris radius ratio, and the subscripts refer to the mated enrollment and search image. The pathologically compressed 330x330 images are excluded from this analysis. The second figure breaks out dilation effects for interoperating camera pairs, CM and L1.

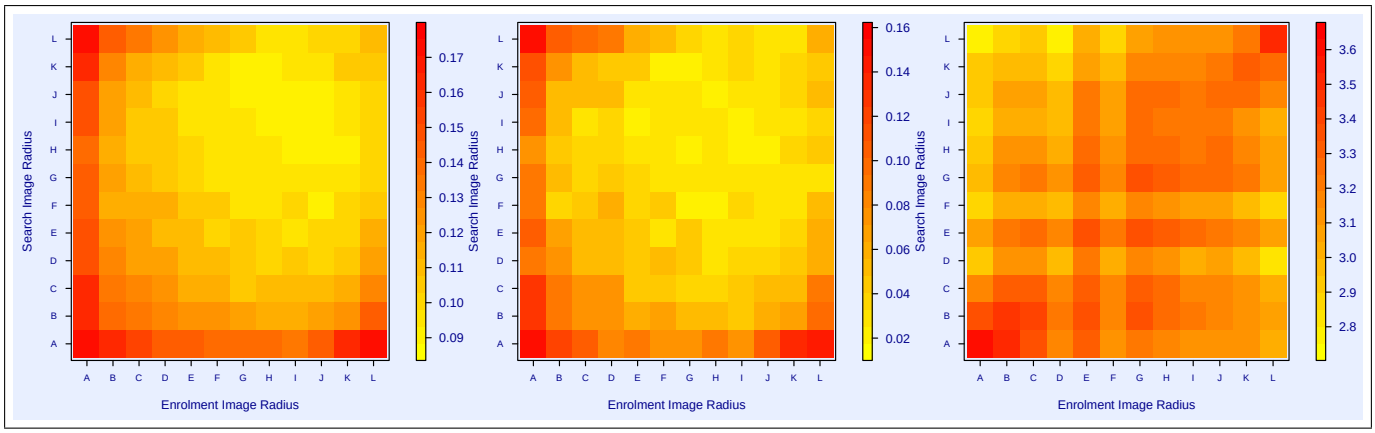

(a) Iris radius: Dis-similarity Score, Miss Rate, $\log_{10}(1+\text{Count})$

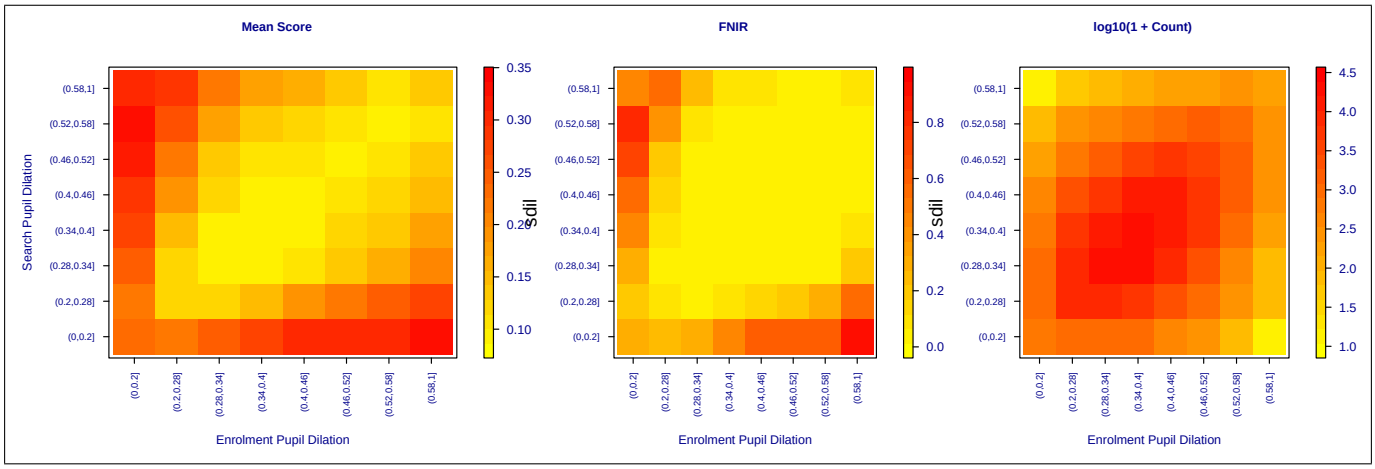

(b) Mate Dilation: Dis-similarity Score, Miss Rate, $\log_{10}(1+\text{Count})$

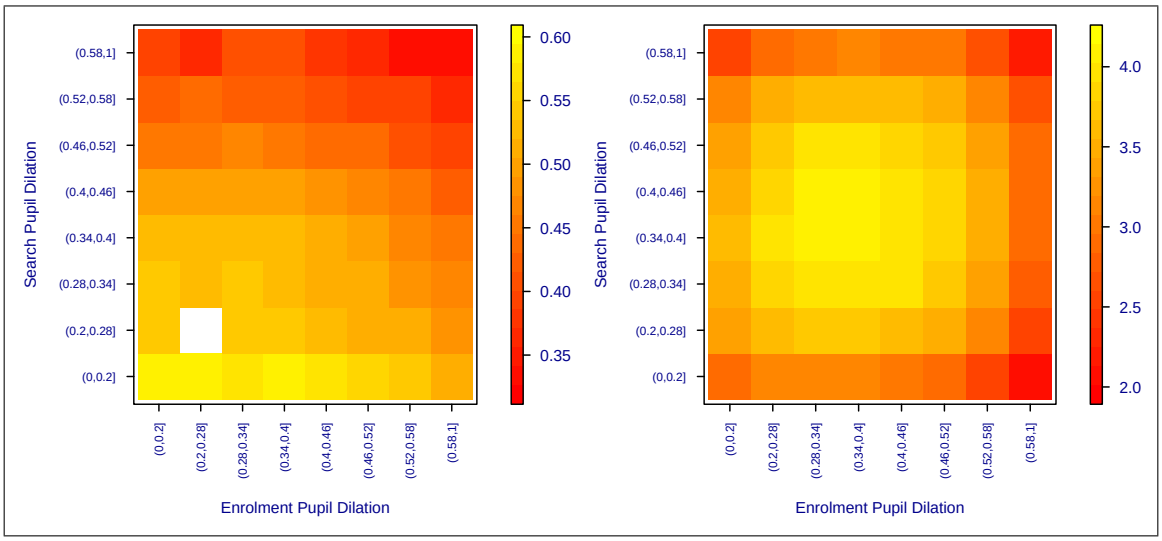

(c) Nonmate Dilation, Dis-similarity Score, Miss Rate, $\log_{10}(1+\text{Count})$

Figure 353: Heatmaps for implementation T03A executing mate searches in an enrolled population of N = 1.6 million. The radius images are binned by into twelve quantiles spanning $[0, 1]$. The dilation values are cut into ranges bounded by: $(0, 0.2, 0.28, 0.34, 0.40, 0.46, 0.52, 0.58, 1)$. The pathologically compressed 330x330 images are excluded from this analysis.

Heatmaps for implementation T03A executing mate searches in an enrolled population of N = 1.6 million.

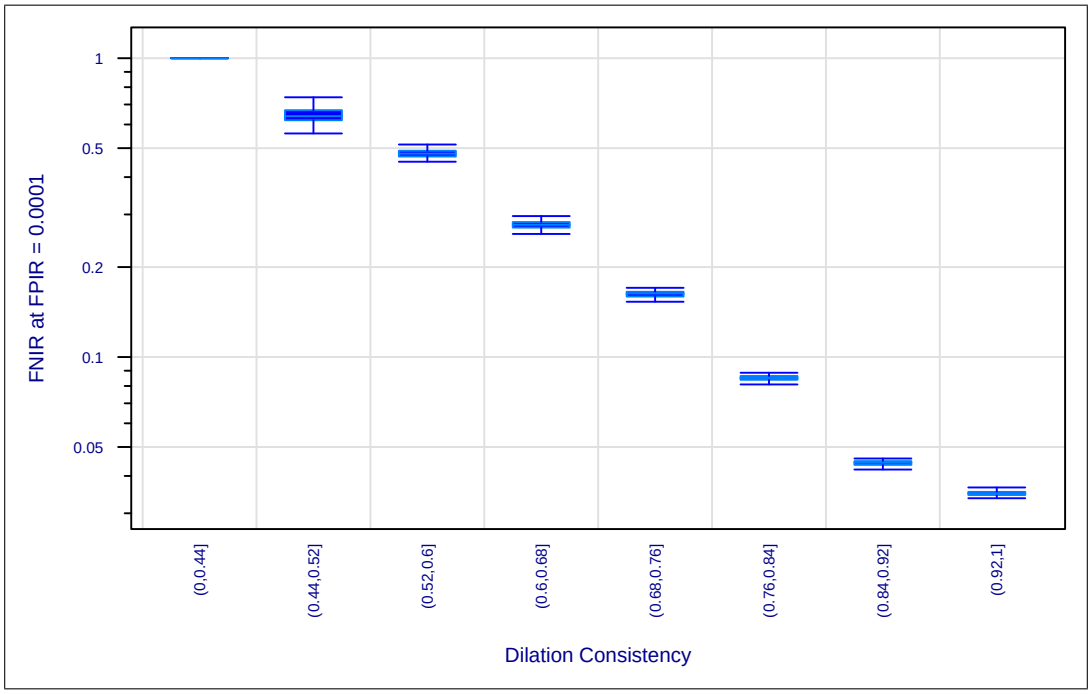

(a) Boxplot, all images

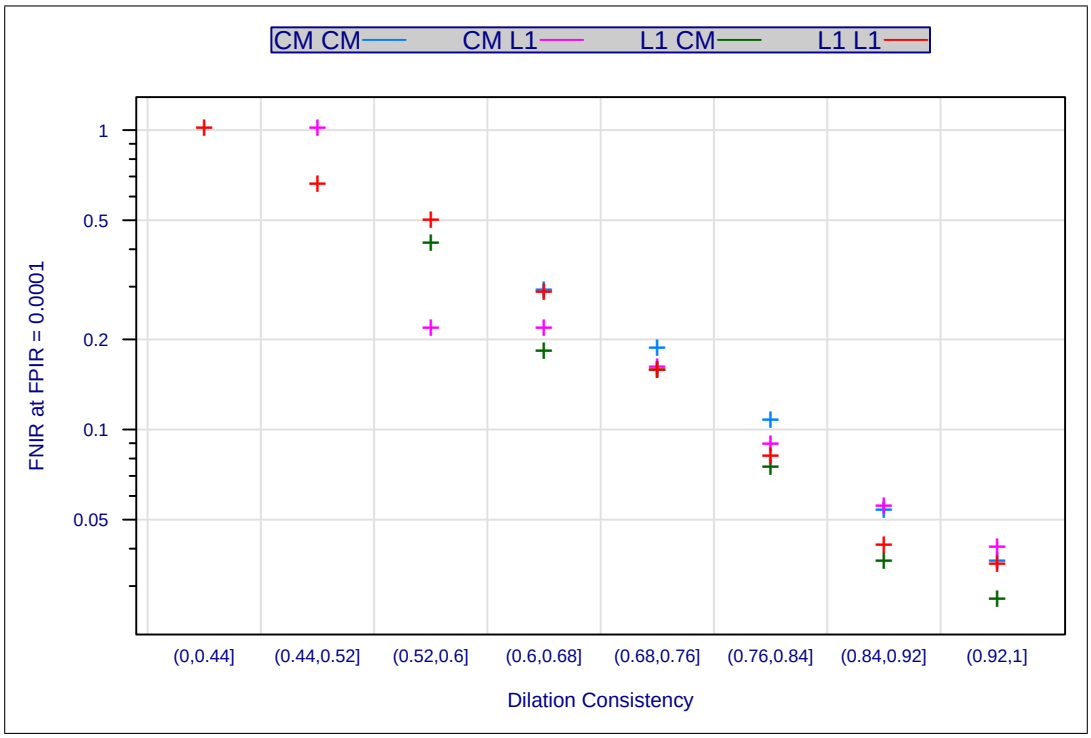

(b) Mean, L1 and CM images

Figure 354: Miss rate statistics for implementation T03A executing mate searches in an enrolled population of N = 1.6 million. The figures plots FNIR at FPIR = 0.0001 versus the IREX I metric for dilation consistency $(1 - \max(D_1, D_2))/(1 - \min(D_1, D_2))$ where D_i is pupil-iris radius ratio, and the subscripts refer to the mated enrollment and search image. The pathologically compressed 330x330 images are excluded from this analysis. The second figure breaks out dilation effects for interoperating camera pairs, CM and L1.

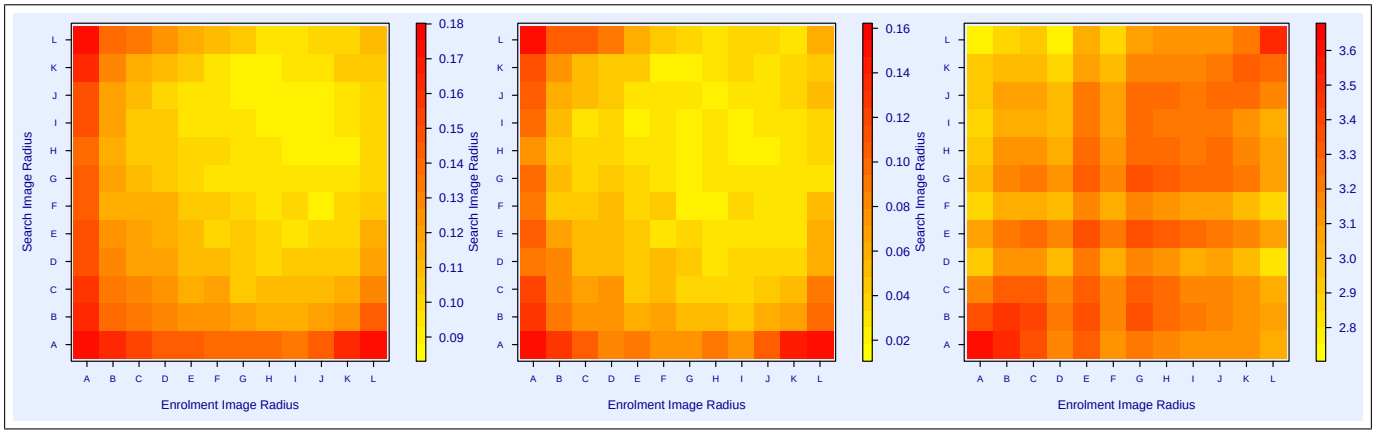

(a) Iris radius: Dis-similarity Score, Miss Rate, $\log_{10}(1+\text{Count})$

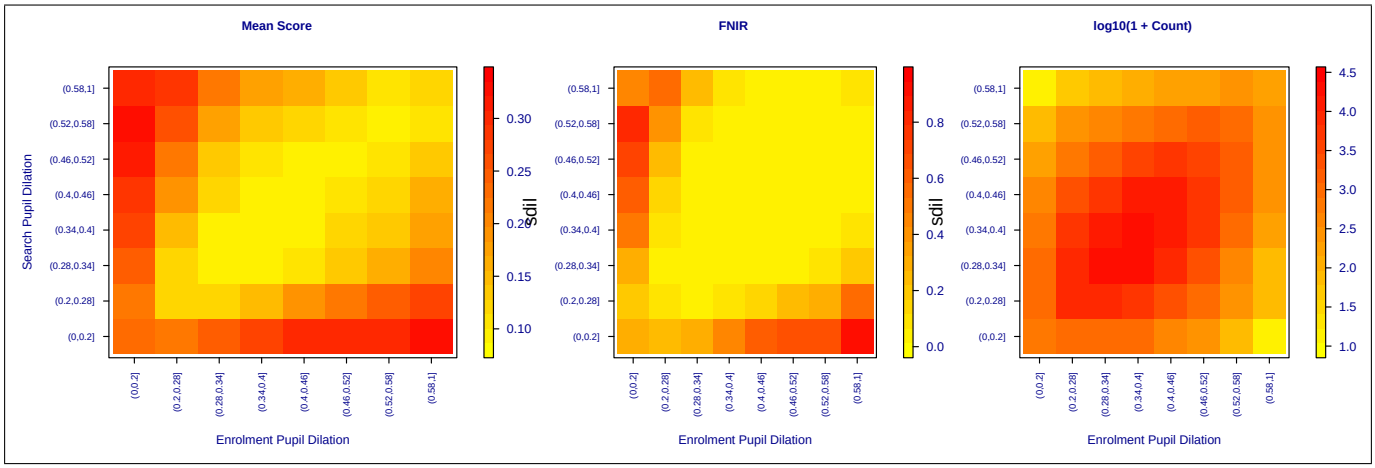

(b) Mate Dilation: Dis-similarity Score, Miss Rate, $\log_{10}(1+\text{Count})$

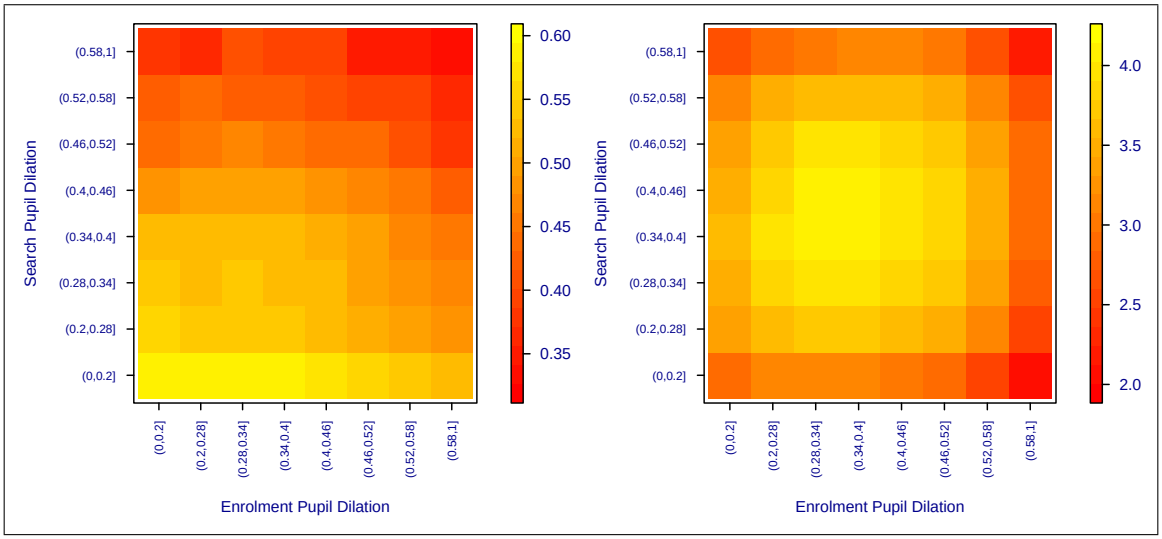

(c) Nonmate Dilation, Dis-similarity Score, Miss Rate, $\log_{10}(1+\text{Count})$

Figure 355: Heatmaps for implementation T03B executing mate searches in an enrolled population of N = 1.6 million. The radius images are binned by into twelve quantiles spanning $[0, 1]$. The dilation values are cut into ranges bounded by: $(0, 0.2, 0.28, 0.34, 0.40, 0.46, 0.52, 0.58, 1)$. The pathologically compressed 330x330 images are excluded from this analysis.

Heatmaps for implementation T03B executing mate searches in an enrolled population of N = 1.6 million.

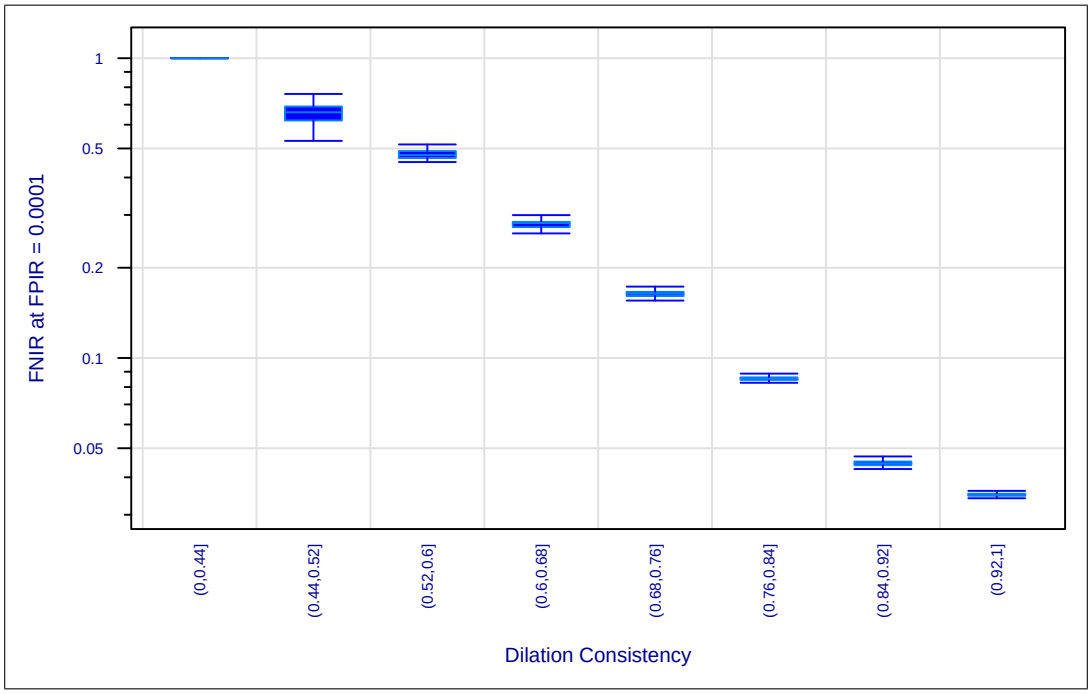

(a) Boxplot, all images

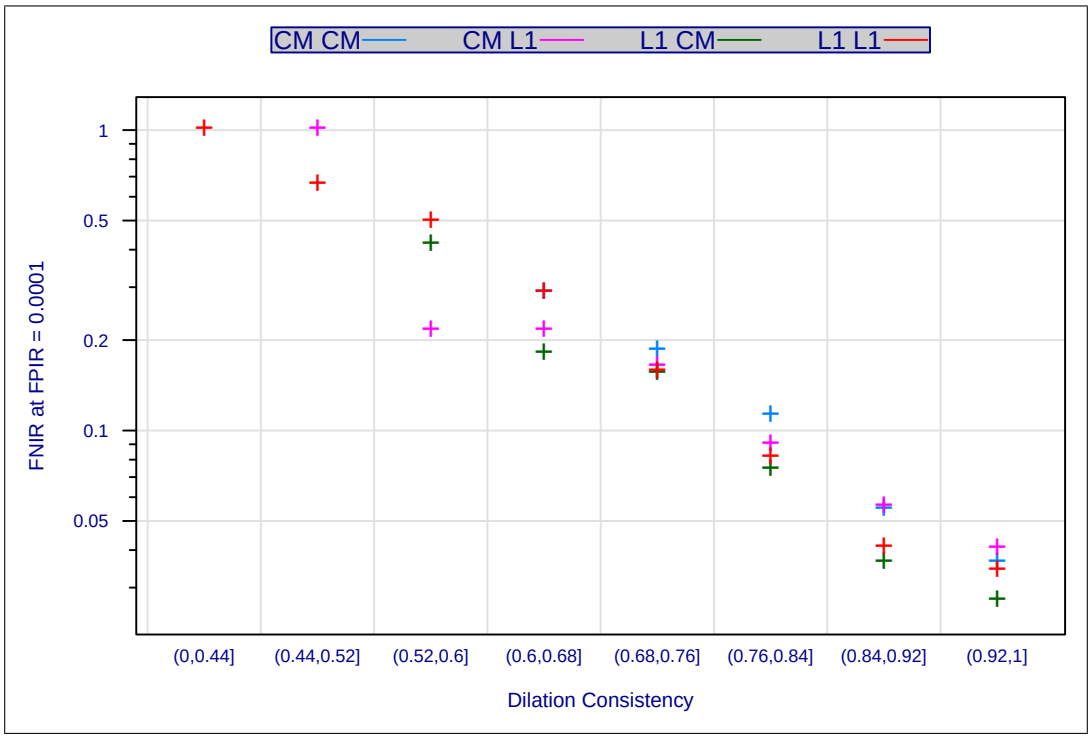

(b) Mean, L1 and CM images

Figure 356: Miss rate statistics for implementation T03B executing mate searches in an enrolled population of N = 1.6 million. The figures plots FNIR at FPIR = 0.0001 versus the IREX I metric for dilation consistency $(1 - \max(D_1, D_2))/(1 - \min(D_1, D_2))$ where D_i is pupil-iris radius ratio, and the subscripts refer to the mated enrollment and search image. The pathologically compressed 330x330 images are excluded from this analysis. The second figure breaks out dilation effects for interoperating camera pairs, CM and L1.

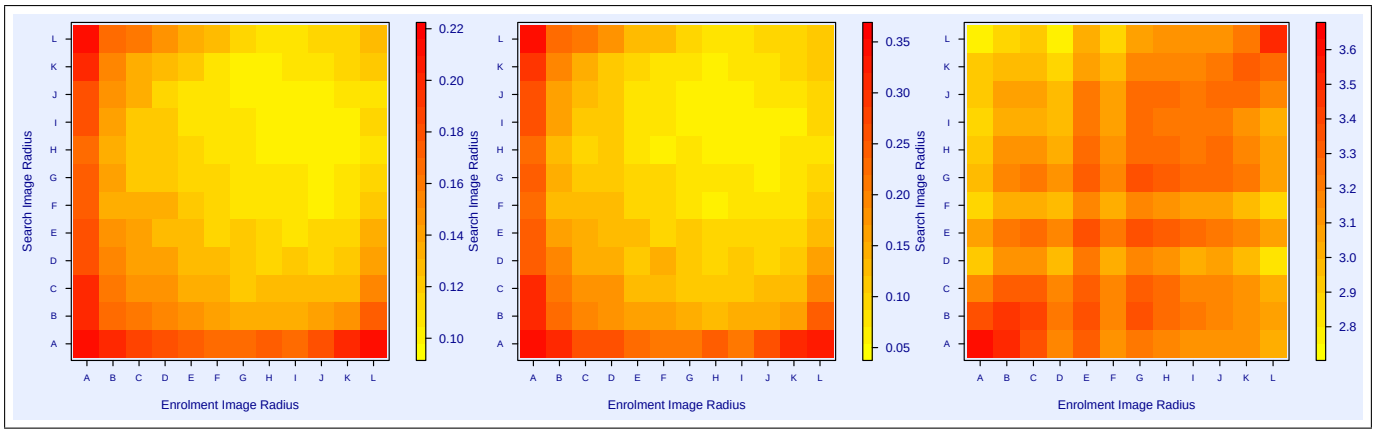

(a) Iris radius: Dis-similarity Score, Miss Rate, $\log_{10}(1+\text{Count})$

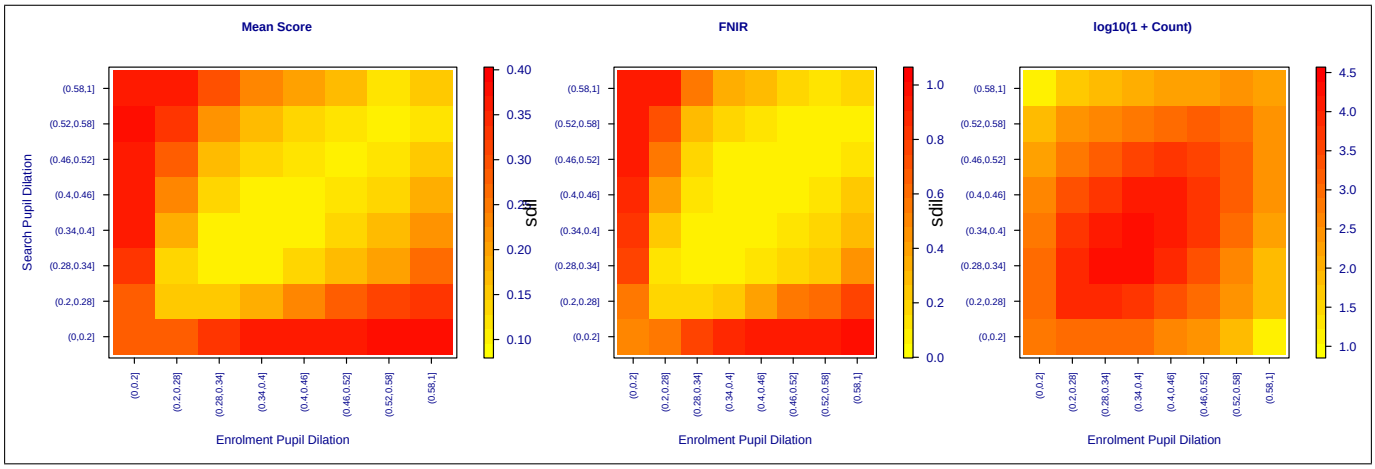

(b) Mate Dilation: Dis-similarity Score, Miss Rate, $\log_{10}(1+\text{Count})$

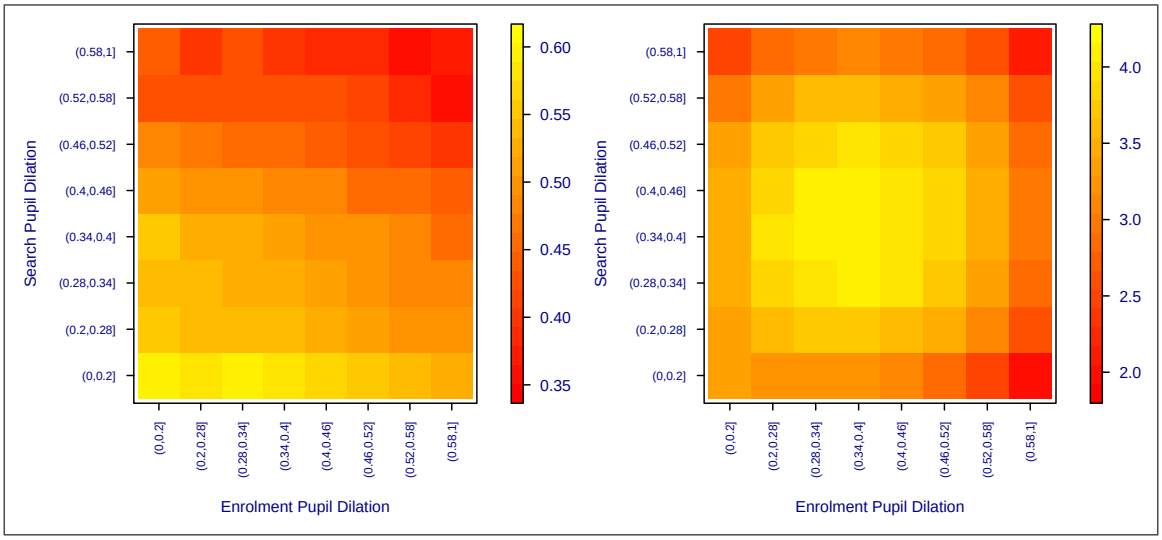

(c) Nonmate Dilation, Dis-similarity Score, Miss Rate, $\log_{10}(1+\text{Count})$

Figure 357: Heatmaps for implementation T04A executing mate searches in an enrolled population of N = 1.6 million. The radius images are binned by into twelve quantiles spanning $[0, 1]$. The dilation values are cut into ranges bounded by: $(0, 0.2, 0.28, 0.34, 0.40, 0.46, 0.52, 0.58, 1)$. The pathologically compressed 330x330 images are excluded from this analysis.

Heatmaps for implementation T04A executing mate searches in an enrolled population of N = 1.6 million.

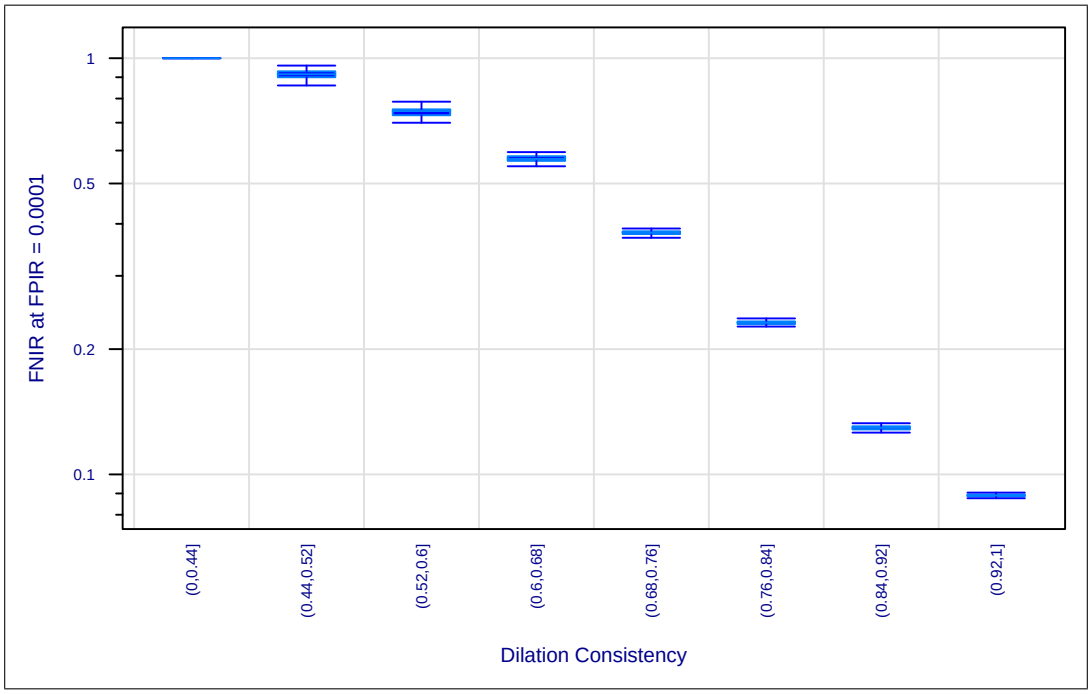

(a) Boxplot, all images

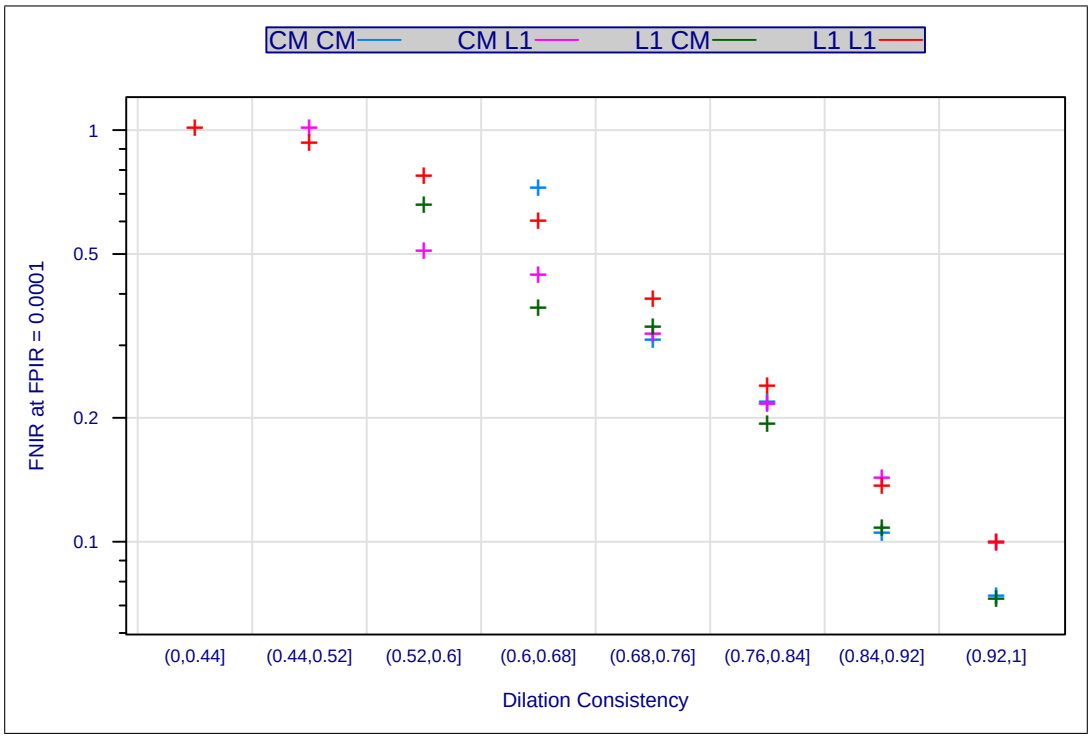

(b) Mean, L1 and CM images

Figure 358: Miss rate statistics for implementation T04A executing mate searches in an enrolled population of N = 1.6 million. The figures plots FNIR at FPIR = 0.0001 versus the IREX I metric for dilation consistency $(1 - \max(D_1, D_2))/(1 - \min(D_1, D_2))$ where D_i is pupil-iris radius ratio, and the subscripts refer to the mated enrollment and search image. The pathologically compressed 330x330 images are excluded from this analysis. The second figure breaks out dilation effects for interoperating camera pairs, CM and L1.

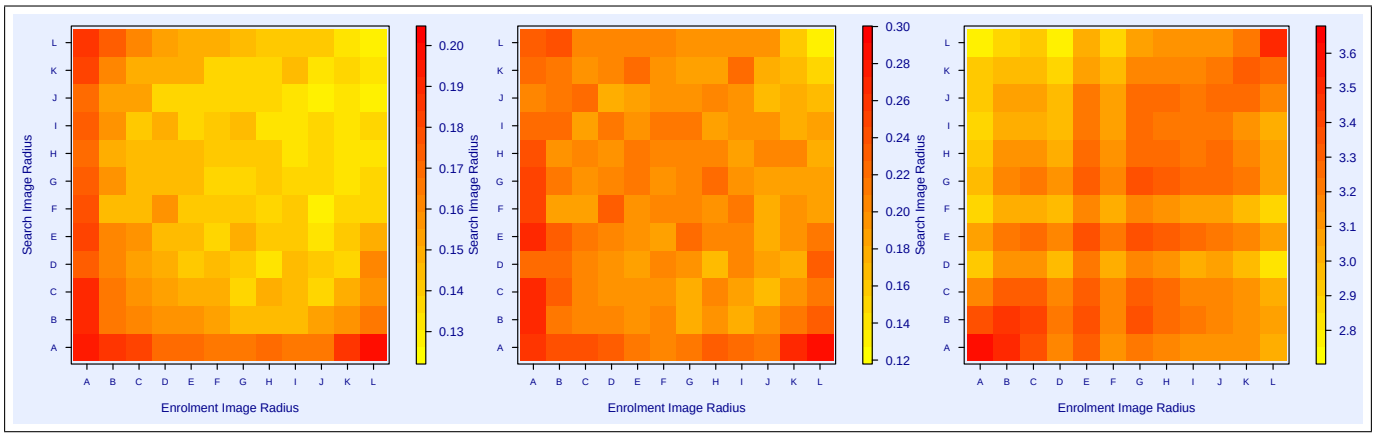

(a) Iris radius: Dis-similarity Score, Miss Rate, $\log_{10}(1+\text{Count})$

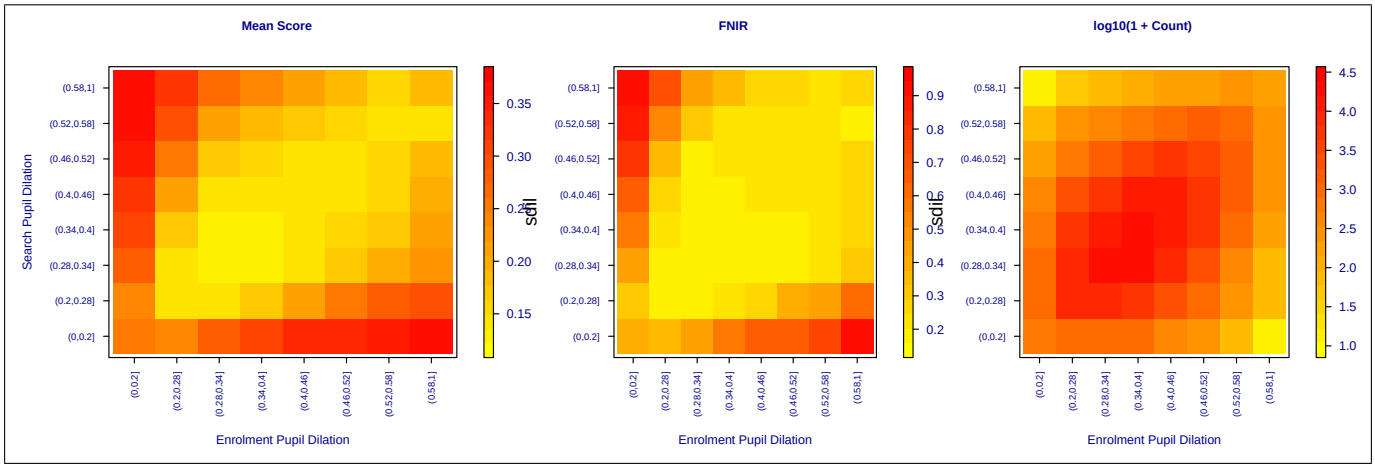

(b) Mate Dilation: Dis-similarity Score, Miss Rate, $\log_{10}(1+\text{Count})$

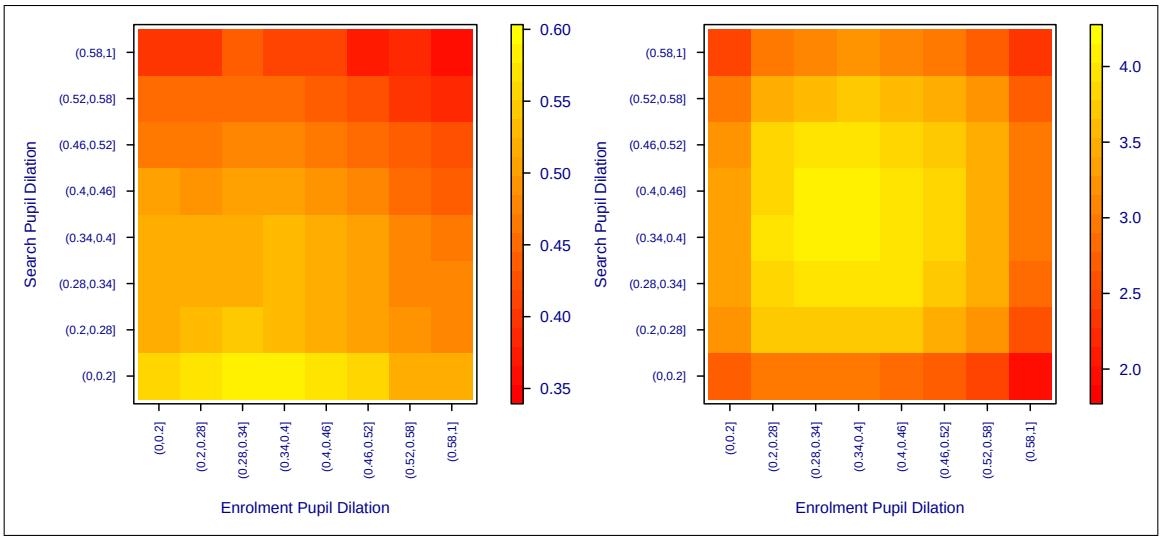

(c) Nonmate Dilation, Dis-similarity Score, Miss Rate, $\log_{10}(1+\text{Count})$

Figure 359: Heatmaps for implementation T11A executing mate searches in an enrolled population of N = 1.6 million. The radius images are binned by into twelve quantiles spanning $[0, 1]$. The dilation values are cut into ranges bounded by: $(0, 0.2, 0.28, 0.34, 0.40, 0.46, 0.52, 0.58, 1)$. The pathologically compressed 330x330 images are excluded from this analysis.

Heatmaps for implementation T11A executing mate searches in an enrolled population of N = 1.6 million.

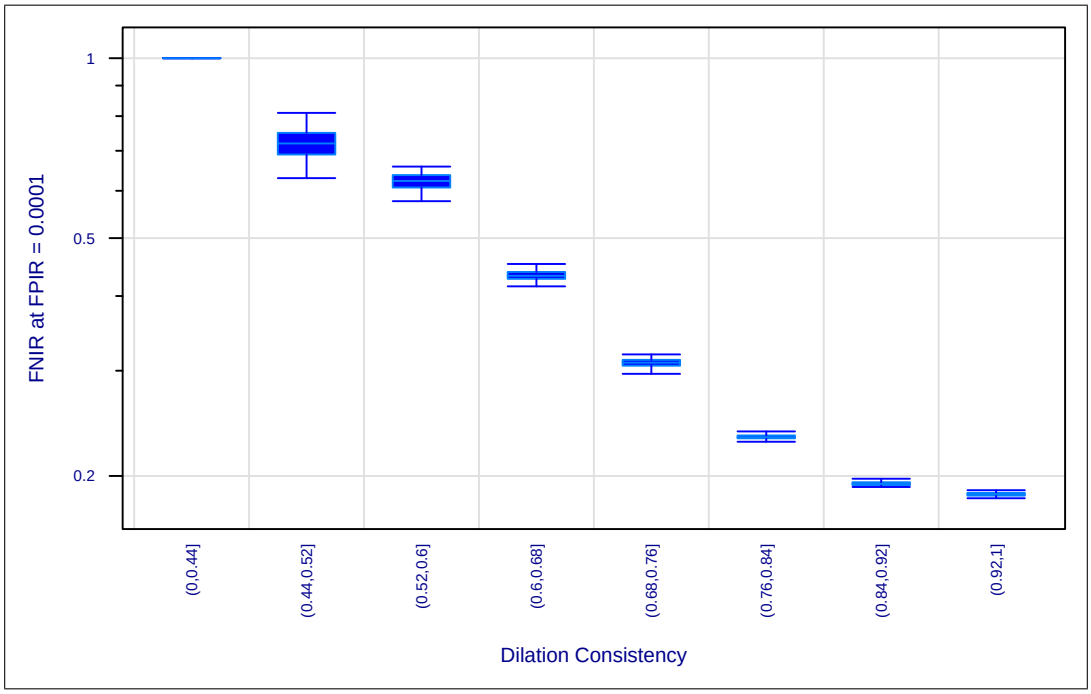

(a) Boxplot, all images

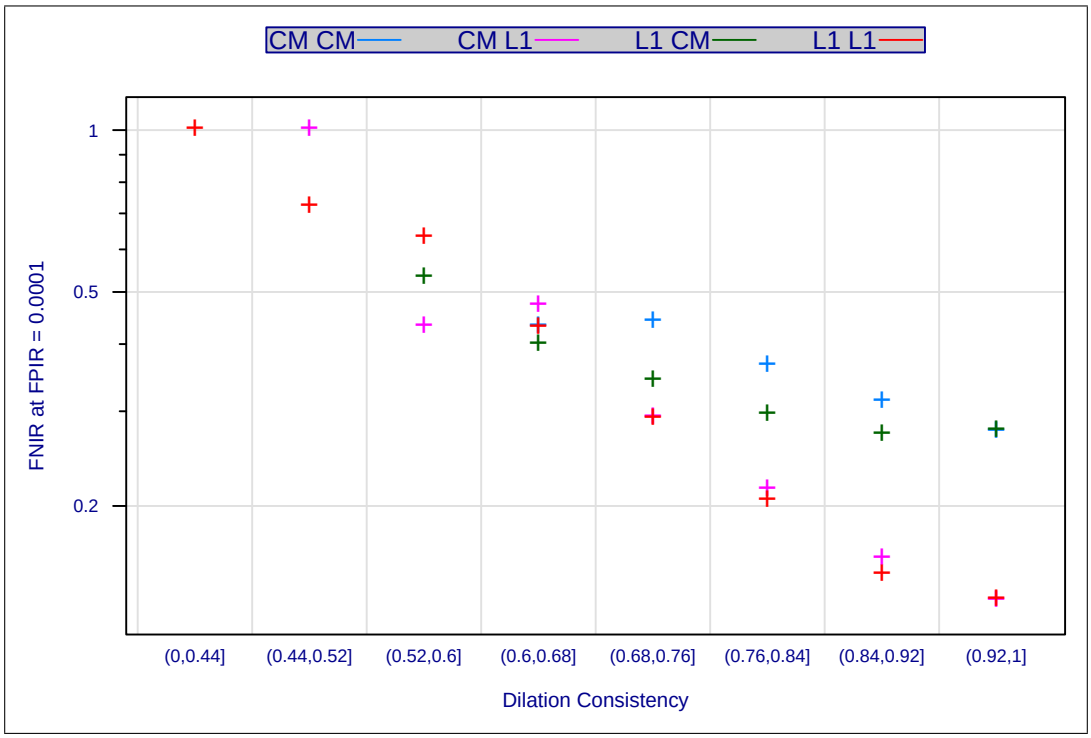

(b) Mean, L1 and CM images

Figure 360: Miss rate statistics for implementation T11A executing mate searches in an enrolled population of N = 1.6 million. The figures plots FNIR at FPIR = 0.0001 versus the IREX I metric for dilation consistency $(1 - \max(D_1, D_2))/(1 - \min(D_1, D_2))$ where D_i is pupil-iris radius ratio, and the subscripts refer to the mated enrollment and search image. The pathologically compressed 330x330 images are excluded from this analysis. The second figure breaks out dilation effects for interoperating camera pairs, CM and L1.

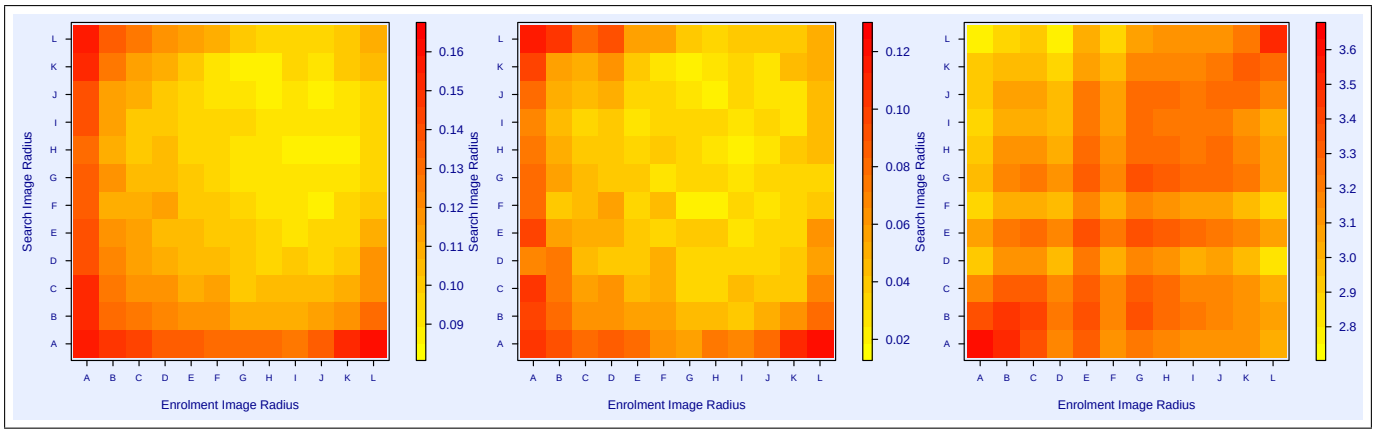

(a) Iris radius: Dis-similarity Score, Miss Rate, $\log_{10}(1+\text{Count})$

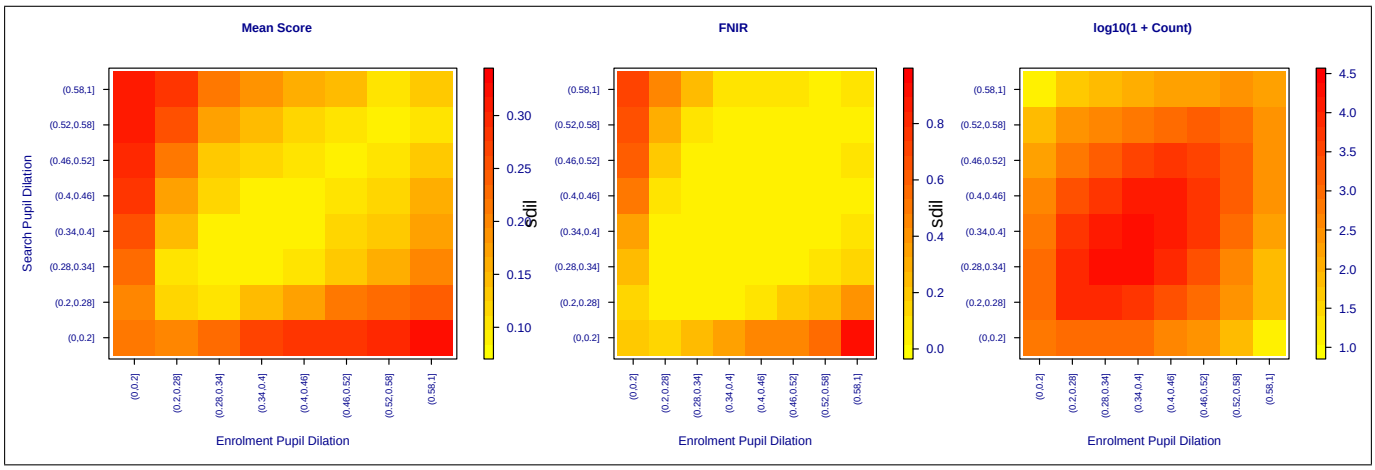

(b) Mate Dilation: Dis-similarity Score, Miss Rate, $\log_{10}(1+\text{Count})$

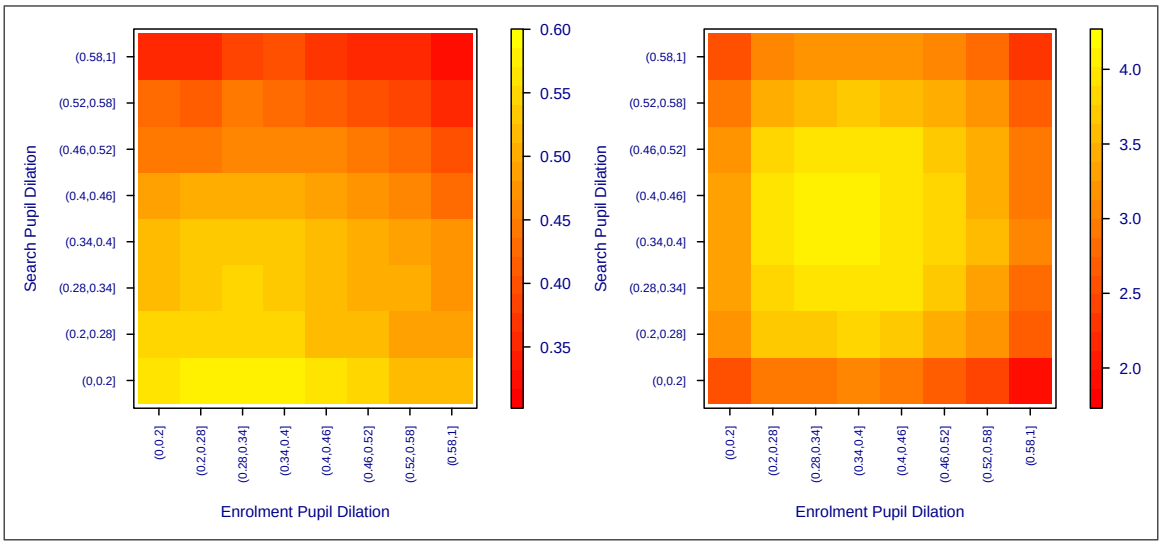

(c) Nonmate Dilation, Dis-similarity Score, Miss Rate, $\log_{10}(1+\text{Count})$

Figure 361: Heatmaps for implementation T11B executing mate searches in an enrolled population of N = 1.6 million. The radius images are binned by into twelve quantiles spanning $[0, 1]$. The dilation values are cut into ranges bounded by: $(0, 0.2, 0.28, 0.34, 0.40, 0.46, 0.52, 0.58, 1)$. The pathologically compressed 330x330 images are excluded from this analysis.

Heatmaps for implementation T11B executing mate searches in an enrolled population of N = 1.6 million.

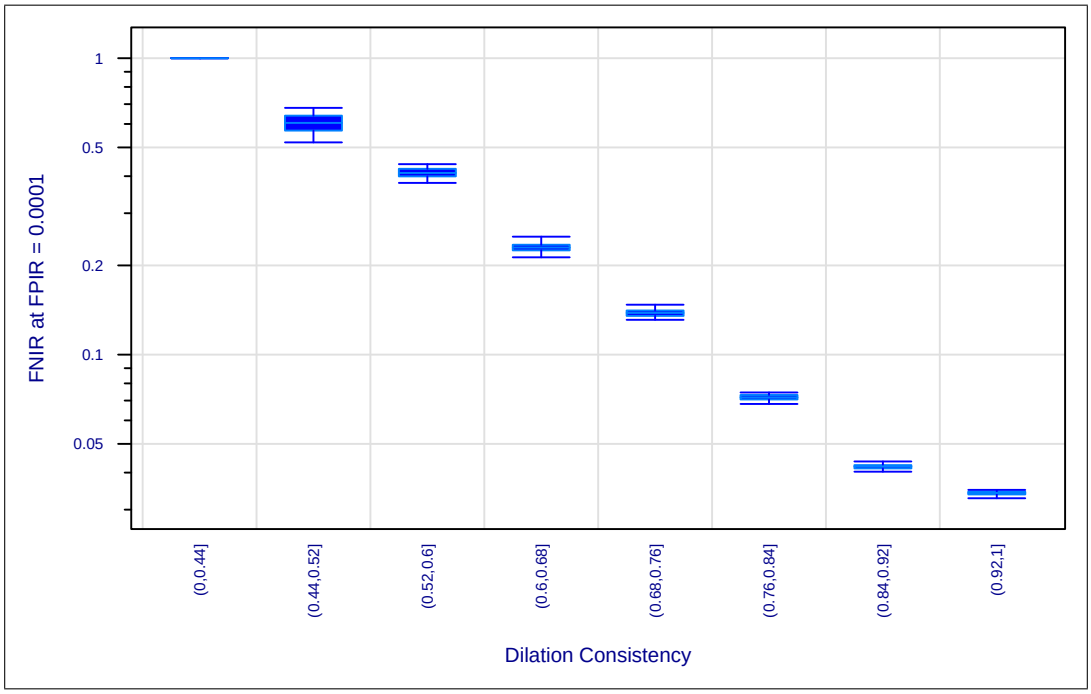

(a) Boxplot, all images

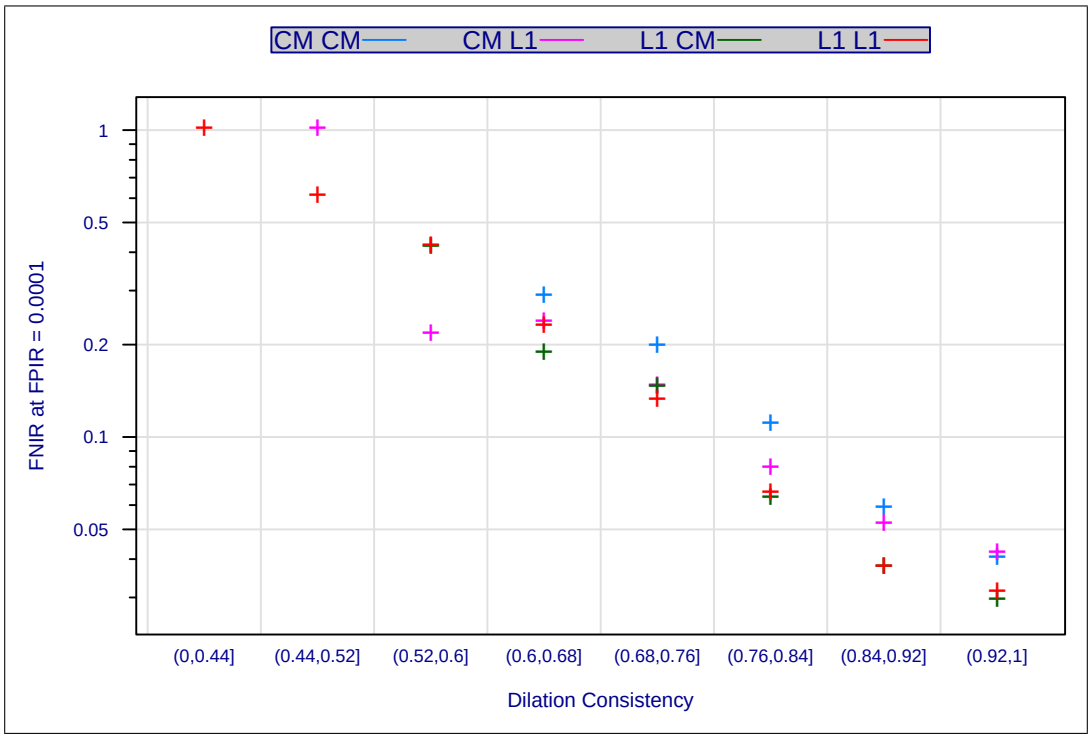

(b) Mean, L1 and CM images

Figure 362: Miss rate statistics for implementation T11B executing mate searches in an enrolled population of N = 1.6 million. The figures plots FNIR at FPIR = 0.0001 versus the IREX I metric for dilation consistency $(1 - \max(D_1, D_2))/(1 - \min(D_1, D_2))$ where D_i is pupil-iris radius ratio, and the subscripts refer to the mated enrollment and search image. The pathologically compressed 330x330 images are excluded from this analysis. The second figure breaks out dilation effects for interoperating camera pairs, CM and L1.

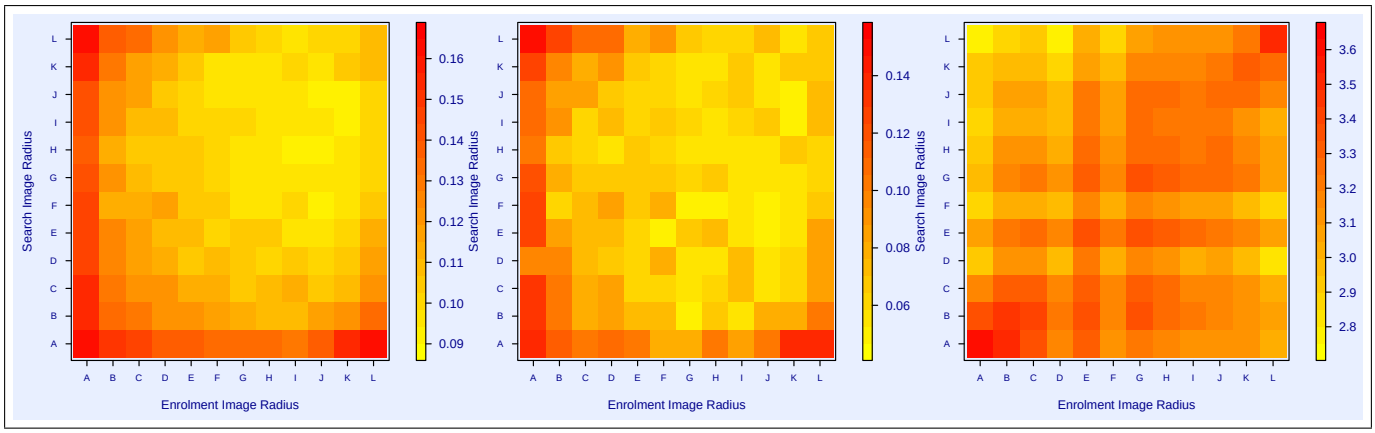

(a) Iris radius: Dis-similarity Score, Miss Rate, $\log_{10}(1+\text{Count})$

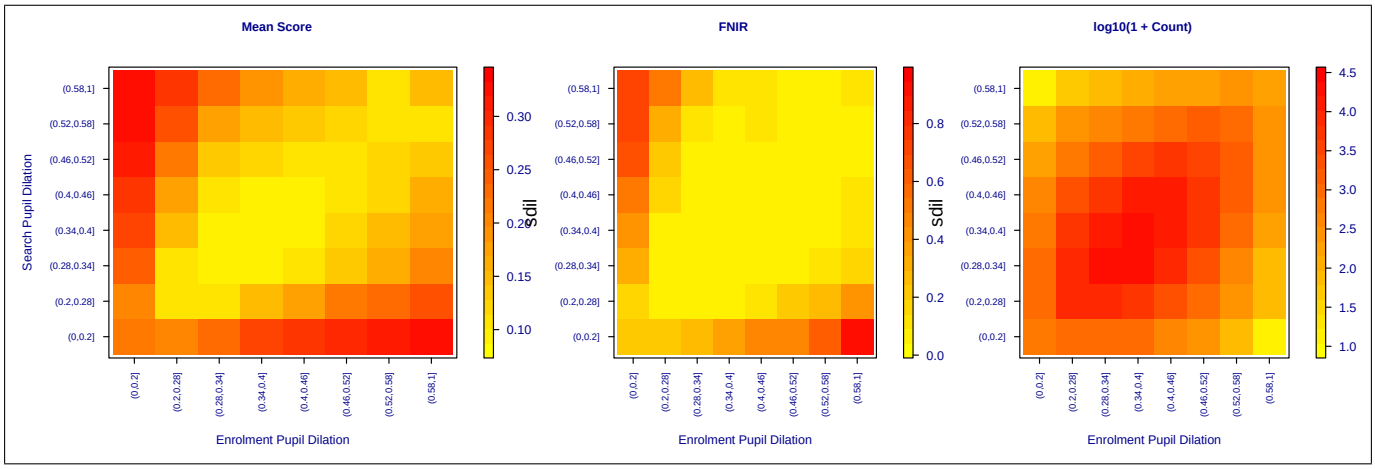

(b) Mate Dilation: Dis-similarity Score, Miss Rate, $\log_{10}(1+\text{Count})$

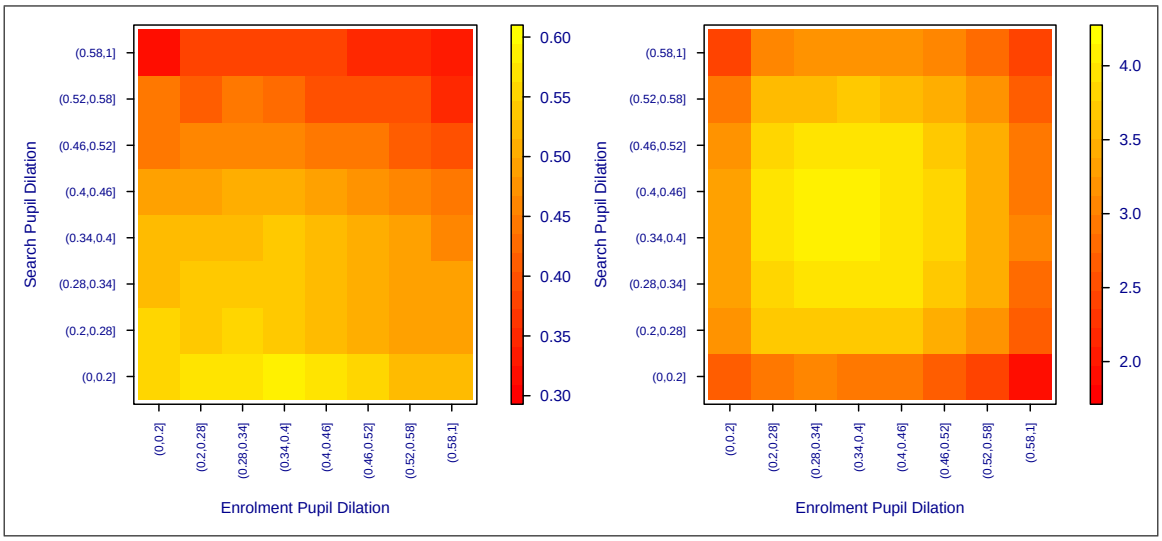

(c) Nonmate Dilation, Dis-similarity Score, Miss Rate, $\log_{10}(1+\text{Count})$

Figure 363: Heatmaps for implementation T12B executing mate searches in an enrolled population of N = 1.6 million. The radius images are binned by into twelve quantiles spanning $[0, 1]$. The dilation values are cut into ranges bounded by: $(0, 0.2, 0.28, 0.34, 0.40, 0.46, 0.52, 0.58, 1)$. The pathologically compressed 330x330 images are excluded from this analysis.

Heatmaps for implementation T12B executing mate searches in an enrolled population of N = 1.6 million.

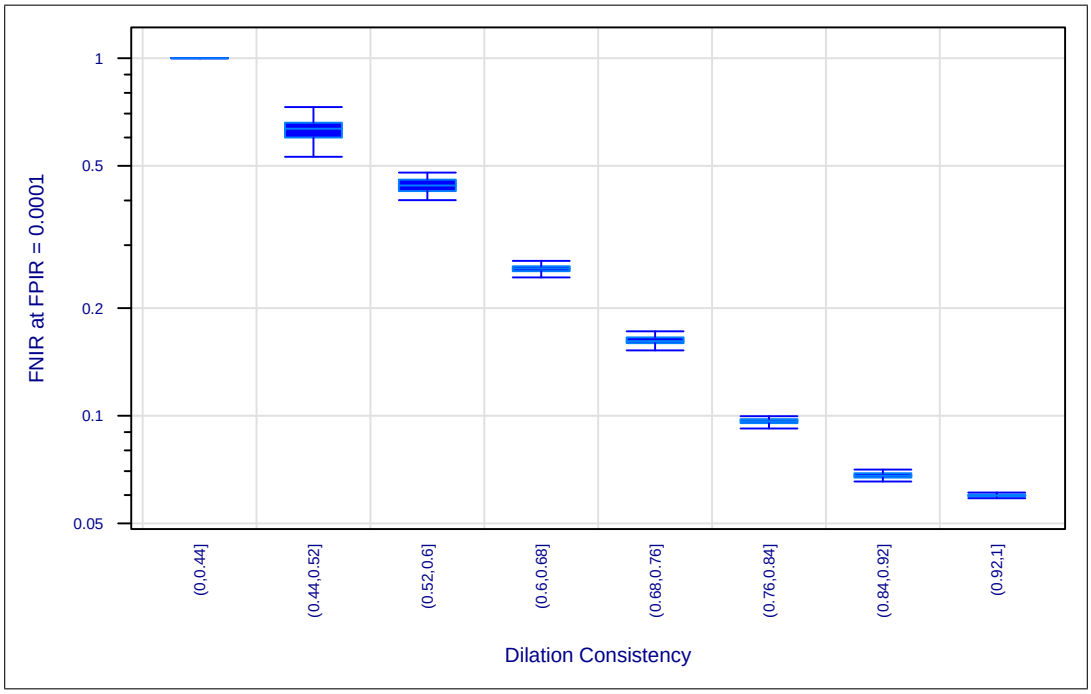

(a) Boxplot, all images

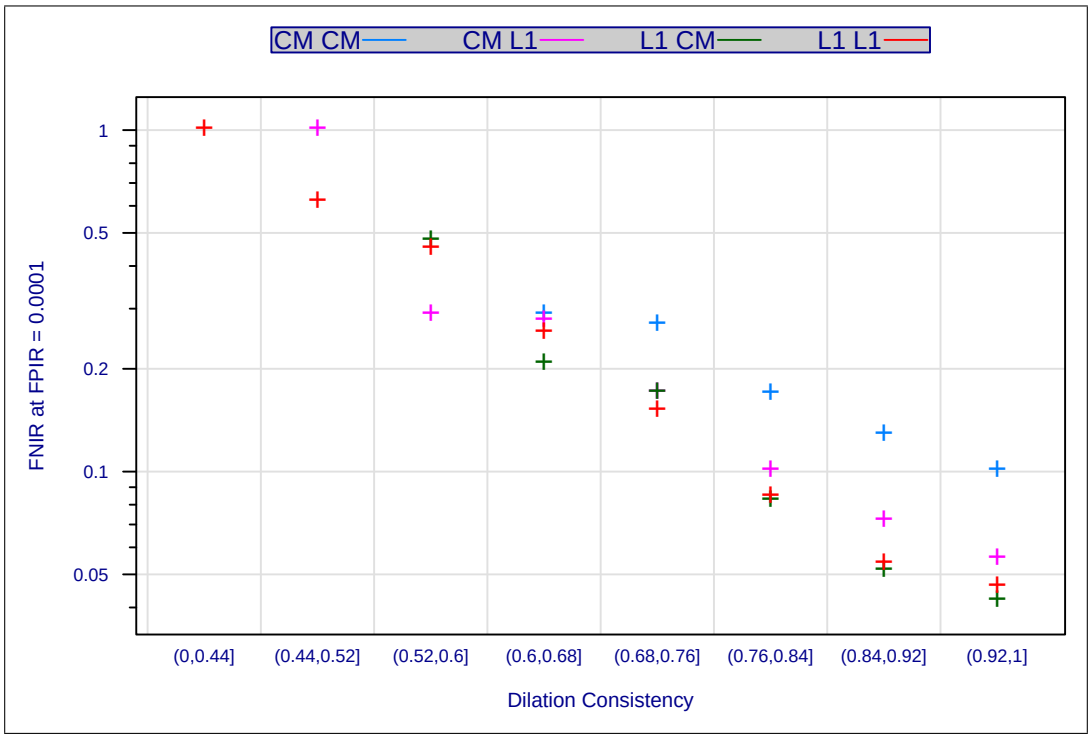

(b) Mean, L1 and CM images

Figure 364: Miss rate statistics for implementation T12B executing mate searches in an enrolled population of N = 1.6 million. The figures plots FNIR at FPIR = 0.0001 versus the IREX I metric for dilation consistency $(1 - \max(D_1, D_2))/(1 - \min(D_1, D_2))$ where D_i is pupil-iris radius ratio, and the subscripts refer to the mated enrollment and search image. The pathologically compressed 330x330 images are excluded from this analysis. The second figure breaks out dilation effects for interoperating camera pairs, CM and L1.

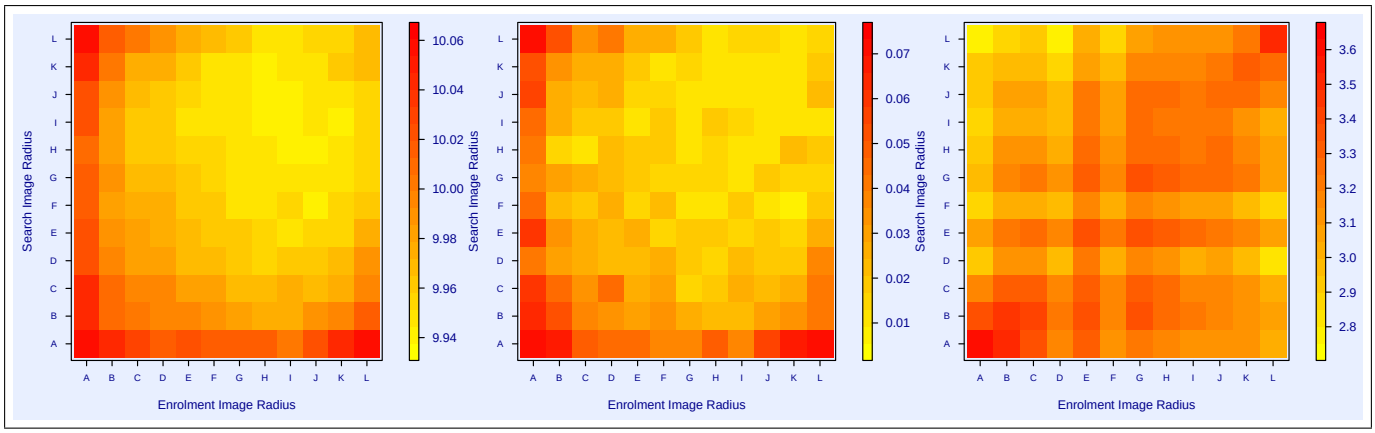

(a) Iris radius: Dis-similarity Score, Miss Rate, $\log_{10}(1+\text{Count})$

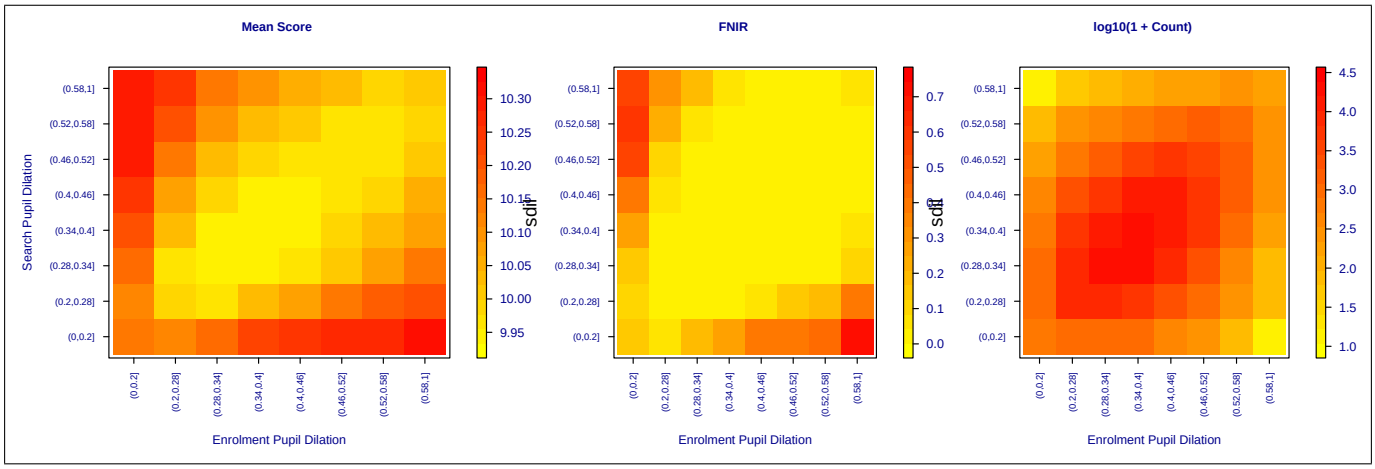

(b) Mate Dilation: Dis-similarity Score, Miss Rate, $\log_{10}(1+\text{Count})$

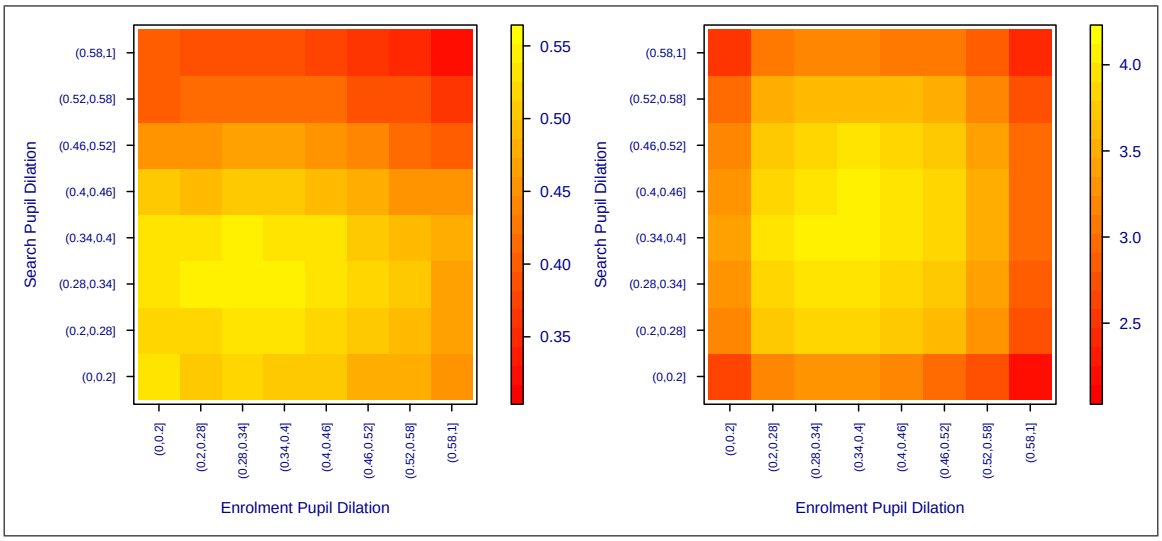

(c) Nonmate Dilation, Dis-similarity Score, Miss Rate, $\log_{10}(1+\text{Count})$

Figure 365: Heatmaps for implementation U01A executing mate searches in an enrolled population of N = 1.6 million. The radius images are binned by into twelve quantiles spanning $[0, 1]$. The dilation values are cut into ranges bounded by: $(0, 0.2, 0.28, 0.34, 0.40, 0.46, 0.52, 0.58, 1)$. The pathologically compressed 330x330 images are excluded from this analysis.

Heatmaps for implementation U01A executing mate searches in an enrolled population of N = 1.6 million.

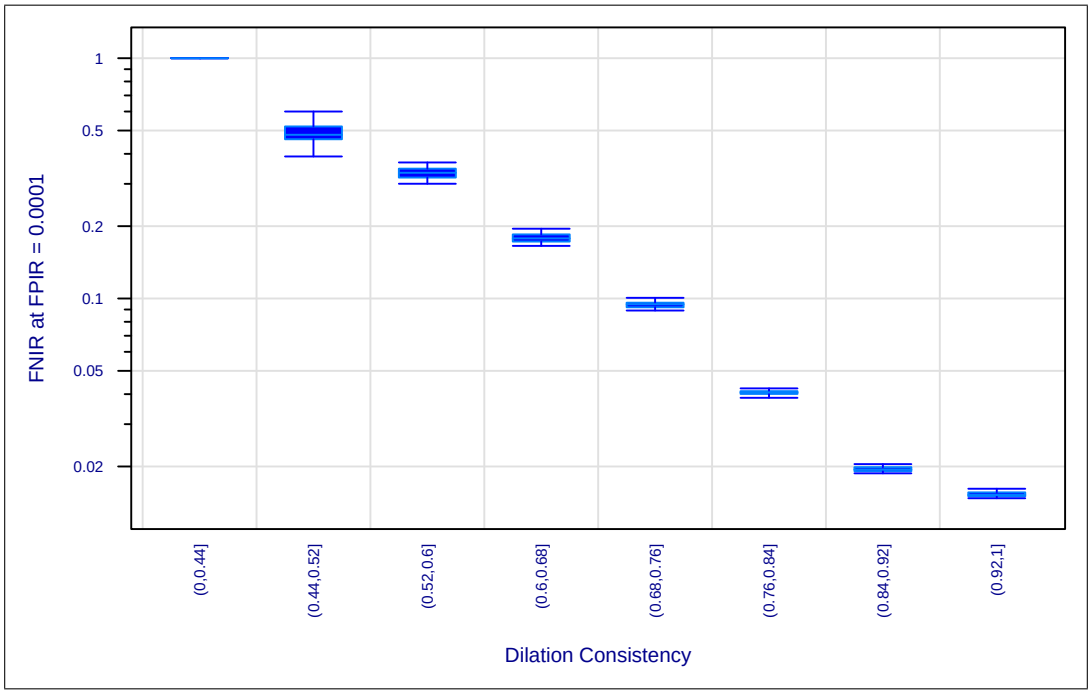

(a) Boxplot, all images

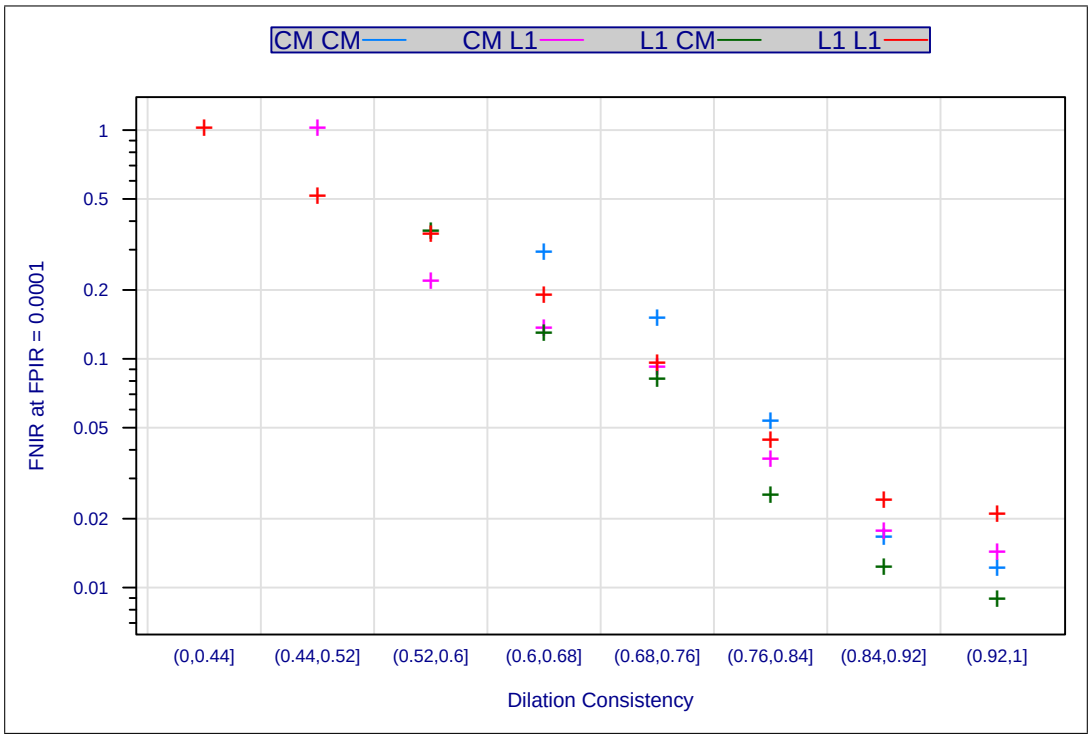

(b) Mean, L1 and CM images

Figure 366: Miss rate statistics for implementation U01A executing mate searches in an enrolled population of N = 1.6 million. The figures plots FNIR at FPIR = 0.0001 versus the IREX I metric for dilation consistency $(1 - \max(D_1, D_2))/(1 - \min(D_1, D_2))$ where D_i is pupil-iris radius ratio, and the subscripts refer to the mated enrollment and search image. The pathologically compressed 330x330 images are excluded from this analysis. The second figure breaks out dilation effects for interoperating camera pairs, CM and L1.

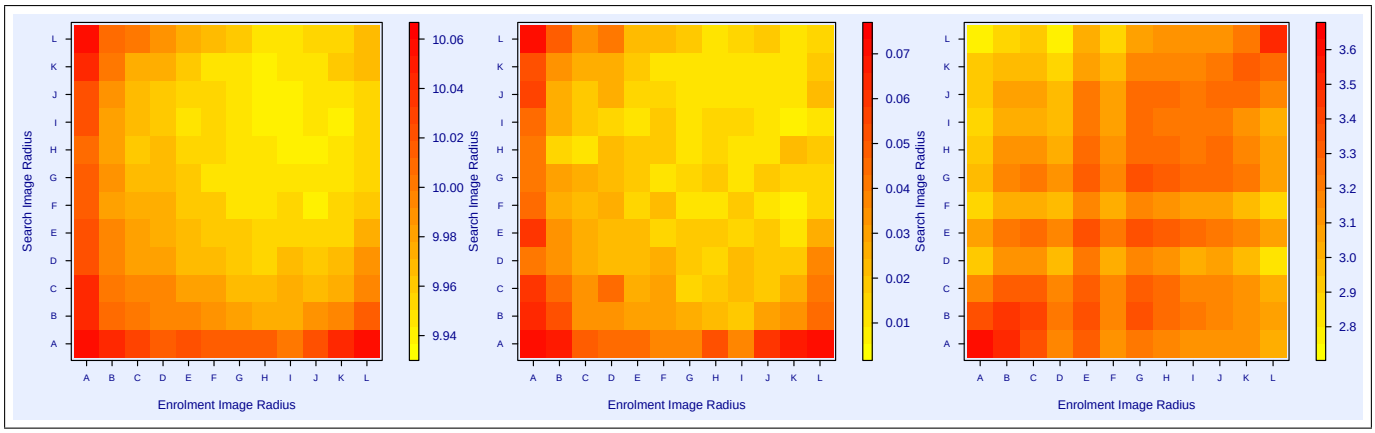

(a) Iris radius: Dis-similarity Score, Miss Rate, $\log_{10}(1+\text{Count})$

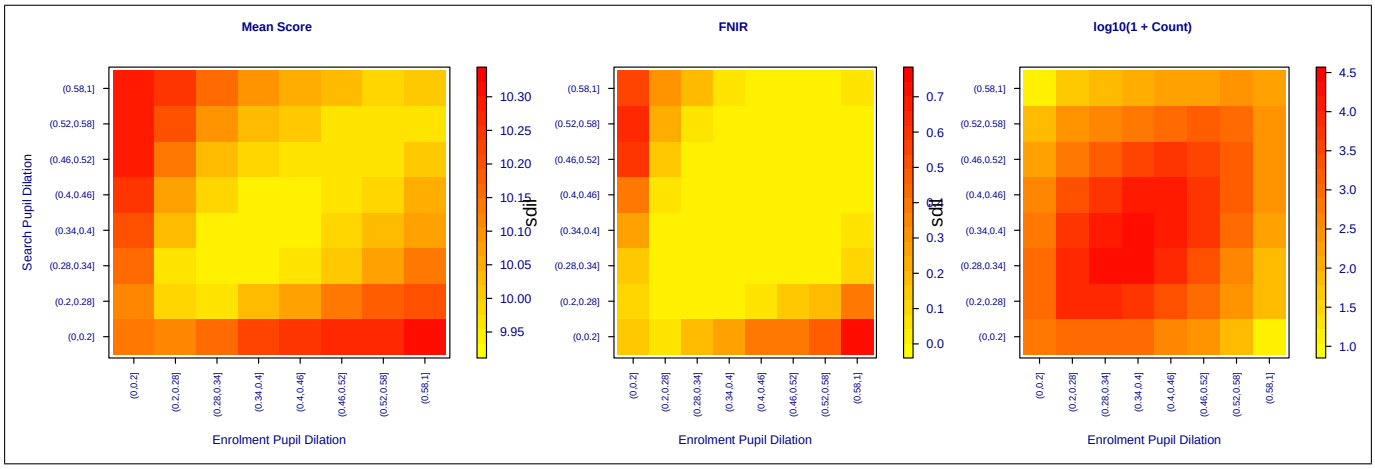

(b) Mate Dilation: Dis-similarity Score, Miss Rate, $\log_{10}(1+\text{Count})$

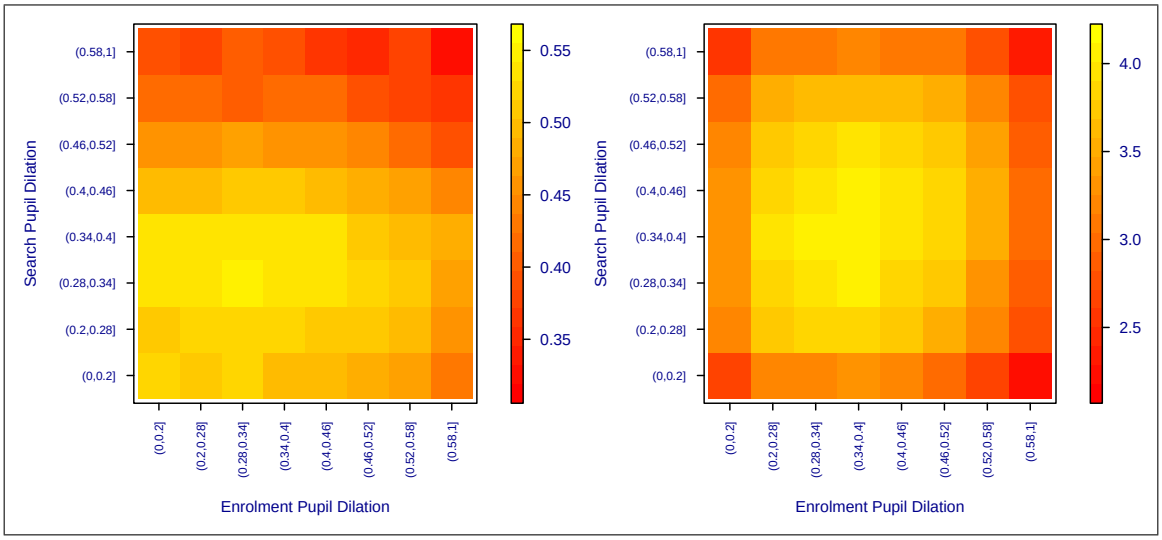

(c) Nonmate Dilation, Dis-similarity Score, Miss Rate, $\log_{10}(1+\text{Count})$

Figure 367: Heatmaps for implementation U01B executing mate searches in an enrolled population of N = 1.6 million. The radius images are binned by into twelve quantiles spanning $[0, 1]$. The dilation values are cut into ranges bounded by: $(0, 0.2, 0.28, 0.34, 0.40, 0.46, 0.52, 0.58, 1)$. The pathologically compressed 330x330 images are excluded from this analysis.

Heatmaps for implementation U01B executing mate searches in an enrolled population of N = 1.6 million.

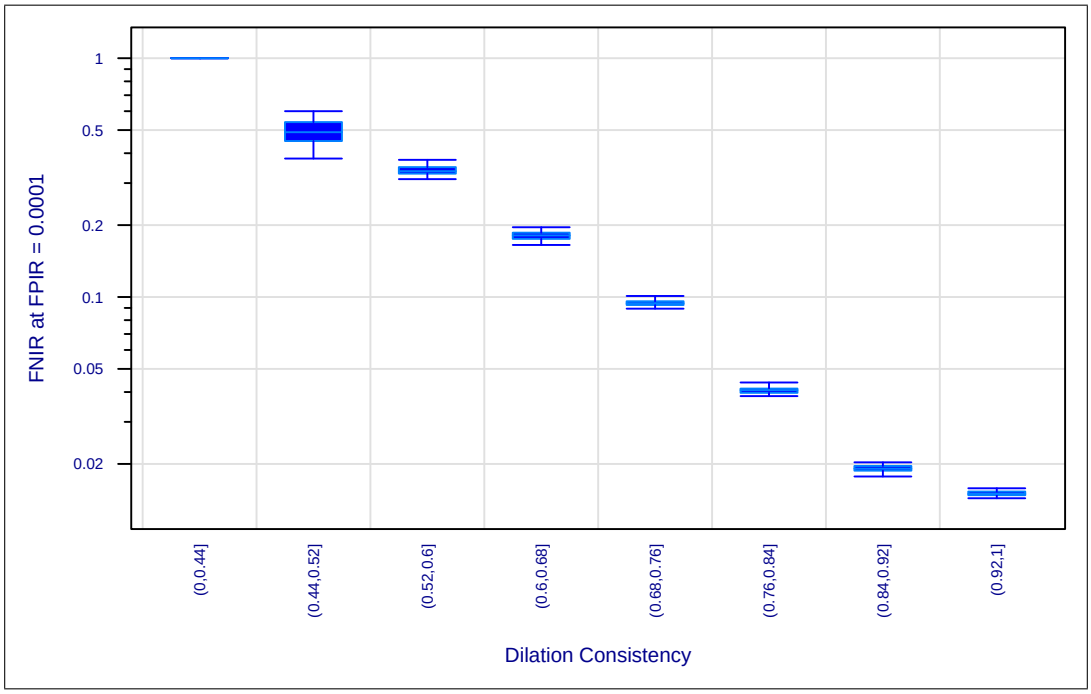

(a) Boxplot, all images

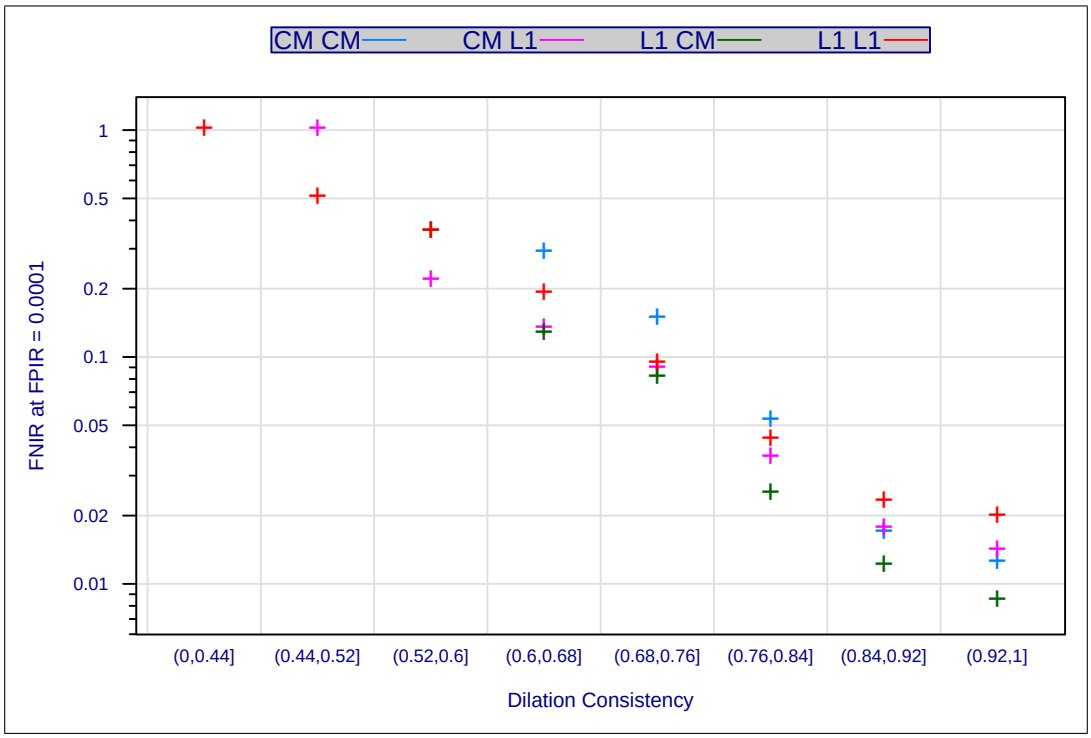

(b) Mean, L1 and CM images

Figure 368: Miss rate statistics for implementation U01B executing mate searches in an enrolled population of N = 1.6 million. The figures plots FNIR at FPIR = 0.0001 versus the IREX I metric for dilation consistency $(1 - \max(D_1, D_2))/(1 - \min(D_1, D_2))$ where D_i is pupil-iris radius ratio, and the subscripts refer to the mated enrollment and search image. The pathologically compressed 330x330 images are excluded from this analysis. The second figure breaks out dilation effects for interoperating camera pairs, CM and L1.

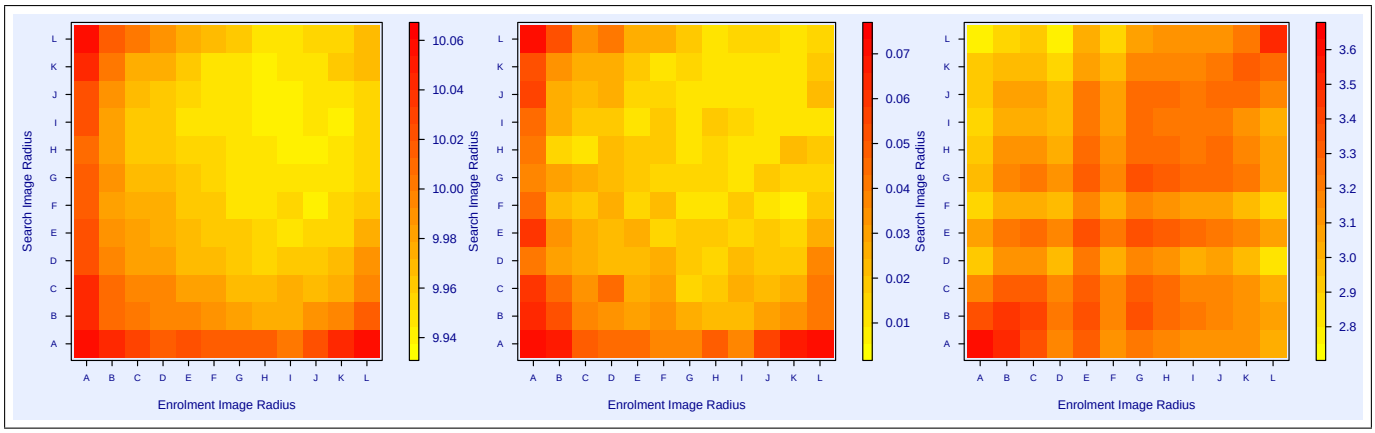

(a) Iris radius: Dis-similarity Score, Miss Rate, $\log_{10}(1+\text{Count})$

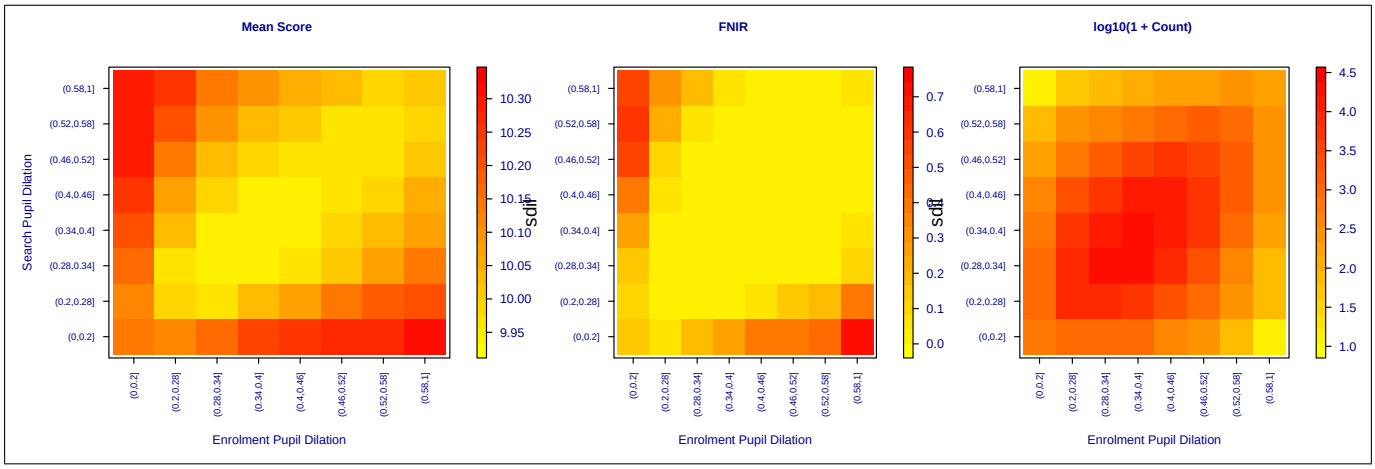

(b) Mate Dilation: Dis-similarity Score, Miss Rate, $\log_{10}(1+\text{Count})$

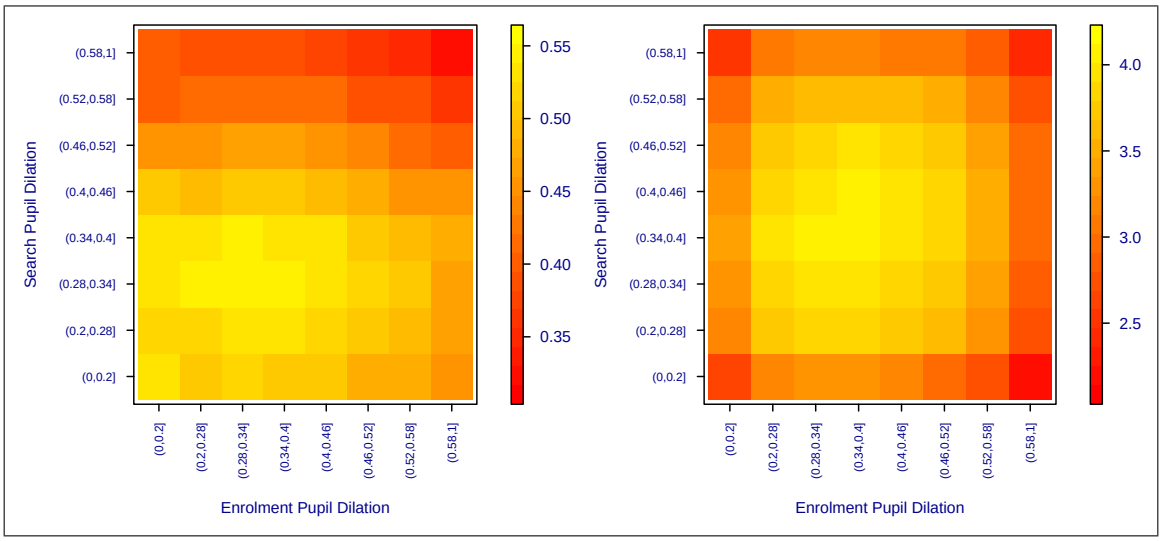

(c) Nonmate Dilation, Dis-similarity Score, Miss Rate, $\log_{10}(1+\text{Count})$

Figure 369: Heatmaps for implementation U02A executing mate searches in an enrolled population of N = 1.6 million. The radius images are binned by into twelve quantiles spanning $[0, 1]$. The dilation values are cut into ranges bounded by: $(0, 0.2, 0.28, 0.34, 0.40, 0.46, 0.52, 0.58, 1)$. The pathologically compressed 330x330 images are excluded from this analysis.

Heatmaps for implementation U02A executing mate searches in an enrolled population of N = 1.6 million.

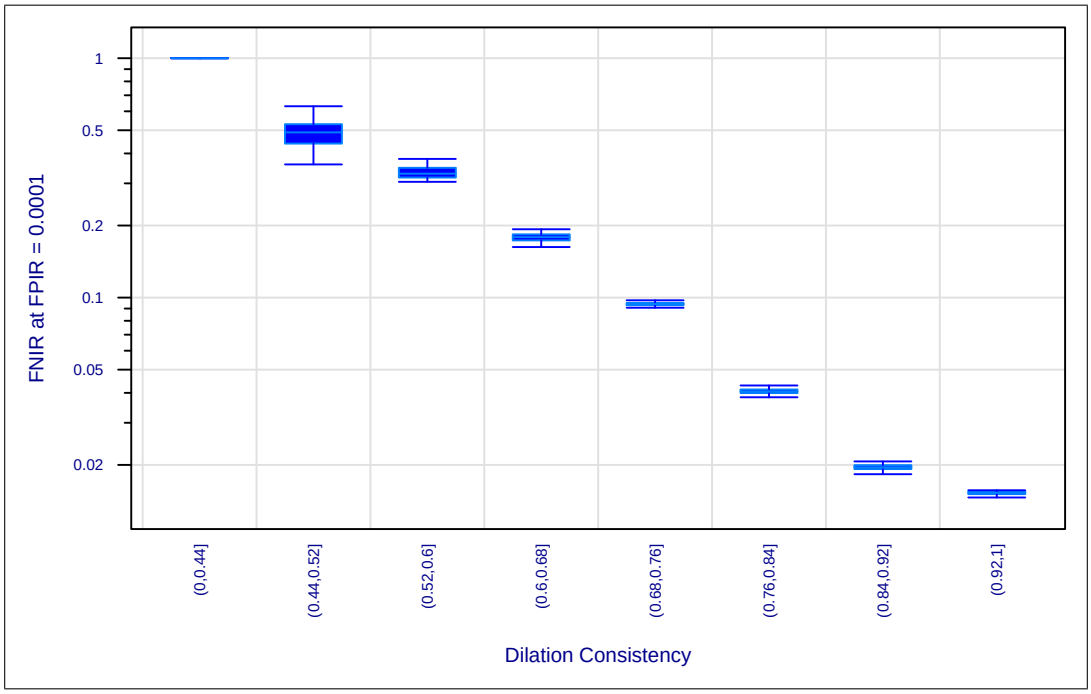

(a) Boxplot, all images

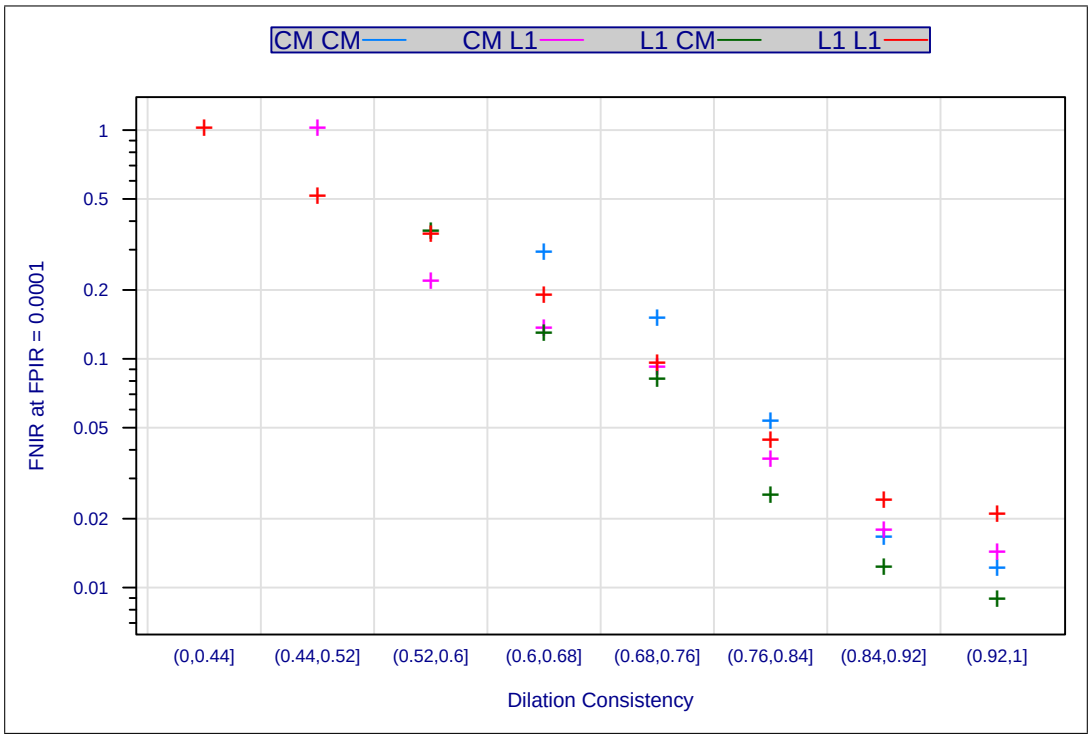

(b) Mean, L1 and CM images

Figure 370: Miss rate statistics for implementation U02A executing mate searches in an enrolled population of N = 1.6 million. The figures plots FNIR at FPIR = 0.0001 versus the IREX I metric for dilation consistency $(1 - \max(D_1, D_2))/(1 - \min(D_1, D_2))$ where D_i is pupil-iris radius ratio, and the subscripts refer to the mated enrollment and search image. The pathologically compressed 330x330 images are excluded from this analysis. The second figure breaks out dilation effects for interoperating camera pairs, CM and L1.

(a) Iris radius: Dis-similarity Score, Miss Rate, $\log_{10}(1+\text{Count})$

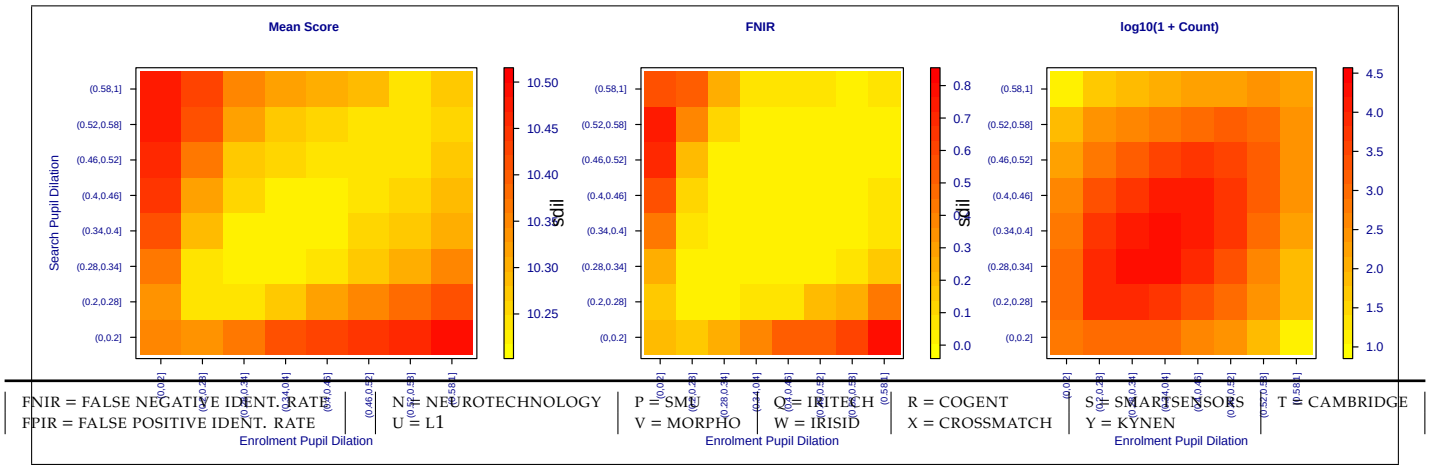

(b) Mate Dilation: Dis-similarity Score, Miss Rate, $\log_{10}(1+\text{Count})$

Heatmaps for implementation U03A executing mate searches in an enrolled population of N = 1.6 million.

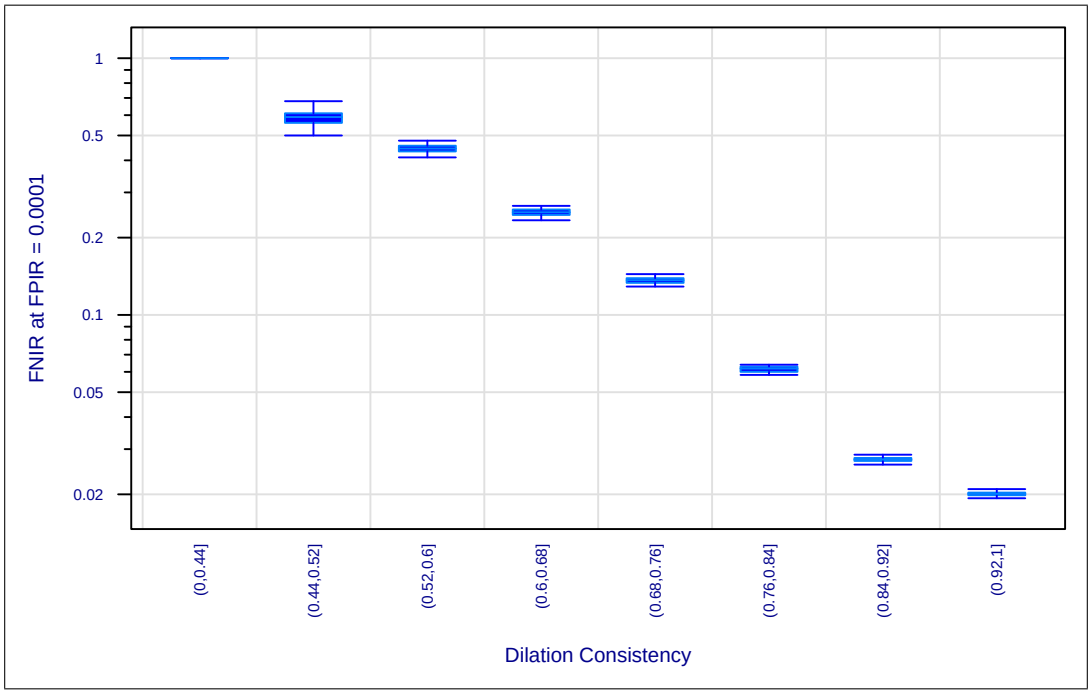

(a) Boxplot, all images

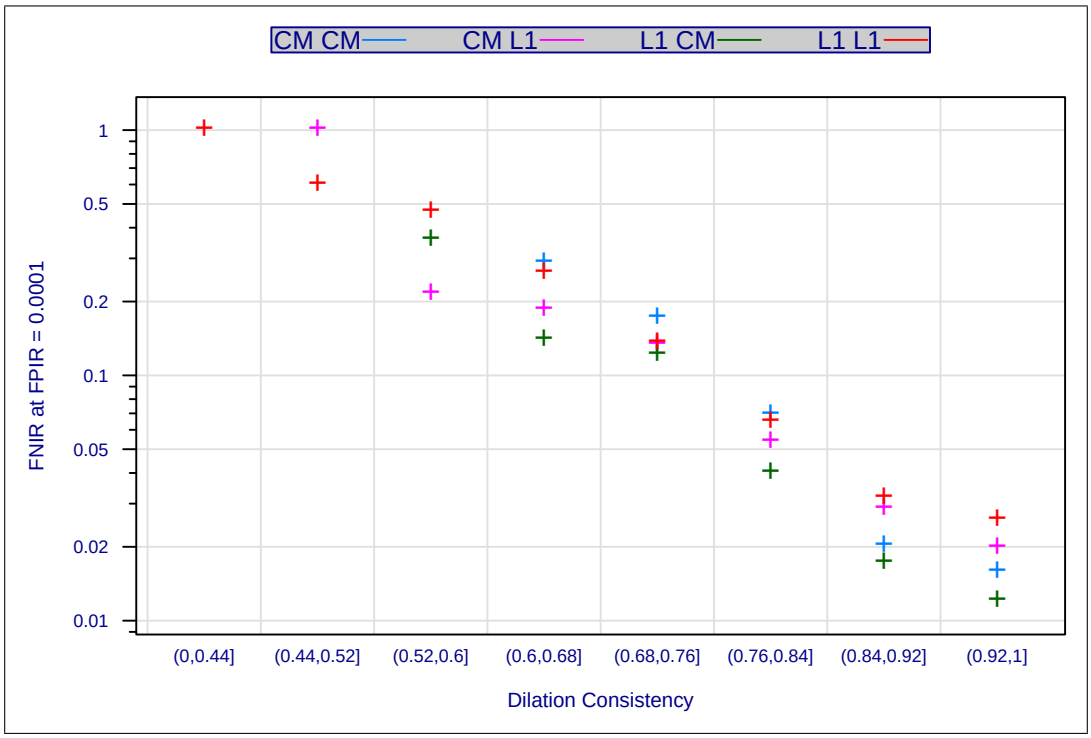

(b) Mean, L1 and CM images

Figure 372: Miss rate statistics for implementation U03A executing mate searches in an enrolled population of N = 1.6 million. The figures plots FNIR at FPIR = 0.0001 versus the IREX I metric for dilation consistency $(1 - \max(D_1, D_2))/(1 - \min(D_1, D_2))$ where D_i is pupil-iris radius ratio, and the subscripts refer to the mated enrollment and search image. The pathologically compressed 330x330 images are excluded from this analysis. The second figure breaks out dilation effects for interoperating camera pairs, CM and L1.

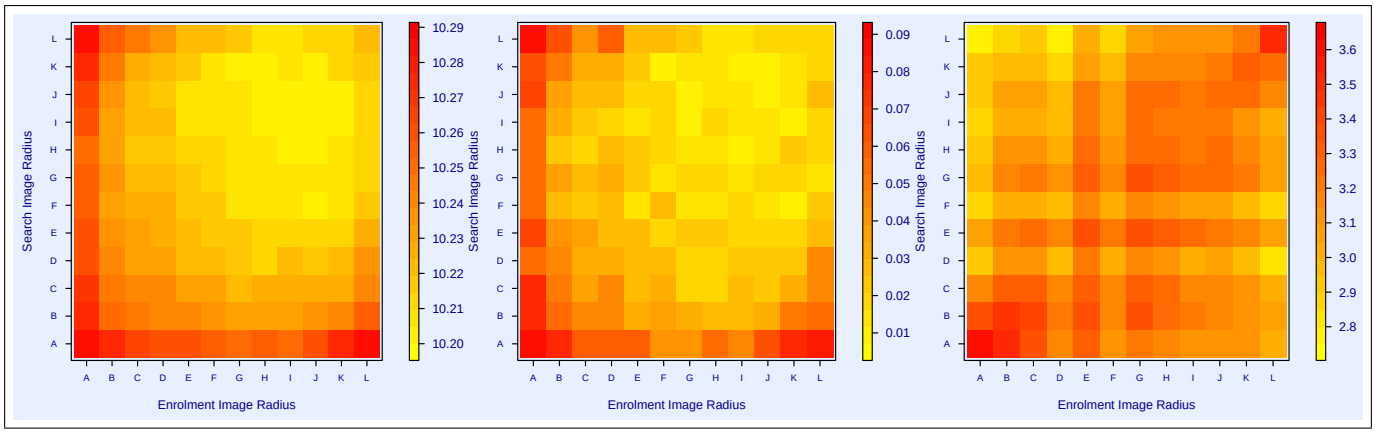

(a) Iris radius: Dis-similarity Score, Miss Rate, $\log_{10}(1+\text{Count})$

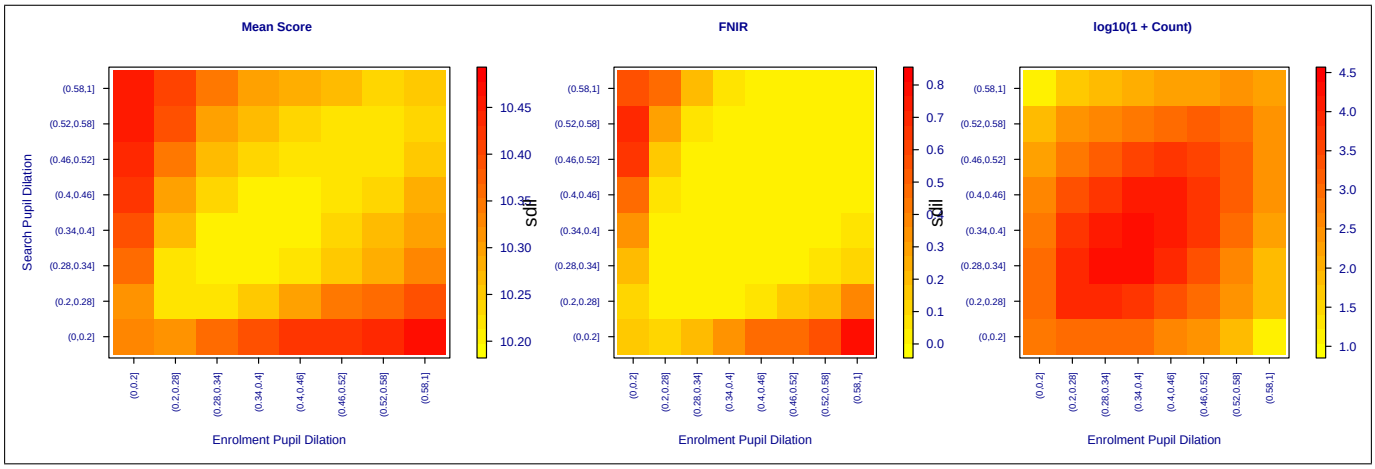

(b) Mate Dilation: Dis-similarity Score, Miss Rate, $\log_{10}(1+\text{Count})$

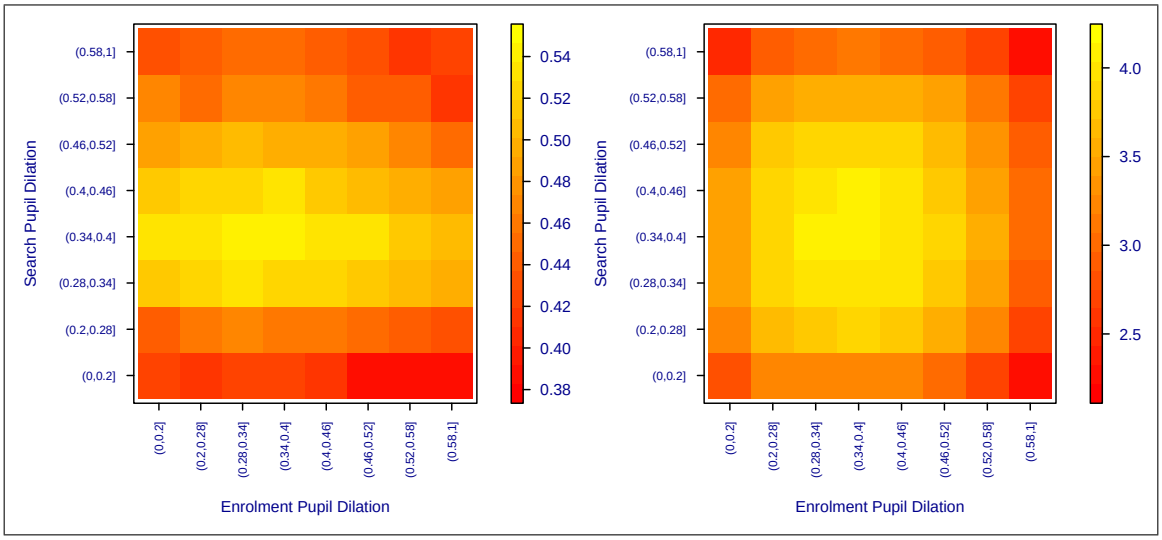

(c) Nonmate Dilation, Dis-similarity Score, Miss Rate, $\log_{10}(1+\text{Count})$

Figure 373: Heatmaps for implementation U03B executing mate searches in an enrolled population of N = 1.6 million. The radius images are binned by into twelve quantiles spanning $[0, 1]$. The dilation values are cut into ranges bounded by: $(0, 0.2, 0.28, 0.34, 0.40, 0.46, 0.52, 0.58, 1)$. The pathologically compressed 330x330 images are excluded from this analysis.

Heatmaps for implementation U03B executing mate searches in an enrolled population of N = 1.6 million.

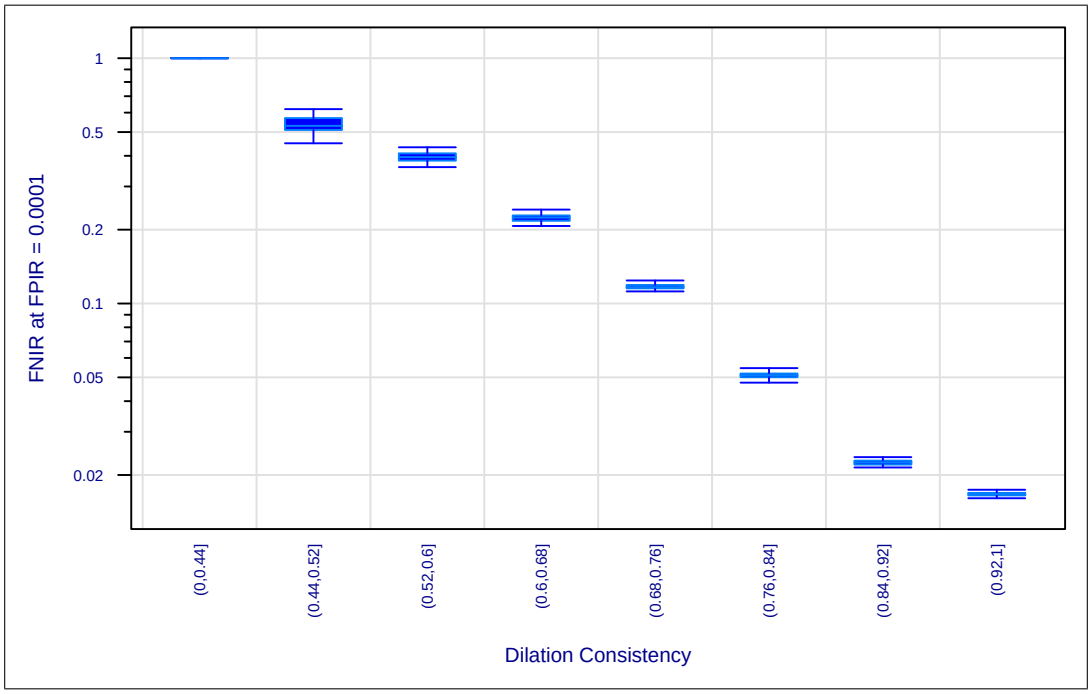

(a) Boxplot, all images

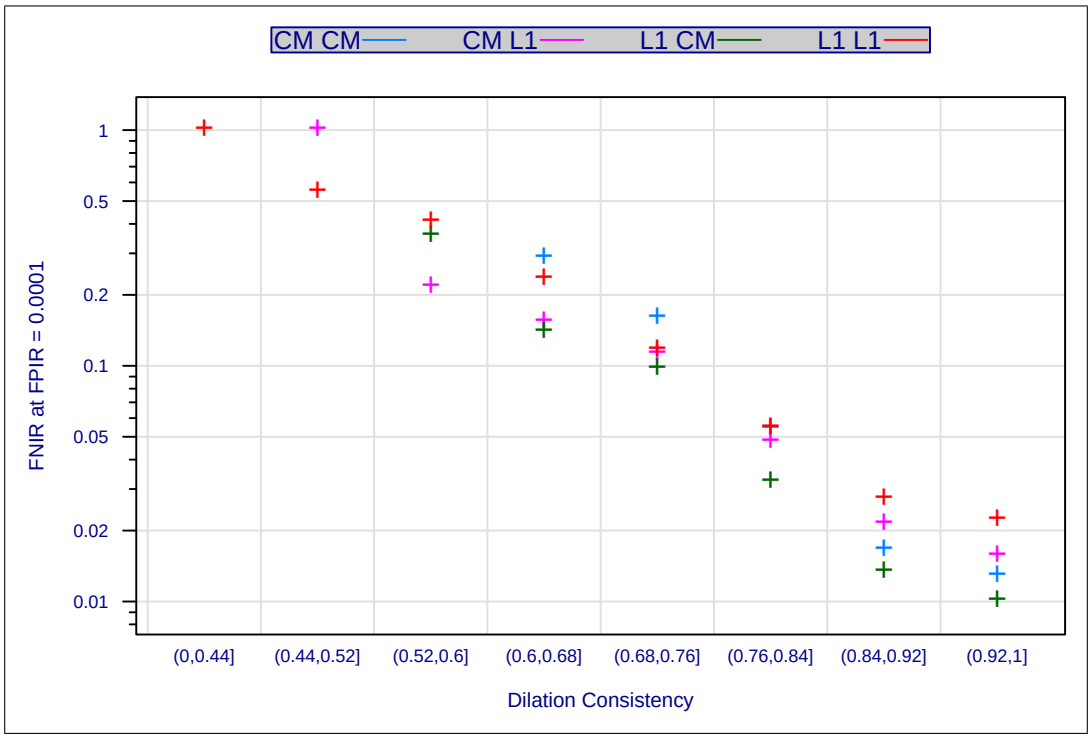

(b) Mean, L1 and CM images

Figure 374: Miss rate statistics for implementation U03B executing mate searches in an enrolled population of N = 1.6 million. The figures plots FNIR at FPIR = 0.0001 versus the IREX I metric for dilation consistency $(1 - \max(D_1, D_2))/(1 - \min(D_1, D_2))$ where D_i is pupil-iris radius ratio, and the subscripts refer to the mated enrollment and search image. The pathologically compressed 330x330 images are excluded from this analysis. The second figure breaks out dilation effects for interoperating camera pairs, CM and L1.

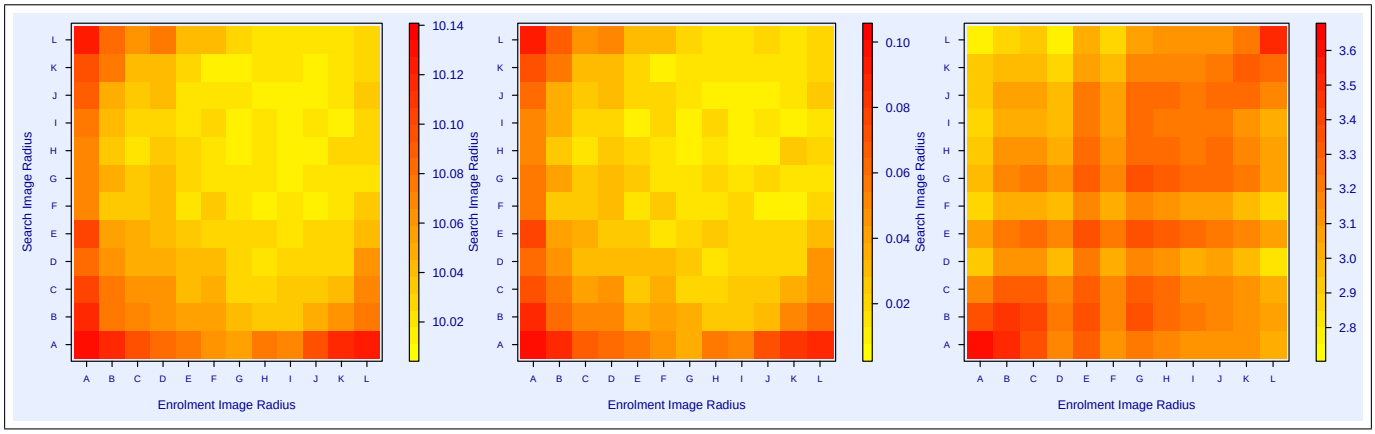

(a) Iris radius: Dis-similarity Score, Miss Rate, $\log_{10}(1+\text{Count})$

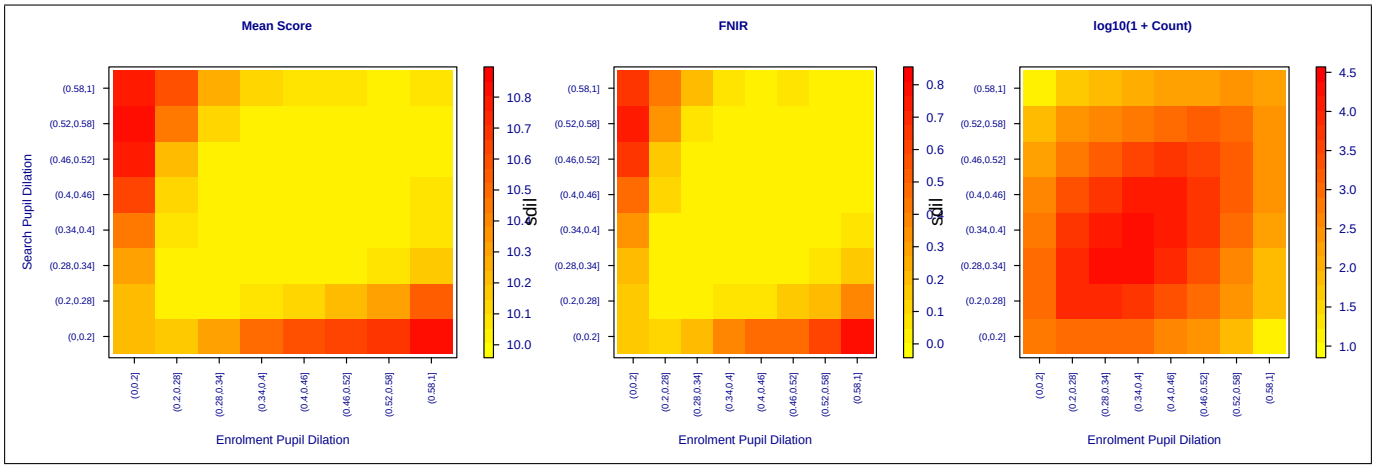

(b) Mate Dilation: Dis-similarity Score, Miss Rate, $\log_{10}(1+\text{Count})$

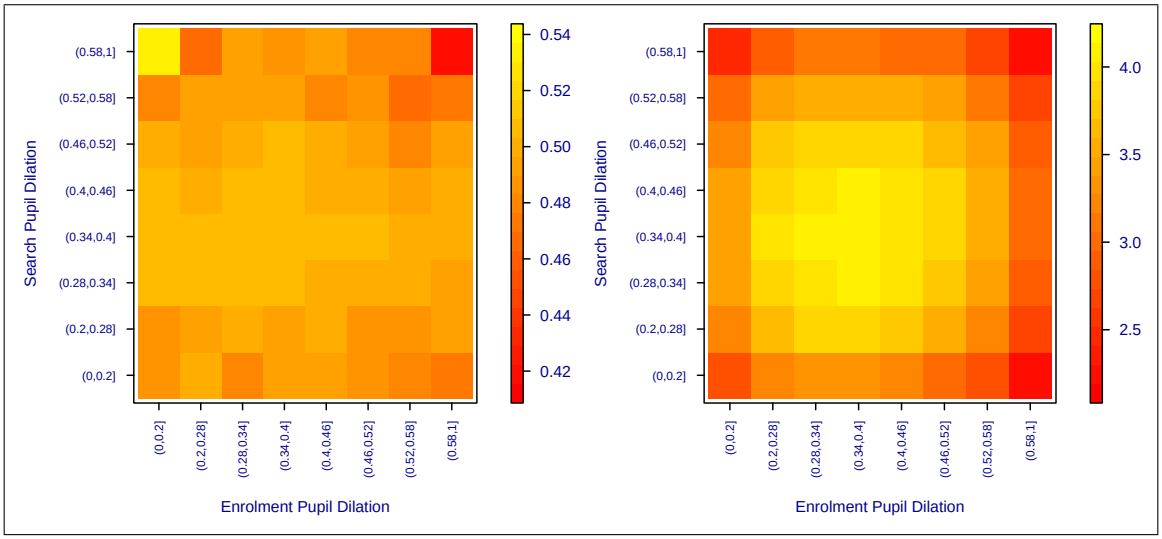

(c) Nonmate Dilation, Dis-similarity Score, Miss Rate, $\log_{10}(1+\text{Count})$

Figure 375: Heatmaps for implementation U04A executing mate searches in an enrolled population of N = 1.6 million. The radius images are binned by into twelve quantiles spanning $[0, 1]$. The dilation values are cut into ranges bounded by: $(0, 0.2, 0.28, 0.34, 0.40, 0.46, 0.52, 0.58, 1)$. The pathologically compressed 330x330 images are excluded from this analysis.

Heatmaps for implementation U04A executing mate searches in an enrolled population of N = 1.6 million.

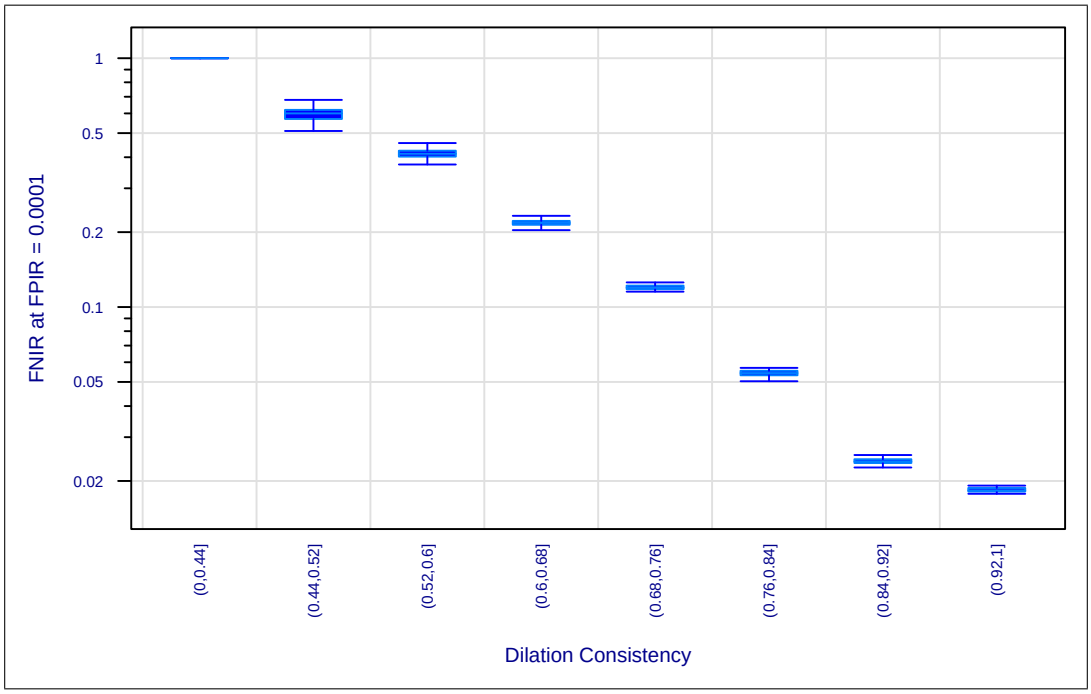

(a) Boxplot, all images

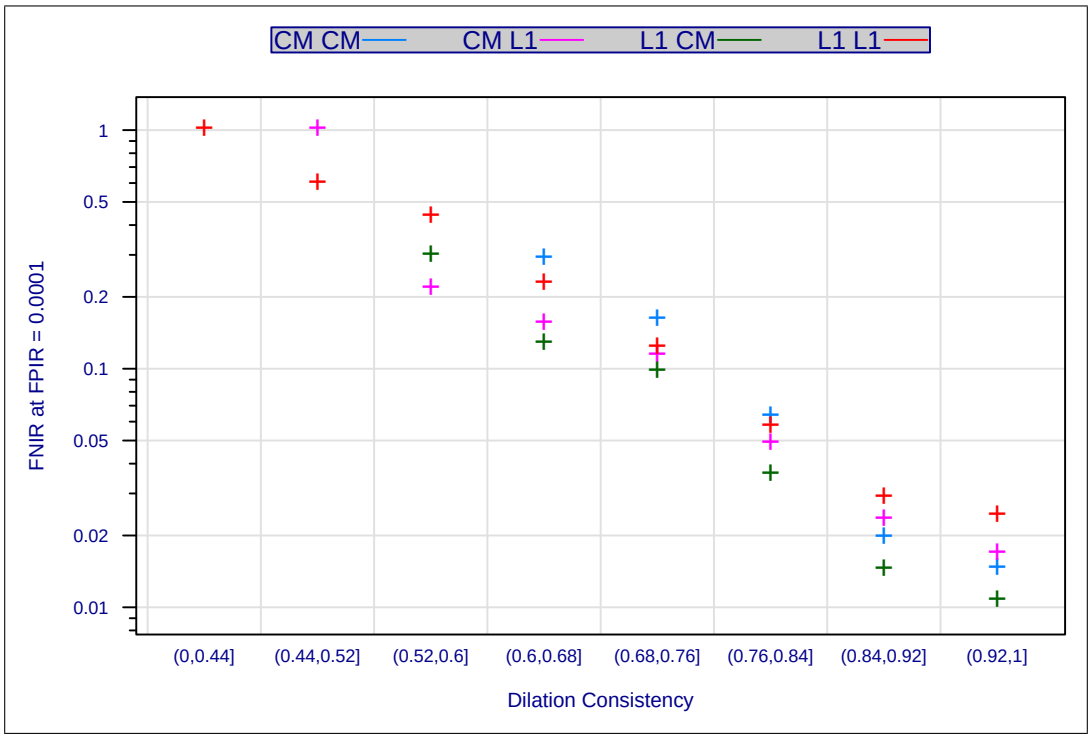

(b) Mean, L1 and CM images

Figure 376: Miss rate statistics for implementation U04A executing mate searches in an enrolled population of N = 1.6 million. The figures plots FNIR at FPIR = 0.0001 versus the IREX I metric for dilation consistency $(1 - \max(D_1, D_2))/(1 - \min(D_1, D_2))$ where D_i is pupil-iris radius ratio, and the subscripts refer to the mated enrollment and search image. The pathologically compressed 330x330 images are excluded from this analysis. The second figure breaks out dilation effects for interoperating camera pairs, CM and L1.

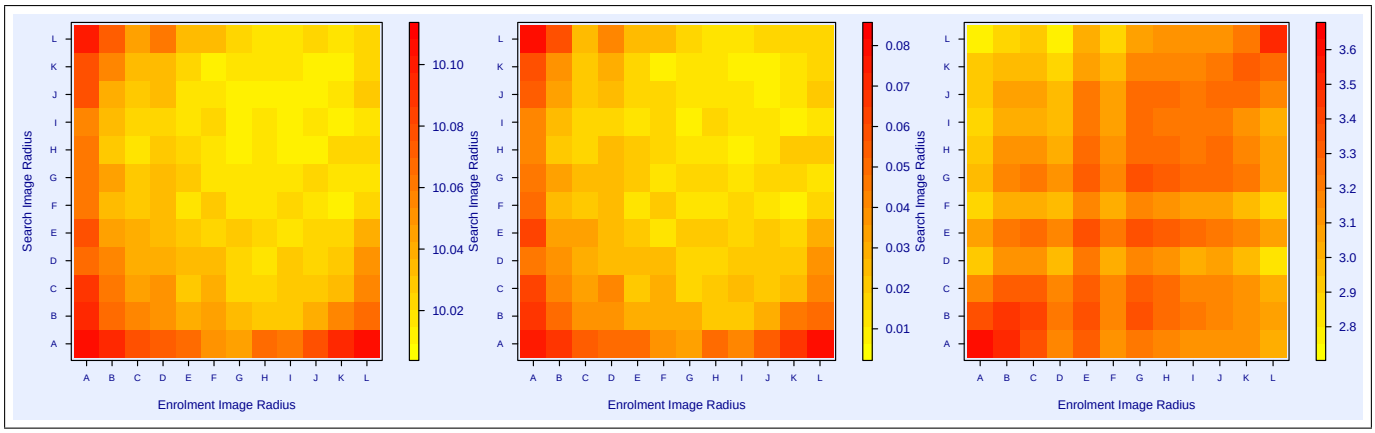

(a) Iris radius: Dis-similarity Score, Miss Rate, $\log_{10}(1+\text{Count})$

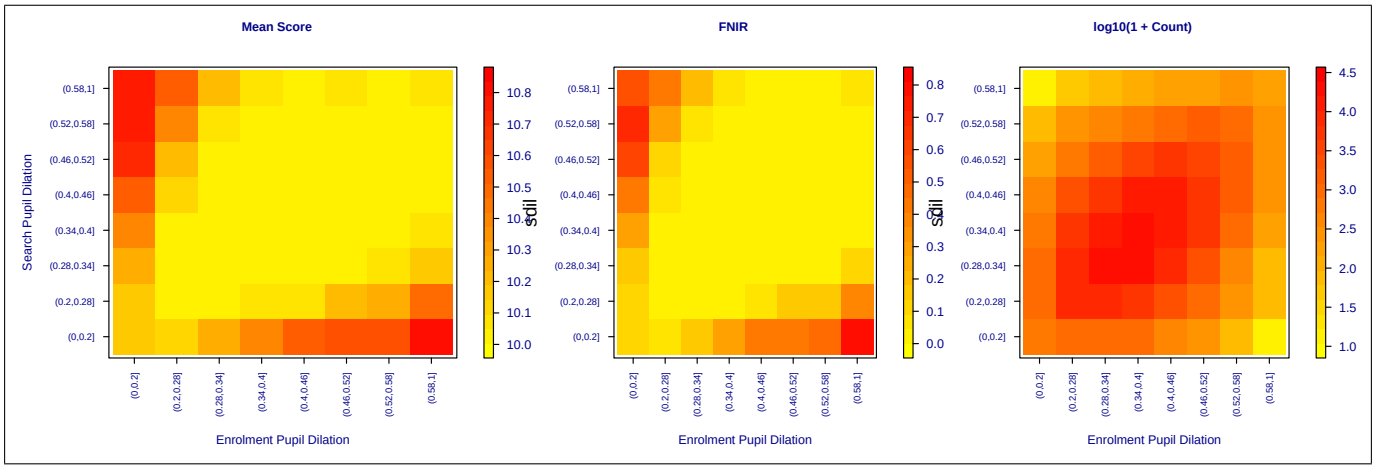

(b) Mate Dilation: Dis-similarity Score, Miss Rate, $\log_{10}(1+\text{Count})$

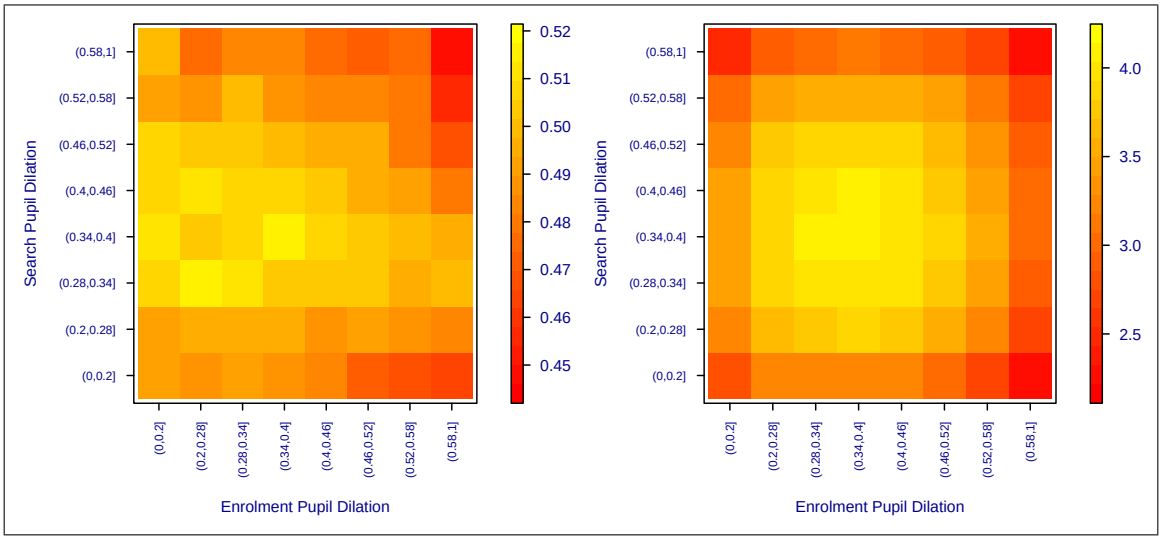

(c) Nonmate Dilation, Dis-similarity Score, Miss Rate, $\log_{10}(1+\text{Count})$

Figure 377: Heatmaps for implementation U04B executing mate searches in an enrolled population of N = 1.6 million. The radius images are binned by into twelve quantiles spanning $[0, 1]$. The dilation values are cut into ranges bounded by: $(0, 0.2, 0.28, 0.34, 0.40, 0.46, 0.52, 0.58, 1)$. The pathologically compressed 330x330 images are excluded from this analysis.

Heatmaps for implementation U04B executing mate searches in an enrolled population of N = 1.6 million.

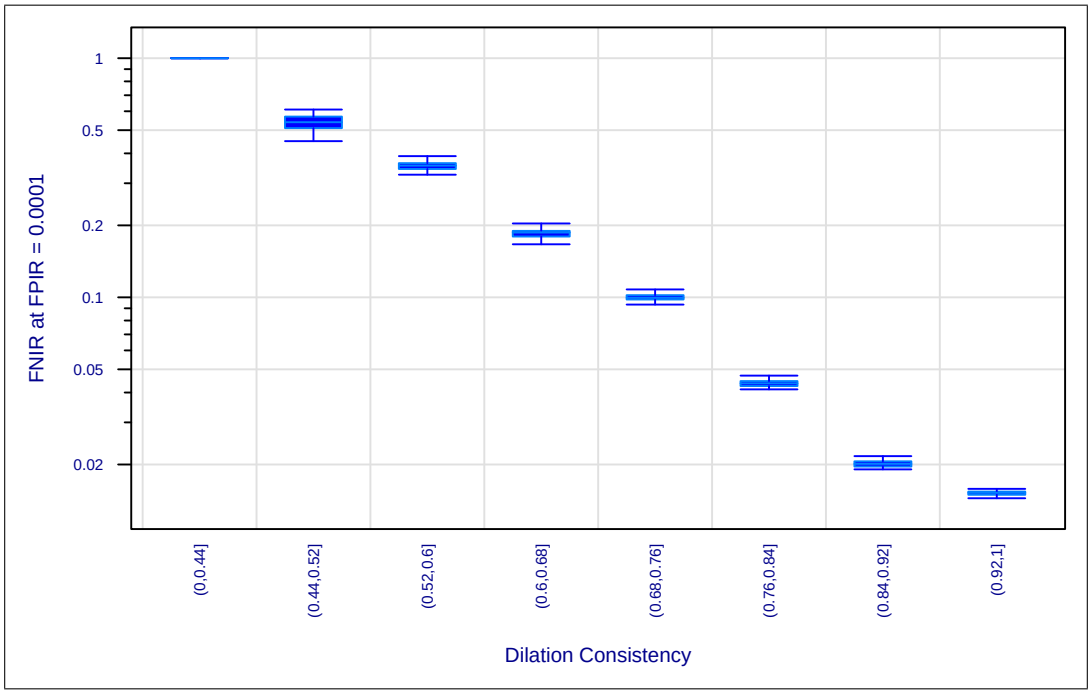

(a) Boxplot, all images

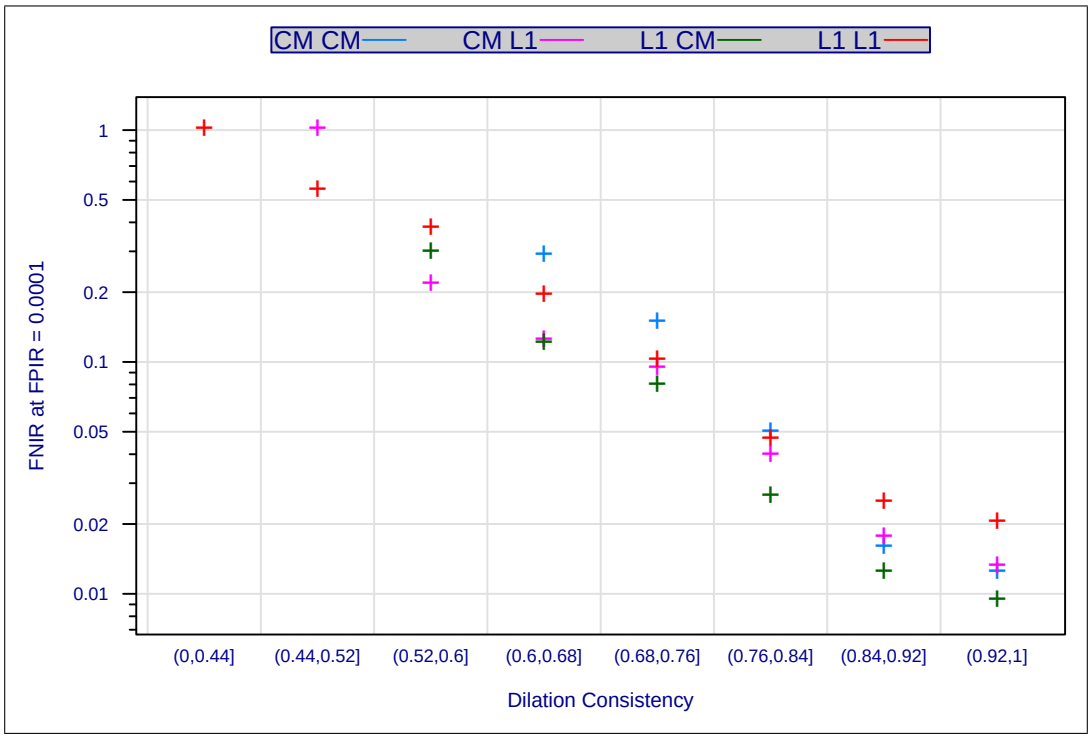

(b) Mean, L1 and CM images

Figure 378: Miss rate statistics for implementation U04B executing mate searches in an enrolled population of N = 1.6 million. The figures plots FNIR at FPIR = 0.0001 versus the IREX I metric for dilation consistency $(1 - \max(D_1, D_2))/(1 - \min(D_1, D_2))$ where D_i is pupil-iris radius ratio, and the subscripts refer to the mated enrollment and search image. The pathologically compressed 330x330 images are excluded from this analysis. The second figure breaks out dilation effects for interoperating camera pairs, CM and L1.

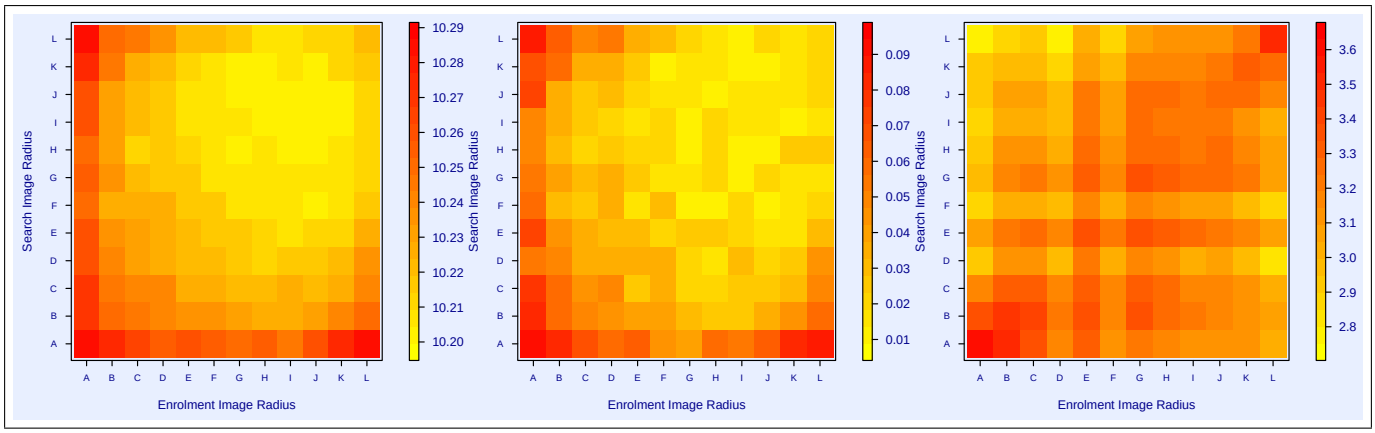

(a) Iris radius: Dis-similarity Score, Miss Rate, $\log_{10}(1+\text{Count})$

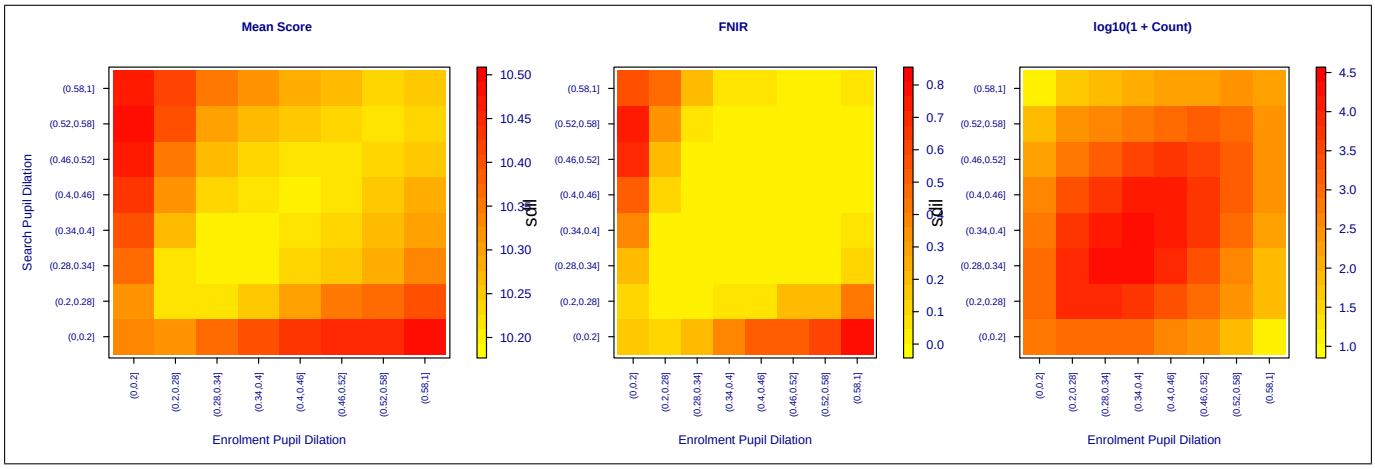

(b) Mate Dilation: Dis-similarity Score, Miss Rate, $\log_{10}(1+\text{Count})$

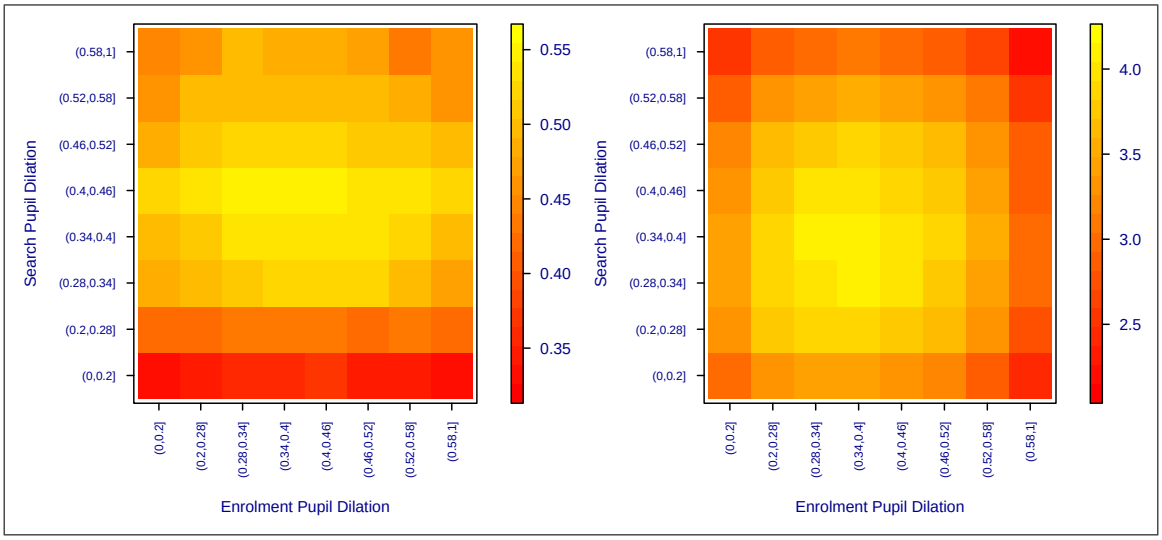

(c) Nonmate Dilation, Dis-similarity Score, Miss Rate, $\log_{10}(1+\text{Count})$

Figure 379: Heatmaps for implementation U11A executing mate searches in an enrolled population of N = 1.6 million. The radius images are binned by into twelve quantiles spanning $[0, 1]$. The dilation values are cut into ranges bounded by: $(0, 0.2, 0.28, 0.34, 0.40, 0.46, 0.52, 0.58, 1)$. The pathologically compressed 330x330 images are excluded from this analysis.

Heatmaps for implementation U11A executing mate searches in an enrolled population of N = 1.6 million.

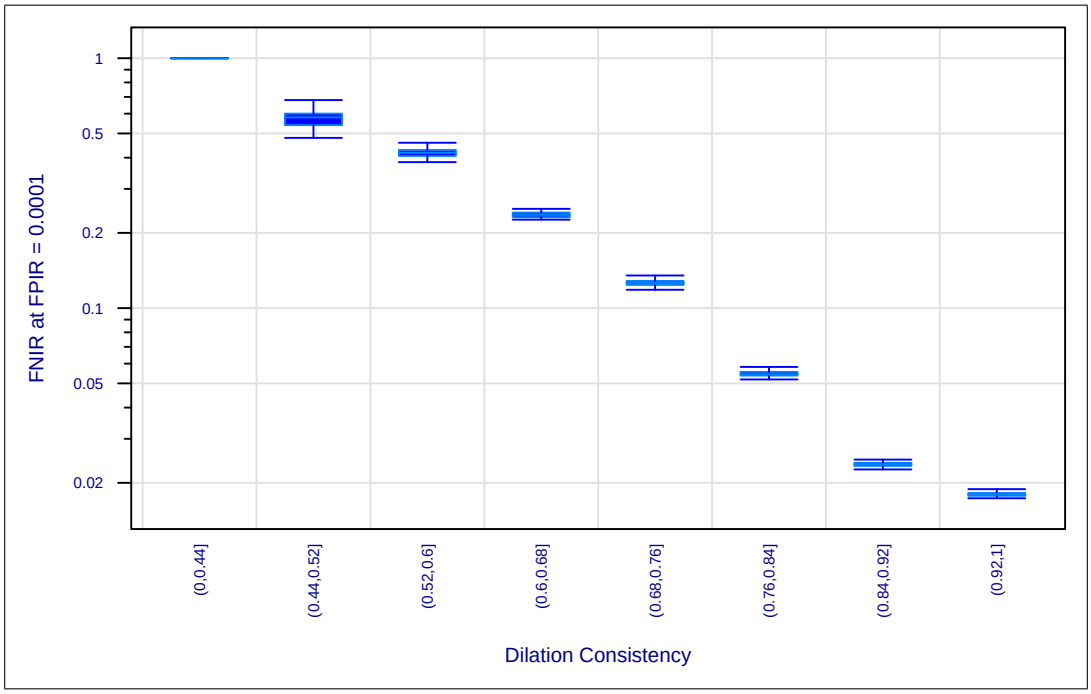

(a) Boxplot, all images

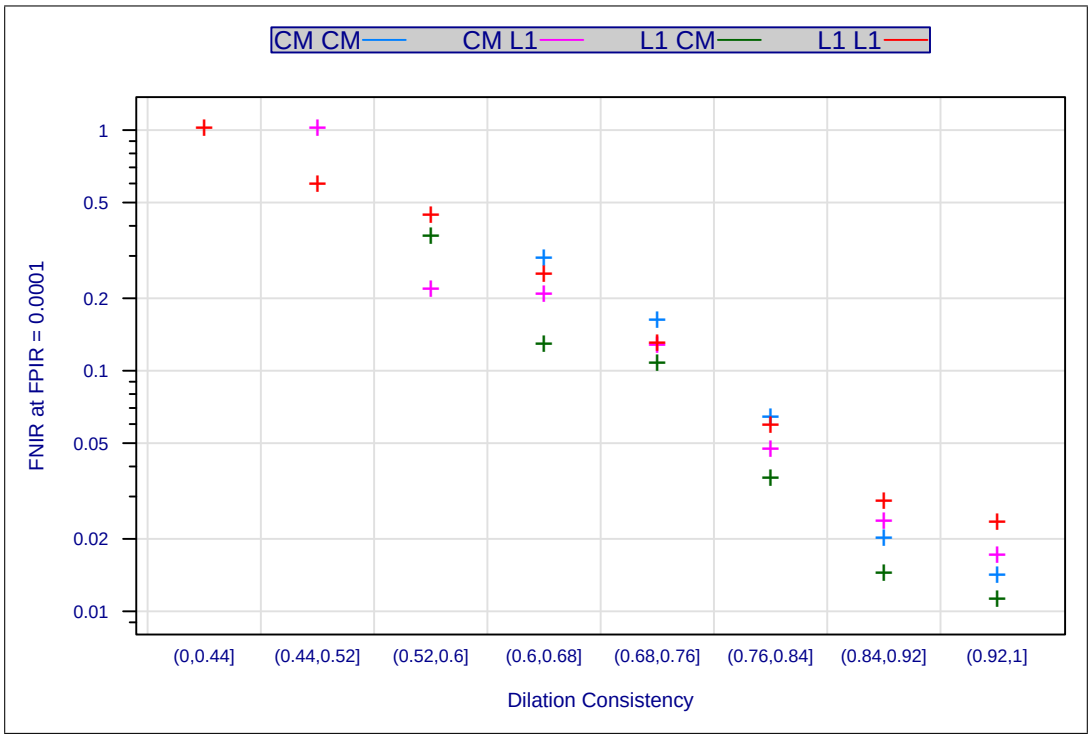

(b) Mean, L1 and CM images

Figure 380: Miss rate statistics for implementation U11A executing mate searches in an enrolled population of N = 1.6 million. The figures plots FNIR at FPIR = 0.0001 versus the IREX I metric for dilation consistency $(1 - \max(D_1, D_2))/(1 - \min(D_1, D_2))$ where D_i is pupil-iris radius ratio, and the subscripts refer to the mated enrollment and search image. The pathologically compressed 330x330 images are excluded from this analysis. The second figure breaks out dilation effects for interoperating camera pairs, CM and L1.

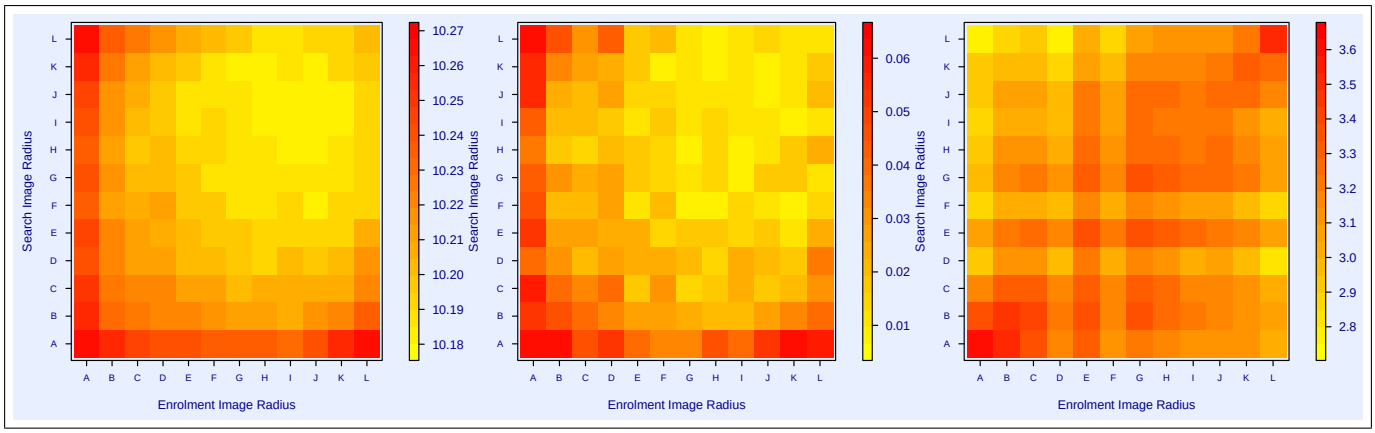

(a) Iris radius: Dis-similarity Score, Miss Rate, $\log_{10}(1+\text{Count})$

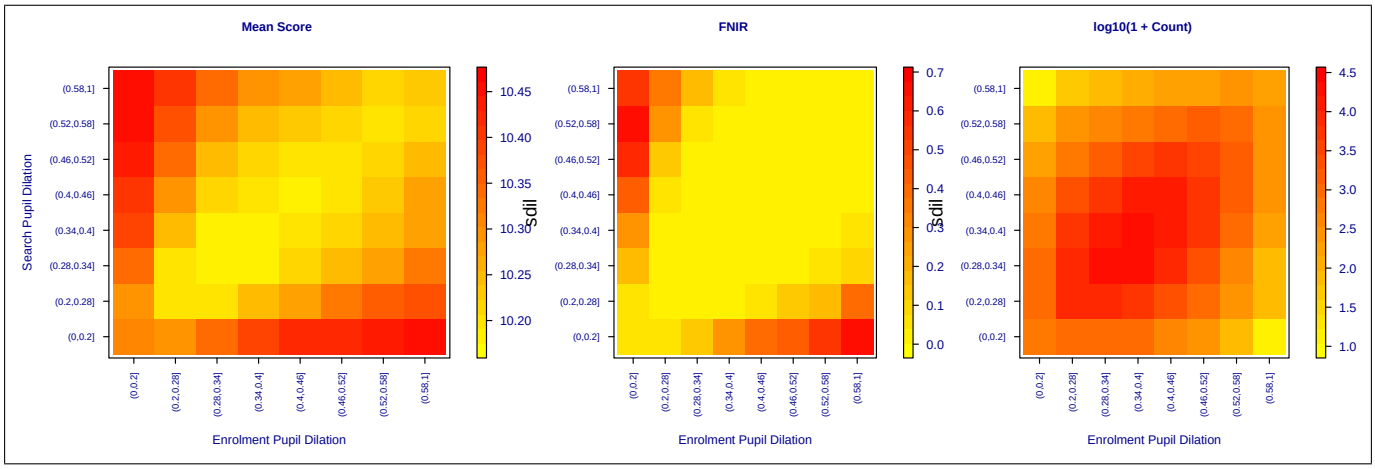

(b) Mate Dilation: Dis-similarity Score, Miss Rate, $\log_{10}(1+\text{Count})$

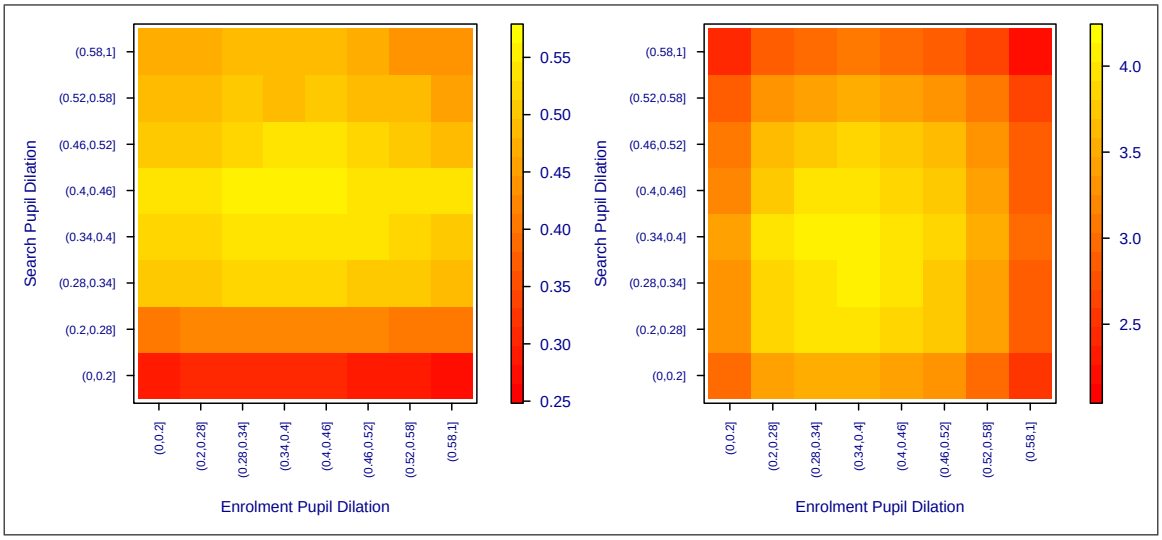

(c) Nonmate Dilation, Dis-similarity Score, Miss Rate, $\log_{10}(1+\text{Count})$

Figure 381: Heatmaps for implementation U11B executing mate searches in an enrolled population of N = 1.6 million. The radius images are binned by into twelve quantiles spanning $[0, 1]$. The dilation values are cut into ranges bounded by: $(0, 0.2, 0.28, 0.34, 0.40, 0.46, 0.52, 0.58, 1)$. The pathologically compressed 330x330 images are excluded from this analysis.

Heatmaps for implementation U11B executing mate searches in an enrolled population of N = 1.6 million.

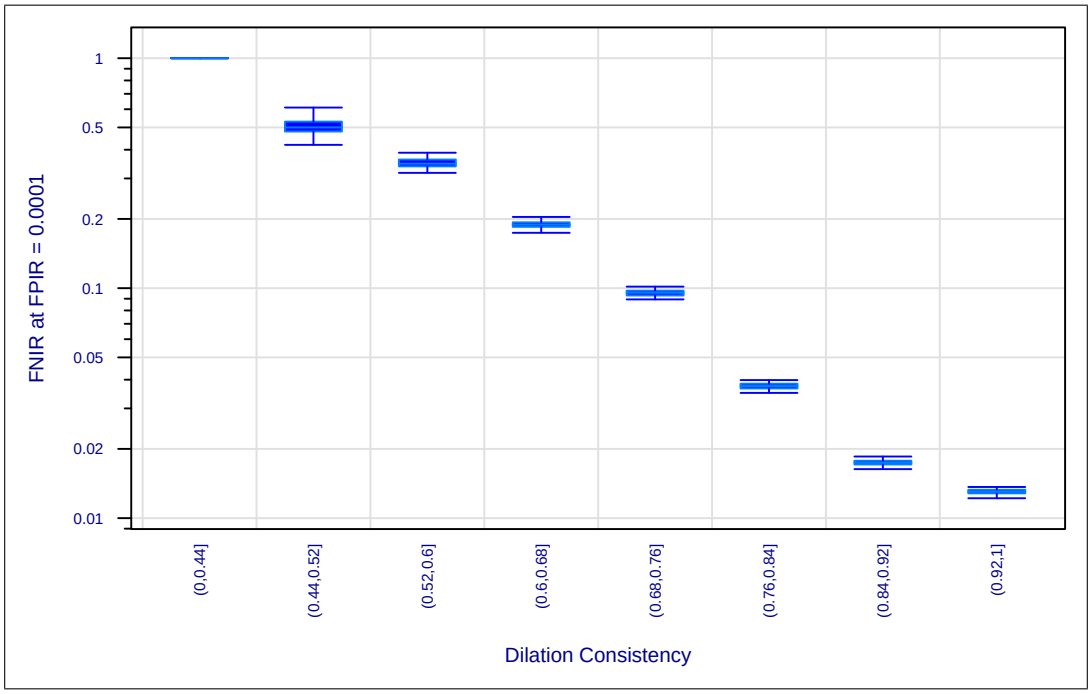

(a) Boxplot, all images

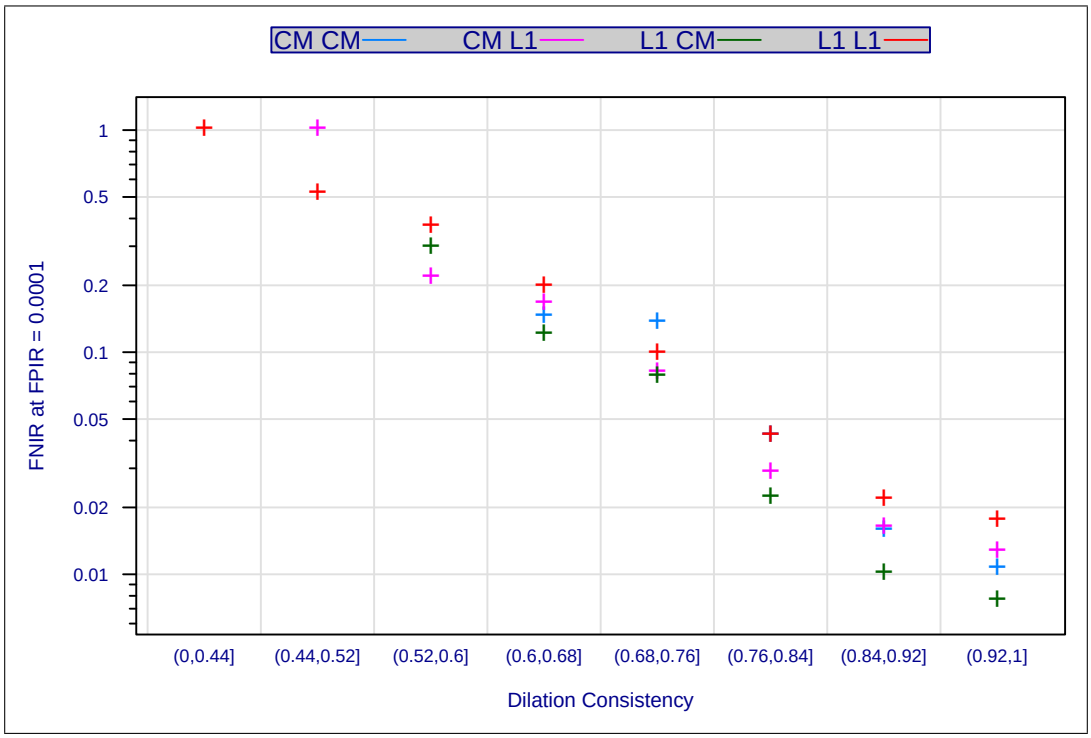

(b) Mean, L1 and CM images

Figure 382: Miss rate statistics for implementation U11B executing mate searches in an enrolled population of N = 1.6 million. The figures plots FNIR at FPIR = 0.0001 versus the IREX I metric for dilation consistency $(1 - \max(D_1, D_2))/(1 - \min(D_1, D_2))$ where D_i is pupil-iris radius ratio, and the subscripts refer to the mated enrollment and search image. The pathologically compressed 330x330 images are excluded from this analysis. The second figure breaks out dilation effects for interoperating camera pairs, CM and L1.

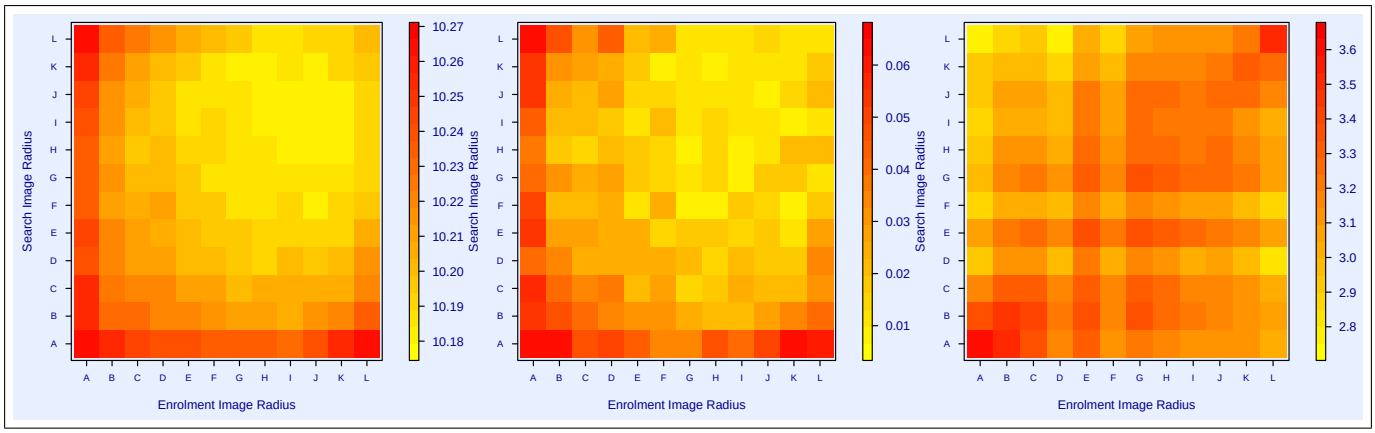

(a) Iris radius: Dis-similarity Score, Miss Rate, $\log_{10}(1+\text{Count})$

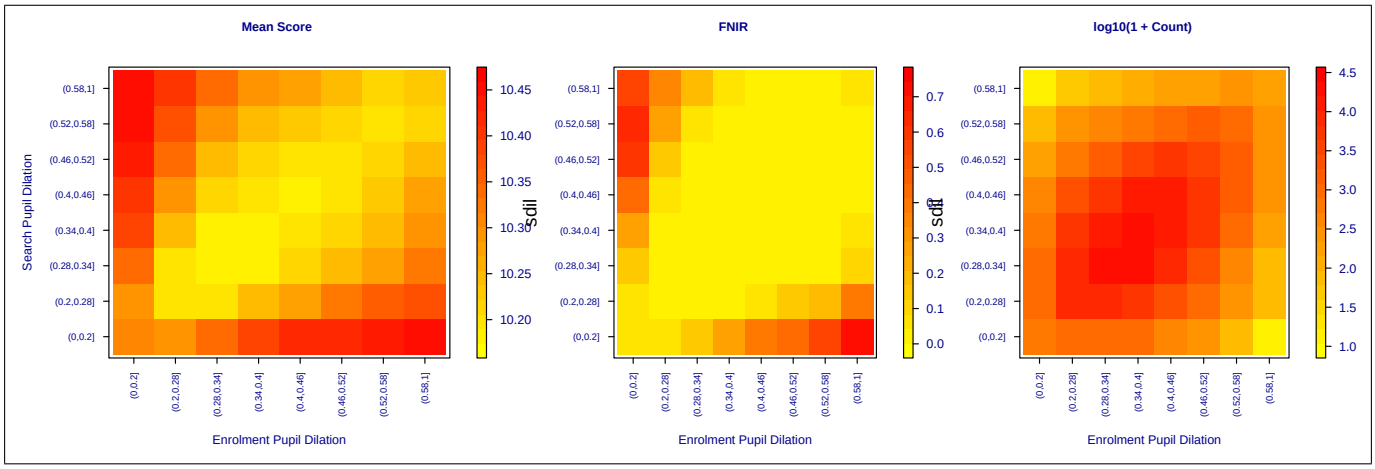

(b) Mate Dilation: Dis-similarity Score, Miss Rate, $\log_{10}(1+\text{Count})$

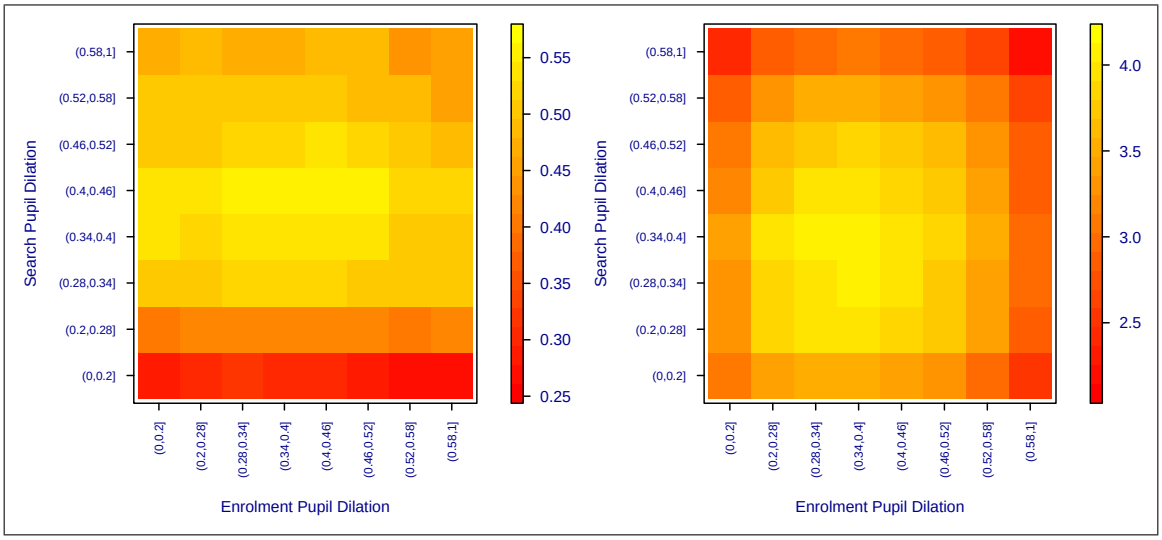

(c) Nonmate Dilation, Dis-similarity Score, Miss Rate, $\log_{10}(1+\text{Count})$

Figure 383: Heatmaps for implementation U12A executing mate searches in an enrolled population of N = 1.6 million. The radius images are binned by into twelve quantiles spanning $[0, 1]$. The dilation values are cut into ranges bounded by: $(0, 0.2, 0.28, 0.34, 0.40, 0.46, 0.52, 0.58, 1)$. The pathologically compressed 330x330 images are excluded from this analysis.

Heatmaps for implementation U12A executing mate searches in an enrolled population of N = 1.6 million.

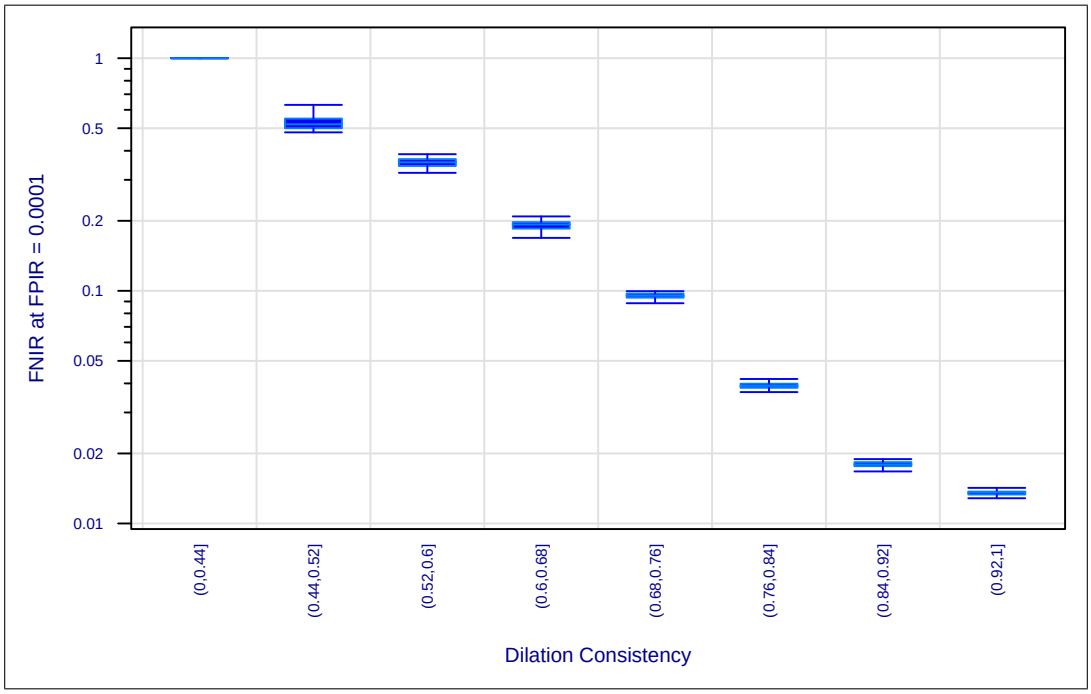

(a) Boxplot, all images

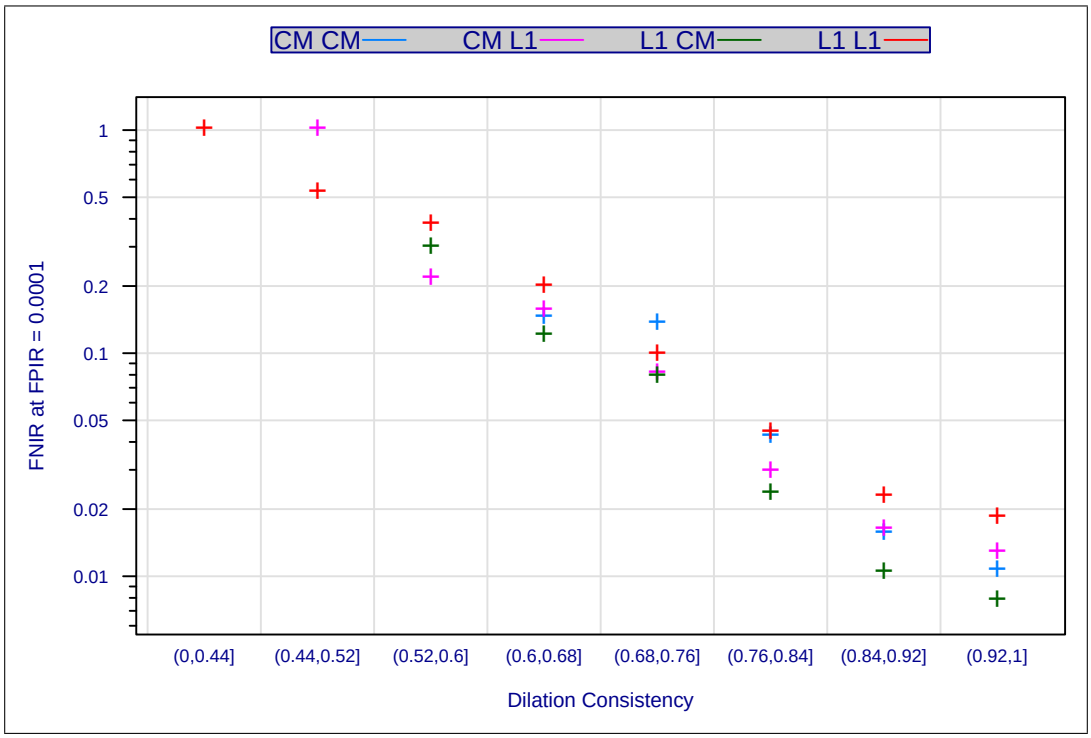

(b) Mean, L1 and CM images

Figure 384: Miss rate statistics for implementation U12A executing mate searches in an enrolled population of N = 1.6 million. The figures plots FNIR at FPIR = 0.0001 versus the IREX I metric for dilation consistency $(1 - \max(D_1, D_2))/(1 - \min(D_1, D_2))$ where D_i is pupil-iris radius ratio, and the subscripts refer to the mated enrollment and search image. The pathologically compressed 330x330 images are excluded from this analysis. The second figure breaks out dilation effects for interoperating camera pairs, CM and L1.

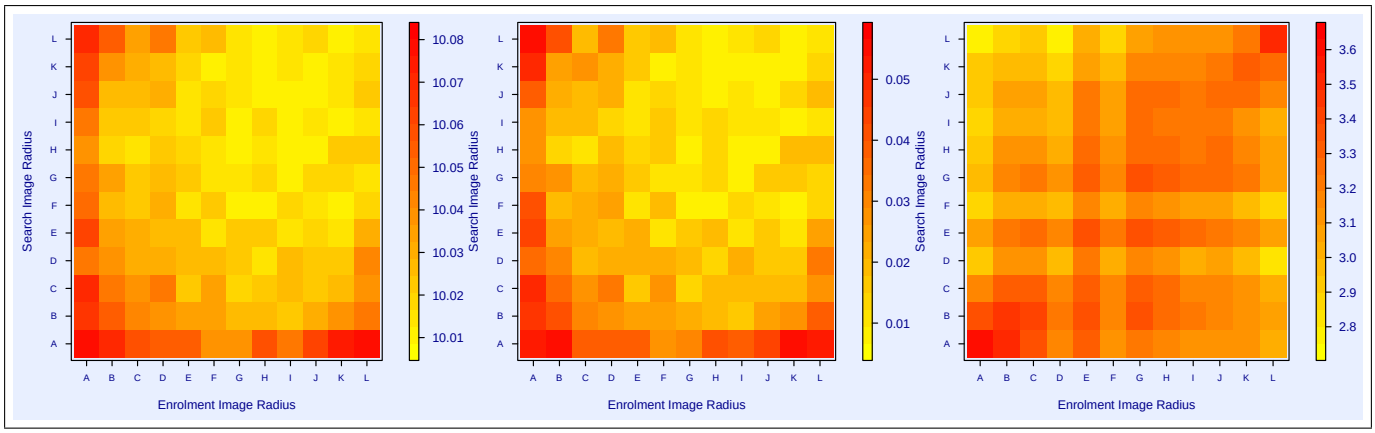

(a) Iris radius: Dis-similarity Score, Miss Rate, $\log_{10}(1+\text{Count})$

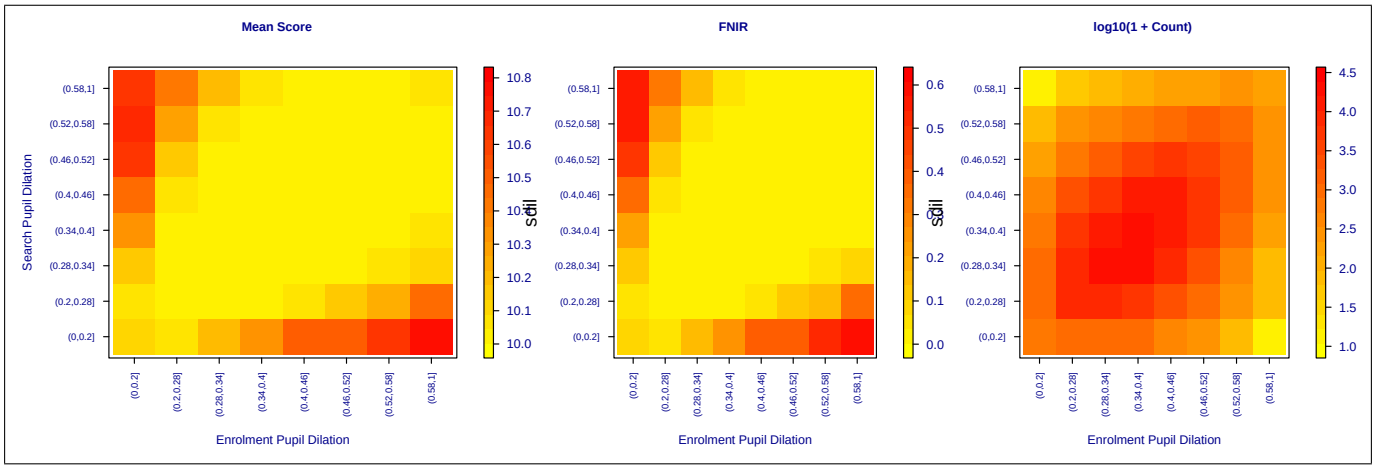

(b) Mate Dilation: Dis-similarity Score, Miss Rate, $\log_{10}(1+\text{Count})$

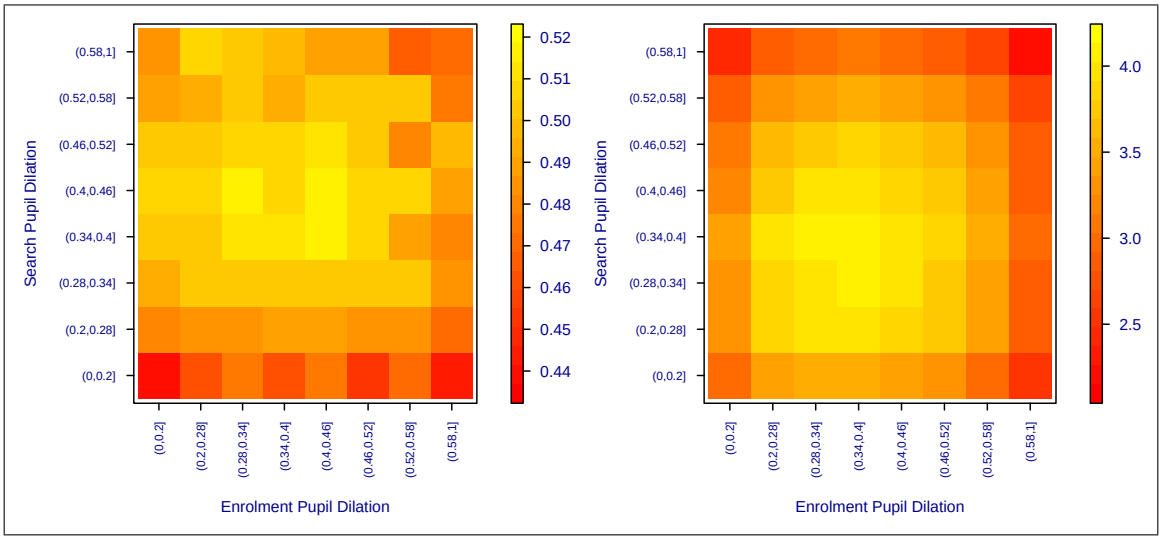

(c) Nonmate Dilation, Dis-similarity Score, Miss Rate, $\log_{10}(1+\text{Count})$

Figure 385: Heatmaps for implementation U12B executing mate searches in an enrolled population of N = 1.6 million. The radius images are binned by into twelve quantiles spanning $[0, 1]$. The dilation values are cut into ranges bounded by: $(0, 0.2, 0.28, 0.34, 0.40, 0.46, 0.52, 0.58, 1)$. The pathologically compressed 330x330 images are excluded from this analysis.

Heatmaps for implementation U12B executing mate searches in an enrolled population of N = 1.6 million.

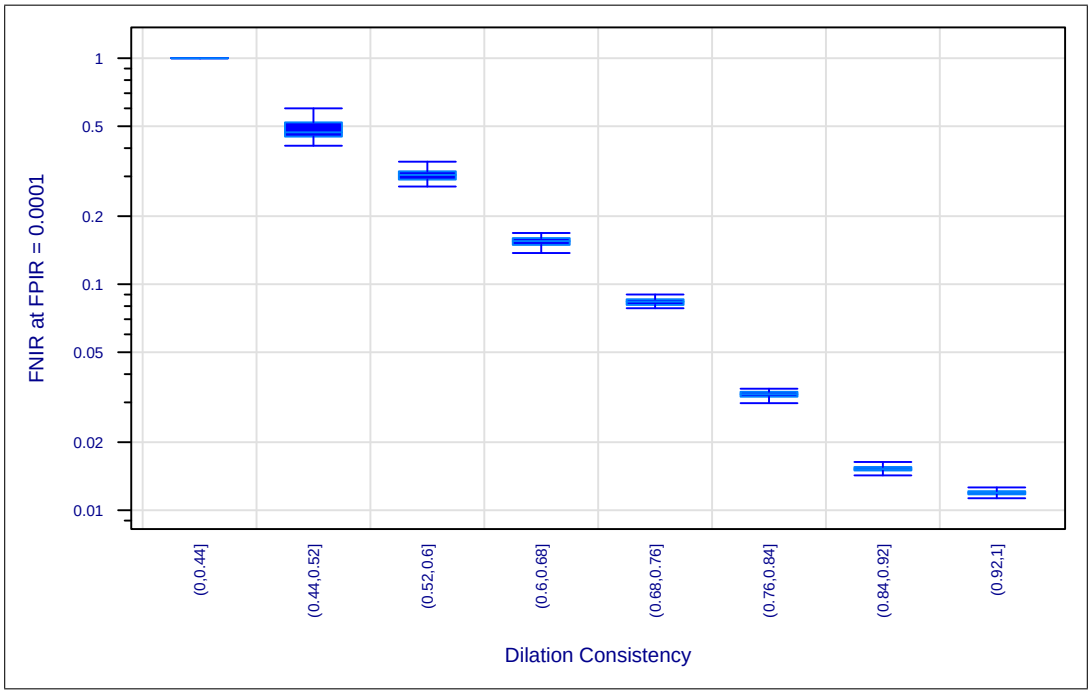

(a) Boxplot, all images

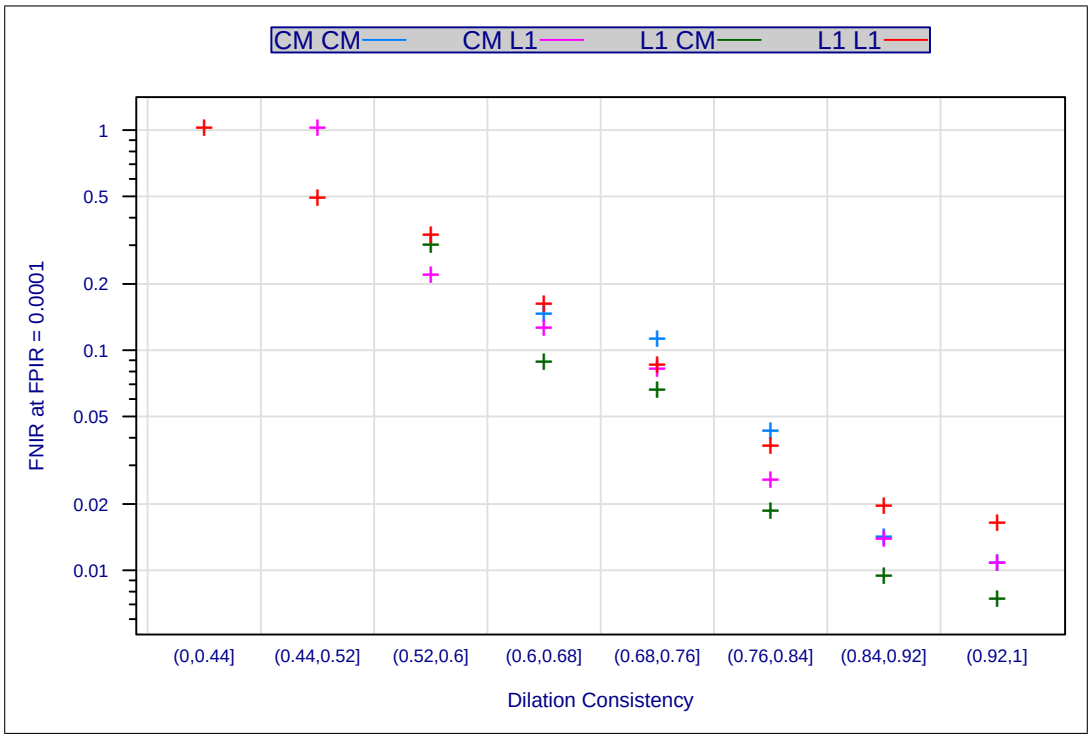

(b) Mean, L1 and CM images

Figure 386: Miss rate statistics for implementation U12B executing mate searches in an enrolled population of N = 1.6 million. The figures plots FNIR at FPIR = 0.0001 versus the IREX I metric for dilation consistency $(1 - \max(D_1, D_2))/(1 - \min(D_1, D_2))$ where D_i is pupil-iris radius ratio, and the subscripts refer to the mated enrollment and search image. The pathologically compressed 330x330 images are excluded from this analysis. The second figure breaks out dilation effects for interoperating camera pairs, CM and L1.

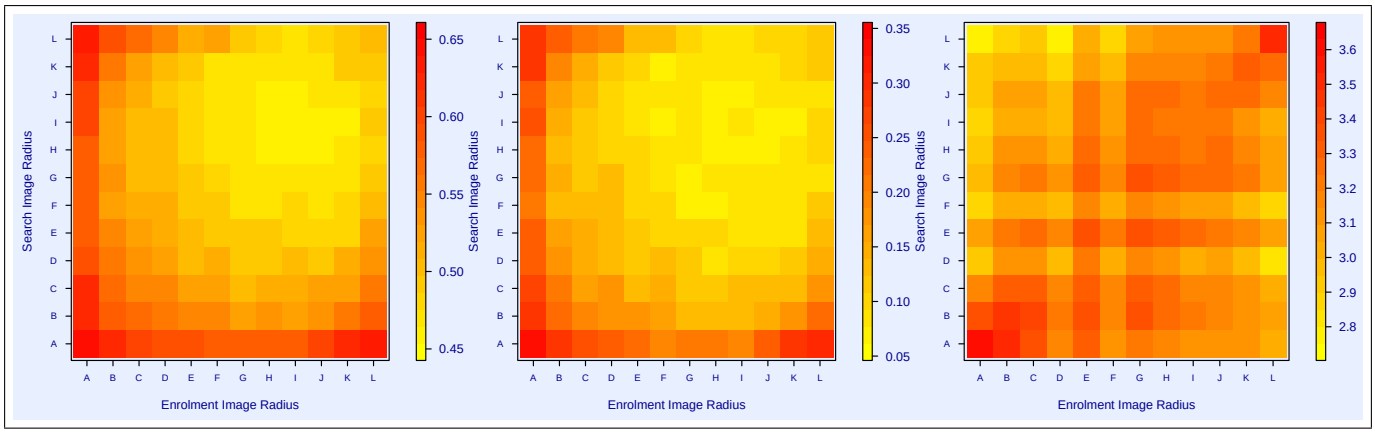

(a) Iris radius: Dis-similarity Score, Miss Rate, $\log_{10}(1+\text{Count})$

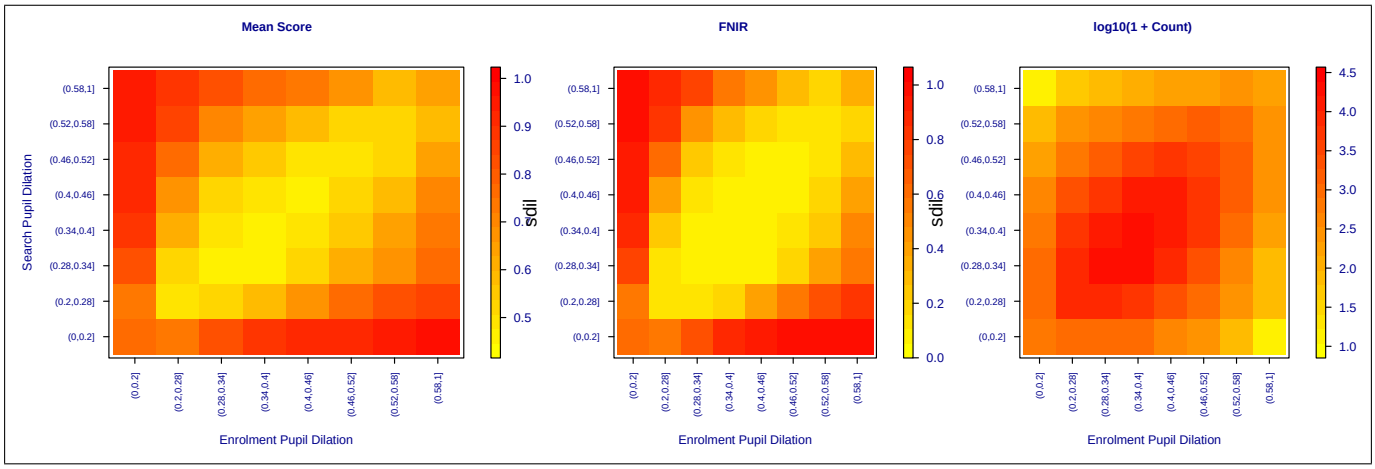

(b) Mate Dilation: Dis-similarity Score, Miss Rate, $\log_{10}(1+\text{Count})$

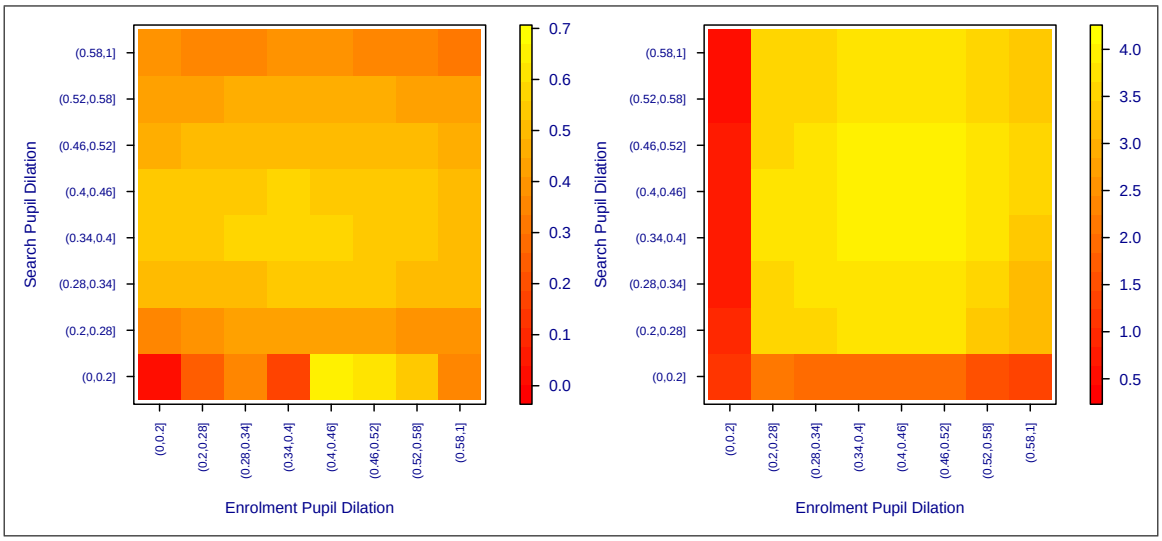

(c) Nonmate Dilation, Dis-similarity Score, Miss Rate, $\log_{10}(1+\text{Count})$

Figure 387: Heatmaps for implementation V01A executing mate searches in an enrolled population of N = 1.6 million. The radius images are binned by into twelve quantiles spanning $[0, 1]$. The dilation values are cut into ranges bounded by: $(0, 0.2, 0.28, 0.34, 0.40, 0.46, 0.52, 0.58, 1)$. The pathologically compressed 330x330 images are excluded from this analysis.

Heatmaps for implementation V01A executing mate searches in an enrolled population of N = 1.6 million.

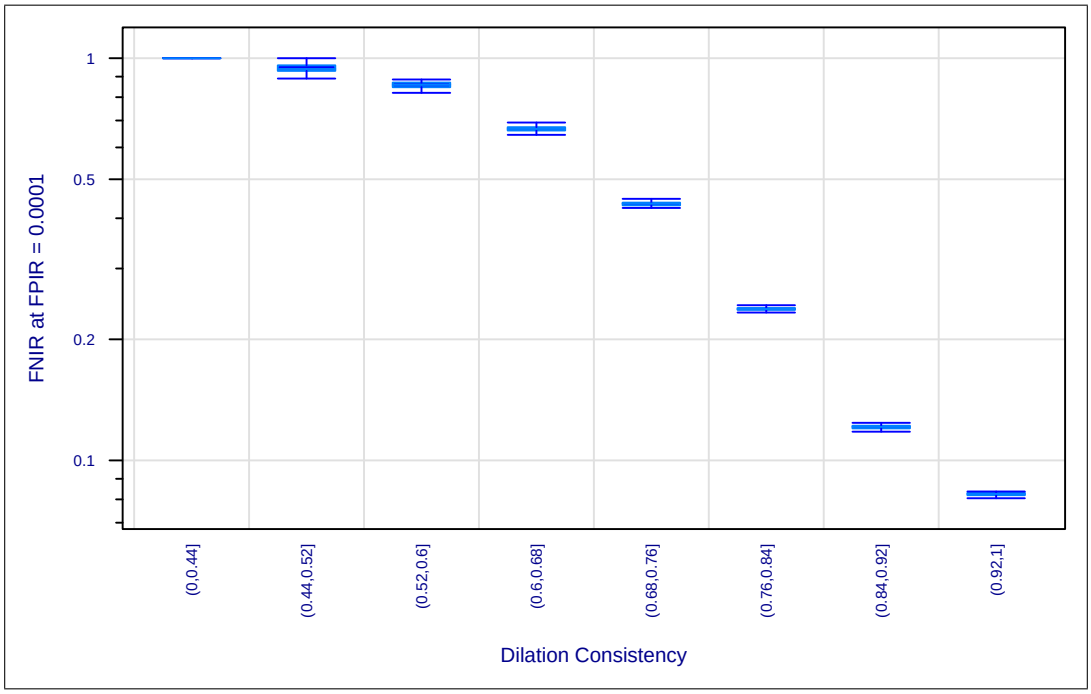

(a) Boxplot, all images

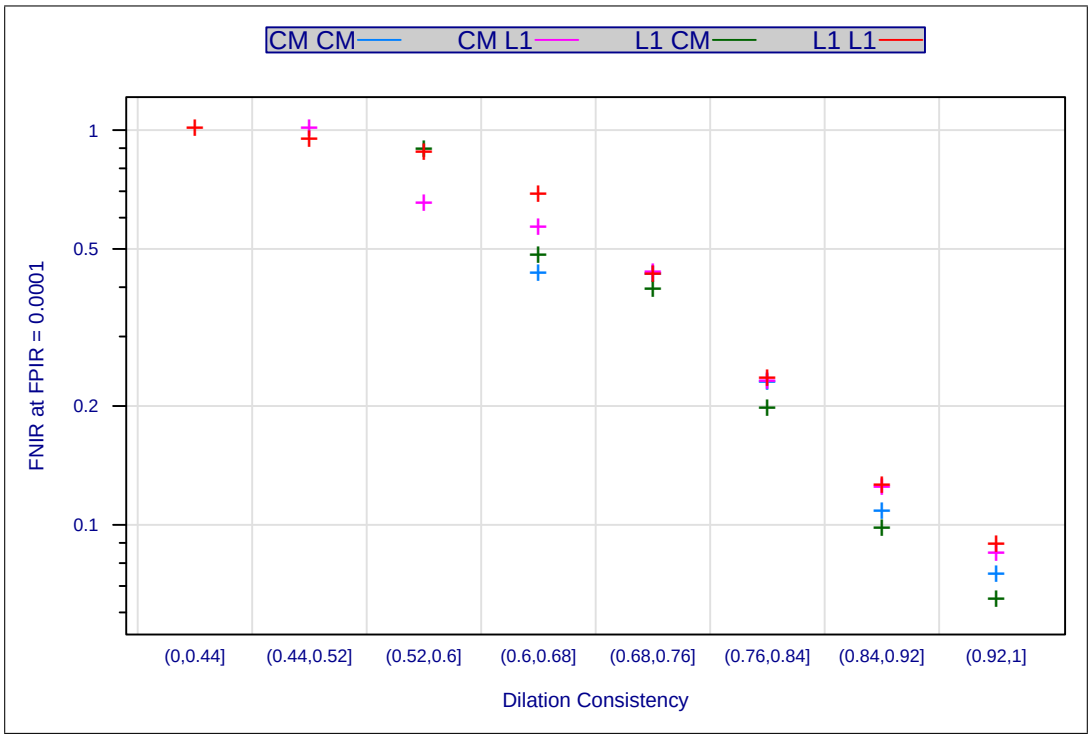

(b) Mean, L1 and CM images

Figure 388: Miss rate statistics for implementation V01A executing mate searches in an enrolled population of N = 1.6 million. The figures plots FNIR at FPIR = 0.0001 versus the IREX I metric for dilation consistency $(1 - \max(D_1, D_2))/(1 - \min(D_1, D_2))$ where D_i is pupil-iris radius ratio, and the subscripts refer to the mated enrollment and search image. The pathologically compressed 330x330 images are excluded from this analysis. The second figure breaks out dilation effects for interoperating camera pairs, CM and L1.

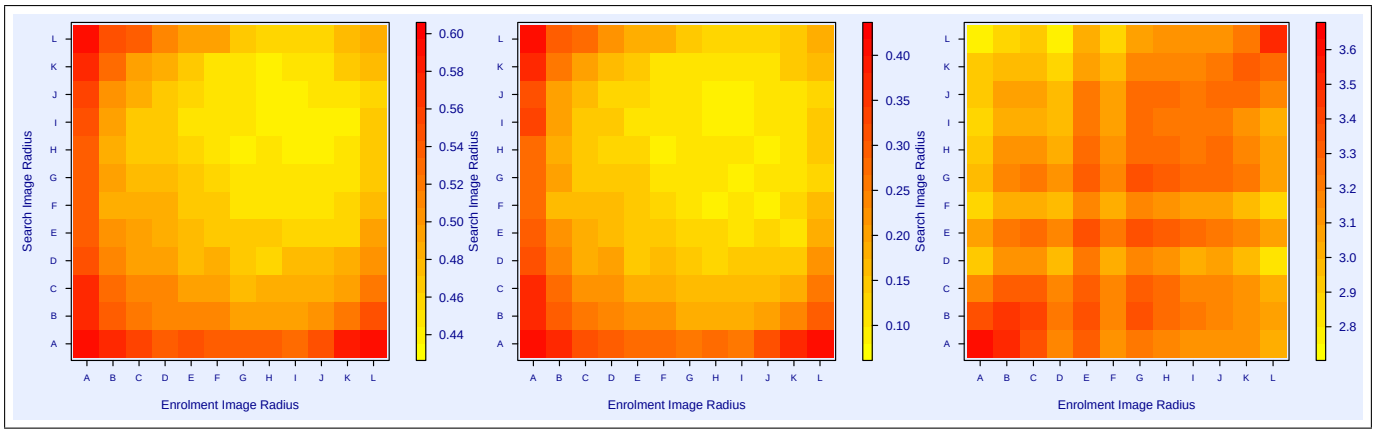

(a) Iris radius: Dis-similarity Score, Miss Rate, $\log_{10}(1+\text{Count})$

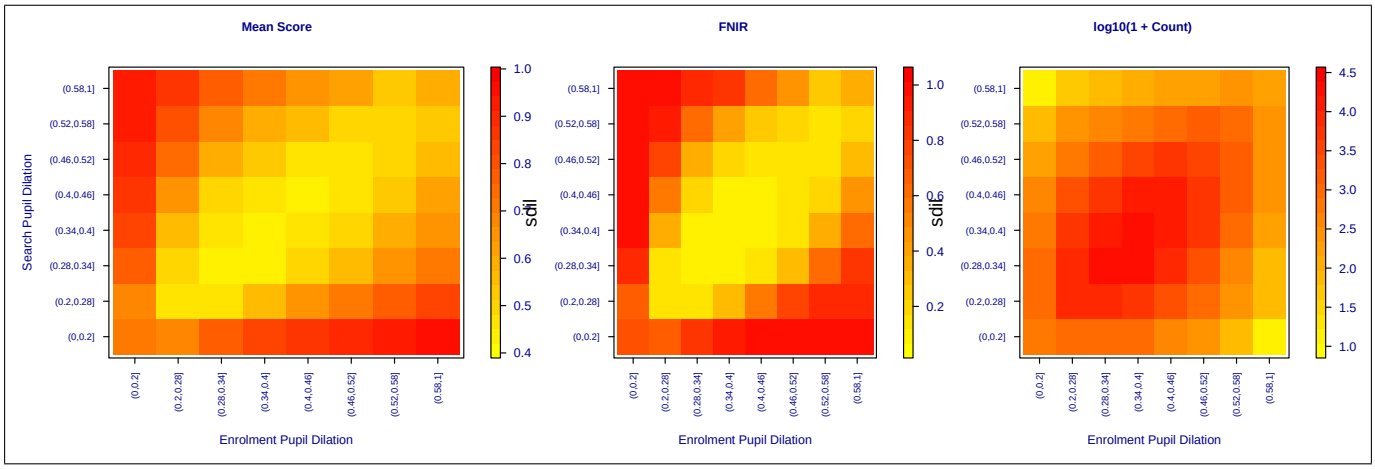

(b) Mate Dilation: Dis-similarity Score, Miss Rate, $\log_{10}(1+\text{Count})$

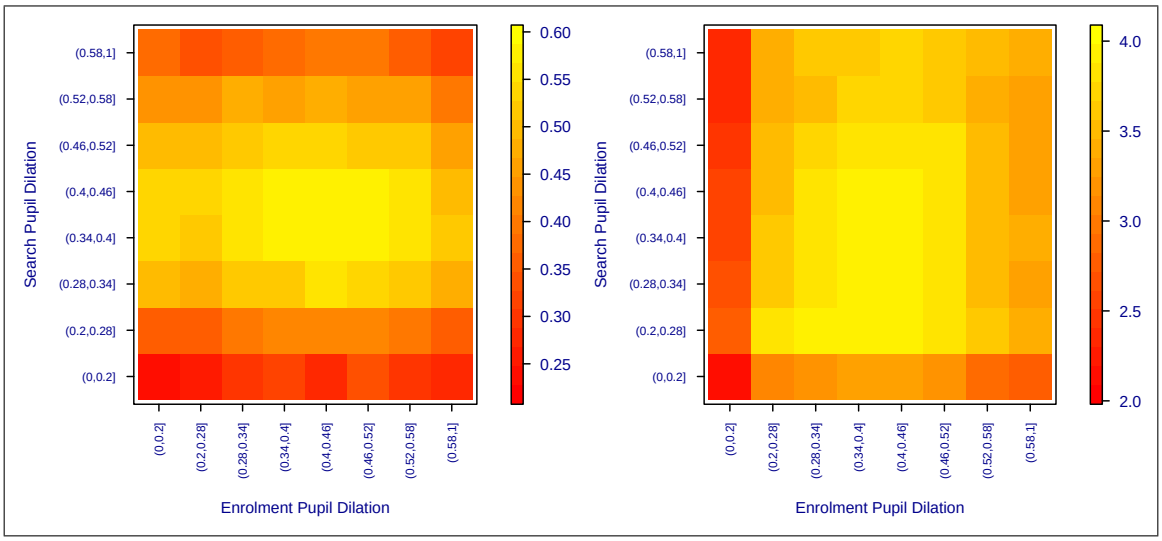

(c) Nonmate Dilation, Dis-similarity Score, Miss Rate, $\log_{10}(1+\text{Count})$

Figure 389: Heatmaps for implementation V02A executing mate searches in an enrolled population of N = 1.6 million. The radius images are binned by into twelve quantiles spanning $[0, 1]$. The dilation values are cut into ranges bounded by: $(0, 0.2, 0.28, 0.34, 0.40, 0.46, 0.52, 0.58, 1)$. The pathologically compressed 330x330 images are excluded from this analysis.

Heatmaps for implementation V02A executing mate searches in an enrolled population of N = 1.6 million.

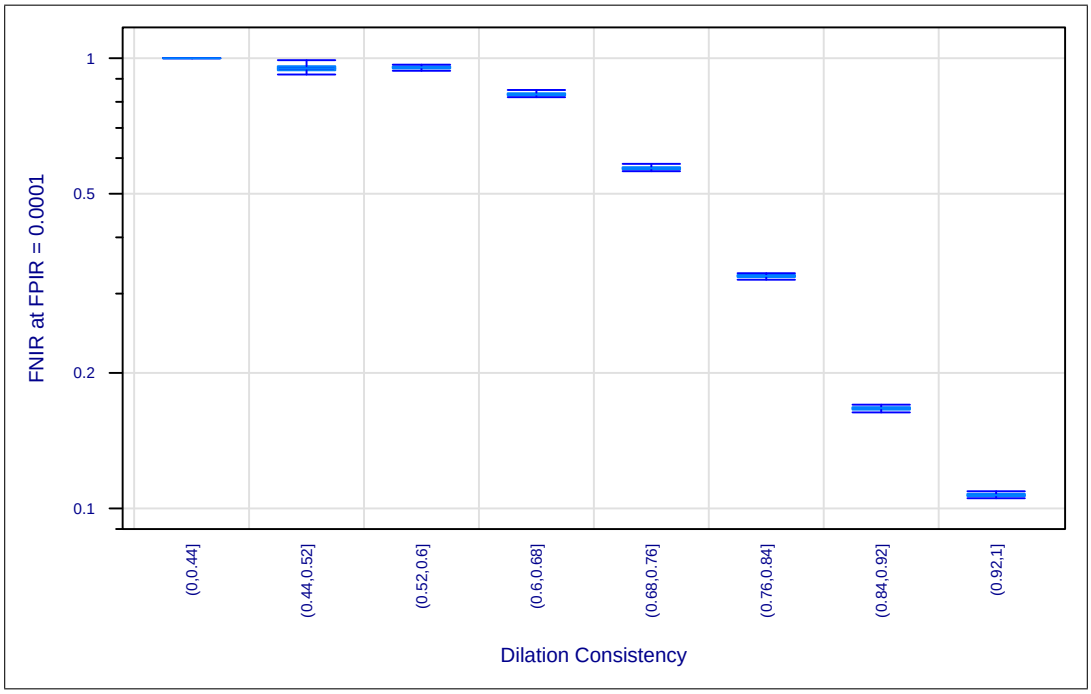

(a) Boxplot, all images

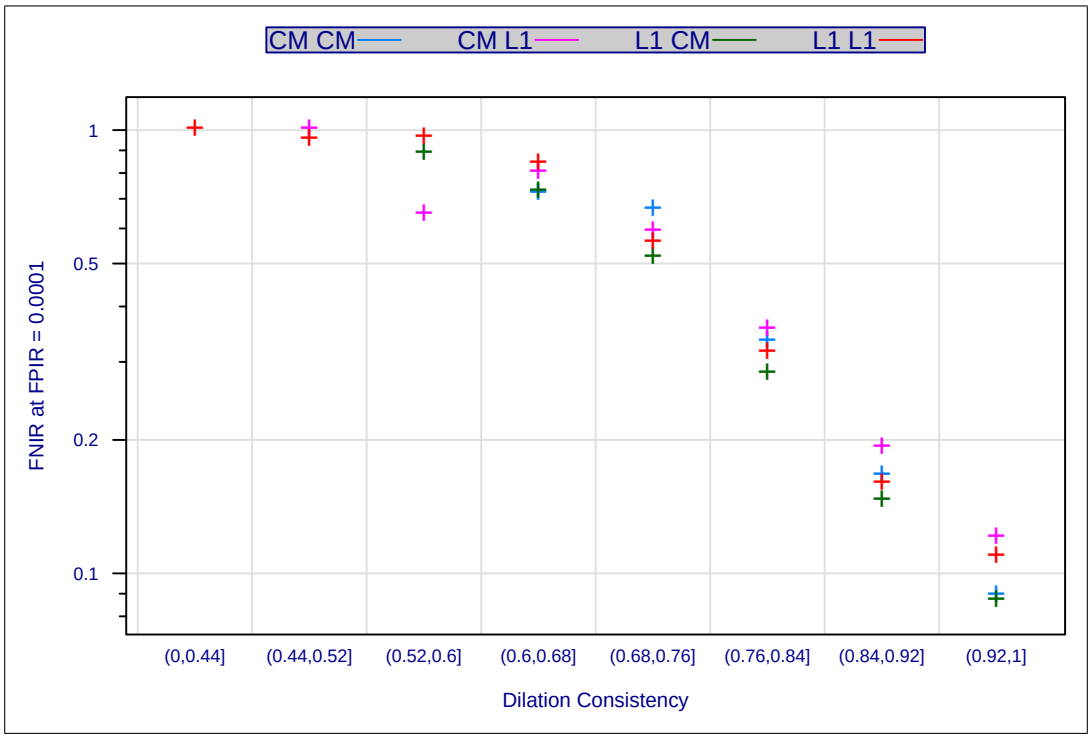

(b) Mean, L1 and CM images

Figure 390: Miss rate statistics for implementation V02A executing mate searches in an enrolled population of N = 1.6 million. The figures plots FNIR at FPIR = 0.0001 versus the IREX I metric for dilation consistency $(1 - \max(D_1, D_2))/(1 - \min(D_1, D_2))$ where D_i is pupil-iris radius ratio, and the subscripts refer to the mated enrollment and search image. The pathologically compressed 330x330 images are excluded from this analysis. The second figure breaks out dilation effects for interoperating camera pairs, CM and L1.

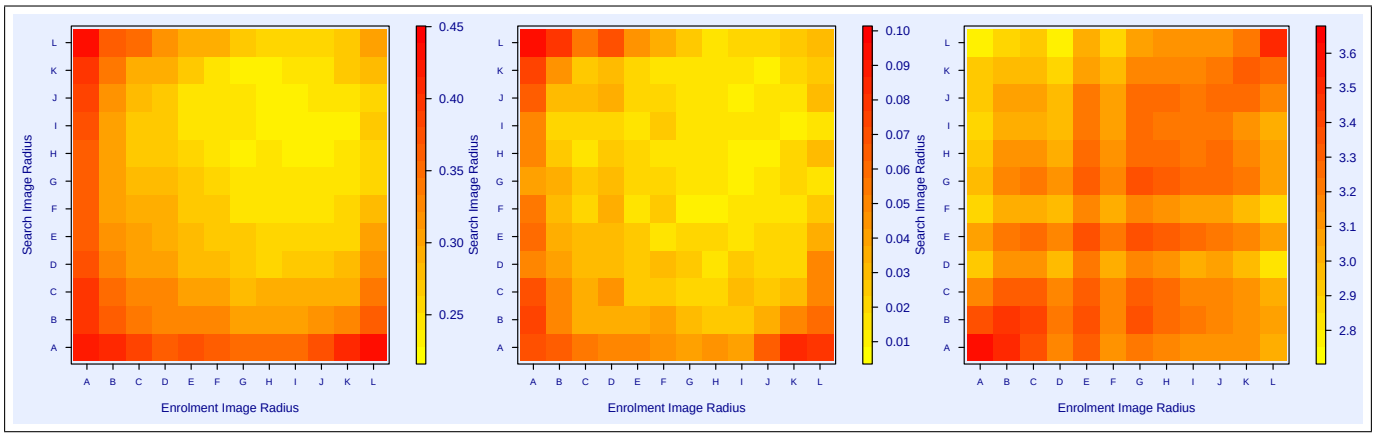

(a) Iris radius: Dis-similarity Score, Miss Rate, $\log_{10}(1+\text{Count})$

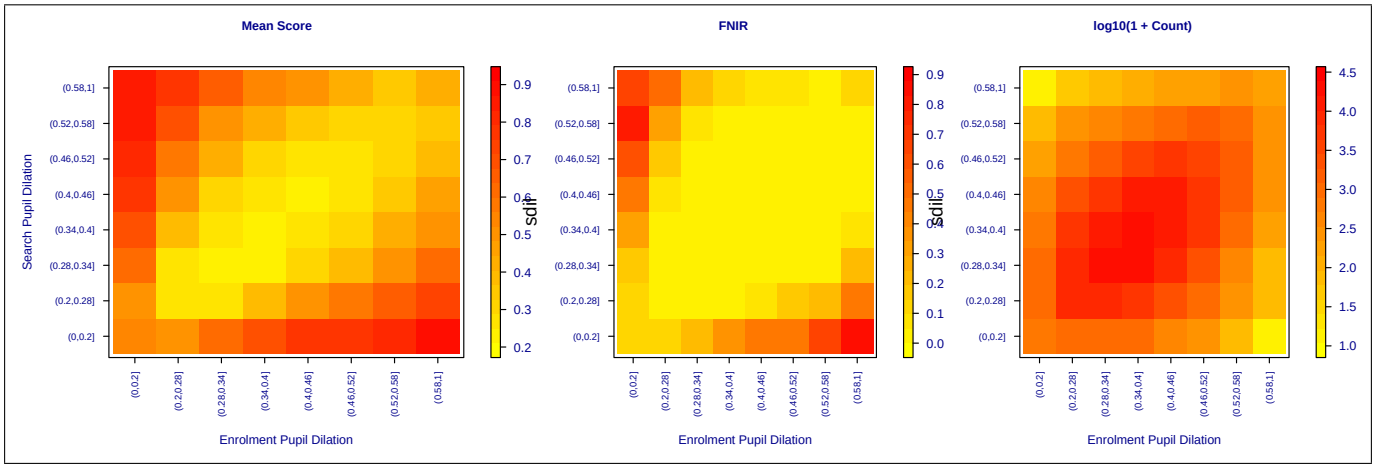

(b) Mate Dilation: Dis-similarity Score, Miss Rate, $\log_{10}(1+\text{Count})$

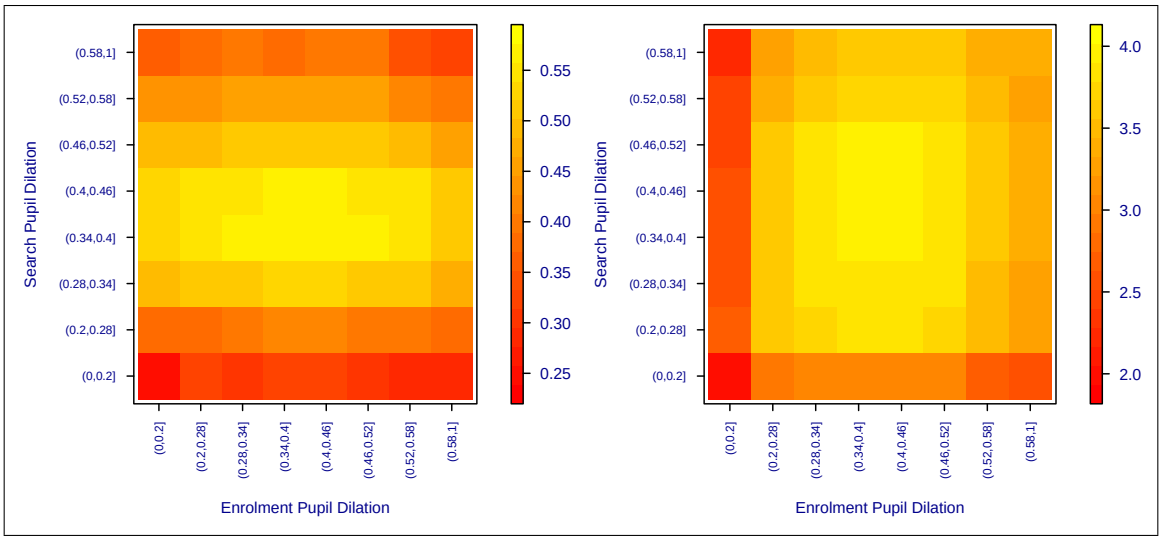

(c) Nonmate Dilation, Dis-similarity Score, Miss Rate, $\log_{10}(1+\text{Count})$

Figure 391: Heatmaps for implementation V03A executing mate searches in an enrolled population of N = 1.6 million. The radius images are binned by into twelve quantiles spanning $[0, 1]$. The dilation values are cut into ranges bounded by: $(0, 0.2, 0.28, 0.34, 0.40, 0.46, 0.52, 0.58, 1)$. The pathologically compressed 330x330 images are excluded from this analysis.

Heatmaps for implementation V03A executing mate searches in an enrolled population of N = 1.6 million.

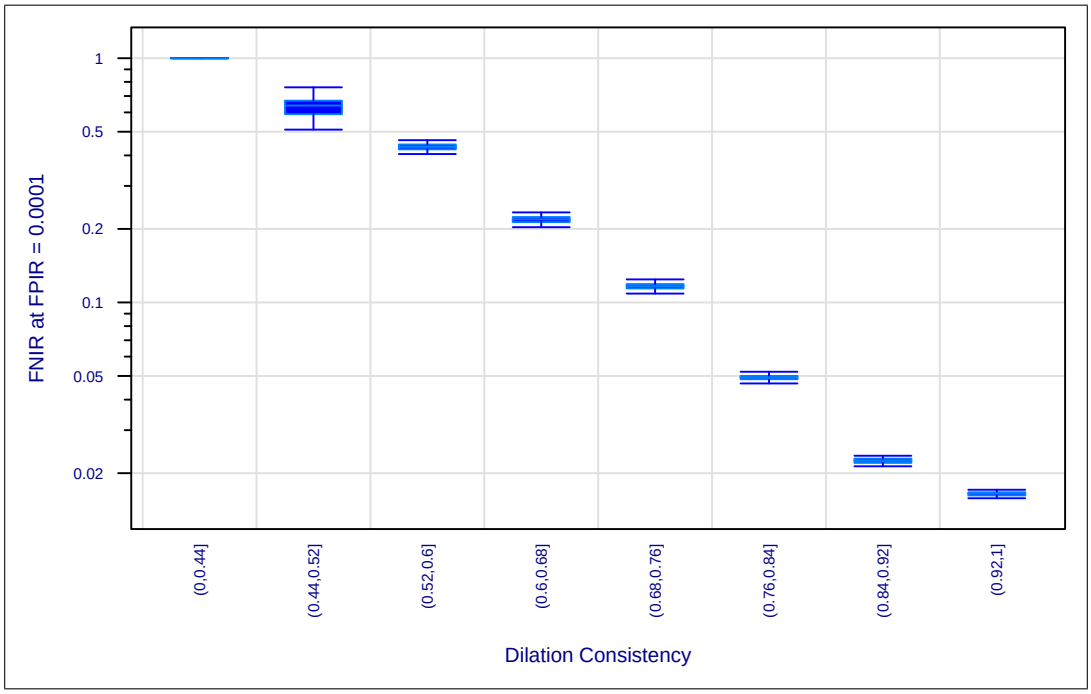

(a) Boxplot, all images

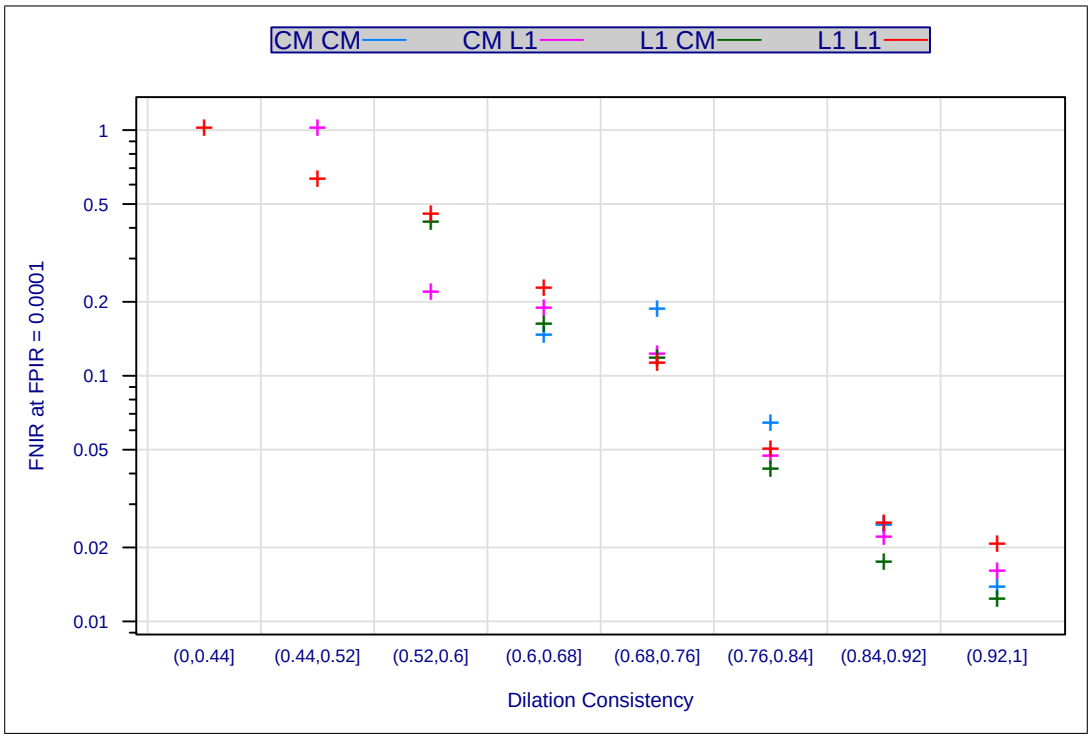

(b) Mean, L1 and CM images

Figure 392: Miss rate statistics for implementation V03A executing mate searches in an enrolled population of N = 1.6 million. The figures plots FNIR at FPIR = 0.0001 versus the IREX I metric for dilation consistency $(1 - \max(D_1, D_2))/(1 - \min(D_1, D_2))$ where D_i is pupil-iris radius ratio, and the subscripts refer to the mated enrollment and search image. The pathologically compressed 330x330 images are excluded from this analysis. The second figure breaks out dilation effects for interoperating camera pairs, CM and L1.

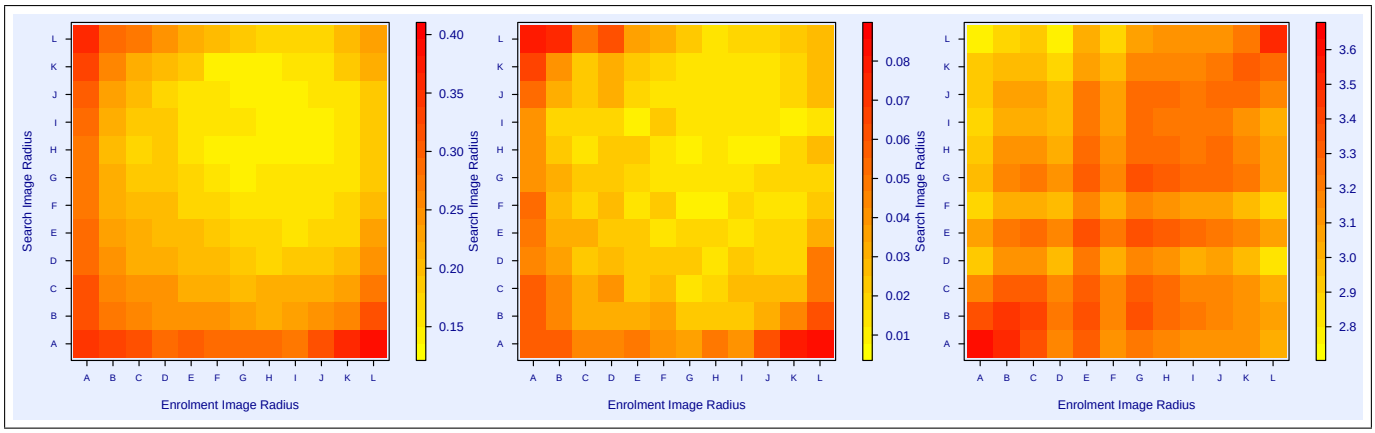

(a) Iris radius: Dis-similarity Score, Miss Rate, $\log_{10}(1+\text{Count})$

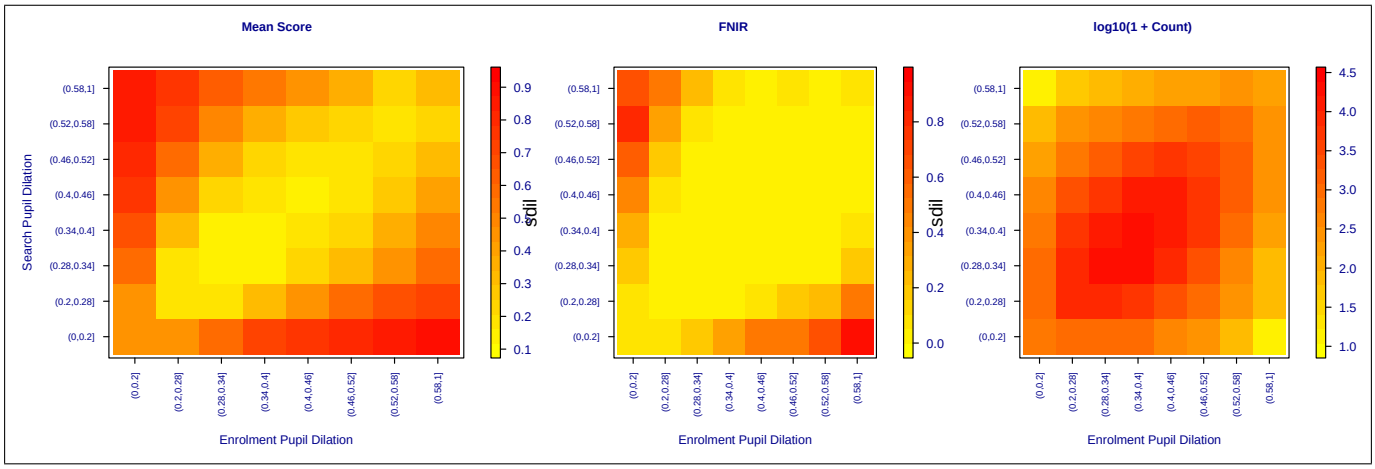

(b) Mate Dilation: Dis-similarity Score, Miss Rate, $\log_{10}(1+\text{Count})$

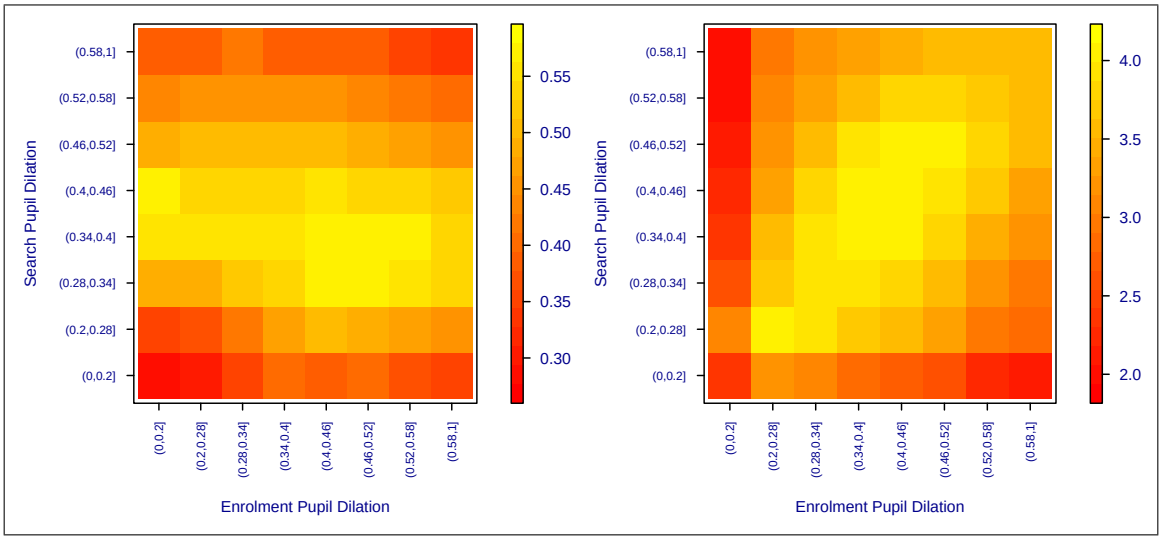

(c) Nonmate Dilation, Dis-similarity Score, Miss Rate, $\log_{10}(1+\text{Count})$

Figure 393: Heatmaps for implementation V03B executing mate searches in an enrolled population of N = 1.6 million. The radius images are binned by into twelve quantiles spanning $[0, 1]$. The dilation values are cut into ranges bounded by: $(0, 0.2, 0.28, 0.34, 0.40, 0.46, 0.52, 0.58, 1)$. The pathologically compressed 330x330 images are excluded from this analysis.

Heatmaps for implementation V03B executing mate searches in an enrolled population of N = 1.6 million.

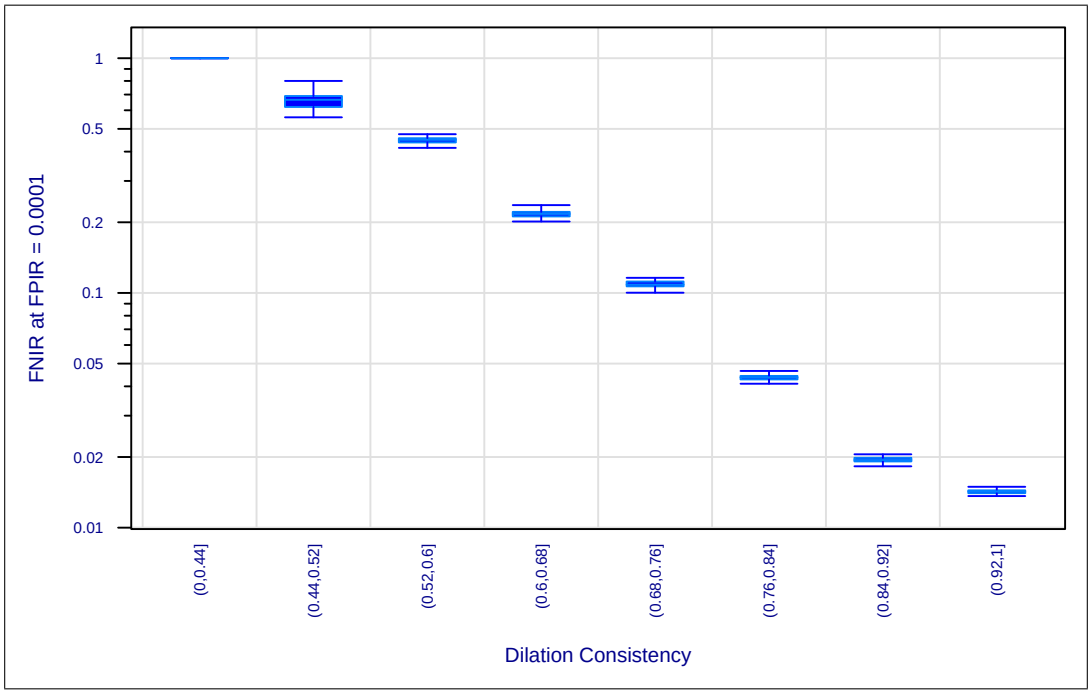

(a) Boxplot, all images

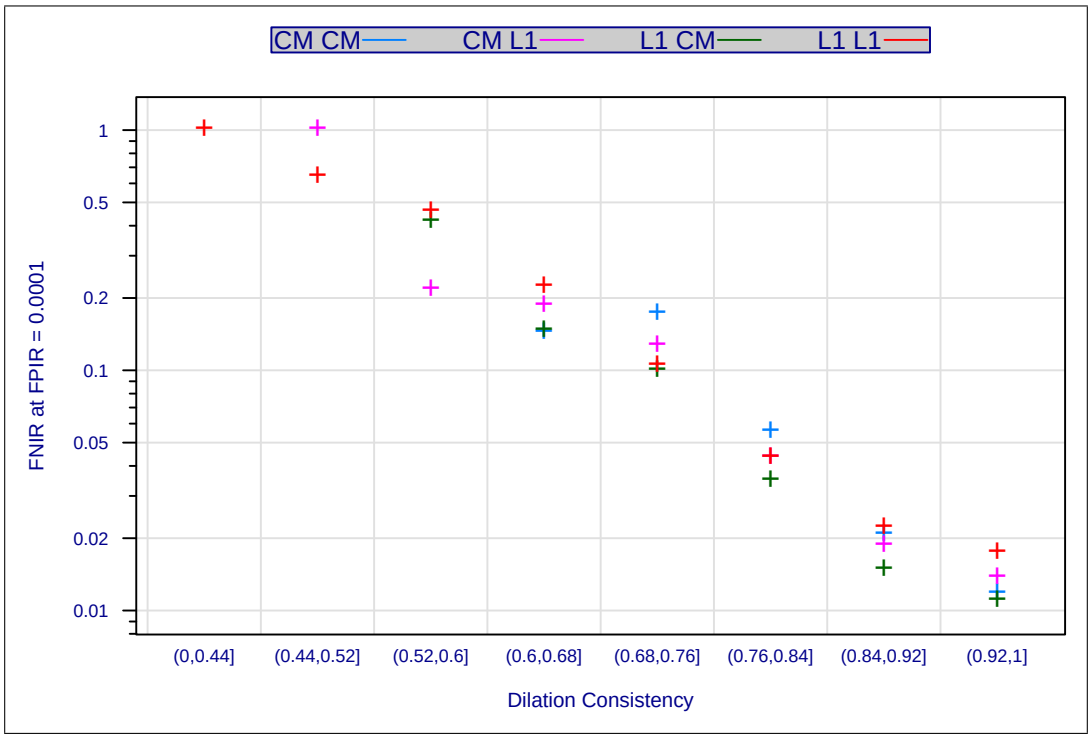

(b) Mean, L1 and CM images

Figure 394: Miss rate statistics for implementation V03B executing mate searches in an enrolled population of N = 1.6 million. The figures plots FNIR at FPIR = 0.0001 versus the IREX I metric for dilation consistency $(1 - \max(D_1, D_2))/(1 - \min(D_1, D_2))$ where D_i is pupil-iris radius ratio, and the subscripts refer to the mated enrollment and search image. The pathologically compressed 330x330 images are excluded from this analysis. The second figure breaks out dilation effects for interoperating camera pairs, CM and L1.

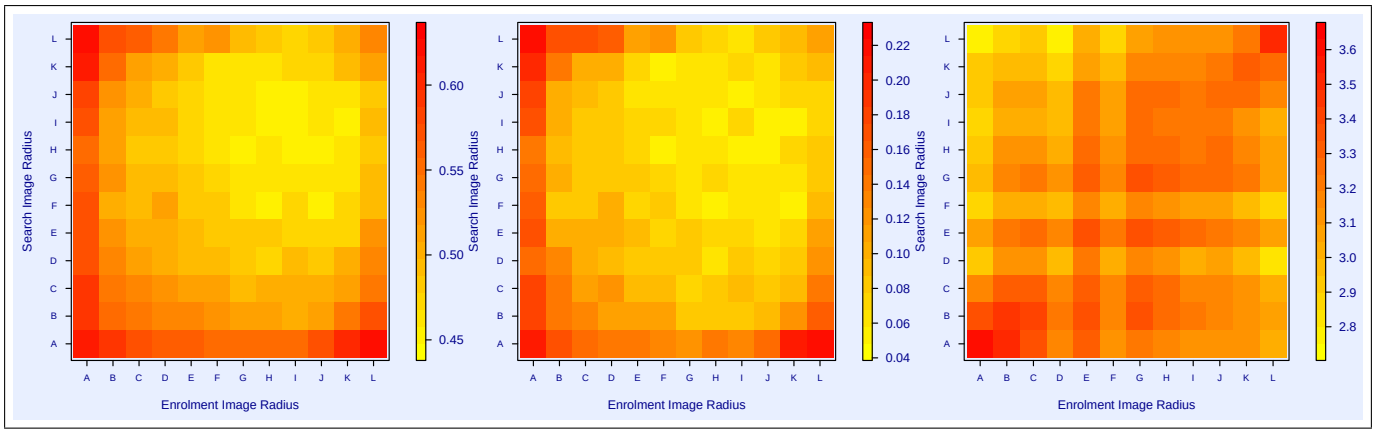

(a) Iris radius: Dis-similarity Score, Miss Rate, $\log_{10}(1+\text{Count})$

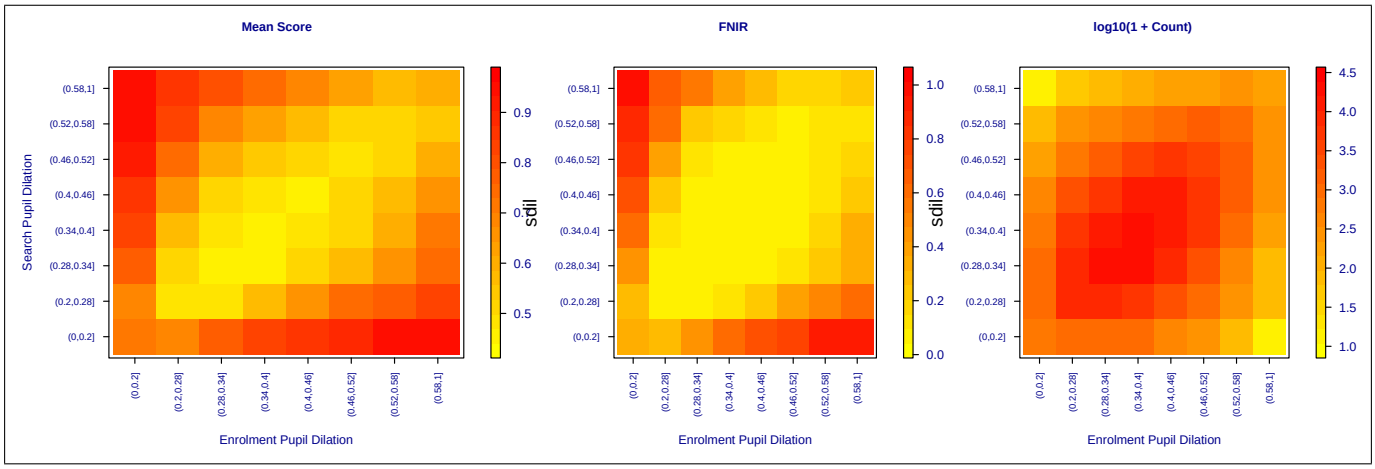

(b) Mate Dilation: Dis-similarity Score, Miss Rate, $\log_{10}(1+\text{Count})$

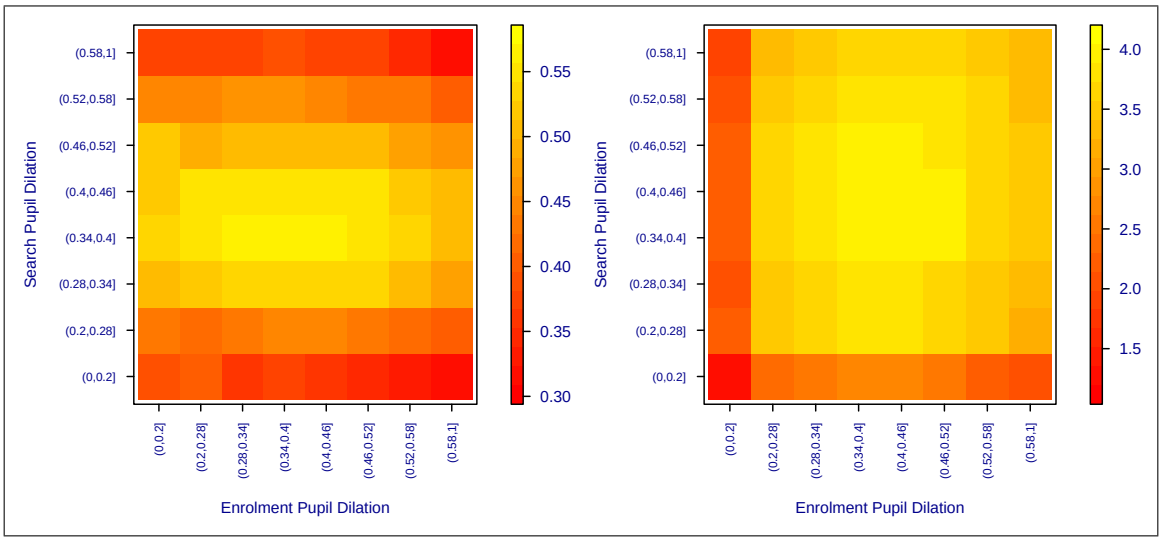

(c) Nonmate Dilation, Dis-similarity Score, Miss Rate, $\log_{10}(1+\text{Count})$

Figure 395: Heatmaps for implementation V04A executing mate searches in an enrolled population of N = 1.6 million. The radius images are binned by into twelve quantiles spanning $[0, 1]$. The dilation values are cut into ranges bounded by: $(0, 0.2, 0.28, 0.34, 0.40, 0.46, 0.52, 0.58, 1)$. The pathologically compressed 330x330 images are excluded from this analysis.

Heatmaps for implementation V04A executing mate searches in an enrolled population of N = 1.6 million.

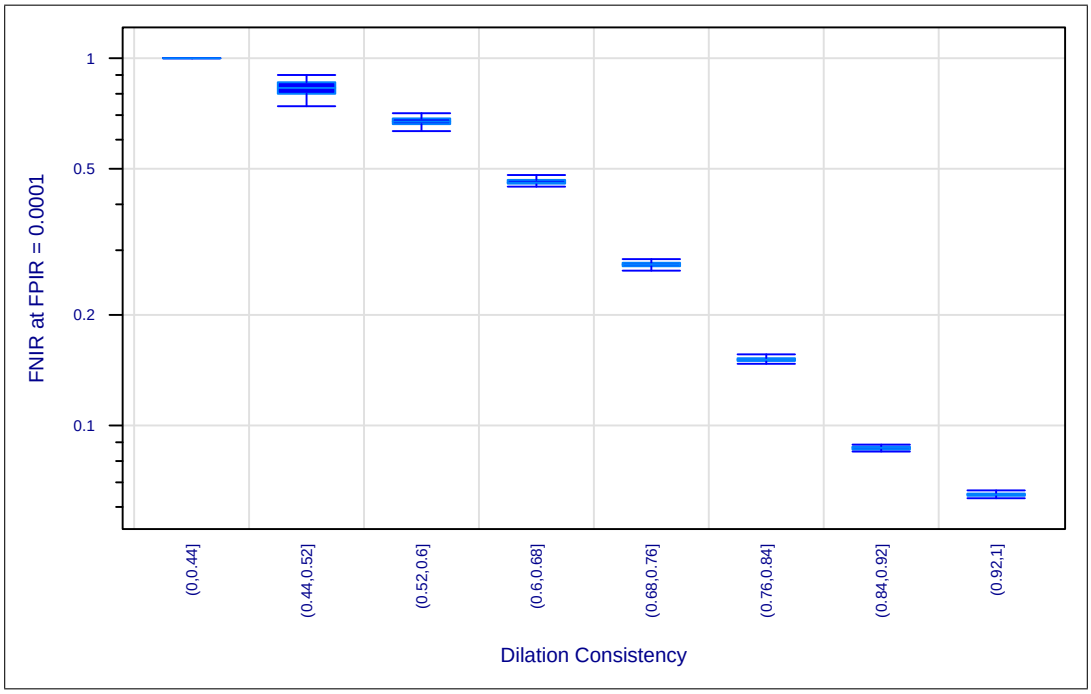

(a) Boxplot, all images

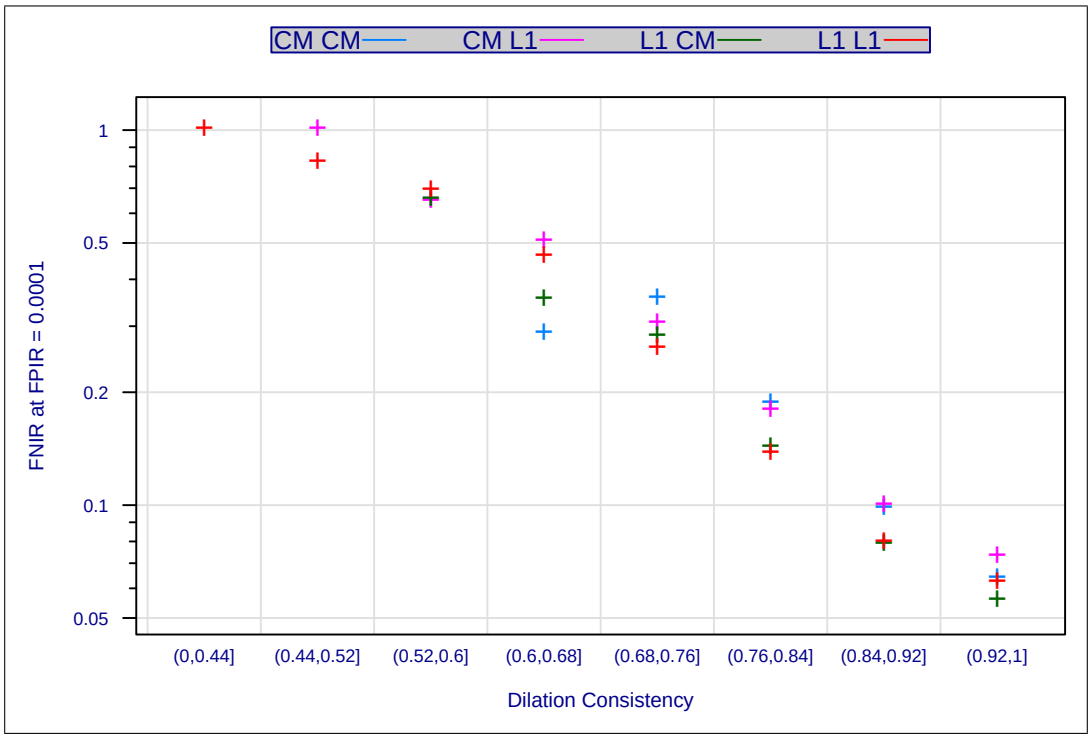

(b) Mean, L1 and CM images

Figure 396: Miss rate statistics for implementation V04A executing mate searches in an enrolled population of N = 1.6 million. The figures plots FNIR at FPIR = 0.0001 versus the IREX I metric for dilation consistency $(1 - \max(D_1, D_2))/(1 - \min(D_1, D_2))$ where D_i is pupil-iris radius ratio, and the subscripts refer to the mated enrollment and search image. The pathologically compressed 330x330 images are excluded from this analysis. The second figure breaks out dilation effects for interoperating camera pairs, CM and L1.

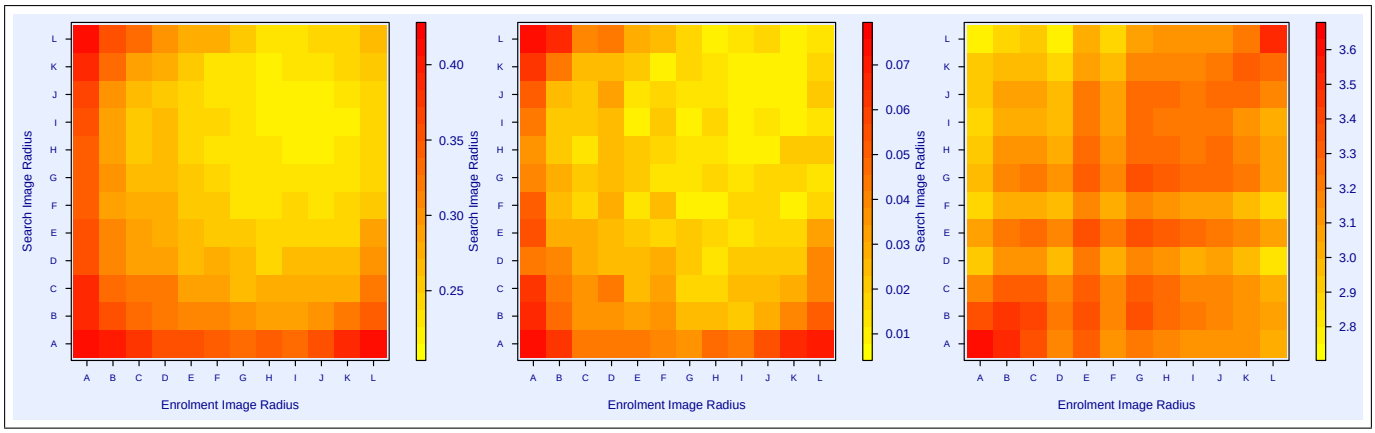

(a) Iris radius: Dis-similarity Score, Miss Rate, $\log_{10}(1+\text{Count})$

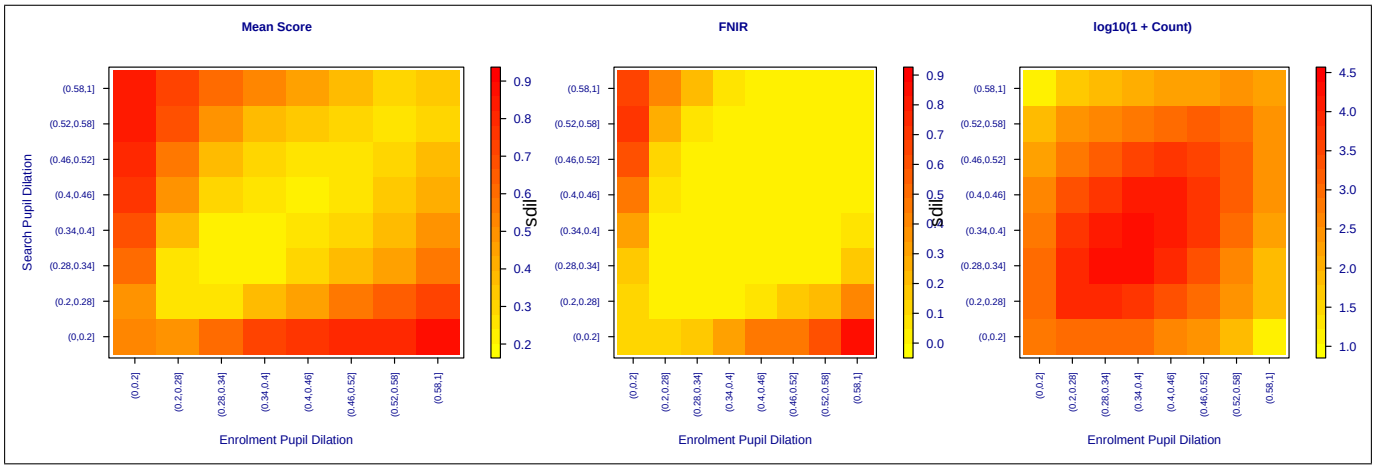

(b) Mate Dilation: Dis-similarity Score, Miss Rate, $\log_{10}(1+\text{Count})$

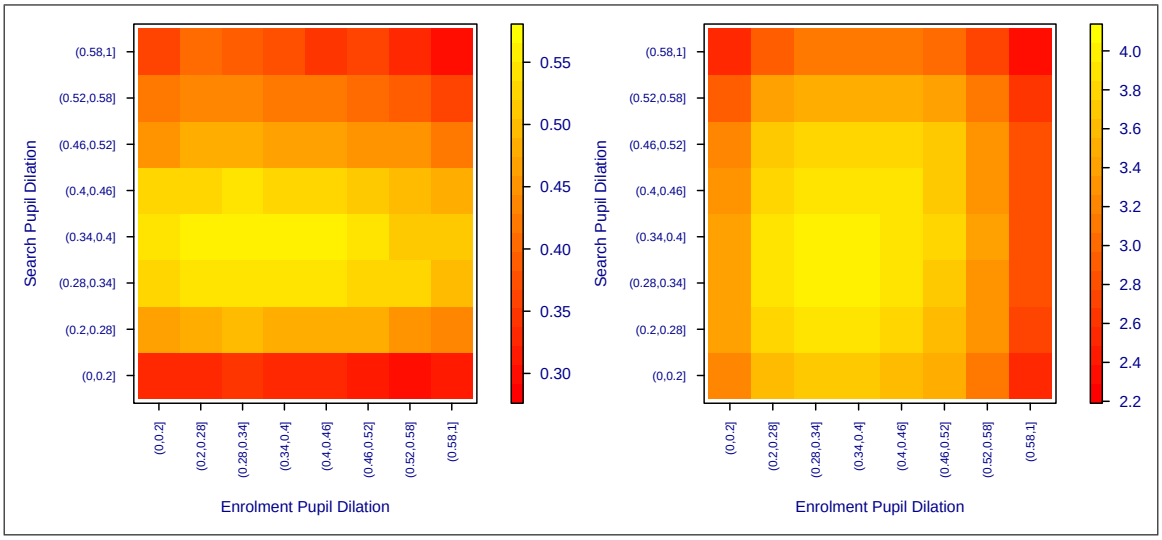

(c) Nonmate Dilation, Dis-similarity Score, Miss Rate, $\log_{10}(1+\text{Count})$

Figure 397: Heatmaps for implementation V11A executing mate searches in an enrolled population of N = 1.6 million. The radius images are binned by into twelve quantiles spanning $[0, 1]$. The dilation values are cut into ranges bounded by: $(0, 0.2, 0.28, 0.34, 0.40, 0.46, 0.52, 0.58, 1)$. The pathologically compressed 330x330 images are excluded from this analysis.

Heatmaps for implementation V11A executing mate searches in an enrolled population of N = 1.6 million.

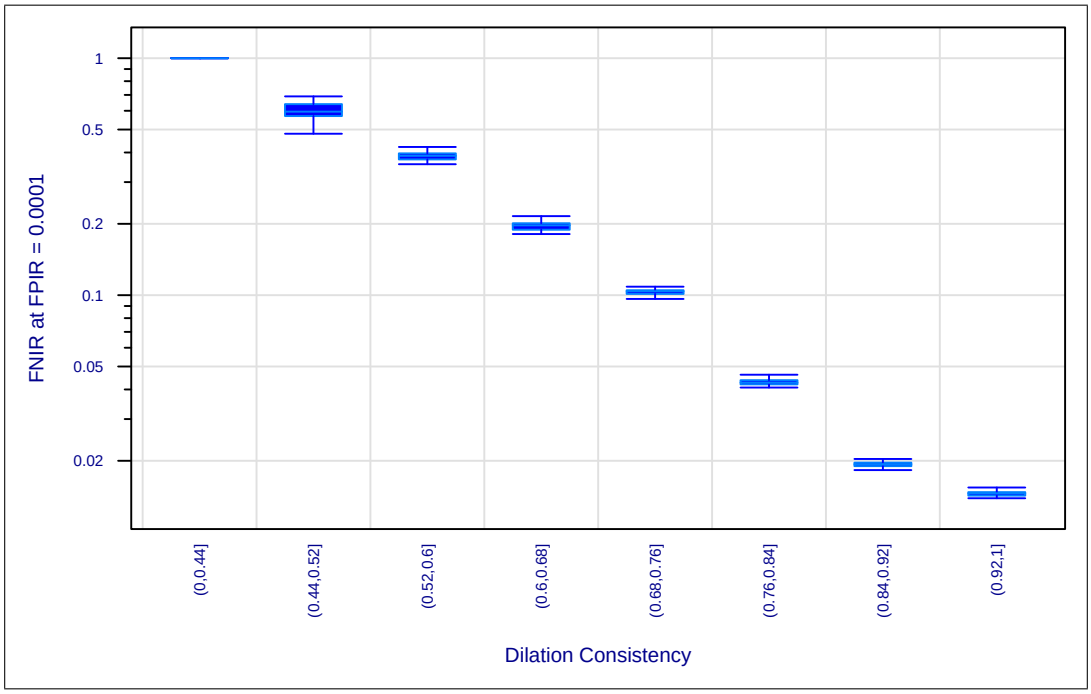

(a) Boxplot, all images

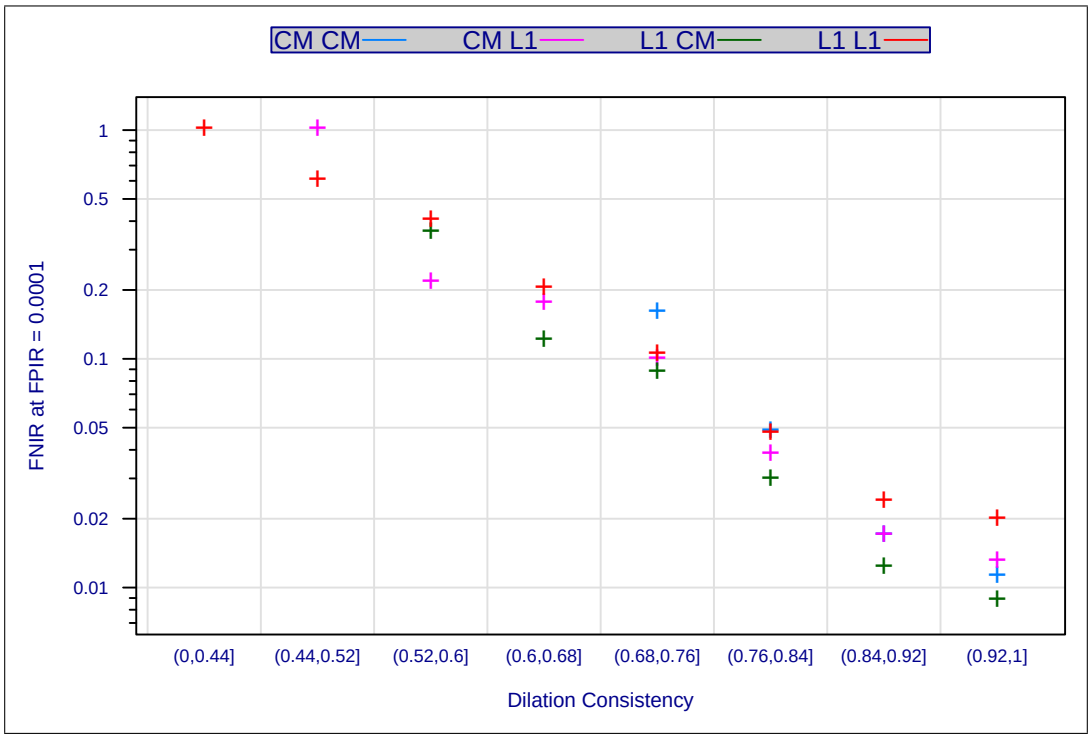

(b) Mean, L1 and CM images

Figure 398: Miss rate statistics for implementation V11A executing mate searches in an enrolled population of N = 1.6 million. The figures plots FNIR at FPIR = 0.0001 versus the IREX I metric for dilation consistency $(1 - \max(D_1, D_2))/(1 - \min(D_1, D_2))$ where D_i is pupil-iris radius ratio, and the subscripts refer to the mated enrollment and search image. The pathologically compressed 330x330 images are excluded from this analysis. The second figure breaks out dilation effects for interoperating camera pairs, CM and L1.

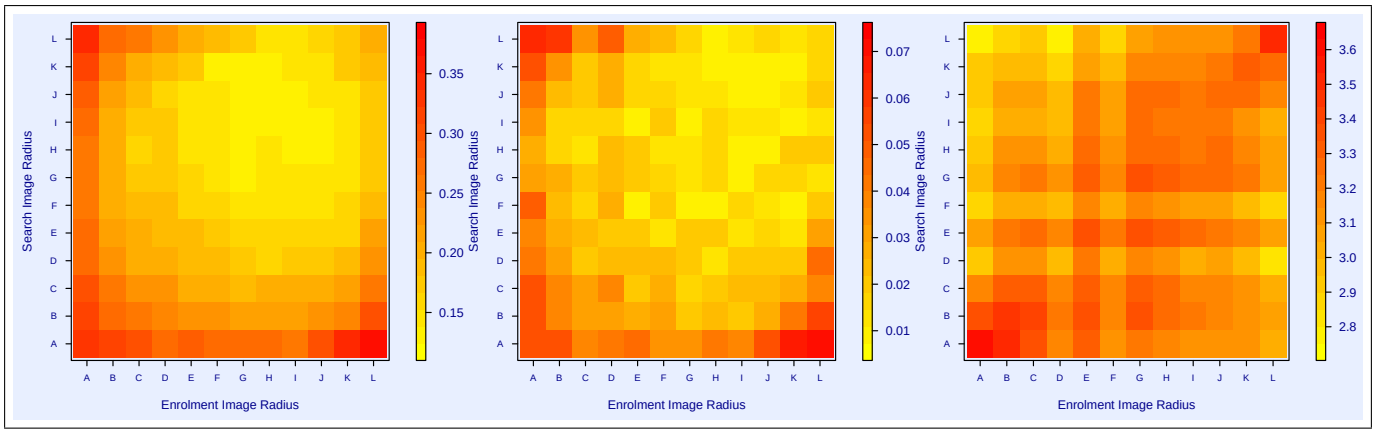

(a) Iris radius: Dis-similarity Score, Miss Rate, $\log_{10}(1+\text{Count})$

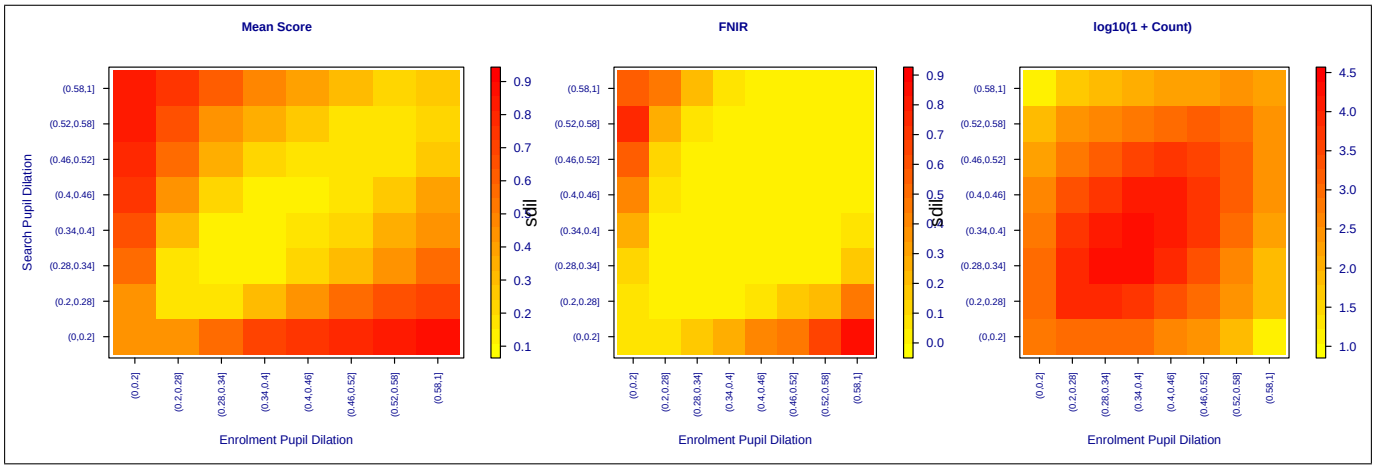

(b) Mate Dilation: Dis-similarity Score, Miss Rate, $\log_{10}(1+\text{Count})$

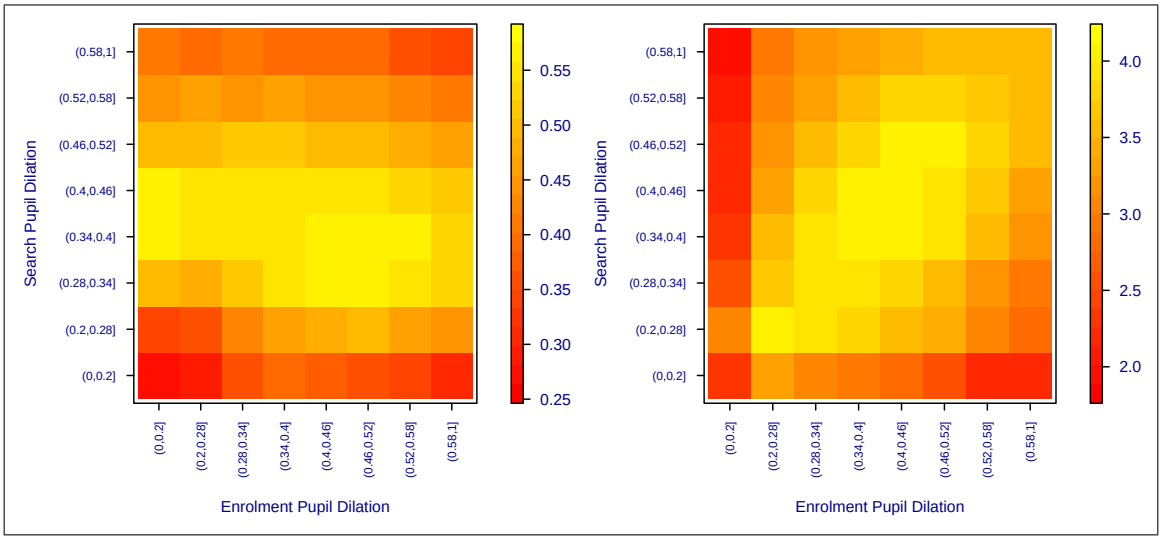

(c) Nonmate Dilation, Dis-similarity Score, Miss Rate, $\log_{10}(1+\text{Count})$

Figure 399: Heatmaps for implementation V11B executing mate searches in an enrolled population of N = 1.6 million. The radius images are binned by into twelve quantiles spanning $[0, 1]$. The dilation values are cut into ranges bounded by: $(0, 0.2, 0.28, 0.34, 0.40, 0.46, 0.52, 0.58, 1)$. The pathologically compressed 330x330 images are excluded from this analysis.

Heatmaps for implementation V11B executing mate searches in an enrolled population of N = 1.6 million.

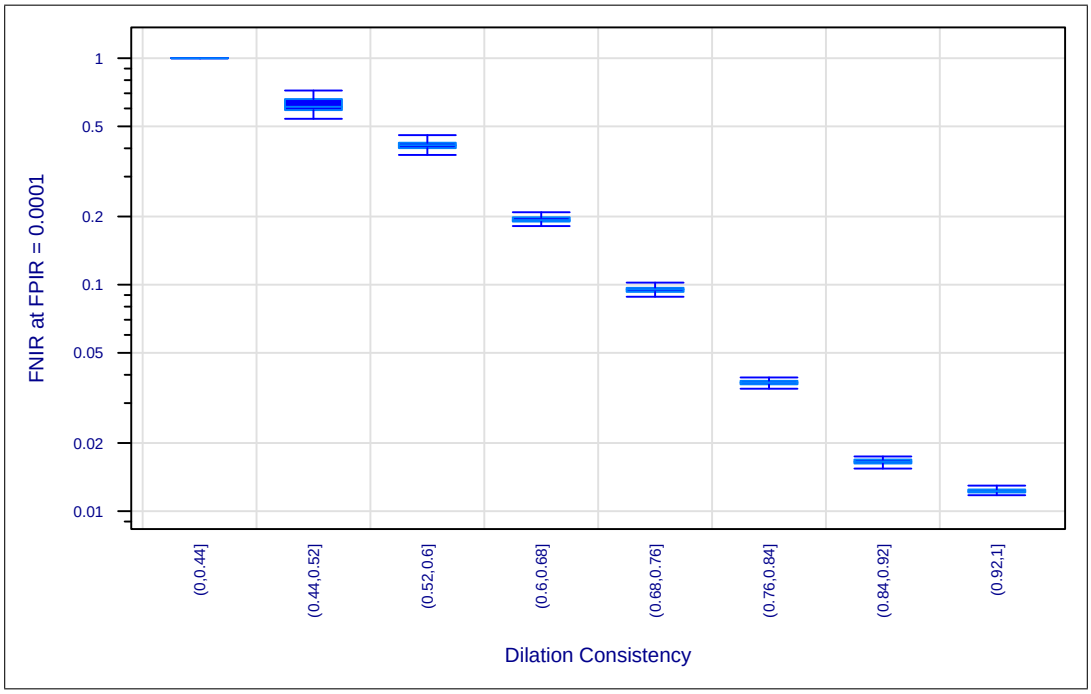

(a) Boxplot, all images

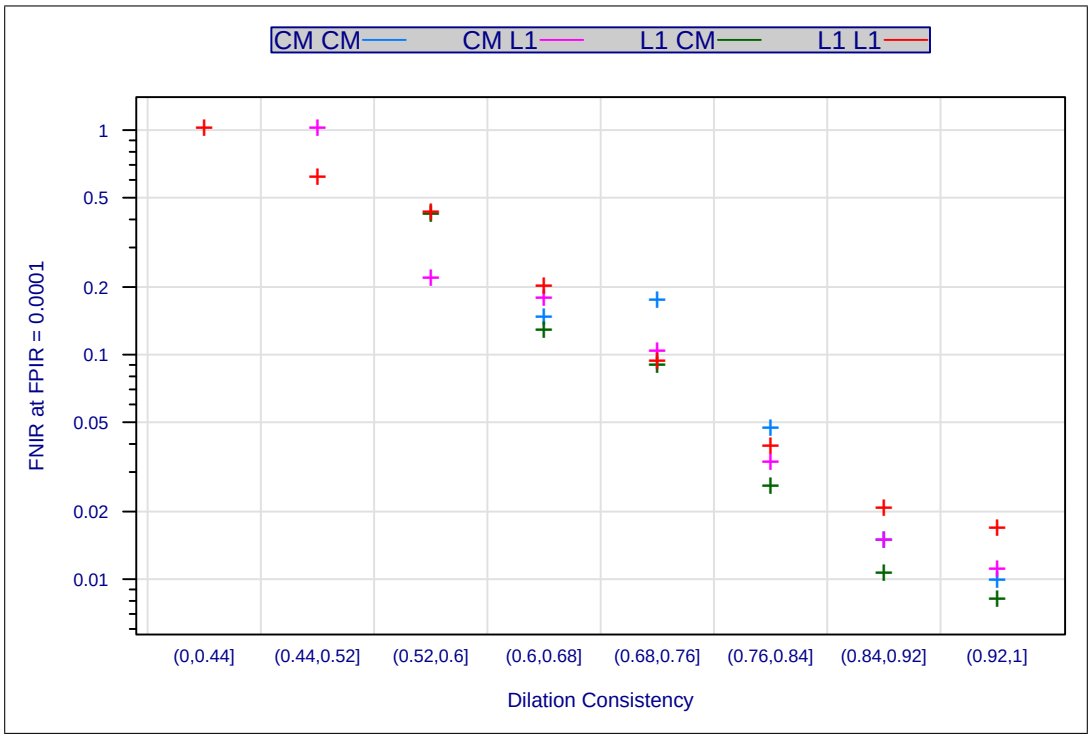

(b) Mean, L1 and CM images

Figure 400: Miss rate statistics for implementation V11B executing mate searches in an enrolled population of N = 1.6 million. The figures plots FNIR at FPIR = 0.0001 versus the IREX I metric for dilation consistency $(1 - \max(D_1, D_2))/(1 - \min(D_1, D_2))$ where D_i is pupil-iris radius ratio, and the subscripts refer to the mated enrollment and search image. The pathologically compressed 330x330 images are excluded from this analysis. The second figure breaks out dilation effects for interoperating camera pairs, CM and L1.

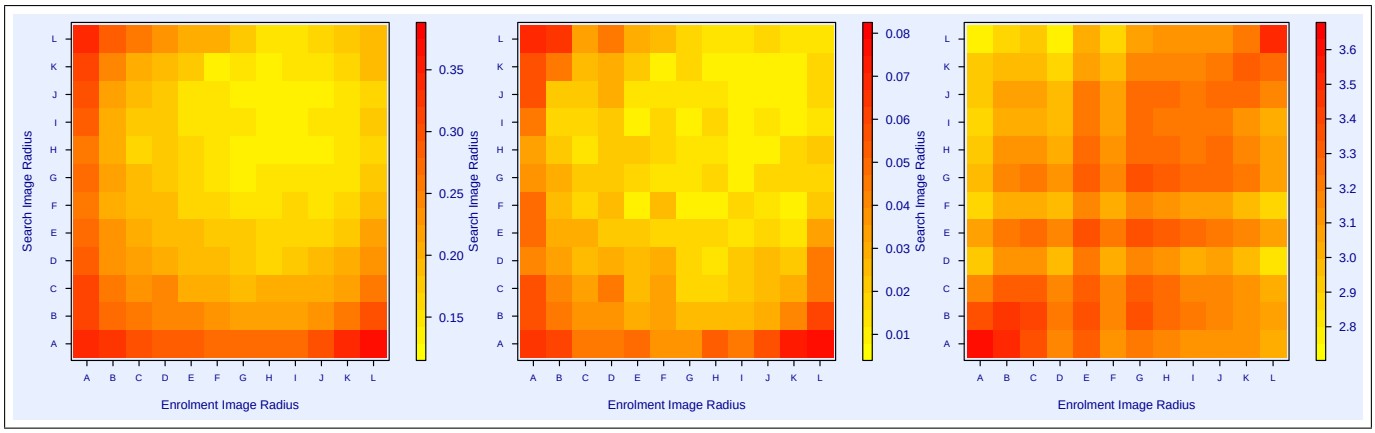

(a) Iris radius: Dis-similarity Score, Miss Rate, $\log_{10}(1+\text{Count})$

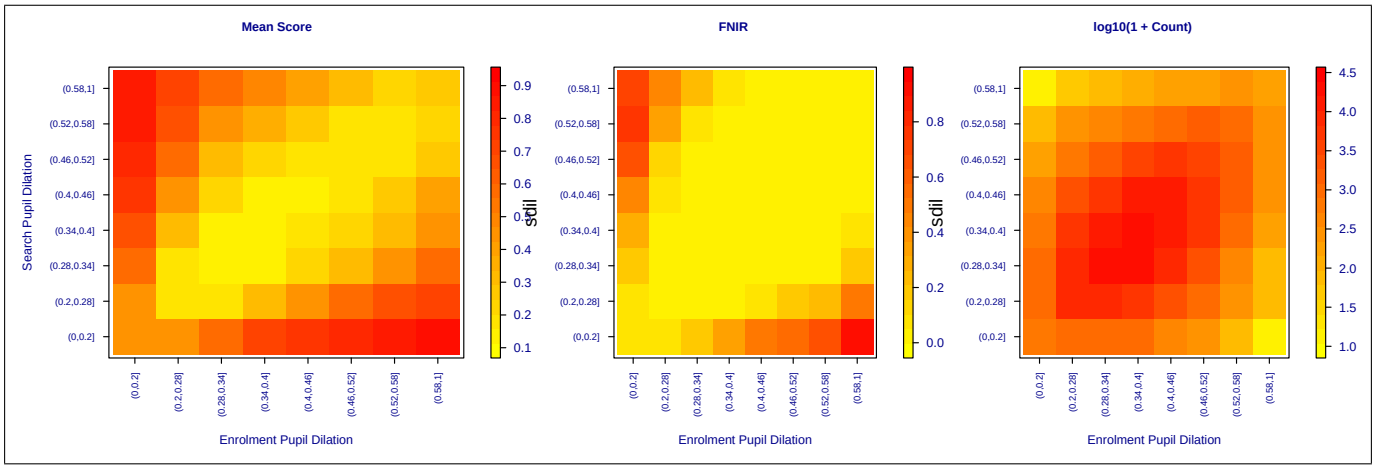

(b) Mate Dilation: Dis-similarity Score, Miss Rate, $\log_{10}(1+\text{Count})$

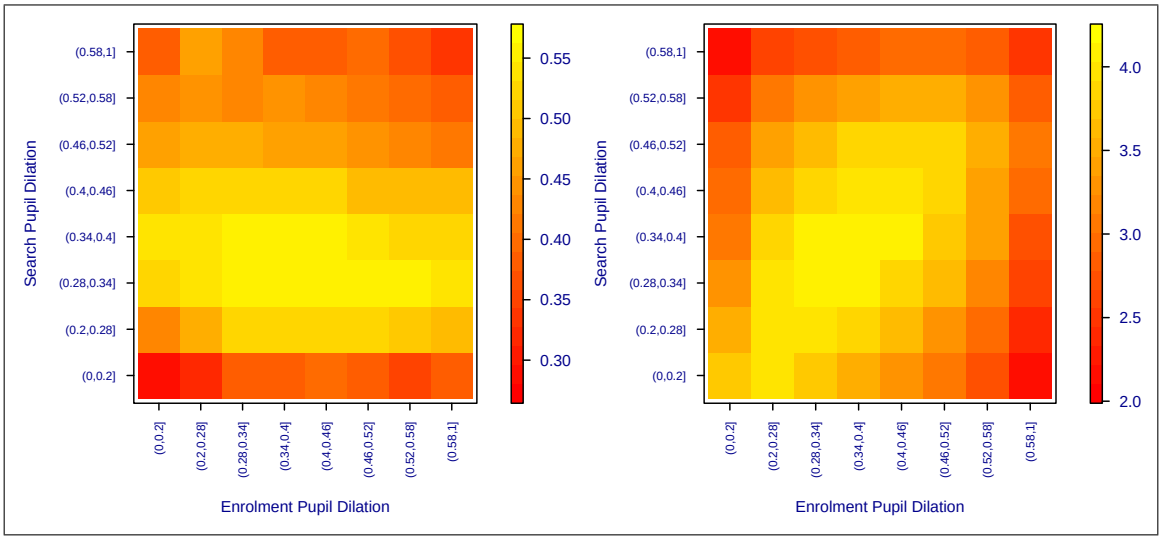

(c) Nonmate Dilation, Dis-similarity Score, Miss Rate, $\log_{10}(1+\text{Count})$

Figure 401: Heatmaps for implementation V12A executing mate searches in an enrolled population of N = 1.6 million. The radius images are binned by into twelve quantiles spanning $[0, 1]$. The dilation values are cut into ranges bounded by: $(0, 0.2, 0.28, 0.34, 0.40, 0.46, 0.52, 0.58, 1)$. The pathologically compressed 330x330 images are excluded from this analysis.

Heatmaps for implementation V12A executing mate searches in an enrolled population of N = 1.6 million.

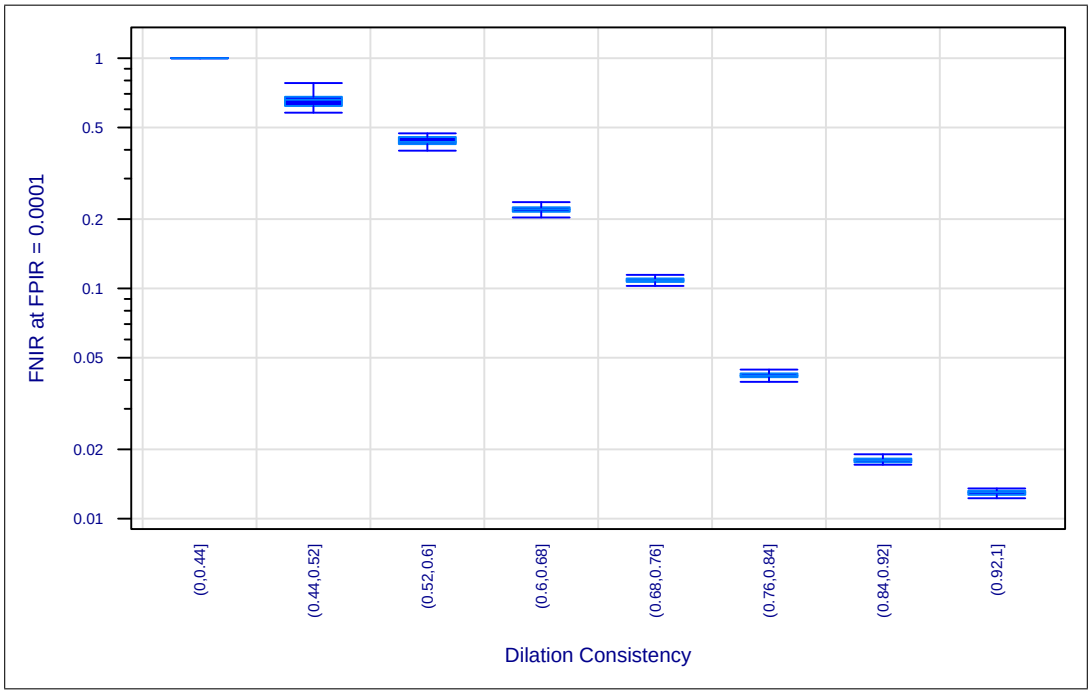

(a) Boxplot, all images

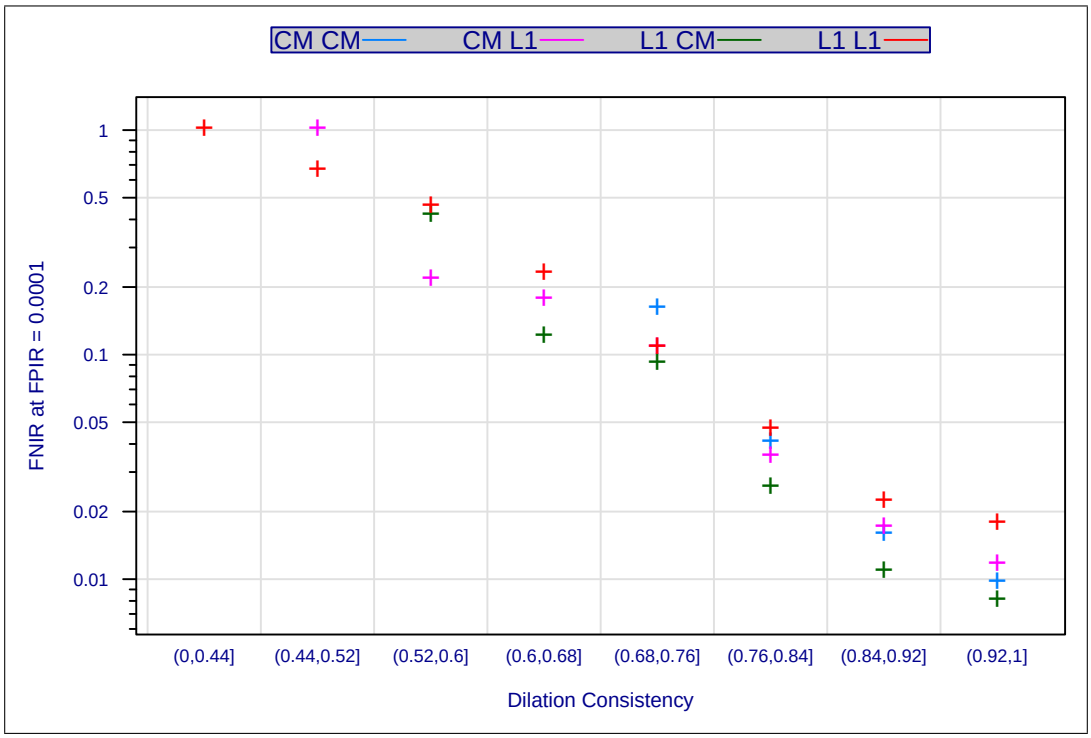

(b) Mean, L1 and CM images

Figure 402: Miss rate statistics for implementation V12A executing mate searches in an enrolled population of N = 1.6 million. The figures plots FNIR at FPIR = 0.0001 versus the IREX I metric for dilation consistency $(1 - \max(D_1, D_2))/(1 - \min(D_1, D_2))$ where D_i is pupil-iris radius ratio, and the subscripts refer to the mated enrollment and search image. The pathologically compressed 330x330 images are excluded from this analysis. The second figure breaks out dilation effects for interoperating camera pairs, CM and L1.

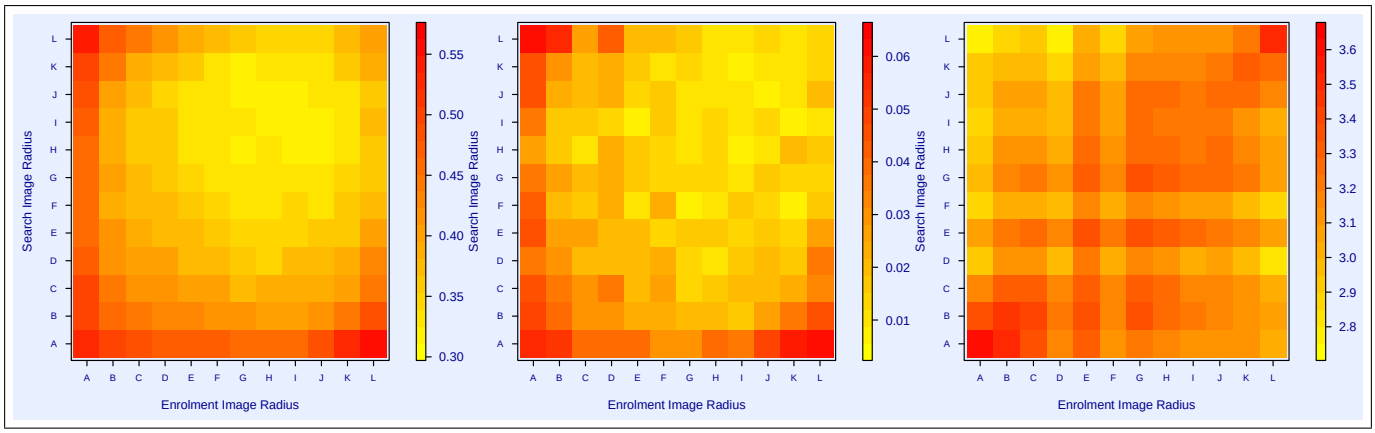

(a) Iris radius: Dis-similarity Score, Miss Rate, $\log_{10}(1+\text{Count})$

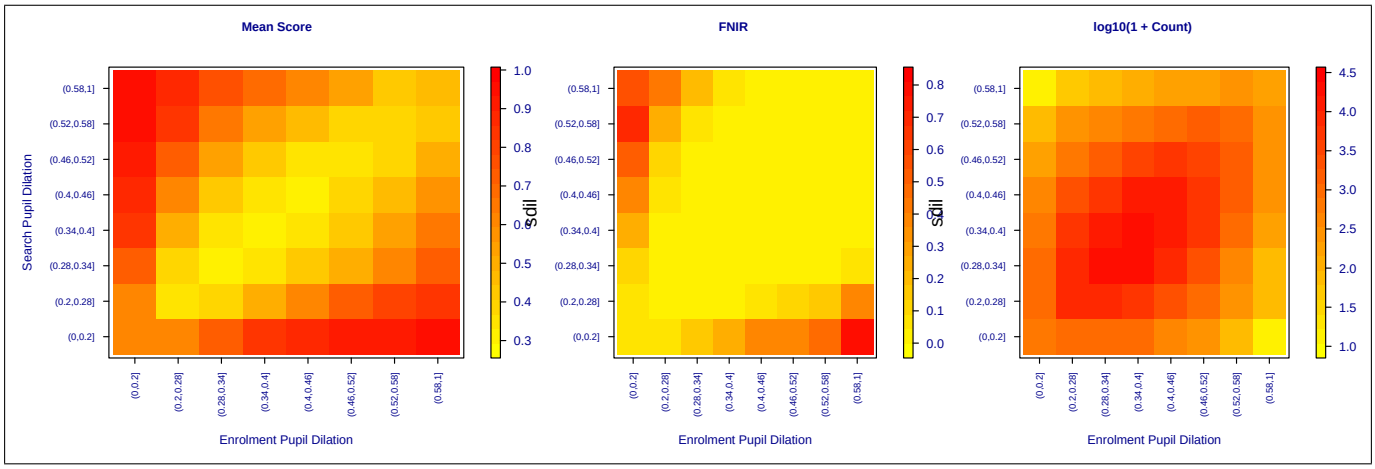

(b) Mate Dilation: Dis-similarity Score, Miss Rate, $\log_{10}(1+\text{Count})$

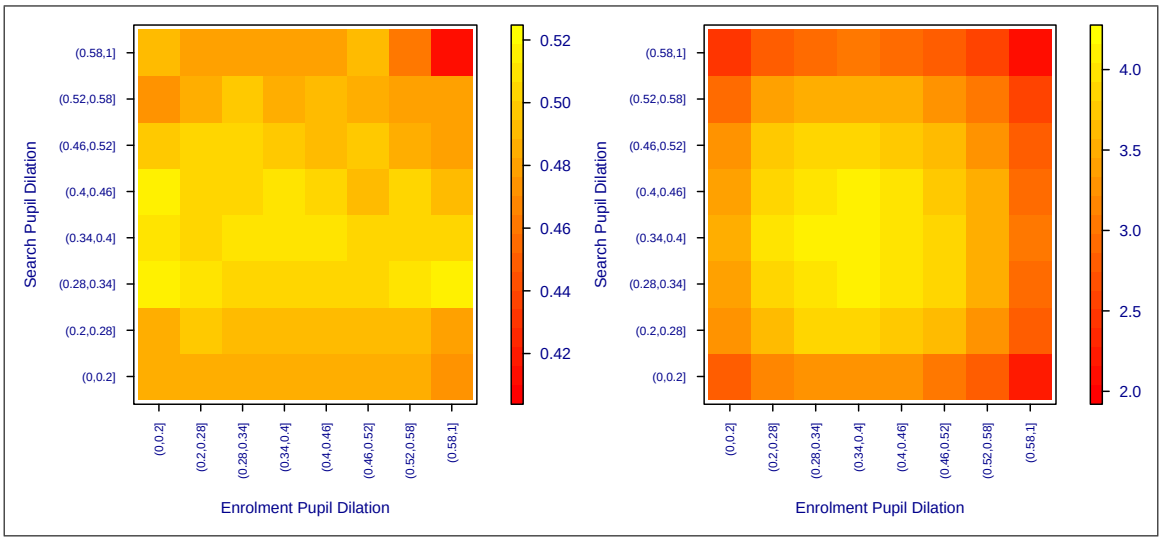

(c) Nonmate Dilation, Dis-similarity Score, Miss Rate, $\log_{10}(1+\text{Count})$

Figure 403: Heatmaps for implementation V12B executing mate searches in an enrolled population of N = 1.6 million. The radius images are binned by into twelve quantiles spanning $[0, 1]$. The dilation values are cut into ranges bounded by: $(0, 0.2, 0.28, 0.34, 0.40, 0.46, 0.52, 0.58, 1)$. The pathologically compressed 330x330 images are excluded from this analysis.

Heatmaps for implementation V12B executing mate searches in an enrolled population of N = 1.6 million.

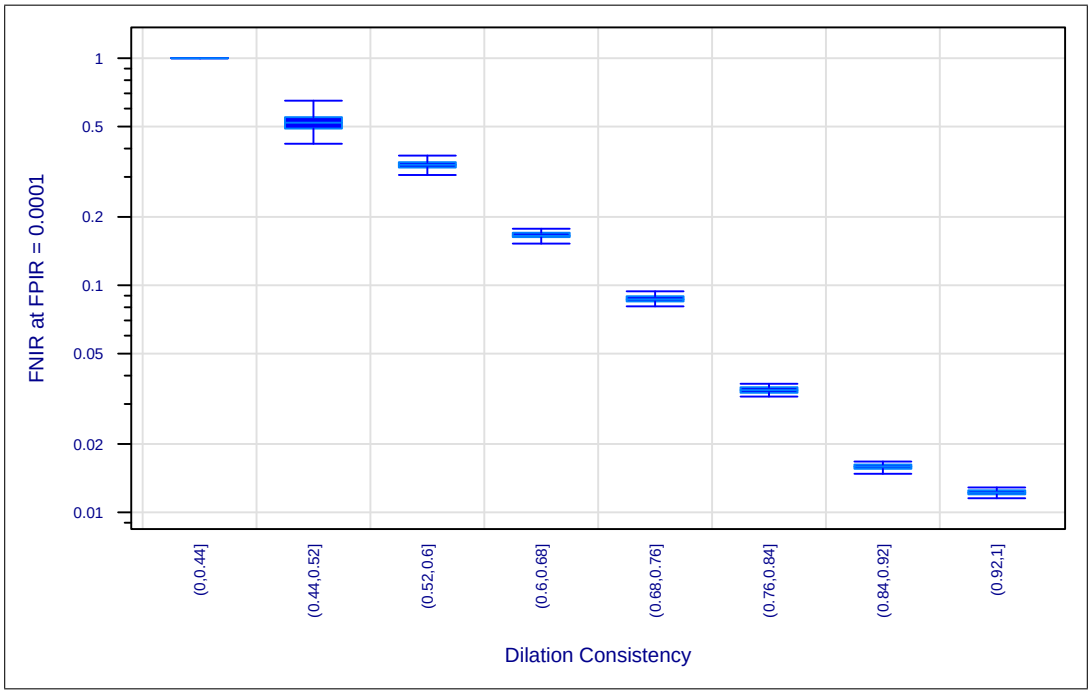

(a) Boxplot, all images

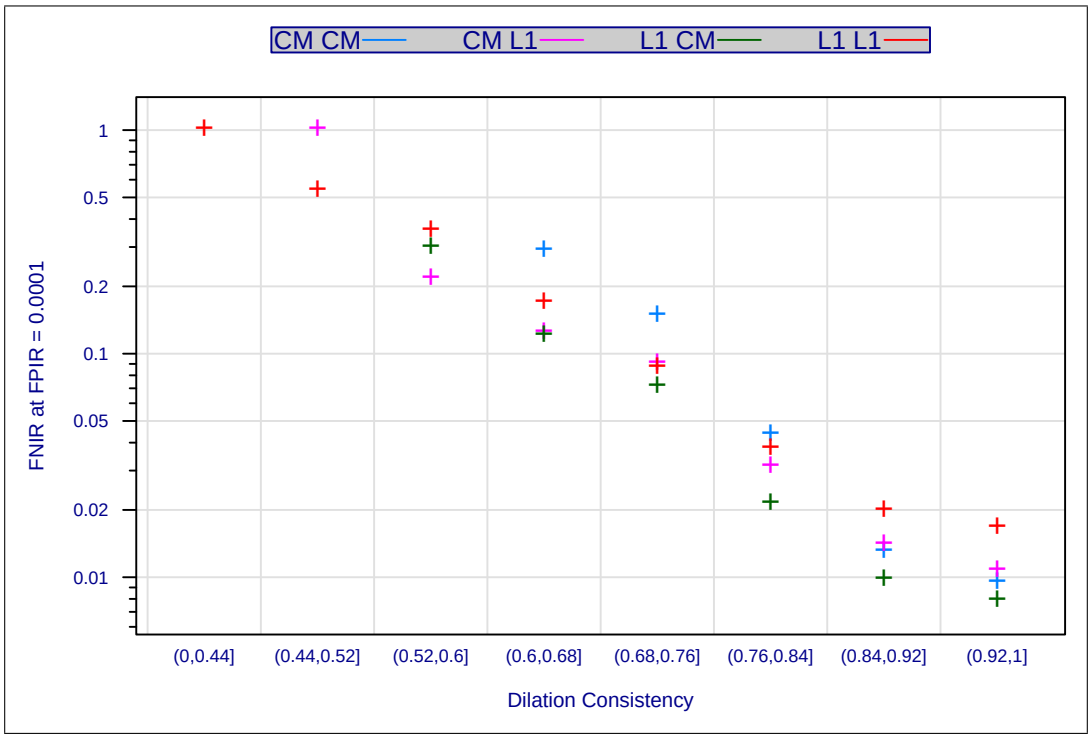

(b) Mean, L1 and CM images

Figure 404: Miss rate statistics for implementation V12B executing mate searches in an enrolled population of N = 1.6 million. The figures plots FNIR at FPIR = 0.0001 versus the IREX I metric for dilation consistency $(1 - \max(D_1, D_2))/(1 - \min(D_1, D_2))$ where D_i is pupil-iris radius ratio, and the subscripts refer to the mated enrollment and search image. The pathologically compressed 330x330 images are excluded from this analysis. The second figure breaks out dilation effects for interoperating camera pairs, CM and L1.

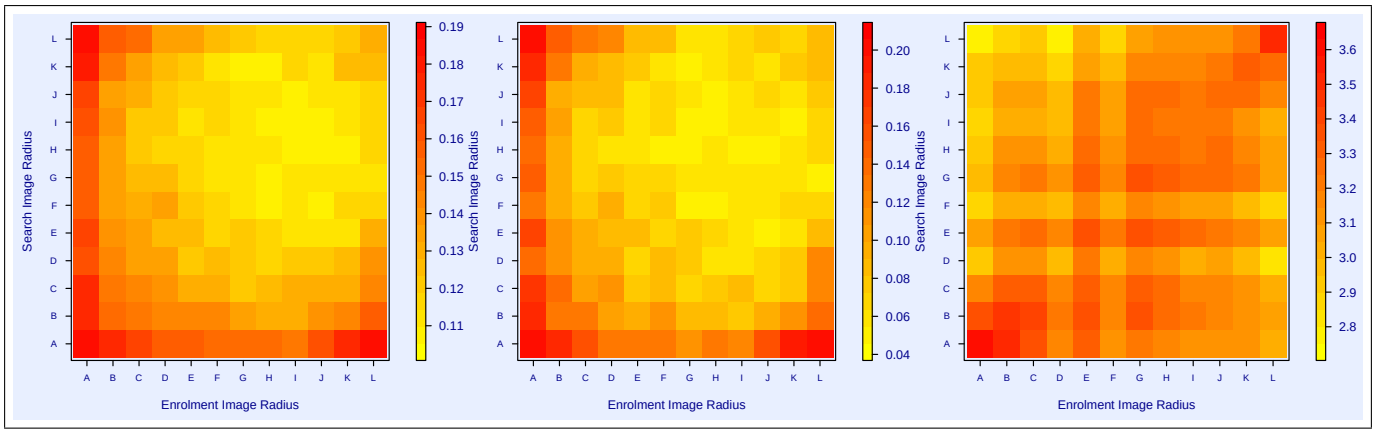

(a) Iris radius: Dis-similarity Score, Miss Rate, $\log_{10}(1+\text{Count})$

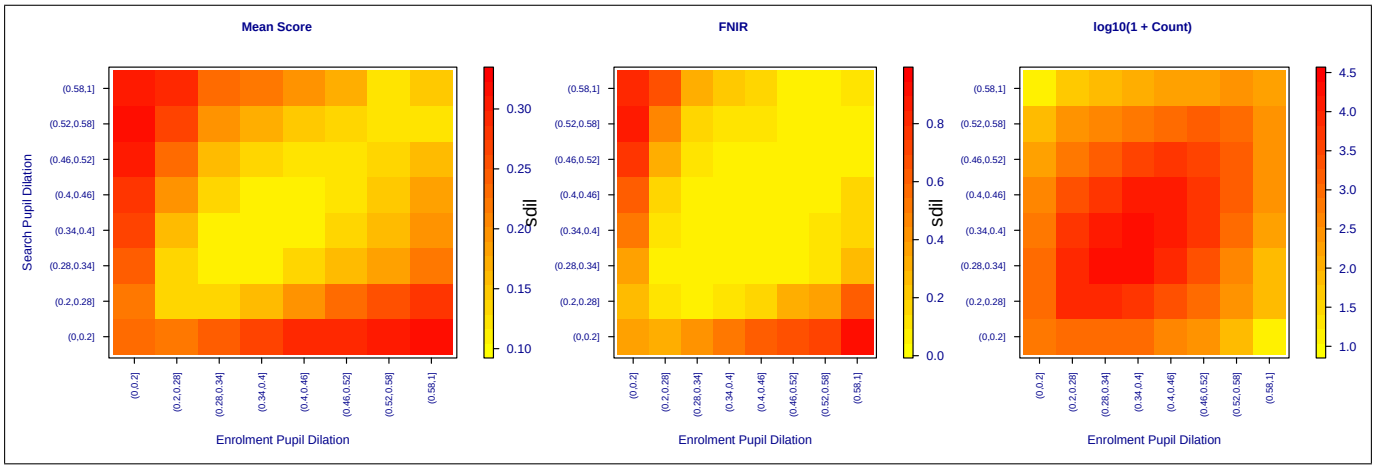

(b) Mate Dilation: Dis-similarity Score, Miss Rate, $\log_{10}(1+\text{Count})$

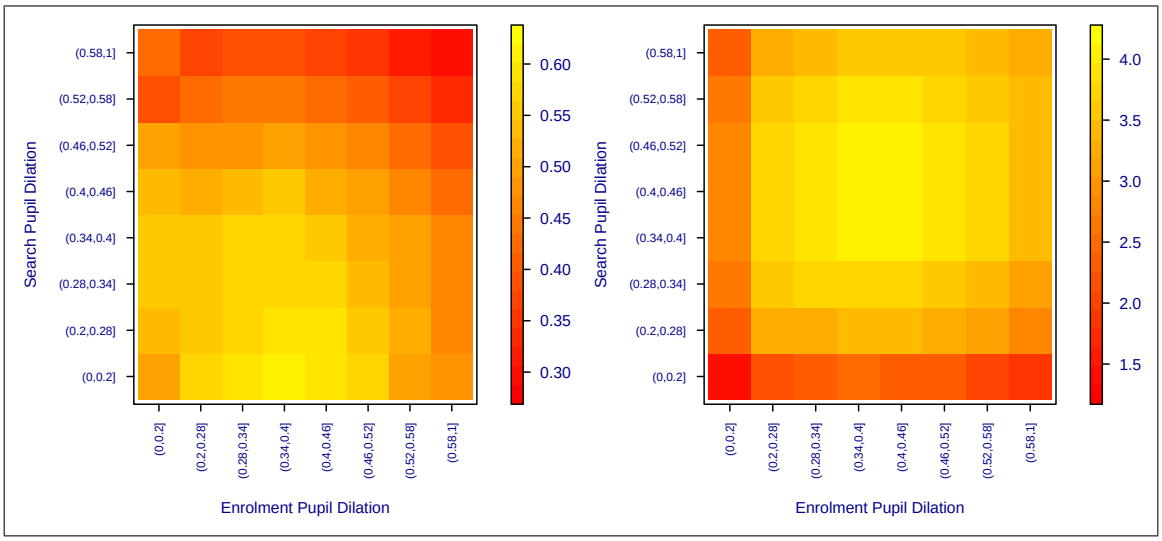

(c) Nonmate Dilation, Dis-similarity Score, Miss Rate, $\log_{10}(1+\text{Count})$

Figure 405: Heatmaps for implementation W01A executing mate searches in an enrolled population of N = 1.6 million. The radius images are binned by into twelve quantiles spanning $[0, 1]$. The dilation values are cut into ranges bounded by: $(0, 0.2, 0.28, 0.34, 0.40, 0.46, 0.52, 0.58, 1)$. The pathologically compressed 330x330 images are excluded from this analysis.

Heatmaps for implementation W01A executing mate searches in an enrolled population of N = 1.6 million.

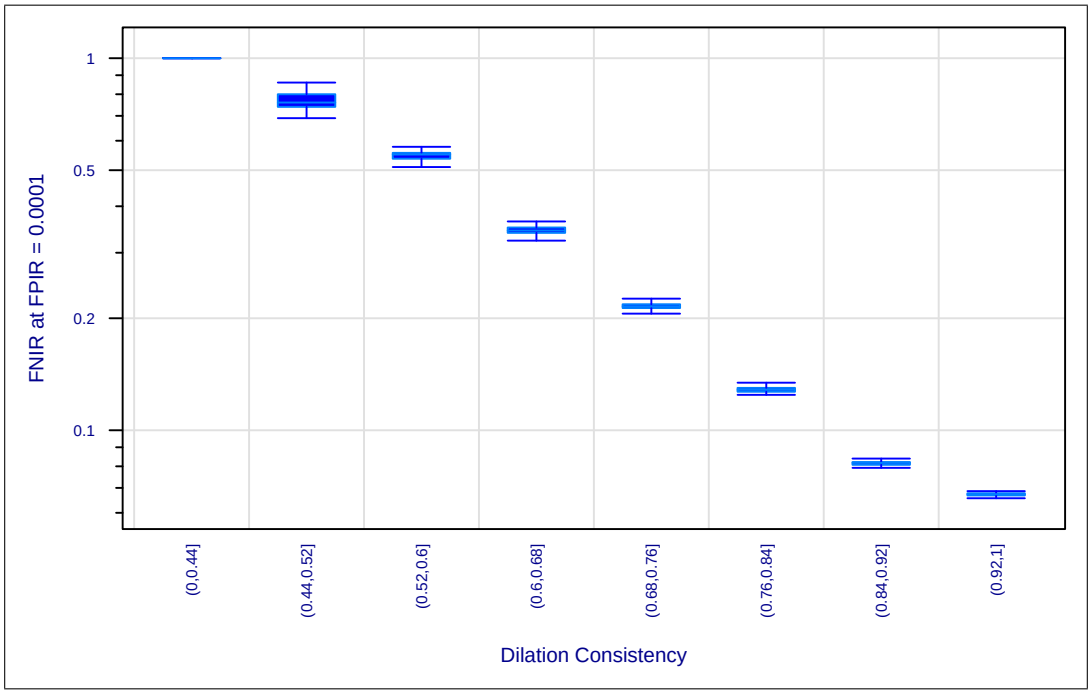

(a) Boxplot, all images

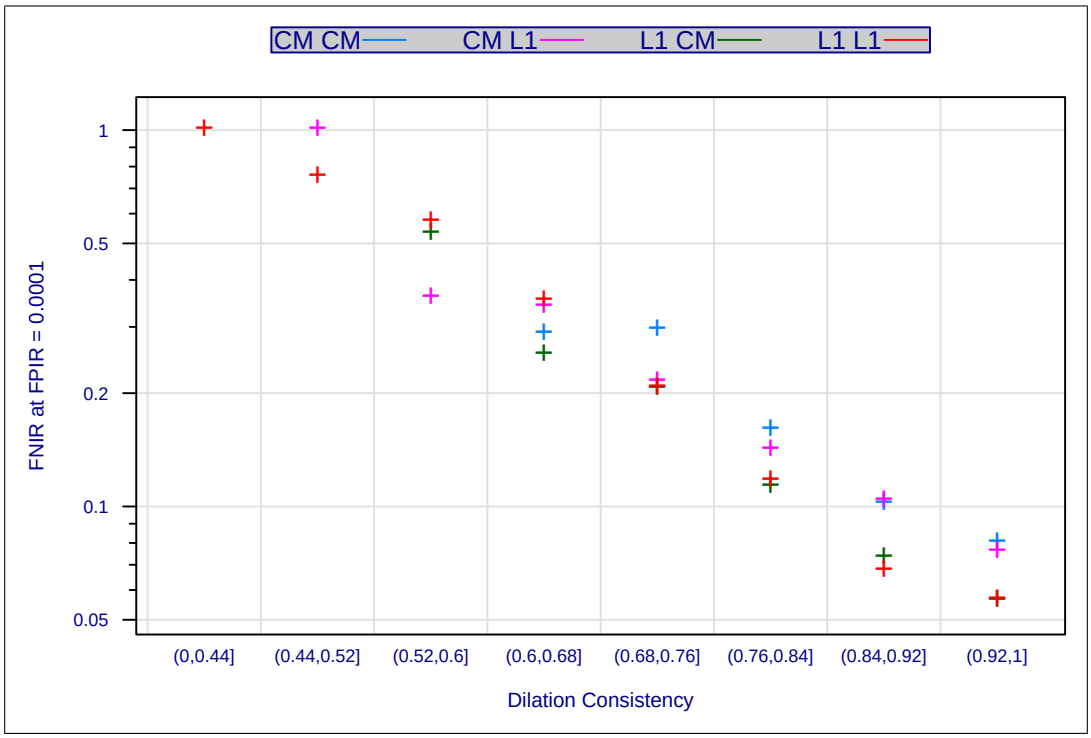

(b) Mean, L1 and CM images

Figure 406: Miss rate statistics for implementation W01A executing mate searches in an enrolled population of N = 1.6 million. The figures plots FNIR at FPIR = 0.0001 versus the IREX I metric for dilation consistency $(1-\max(D_1, D_2))/(1-\min(D_1, D_2))$ where D_i is pupil-iris radius ratio, and the subscripts refer to the mated enrollment and search image. The pathologically compressed 330x330 images are excluded from this analysis. The second figure breaks out dilation effects for interoperating camera pairs, CM and L1.

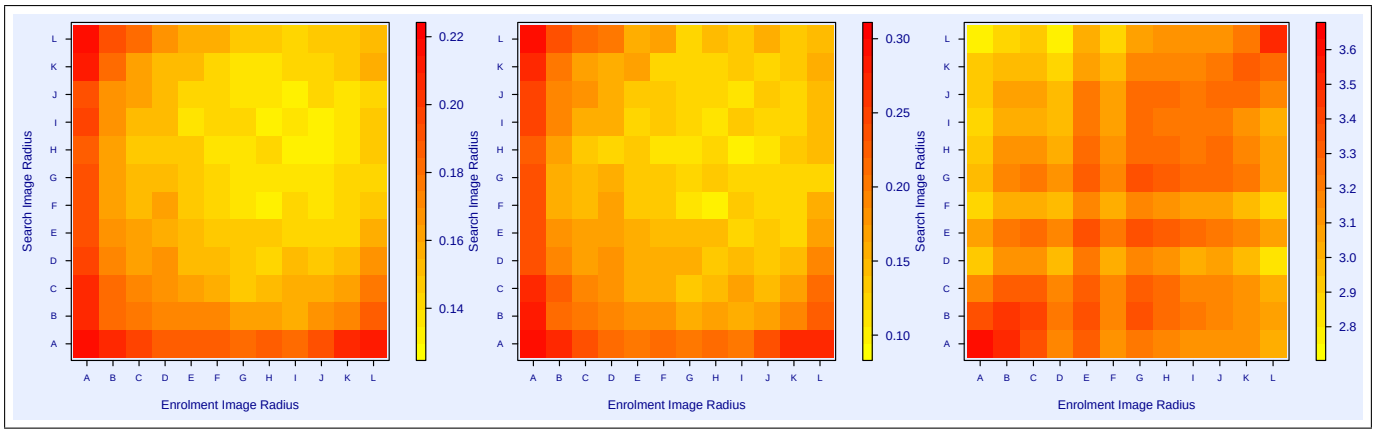

(a) Iris radius: Dis-similarity Score, Miss Rate, $\log_{10}(1+\text{Count})$

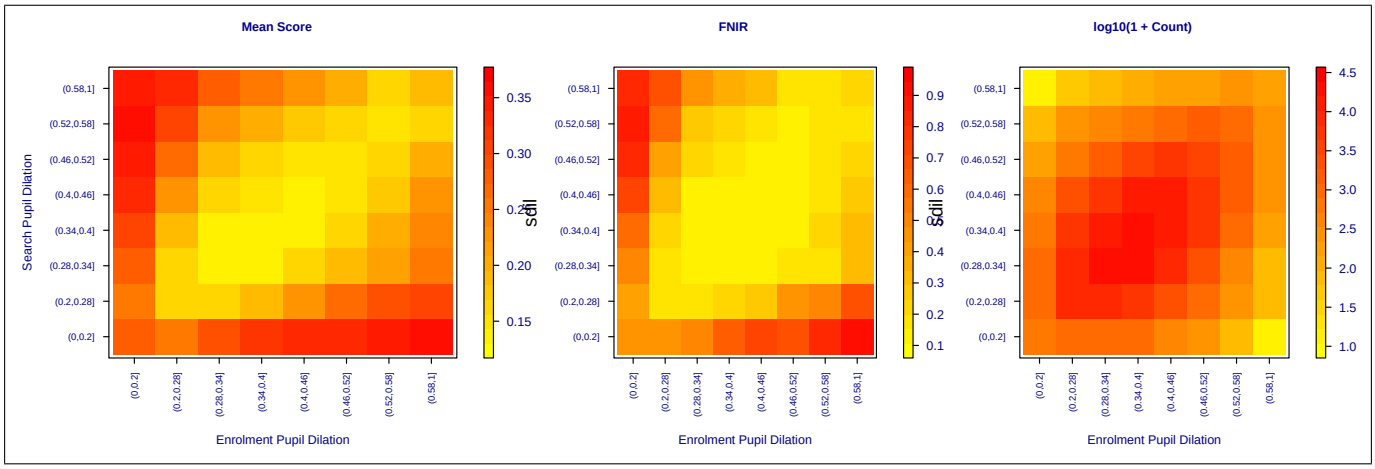

(b) Mate Dilation: Dis-similarity Score, Miss Rate, $\log_{10}(1+\text{Count})$

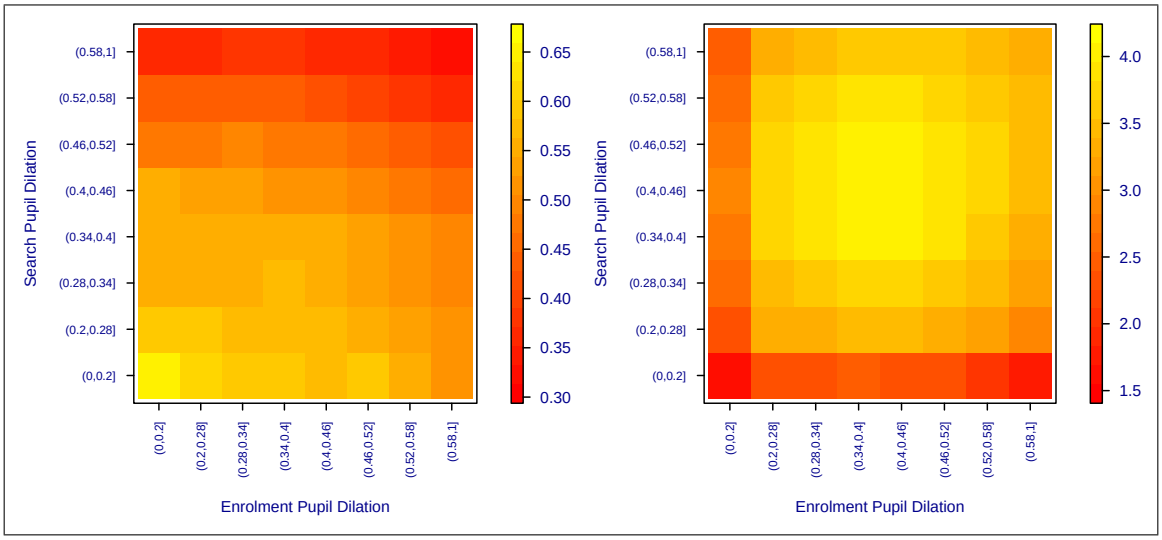

(c) Nonmate Dilation, Dis-similarity Score, Miss Rate, $\log_{10}(1+\text{Count})$

Figure 407: Heatmaps for implementation W01B executing mate searches in an enrolled population of N = 1.6 million. The radius images are binned by into twelve quantiles spanning $[0, 1]$. The dilation values are cut into ranges bounded by: $(0, 0.2, 0.28, 0.34, 0.40, 0.46, 0.52, 0.58, 1)$. The pathologically compressed 330x330 images are excluded from this analysis.

Heatmaps for implementation W01B executing mate searches in an enrolled population of N = 1.6 million.

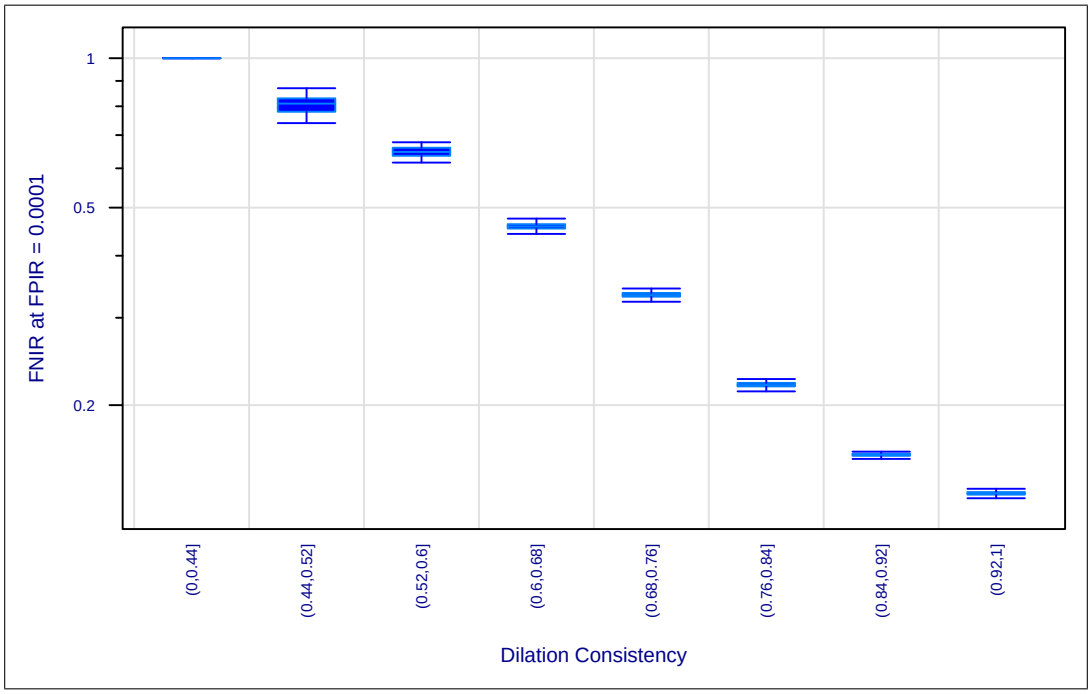

(a) Boxplot, all images

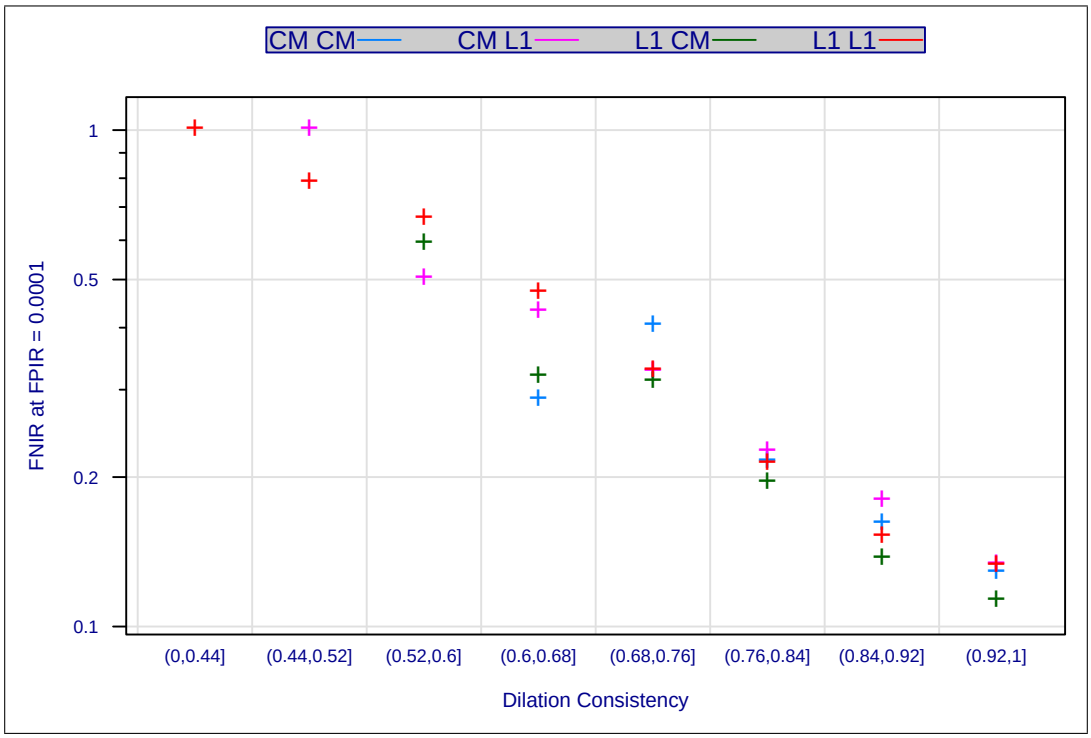

(b) Mean, L1 and CM images

Figure 408: Miss rate statistics for implementation W01B executing mate searches in an enrolled population of N = 1.6 million. The figures plots FNIR at FPIR = 0.0001 versus the IREX I metric for dilation consistency $(1 - \max(D_1, D_2))/(1 - \min(D_1, D_2))$ where D_i is pupil-iris radius ratio, and the subscripts refer to the mated enrollment and search image. The pathologically compressed 330x330 images are excluded from this analysis. The second figure breaks out dilation effects for interoperating camera pairs, CM and L1.

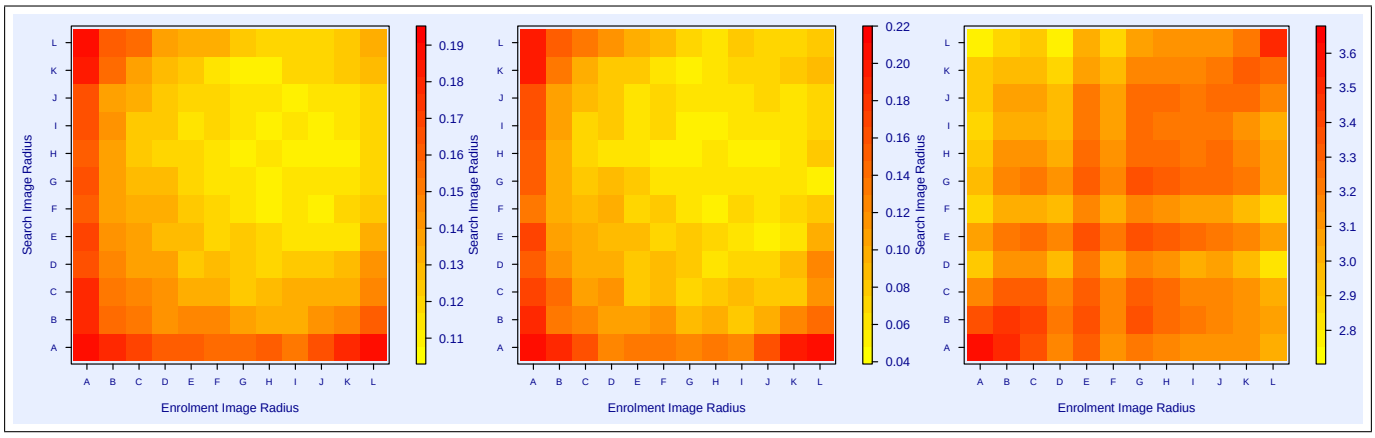

(a) Iris radius: Dis-similarity Score, Miss Rate, $\log_{10}(1+\text{Count})$

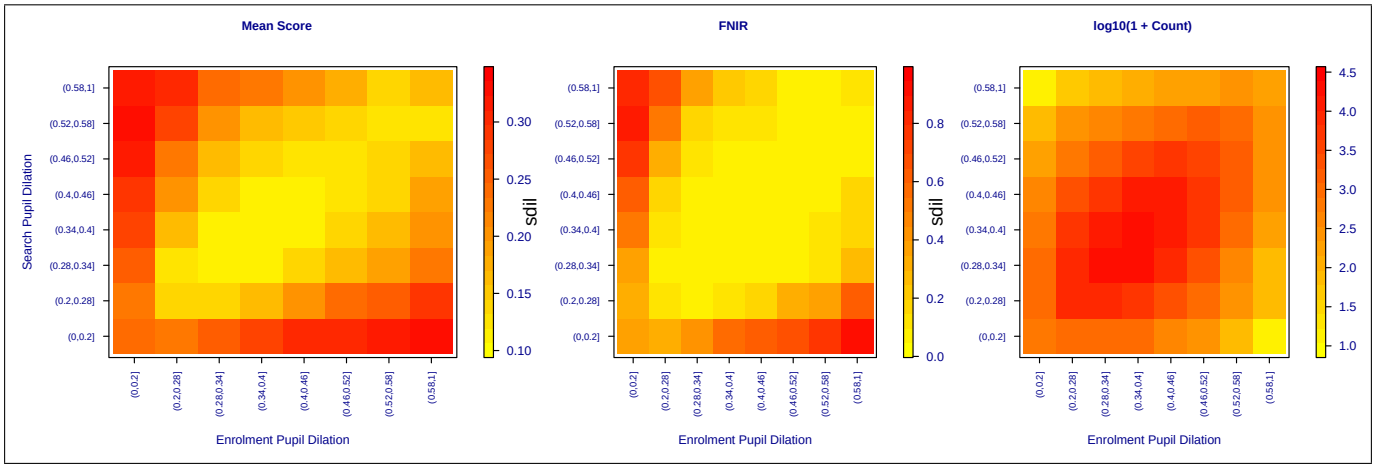

(b) Mate Dilation: Dis-similarity Score, Miss Rate, $\log_{10}(1+\text{Count})$

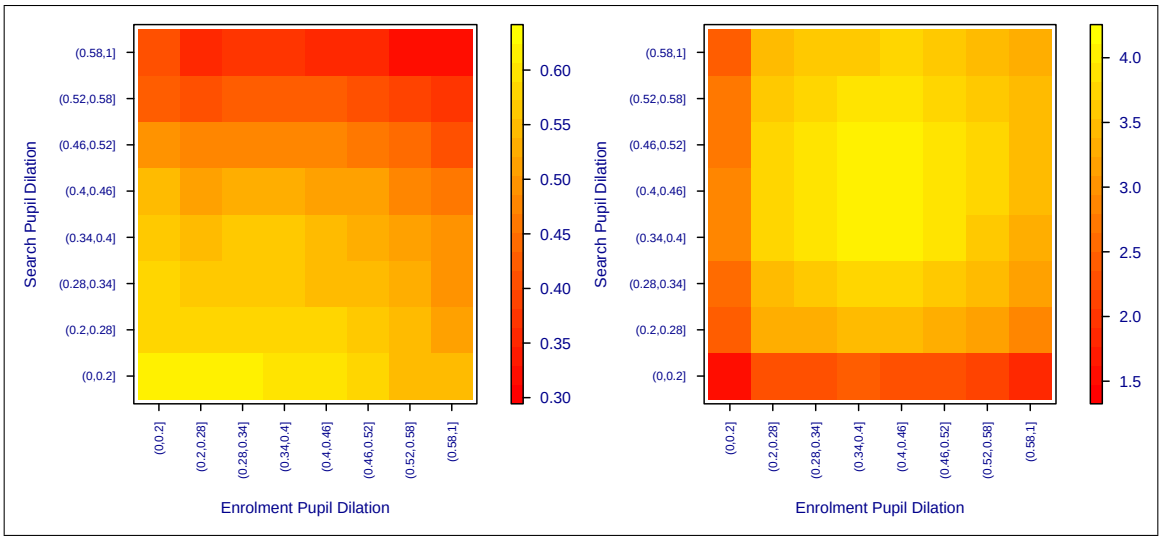

(c) Nonmate Dilation, Dis-similarity Score, Miss Rate, $\log_{10}(1+\text{Count})$

Figure 409: Heatmaps for implementation W02A executing mate searches in an enrolled population of N = 1.6 million. The radius images are binned by into twelve quantiles spanning $[0, 1]$. The dilation values are cut into ranges bounded by: $(0, 0.2, 0.28, 0.34, 0.40, 0.46, 0.52, 0.58, 1)$. The pathologically compressed 330x330 images are excluded from this analysis.

Heatmaps for implementation W02A executing mate searches in an enrolled population of N = 1.6 million.

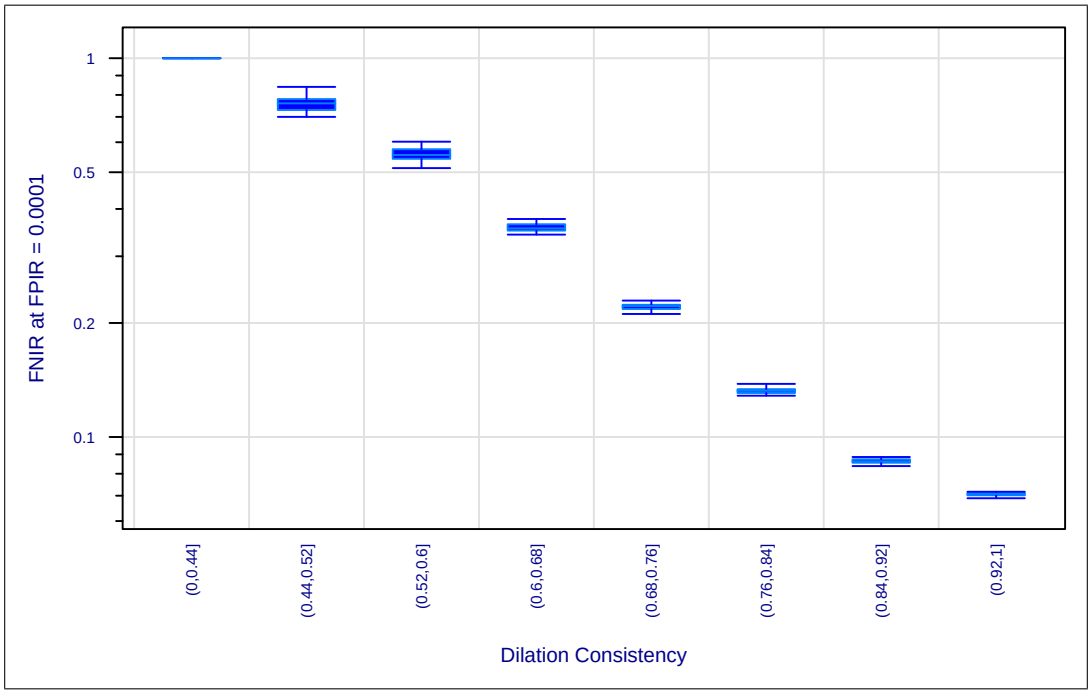

(a) Boxplot, all images

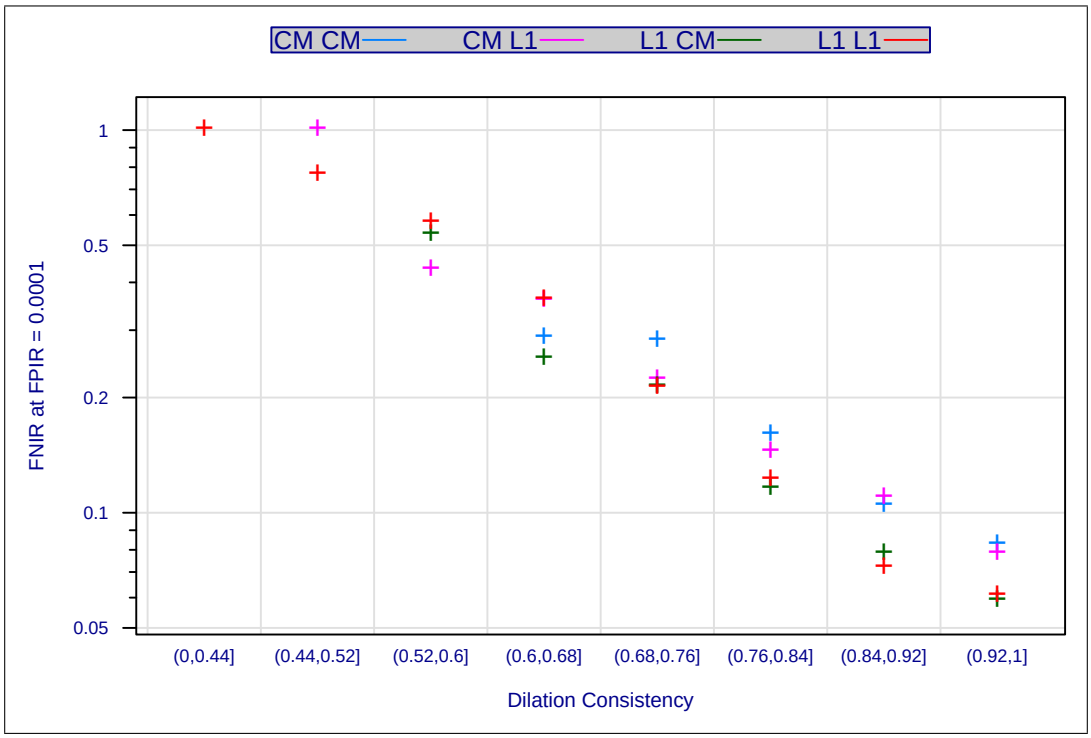

(b) Mean, L1 and CM images

Figure 410: Miss rate statistics for implementation W02A executing mate searches in an enrolled population of N = 1.6 million. The figures plots FNIR at FPIR = 0.0001 versus the IREX I metric for dilation consistency $(1 - \max(D_1, D_2))/(1 - \min(D_1, D_2))$ where D_i is pupil-iris radius ratio, and the subscripts refer to the mated enrollment and search image. The pathologically compressed 330x330 images are excluded from this analysis. The second figure breaks out dilation effects for interoperating camera pairs, CM and L1.

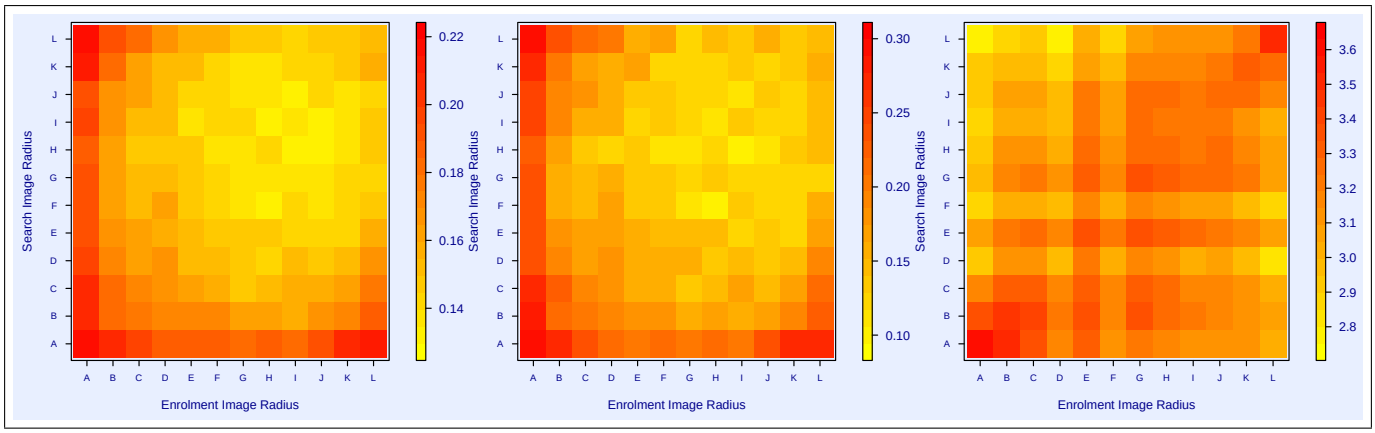

(a) Iris radius: Dis-similarity Score, Miss Rate, $\log_{10}(1+\text{Count})$

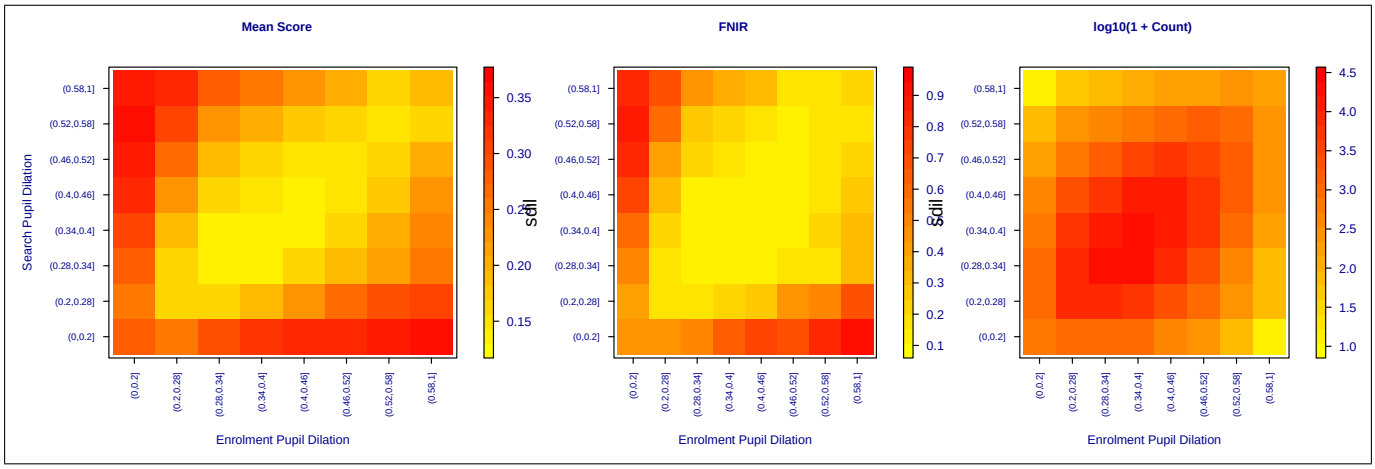

(b) Mate Dilation: Dis-similarity Score, Miss Rate, $\log_{10}(1+\text{Count})$

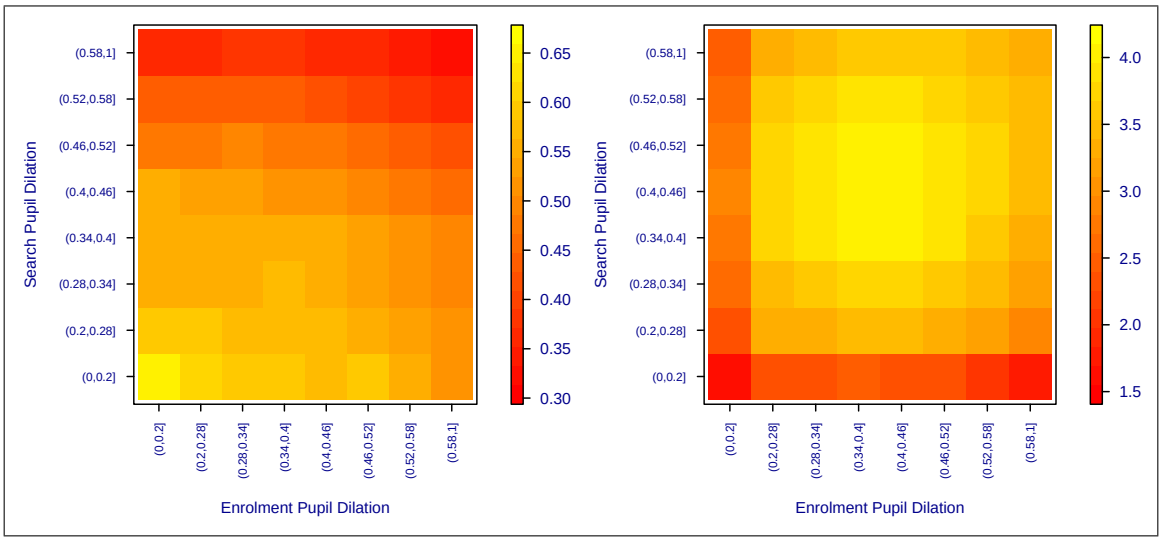

(c) Nonmate Dilation, Dis-similarity Score, Miss Rate, $\log_{10}(1+\text{Count})$

Figure 411: Heatmaps for implementation W02B executing mate searches in an enrolled population of N = 1.6 million. The radius images are binned by into twelve quantiles spanning $[0, 1]$. The dilation values are cut into ranges bounded by: $(0, 0.2, 0.28, 0.34, 0.40, 0.46, 0.52, 0.58, 1)$. The pathologically compressed 330x330 images are excluded from this analysis.

Heatmaps for implementation W02B executing mate searches in an enrolled population of N = 1.6 million.

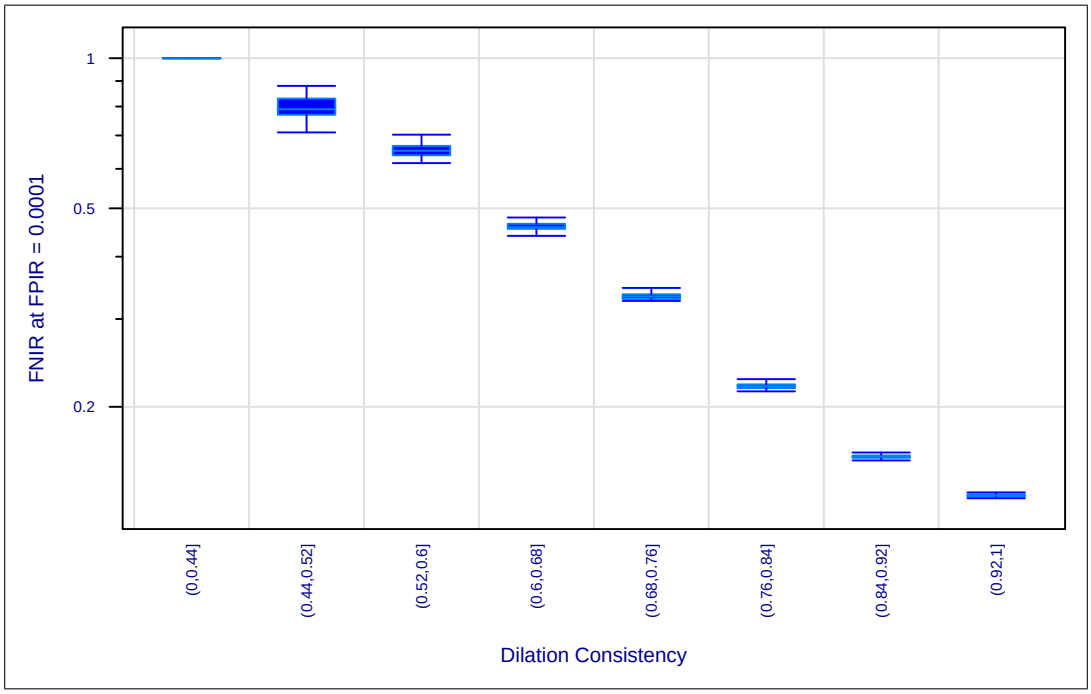

(a) Boxplot, all images

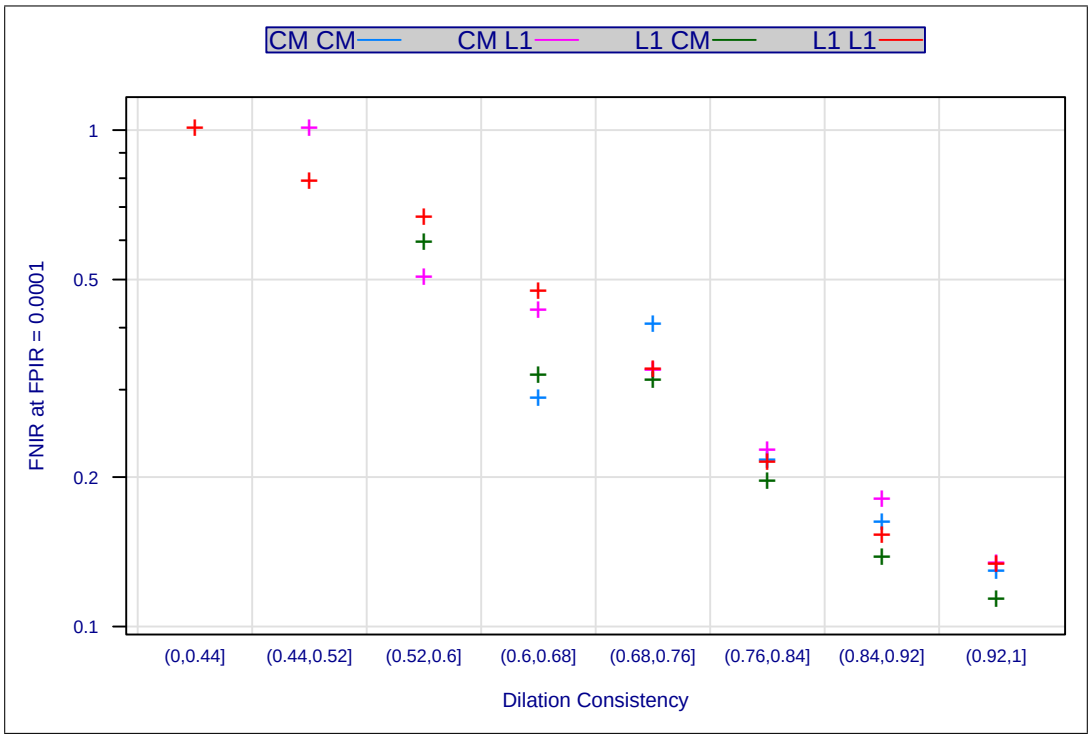

(b) Mean, L1 and CM images

Figure 412: Miss rate statistics for implementation W02B executing mate searches in an enrolled population of N = 1.6 million. The figures plots FNIR at FPIR = 0.0001 versus the IREX I metric for dilation consistency $(1 - \max(D_1, D_2))/(1 - \min(D_1, D_2))$ where D_i is pupil-iris radius ratio, and the subscripts refer to the mated enrollment and search image. The pathologically compressed 330x330 images are excluded from this analysis. The second figure breaks out dilation effects for interoperating camera pairs, CM and L1.

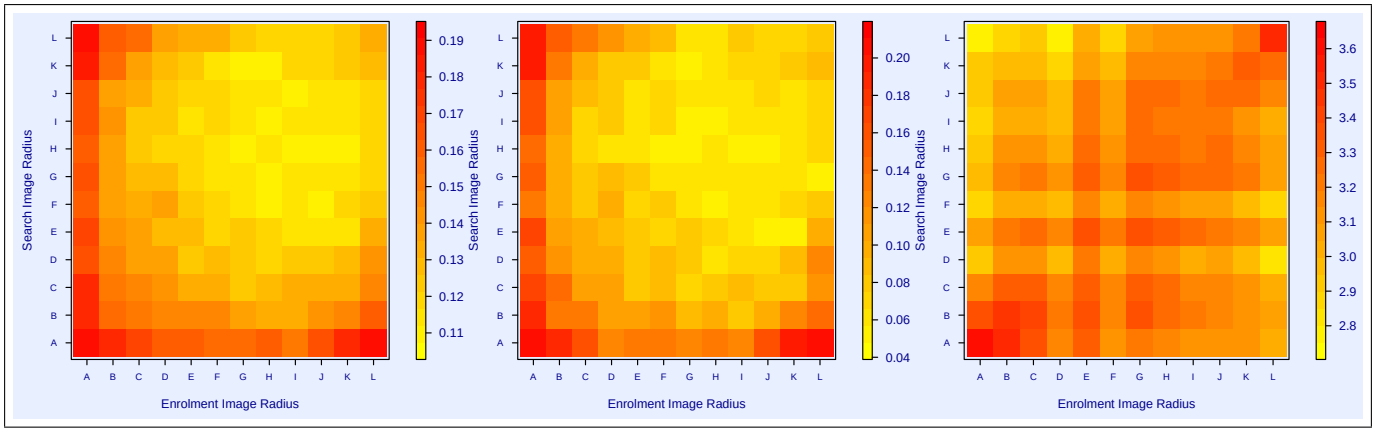

(a) Iris radius: Dis-similarity Score, Miss Rate, $\log_{10}(1+\text{Count})$

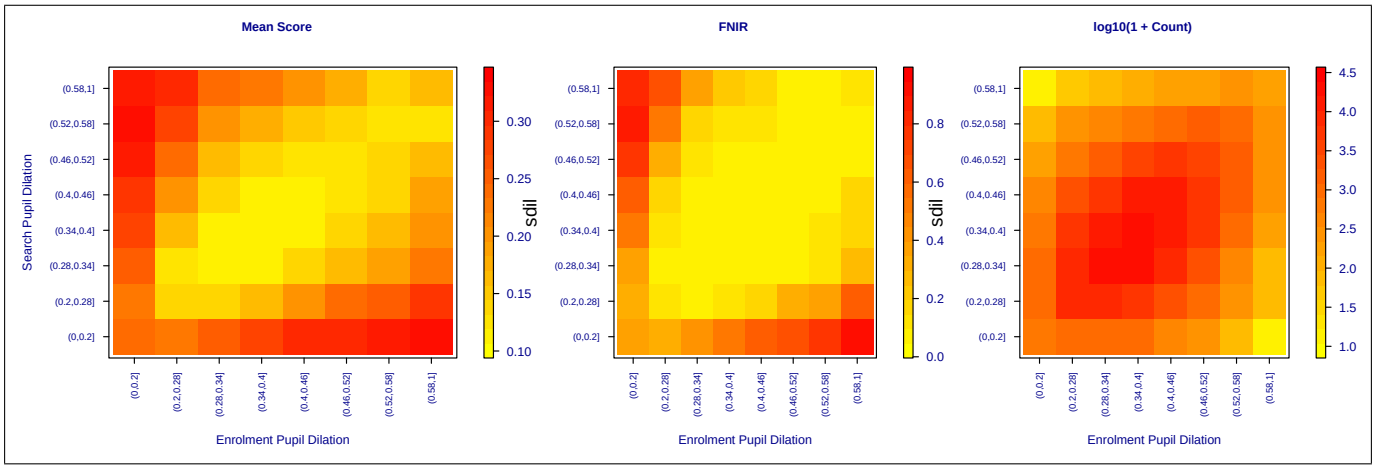

(b) Mate Dilation: Dis-similarity Score, Miss Rate, $\log_{10}(1+\text{Count})$

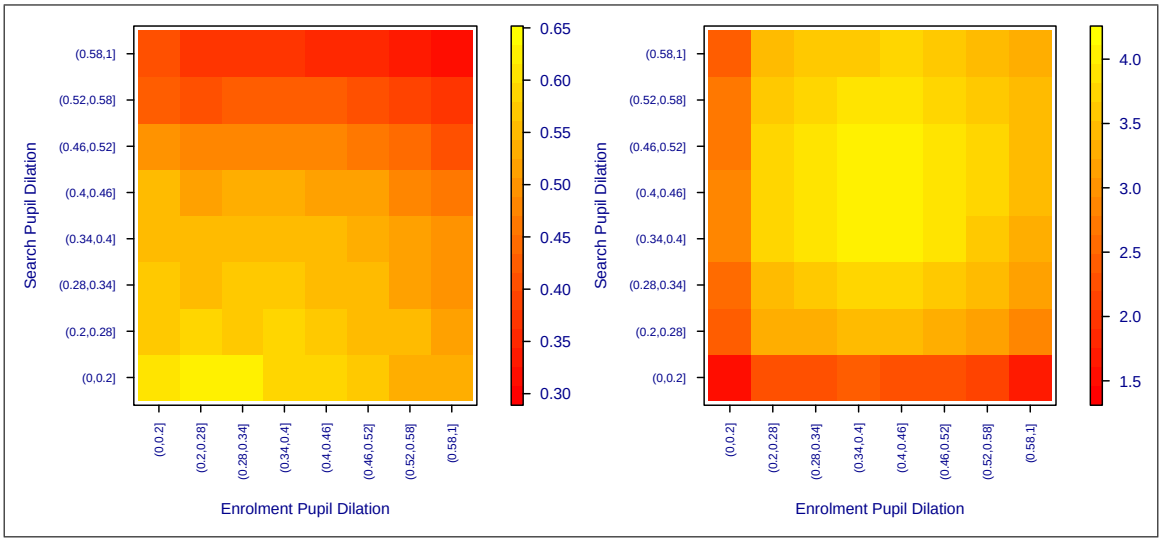

(c) Nonmate Dilation, Dis-similarity Score, Miss Rate, $\log_{10}(1+\text{Count})$

Figure 413: Heatmaps for implementation W03A executing mate searches in an enrolled population of N = 1.6 million. The radius images are binned by into twelve quantiles spanning $[0, 1]$. The dilation values are cut into ranges bounded by: $(0, 0.2, 0.28, 0.34, 0.40, 0.46, 0.52, 0.58, 1)$. The pathologically compressed 330x330 images are excluded from this analysis.

Heatmaps for implementation W03A executing mate searches in an enrolled population of N = 1.6 million.

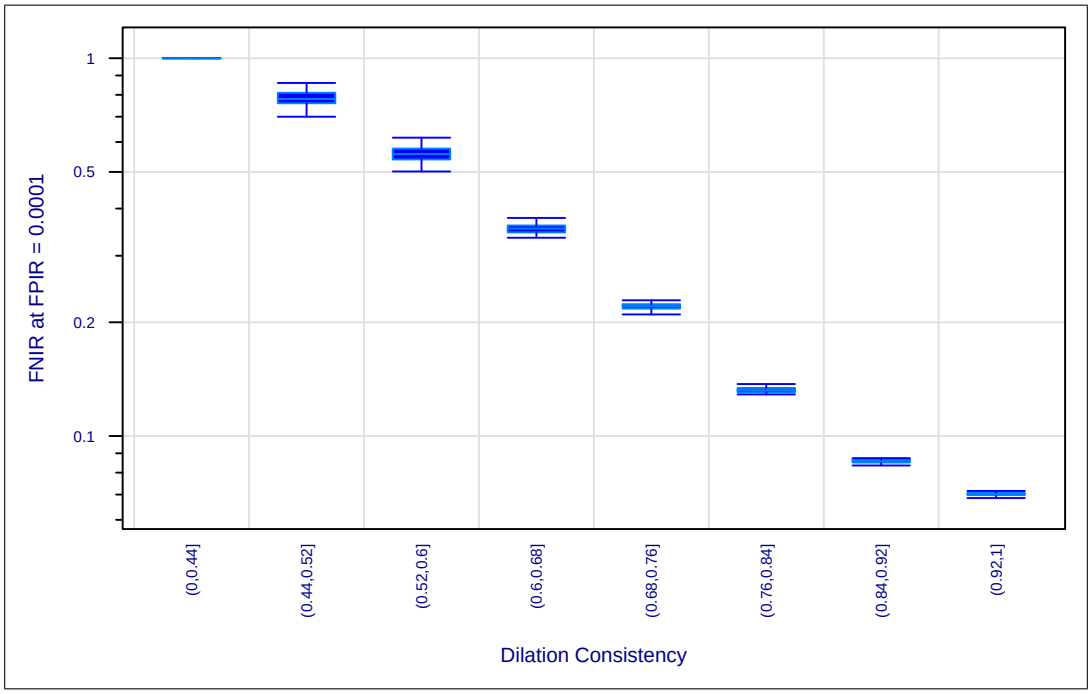

(a) Boxplot, all images

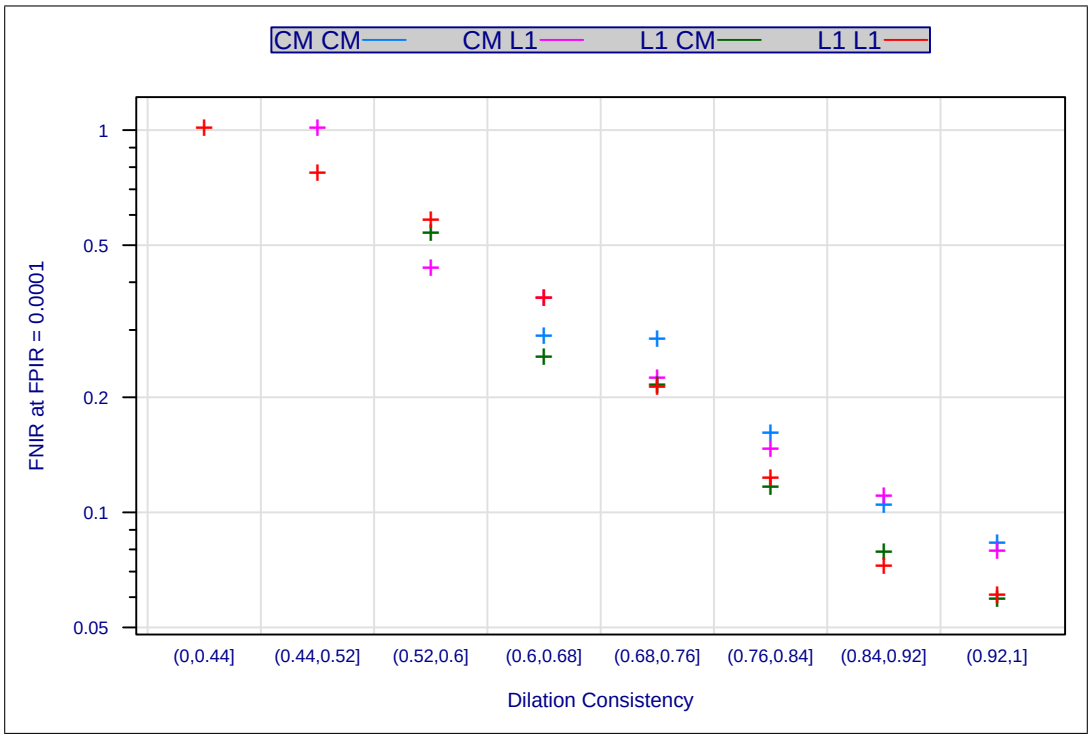

(b) Mean, L1 and CM images

Figure 414: Miss rate statistics for implementation W03A executing mate searches in an enrolled population of N = 1.6 million. The figures plots FNIR at FPIR = 0.0001 versus the IREX I metric for dilation consistency $(1 - \max(D_1, D_2))/(1 - \min(D_1, D_2))$ where D_i is pupil-iris radius ratio, and the subscripts refer to the mated enrollment and search image. The pathologically compressed 330x330 images are excluded from this analysis. The second figure breaks out dilation effects for interoperating camera pairs, CM and L1.

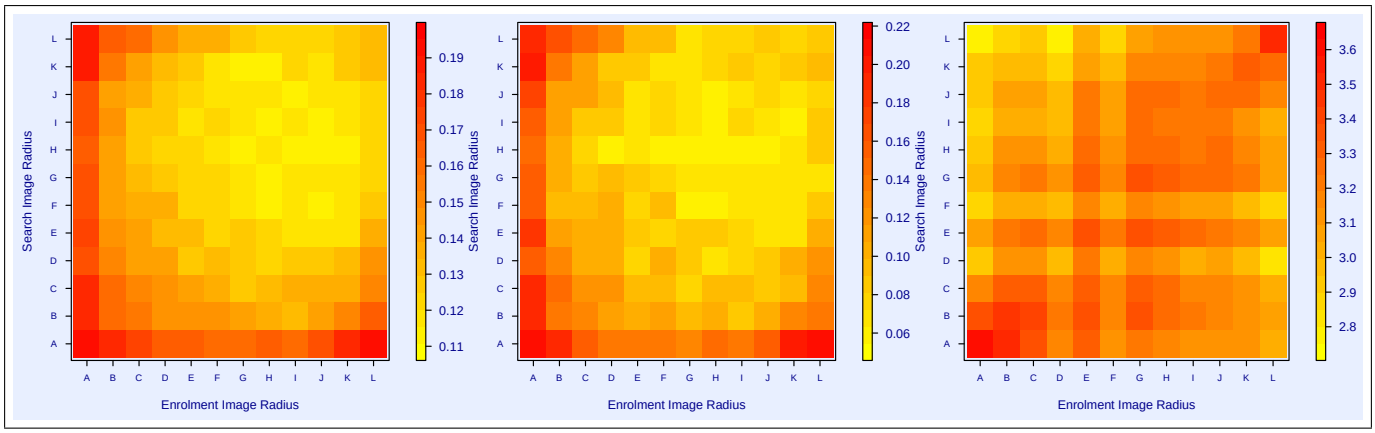

(a) Iris radius: Dis-similarity Score, Miss Rate, $\log_{10}(1+\text{Count})$

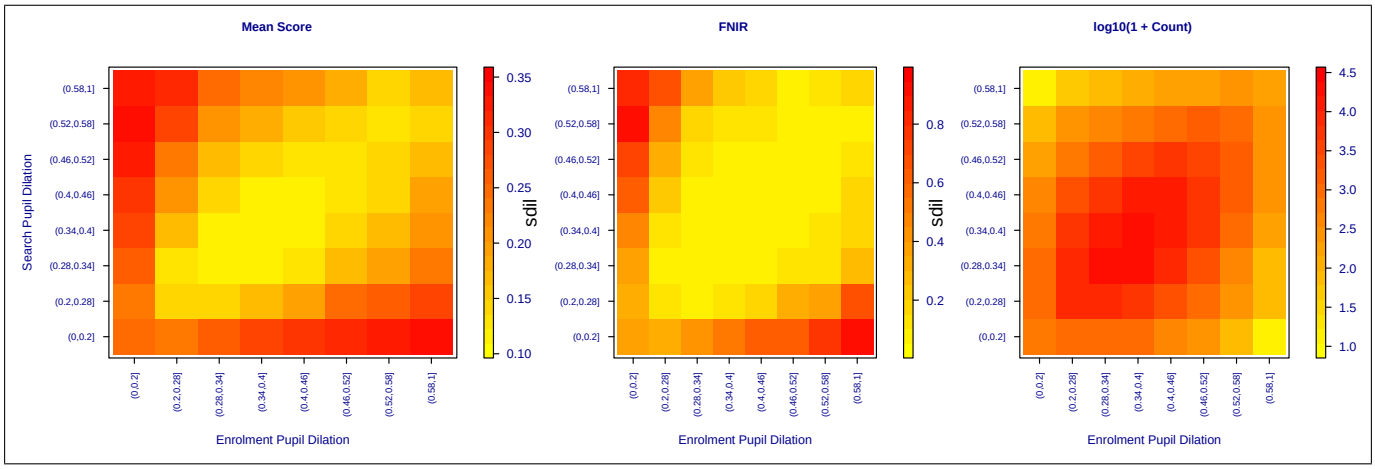

(b) Mate Dilation: Dis-similarity Score, Miss Rate, $\log_{10}(1+\text{Count})$

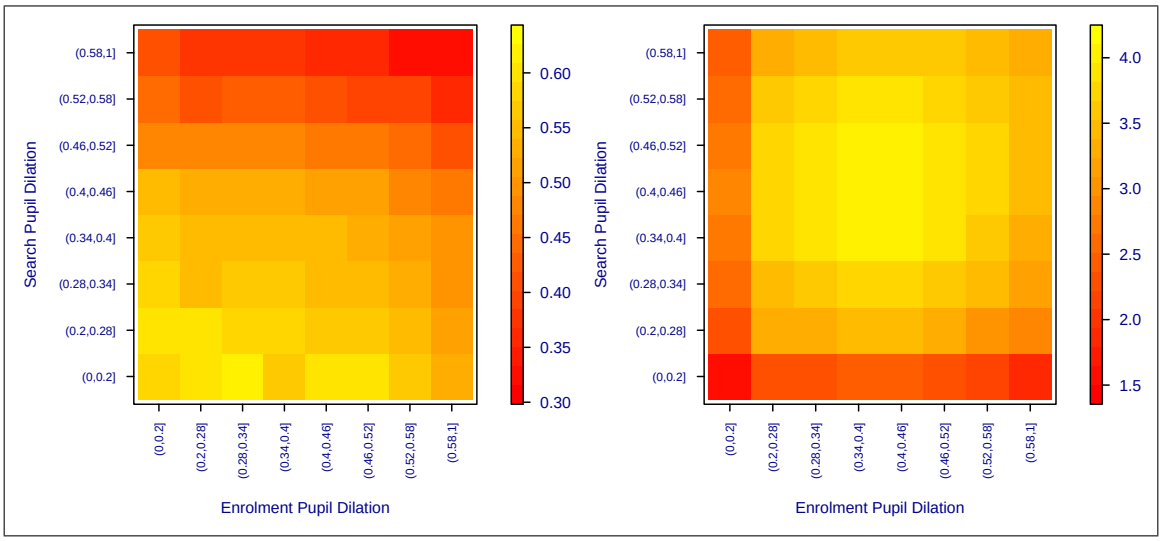

(c) Nonmate Dilation, Dis-similarity Score, Miss Rate, $\log_{10}(1+\text{Count})$

Figure 415: Heatmaps for implementation W04A executing mate searches in an enrolled population of N = 1.6 million. The radius images are binned by into twelve quantiles spanning $[0, 1]$. The dilation values are cut into ranges bounded by: $(0, 0.2, 0.28, 0.34, 0.40, 0.46, 0.52, 0.58, 1)$. The pathologically compressed 330x330 images are excluded from this analysis.

Heatmaps for implementation W04A executing mate searches in an enrolled population of N = 1.6 million.

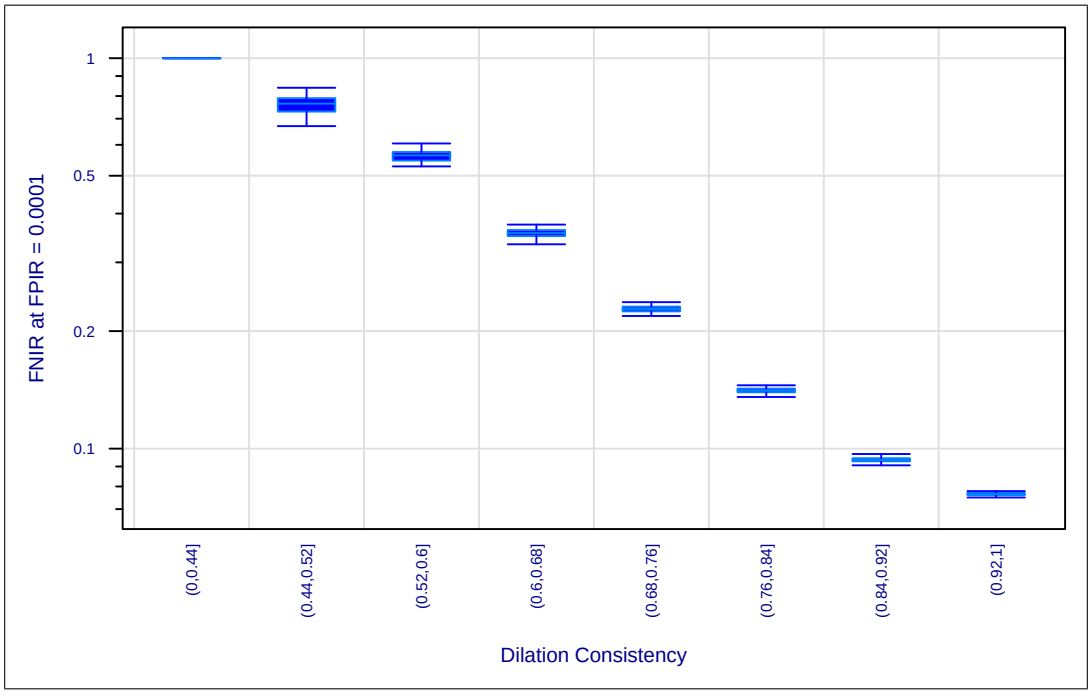

(a) Boxplot, all images

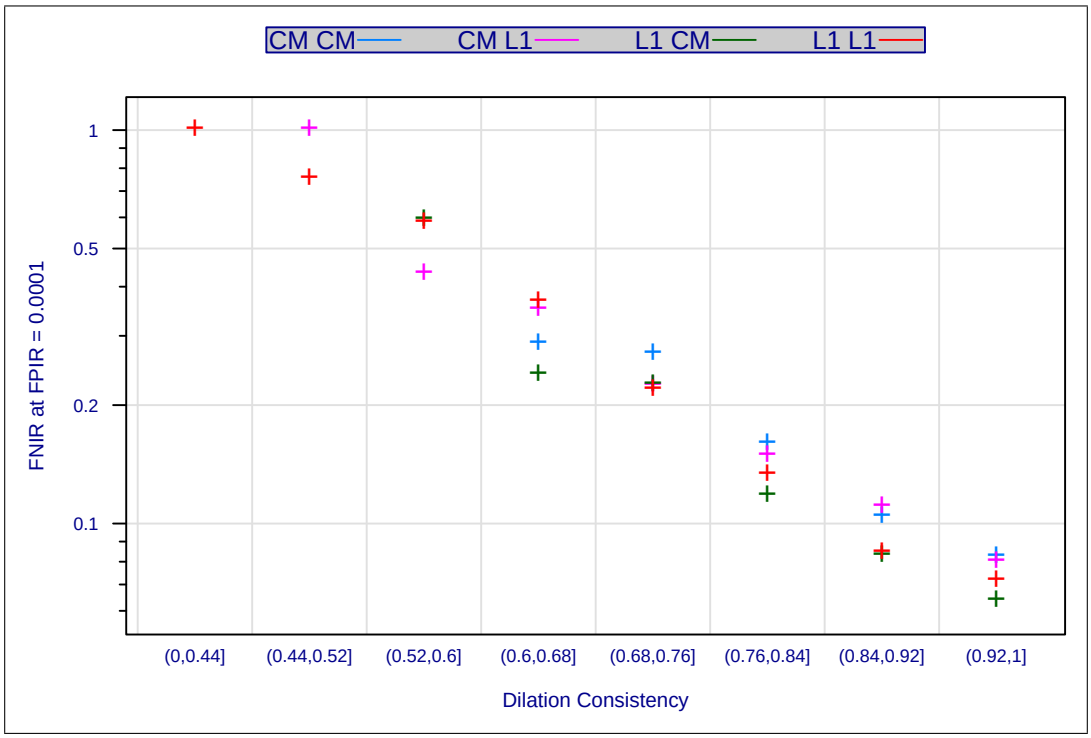

(b) Mean, L1 and CM images

Figure 416: Miss rate statistics for implementation W04A executing mate searches in an enrolled population of N = 1.6 million. The figures plots FNIR at FPIR = 0.0001 versus the IREX I metric for dilation consistency $(1 - \max(D_1, D_2))/(1 - \min(D_1, D_2))$ where D_i is pupil-iris radius ratio, and the subscripts refer to the mated enrollment and search image. The pathologically compressed 330x330 images are excluded from this analysis. The second figure breaks out dilation effects for interoperating camera pairs, CM and L1.

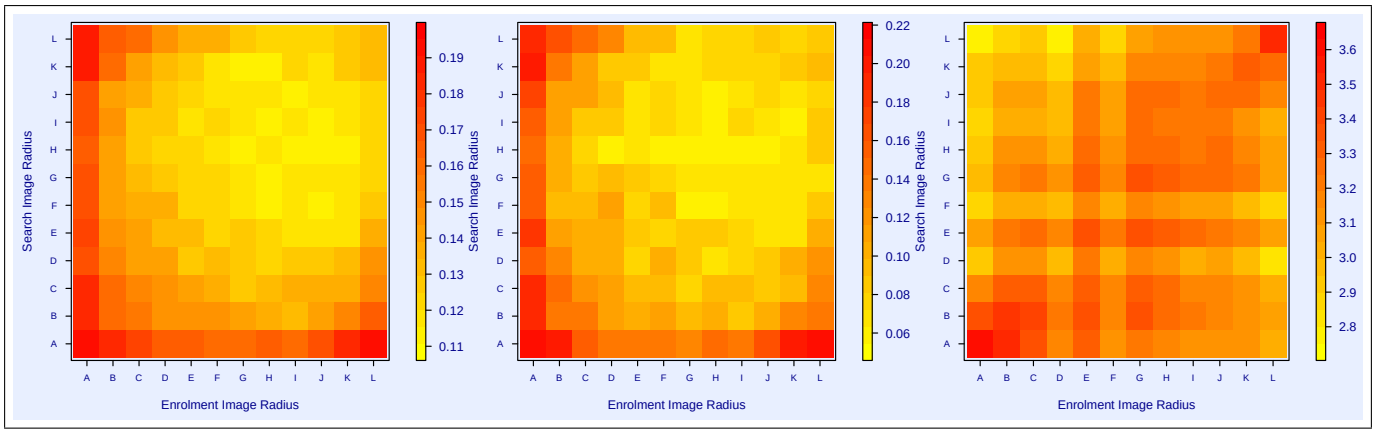

(a) Iris radius: Dis-similarity Score, Miss Rate, $\log_{10}(1+\text{Count})$

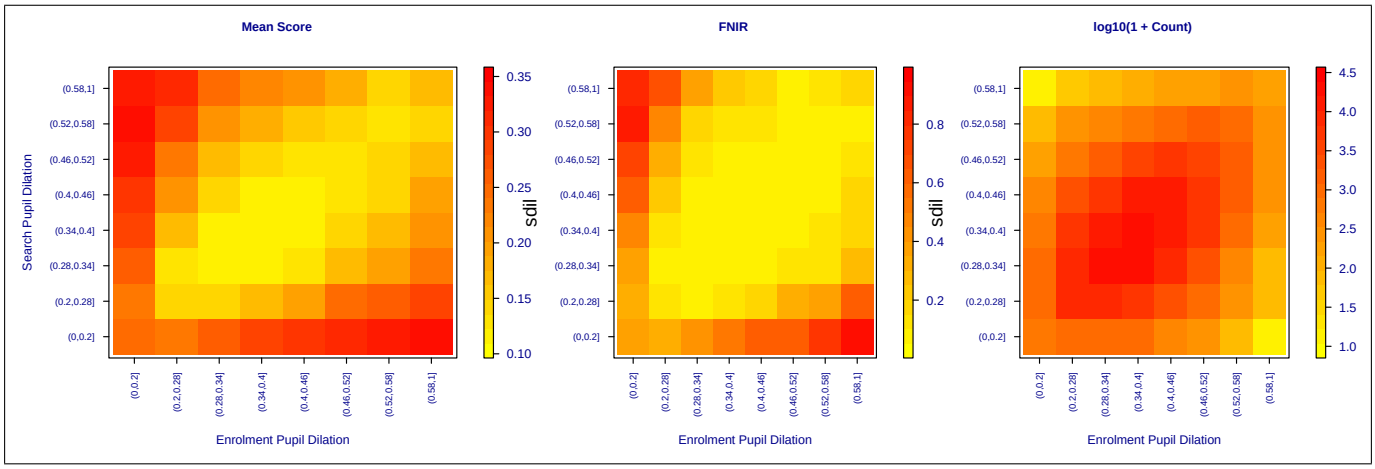

(b) Mate Dilation: Dis-similarity Score, Miss Rate, $\log_{10}(1+\text{Count})$

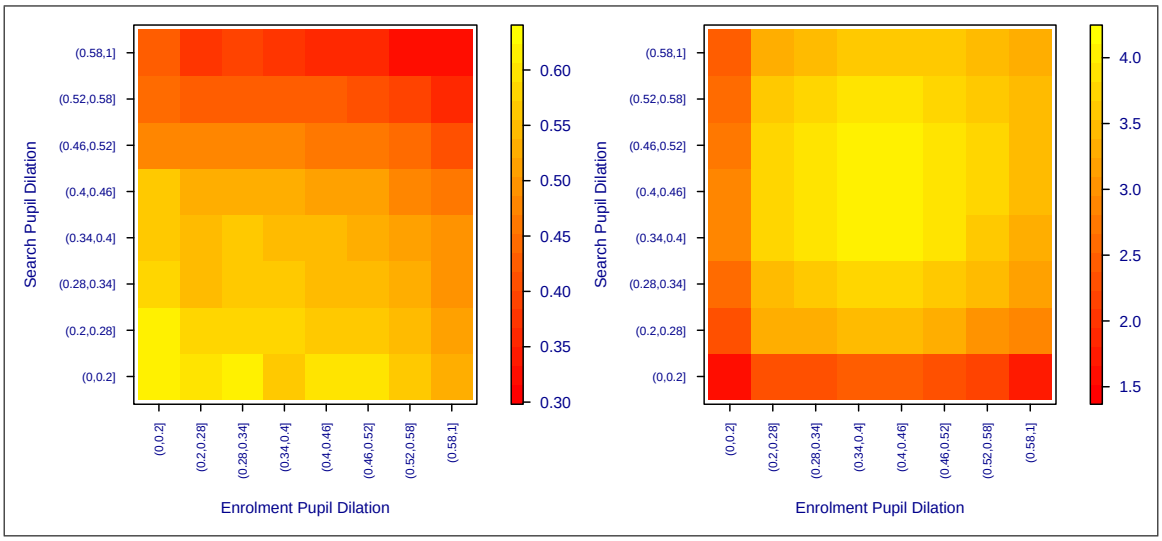

(c) Nonmate Dilation, Dis-similarity Score, Miss Rate, $\log_{10}(1+\text{Count})$

Figure 417: Heatmaps for implementation W05A executing mate searches in an enrolled population of N = 1.6 million. The radius images are binned by into twelve quantiles spanning $[0, 1]$. The dilation values are cut into ranges bounded by: $(0, 0.2, 0.28, 0.34, 0.40, 0.46, 0.52, 0.58, 1)$. The pathologically compressed 330x330 images are excluded from this analysis.

Heatmaps for implementation W05A executing mate searches in an enrolled population of N = 1.6 million.

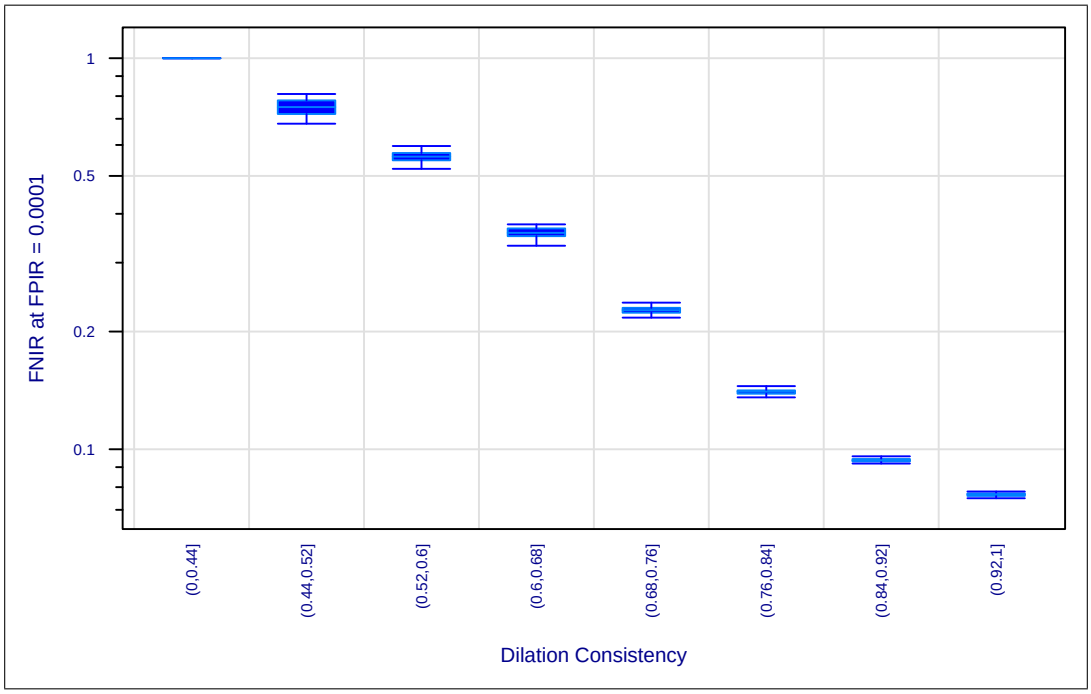

(a) Boxplot, all images

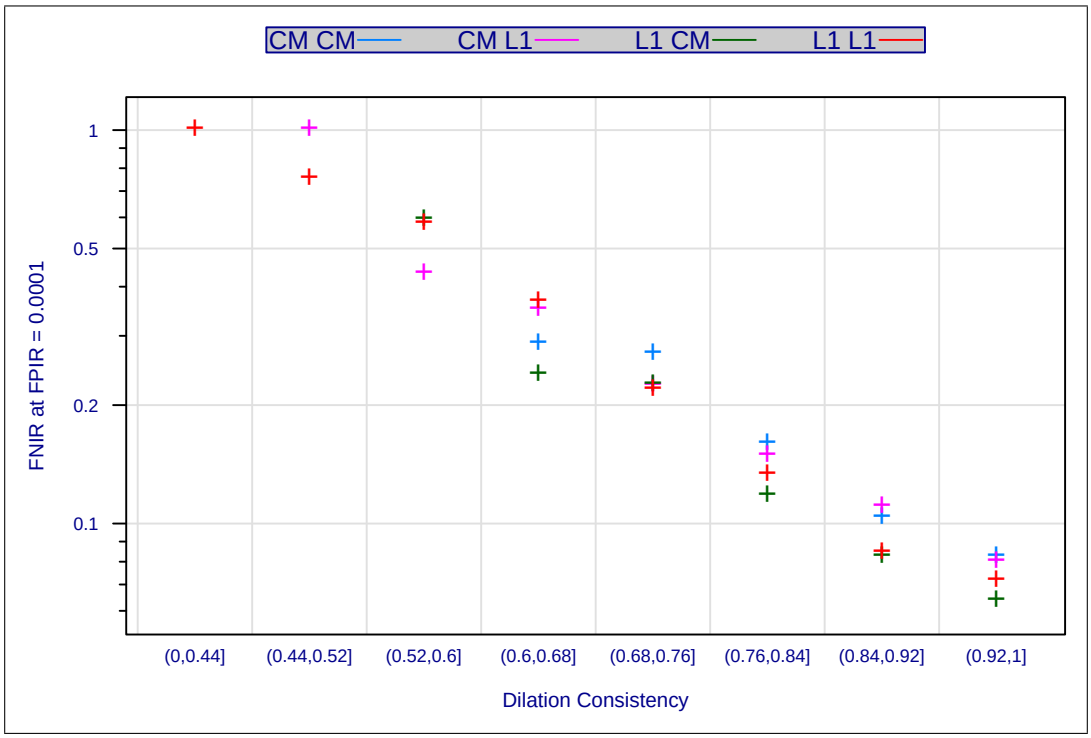

(b) Mean, L1 and CM images

Figure 418: Miss rate statistics for implementation W05A executing mate searches in an enrolled population of N = 1.6 million. The figures plots FNIR at FPIR = 0.0001 versus the IREX I metric for dilation consistency $(1-\max(D_1,D_2))/(1-\min(D_1,D_2))$ where D_i is pupil-iris radius ratio, and the subscripts refer to the mated enrollment and search image. The pathologically compressed 330x330 images are excluded from this analysis. The second figure breaks out dilation effects for interoperating camera pairs, CM and L1.

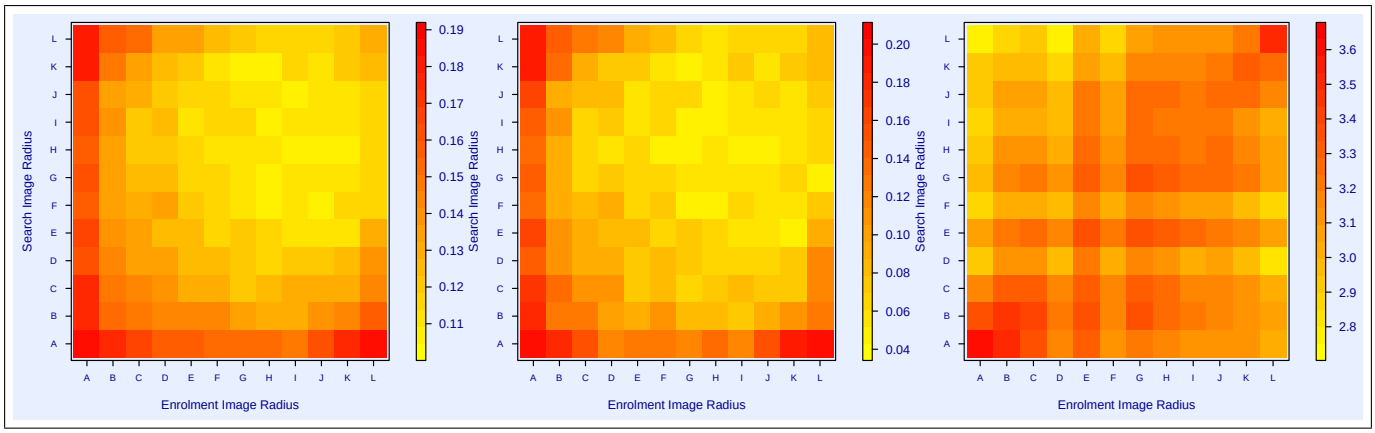

(a) Iris radius: Dis-similarity Score, Miss Rate, $\log_{10}(1+\text{Count})$

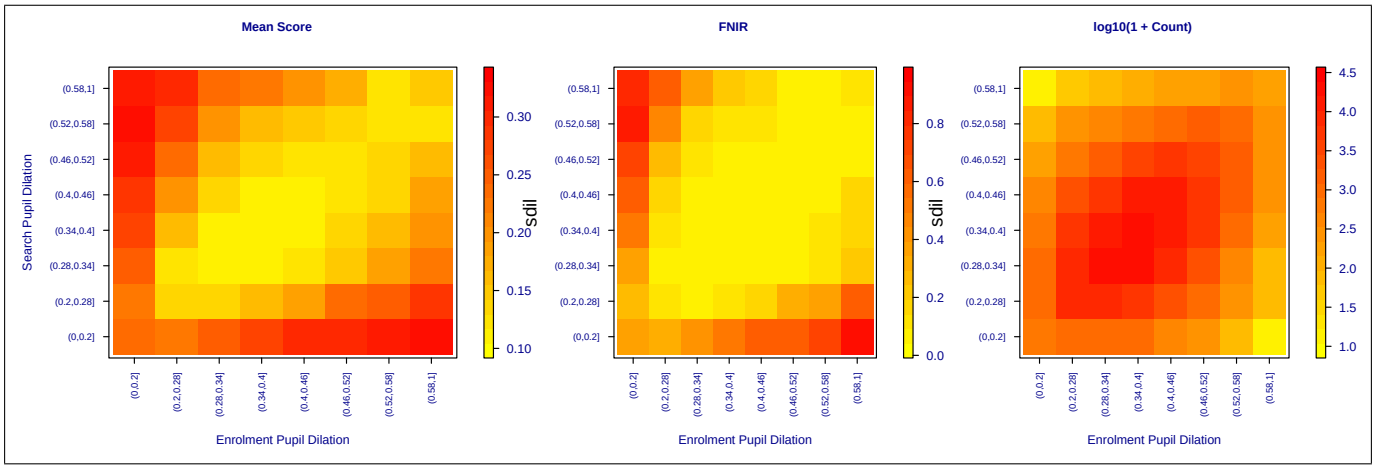

(b) Mate Dilation: Dis-similarity Score, Miss Rate, $\log_{10}(1+\text{Count})$

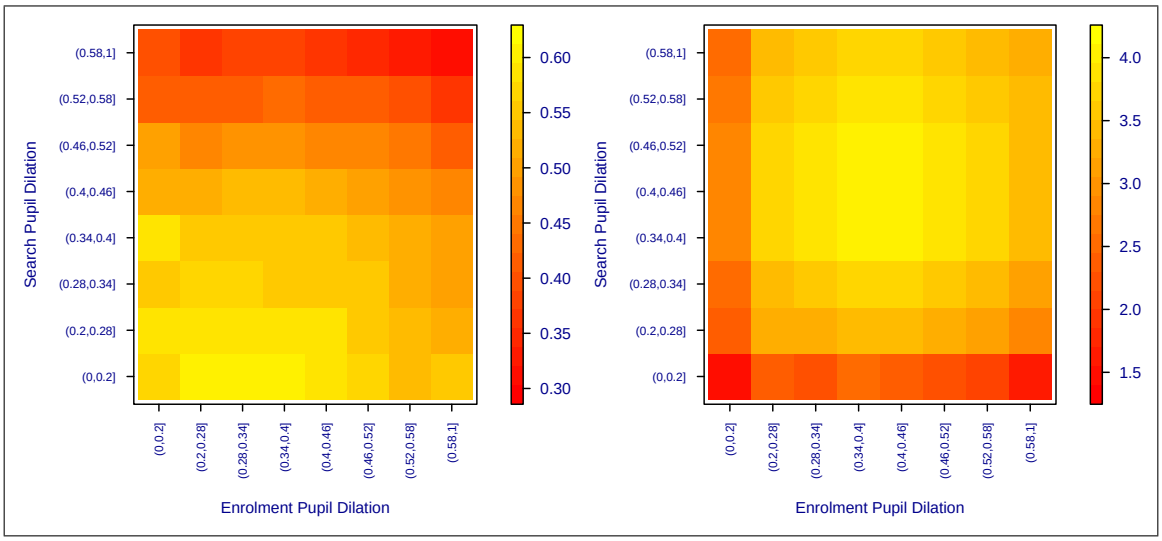

(c) Nonmate Dilation, Dis-similarity Score, Miss Rate, $\log_{10}(1+\text{Count})$

Figure 419: Heatmaps for implementation W11A executing mate searches in an enrolled population of N = 1.6 million. The radius images are binned by into twelve quantiles spanning $[0, 1]$. The dilation values are cut into ranges bounded by: $(0, 0.2, 0.28, 0.34, 0.40, 0.46, 0.52, 0.58, 1)$. The pathologically compressed 330x330 images are excluded from this analysis.

Heatmaps for implementation W11A executing mate searches in an enrolled population of N = 1.6 million.

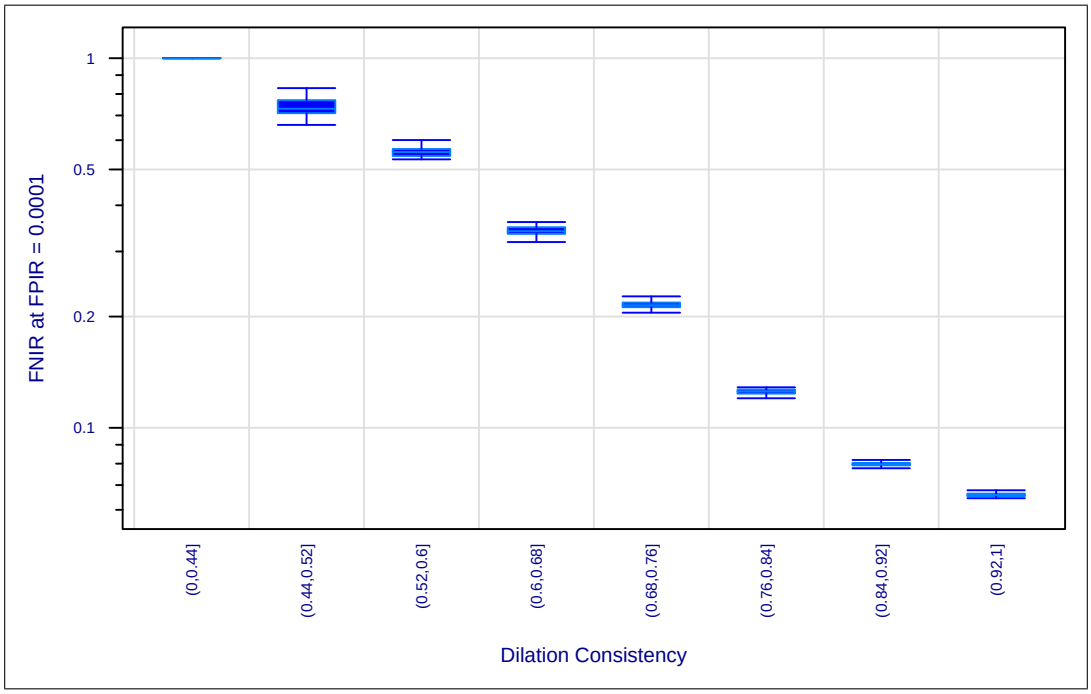

(a) Boxplot, all images

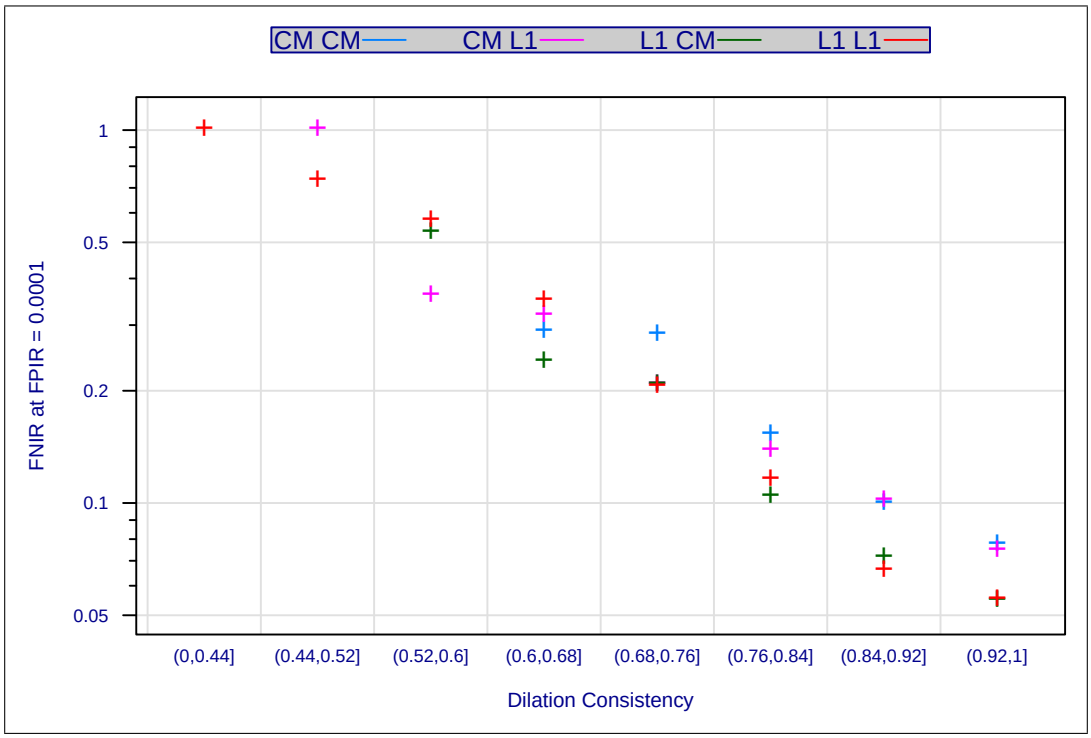

(b) Mean, L1 and CM images

Figure 420: Miss rate statistics for implementation W11A executing mate searches in an enrolled population of N = 1.6 million. The figures plots FNIR at FPIR = 0.0001 versus the IREX I metric for dilation consistency $(1-\max(D_1, D_2))/(1-\min(D_1, D_2))$ where D_i is pupil-iris radius ratio, and the subscripts refer to the mated enrollment and search image. The pathologically compressed 330x330 images are excluded from this analysis. The second figure breaks out dilation effects for interoperating camera pairs, CM and L1.

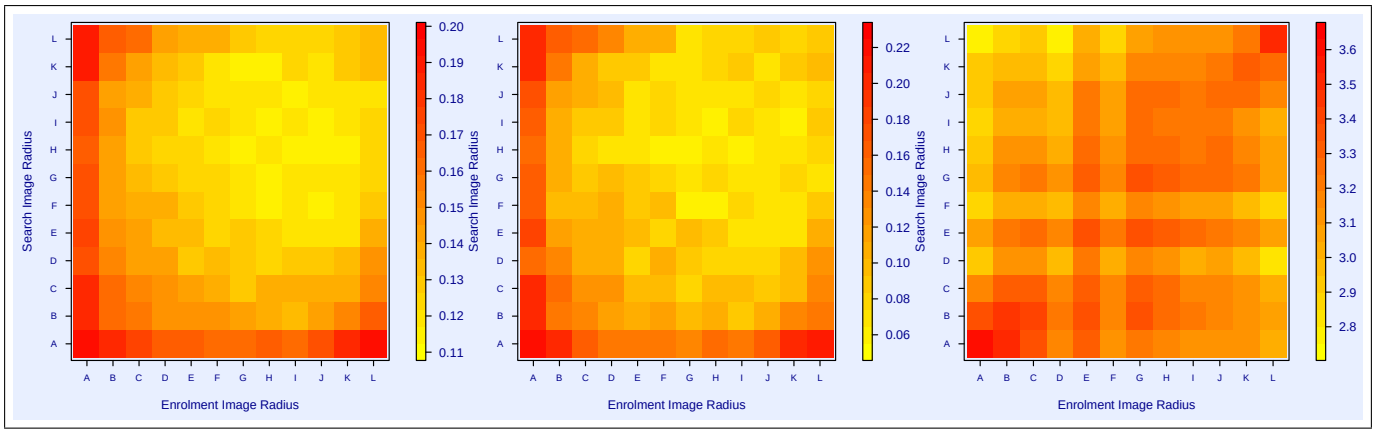

(a) Iris radius: Dis-similarity Score, Miss Rate, $\log_{10}(1+\text{Count})$

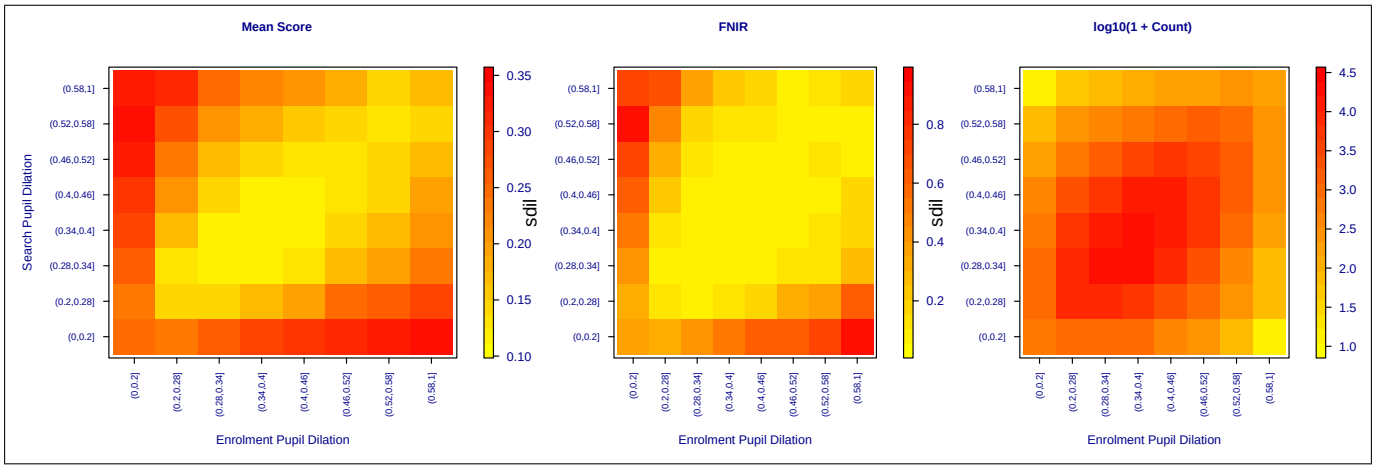

(b) Mate Dilation: Dis-similarity Score, Miss Rate, $\log_{10}(1+\text{Count})$

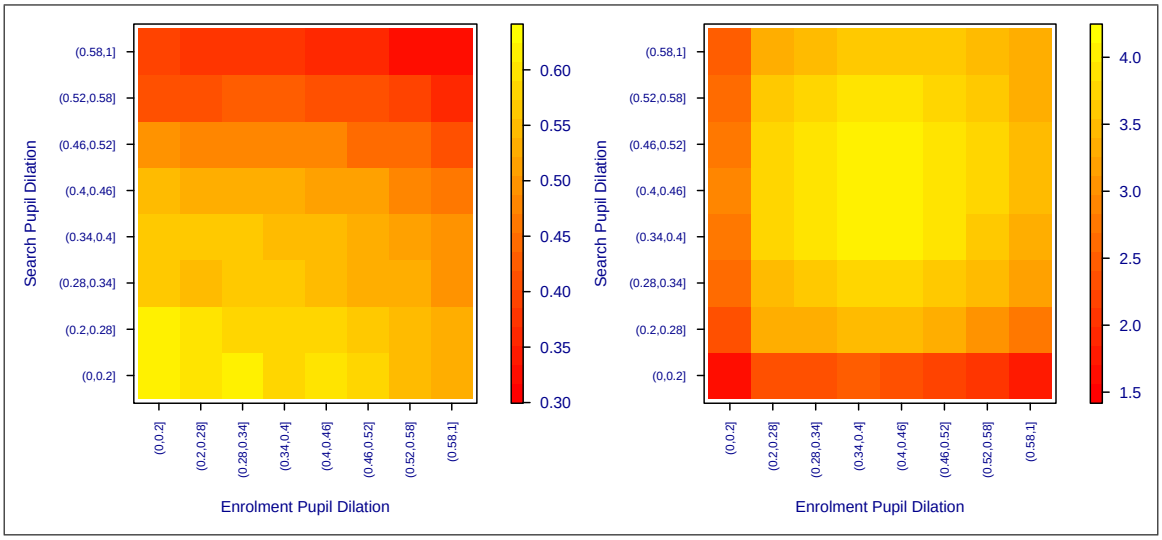

(c) Nonmate Dilation, Dis-similarity Score, Miss Rate, $\log_{10}(1+\text{Count})$

Figure 421: Heatmaps for implementation W11B executing mate searches in an enrolled population of N = 1.6 million. The radius images are binned by into twelve quantiles spanning $[0, 1]$. The dilation values are cut into ranges bounded by: $(0, 0.2, 0.28, 0.34, 0.40, 0.46, 0.52, 0.58, 1)$. The pathologically compressed 330x330 images are excluded from this analysis.

Heatmaps for implementation W11B executing mate searches in an enrolled population of N = 1.6 million.

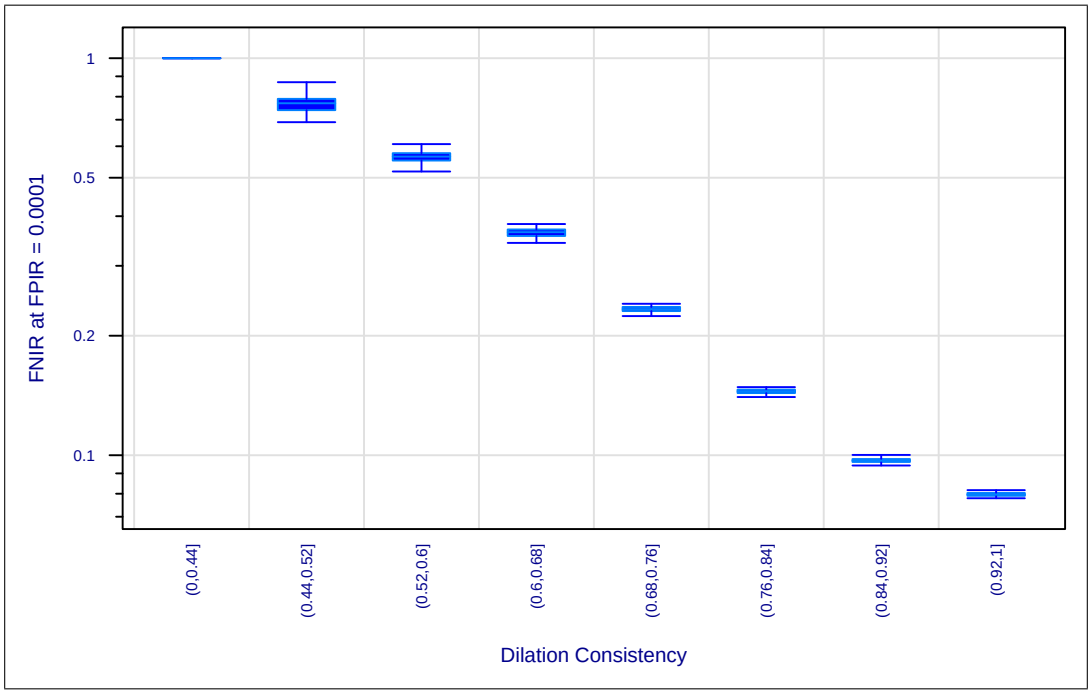

(a) Boxplot, all images

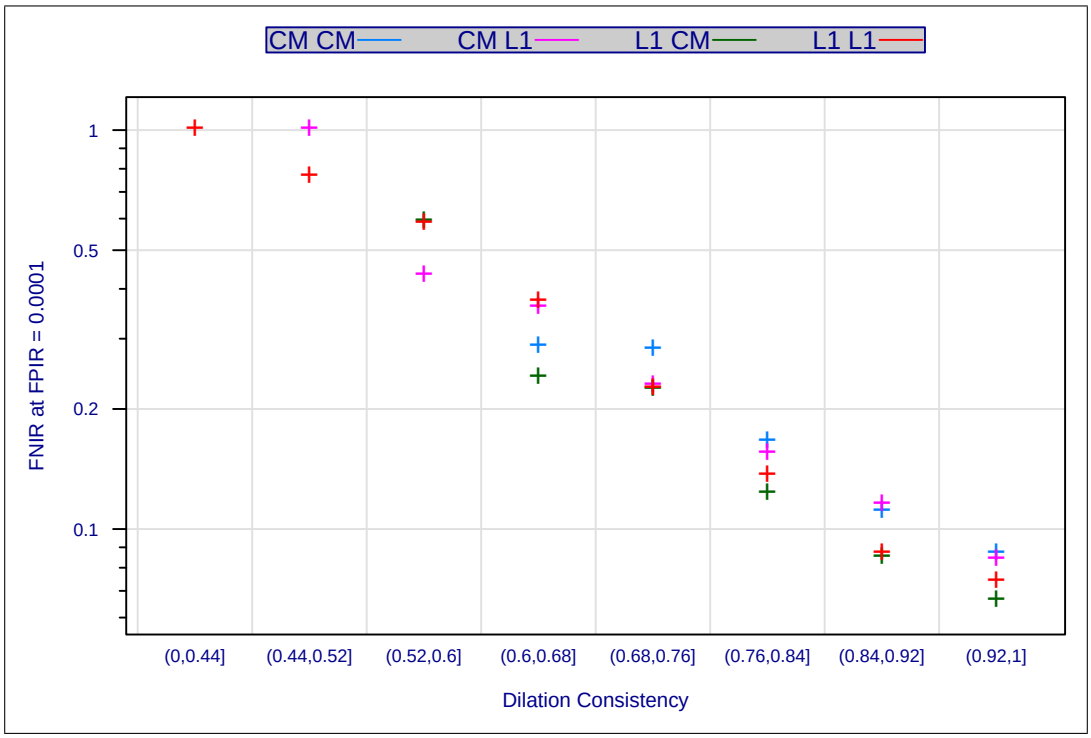

(b) Mean, L1 and CM images

Figure 422: Miss rate statistics for implementation W11B executing mate searches in an enrolled population of N = 1.6 million. The figures plots FNIR at FPIR = 0.0001 versus the IREX I metric for dilation consistency $(1 - \max(D_1, D_2))/(1 - \min(D_1, D_2))$ where D_i is pupil-iris radius ratio, and the subscripts refer to the mated enrollment and search image. The pathologically compressed 330x330 images are excluded from this analysis. The second figure breaks out dilation effects for interoperating camera pairs, CM and L1.

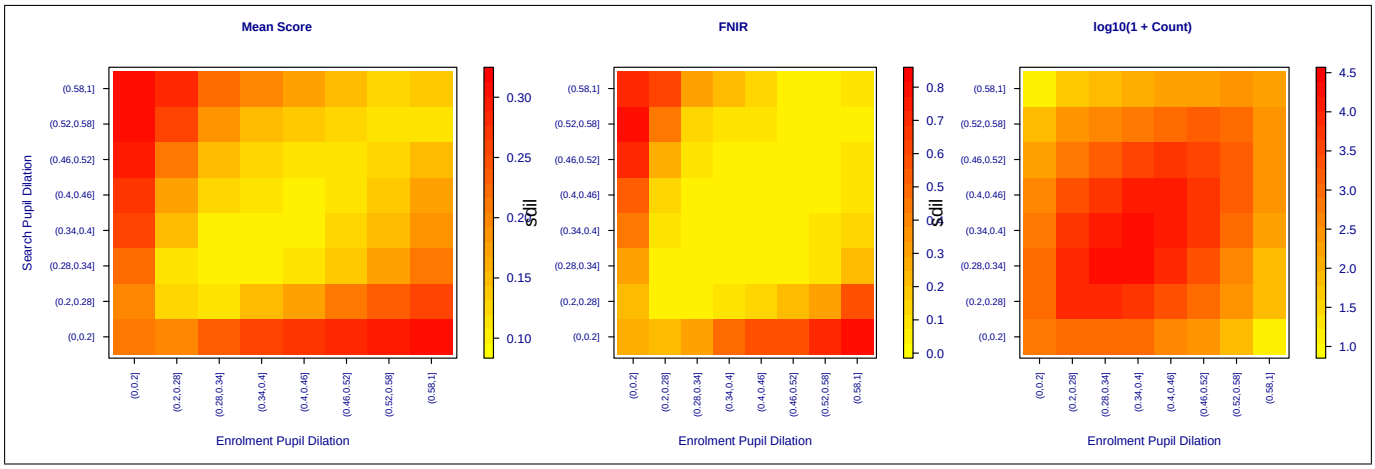

(a) Mate Dilation: Dis-similarity Score, Miss Rate, $\log_{10}(1+\text{Count})$

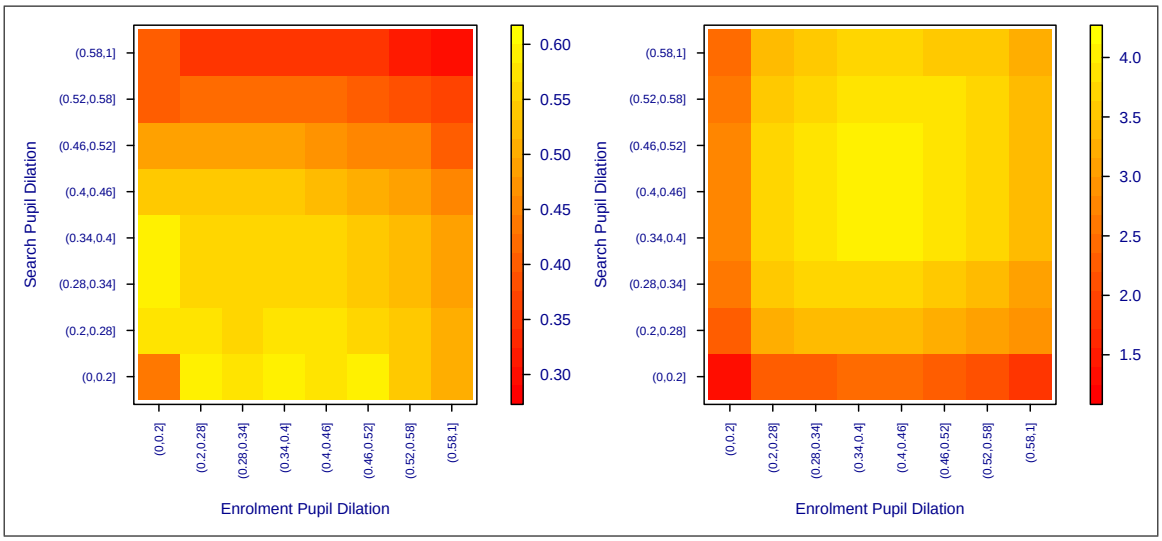

(b) Nonmate Dilation, Dis-similarity Score, Miss Rate, $\log_{10}(1+\text{Count})$

Figure 423: Heatmaps for implementation W12A executing mate searches in an enrolled population of N = 1.6 million. The radius images are binned by into twelve quantiles spanning $[0, 1]$. The dilation values are cut into ranges bounded by: $(0, 0.2, 0.28, 0.34, 0.40, 0.46, 0.52, 0.58, 1)$. The pathologically compressed 330x330 images are excluded from this analysis.

Heatmaps for implementation W12A executing mate searches in an enrolled population of N = 1.6 million.

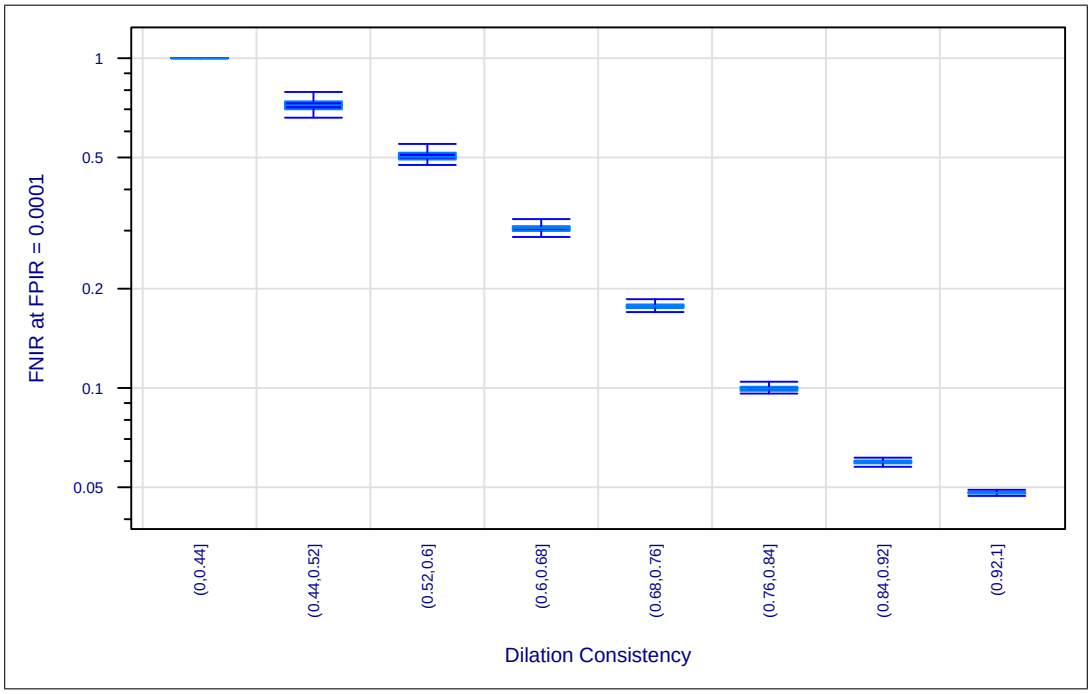

(a) Boxplot, all images

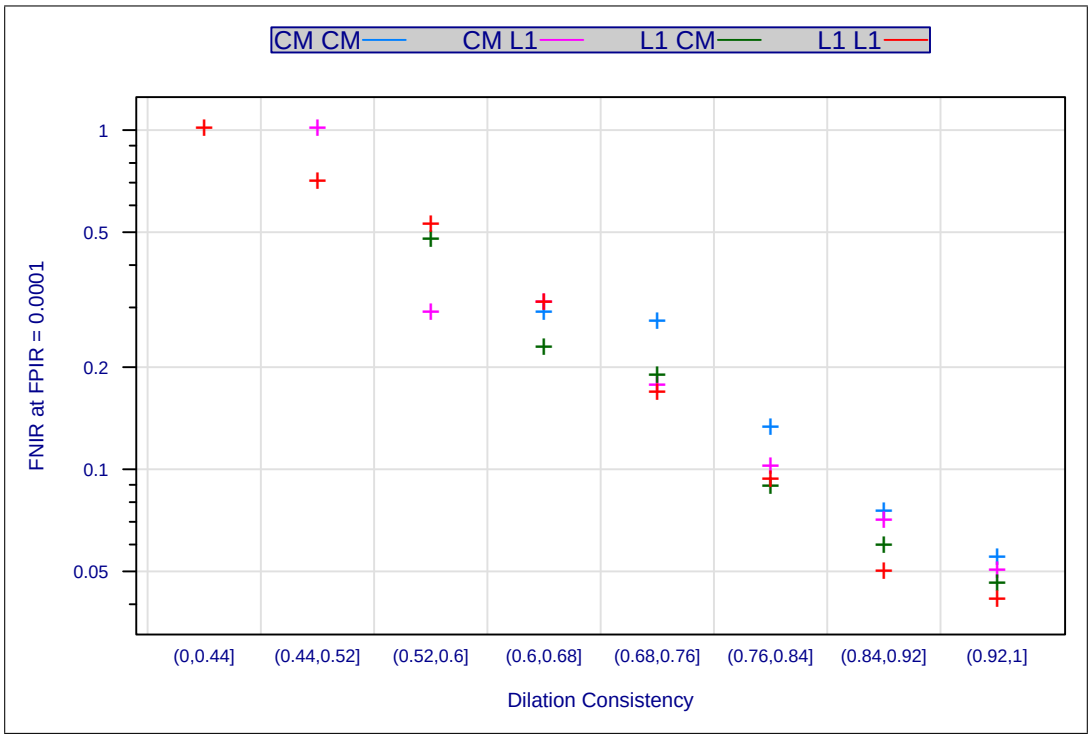

(b) Mean, L1 and CM images

Figure 424: Miss rate statistics for implementation W12A executing mate searches in an enrolled population of N = 1.6 million. The figures plots FNIR at FPIR = 0.0001 versus the IREX I metric for dilation consistency $(1-\max(D_1, D_2))/(1-\min(D_1, D_2))$ where D_i is pupil-iris radius ratio, and the subscripts refer to the mated enrollment and search image. The pathologically compressed 330x330 images are excluded from this analysis. The second figure breaks out dilation effects for interoperating camera pairs, CM and L1.

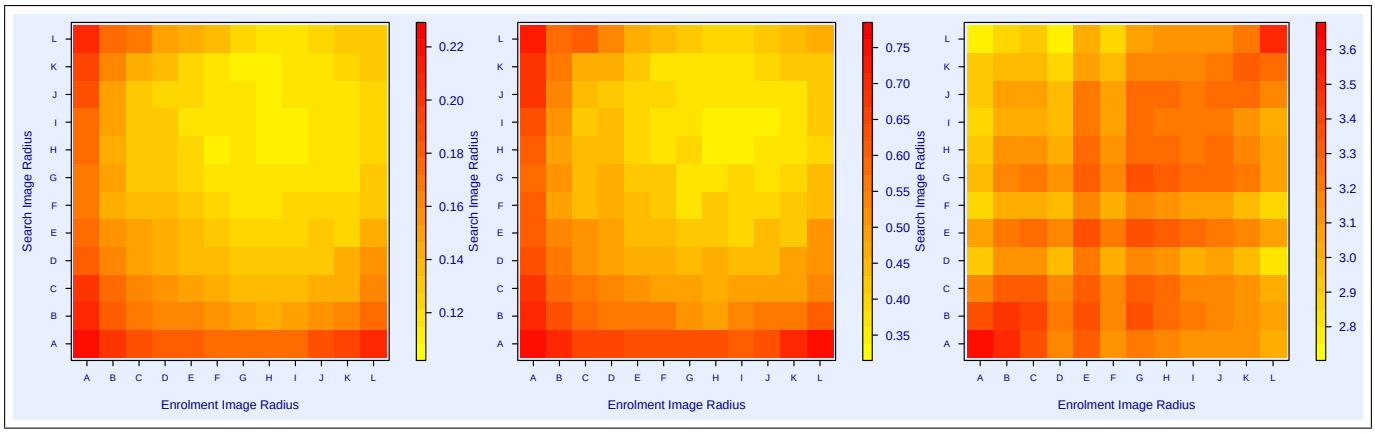

(a) Iris radius: Dis-similarity Score, Miss Rate, $\log_{10}(1+\text{Count})$

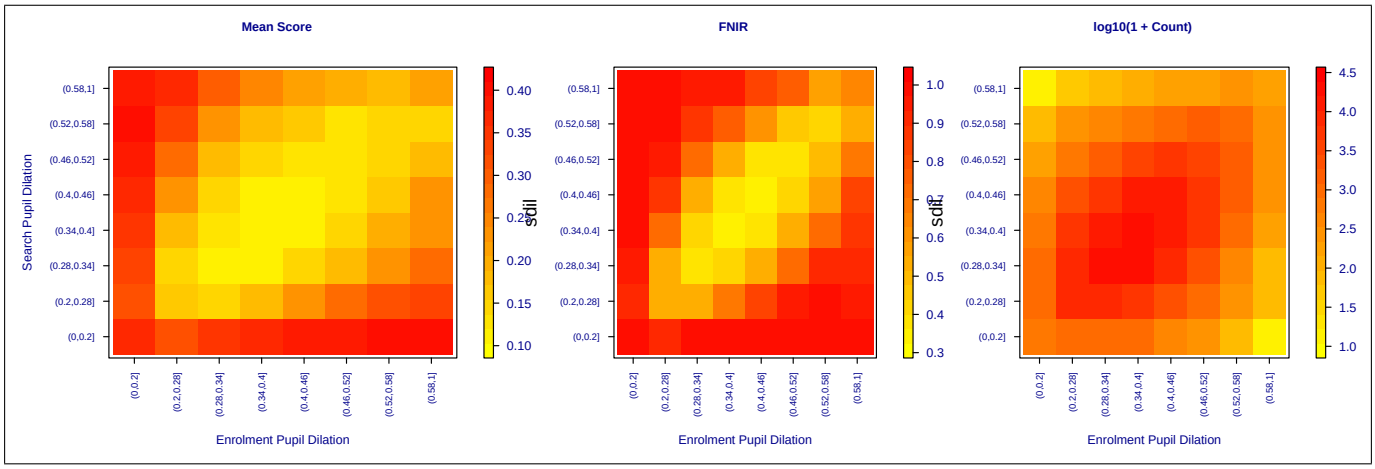

(b) Mate Dilation: Dis-similarity Score, Miss Rate, $\log_{10}(1+\text{Count})$

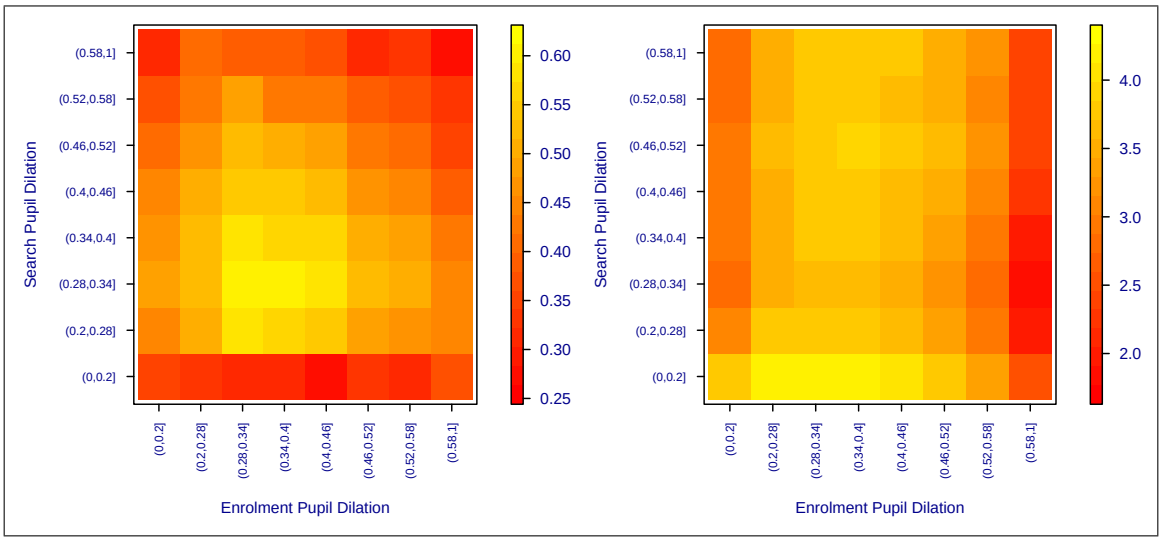

(c) Nonmate Dilation, Dis-similarity Score, Miss Rate, $\log_{10}(1+\text{Count})$

Figure 425: Heatmaps for implementation X02A executing mate searches in an enrolled population of N = 1.6 million. The radius images are binned by into twelve quantiles spanning $[0, 1]$. The dilation values are cut into ranges bounded by: $(0, 0.2, 0.28, 0.34, 0.40, 0.46, 0.52, 0.58, 1)$. The pathologically compressed 330x330 images are excluded from this analysis.

Heatmaps for implementation X02A executing mate searches in an enrolled population of N = 1.6 million.

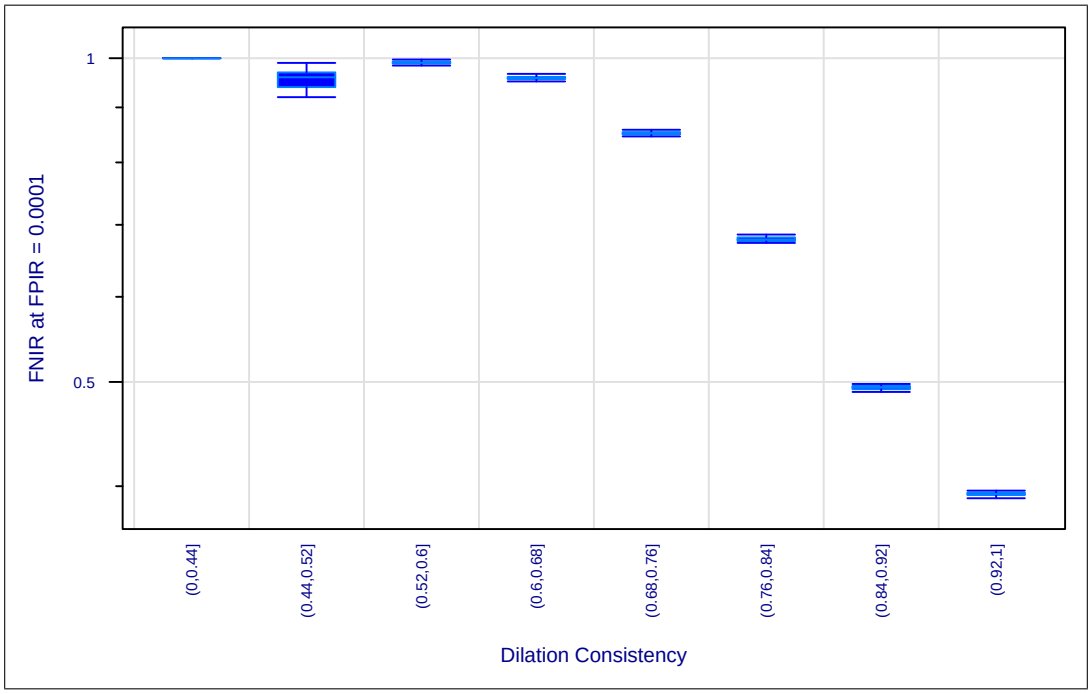

(a) Boxplot, all images

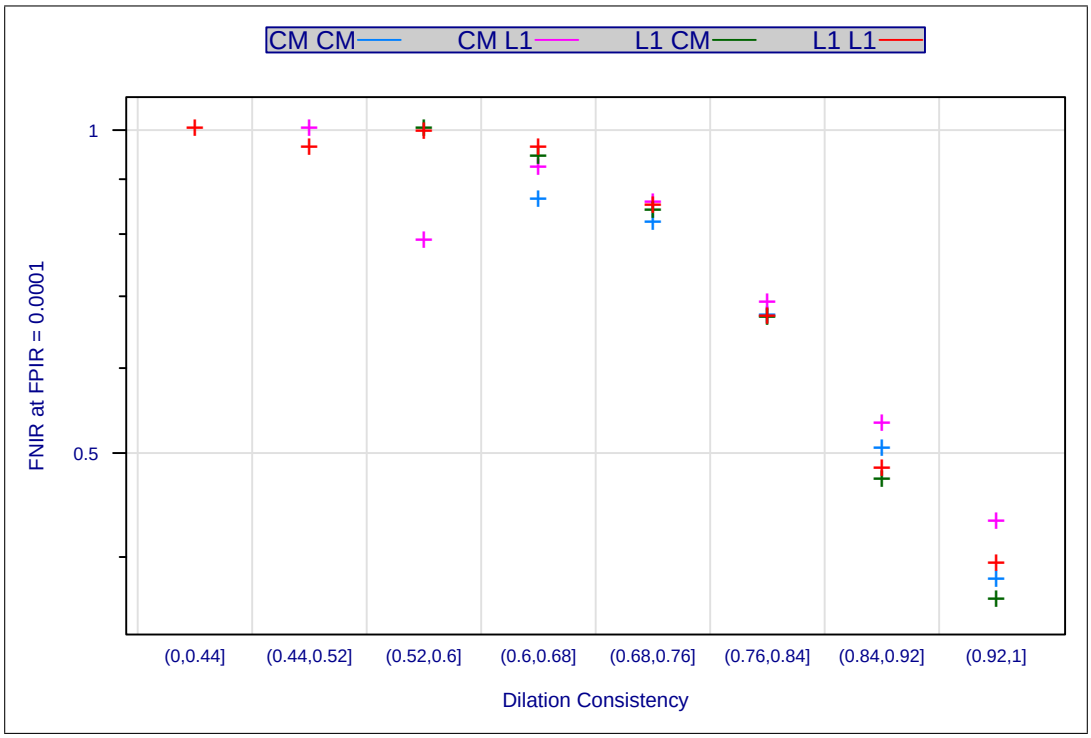

(b) Mean, L1 and CM images

Figure 426: Miss rate statistics for implementation X02A executing mate searches in an enrolled population of N = 1.6 million. The figures plots FNIR at FPIR = 0.0001 versus the IREX I metric for dilation consistency $(1 - \max(D_1, D_2))/(1 - \min(D_1, D_2))$ where D_i is pupil-iris radius ratio, and the subscripts refer to the mated enrollment and search image. The pathologically compressed 330x330 images are excluded from this analysis. The second figure breaks out dilation effects for interoperating camera pairs, CM and L1.

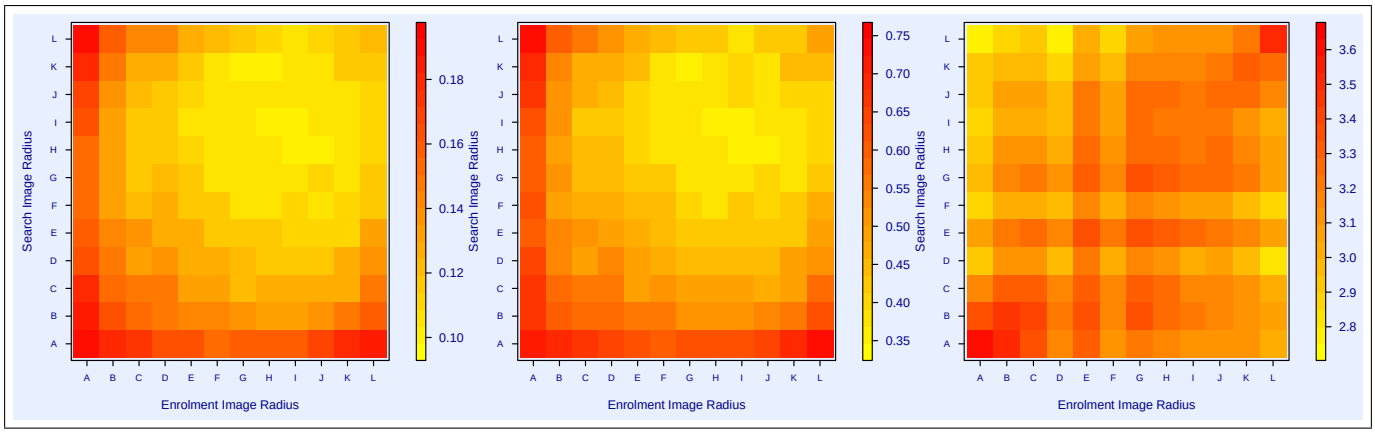

(a) Iris radius: Dis-similarity Score, Miss Rate, $\log_{10}(1+\text{Count})$

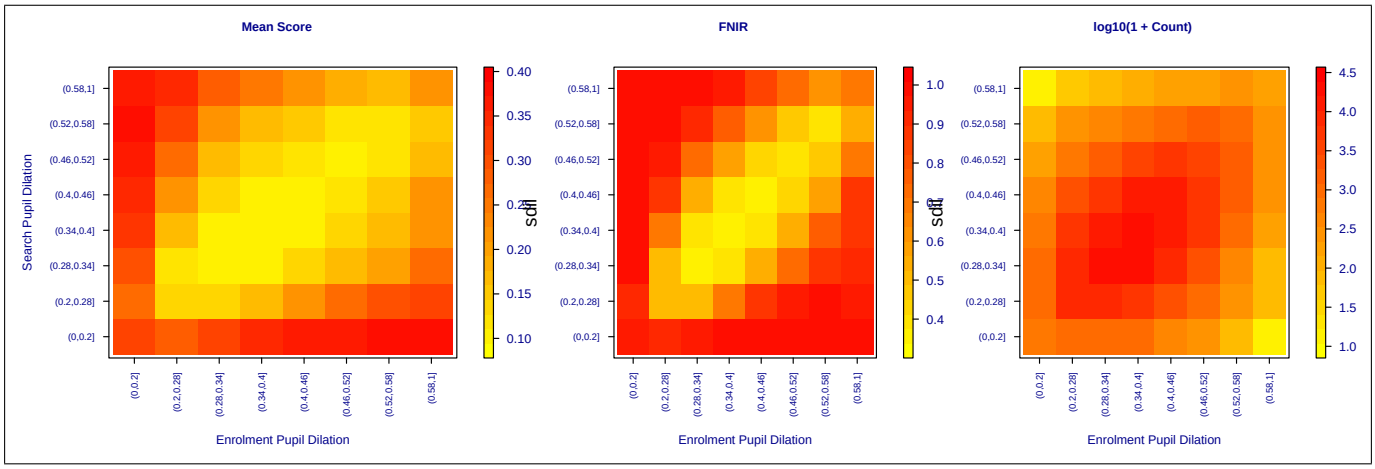

(b) Mate Dilation: Dis-similarity Score, Miss Rate, $\log_{10}(1+\text{Count})$

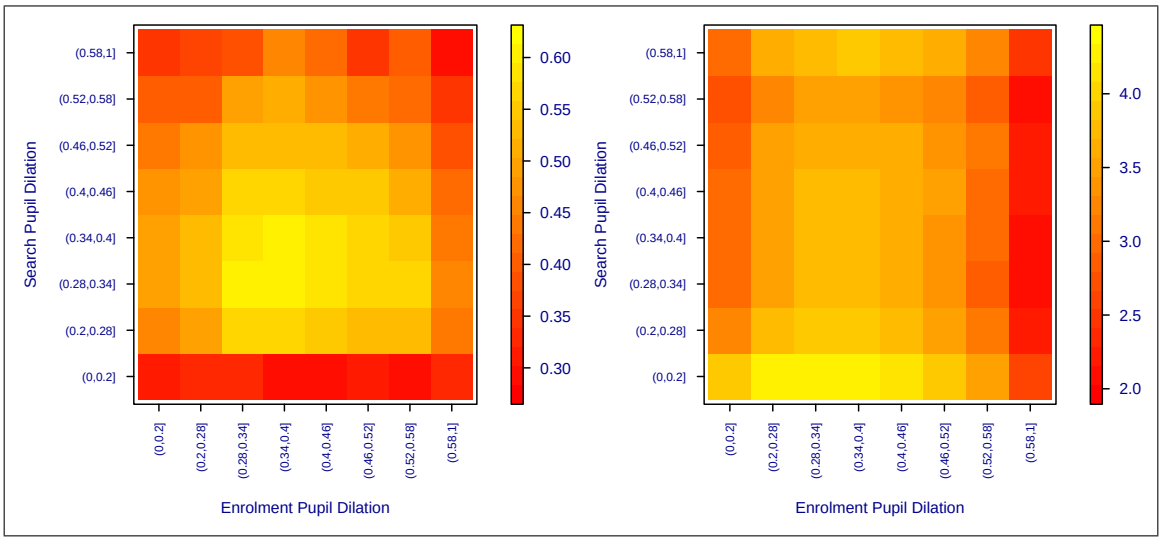

(c) Nonmate Dilation, Dis-similarity Score, Miss Rate, $\log_{10}(1+\text{Count})$

Figure 427: Heatmaps for implementation X03A executing mate searches in an enrolled population of N = 1.6 million. The radius images are binned by into twelve quantiles spanning $[0, 1]$. The dilation values are cut into ranges bounded by: $(0, 0.2, 0.28, 0.34, 0.40, 0.46, 0.52, 0.58, 1)$. The pathologically compressed 330x330 images are excluded from this analysis.

Heatmaps for implementation X03A executing mate searches in an enrolled population of N = 1.6 million.

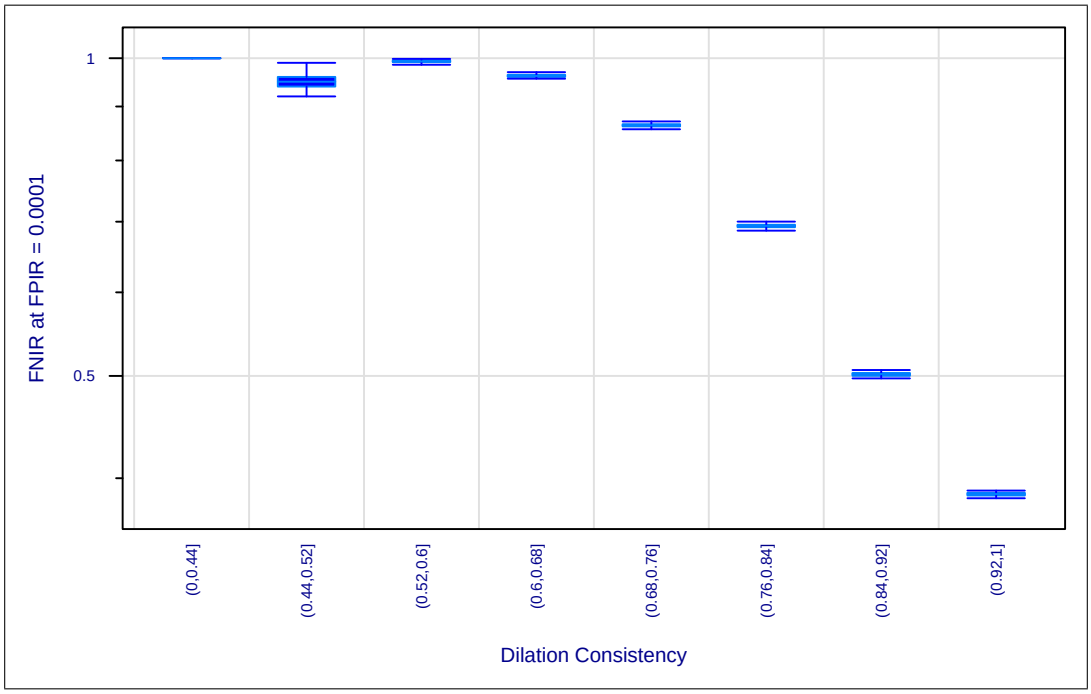

(a) Boxplot, all images

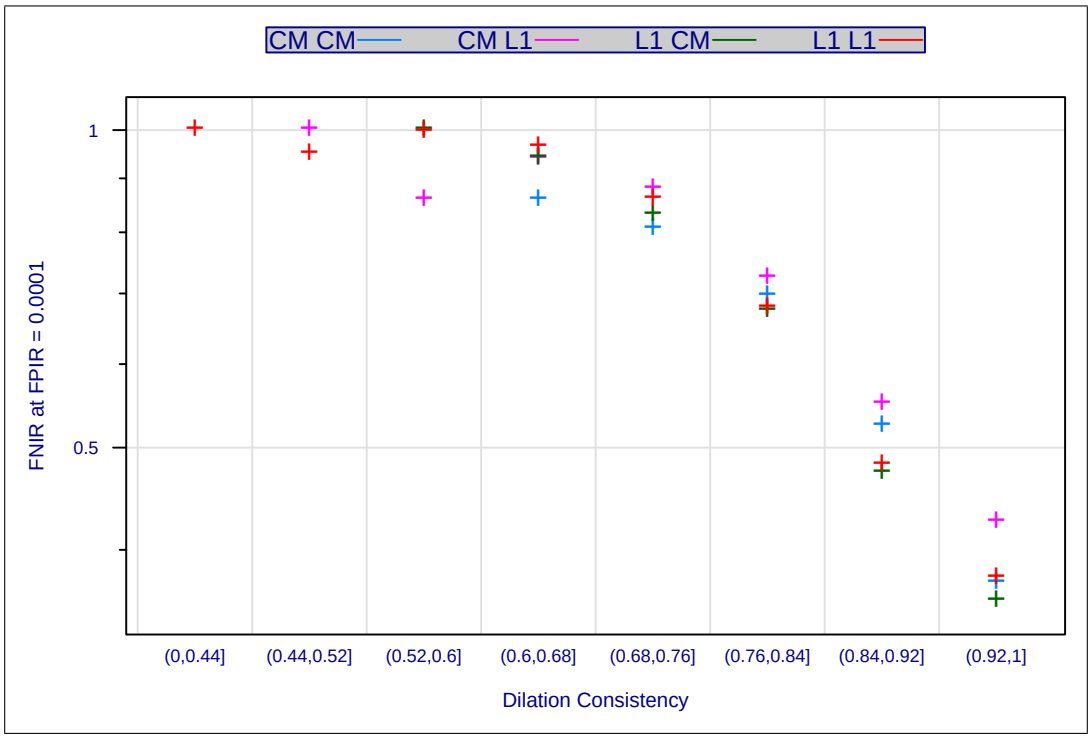

(b) Mean, L1 and CM images

Figure 428: Miss rate statistics for implementation X03A executing mate searches in an enrolled population of N = 1.6 million. The figures plots FNIR at FPIR = 0.0001 versus the IREX I metric for dilation consistency $(1 - \max(D_1, D_2))/(1 - \min(D_1, D_2))$ where D_i is pupil-iris radius ratio, and the subscripts refer to the mated enrollment and search image. The pathologically compressed 330x330 images are excluded from this analysis. The second figure breaks out dilation effects for interoperating camera pairs, CM and L1.

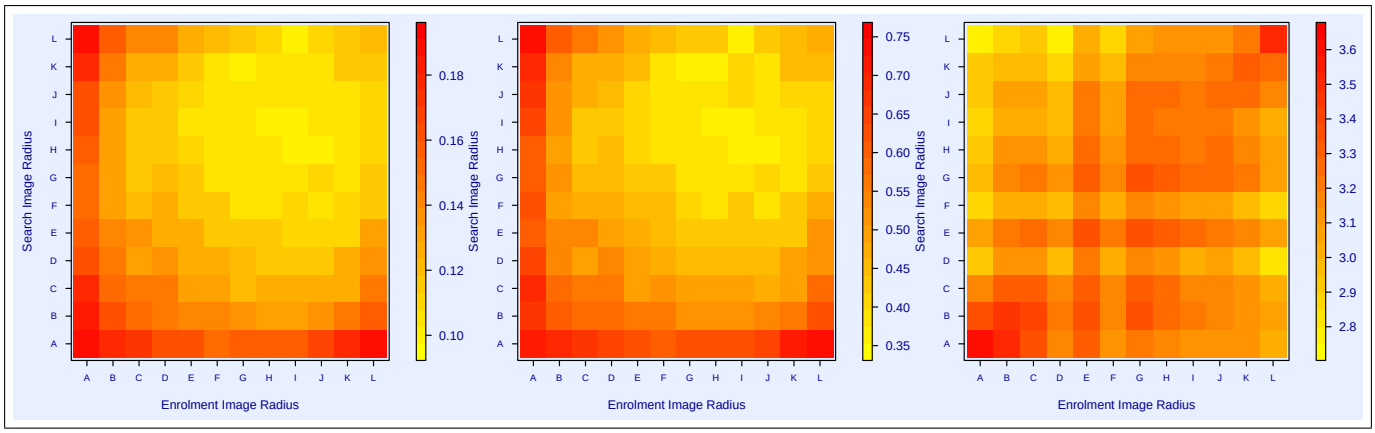

(a) Iris radius: Dis-similarity Score, Miss Rate, $\log_{10}(1+\text{Count})$

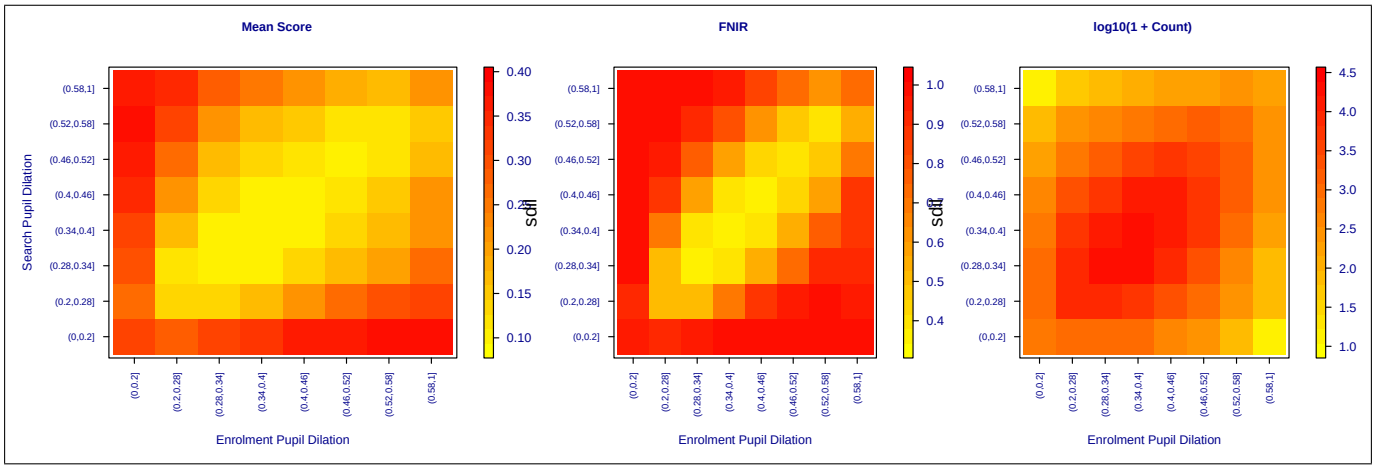

(b) Mate Dilation: Dis-similarity Score, Miss Rate, $\log_{10}(1+\text{Count})$

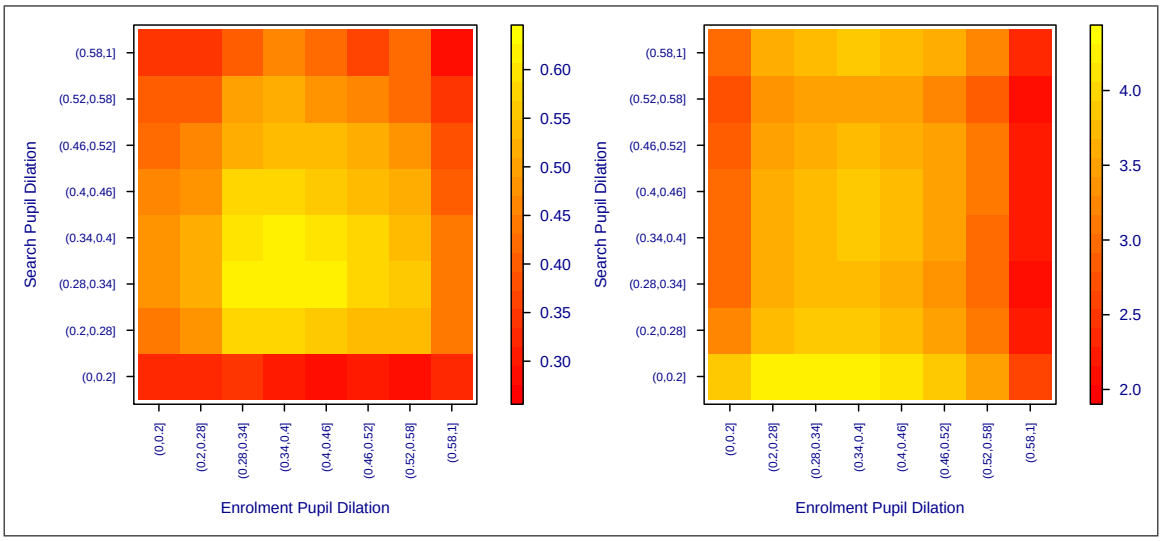

(c) Nonmate Dilation, Dis-similarity Score, Miss Rate, $\log_{10}(1+\text{Count})$

Figure 429: Heatmaps for implementation X04A executing mate searches in an enrolled population of N = 1.6 million. The radius images are binned by into twelve quantiles spanning $[0, 1]$. The dilation values are cut into ranges bounded by: $(0, 0.2, 0.28, 0.34, 0.40, 0.46, 0.52, 0.58, 1)$. The pathologically compressed 330x330 images are excluded from this analysis.

Heatmaps for implementation X04A executing mate searches in an enrolled population of N = 1.6 million.

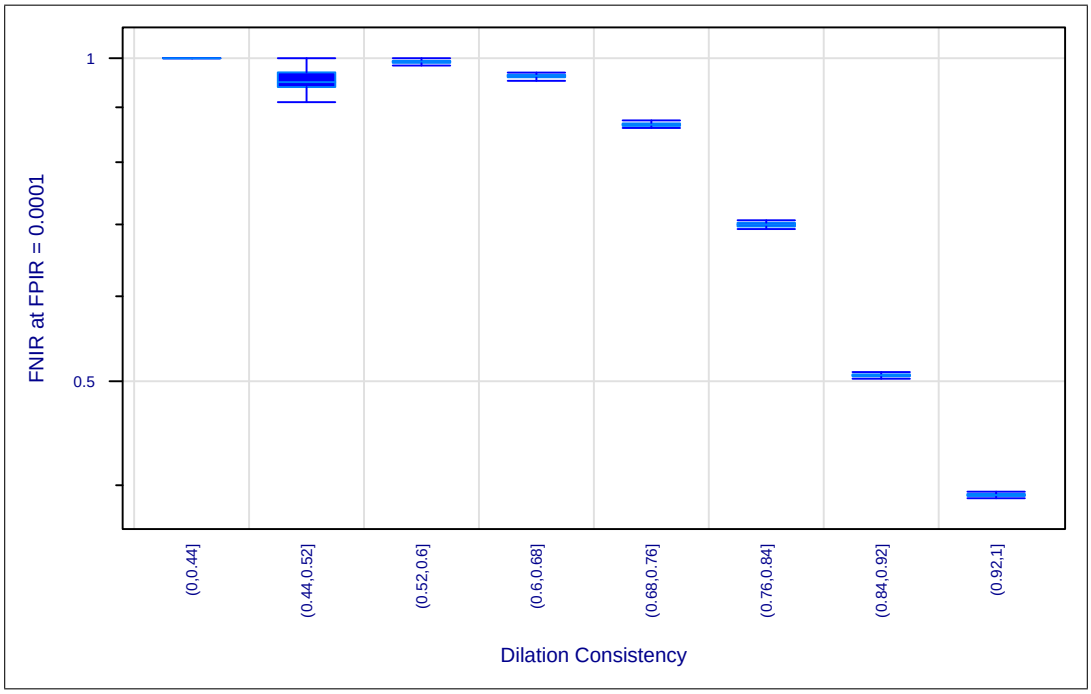

(a) Boxplot, all images

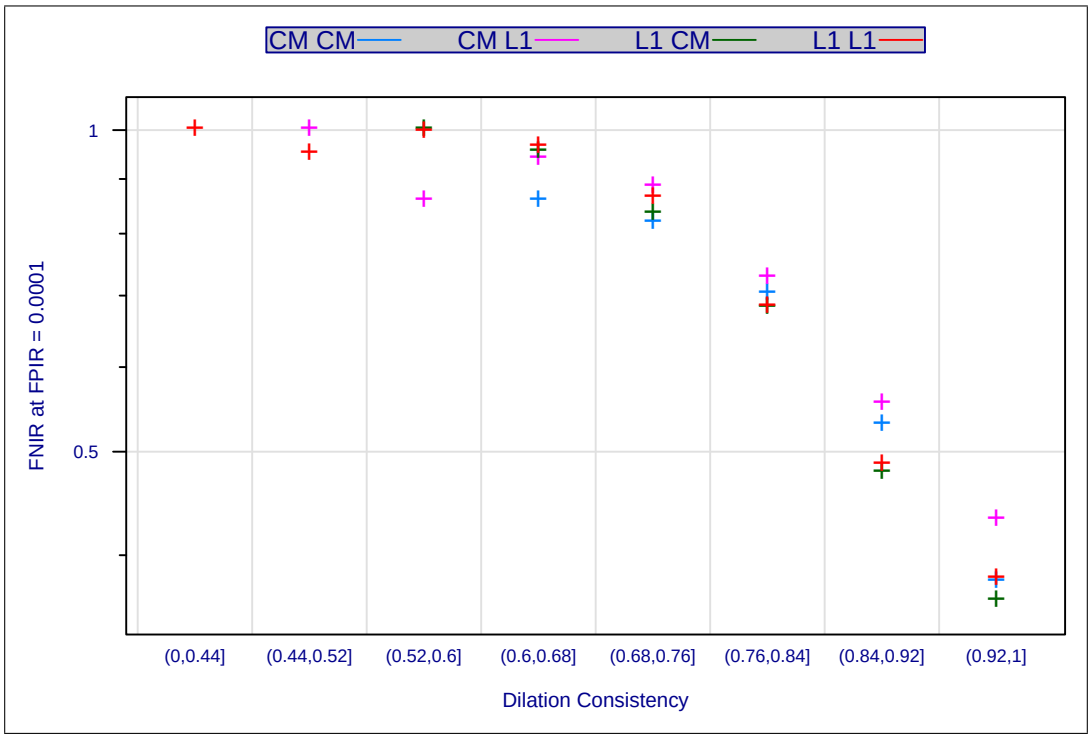

(b) Mean, L1 and CM images

Figure 430: Miss rate statistics for implementation X04A executing mate searches in an enrolled population of N = 1.6 million. The figures plots FNIR at FPIR = 0.0001 versus the IREX I metric for dilation consistency $(1 - \max(D_1, D_2))/(1 - \min(D_1, D_2))$ where D_i is pupil-iris radius ratio, and the subscripts refer to the mated enrollment and search image. The pathologically compressed 330x330 images are excluded from this analysis. The second figure breaks out dilation effects for interoperating camera pairs, CM and L1.

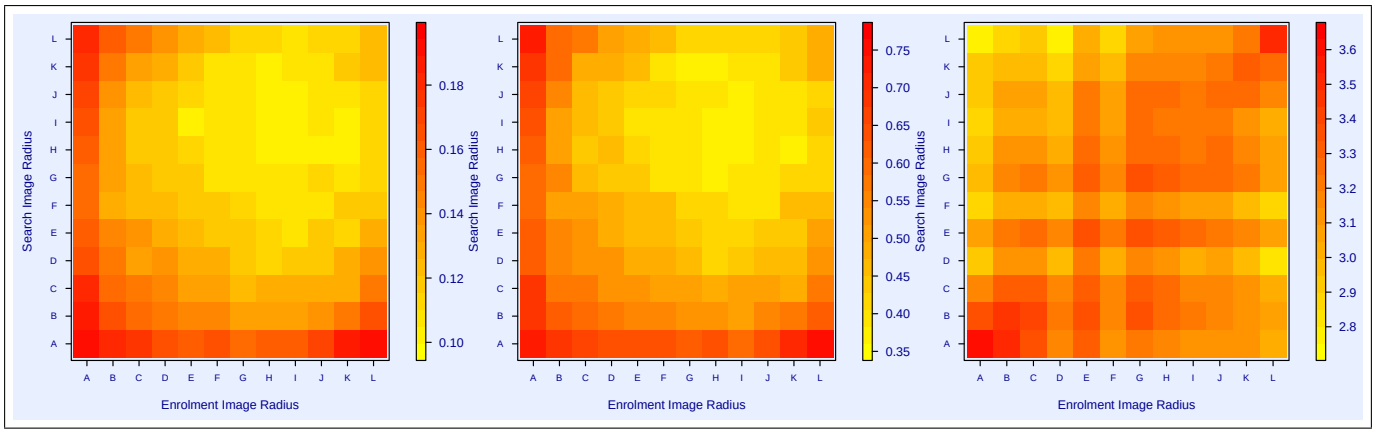

(a) Iris radius: Dis-similarity Score, Miss Rate, $\log_{10}(1+\text{Count})$

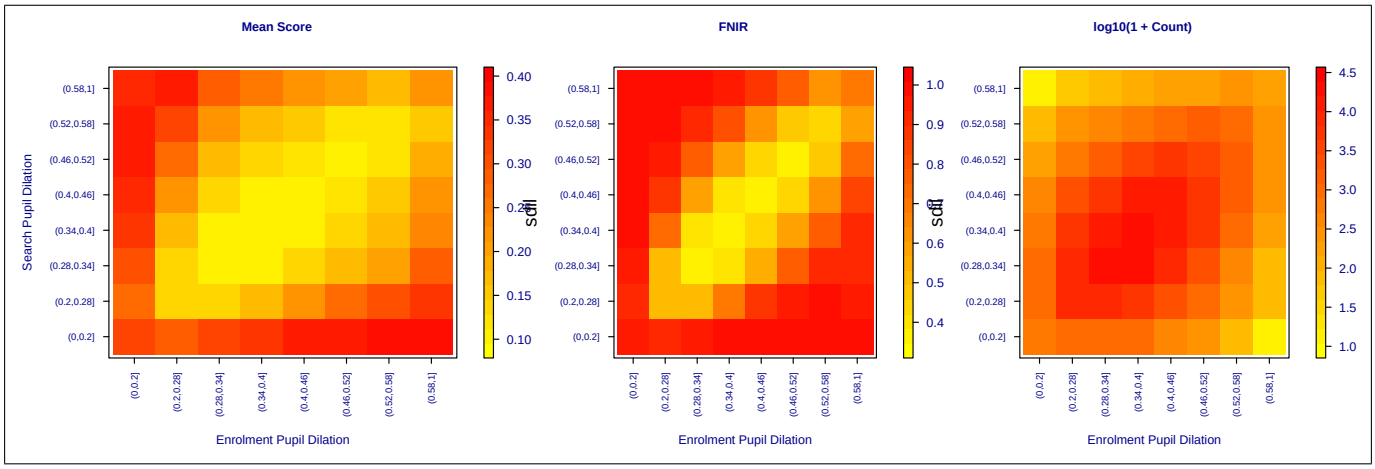

(b) Mate Dilation: Dis-similarity Score, Miss Rate, $\log_{10}(1+\text{Count})$

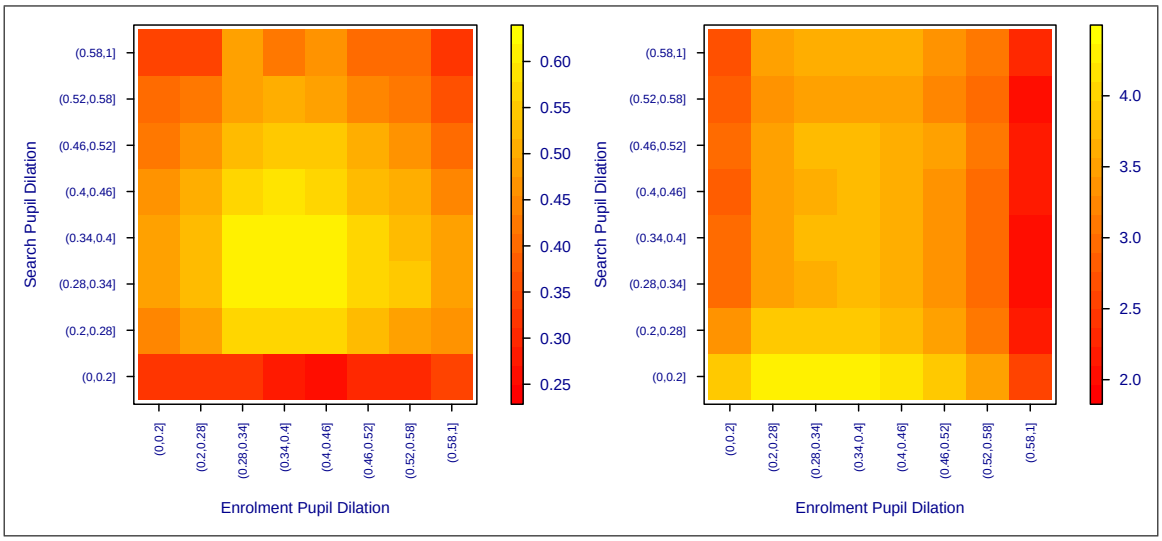

(c) Nonmate Dilation, Dis-similarity Score, Miss Rate, $\log_{10}(1+\text{Count})$

Figure 431: Heatmaps for implementation X11A executing mate searches in an enrolled population of N = 1.6 million. The radius images are binned by into twelve quantiles spanning $[0, 1]$. The dilation values are cut into ranges bounded by: $(0, 0.2, 0.28, 0.34, 0.40, 0.46, 0.52, 0.58, 1)$. The pathologically compressed 330x330 images are excluded from this analysis.

Heatmaps for implementation X11A executing mate searches in an enrolled population of N = 1.6 million.

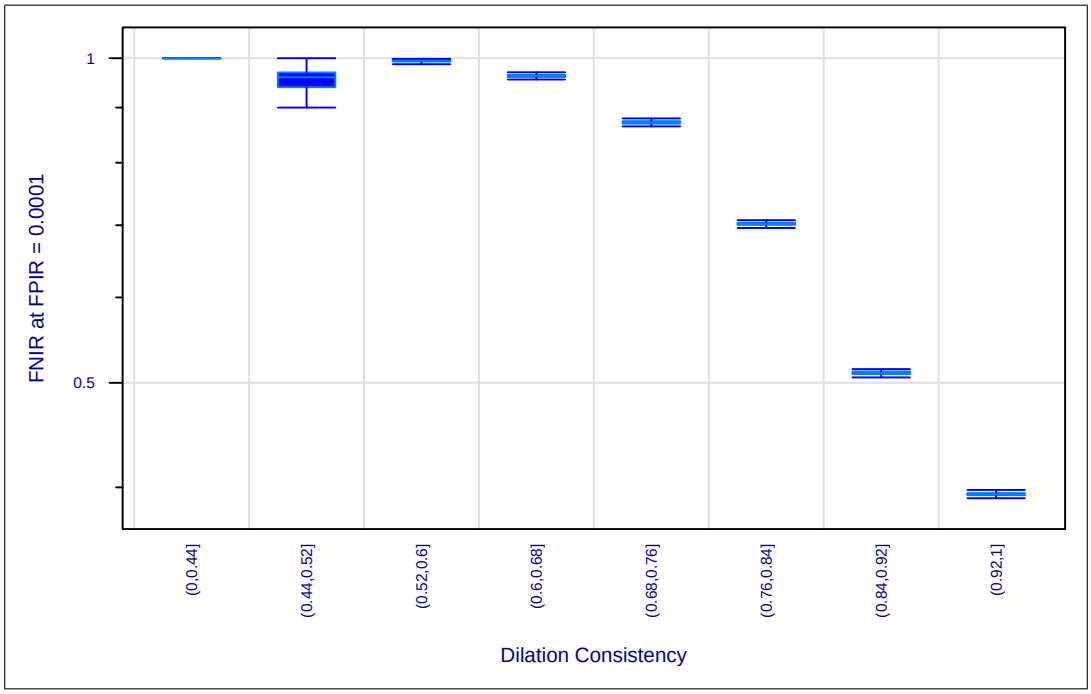

(a) Boxplot, all images

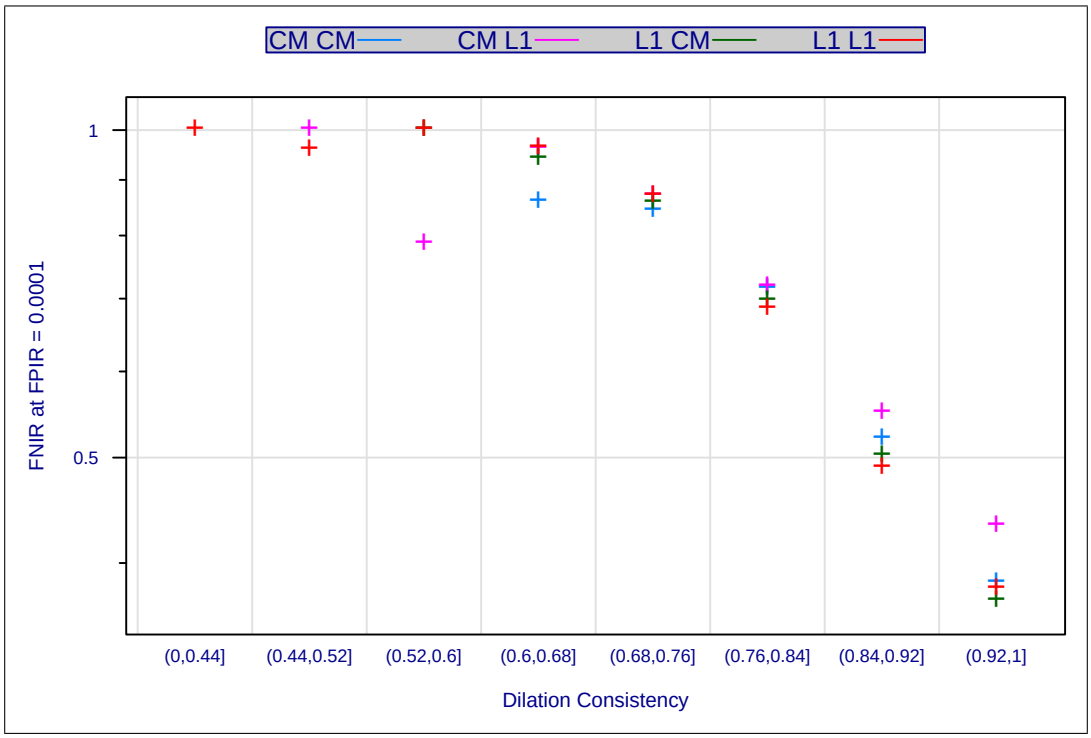

(b) Mean, L1 and CM images

Figure 432: Miss rate statistics for implementation X11A executing mate searches in an enrolled population of N = 1.6 million. The figures plots FNIR at FPIR = 0.0001 versus the IREX I metric for dilation consistency $(1 - \max(D_1, D_2))/(1 - \min(D_1, D_2))$ where D_i is pupil-iris radius ratio, and the subscripts refer to the mated enrollment and search image. The pathologically compressed 330x330 images are excluded from this analysis. The second figure breaks out dilation effects for interoperating camera pairs, CM and L1.

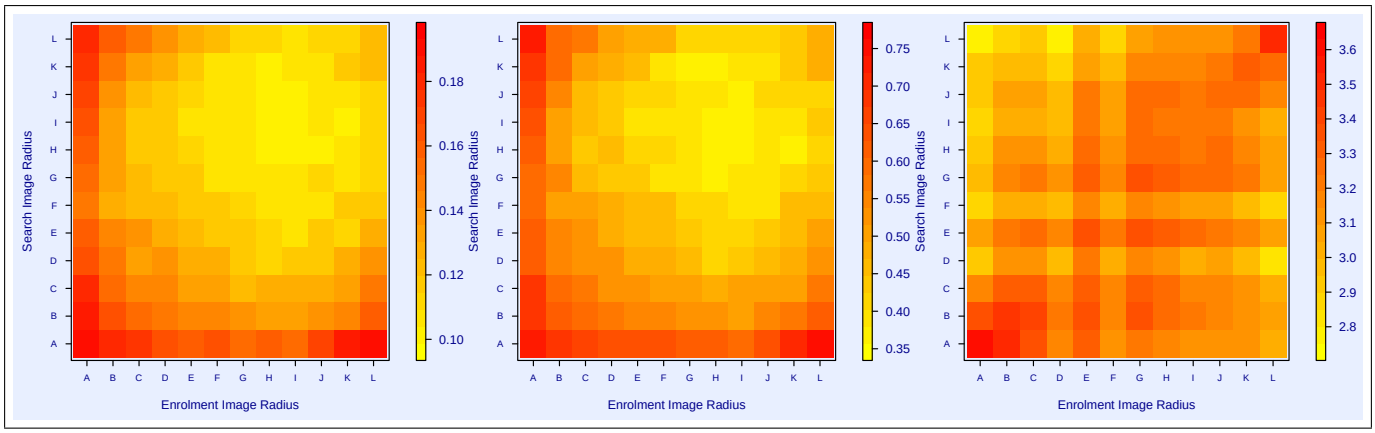

(a) Iris radius: Dis-similarity Score, Miss Rate, $\log_{10}(1+\text{Count})$

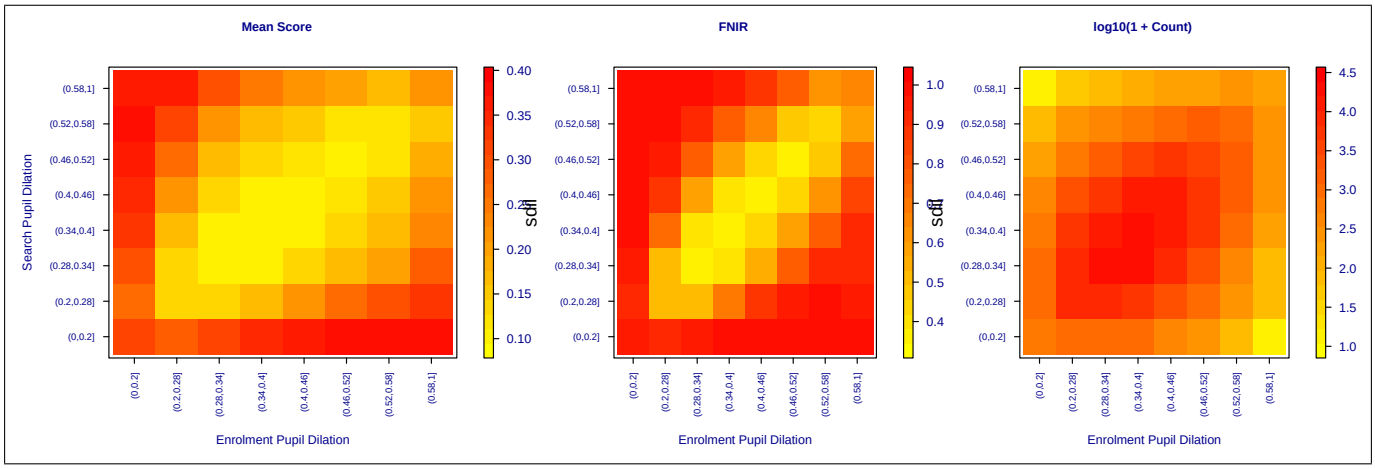

(b) Mate Dilation: Dis-similarity Score, Miss Rate, $\log_{10}(1+\text{Count})$

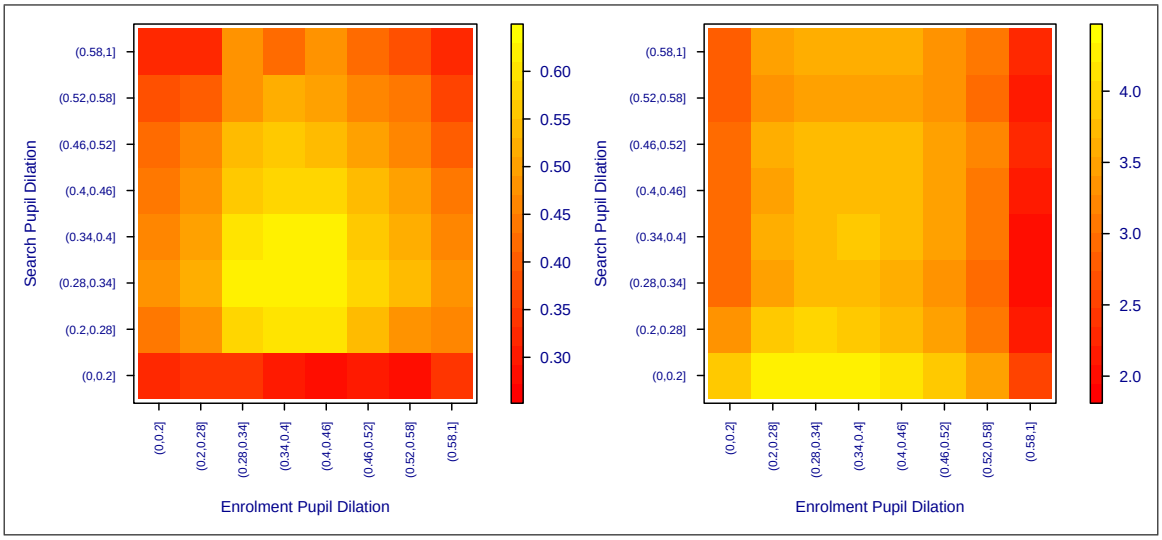

(c) Nonmate Dilation, Dis-similarity Score, Miss Rate, $\log_{10}(1+\text{Count})$

Figure 433: Heatmaps for implementation X11B executing mate searches in an enrolled population of N = 1.6 million. The radius images are binned by into twelve quantiles spanning $[0, 1]$. The dilation values are cut into ranges bounded by: $(0, 0.2, 0.28, 0.34, 0.40, 0.46, 0.52, 0.58, 1)$. The pathologically compressed 330x330 images are excluded from this analysis.

Heatmaps for implementation X11B executing mate searches in an enrolled population of N = 1.6 million.

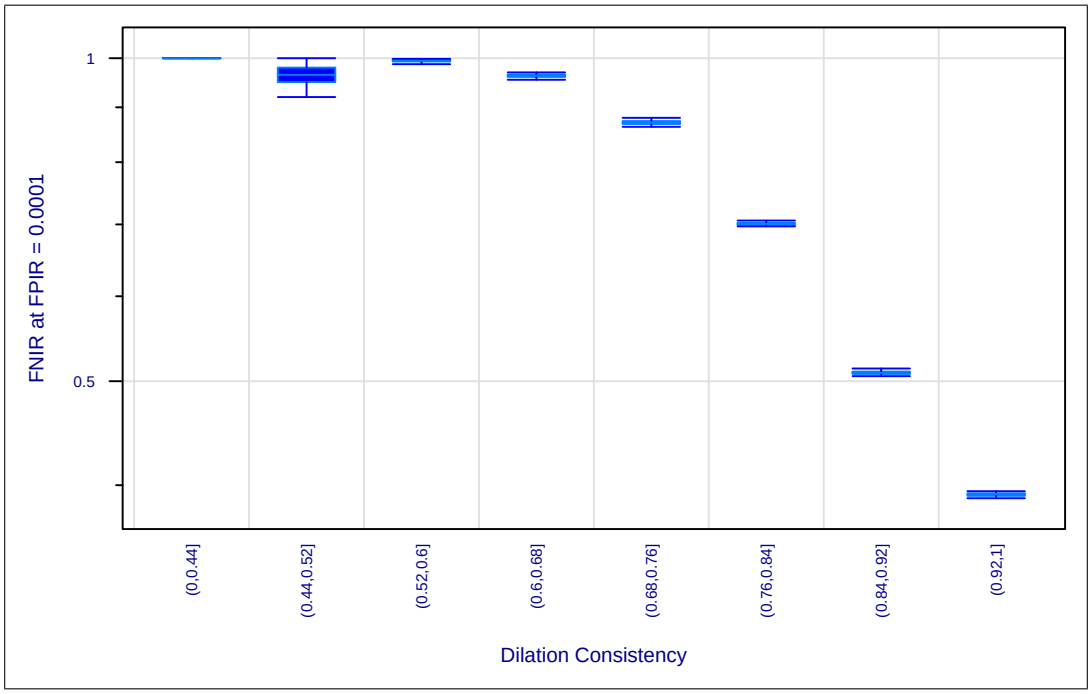

(a) Boxplot, all images

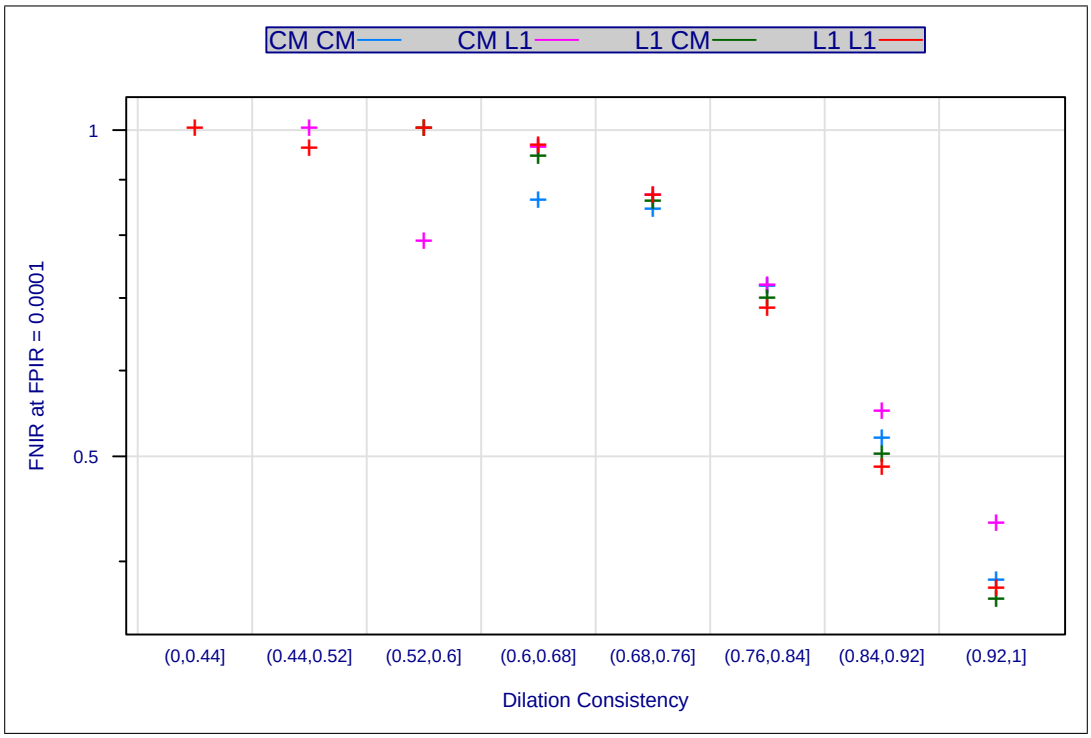

(b) Mean, L1 and CM images

Figure 434: Miss rate statistics for implementation X11B executing mate searches in an enrolled population of N = 1.6 million. The figures plots FNIR at FPIR = 0.0001 versus the IREX I metric for dilation consistency $(1 - \max(D_1, D_2))/(1 - \min(D_1, D_2))$ where D_i is pupil-iris radius ratio, and the subscripts refer to the mated enrollment and search image. The pathologically compressed 330x330 images are excluded from this analysis. The second figure breaks out dilation effects for interoperating camera pairs, CM and L1.

Figure 435: Heatmaps for implementation Y02A executing mate searches in an enrolled population of N = 1.6 million. The radius images are binned by into twelve quantiles spanning $[0, 1]$. The dilation values are cut into ranges bounded by: $(0, 0.2, 0.28, 0.34, 0.40, 0.46, 0.52, 0.58, 1)$. The pathologically compressed 330x330 images are excluded from this analysis.

Figure 436: Miss rate statistics for implementation Y02A executing mate searches in an enrolled population of N = 1.6 million. The figures plots FNIR at FPIR = 0.0001 versus the IREX I metric for dilation consistency $(1 - \max(D_1, D_2))/(1 - \min(D_1, D_2))$ where D_i is pupil-iris radius ratio, and the subscripts refer to the mated enrollment and search image. The pathologically compressed 330x330 images are excluded from this analysis. The second figure breaks out dilation effects for interoperating camera pairs, CM and L1.

Figure 437: Heatmaps for implementation Y02B executing mate searches in an enrolled population of N = 1.6 million. The radius images are binned by into twelve quantiles spanning $[0, 1]$. The dilation values are cut into ranges bounded by: $(0, 0.2, 0.28, 0.34, 0.40, 0.46, 0.52, 0.58, 1)$. The pathologically compressed 330x330 images are excluded from this analysis.

Heatmaps for implementation Y02A executing mate searches in an enrolled population of N = 1.6 million.

Figure 438: Miss rate statistics for implementation Y02B executing mate searches in an enrolled population of N = 1.6 million. The figures plots FNIR at FPIR = 0.0001 versus the IREX I metric for dilation consistency $(1 - \max(D_1, D_2))/(1 - \min(D_1, D_2))$ where D_i is pupil-iris radius ratio, and the subscripts refer to the mated enrollment and search image. The pathologically compressed 330x330 images are excluded from this analysis. The second figure breaks out dilation effects for interoperating camera pairs, CM and L1.

Figure 439: Heatmaps for implementation Y03A executing mate searches in an enrolled population of N = 1.6 million. The radius images are binned by into twelve quantiles spanning $[0, 1]$. The dilation values are cut into ranges bounded by: $(0, 0.2, 0.28, 0.34, 0.40, 0.46, 0.52, 0.58, 1)$. The pathologically compressed 330x330 images are excluded from this analysis.

Heatmaps for implementation Y02B executing mate searches in an enrolled population of N = 1.6 million.

Figure 440: Miss rate statistics for implementation Y03A executing mate searches in an enrolled population of N = 1.6 million. The figures plots FNIR at FPIR = 0.0001 versus the IREX I metric for dilation consistency $(1 - \max(D_1, D_2))/(1 - \min(D_1, D_2))$ where D_i is pupil-iris radius ratio, and the subscripts refer to the mated enrollment and search image. The pathologically compressed 330x330 images are excluded from this analysis. The second figure breaks out dilation effects for interoperating camera pairs, CM and L1.

Figure 441: Heatmaps for implementation Y03B executing mate searches in an enrolled population of N = 1.6 million. The radius images are binned by into twelve quantiles spanning $[0, 1]$. The dilation values are cut into ranges bounded by: $(0, 0.2, 0.28, 0.34, 0.40, 0.46, 0.52, 0.58, 1)$. The pathologically compressed 330x330 images are excluded from this analysis.

Heatmaps for implementation Y03A executing mate searches in an enrolled population of N = 1.6 million.

Figure 442: Miss rate statistics for implementation Y03B executing mate searches in an enrolled population of N = 1.6 million. The figures plots FNIR at FPIR = 0.0001 versus the IREX I metric for dilation consistency $(1 - \max(D_1, D_2))/(1 - \min(D_1, D_2))$ where D_i is pupil-iris radius ratio, and the subscripts refer to the mated enrollment and search image. The pathologically compressed 330x330 images are excluded from this analysis. The second figure breaks out dilation effects for interoperating camera pairs, CM and L1.

Heatmaps for implementation Y03B executing mate searches in an enrolled population of N = 1.6 million.

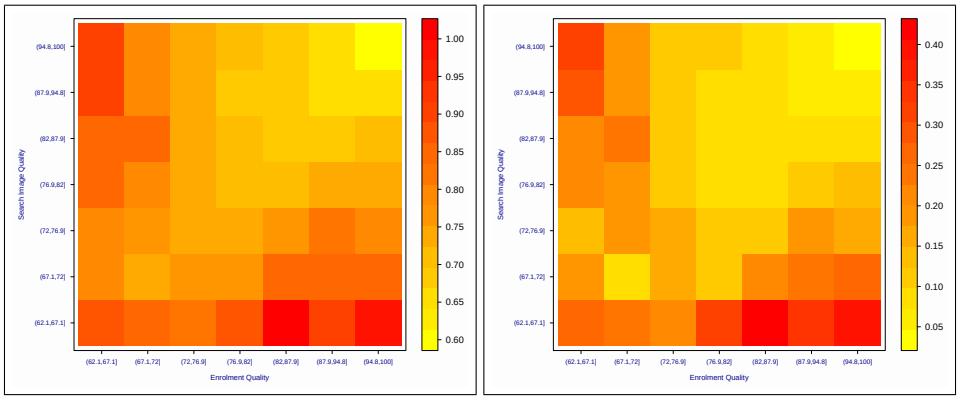

(a) Score (b) FNIR

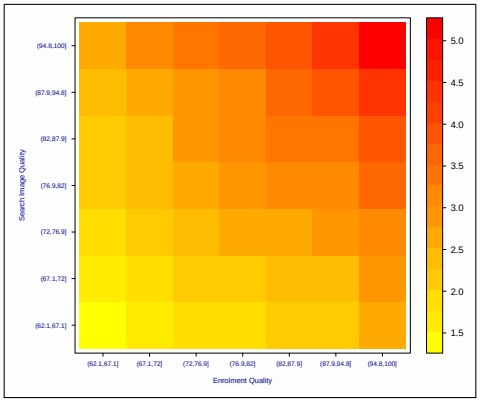

(c) $log_{10}(1 + Count)$

Figure 443: **Effectiveness of quality assessments**: Heatmaps for implementation Q02A executing mate searches in an enrolled population of N = 1600000. The quality values of the enrolled and search images are binned by their mutual $0.005, 0.01, 0.02, 0.04, 0.16, 0.32$ quantiles. From left to right, the color gives the mean reported dis-similarity score, the FNIR at FPIR = 0.0001, and the log of count of the images in each quality bin.

Appendix G: Relation of Image Quality Estimates and Accuracy

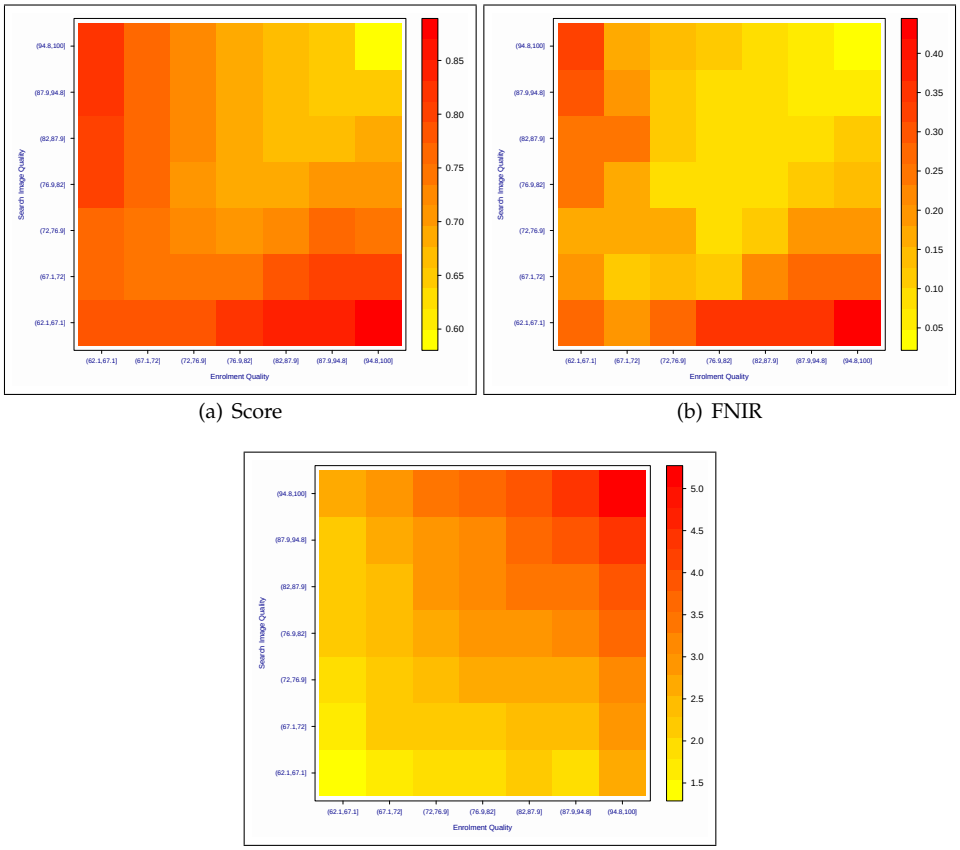

(a) Score (b) FNIR

(c) $log_{10}(1 + Count)$

Figure 444: **Effectiveness of quality assessments**: Heatmaps for implementation Q02B executing mate searches in an enrolled population of N = 1600000. The quality values of the enrolled and search images are binned by their mutual $0.005, 0.01, 0.02, 0.04, 0.16, 0.32$ quantiles. From left to right, the color gives the mean reported dis-similarity score, the FNIR at FPIR = 0.0001, and the log of count of the images in each quality bin.

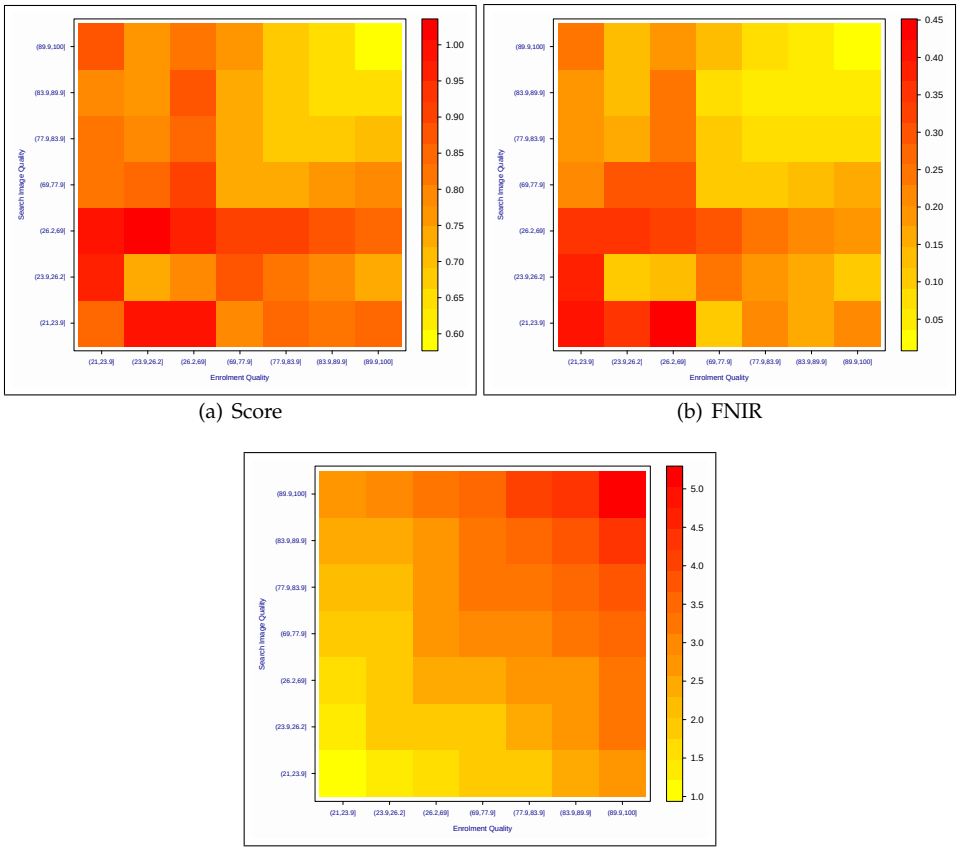

(a) Score (b) FNIR

(c) $log_{10}(1 + Count)$

Figure 445: **Effectiveness of quality assessments**: Heatmaps for implementation Q03A executing mate searches in an enrolled population of N = 1600000. The quality values of the enrolled and search images are binned by their mutual $0.005, 0.01, 0.02, 0.04, 0.16, 0.32$ quantiles. From left to right, the color gives the mean reported dis-similarity score, the FNIR at FPIR = 0.0001, and the log of count of the images in each quality bin.

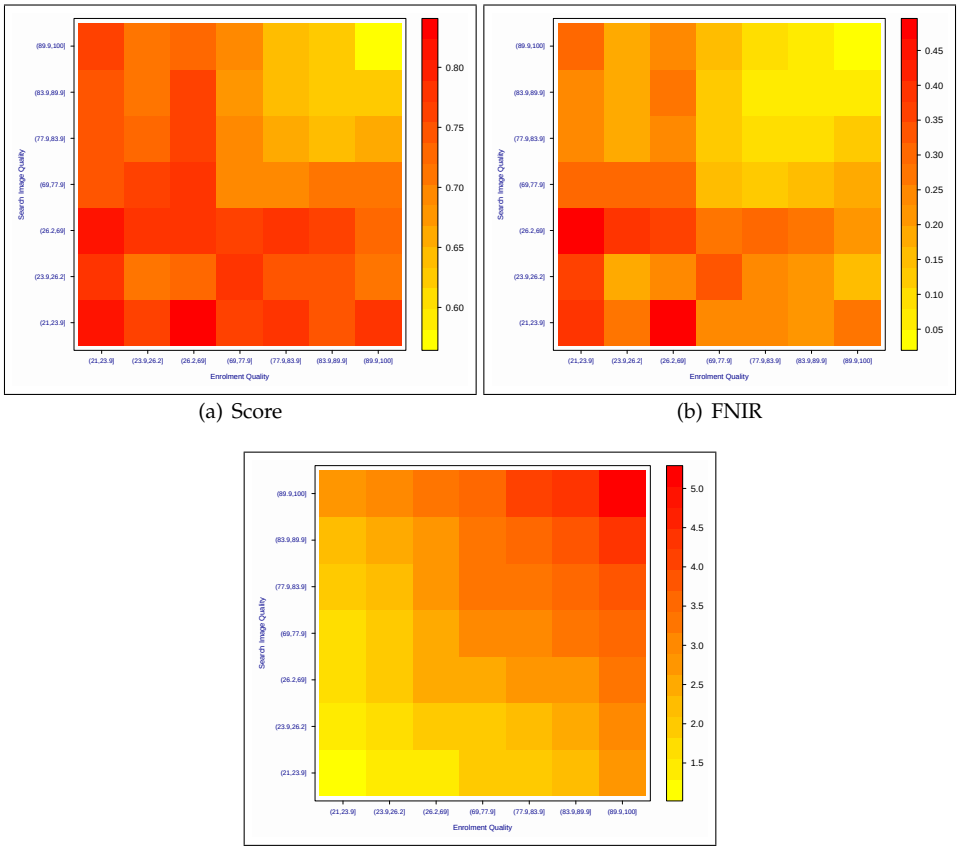

(a) Score (b) FNIR

(c) $log_{10}(1 + Count)$

Figure 446: **Effectiveness of quality assessments**: Heatmaps for implementation Q03B executing mate searches in an enrolled population of N = 1600000. The quality values of the enrolled and search images are binned by their mutual $0.005, 0.01, 0.02, 0.04, 0.16, 0.32$ quantiles. From left to right, the color gives the mean reported dis-similarity score, the FNIR at FPIR = 0.0001, and the log of count of the images in each quality bin.

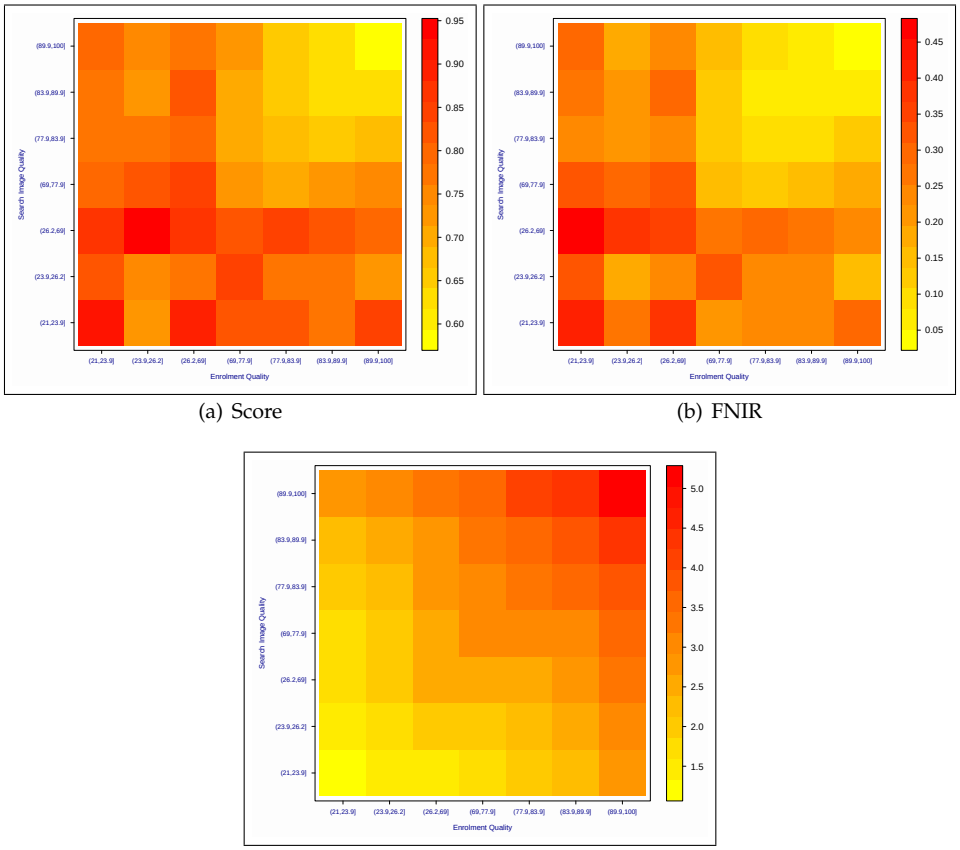

(a) Score (b) FNIR

(c) $log_{10}(1 + Count)$

Figure 447: **Effectiveness of quality assessments**: Heatmaps for implementation Q04B executing mate searches in an enrolled population of N = 1600000. The quality values of the enrolled and search images are binned by their mutual $0.005, 0.01, 0.02, 0.04, 0.16, 0.32$ quantiles. From left to right, the color gives the mean reported dis-similarity score, the FNIR at FPIR = 0.0001, and the log of count of the images in each quality bin.

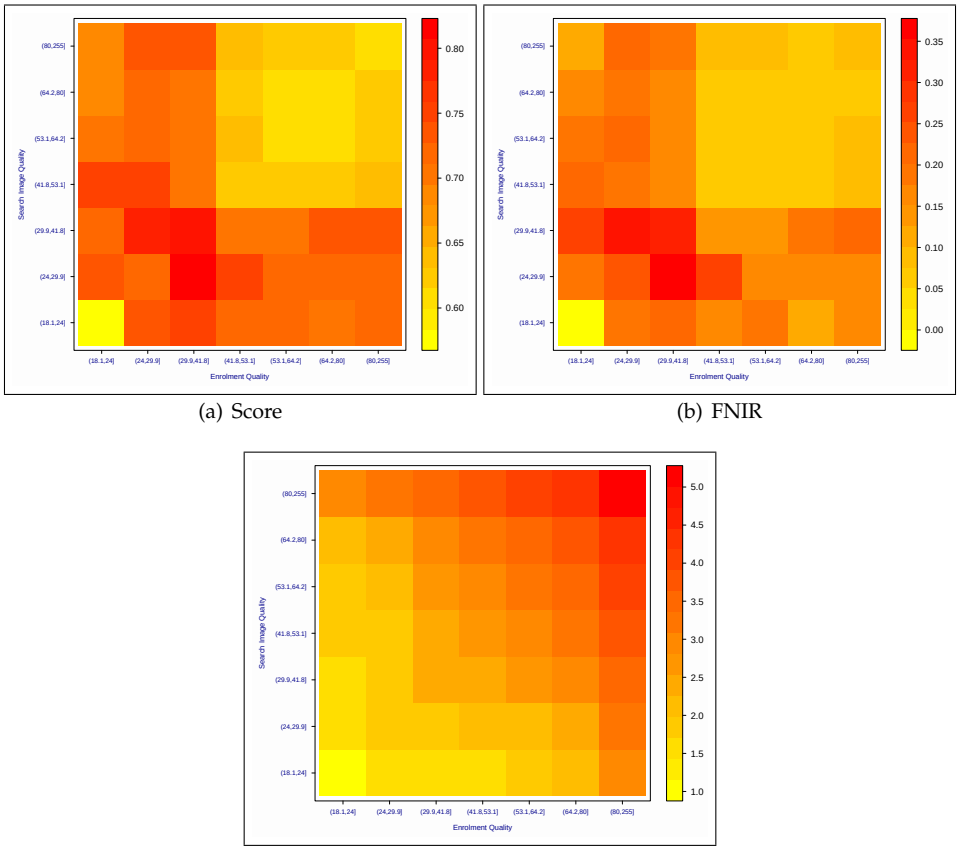

(a) Score (b) FNIR

(c) $log_{10}(1 + Count)$

Figure 448: **Effectiveness of quality assessments**: Heatmaps for implementation Q11B executing mate searches in an enrolled population of N = 1600000. The quality values of the enrolled and search images are binned by their mutual $0.005, 0.01, 0.02, 0.04, 0.16, 0.32$ quantiles. From left to right, the color gives the mean reported dis-similarity score, the FNIR at FPIR = 0.0001, and the log of count of the images in each quality bin.

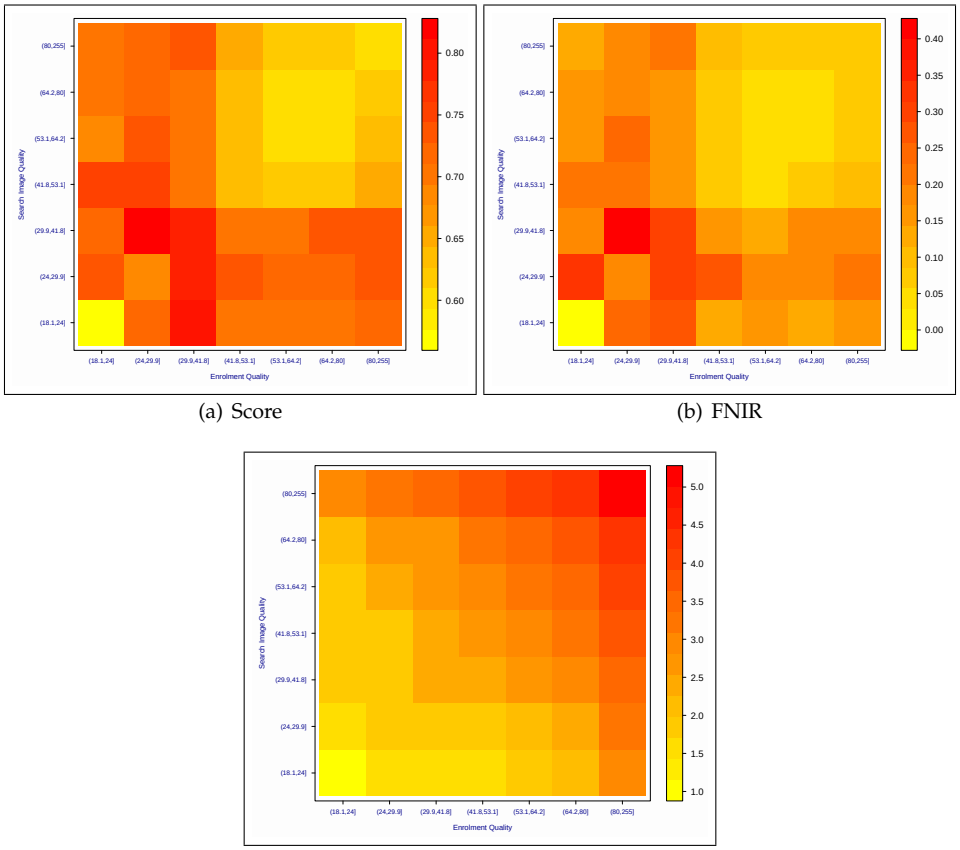

(a) Score (b) FNIR

(c) $log_{10}(1 + Count)$

Figure 449: **Effectiveness of quality assessments**: Heatmaps for implementation Q12B executing mate searches in an enrolled population of N = 1600000. The quality values of the enrolled and search images are binned by their mutual $0.005, 0.01, 0.02, 0.04, 0.16, 0.32$ quantiles. From left to right, the color gives the mean reported dis-similarity score, the FNIR at FPIR = 0.0001, and the log of count of the images in each quality bin.

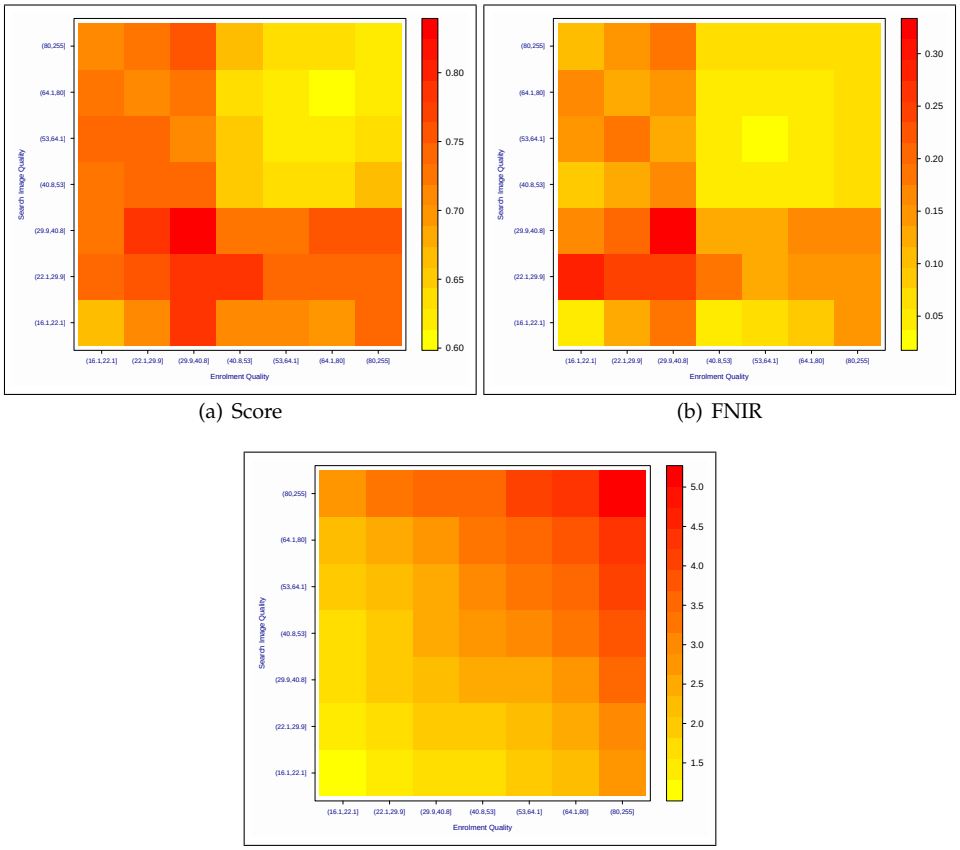

(a) Score (b) FNIR

(c) $log_{10}(1 + Count)$

Figure 450: **Effectiveness of quality assessments**: Heatmaps for implementation Q13B executing mate searches in an enrolled population of N = 1600000. The quality values of the enrolled and search images are binned by their mutual $0.005, 0.01, 0.02, 0.04, 0.16, 0.32$ quantiles. From left to right, the color gives the mean reported dis-similarity score, the FNIR at FPIR = 0.0001, and the log of count of the images in each quality bin.

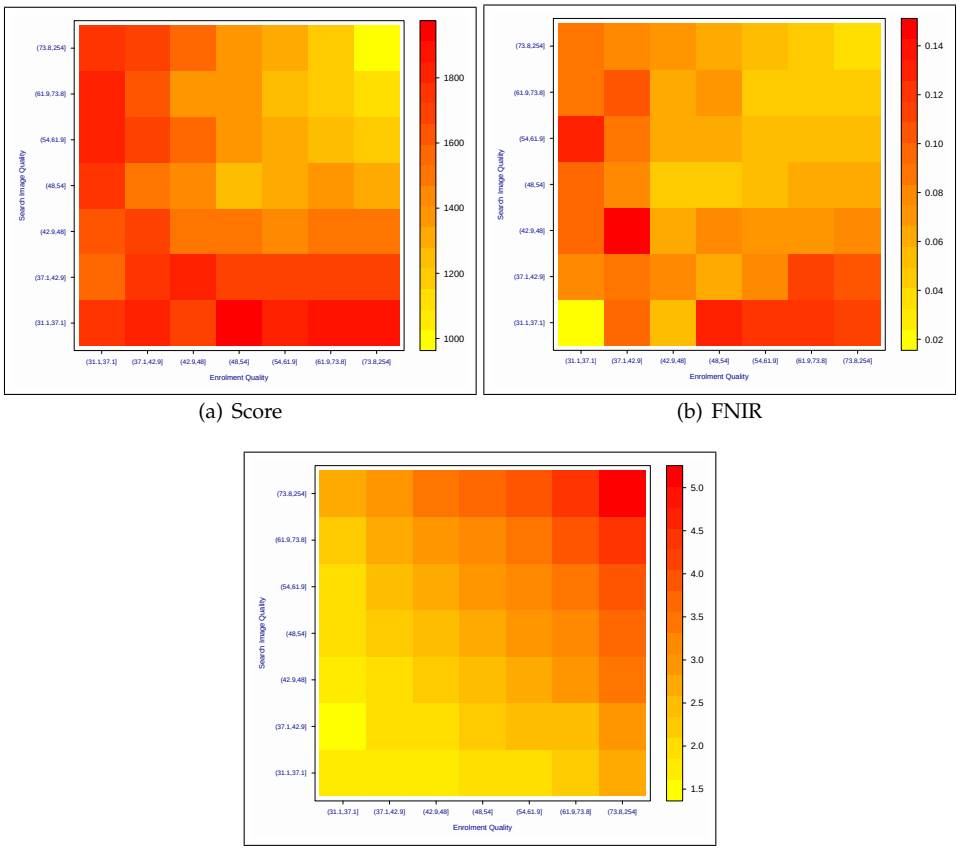

(a) Score (b) FNIR

(c) $log_{10}(1 + Count)$

Figure 451: **Effectiveness of quality assessments**: Heatmaps for implementation R02A executing mate searches in an enrolled population of N = 1600000. The quality values of the enrolled and search images are binned by their mutual $0.005, 0.01, 0.02, 0.04, 0.16, 0.32$ quantiles. From left to right, the color gives the mean reported dis-similarity score, the FNIR at FPIR = 0.0001, and the log of count of the images in each quality bin.

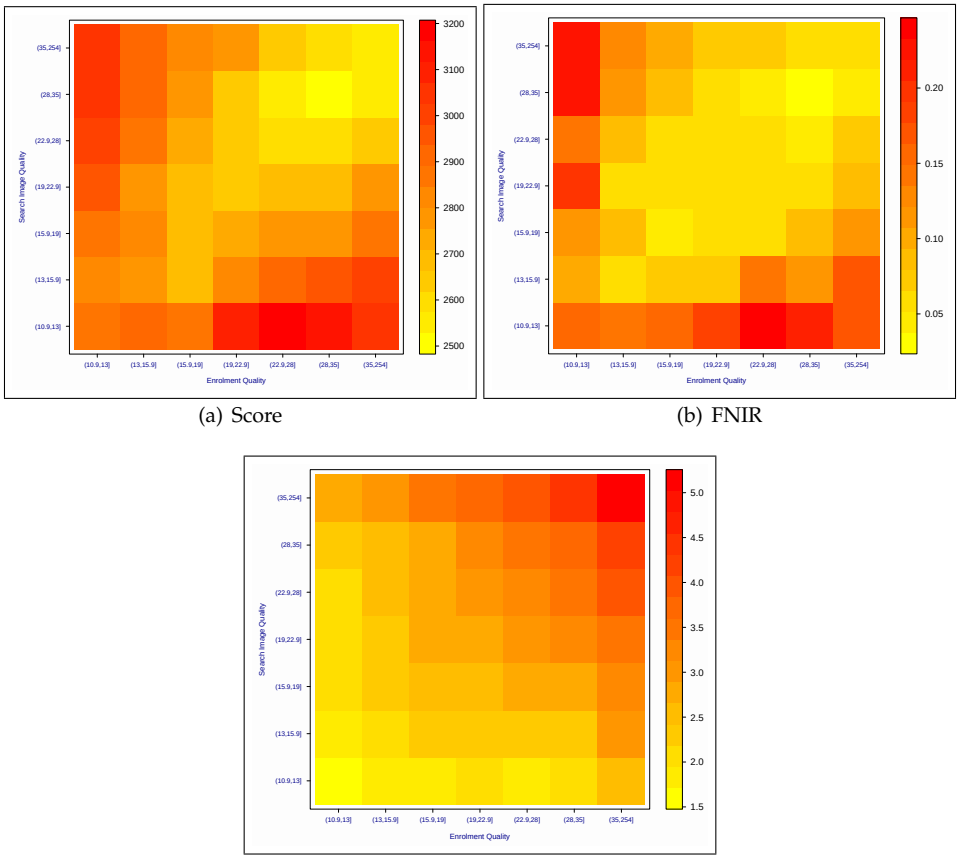

(a) Score (b) FNIR

(c) $log_{10}(1 + Count)$

Figure 452: **Effectiveness of quality assessments**: Heatmaps for implementation R02B executing mate searches in an enrolled population of N = 1600000. The quality values of the enrolled and search images are binned by their mutual $0.005, 0.01, 0.02, 0.04, 0.16, 0.32$ quantiles. From left to right, the color gives the mean reported dis-similarity score, the FNIR at FPIR = 0.0001, and the log of count of the images in each quality bin.

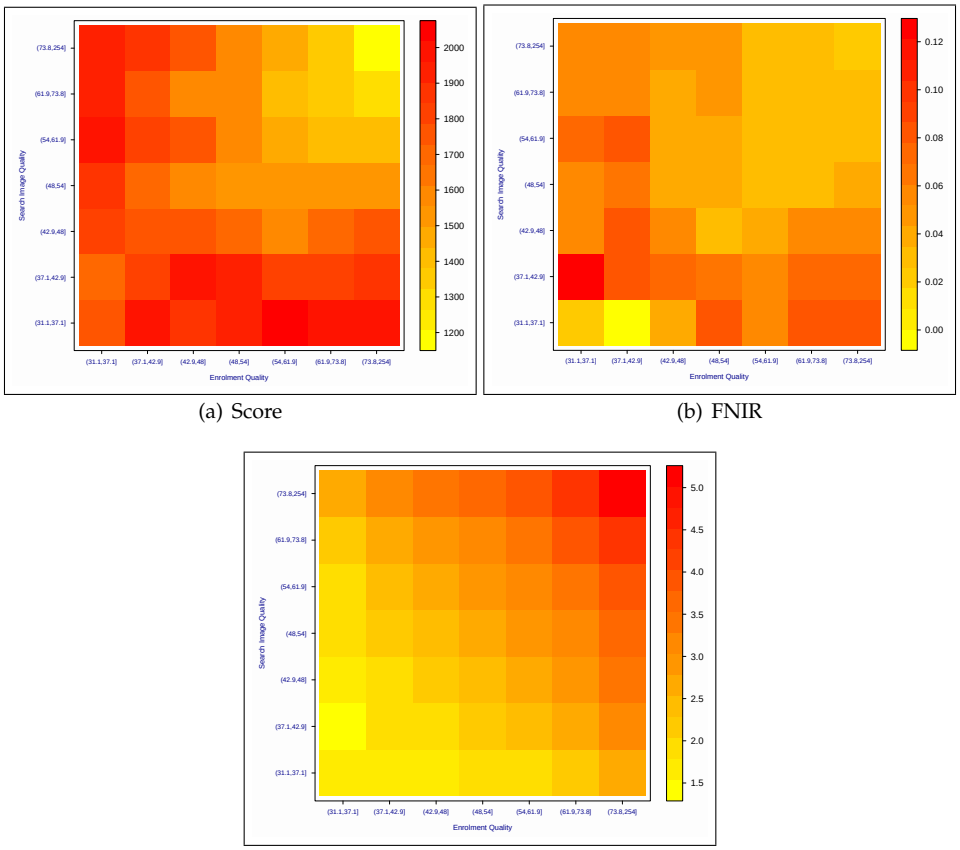

(a) Score (b) FNIR

(c) $log_{10}(1 + Count)$

Figure 453: **Effectiveness of quality assessments**: Heatmaps for implementation R03A executing mate searches in an enrolled population of N = 1600000. The quality values of the enrolled and search images are binned by their mutual $0.005, 0.01, 0.02, 0.04, 0.16, 0.32$ quantiles. From left to right, the color gives the mean reported dis-similarity score, the FNIR at FPIR = 0.0001, and the log of count of the images in each quality bin.

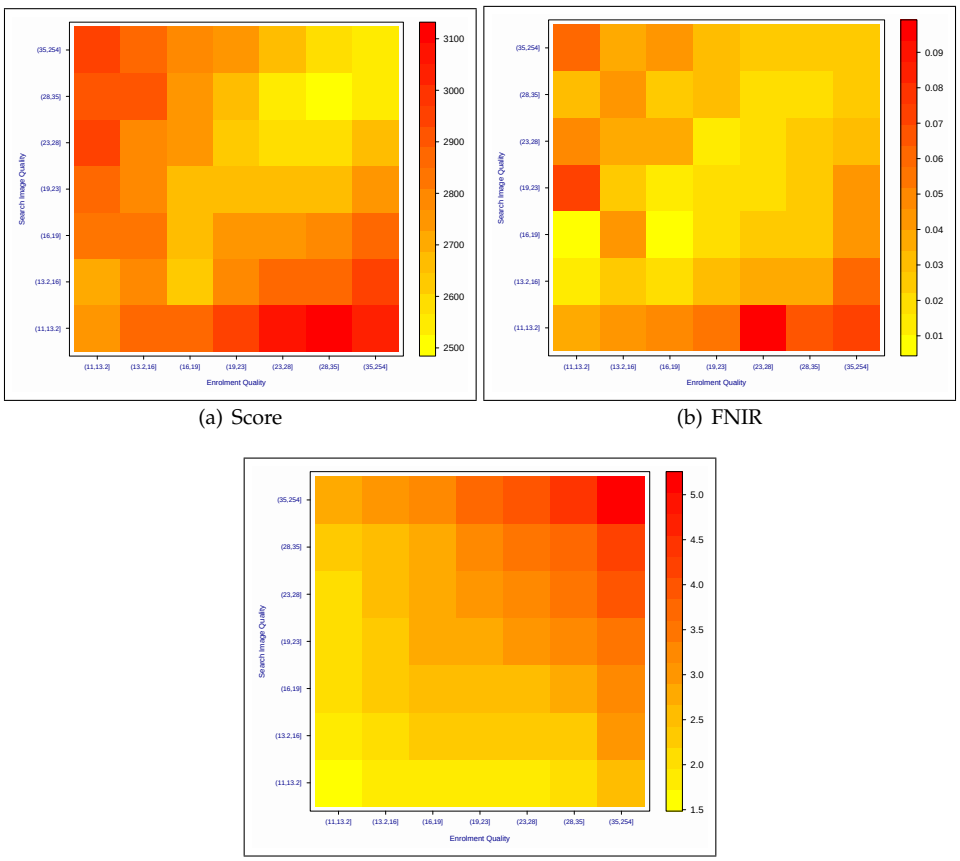

(a) Score (b) FNIR

(c) $log_{10}(1 + Count)$

Figure 454: **Effectiveness of quality assessments**: Heatmaps for implementation R03B executing mate searches in an enrolled population of N = 1600000. The quality values of the enrolled and search images are binned by their mutual $0.005, 0.01, 0.02, 0.04, 0.16, 0.32$ quantiles. From left to right, the color gives the mean reported dis-similarity score, the FNIR at FPIR = 0.0001, and the log of count of the images in each quality bin.

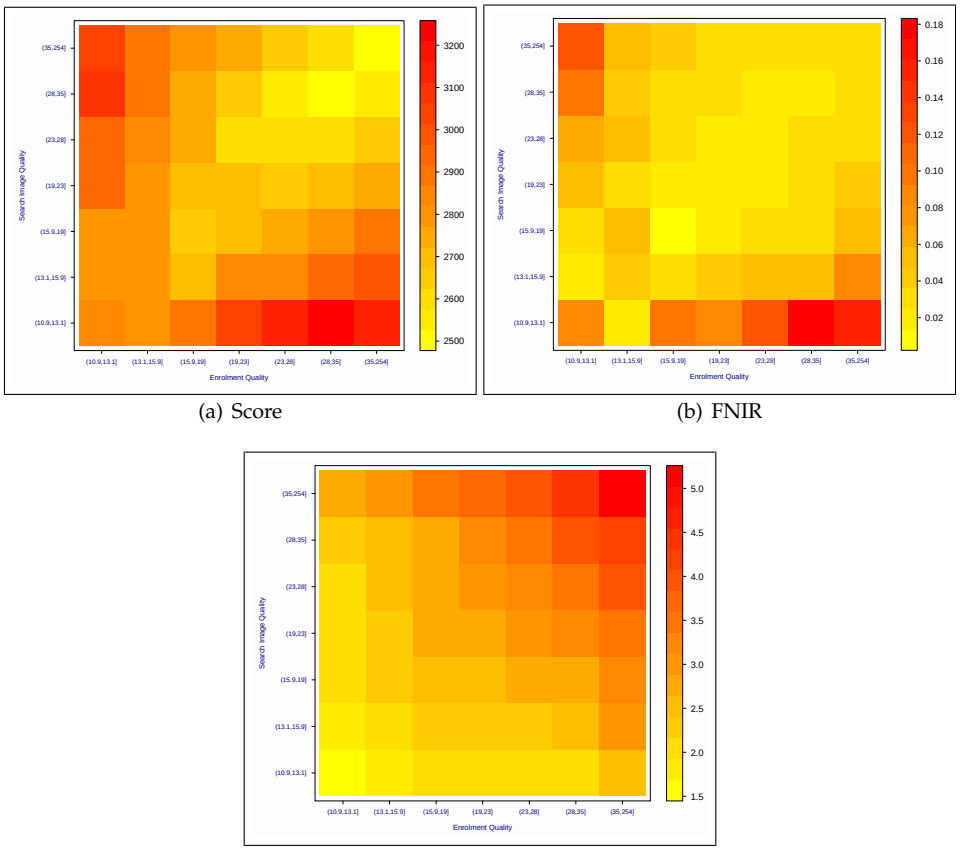

(a) Score (b) FNIR

(c) $log_{10}(1 + Count)$

Figure 455: **Effectiveness of quality assessments**: Heatmaps for implementation R04B executing mate searches in an enrolled population of N = 1600000. The quality values of the enrolled and search images are binned by their mutual $0.005, 0.01, 0.02, 0.04, 0.16, 0.32$ quantiles. From left to right, the color gives the mean reported dis-similarity score, the FNIR at FPIR = 0.0001, and the log of count of the images in each quality bin.

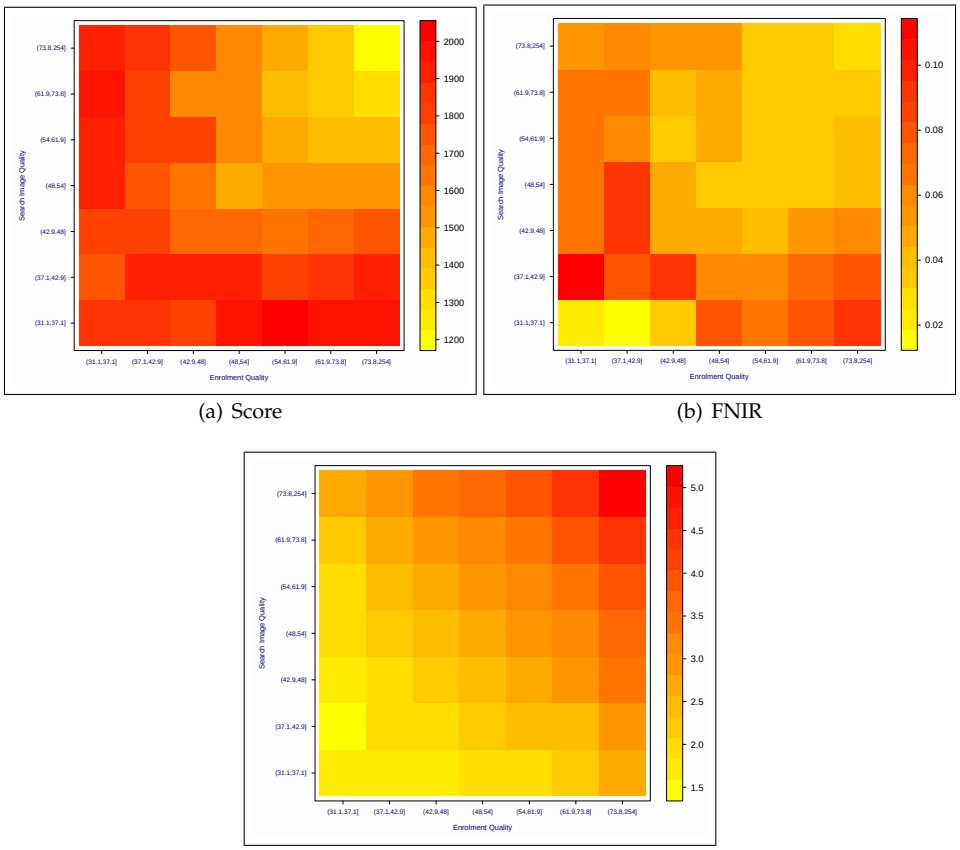

(a) Score (b) FNIR

(c) $log_{10}(1 + Count)$

Figure 456: **Effectiveness of quality assessments**: Heatmaps for implementation R11A executing mate searches in an enrolled population of N = 1600000. The quality values of the enrolled and search images are binned by their mutual $0.005, 0.01, 0.02, 0.04, 0.16, 0.32$ quantiles. From left to right, the color gives the mean reported dis-similarity score, the FNIR at FPIR = 0.0001, and the log of count of the images in each quality bin.

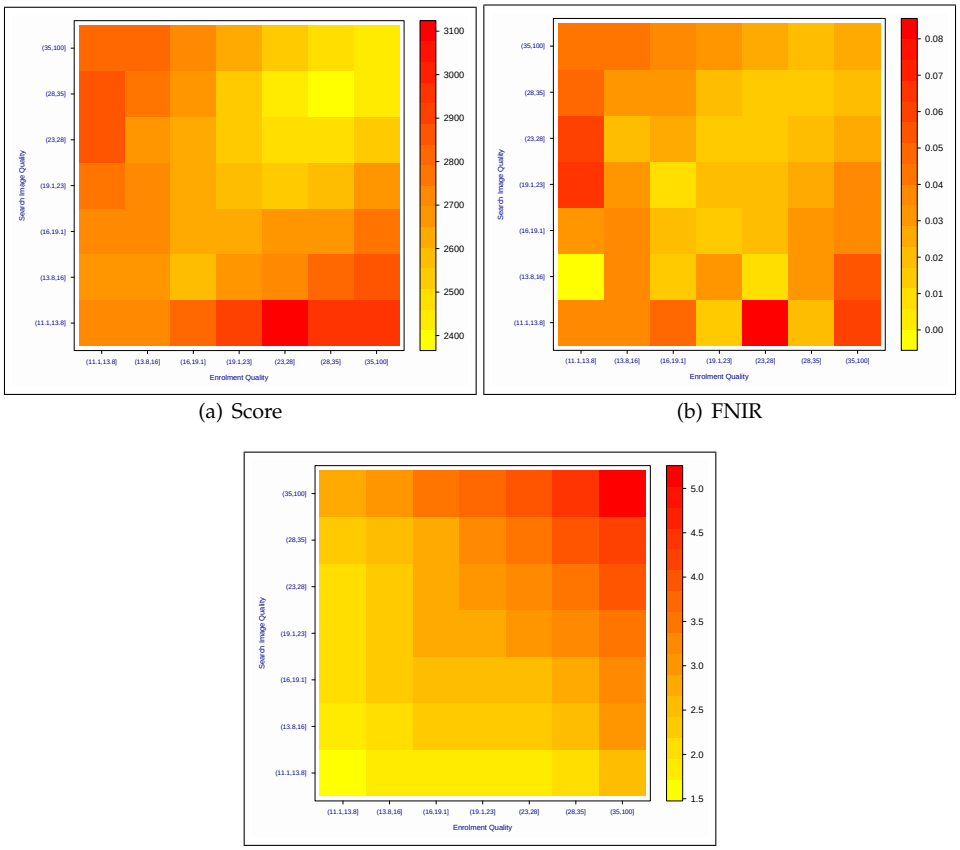

(a) Score (b) FNIR

(c) $log_{10}(1 + Count)$

Figure 457: **Effectiveness of quality assessments**: Heatmaps for implementation R11B executing mate searches in an enrolled population of N = 1600000. The quality values of the enrolled and search images are binned by their mutual $0.005, 0.01, 0.02, 0.04, 0.16, 0.32$ quantiles. From left to right, the color gives the mean reported dis-similarity score, the FNIR at FPIR = 0.0001, and the log of count of the images in each quality bin.

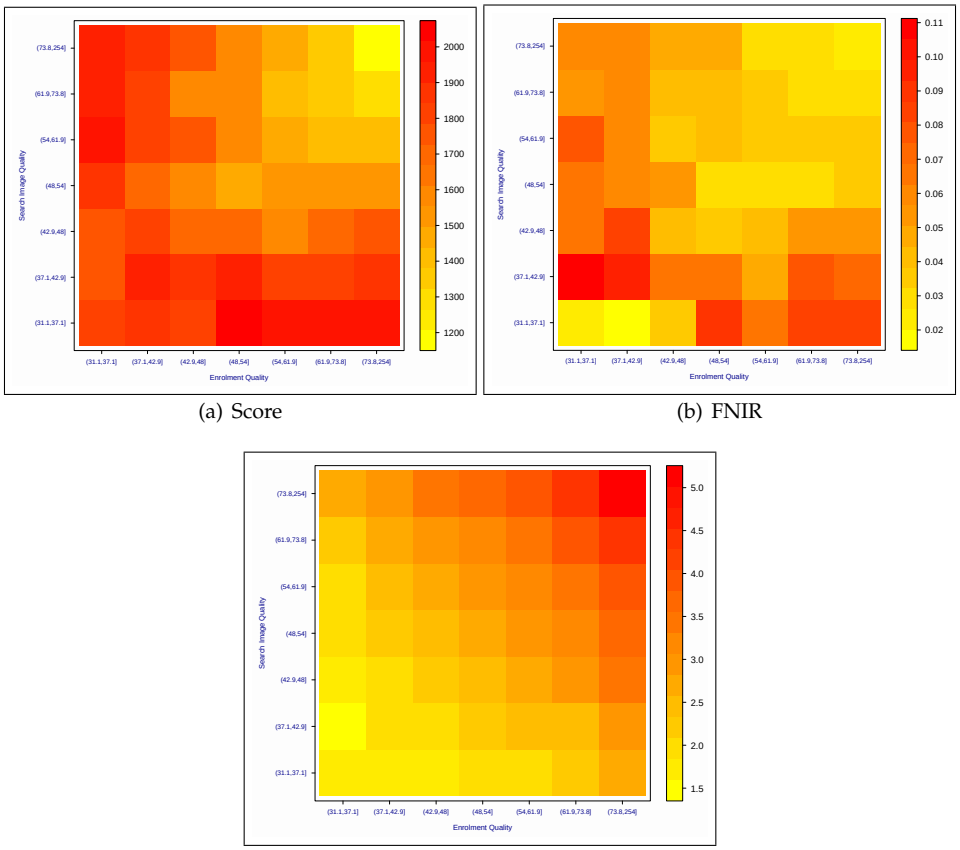

(a) Score (b) FNIR

(c) $log_{10}(1 + Count)$

Figure 458: **Effectiveness of quality assessments**: Heatmaps for implementation R12A executing mate searches in an enrolled population of N = 1600000. The quality values of the enrolled and search images are binned by their mutual $0.005, 0.01, 0.02, 0.04, 0.16, 0.32$ quantiles. From left to right, the color gives the mean reported dis-similarity score, the FNIR at FPIR = 0.0001, and the log of count of the images in each quality bin.

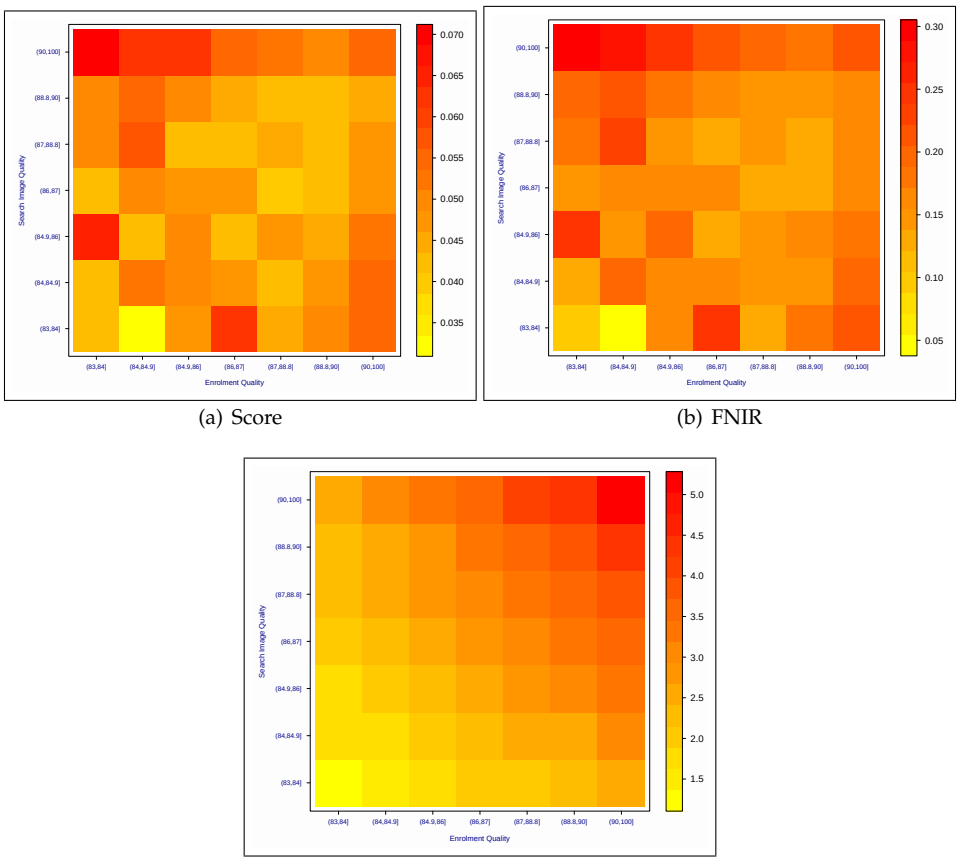

(a) Score (b) FNIR

(c) $log_{10}(1 + Count)$

Figure 459: **Effectiveness of quality assessments**: Heatmaps for implementation S03A executing mate searches in an enrolled population of N = 1600000. The quality values of the enrolled and search images are binned by their mutual $0.005, 0.01, 0.02, 0.04, 0.16, 0.32$ quantiles. From left to right, the color gives the mean reported dis-similarity score, the FNIR at FPIR = 0.0001, and the log of count of the images in each quality bin.

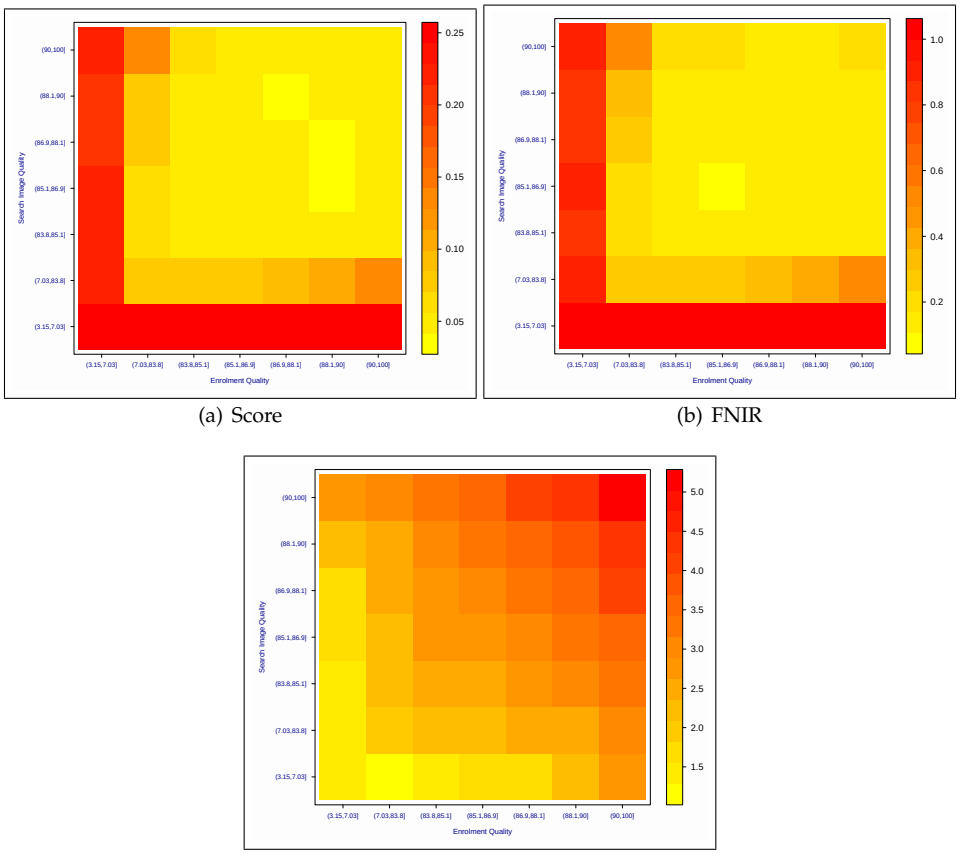

(a) Score (b) FNIR

(c) $log_{10}(1 + Count)$

Figure 460: **Effectiveness of quality assessments**: Heatmaps for implementation S04A executing mate searches in an enrolled population of N = 1600000. The quality values of the enrolled and search images are binned by their mutual $0.005, 0.01, 0.02, 0.04, 0.16, 0.32$ quantiles. From left to right, the color gives the mean reported dis-similarity score, the FNIR at FPIR = 0.0001, and the log of count of the images in each quality bin.

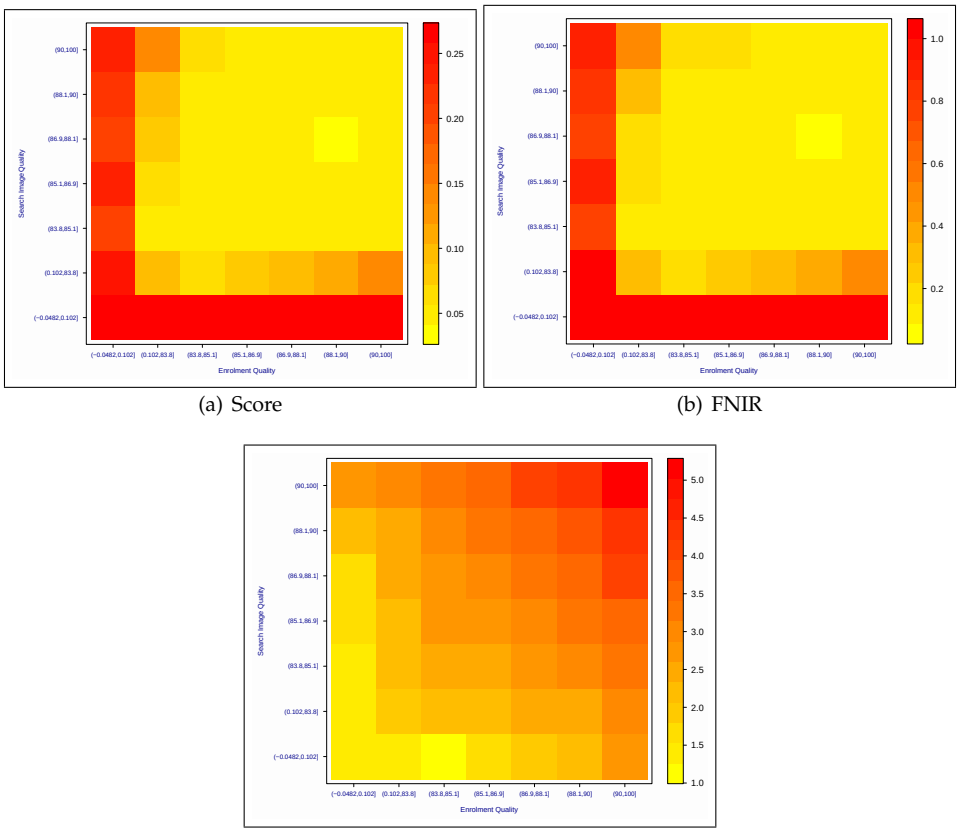

(a) Score (b) FNIR

(c) $log_{10}(1 + Count)$

Figure 461: **Effectiveness of quality assessments**: Heatmaps for implementation S05A executing mate searches in an enrolled population of N = 1600000. The quality values of the enrolled and search images are binned by their mutual $0.005, 0.01, 0.02, 0.04, 0.16, 0.32$ quantiles. From left to right, the color gives the mean reported dis-similarity score, the FNIR at FPIR = 0.0001, and the log of count of the images in each quality bin.

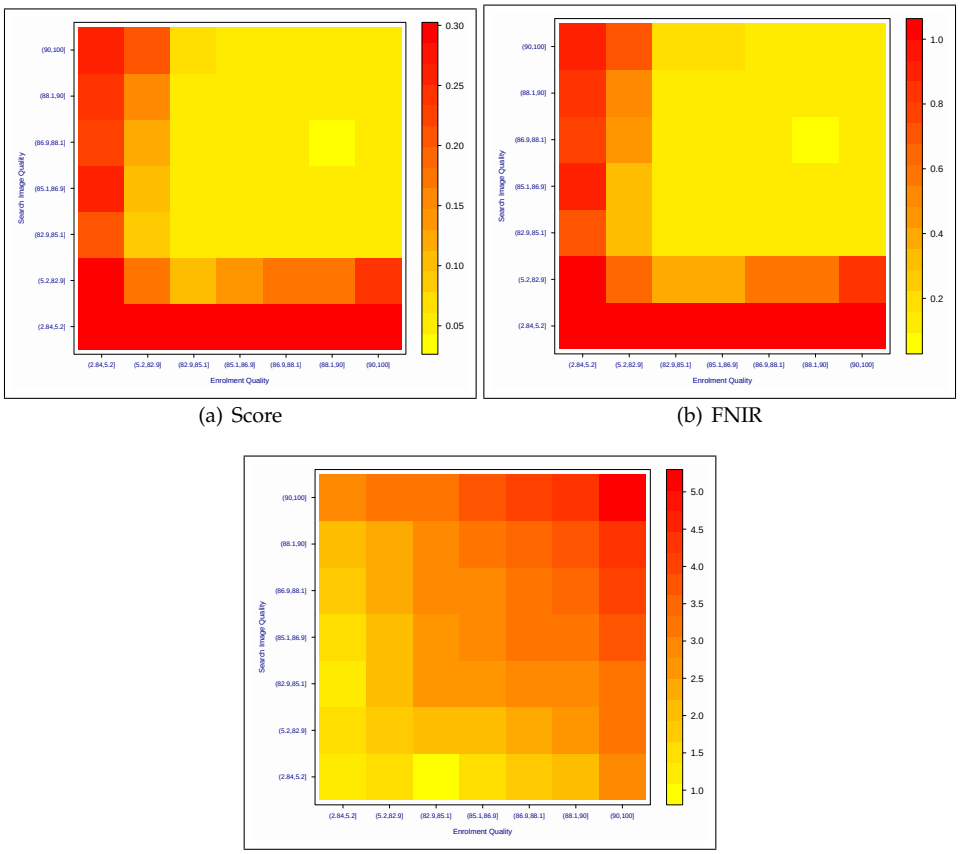

(a) Score (b) FNIR

(c) $log_{10}(1 + Count)$

Figure 462: **Effectiveness of quality assessments**: Heatmaps for implementation S11A executing mate searches in an enrolled population of N = 1600000. The quality values of the enrolled and search images are binned by their mutual $0.005, 0.01, 0.02, 0.04, 0.16, 0.32$ quantiles. From left to right, the color gives the mean reported dis-similarity score, the FNIR at FPIR = 0.0001, and the log of count of the images in each quality bin.

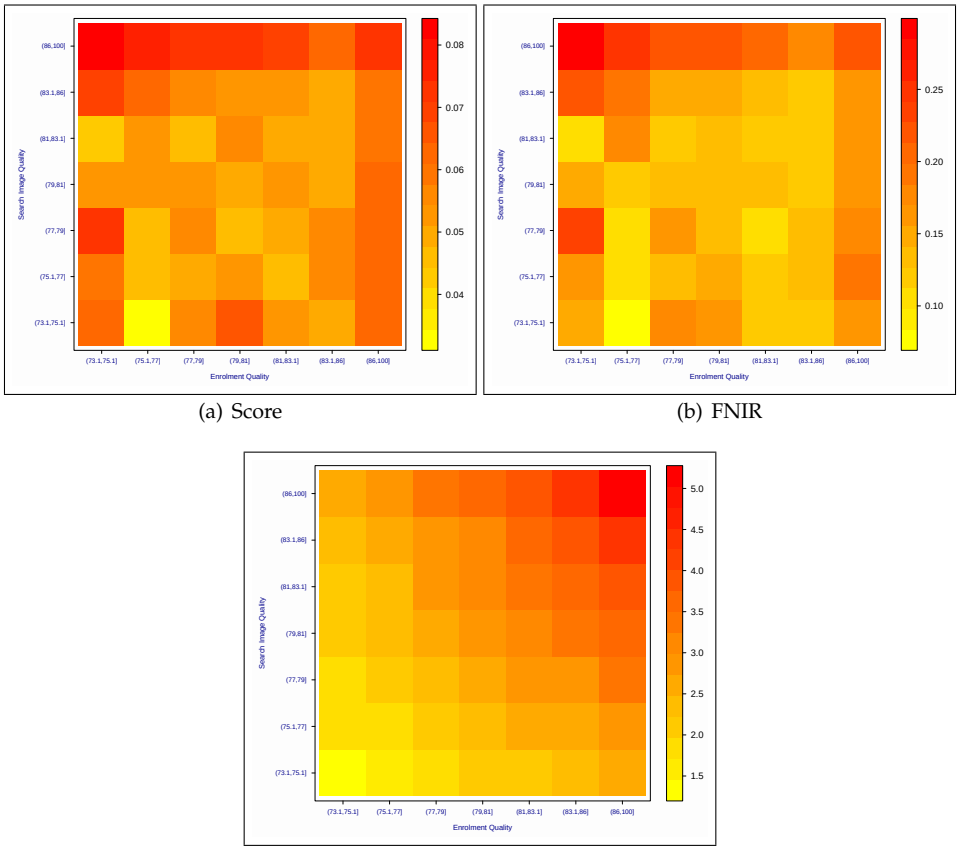

(a) Score (b) FNIR

(c) $log_{10}(1 + Count)$

Figure 463: **Effectiveness of quality assessments**: Heatmaps for implementation S11B executing mate searches in an enrolled population of N = 1600000. The quality values of the enrolled and search images are binned by their mutual $0.005, 0.01, 0.02, 0.04, 0.16, 0.32$ quantiles. From left to right, the color gives the mean reported dis-similarity score, the FNIR at FPIR = 0.0001, and the log of count of the images in each quality bin.

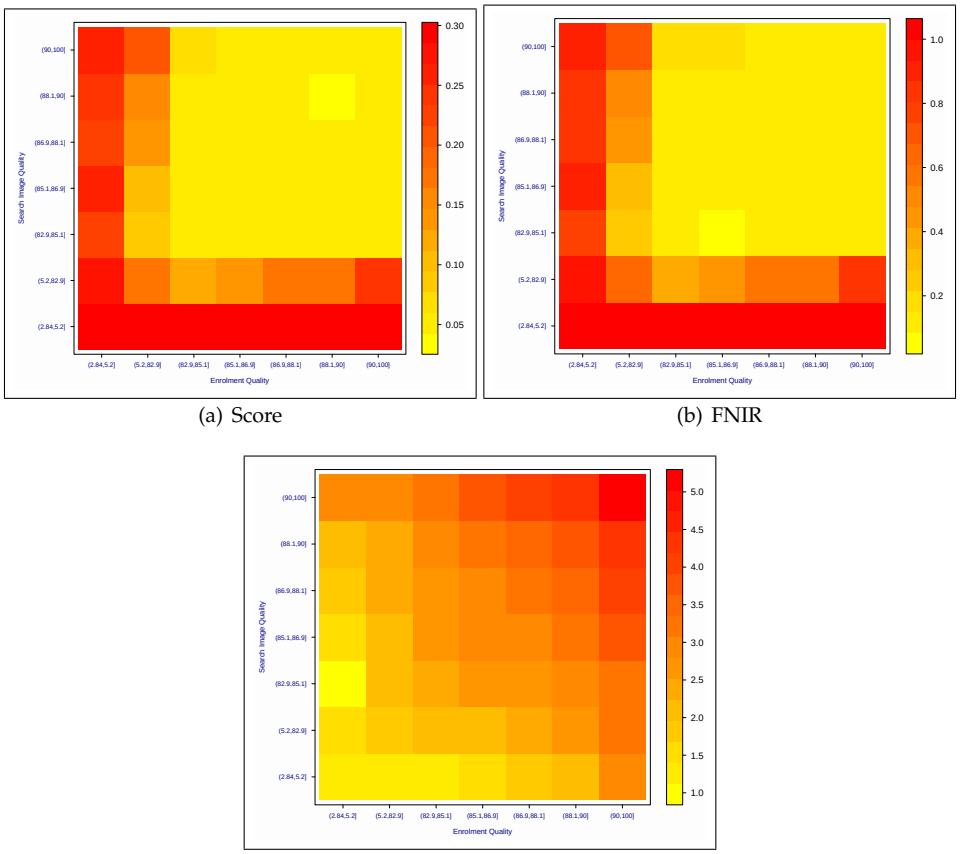

(a) Score (b) FNIR

(c) $log_{10}(1 + Count)$

Figure 464: **Effectiveness of quality assessments**: Heatmaps for implementation S12A executing mate searches in an enrolled population of N = 1600000. The quality values of the enrolled and search images are binned by their mutual $0.005, 0.01, 0.02, 0.04, 0.16, 0.32$ quantiles. From left to right, the color gives the mean reported dis-similarity score, the FNIR at FPIR = 0.0001, and the log of count of the images in each quality bin.

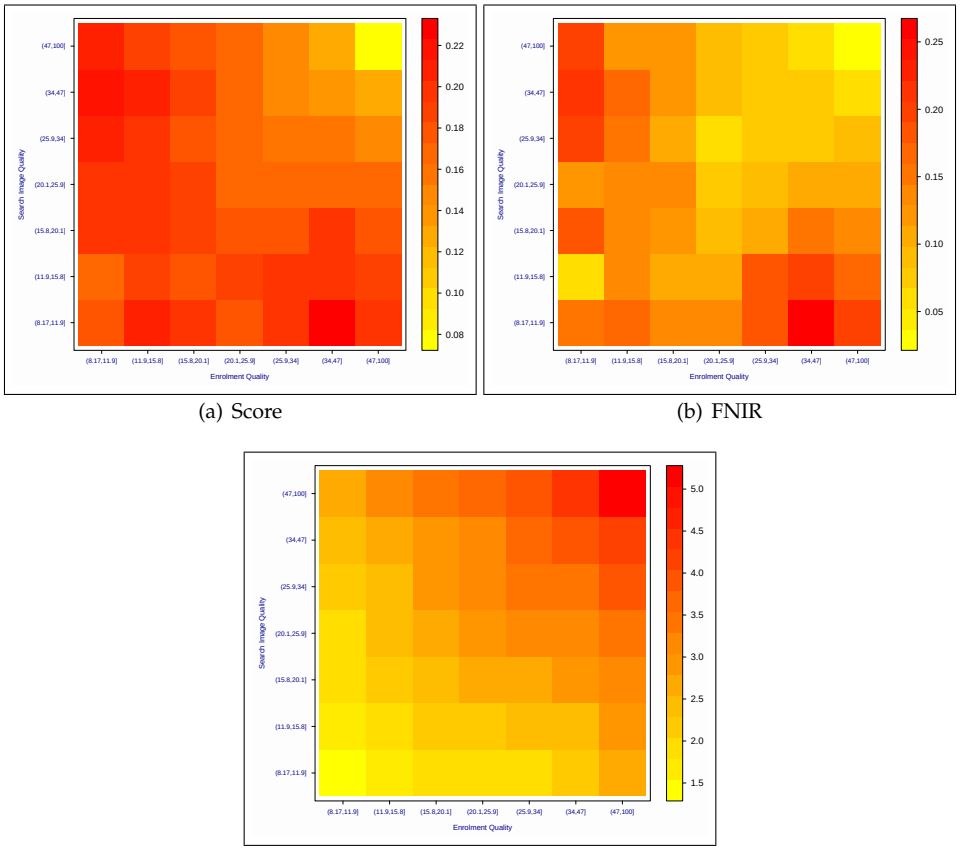

(a) Score (b) FNIR

(c) $log_{10}(1 + Count)$

Figure 465: **Effectiveness of quality assessments**: Heatmaps for implementation T01A executing mate searches in an enrolled population of N = 1600000. The quality values of the enrolled and search images are binned by their mutual $0.005, 0.01, 0.02, 0.04, 0.16, 0.32$ quantiles. From left to right, the color gives the mean reported dis-similarity score, the FNIR at FPIR = 0.0001, and the log of count of the images in each quality bin.

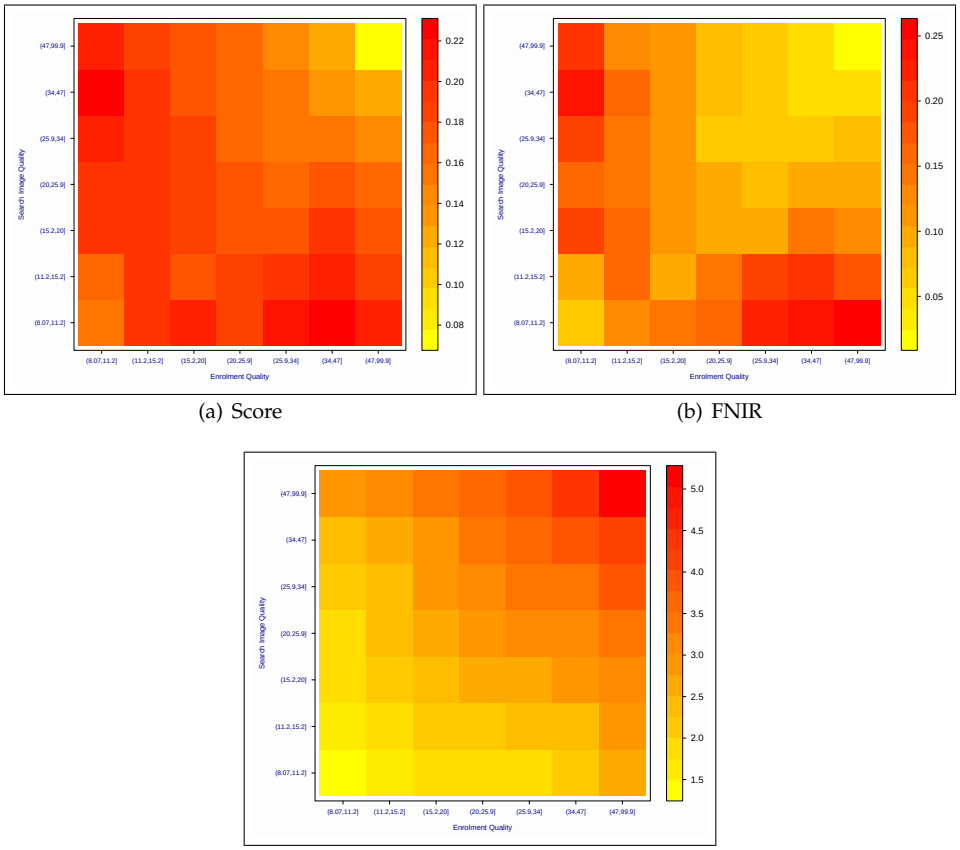

(a) Score (b) FNIR

(c) $log_{10}(1 + Count)$

Figure 466: **Effectiveness of quality assessments**: Heatmaps for implementation T01B executing mate searches in an enrolled population of N = 1600000. The quality values of the enrolled and search images are binned by their mutual $0.005, 0.01, 0.02, 0.04, 0.16, 0.32$ quantiles. From left to right, the color gives the mean reported dis-similarity score, the FNIR at FPIR = 0.0001, and the log of count of the images in each quality bin.

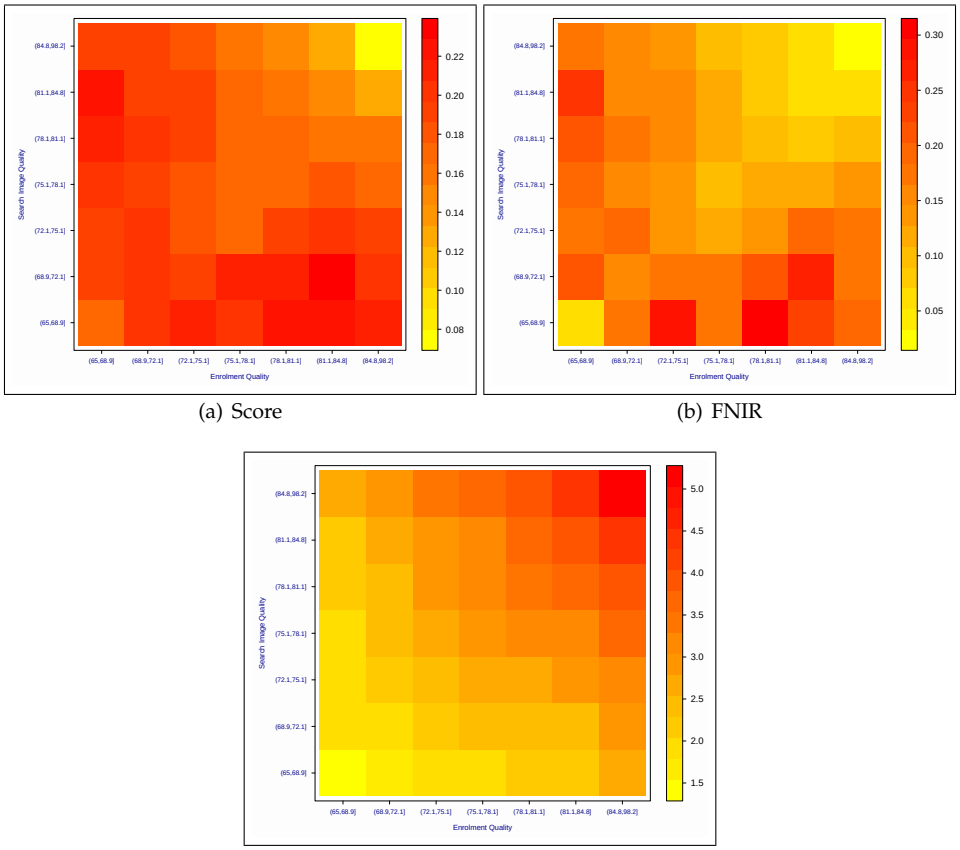

(a) Score (b) FNIR

(c) $log_{10}(1 + Count)$

Figure 467: **Effectiveness of quality assessments**: Heatmaps for implementation T02A executing mate searches in an enrolled population of N = 1600000. The quality values of the enrolled and search images are binned by their mutual $0.005, 0.01, 0.02, 0.04, 0.16, 0.32$ quantiles. From left to right, the color gives the mean reported dis-similarity score, the FNIR at FPIR = 0.0001, and the log of count of the images in each quality bin.

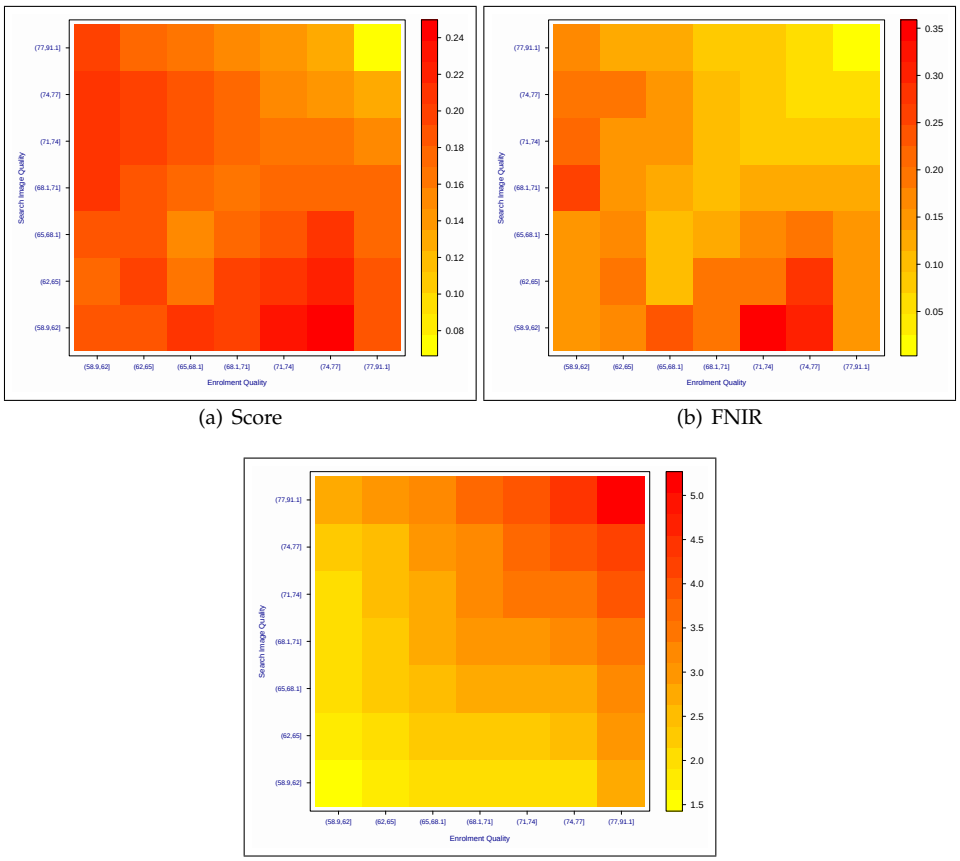

(a) Score (b) FNIR

(c) $log_{10}(1 + Count)$

Figure 468: **Effectiveness of quality assessments**: Heatmaps for implementation T02B executing mate searches in an enrolled population of N = 1600000. The quality values of the enrolled and search images are binned by their mutual $0.005, 0.01, 0.02, 0.04, 0.16, 0.32$ quantiles. From left to right, the color gives the mean reported dis-similarity score, the FNIR at FPIR = 0.0001, and the log of count of the images in each quality bin.

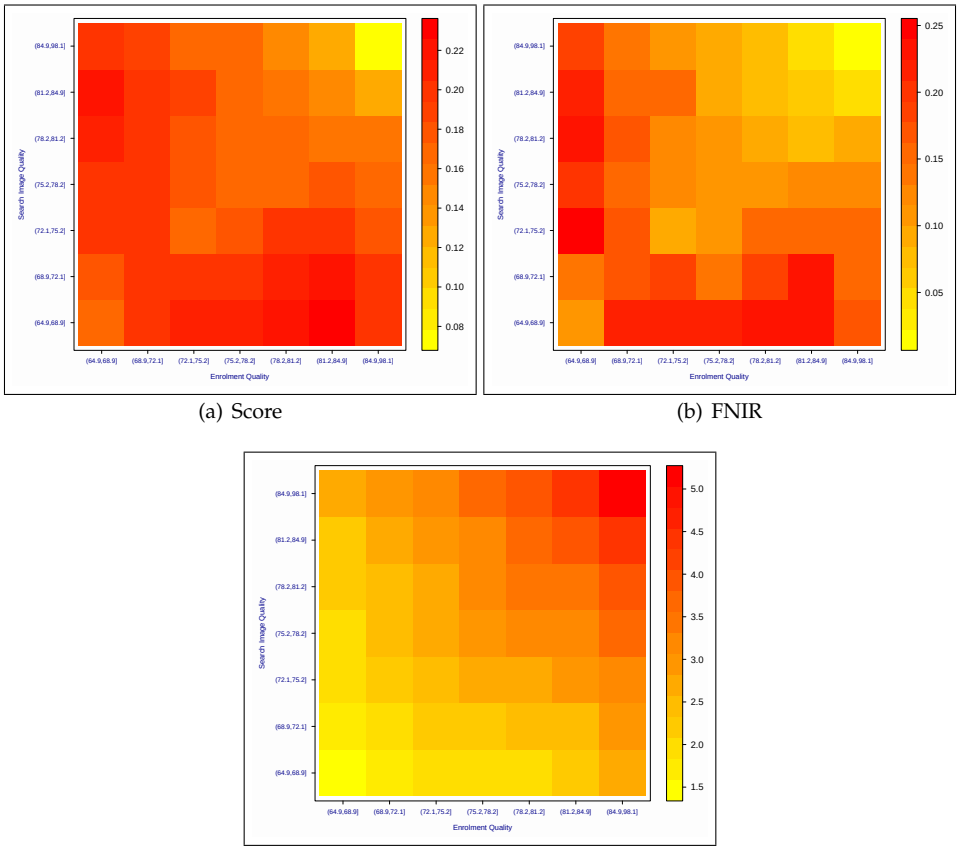

(a) Score (b) FNIR

(c) $log_{10}(1 + Count)$

Figure 469: **Effectiveness of quality assessments**: Heatmaps for implementation T03A executing mate searches in an enrolled population of N = 1600000. The quality values of the enrolled and search images are binned by their mutual $0.005, 0.01, 0.02, 0.04, 0.16, 0.32$ quantiles. From left to right, the color gives the mean reported dis-similarity score, the FNIR at FPIR = 0.0001, and the log of count of the images in each quality bin.

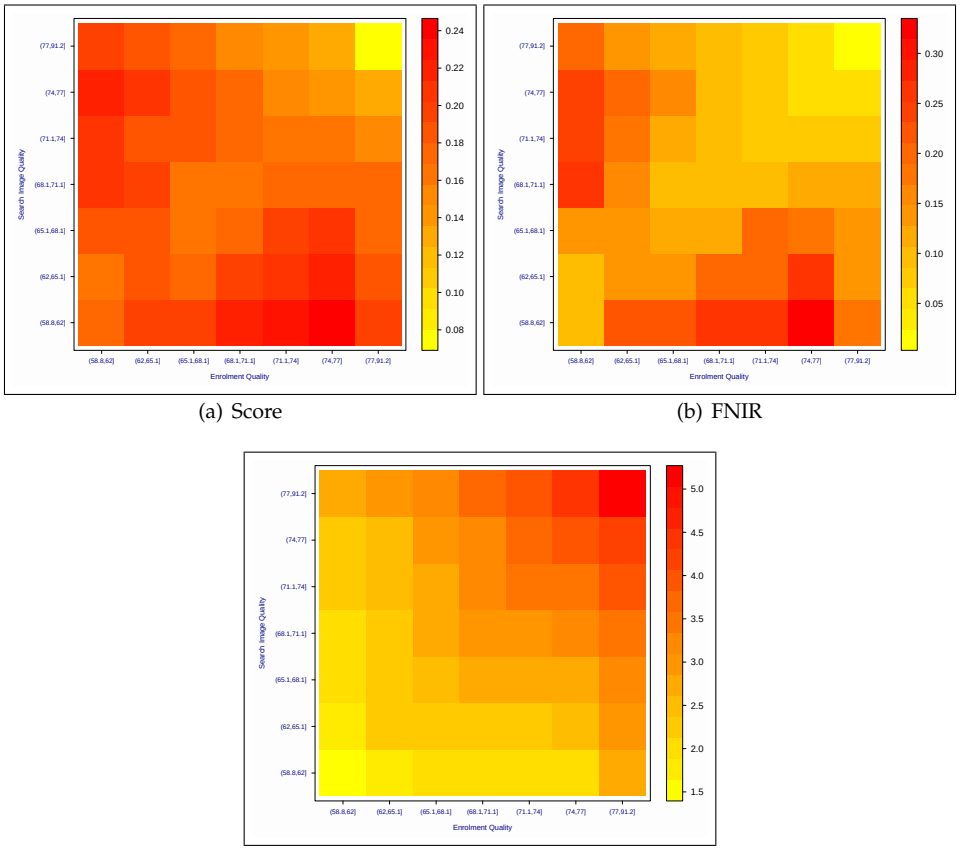

(a) Score (b) FNIR

(c) $log_{10}(1 + Count)$

Figure 470: **Effectiveness of quality assessments**: Heatmaps for implementation T03B executing mate searches in an enrolled population of N = 1600000. The quality values of the enrolled and search images are binned by their mutual $0.005, 0.01, 0.02, 0.04, 0.16, 0.32$ quantiles. From left to right, the color gives the mean reported dis-similarity score, the FNIR at FPIR = 0.0001, and the log of count of the images in each quality bin.

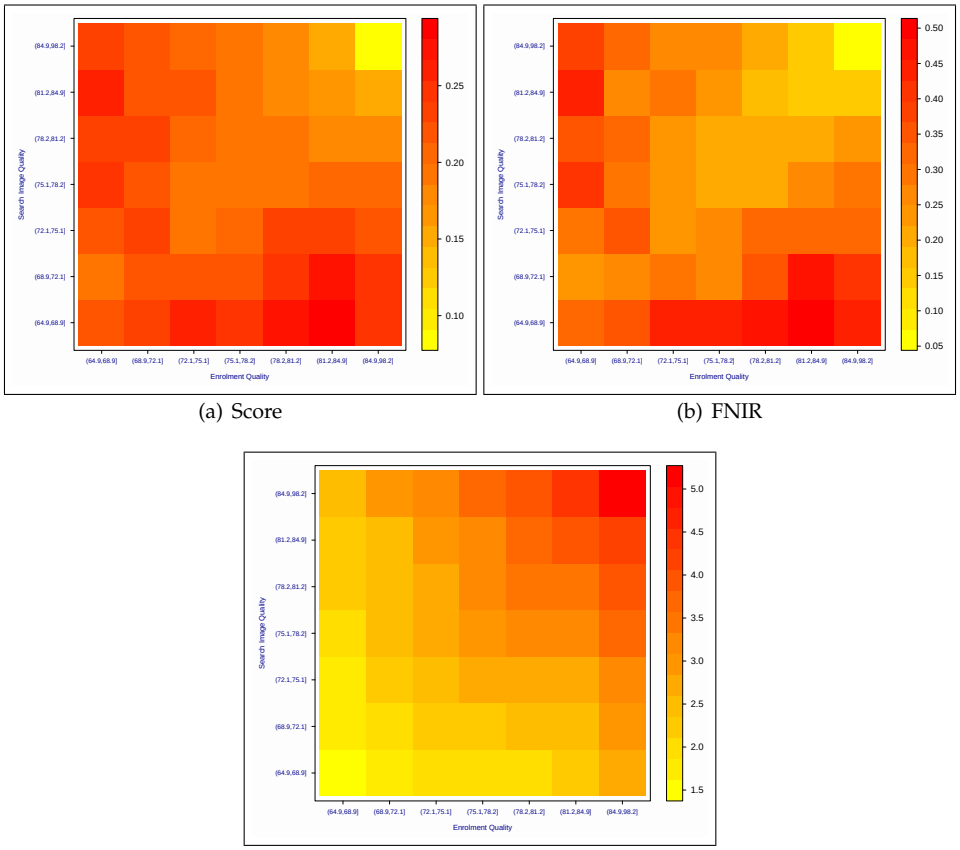

(a) Score (b) FNIR

(c) $log_{10}(1 + Count)$

Figure 471: **Effectiveness of quality assessments**: Heatmaps for implementation T04A executing mate searches in an enrolled population of N = 1600000. The quality values of the enrolled and search images are binned by their mutual $0.005, 0.01, 0.02, 0.04, 0.16, 0.32$ quantiles. From left to right, the color gives the mean reported dis-similarity score, the FNIR at FPIR = 0.0001, and the log of count of the images in each quality bin.

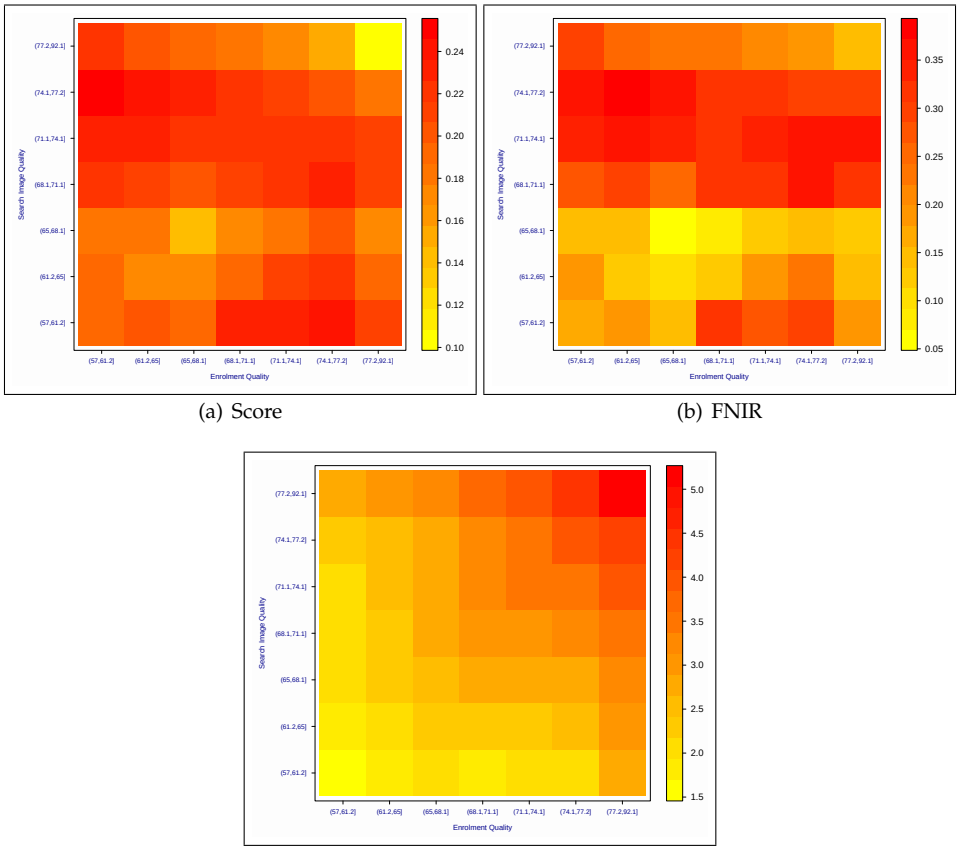

(a) Score (b) FNIR

(c) $log_{10}(1 + Count)$

Figure 472: **Effectiveness of quality assessments**: Heatmaps for implementation T11A executing mate searches in an enrolled population of N = 1600000. The quality values of the enrolled and search images are binned by their mutual $0.005, 0.01, 0.02, 0.04, 0.16, 0.32$ quantiles. From left to right, the color gives the mean reported dis-similarity score, the FNIR at FPIR = 0.0001, and the log of count of the images in each quality bin.

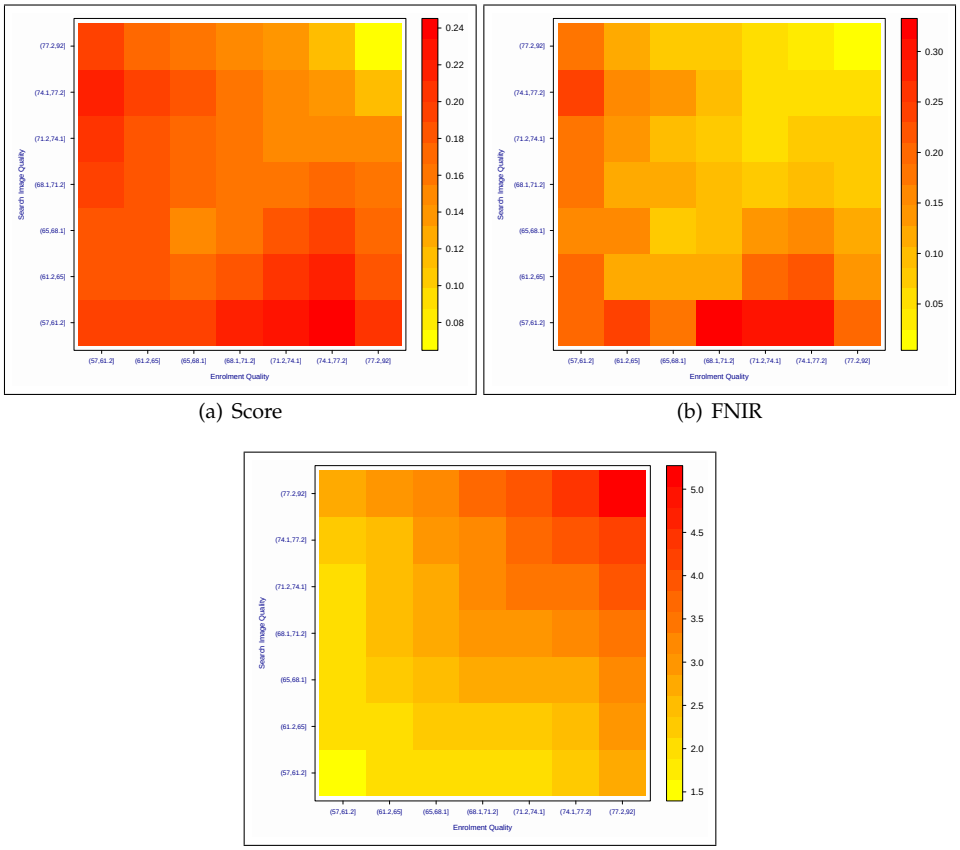

(a) Score (b) FNIR

(c) $log_{10}(1 + Count)$

Figure 473: **Effectiveness of quality assessments**: Heatmaps for implementation T11B executing mate searches in an enrolled population of N = 1600000. The quality values of the enrolled and search images are binned by their mutual $0.005, 0.01, 0.02, 0.04, 0.16, 0.32$ quantiles. From left to right, the color gives the mean reported dis-similarity score, the FNIR at FPIR = 0.0001, and the log of count of the images in each quality bin.

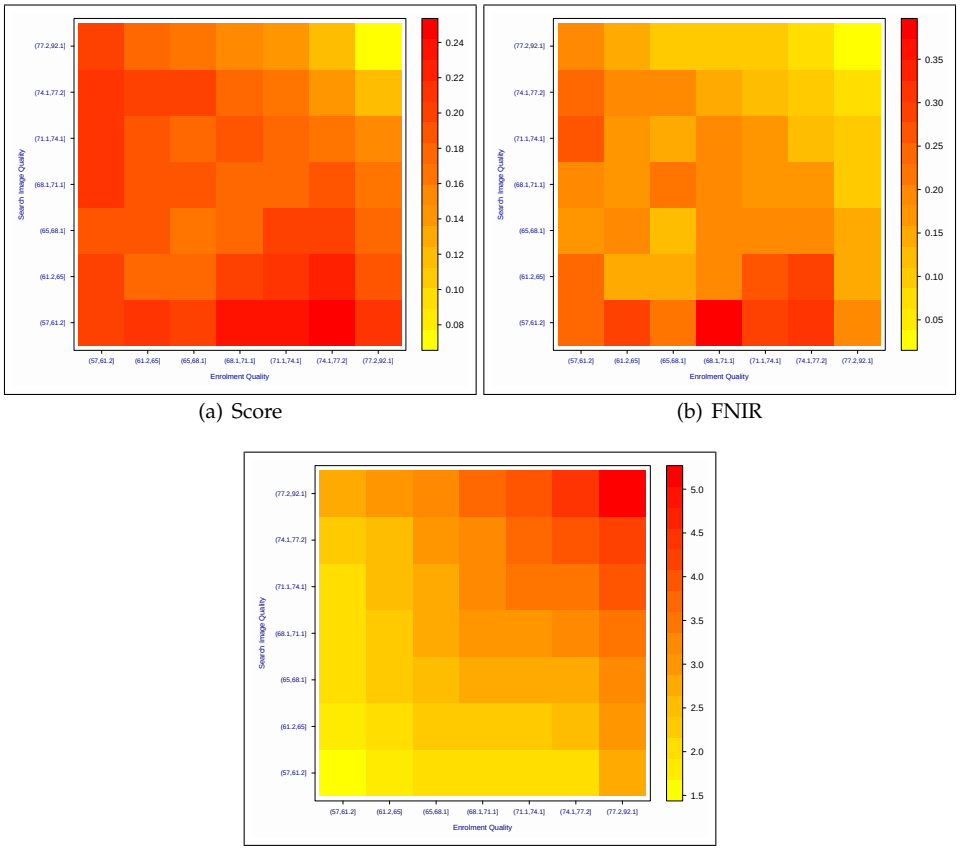

(a) Score (b) FNIR

(c) $log_{10}(1 + Count)$

Figure 474: **Effectiveness of quality assessments**: Heatmaps for implementation T12B executing mate searches in an enrolled population of N = 1600000. The quality values of the enrolled and search images are binned by their mutual $0.005, 0.01, 0.02, 0.04, 0.16, 0.32$ quantiles. From left to right, the color gives the mean reported dis-similarity score, the FNIR at FPIR = 0.0001, and the log of count of the images in each quality bin.

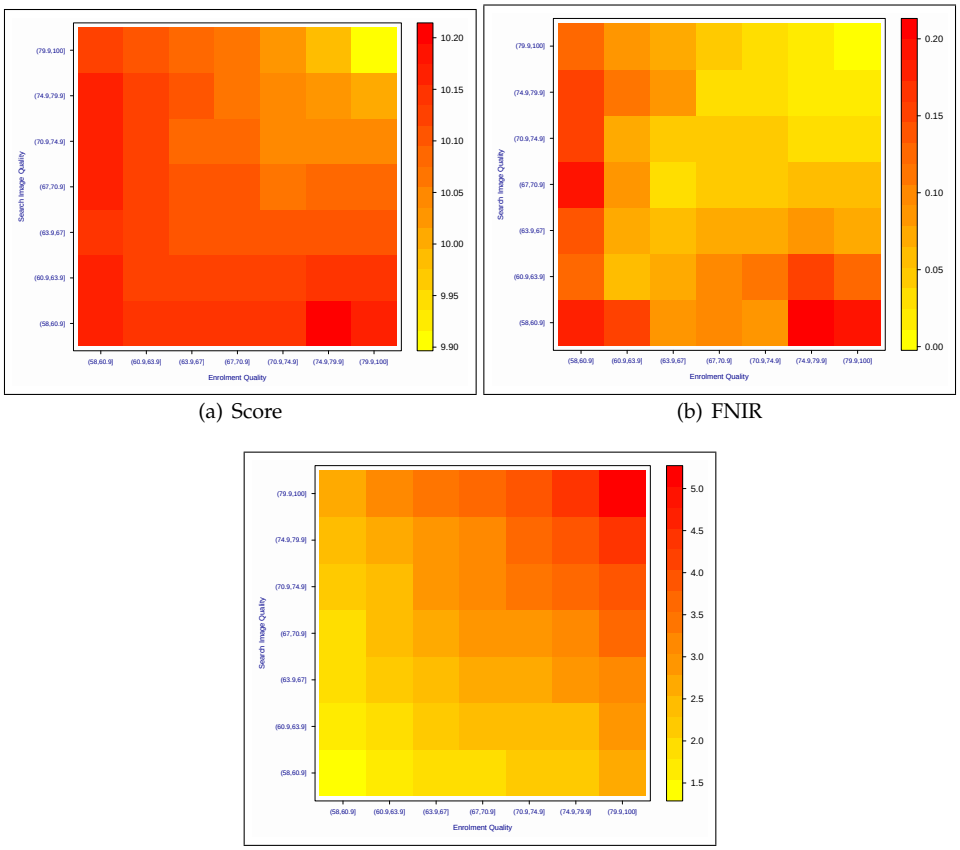

(a) Score (b) FNIR

(c) $log_{10}(1 + Count)$

Figure 475: **Effectiveness of quality assessments**: Heatmaps for implementation U01A executing mate searches in an enrolled population of N = 1600000. The quality values of the enrolled and search images are binned by their mutual $0.005, 0.01, 0.02, 0.04, 0.16, 0.32$ quantiles. From left to right, the color gives the mean reported dis-similarity score, the FNIR at FPIR = 0.0001, and the log of count of the images in each quality bin.

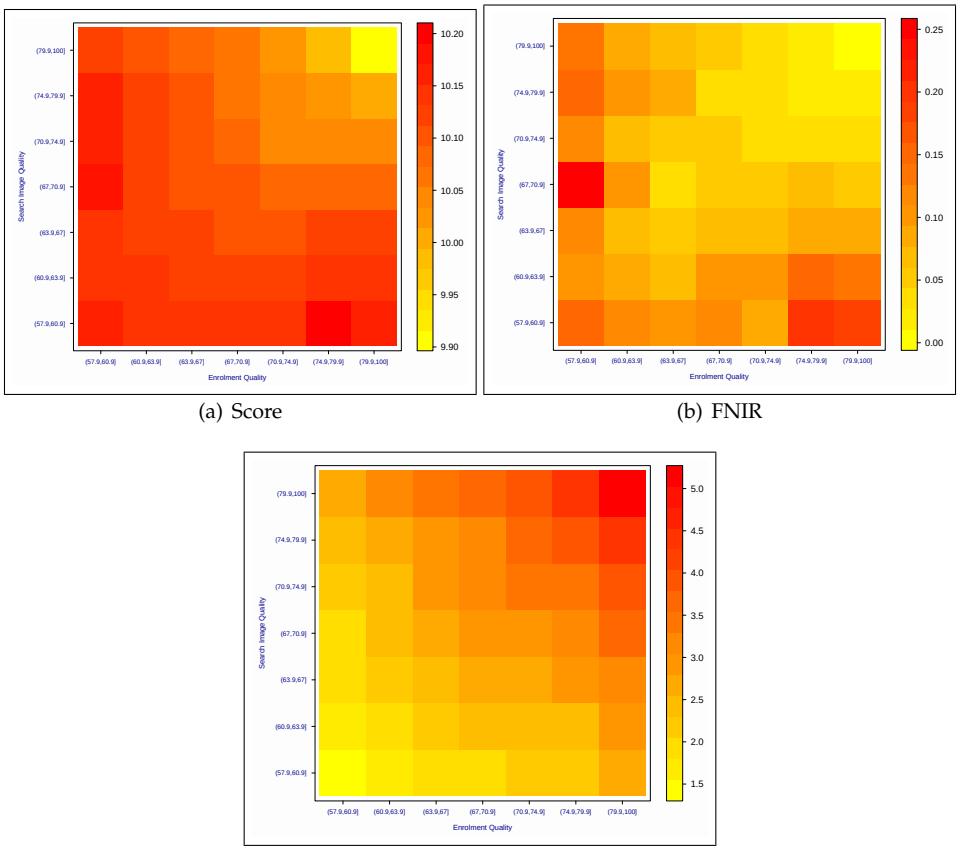

(a) Score (b) FNIR

(c) $log_{10}(1 + Count)$

Figure 476: **Effectiveness of quality assessments**: Heatmaps for implementation U01B executing mate searches in an enrolled population of N = 1600000. The quality values of the enrolled and search images are binned by their mutual $0.005, 0.01, 0.02, 0.04, 0.16, 0.32$ quantiles. From left to right, the color gives the mean reported dis-similarity score, the FNIR at FPIR = 0.0001, and the log of count of the images in each quality bin.

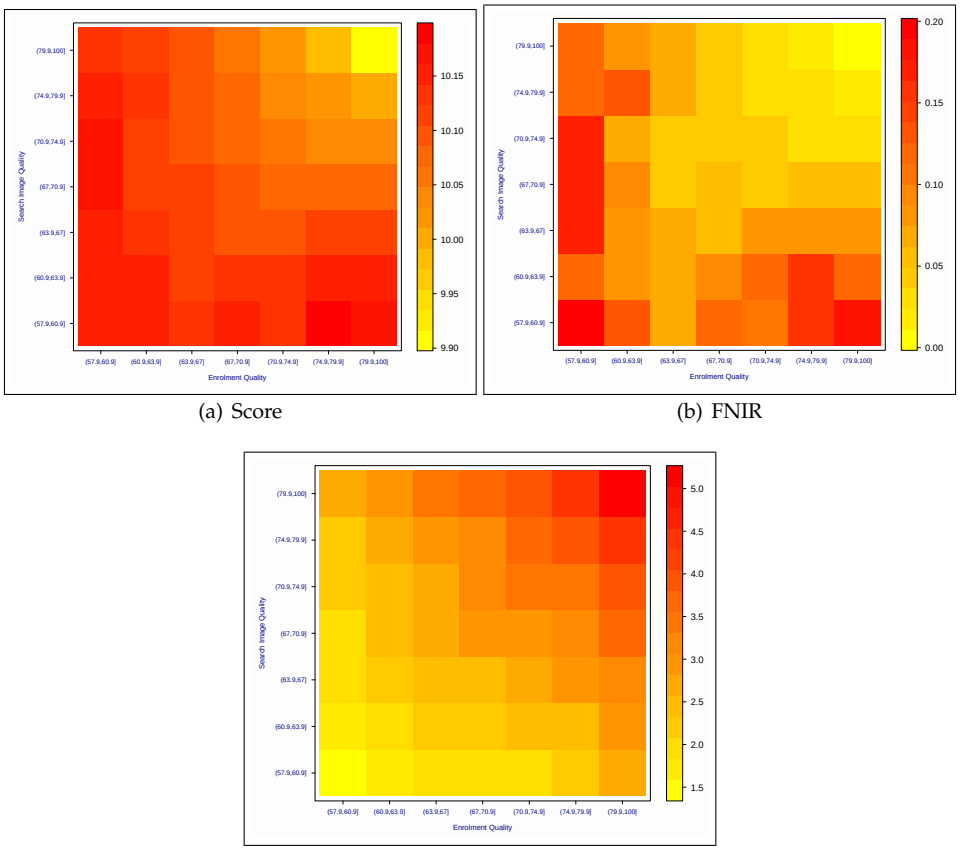

(a) Score (b) FNIR

(c) $log_{10}(1 + Count)$

Figure 477: **Effectiveness of quality assessments**: Heatmaps for implementation U02A executing mate searches in an enrolled population of N = 1600000. The quality values of the enrolled and search images are binned by their mutual $0.005, 0.01, 0.02, 0.04, 0.16, 0.32$ quantiles. From left to right, the color gives the mean reported dis-similarity score, the FNIR at FPIR = 0.0001, and the log of count of the images in each quality bin.

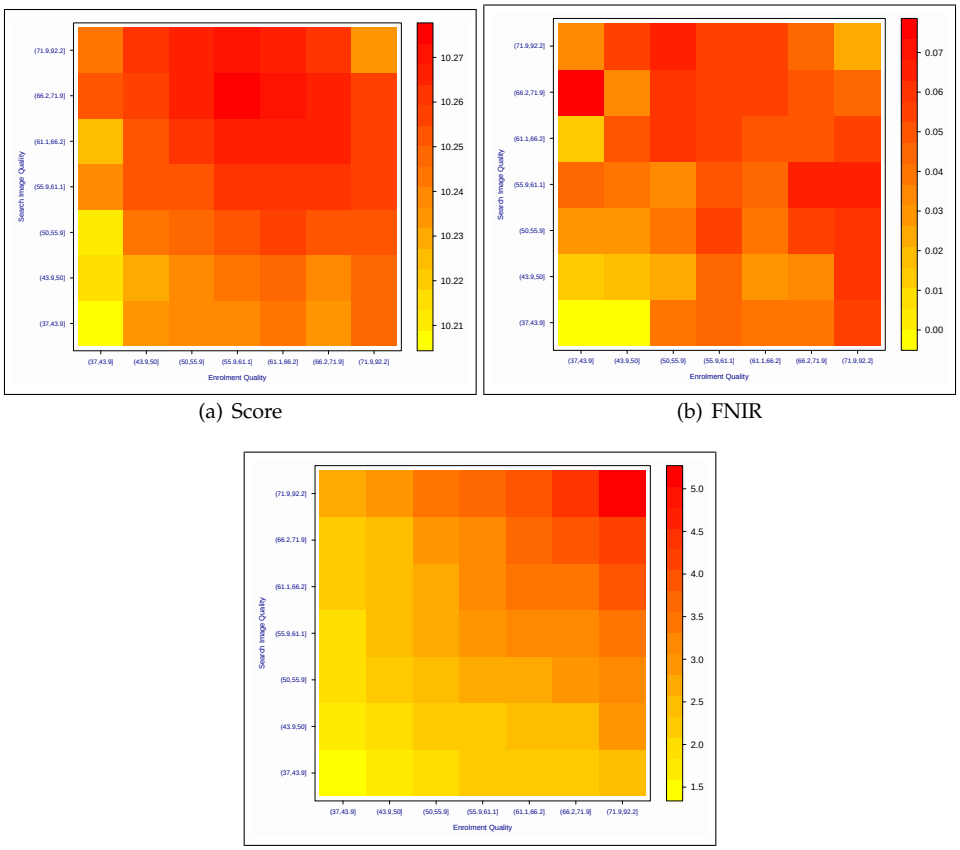

(a) Score (b) FNIR

(c) $log_{10}(1 + Count)$

Figure 478: **Effectiveness of quality assessments**: Heatmaps for implementation U03A executing mate searches in an enrolled population of N = 1600000. The quality values of the enrolled and search images are binned by their mutual $0.005, 0.01, 0.02, 0.04, 0.16, 0.32$ quantiles. From left to right, the color gives the mean reported dis-similarity score, the FNIR at FPIR = 0.0001, and the log of count of the images in each quality bin.

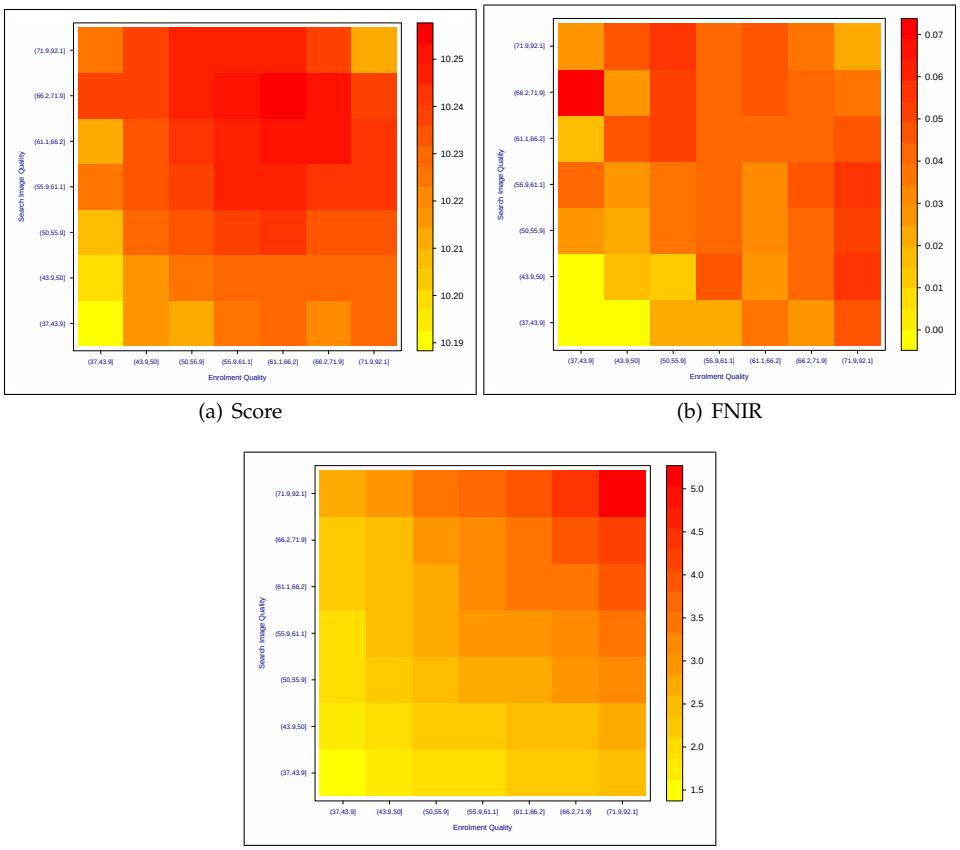

(a) Score (b) FNIR

(c) $log_{10}(1 + Count)$

Figure 479: **Effectiveness of quality assessments**: Heatmaps for implementation U03B executing mate searches in an enrolled population of N = 1600000. The quality values of the enrolled and search images are binned by their mutual $0.005, 0.01, 0.02, 0.04, 0.16, 0.32$ quantiles. From left to right, the color gives the mean reported dis-similarity score, the FNIR at FPIR = 0.0001, and the log of count of the images in each quality bin.

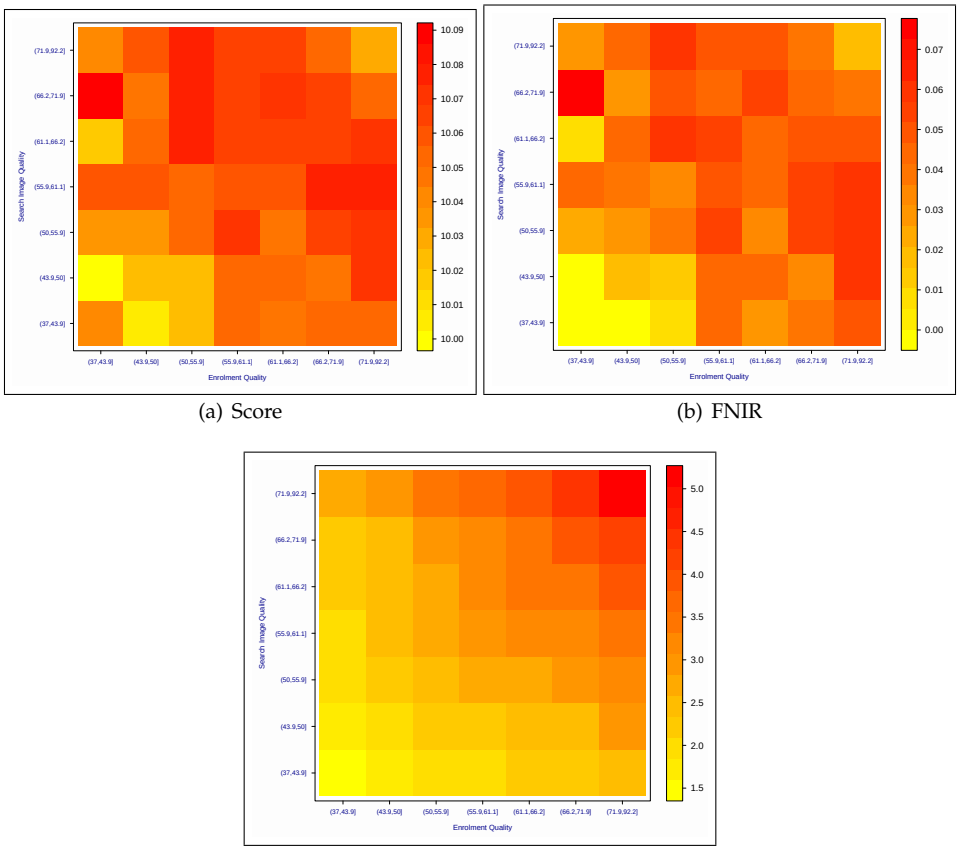

(a) Score (b) FNIR

(c) $log_{10}(1 + Count)$

Figure 480: **Effectiveness of quality assessments**: Heatmaps for implementation U04A executing mate searches in an enrolled population of N = 1600000. The quality values of the enrolled and search images are binned by their mutual $0.005, 0.01, 0.02, 0.04, 0.16, 0.32$ quantiles. From left to right, the color gives the mean reported dis-similarity score, the FNIR at FPIR = 0.0001, and the log of count of the images in each quality bin.

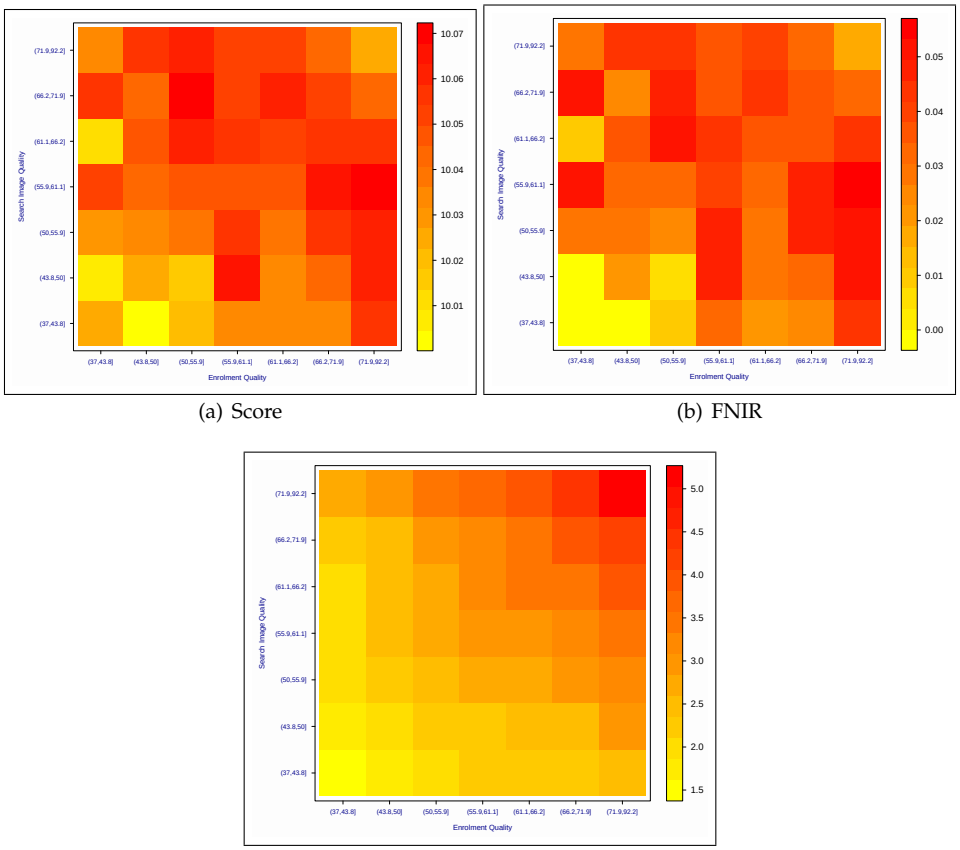

(a) Score (b) FNIR

(c) $log_{10}(1 + Count)$

Figure 481: **Effectiveness of quality assessments**: Heatmaps for implementation U04B executing mate searches in an enrolled population of N = 1600000. The quality values of the enrolled and search images are binned by their mutual $0.005, 0.01, 0.02, 0.04, 0.16, 0.32$ quantiles. From left to right, the color gives the mean reported dis-similarity score, the FNIR at FPIR = 0.0001, and the log of count of the images in each quality bin.

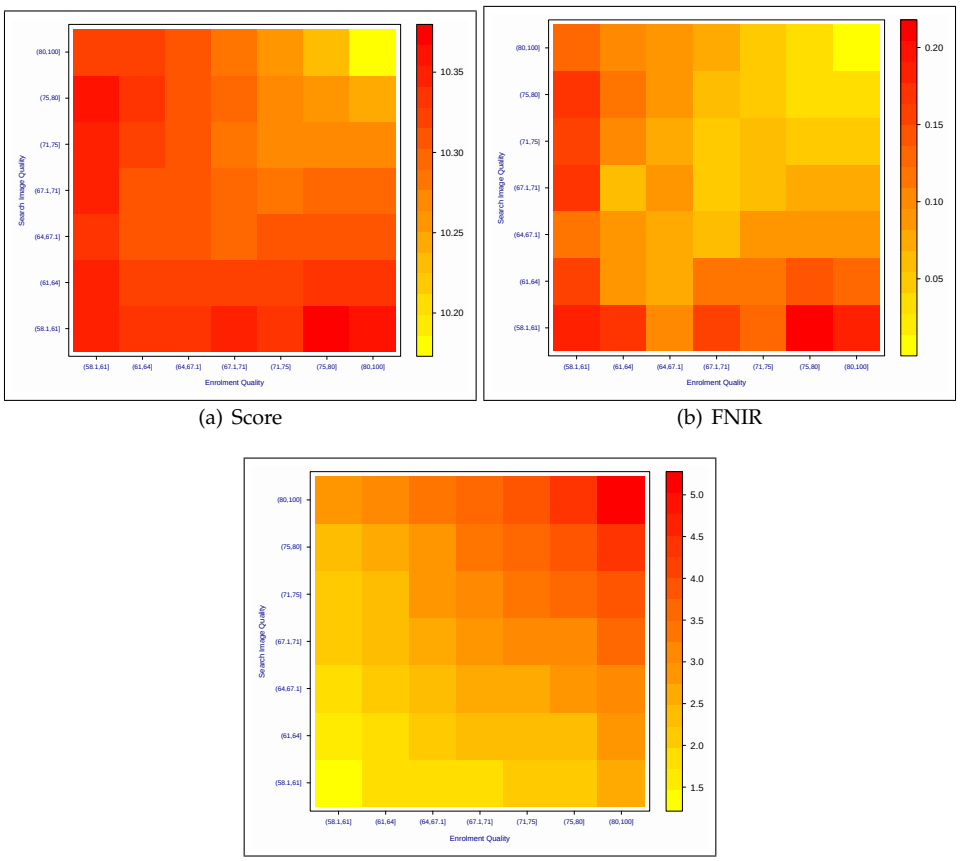

(a) Score (b) FNIR

(c) $log_{10}(1 + Count)$

Figure 482: **Effectiveness of quality assessments**: Heatmaps for implementation U11A executing mate searches in an enrolled population of N = 1600000. The quality values of the enrolled and search images are binned by their mutual $0.005, 0.01, 0.02, 0.04, 0.16, 0.32$ quantiles. From left to right, the color gives the mean reported dis-similarity score, the FNIR at FPIR = 0.0001, and the log of count of the images in each quality bin.

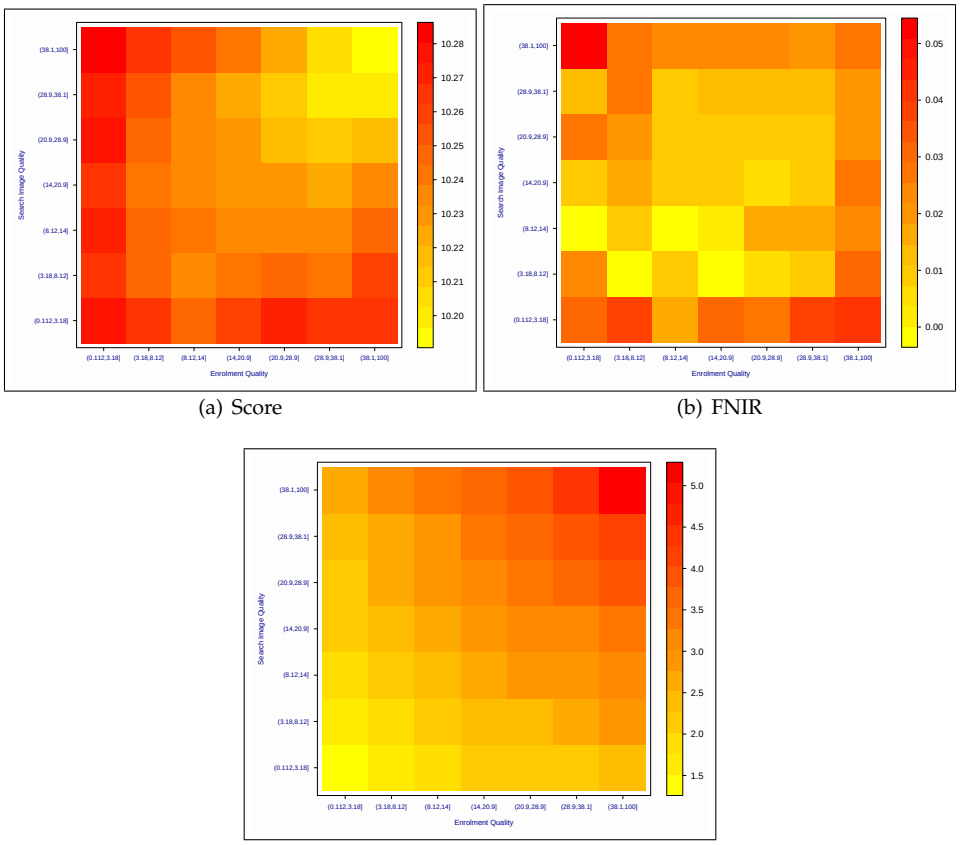

(a) Score (b) FNIR

(c) $log_{10}(1 + Count)$

Figure 483: **Effectiveness of quality assessments**: Heatmaps for implementation U11B executing mate searches in an enrolled population of N = 1600000. The quality values of the enrolled and search images are binned by their mutual $0.005, 0.01, 0.02, 0.04, 0.16, 0.32$ quantiles. From left to right, the color gives the mean reported dis-similarity score, the FNIR at FPIR = 0.0001, and the log of count of the images in each quality bin.

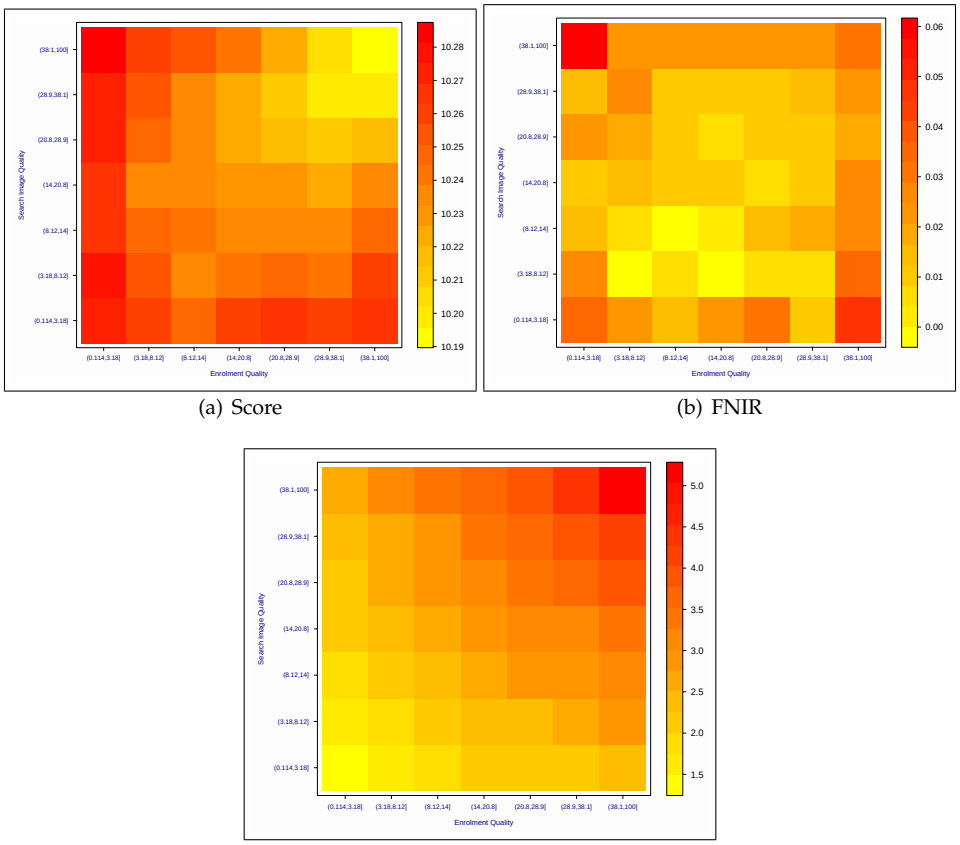

(a) Score (b) FNIR

(c) $log_{10}(1 + Count)$

Figure 484: **Effectiveness of quality assessments**: Heatmaps for implementation U12A executing mate searches in an enrolled population of N = 1600000. The quality values of the enrolled and search images are binned by their mutual $0.005, 0.01, 0.02, 0.04, 0.16, 0.32$ quantiles. From left to right, the color gives the mean reported dis-similarity score, the FNIR at FPIR = 0.0001, and the log of count of the images in each quality bin.

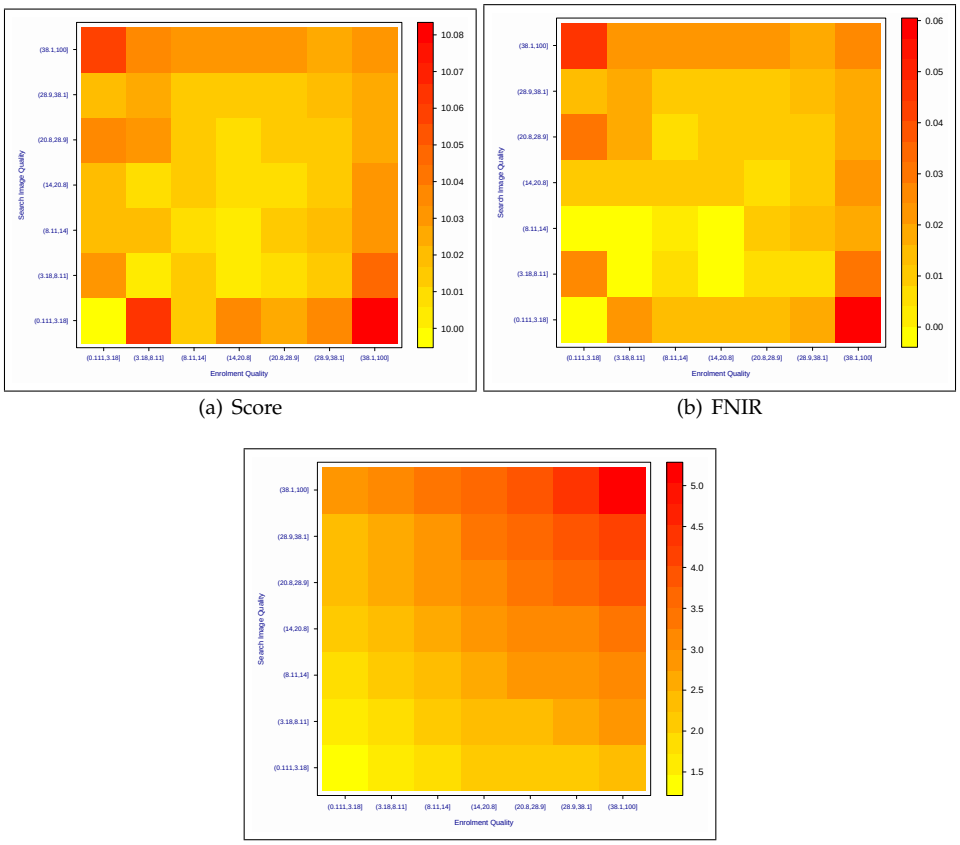

(a) Score (b) FNIR

(c) $log_{10}(1 + Count)$

Figure 485: **Effectiveness of quality assessments**: Heatmaps for implementation U12B executing mate searches in an enrolled population of N = 1600000. The quality values of the enrolled and search images are binned by their mutual $0.005, 0.01, 0.02, 0.04, 0.16, 0.32$ quantiles. From left to right, the color gives the mean reported dis-similarity score, the FNIR at FPIR = 0.0001, and the log of count of the images in each quality bin.

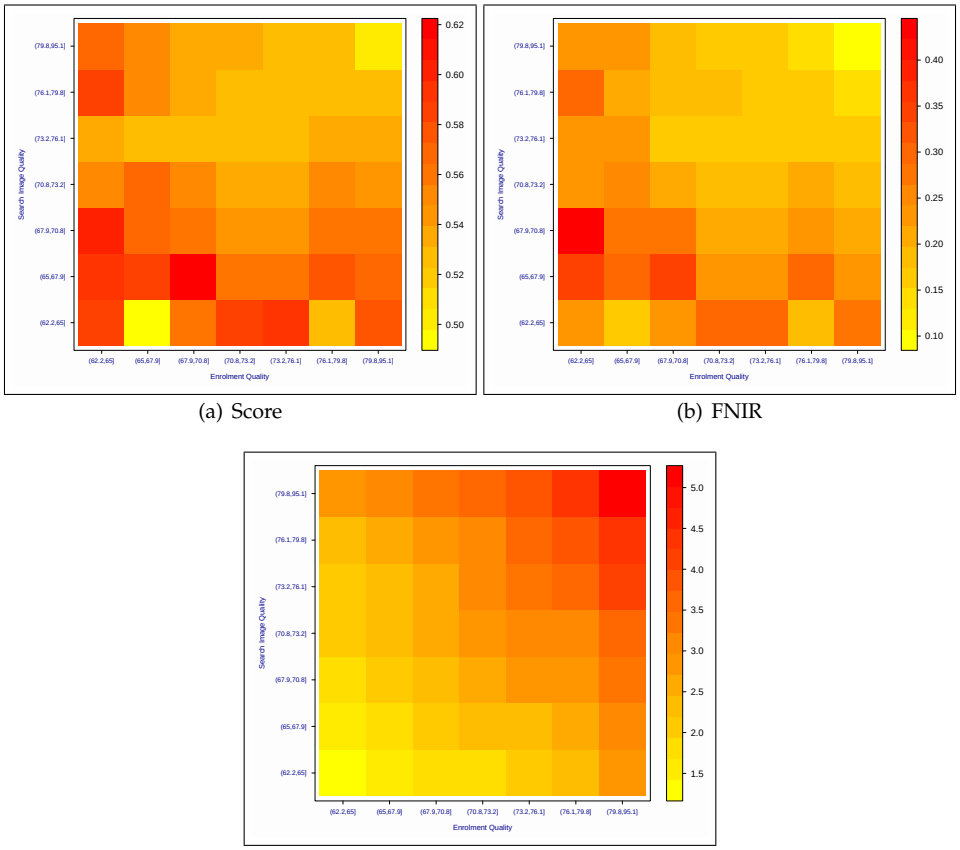

(a) Score (b) FNIR

(c) $log_{10}(1 + Count)$

Figure 486: **Effectiveness of quality assessments**: Heatmaps for implementation V01A executing mate searches in an enrolled population of N = 1600000. The quality values of the enrolled and search images are binned by their mutual $0.005, 0.01, 0.02, 0.04, 0.16, 0.32$ quantiles. From left to right, the color gives the mean reported dis-similarity score, the FNIR at FPIR = 0.0001, and the log of count of the images in each quality bin.

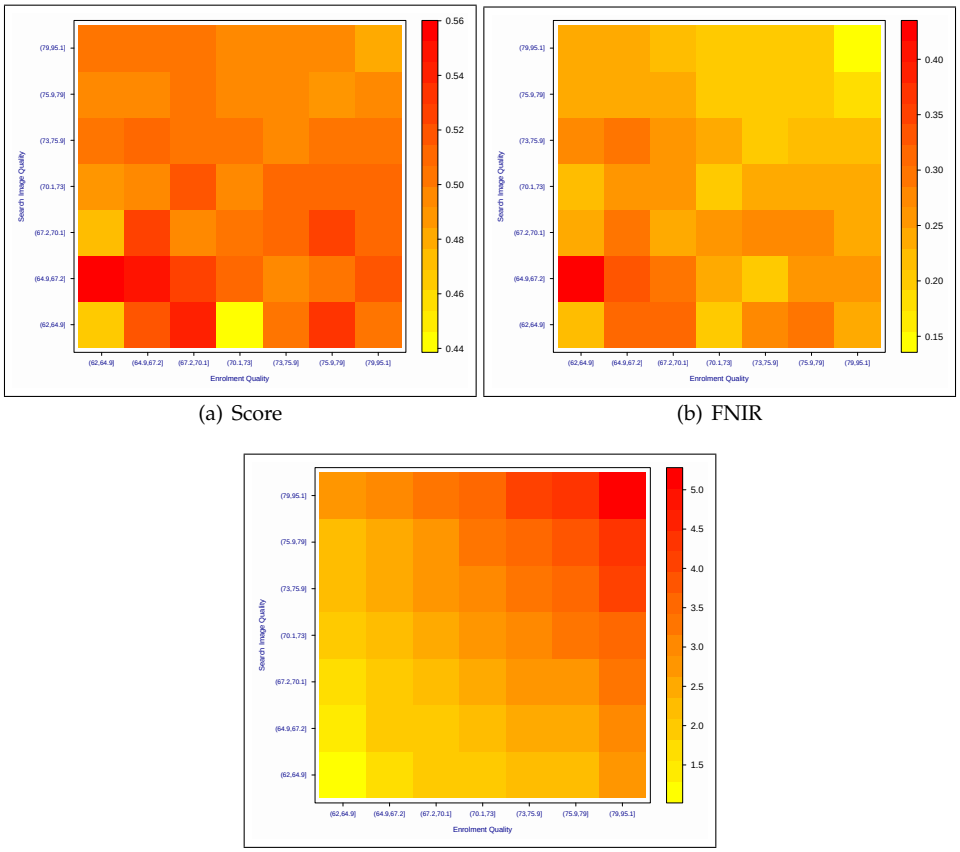

(a) Score (b) FNIR

(c) $log_{10}(1 + Count)$

Figure 487: **Effectiveness of quality assessments**: Heatmaps for implementation V02A executing mate searches in an enrolled population of N = 1600000. The quality values of the enrolled and search images are binned by their mutual $0.005, 0.01, 0.02, 0.04, 0.16, 0.32$ quantiles. From left to right, the color gives the mean reported dis-similarity score, the FNIR at FPIR = 0.0001, and the log of count of the images in each quality bin.

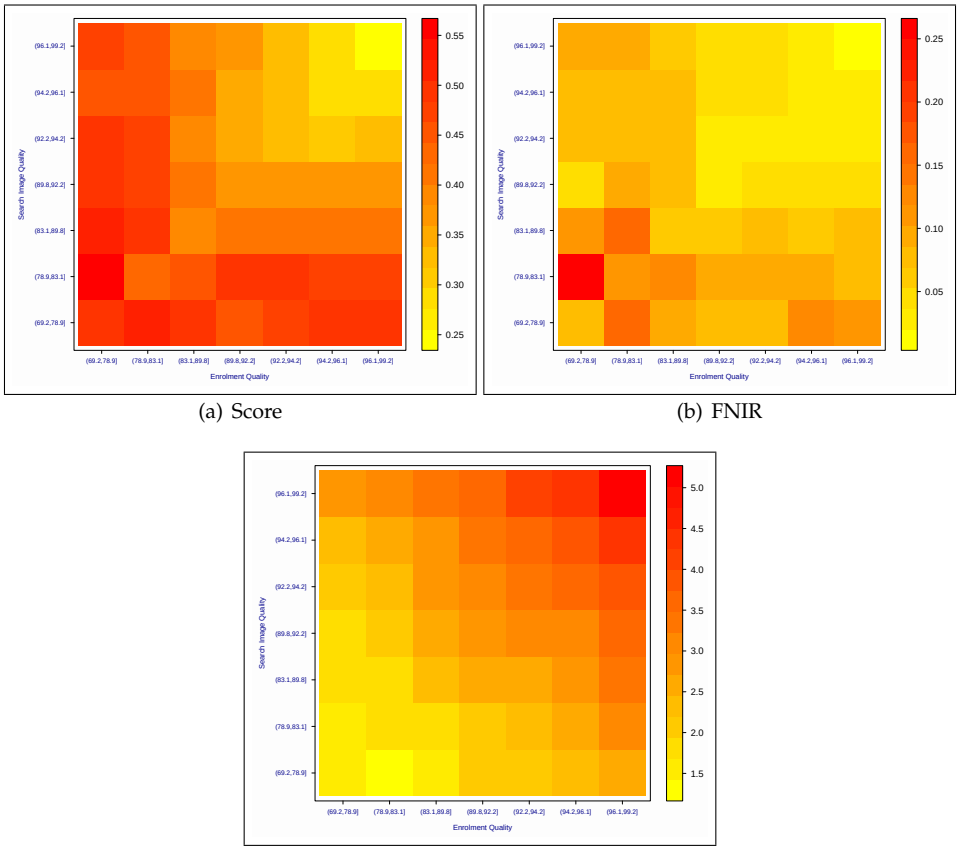

(a) Score (b) FNIR

(c) $log_{10}(1 + Count)$

Figure 488: **Effectiveness of quality assessments**: Heatmaps for implementation V03A executing mate searches in an enrolled population of N = 1600000. The quality values of the enrolled and search images are binned by their mutual $0.005, 0.01, 0.02, 0.04, 0.16, 0.32$ quantiles. From left to right, the color gives the mean reported dis-similarity score, the FNIR at FPIR = 0.0001, and the log of count of the images in each quality bin.

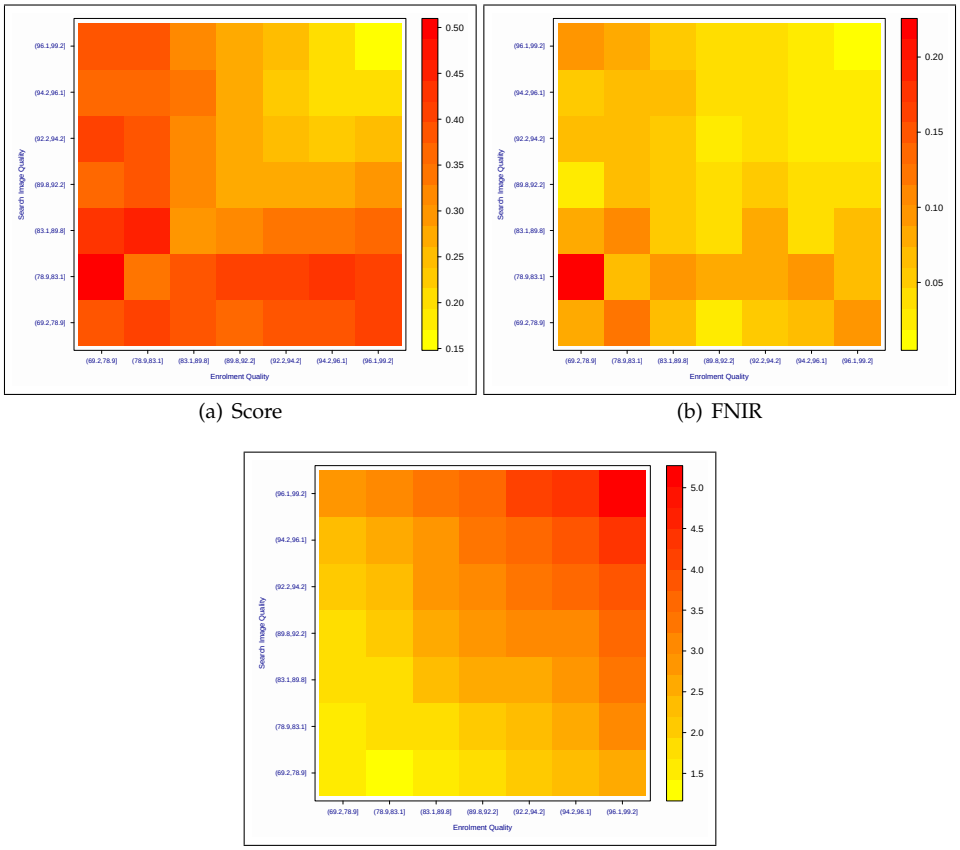

(a) Score (b) FNIR

(c) $log_{10}(1 + Count)$

Figure 489: **Effectiveness of quality assessments**: Heatmaps for implementation V03B executing mate searches in an enrolled population of N = 1600000. The quality values of the enrolled and search images are binned by their mutual $0.005, 0.01, 0.02, 0.04, 0.16, 0.32$ quantiles. From left to right, the color gives the mean reported dis-similarity score, the FNIR at FPIR = 0.0001, and the log of count of the images in each quality bin.

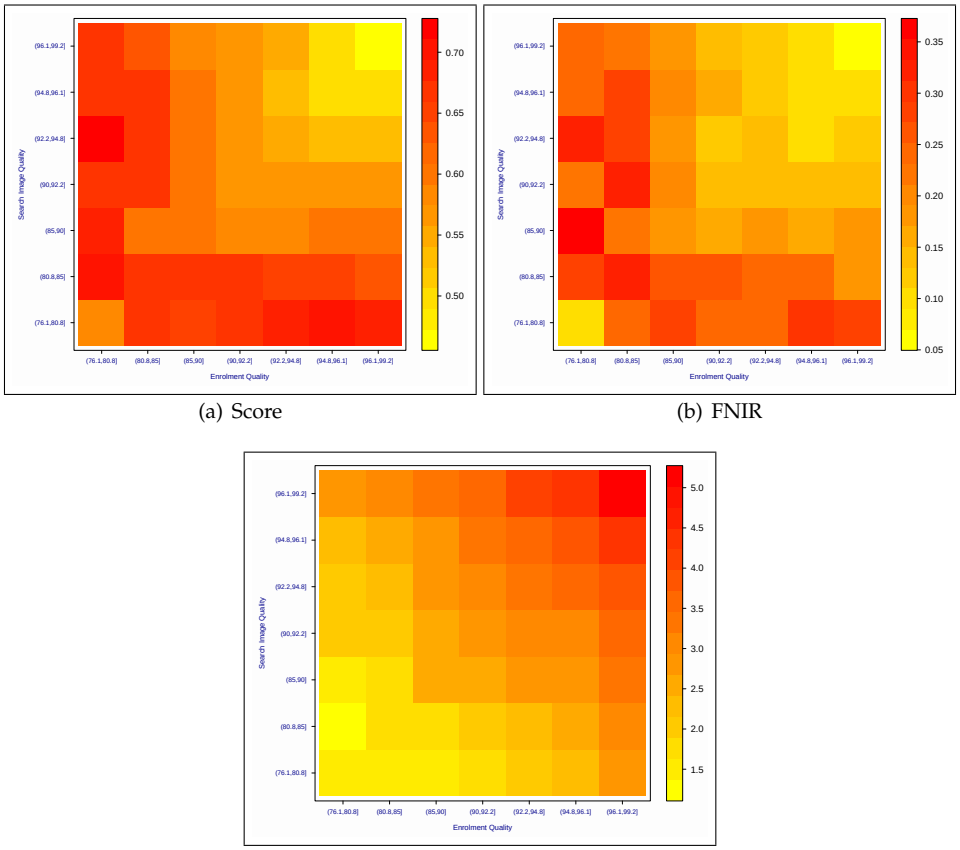

(a) Score (b) FNIR

(c) $log_{10}(1 + Count)$

Figure 490: **Effectiveness of quality assessments**: Heatmaps for implementation V04A executing mate searches in an enrolled population of N = 1600000. The quality values of the enrolled and search images are binned by their mutual $0.005, 0.01, 0.02, 0.04, 0.16, 0.32$ quantiles. From left to right, the color gives the mean reported dis-similarity score, the FNIR at FPIR = 0.0001, and the log of count of the images in each quality bin.

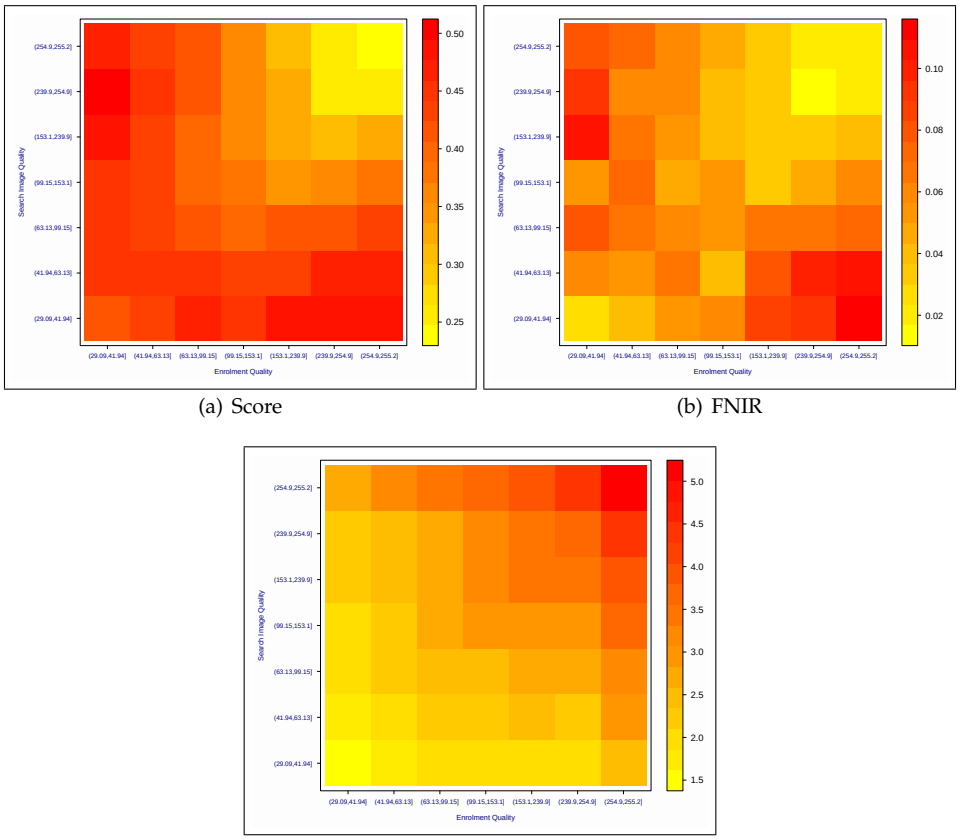

(a) Score (b) FNIR

(c) $log_{10}(1 + Count)$

Figure 491: **Effectiveness of quality assessments**: Heatmaps for implementation V11A executing mate searches in an enrolled population of N = 1600000. The quality values of the enrolled and search images are binned by their mutual $0.005, 0.01, 0.02, 0.04, 0.16, 0.32$ quantiles. From left to right, the color gives the mean reported dis-similarity score, the FNIR at FPIR = 0.0001, and the log of count of the images in each quality bin.

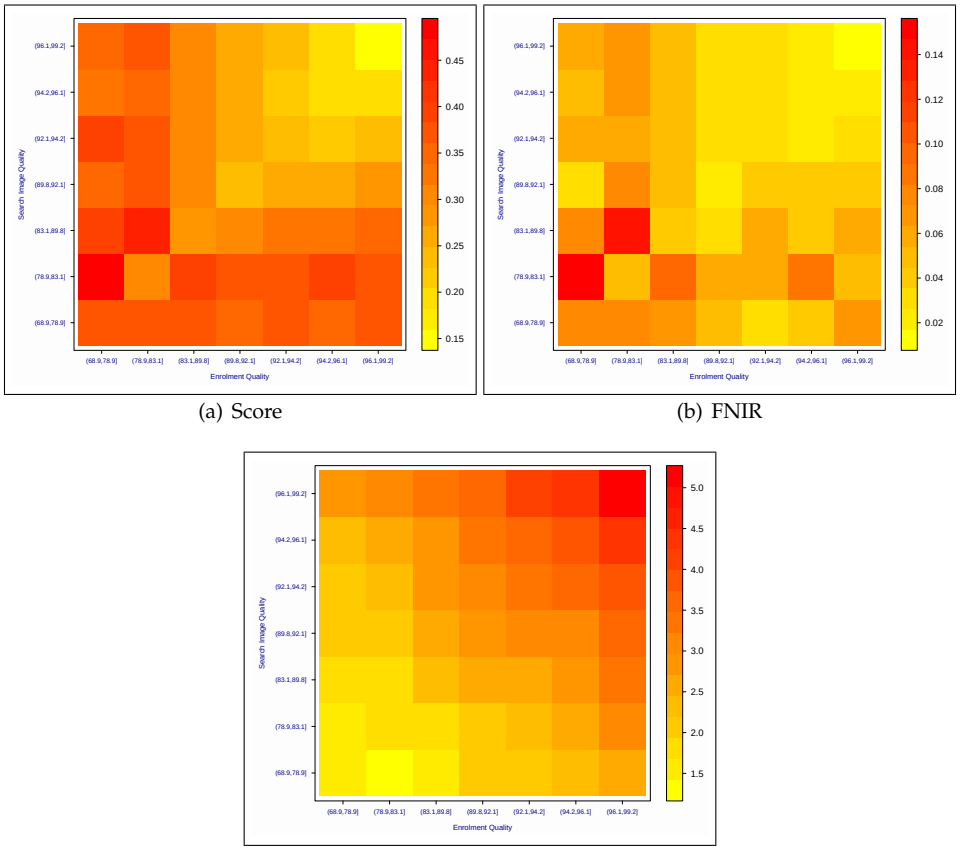

(a) Score (b) FNIR

(c) $log_{10}(1 + Count)$

Figure 492: **Effectiveness of quality assessments**: Heatmaps for implementation V11B executing mate searches in an enrolled population of N = 1600000. The quality values of the enrolled and search images are binned by their mutual $0.005, 0.01, 0.02, 0.04, 0.16, 0.32$ quantiles. From left to right, the color gives the mean reported dis-similarity score, the FNIR at FPIR = 0.0001, and the log of count of the images in each quality bin.

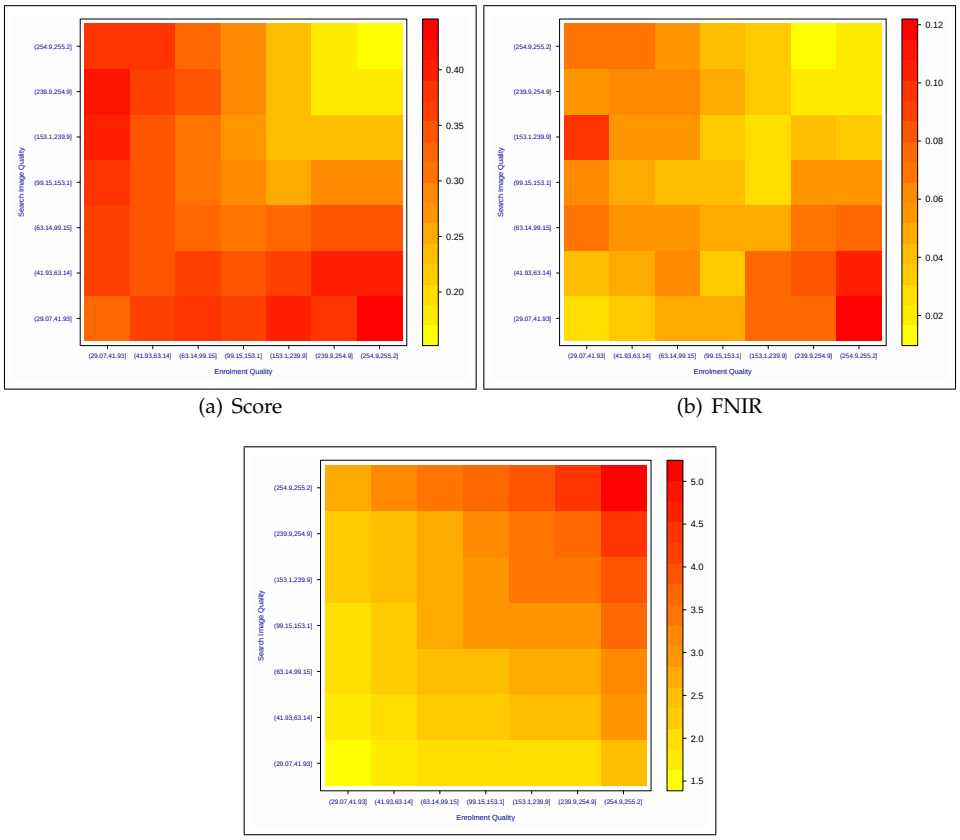

(a) Score (b) FNIR

(c) $log_{10}(1 + Count)$

Figure 493: **Effectiveness of quality assessments**: Heatmaps for implementation V12A executing mate searches in an enrolled population of N = 1600000. The quality values of the enrolled and search images are binned by their mutual $0.005, 0.01, 0.02, 0.04, 0.16, 0.32$ quantiles. From left to right, the color gives the mean reported dis-similarity score, the FNIR at FPIR = 0.0001, and the log of count of the images in each quality bin.

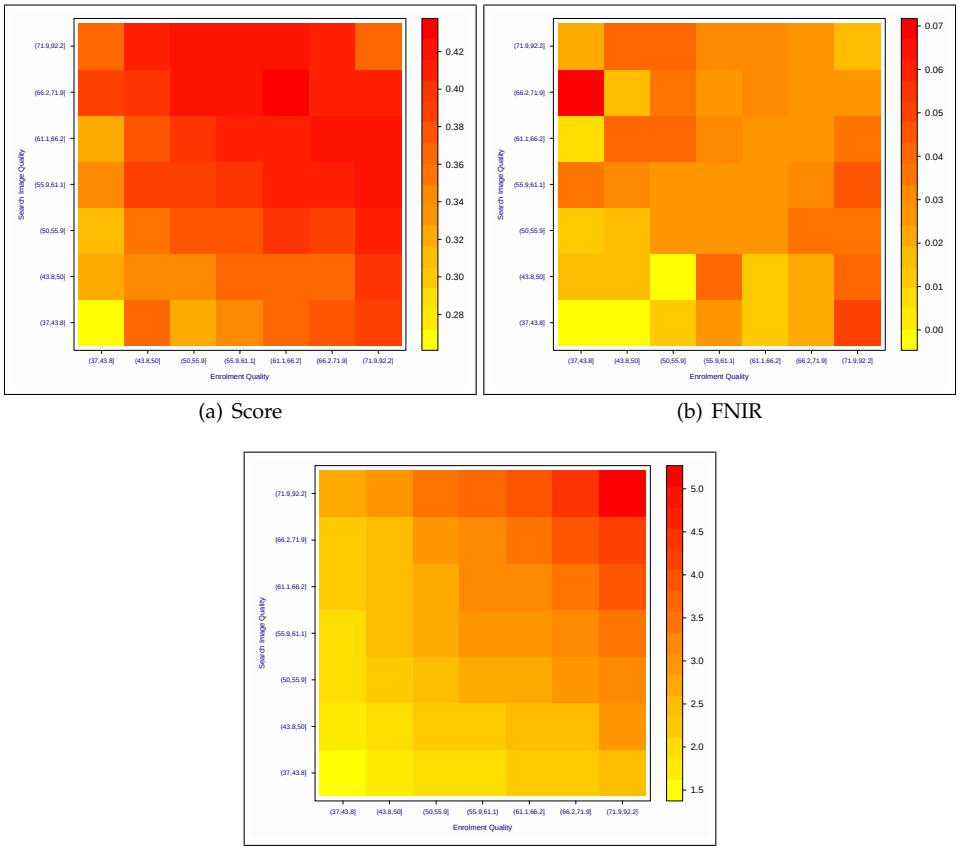

(a) Score (b) FNIR

(c) $log_{10}(1 + Count)$

Figure 494: **Effectiveness of quality assessments**: Heatmaps for implementation V12B executing mate searches in an enrolled population of N = 1600000. The quality values of the enrolled and search images are binned by their mutual $0.005, 0.01, 0.02, 0.04, 0.16, 0.32$ quantiles. From left to right, the color gives the mean reported dis-similarity score, the FNIR at FPIR = 0.0001, and the log of count of the images in each quality bin.

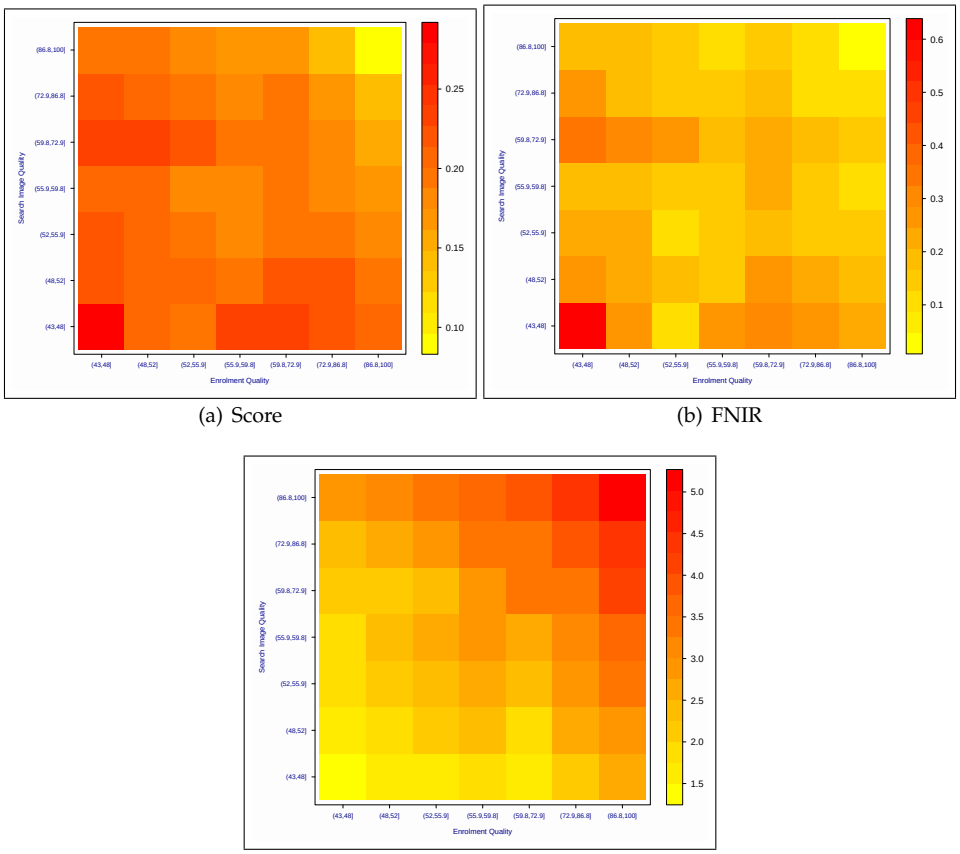

(a) Score (b) FNIR

(c) $log_{10}(1 + Count)$

Figure 495: **Effectiveness of quality assessments**: Heatmaps for implementation W01A executing mate searches in an enrolled population of N = 1600000. The quality values of the enrolled and search images are binned by their mutual $0.005, 0.01, 0.02, 0.04, 0.16, 0.32$ quantiles. From left to right, the color gives the mean reported dis-similarity score, the FNIR at FPIR = 0.0001, and the log of count of the images in each quality bin.

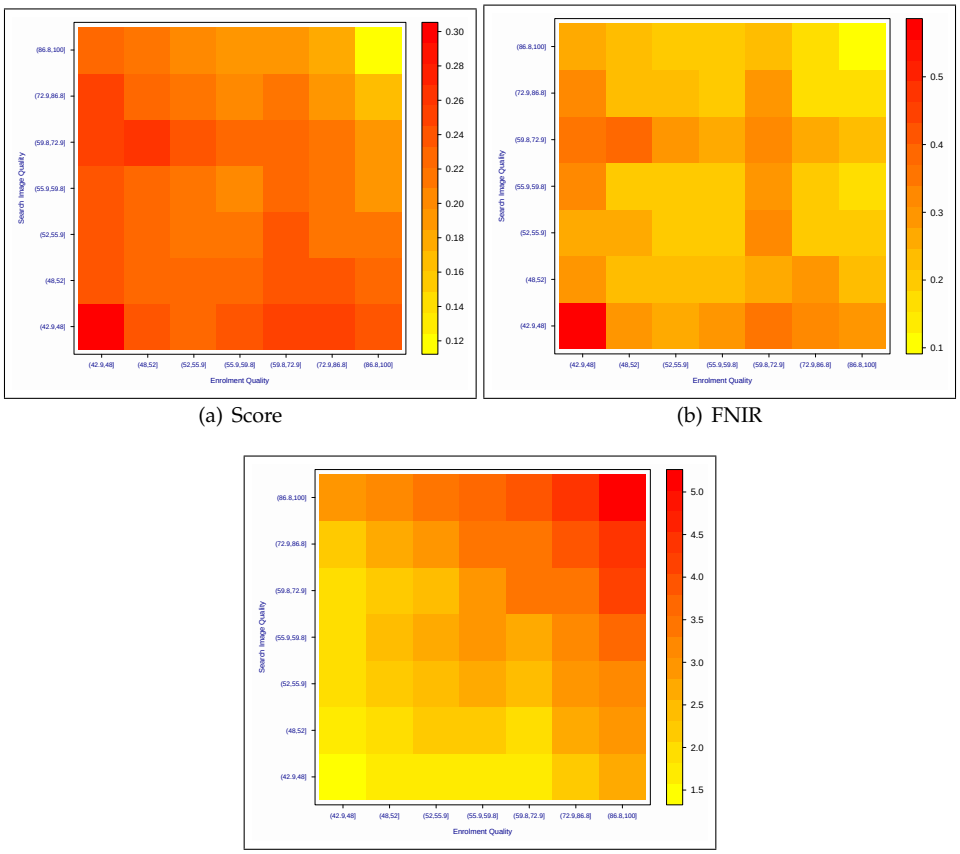

(a) Score (b) FNIR

(c) $log_{10}(1 + Count)$

Figure 496: **Effectiveness of quality assessments**: Heatmaps for implementation W01B executing mate searches in an enrolled population of N = 1600000. The quality values of the enrolled and search images are binned by their mutual $0.005, 0.01, 0.02, 0.04, 0.16, 0.32$ quantiles. From left to right, the color gives the mean reported dis-similarity score, the FNIR at FPIR = 0.0001, and the log of count of the images in each quality bin.

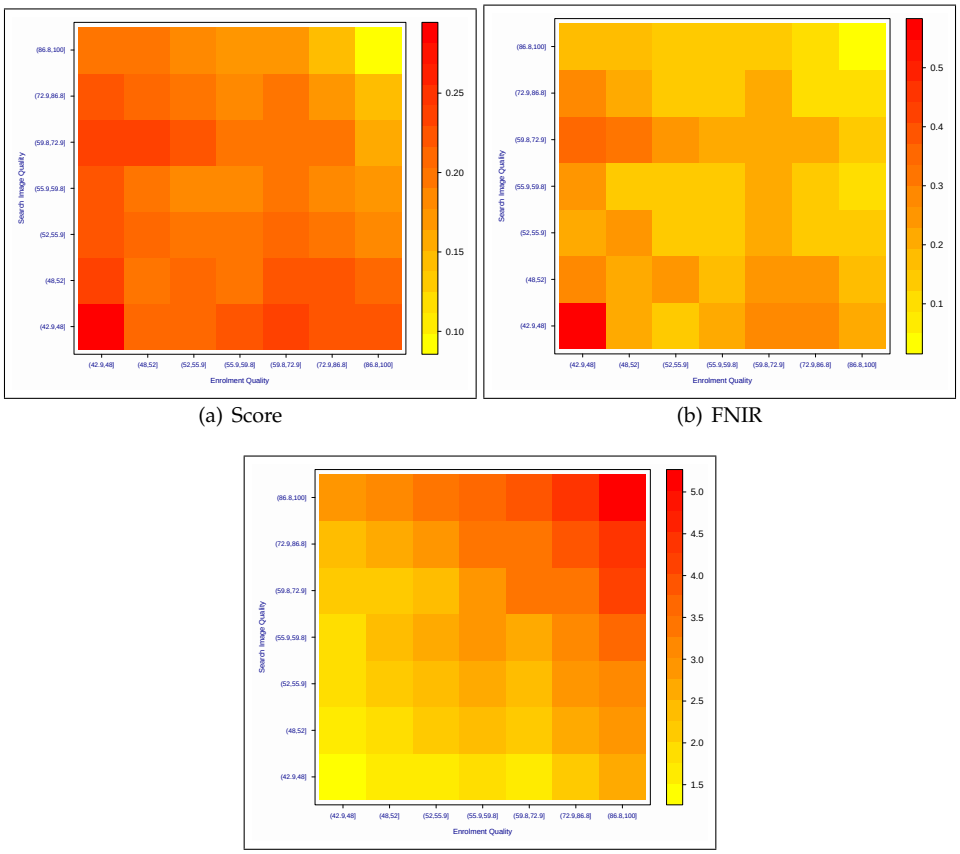

(a) Score (b) FNIR

(c) $log_{10}(1 + Count)$

Figure 497: **Effectiveness of quality assessments**: Heatmaps for implementation W02A executing mate searches in an enrolled population of N = 1600000. The quality values of the enrolled and search images are binned by their mutual $0.005, 0.01, 0.02, 0.04, 0.16, 0.32$ quantiles. From left to right, the color gives the mean reported dis-similarity score, the FNIR at FPIR = 0.0001, and the log of count of the images in each quality bin.

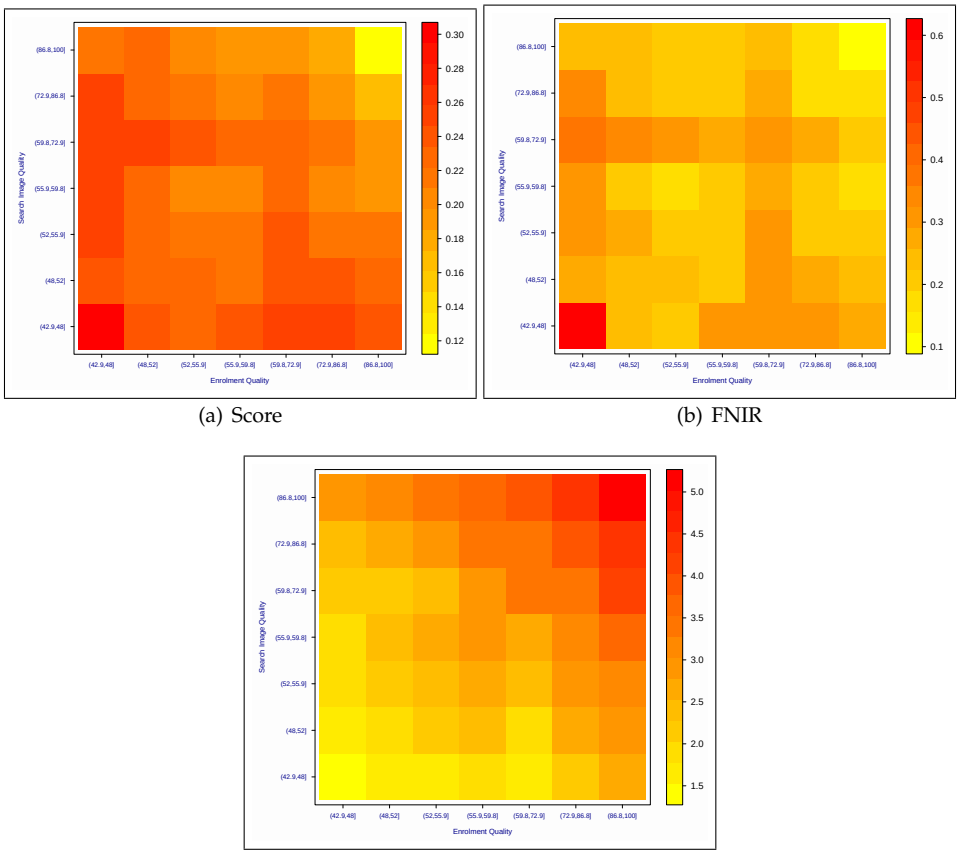

(a) Score (b) FNIR

(c) $log_{10}(1 + Count)$

Figure 498: **Effectiveness of quality assessments**: Heatmaps for implementation W02B executing mate searches in an enrolled population of N = 1600000. The quality values of the enrolled and search images are binned by their mutual $0.005, 0.01, 0.02, 0.04, 0.16, 0.32$ quantiles. From left to right, the color gives the mean reported dis-similarity score, the FNIR at FPIR = 0.0001, and the log of count of the images in each quality bin.

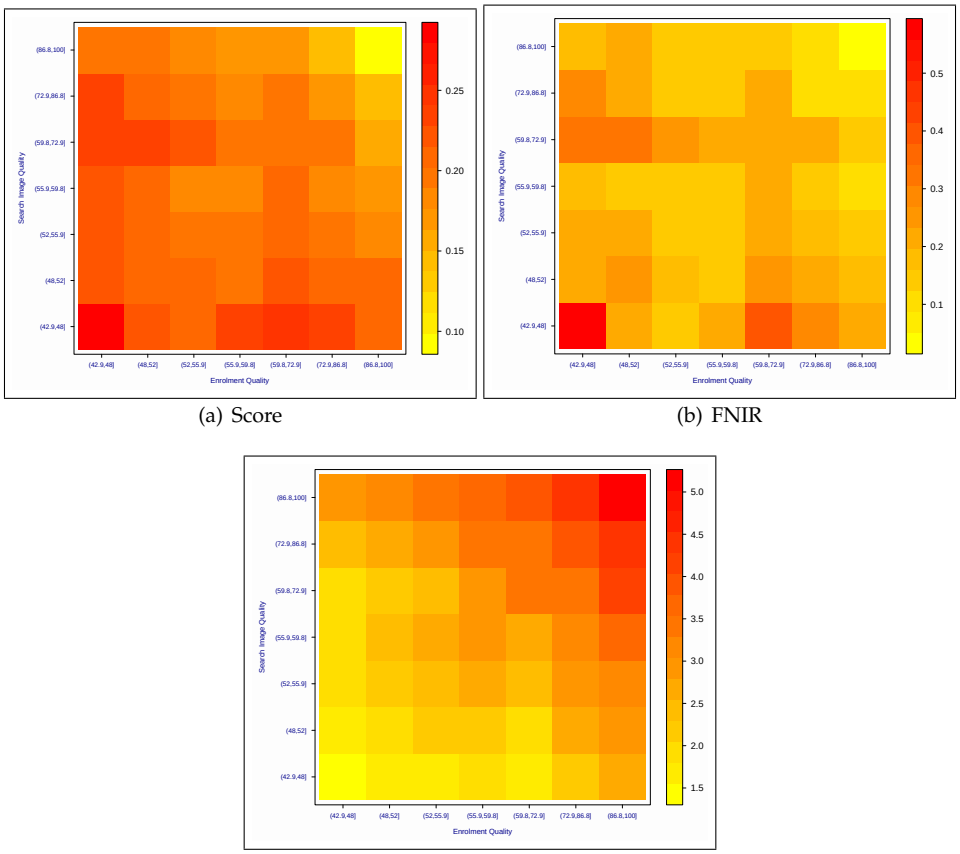

(a) Score (b) FNIR

(c) $log_{10}(1 + Count)$

Figure 499: **Effectiveness of quality assessments**: Heatmaps for implementation W03A executing mate searches in an enrolled population of N = 1600000. The quality values of the enrolled and search images are binned by their mutual $0.005, 0.01, 0.02, 0.04, 0.16, 0.32$ quantiles. From left to right, the color gives the mean reported dis-similarity score, the FNIR at FPIR = 0.0001, and the log of count of the images in each quality bin.

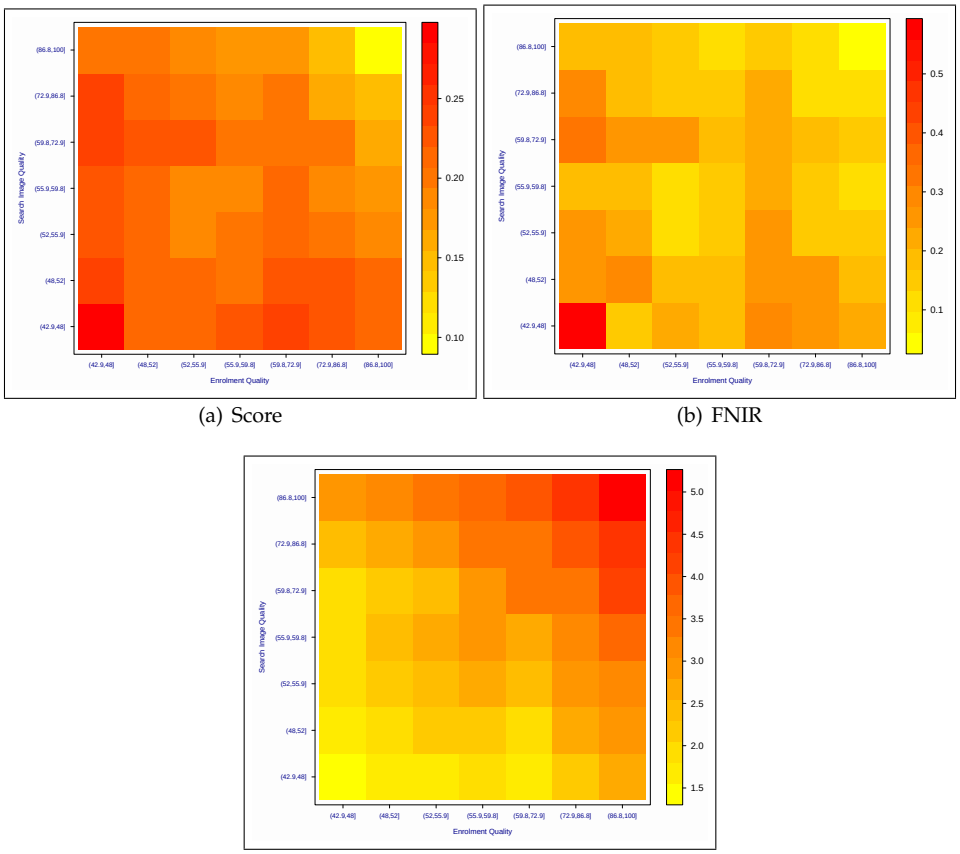

(a) Score (b) FNIR

(c) $log_{10}(1 + Count)$

Figure 500: **Effectiveness of quality assessments**: Heatmaps for implementation W04A executing mate searches in an enrolled population of N = 1600000. The quality values of the enrolled and search images are binned by their mutual $0.005, 0.01, 0.02, 0.04, 0.16, 0.32$ quantiles. From left to right, the color gives the mean reported dis-similarity score, the FNIR at FPIR = 0.0001, and the log of count of the images in each quality bin.

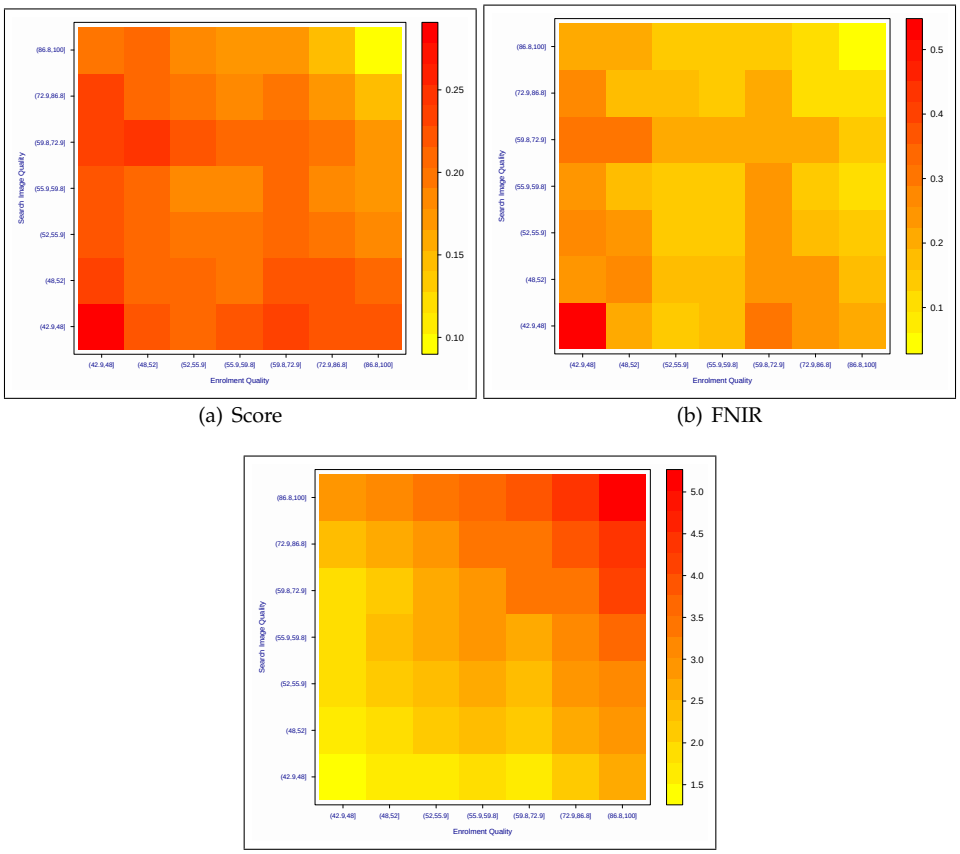

(a) Score (b) FNIR

(c) $log_{10}(1 + Count)$

Figure 501: **Effectiveness of quality assessments**: Heatmaps for implementation W05A executing mate searches in an enrolled population of N = 1600000. The quality values of the enrolled and search images are binned by their mutual $0.005, 0.01, 0.02, 0.04, 0.16, 0.32$ quantiles. From left to right, the color gives the mean reported dis-similarity score, the FNIR at FPIR = 0.0001, and the log of count of the images in each quality bin.

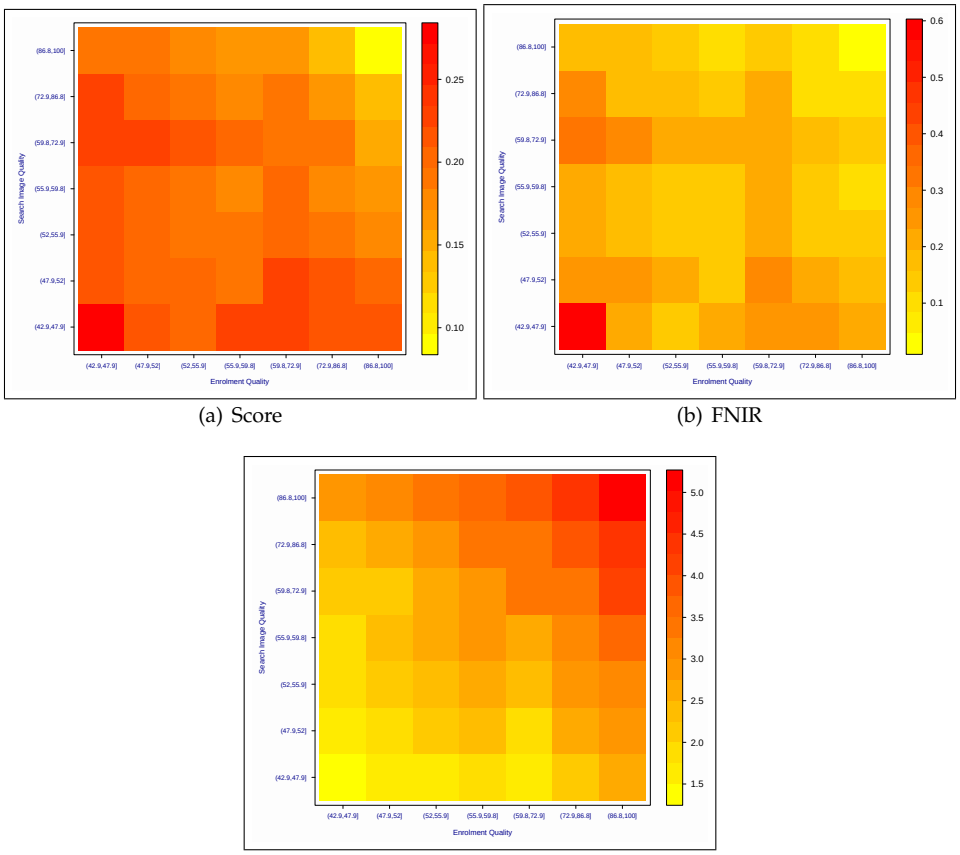

(a) Score (b) FNIR

(c) $log_{10}(1 + Count)$

Figure 502: **Effectiveness of quality assessments**: Heatmaps for implementation W11A executing mate searches in an enrolled population of N = 1600000. The quality values of the enrolled and search images are binned by their mutual $0.005, 0.01, 0.02, 0.04, 0.16, 0.32$ quantiles. From left to right, the color gives the mean reported dis-similarity score, the FNIR at FPIR = 0.0001, and the log of count of the images in each quality bin.

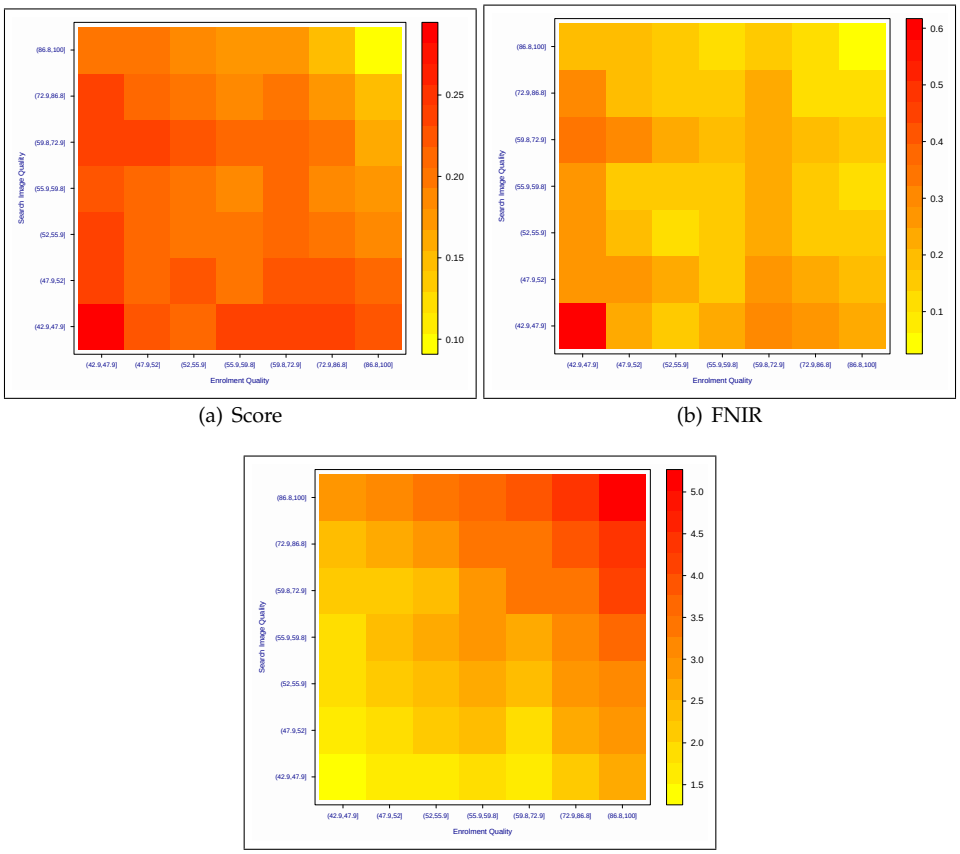

(a) Score (b) FNIR

(c) $log_{10}(1 + Count)$

Figure 503: **Effectiveness of quality assessments**: Heatmaps for implementation W11B executing mate searches in an enrolled population of N = 1600000. The quality values of the enrolled and search images are binned by their mutual $0.005, 0.01, 0.02, 0.04, 0.16, 0.32$ quantiles. From left to right, the color gives the mean reported dis-similarity score, the FNIR at FPIR = 0.0001, and the log of count of the images in each quality bin.

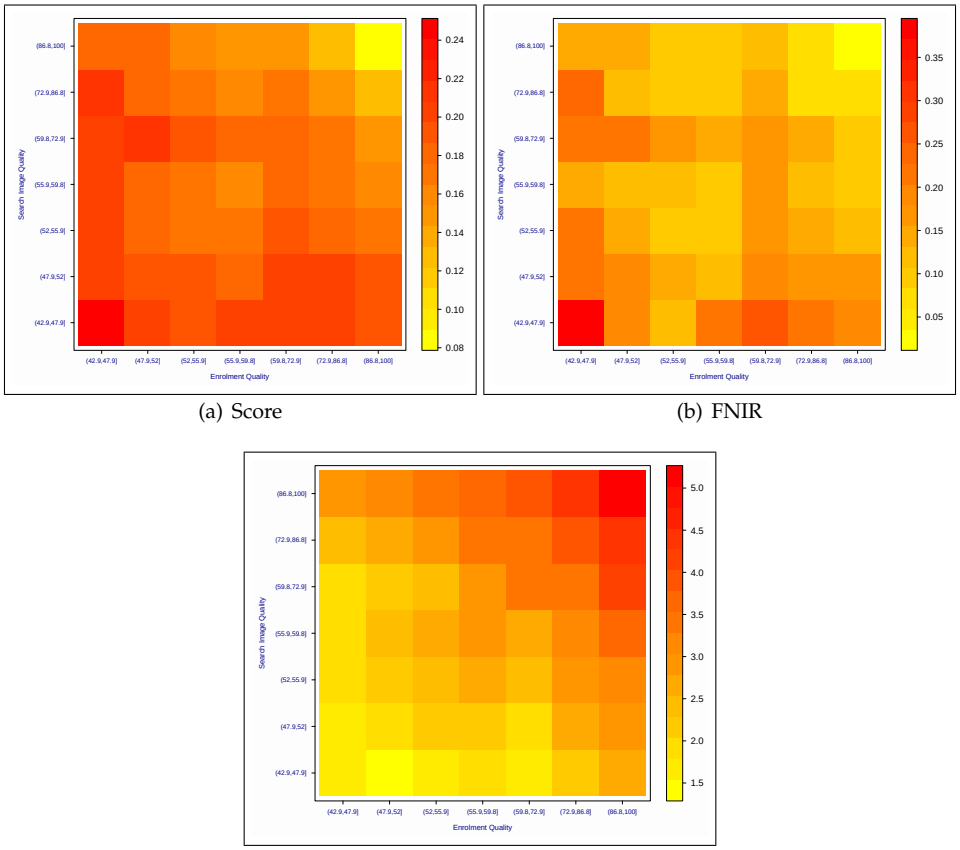

(a) Score (b) FNIR

(c) $log_{10}(1 + Count)$

Figure 504: **Effectiveness of quality assessments**: Heatmaps for implementation W12A executing mate searches in an enrolled population of N = 1600000. The quality values of the enrolled and search images are binned by their mutual $0.005, 0.01, 0.02, 0.04, 0.16, 0.32$ quantiles. From left to right, the color gives the mean reported dis-similarity score, the FNIR at FPIR = 0.0001, and the log of count of the images in each quality bin.

Appendix H: Effect of Image Size

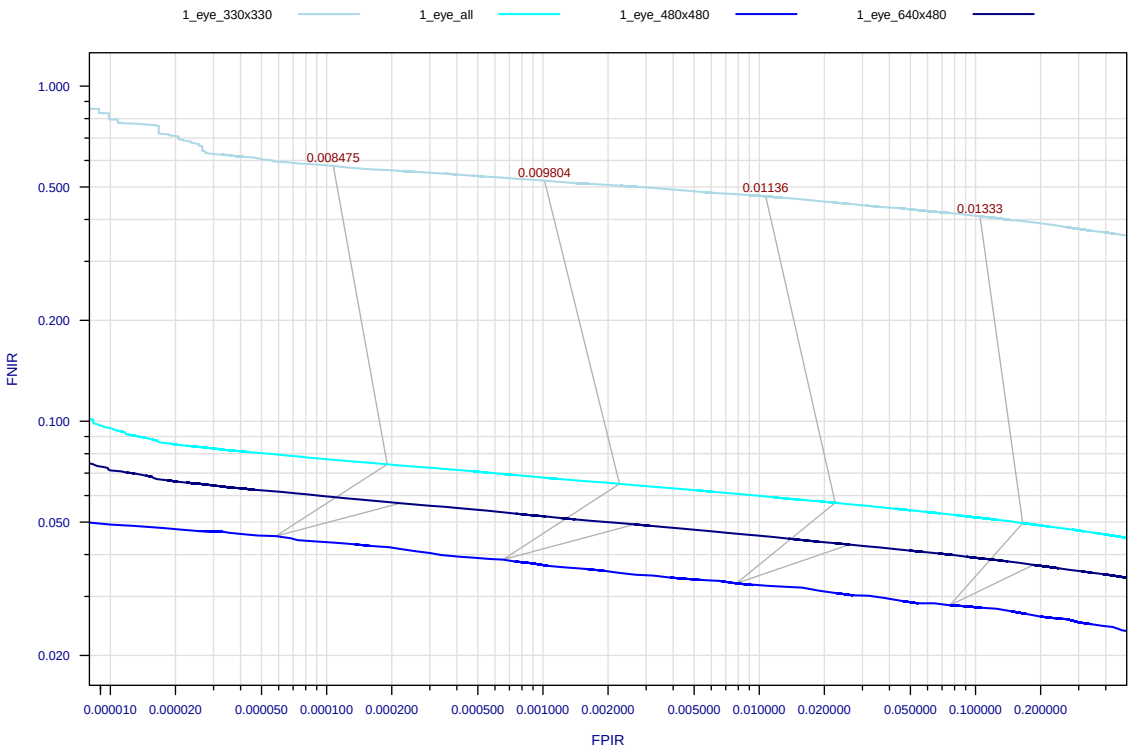

(a) Large search set, $\mathcal{S}_{nb}$

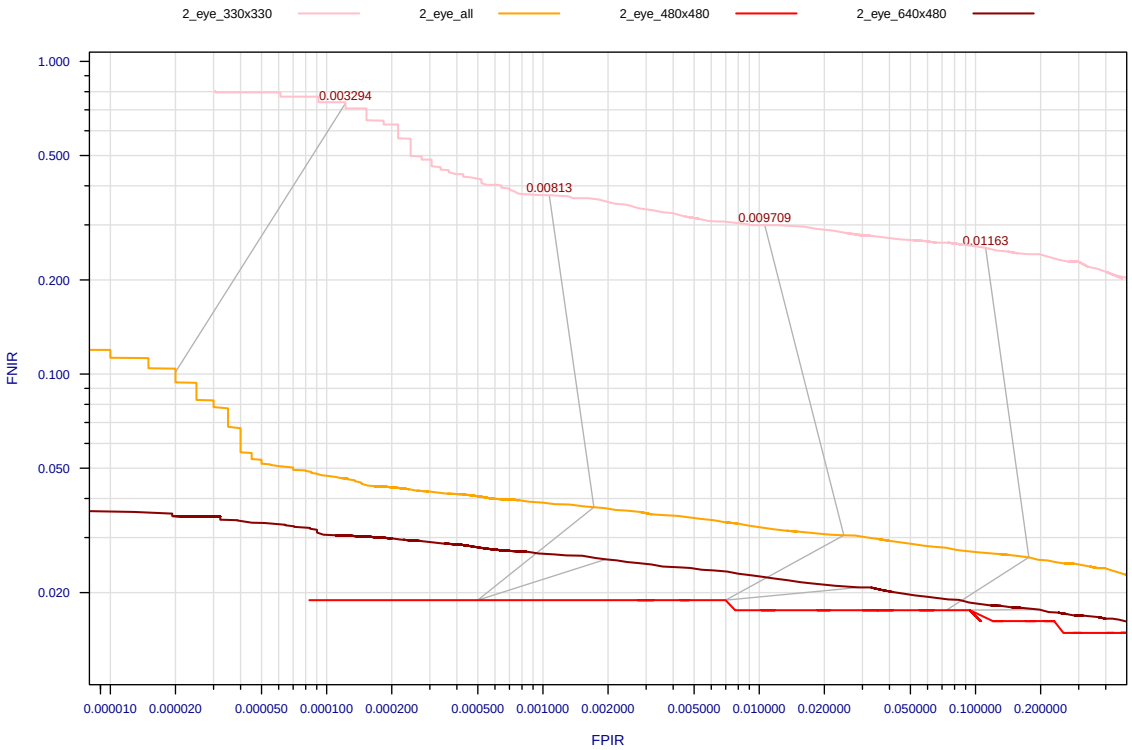

(b) Small search set, $\mathcal{S}_{na}$

Figure 505: DET for implementation N02A executing searches in an enrolled population of N = 1.6 million, broken out for three different image sizes (corresponding broadly to three camera plus ancillary software combinations) of the search image. The acquisition system used for the enrollment image (if any) is ignored in this breakout. Results for single-eye and two-eyes are plotted with two families of color. The straight lines, which link points of constant threshold, show how the two error rates would vary if a fixed threshold were adopted operationally.

FNIR = FALSE NEGATIVE IDENT. RATE FPIR = FALSE POSITIVE IDENT. RATE	N = NEUROTECHNOLOGY U = L1	P = SMU V = MORPHO	Q = IRITECH W = IRISID	R = COGENT X = CROSSMATCH	S = SMARTSENSORS Y = KYNEN	T = CAMBRIDGE

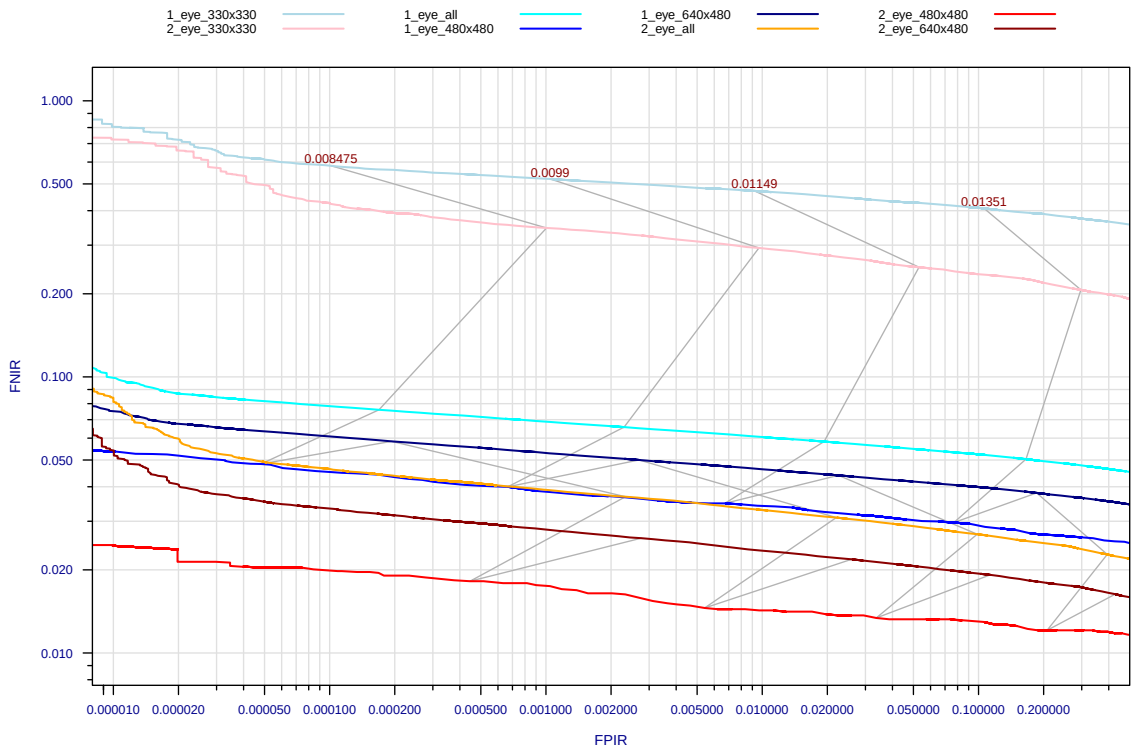

(a) Large search set, $\mathcal{S}_{nb}$

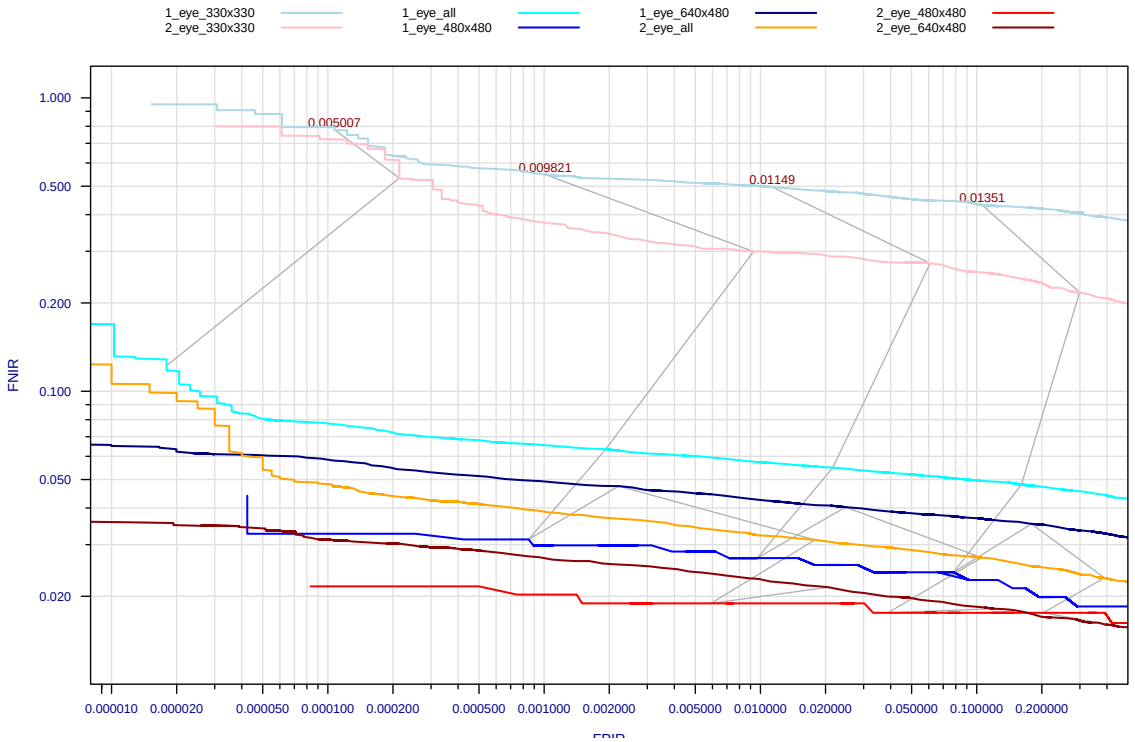

(b) Small search set, $\mathcal{S}_{na}$

Figure 506: DET for implementation N02B executing searches in an enrolled population of N = 1.6 million, broken out for three different image sizes (corresponding broadly to three camera plus ancillary software combinations) of the search image. The acquisition system used for the enrollment image (if any) is ignored in this breakout. Results for single-eye and two-eyes are plotted with two families of color. The straight lines, which link points of constant threshold, show how the two error rates would vary if a fixed threshold were adopted operationally.

FNIR = FALSE NEGATIVE IDENT. RATE FPIR = FALSE POSITIVE IDENT. RATE	N = NEUROTECHNOLOGY U = L1	P = SMU V = MORPHO	Q = IRITECH W = IRISID	R = COGENT X = CROSSMATCH	S = SMARTSENSORS Y = KYNEN	T = CAMBRIDGE

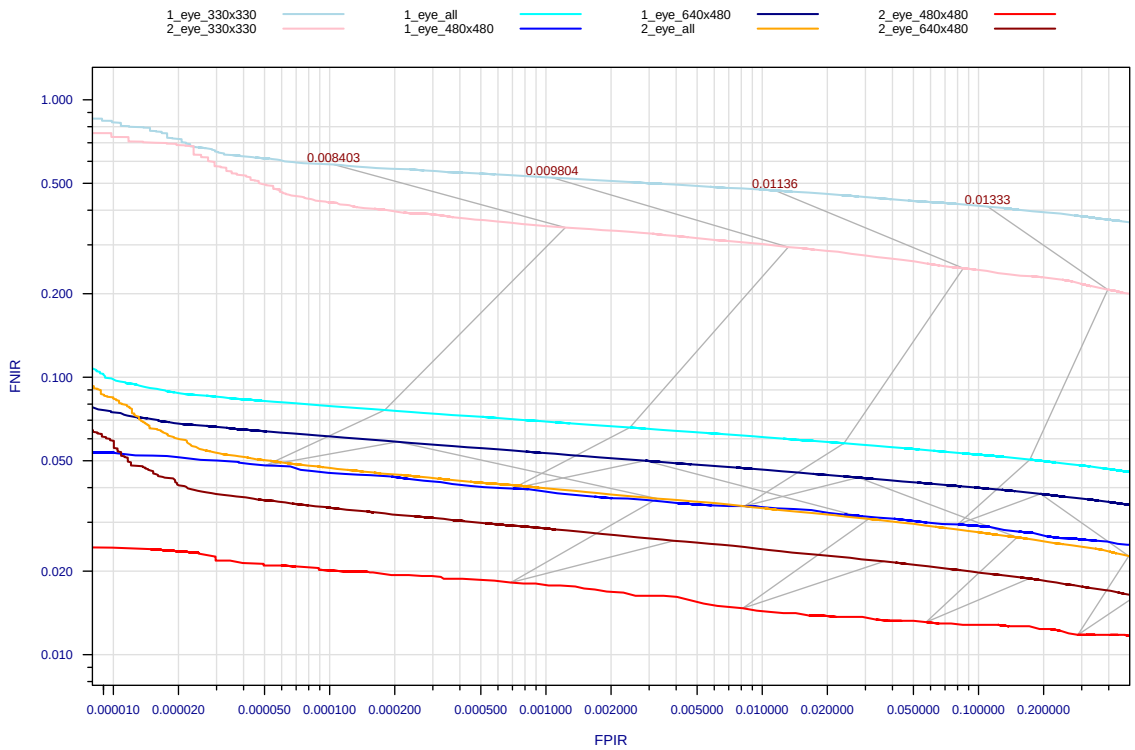

(a) Large search set, $\mathcal{S}_{nb}$

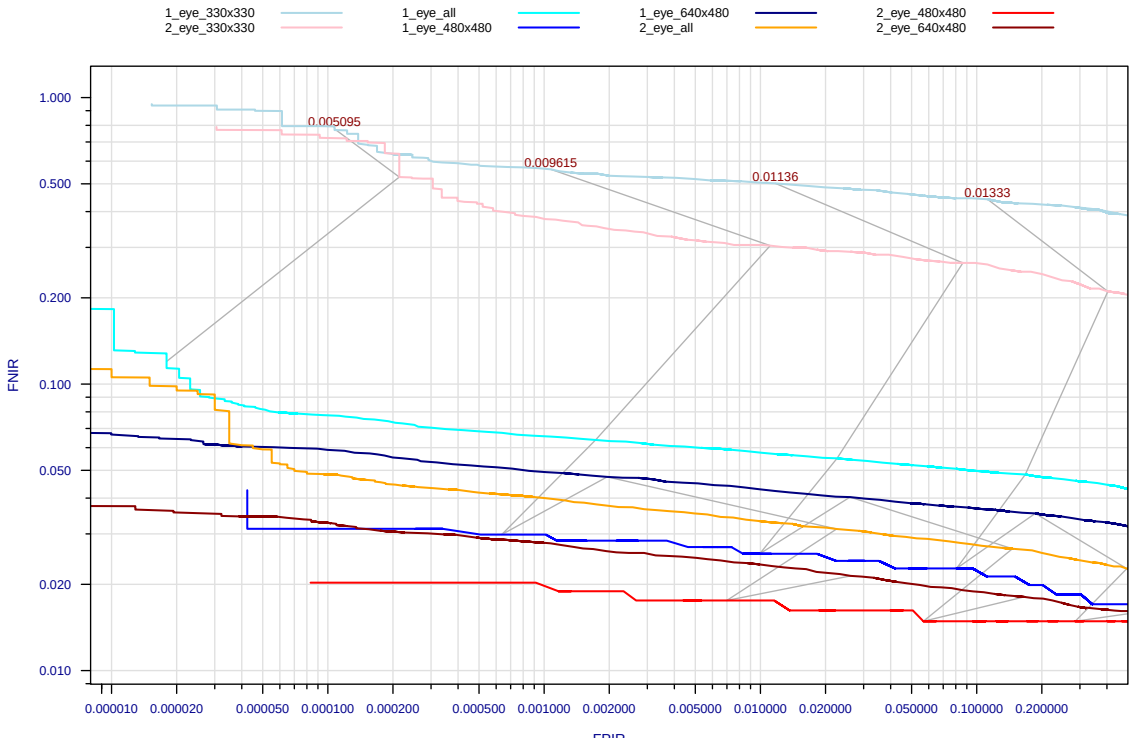

(b) Small search set, $\mathcal{S}_{na}$

Figure 507: DET for implementation N03A executing searches in an enrolled population of N = 1.6 million, broken out for three different image sizes (corresponding broadly to three camera plus ancillary software combinations) of the search image. The acquisition system used for the enrollment image (if any) is ignored in this breakout. Results for single-eye and two-eyes are plotted with two families of color. The straight lines, which link points of constant threshold, show how the two error rates would vary if a fixed threshold were adopted operationally.

FNIR = FALSE NEGATIVE IDENT. RATE FPIR = FALSE POSITIVE IDENT. RATE	N = NEUROTECHNOLOGY U = L1	P = SMU V = MORPHO	Q = IRITECH W = IRISID	R = COGENT X = CROSSMATCH	S = SMARTSENSORS Y = KYNEN	T = CAMBRIDGE

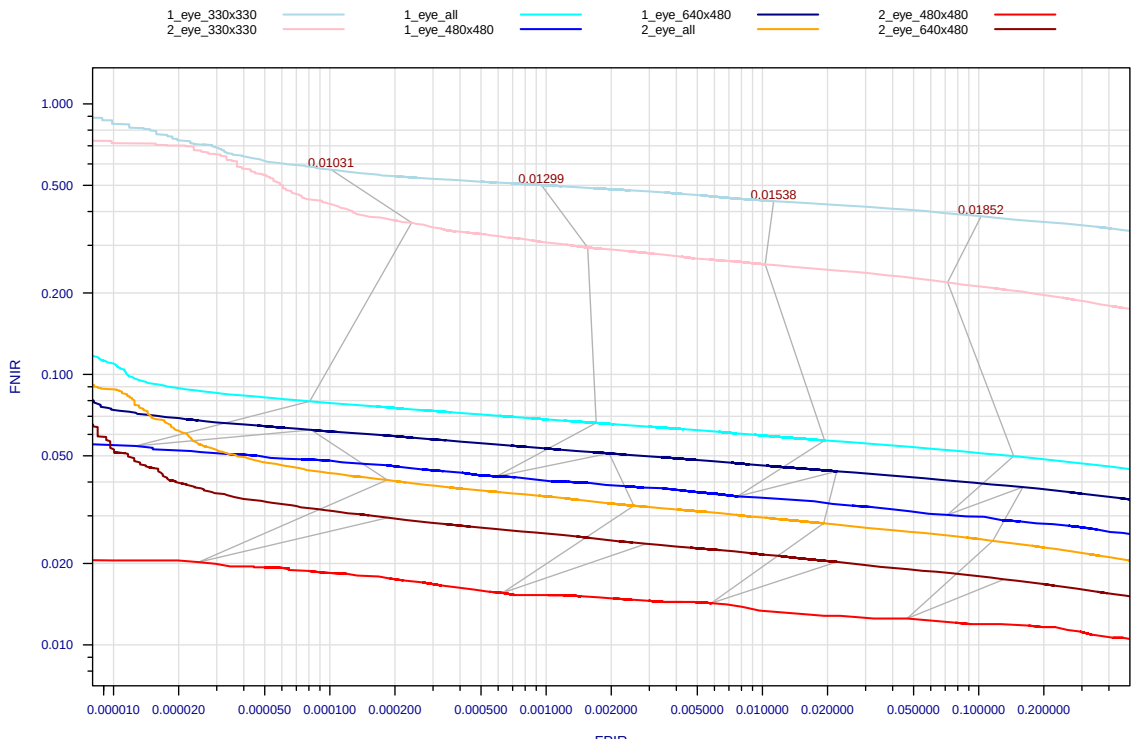

(a) Large search set, $\mathcal{S}_{nb}$

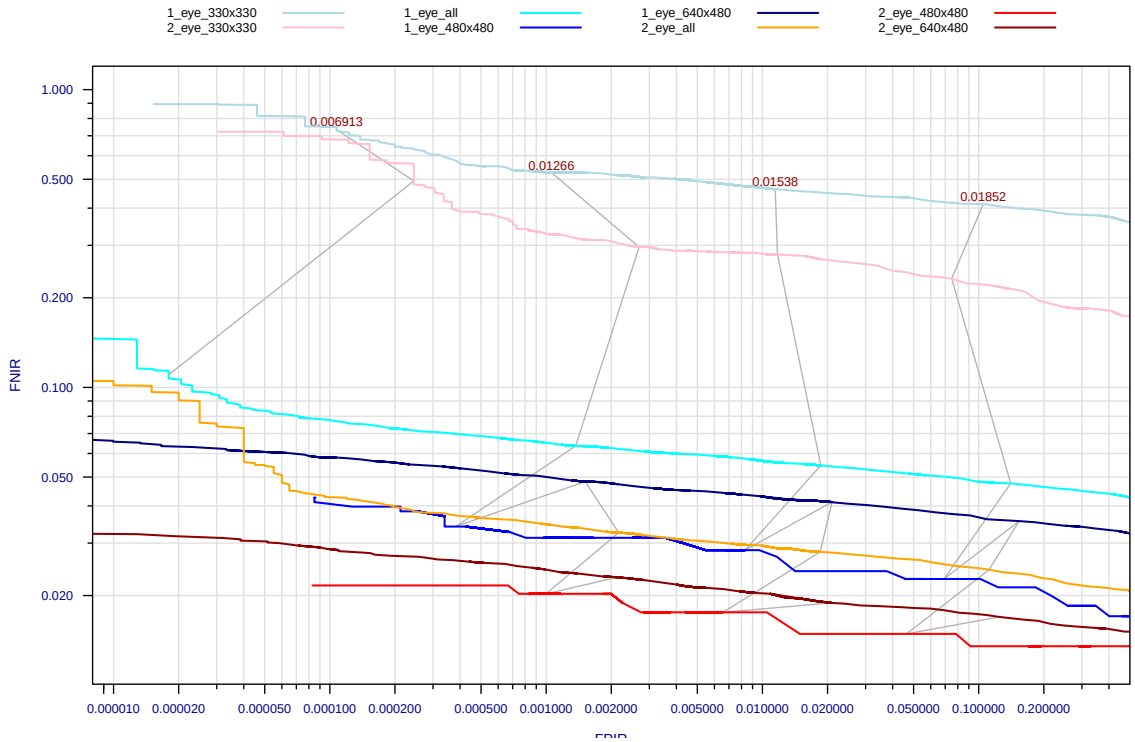

(b) Small search set, $\mathcal{S}_{na}$

Figure 508: DET for implementation N03B executing searches in an enrolled population of N = 1.6 million, broken out for three different image sizes (corresponding broadly to three camera plus ancillary software combinations) of the search image. The acquisition system used for the enrollment image (if any) is ignored in this breakout. Results for single-eye and two-eyes are plotted with two families of color. The straight lines, which link points of constant threshold, show how the two error rates would vary if a fixed threshold were adopted operationally.

FNIR = FALSE NEGATIVE IDENT. RATE FPIR = FALSE POSITIVE IDENT. RATE	N = NEUROTECHNOLOGY U = L1	P = SMU V = MORPHO	Q = IRITECH W = IRISID	R = COGENT X = CROSSMATCH	S = SMARTSENSORS Y = KYNEN	T = CAMBRIDGE

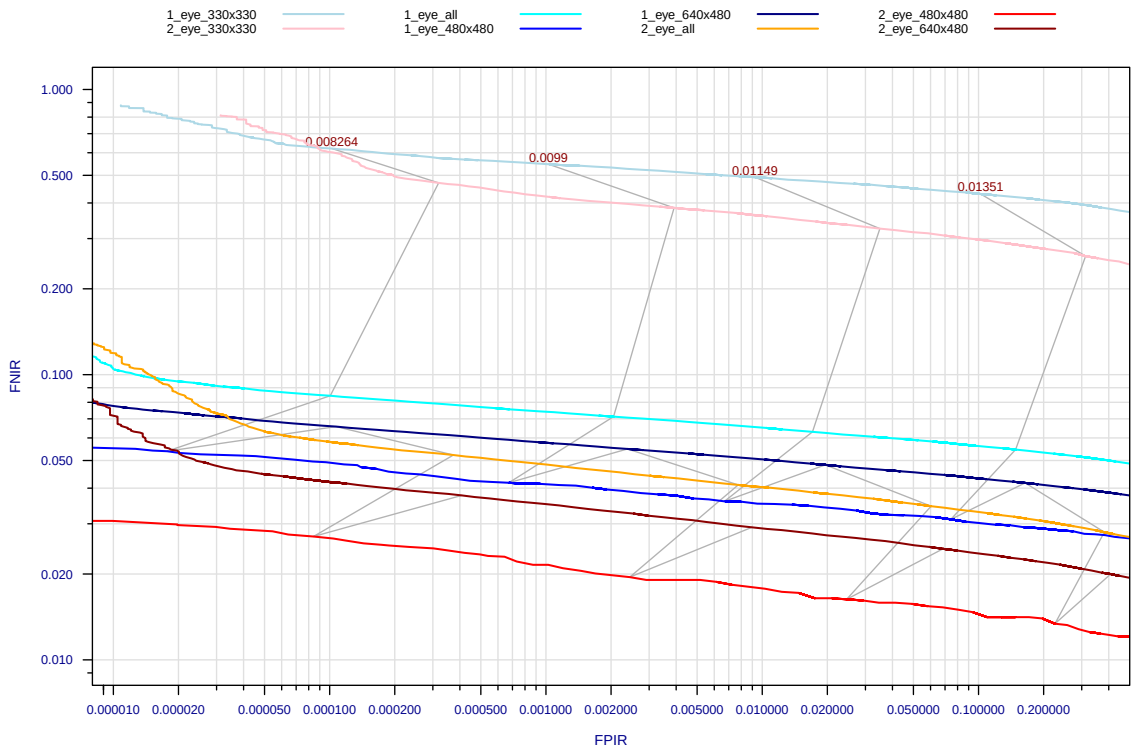

(a) Large search set, $\mathcal{S}_{nb}$

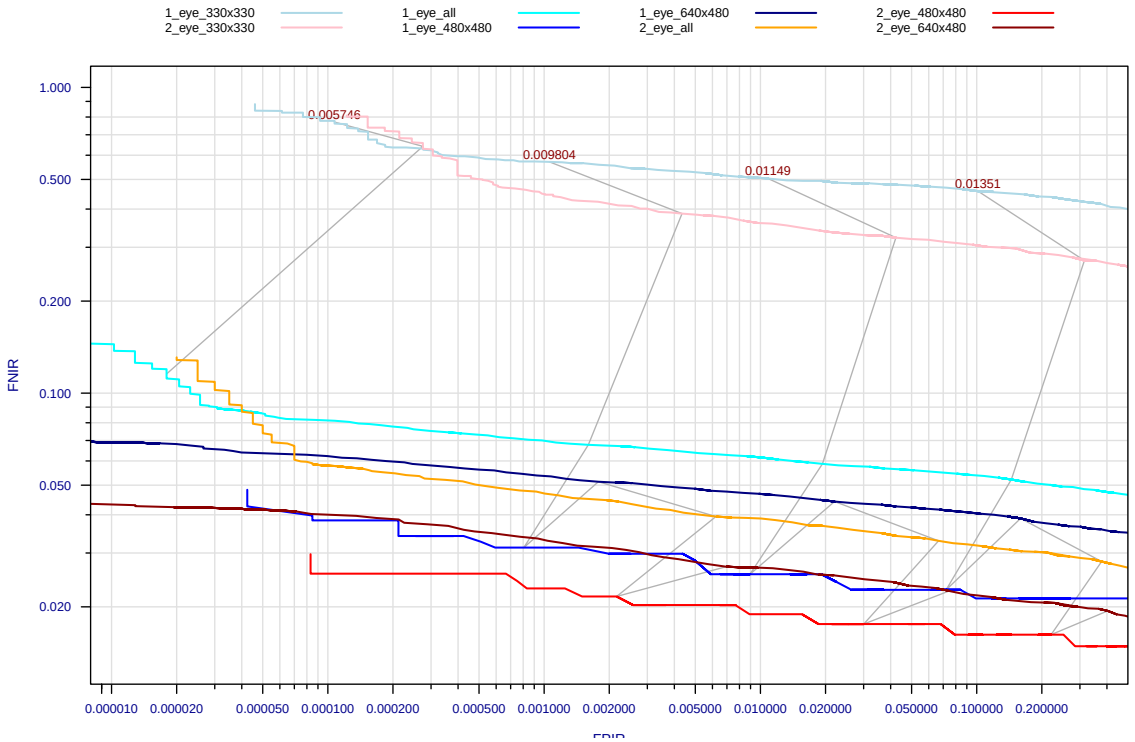

(b) Small search set, $\mathcal{S}_{na}$

Figure 509: DET for implementation N04A executing searches in an enrolled population of N = 1.6 million, broken out for three different image sizes (corresponding broadly to three camera plus ancillary software combinations) of the search image. The acquisition system used for the enrollment image (if any) is ignored in this breakout. Results for single-eye and two-eyes are plotted with two families of color. The straight lines, which link points of constant threshold, show how the two error rates would vary if a fixed threshold were adopted operationally.

FNIR = FALSE NEGATIVE IDENT. RATE FPIR = FALSE POSITIVE IDENT. RATE	N = NEUROTECHNOLOGY U = L1	P = SMU V = MORPHO	Q = IRITECH W = IRISID	R = COGENT X = CROSSMATCH	S = SMARTSENSORS Y = KYNEN	T = CAMBRIDGE

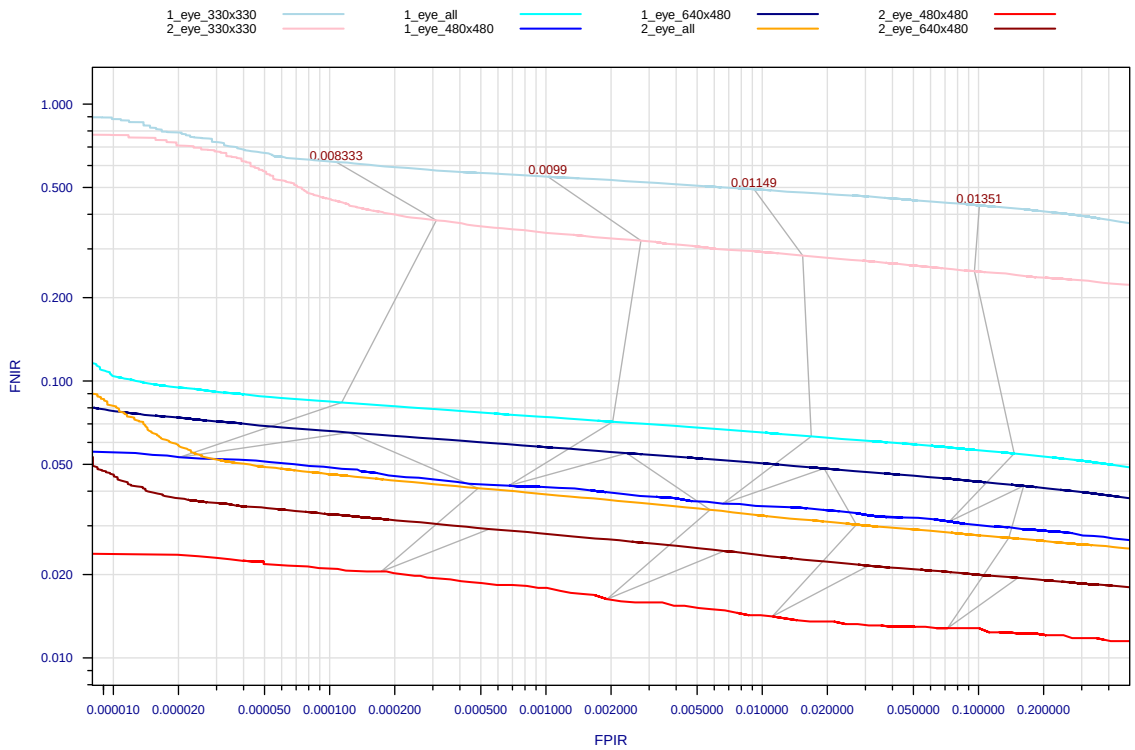

(a) Large search set, $\mathcal{S}_{nb}$

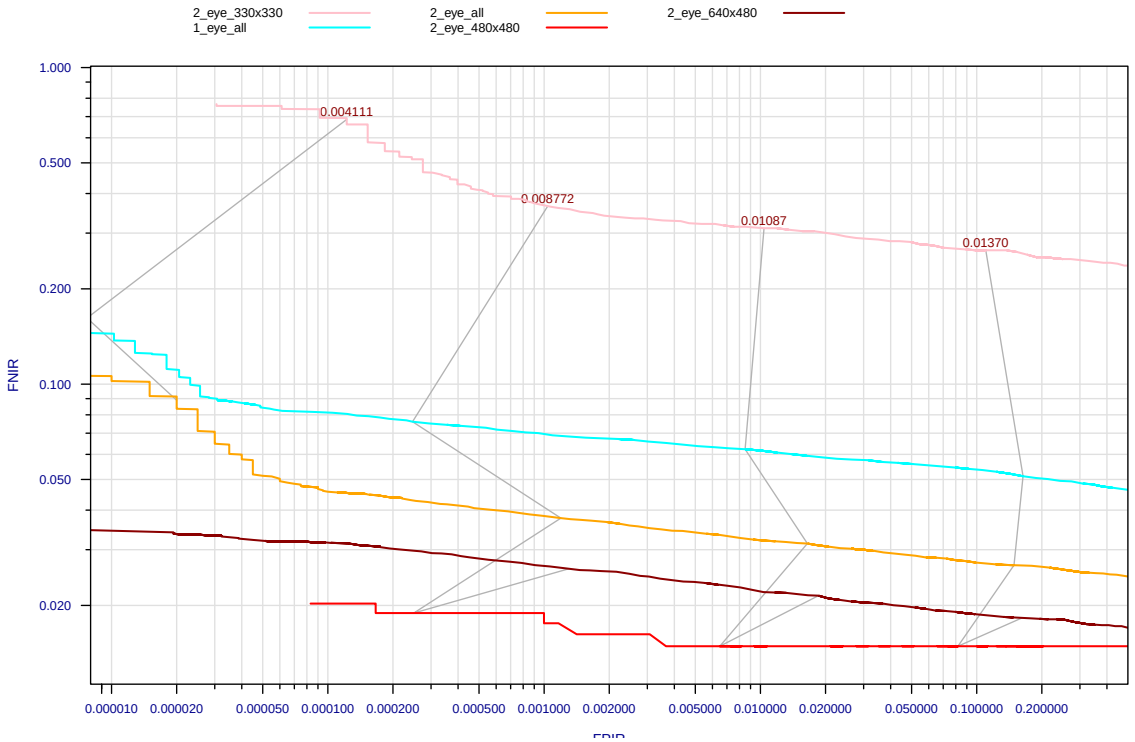

(b) Small search set, $\mathcal{S}_{na}$

Figure 510: DET for implementation N11A executing searches in an enrolled population of N = 1.6 million, broken out for three different image sizes (corresponding broadly to three camera plus ancillary software combinations) of the search image. The acquisition system used for the enrollment image (if any) is ignored in this breakout. Results for single-eye and two-eyes are plotted with two families of color. The straight lines, which link points of constant threshold, show how the two error rates would vary if a fixed threshold were adopted operationally.

FNIR = FALSE NEGATIVE IDENT. RATE FPIR = FALSE POSITIVE IDENT. RATE	N = NEUROTECHNOLOGY U = L1	P = SMU V = MORPHO	Q = IRITECH W = IRISID	R = COGENT X = CROSSMATCH	S = SMARTSENSORS Y = KYNEN	T = CAMBRIDGE

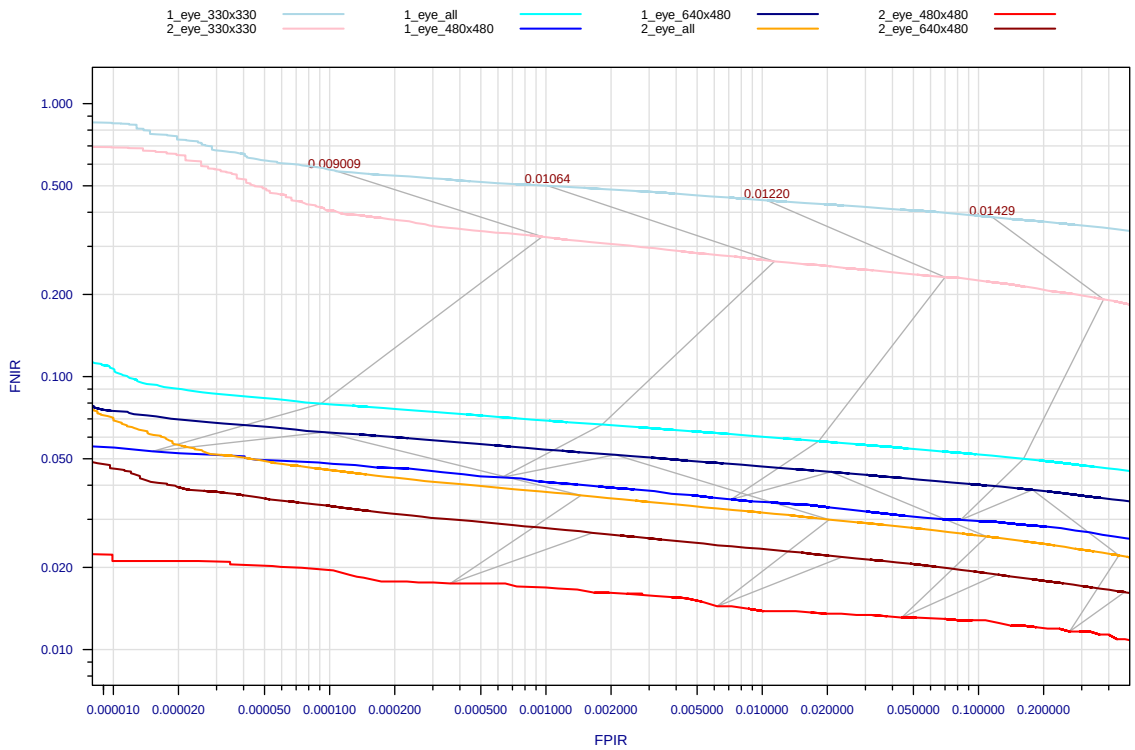

(a) Large search set, $\mathcal{S}_{nb}$

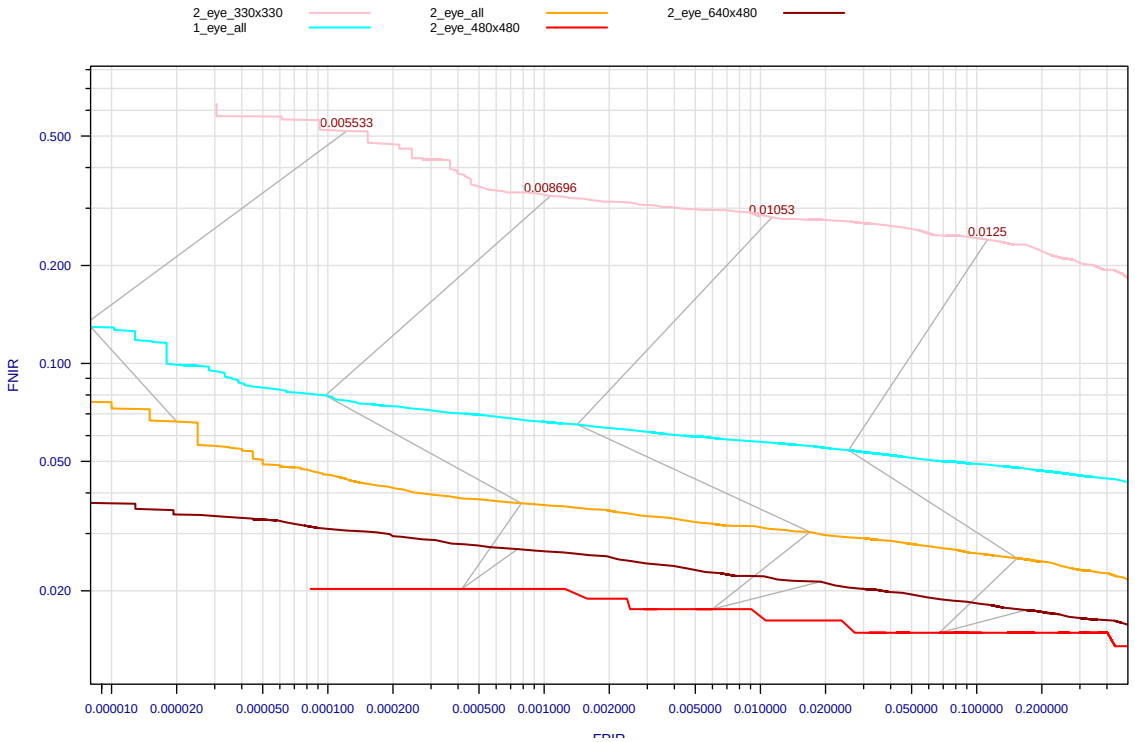

(b) Small search set, $\mathcal{S}_{na}$

Figure 511: DET for implementation N11B executing searches in an enrolled population of N = 1.6 million, broken out for three different image sizes (corresponding broadly to three camera plus ancillary software combinations) of the search image. The acquisition system used for the enrollment image (if any) is ignored in this breakout. Results for single-eye and two-eyes are plotted with two families of color. The straight lines, which link points of constant threshold, show how the two error rates would vary if a fixed threshold were adopted operationally.

FNIR = FALSE NEGATIVE IDENT. RATE FPIR = FALSE POSITIVE IDENT. RATE	N = NEUROTECHNOLOGY U = L1	P = SMU V = MORPHO	Q = IRITECH W = IRISID	R = COGENT X = CROSSMATCH	S = SMARTSENSORS Y = KYNEN	T = CAMBRIDGE

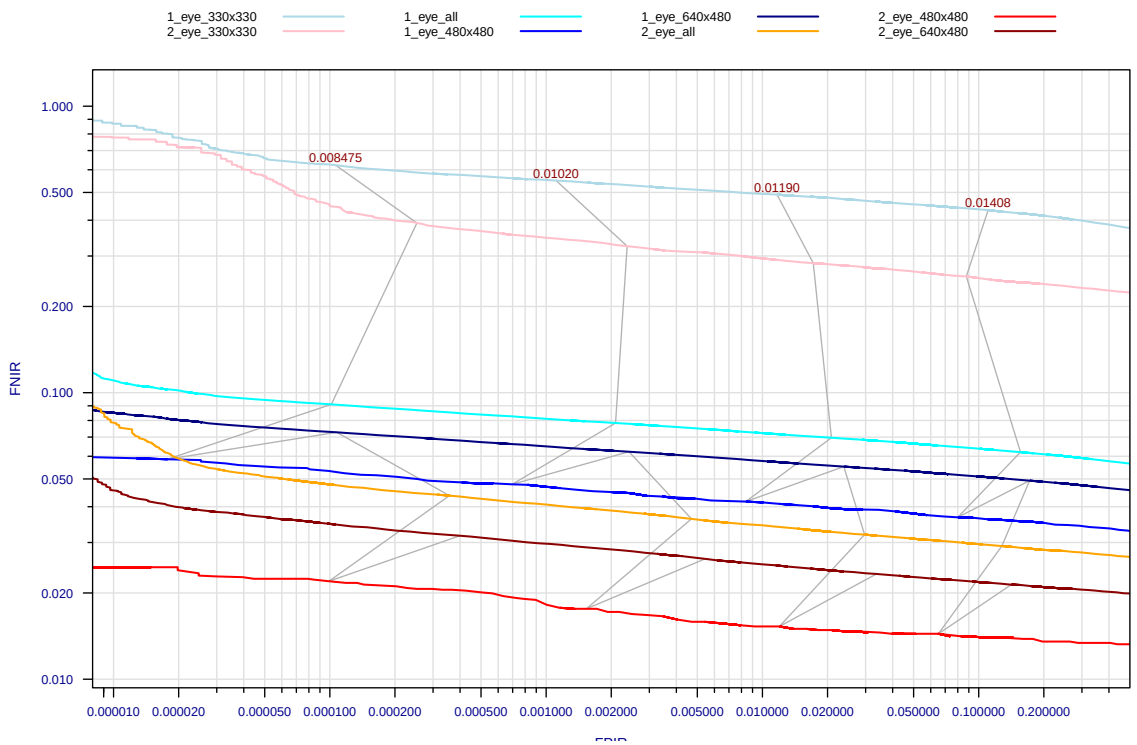

(a) Large search set, $\mathcal{S}_{nb}$

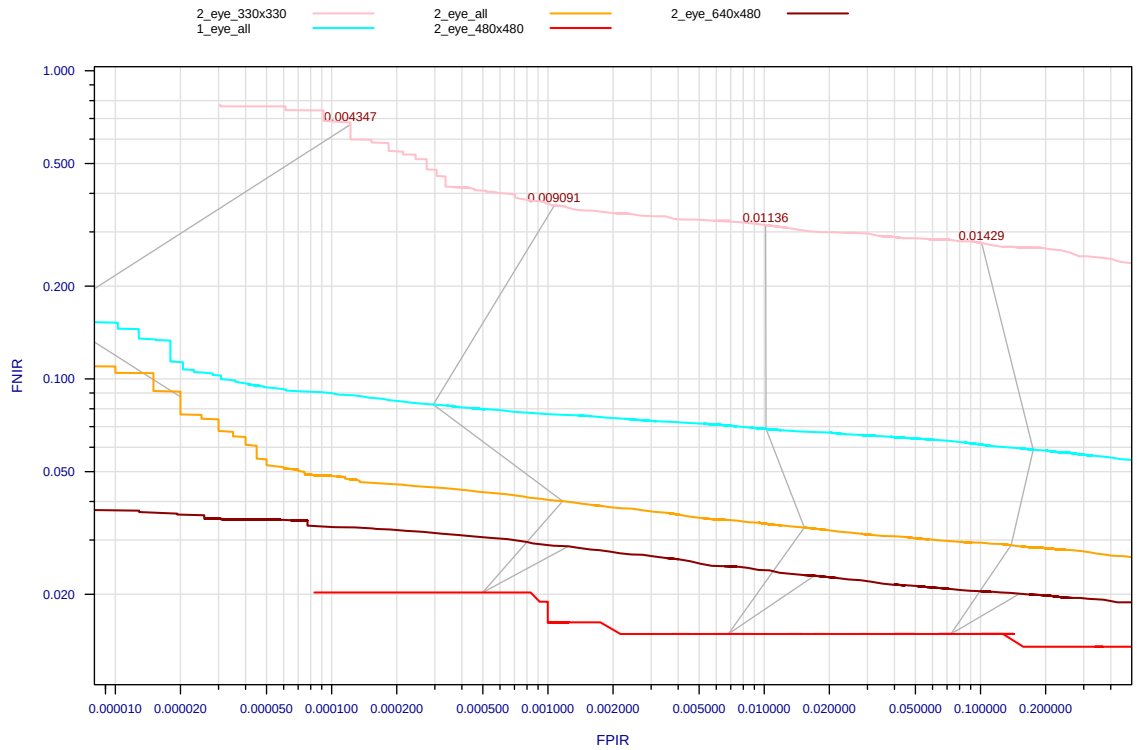

(b) Small search set, $\mathcal{S}_{na}$

Figure 512: DET for implementation N12A executing searches in an enrolled population of N = 1.6 million, broken out for three different image sizes (corresponding broadly to three camera plus ancillary software combinations) of the search image. The acquisition system used for the enrollment image (if any) is ignored in this breakout. Results for single-eye and two-eyes are plotted with two families of color. The straight lines, which link points of constant threshold, show how the two error rates would vary if a fixed threshold were adopted operationally.

FNIR = FALSE NEGATIVE IDENT. RATE FPIR = FALSE POSITIVE IDENT. RATE	N = NEUROTECHNOLOGY U = L1	P = SMU V = MORPHO	Q = IRITECH W = IRISID	R = COGENT X = CROSSMATCH	S = SMARTSENSORS Y = KYNEN	T = CAMBRIDGE

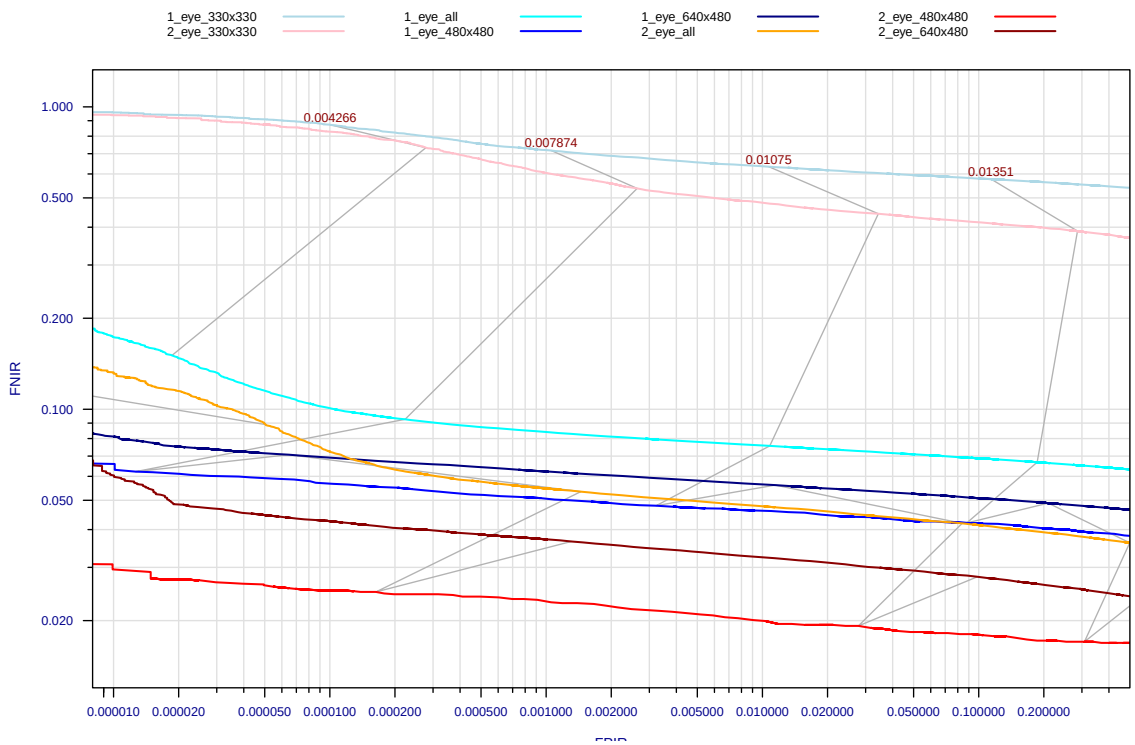

(a) Large search set, $\mathcal{S}_{nb}$

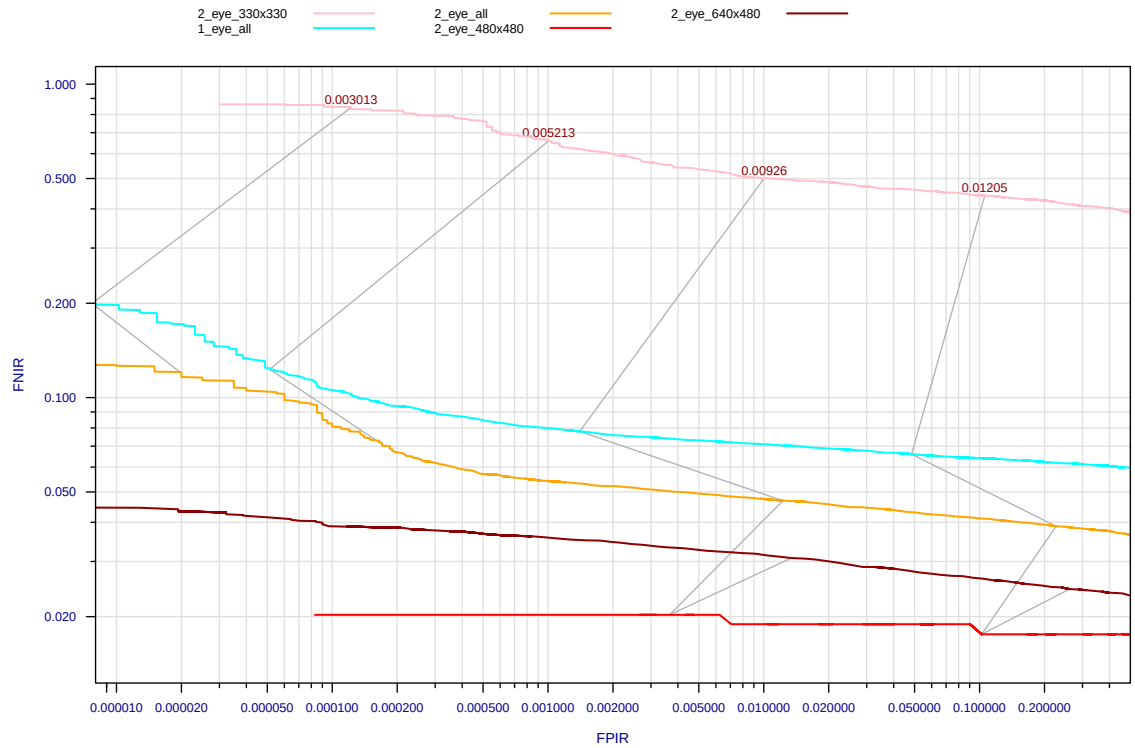

(b) Small search set, $\mathcal{S}_{na}$

Figure 513: DET for implementation N12B executing searches in an enrolled population of N = 1.6 million, broken out for three different image sizes (corresponding broadly to three camera plus ancillary software combinations) of the search image. The acquisition system used for the enrollment image (if any) is ignored in this breakout. Results for single-eye and two-eyes are plotted with two families of color. The straight lines, which link points of constant threshold, show how the two error rates would vary if a fixed threshold were adopted operationally.

FNIR = FALSE NEGATIVE IDENT. RATE FPIR = FALSE POSITIVE IDENT. RATE	N = NEUROTECHNOLOGY U = L1	P = SMU V = MORPHO	Q = IRITECH W = IRISID	R = COGENT X = CROSSMATCH	S = SMARTSENSORS Y = KYNEN	T = CAMBRIDGE

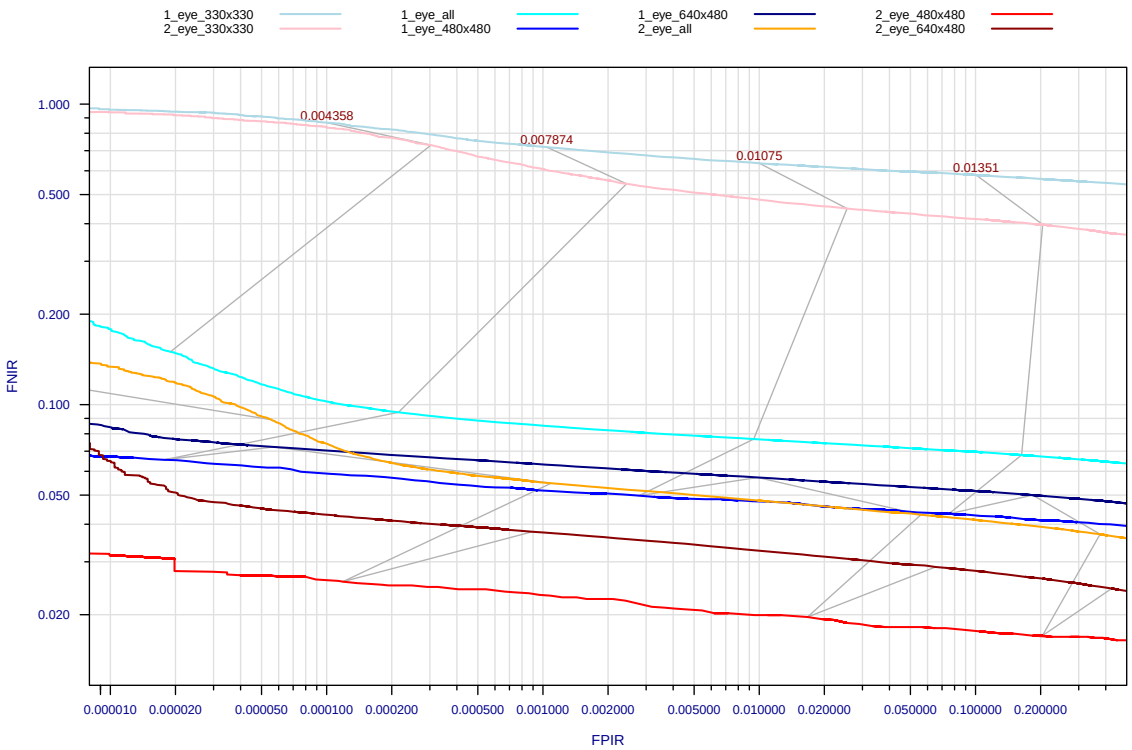

(a) Large search set, $\mathcal{S}_{nb}$

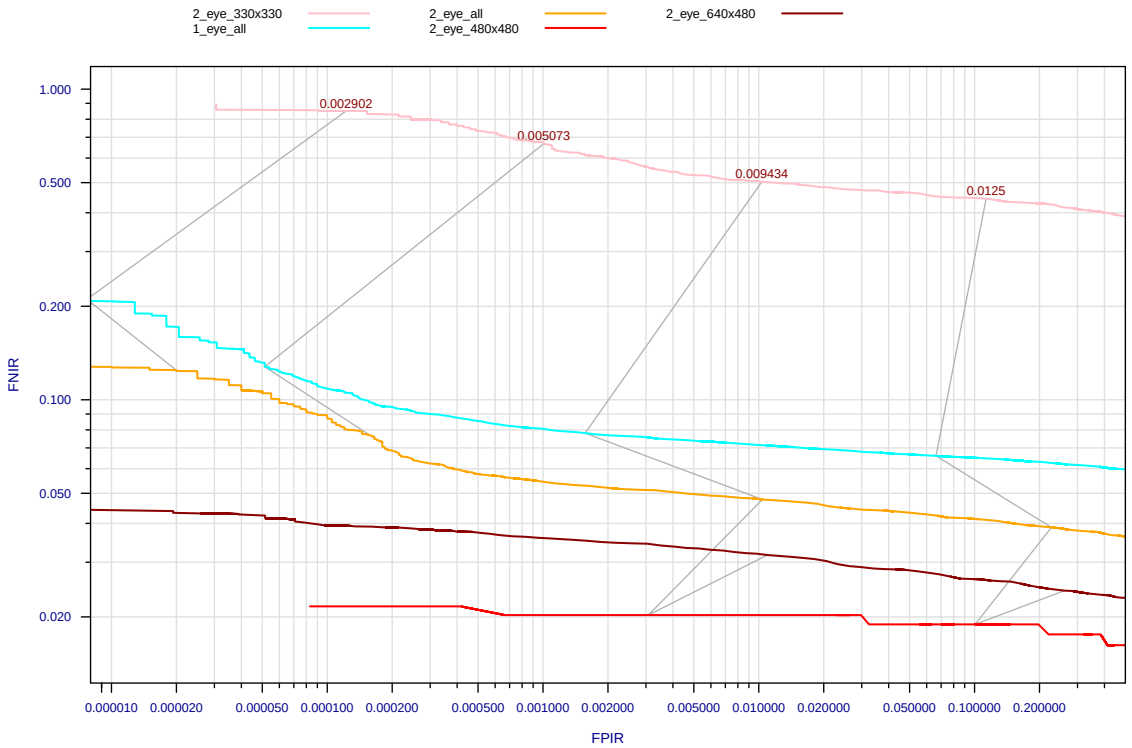

(b) Small search set, $\mathcal{S}_{na}$

Figure 514: DET for implementation N13B executing searches in an enrolled population of N = 1.6 million, broken out for three different image sizes (corresponding broadly to three camera plus ancillary software combinations) of the search image. The acquisition system used for the enrollment image (if any) is ignored in this breakout. Results for single-eye and two-eyes are plotted with two families of color. The straight lines, which link points of constant threshold, show how the two error rates would vary if a fixed threshold were adopted operationally.

FNIR = FALSE NEGATIVE IDENT. RATE FPIR = FALSE POSITIVE IDENT. RATE	N = NEUROTECHNOLOGY U = L1	P = SMU V = MORPHO	Q = IRITECH W = IRISID	R = COGENT X = CROSSMATCH	S = SMARTSENSORS Y = KYNEN	T = CAMBRIDGE

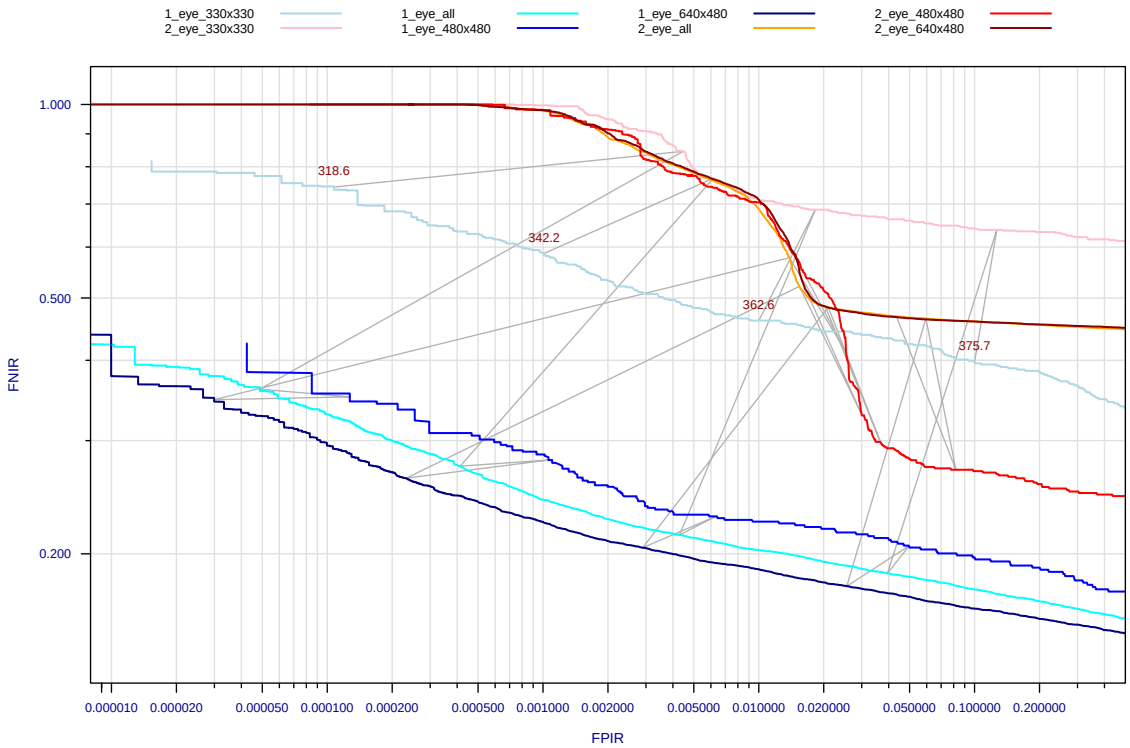

(a) Small search set, $\mathcal{S}_{na}$

Figure 515: DET for implementation P02A executing searches in an enrolled population of N = 1.6 million, broken out for three different image sizes (corresponding broadly to three camera plus ancillary software combinations) of the search image. The acquisition system used for the enrollment image (if any) is ignored in this breakout. Results for single-eye and two-eyes are plotted with two families of color. The straight lines, which link points of constant threshold, show how the two error rates would vary if a fixed threshold were adopted operationally.

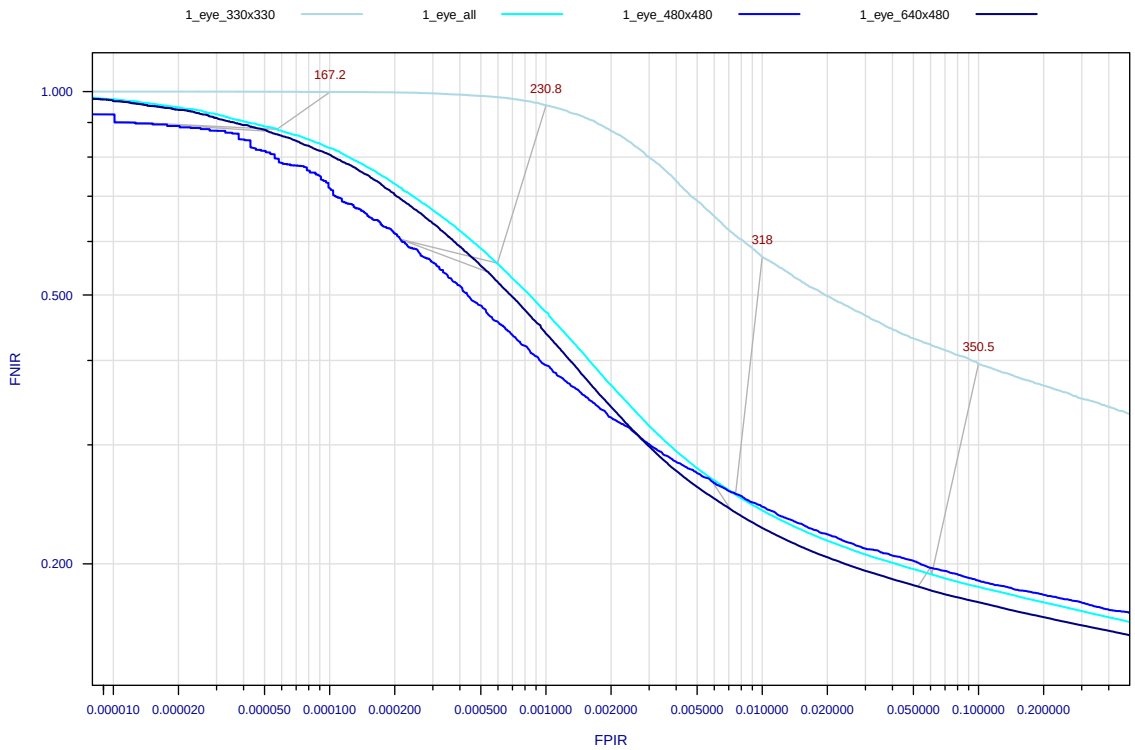

(a) Large search set, $\mathcal{S}_{nb}$

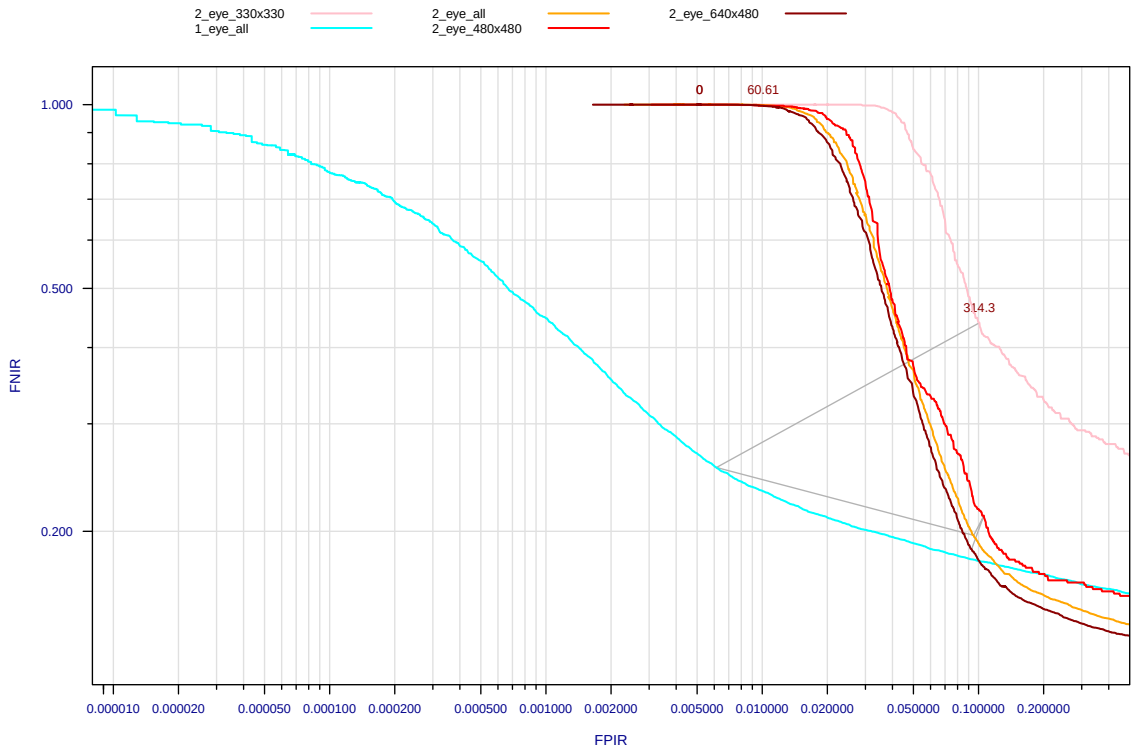

(b) Small search set, $\mathcal{S}_{na}$

Figure 516: DET for implementation P11A executing searches in an enrolled population of N = 1.6 million, broken out for three different image sizes (corresponding broadly to three camera plus ancillary software combinations) of the search image. The acquisition system used for the enrollment image (if any) is ignored in this breakout. Results for single-eye and two-eyes are plotted with two families of color. The straight lines, which link points of constant threshold, show how the two error rates would vary if a fixed threshold were adopted operationally.

FNIR = FALSE NEGATIVE IDENT. RATE FPIR = FALSE POSITIVE IDENT. RATE	N = NEUROTECHNOLOGY U = L1	P = SMU V = MORPHO	Q = IRITECH W = IRISID	R = COGENT X = CROSSMATCH	S = SMARTSENSORS Y = KYNEN	T = CAMBRIDGE

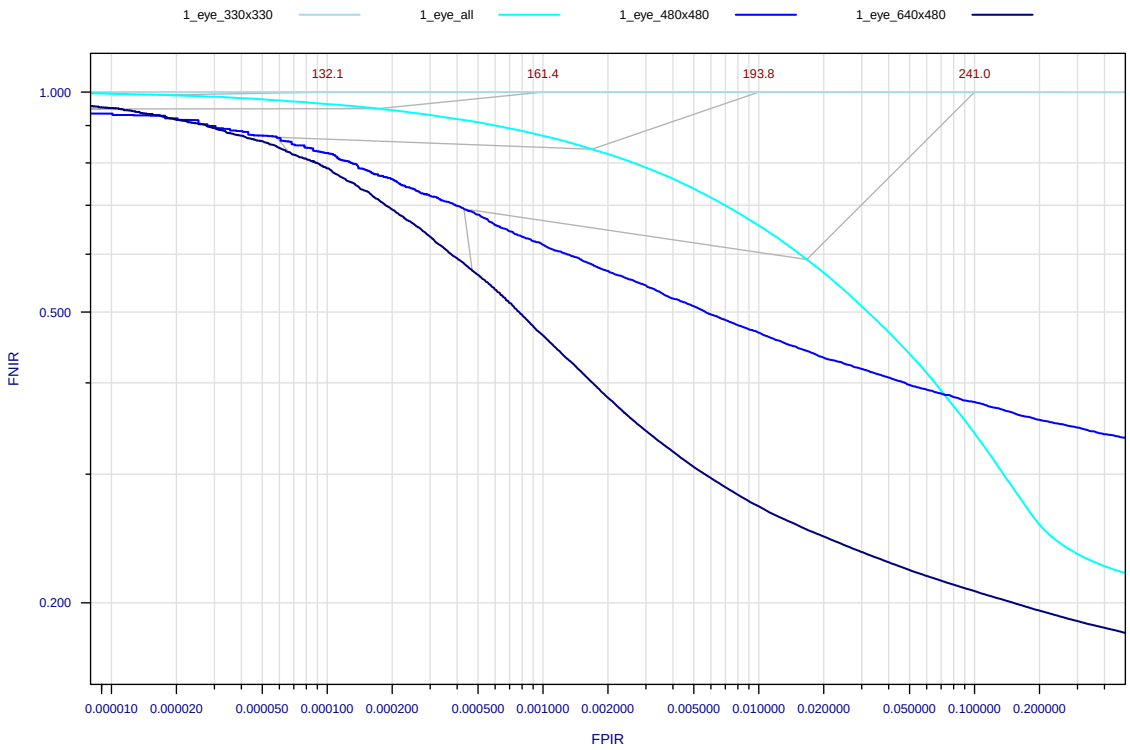

(a) Large search set, $\mathcal{S}_{nb}$

Figure 517: DET for implementation P11B executing searches in an enrolled population of N = 1.6 million, broken out for three different image sizes (corresponding broadly to three camera plus ancillary software combinations) of the search image. The acquisition system used for the enrollment image (if any) is ignored in this breakout. Results for single-eye and two-eyes are plotted with two families of color. The straight lines, which link points of constant threshold, show how the two error rates would vary if a fixed threshold were adopted operationally.

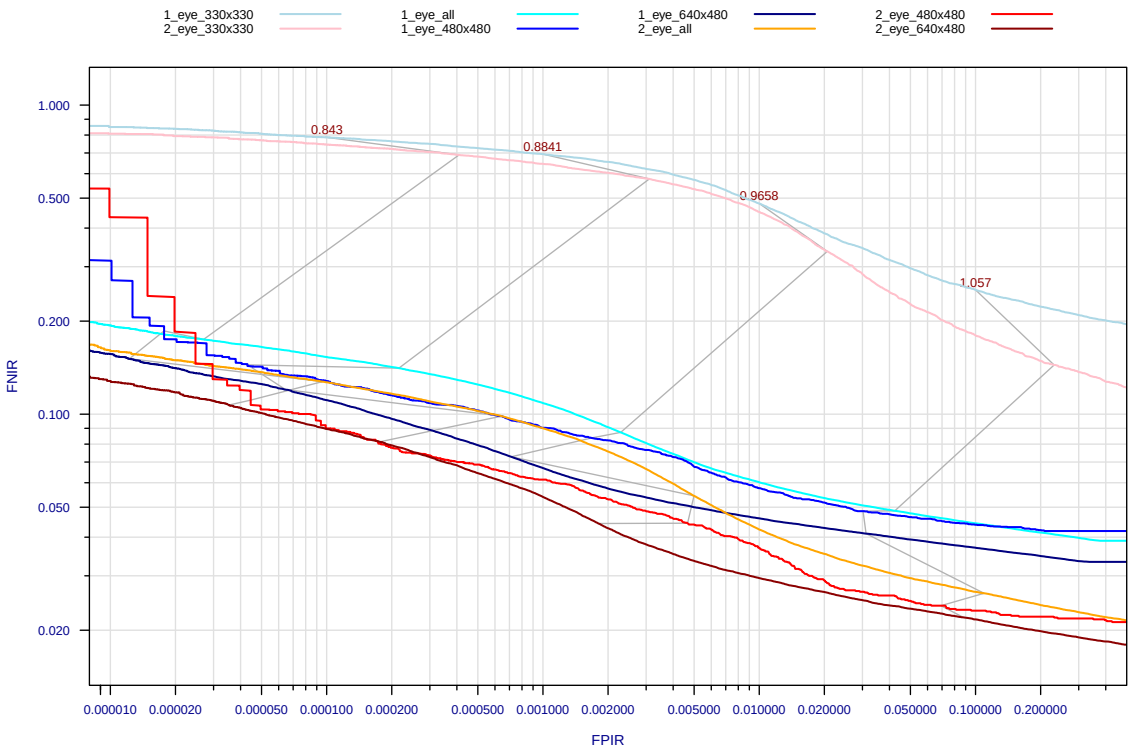

(a) Large search set, $\mathcal{S}_{nb}$

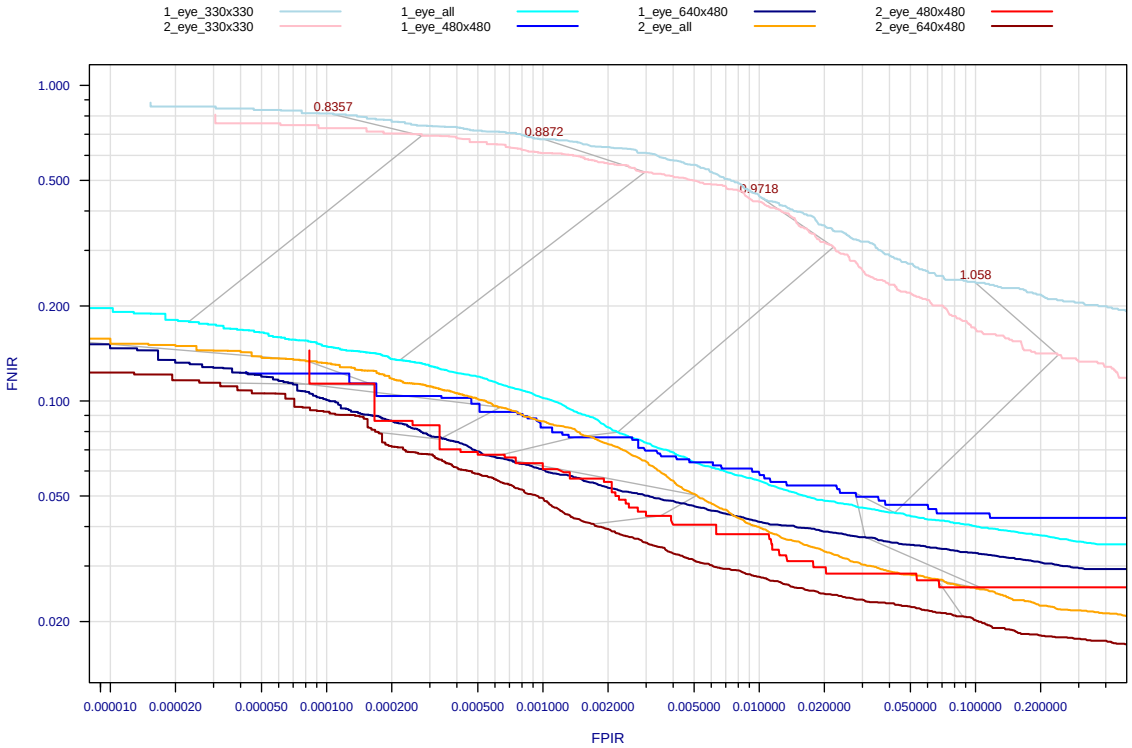

(b) Small search set, $\mathcal{S}_{na}$

Figure 518: DET for implementation Q02A executing searches in an enrolled population of N = 1.6 million, broken out for three different image sizes (corresponding broadly to three camera plus ancillary software combinations) of the search image. The acquisition system used for the enrollment image (if any) is ignored in this breakout. Results for single-eye and two-eyes are plotted with two families of color. The straight lines, which link points of constant threshold, show how the two error rates would vary if a fixed threshold were adopted operationally.

FNIR = FALSE NEGATIVE IDENT. RATE FPIR = FALSE POSITIVE IDENT. RATE	N = NEUROTECHNOLOGY U = L1	P = SMU V = MORPHO	Q = IRITECH W = IRISID	R = COGENT X = CROSSMATCH	S = SMARTSENSORS Y = KYNEN	T = CAMBRIDGE

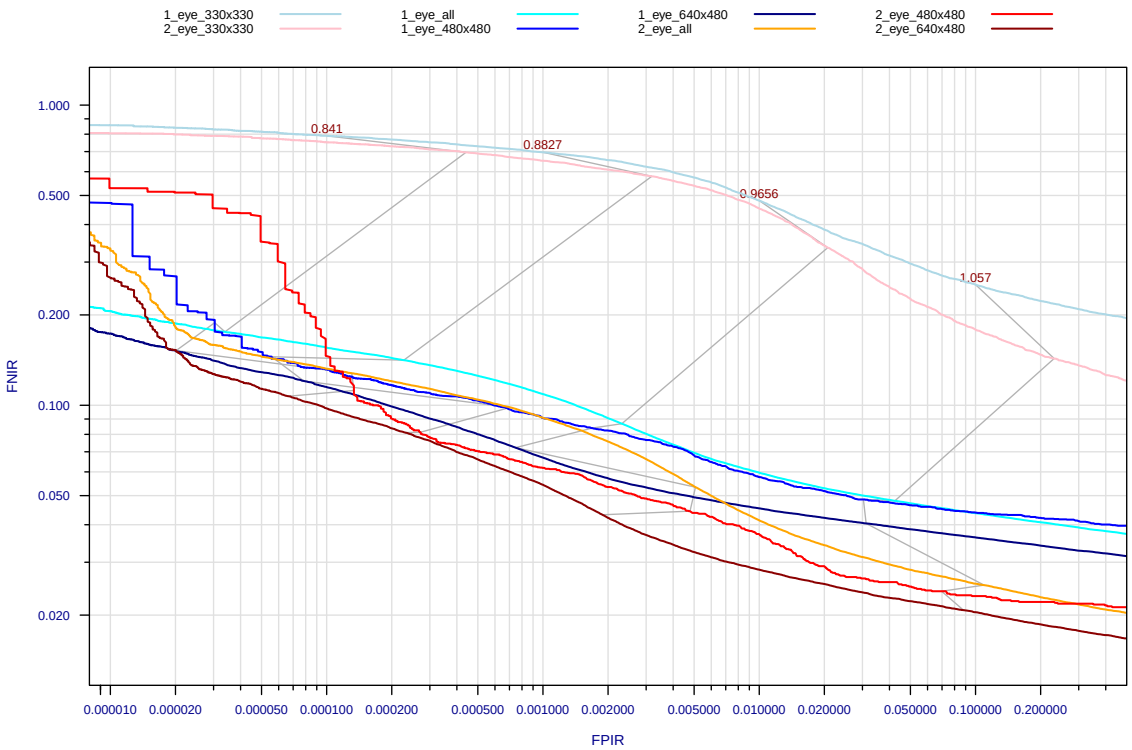

(a) Large search set, $\mathcal{S}_{nb}$

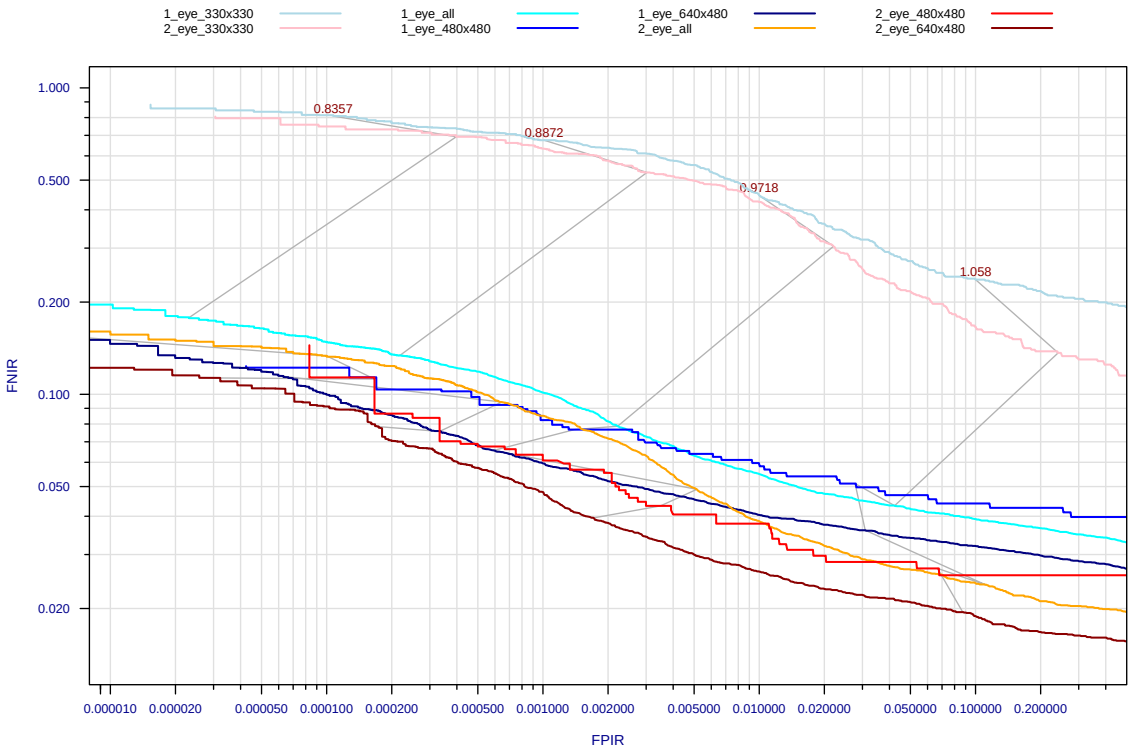

(b) Small search set, $\mathcal{S}_{na}$

Figure 519: DET for implementation Q02B executing searches in an enrolled population of N = 1.6 million, broken out for three different image sizes (corresponding broadly to three camera plus ancillary software combinations) of the search image. The acquisition system used for the enrollment image (if any) is ignored in this breakout. Results for single-eye and two-eyes are plotted with two families of color. The straight lines, which link points of constant threshold, show how the two error rates would vary if a fixed threshold were adopted operationally.

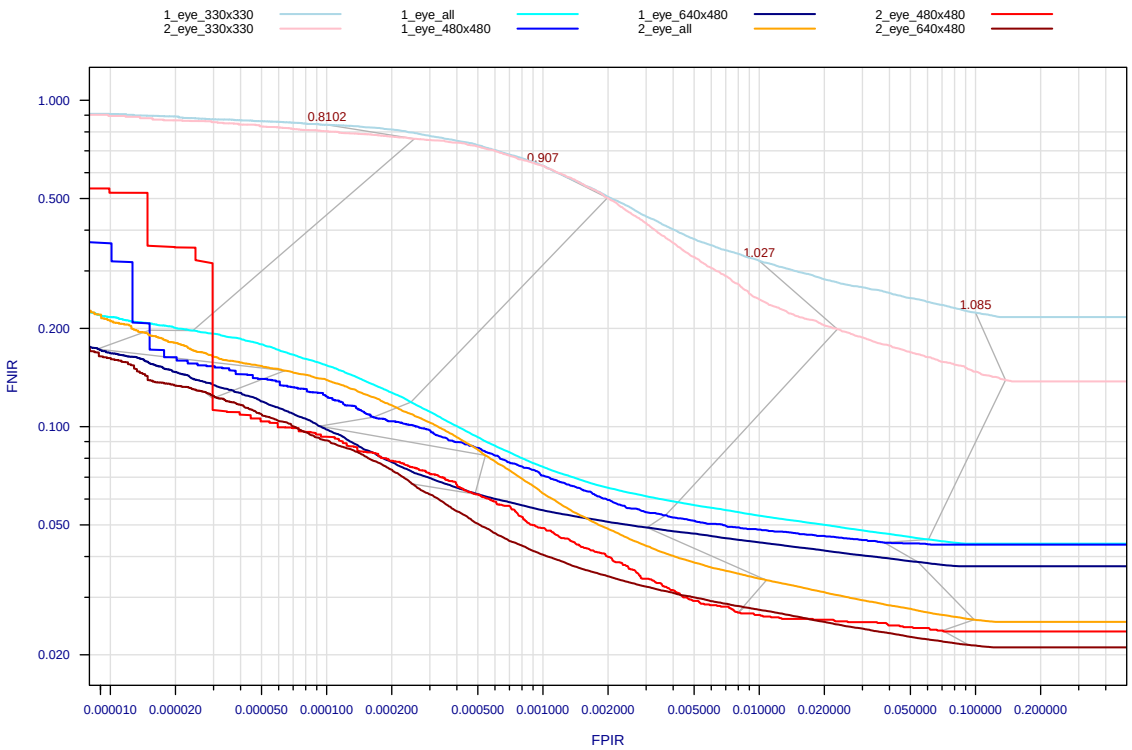

(a) Large search set, $\mathcal{S}_{nb}$

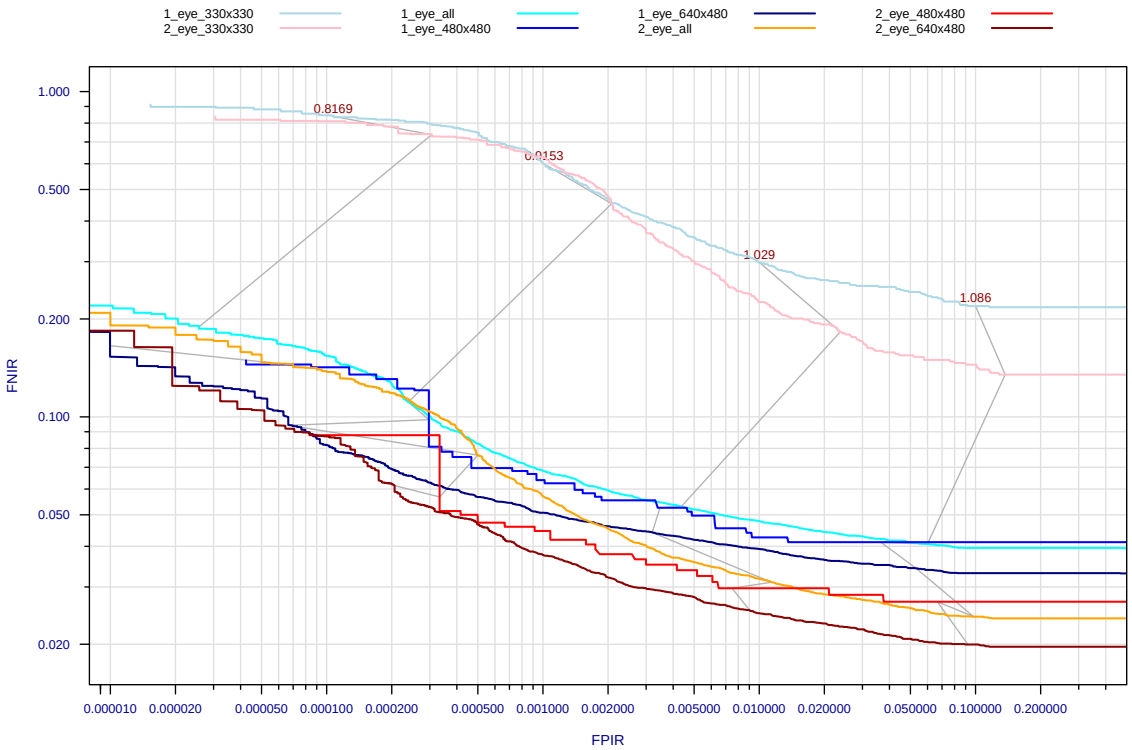

(b) Small search set, $\mathcal{S}_{na}$

Figure 520: DET for implementation Q03A executing searches in an enrolled population of N = 1.6 million, broken out for three different image sizes (corresponding broadly to three camera plus ancillary software combinations) of the search image. The acquisition system used for the enrollment image (if any) is ignored in this breakout. Results for single-eye and two-eyes are plotted with two families of color. The straight lines, which link points of constant threshold, show how the two error rates would vary if a fixed threshold were adopted operationally.

FNIR = FALSE NEGATIVE IDENT. RATE FPIR = FALSE POSITIVE IDENT. RATE	N = NEUROTECHNOLOGY U = L1	P = SMU V = MORPHO	Q = IRITECH W = IRISID	R = COGENT X = CROSSMATCH	S = SMARTSENSORS Y = KYNEN	T = CAMBRIDGE

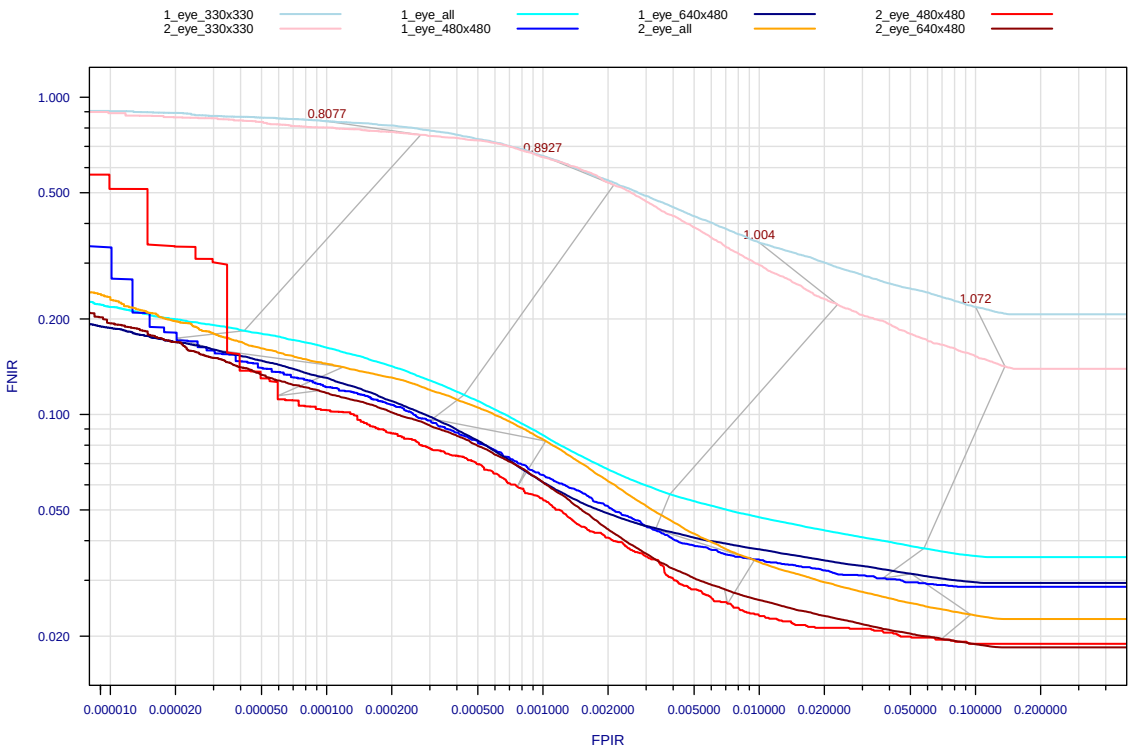

(a) Large search set, $\mathcal{S}_{nb}$

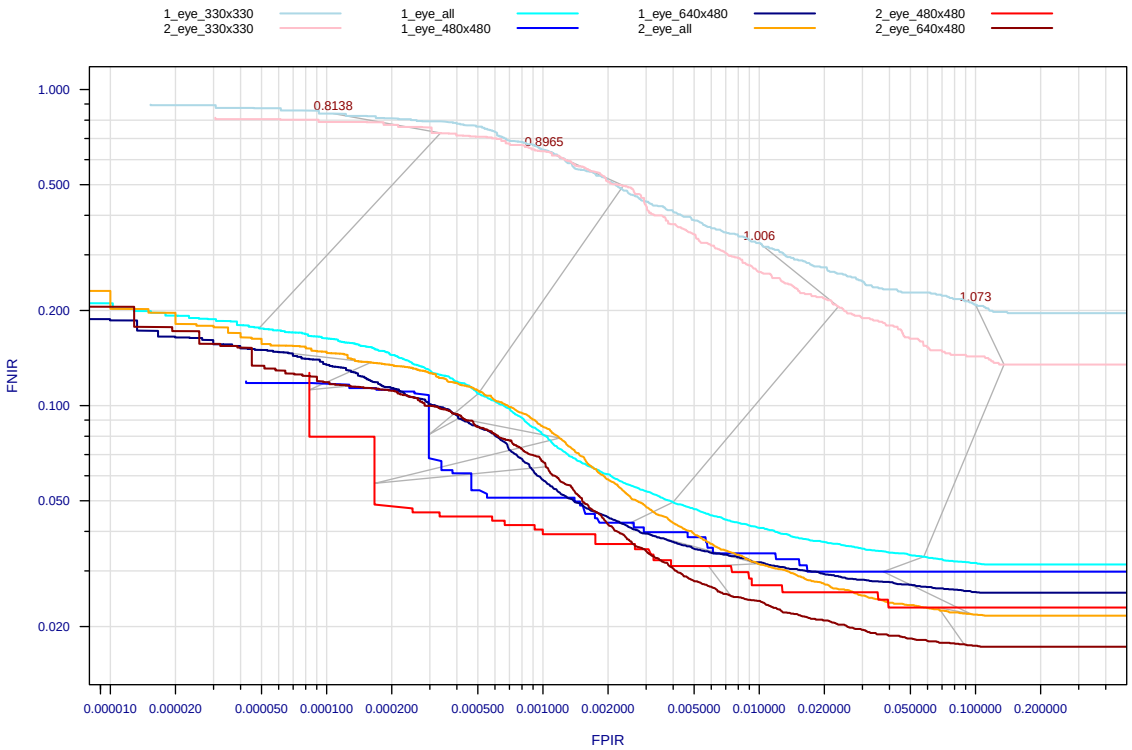

(b) Small search set, $\mathcal{S}_{na}$

Figure 521: DET for implementation Q03B executing searches in an enrolled population of N = 1.6 million, broken out for three different image sizes (corresponding broadly to three camera plus ancillary software combinations) of the search image. The acquisition system used for the enrollment image (if any) is ignored in this breakout. Results for single-eye and two-eyes are plotted with two families of color. The straight lines, which link points of constant threshold, show how the two error rates would vary if a fixed threshold were adopted operationally.

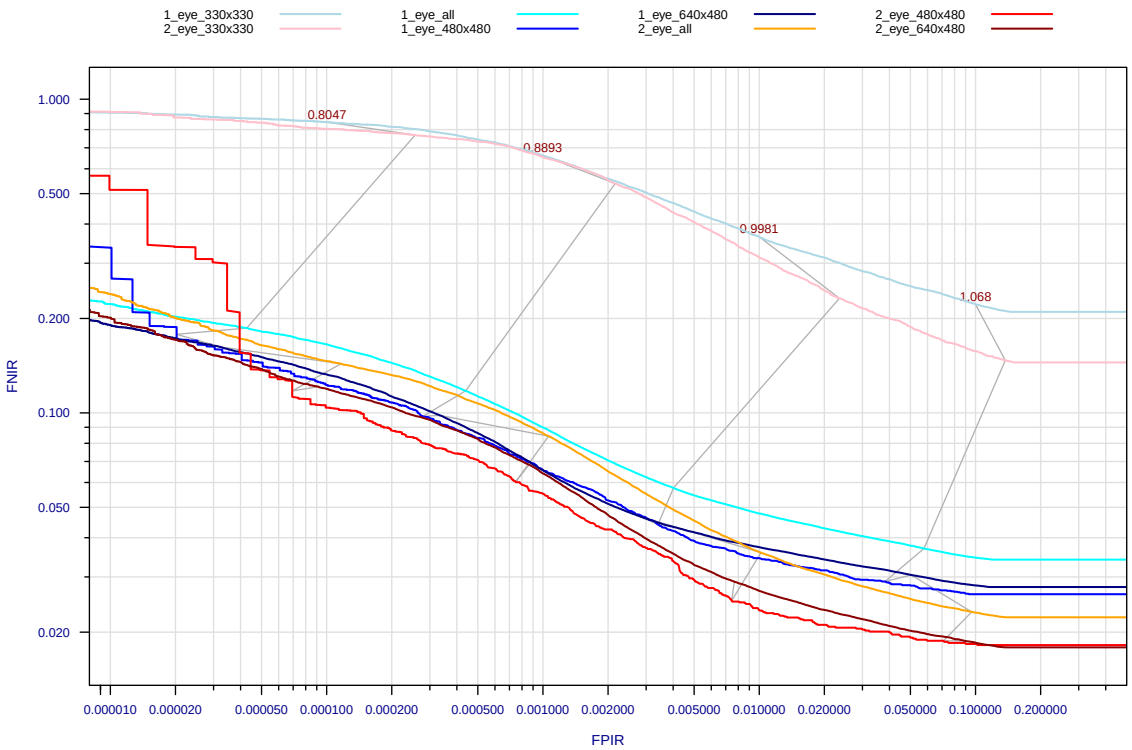

(a) Large search set, $\mathcal{S}_{nb}$

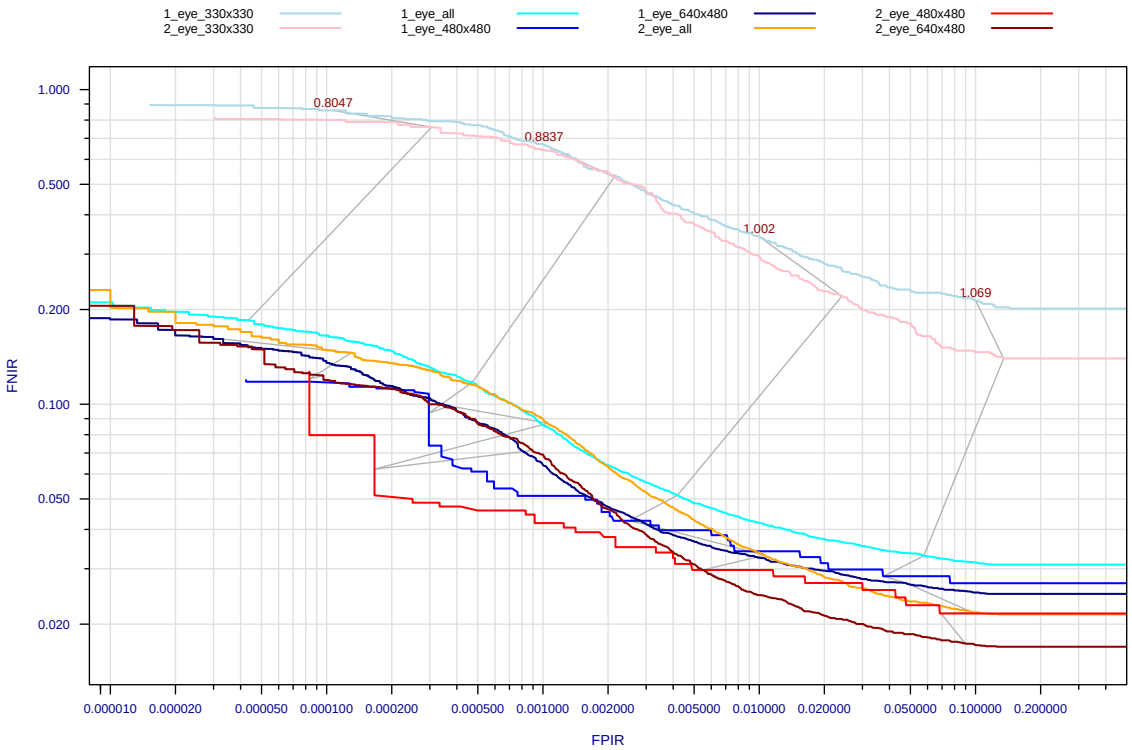

(b) Small search set, $\mathcal{S}_{na}$

Figure 522: DET for implementation Q04B executing searches in an enrolled population of N = 1.6 million, broken out for three different image sizes (corresponding broadly to three camera plus ancillary software combinations) of the search image. The acquisition system used for the enrollment image (if any) is ignored in this breakout. Results for single-eye and two-eyes are plotted with two families of color. The straight lines, which link points of constant threshold, show how the two error rates would vary if a fixed threshold were adopted operationally.

FNIR = FALSE NEGATIVE IDENT. RATE FPIR = FALSE POSITIVE IDENT. RATE	N = NEUROTECHNOLOGY U = L1	P = SMU V = MORPHO	Q = IRITECH W = IRISID	R = COGENT X = CROSSMATCH	S = SMARTSENSORS Y = KYNEN	T = CAMBRIDGE

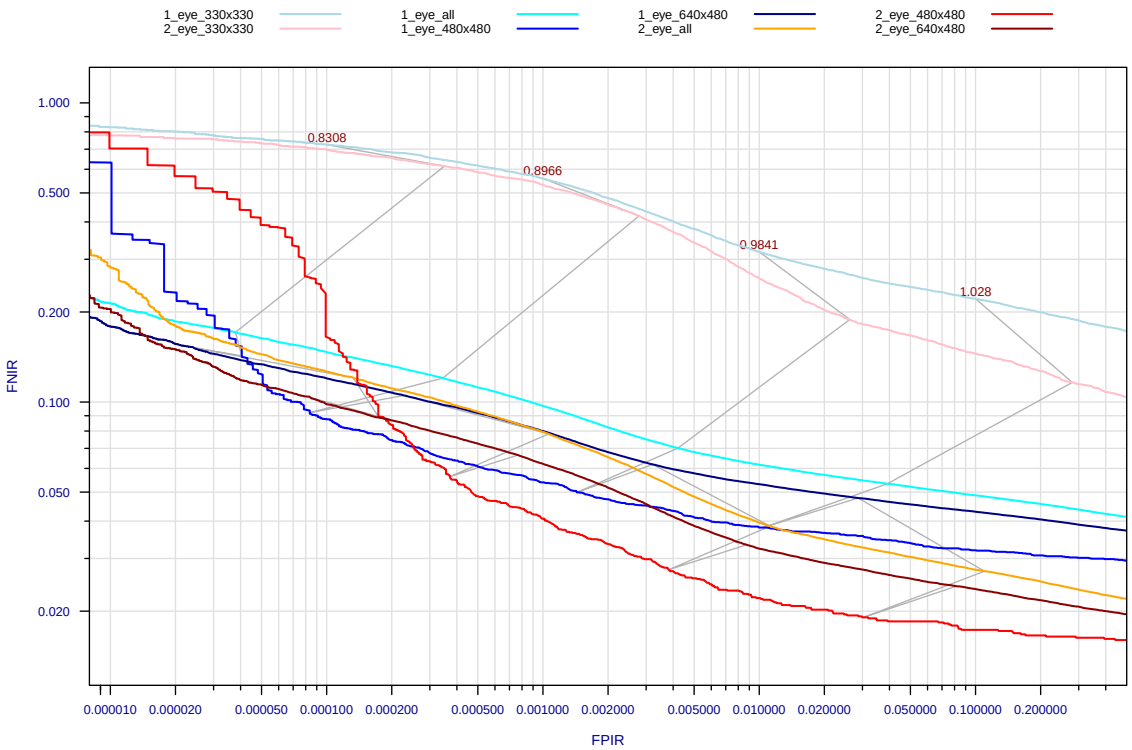

(a) Large search set, $\mathcal{S}_{nb}$

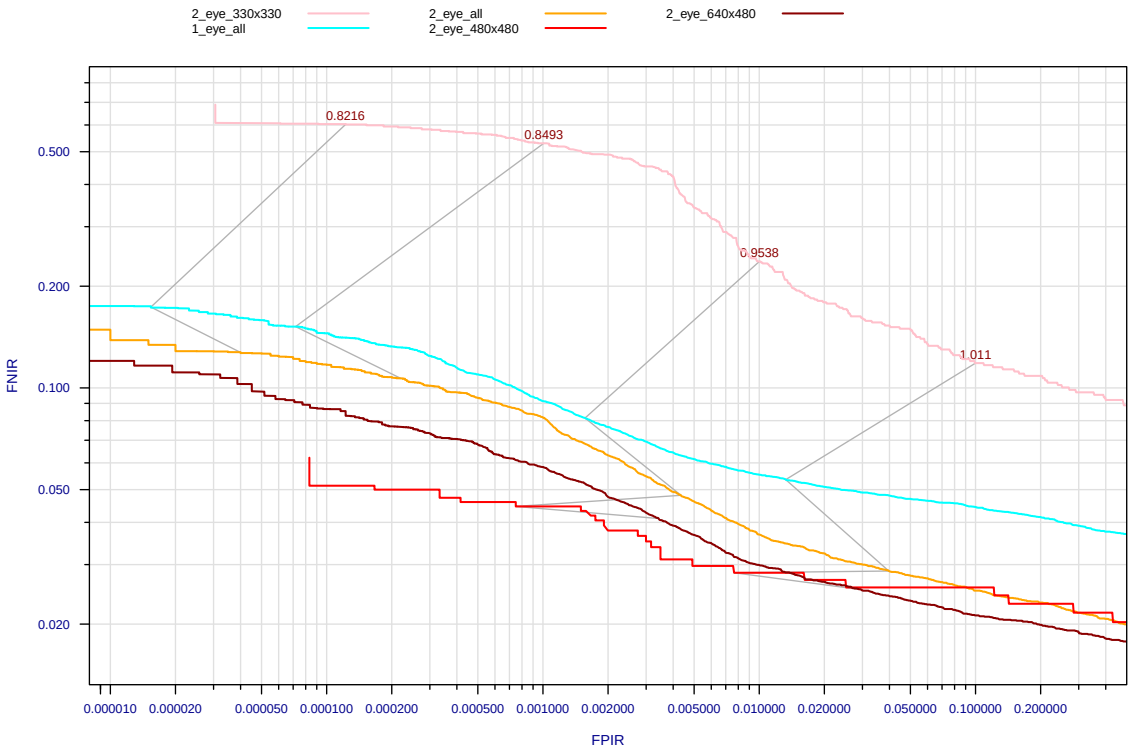

(b) Small search set, $\mathcal{S}_{na}$

Figure 523: DET for implementation Q11B executing searches in an enrolled population of N = 1.6 million, broken out for three different image sizes (corresponding broadly to three camera plus ancillary software combinations) of the search image. The acquisition system used for the enrollment image (if any) is ignored in this breakout. Results for single-eye and two-eyes are plotted with two families of color. The straight lines, which link points of constant threshold, show how the two error rates would vary if a fixed threshold were adopted operationally.

FNIR = FALSE NEGATIVE IDENT. RATE FPIR = FALSE POSITIVE IDENT. RATE	N = NEUROTECHNOLOGY U = L1	P = SMU V = MORPHO	Q = IRITECH W = IRISID	R = COGENT X = CROSSMATCH	S = SMARTSENSORS Y = KYNEN	T = CAMBRIDGE

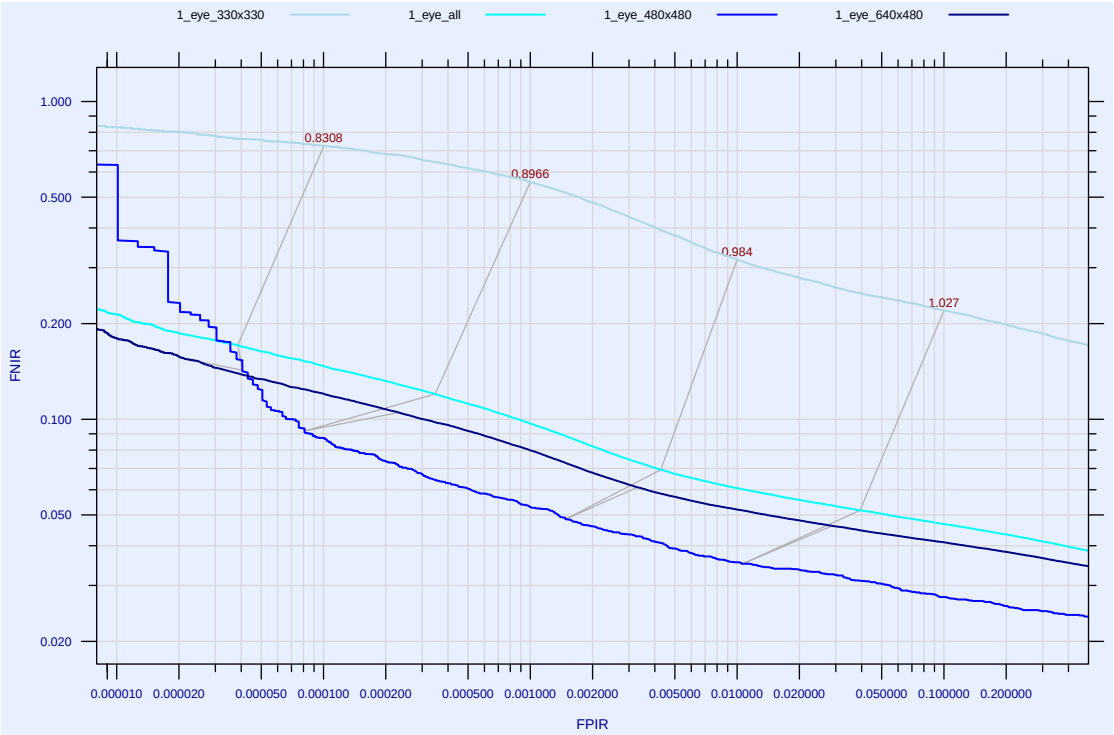

(a) Large search set, $\mathcal{S}_{nb}$

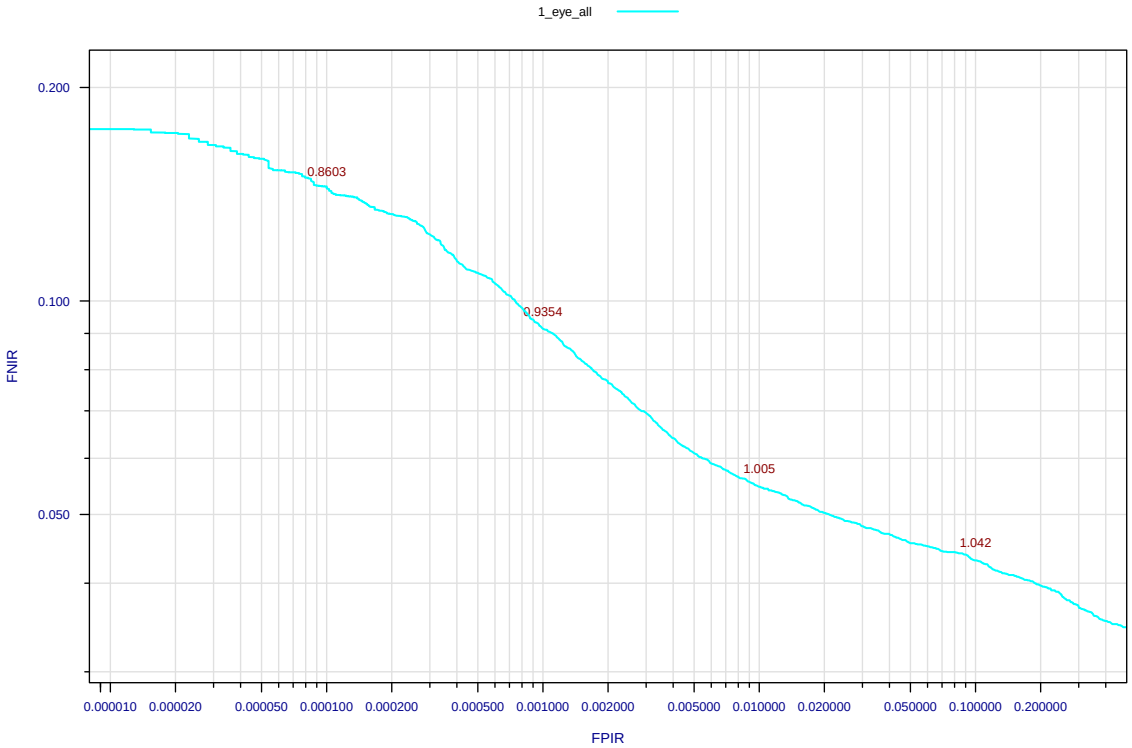

(b) Small search set, $\mathcal{S}_{na}$

Figure 524: DET for implementation Q12B executing searches in an enrolled population of N = 1.6 million, broken out for three different image sizes (corresponding broadly to three camera plus ancillary software combinations) of the search image. The acquisition system used for the enrollment image (if any) is ignored in this breakout. Results for single-eye and two-eyes are plotted with two families of color. The straight lines, which link points of constant threshold, show how the two error rates would vary if a fixed threshold were adopted operationally.

FNIR = FALSE NEGATIVE IDENT. RATE FPIR = FALSE POSITIVE IDENT. RATE	N = NEUROTECHNOLOGY U = L1	P = SMU V = MORPHO	Q = IRITECH W = IRISID	R = COGENT X = CROSSMATCH	S = SMARTSENSORS Y = KYNEN	T = CAMBRIDGE

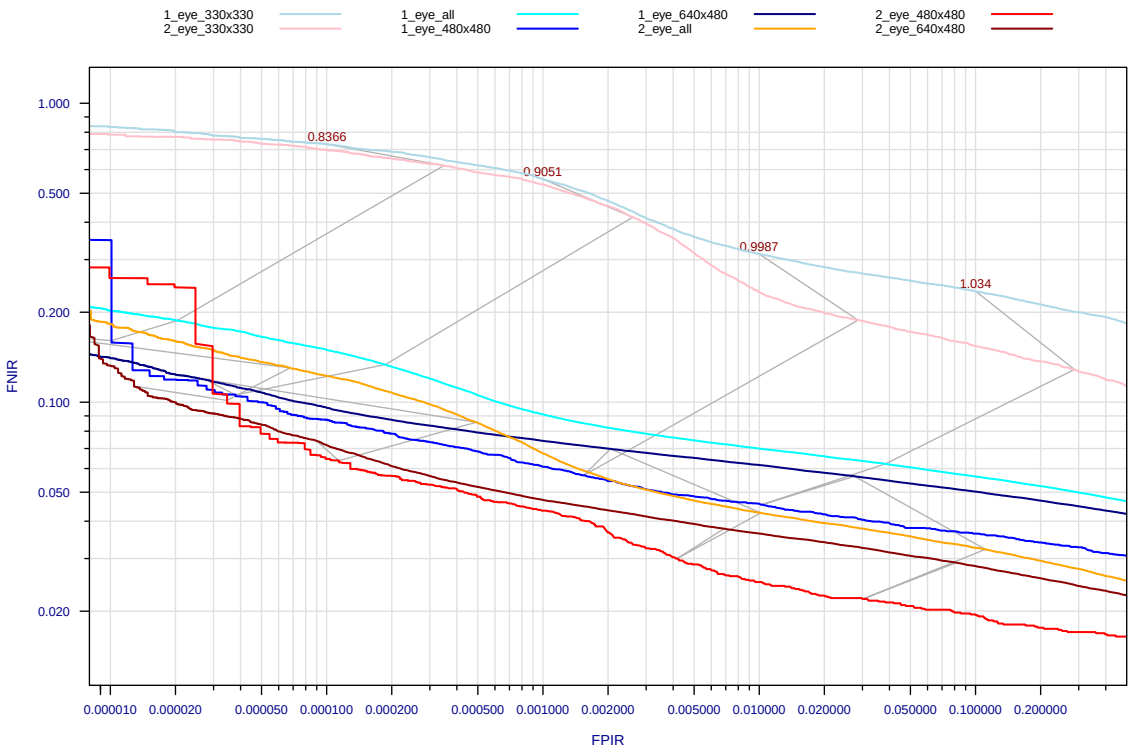

(a) Large search set, $\mathcal{S}_{nb}$

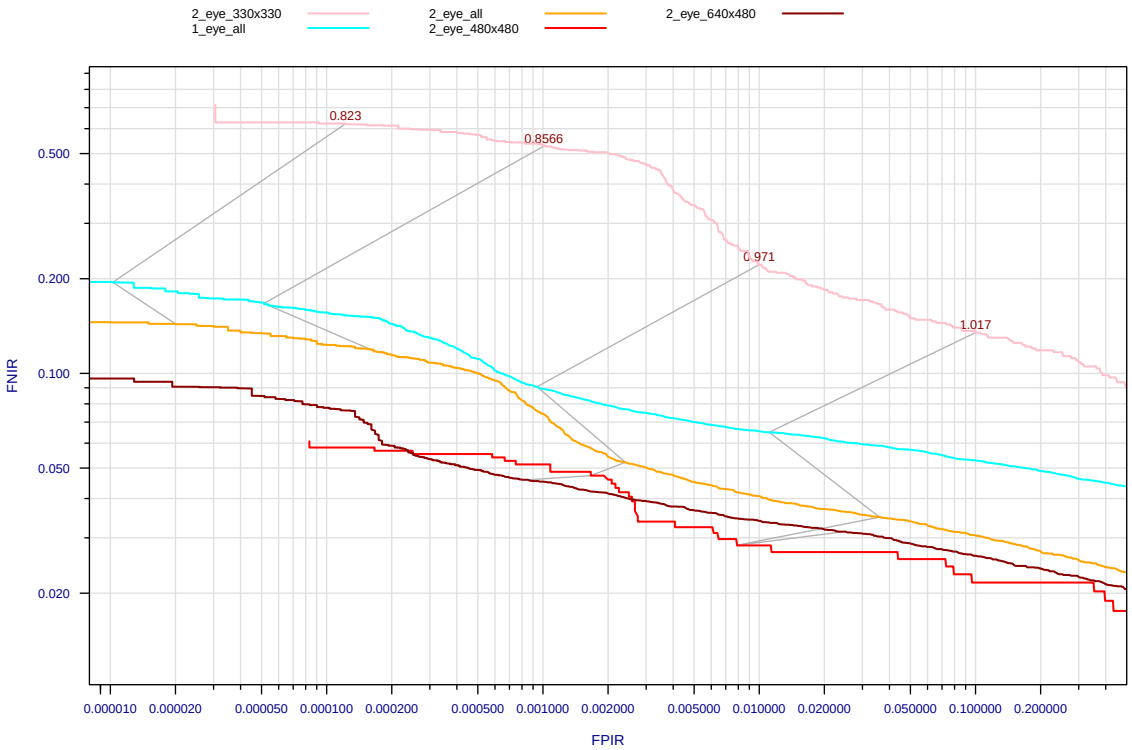

(b) Small search set, $\mathcal{S}_{na}$

Figure 525: DET for implementation Q13B executing searches in an enrolled population of N = 1.6 million, broken out for three different image sizes (corresponding broadly to three camera plus ancillary software combinations) of the search image. The acquisition system used for the enrollment image (if any) is ignored in this breakout. Results for single-eye and two-eyes are plotted with two families of color. The straight lines, which link points of constant threshold, show how the two error rates would vary if a fixed threshold were adopted operationally.

FNIR = FALSE NEGATIVE IDENT. RATE FPIR = FALSE POSITIVE IDENT. RATE	N = NEUROTECHNOLOGY U = L1	P = SMU V = MORPHO	Q = IRITECH W = IRISID	R = COGENT X = CROSSMATCH	S = SMARTSENSORS Y = KYNEN	T = CAMBRIDGE

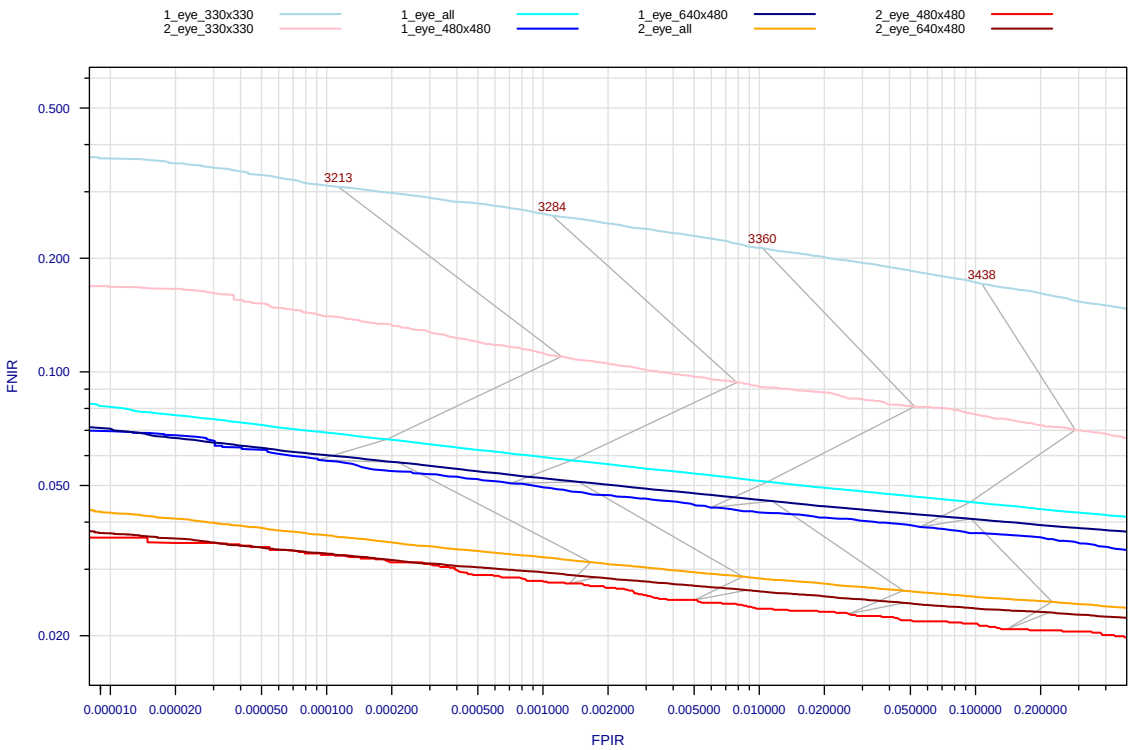

(a) Large search set, $\mathcal{S}_{nb}$

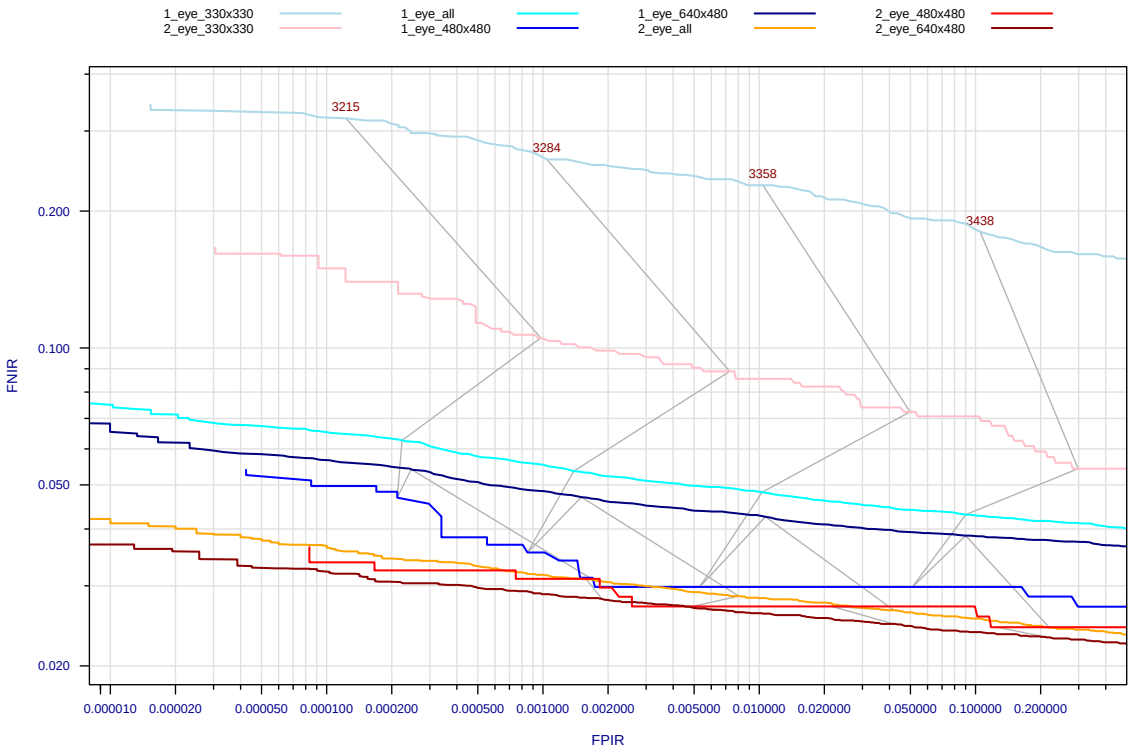

(b) Small search set, $\mathcal{S}_{na}$

Figure 526: DET for implementation R02A executing searches in an enrolled population of N = 1.6 million, broken out for three different image sizes (corresponding broadly to three camera plus ancillary software combinations) of the search image. The acquisition system used for the enrollment image (if any) is ignored in this breakout. Results for single-eye and two-eyes are plotted with two families of color. The straight lines, which link points of constant threshold, show how the two error rates would vary if a fixed threshold were adopted operationally.

FNIR = FALSE NEGATIVE IDENT. RATE FPIR = FALSE POSITIVE IDENT. RATE	N = NEUROTECHNOLOGY U = L1	P = SMU V = MORPHO	Q = IRITECH W = IRISID	R = COGENT X = CROSSMATCH	S = SMARTSENSORS Y = KYNEN	T = CAMBRIDGE

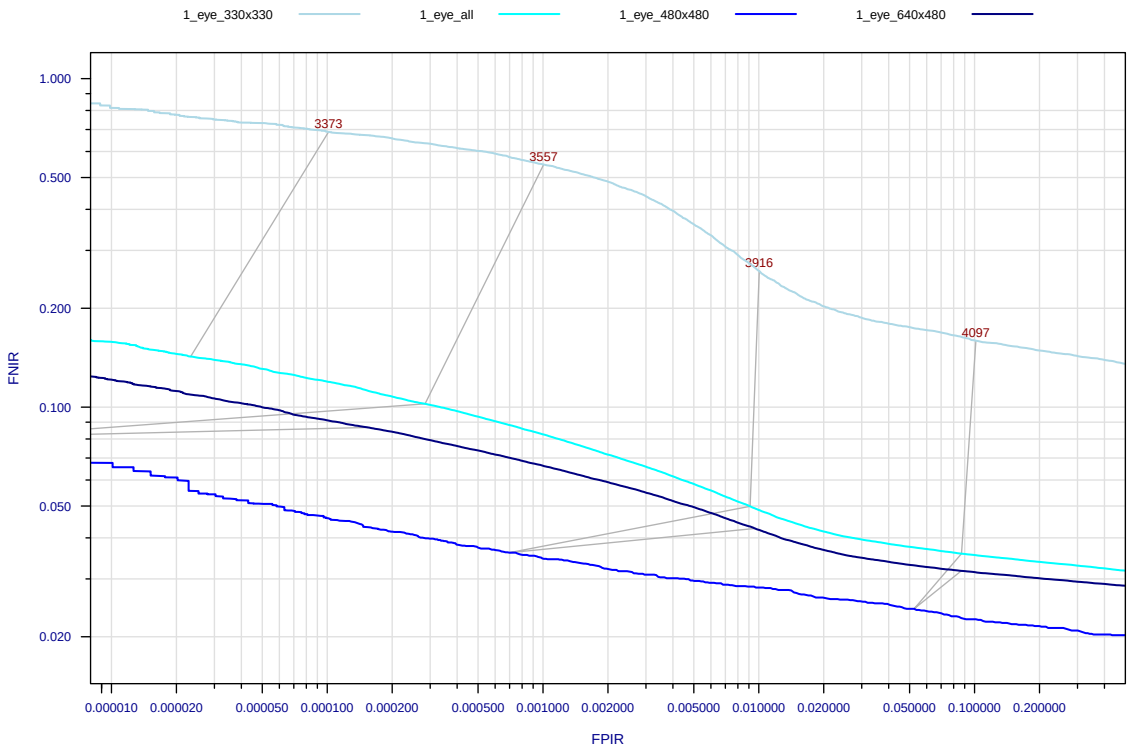

(a) Large search set, $\mathcal{S}_{nb}$

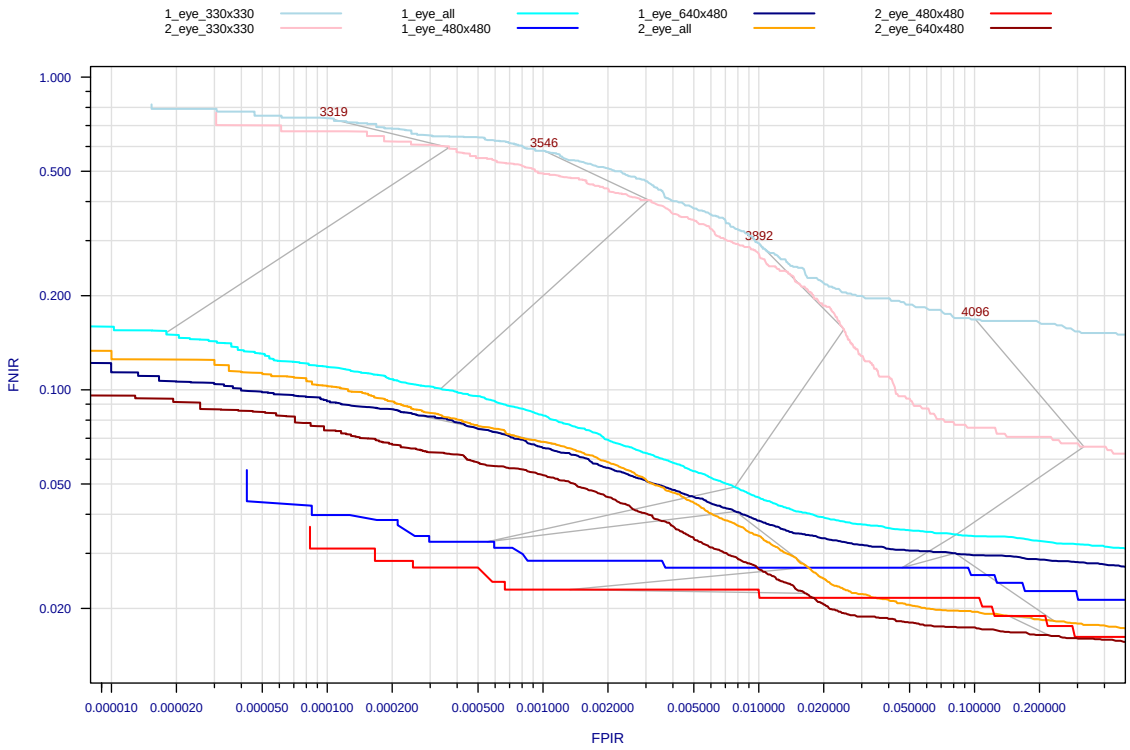

(b) Small search set, $\mathcal{S}_{na}$

Figure 527: DET for implementation R02B executing searches in an enrolled population of N = 1.6 million, broken out for three different image sizes (corresponding broadly to three camera plus ancillary software combinations) of the search image. The acquisition system used for the enrollment image (if any) is ignored in this breakout. Results for single-eye and two-eyes are plotted with two families of color. The straight lines, which link points of constant threshold, show how the two error rates would vary if a fixed threshold were adopted operationally.

FNIR = FALSE NEGATIVE IDENT. RATE FPIR = FALSE POSITIVE IDENT. RATE	N = NEUROTECHNOLOGY U = L1	P = SMU V = MORPHO	Q = IRITECH W = IRISID	R = COGENT X = CROSSMATCH	S = SMARTSENSORS Y = KYNEN	T = CAMBRIDGE

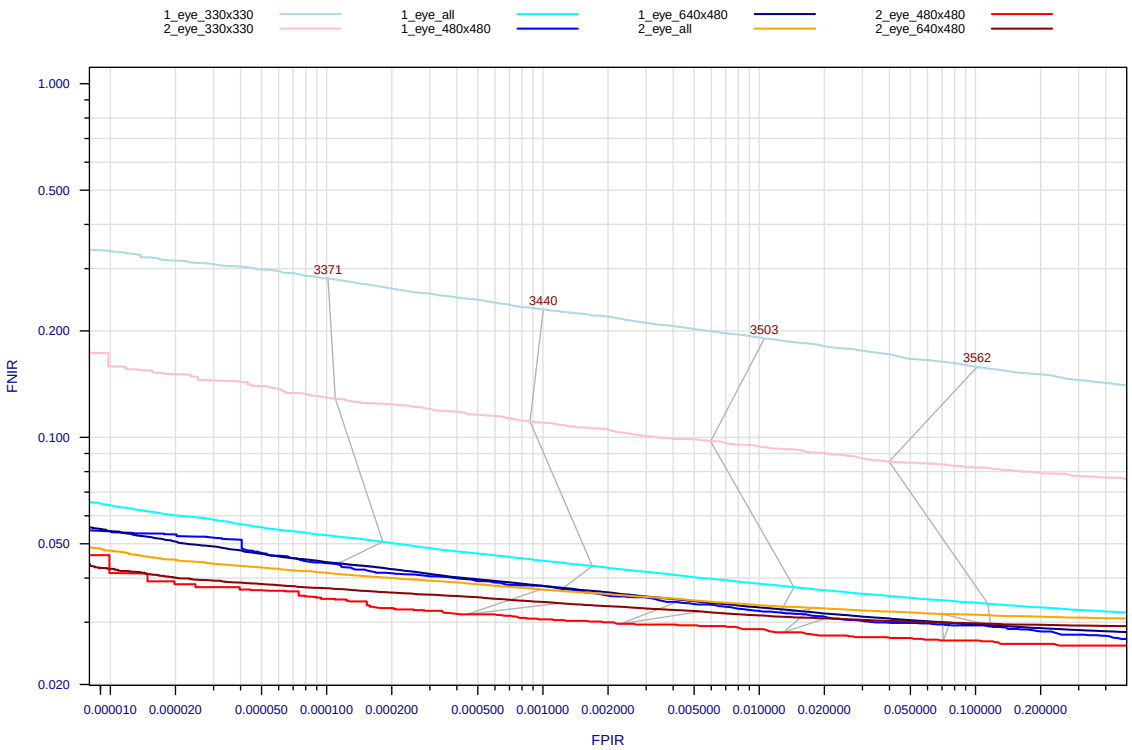

(a) Large search set, $\mathcal{S}_{nb}$

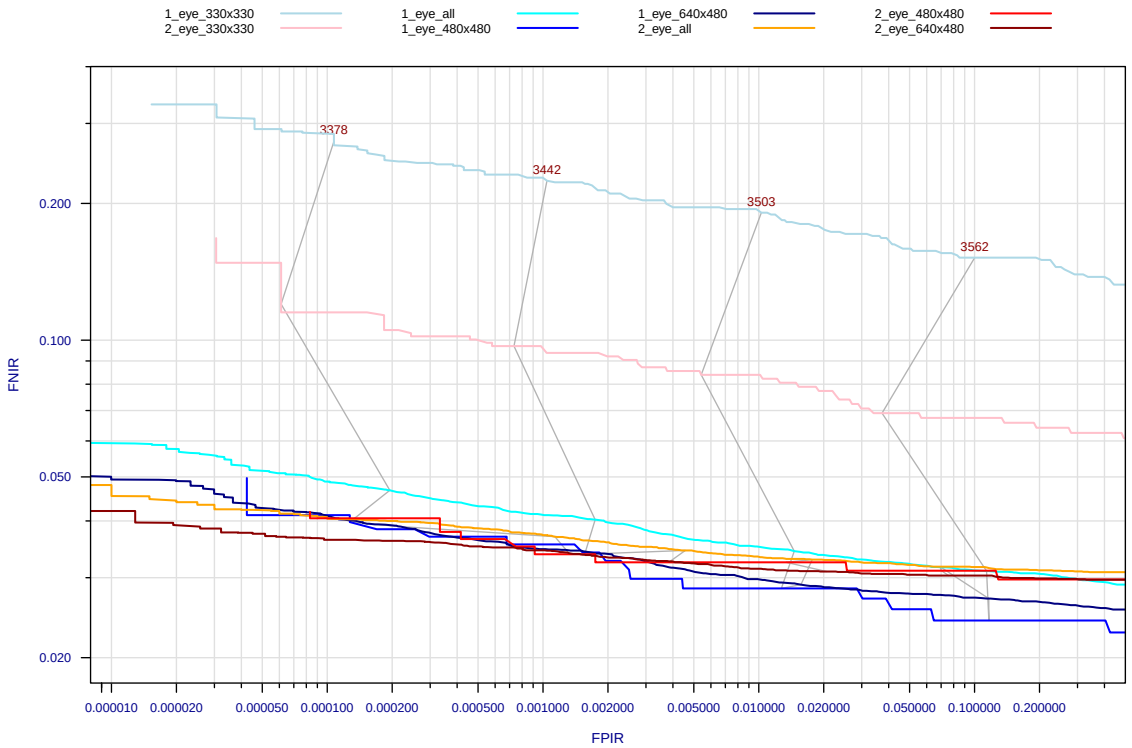

(b) Small search set, $\mathcal{S}_{na}$

Figure 528: DET for implementation R03A executing searches in an enrolled population of N = 1.6 million, broken out for three different image sizes (corresponding broadly to three camera plus ancillary software combinations) of the search image. The acquisition system used for the enrollment image (if any) is ignored in this breakout. Results for single-eye and two-eyes are plotted with two families of color. The straight lines, which link points of constant threshold, show how the two error rates would vary if a fixed threshold were adopted operationally.

FNIR = FALSE NEGATIVE IDENT. RATE FPIR = FALSE POSITIVE IDENT. RATE	N = NEUROTECHNOLOGY U = L1	P = SMU V = MORPHO	Q = IRITECH W = IRISID	R = COGENT X = CROSSMATCH	S = SMARTSENSORS Y = KYNEN	T = CAMBRIDGE

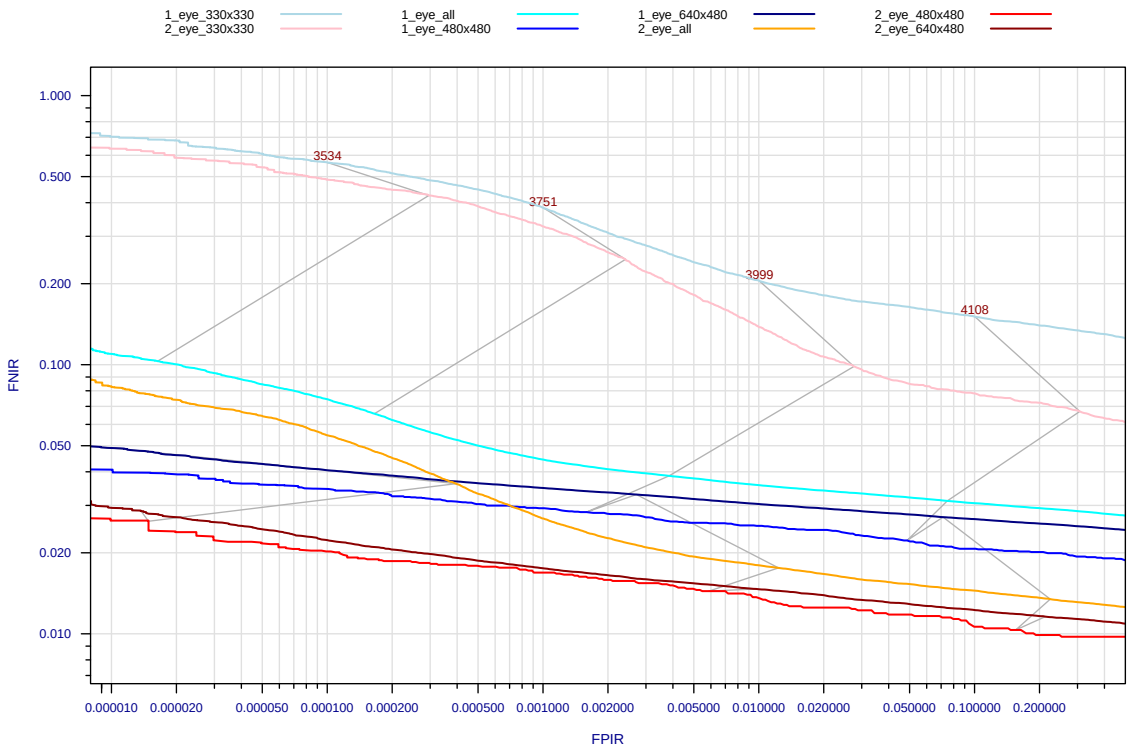

(a) Large search set, $\mathcal{S}_{nb}$

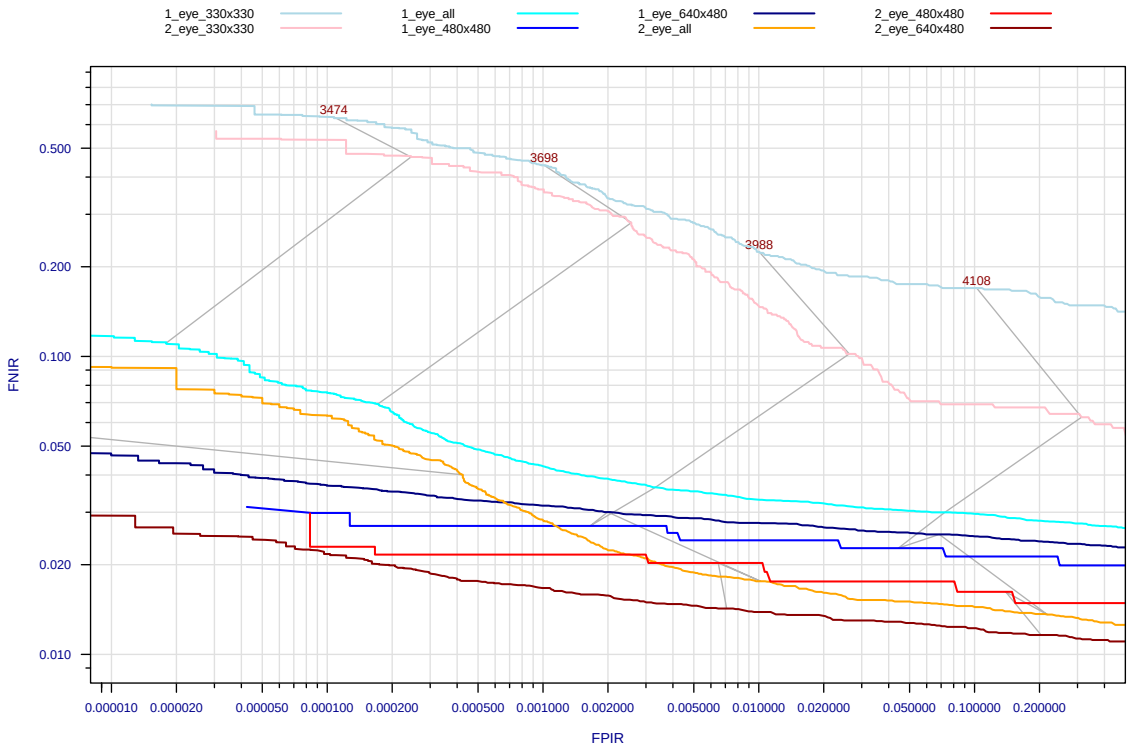

(b) Small search set, $\mathcal{S}_{na}$

Figure 529: DET for implementation R03B executing searches in an enrolled population of N = 1.6 million, broken out for three different image sizes (corresponding broadly to three camera plus ancillary software combinations) of the search image. The acquisition system used for the enrollment image (if any) is ignored in this breakout. Results for single-eye and two-eyes are plotted with two families of color. The straight lines, which link points of constant threshold, show how the two error rates would vary if a fixed threshold were adopted operationally.

FNIR = FALSE NEGATIVE IDENT. RATE FPIR = FALSE POSITIVE IDENT. RATE	N = NEUROTECHNOLOGY U = L1	P = SMU V = MORPHO	Q = IRITECH W = IRISID	R = COGENT X = CROSSMATCH	S = SMARTSENSORS Y = KYNEN	T = CAMBRIDGE

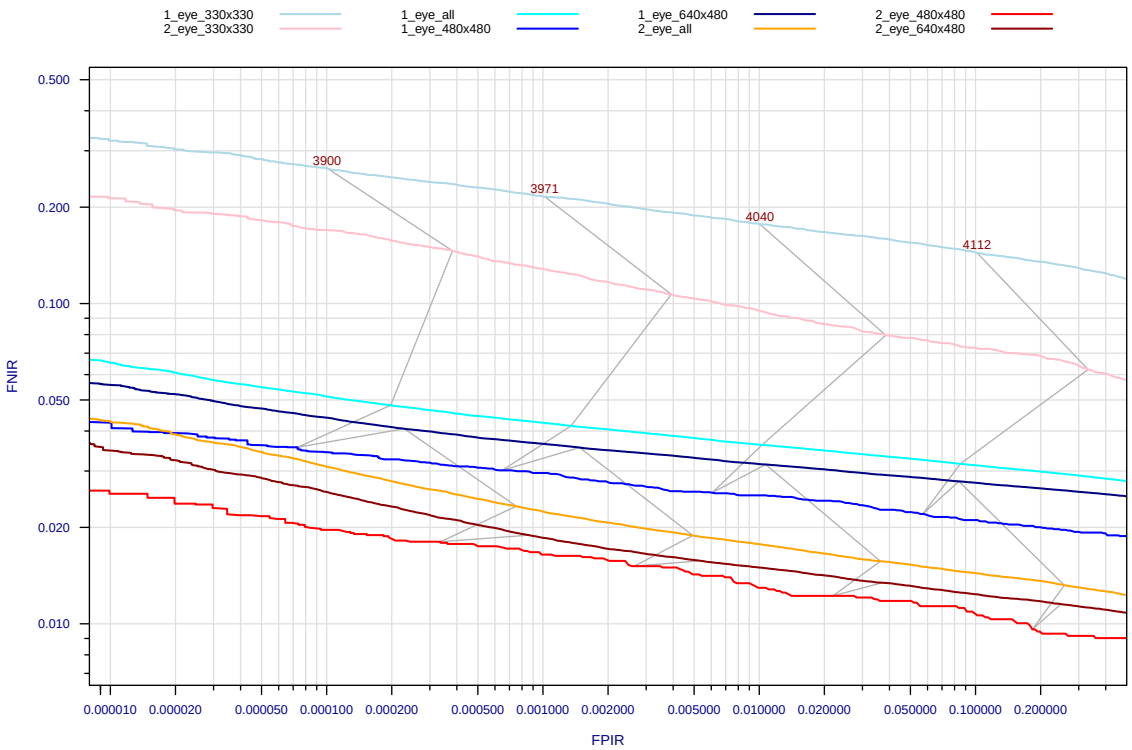

(a) Large search set, $\mathcal{S}_{nb}$

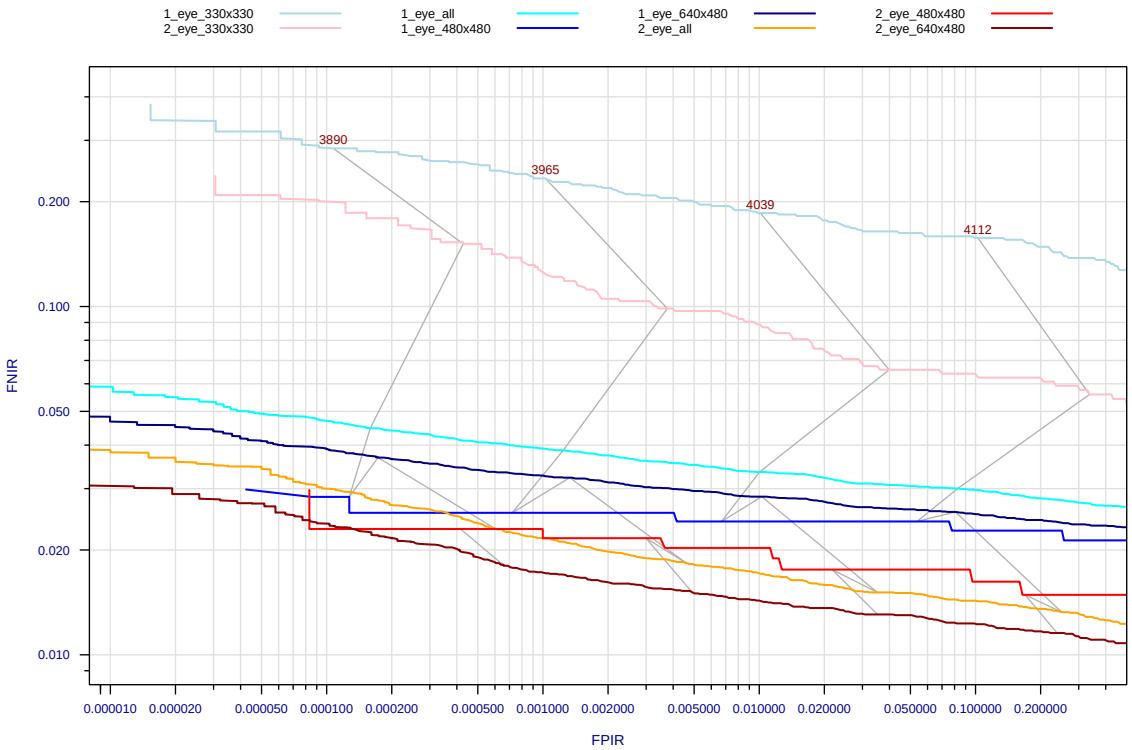

(b) Small search set, $\mathcal{S}_{na}$

Figure 530: DET for implementation R04B executing searches in an enrolled population of N = 1.6 million, broken out for three different image sizes (corresponding broadly to three camera plus ancillary software combinations) of the search image. The acquisition system used for the enrollment image (if any) is ignored in this breakout. Results for single-eye and two-eyes are plotted with two families of color. The straight lines, which link points of constant threshold, show how the two error rates would vary if a fixed threshold were adopted operationally.

FNIR = FALSE NEGATIVE IDENT. RATE FPIR = FALSE POSITIVE IDENT. RATE	N = NEUROTECHNOLOGY U = L1	P = SMU V = MORPHO	Q = IRITECH W = IRISID	R = COGENT X = CROSSMATCH	S = SMARTSENSORS Y = KYNEN	T = CAMBRIDGE

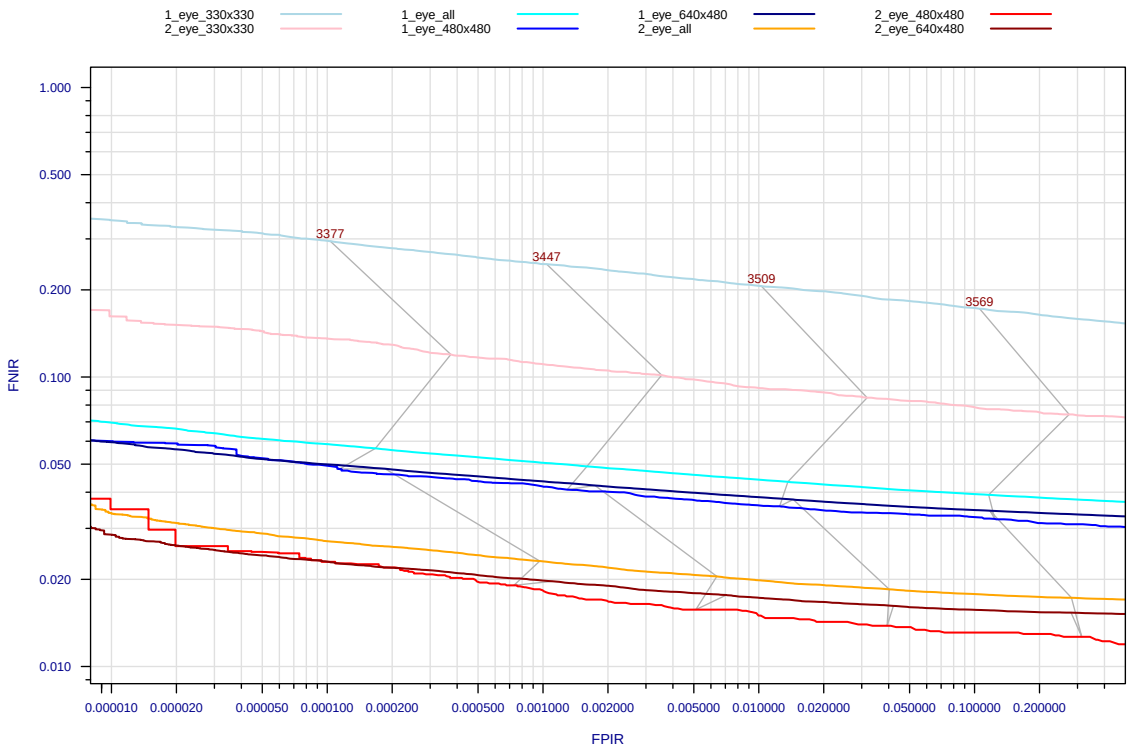

(a) Large search set, $\mathcal{S}_{nb}$

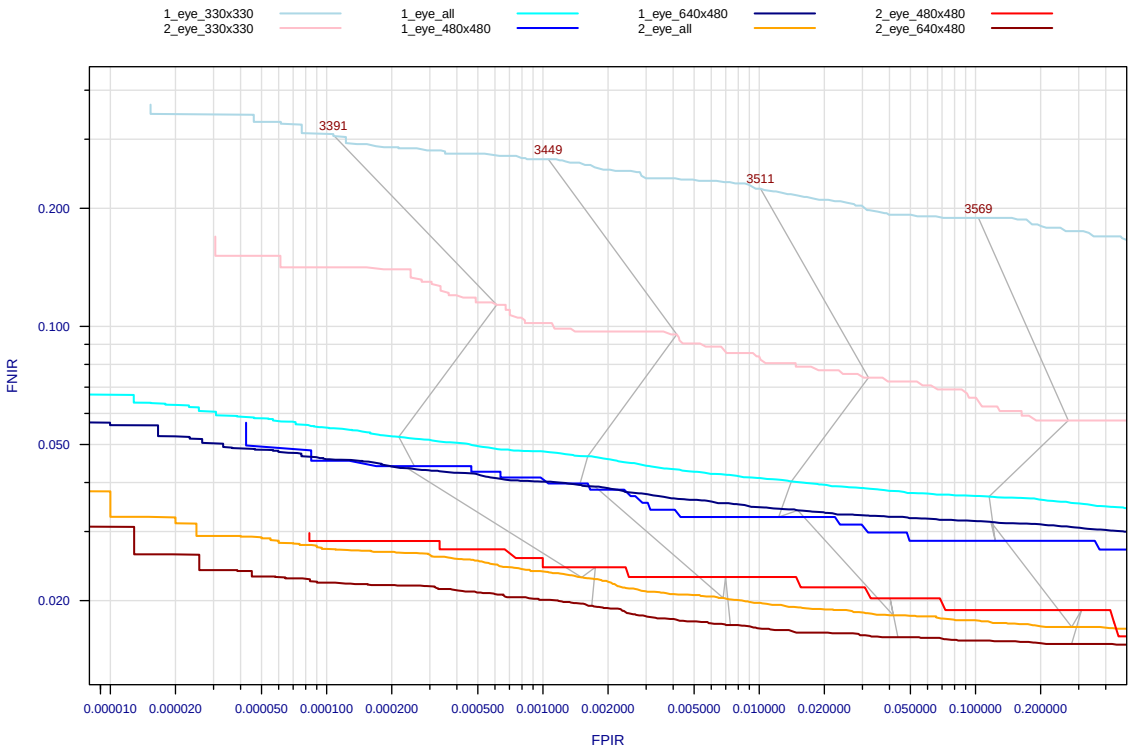

(b) Small search set, $\mathcal{S}_{na}$

Figure 531: DET for implementation R11A executing searches in an enrolled population of N = 1.6 million, broken out for three different image sizes (corresponding broadly to three camera plus ancillary software combinations) of the search image. The acquisition system used for the enrollment image (if any) is ignored in this breakout. Results for single-eye and two-eyes are plotted with two families of color. The straight lines, which link points of constant threshold, show how the two error rates would vary if a fixed threshold were adopted operationally.

FNIR = FALSE NEGATIVE IDENT. RATE FPIR = FALSE POSITIVE IDENT. RATE	N = NEUROTECHNOLOGY U = L1	P = SMU V = MORPHO	Q = IRITECH W = IRISID	R = COGENT X = CROSSMATCH	S = SMARTSENSORS Y = KYNEN	T = CAMBRIDGE

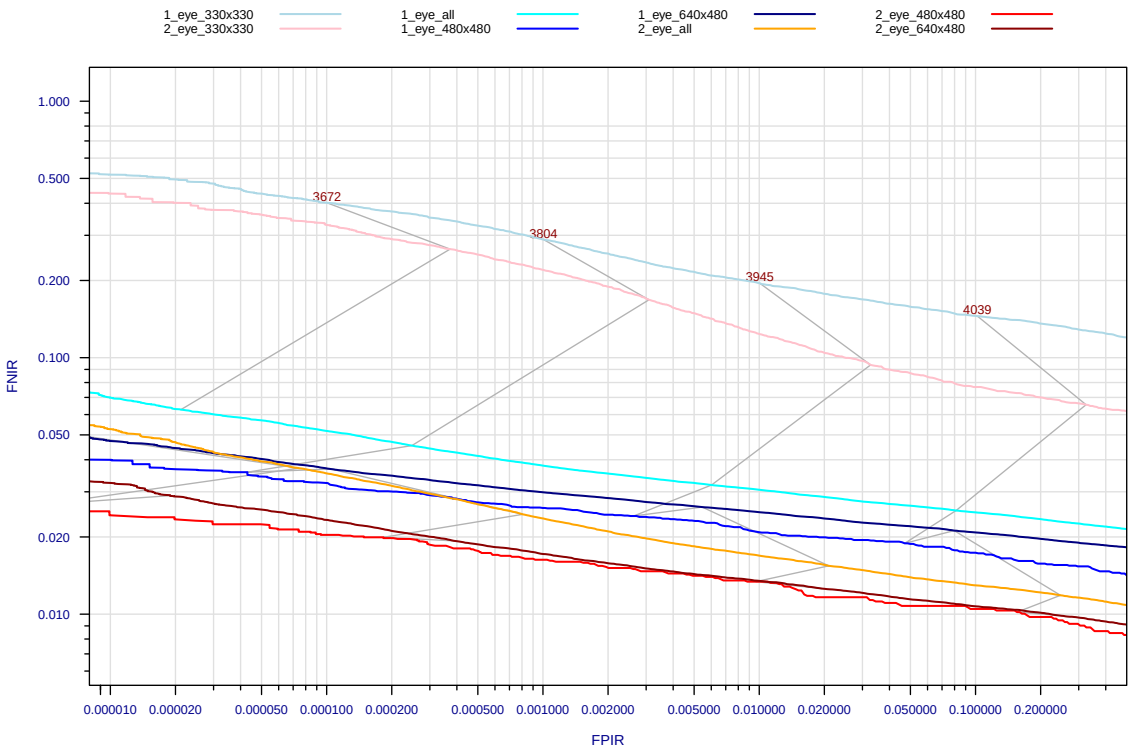

(a) Large search set, $\mathcal{S}_{nb}$

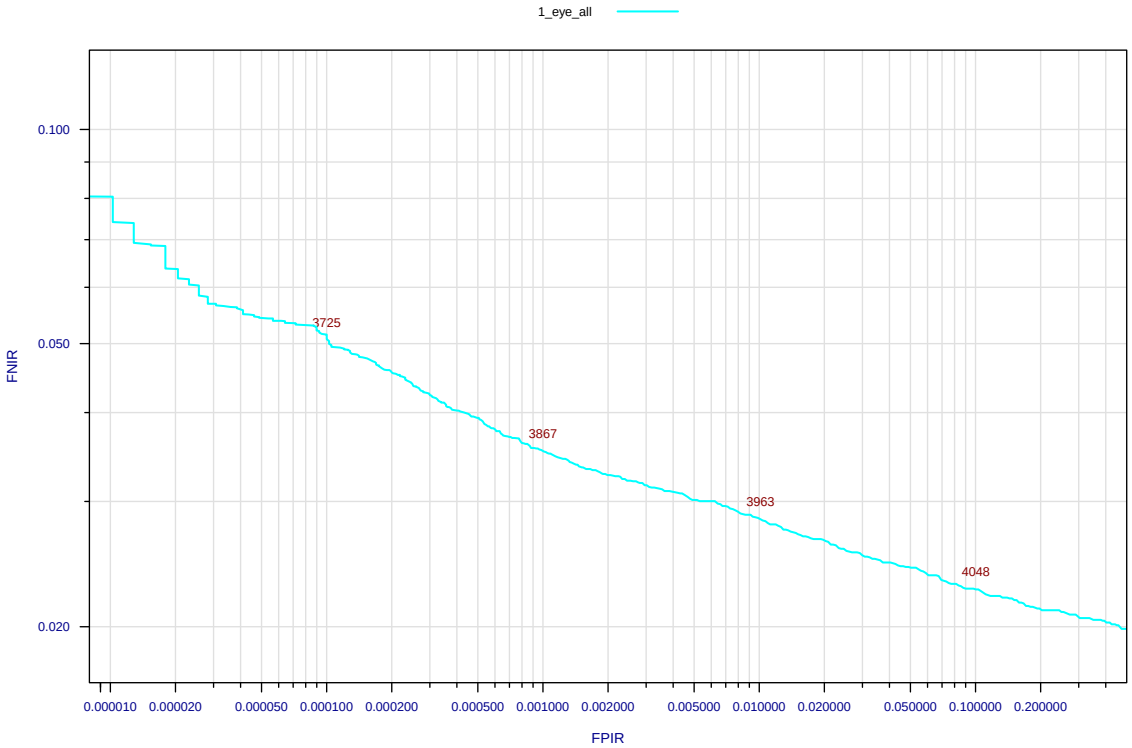

(b) Small search set, $\mathcal{S}_{na}$

Figure 532: DET for implementation R11B executing searches in an enrolled population of N = 1.6 million, broken out for three different image sizes (corresponding broadly to three camera plus ancillary software combinations) of the search image. The acquisition system used for the enrollment image (if any) is ignored in this breakout. Results for single-eye and two-eyes are plotted with two families of color. The straight lines, which link points of constant threshold, show how the two error rates would vary if a fixed threshold were adopted operationally.

FNIR = FALSE NEGATIVE IDENT. RATE FPIR = FALSE POSITIVE IDENT. RATE	N = NEUROTECHNOLOGY U = L1	P = SMU V = MORPHO	Q = IRITECH W = IRISID	R = COGENT X = CROSSMATCH	S = SMARTSENSORS Y = KYNEN	T = CAMBRIDGE

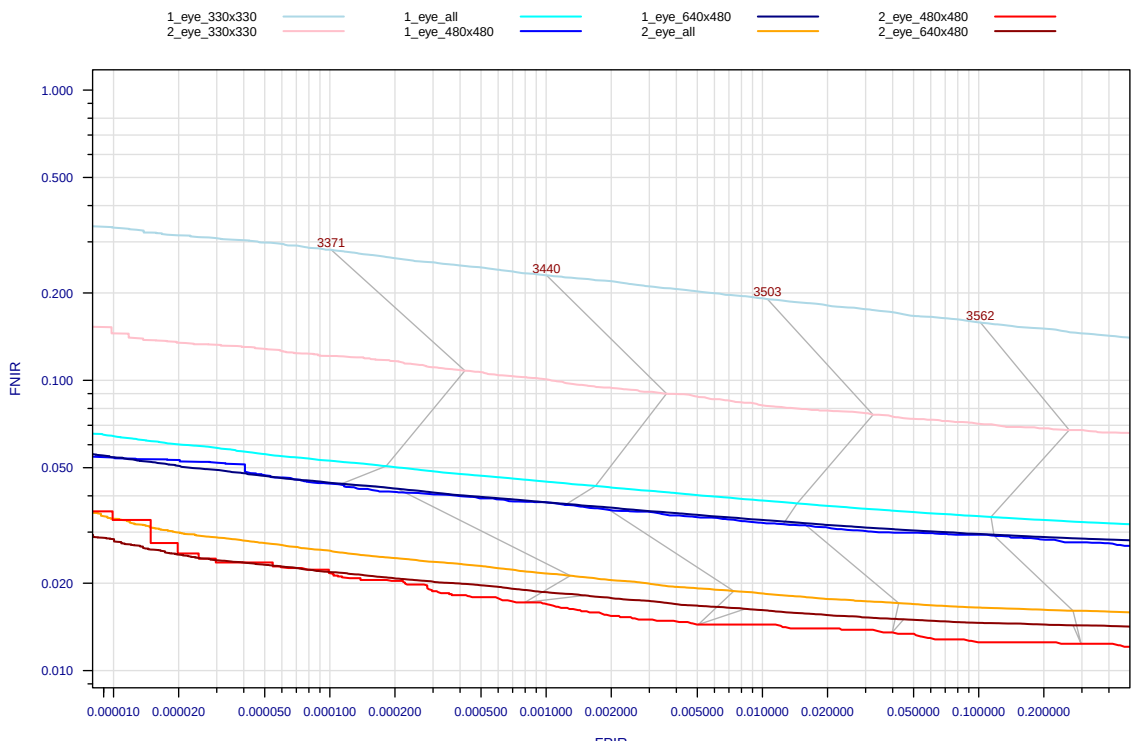

(a) Large search set, $\mathcal{S}_{nb}$

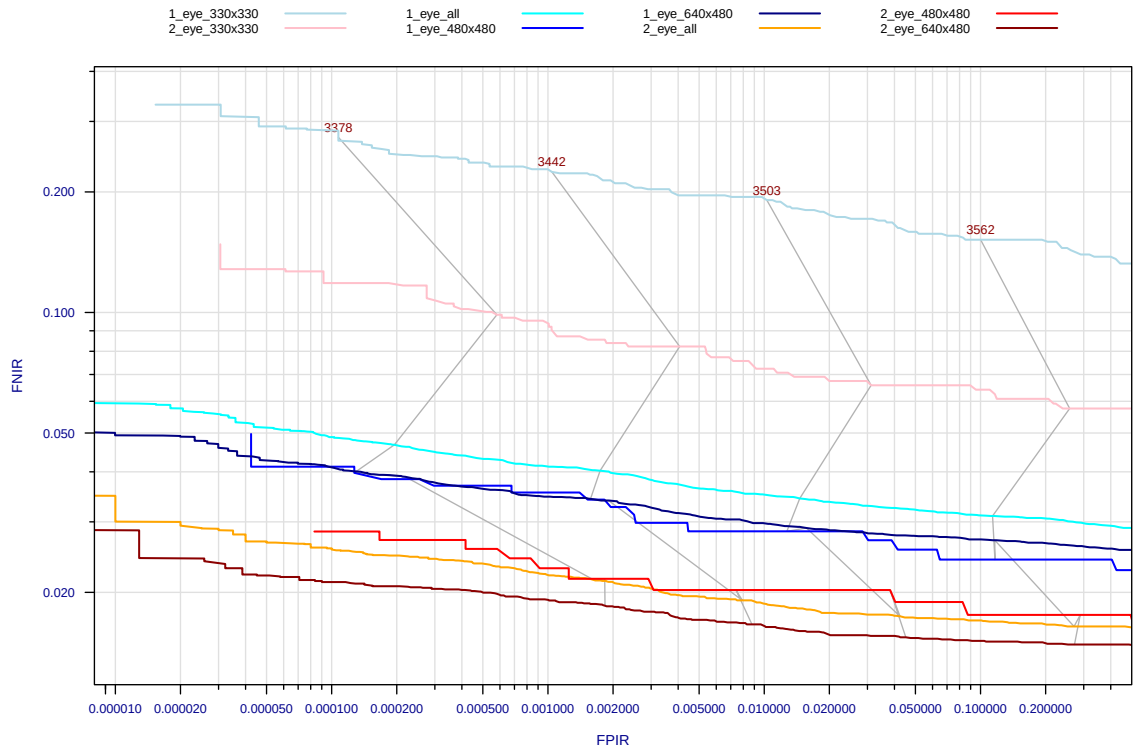

(b) Small search set, $\mathcal{S}_{na}$

Figure 533: DET for implementation R12A executing searches in an enrolled population of N = 1.6 million, broken out for three different image sizes (corresponding broadly to three camera plus ancillary software combinations) of the search image. The acquisition system used for the enrollment image (if any) is ignored in this breakout. Results for single-eye and two-eyes are plotted with two families of color. The straight lines, which link points of constant threshold, show how the two error rates would vary if a fixed threshold were adopted operationally.

FNIR = FALSE NEGATIVE IDENT. RATE FPIR = FALSE POSITIVE IDENT. RATE	N = NEUROTECHNOLOGY U = L1	P = SMU V = MORPHO	Q = IRITECH W = IRISID	R = COGENT X = CROSSMATCH	S = SMARTSENSORS Y = KYNEN	T = CAMBRIDGE

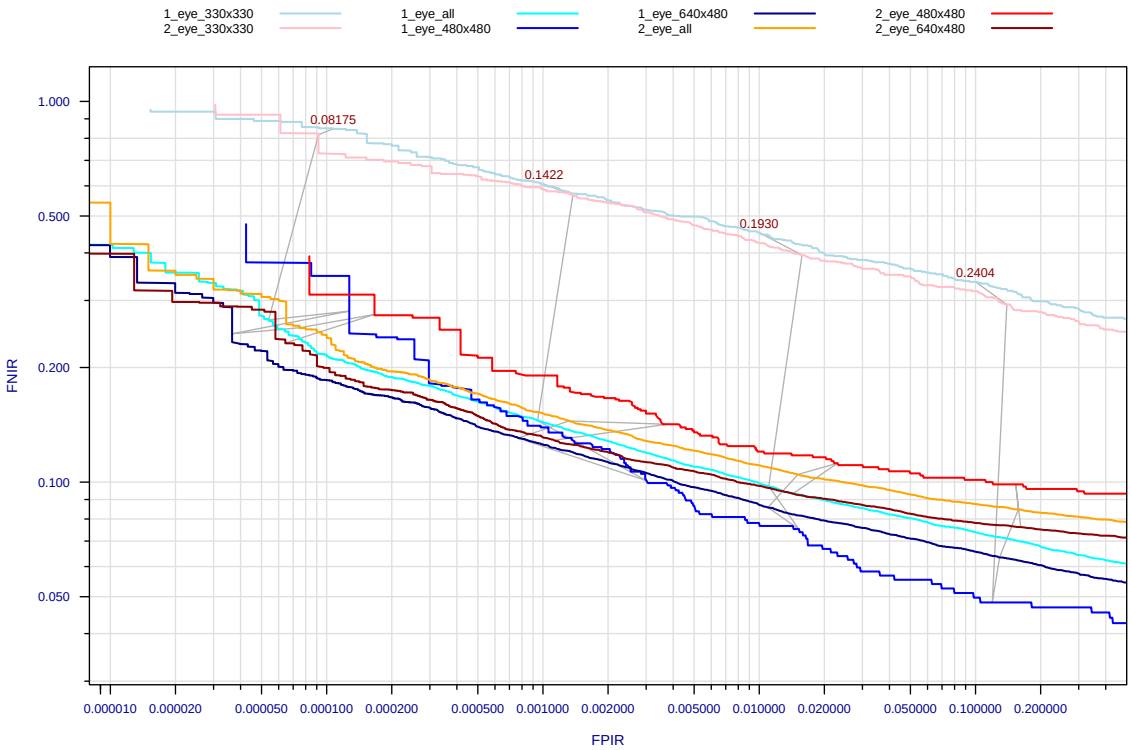

(a) Small search set, $\mathcal{S}_{na}$

Figure 534: DET for implementation S01B executing searches in an enrolled population of N = 1.6 million, broken out for three different image sizes (corresponding broadly to three camera plus ancillary software combinations) of the search image. The acquisition system used for the enrollment image (if any) is ignored in this breakout. Results for single-eye and two-eyes are plotted with two families of color. The straight lines, which link points of constant threshold, show how the two error rates would vary if a fixed threshold were adopted operationally.

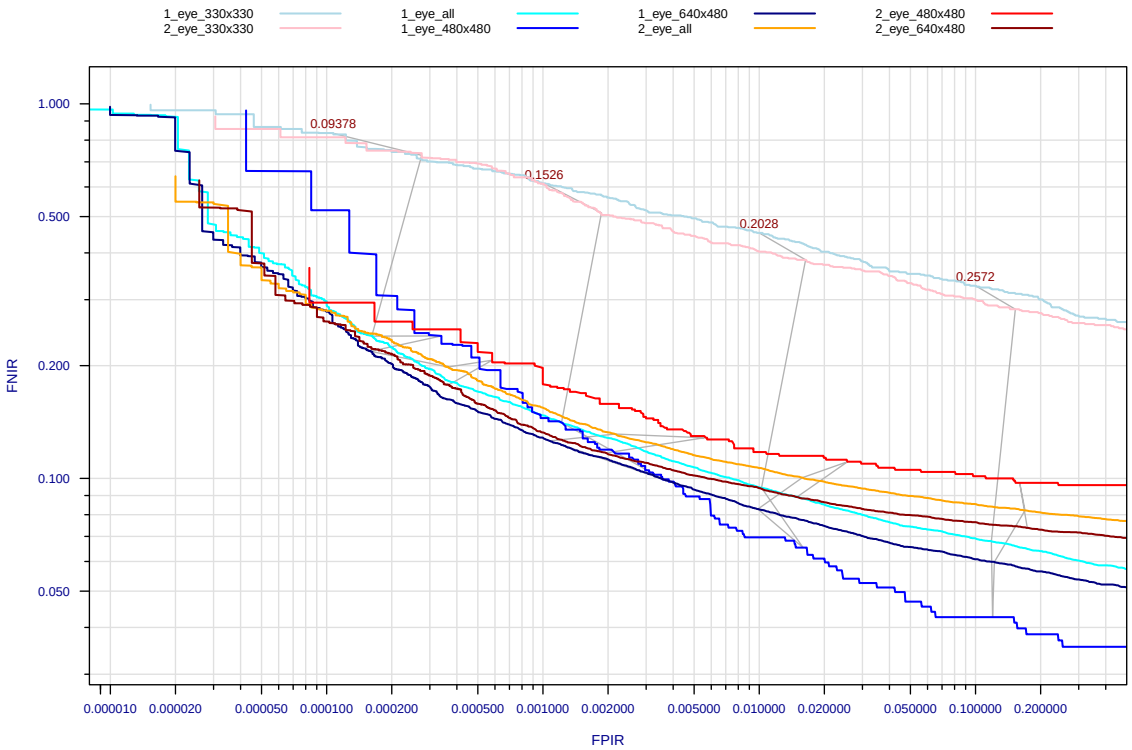

(a) Small search set, $\mathcal{S}_{na}$

Figure 535: DET for implementation S02B executing searches in an enrolled population of N = 1.6 million, broken out for three different image sizes (corresponding broadly to three camera plus ancillary software combinations) of the search image. The acquisition system used for the enrollment image (if any) is ignored in this breakout. Results for single-eye and two-eyes are plotted with two families of color. The straight lines, which link points of constant threshold, show how the two error rates would vary if a fixed threshold were adopted operationally.

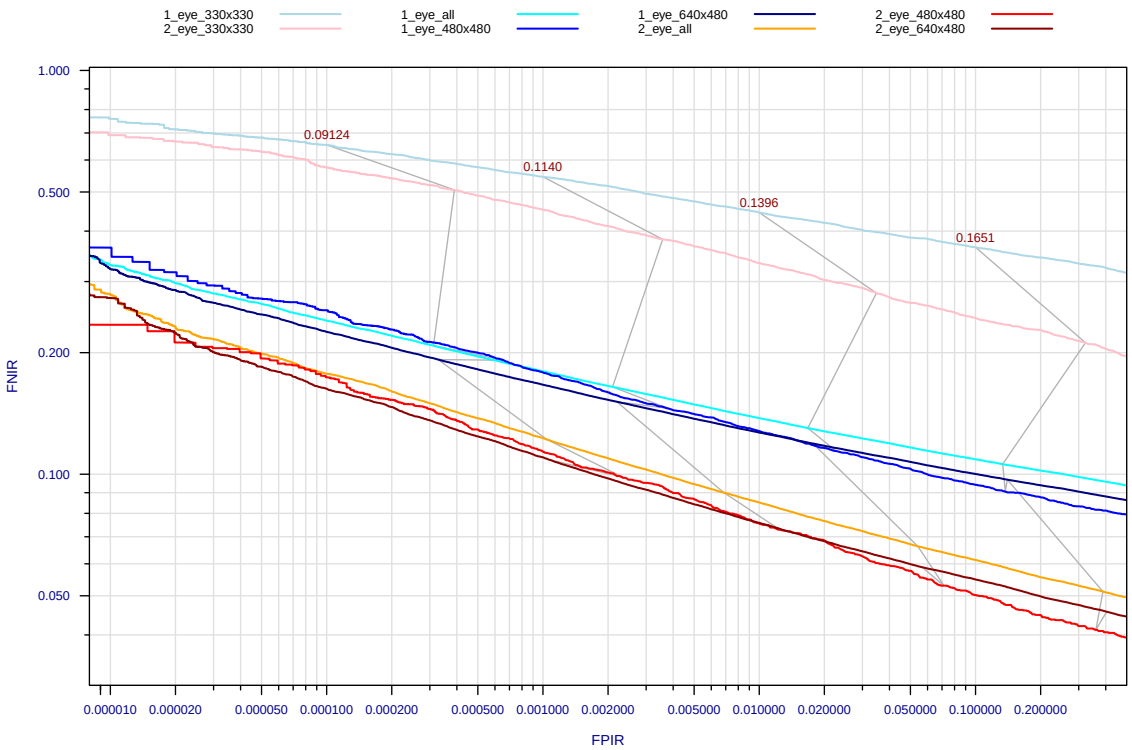

(a) Large search set, $\mathcal{S}_{nb}$

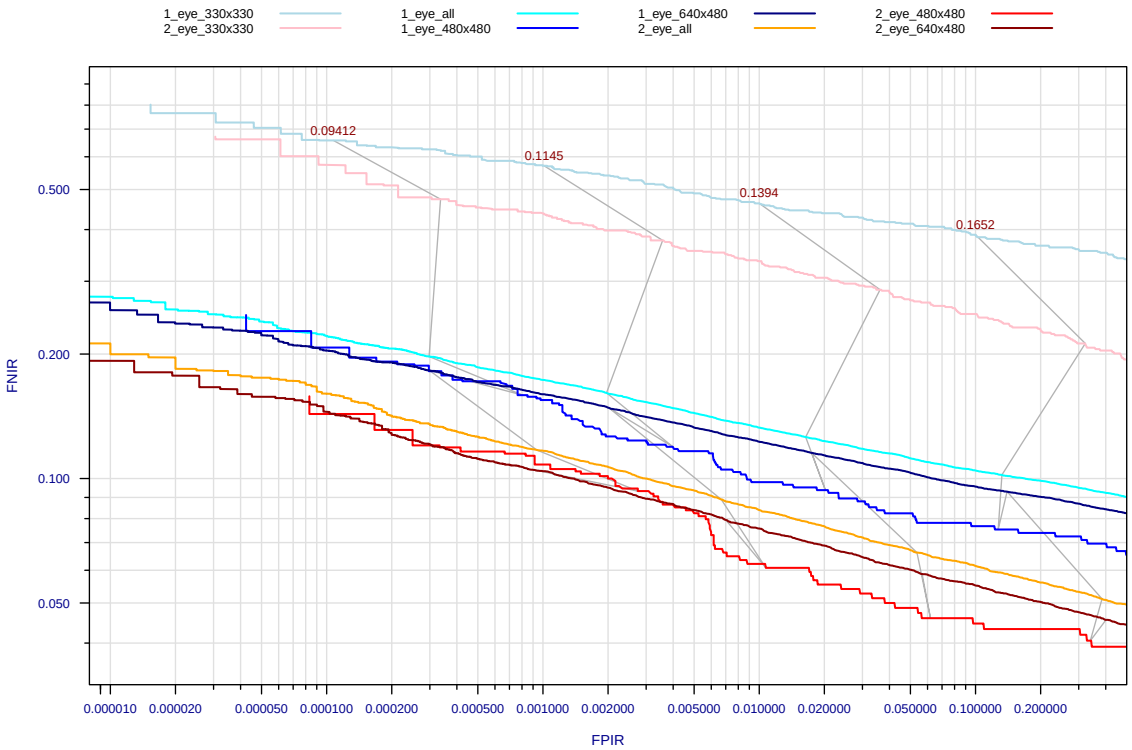

(b) Small search set, $\mathcal{S}_{na}$

Figure 536: DET for implementation S03A executing searches in an enrolled population of N = 1.6 million, broken out for three different image sizes (corresponding broadly to three camera plus ancillary software combinations) of the search image. The acquisition system used for the enrollment image (if any) is ignored in this breakout. Results for single-eye and two-eyes are plotted with two families of color. The straight lines, which link points of constant threshold, show how the two error rates would vary if a fixed threshold were adopted operationally.

FNIR = FALSE NEGATIVE IDENT. RATE FPIR = FALSE POSITIVE IDENT. RATE	N = NEUROTECHNOLOGY U = L1	P = SMU V = MORPHO	Q = IRITECH W = IRISID	R = COGENT X = CROSSMATCH	S = SMARTSENSORS Y = KYNEN	T = CAMBRIDGE

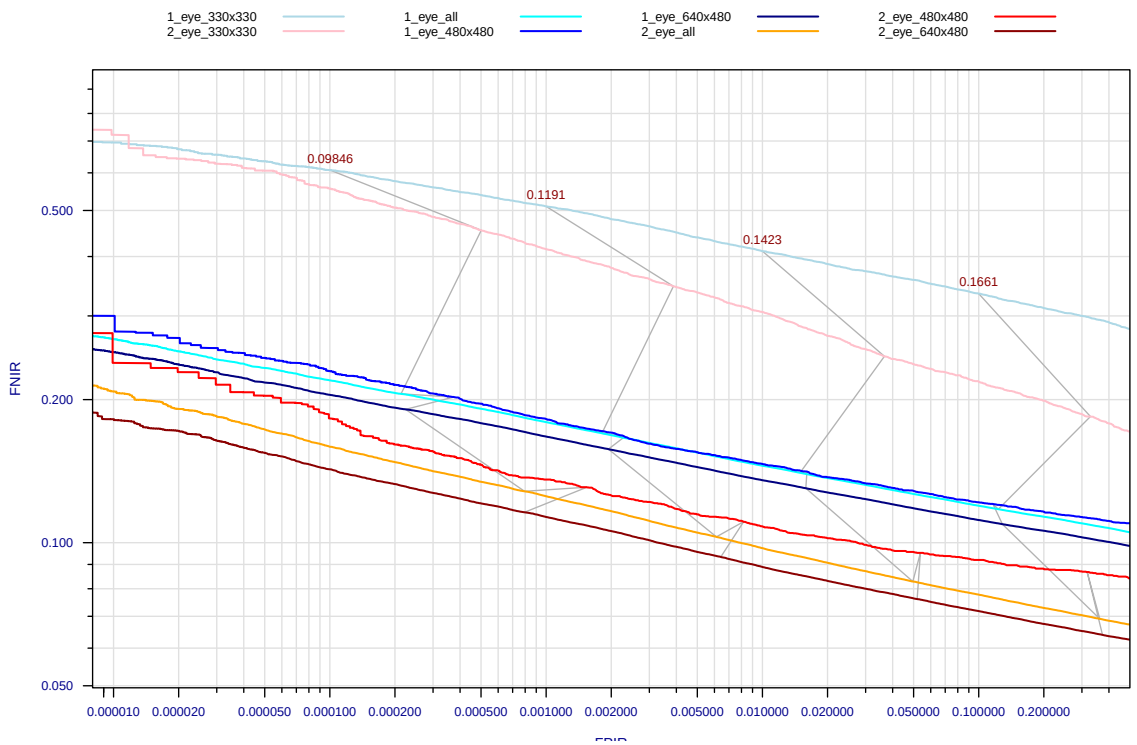

(a) Large search set, $\mathcal{S}_{nb}$

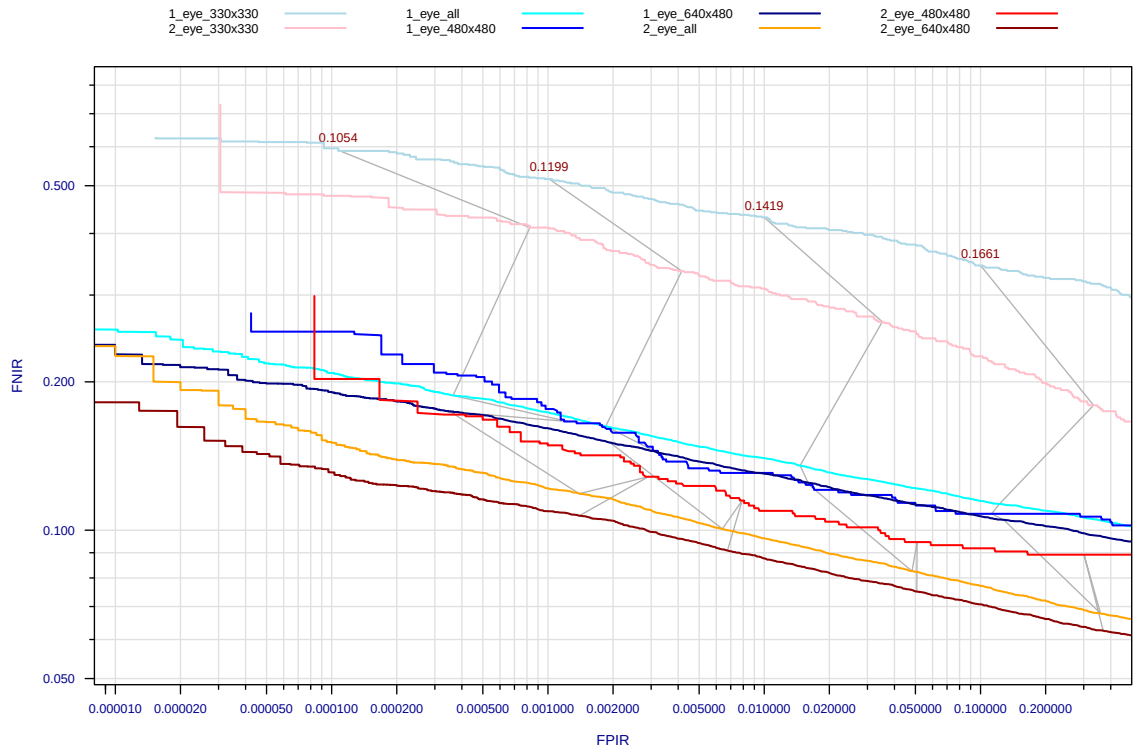

(b) Small search set, $\mathcal{S}_{na}$

Figure 537: DET for implementation S04A executing searches in an enrolled population of N = 1.6 million, broken out for three different image sizes (corresponding broadly to three camera plus ancillary software combinations) of the search image. The acquisition system used for the enrollment image (if any) is ignored in this breakout. Results for single-eye and two-eyes are plotted with two families of color. The straight lines, which link points of constant threshold, show how the two error rates would vary if a fixed threshold were adopted operationally.

FNIR = FALSE NEGATIVE IDENT. RATE FPIR = FALSE POSITIVE IDENT. RATE	N = NEUROTECHNOLOGY U = L1	P = SMU V = MORPHO	Q = IRITECH W = IRISID	R = COGENT X = CROSSMATCH	S = SMARTSENSORS Y = KYNEN	T = CAMBRIDGE

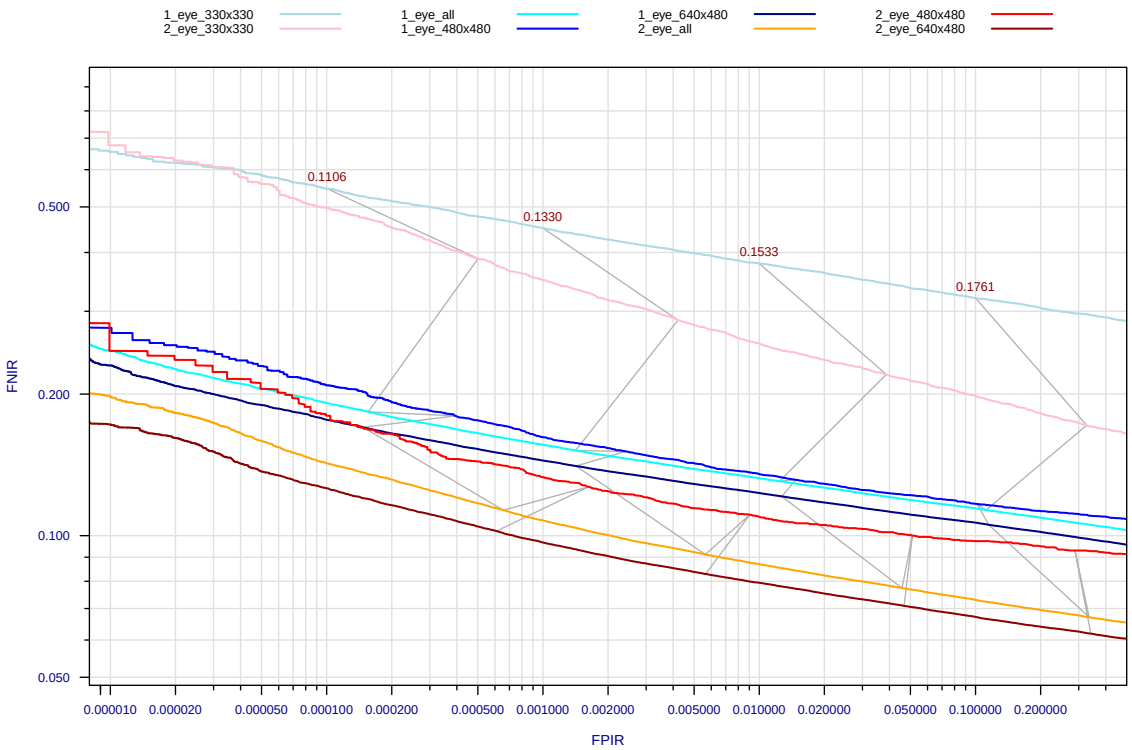

(a) Large search set, $\mathcal{S}_{nb}$

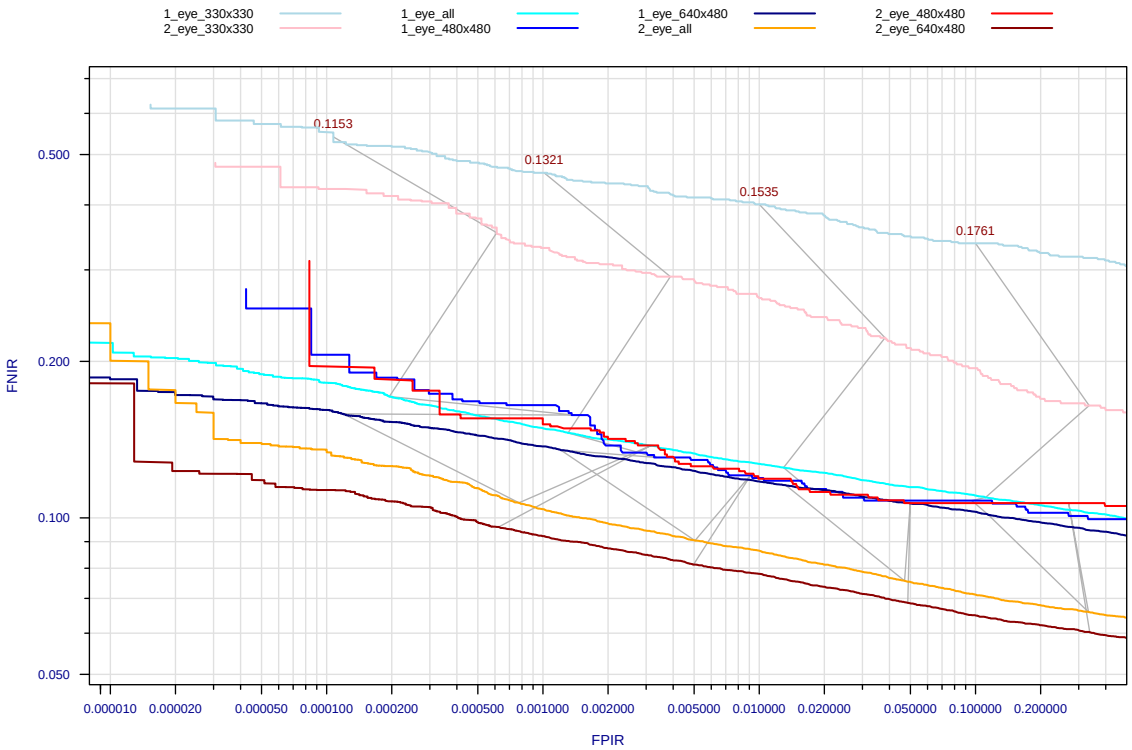

(b) Small search set, $\mathcal{S}_{na}$

Figure 538: DET for implementation S05A executing searches in an enrolled population of N = 1.6 million, broken out for three different image sizes (corresponding broadly to three camera plus ancillary software combinations) of the search image. The acquisition system used for the enrollment image (if any) is ignored in this breakout. Results for single-eye and two-eyes are plotted with two families of color. The straight lines, which link points of constant threshold, show how the two error rates would vary if a fixed threshold were adopted operationally.

FNIR = FALSE NEGATIVE IDENT. RATE FPIR = FALSE POSITIVE IDENT. RATE	N = NEUROTECHNOLOGY U = L1	P = SMU V = MORPHO	Q = IRITECH W = IRISID	R = COGENT X = CROSSMATCH	S = SMARTSENSORS Y = KYNEN	T = CAMBRIDGE

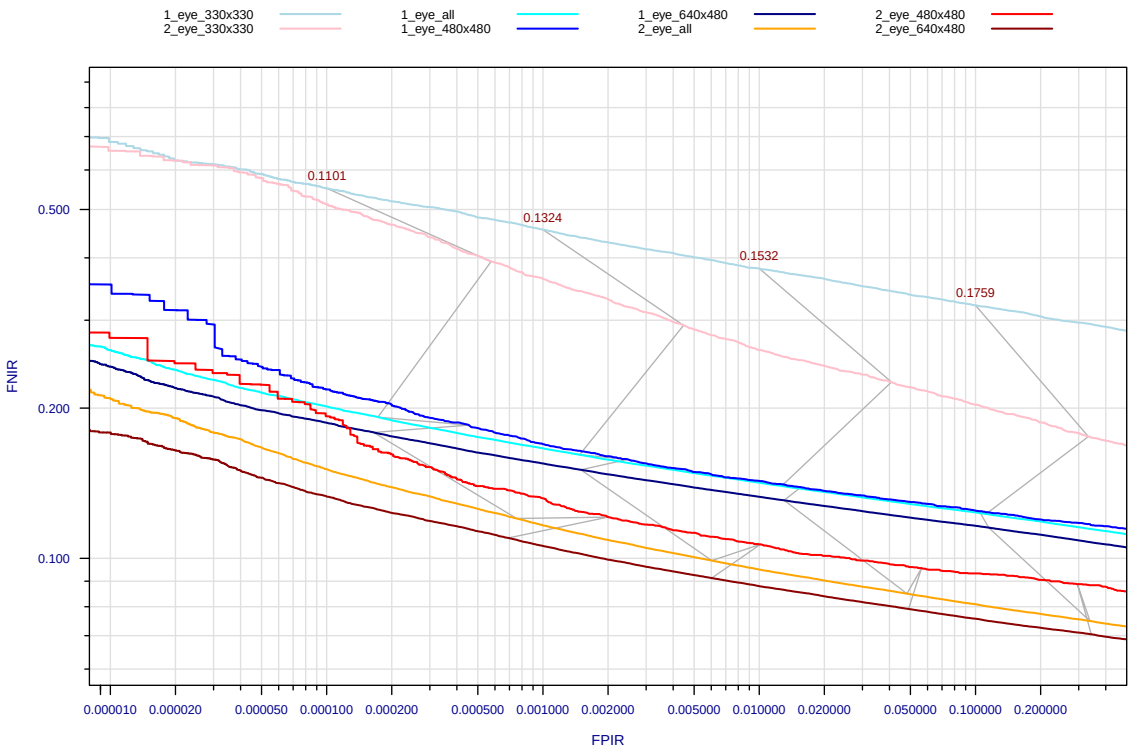

(a) Large search set, $\mathcal{S}_{nb}$

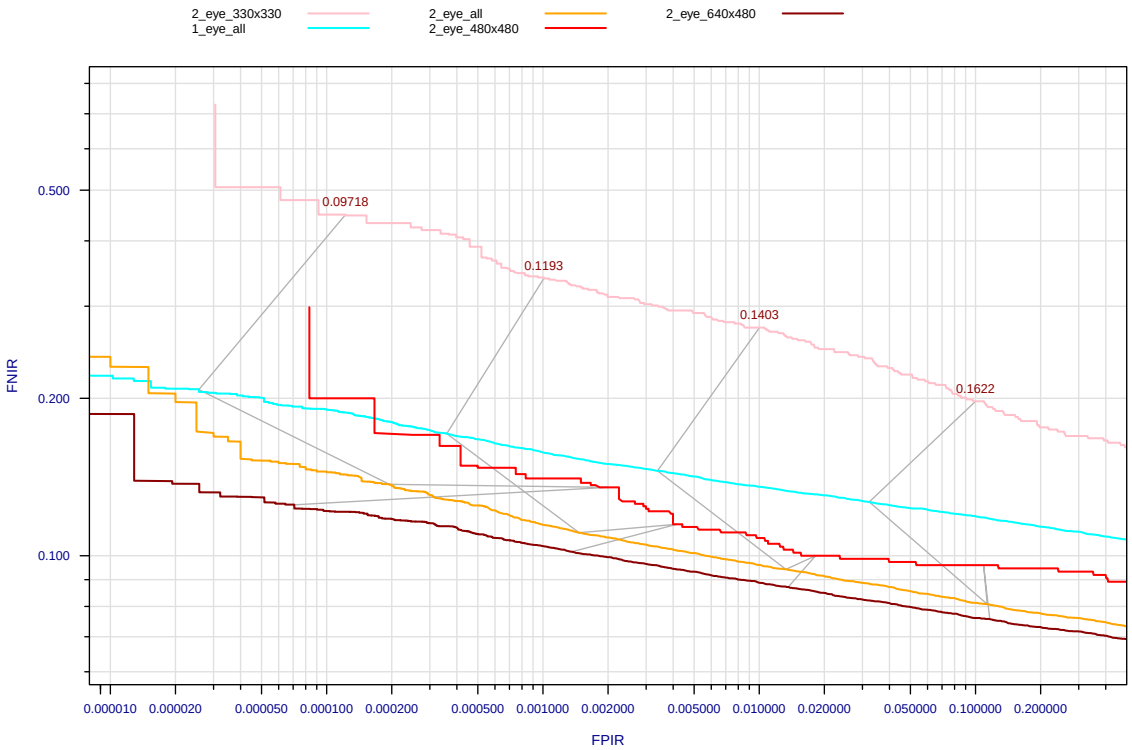

(b) Small search set, $\mathcal{S}_{na}$

Figure 539: DET for implementation S11A executing searches in an enrolled population of N = 1.6 million, broken out for three different image sizes (corresponding broadly to three camera plus ancillary software combinations) of the search image. The acquisition system used for the enrollment image (if any) is ignored in this breakout. Results for single-eye and two-eyes are plotted with two families of color. The straight lines, which link points of constant threshold, show how the two error rates would vary if a fixed threshold were adopted operationally.

FNIR = FALSE NEGATIVE IDENT. RATE FPIR = FALSE POSITIVE IDENT. RATE	N = NEUROTECHNOLOGY U = L1	P = SMU V = MORPHO	Q = IRITECH W = IRISID	R = COGENT X = CROSSMATCH	S = SMARTSENSORS Y = KYNEN	T = CAMBRIDGE

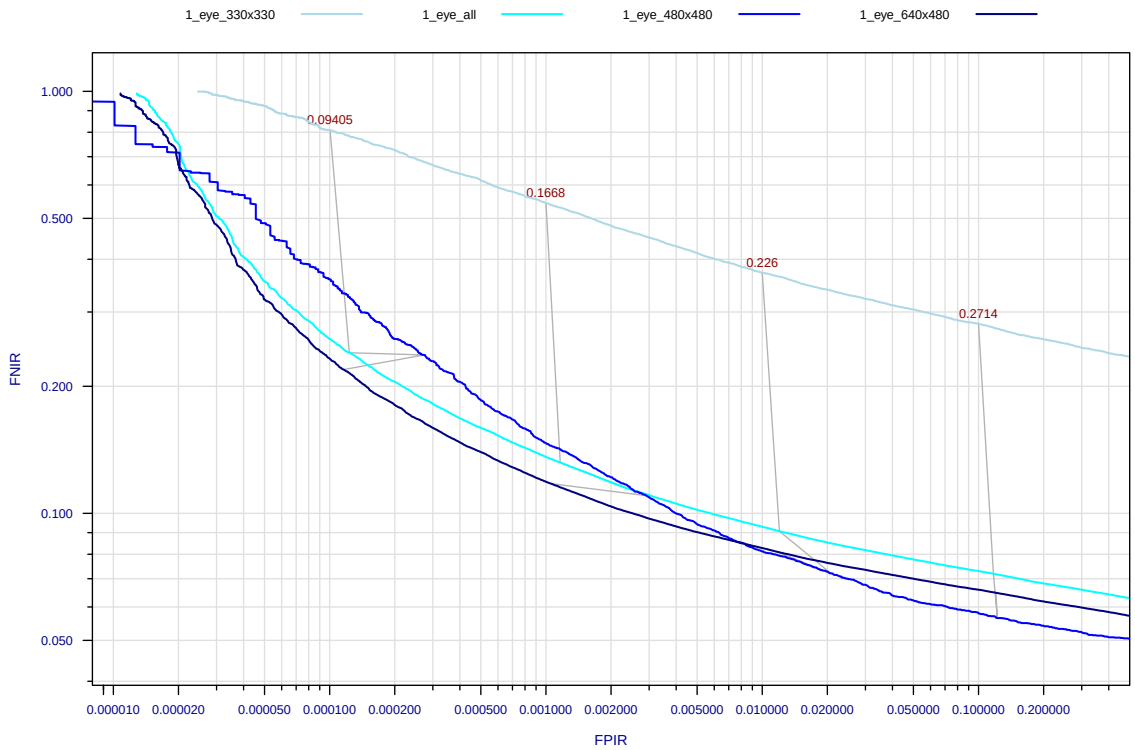

(a) Large search set, $\mathcal{S}_{nb}$

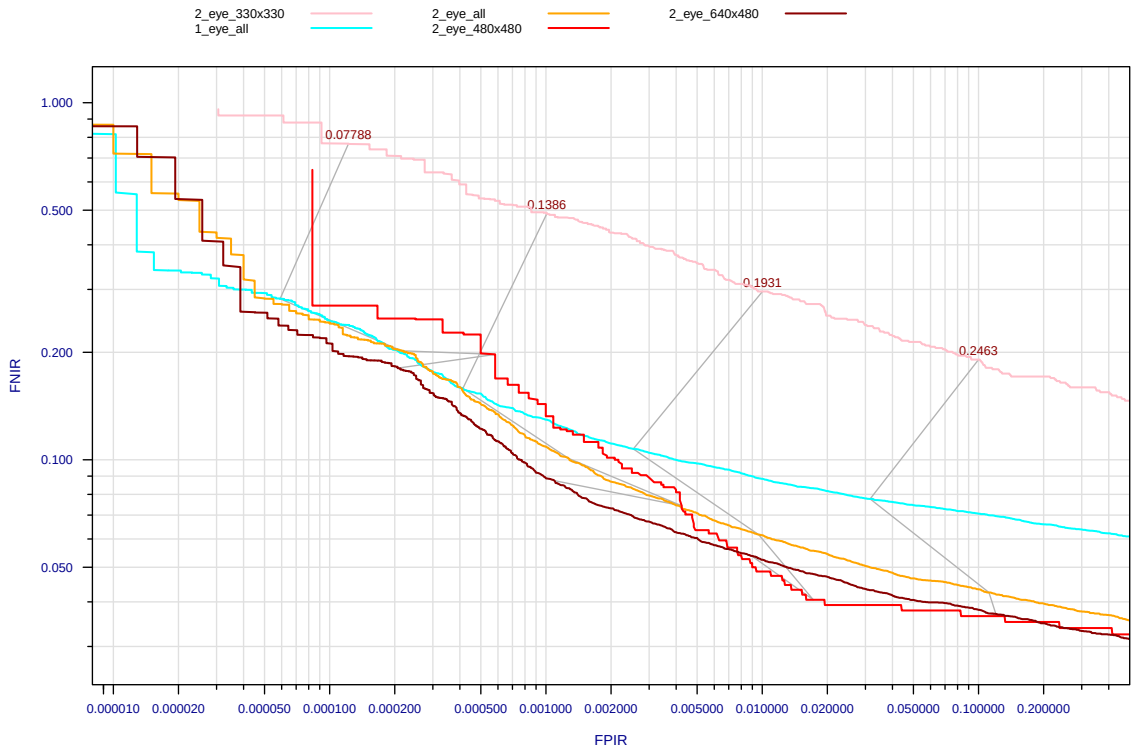

(b) Small search set, $\mathcal{S}_{na}$

Figure 540: DET for implementation S11B executing searches in an enrolled population of N = 1.6 million, broken out for three different image sizes (corresponding broadly to three camera plus ancillary software combinations) of the search image. The acquisition system used for the enrollment image (if any) is ignored in this breakout. Results for single-eye and two-eyes are plotted with two families of color. The straight lines, which link points of constant threshold, show how the two error rates would vary if a fixed threshold were adopted operationally.

FNIR = FALSE NEGATIVE IDENT. RATE FPIR = FALSE POSITIVE IDENT. RATE	N = NEUROTECHNOLOGY U = L1	P = SMU V = MORPHO	Q = IRITECH W = IRISID	R = COGENT X = CROSSMATCH	S = SMARTSENSORS Y = KYNEN	T = CAMBRIDGE

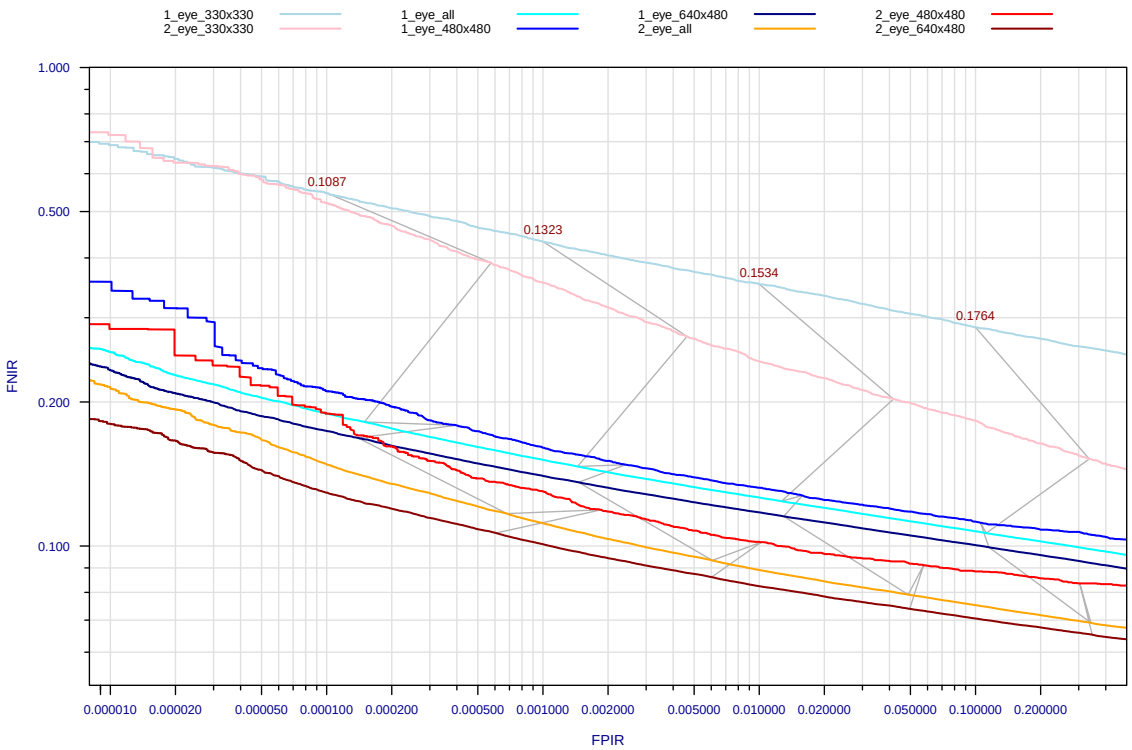

(a) Large search set, $\mathcal{S}_{nb}$

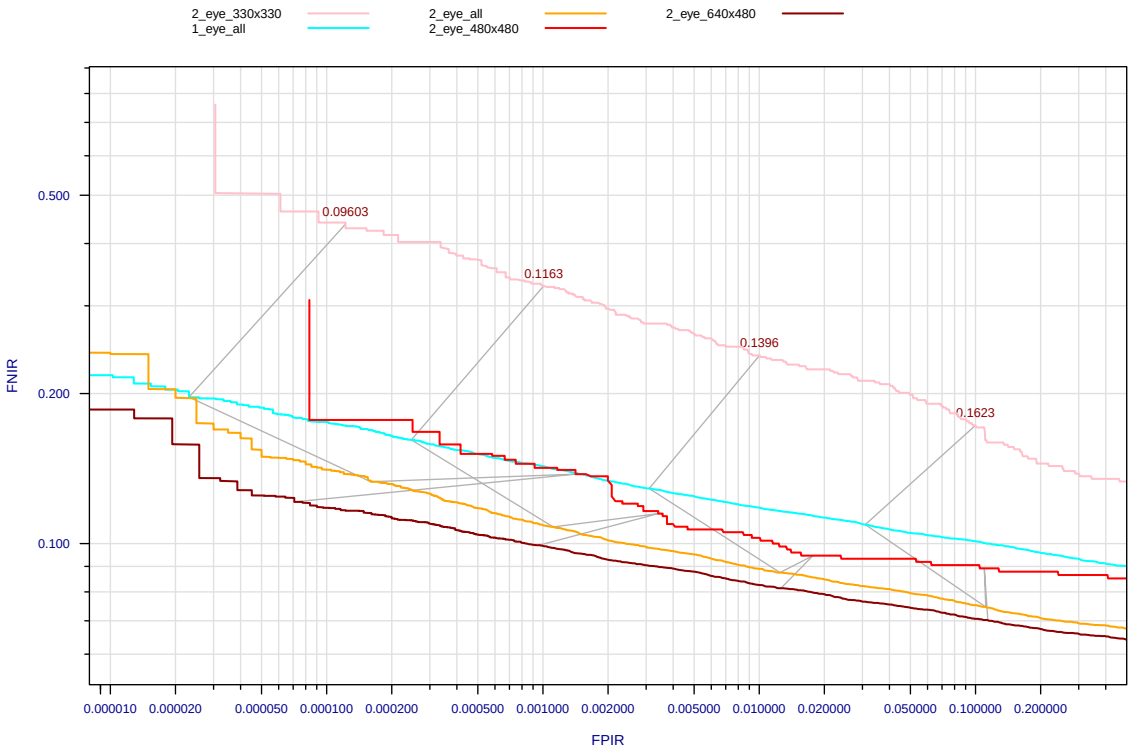

(b) Small search set, $\mathcal{S}_{na}$

Figure 541: DET for implementation S12A executing searches in an enrolled population of N = 1.6 million, broken out for three different image sizes (corresponding broadly to three camera plus ancillary software combinations) of the search image. The acquisition system used for the enrollment image (if any) is ignored in this breakout. Results for single-eye and two-eyes are plotted with two families of color. The straight lines, which link points of constant threshold, show how the two error rates would vary if a fixed threshold were adopted operationally.

FNIR = FALSE NEGATIVE IDENT. RATE FPIR = FALSE POSITIVE IDENT. RATE	N = NEUROTECHNOLOGY U = L1	P = SMU V = MORPHO	Q = IRITECH W = IRISID	R = COGENT X = CROSSMATCH	S = SMARTSENSORS Y = KYNEN	T = CAMBRIDGE

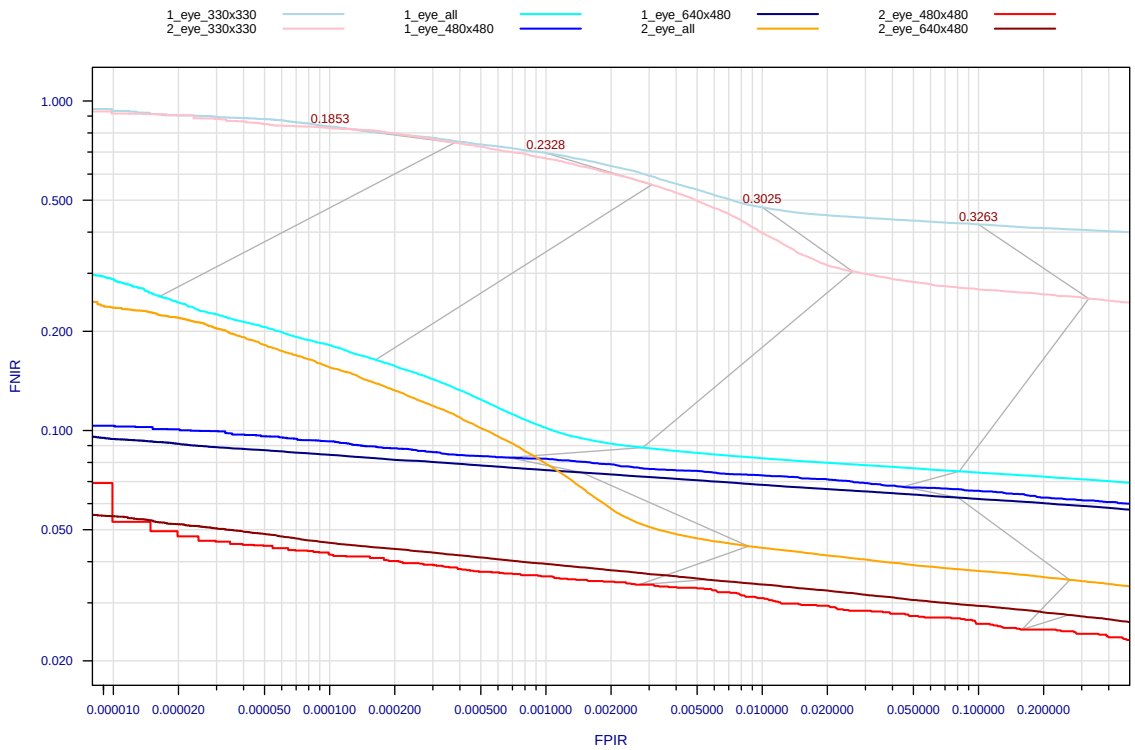

(a) Large search set, $\mathcal{S}_{nb}$

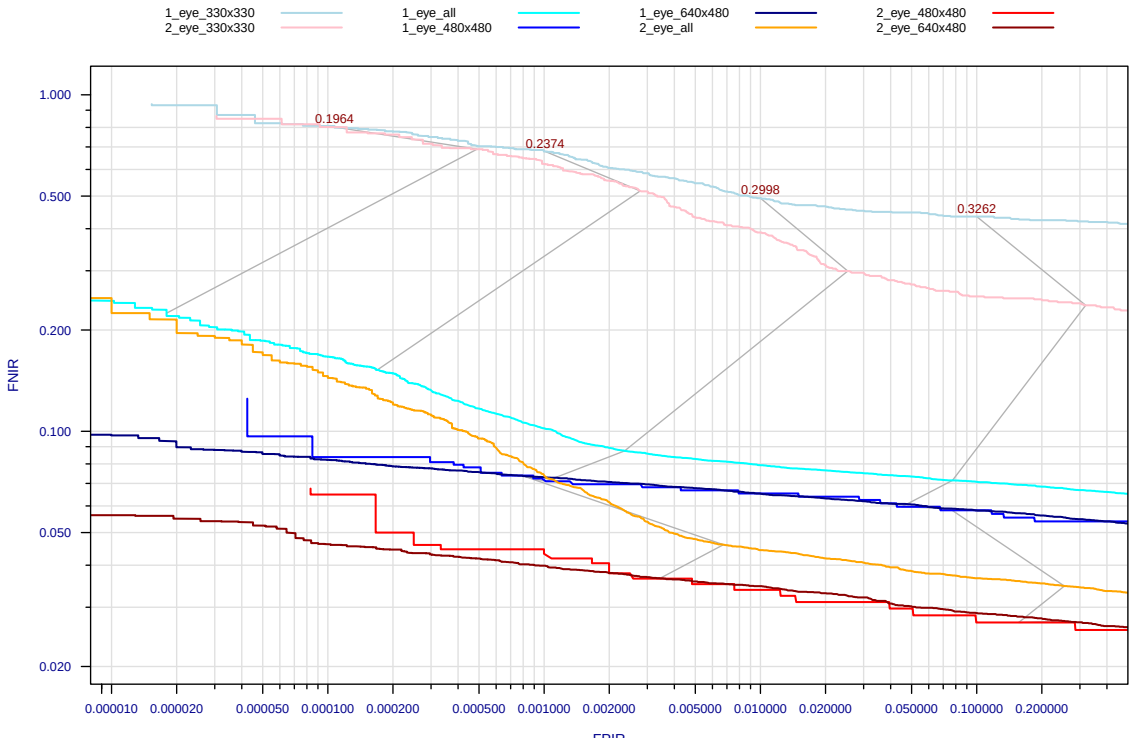

(b) Small search set, $\mathcal{S}_{na}$

Figure 542: DET for implementation T01A executing searches in an enrolled population of N = 1.6 million, broken out for three different image sizes (corresponding broadly to three camera plus ancillary software combinations) of the search image. The acquisition system used for the enrollment image (if any) is ignored in this breakout. Results for single-eye and two-eyes are plotted with two families of color. The straight lines, which link points of constant threshold, show how the two error rates would vary if a fixed threshold were adopted operationally.

FNIR = FALSE NEGATIVE IDENT. RATE FPIR = FALSE POSITIVE IDENT. RATE	N = NEUROTECHNOLOGY U = L1	P = SMU V = MORPHO	Q = IRITECH W = IRISID	R = COGENT X = CROSSMATCH	S = SMARTSENSORS Y = KYNEN	T = CAMBRIDGE

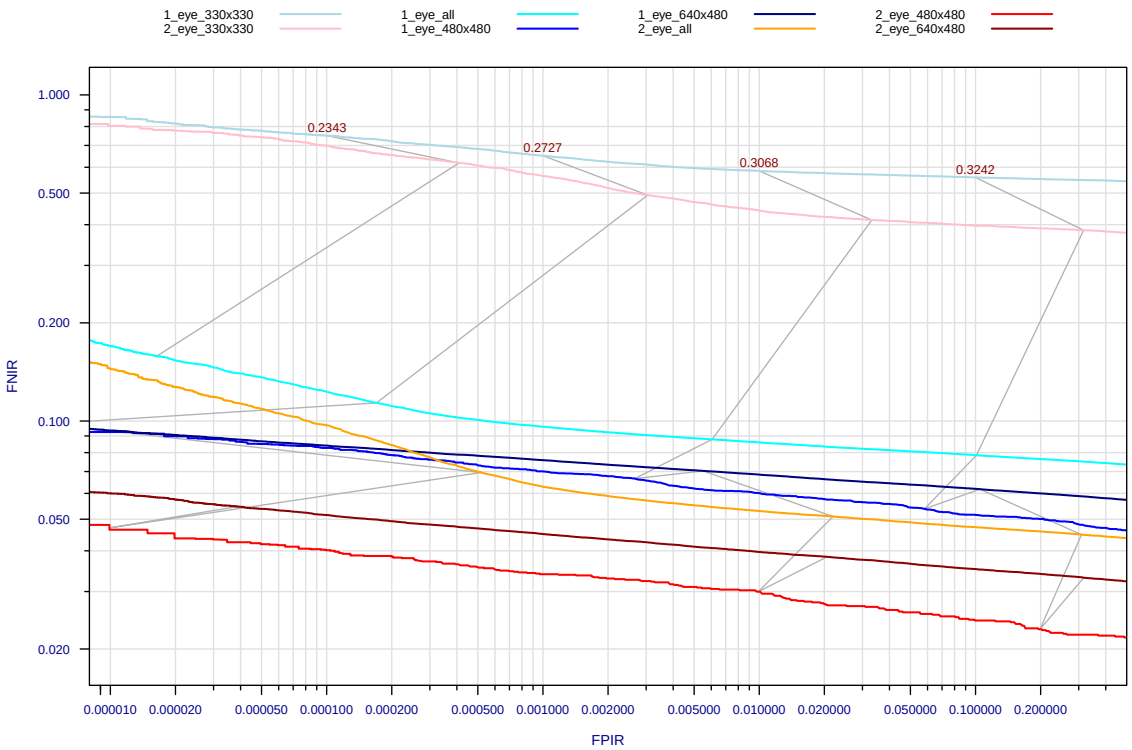

(a) Large search set, $\mathcal{S}_{nb}$

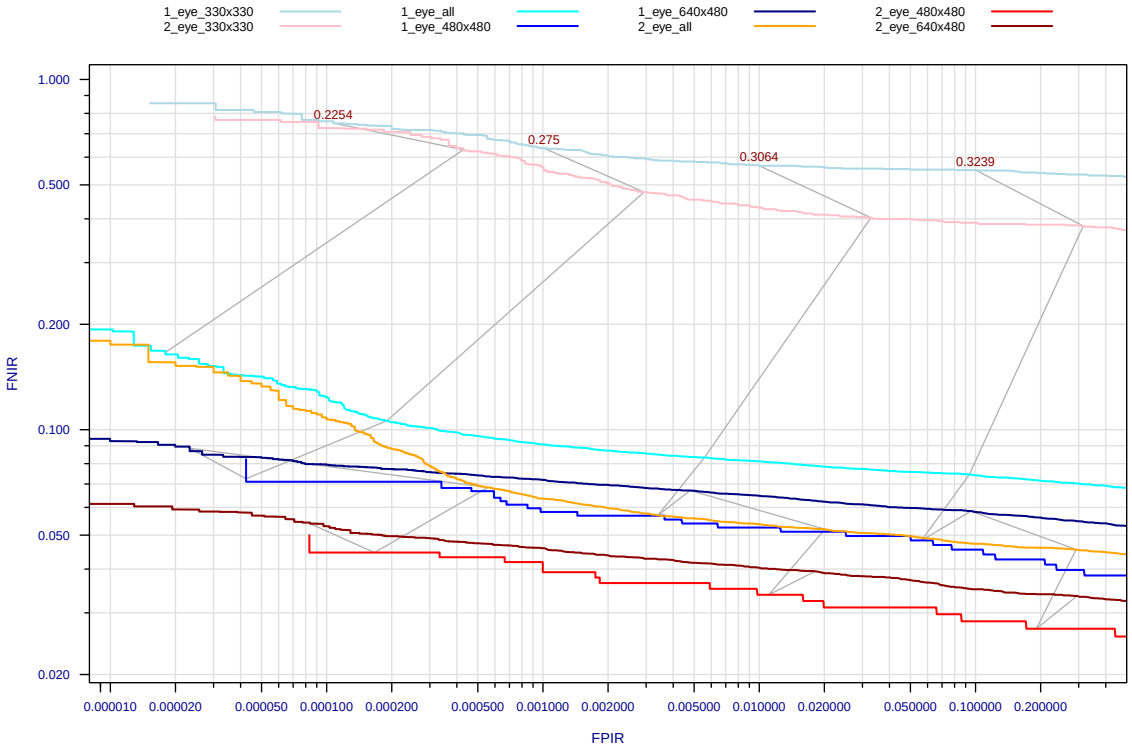

(b) Small search set, $\mathcal{S}_{na}$

Figure 543: DET for implementation T01B executing searches in an enrolled population of N = 1.6 million, broken out for three different image sizes (corresponding broadly to three camera plus ancillary software combinations) of the search image. The acquisition system used for the enrollment image (if any) is ignored in this breakout. Results for single-eye and two-eyes are plotted with two families of color. The straight lines, which link points of constant threshold, show how the two error rates would vary if a fixed threshold were adopted operationally.

FNIR = FALSE NEGATIVE IDENT. RATE FPIR = FALSE POSITIVE IDENT. RATE	N = NEUROTECHNOLOGY U = L1	P = SMU V = MORPHO	Q = IRITECH W = IRISID	R = COGENT X = CROSSMATCH	S = SMARTSENSORS Y = KYNEN	T = CAMBRIDGE

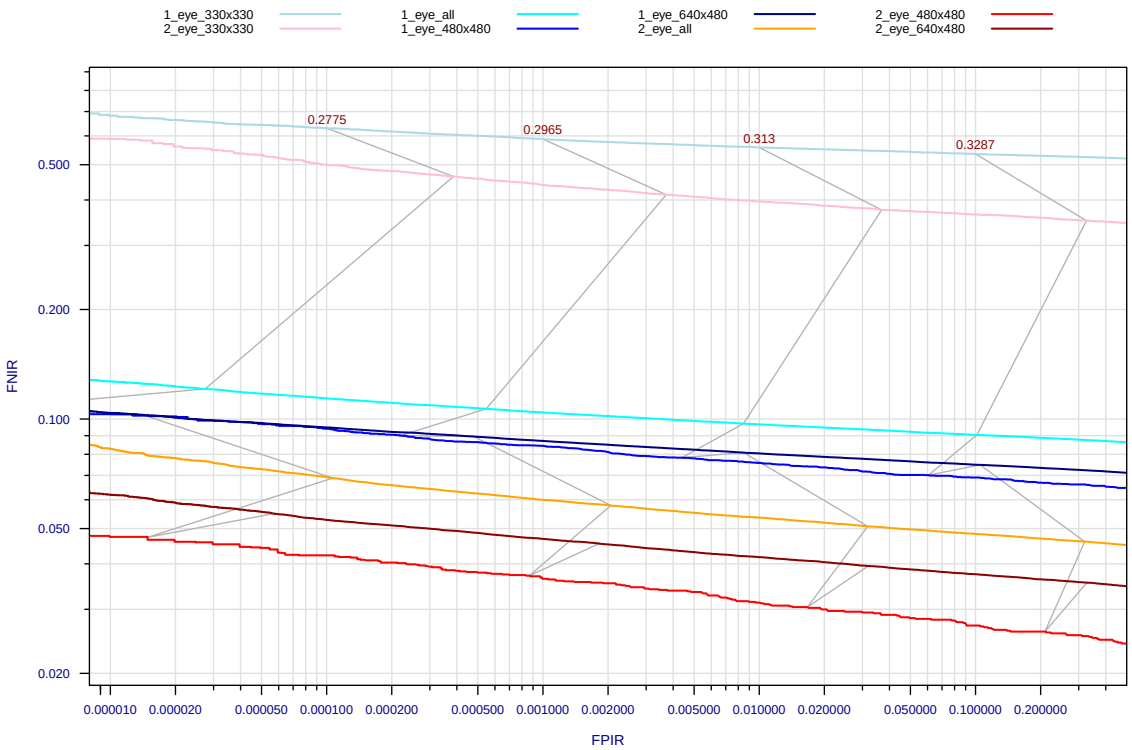

(a) Large search set, $\mathcal{S}_{nb}$

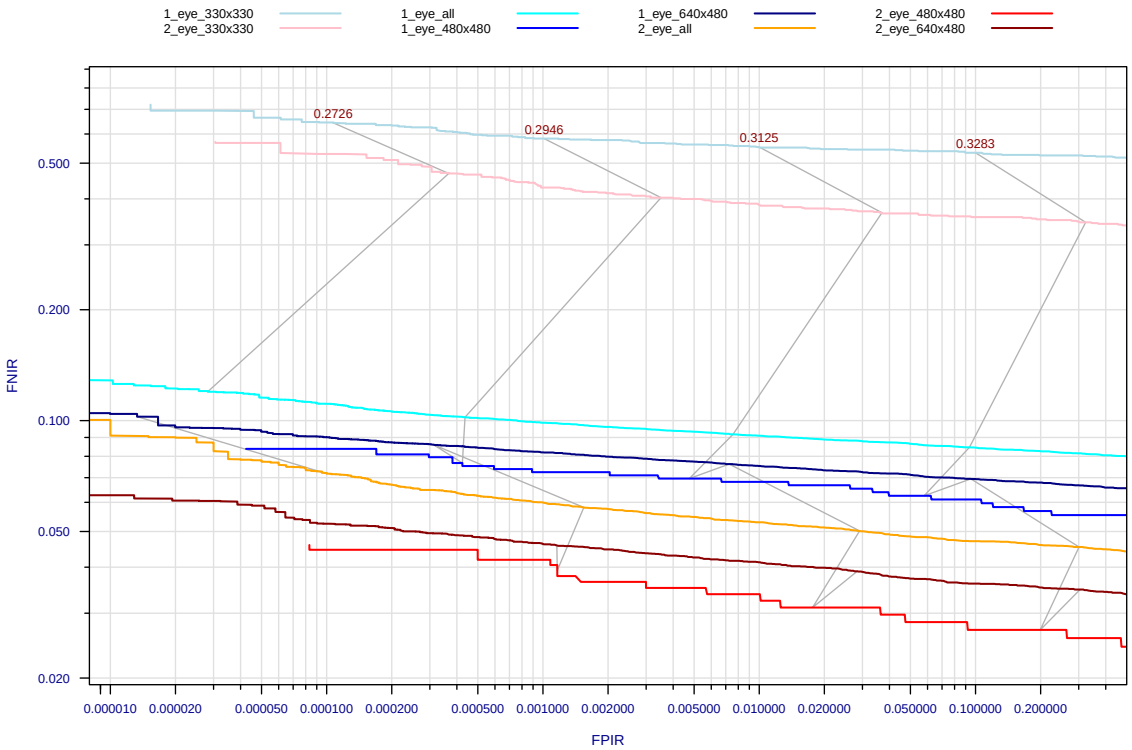

(b) Small search set, $\mathcal{S}_{na}$

Figure 544: DET for implementation T02A executing searches in an enrolled population of N = 1.6 million, broken out for three different image sizes (corresponding broadly to three camera plus ancillary software combinations) of the search image. The acquisition system used for the enrollment image (if any) is ignored in this breakout. Results for single-eye and two-eyes are plotted with two families of color. The straight lines, which link points of constant threshold, show how the two error rates would vary if a fixed threshold were adopted operationally.

FNIR = FALSE NEGATIVE IDENT. RATE FPIR = FALSE POSITIVE IDENT. RATE	N = NEUROTECHNOLOGY U = L1	P = SMU V = MORPHO	Q = IRITECH W = IRISID	R = COGENT X = CROSSMATCH	S = SMARTSENSORS Y = KYNEN	T = CAMBRIDGE

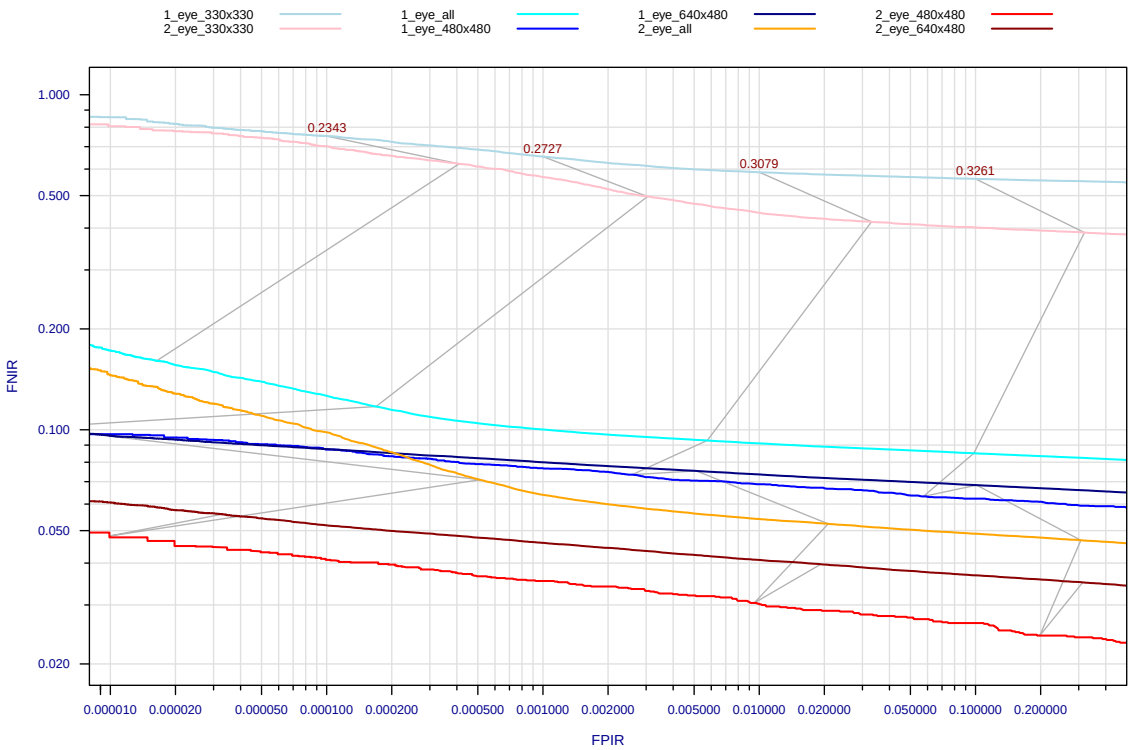

(a) Large search set, $\mathcal{S}_{nb}$

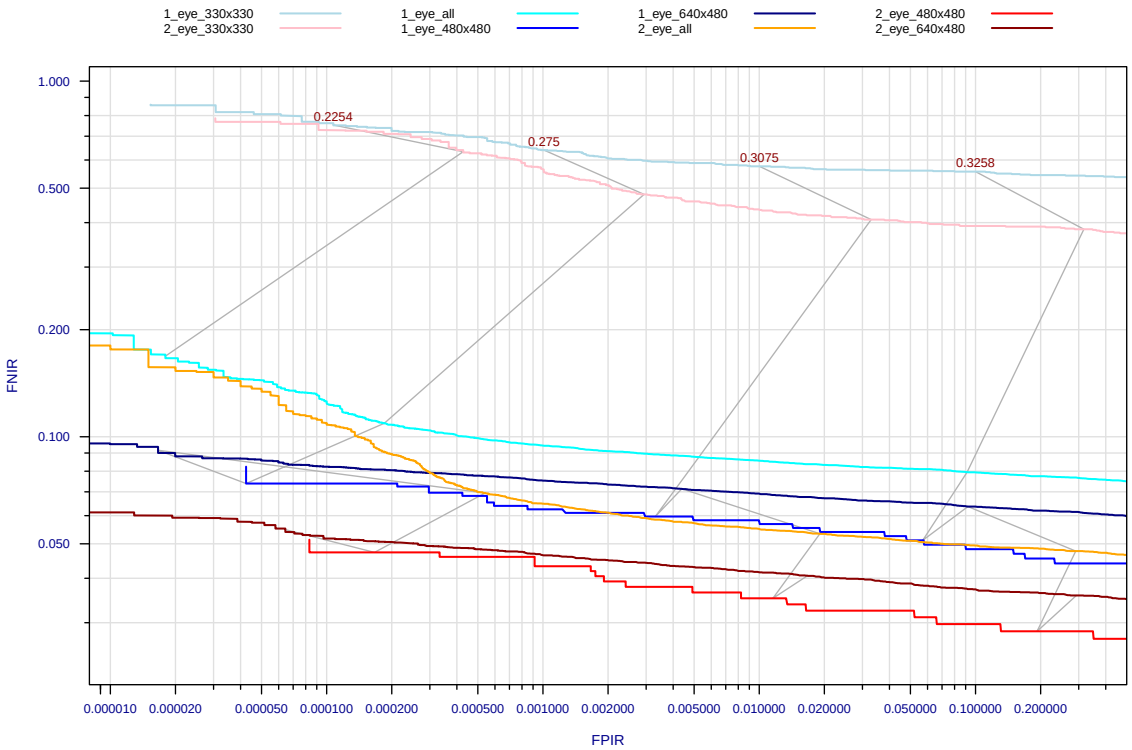

(b) Small search set, $\mathcal{S}_{na}$

Figure 545: DET for implementation T02B executing searches in an enrolled population of N = 1.6 million, broken out for three different image sizes (corresponding broadly to three camera plus ancillary software combinations) of the search image. The acquisition system used for the enrollment image (if any) is ignored in this breakout. Results for single-eye and two-eyes are plotted with two families of color. The straight lines, which link points of constant threshold, show how the two error rates would vary if a fixed threshold were adopted operationally.

FNIR = FALSE NEGATIVE IDENT. RATE FPIR = FALSE POSITIVE IDENT. RATE	N = NEUROTECHNOLOGY U = L1	P = SMU V = MORPHO	Q = IRITECH W = IRISID	R = COGENT X = CROSSMATCH	S = SMARTSENSORS Y = KYNEN	T = CAMBRIDGE

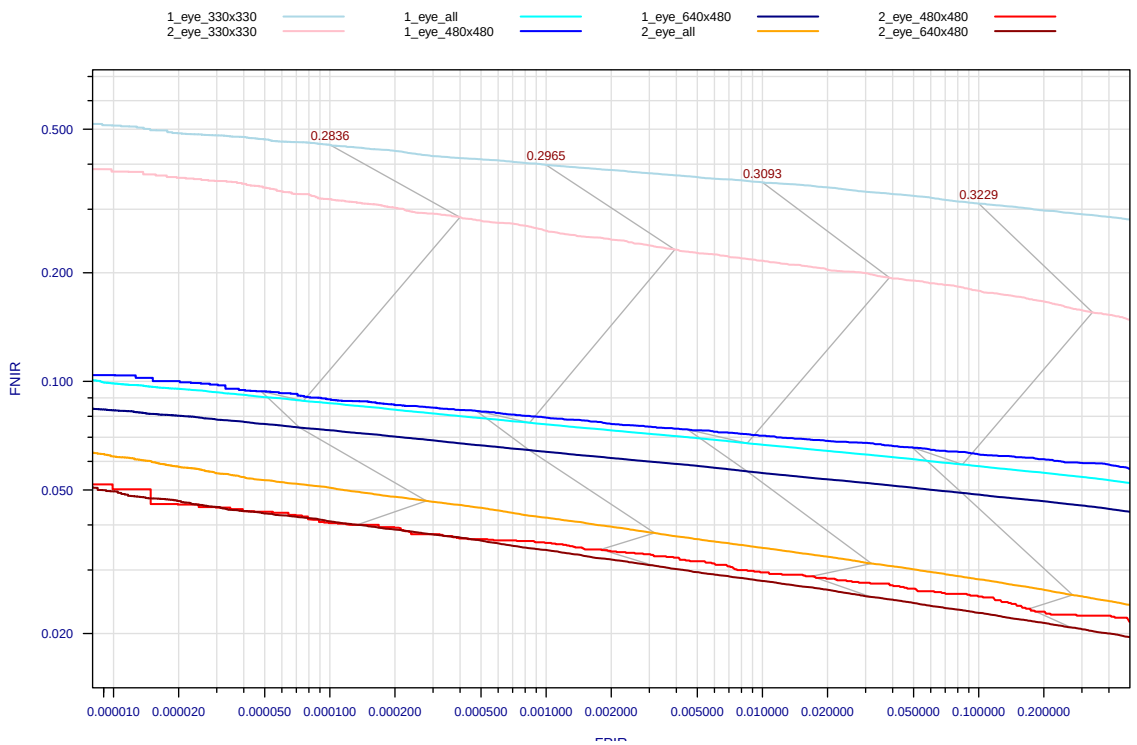

(a) Large search set, $\mathcal{S}_{nb}$

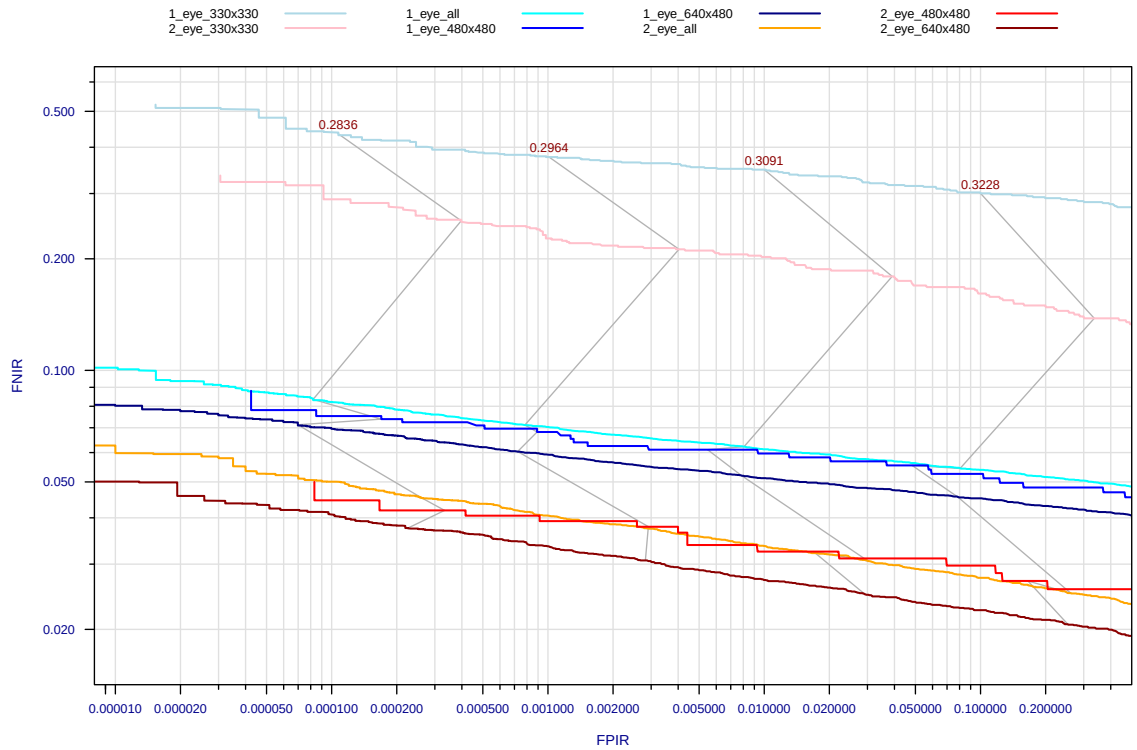

(b) Small search set, $\mathcal{S}_{na}$

Figure 546: DET for implementation T03A executing searches in an enrolled population of N = 1.6 million, broken out for three different image sizes (corresponding broadly to three camera plus ancillary software combinations) of the search image. The acquisition system used for the enrollment image (if any) is ignored in this breakout. Results for single-eye and two-eyes are plotted with two families of color. The straight lines, which link points of constant threshold, show how the two error rates would vary if a fixed threshold were adopted operationally.

FNIR = FALSE NEGATIVE IDENT. RATE FPIR = FALSE POSITIVE IDENT. RATE	N = NEUROTECHNOLOGY U = L1	P = SMU V = MORPHO	Q = IRITECH W = IRISID	R = COGENT X = CROSSMATCH	S = SMARTSENSORS Y = KYNEN	T = CAMBRIDGE

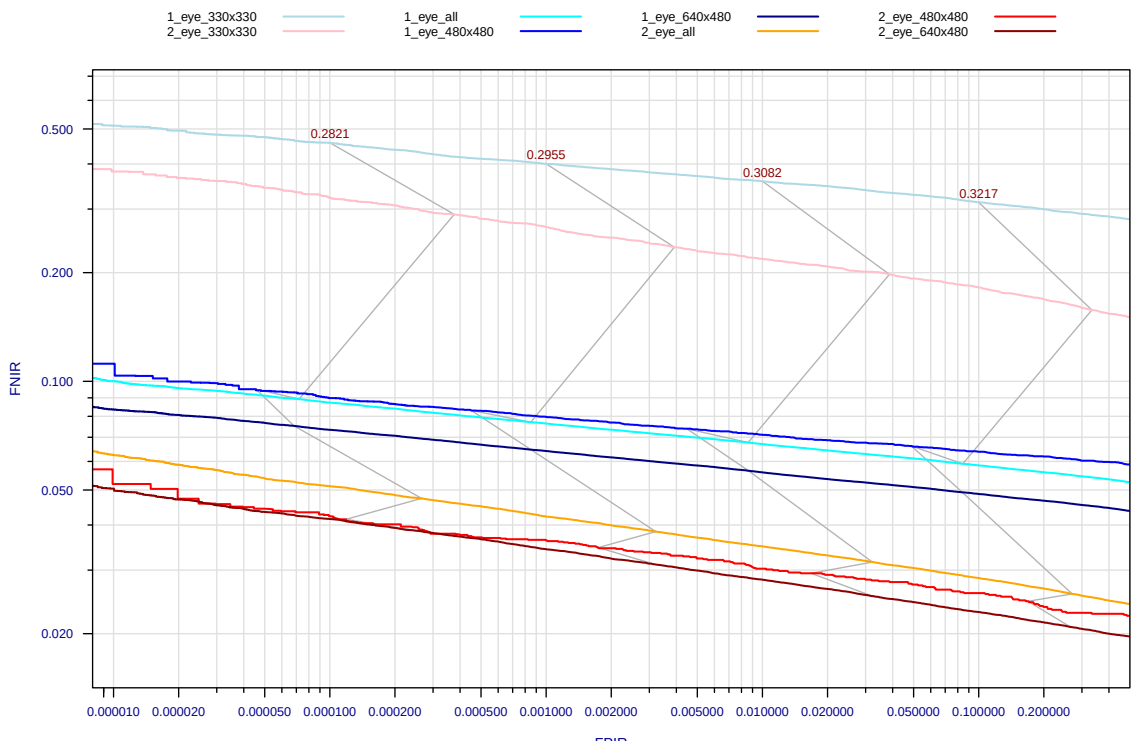

(a) Large search set, $\mathcal{S}_{nb}$

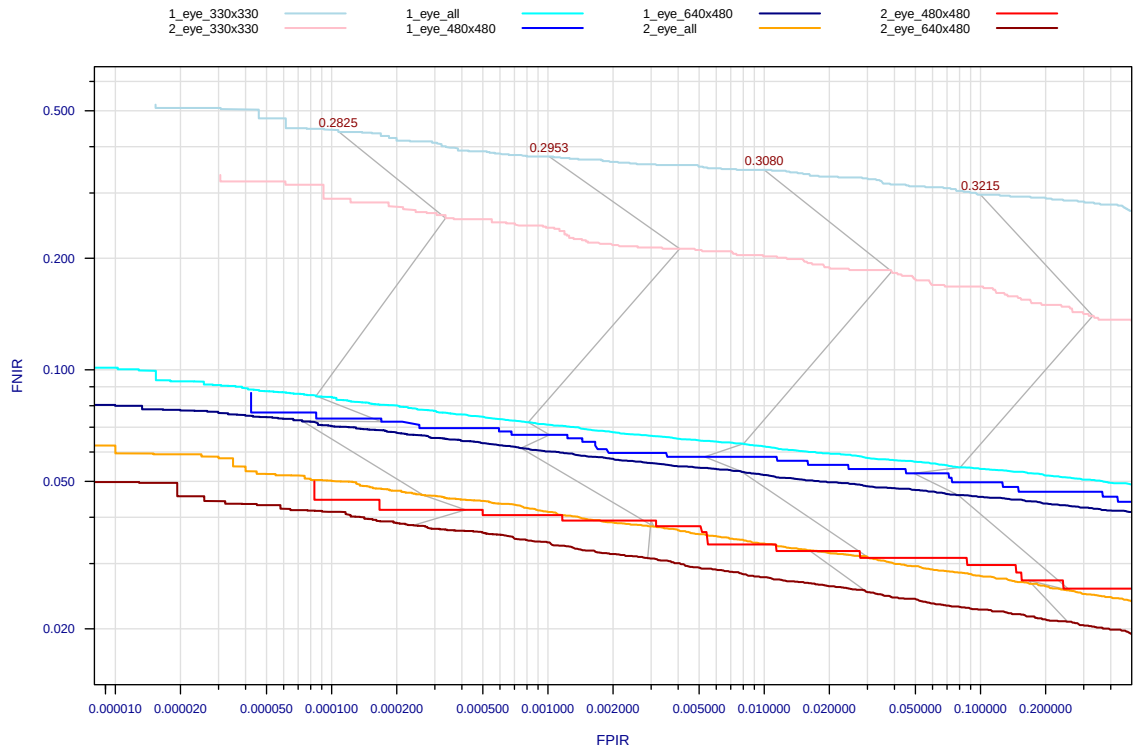

(b) Small search set, $\mathcal{S}_{na}$

Figure 547: DET for implementation T03B executing searches in an enrolled population of N = 1.6 million, broken out for three different image sizes (corresponding broadly to three camera plus ancillary software combinations) of the search image. The acquisition system used for the enrollment image (if any) is ignored in this breakout. Results for single-eye and two-eyes are plotted with two families of color. The straight lines, which link points of constant threshold, show how the two error rates would vary if a fixed threshold were adopted operationally.

FNIR = FALSE NEGATIVE IDENT. RATE FPIR = FALSE POSITIVE IDENT. RATE	N = NEUROTECHNOLOGY U = L1	P = SMU V = MORPHO	Q = IRITECH W = IRISID	R = COGENT X = CROSSMATCH	S = SMARTSENSORS Y = KYNEN	T = CAMBRIDGE

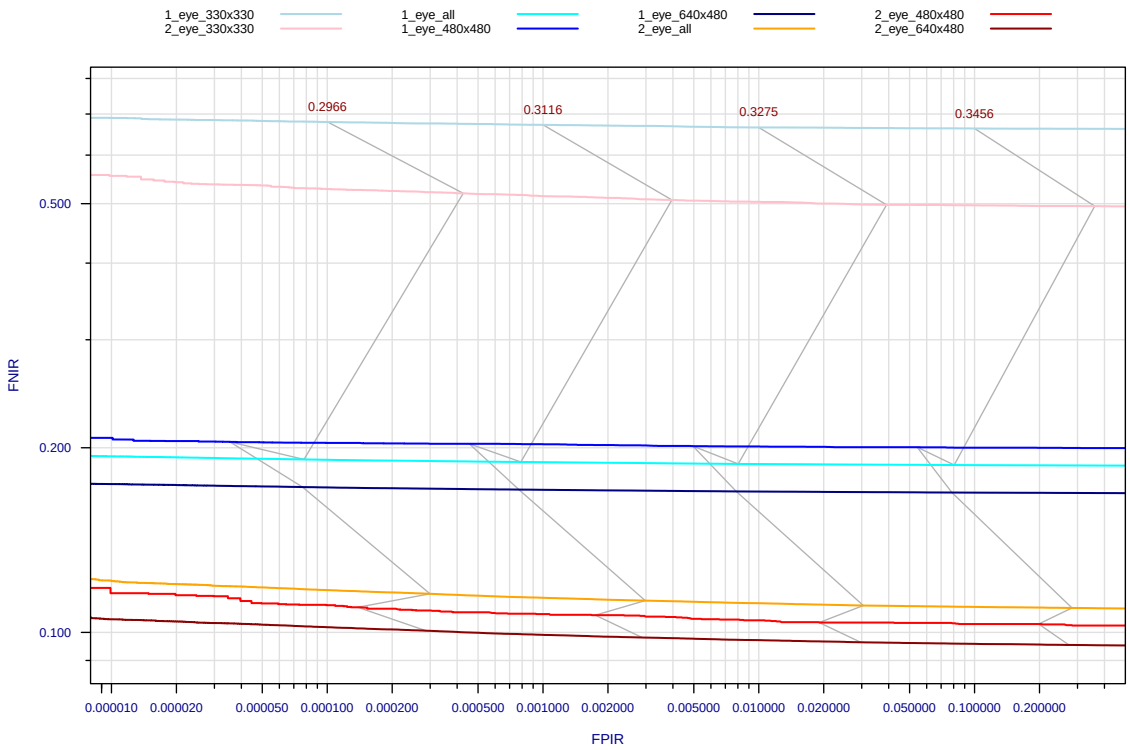

(a) Large search set, $\mathcal{S}_{nb}$

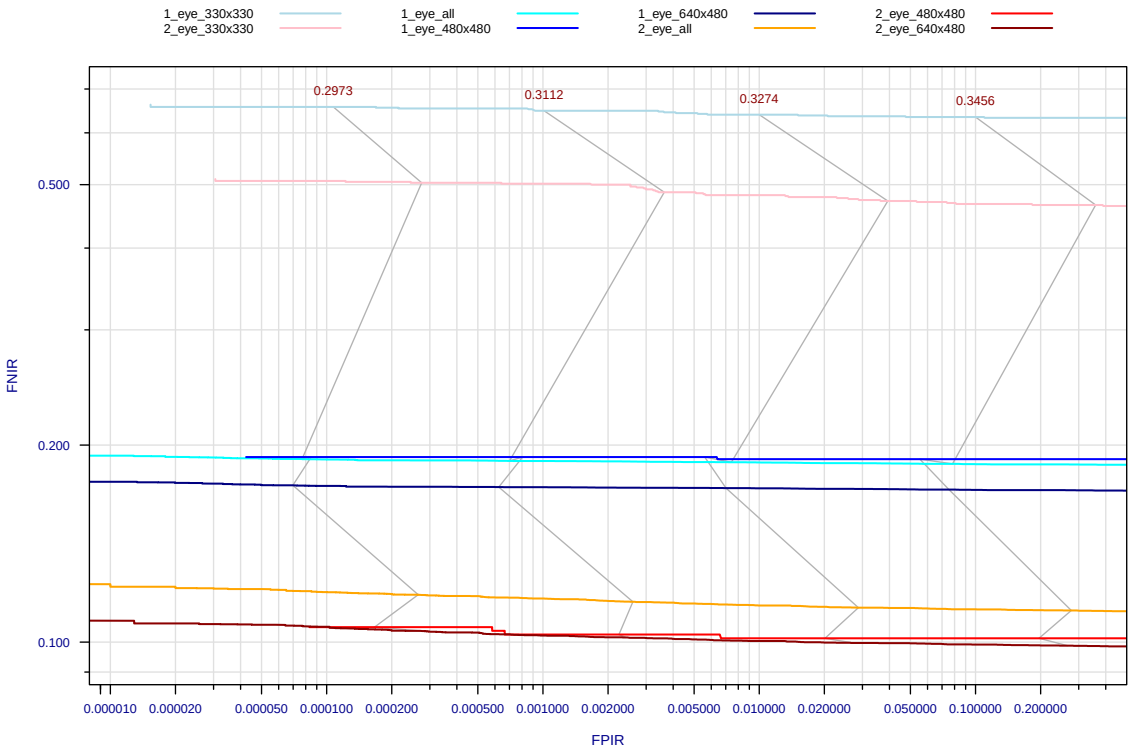

(b) Small search set, $\mathcal{S}_{na}$

Figure 548: DET for implementation T04A executing searches in an enrolled population of N = 1.6 million, broken out for three different image sizes (corresponding broadly to three camera plus ancillary software combinations) of the search image. The acquisition system used for the enrollment image (if any) is ignored in this breakout. Results for single-eye and two-eyes are plotted with two families of color. The straight lines, which link points of constant threshold, show how the two error rates would vary if a fixed threshold were adopted operationally.

FNIR = FALSE NEGATIVE IDENT. RATE FPIR = FALSE POSITIVE IDENT. RATE	N = NEUROTECHNOLOGY U = L1	P = SMU V = MORPHO	Q = IRITECH W = IRISID	R = COGENT X = CROSSMATCH	S = SMARTSENSORS Y = KYNEN	T = CAMBRIDGE

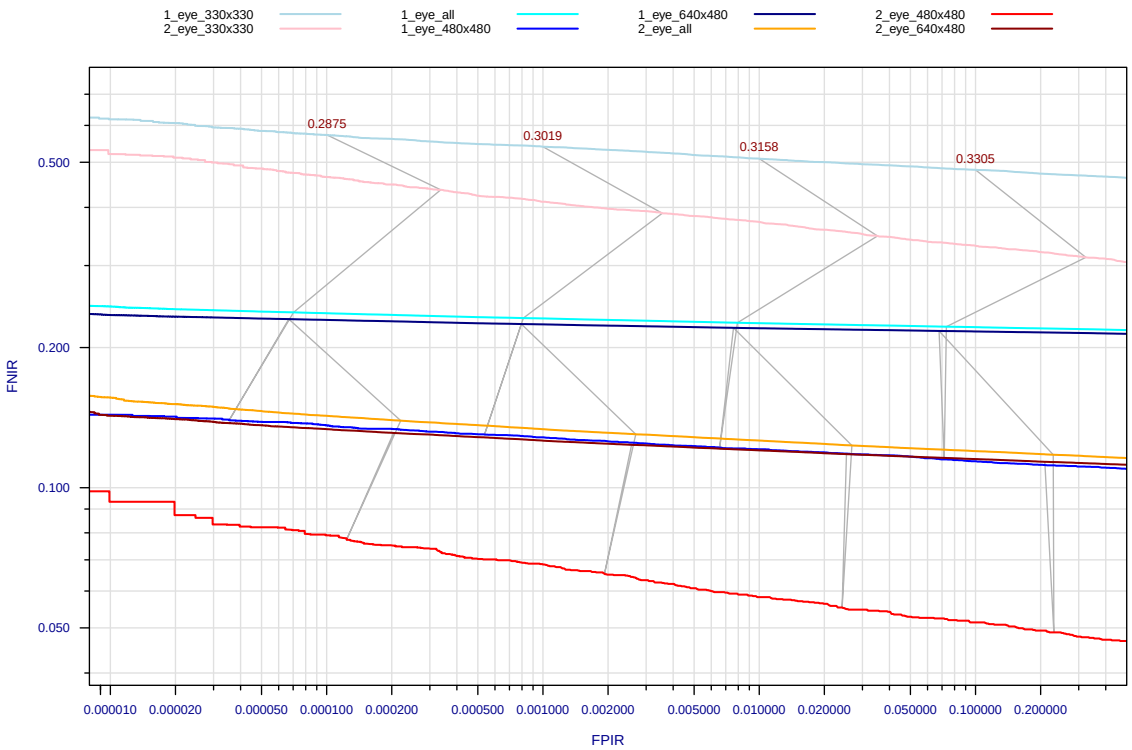

(a) Large search set, $\mathcal{S}_{nb}$

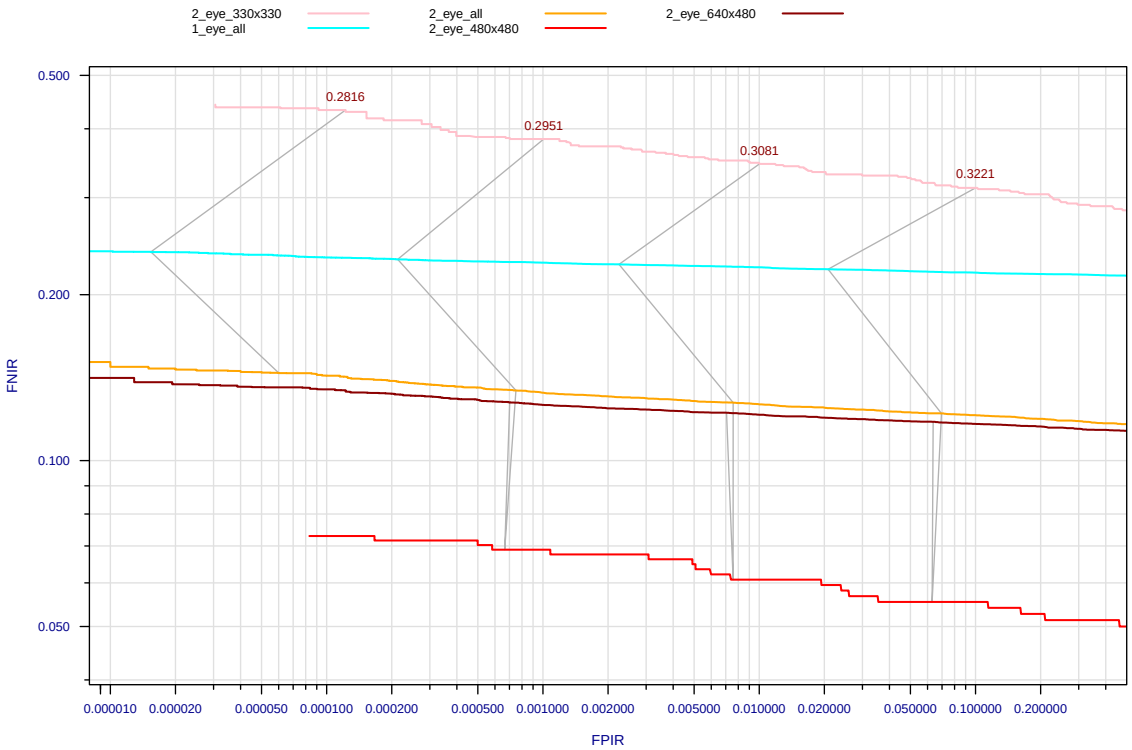

(b) Small search set, $\mathcal{S}_{na}$

Figure 549: DET for implementation T11A executing searches in an enrolled population of N = 1.6 million, broken out for three different image sizes (corresponding broadly to three camera plus ancillary software combinations) of the search image. The acquisition system used for the enrollment image (if any) is ignored in this breakout. Results for single-eye and two-eyes are plotted with two families of color. The straight lines, which link points of constant threshold, show how the two error rates would vary if a fixed threshold were adopted operationally.

FNIR = FALSE NEGATIVE IDENT. RATE FPIR = FALSE POSITIVE IDENT. RATE	N = NEUROTECHNOLOGY U = L1	P = SMU V = MORPHO	Q = IRITECH W = IRISID	R = COGENT X = CROSSMATCH	S = SMARTSENSORS Y = KYNEN	T = CAMBRIDGE

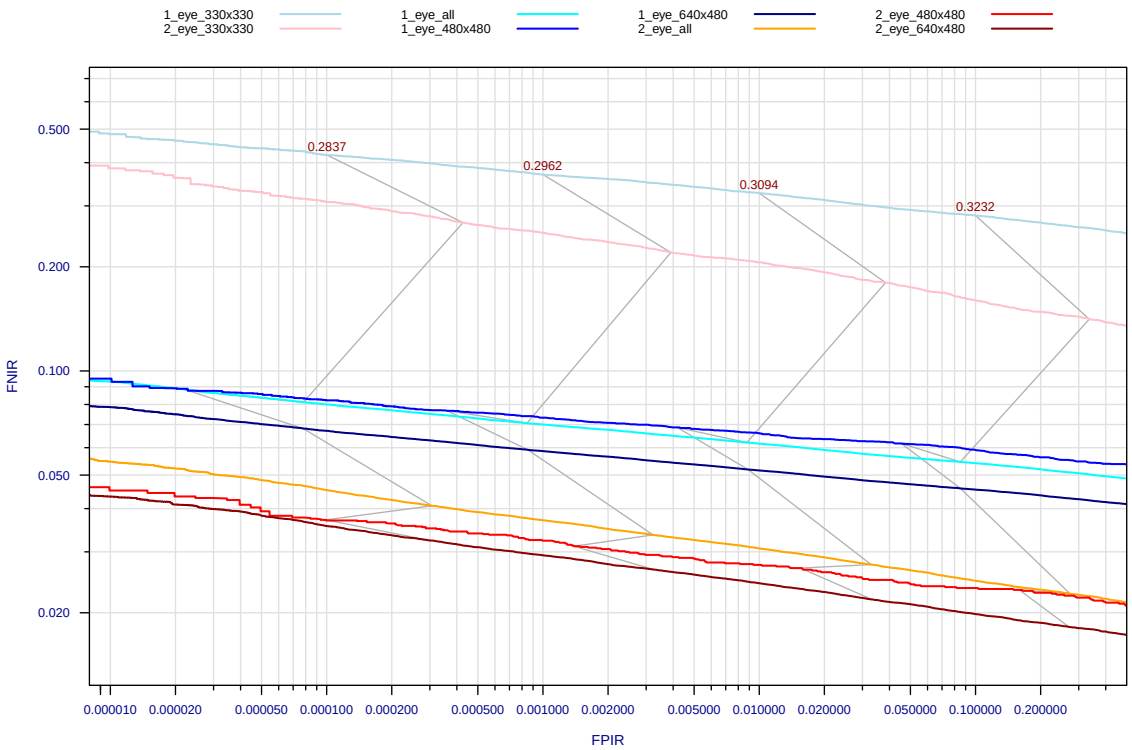

(a) Large search set, $\mathcal{S}_{nb}$

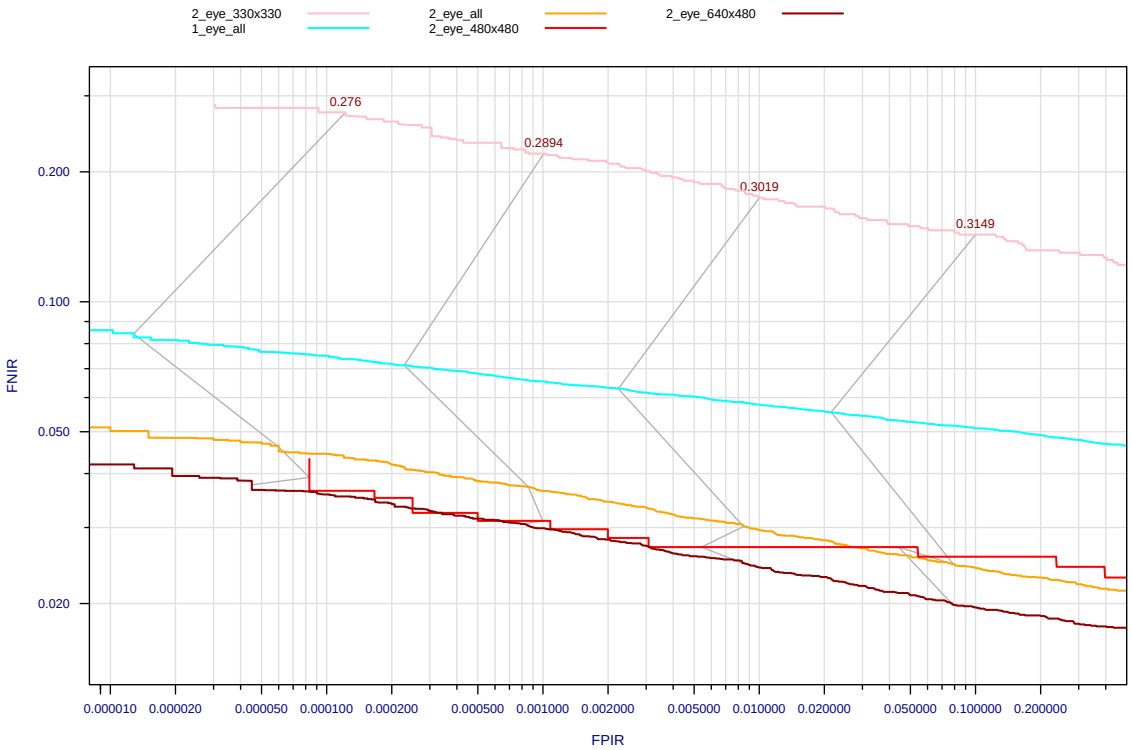

(b) Small search set, $\mathcal{S}_{na}$

Figure 550: DET for implementation T11B executing searches in an enrolled population of N = 1.6 million, broken out for three different image sizes (corresponding broadly to three camera plus ancillary software combinations) of the search image. The acquisition system used for the enrollment image (if any) is ignored in this breakout. Results for single-eye and two-eyes are plotted with two families of color. The straight lines, which link points of constant threshold, show how the two error rates would vary if a fixed threshold were adopted operationally.

FNIR = FALSE NEGATIVE IDENT. RATE FPIR = FALSE POSITIVE IDENT. RATE	N = NEUROTECHNOLOGY U = L1	P = SMU V = MORPHO	Q = IRITECH W = IRISID	R = COGENT X = CROSSMATCH	S = SMARTSENSORS Y = KYNEN	T = CAMBRIDGE

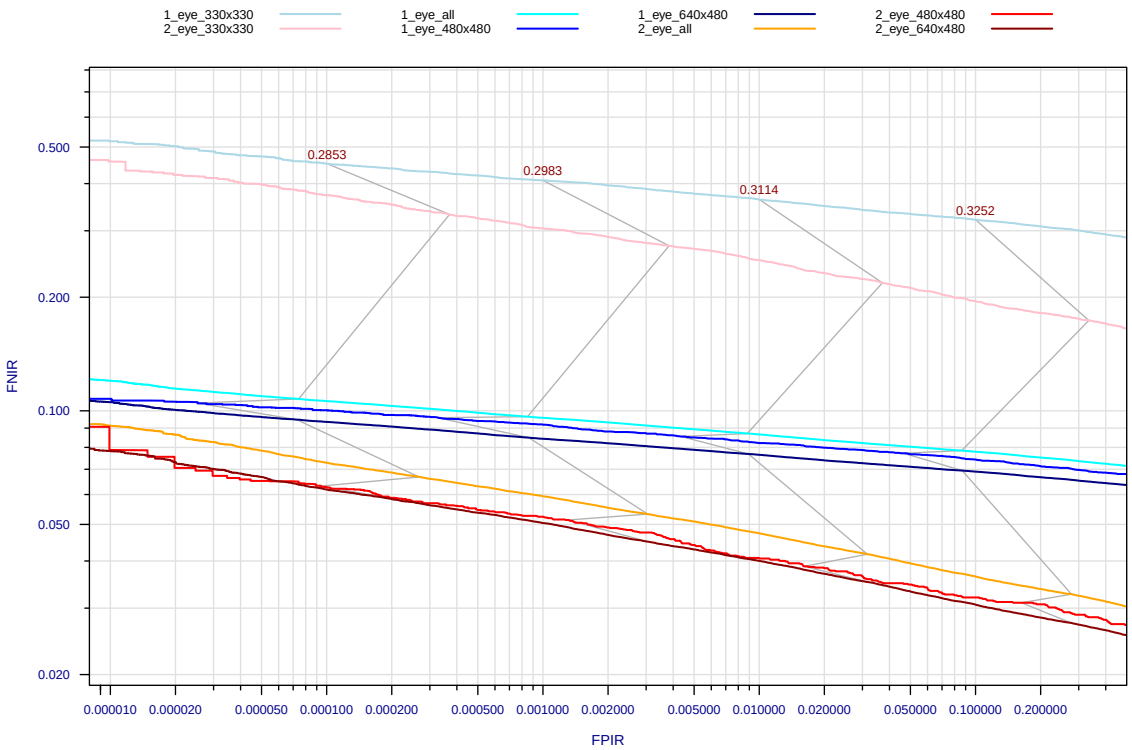

(a) Large search set, $\mathcal{S}_{nb}$

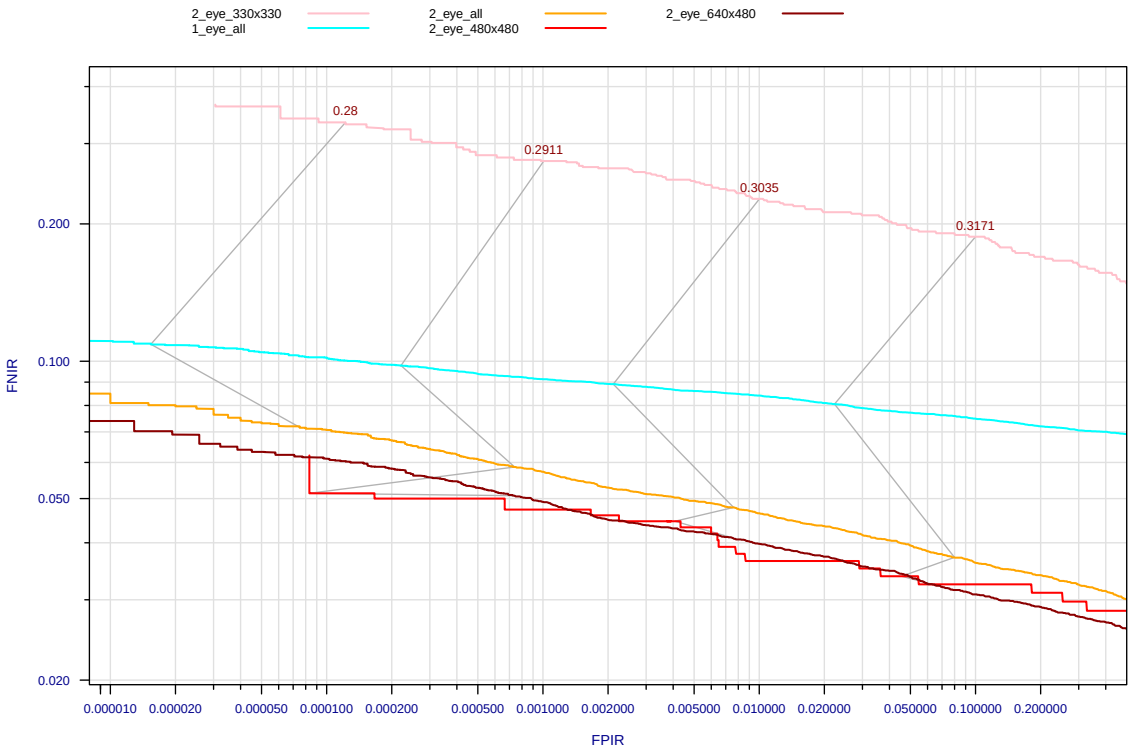

(b) Small search set, $\mathcal{S}_{na}$

Figure 551: DET for implementation T12B executing searches in an enrolled population of N = 1.6 million, broken out for three different image sizes (corresponding broadly to three camera plus ancillary software combinations) of the search image. The acquisition system used for the enrollment image (if any) is ignored in this breakout. Results for single-eye and two-eyes are plotted with two families of color. The straight lines, which link points of constant threshold, show how the two error rates would vary if a fixed threshold were adopted operationally.

FNIR = FALSE NEGATIVE IDENT. RATE FPIR = FALSE POSITIVE IDENT. RATE	N = NEUROTECHNOLOGY U = L1	P = SMU V = MORPHO	Q = IRITECH W = IRISID	R = COGENT X = CROSSMATCH	S = SMARTSENSORS Y = KYNEN	T = CAMBRIDGE

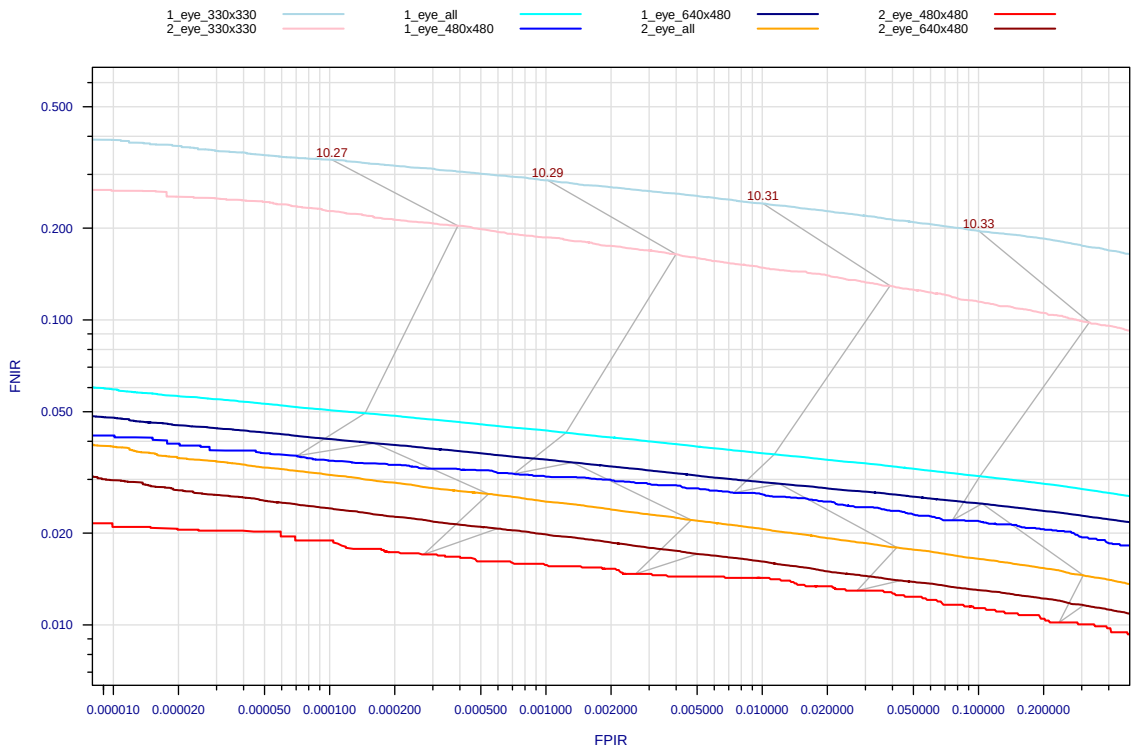

(a) Large search set, $\mathcal{S}_{nb}$

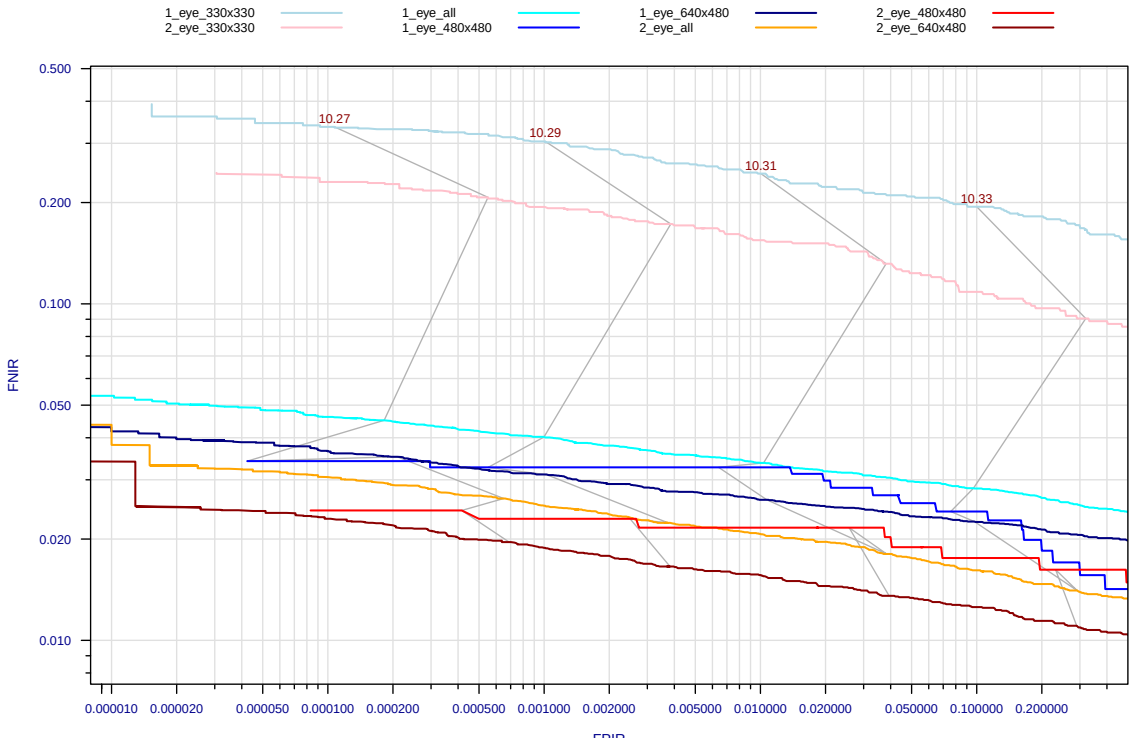

(b) Small search set, $\mathcal{S}_{na}$

Figure 552: DET for implementation U01A executing searches in an enrolled population of N = 1.6 million, broken out for three different image sizes (corresponding broadly to three camera plus ancillary software combinations) of the search image. The acquisition system used for the enrollment image (if any) is ignored in this breakout. Results for single-eye and two-eyes are plotted with two families of color. The straight lines, which link points of constant threshold, show how the two error rates would vary if a fixed threshold were adopted operationally.

FNIR = FALSE NEGATIVE IDENT. RATE FPIR = FALSE POSITIVE IDENT. RATE	N = NEUROTECHNOLOGY U = L1	P = SMU V = MORPHO	Q = IRITECH W = IRISID	R = COGENT X = CROSSMATCH	S = SMARTSENSORS Y = KYNEN	T = CAMBRIDGE

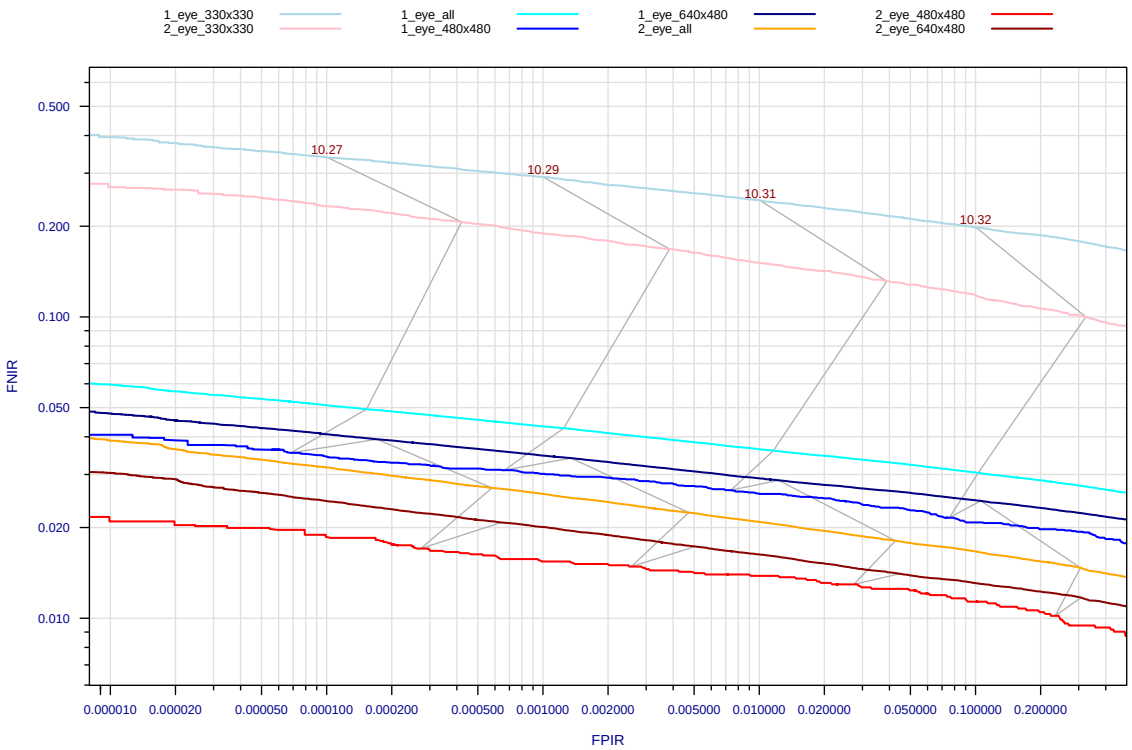

(a) Large search set, $\mathcal{S}_{nb}$

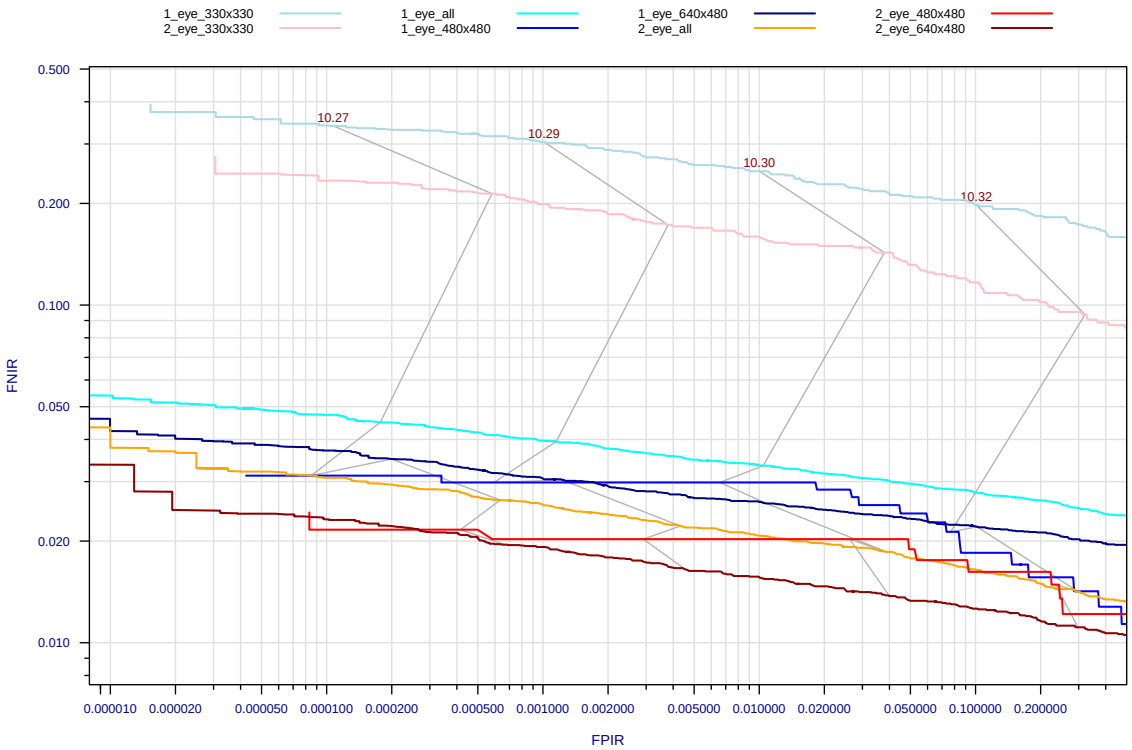

(b) Small search set, $\mathcal{S}_{na}$

Figure 553: DET for implementation U01B executing searches in an enrolled population of N = 1.6 million, broken out for three different image sizes (corresponding broadly to three camera plus ancillary software combinations) of the search image. The acquisition system used for the enrollment image (if any) is ignored in this breakout. Results for single-eye and two-eyes are plotted with two families of color. The straight lines, which link points of constant threshold, show how the two error rates would vary if a fixed threshold were adopted operationally.

FNIR = FALSE NEGATIVE IDENT. RATE FPIR = FALSE POSITIVE IDENT. RATE	N = NEUROTECHNOLOGY U = L1	P = SMU V = MORPHO	Q = IRITECH W = IRISID	R = COGENT X = CROSSMATCH	S = SMARTSENSORS Y = KYNEN	T = CAMBRIDGE

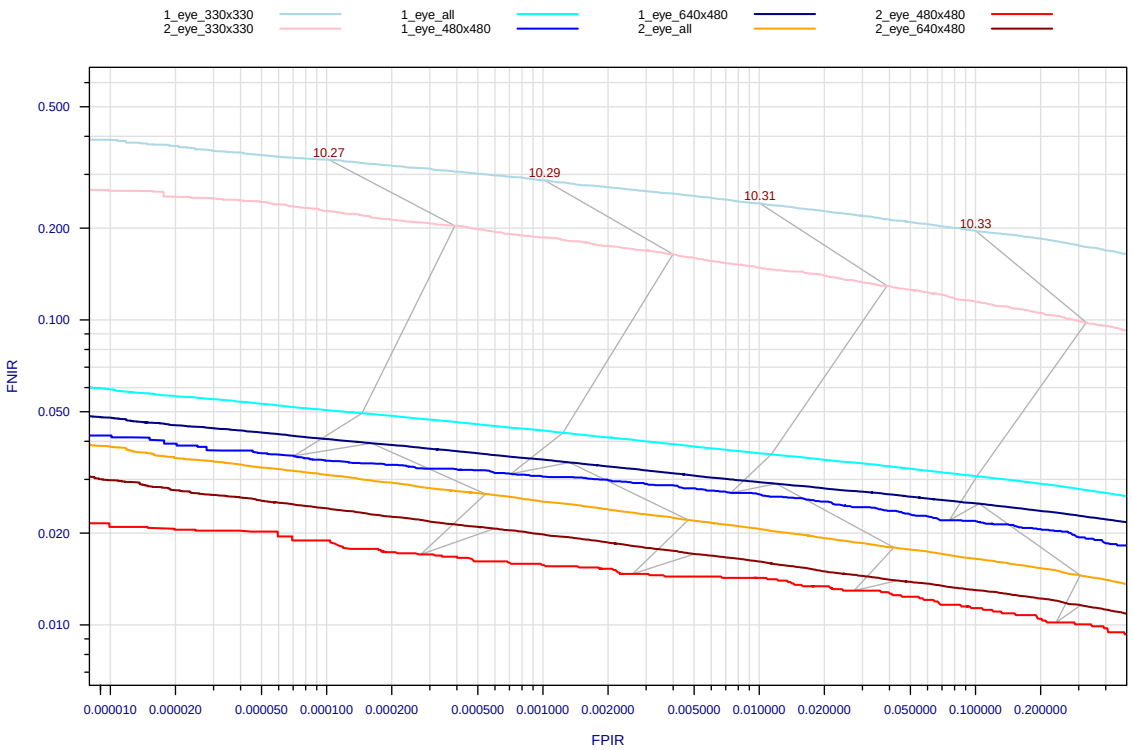

(a) Large search set, $\mathcal{S}_{nb}$

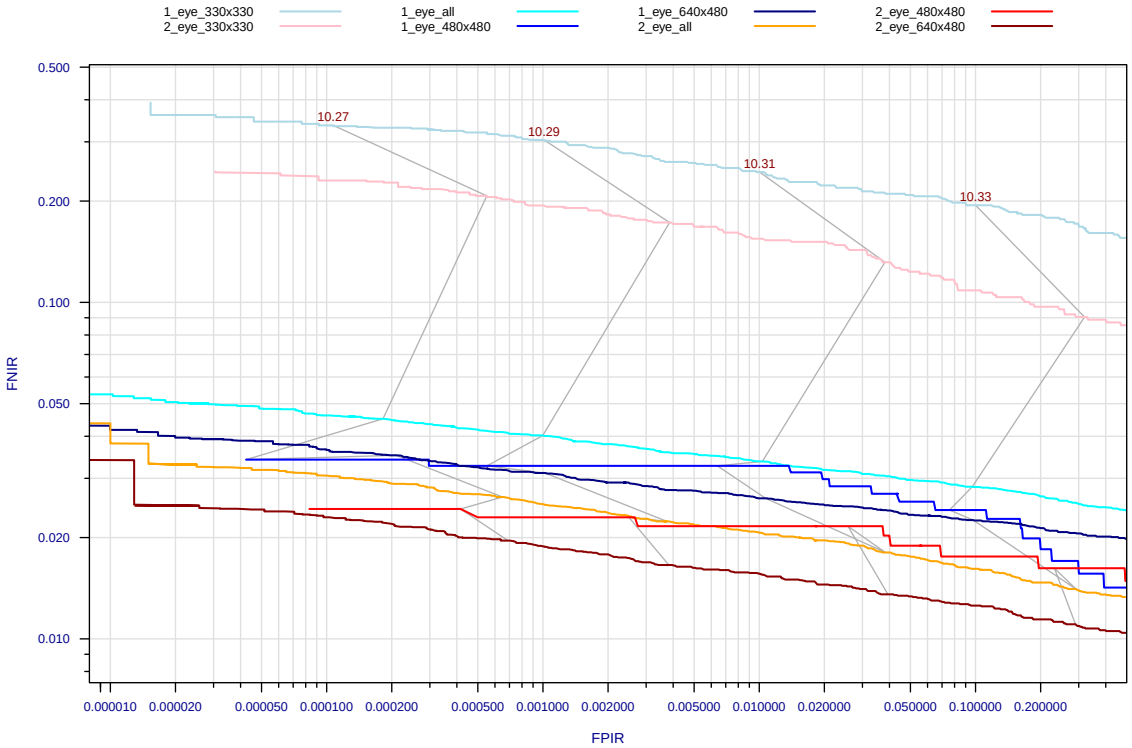

(b) Small search set, $\mathcal{S}_{na}$

Figure 554: DET for implementation U02A executing searches in an enrolled population of N = 1.6 million, broken out for three different image sizes (corresponding broadly to three camera plus ancillary software combinations) of the search image. The acquisition system used for the enrollment image (if any) is ignored in this breakout. Results for single-eye and two-eyes are plotted with two families of color. The straight lines, which link points of constant threshold, show how the two error rates would vary if a fixed threshold were adopted operationally.

FNIR = FALSE NEGATIVE IDENT. RATE FPIR = FALSE POSITIVE IDENT. RATE	N = NEUROTECHNOLOGY U = L1	P = SMU V = MORPHO	Q = IRITECH W = IRISID	R = COGENT X = CROSSMATCH	S = SMARTSENSORS Y = KYNEN	T = CAMBRIDGE

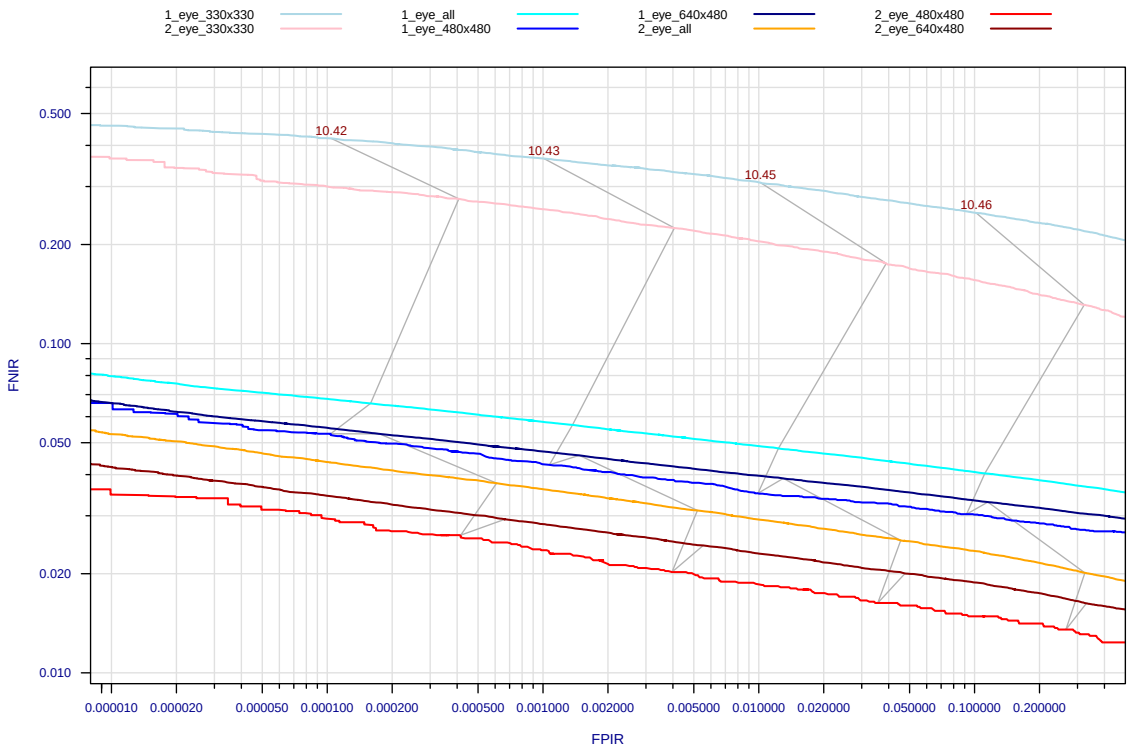

(a) Large search set, $\mathcal{S}_{nb}$

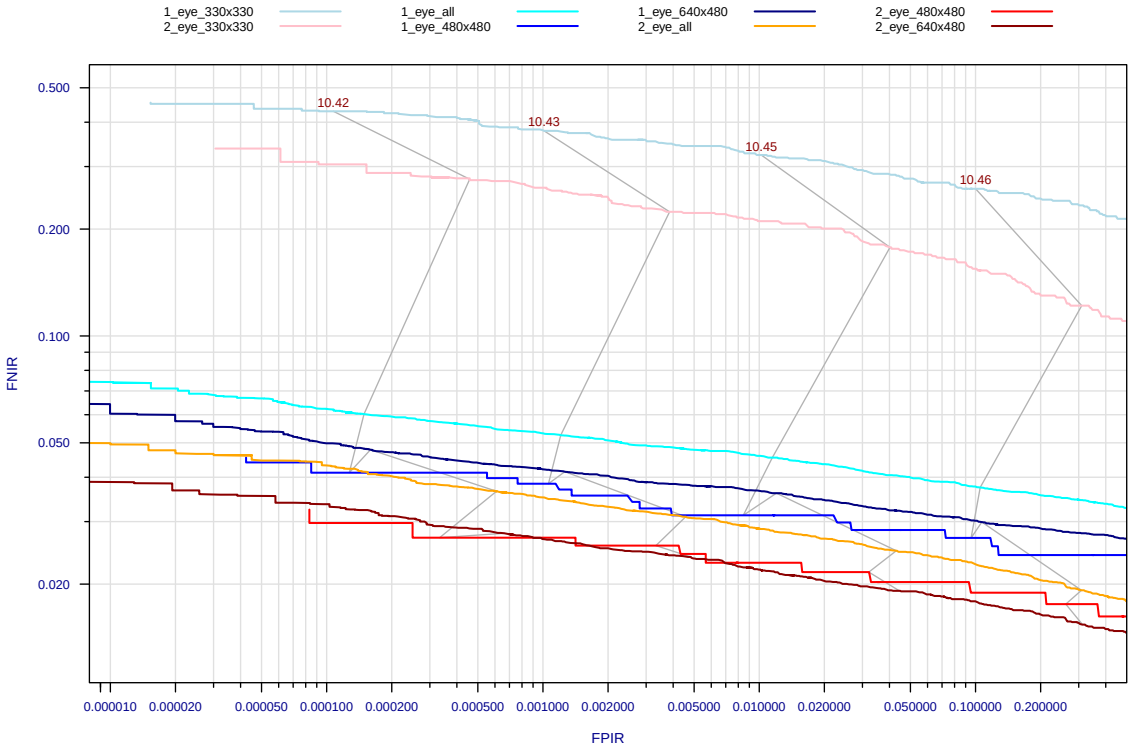

(b) Small search set, $\mathcal{S}_{na}$

Figure 555: DET for implementation U03A executing searches in an enrolled population of N = 1.6 million, broken out for three different image sizes (corresponding broadly to three camera plus ancillary software combinations) of the search image. The acquisition system used for the enrollment image (if any) is ignored in this breakout. Results for single-eye and two-eyes are plotted with two families of color. The straight lines, which link points of constant threshold, show how the two error rates would vary if a fixed threshold were adopted operationally.

FNIR = FALSE NEGATIVE IDENT. RATE FPIR = FALSE POSITIVE IDENT. RATE	N = NEUROTECHNOLOGY U = L1	P = SMU V = MORPHO	Q = IRITECH W = IRISID	R = COGENT X = CROSSMATCH	S = SMARTSENSORS Y = KYNEN	T = CAMBRIDGE

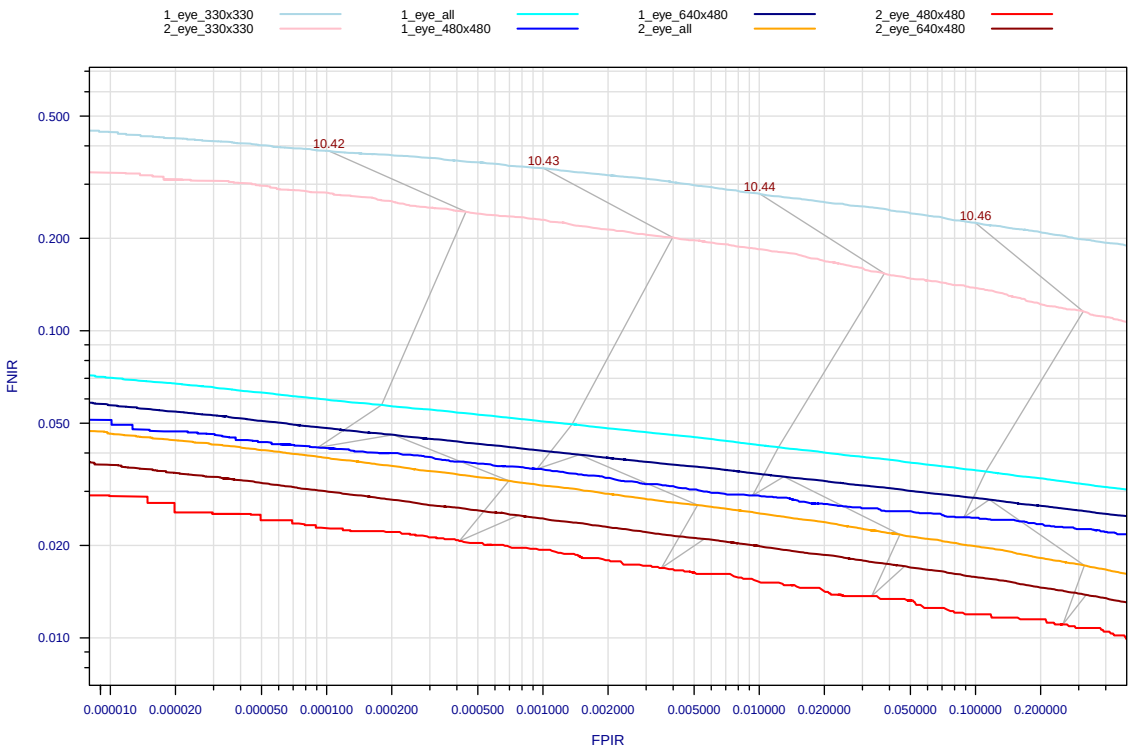

(a) Large search set, $\mathcal{S}_{nb}$

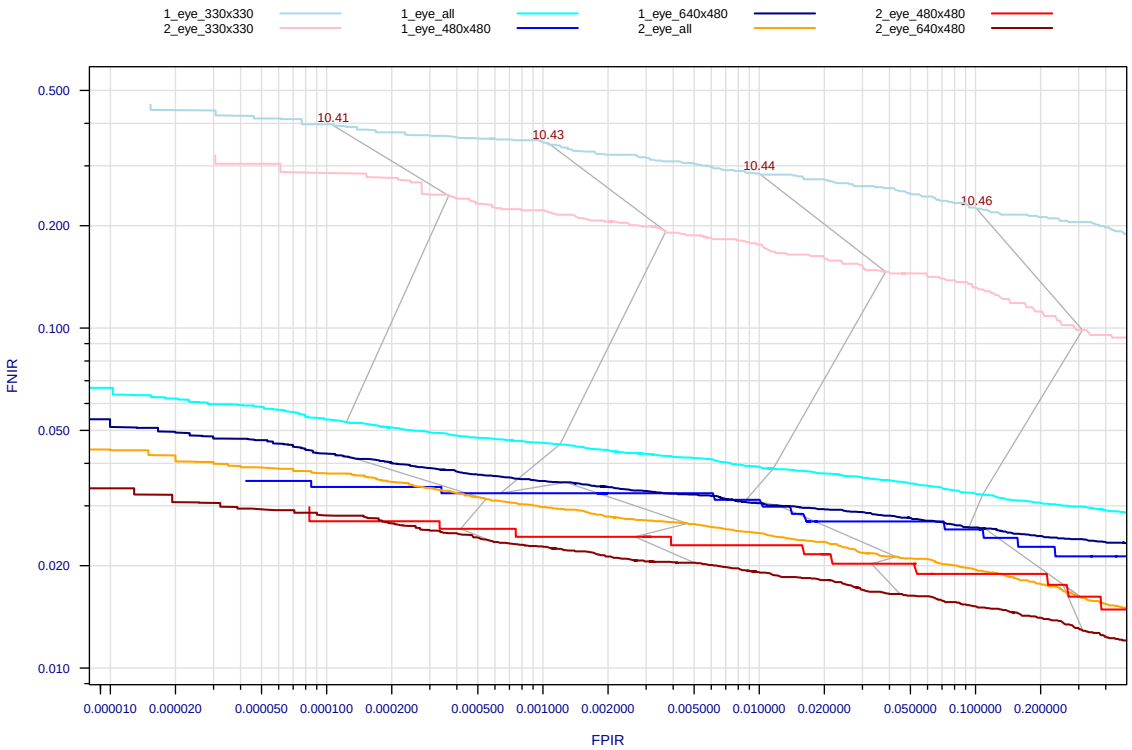

(b) Small search set, $\mathcal{S}_{na}$

Figure 556: DET for implementation U03B executing searches in an enrolled population of N = 1.6 million, broken out for three different image sizes (corresponding broadly to three camera plus ancillary software combinations) of the search image. The acquisition system used for the enrollment image (if any) is ignored in this breakout. Results for single-eye and two-eyes are plotted with two families of color. The straight lines, which link points of constant threshold, show how the two error rates would vary if a fixed threshold were adopted operationally.

FNIR = FALSE NEGATIVE IDENT. RATE FPIR = FALSE POSITIVE IDENT. RATE	N = NEUROTECHNOLOGY U = L1	P = SMU V = MORPHO	Q = IRITECH W = IRISID	R = COGENT X = CROSSMATCH	S = SMARTSENSORS Y = KYNEN	T = CAMBRIDGE

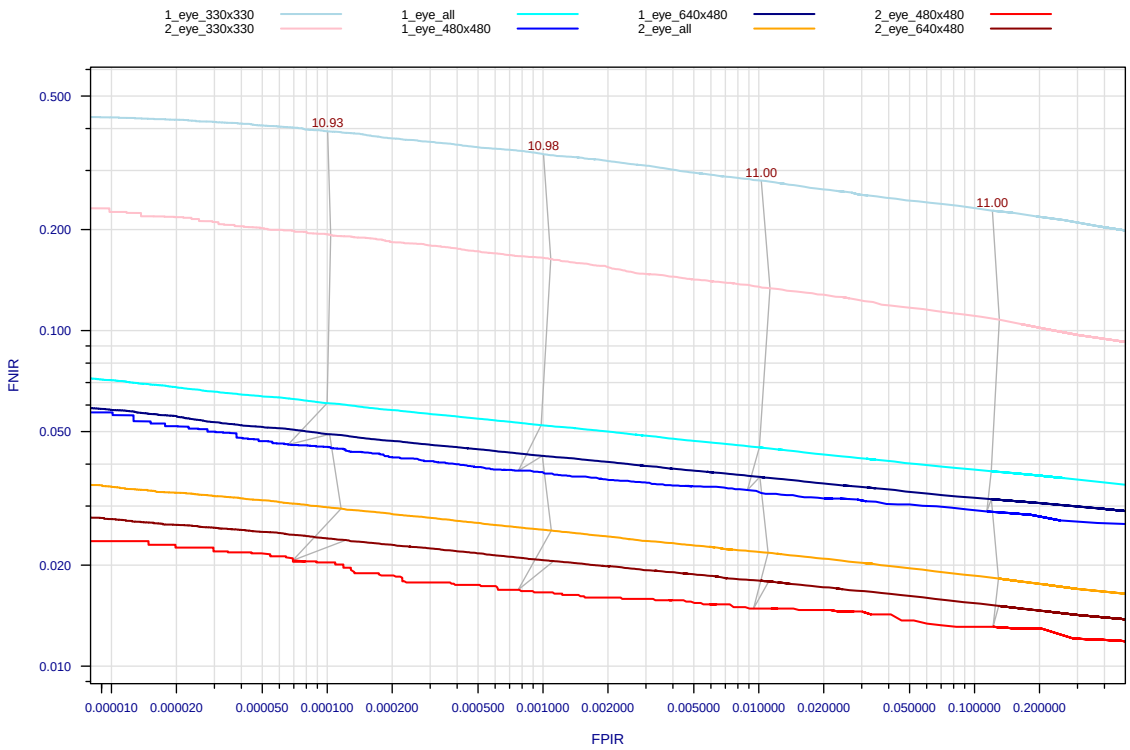

(a) Large search set, $\mathcal{S}_{nb}$

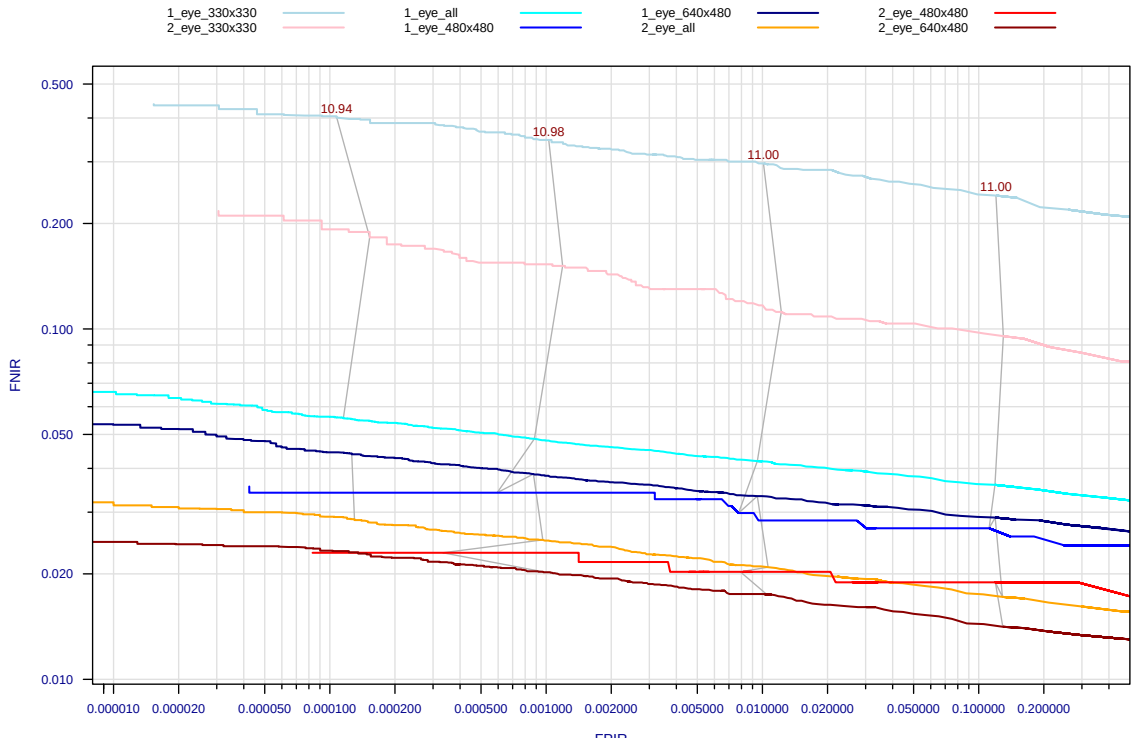

(b) Small search set, $\mathcal{S}_{na}$

Figure 557: DET for implementation U04A executing searches in an enrolled population of N = 1.6 million, broken out for three different image sizes (corresponding broadly to three camera plus ancillary software combinations) of the search image. The acquisition system used for the enrollment image (if any) is ignored in this breakout. Results for single-eye and two-eyes are plotted with two families of color. The straight lines, which link points of constant threshold, show how the two error rates would vary if a fixed threshold were adopted operationally.

FNIR = FALSE NEGATIVE IDENT. RATE FPIR = FALSE POSITIVE IDENT. RATE	N = NEUROTECHNOLOGY U = L1	P = SMU V = MORPHO	Q = IRITECH W = IRISID	R = COGENT X = CROSSMATCH	S = SMARTSENSORS Y = KYNEN	T = CAMBRIDGE

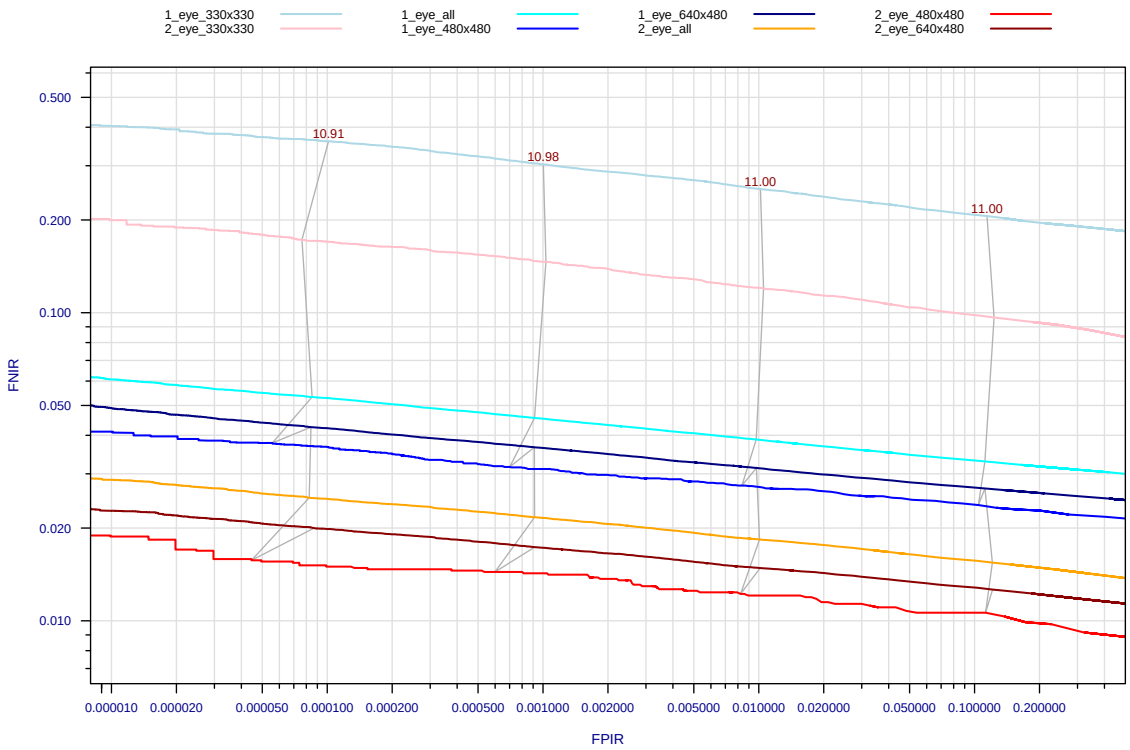

(a) Large search set, $\mathcal{S}_{nb}$

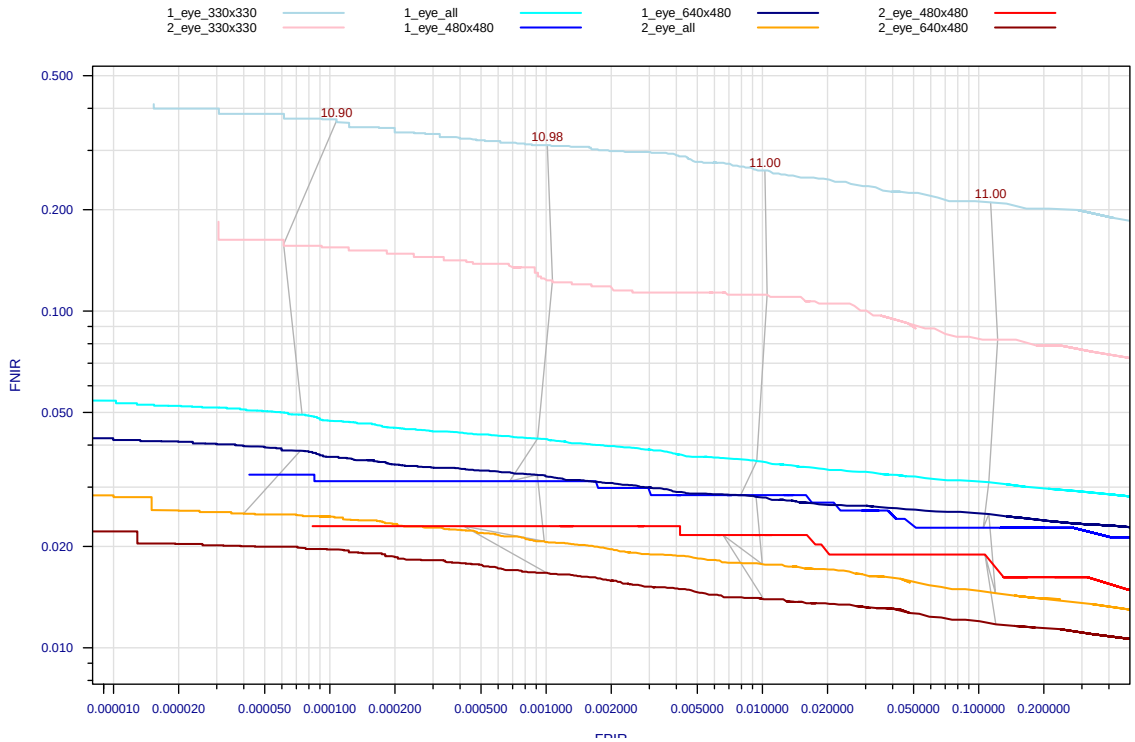

(b) Small search set, $\mathcal{S}_{na}$

Figure 558: DET for implementation U04B executing searches in an enrolled population of N = 1.6 million, broken out for three different image sizes (corresponding broadly to three camera plus ancillary software combinations) of the search image. The acquisition system used for the enrollment image (if any) is ignored in this breakout. Results for single-eye and two-eyes are plotted with two families of color. The straight lines, which link points of constant threshold, show how the two error rates would vary if a fixed threshold were adopted operationally.

FNIR = FALSE NEGATIVE IDENT. RATE FPIR = FALSE POSITIVE IDENT. RATE	N = NEUROTECHNOLOGY U = L1	P = SMU V = MORPHO	Q = IRITECH W = IRISID	R = COGENT X = CROSSMATCH	S = SMARTSENSORS Y = KYNEN	T = CAMBRIDGE

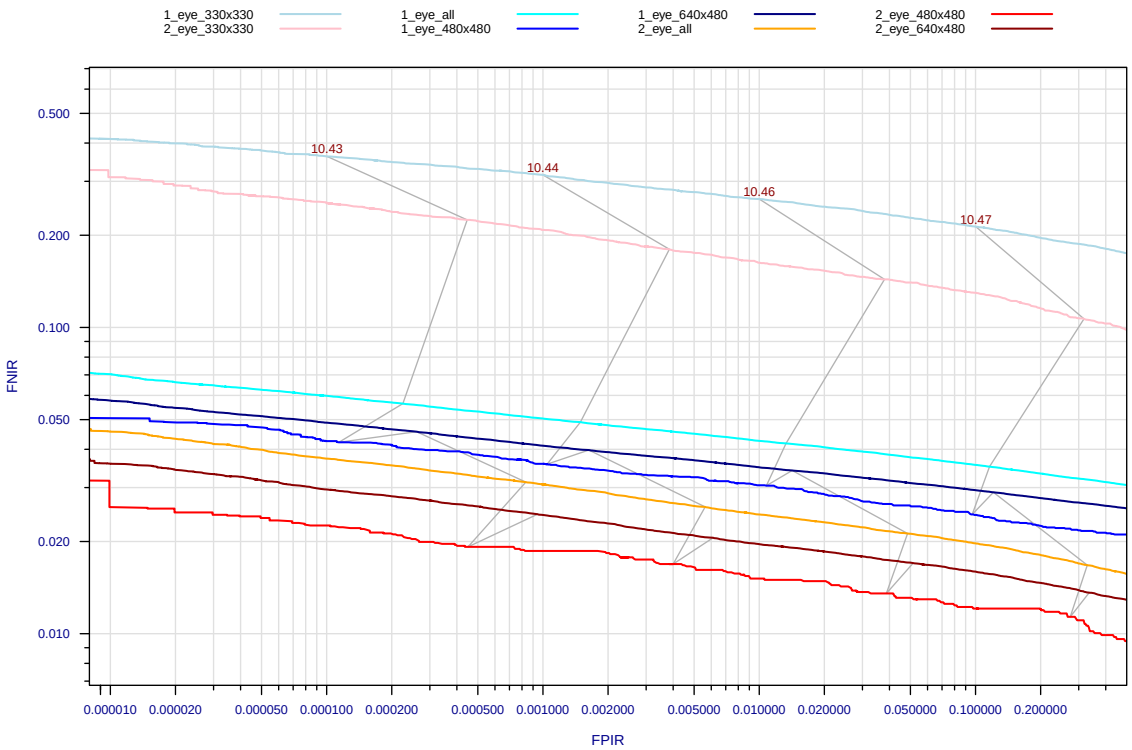

(a) Large search set, $\mathcal{S}_{nb}$

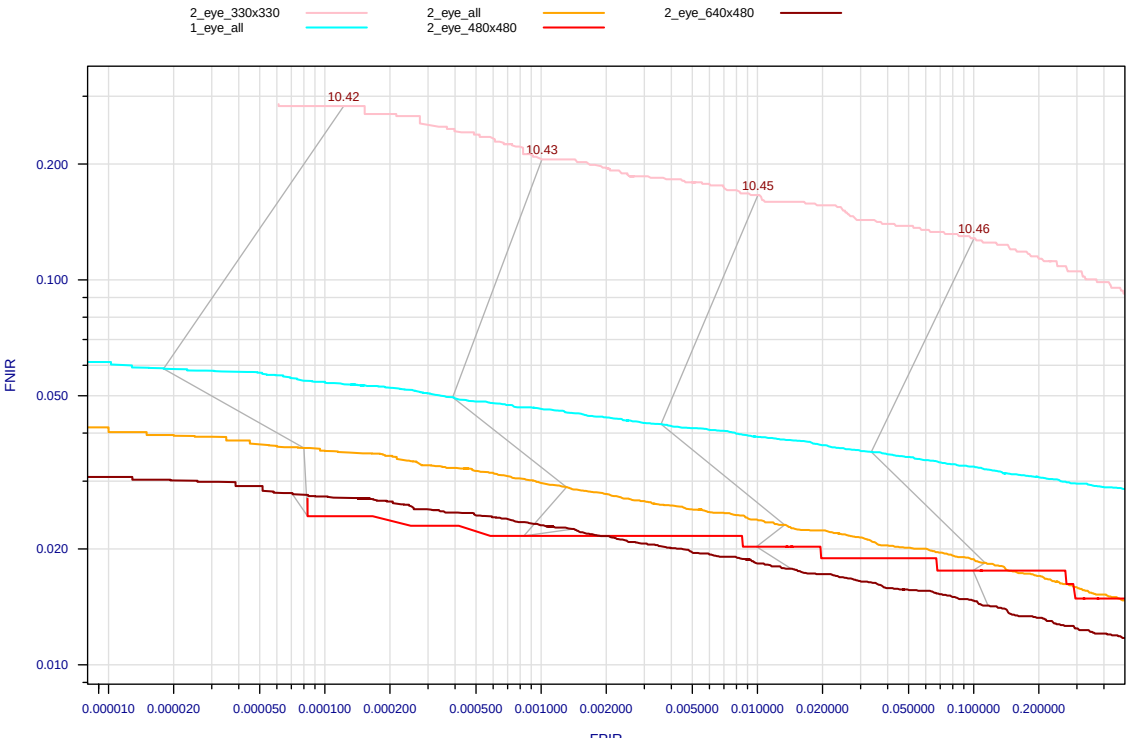

(b) Small search set, $\mathcal{S}_{na}$

Figure 559: DET for implementation U11A executing searches in an enrolled population of N = 1.6 million, broken out for three different image sizes (corresponding broadly to three camera plus ancillary software combinations) of the search image. The acquisition system used for the enrollment image (if any) is ignored in this breakout. Results for single-eye and two-eyes are plotted with two families of color. The straight lines, which link points of constant threshold, show how the two error rates would vary if a fixed threshold were adopted operationally.

FNIR = FALSE NEGATIVE IDENT. RATE FPIR = FALSE POSITIVE IDENT. RATE	N = NEUROTECHNOLOGY U = L1	P = SMU V = MORPHO	Q = IRITECH W = IRISID	R = COGENT X = CROSSMATCH	S = SMARTSENSORS Y = KYNEN	T = CAMBRIDGE

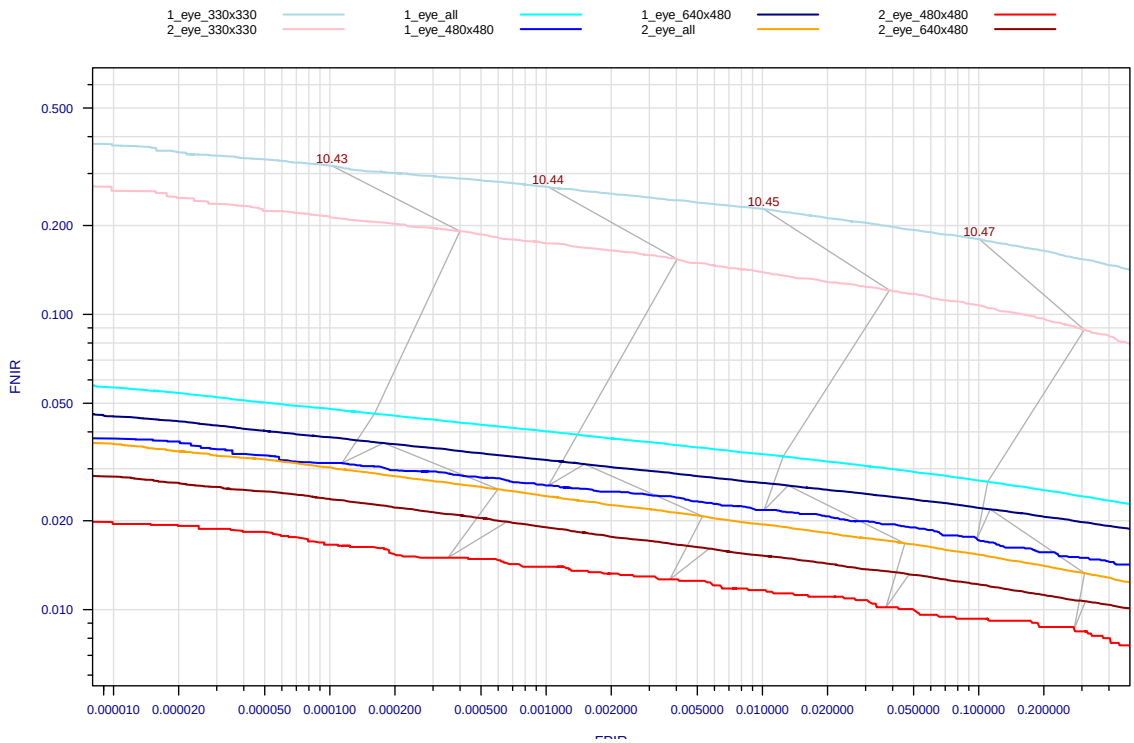

(a) Large search set, $\mathcal{S}_{nb}$

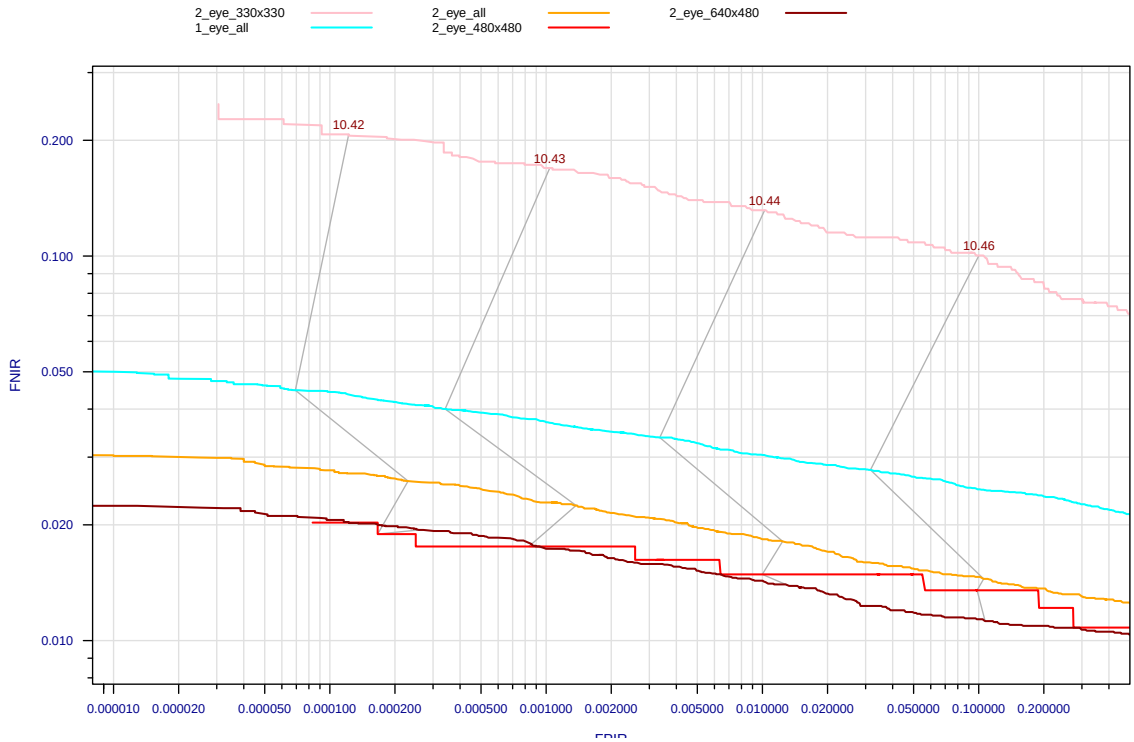

(b) Small search set, $\mathcal{S}_{na}$

Figure 560: DET for implementation U11B executing searches in an enrolled population of N = 1.6 million, broken out for three different image sizes (corresponding broadly to three camera plus ancillary software combinations) of the search image. The acquisition system used for the enrollment image (if any) is ignored in this breakout. Results for single-eye and two-eyes are plotted with two families of color. The straight lines, which link points of constant threshold, show how the two error rates would vary if a fixed threshold were adopted operationally.

FNIR = FALSE NEGATIVE IDENT. RATE FPIR = FALSE POSITIVE IDENT. RATE	N = NEUROTECHNOLOGY U = L1	P = SMU V = MORPHO	Q = IRITECH W = IRISID	R = COGENT X = CROSSMATCH	S = SMARTSENSORS Y = KYNEN	T = CAMBRIDGE

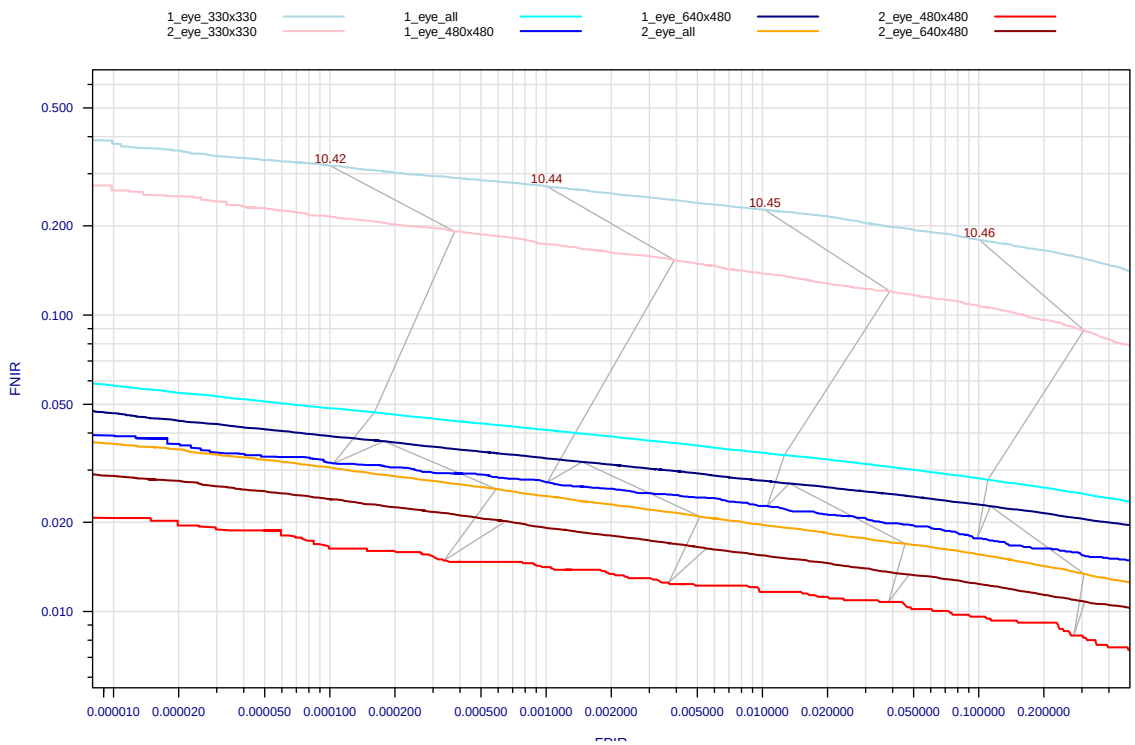

(a) Large search set, $\mathcal{S}_{nb}$

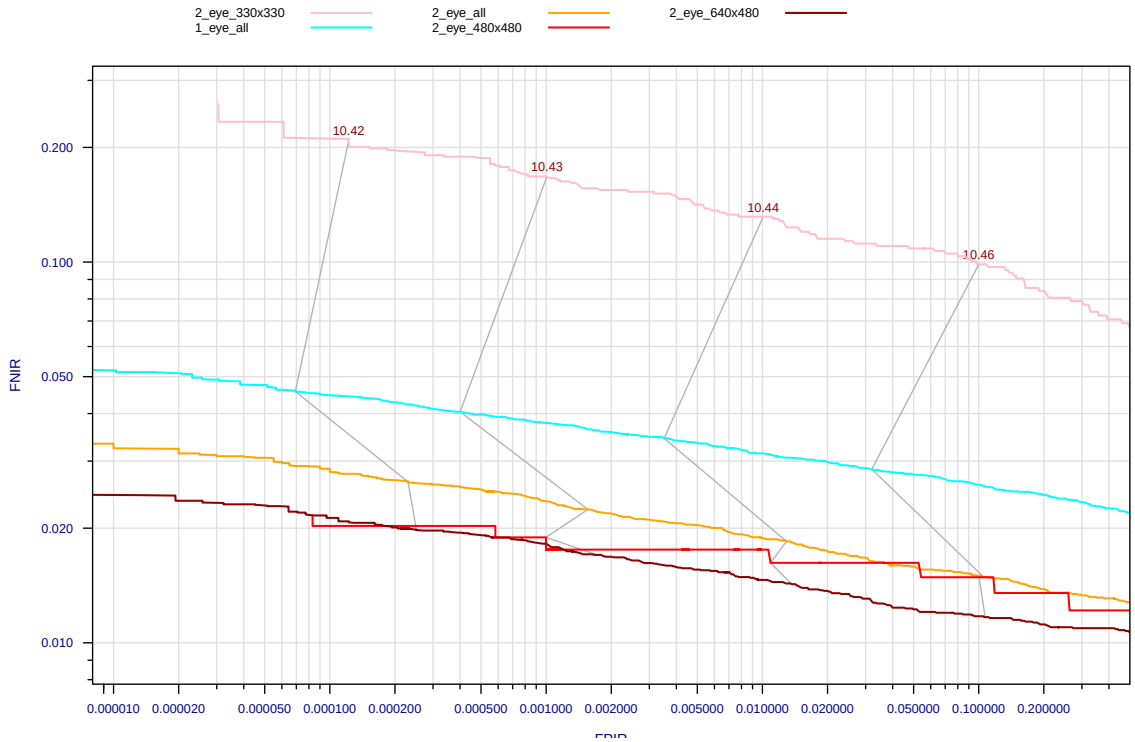

(b) Small search set, $\mathcal{S}_{na}$

Figure 561: DET for implementation U12A executing searches in an enrolled population of N = 1.6 million, broken out for three different image sizes (corresponding broadly to three camera plus ancillary software combinations) of the search image. The acquisition system used for the enrollment image (if any) is ignored in this breakout. Results for single-eye and two-eyes are plotted with two families of color. The straight lines, which link points of constant threshold, show how the two error rates would vary if a fixed threshold were adopted operationally.

FNIR = FALSE NEGATIVE IDENT. RATE FPIR = FALSE POSITIVE IDENT. RATE	N = NEUROTECHNOLOGY U = L1	P = SMU V = MORPHO	Q = IRITECH W = IRISID	R = COGENT X = CROSSMATCH	S = SMARTSENSORS Y = KYNEN	T = CAMBRIDGE

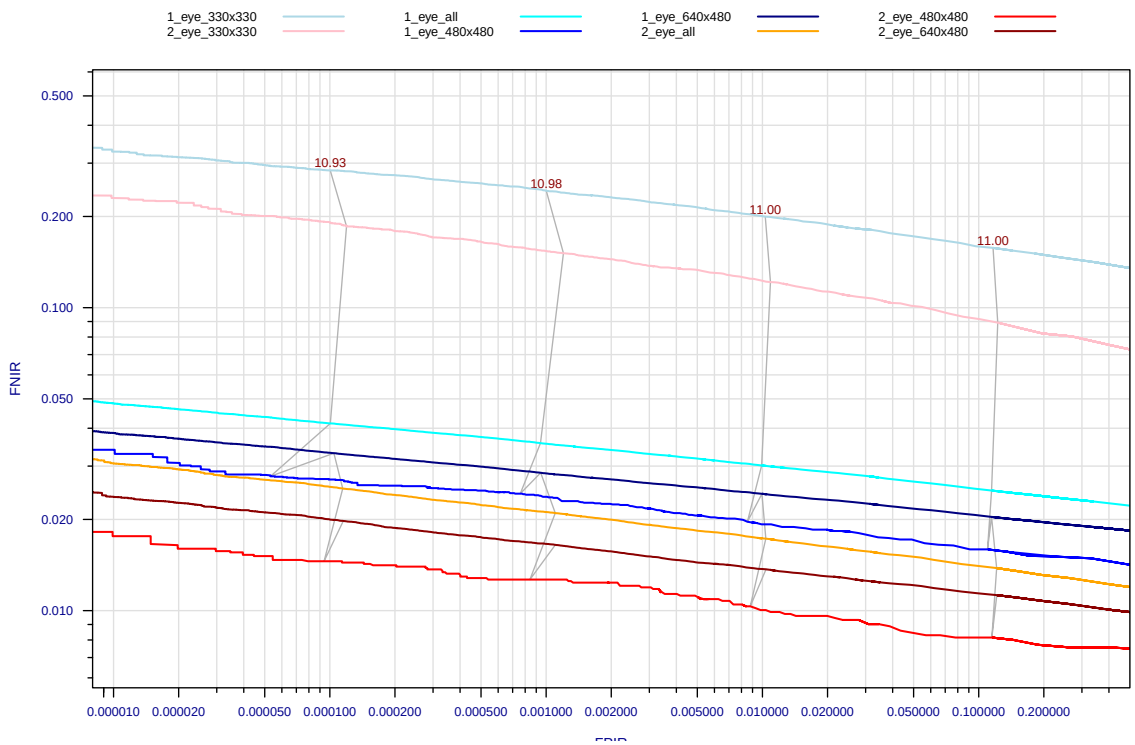

(a) Large search set, $\mathcal{S}_{nb}$

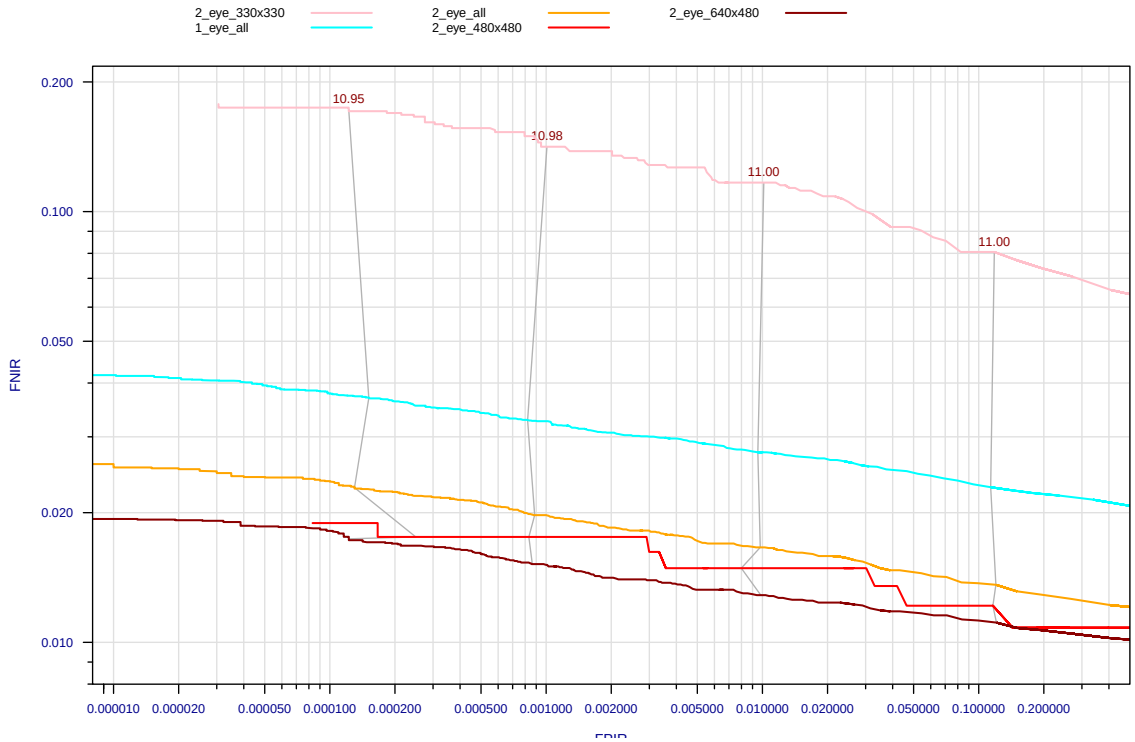

(b) Small search set, $\mathcal{S}_{na}$

Figure 562: DET for implementation U12B executing searches in an enrolled population of N = 1.6 million, broken out for three different image sizes (corresponding broadly to three camera plus ancillary software combinations) of the search image. The acquisition system used for the enrollment image (if any) is ignored in this breakout. Results for single-eye and two-eyes are plotted with two families of color. The straight lines, which link points of constant threshold, show how the two error rates would vary if a fixed threshold were adopted operationally.

FNIR = FALSE NEGATIVE IDENT. RATE FPIR = FALSE POSITIVE IDENT. RATE	N = NEUROTECHNOLOGY U = L1	P = SMU V = MORPHO	Q = IRITECH W = IRISID	R = COGENT X = CROSSMATCH	S = SMARTSENSORS Y = KYNEN	T = CAMBRIDGE

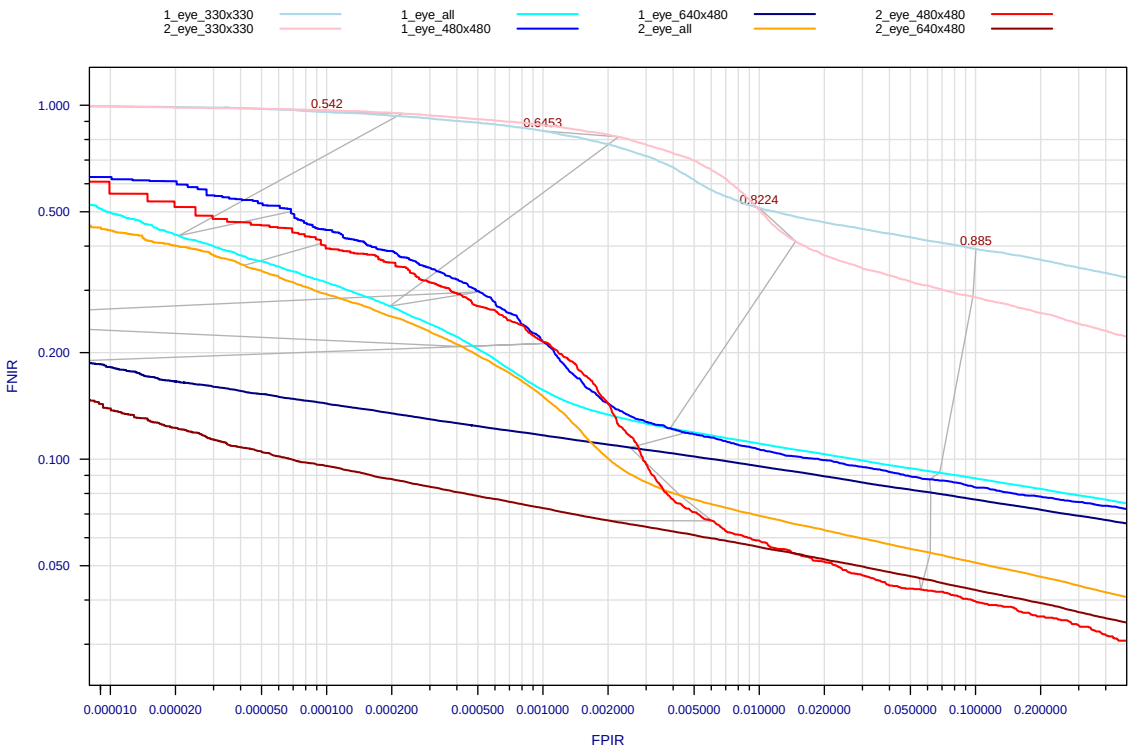

(a) Large search set, $\mathcal{S}_{nb}$

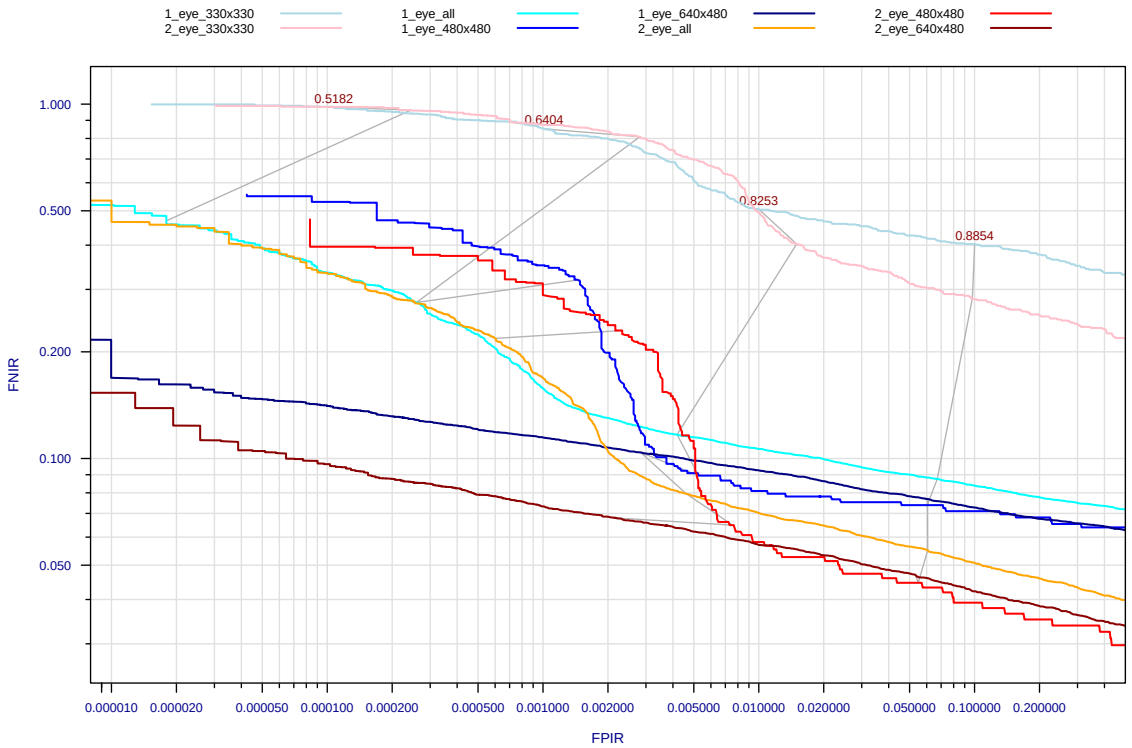

(b) Small search set, $\mathcal{S}_{na}$

Figure 563: DET for implementation V01A executing searches in an enrolled population of N = 1.6 million, broken out for three different image sizes (corresponding broadly to three camera plus ancillary software combinations) of the search image. The acquisition system used for the enrollment image (if any) is ignored in this breakout. Results for single-eye and two-eyes are plotted with two families of color. The straight lines, which link points of constant threshold, show how the two error rates would vary if a fixed threshold were adopted operationally.

FNIR = FALSE NEGATIVE IDENT. RATE FPIR = FALSE POSITIVE IDENT. RATE	N = NEUROTECHNOLOGY U = L1	P = SMU V = MORPHO	Q = IRITECH W = IRISID	R = COGENT X = CROSSMATCH	S = SMARTSENSORS Y = KYNEN	T = CAMBRIDGE

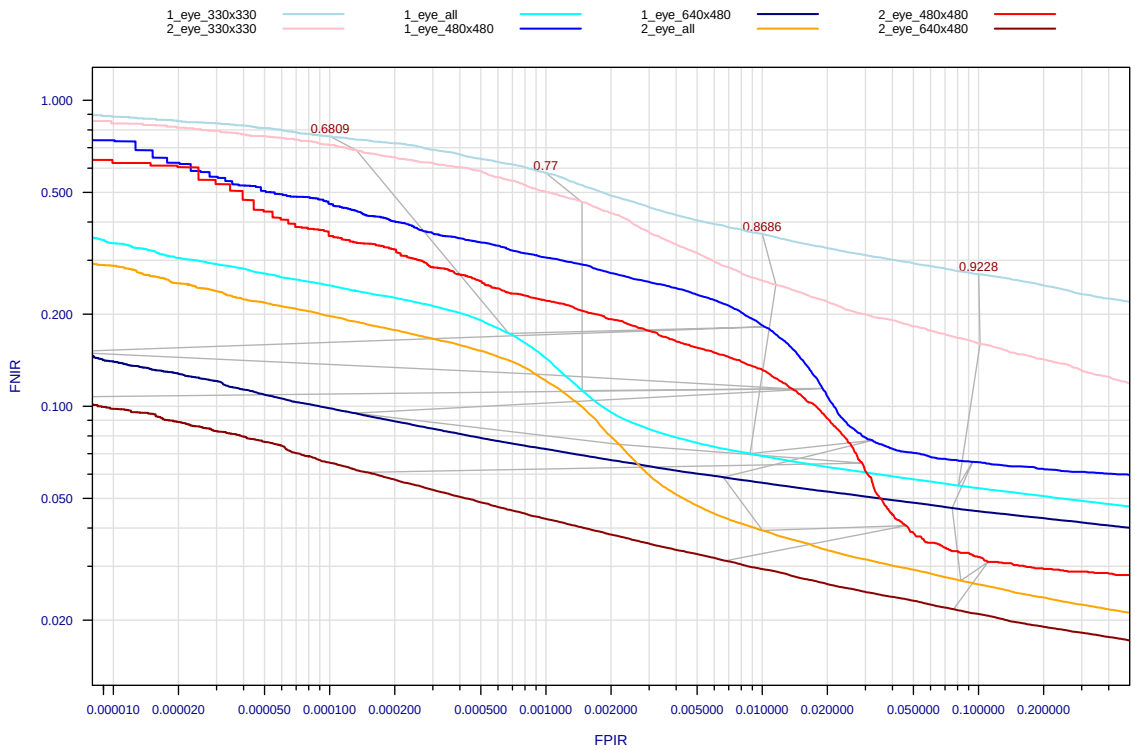

(a) Large search set, $\mathcal{S}_{nb}$

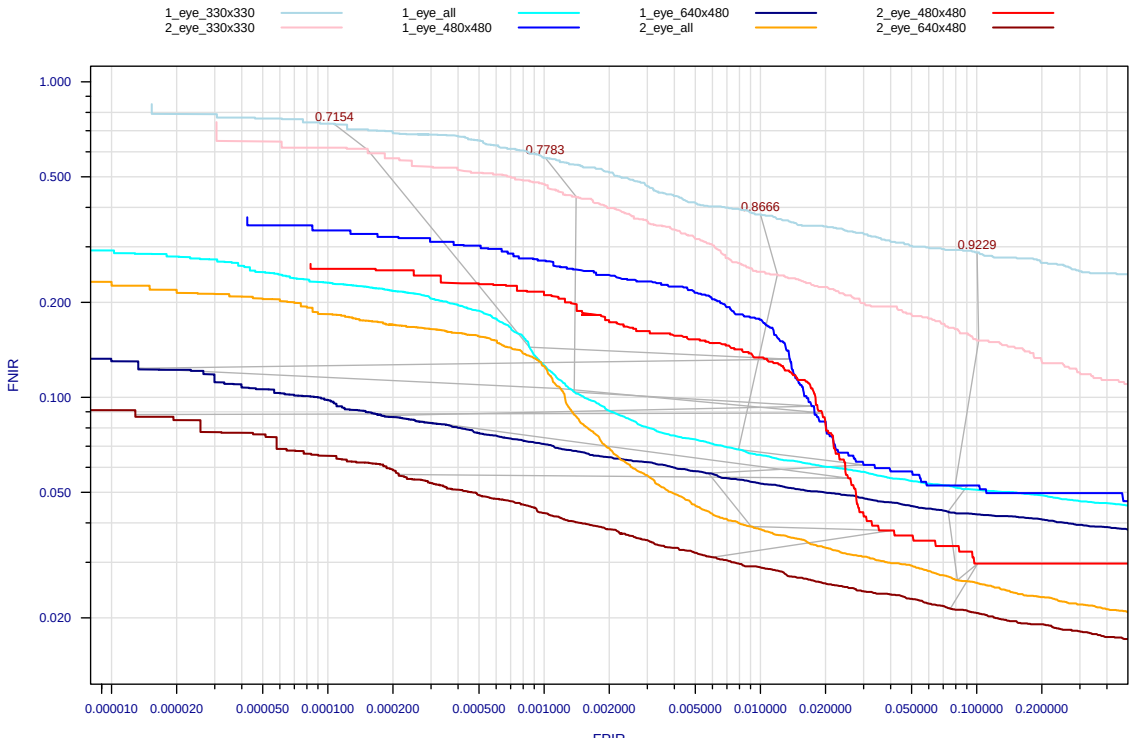

(b) Small search set, $\mathcal{S}_{na}$

Figure 564: DET for implementation V02A executing searches in an enrolled population of N = 1.6 million, broken out for three different image sizes (corresponding broadly to three camera plus ancillary software combinations) of the search image. The acquisition system used for the enrollment image (if any) is ignored in this breakout. Results for single-eye and two-eyes are plotted with two families of color. The straight lines, which link points of constant threshold, show how the two error rates would vary if a fixed threshold were adopted operationally.

FNIR = FALSE NEGATIVE IDENT. RATE FPIR = FALSE POSITIVE IDENT. RATE	N = NEUROTECHNOLOGY U = L1	P = SMU V = MORPHO	Q = IRITECH W = IRISID	R = COGENT X = CROSSMATCH	S = SMARTSENSORS Y = KYNEN	T = CAMBRIDGE

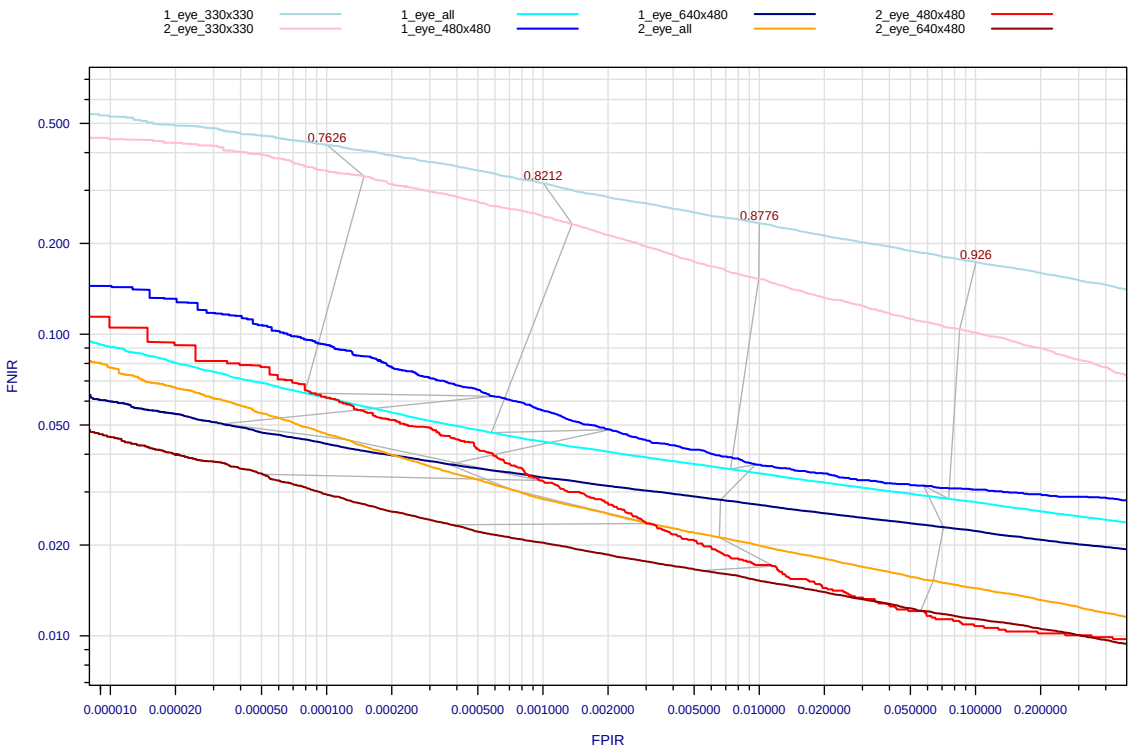

(a) Large search set, $\mathcal{S}_{nb}$

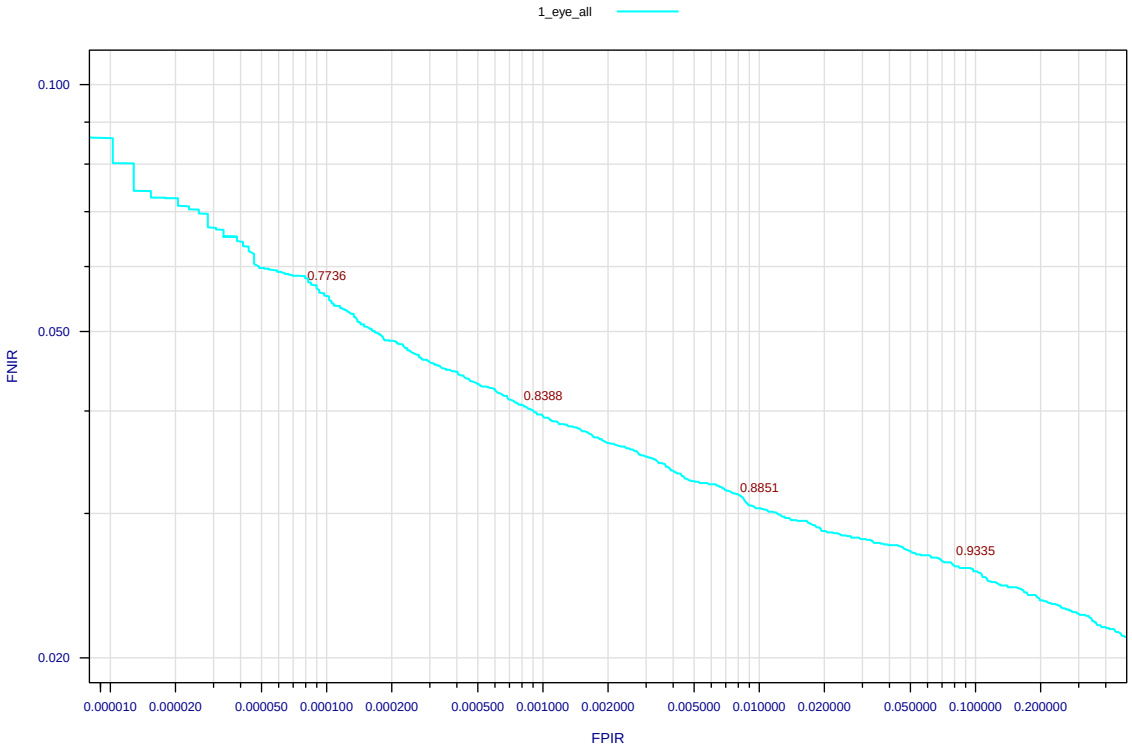

(b) Small search set, $\mathcal{S}_{na}$

Figure 565: DET for implementation V03A executing searches in an enrolled population of N = 1.6 million, broken out for three different image sizes (corresponding broadly to three camera plus ancillary software combinations) of the search image. The acquisition system used for the enrollment image (if any) is ignored in this breakout. Results for single-eye and two-eyes are plotted with two families of color. The straight lines, which link points of constant threshold, show how the two error rates would vary if a fixed threshold were adopted operationally.

FNIR = FALSE NEGATIVE IDENT. RATE FPIR = FALSE POSITIVE IDENT. RATE	N = NEUROTECHNOLOGY U = L1	P = SMU V = MORPHO	Q = IRITECH W = IRISID	R = COGENT X = CROSSMATCH	S = SMARTSENSORS Y = KYNEN	T = CAMBRIDGE

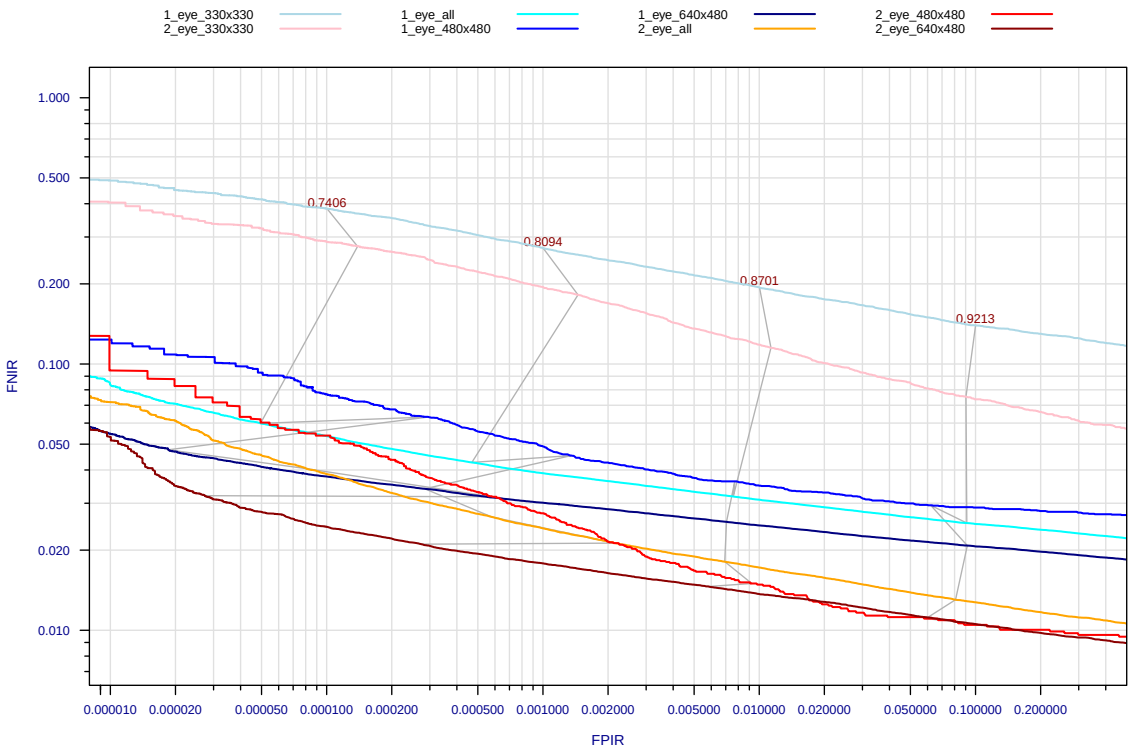

(a) Large search set, $\mathcal{S}_{nb}$

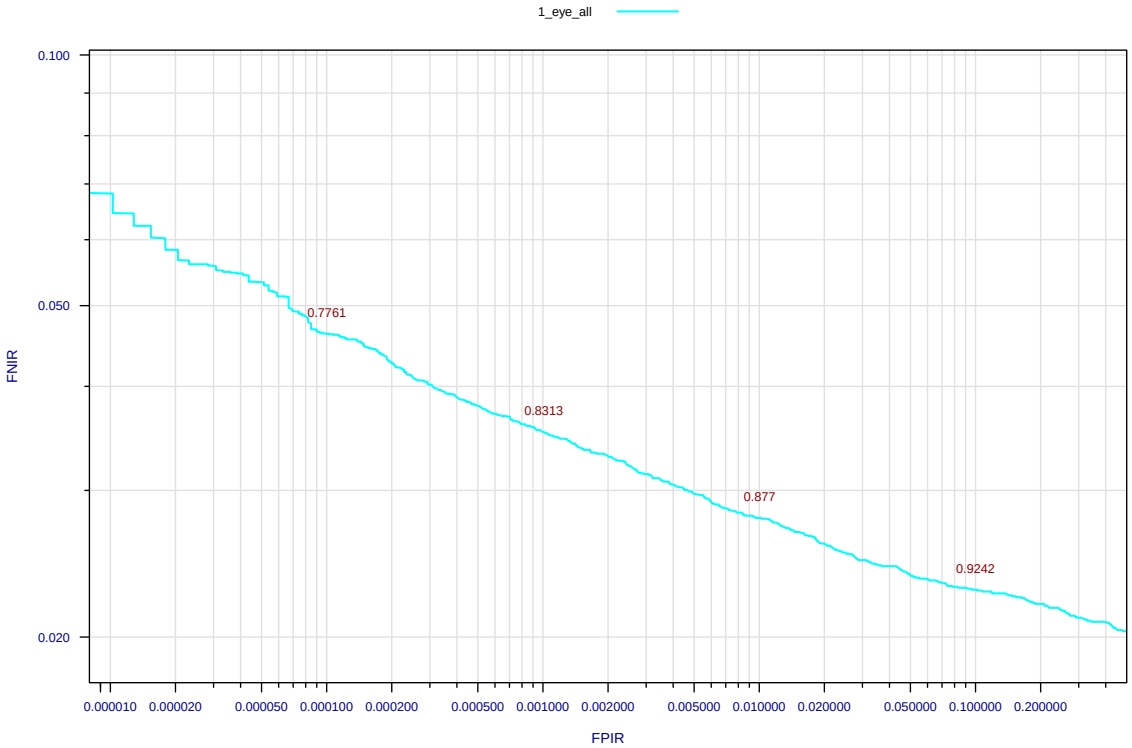

(b) Small search set, $\mathcal{S}_{na}$

Figure 566: DET for implementation V03B executing searches in an enrolled population of N = 1.6 million, broken out for three different image sizes (corresponding broadly to three camera plus ancillary software combinations) of the search image. The acquisition system used for the enrollment image (if any) is ignored in this breakout. Results for single-eye and two-eyes are plotted with two families of color. The straight lines, which link points of constant threshold, show how the two error rates would vary if a fixed threshold were adopted operationally.

FNIR = FALSE NEGATIVE IDENT. RATE FPIR = FALSE POSITIVE IDENT. RATE	N = NEUROTECHNOLOGY U = L1	P = SMU V = MORPHO	Q = IRITECH W = IRISID	R = COGENT X = CROSSMATCH	S = SMARTSENSORS Y = KYNEN	T = CAMBRIDGE

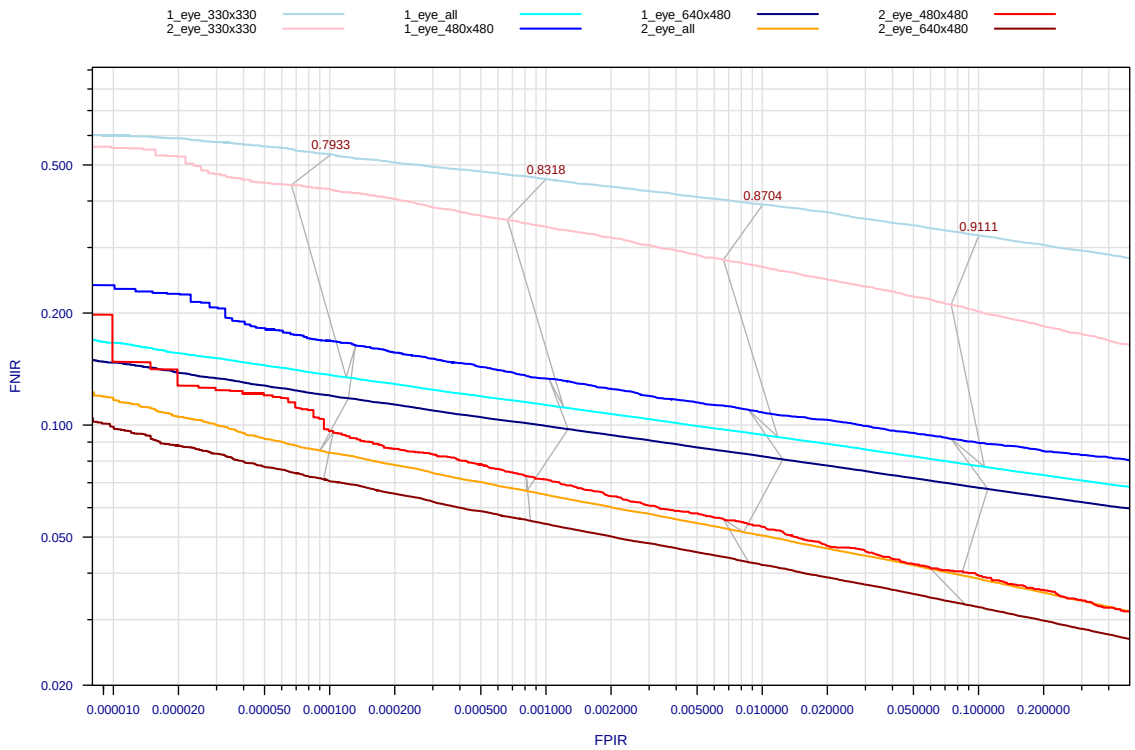

(a) Large search set, $\mathcal{S}_{nb}$

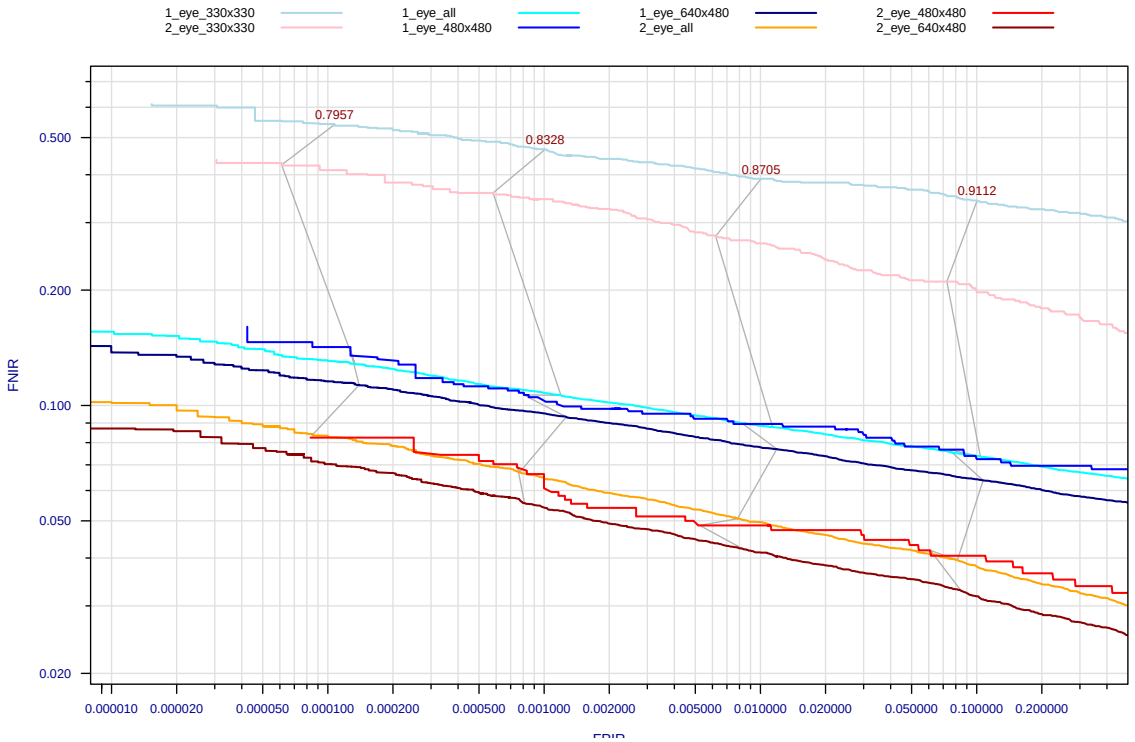

(b) Small search set, $\mathcal{S}_{na}$

Figure 567: DET for implementation V04A executing searches in an enrolled population of N = 1.6 million, broken out for three different image sizes (corresponding broadly to three camera plus ancillary software combinations) of the search image. The acquisition system used for the enrollment image (if any) is ignored in this breakout. Results for single-eye and two-eyes are plotted with two families of color. The straight lines, which link points of constant threshold, show how the two error rates would vary if a fixed threshold were adopted operationally.

FNIR = FALSE NEGATIVE IDENT. RATE FPIR = FALSE POSITIVE IDENT. RATE	N = NEUROTECHNOLOGY U = L1	P = SMU V = MORPHO	Q = IRITECH W = IRISID	R = COGENT X = CROSSMATCH	S = SMARTSENSORS Y = KYNEN	T = CAMBRIDGE

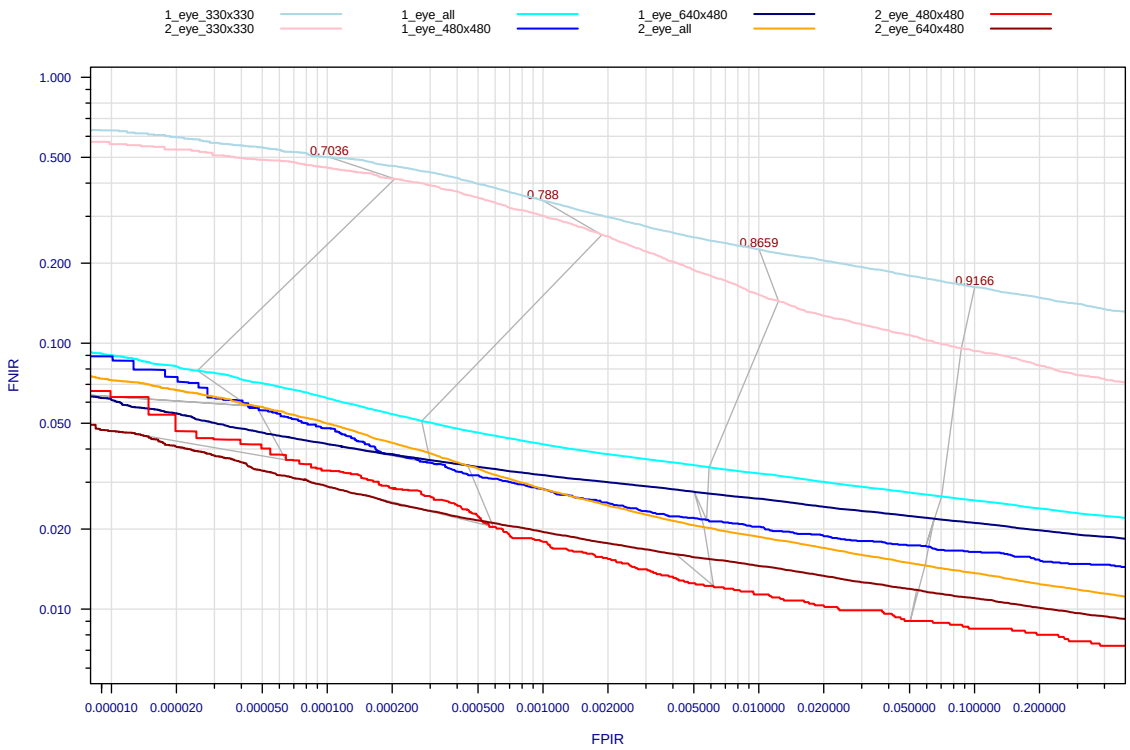

(a) Large search set, $\mathcal{S}_{nb}$

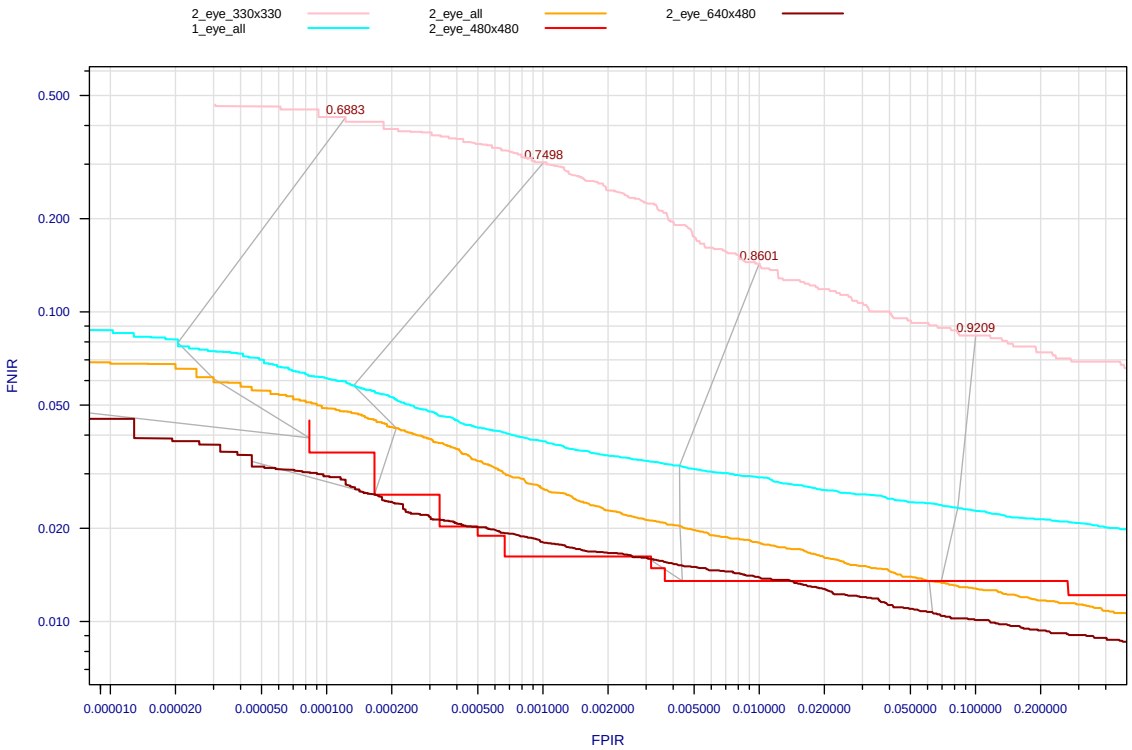

(b) Small search set, $\mathcal{S}_{na}$

Figure 568: DET for implementation V11A executing searches in an enrolled population of N = 1.6 million, broken out for three different image sizes (corresponding broadly to three camera plus ancillary software combinations) of the search image. The acquisition system used for the enrollment image (if any) is ignored in this breakout. Results for single-eye and two-eyes are plotted with two families of color. The straight lines, which link points of constant threshold, show how the two error rates would vary if a fixed threshold were adopted operationally.

FNIR = FALSE NEGATIVE IDENT. RATE FPIR = FALSE POSITIVE IDENT. RATE	N = NEUROTECHNOLOGY U = L1	P = SMU V = MORPHO	Q = IRITECH W = IRISID	R = COGENT X = CROSSMATCH	S = SMARTSENSORS Y = KYNEN	T = CAMBRIDGE

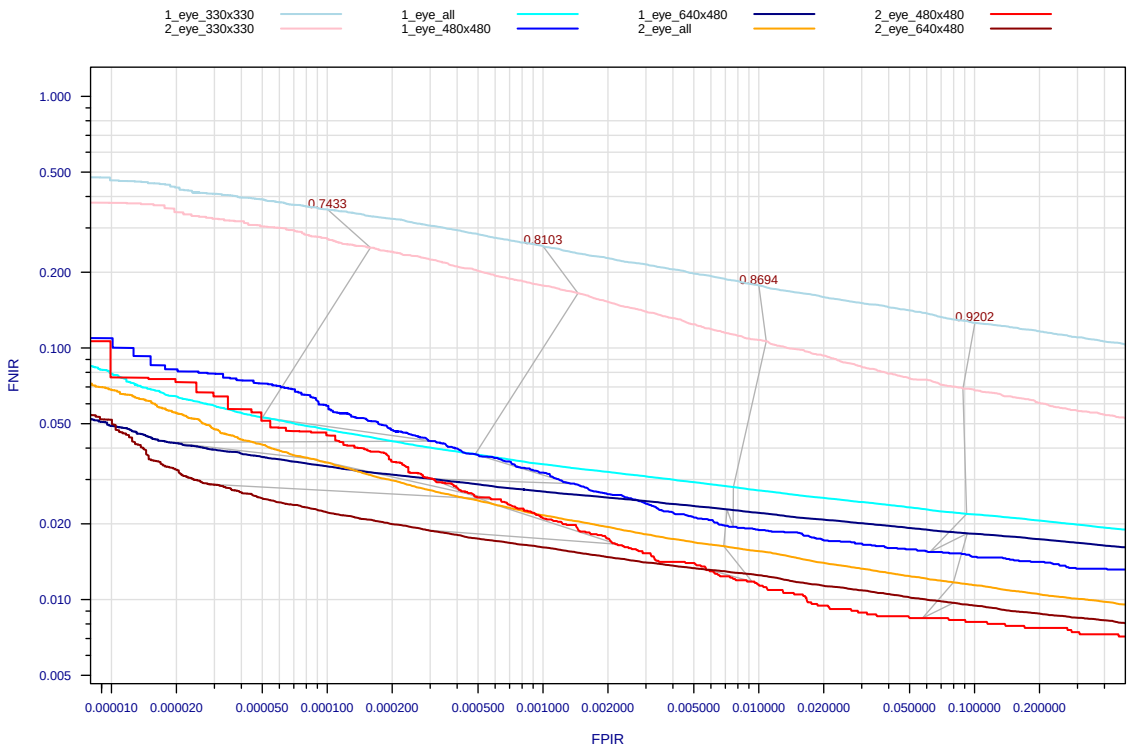

(a) Large search set, $\mathcal{S}_{nb}$

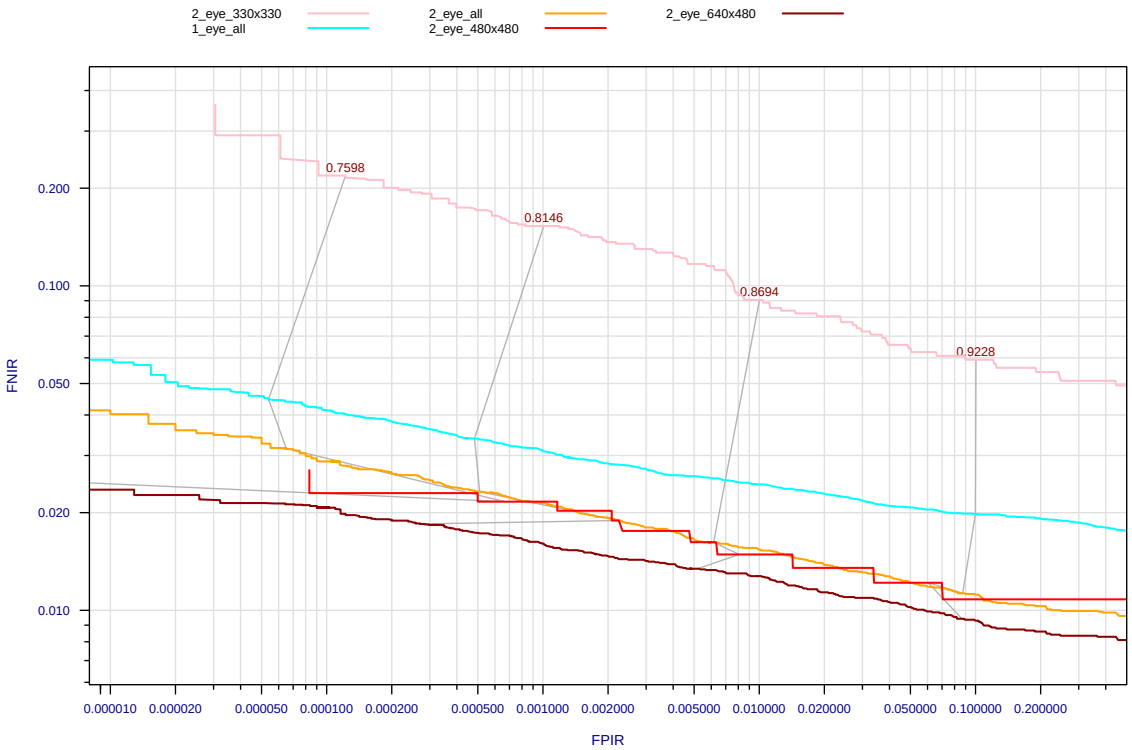

(b) Small search set, $\mathcal{S}_{na}$

Figure 569: DET for implementation V11B executing searches in an enrolled population of N = 1.6 million, broken out for three different image sizes (corresponding broadly to three camera plus ancillary software combinations) of the search image. The acquisition system used for the enrollment image (if any) is ignored in this breakout. Results for single-eye and two-eyes are plotted with two families of color. The straight lines, which link points of constant threshold, show how the two error rates would vary if a fixed threshold were adopted operationally.

FNIR = FALSE NEGATIVE IDENT. RATE FPIR = FALSE POSITIVE IDENT. RATE	N = NEUROTECHNOLOGY U = L1	P = SMU V = MORPHO	Q = IRITECH W = IRISID	R = COGENT X = CROSSMATCH	S = SMARTSENSORS Y = KYNEN	T = CAMBRIDGE

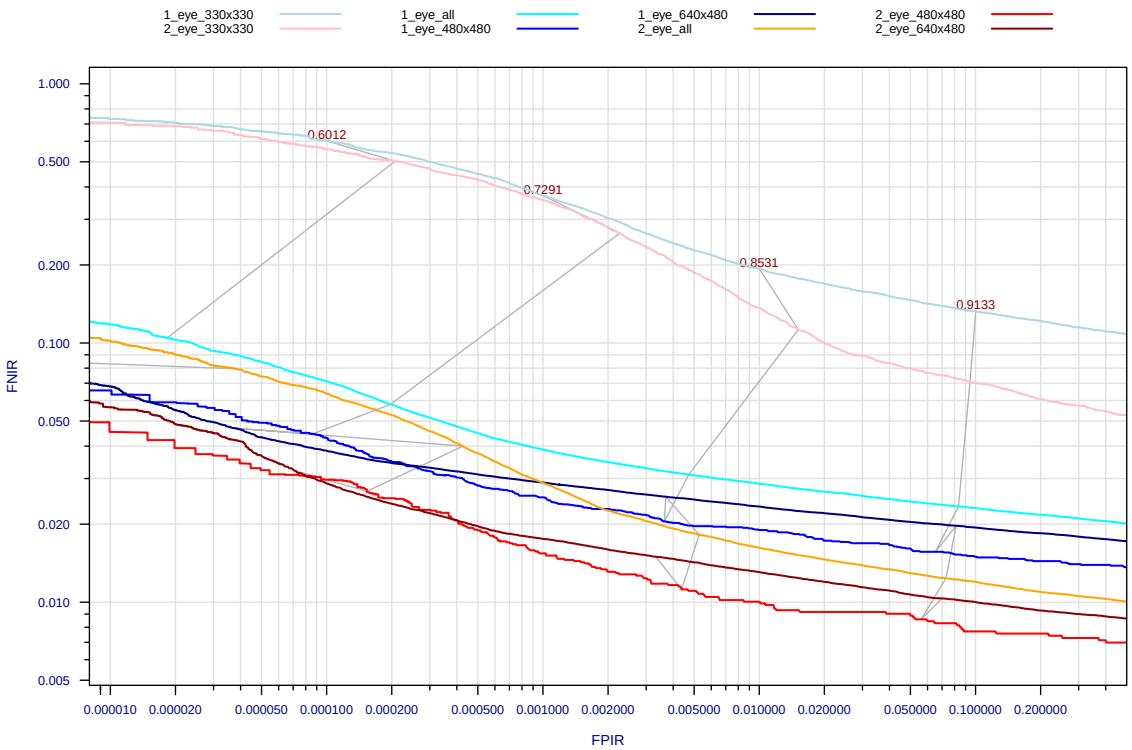

(a) Large search set, $\mathcal{S}_{nb}$

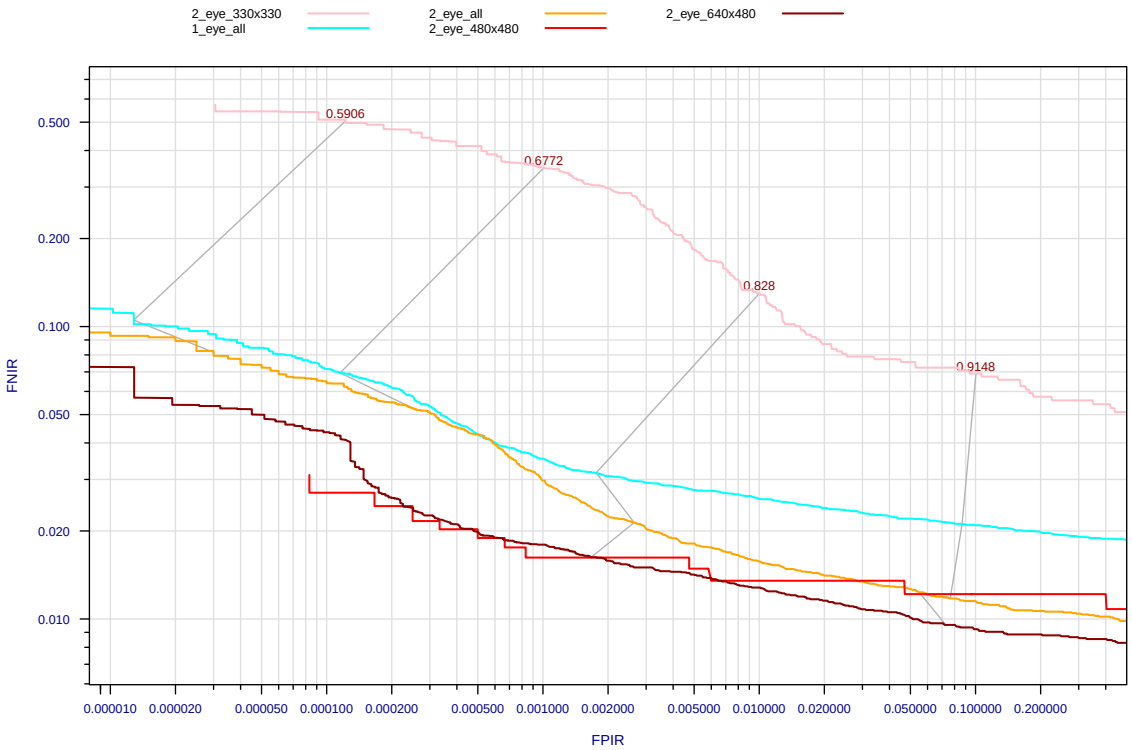

(b) Small search set, $\mathcal{S}_{na}$

Figure 570: DET for implementation V12A executing searches in an enrolled population of N = 1.6 million, broken out for three different image sizes (corresponding broadly to three camera plus ancillary software combinations) of the search image. The acquisition system used for the enrollment image (if any) is ignored in this breakout. Results for single-eye and two-eyes are plotted with two families of color. The straight lines, which link points of constant threshold, show how the two error rates would vary if a fixed threshold were adopted operationally.

FNIR = FALSE NEGATIVE IDENT. RATE FPIR = FALSE POSITIVE IDENT. RATE	N = NEUROTECHNOLOGY U = L1	P = SMU V = MORPHO	Q = IRITECH W = IRISID	R = COGENT X = CROSSMATCH	S = SMARTSENSORS Y = KYNEN	T = CAMBRIDGE

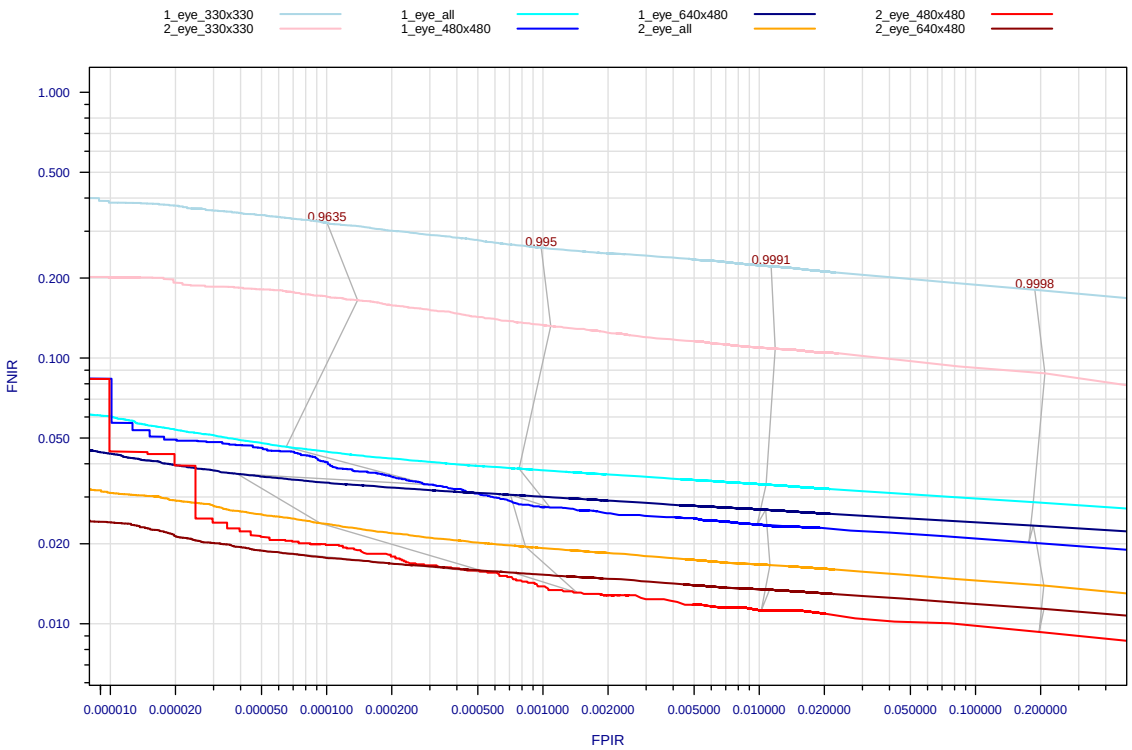

(a) Large search set, $\mathcal{S}_{nb}$

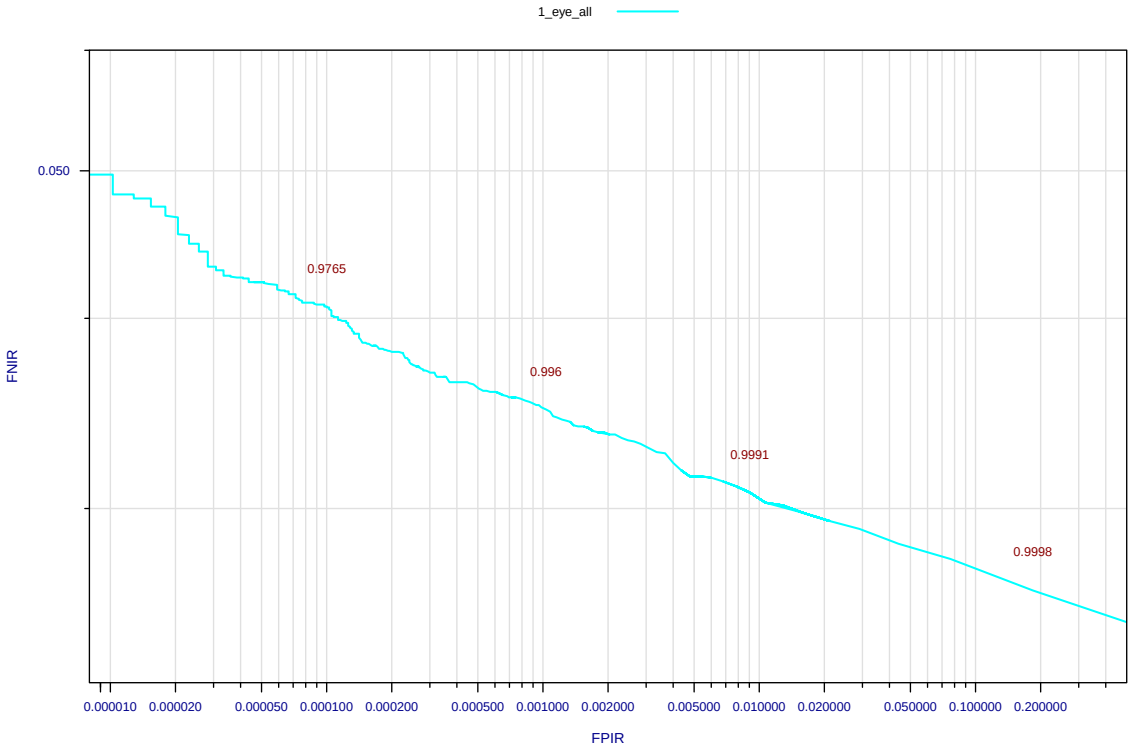

(b) Small search set, $\mathcal{S}_{na}$

Figure 571: DET for implementation V12B executing searches in an enrolled population of N = 1.6 million, broken out for three different image sizes (corresponding broadly to three camera plus ancillary software combinations) of the search image. The acquisition system used for the enrollment image (if any) is ignored in this breakout. Results for single-eye and two-eyes are plotted with two families of color. The straight lines, which link points of constant threshold, show how the two error rates would vary if a fixed threshold were adopted operationally.

FNIR = FALSE NEGATIVE IDENT. RATE FPIR = FALSE POSITIVE IDENT. RATE	N = NEUROTECHNOLOGY U = L1	P = SMU V = MORPHO	Q = IRITECH W = IRISID	R = COGENT X = CROSSMATCH	S = SMARTSENSORS Y = KYNEN	T = CAMBRIDGE

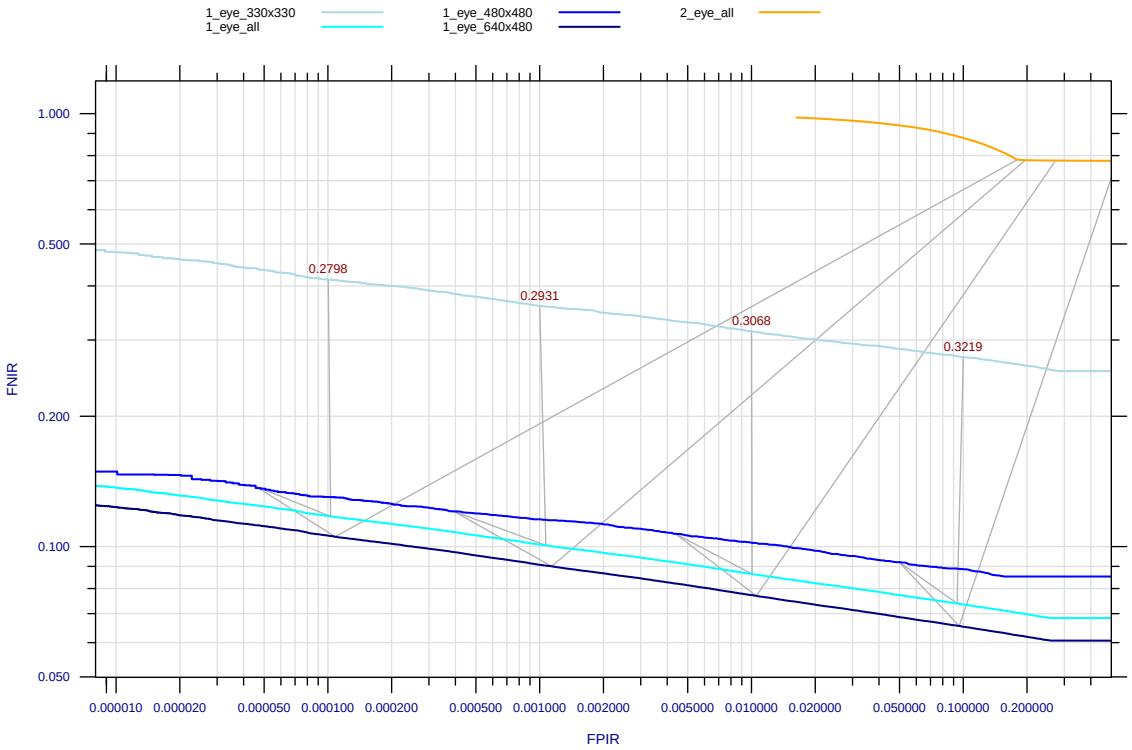

(a) Large search set, $\mathcal{S}_{nb}$

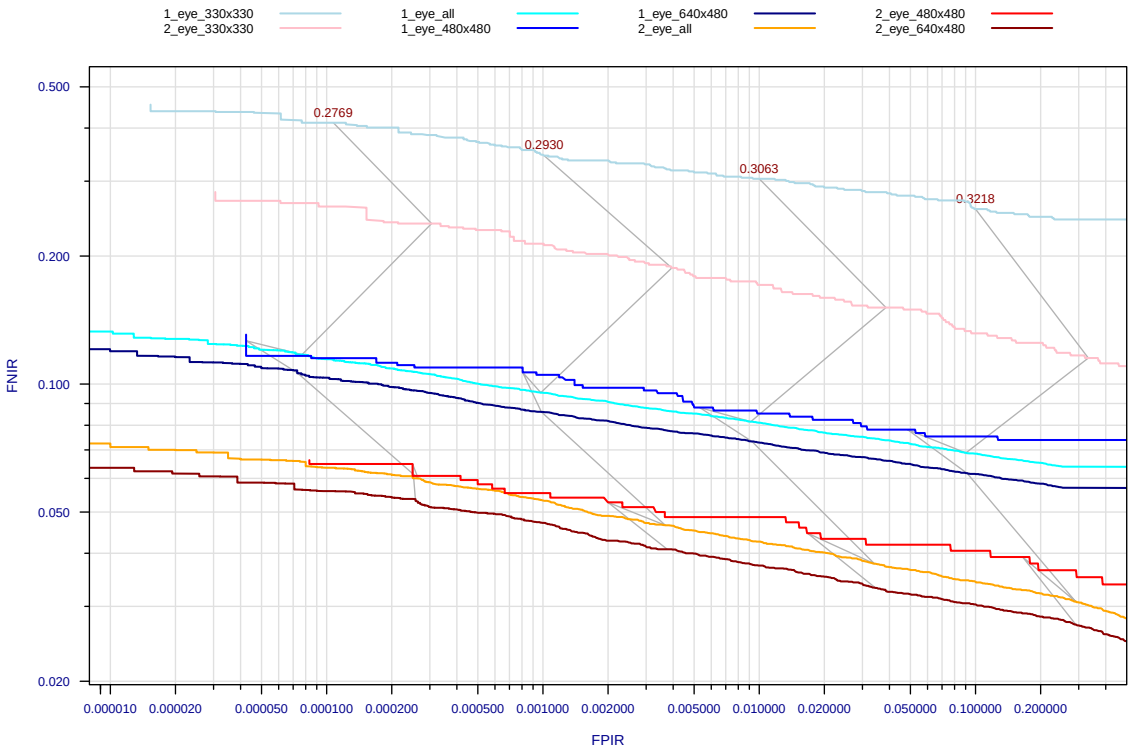

(b) Small search set, $\mathcal{S}_{na}$

Figure 572: DET for implementation W01A executing searches in an enrolled population of N = 1.6 million, broken out for three different image sizes (corresponding broadly to three camera plus ancillary software combinations) of the search image. The acquisition system used for the enrollment image (if any) is ignored in this breakout. Results for single-eye and two-eyes are plotted with two families of color. The straight lines, which link points of constant threshold, show how the two error rates would vary if a fixed threshold were adopted operationally.

FNIR = FALSE NEGATIVE IDENT. RATE FPIR = FALSE POSITIVE IDENT. RATE	N = NEUROTECHNOLOGY U = L1	P = SMU V = MORPHO	Q = IRITECH W = IRISID	R = COGENT X = CROSSMATCH	S = SMARTSENSORS Y = KYNEN	T = CAMBRIDGE

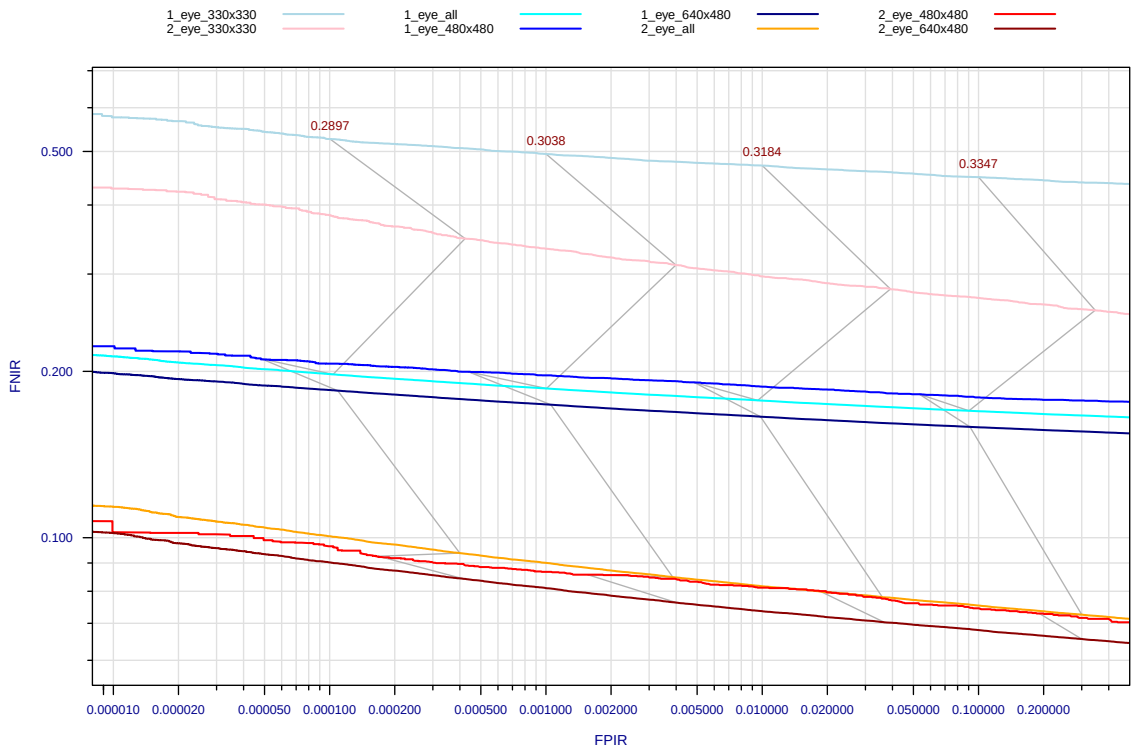

(a) Large search set, $\mathcal{S}_{nb}$

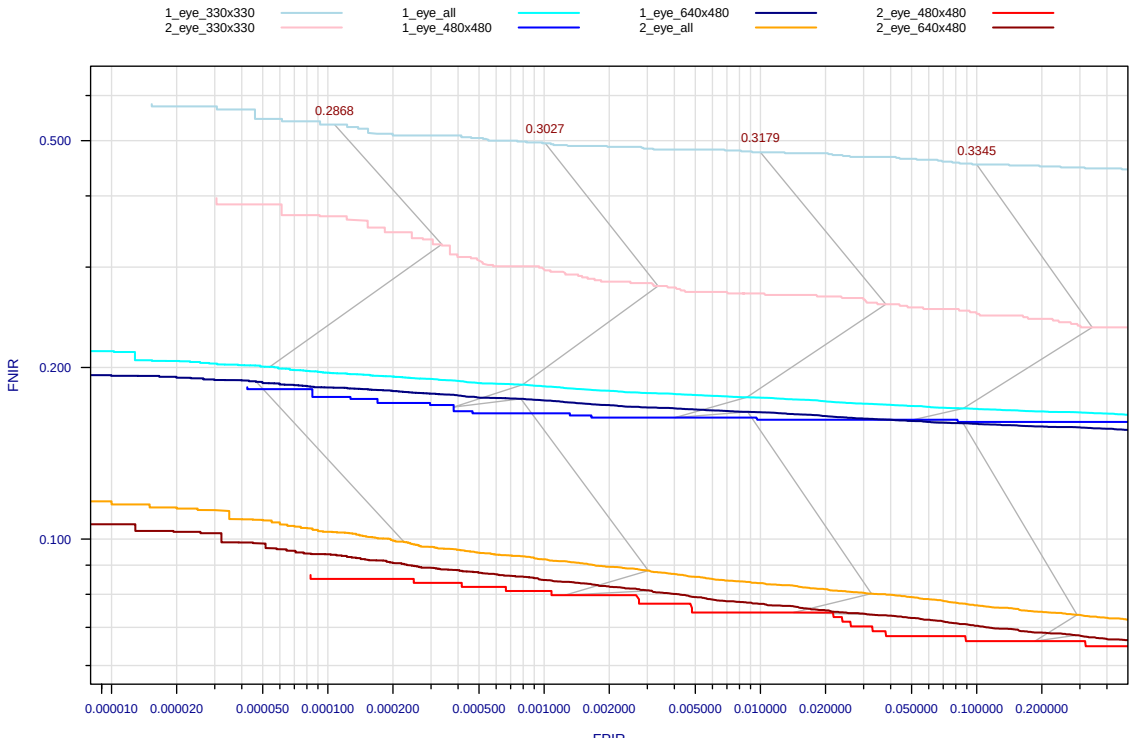

(b) Small search set, $\mathcal{S}_{na}$

Figure 573: DET for implementation W01B executing searches in an enrolled population of N = 1.6 million, broken out for three different image sizes (corresponding broadly to three camera plus ancillary software combinations) of the search image. The acquisition system used for the enrollment image (if any) is ignored in this breakout. Results for single-eye and two-eyes are plotted with two families of color. The straight lines, which link points of constant threshold, show how the two error rates would vary if a fixed threshold were adopted operationally.

FNIR = FALSE NEGATIVE IDENT. RATE FPIR = FALSE POSITIVE IDENT. RATE	N = NEUROTECHNOLOGY U = L1	P = SMU V = MORPHO	Q = IRITECH W = IRISID	R = COGENT X = CROSSMATCH	S = SMARTSENSORS Y = KYNEN	T = CAMBRIDGE

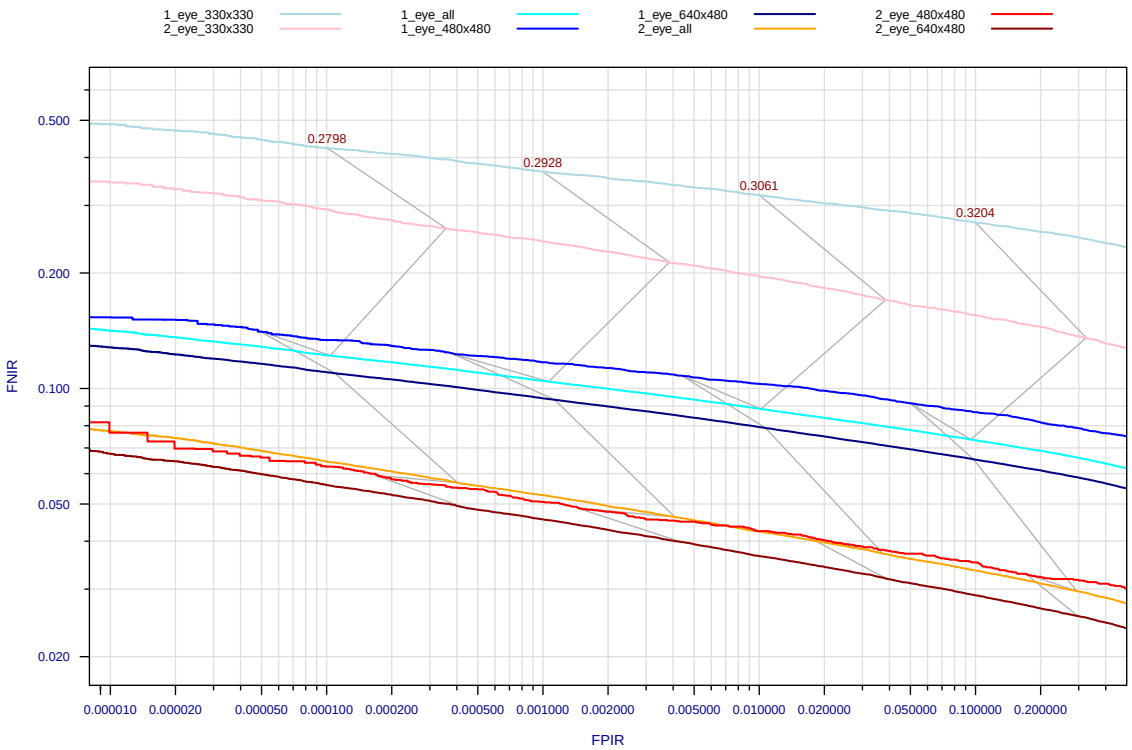

(a) Large search set, $\mathcal{S}_{nb}$

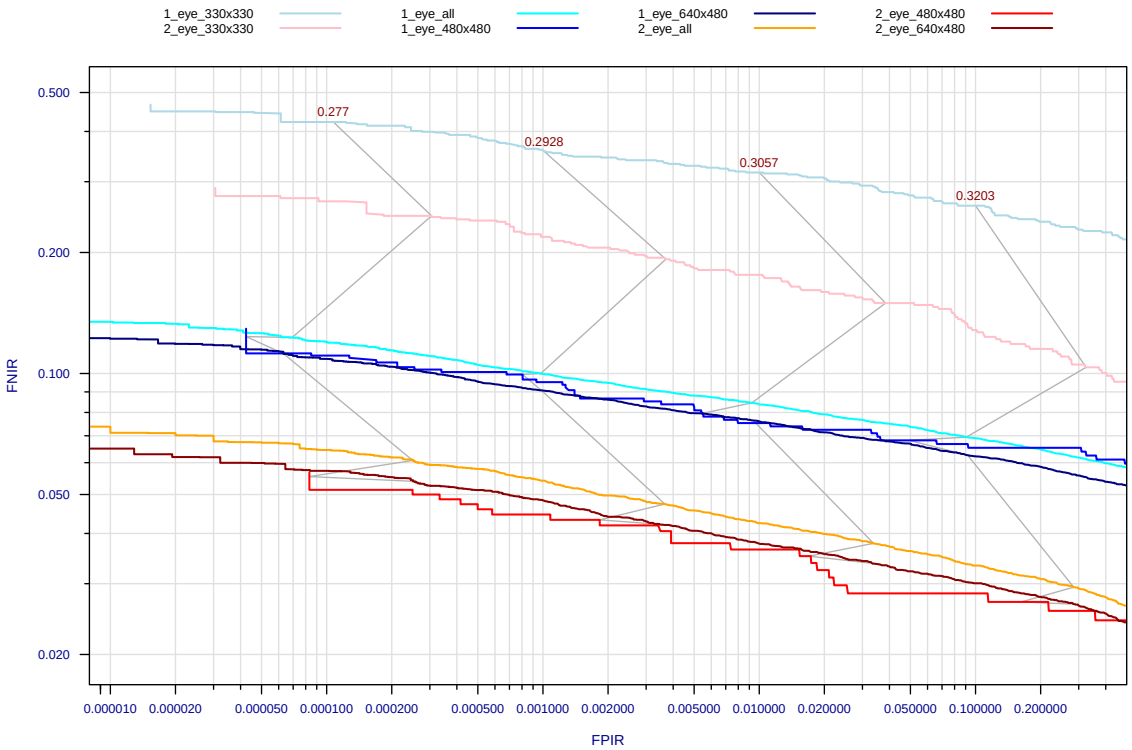

(b) Small search set, $\mathcal{S}_{na}$

Figure 574: DET for implementation W02A executing searches in an enrolled population of N = 1.6 million, broken out for three different image sizes (corresponding broadly to three camera plus ancillary software combinations) of the search image. The acquisition system used for the enrollment image (if any) is ignored in this breakout. Results for single-eye and two-eyes are plotted with two families of color. The straight lines, which link points of constant threshold, show how the two error rates would vary if a fixed threshold were adopted operationally.

FNIR = FALSE NEGATIVE IDENT. RATE FPIR = FALSE POSITIVE IDENT. RATE	N = NEUROTECHNOLOGY U = L1	P = SMU V = MORPHO	Q = IRITECH W = IRISID	R = COGENT X = CROSSMATCH	S = SMARTSENSORS Y = KYNEN	T = CAMBRIDGE

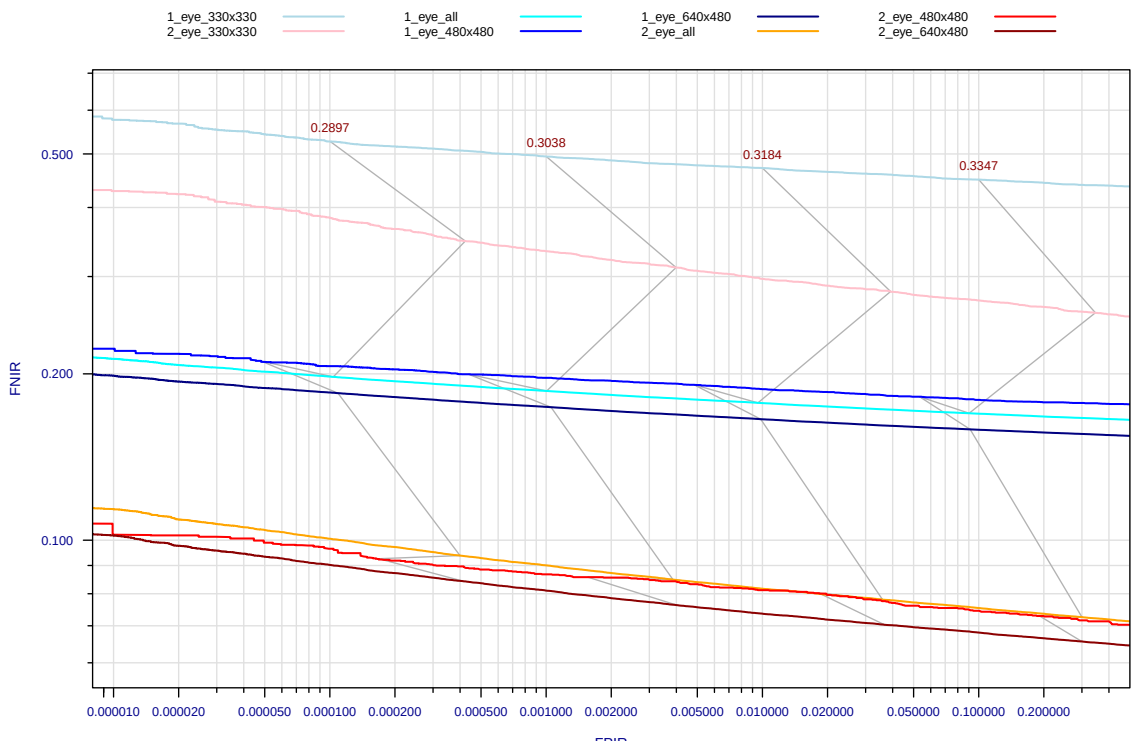

(a) Large search set, $\mathcal{S}_{nb}$

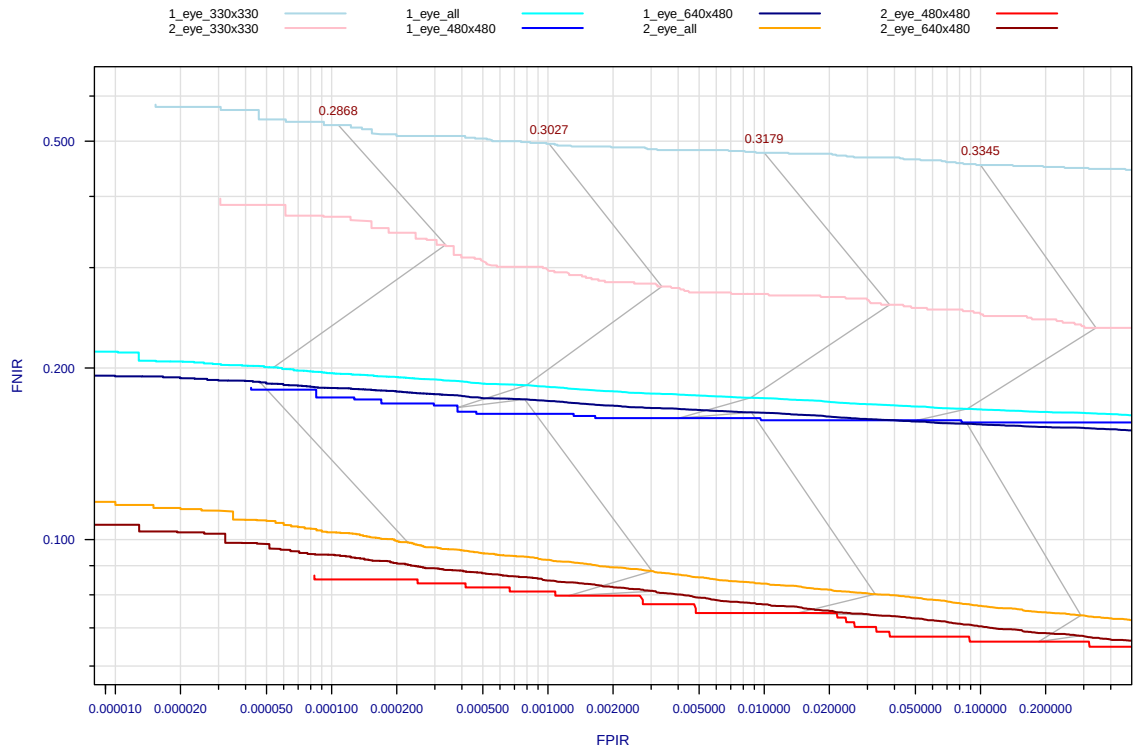

(b) Small search set, $\mathcal{S}_{na}$

Figure 575: DET for implementation W02B executing searches in an enrolled population of N = 1.6 million, broken out for three different image sizes (corresponding broadly to three camera plus ancillary software combinations) of the search image. The acquisition system used for the enrollment image (if any) is ignored in this breakout. Results for single-eye and two-eyes are plotted with two families of color. The straight lines, which link points of constant threshold, show how the two error rates would vary if a fixed threshold were adopted operationally.

FNIR = FALSE NEGATIVE IDENT. RATE FPIR = FALSE POSITIVE IDENT. RATE	N = NEUROTECHNOLOGY U = L1	P = SMU V = MORPHO	Q = IRITECH W = IRISID	R = COGENT X = CROSSMATCH	S = SMARTSENSORS Y = KYNEN	T = CAMBRIDGE

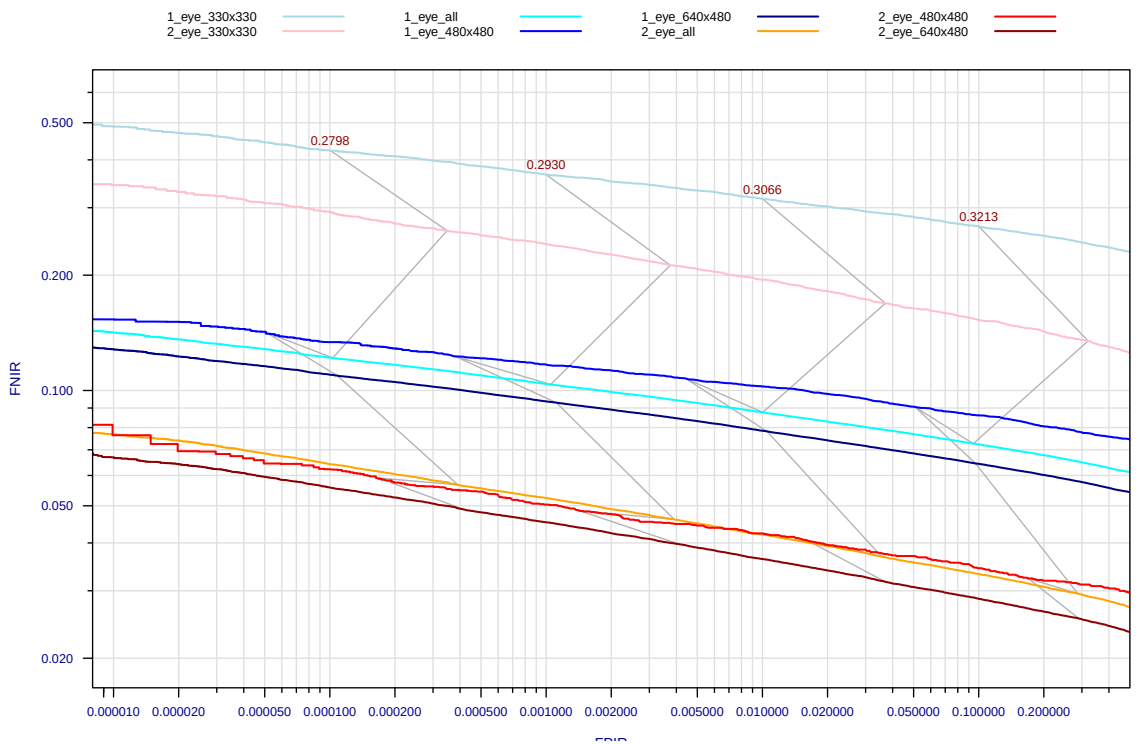

(a) Large search set, $\mathcal{S}_{nb}$

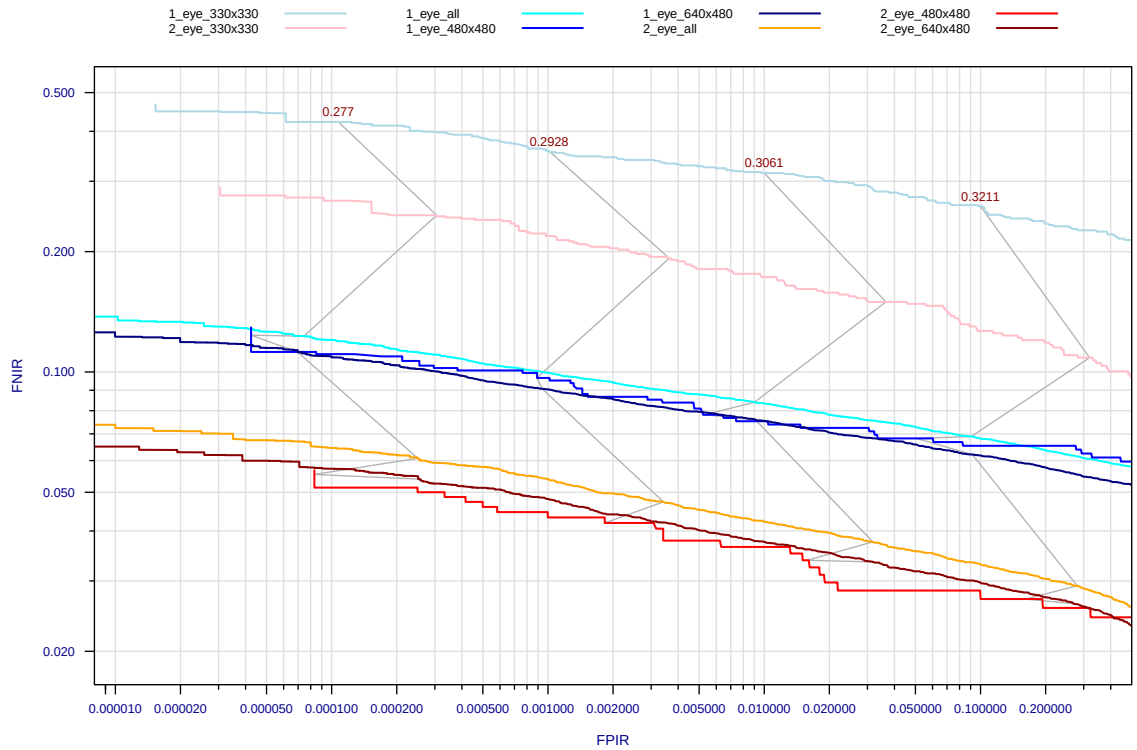

(b) Small search set, $\mathcal{S}_{na}$

Figure 576: DET for implementation W03A executing searches in an enrolled population of N = 1.6 million, broken out for three different image sizes (corresponding broadly to three camera plus ancillary software combinations) of the search image. The acquisition system used for the enrollment image (if any) is ignored in this breakout. Results for single-eye and two-eyes are plotted with two families of color. The straight lines, which link points of constant threshold, show how the two error rates would vary if a fixed threshold were adopted operationally.

FNIR = FALSE NEGATIVE IDENT. RATE FPIR = FALSE POSITIVE IDENT. RATE	N = NEUROTECHNOLOGY U = L1	P = SMU V = MORPHO	Q = IRITECH W = IRISID	R = COGENT X = CROSSMATCH	S = SMARTSENSORS Y = KYNEN	T = CAMBRIDGE

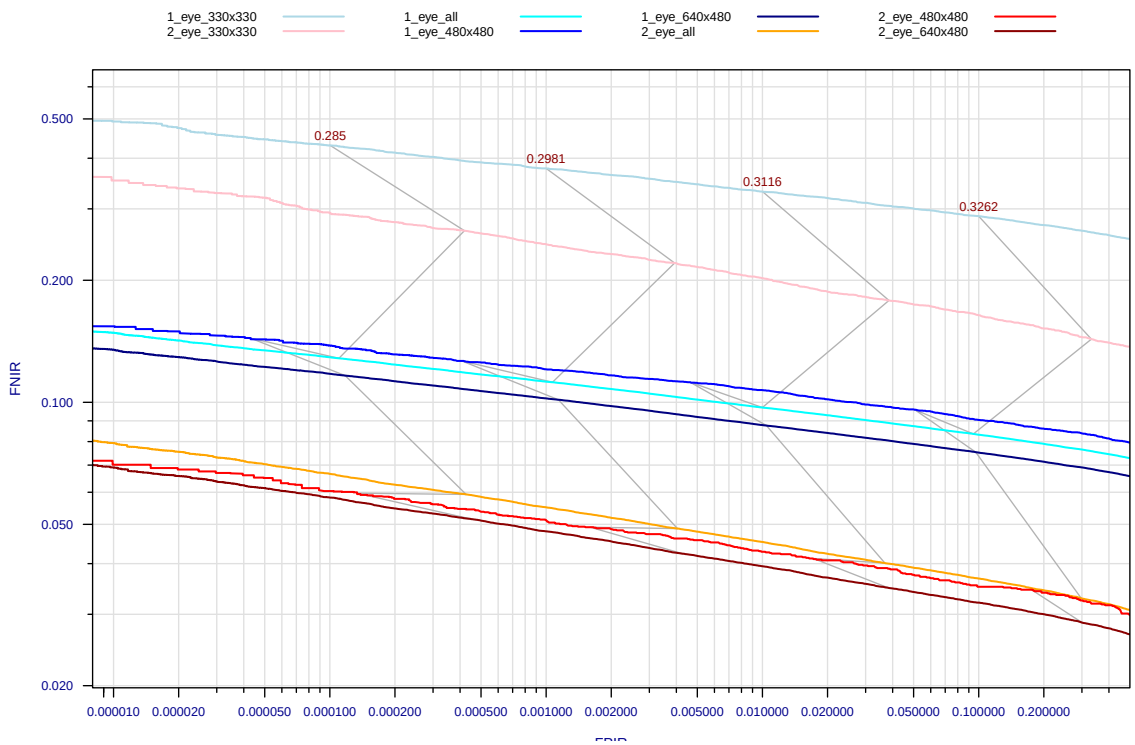

(a) Large search set, $\mathcal{S}_{nb}$

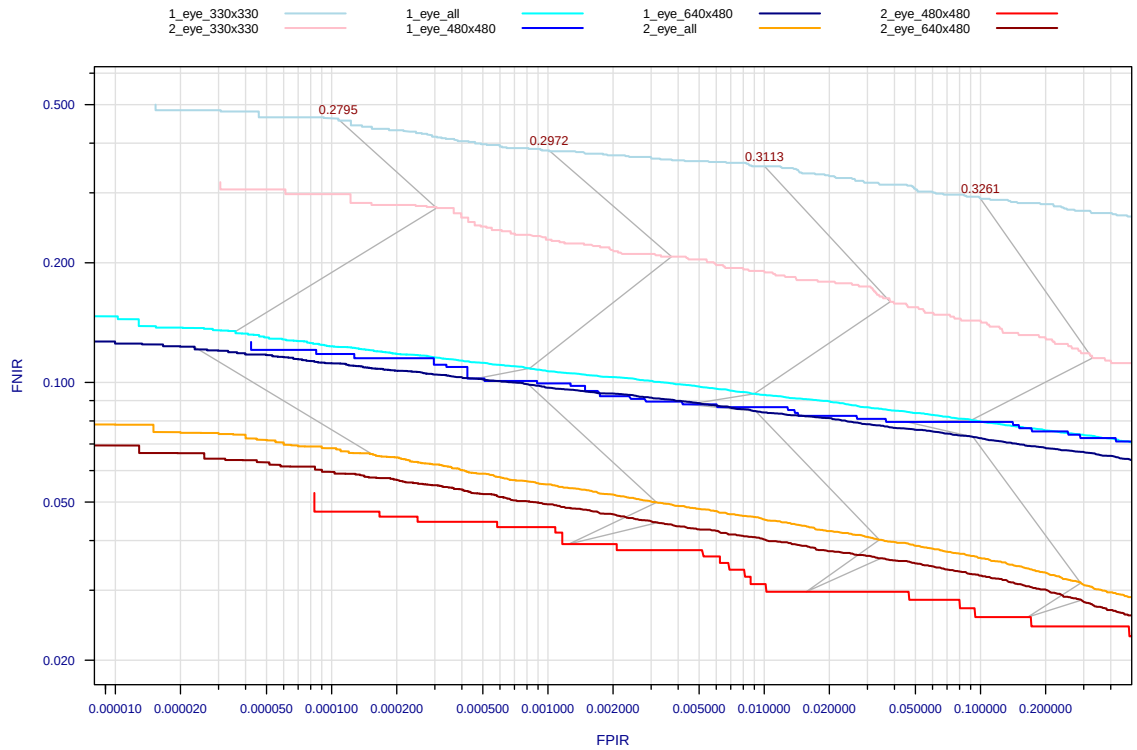

(b) Small search set, $\mathcal{S}_{na}$

Figure 577: DET for implementation W04A executing searches in an enrolled population of N = 1.6 million, broken out for three different image sizes (corresponding broadly to three camera plus ancillary software combinations) of the search image. The acquisition system used for the enrollment image (if any) is ignored in this breakout. Results for single-eye and two-eyes are plotted with two families of color. The straight lines, which link points of constant threshold, show how the two error rates would vary if a fixed threshold were adopted operationally.

FNIR = FALSE NEGATIVE IDENT. RATE FPIR = FALSE POSITIVE IDENT. RATE	N = NEUROTECHNOLOGY U = L1	P = SMU V = MORPHO	Q = IRITECH W = IRISID	R = COGENT X = CROSSMATCH	S = SMARTSENSORS Y = KYNEN	T = CAMBRIDGE

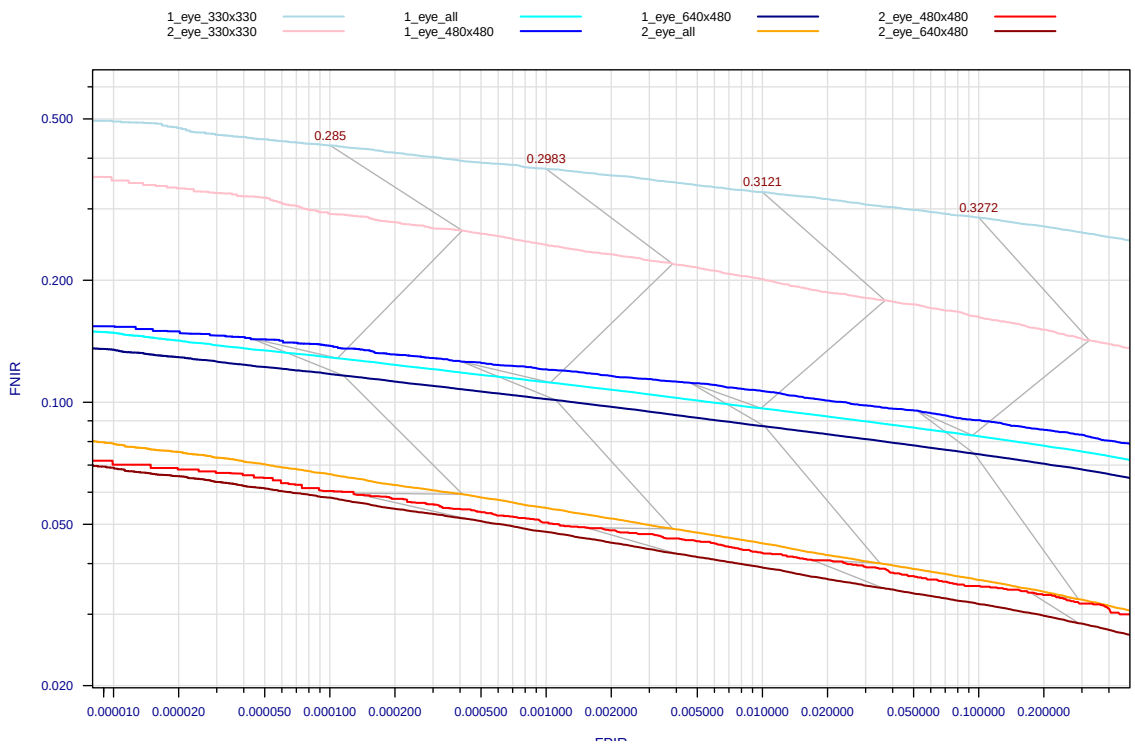

(a) Large search set, $\mathcal{S}_{nb}$

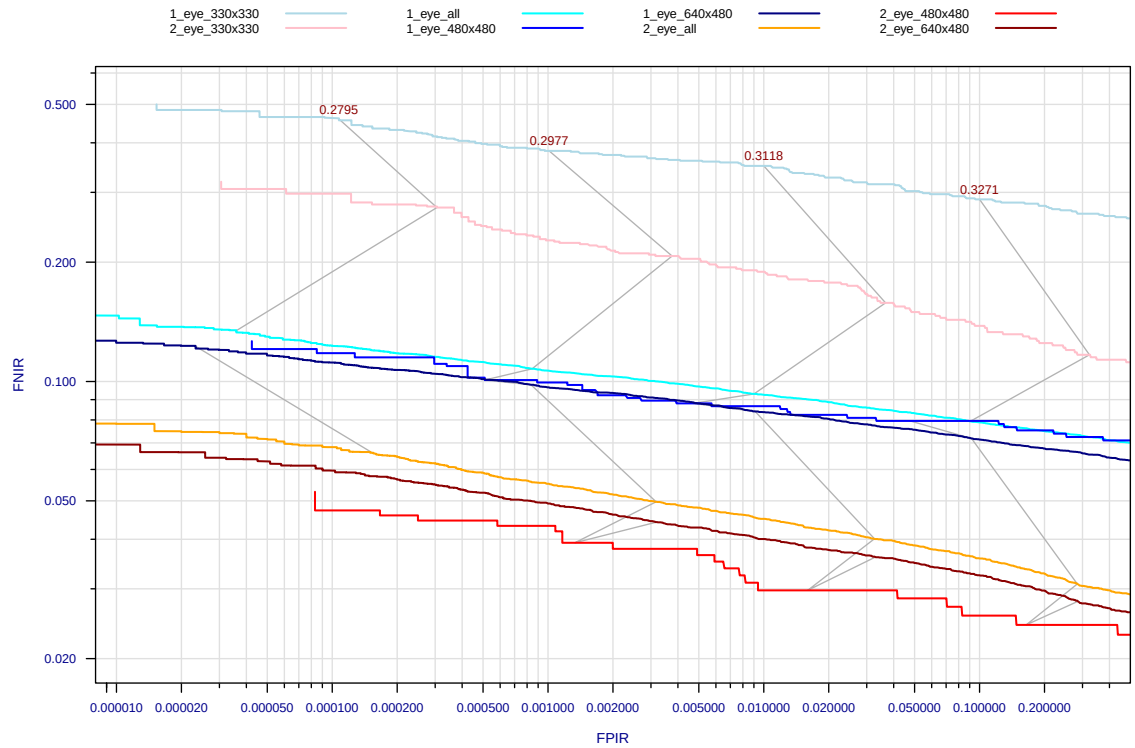

(b) Small search set, $\mathcal{S}_{na}$

Figure 578: DET for implementation W05A executing searches in an enrolled population of N = 1.6 million, broken out for three different image sizes (corresponding broadly to three camera plus ancillary software combinations) of the search image. The acquisition system used for the enrollment image (if any) is ignored in this breakout. Results for single-eye and two-eyes are plotted with two families of color. The straight lines, which link points of constant threshold, show how the two error rates would vary if a fixed threshold were adopted operationally.

FNIR = FALSE NEGATIVE IDENT. RATE FPIR = FALSE POSITIVE IDENT. RATE	N = NEUROTECHNOLOGY U = L1	P = SMU V = MORPHO	Q = IRITECH W = IRISID	R = COGENT X = CROSSMATCH	S = SMARTSENSORS Y = KYNEN	T = CAMBRIDGE

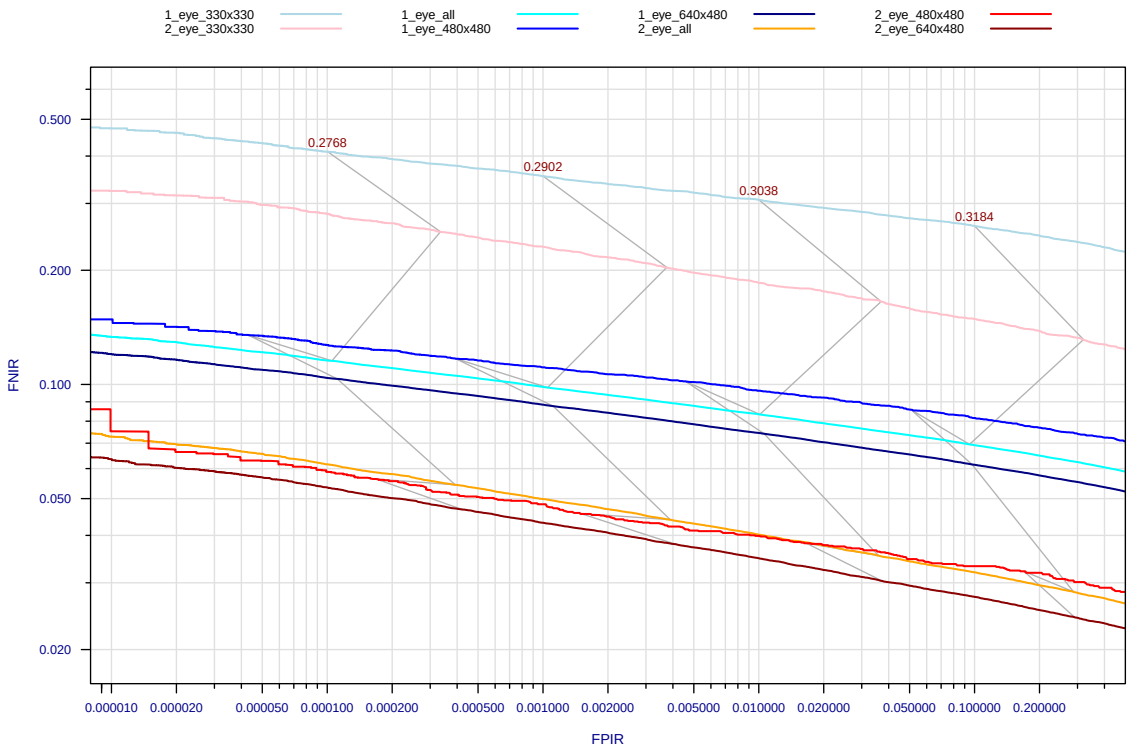

(a) Large search set, $\mathcal{S}_{nb}$

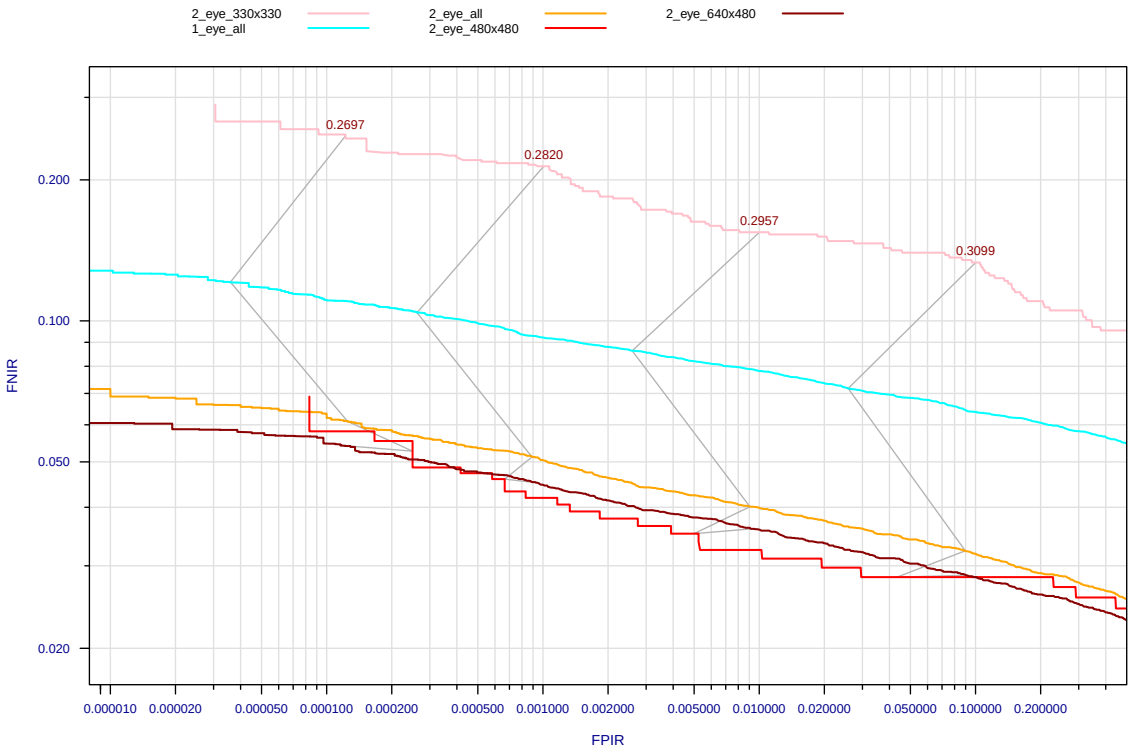

(b) Small search set, $\mathcal{S}_{na}$

Figure 579: DET for implementation W11A executing searches in an enrolled population of N = 1.6 million, broken out for three different image sizes (corresponding broadly to three camera plus ancillary software combinations) of the search image. The acquisition system used for the enrollment image (if any) is ignored in this breakout. Results for single-eye and two-eyes are plotted with two families of color. The straight lines, which link points of constant threshold, show how the two error rates would vary if a fixed threshold were adopted operationally.

FNIR = FALSE NEGATIVE IDENT. RATE FPIR = FALSE POSITIVE IDENT. RATE	N = NEUROTECHNOLOGY U = L1	P = SMU V = MORPHO	Q = IRITECH W = IRISID	R = COGENT X = CROSSMATCH	S = SMARTSENSORS Y = KYNEN	T = CAMBRIDGE

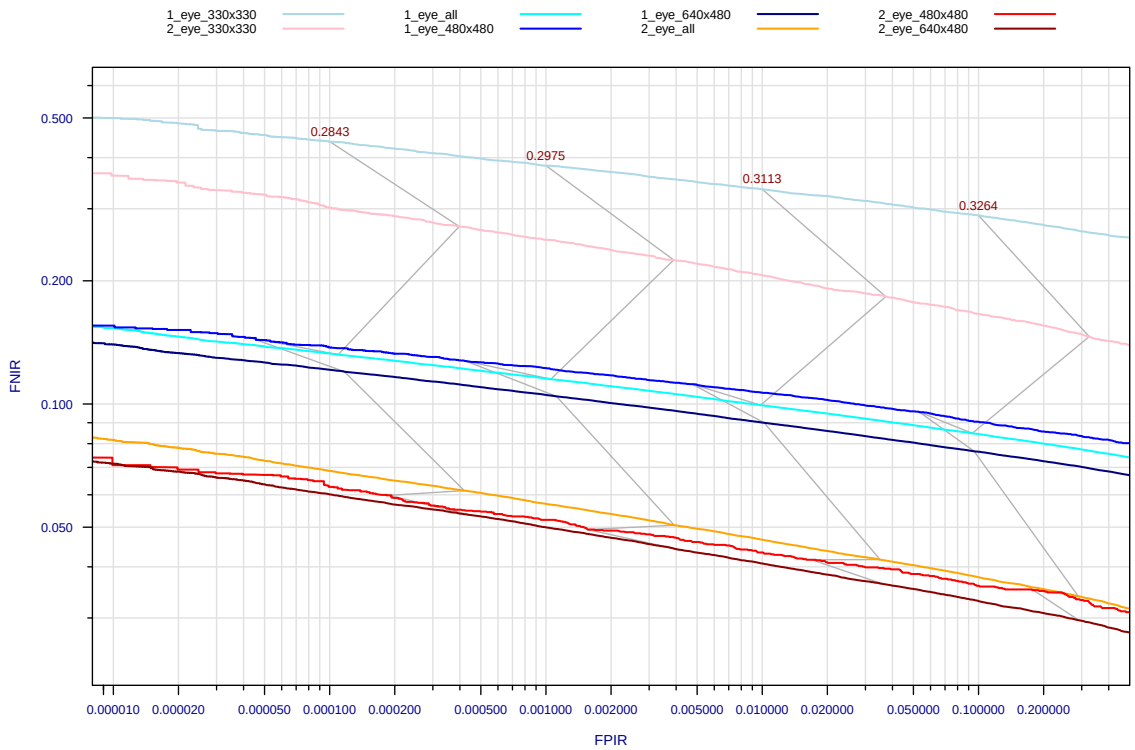

(a) Large search set, $\mathcal{S}_{nb}$

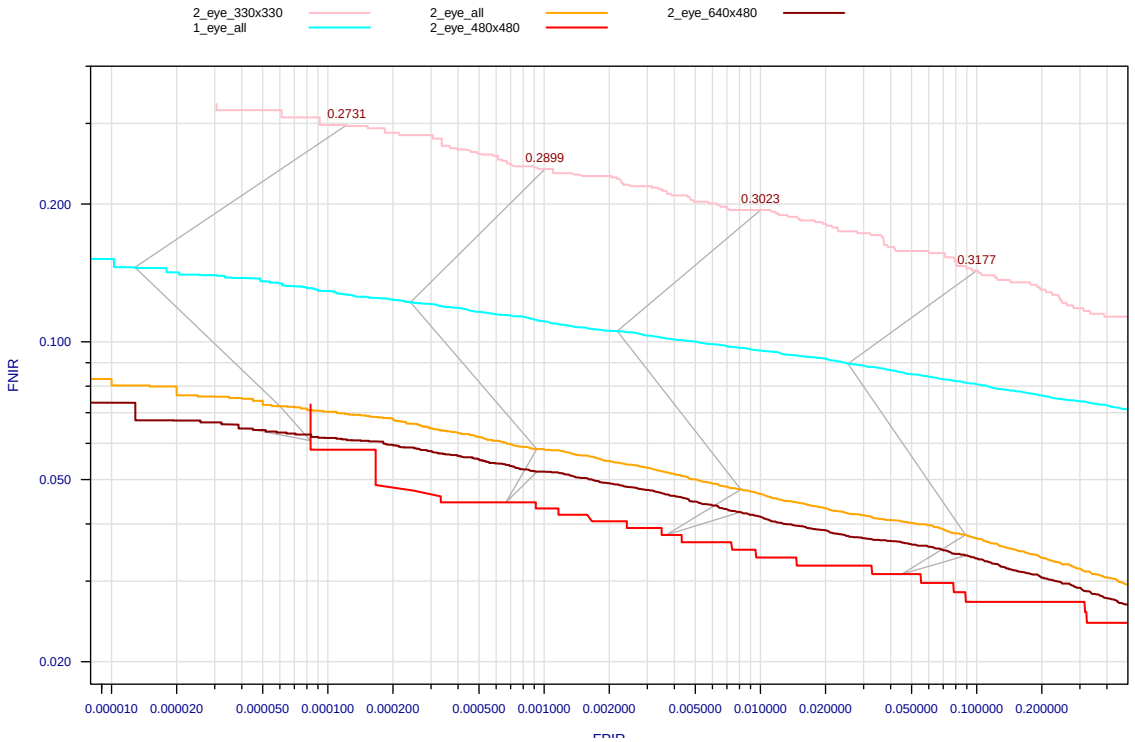

(b) Small search set, $\mathcal{S}_{na}$

Figure 580: DET for implementation W11B executing searches in an enrolled population of N = 1.6 million, broken out for three different image sizes (corresponding broadly to three camera plus ancillary software combinations) of the search image. The acquisition system used for the enrollment image (if any) is ignored in this breakout. Results for single-eye and two-eyes are plotted with two families of color. The straight lines, which link points of constant threshold, show how the two error rates would vary if a fixed threshold were adopted operationally.

FNIR = FALSE NEGATIVE IDENT. RATE FPIR = FALSE POSITIVE IDENT. RATE	N = NEUROTECHNOLOGY U = L1	P = SMU V = MORPHO	Q = IRITECH W = IRISID	R = COGENT X = CROSSMATCH	S = SMARTSENSORS Y = KYNEN	T = CAMBRIDGE

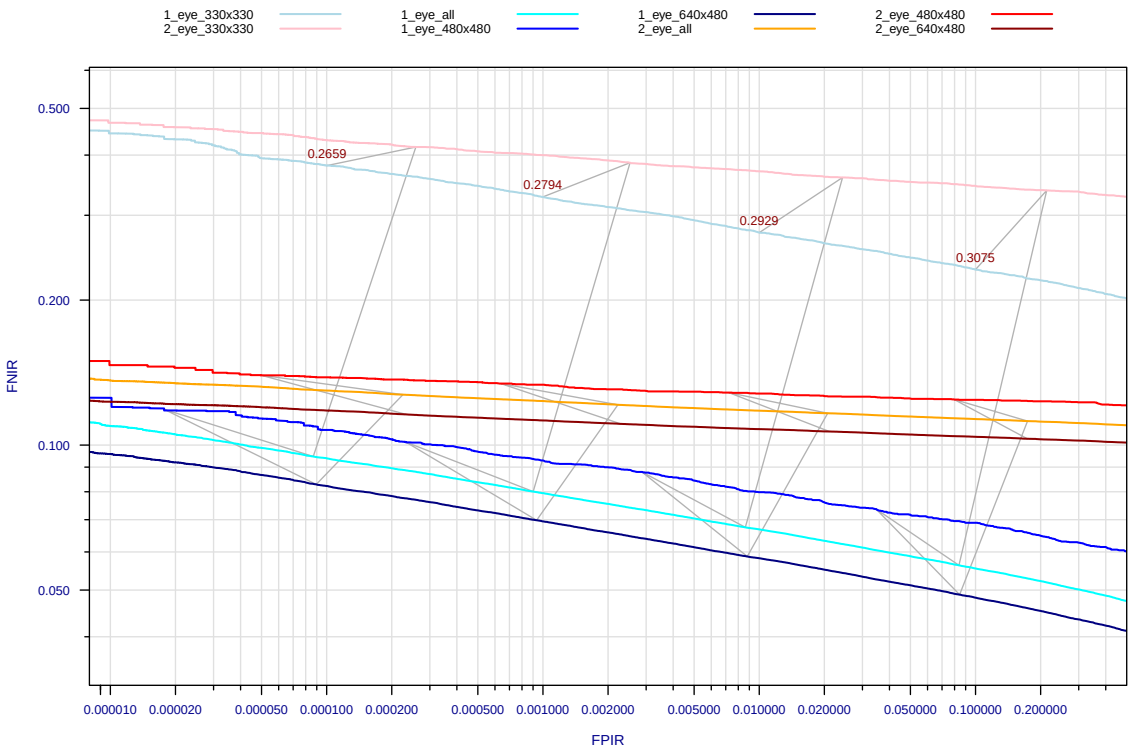

(a) Large search set, $\mathcal{S}_{nb}$

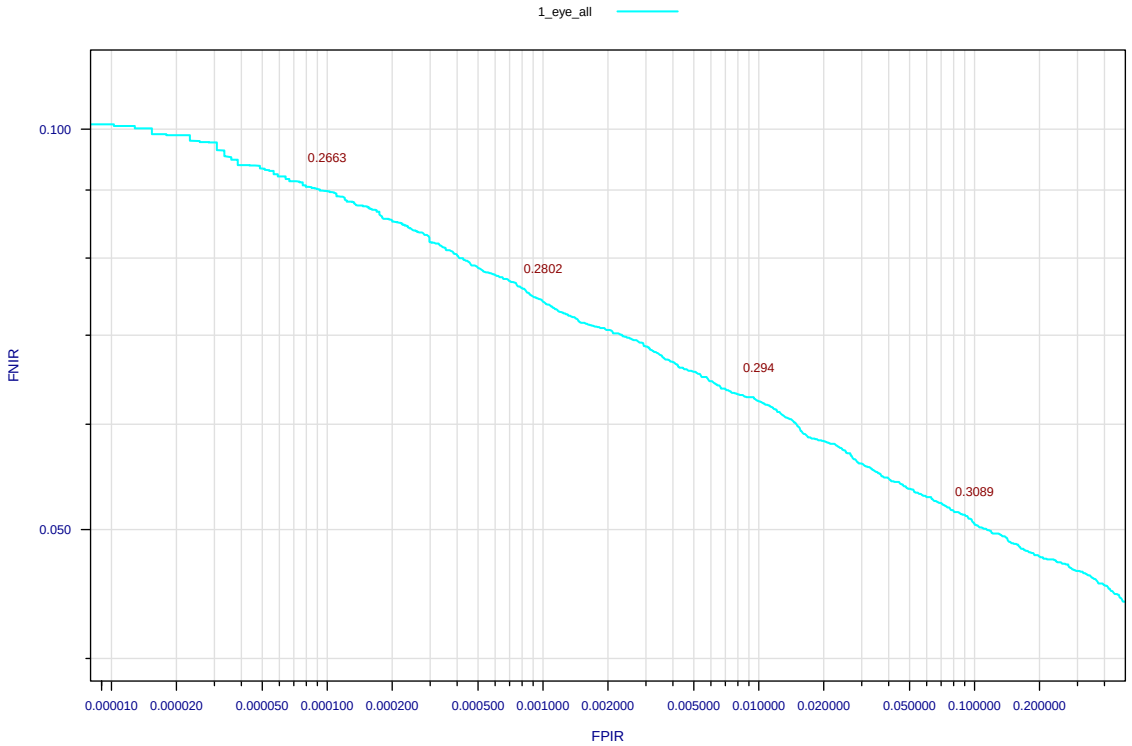

(b) Small search set, $\mathcal{S}_{na}$

Figure 581: DET for implementation W12A executing searches in an enrolled population of N = 1.6 million, broken out for three different image sizes (corresponding broadly to three camera plus ancillary software combinations) of the search image. The acquisition system used for the enrollment image (if any) is ignored in this breakout. Results for single-eye and two-eyes are plotted with two families of color. The straight lines, which link points of constant threshold, show how the two error rates would vary if a fixed threshold were adopted operationally.

FNIR = FALSE NEGATIVE IDENT. RATE FPIR = FALSE POSITIVE IDENT. RATE	N = NEUROTECHNOLOGY U = L1	P = SMU V = MORPHO	Q = IRITECH W = IRISID	R = COGENT X = CROSSMATCH	S = SMARTSENSORS Y = KYNEN	T = CAMBRIDGE

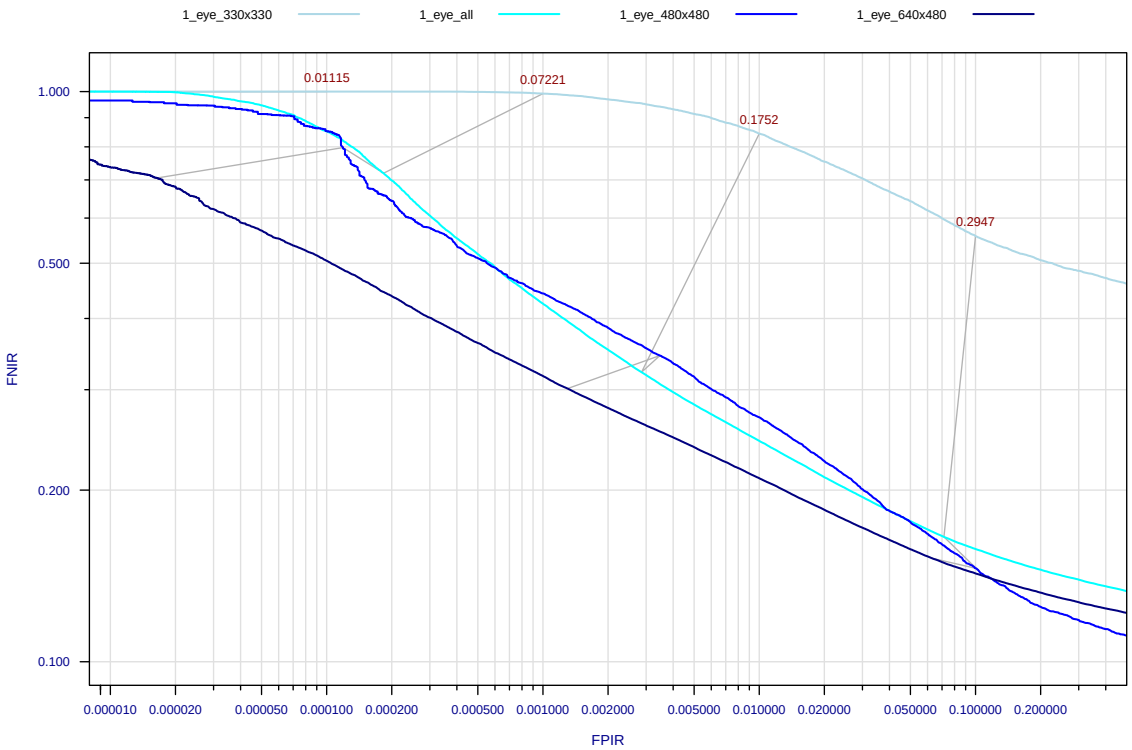

(a) Large search set, $\mathcal{S}_{nb}$

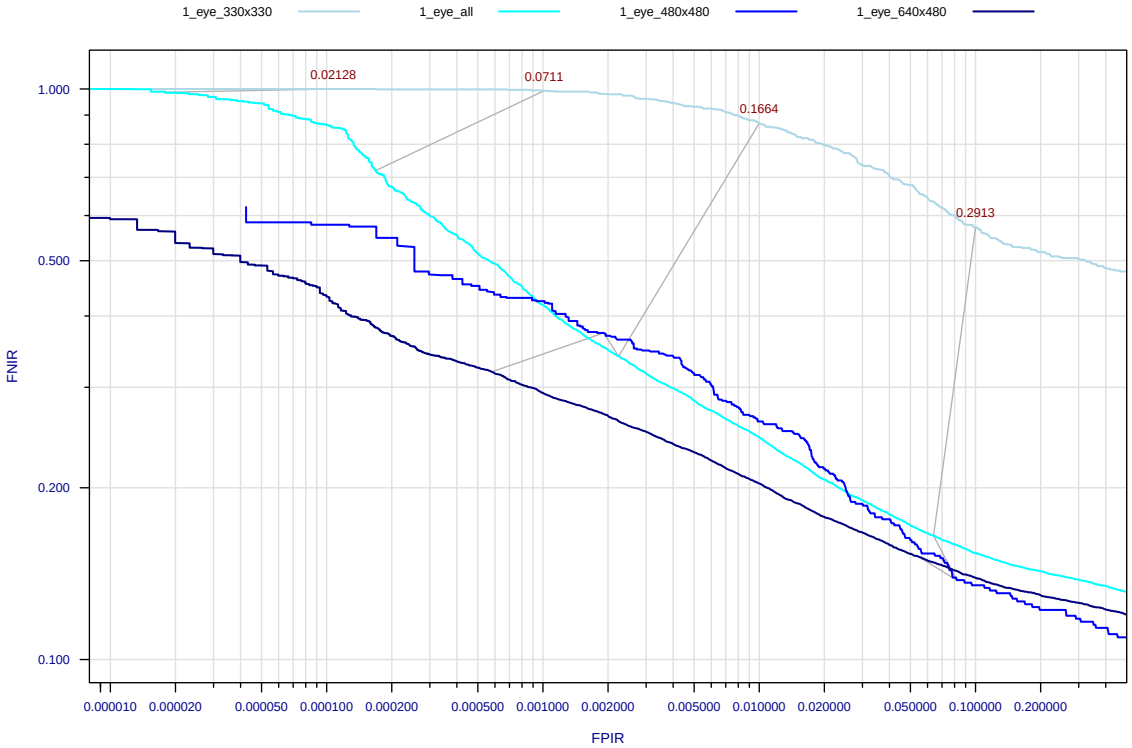

(b) Small search set, $\mathcal{S}_{na}$

Figure 582: DET for implementation X02A executing searches in an enrolled population of N = 1.6 million, broken out for three different image sizes (corresponding broadly to three camera plus ancillary software combinations) of the search image. The acquisition system used for the enrollment image (if any) is ignored in this breakout. Results for single-eye and two-eyes are plotted with two families of color. The straight lines, which link points of constant threshold, show how the two error rates would vary if a fixed threshold were adopted operationally.

FNIR = FALSE NEGATIVE IDENT. RATE FPIR = FALSE POSITIVE IDENT. RATE	N = NEUROTECHNOLOGY U = L1	P = SMU V = MORPHO	Q = IRITECH W = IRISID	R = COGENT X = CROSSMATCH	S = SMARTSENSORS Y = KYNEN	T = CAMBRIDGE

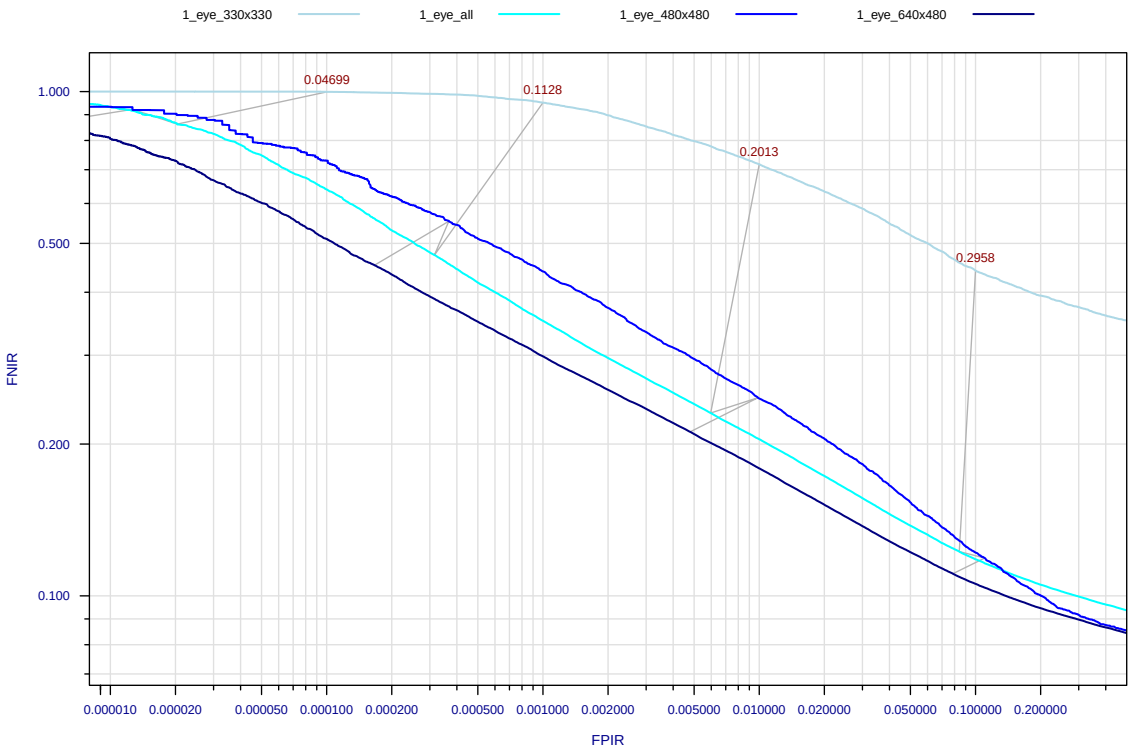

(a) Large search set, $\mathcal{S}_{nb}$

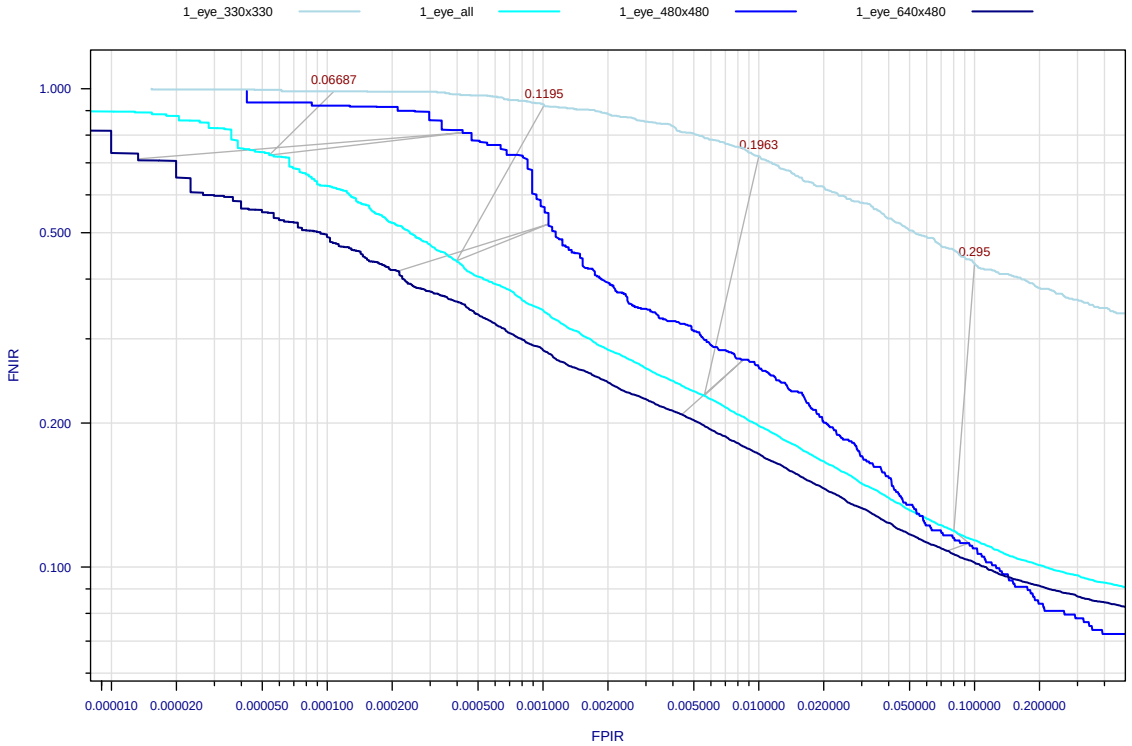

(b) Small search set, $\mathcal{S}_{na}$

Figure 583: DET for implementation X03A executing searches in an enrolled population of N = 1.6 million, broken out for three different image sizes (corresponding broadly to three camera plus ancillary software combinations) of the search image. The acquisition system used for the enrollment image (if any) is ignored in this breakout. Results for single-eye and two-eyes are plotted with two families of color. The straight lines, which link points of constant threshold, show how the two error rates would vary if a fixed threshold were adopted operationally.

FNIR = FALSE NEGATIVE IDENT. RATE FPIR = FALSE POSITIVE IDENT. RATE	N = NEUROTECHNOLOGY U = L1	P = SMU V = MORPHO	Q = IRITECH W = IRISID	R = COGENT X = CROSSMATCH	S = SMARTSENSORS Y = KYNEN	T = CAMBRIDGE

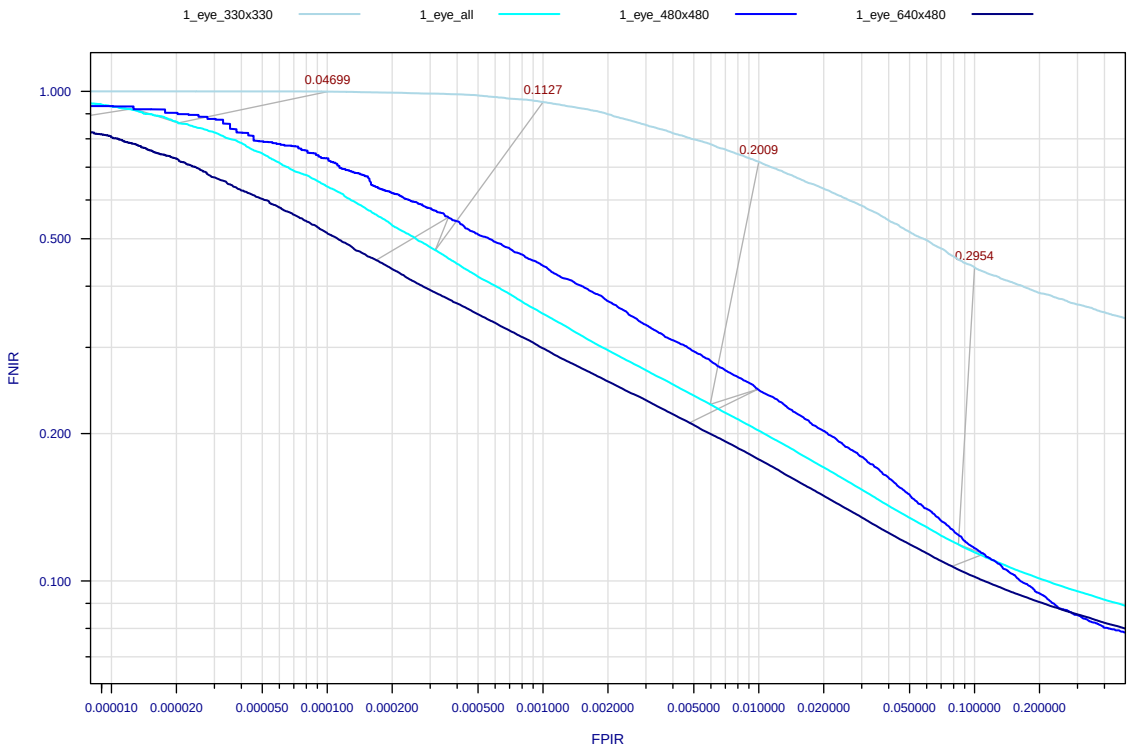

(a) Large search set, $\mathcal{S}_{nb}$

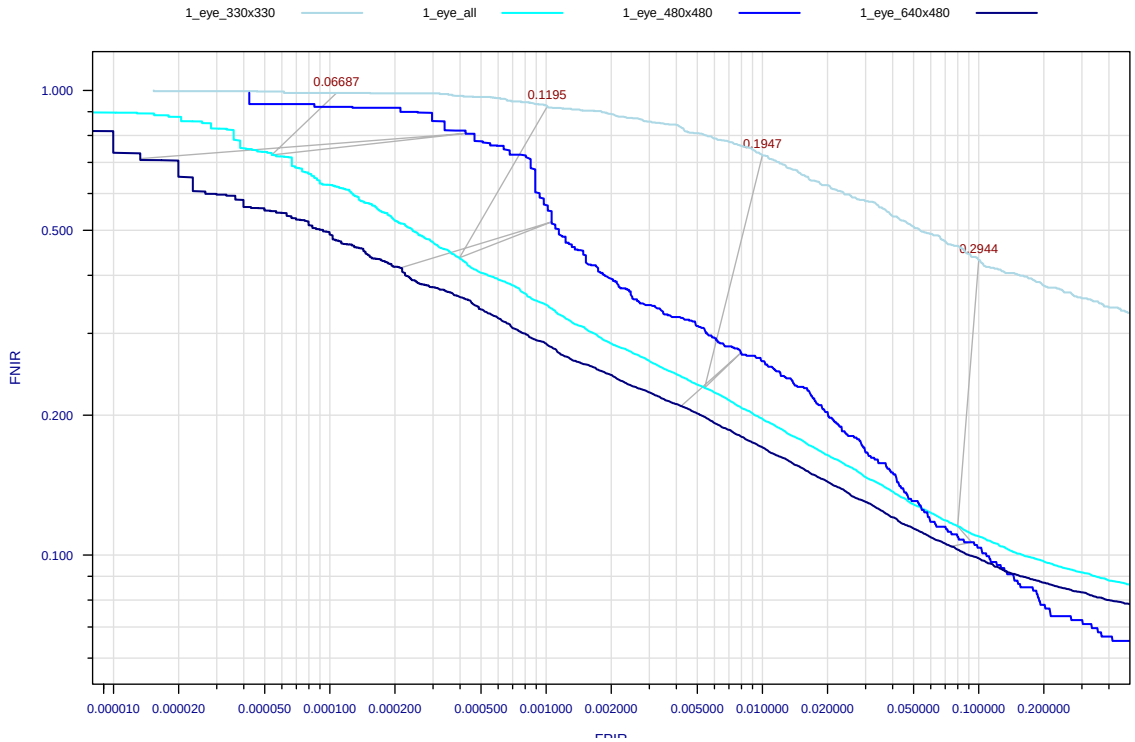

(b) Small search set, $\mathcal{S}_{na}$

Figure 584: DET for implementation X04A executing searches in an enrolled population of N = 1.6 million, broken out for three different image sizes (corresponding broadly to three camera plus ancillary software combinations) of the search image. The acquisition system used for the enrollment image (if any) is ignored in this breakout. Results for single-eye and two-eyes are plotted with two families of color. The straight lines, which link points of constant threshold, show how the two error rates would vary if a fixed threshold were adopted operationally.

FNIR = FALSE NEGATIVE IDENT. RATE FPIR = FALSE POSITIVE IDENT. RATE	N = NEUROTECHNOLOGY U = L1	P = SMU V = MORPHO	Q = IRITECH W = IRISID	R = COGENT X = CROSSMATCH	S = SMARTSENSORS Y = KYNEN	T = CAMBRIDGE

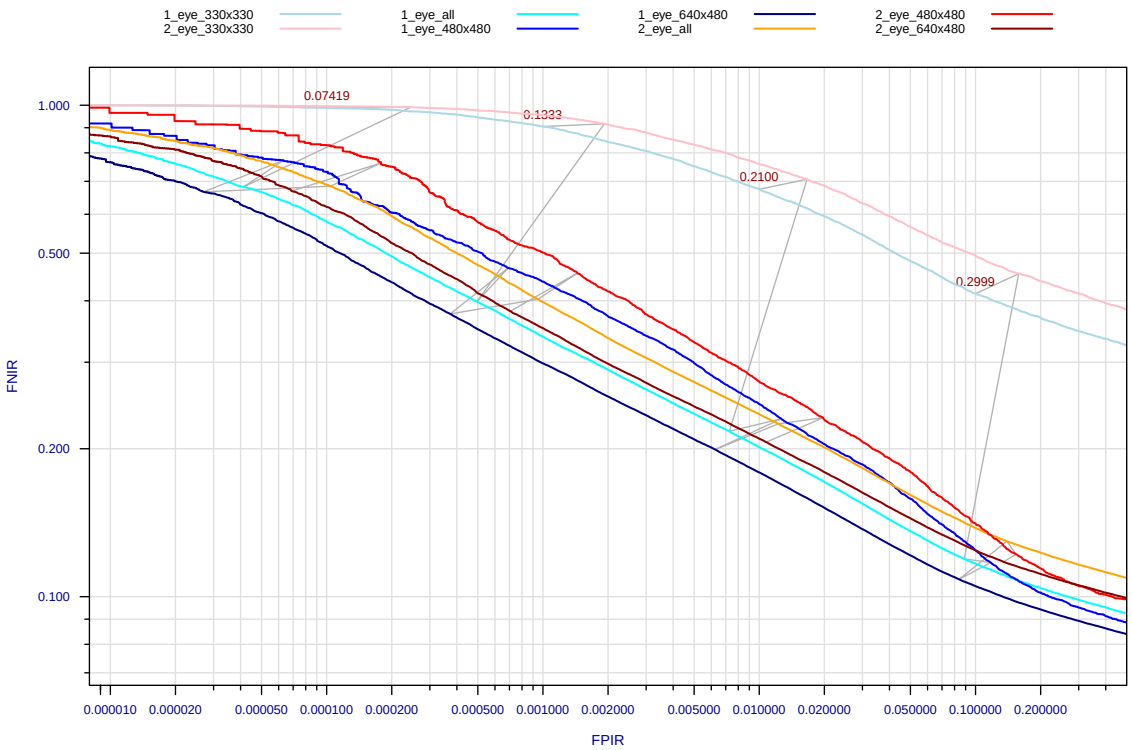

(a) Large search set, $\mathcal{S}_{nb}$

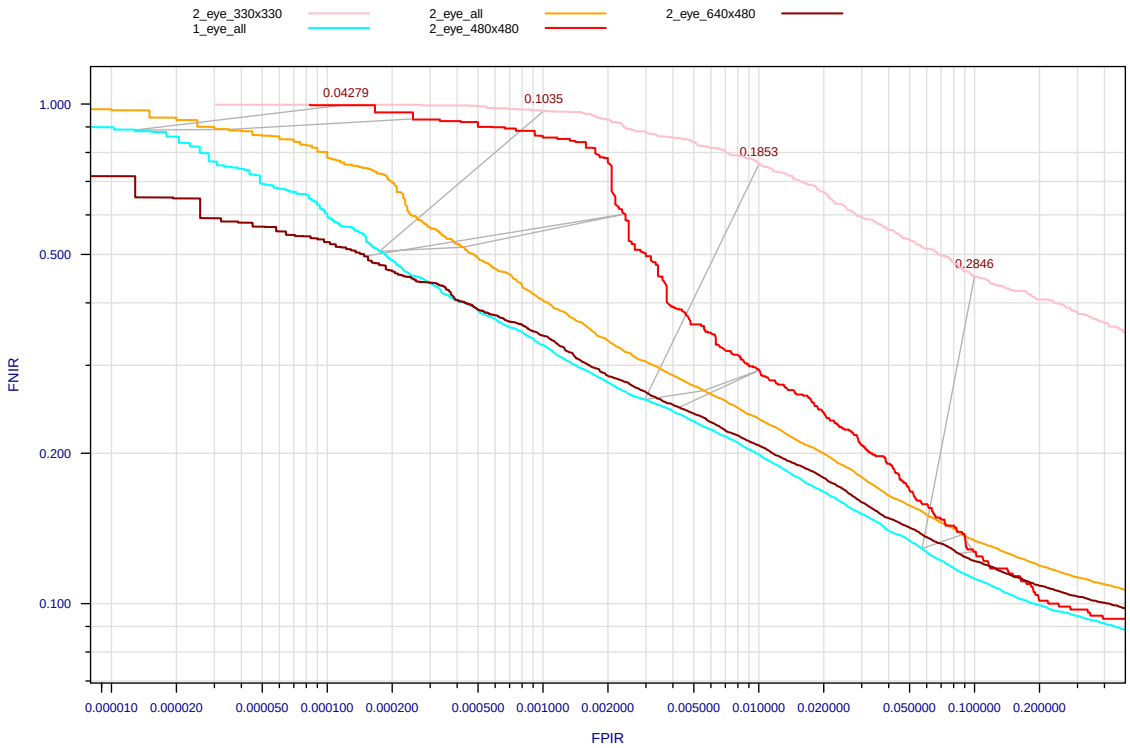

(b) Small search set, $\mathcal{S}_{na}$

Figure 585: DET for implementation X11A executing searches in an enrolled population of N = 1.6 million, broken out for three different image sizes (corresponding broadly to three camera plus ancillary software combinations) of the search image. The acquisition system used for the enrollment image (if any) is ignored in this breakout. Results for single-eye and two-eyes are plotted with two families of color. The straight lines, which link points of constant threshold, show how the two error rates would vary if a fixed threshold were adopted operationally.

FNIR = FALSE NEGATIVE IDENT. RATE FPIR = FALSE POSITIVE IDENT. RATE	N = NEUROTECHNOLOGY U = L1	P = SMU V = MORPHO	Q = IRITECH W = IRISID	R = COGENT X = CROSSMATCH	S = SMARTSENSORS Y = KYNEN	T = CAMBRIDGE

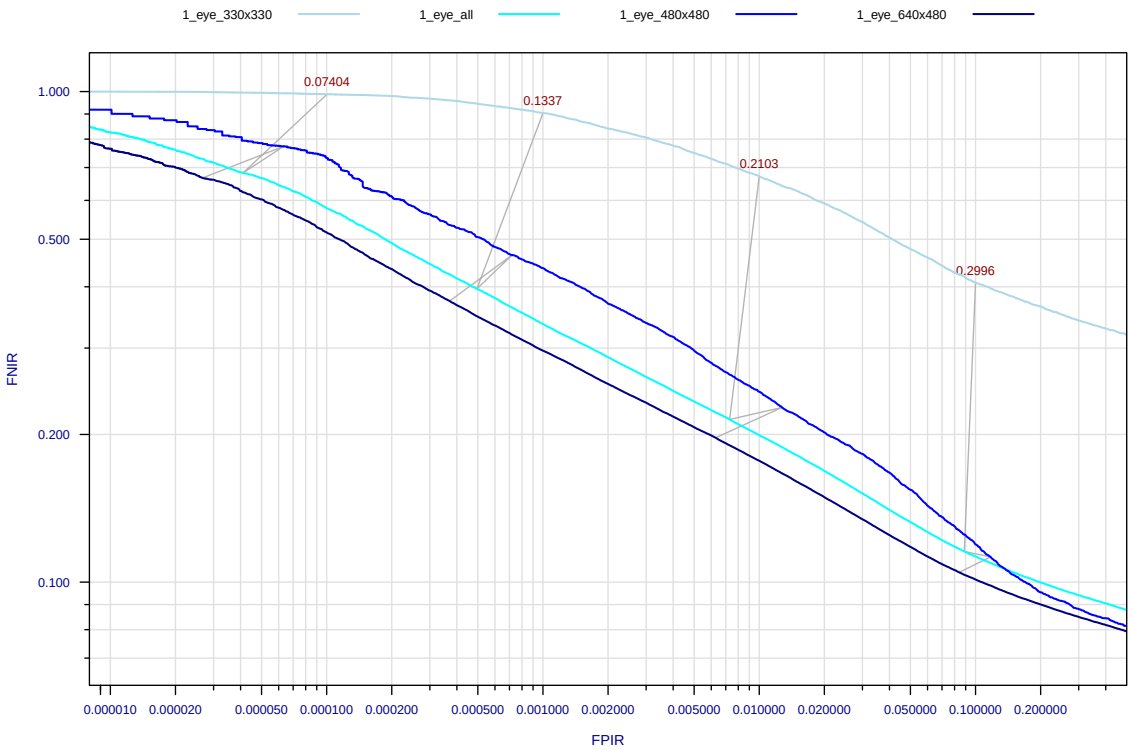

(a) Large search set, $\mathcal{S}_{nb}$

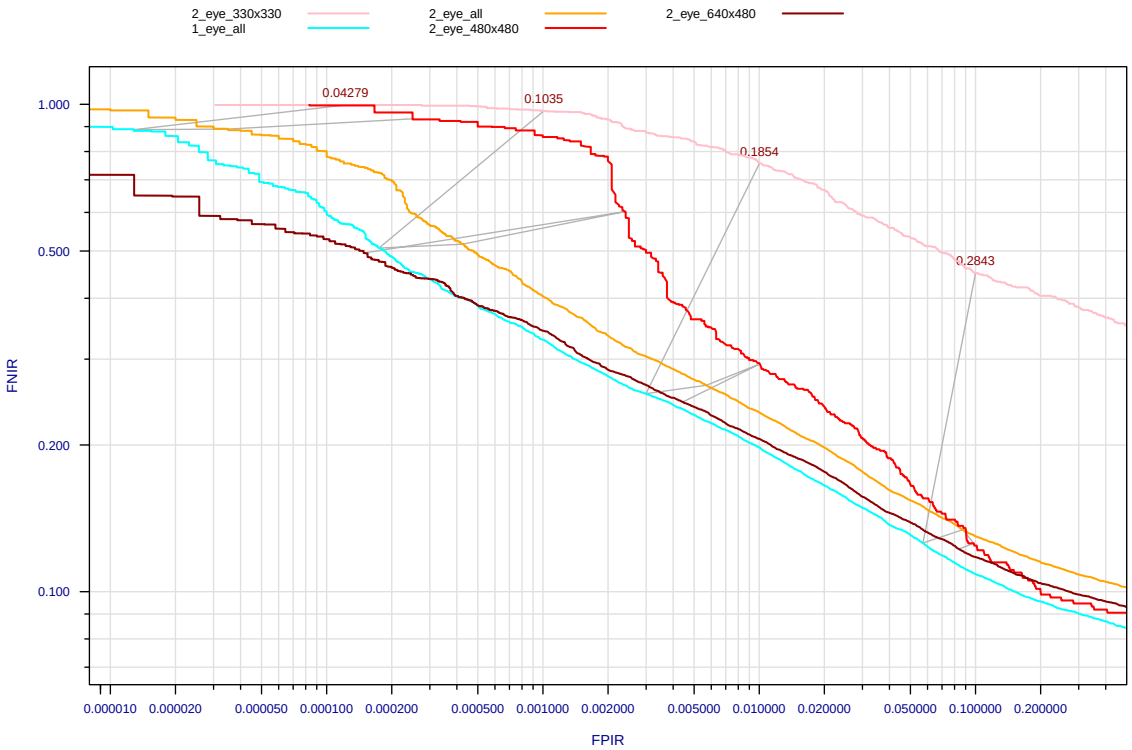

(b) Small search set, $\mathcal{S}_{na}$

Figure 586: DET for implementation X11B executing searches in an enrolled population of N = 1.6 million, broken out for three different image sizes (corresponding broadly to three camera plus ancillary software combinations) of the search image. The acquisition system used for the enrollment image (if any) is ignored in this breakout. Results for single-eye and two-eyes are plotted with two families of color. The straight lines, which link points of constant threshold, show how the two error rates would vary if a fixed threshold were adopted operationally.

FNIR = FALSE NEGATIVE IDENT. RATE FPIR = FALSE POSITIVE IDENT. RATE	N = NEUROTECHNOLOGY U = L1	P = SMU V = MORPHO	Q = IRITECH W = IRISID	R = COGENT X = CROSSMATCH	S = SMARTSENSORS Y = KYNEN	T = CAMBRIDGE

Figure 587: DET for implementation Y02A executing searches in an enrolled population of N = 1.6 million, broken out for three different image sizes (corresponding broadly to three camera plus ancillary software combinations) of the search image. The acquisition system used for the enrollment image (if any) is ignored in this breakout. Results for single-eye and two-eyes are plotted with two families of color. The straight lines, which link points of constant threshold, show how the two error rates would vary if a fixed threshold were adopted operationally.

Figure 588: DET for implementation Y02B executing searches in an enrolled population of N = 1.6 million, broken out for three different image sizes (corresponding broadly to three camera plus ancillary software combinations) of the search image. The acquisition system used for the enrollment image (if any) is ignored in this breakout. Results for single-eye and two-eyes are plotted with two families of color. The straight lines, which link points of constant threshold, show how the two error rates would vary if a fixed threshold were adopted operationally.

Figure 589: DET for implementation Y03A executing searches in an enrolled population of N = 1.6 million, broken out for three different image sizes (corresponding broadly to three camera plus ancillary software combinations) of the search image. The acquisition system used for the enrollment image (if any) is ignored in this breakout. Results for single-eye and two-eyes are plotted with two families of color. The straight lines, which link points of constant threshold, show how the two error rates would vary if a fixed threshold were adopted operationally.

Figure 590: DET for implementation Y03B executing searches in an enrolled population of N = 1.6 million, broken out for three different image sizes (corresponding broadly to three camera plus ancillary software combinations) of the search image. The acquisition system used for the enrollment image (if any) is ignored in this breakout. Results for single-eye and two-eyes are plotted with two families of color. The straight lines, which link points of constant threshold, show how the two error rates would vary if a fixed threshold were adopted operationally.

Appendix I: Relation of Dissimilarity Score and Search Duration

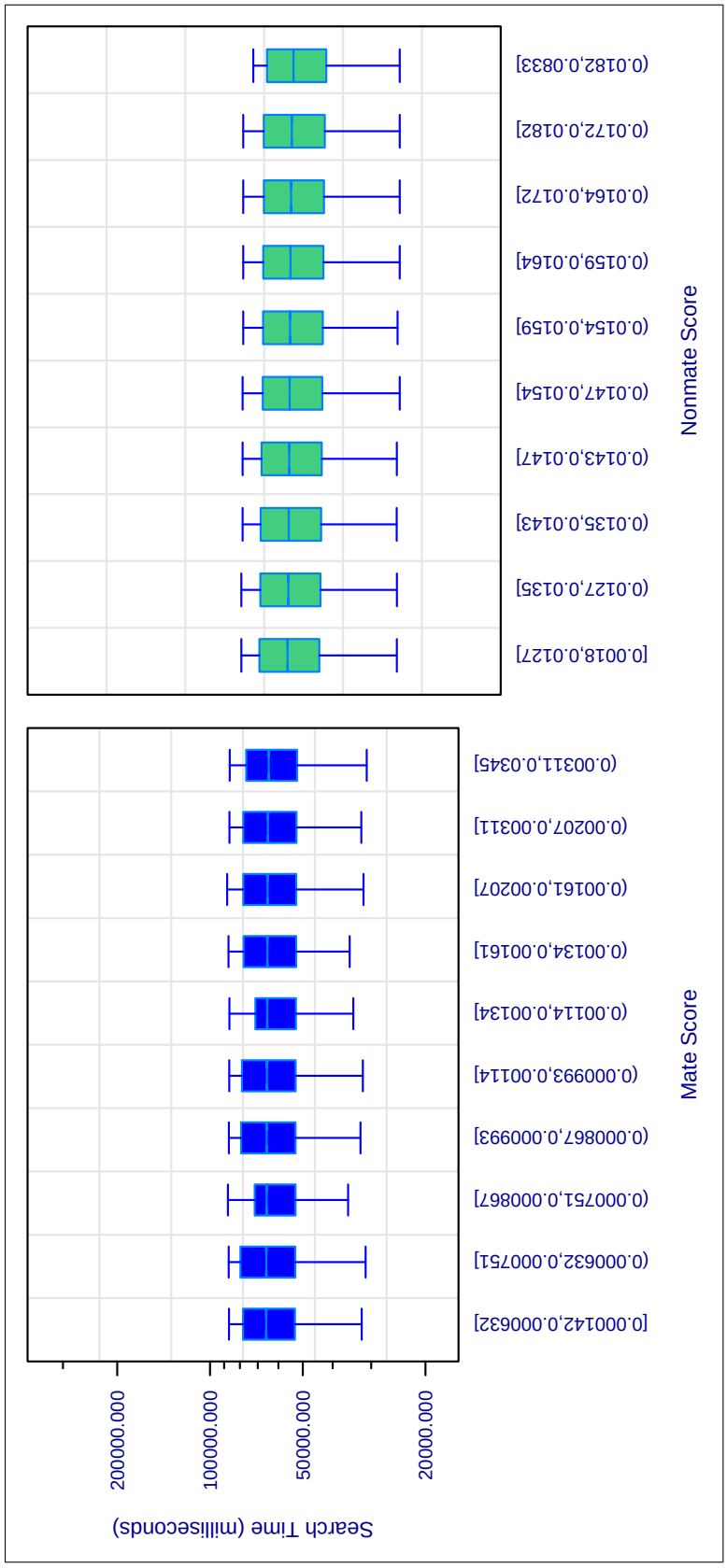

Figure 591: Dependence of speed and comparison score. For the N02A algorithm, the panels show the distribution of the one-to-many search time for ordered intervals of the mate and nonmate dissimilarity scores. For many implementations the duration of the search is independent of the score outcome. For some others (e.g. T11A), however, mate search durations are faster when the ultimate dissimilarity score is low (i.e. good).

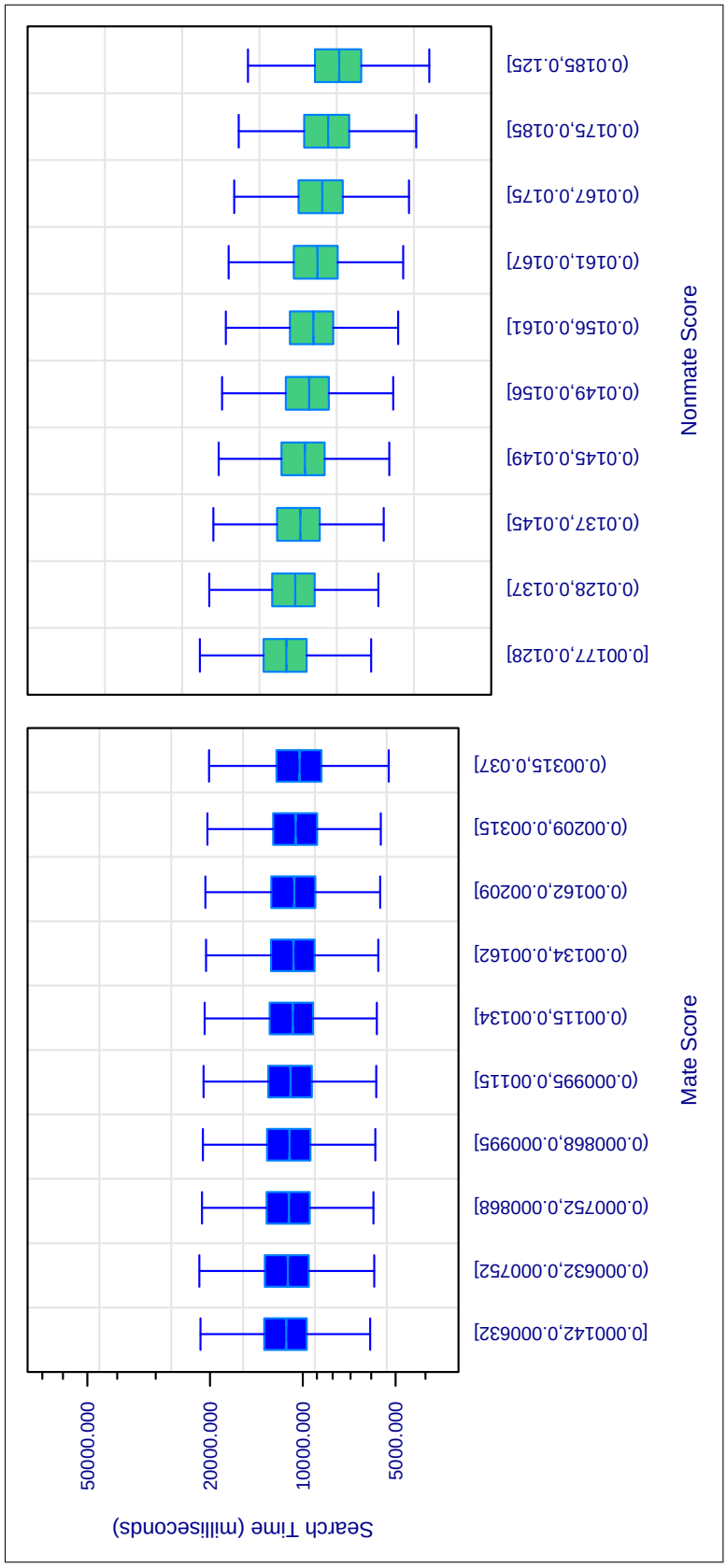

Figure 592: Dependence of speed and comparison score. For the N02B algorithm, the panels show the distribution of the one-to-many search time for ordered intervals of the mate and nonmate dissimilarity scores. For many implementations the duration of the search is independent of the score outcome. For some others (e.g. T11A), however, mate search durations are faster when the ultimate dissimilarity score is low (i.e. good).

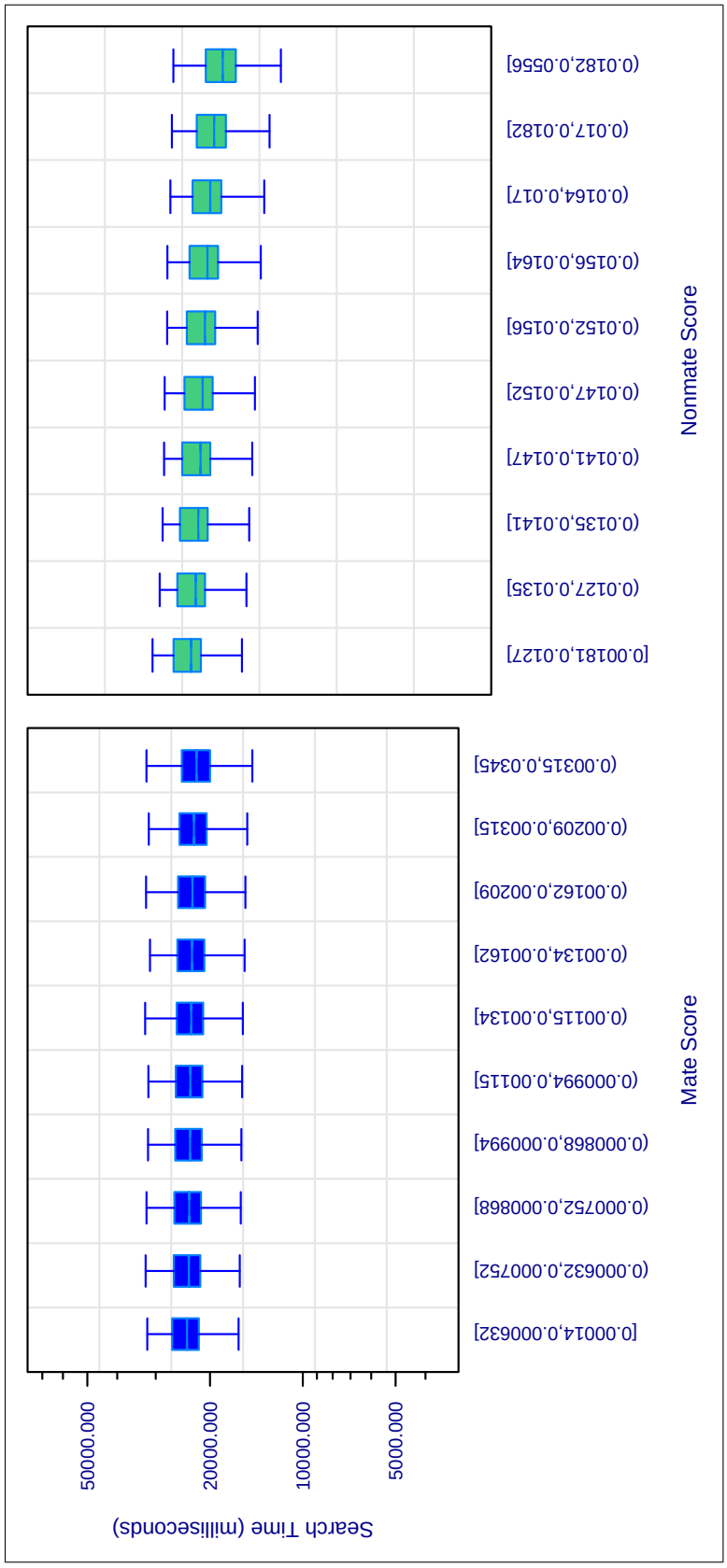

Figure 593: Dependence of speed and comparison score. For the N03A algorithm, the panels show the distribution of the one-to-many search time for ordered intervals of the mate and nonmate dissimilarity scores. For many implementations the duration of the search is independent of the score outcome. For some others (e.g. T11A), however, mate search durations are faster when the ultimate dissimilarity score is low (i.e. good).

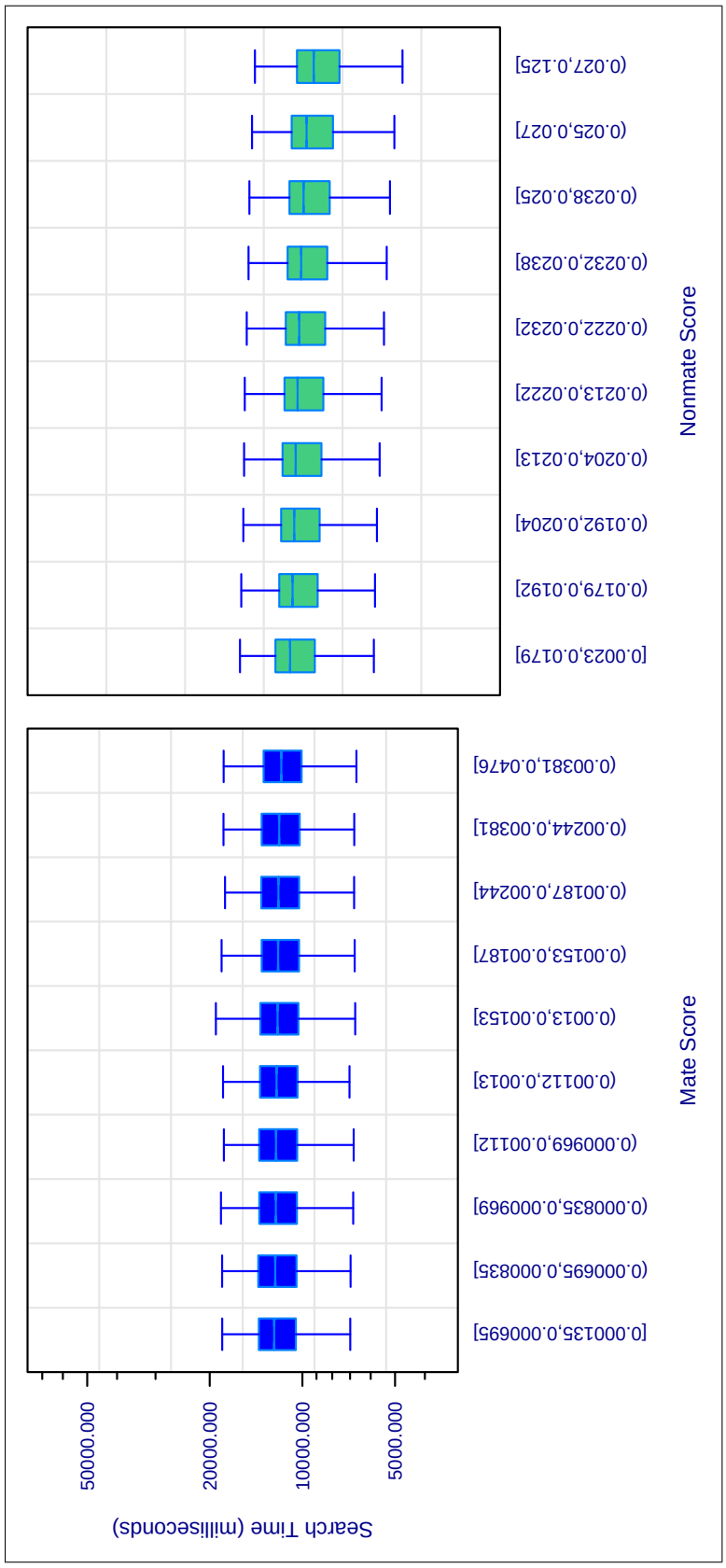

Figure 594: Dependence of speed and comparison score. For the N03B algorithm, the panels show the distribution of the one-to-many search time for ordered intervals of the mate and nonmate dissimilarity scores. For many implementations the duration of the search is independent of the score outcome. For some others (e.g. T11A), however, mate search durations are faster when the ultimate dissimilarity score is low (i.e. good).

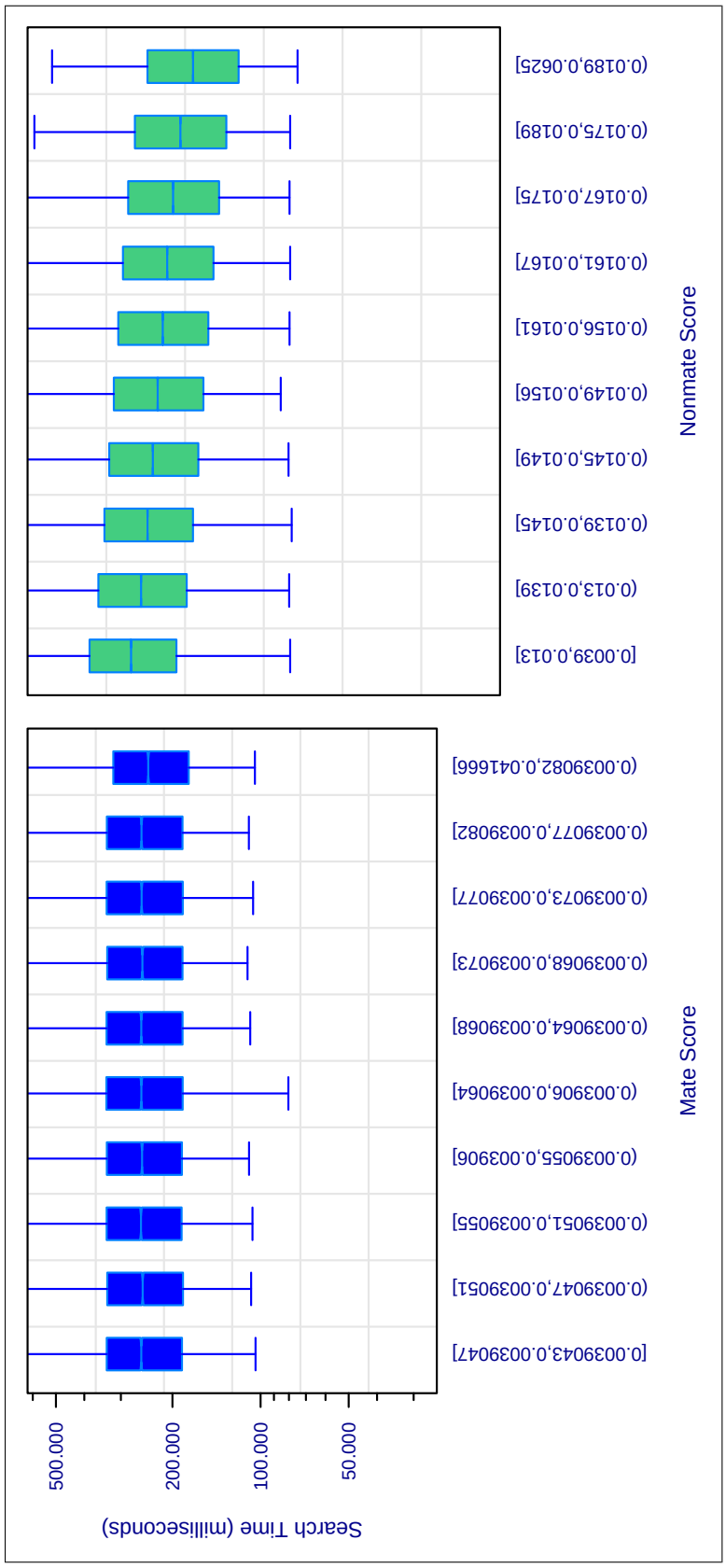

Figure 595: Dependence of speed and comparison score. For the N04A algorithm, the panels show the distribution of the one-to-many search time for ordered intervals of the mate and nonmate dissimilarity scores. For many implementations the duration of the search is independent of the score outcome. For some others (e.g. T11A), however, mate search durations are faster when the ultimate dissimilarity score is low (i.e. good).

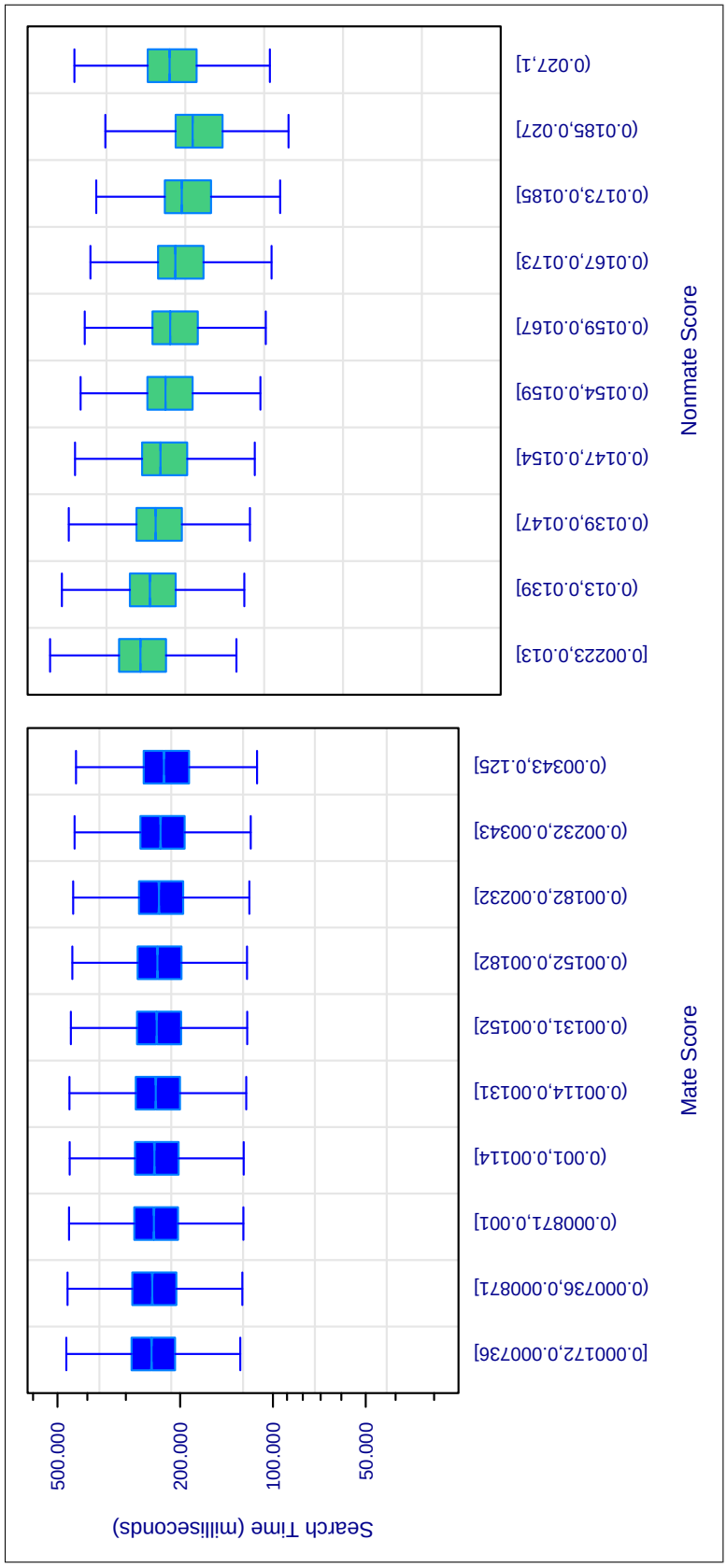

Figure 596: Dependence of speed and comparison score. For the N11A algorithm, the panels show the distribution of the one-to-many search time for ordered intervals of the mate and nonmate dissimilarity scores. For many implementations the duration of the search is independent of the score outcome. For some others (e.g. T11A), however, mate search durations are faster when the ultimate dissimilarity score is low (i.e. good).

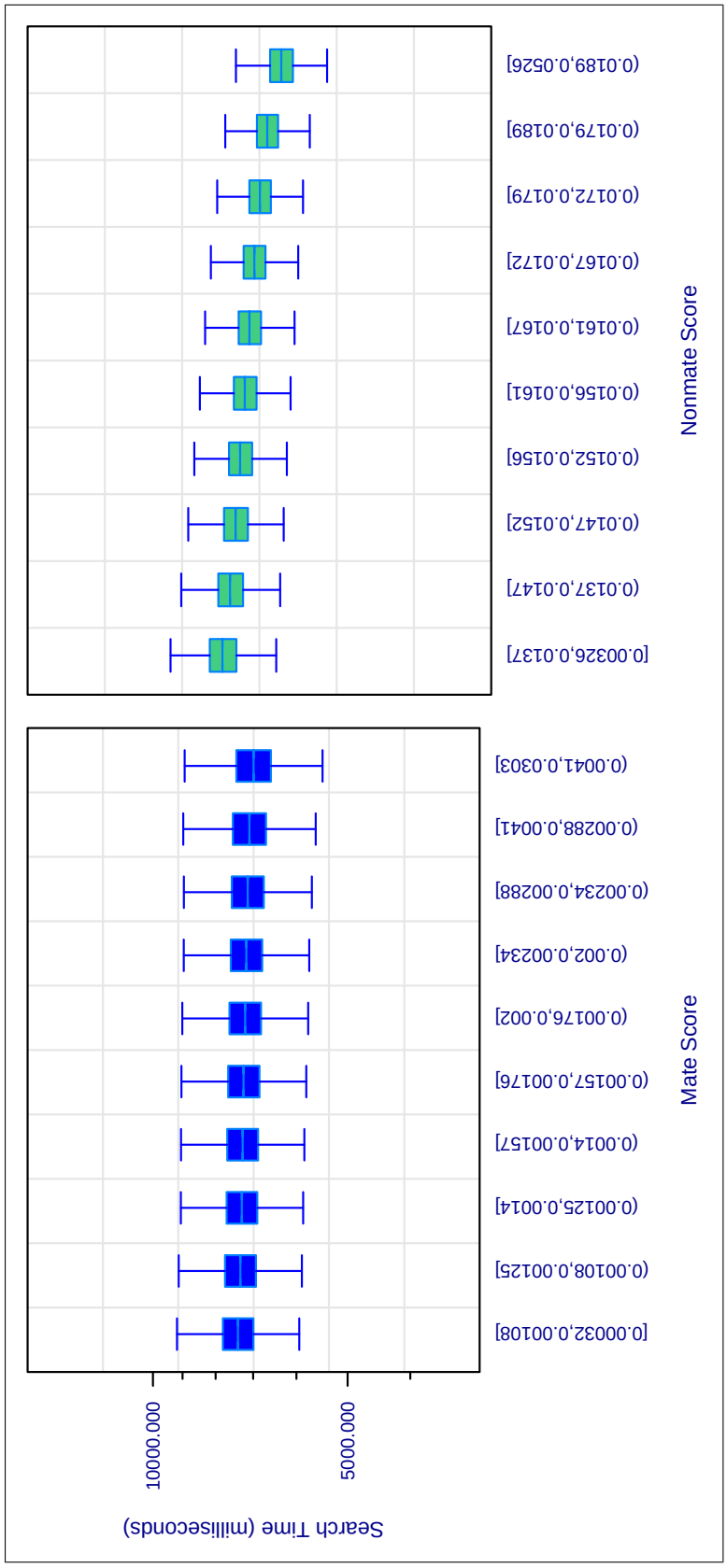

Figure 597: Dependence of speed and comparison score. For the N11B algorithm, the panels show the distribution of the one-to-many search time for ordered intervals of the mate and nonmate dissimilarity scores. For many implementations the duration of the search is independent of the score outcome. For some others (e.g. T11A), however, mate search durations are faster when the ultimate dissimilarity score is low (i.e. good).

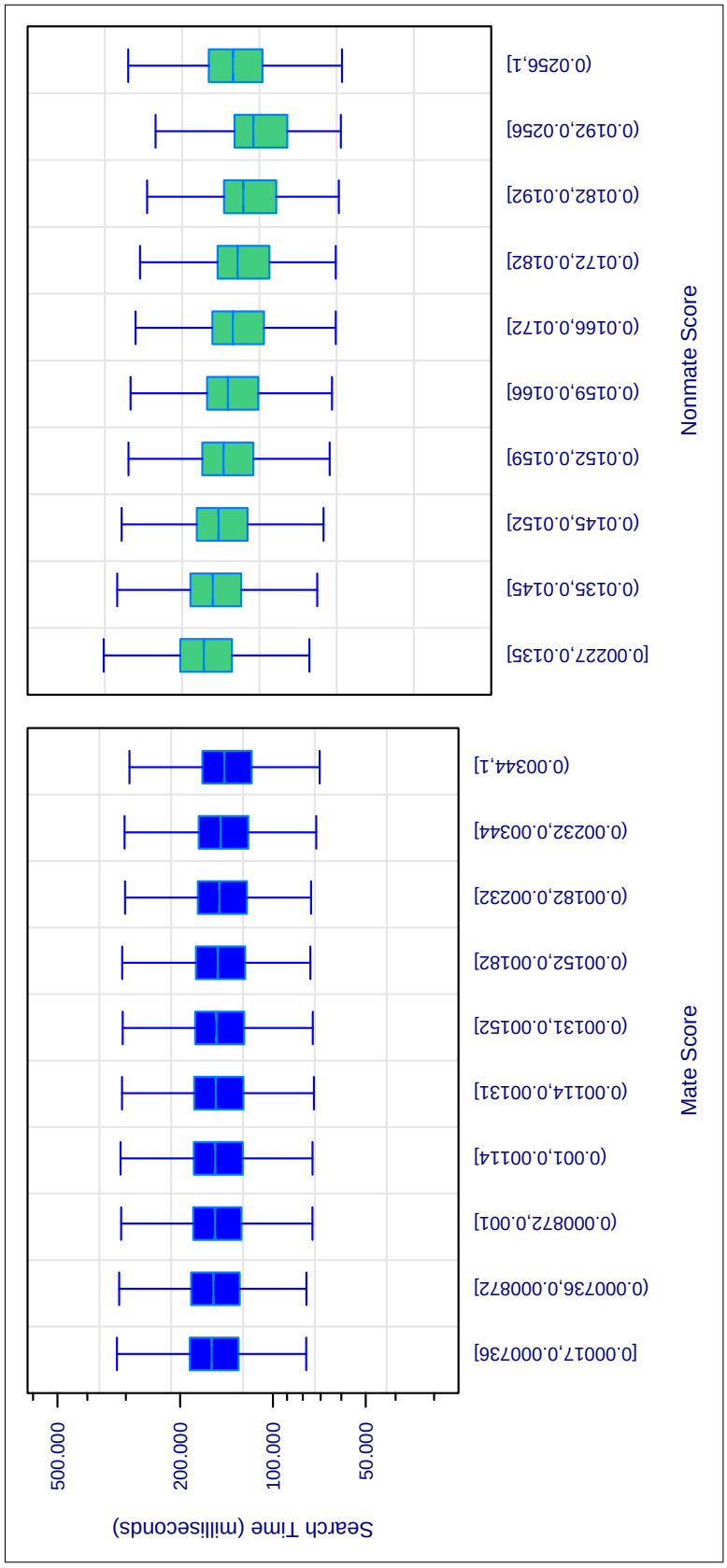

Figure 598: Dependence of speed and comparison score. For the N12A algorithm, the panels show the distribution of the one-to-many search time for ordered intervals of the mate and nonmate dissimilarity scores. For many implementations the duration of the search is independent of the score outcome. For some others (e.g. T11A), however, mate search durations are faster when the ultimate dissimilarity score is low (i.e. good).

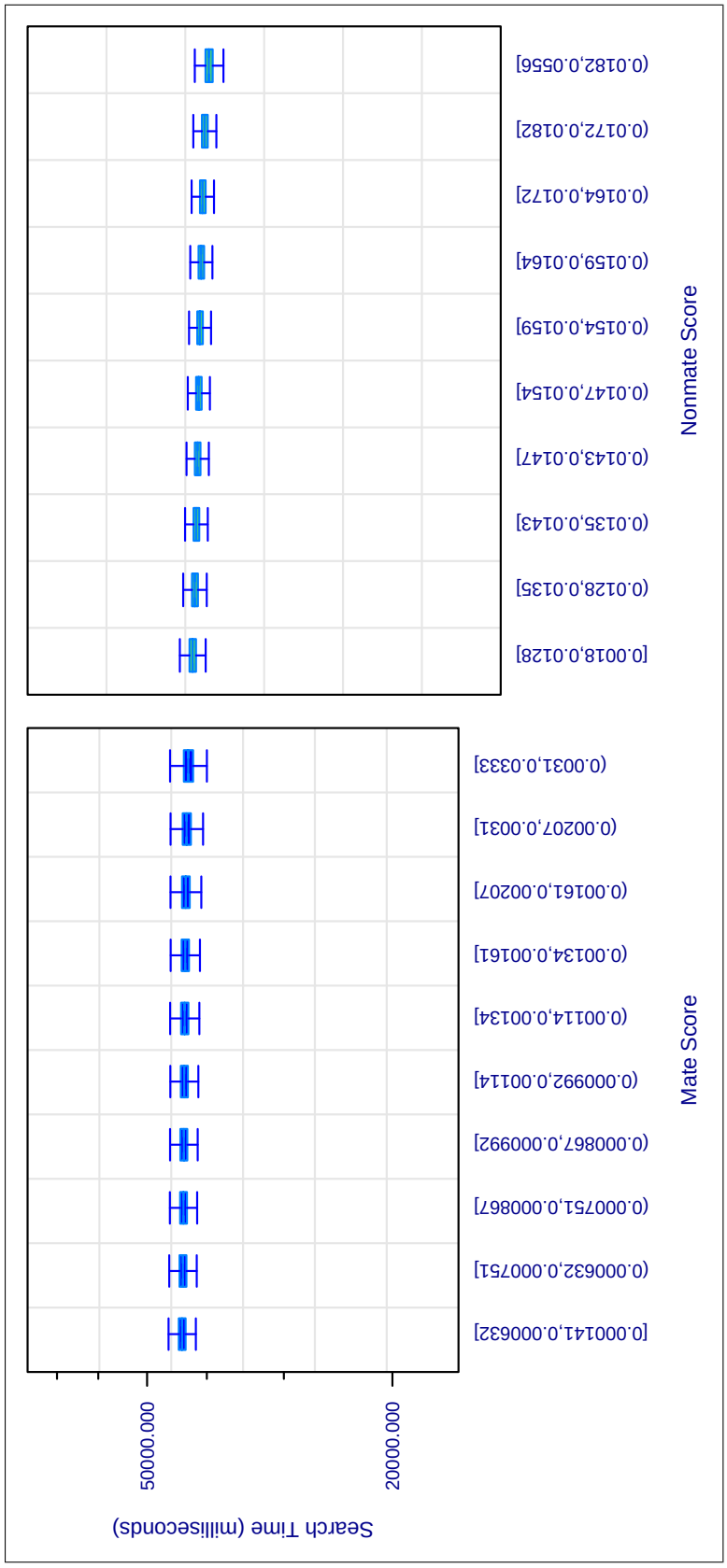

Figure 599: Dependence of speed and comparison score. For the N12B algorithm, the panels show the distribution of the one-to-many search time for ordered intervals of the mate and nonmate dissimilarity scores. For many implementations the duration of the search is independent of the score outcome. For some others (e.g. T11A), however, mate search durations are faster when the ultimate dissimilarity score is low (i.e. good).

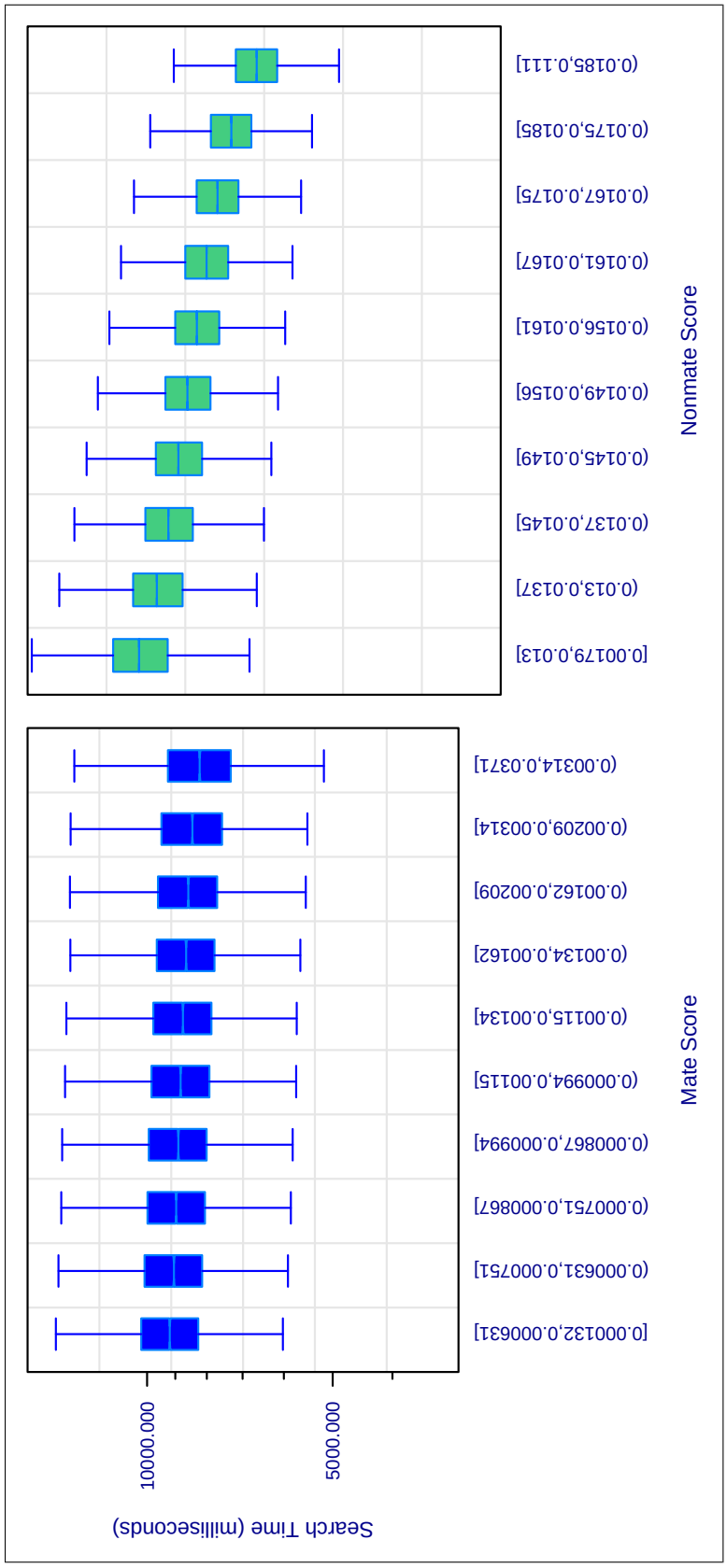

Figure 600: Dependence of speed and comparison score. For the N13B algorithm, the panels show the distribution of the one-to-many search time for ordered intervals of the mate and nonmate dissimilarity scores. For many implementations the duration of the search is independent of the score outcome. For some others (e.g. T11A), however, mate search durations are faster when the ultimate dissimilarity score is low (i.e. good).

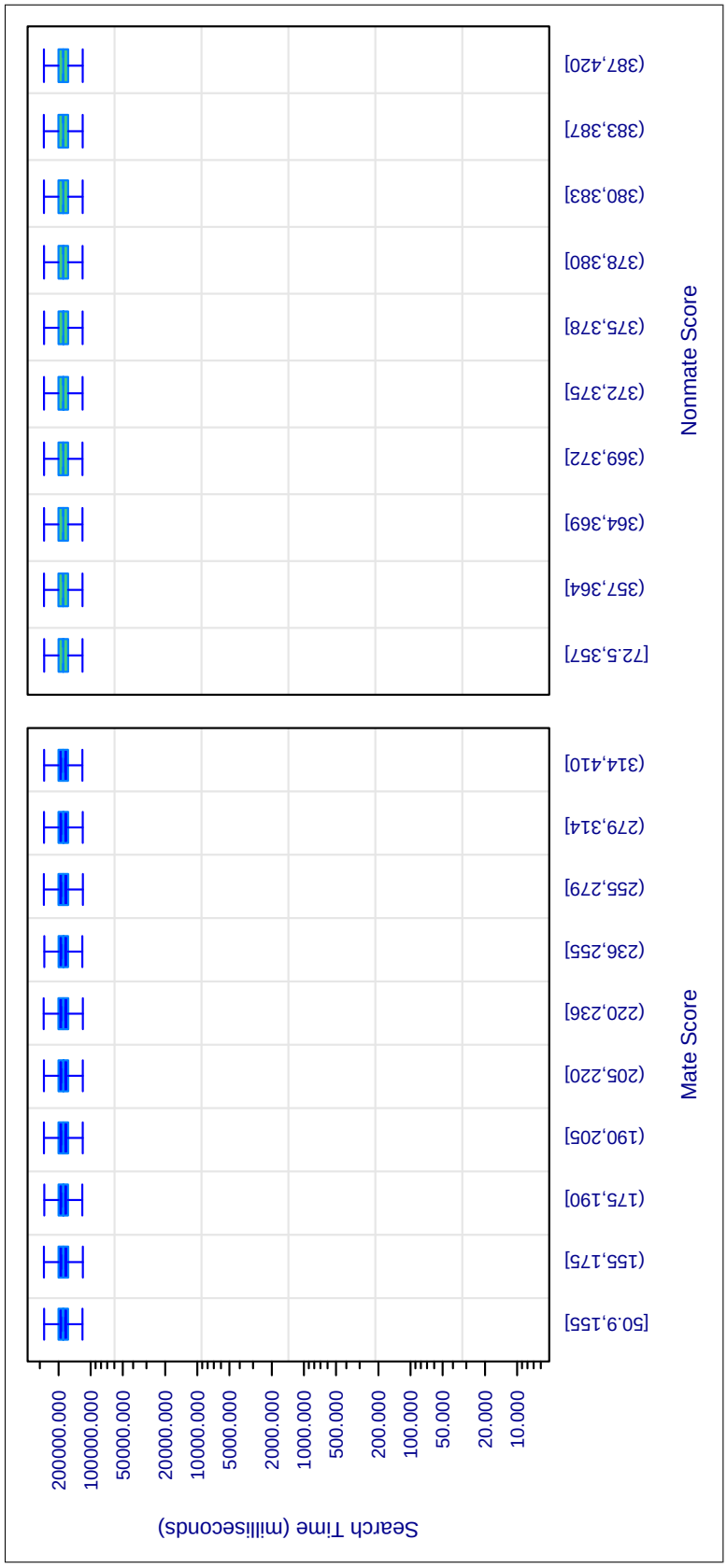

Figure 601: Dependence of speed and comparison score. For the P11A algorithm, the panels show the distribution of the one-to-many search time for ordered intervals of the mate and nonmate dissimilarity scores. For many implementations the duration of the search is independent of the score outcome. For some others (e.g. T11A), however, mate search durations are faster when the ultimate dissimilarity score is low (i.e. good).

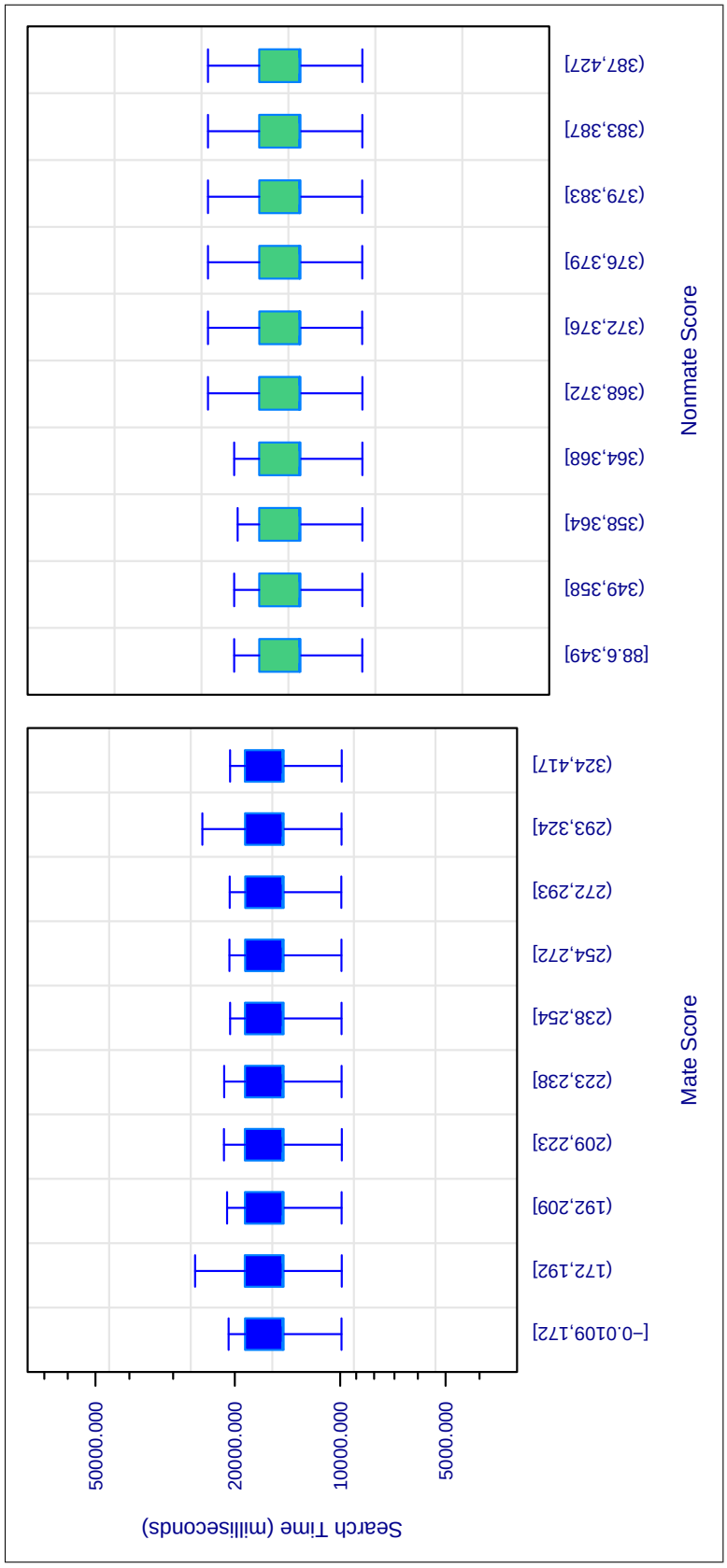

Figure 602: Dependence of speed and comparison score. For the P11B algorithm, the panels show the distribution of the one-to-many search time for ordered intervals of the mate and nonmate dissimilarity scores. For many implementations the duration of the search is independent of the score outcome. For some others (e.g. T11A), however, mate search durations are faster when the ultimate dissimilarity score is low (i.e. good).

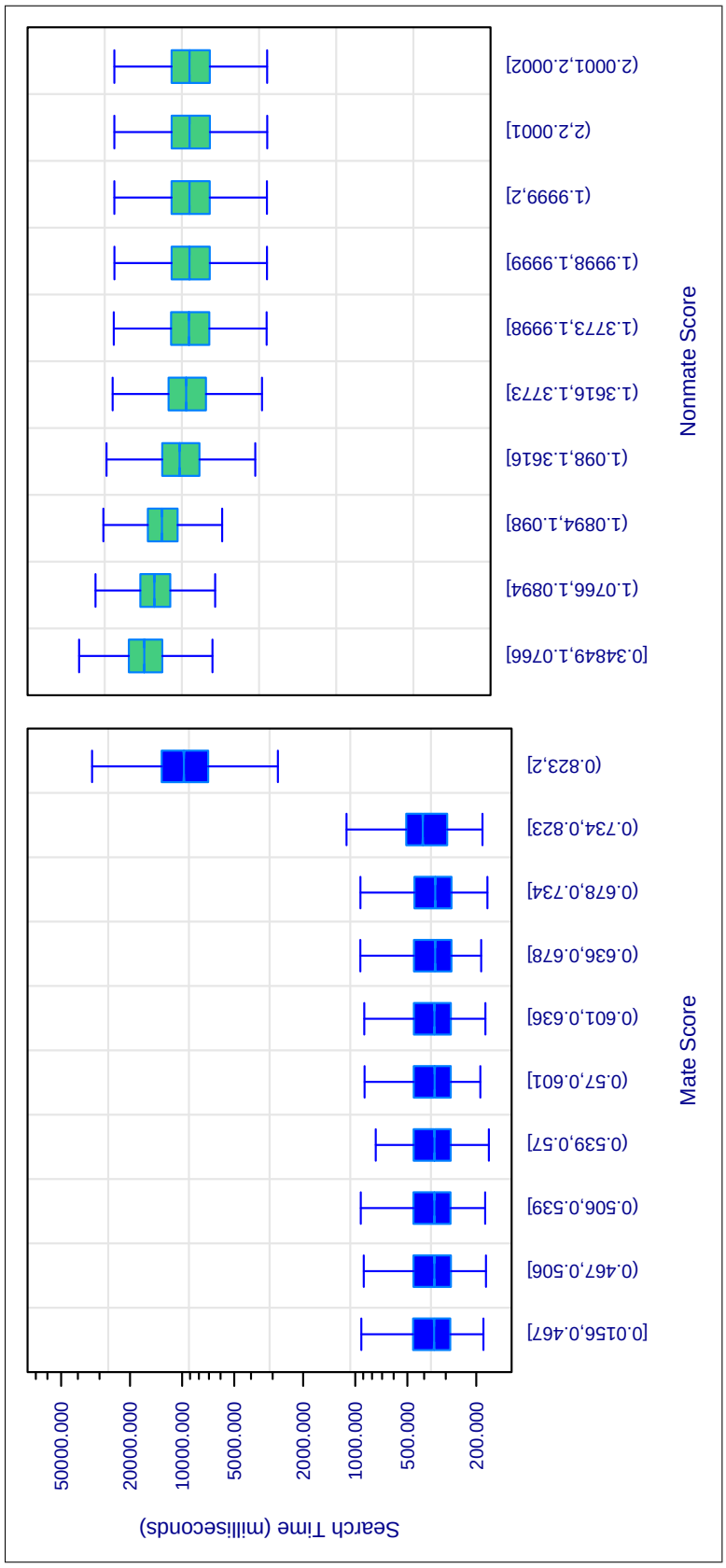

Figure 603: Dependence of speed and comparison score. For the Q02A algorithm, the panels show the distribution of the one-to-many search time for ordered intervals of the mate and nonmate dissimilarity scores. For many implementations the duration of the search is independent of the score outcome. For some others (e.g. T11A), however, mate search durations are faster when the ultimate dissimilarity score is low (i.e. good).

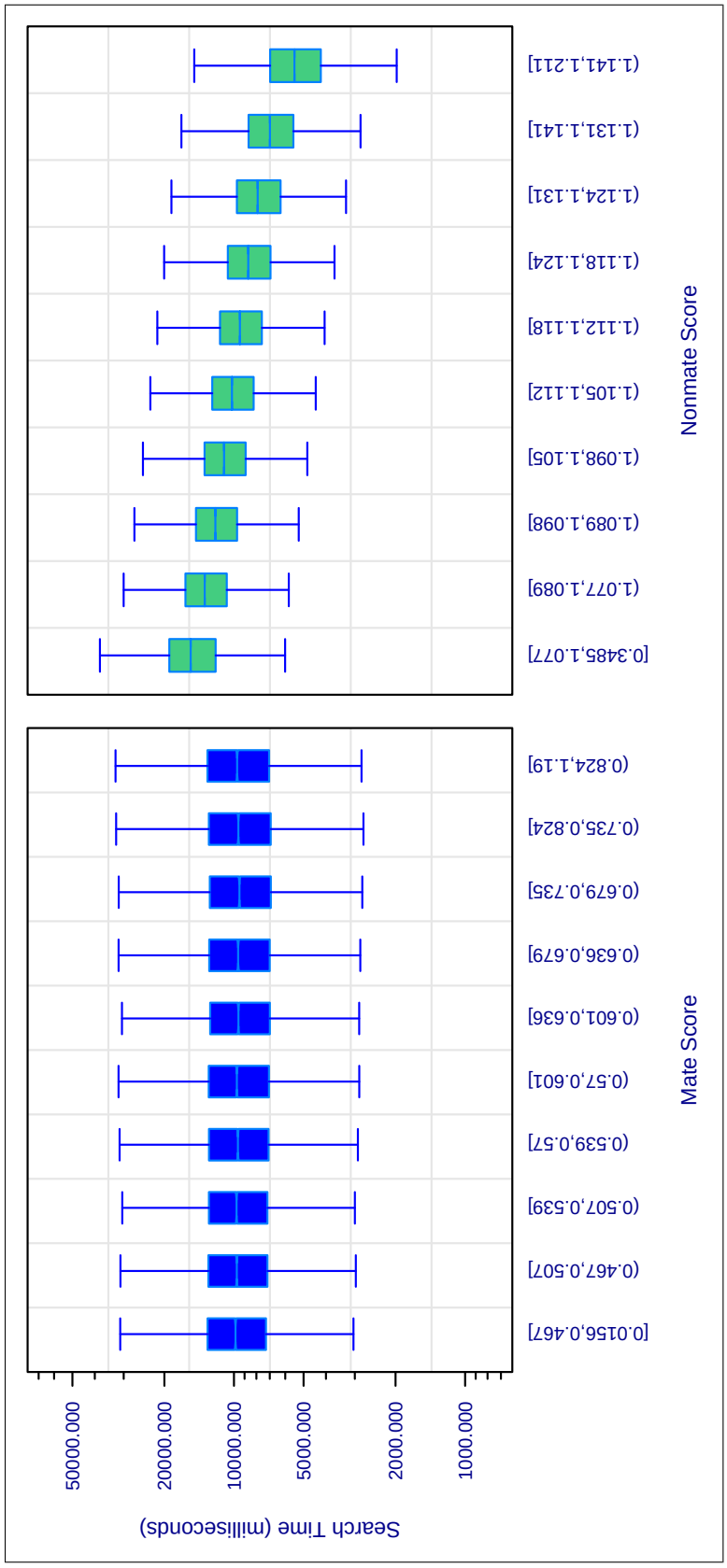

Figure 604: Dependence of speed and comparison score. For the Q02B algorithm, the panels show the distribution of the one-to-many search time for ordered intervals of the mate and nonmate dissimilarity scores. For many implementations the duration of the search is independent of the score outcome. For some others (e.g. T11A), however, mate search durations are faster when the ultimate dissimilarity score is low (i.e. good).

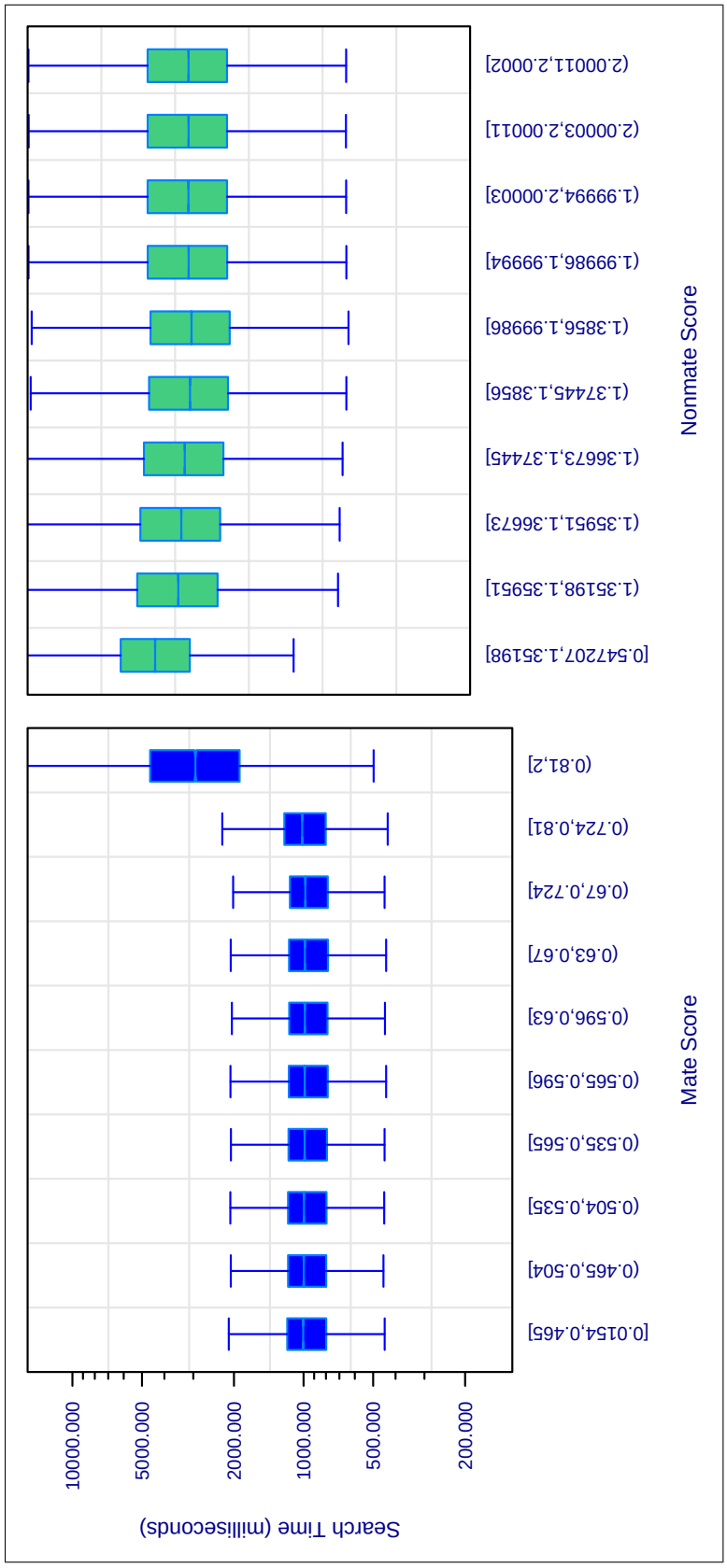

Figure 605: Dependence of speed and comparison score. For the Q03A algorithm, the panels show the distribution of the one-to-many search time for ordered intervals of the mate and nonmate dissimilarity scores. For many implementations the duration of the search is independent of the score outcome. For some others (e.g. T11A), however, mate search durations are faster when the ultimate dissimilarity score is low (i.e. good).

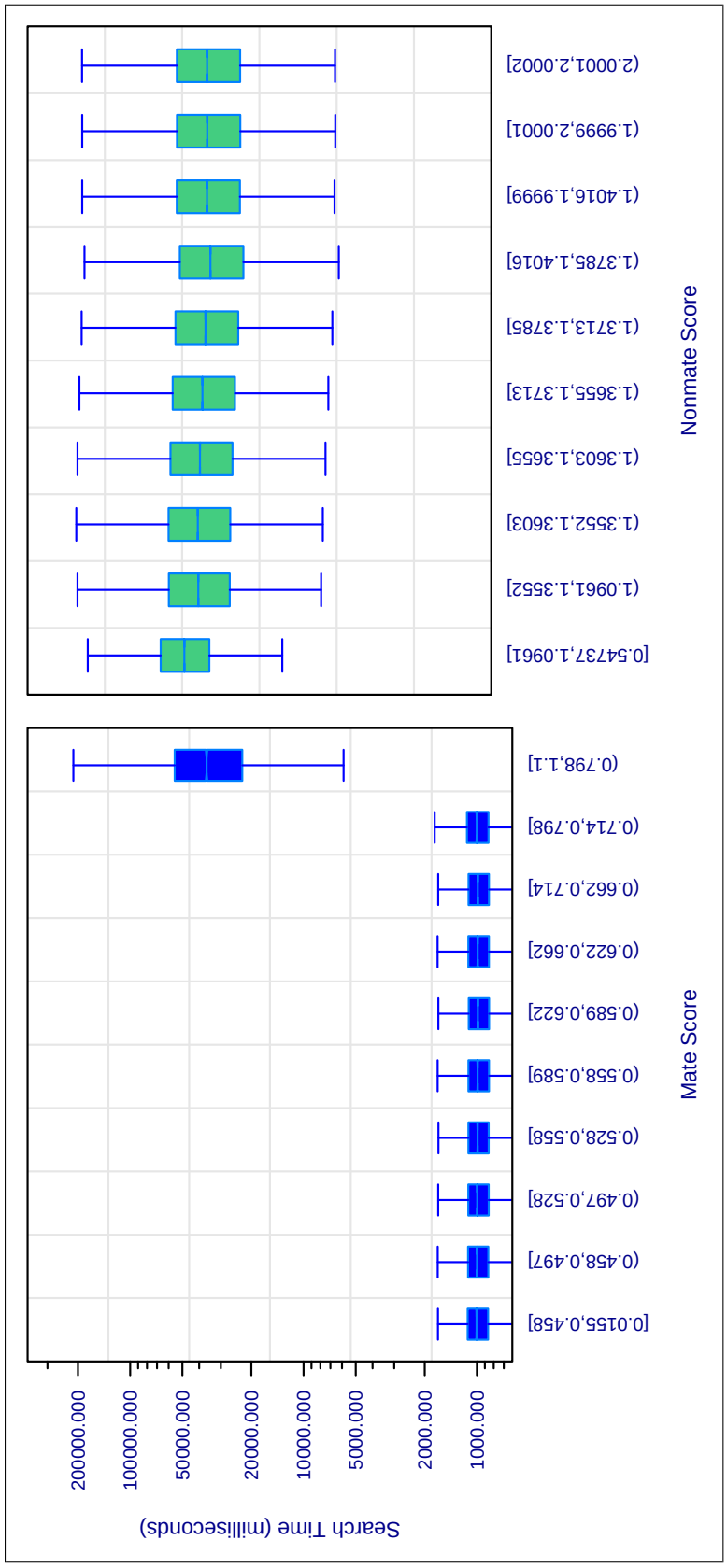

Figure 606: Dependence of speed and comparison score. For the Q03B algorithm, the panels show the distribution of the one-to-many search time for ordered intervals of the mate and nonmate dissimilarity scores. For many implementations the duration of the search is independent of the score outcome. For some others (e.g. T11A), however, mate search durations are faster when the ultimate dissimilarity score is low (i.e. good).

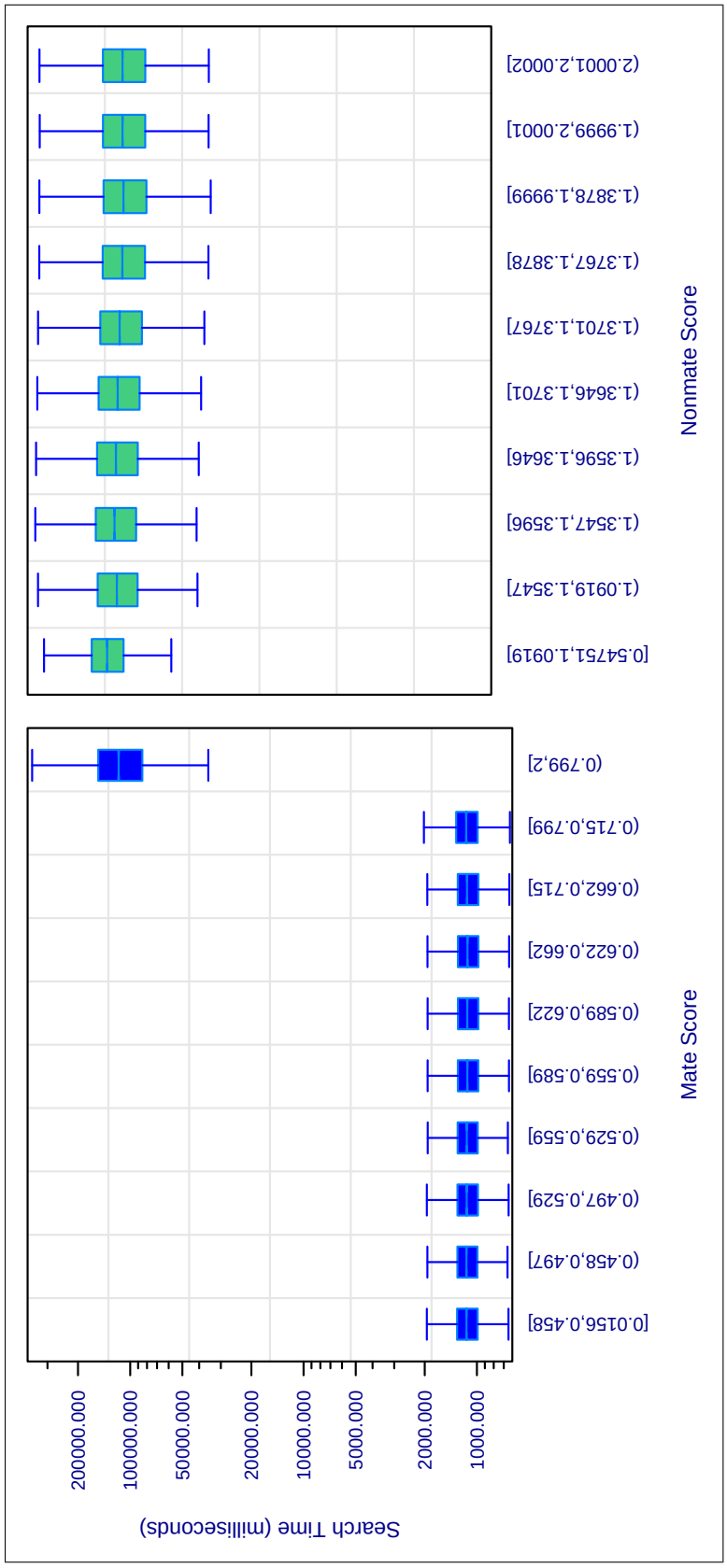

Figure 607: Dependence of speed and comparison score. For the Q04B algorithm, the panels show the distribution of the one-to-many search time for ordered intervals of the mate and nonmate dissimilarity scores. For many implementations the duration of the search is independent of the score outcome. For some others (e.g. T11A), however, mate search durations are faster when the ultimate dissimilarity score is low (i.e. good).

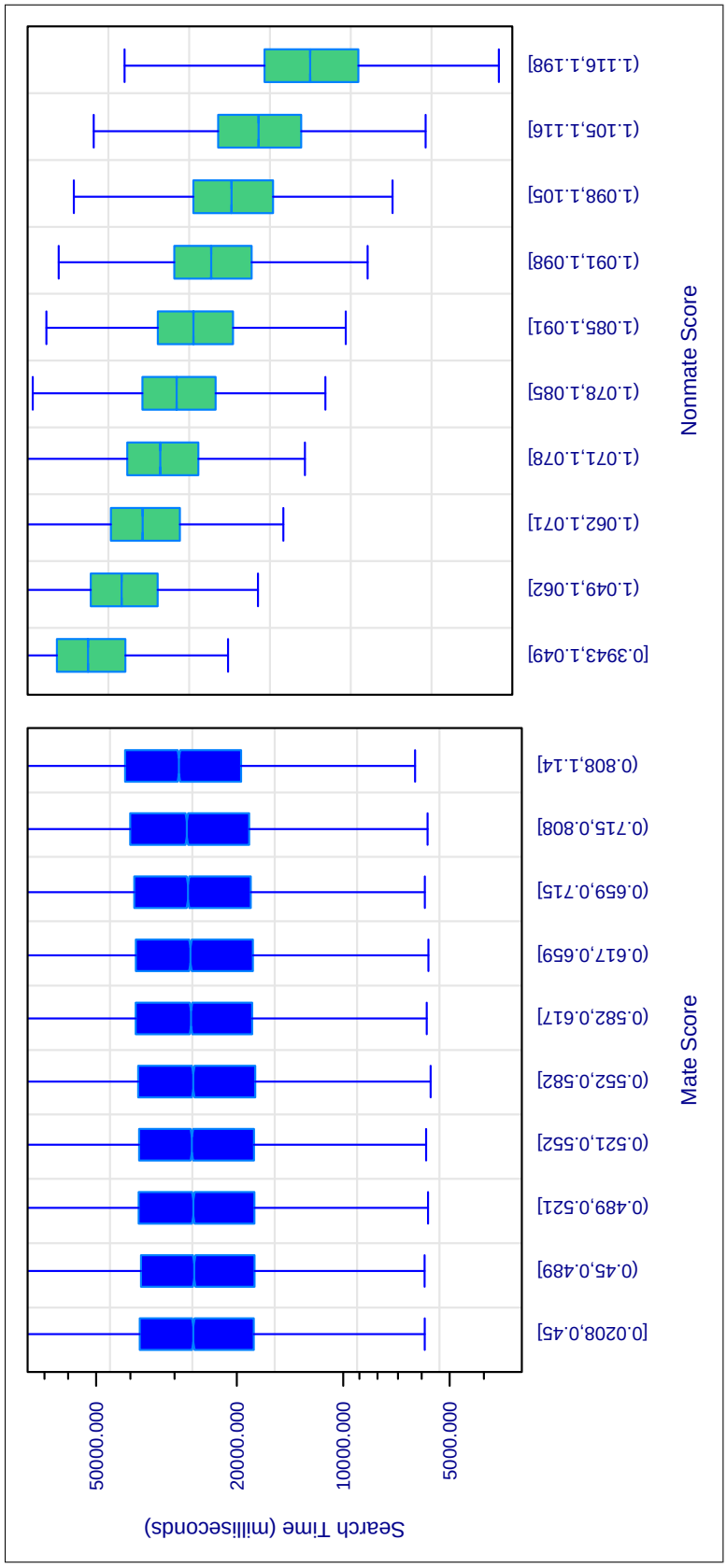

Figure 608: Dependence of speed and comparison score. For the Q11B algorithm, the panels show the distribution of the one-to-many search time for ordered intervals of the mate and nonmate dissimilarity scores. For many implementations the duration of the search is independent of the score outcome. For some others (e.g. T11A), however, mate search durations are faster when the ultimate dissimilarity score is low (i.e. good).

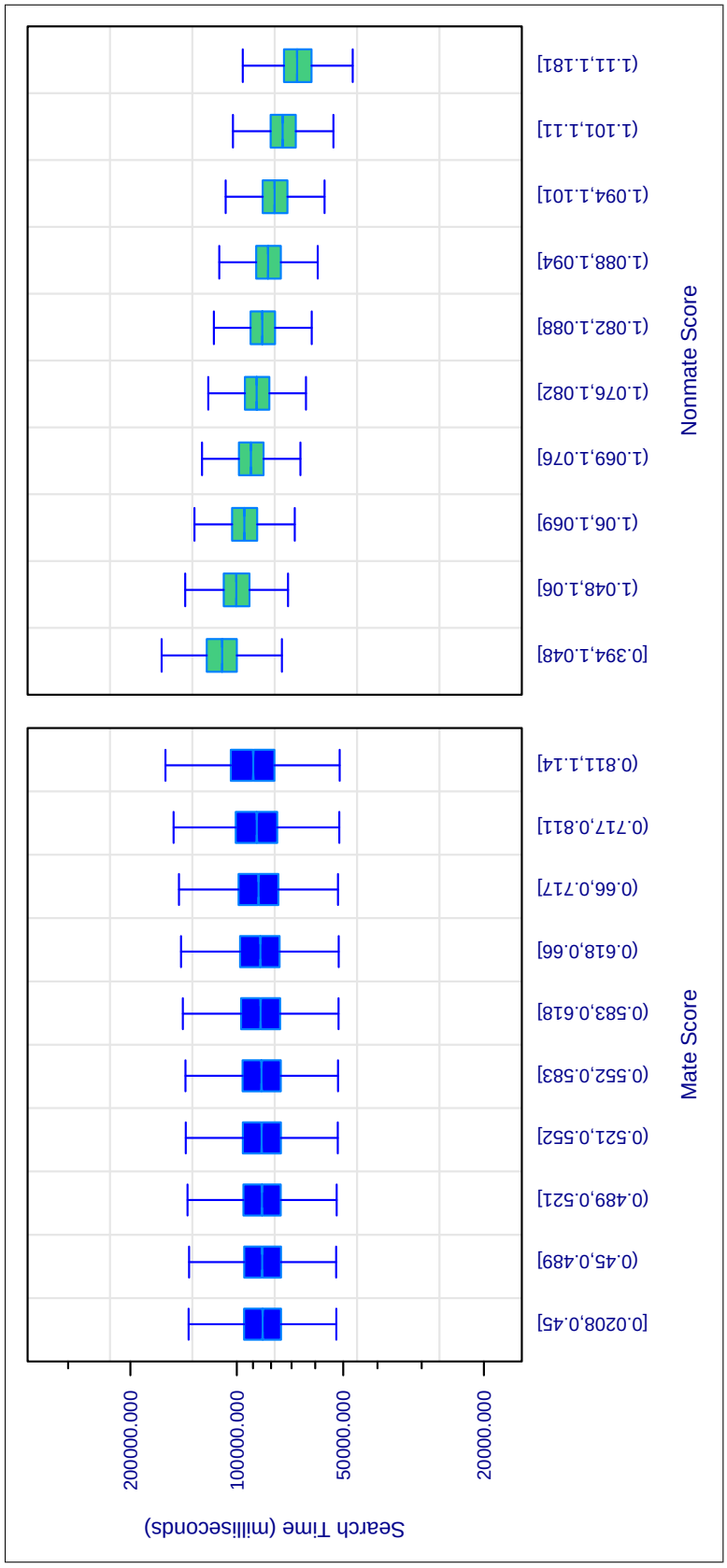

Figure 609: Dependence of speed and comparison score. For the Q12B algorithm, the panels show the distribution of the one-to-many search time for ordered intervals of the mate and nonmate dissimilarity scores. For many implementations the duration of the search is independent of the score outcome. For some others (e.g. T11A), however, mate search durations are faster when the ultimate dissimilarity score is low (i.e. good).

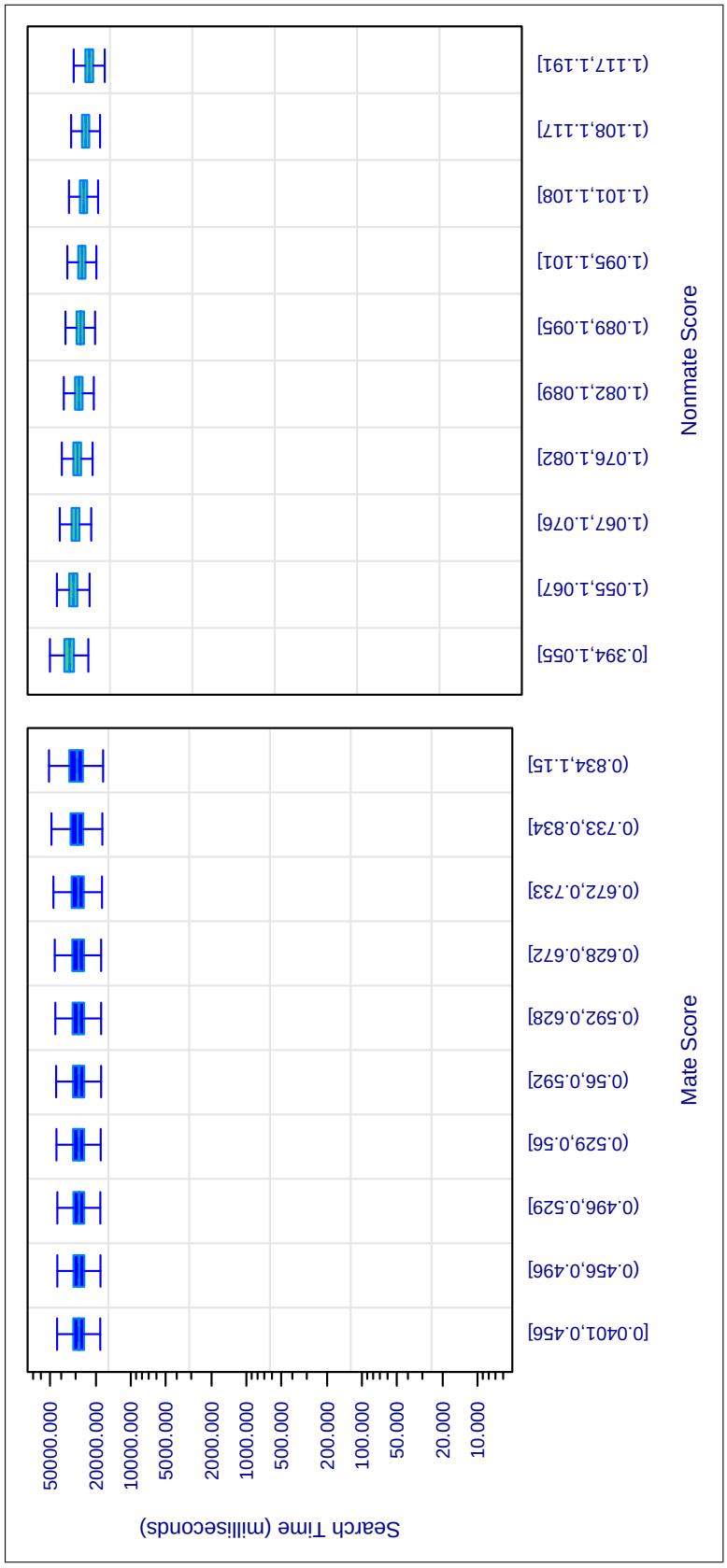

Figure 610: Dependence of speed and comparison score. For the Q13B algorithm, the panels show the distribution of the one-to-many search time for ordered intervals of the mate and nonmate dissimilarity scores. For many implementations the duration of the search is independent of the score outcome. For some others (e.g. T11A), however, mate search durations are faster when the ultimate dissimilarity score is low (i.e. good).

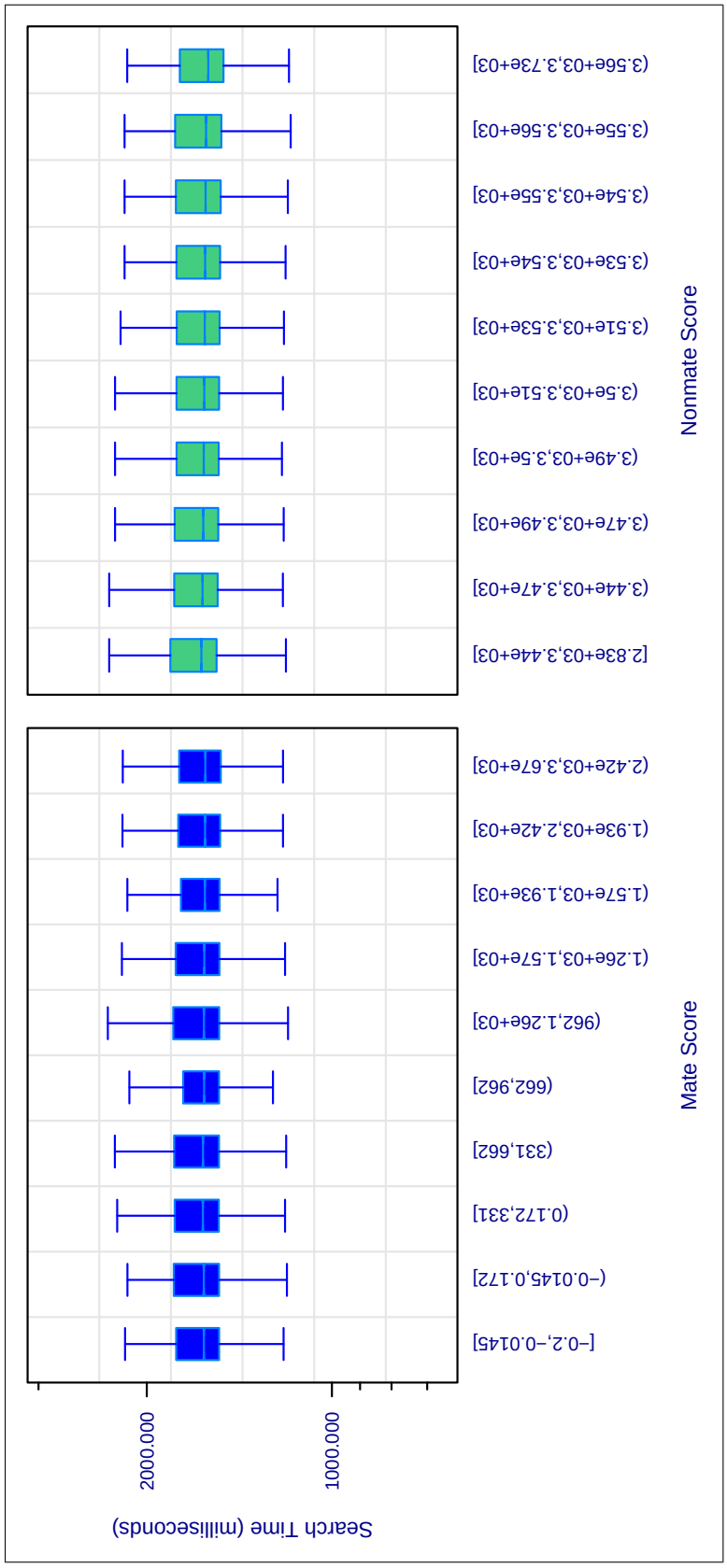

Figure 611: Dependence of speed and comparison score. For the R02A algorithm, the panels show the distribution of the one-to-many search time for ordered intervals of the mate and nonmate dissimilarity scores. For many implementations the duration of the search is independent of the score outcome. For some others (e.g. T11A), however, mate search durations are faster when the ultimate dissimilarity score is low (i.e. good).

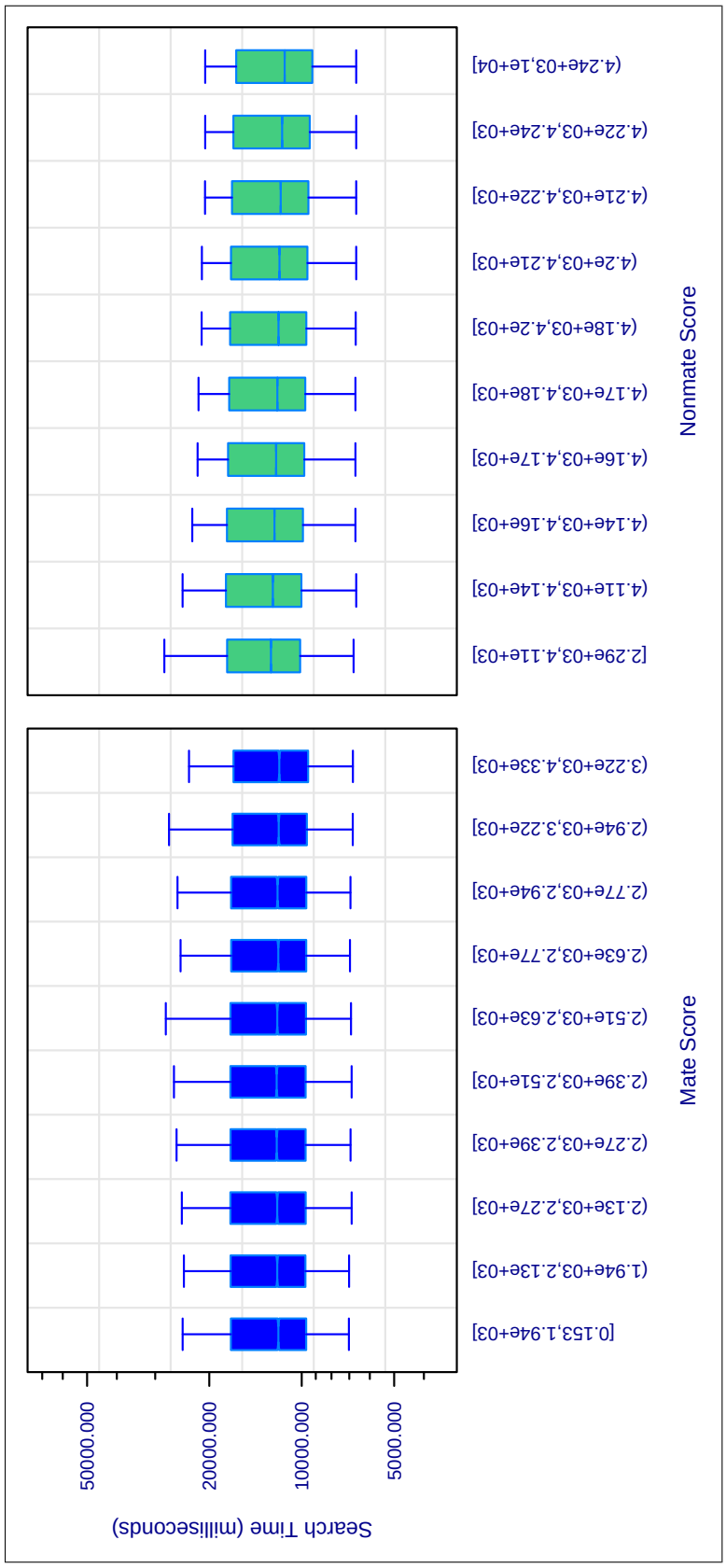

Figure 612: Dependence of speed and comparison score. For the R02B algorithm, the panels show the distribution of the one-to-many search time for ordered intervals of the mate and nonmate dissimilarity scores. For many implementations the duration of the search is independent of the score outcome. For some others (e.g. T11A), however, mate search durations are faster when the ultimate dissimilarity score is low (i.e. good).

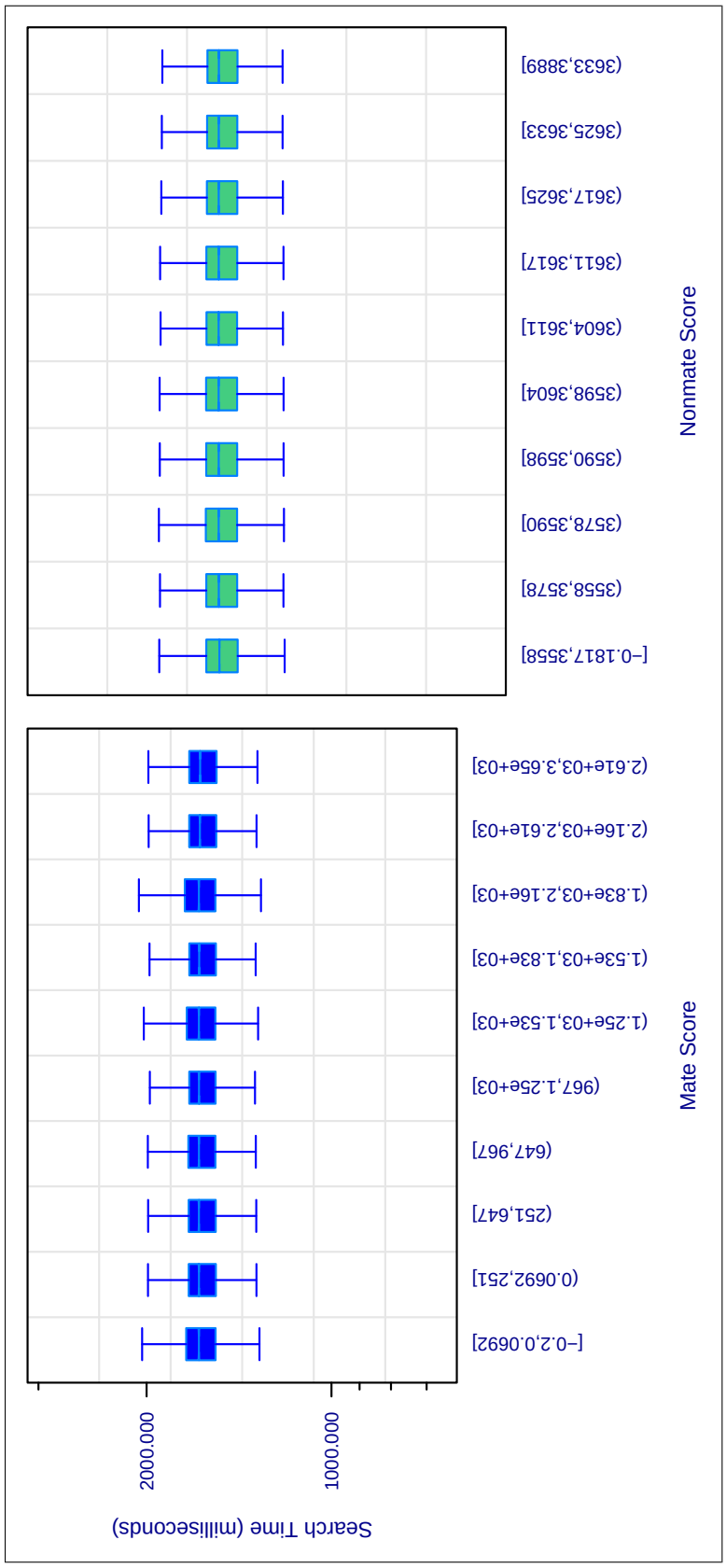

Figure 613: Dependence of speed and comparison score. For the R03A algorithm, the panels show the distribution of the one-to-many search time for ordered intervals of the mate and nonmate dissimilarity scores. For many implementations the duration of the search is independent of the score outcome. For some others (e.g. T11A), however, mate search durations are faster when the ultimate dissimilarity score is low (i.e. good).

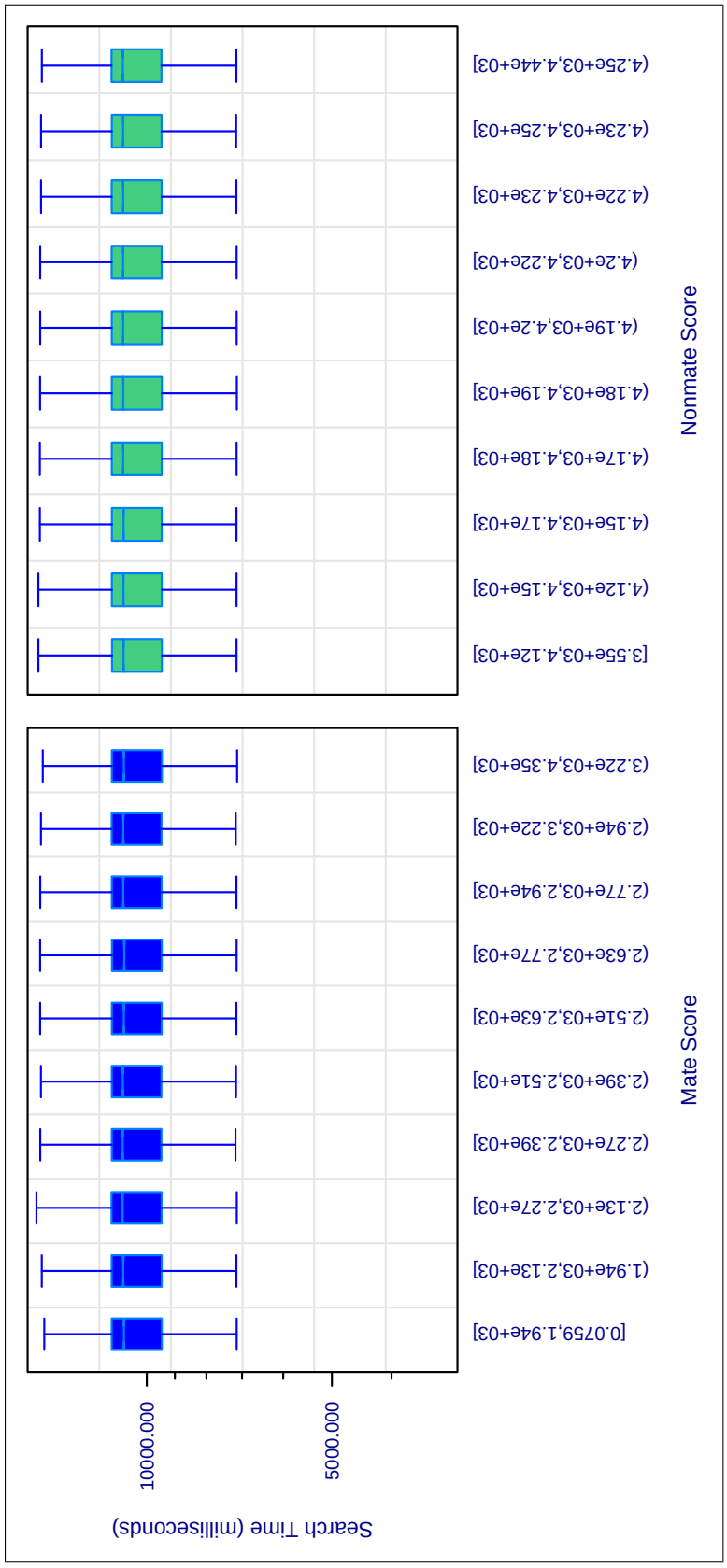

Figure 614: Dependence of speed and comparison score. For the R03B algorithm, the panels show the distribution of the one-to-many search time for ordered intervals of the mate and nonmate dissimilarity scores. For many implementations the duration of the search is independent of the score outcome. For some others (e.g. T11A), however, mate search durations are faster when the ultimate dissimilarity score is low (i.e. good).

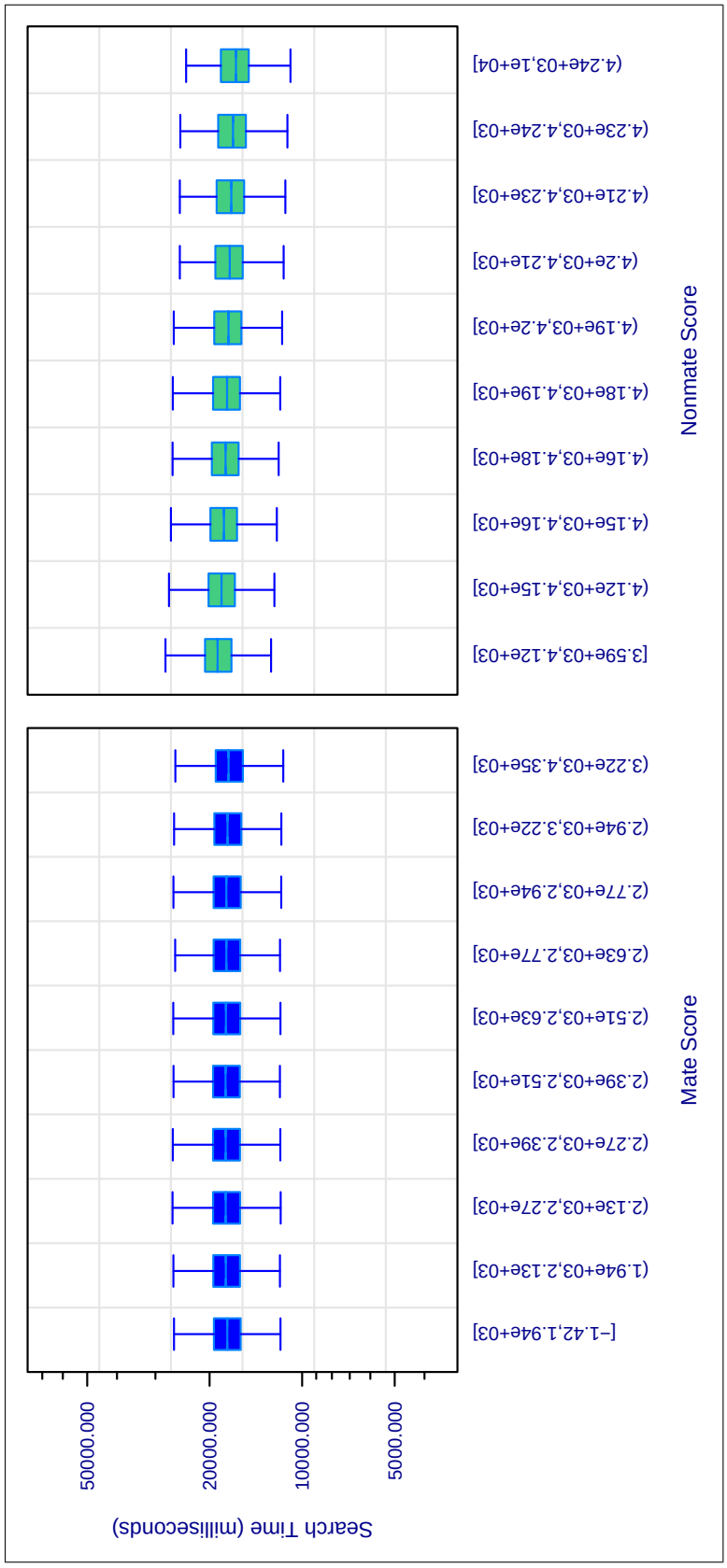

Figure 615: Dependence of speed and comparison score. For the R04B algorithm, the panels show the distribution of the one-to-many search time for ordered intervals of the mate and nonmate dissimilarity scores. For many implementations the duration of the search is independent of the score outcome. For some others (e.g. T11A), however, mate search durations are faster when the ultimate dissimilarity score is low (i.e. good).

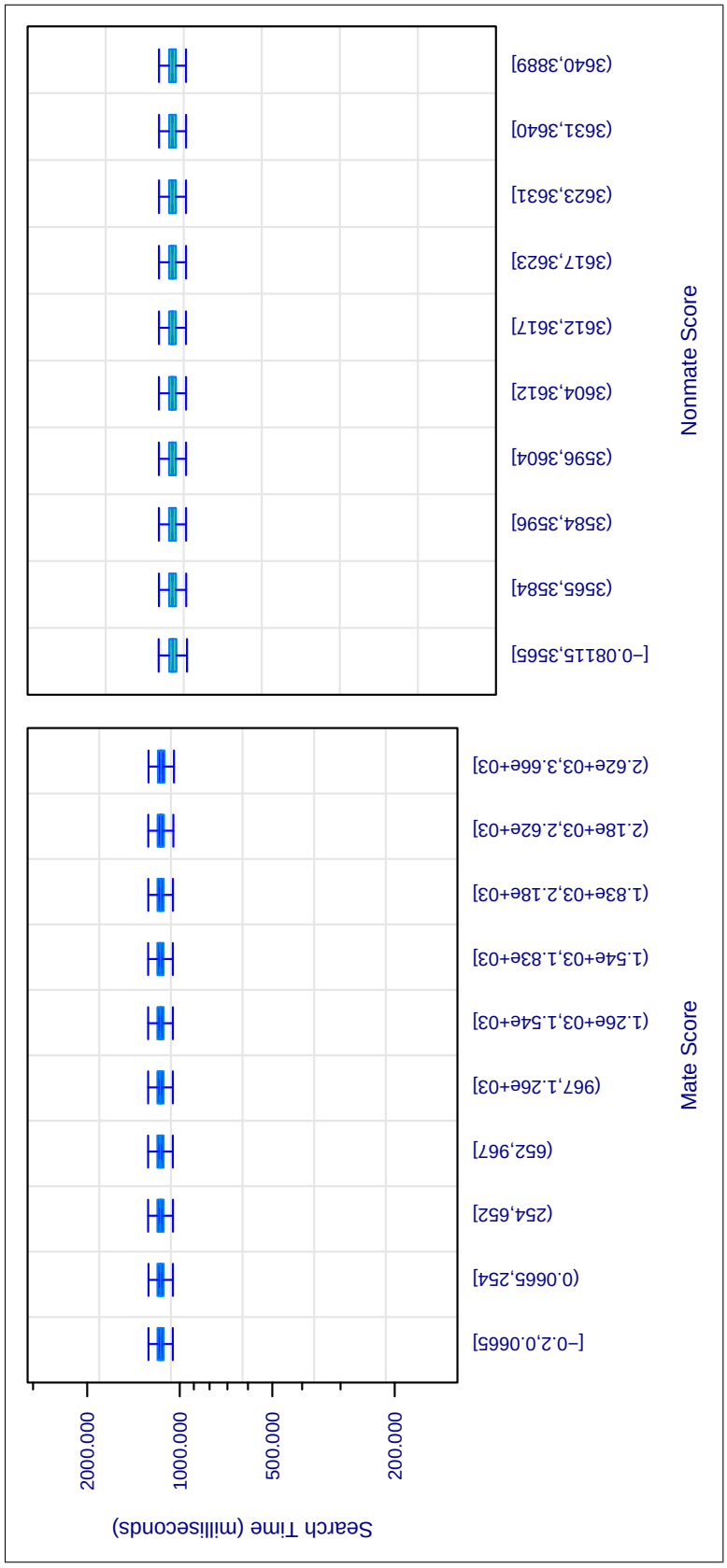

Figure 616: Dependence of speed and comparison score. For the R11A algorithm, the panels show the distribution of the one-to-many search time for ordered intervals of the mate and nonmate dissimilarity scores. For many implementations the duration of the search is independent of the score outcome. For some others (e.g. T11A), however, mate search durations are faster when the ultimate dissimilarity score is low (i.e. good).

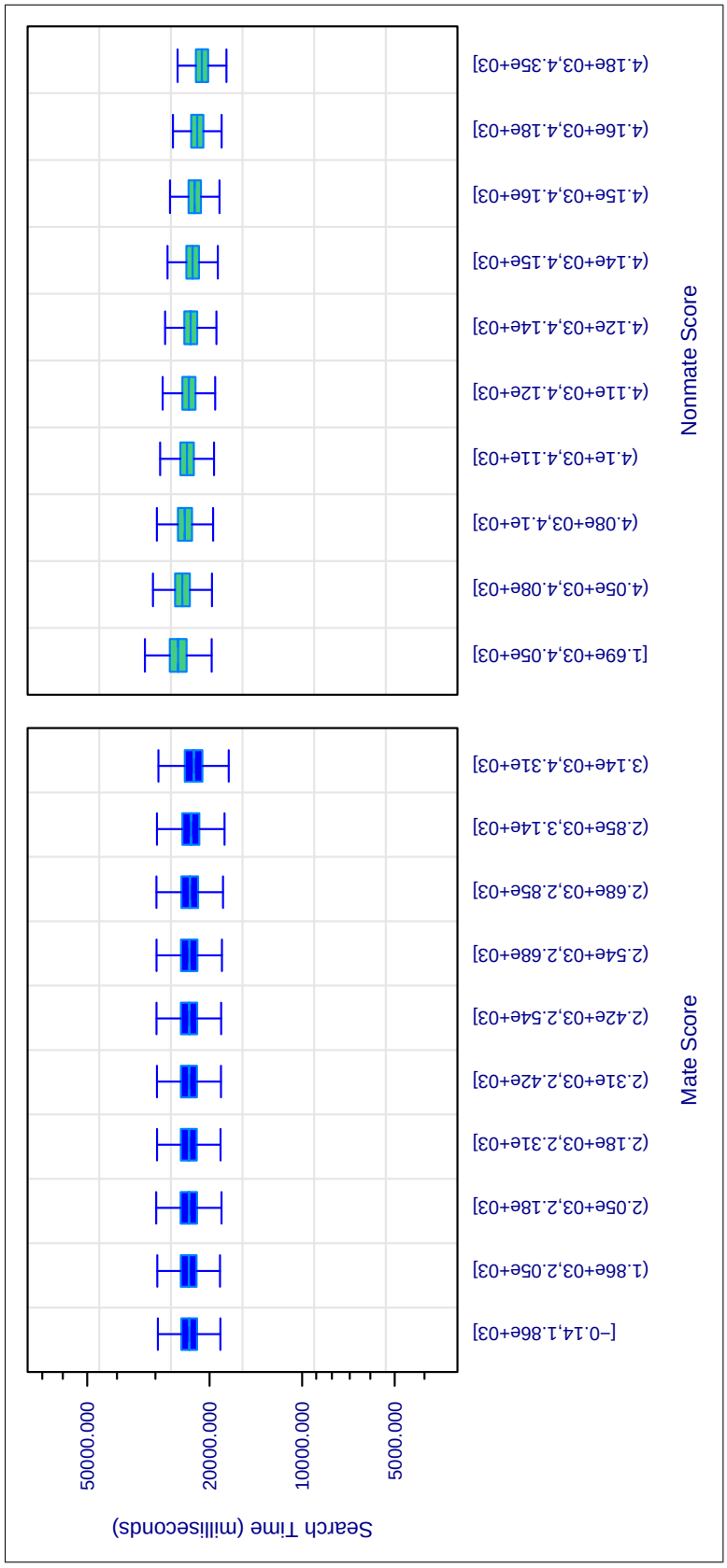

Figure 617: Dependence of speed and comparison score. For the R11B algorithm, the panels show the distribution of the one-to-many search time for ordered intervals of the mate and nonmate dissimilarity scores. For many implementations the duration of the search is independent of the score outcome. For some others (e.g. T11A), however, mate search durations are faster when the ultimate dissimilarity score is low (i.e. good).

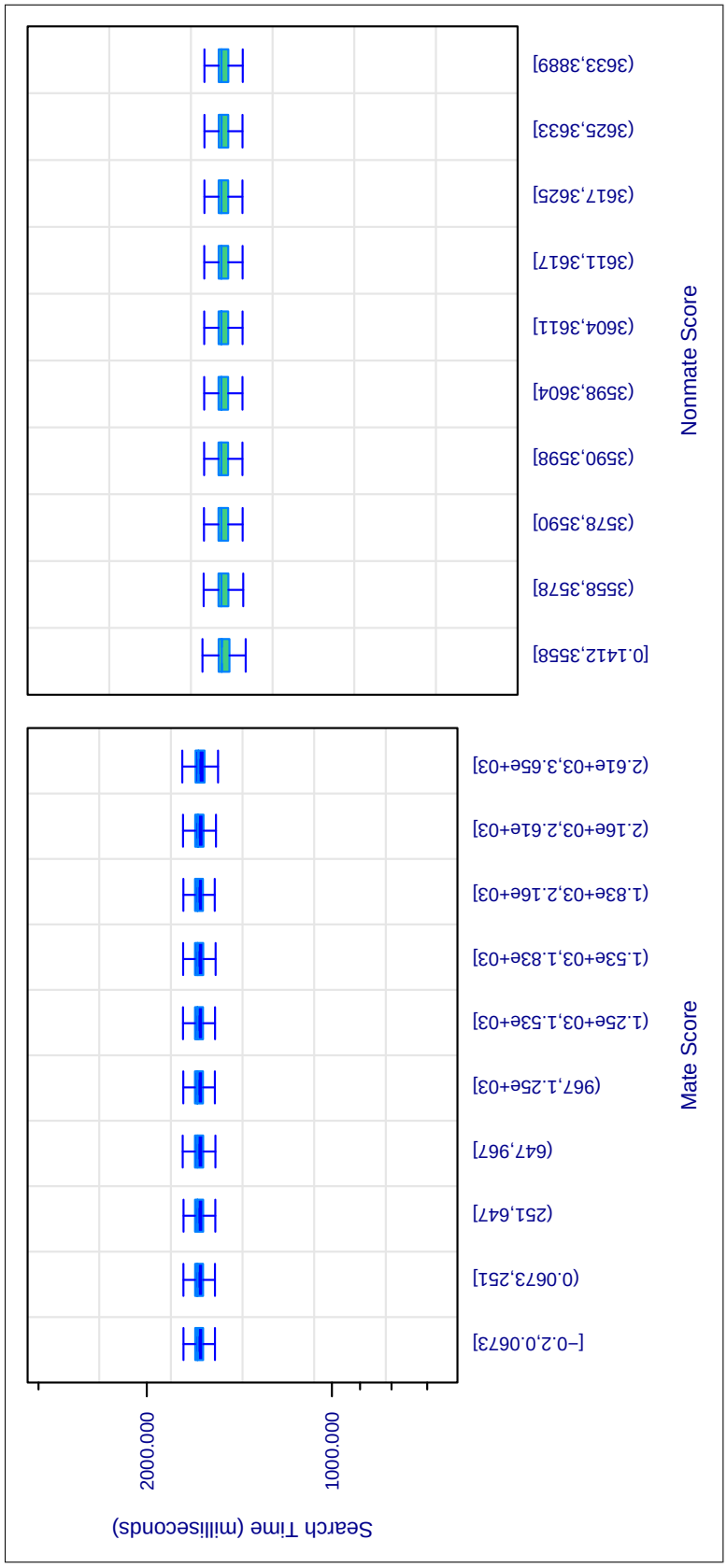

Figure 618: Dependence of speed and comparison score. For the R12A algorithm, the panels show the distribution of the one-to-many search time for ordered intervals of the mate and nonmate dissimilarity scores. For many implementations the duration of the search is independent of the score outcome. For some others (e.g. T11A), however, mate search durations are faster when the ultimate dissimilarity score is low (i.e. good).

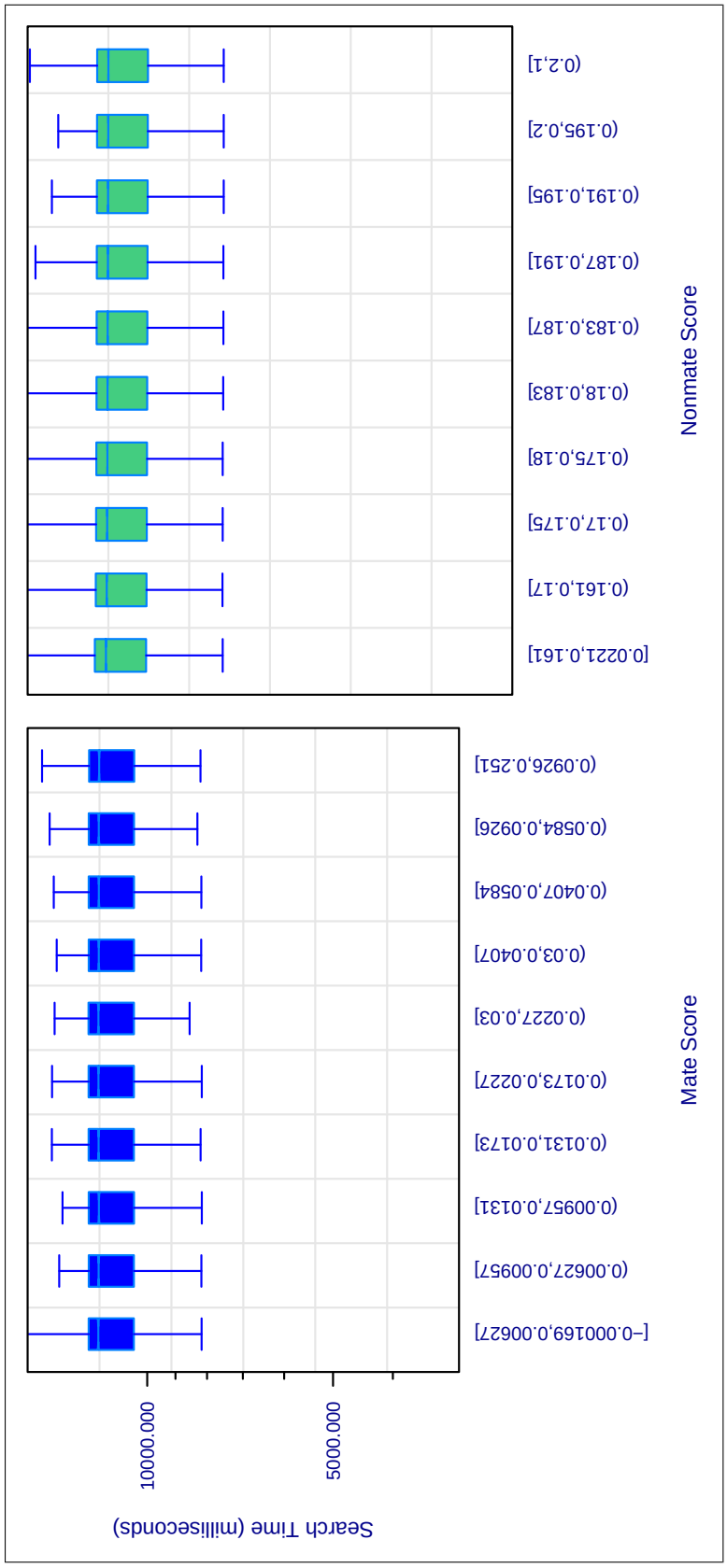

Figure 619: Dependence of speed and comparison score. For the S03A algorithm, the panels show the distribution of the one-to-many search time for ordered intervals of the mate and nonmate dissimilarity scores. For many implementations the duration of the search is independent of the score outcome. For some others (e.g. T11A), however, mate search durations are faster when the ultimate dissimilarity score is low (i.e. good).

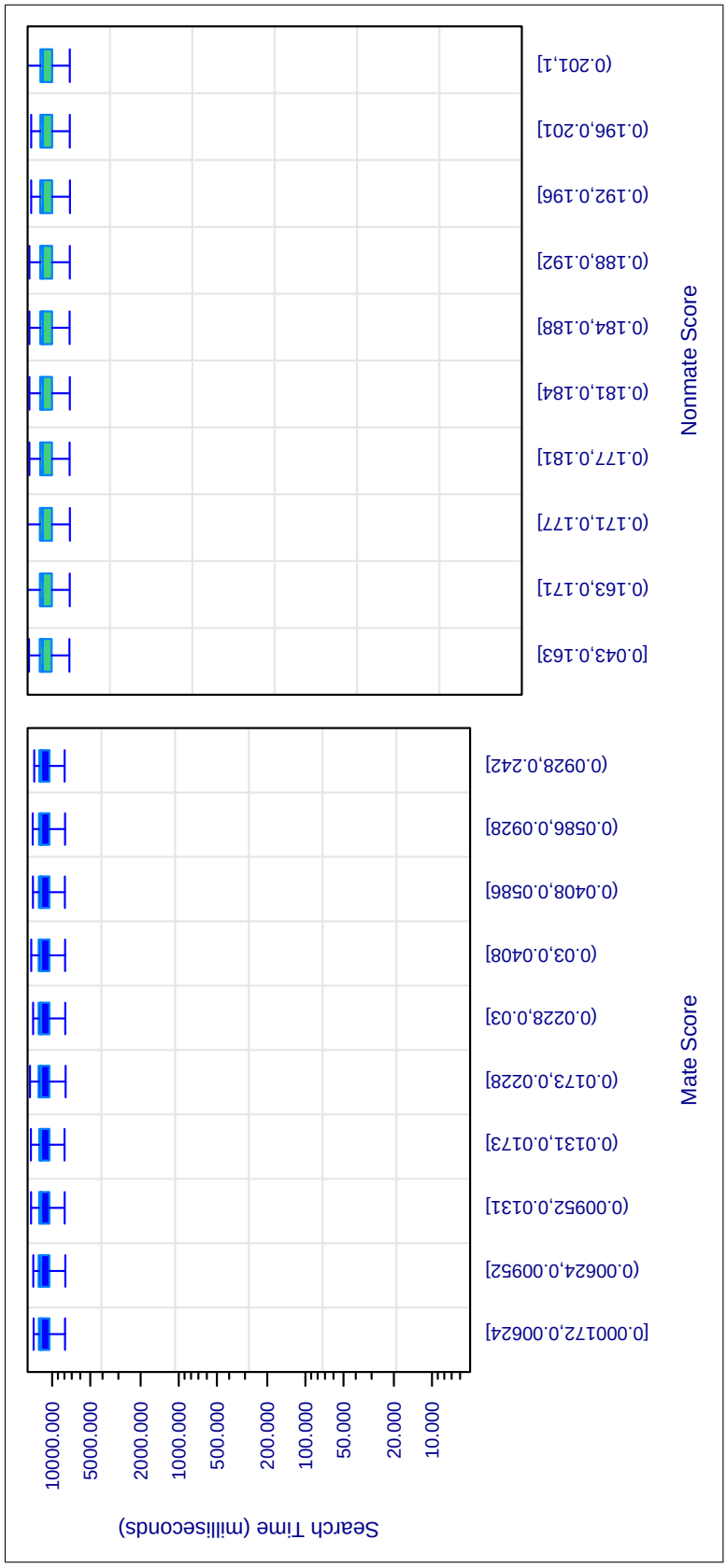

Figure 620: Dependence of speed and comparison score. For the S04A algorithm, the panels show the distribution of the one-to-many search time for ordered intervals of the mate and nonmate dissimilarity scores. For many implementations the duration of the search is independent of the score outcome. For some others (e.g. T11A), however, mate search durations are faster when the ultimate dissimilarity score is low (i.e. good).

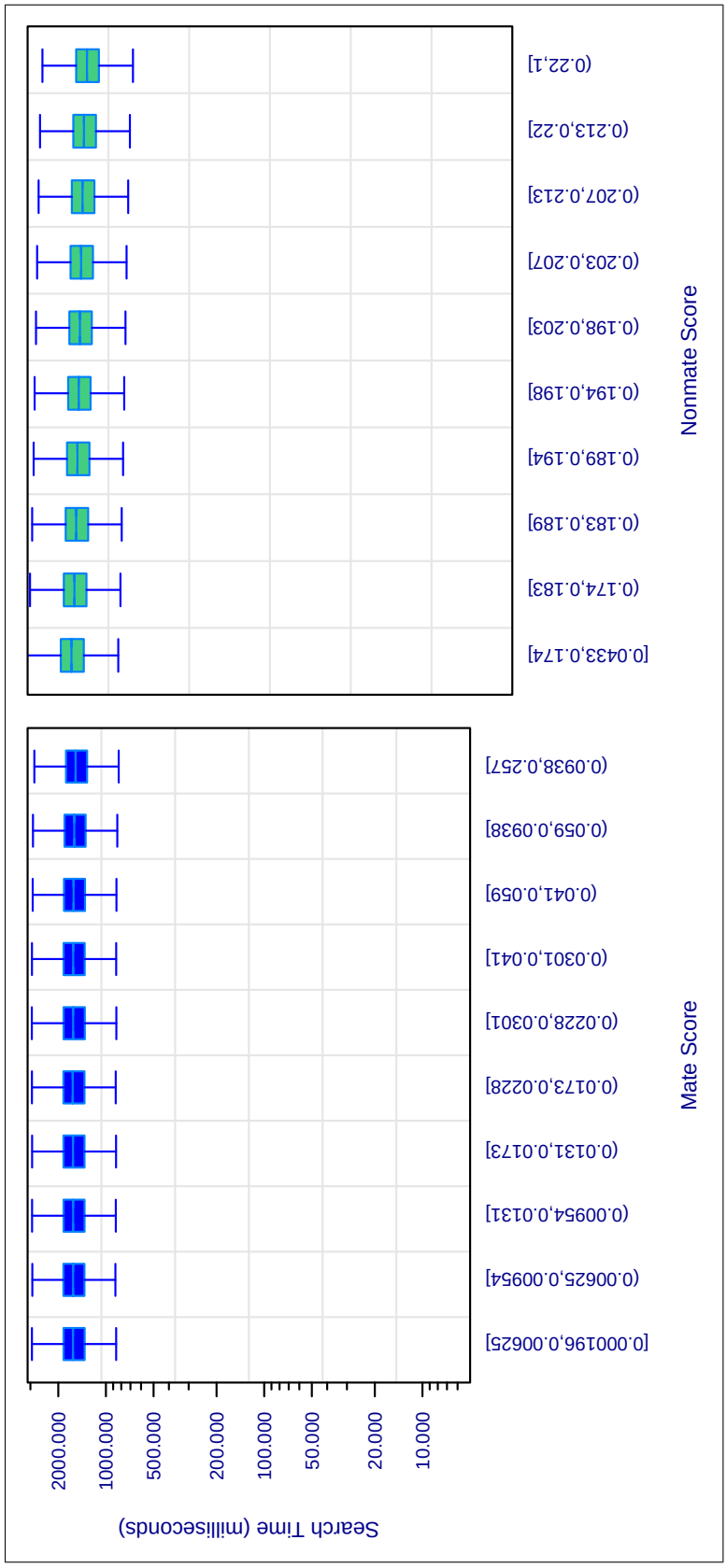

Figure 621: Dependence of speed and comparison score. For the S05A algorithm, the panels show the distribution of the one-to-many search time for ordered intervals of the mate and nonmate dissimilarity scores. For many implementations the duration of the search is independent of the score outcome. For some others (e.g. T11A), however, mate search durations are faster when the ultimate dissimilarity score is low (i.e. good).

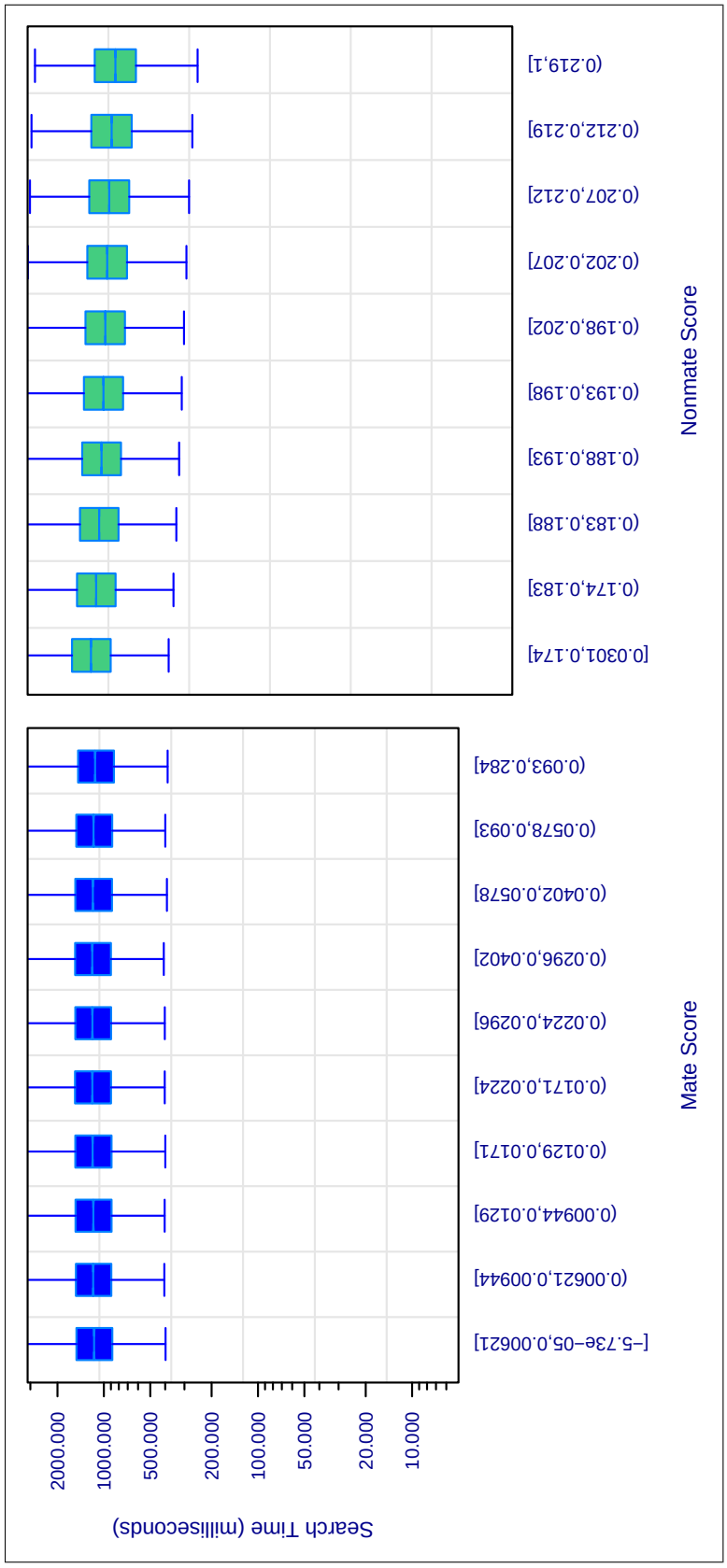

Figure 622: Dependence of speed and comparison score. For the S11A algorithm, the panels show the distribution of the one-to-many search time for ordered intervals of the mate and nonmate dissimilarity scores. For many implementations the duration of the search is independent of the score outcome. For some others (e.g. T11A), however, mate search durations are faster when the ultimate dissimilarity score is low (i.e. good).

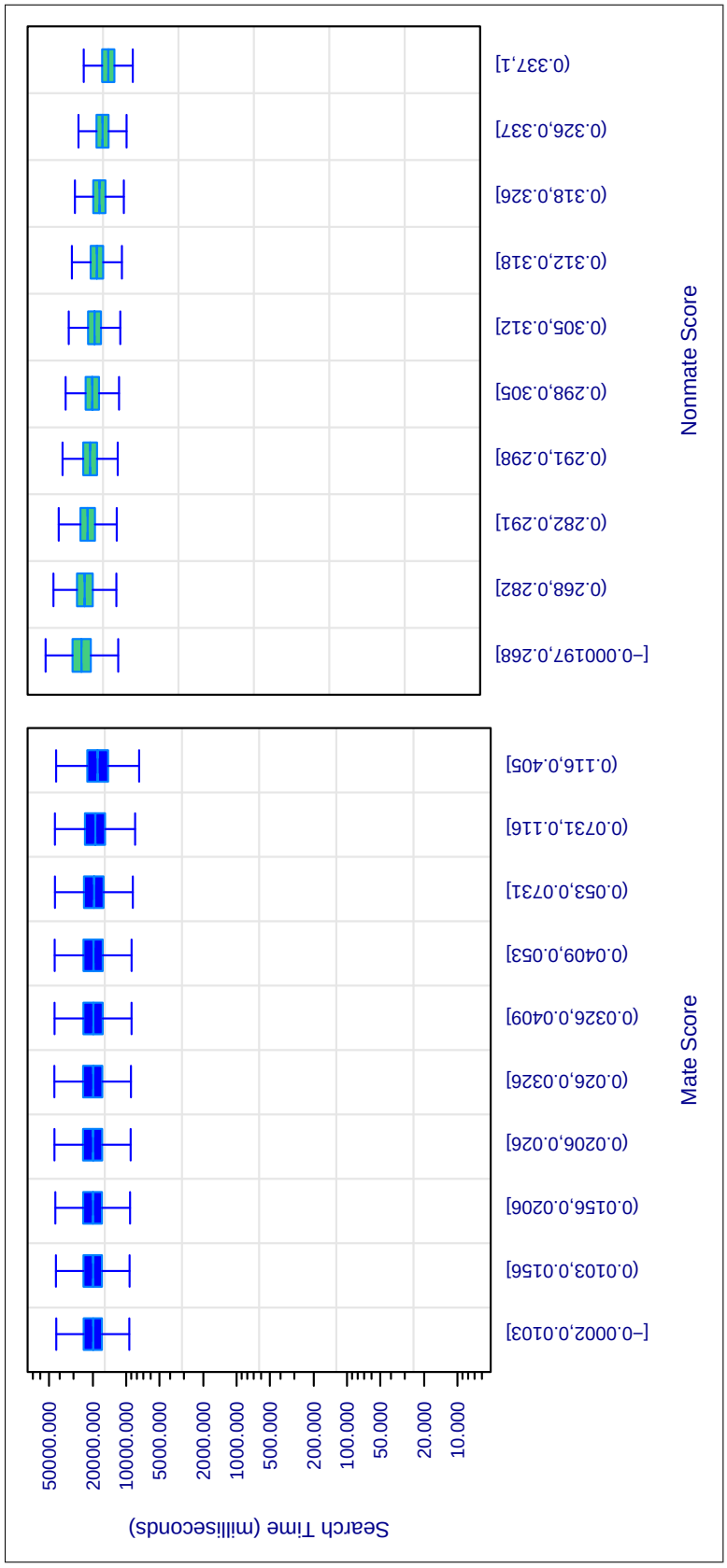

Figure 623: Dependence of speed and comparison score. For the S11B algorithm, the panels show the distribution of the one-to-many search time for ordered intervals of the mate and nonmate dissimilarity scores. For many implementations the duration of the search is independent of the score outcome. For some others (e.g. T11A), however, mate search durations are faster when the ultimate dissimilarity score is low (i.e. good).

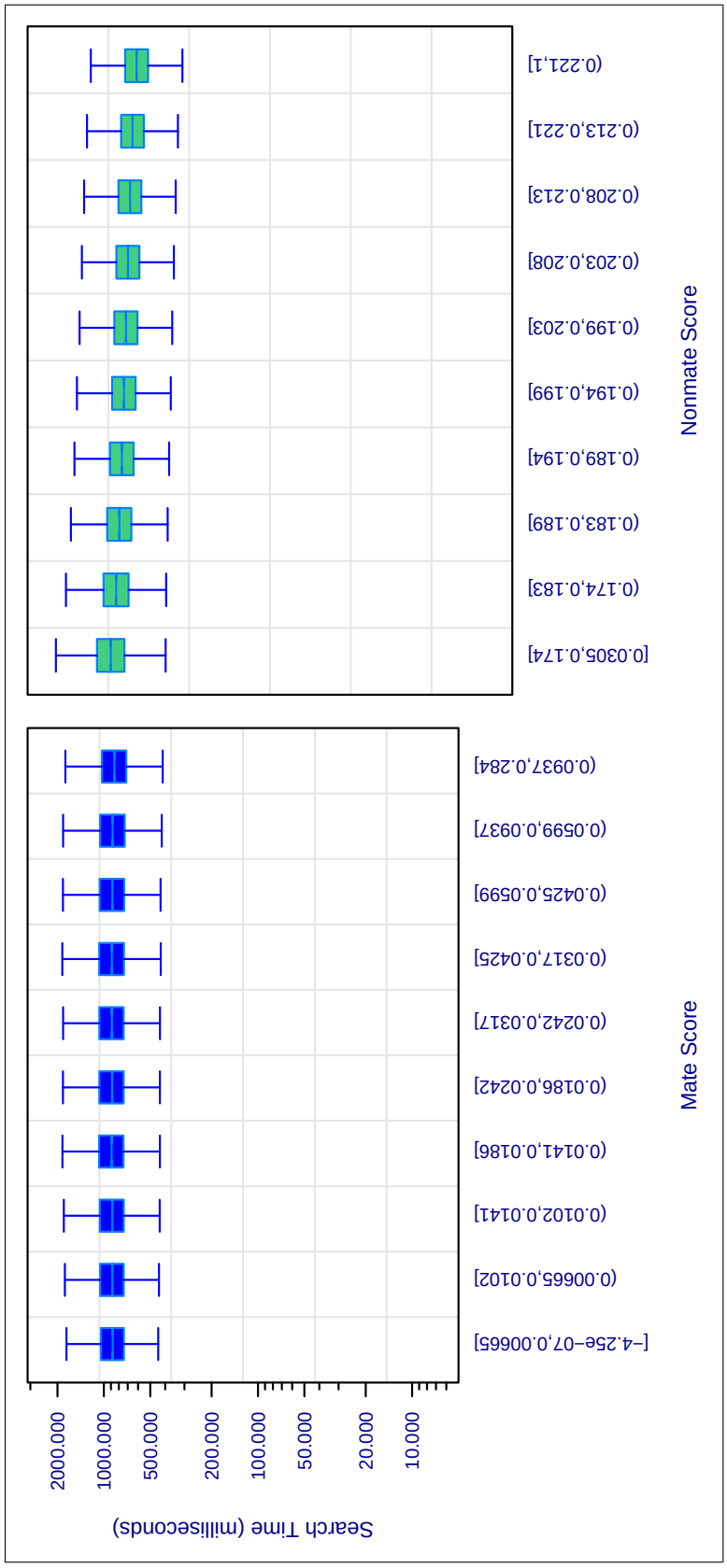

Figure 624: Dependence of speed and comparison score. For the S12A algorithm, the panels show the distribution of the one-to-many search time for ordered intervals of the mate and nonmate dissimilarity scores. For many implementations the duration of the search is independent of the score outcome. For some others (e.g. T11A), however, mate search durations are faster when the ultimate dissimilarity score is low (i.e. good).

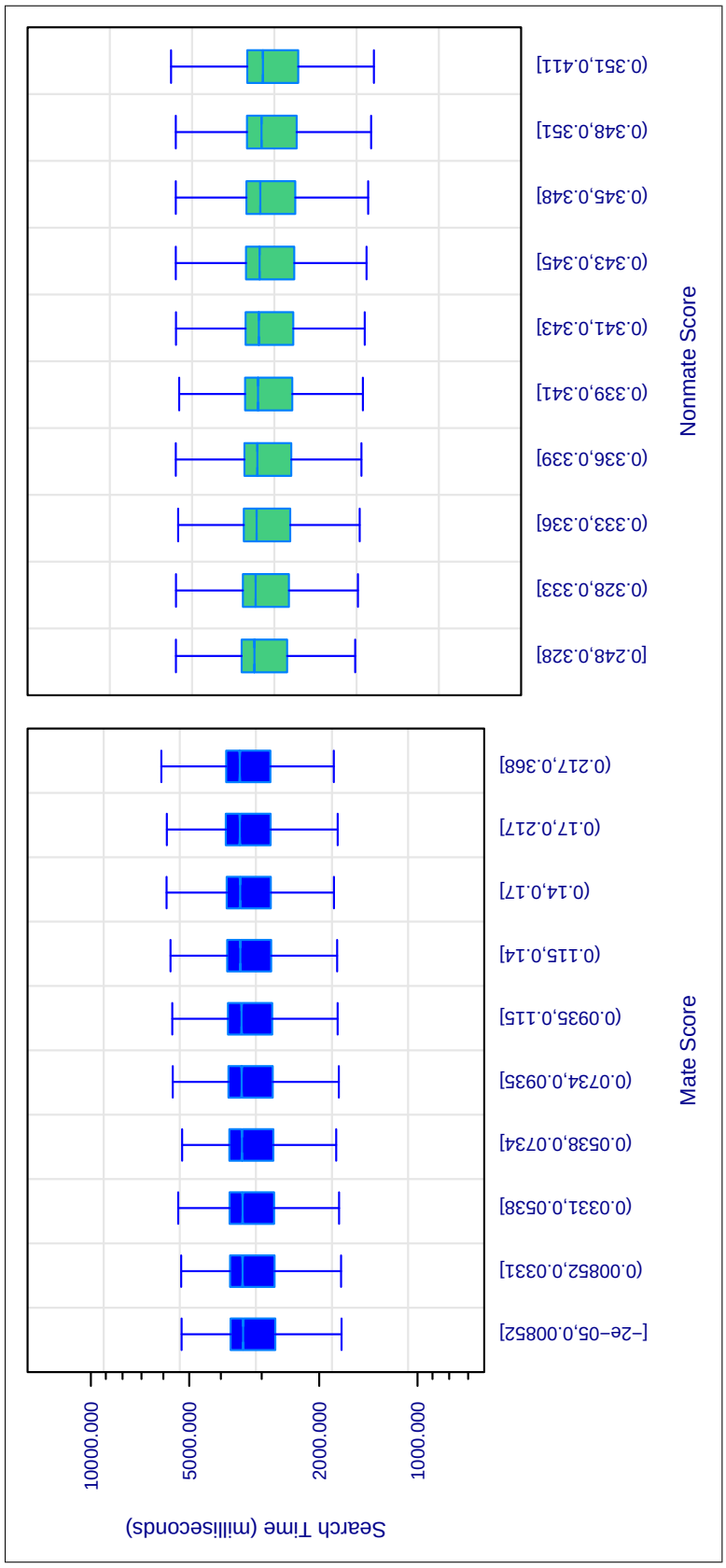

Figure 625: Dependence of speed and comparison score. For the T01A algorithm, the panels show the distribution of the one-to-many search time for ordered intervals of the mate and nonmate dissimilarity scores. For many implementations the duration of the search is independent of the score outcome. For some others (e.g. T11A), however, mate search durations are faster when the ultimate dissimilarity score is low (i.e. good).

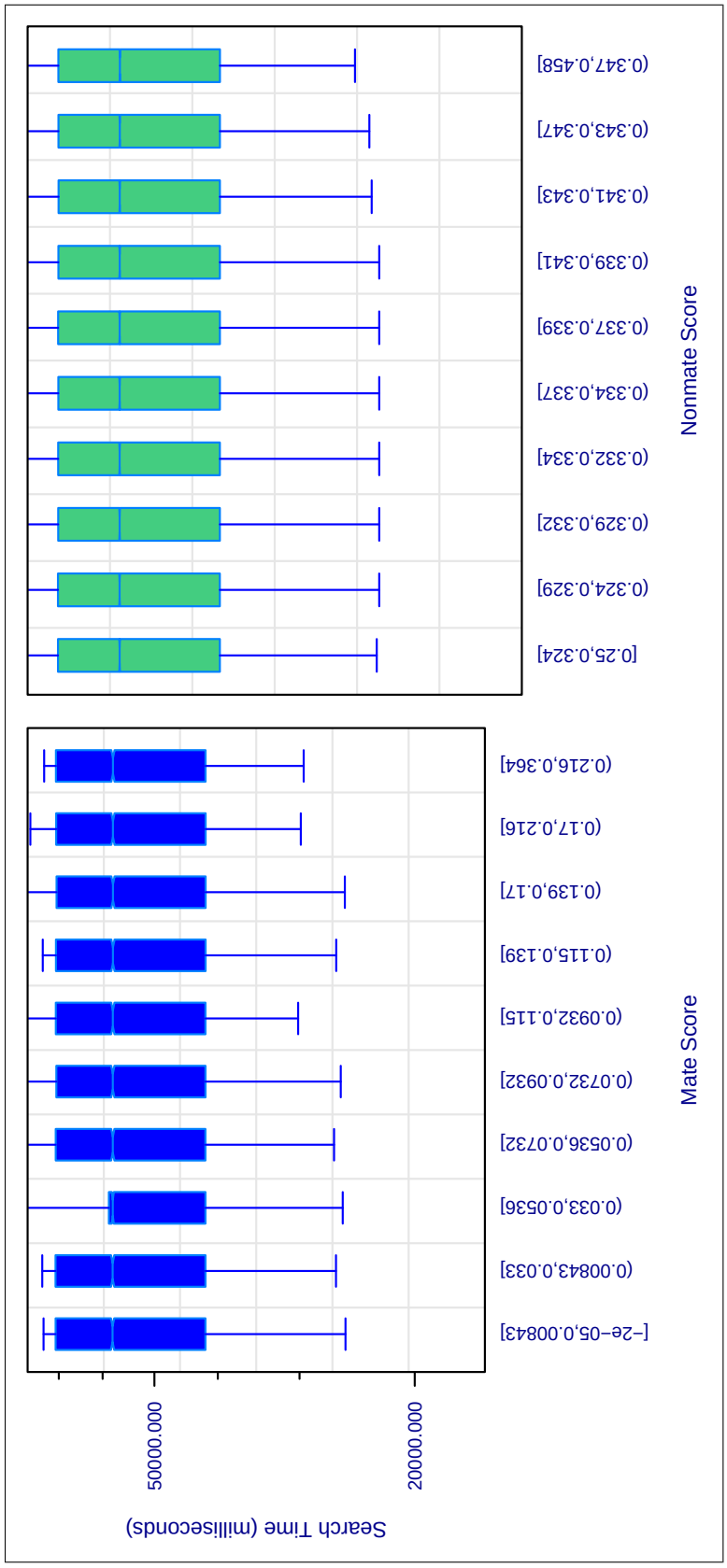

Figure 626: Dependence of speed and comparison score. For the T01B algorithm, the panels show the distribution of the one-to-many search time for ordered intervals of the mate and nonmate dissimilarity scores. For many implementations the duration of the search is independent of the score outcome. For some others (e.g. T11A), however, mate search durations are faster when the ultimate dissimilarity score is low (i.e. good).

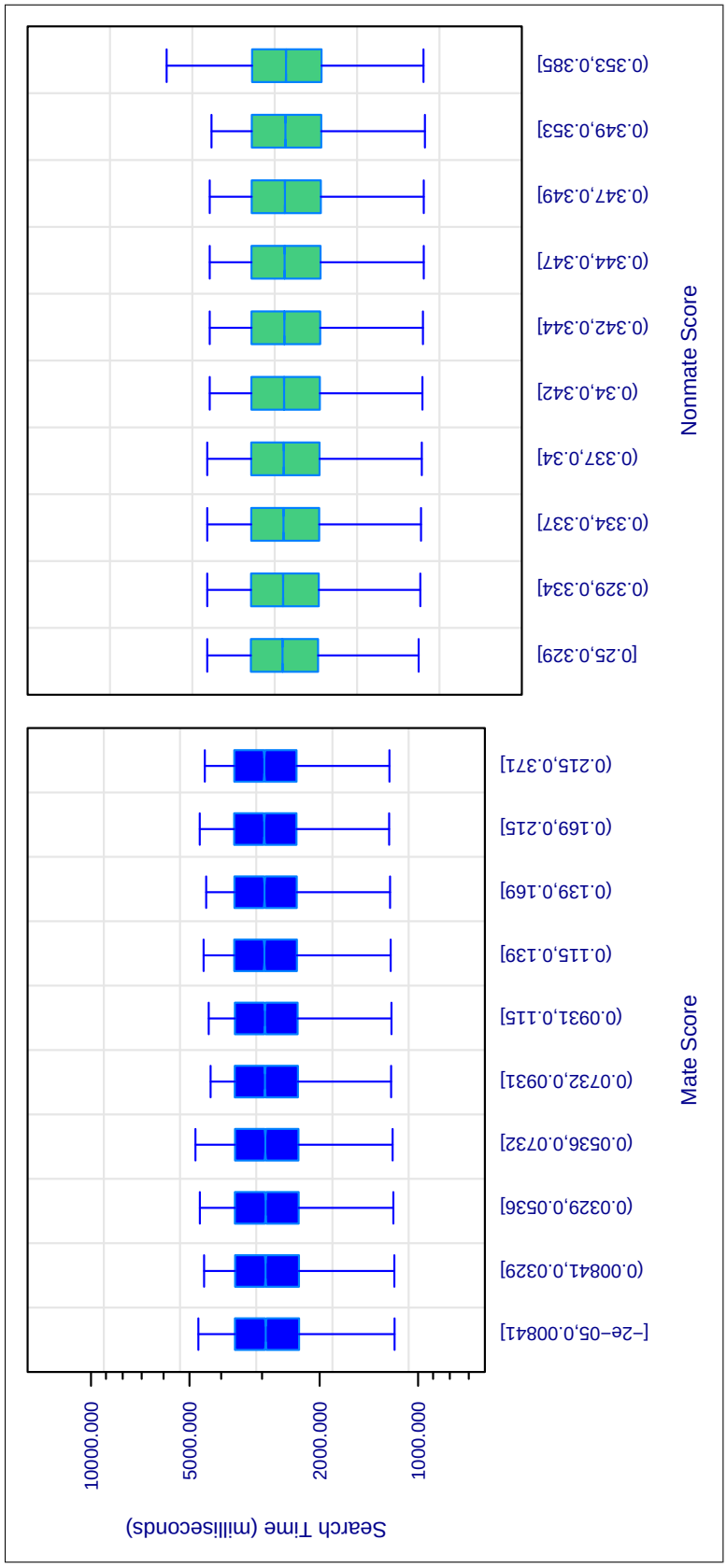

Figure 627: Dependence of speed and comparison score. For the T02A algorithm, the panels show the distribution of the one-to-many search time for ordered intervals of the mate and nonmate dissimilarity scores. For many implementations the duration of the search is independent of the score outcome. For some others (e.g. T11A), however, mate search durations are faster when the ultimate dissimilarity score is low (i.e. good).

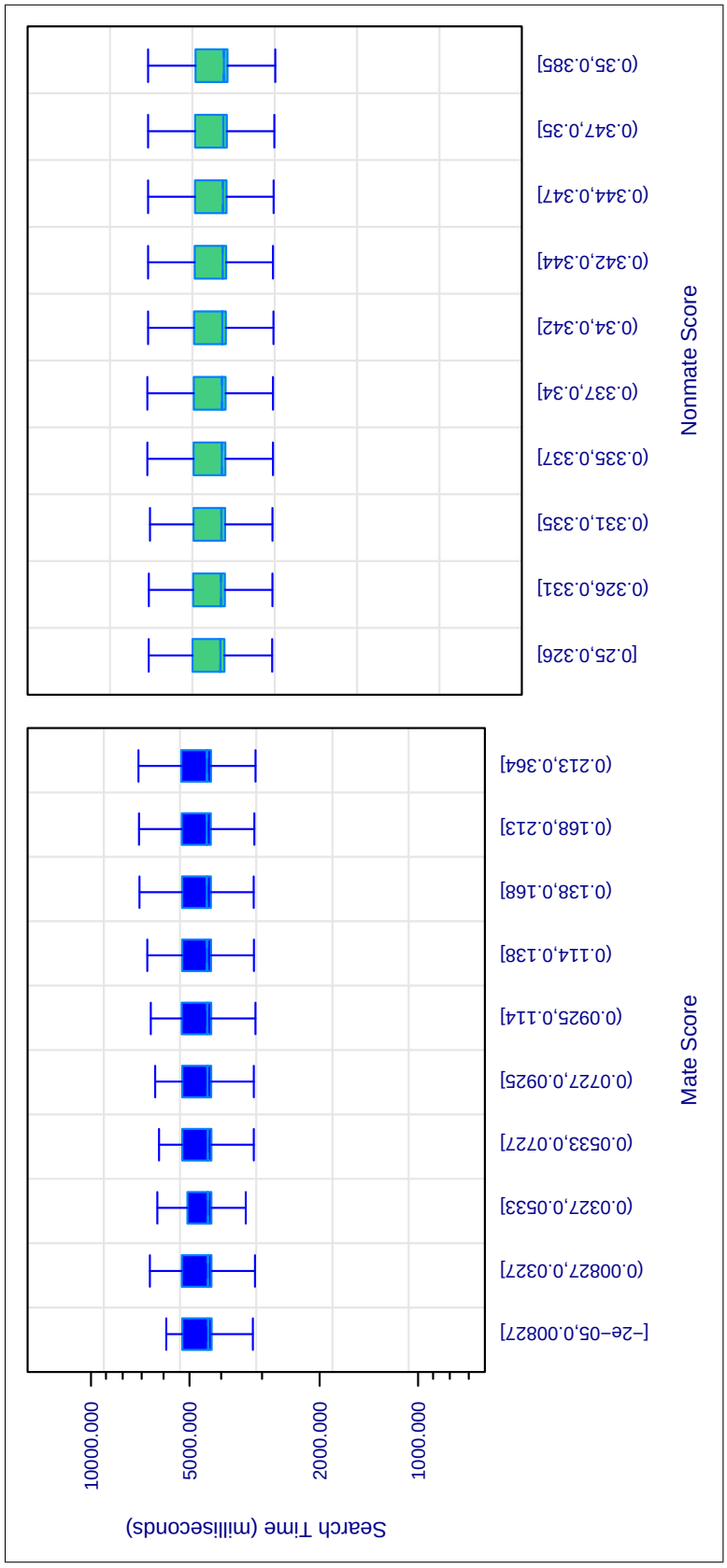

Figure 628: Dependence of speed and comparison score. For the T02B algorithm, the panels show the distribution of the one-to-many search time for ordered intervals of the mate and nonmate dissimilarity scores. For many implementations the duration of the search is independent of the score outcome. For some others (e.g. T11A), however, mate search durations are faster when the ultimate dissimilarity score is low (i.e. good).

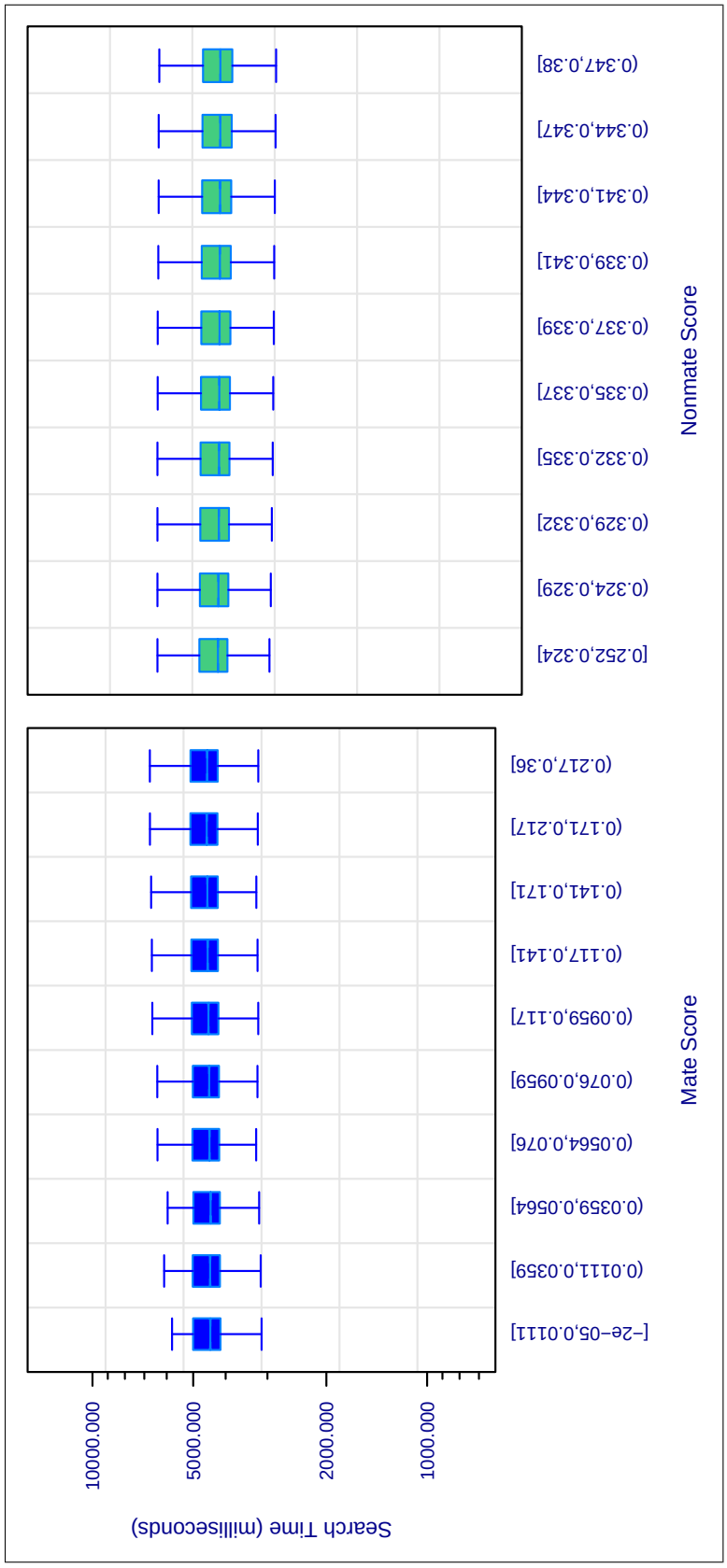

Figure 629: Dependence of speed and comparison score. For the T03A algorithm, the panels show the distribution of the one-to-many search time for ordered intervals of the mate and nonmate dissimilarity scores. For many implementations the duration of the search is independent of the score outcome. For some others (e.g. T11A), however, mate search durations are faster when the ultimate dissimilarity score is low (i.e. good).

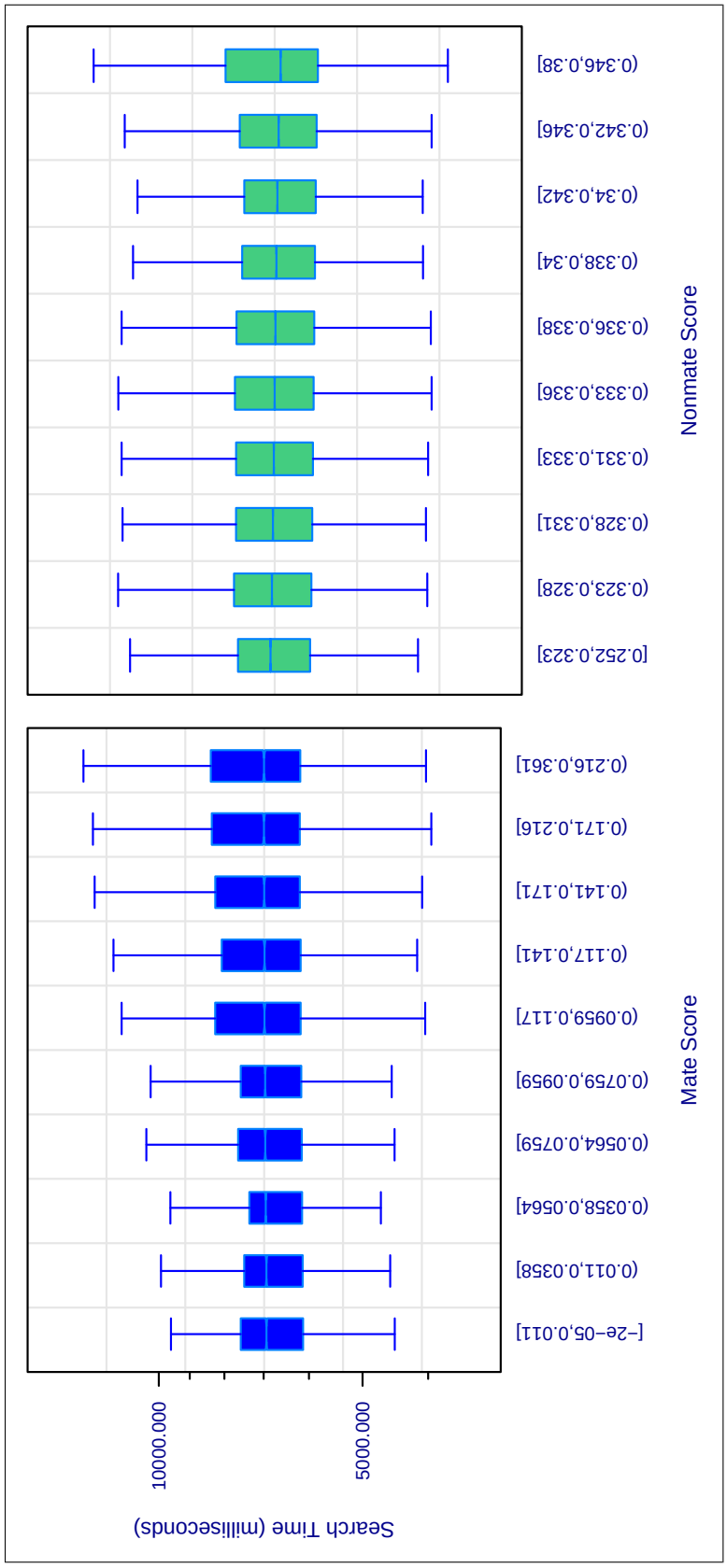

Figure 630: Dependence of speed and comparison score. For the T03B algorithm, the panels show the distribution of the one-to-many search time for ordered intervals of the mate and nonmate dissimilarity scores. For many implementations the duration of the search is independent of the score outcome. For some others (e.g. T11A), however, mate search durations are faster when the ultimate dissimilarity score is low (i.e. good).

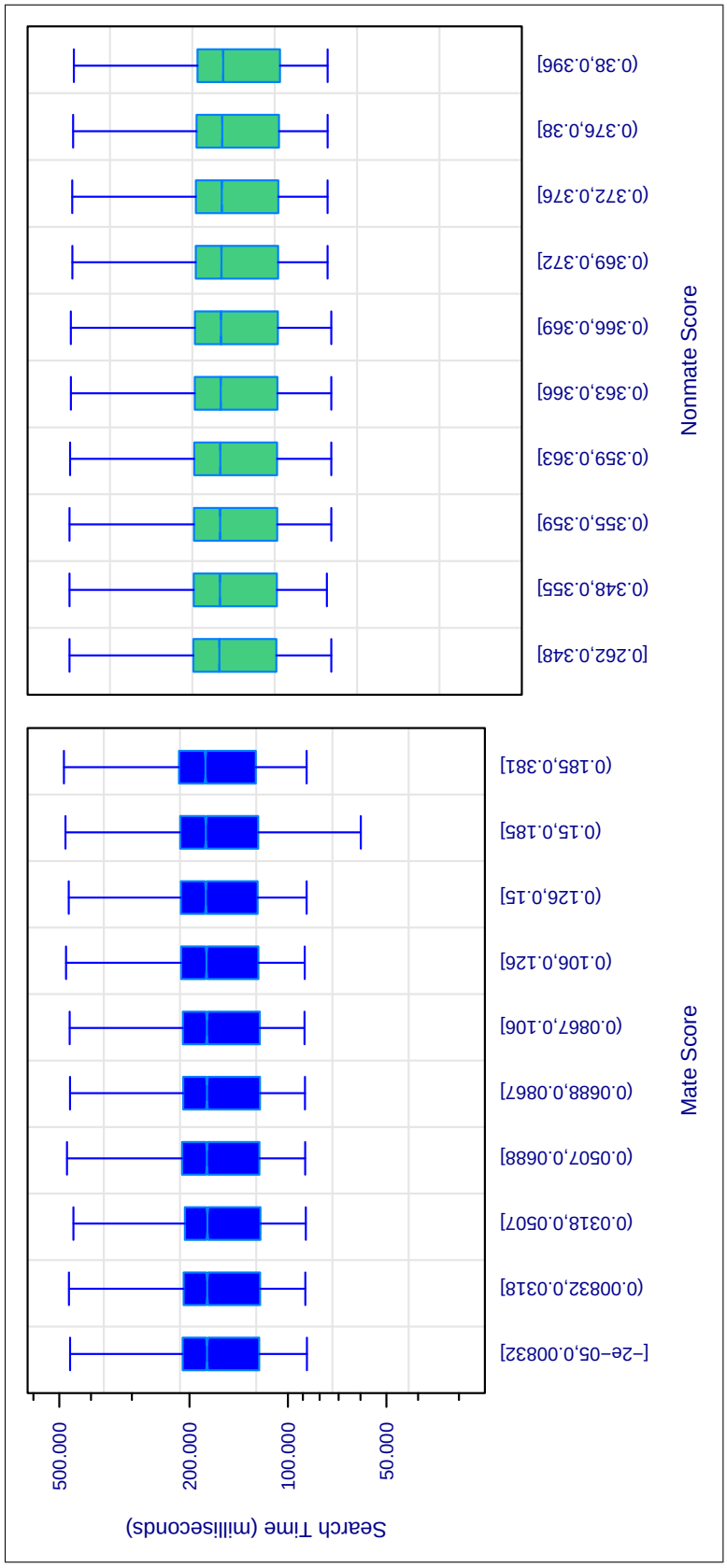

Figure 631: Dependence of speed and comparison score. For the T04A algorithm, the panels show the distribution of the one-to-many search time for ordered intervals of the mate and nonmate dissimilarity scores. For many implementations the duration of the search is independent of the score outcome. For some others (e.g. T11A), however, mate search durations are faster when the ultimate dissimilarity score is low (i.e. good).

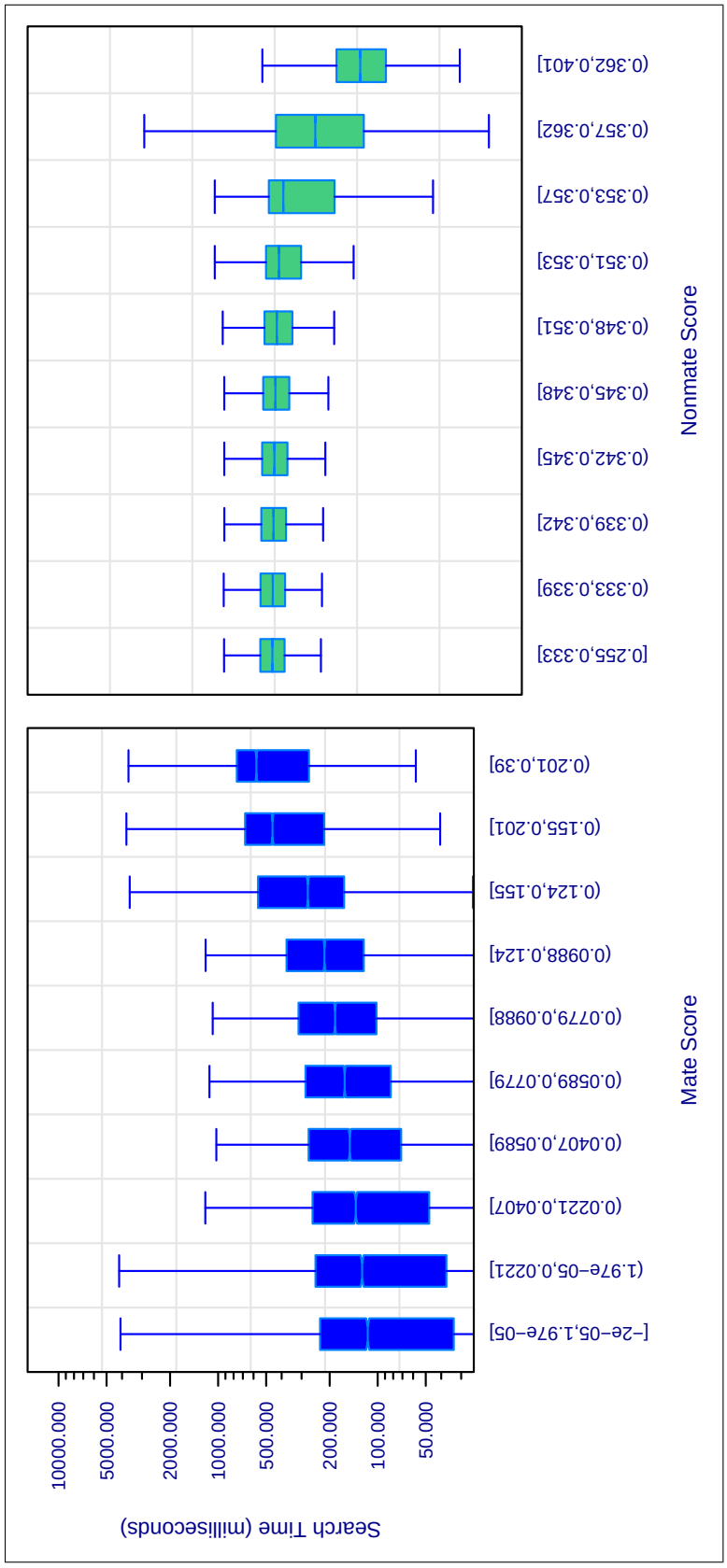

Figure 632: Dependence of speed and comparison score. For the T11A algorithm, the panels show the distribution of the one-to-many search time for ordered intervals of the mate and nonmate dissimilarity scores. For many implementations the duration of the search is independent of the score outcome. For some others (e.g. T11A), however, mate search durations are faster when the ultimate dissimilarity score is low (i.e. good).

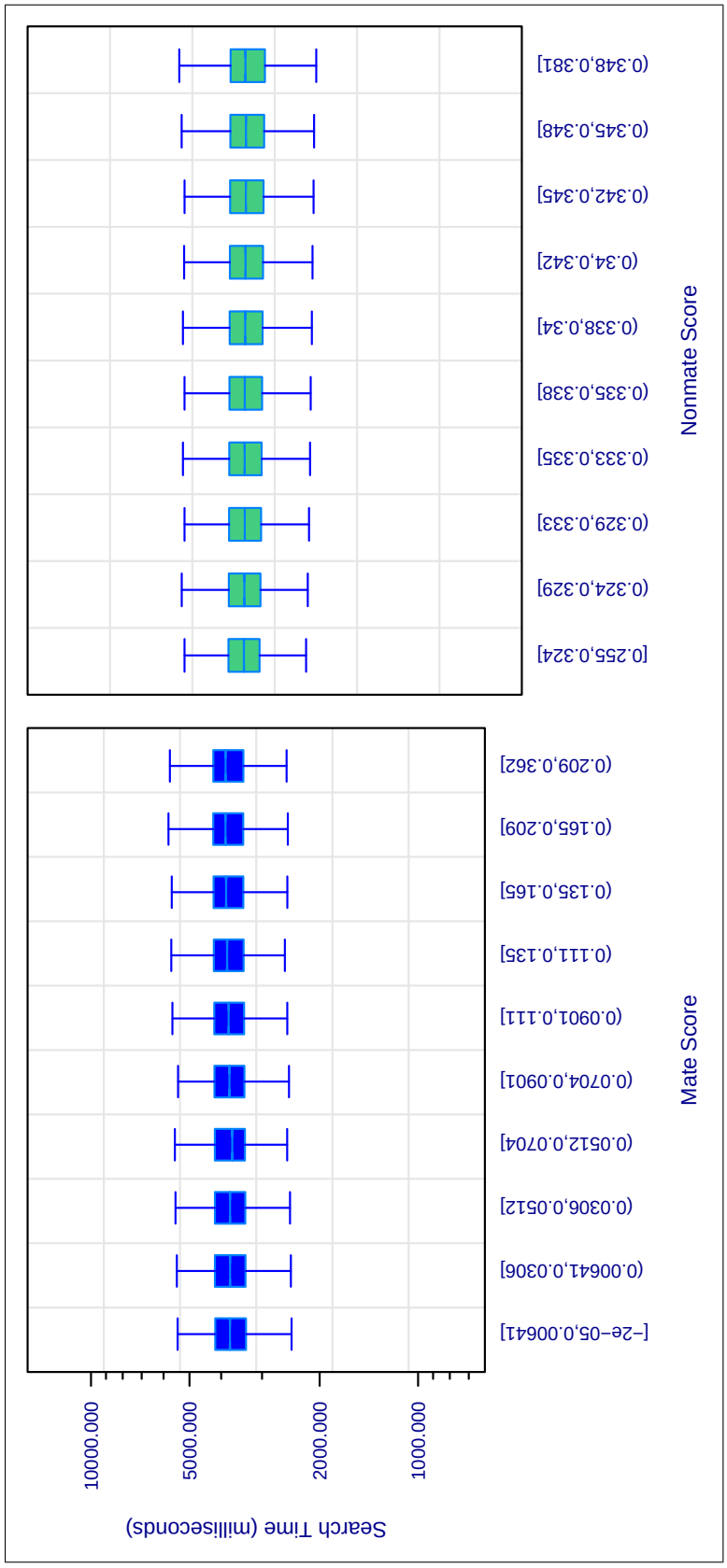

Figure 633: Dependence of speed and comparison score. For the T11B algorithm, the panels show the distribution of the one-to-many search time for ordered intervals of the mate and nonmate dissimilarity scores. For many implementations the duration of the search is independent of the score outcome. For some others (e.g. T11A), however, mate search durations are faster when the ultimate dissimilarity score is low (i.e. good).

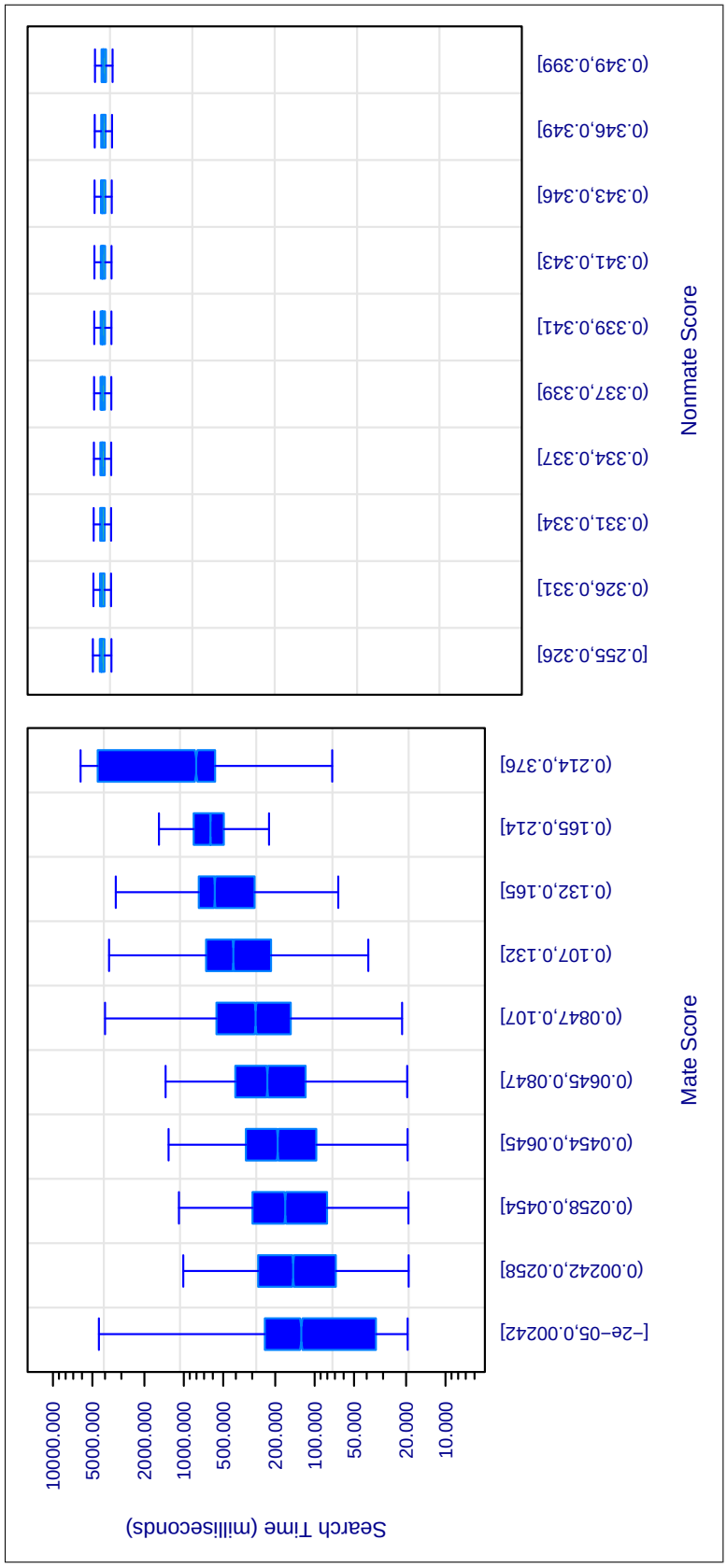

Figure 634: Dependence of speed and comparison score. For the T12B algorithm, the panels show the distribution of the one-to-many search time for ordered intervals of the mate and nonmate dissimilarity scores. For many implementations the duration of the search is independent of the score outcome. For some others (e.g. T11A), however, mate search durations are faster when the ultimate dissimilarity score is low (i.e. good).

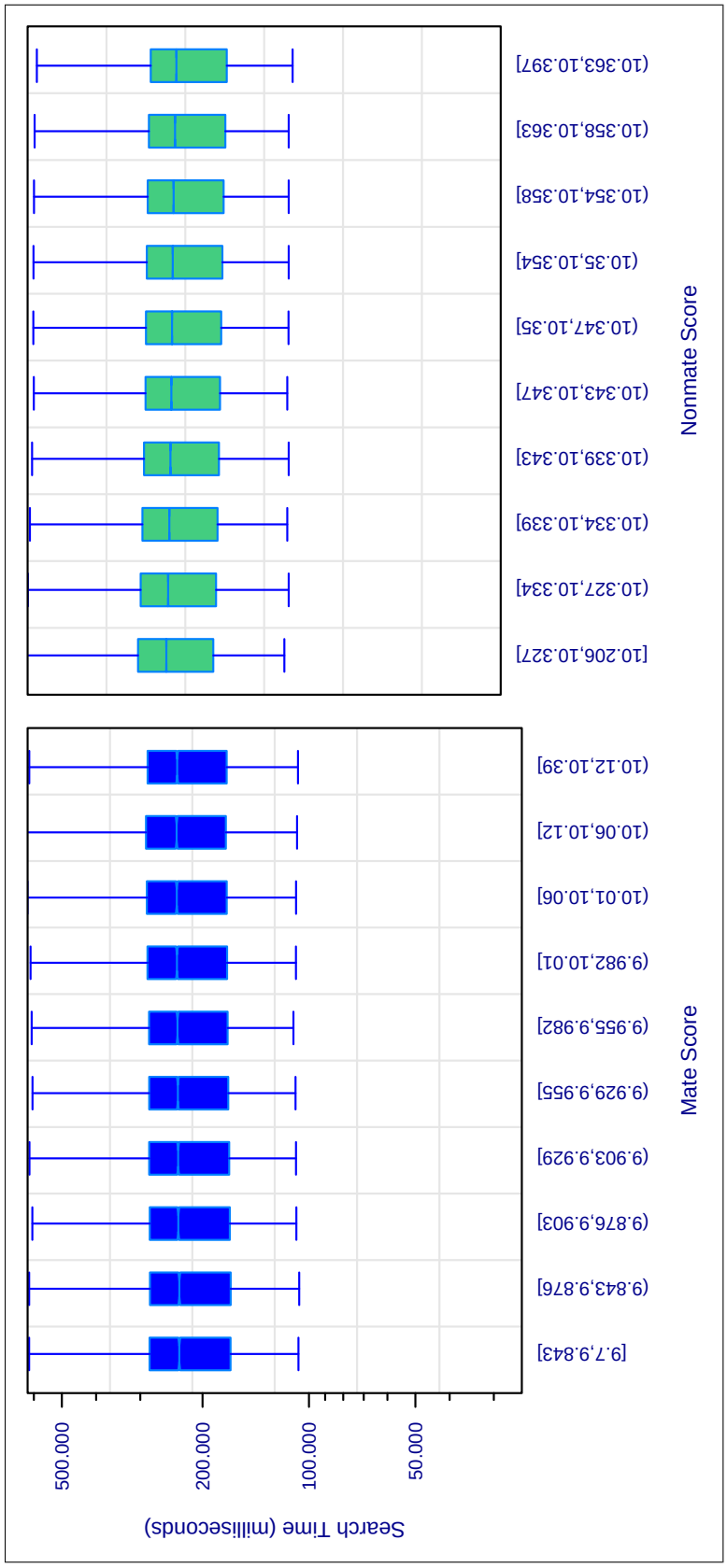

Figure 635: Dependence of speed and comparison score. For the U01A algorithm, the panels show the distribution of the one-to-many search time for ordered intervals of the mate and nonmate dissimilarity scores. For many implementations the duration of the search is independent of the score outcome. For some others (e.g. T11A), however, mate search durations are faster when the ultimate dissimilarity score is low (i.e. good).

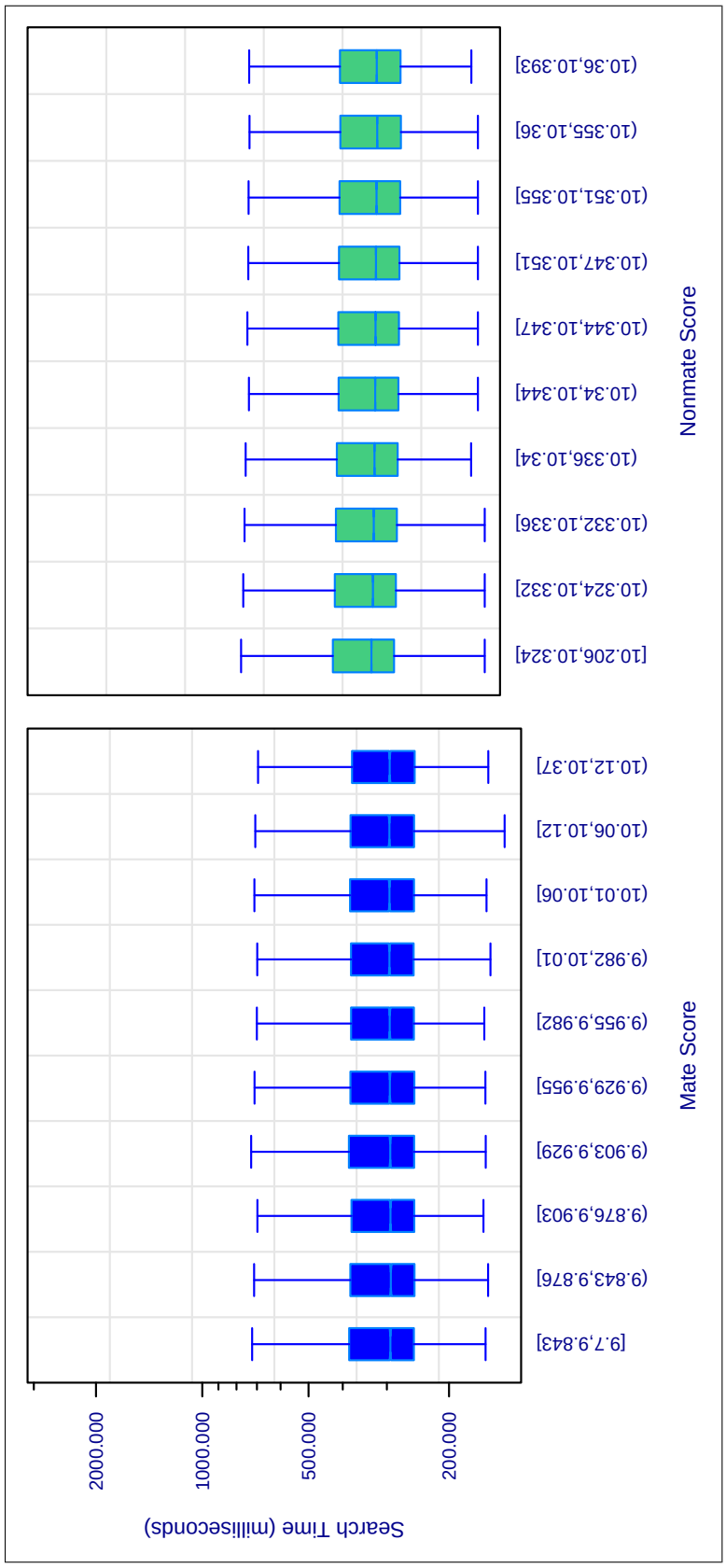

Figure 636: Dependence of speed and comparison score. For the U01B algorithm, the panels show the distribution of the one-to-many search time for ordered intervals of the mate and nonmate dissimilarity scores. For many implementations the duration of the search is independent of the score outcome. For some others (e.g. T11A), however, mate search durations are faster when the ultimate dissimilarity score is low (i.e. good).

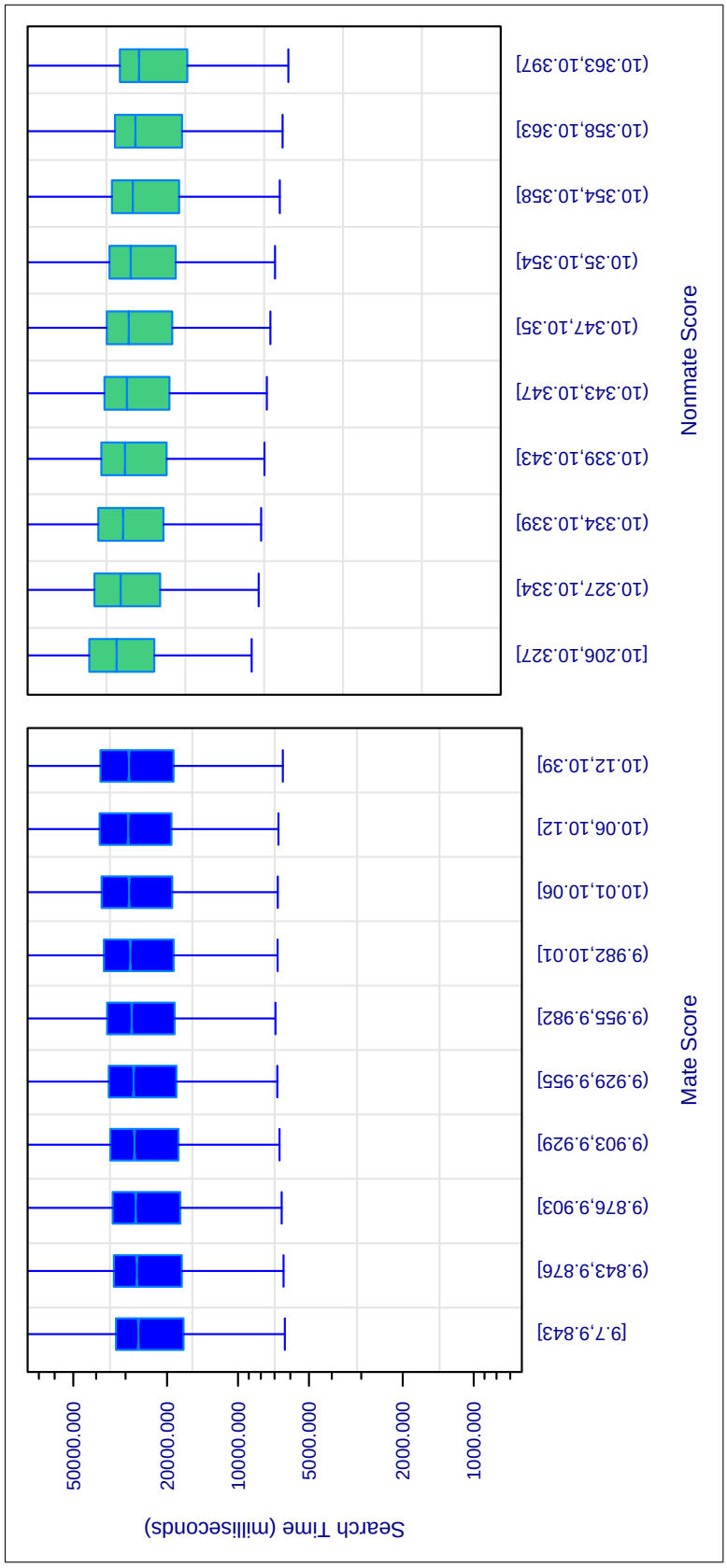

Figure 637: Dependence of speed and comparison score. For the U02A algorithm, the panels show the distribution of the one-to-many search time for ordered intervals of the mate and nonmate dissimilarity scores. For many implementations the duration of the search is independent of the score outcome. For some others (e.g. T11A), however, mate search durations are faster when the ultimate dissimilarity score is low (i.e. good).

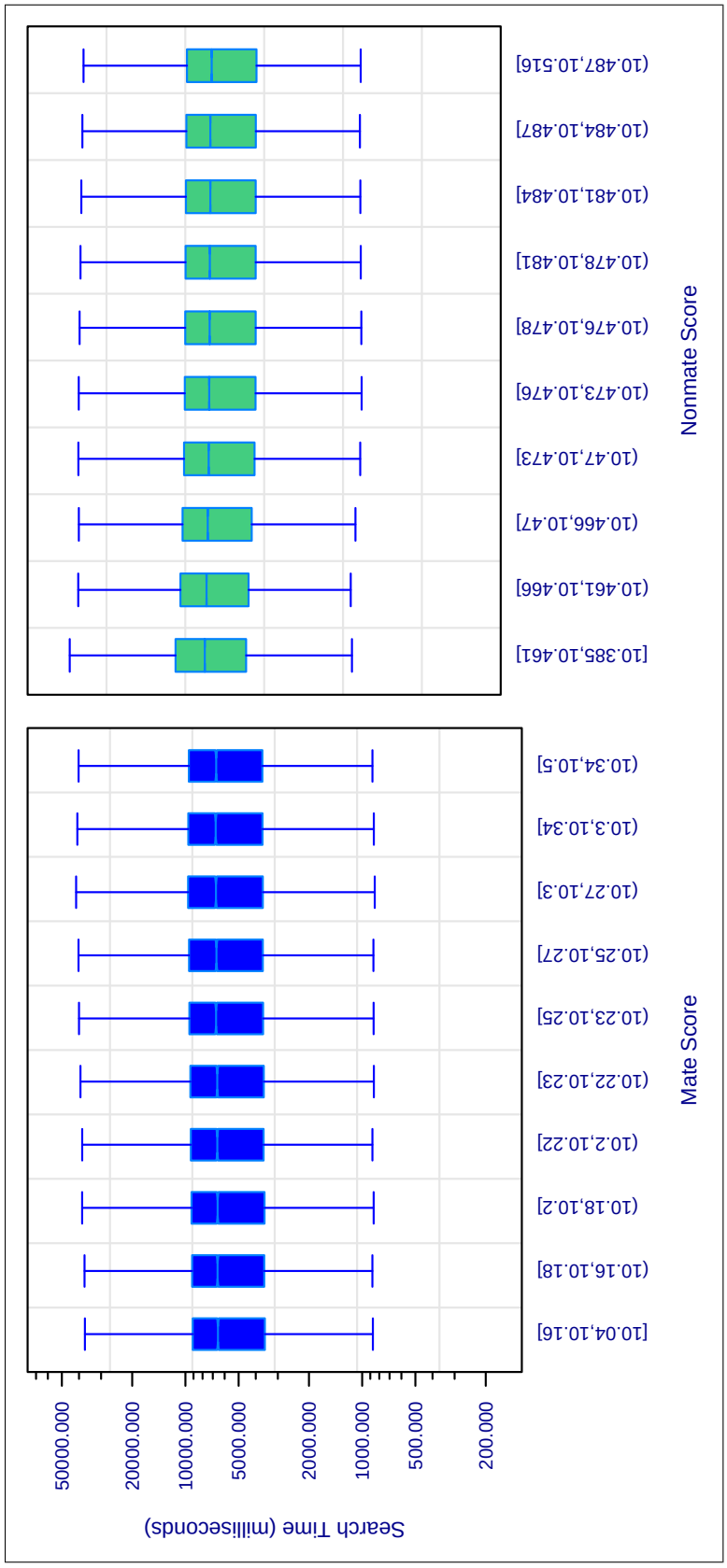

Figure 638: Dependence of speed and comparison score. For the U03A algorithm, the panels show the distribution of the one-to-many search time for ordered intervals of the mate and nonmate dissimilarity scores. For many implementations the duration of the search is independent of the score outcome. For some others (e.g. T11A), however, mate search durations are faster when the ultimate dissimilarity score is low (i.e. good).

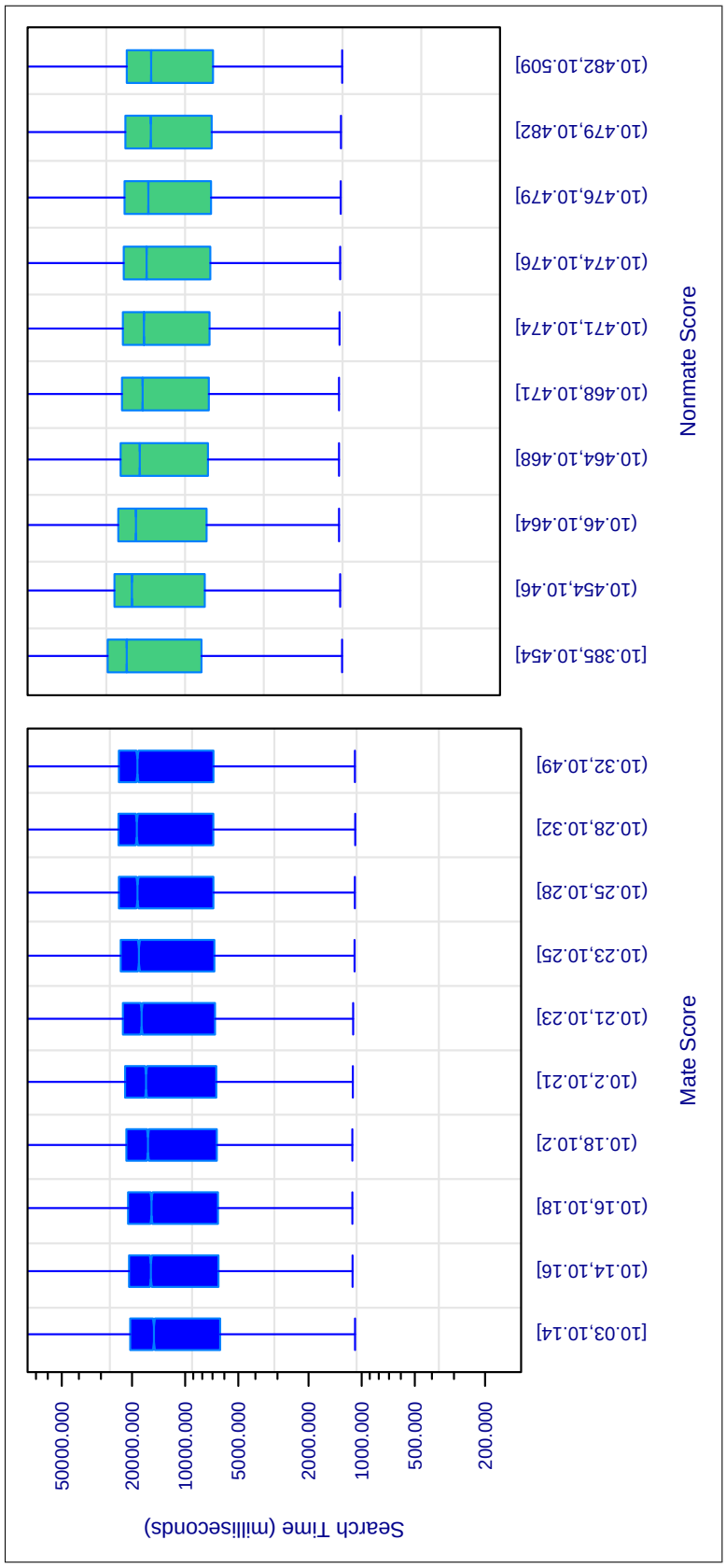

Figure 639: Dependence of speed and comparison score. For the U03B algorithm, the panels show the distribution of the one-to-many search time for ordered intervals of the mate and nonmate dissimilarity scores. For many implementations the duration of the search is independent of the score outcome. For some others (e.g. T11A), however, mate search durations are faster when the ultimate dissimilarity score is low (i.e. good).

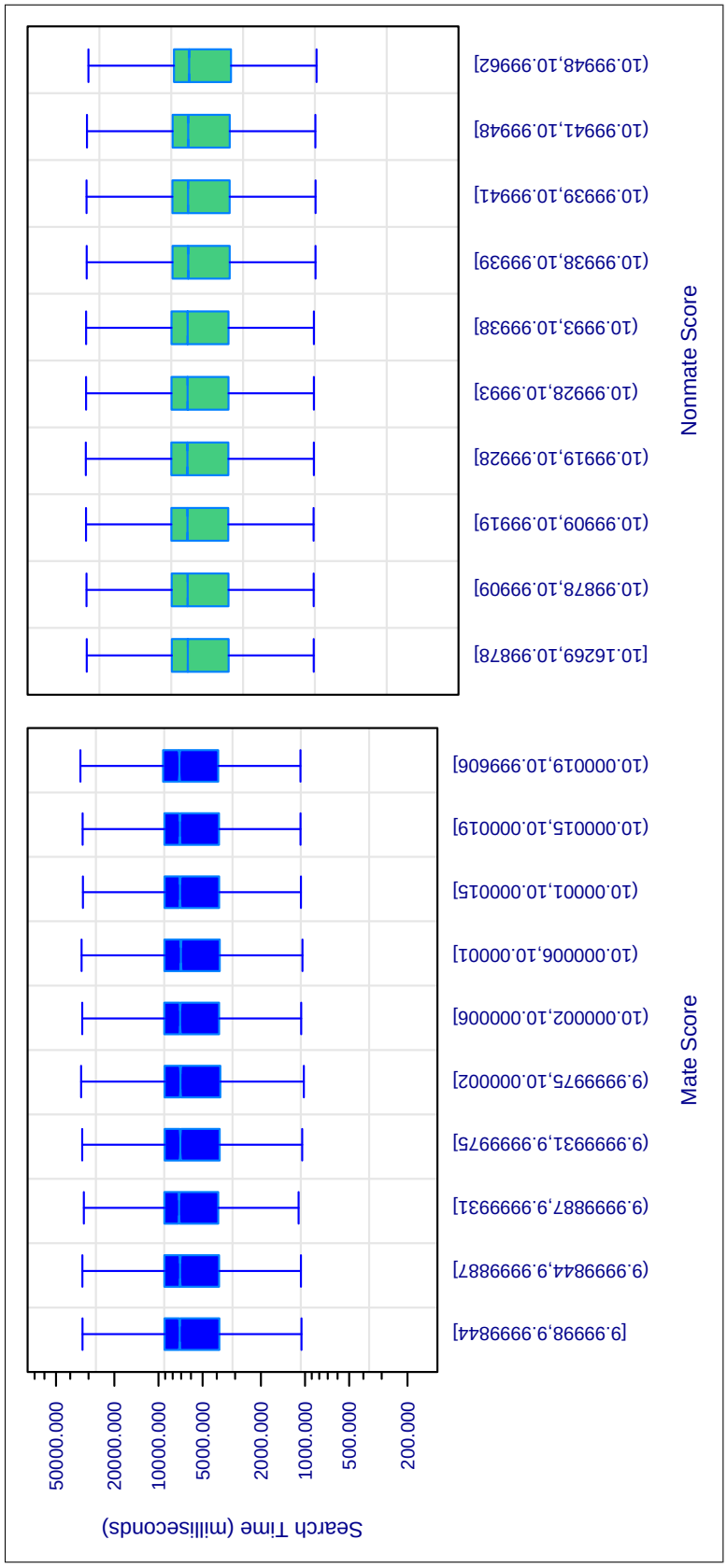

Figure 640: Dependence of speed and comparison score. For the U04A algorithm, the panels show the distribution of the one-to-many search time for ordered intervals of the mate and nonmate dissimilarity scores. For many implementations the duration of the search is independent of the score outcome. For some others (e.g. T11A), however, mate search durations are faster when the ultimate dissimilarity score is low (i.e. good).

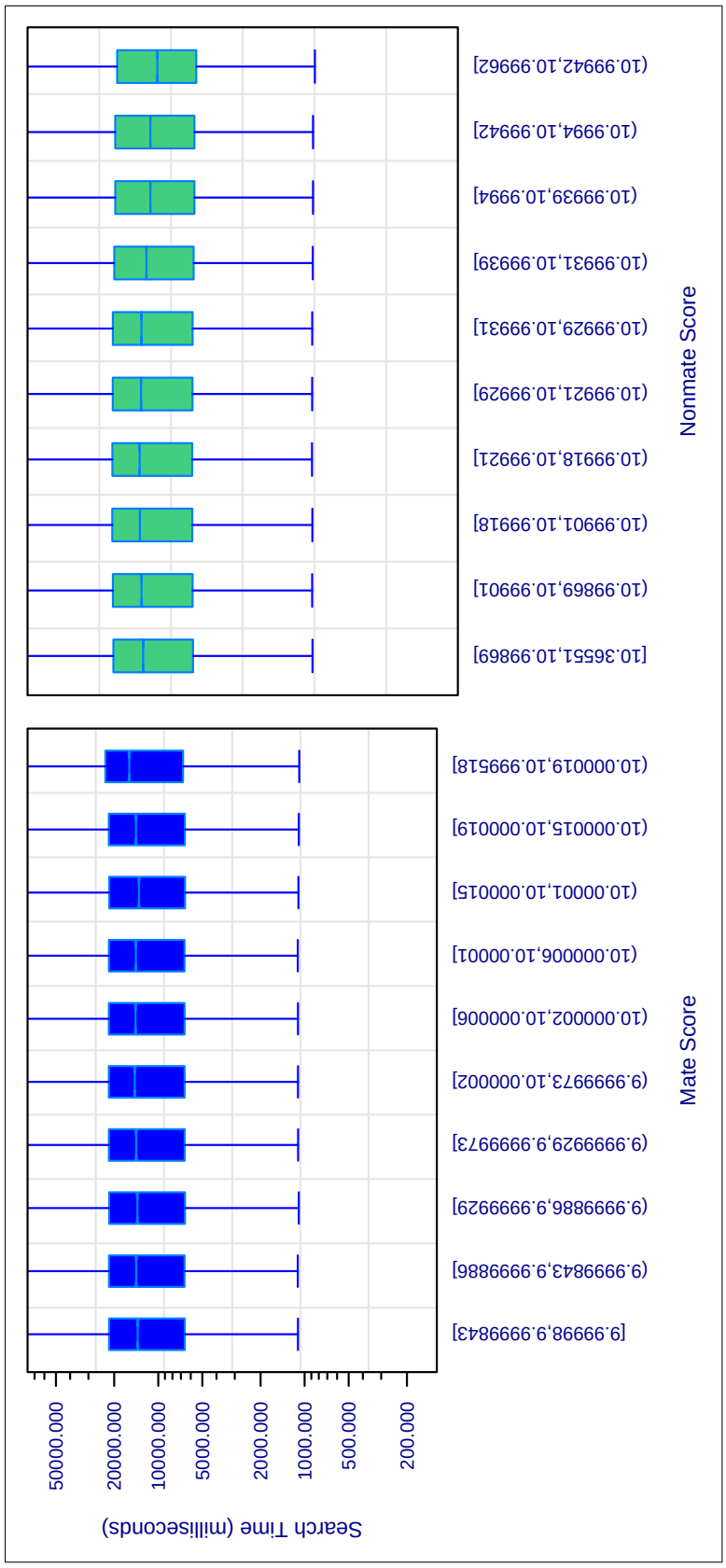

Figure 641: Dependence of speed and comparison score. For the U04B algorithm, the panels show the distribution of the one-to-many search time for ordered intervals of the mate and nonmate dissimilarity scores. For many implementations the duration of the search is independent of the score outcome. For some others (e.g. T11A), however, mate search durations are faster when the ultimate dissimilarity score is low (i.e. good).

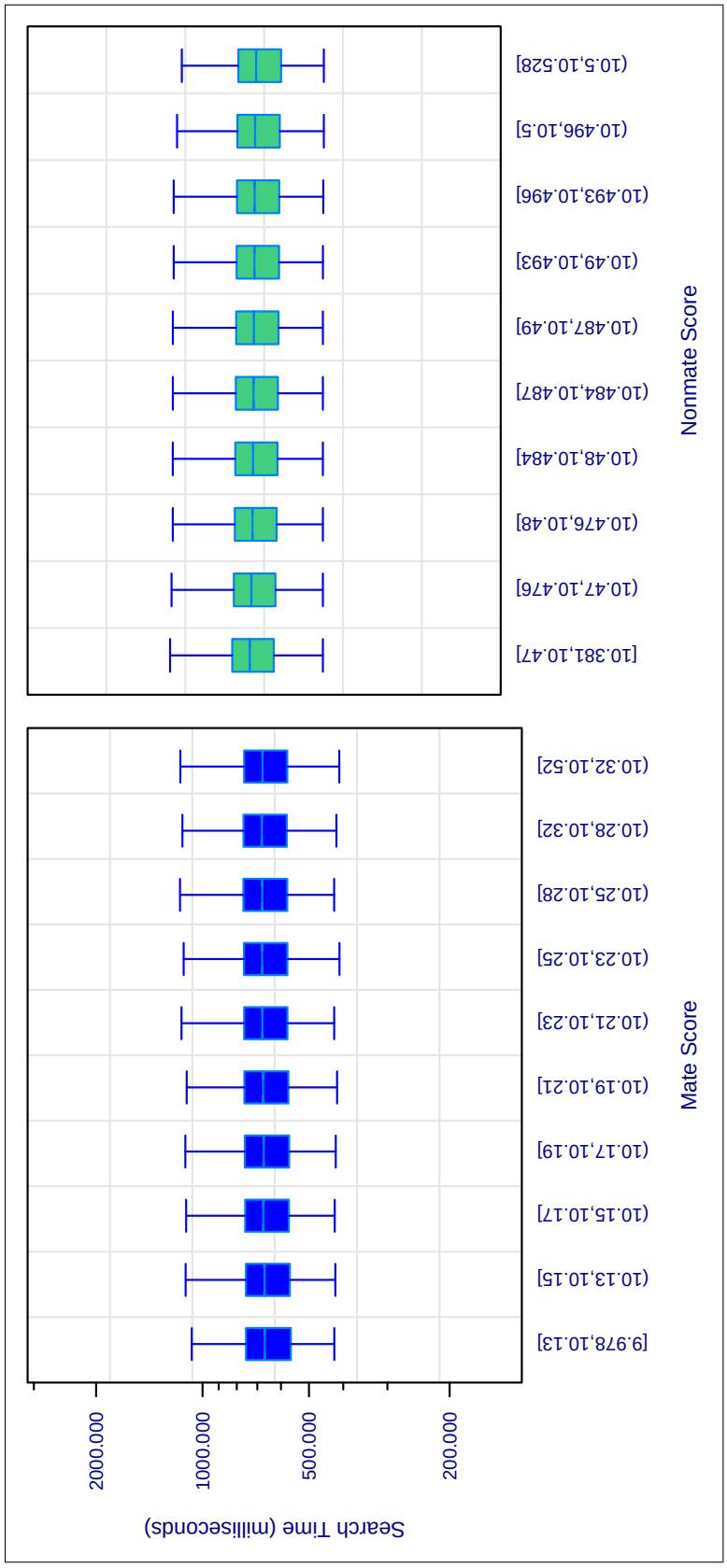

Figure 642: Dependence of speed and comparison score. For the U11A algorithm, the panels show the distribution of the one-to-many search time for ordered intervals of the mate and nonmate dissimilarity scores. For many implementations the duration of the search is independent of the score outcome. For some others (e.g. T11A), however, mate search durations are faster when the ultimate dissimilarity score is low (i.e. good).

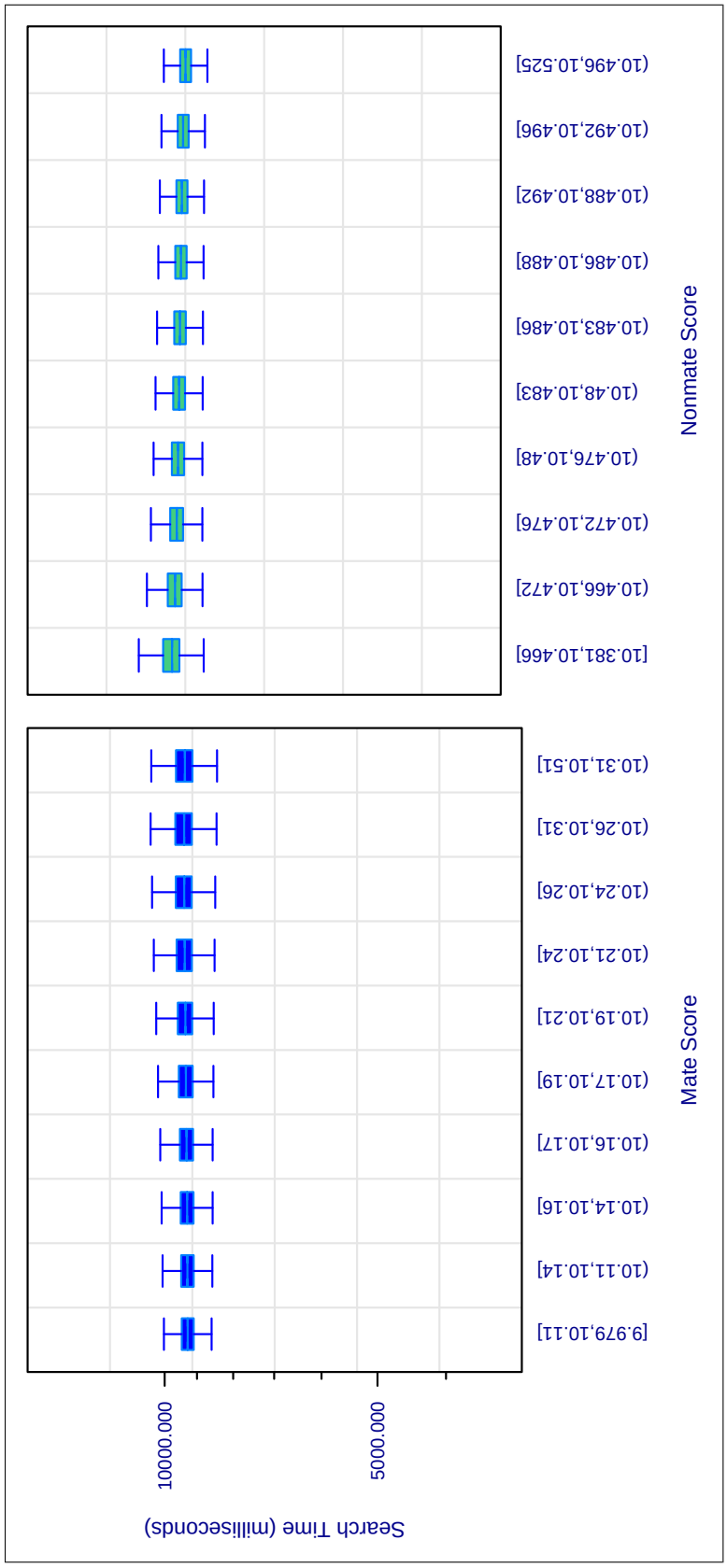

Figure 643: Dependence of speed and comparison score. For the U11B algorithm, the panels show the distribution of the one-to-many search time for ordered intervals of the mate and nonmate dissimilarity scores. For many implementations the duration of the search is independent of the score outcome. For some others (e.g. T11A), however, mate search durations are faster when the ultimate dissimilarity score is low (i.e. good).

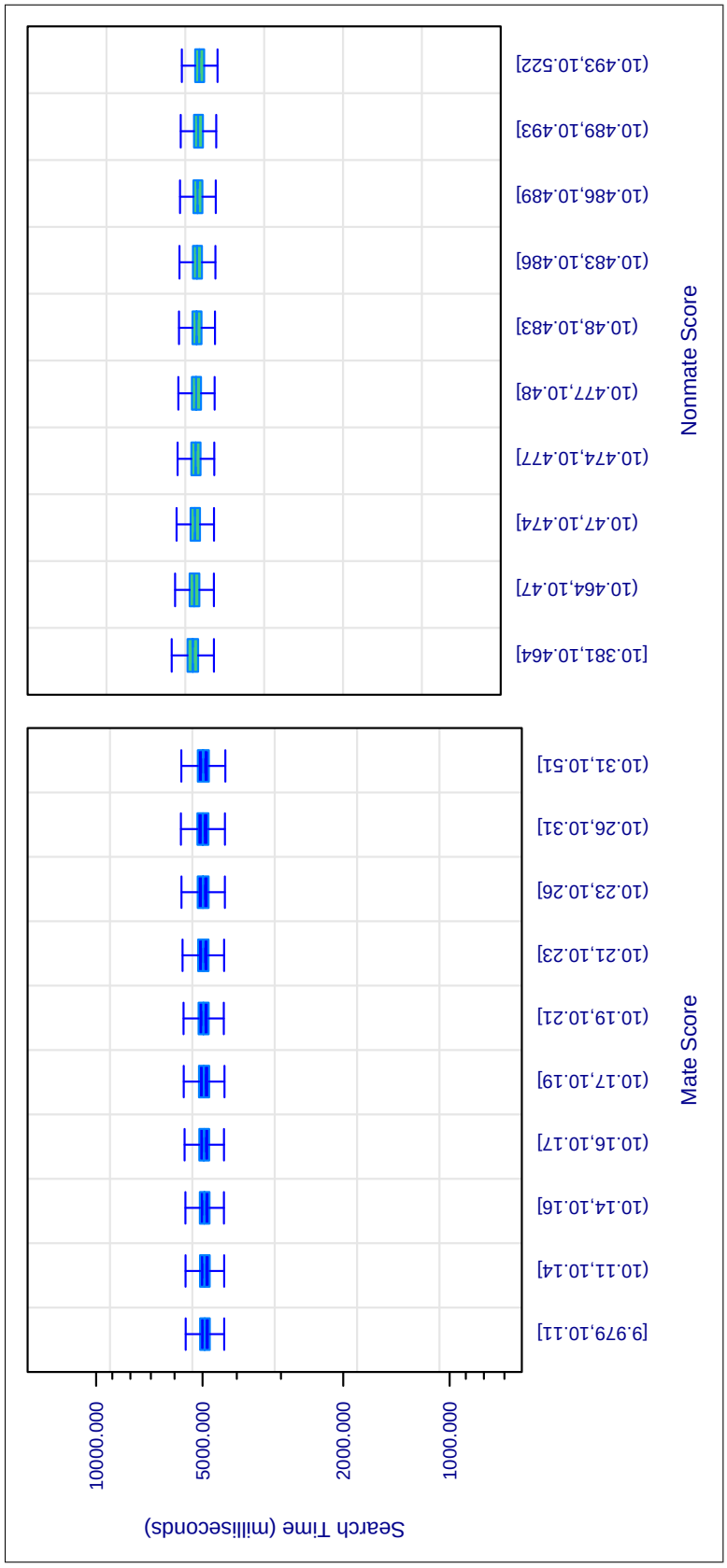

Figure 644: Dependence of speed and comparison score. For the U12A algorithm, the panels show the distribution of the one-to-many search time for ordered intervals of the mate and nonmate dissimilarity scores. For many implementations the duration of the search is independent of the score outcome. For some others (e.g. T11A), however, mate search durations are faster when the ultimate dissimilarity score is low (i.e. good).

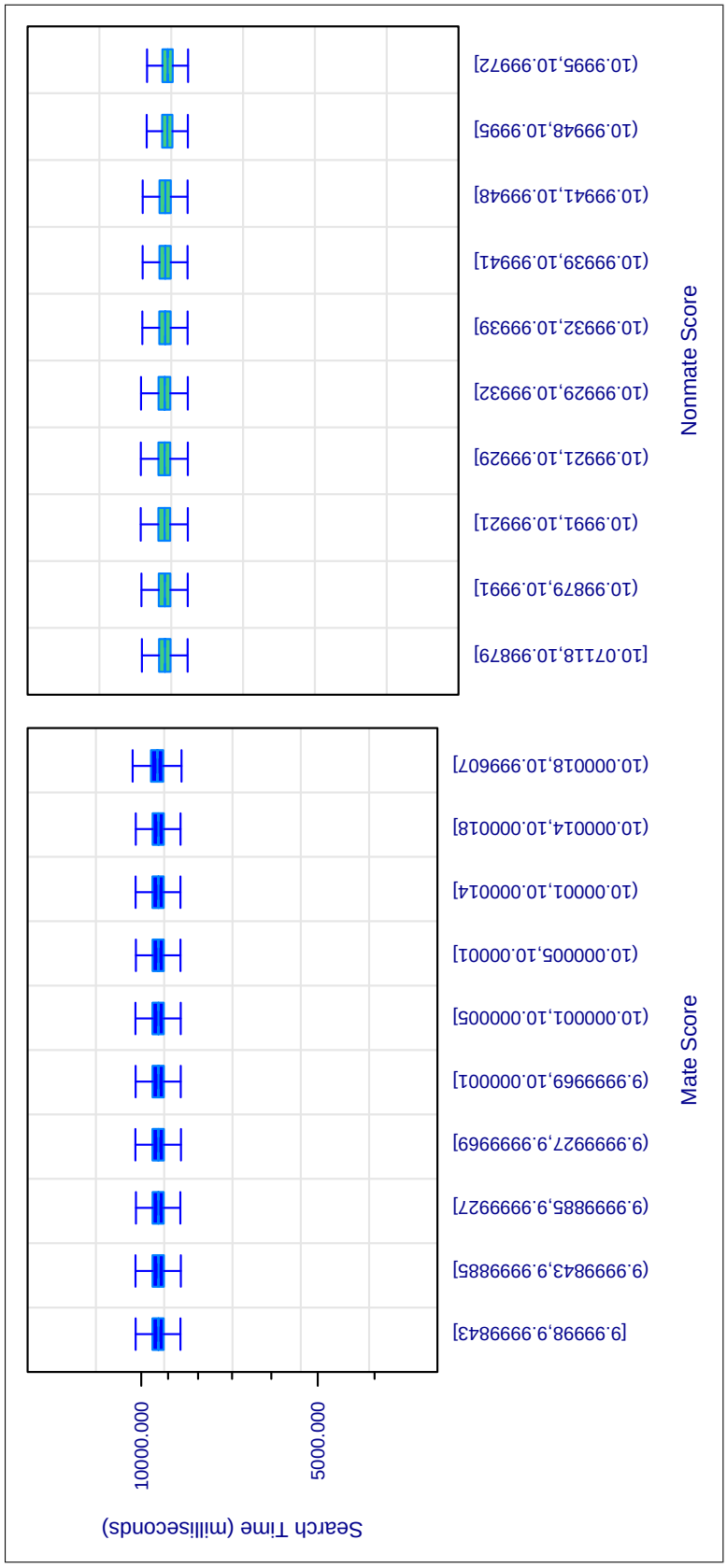

Figure 645: Dependence of speed and comparison score. For the U12B algorithm, the panels show the distribution of the one-to-many search time for ordered intervals of the mate and nonmate dissimilarity scores. For many implementations the duration of the search is independent of the score outcome. For some others (e.g. T11A), however, mate search durations are faster when the ultimate dissimilarity score is low (i.e. good).

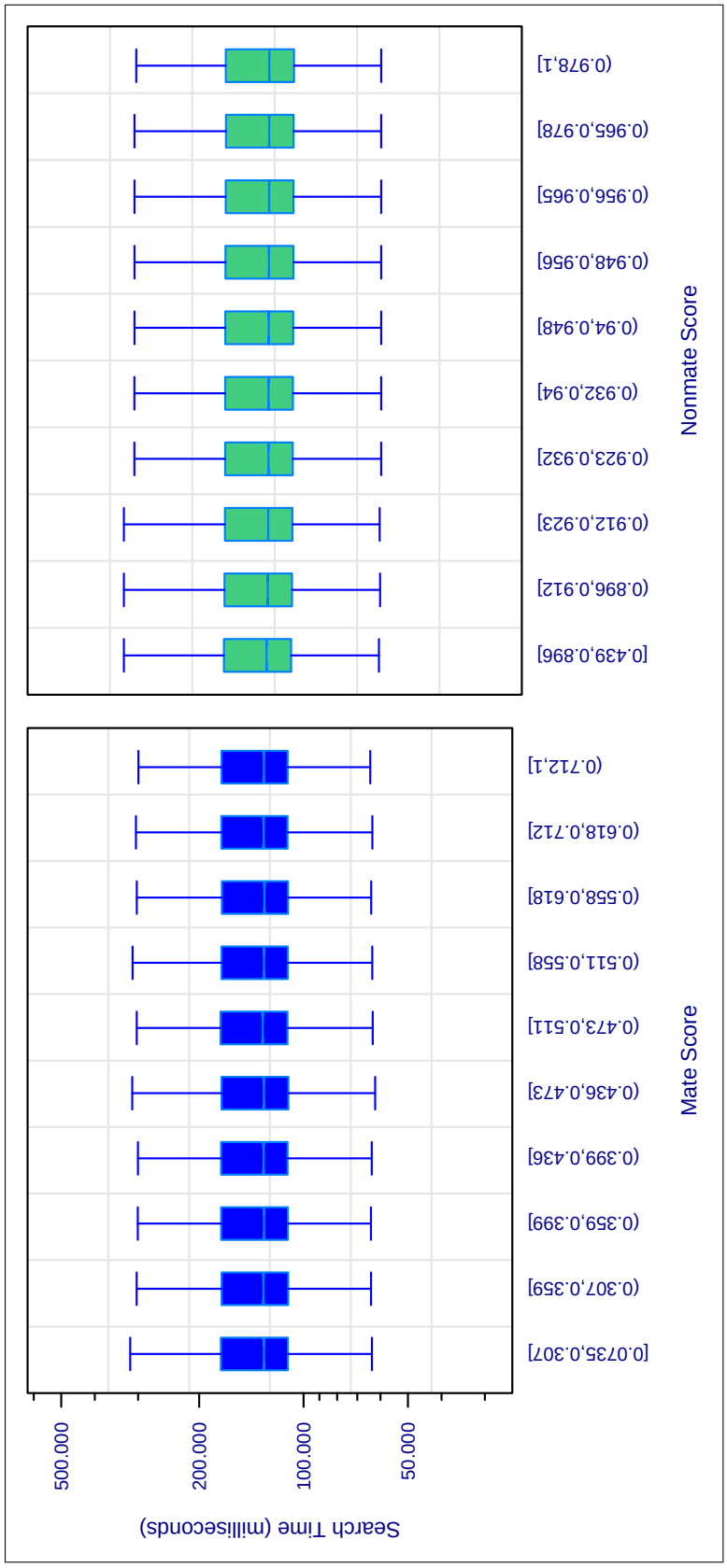

Figure 646: Dependence of speed and comparison score. For the V01A algorithm, the panels show the distribution of the one-to-many search time for ordered intervals of the mate and nonmate dissimilarity scores. For many implementations the duration of the search is independent of the score outcome. For some others (e.g. T11A), however, mate search durations are faster when the ultimate dissimilarity score is low (i.e. good).

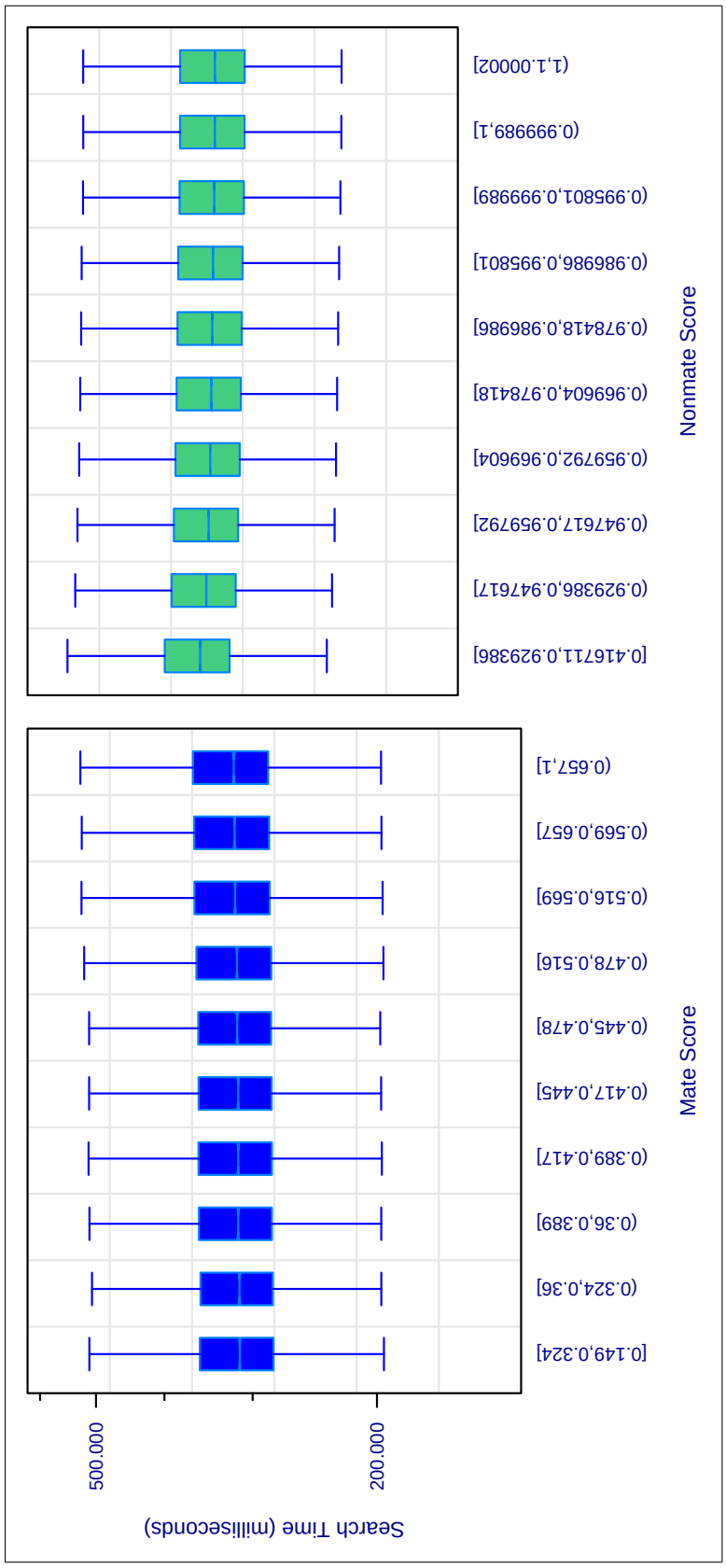

Figure 647: Dependence of speed and comparison score. For the V02A algorithm, the panels show the distribution of the one-to-many search time for ordered intervals of the mate and nonmate dissimilarity scores. For many implementations the duration of the search is independent of the score outcome. For some others (e.g. T11A), however, mate search durations are faster when the ultimate dissimilarity score is low (i.e. good).

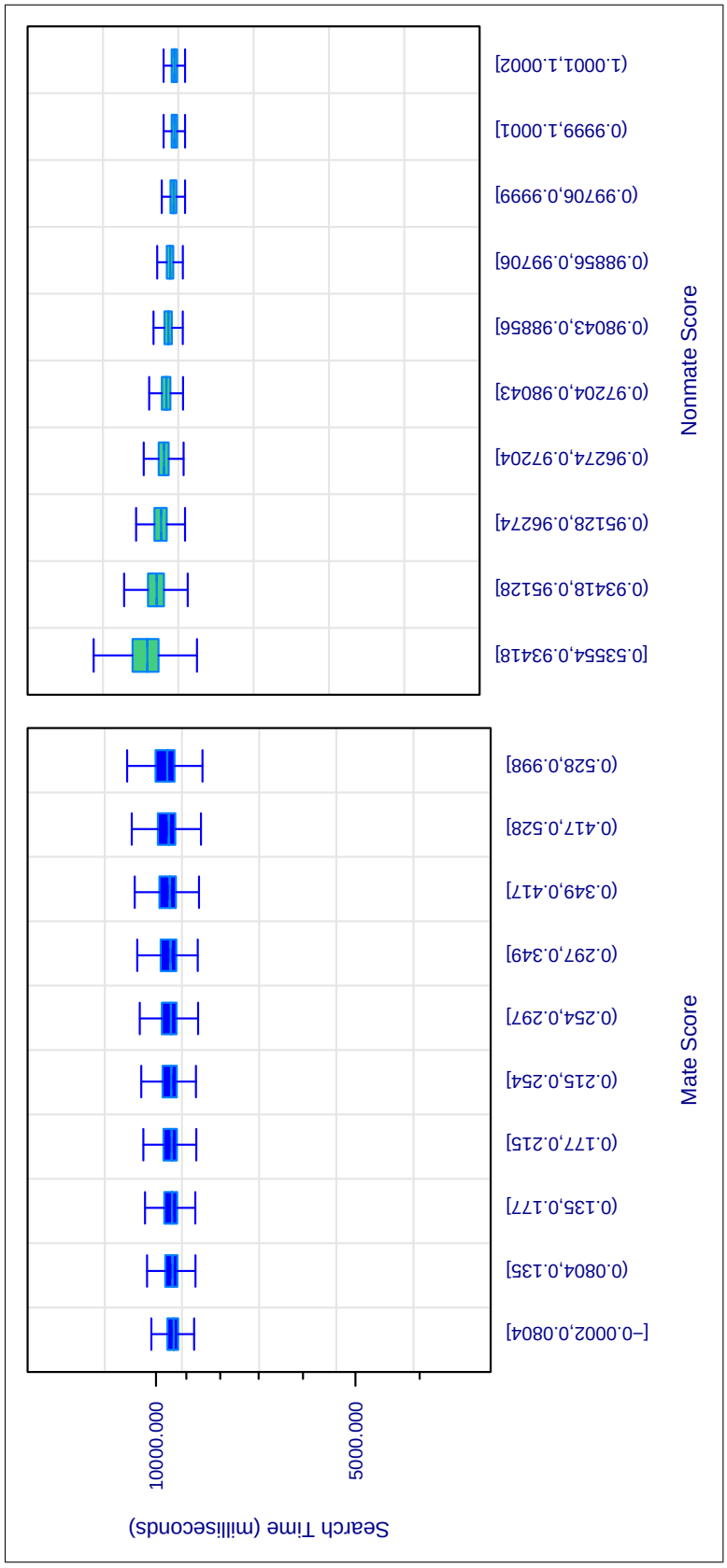

Figure 648: Dependence of speed and comparison score. For the V03A algorithm, the panels show the distribution of the one-to-many search time for ordered intervals of the mate and nonmate dissimilarity scores. For many implementations the duration of the search is independent of the score outcome. For some others (e.g. T11A), however, mate search durations are faster when the ultimate dissimilarity score is low (i.e. good).

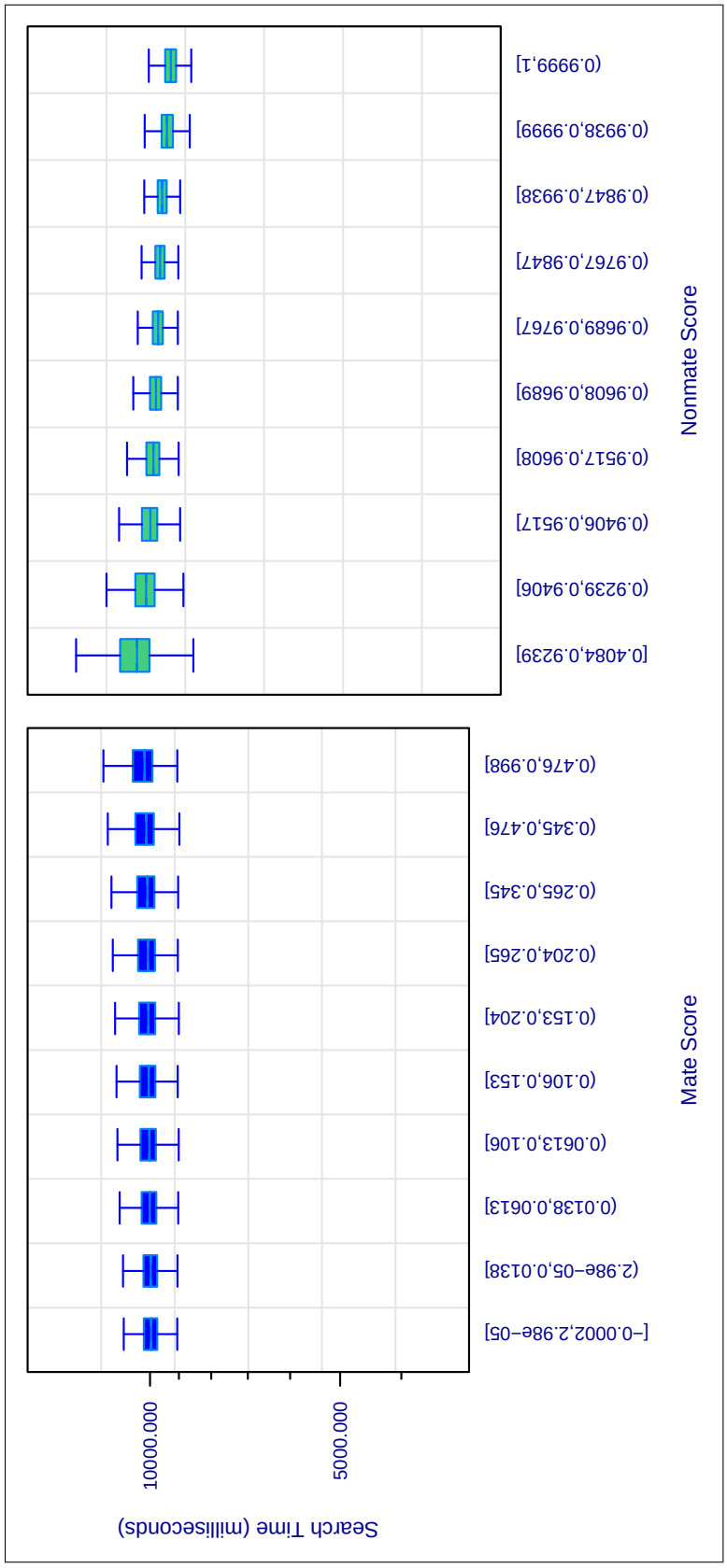

Figure 649: Dependence of speed and comparison score. For the V03B algorithm, the panels show the distribution of the one-to-many search time for ordered intervals of the mate and nonmate dissimilarity scores. For many implementations the duration of the search is independent of the score outcome. For some others (e.g. T11A), however, mate search durations are faster when the ultimate dissimilarity score is low (i.e. good).

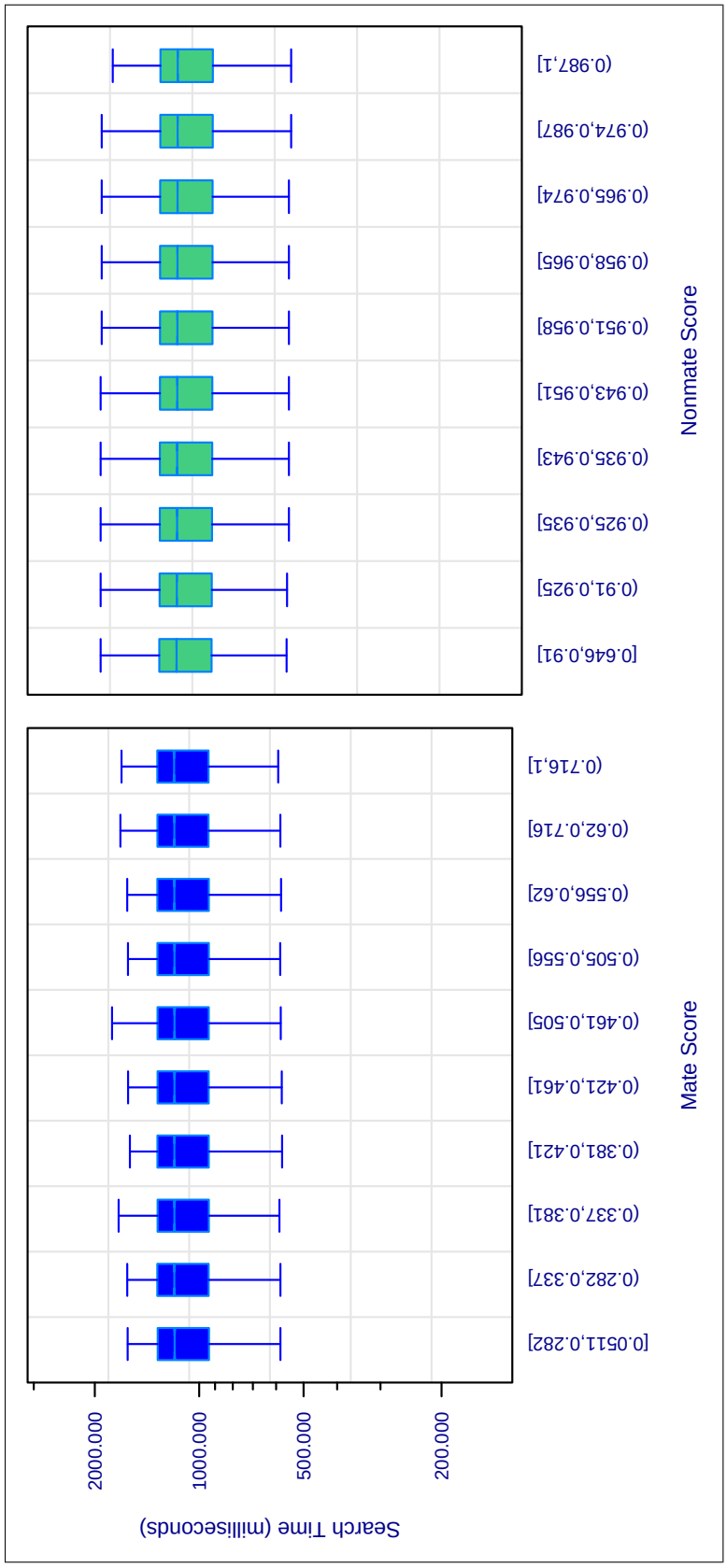

Figure 650: Dependence of speed and comparison score. For the V04A algorithm, the panels show the distribution of the one-to-many search time for ordered intervals of the mate and nonmate dissimilarity scores. For many implementations the duration of the search is independent of the score outcome. For some others (e.g. T11A), however, mate search durations are faster when the ultimate dissimilarity score is low (i.e. good).

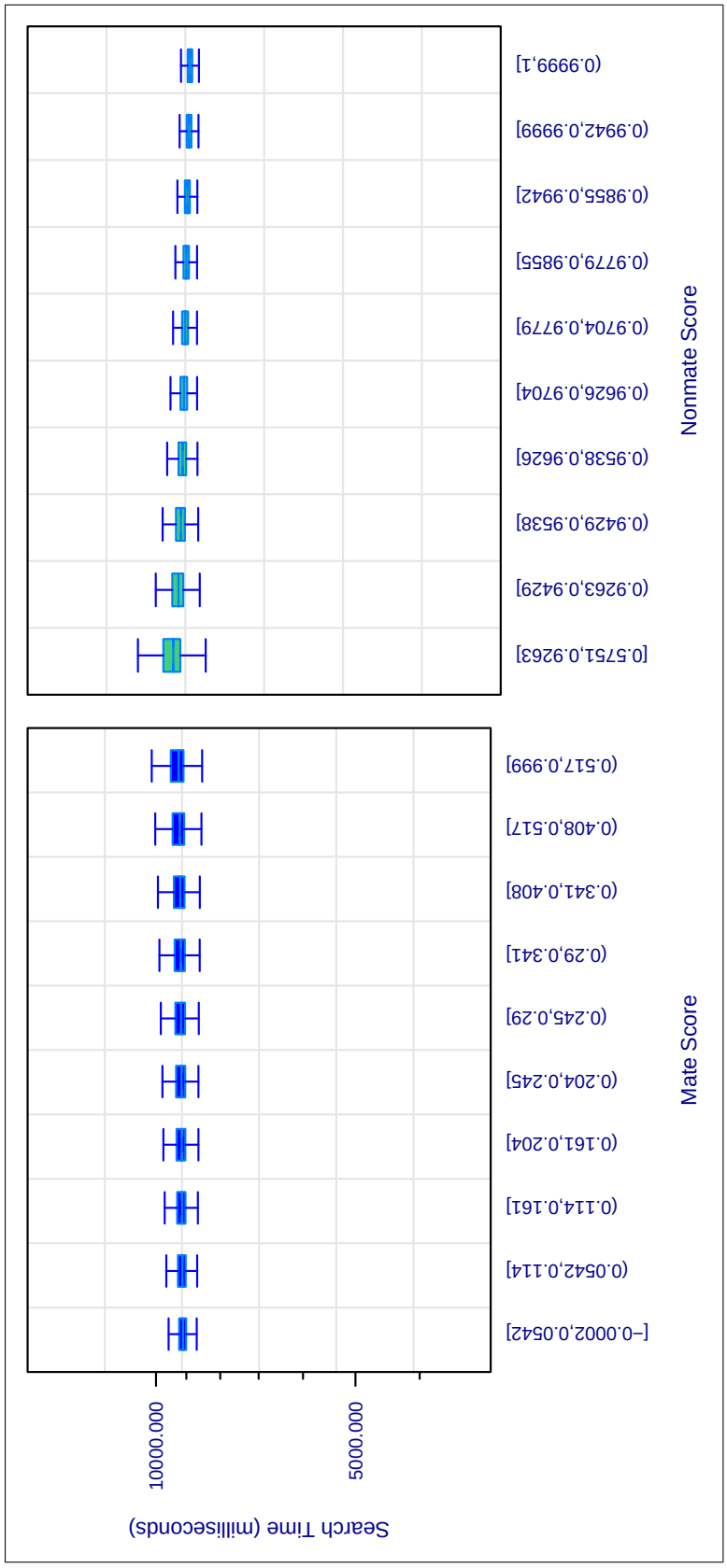

Figure 651: Dependence of speed and comparison score. For the V11A algorithm, the panels show the distribution of the one-to-many search time for ordered intervals of the mate and nonmate dissimilarity scores. For many implementations the duration of the search is independent of the score outcome. For some others (e.g. T11A), however, mate search durations are faster when the ultimate dissimilarity score is low (i.e. good).

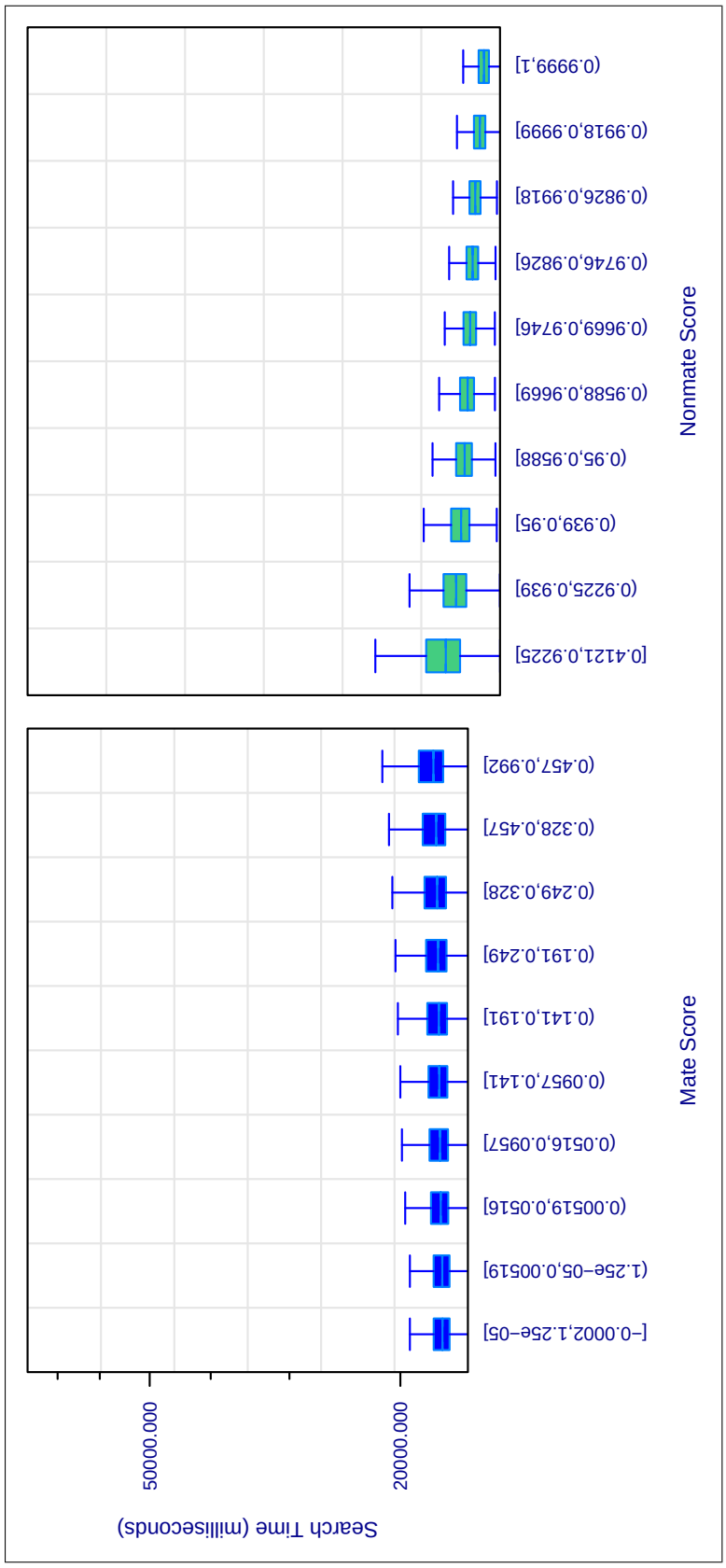

Figure 652: Dependence of speed and comparison score. For the V11B algorithm, the panels show the distribution of the one-to-many search time for ordered intervals of the mate and nonmate dissimilarity scores. For many implementations the duration of the search is independent of the score outcome. For some others (e.g. T11A), however, mate search durations are faster when the ultimate dissimilarity score is low (i.e. good).

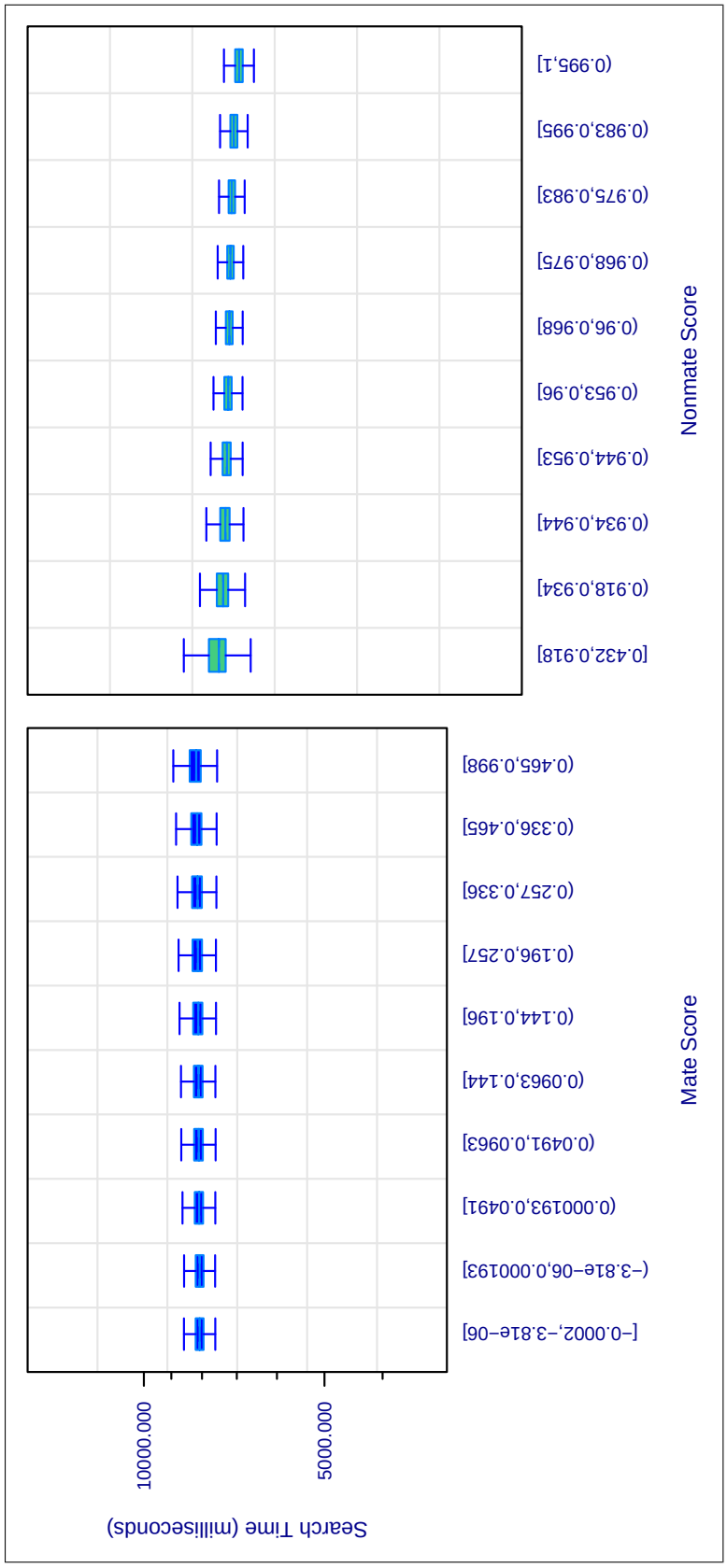

Figure 653: Dependence of speed and comparison score. For the V12A algorithm, the panels show the distribution of the one-to-many search time for ordered intervals of the mate and nonmate dissimilarity scores. For many implementations the duration of the search is independent of the score outcome. For some others (e.g. T11A), however, mate search durations are faster when the ultimate dissimilarity score is low (i.e. good).

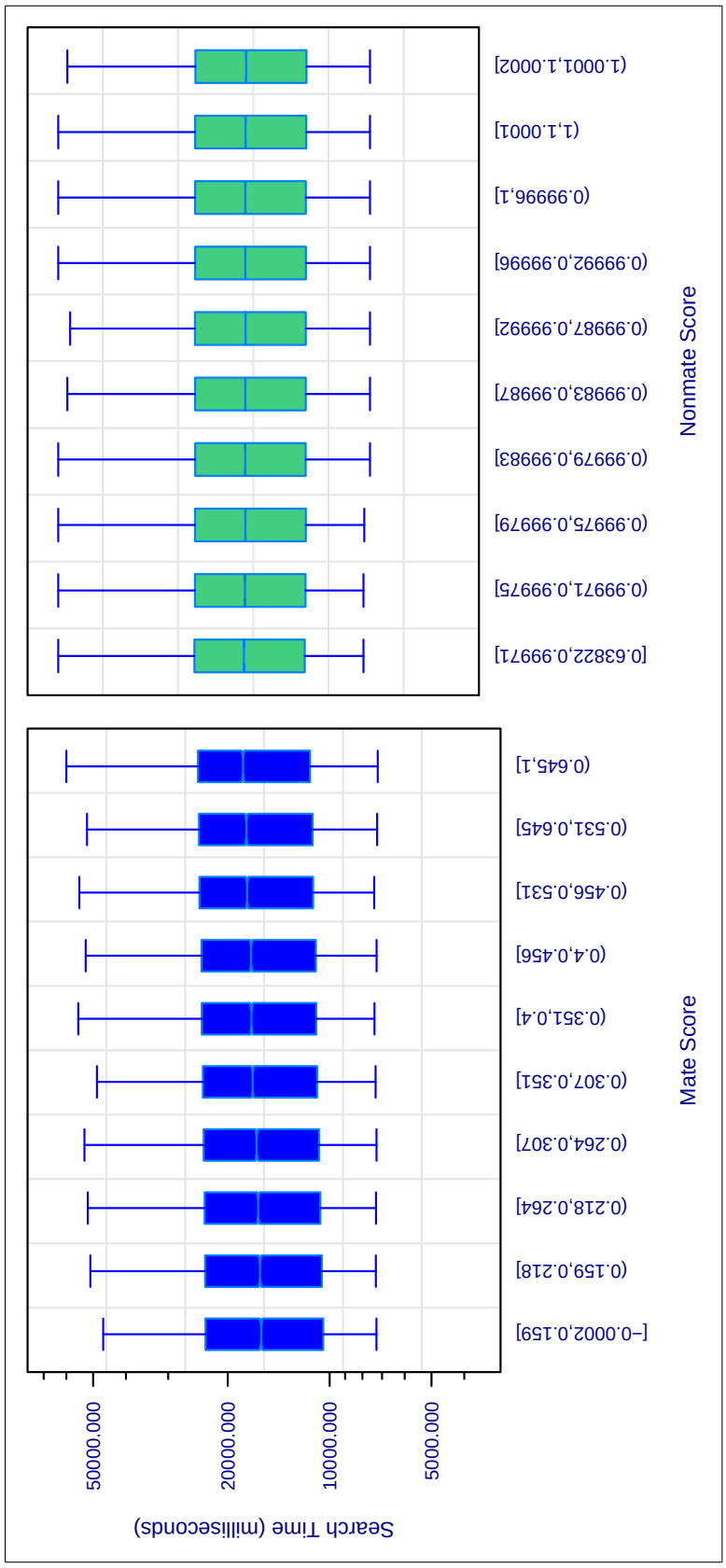

Figure 654: Dependence of speed and comparison score. For the V12B algorithm, the panels show the distribution of the one-to-many search time for ordered intervals of the mate and nonmate dissimilarity scores. For many implementations the duration of the search is independent of the score outcome. For some others (e.g. T11A), however, mate search durations are faster when the ultimate dissimilarity score is low (i.e. good).

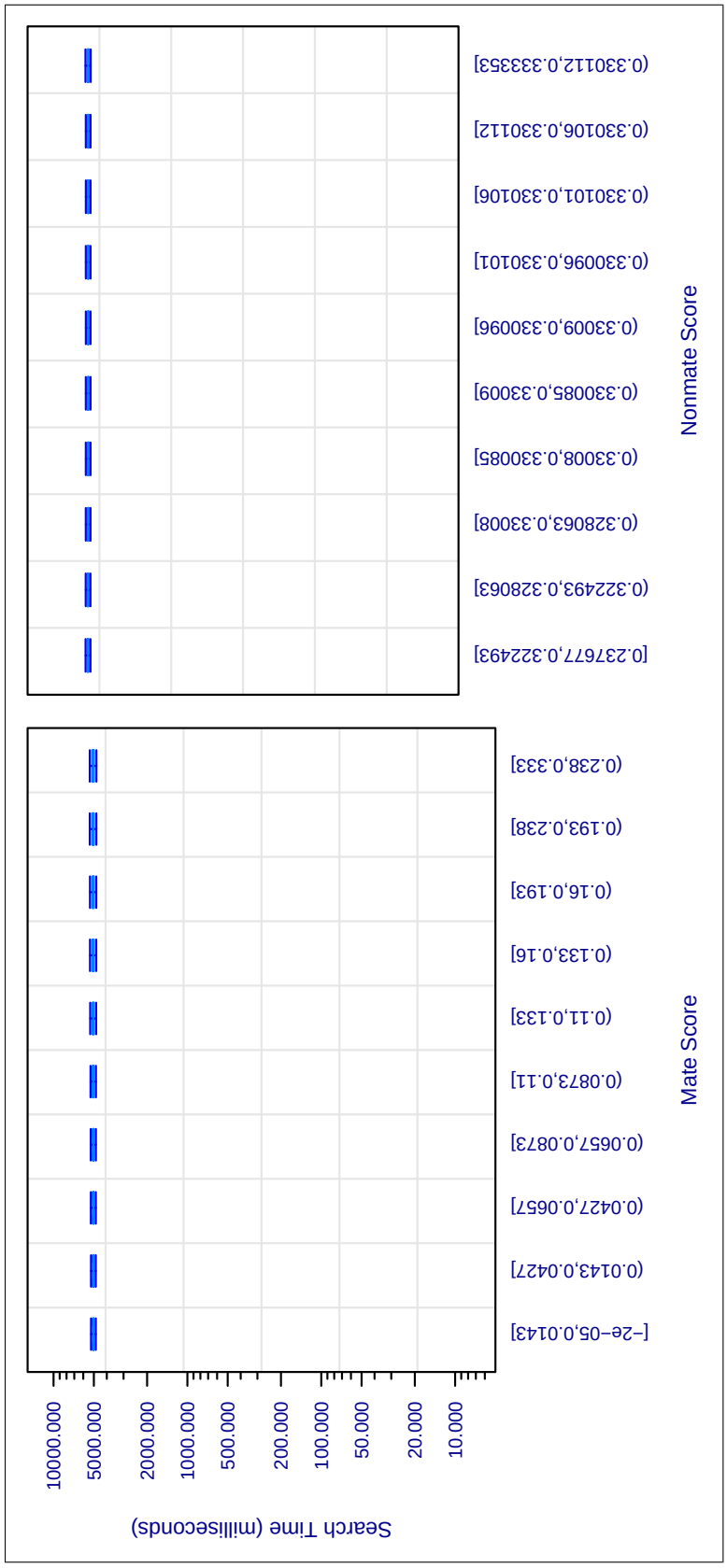

Figure 655: Dependence of speed and comparison score. For the W01A algorithm, the panels show the distribution of the one-to-many search time for ordered intervals of the mate and nonmate dissimilarity scores. For many implementations the duration of the search is independent of the score outcome. For some others (e.g. T11A), however, mate search durations are faster when the ultimate dissimilarity score is low (i.e. good).

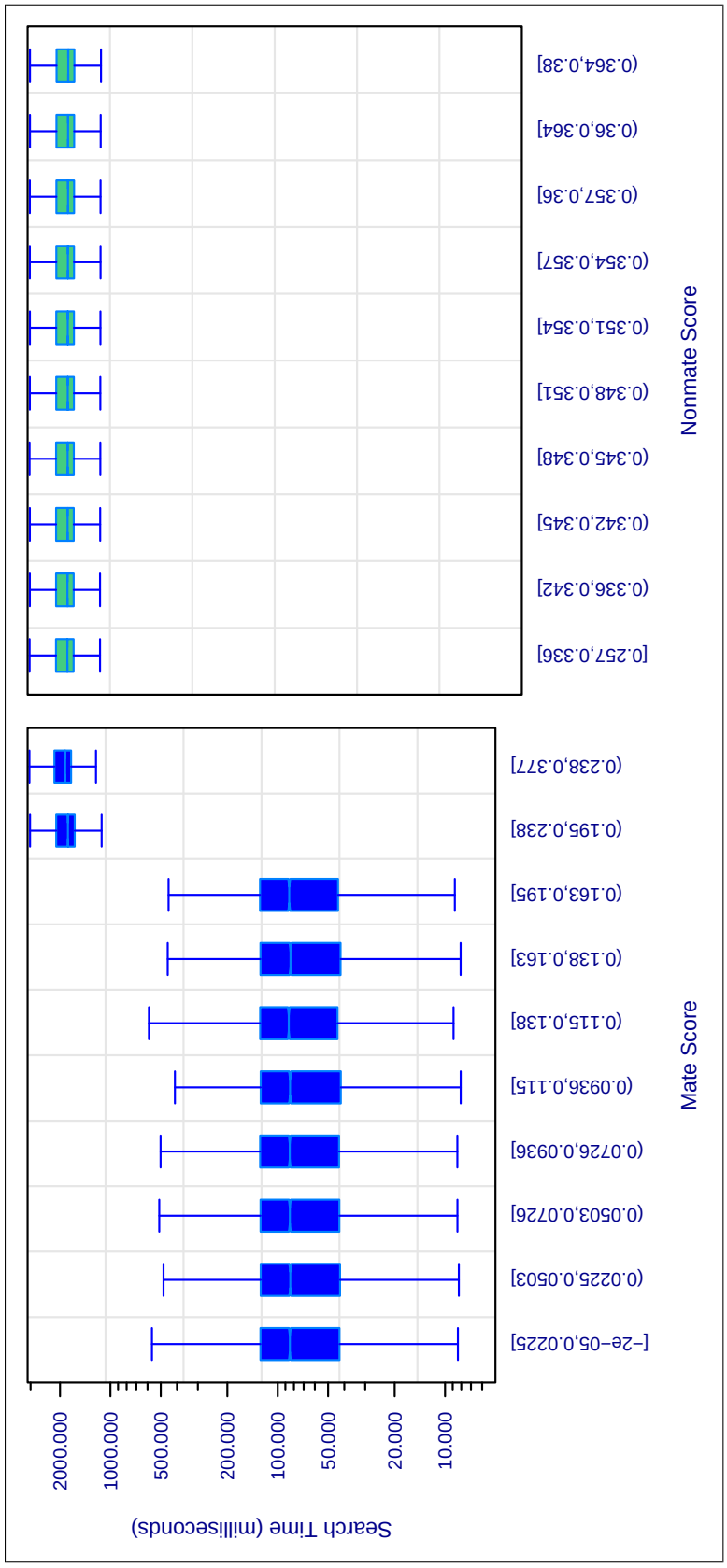

Figure 656: Dependence of speed and comparison score. For the W01B algorithm, the panels show the distribution of the one-to-many search time for ordered intervals of the mate and nonmate dissimilarity scores. For many implementations the duration of the search is independent of the score outcome. For some others (e.g. T11A), however, mate search durations are faster when the ultimate dissimilarity score is low (i.e. good).

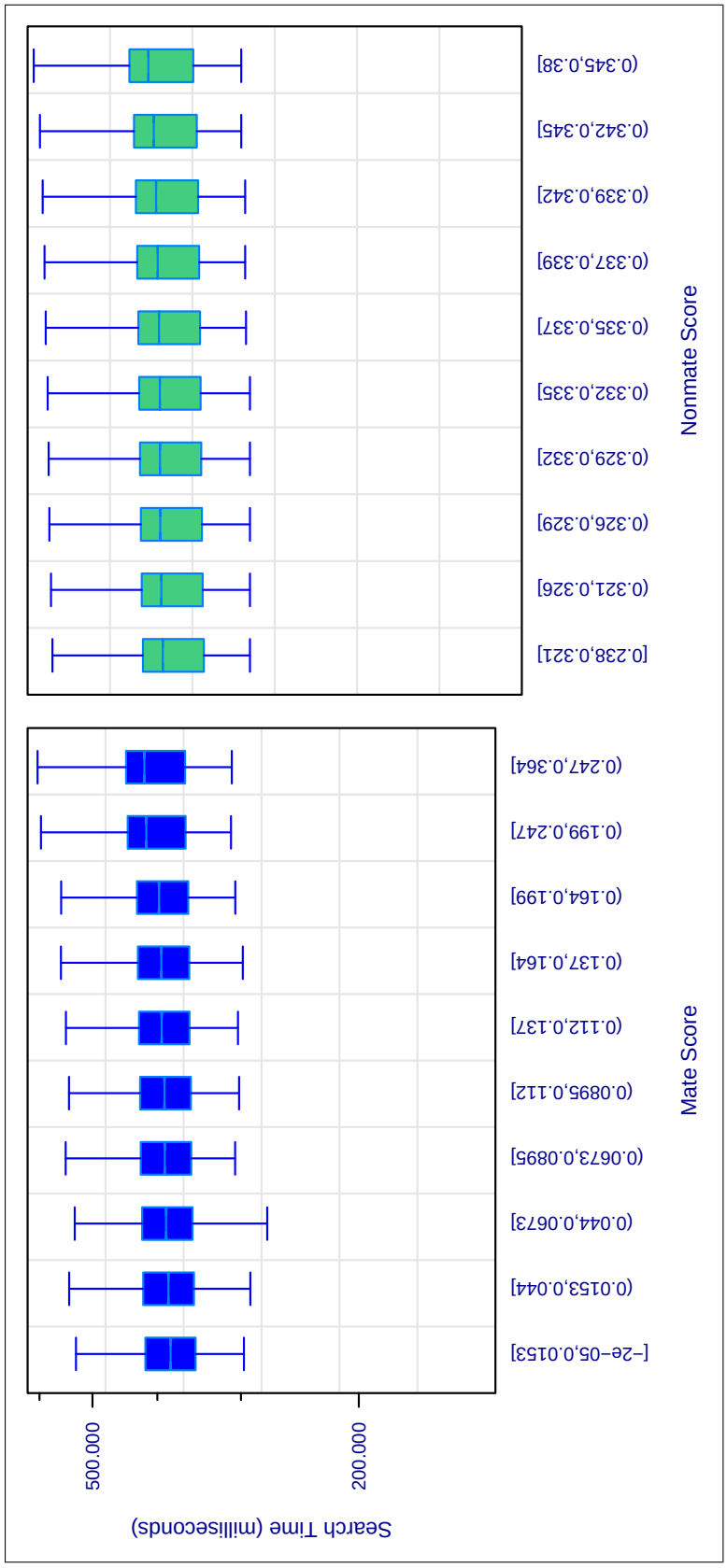

Figure 657: Dependence of speed and comparison score. For the W02A algorithm, the panels show the distribution of the one-to-many search time for ordered intervals of the mate and nonmate dissimilarity scores. For many implementations the duration of the search is independent of the score outcome. For some others (e.g. T11A), however, mate search durations are faster when the ultimate dissimilarity score is low (i.e. good).

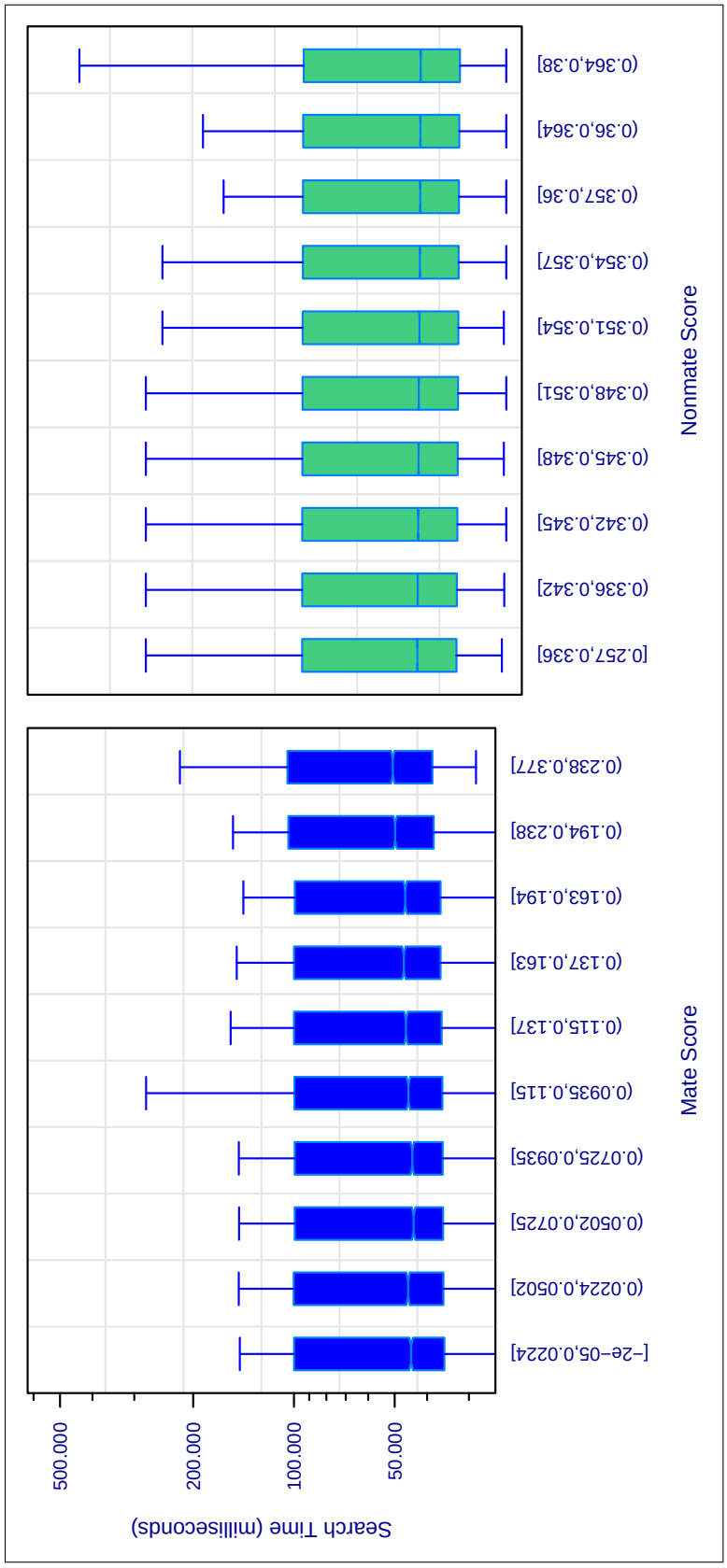

Figure 658: Dependence of speed and comparison score. For the W02B algorithm, the panels show the distribution of the one-to-many search time for ordered intervals of the mate and nonmate dissimilarity scores. For many implementations the duration of the search is independent of the score outcome. For some others (e.g. T11A), however, mate search durations are faster when the ultimate dissimilarity score is low (i.e. good).

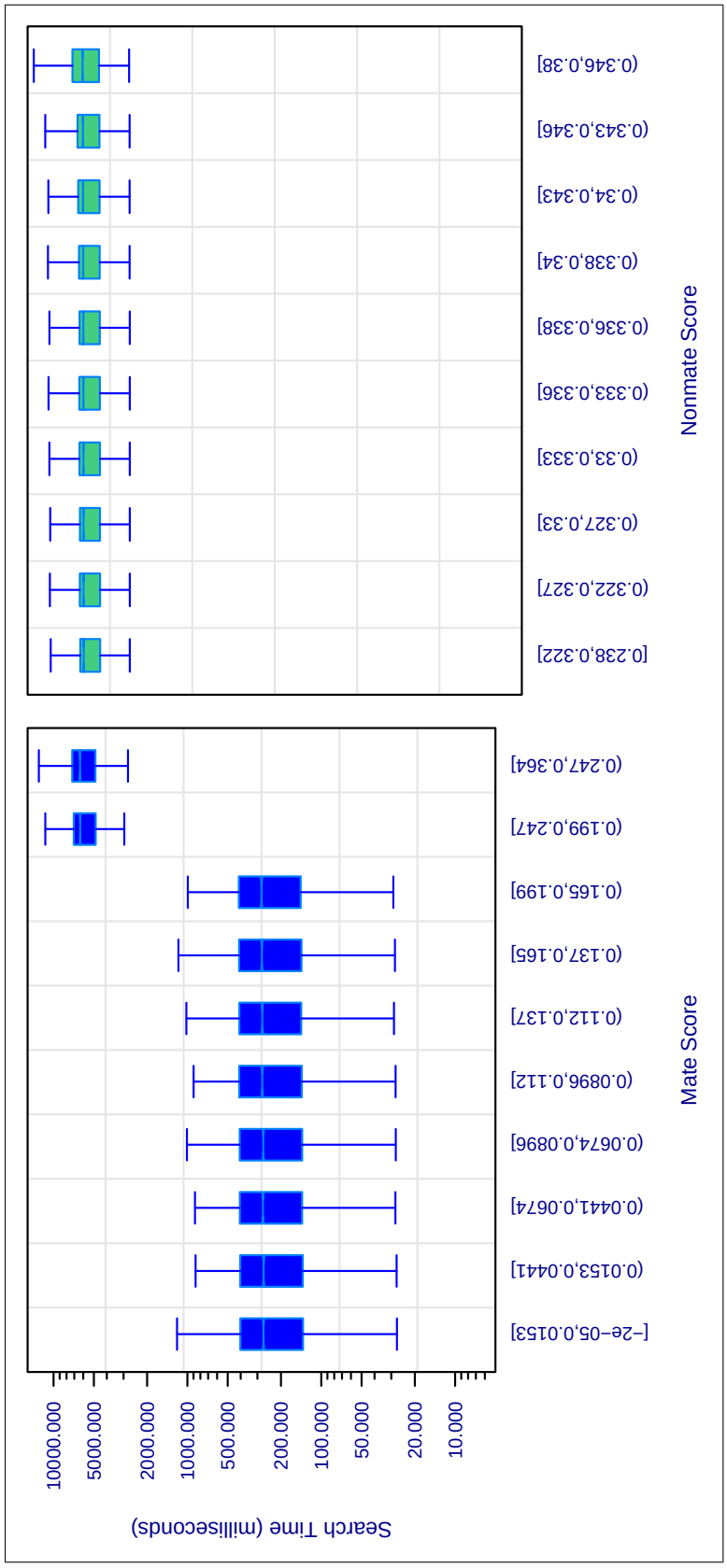

Figure 659: Dependence of speed and comparison score. For the W03A algorithm, the panels show the distribution of the one-to-many search time for ordered intervals of the mate and nonmate dissimilarity scores. For many implementations the duration of the search is independent of the score outcome. For some others (e.g. T11A), however, mate search durations are faster when the ultimate dissimilarity score is low (i.e. good).

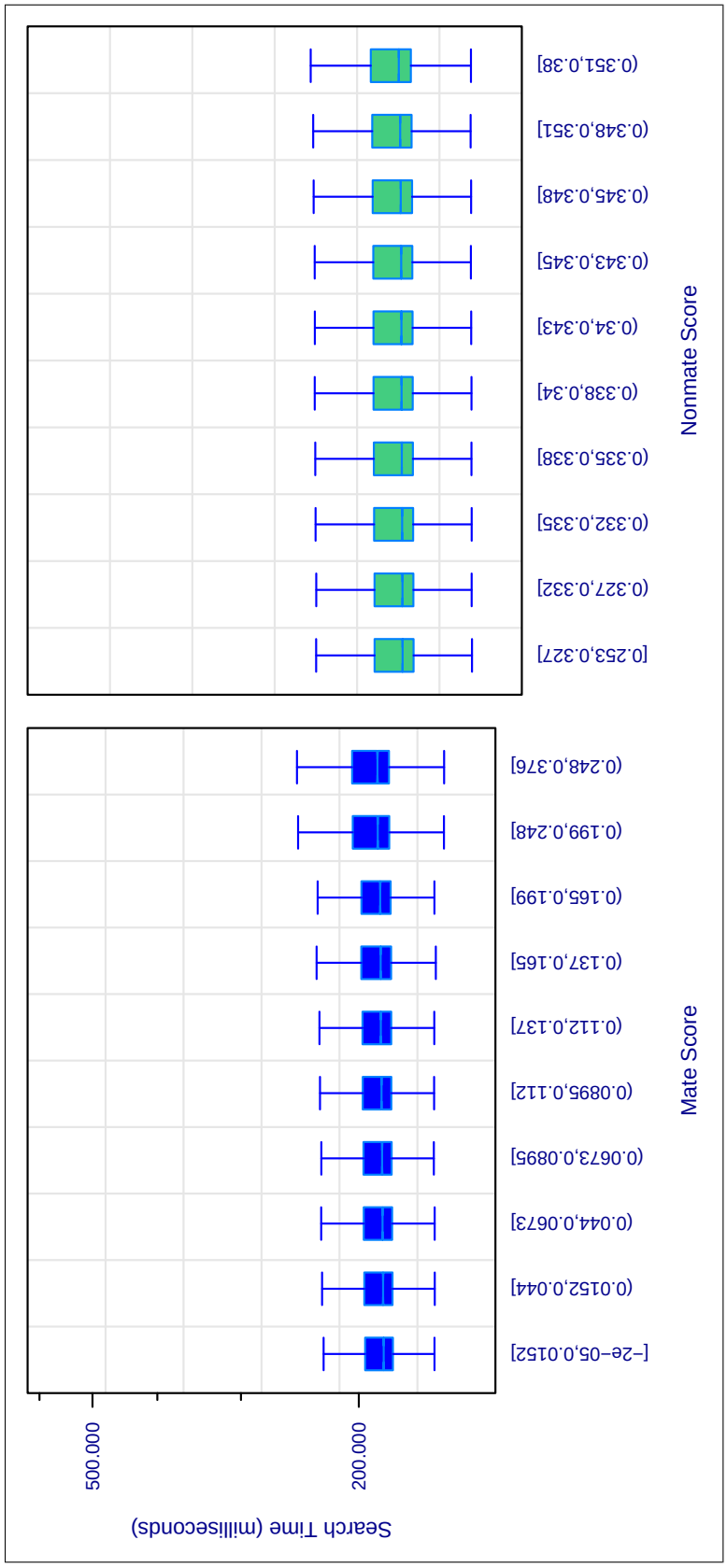

Figure 660: Dependence of speed and comparison score. For the W04A algorithm, the panels show the distribution of the one-to-many search time for ordered intervals of the mate and nonmate dissimilarity scores. For many implementations the duration of the search is independent of the score outcome. For some others (e.g. T11A), however, mate search durations are faster when the ultimate dissimilarity score is low (i.e. good).

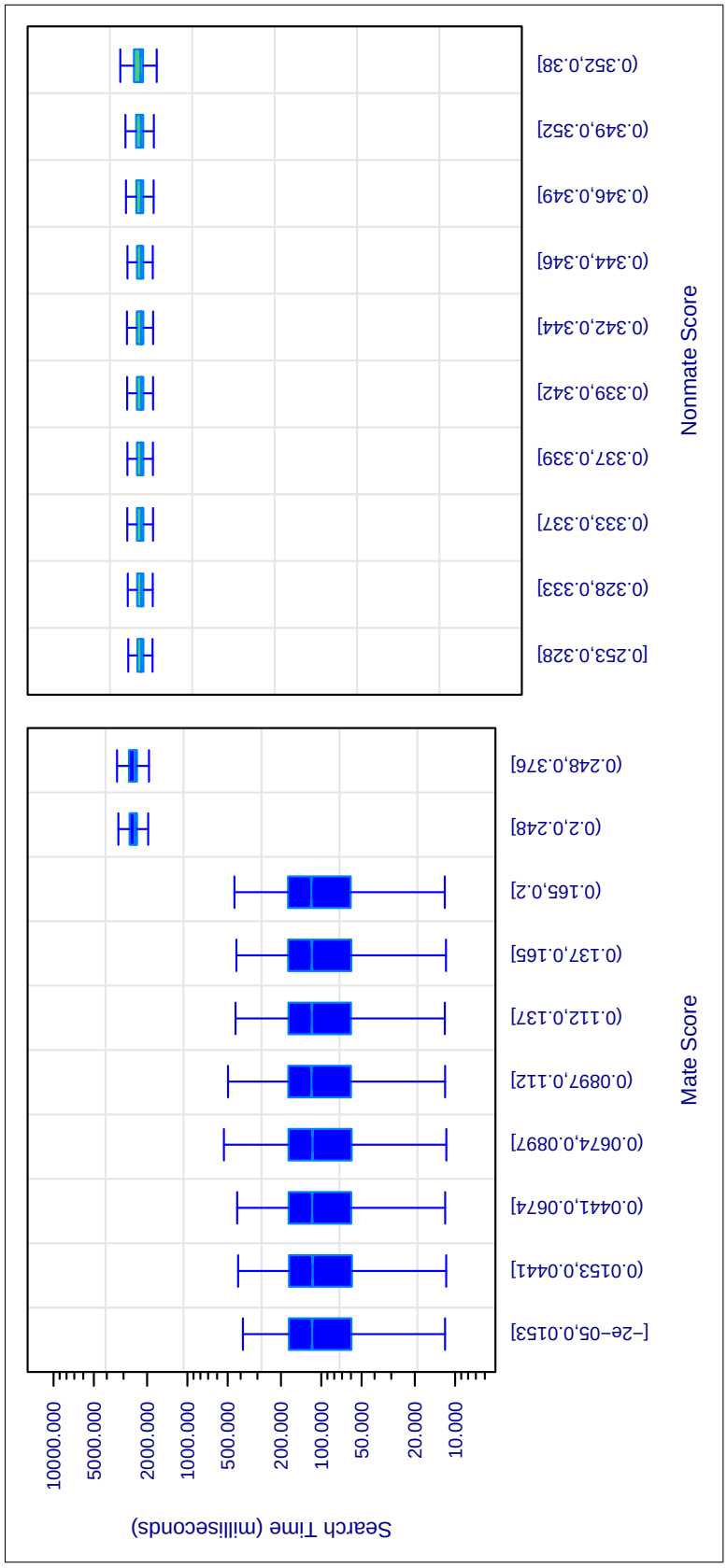

Figure 661: Dependence of speed and comparison score. For the W05A algorithm, the panels show the distribution of the one-to-many search time for ordered intervals of the mate and nonmate dissimilarity scores. For many implementations the duration of the search is independent of the score outcome. For some others (e.g. T11A), however, mate search durations are faster when the ultimate dissimilarity score is low (i.e. good).

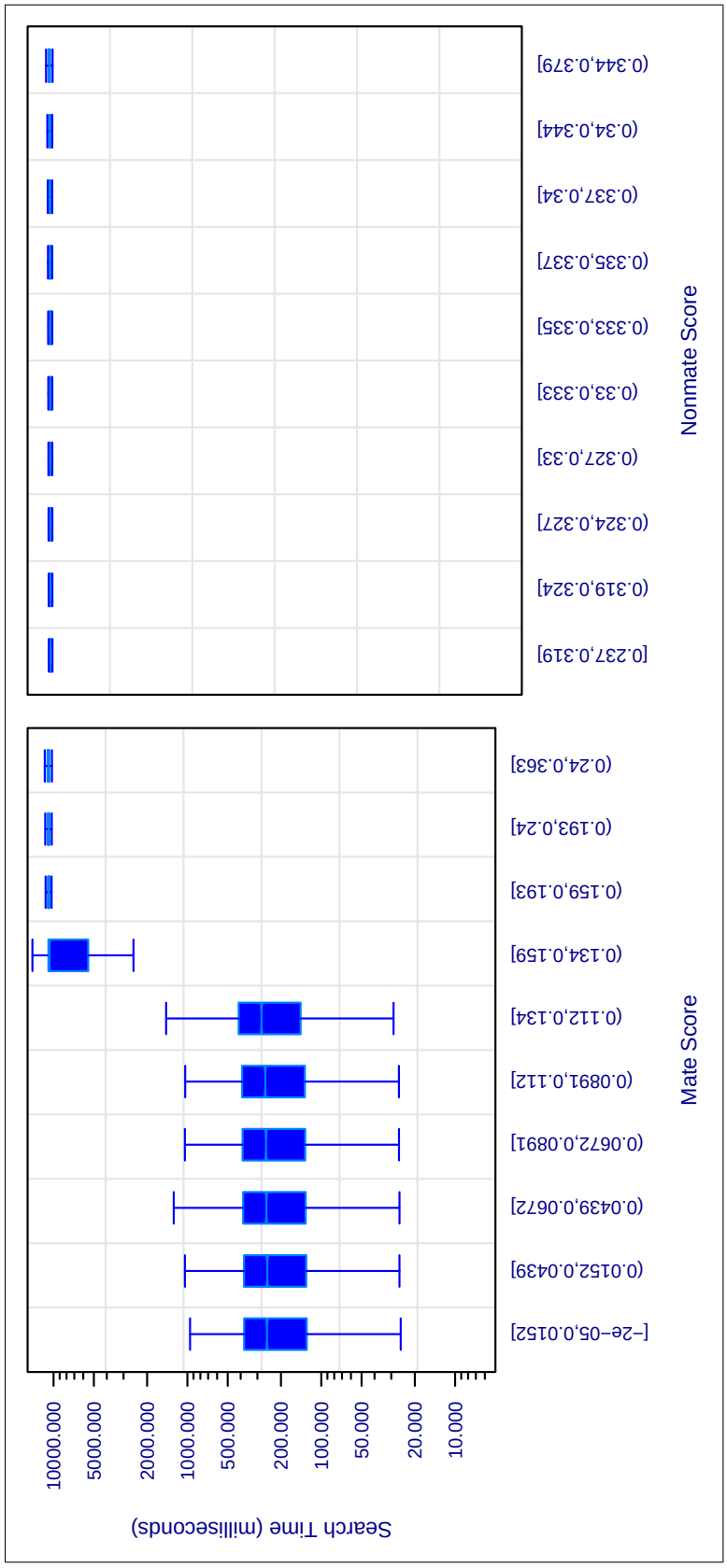

Figure 662: Dependence of speed and comparison score. For the W11A algorithm, the panels show the distribution of the one-to-many search time for ordered intervals of the mate and nonmate dissimilarity scores. For many implementations the duration of the search is independent of the score outcome. For some others (e.g. T11A), however, mate search durations are faster when the ultimate dissimilarity score is low (i.e. good).

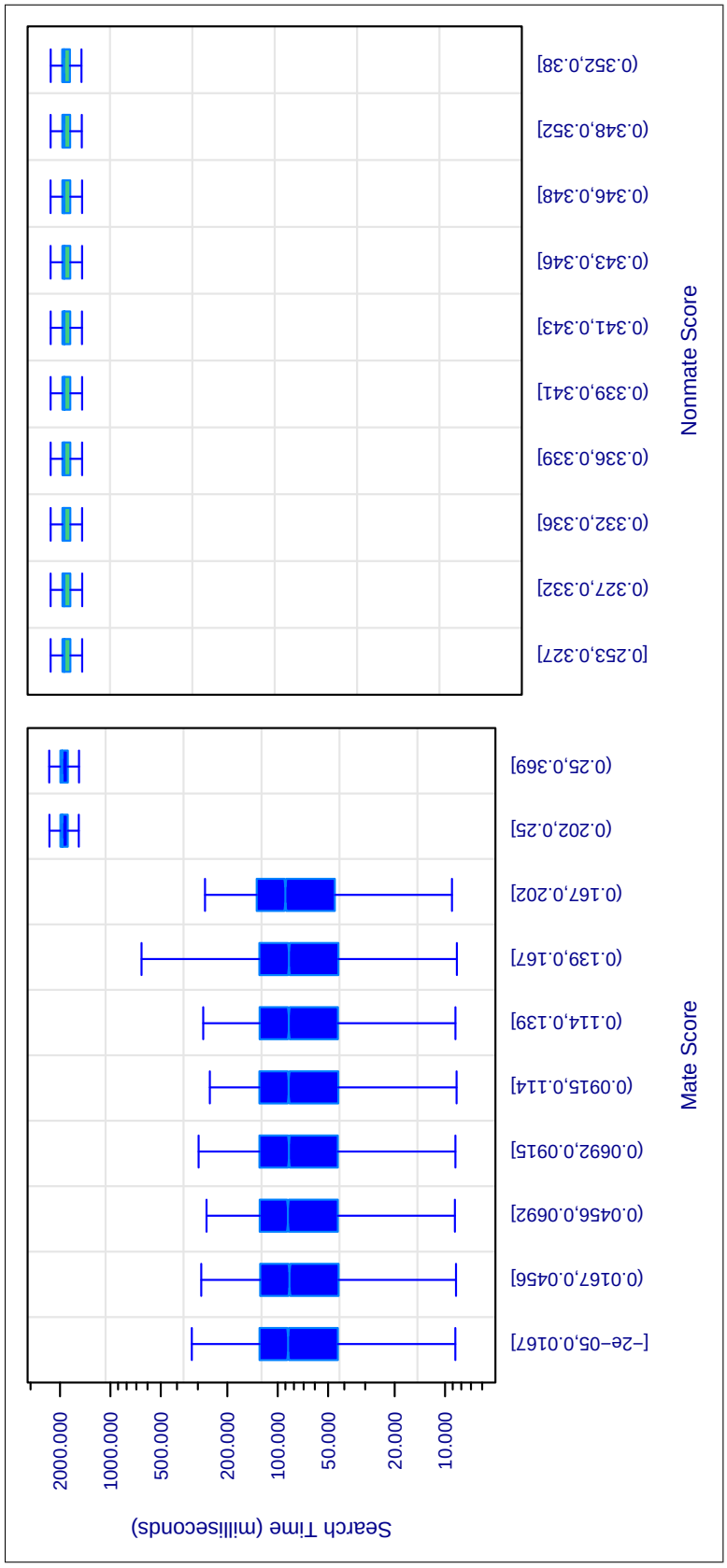

Figure 663: Dependence of speed and comparison score. For the W11B algorithm, the panels show the distribution of the one-to-many search time for ordered intervals of the mate and nonmate dissimilarity scores. For many implementations the duration of the search is independent of the score outcome. For some others (e.g. T11A), however, mate search durations are faster when the ultimate dissimilarity score is low (i.e. good).

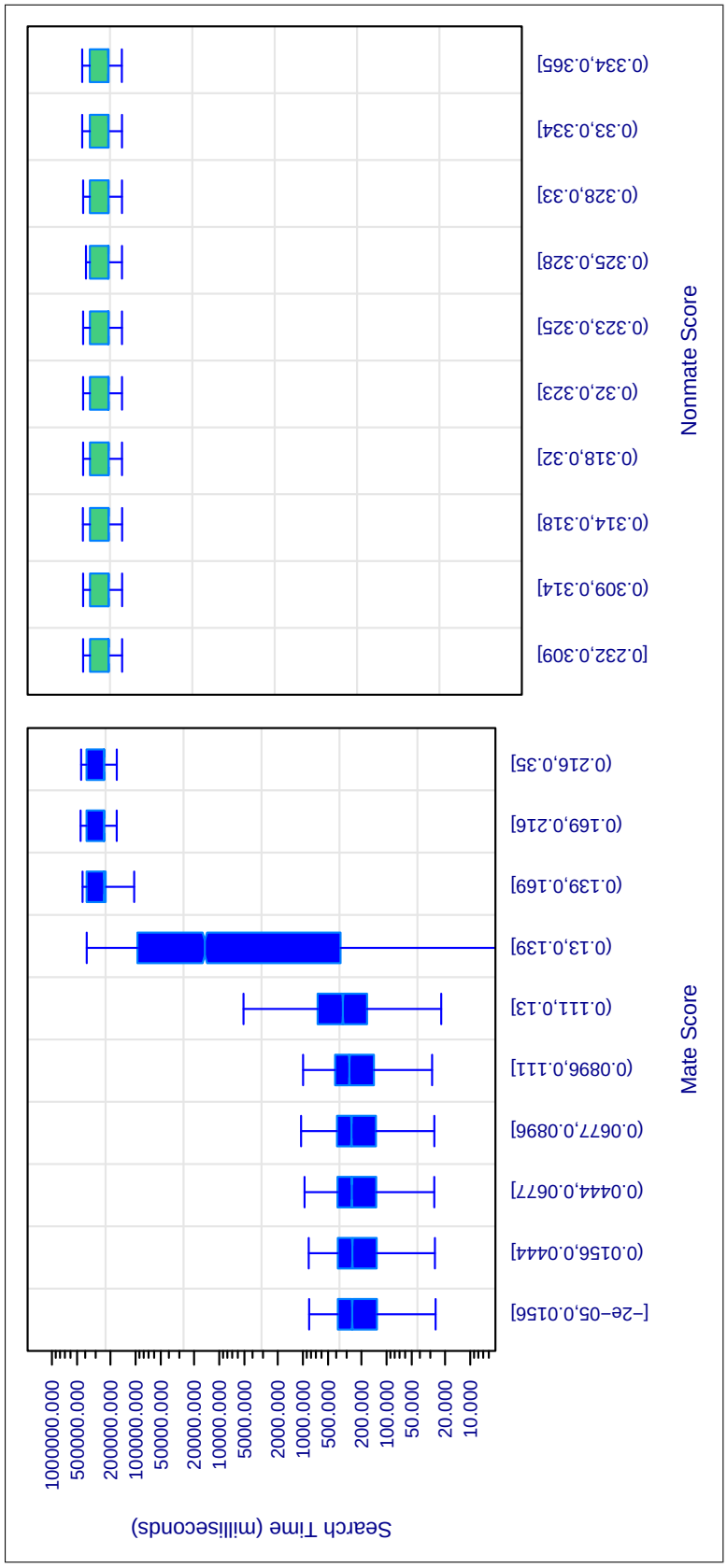

Figure 664: Dependence of speed and comparison score. For the W12A algorithm, the panels show the distribution of the one-to-many search time for ordered intervals of the mate and nonmate dissimilarity scores. For many implementations the duration of the search is independent of the score outcome. For some others (e.g. T11A), however, mate search durations are faster when the ultimate dissimilarity score is low (i.e. good).

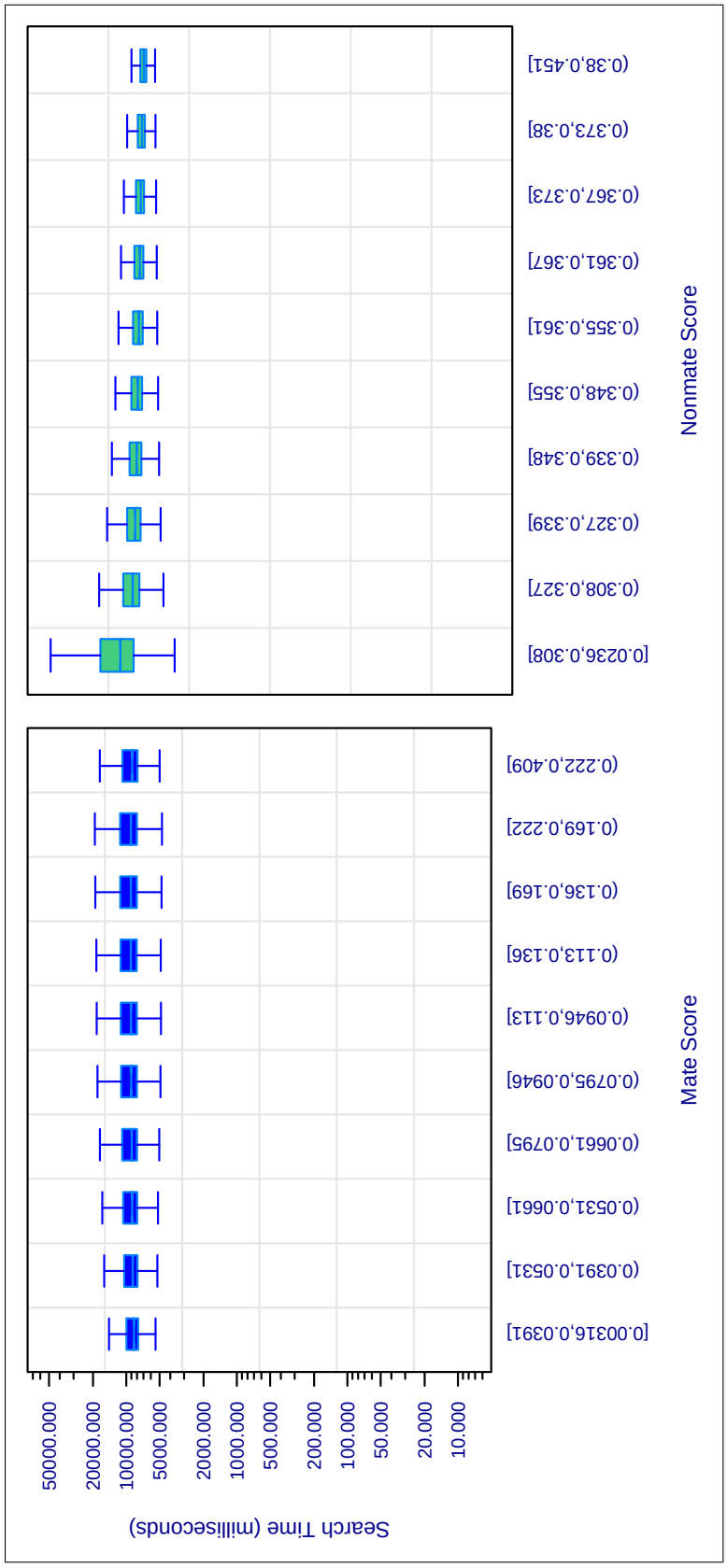

Figure 665: Dependence of speed and comparison score. For the X02A algorithm, the panels show the distribution of the one-to-many search time for ordered intervals of the mate and nonmate dissimilarity scores. For many implementations the duration of the search is independent of the score outcome. For some others (e.g. T11A), however, mate search durations are faster when the ultimate dissimilarity score is low (i.e. good).

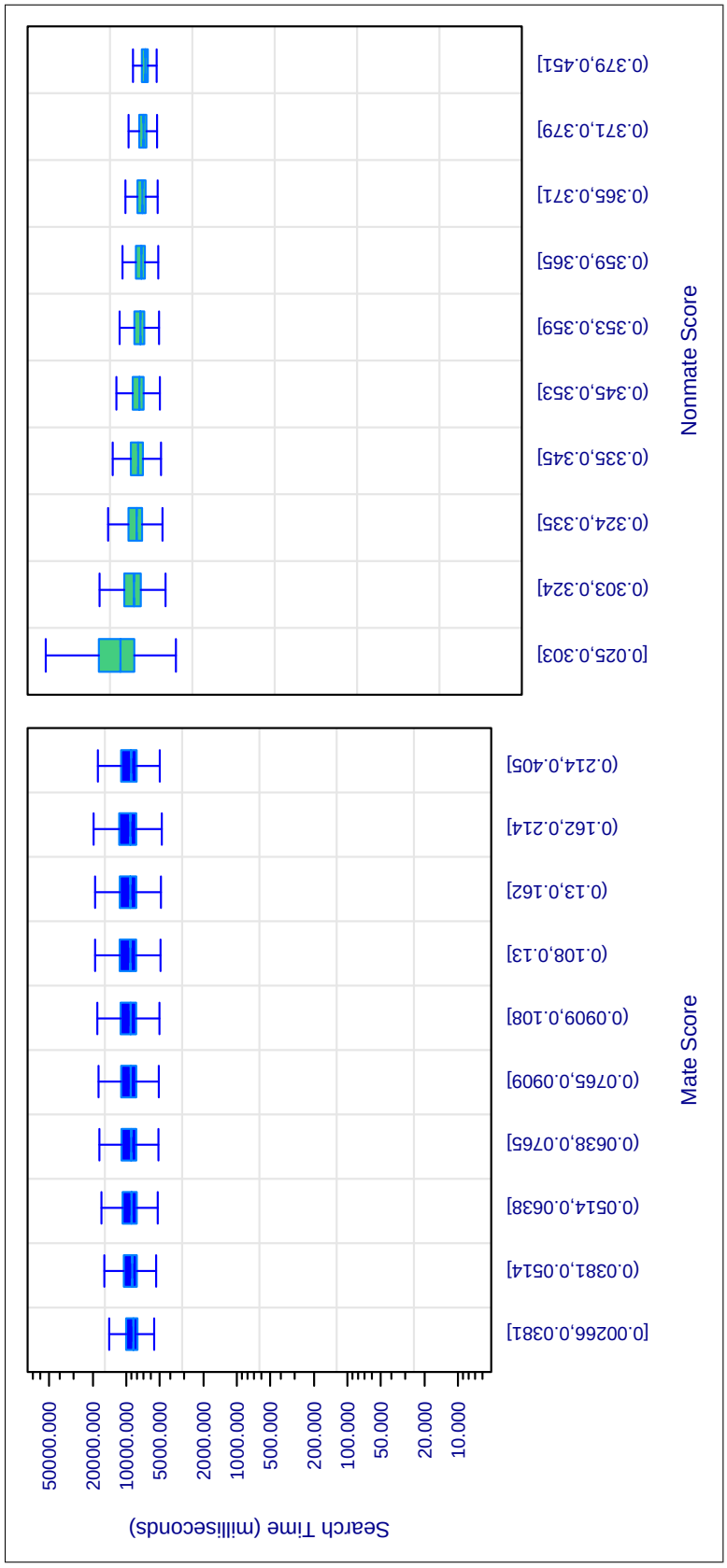

Figure 666: Dependence of speed and comparison score. For the X03A algorithm, the panels show the distribution of the one-to-many search time for ordered intervals of the mate and nonmate dissimilarity scores. For many implementations the duration of the search is independent of the score outcome. For some others (e.g. T11A), however, mate search durations are faster when the ultimate dissimilarity score is low (i.e. good).

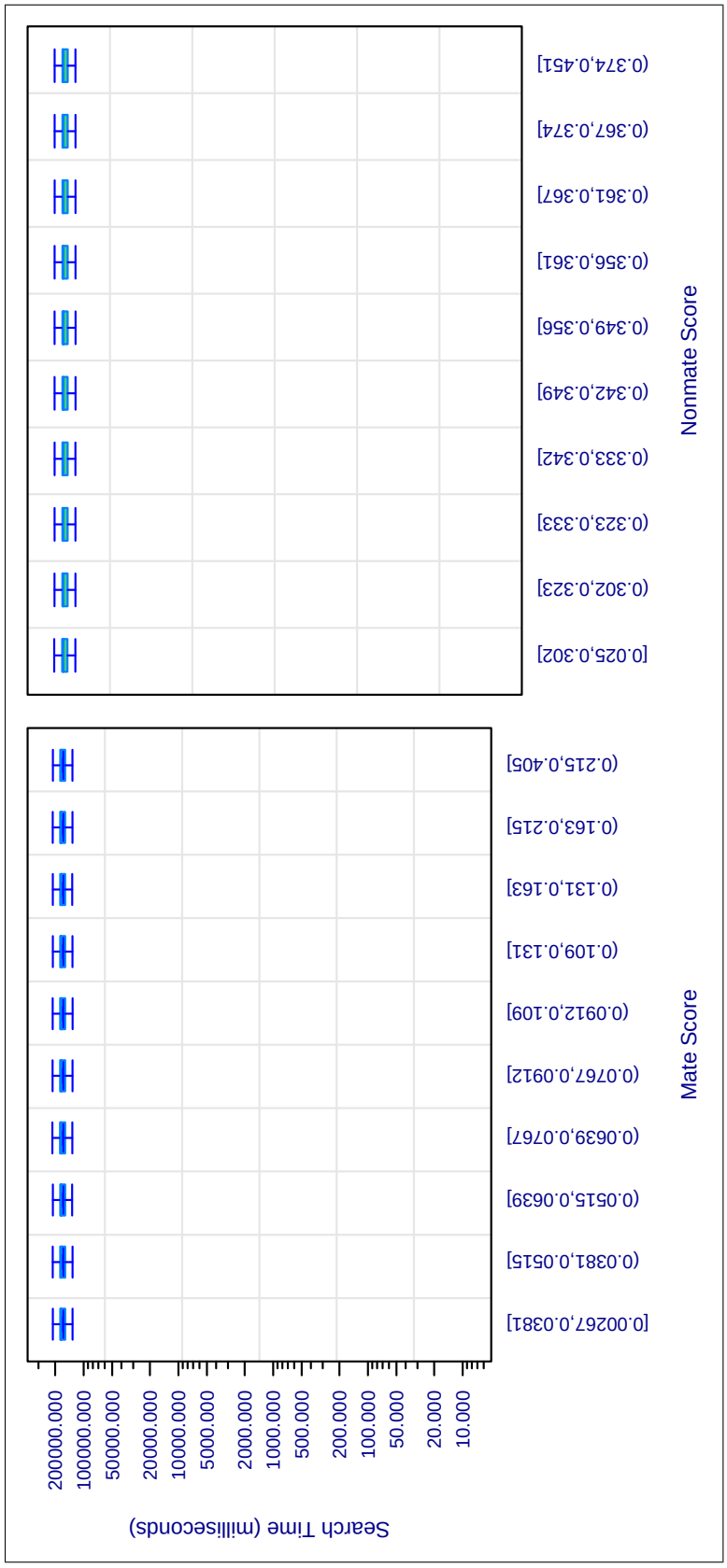

Figure 667: Dependence of speed and comparison score. For the X04A algorithm, the panels show the distribution of the one-to-many search time for ordered intervals of the mate and nonmate dissimilarity scores. For many implementations the duration of the search is independent of the score outcome. For some others (e.g. T11A), however, mate search durations are faster when the ultimate dissimilarity score is low (i.e. good).

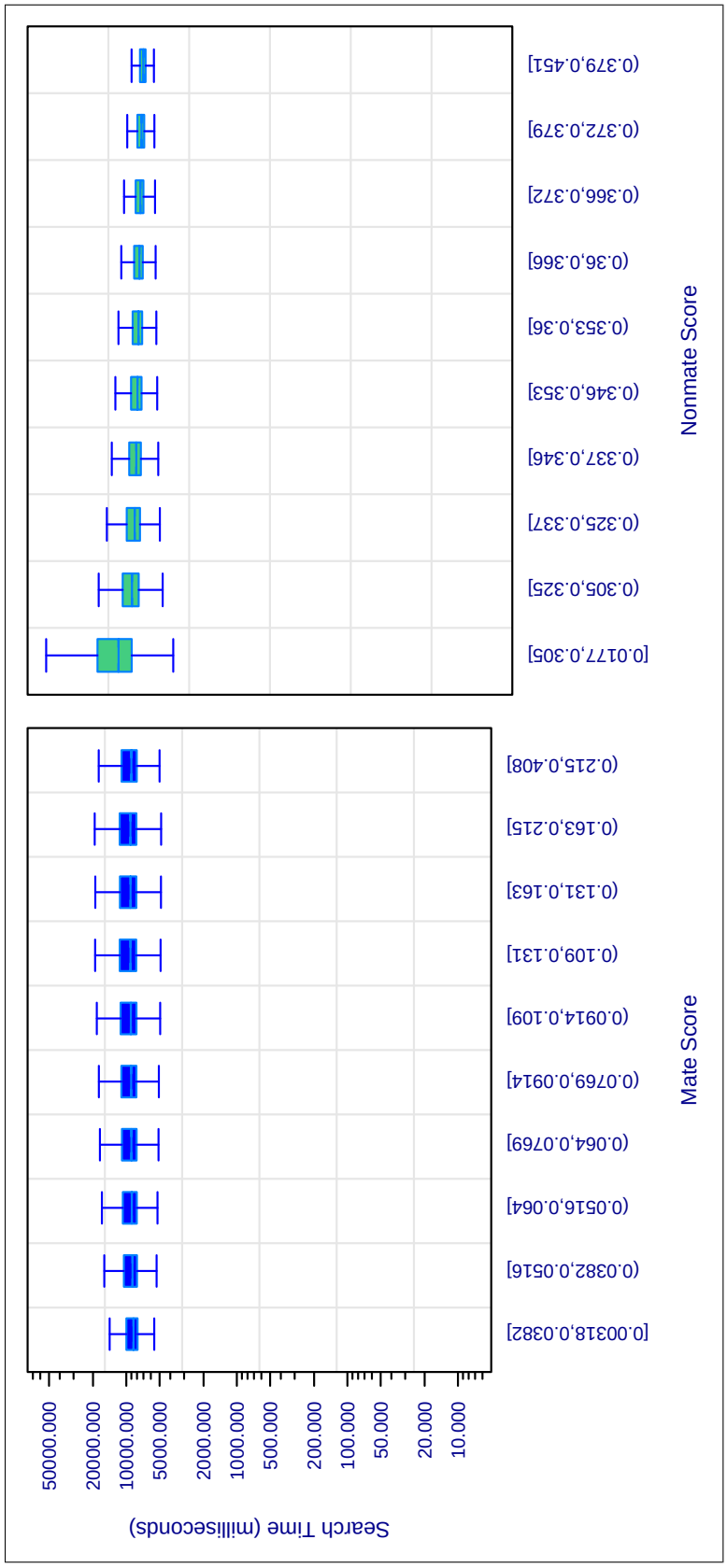

Figure 668: Dependence of speed and comparison score. For the X11A algorithm, the panels show the distribution of the one-to-many search time for ordered intervals of the mate and nonmate dissimilarity scores. For many implementations the duration of the search is independent of the score outcome. For some others (e.g. T11A), however, mate search durations are faster when the ultimate dissimilarity score is low (i.e. good).

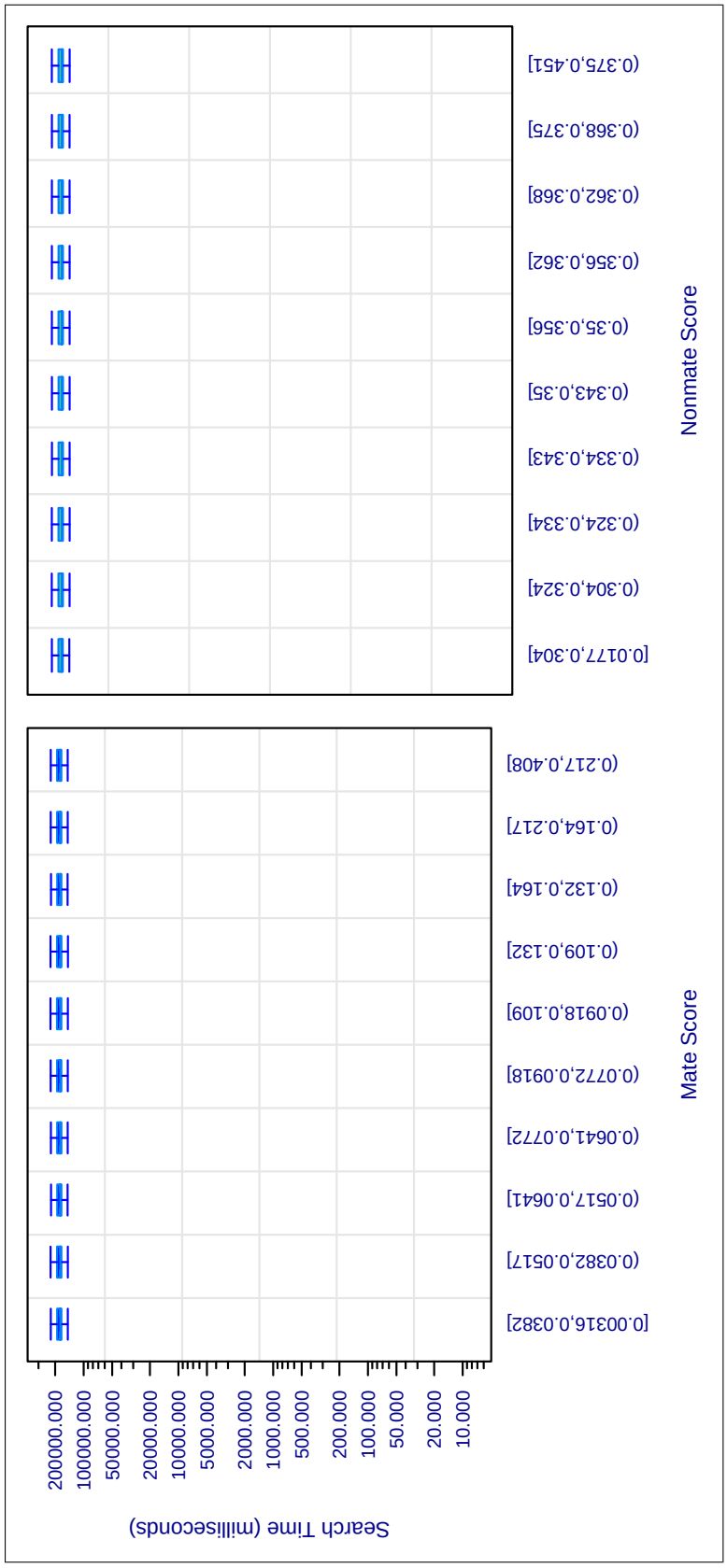

Figure 669: Dependence of speed and comparison score. For the X11B algorithm, the panels show the distribution of the one-to-many search time for ordered intervals of the mate and nonmate dissimilarity scores. For many implementations the duration of the search is independent of the score outcome. For some others (e.g. T11A), however, mate search durations are faster when the ultimate dissimilarity score is low (i.e. good).

N	SDK	MD5 Hash	Size (Bytes)
1	N02A	61f3e8c849313d82255ec30b4defad88	1968277
2	N02B	aef879edccdf7ce2acced642a4d3211e	1968277
3	N03A	1ef50efefdbca5269f49e3fb653566f6	1968277
4	N03B	d7a0e70f4f00806b4769b7adc8e6d1f3	2421940
5	N04A	14479ce6647c8e956aa3b84429a14841	2026836
6	N11A	da29ebe53c7d3da6fd70b9ab67b5505c	2048704
7	N11B	0b7d87e6d7a573653b4f48165e97b88f	2484068
8	N12A	a8bcf466b186b56c9d8543ddccafd5d7	2048704
9	N12B	cf0825608f8674c057bdf2c669383e65	2471012
10	N13B	f8856b8f6ca1e22df8c735f14d6168aa	2471012

Table 1: Hashes and sizes of the libraries comprising the Neurotechnology implementations, denoted by N. The hash values are intended to support version control and verification, and are meaningful only to the supplier of the SDK. The library sizes may have some relevance to deployers, for example on architectures where memory is limited.

P	SDK	MD5 Hash	Size (Bytes)

Table 2: Hashes and sizes of the libraries comprising the SMU implementations, denoted by P. The hash values are intended to support version control and verification, and are meaningful only to the supplier of the SDK. The library sizes may have some relevance to deployers, for example on architectures where memory is limited.

Appendix J: Implementation Traceability

Q	SDK	MD5 Hash	Size (Bytes)
1	Q02A	1cc7ee38f2b3de1d0d66e941d3b62b12	2907635
2	Q02B	2e943be5b92720eab3e7df243e4d0b97	2912177
3	Q03A	94941eed989fbe1c8e4dd43652109182	2967020
4	Q03B	c555e08ad4612dd676b6cd1f54748daa	2971116
5	Q04B	285c887de25207819bc5e7217dad69ea	2971116
6	Q11B	17e919b522aa5d0e1a589ed02baa8a78	3331535
7	Q12B	69fbc3e2ef2d93dd738f9d6658fbac3b	3312175
8	Q13B	21b26c049f19822b58ba48520c6d22f9	3311823

Table 3: Hashes and sizes of the libraries comprising the Iritech implementations, denoted by Q. The hash values are intended to support version control and verification, and are meaningful only to the supplier of the SDK. The library sizes may have some relevance to deployers, for example on architectures where memory is limited.

R	SDK	MD5 Hash	Size (Bytes)
1	R02A	ddf3d5cf7b80d7e6cee453d48658e5fc	815190
2	R02B	a431109a56e3e3b2333e4fe3308562f2	858616
3	R03A	22d51c81758b4796f6acf38accf26bce	817134
4	R03B	23a4ae242de4927828fec24f7f612359	875000
5	R04B	280f284e0524149bfec87bf1d7e66c82	875000
6	R11A	ca98a19e075349e44ff24e1d298dcdaa	818006
7	R11B	3ac13bd6be87cf175c6c05dd88e3a5d8	1066560
8	R12A	72860f963adee3ad922a00267fef1716	818038

Table 4: Hashes and sizes of the libraries comprising the Cogent implementations, denoted by R. The hash values are intended to support version control and verification, and are meaningful only to the supplier of the SDK. The library sizes may have some relevance to deployers, for example on architectures where memory is limited.

S	SDK	MD5 Hash	Size (Bytes)
1	S01B	b90df4457b87c3a10675ac10d3375e97	270424
1	S01B	c1f86a8816813379131d9789f630c57c	1639462
2	S02B	c9ff2e73463ed41461db242190a62b21	274834
2	S02B	5b4bcd9a8f24452c667ac34abfafd8fe	305392
2	S02B	e3122035af627e17b0e56cd207f08bbb	1758460
3	S03A	c47a72b91ddfcc188fd934bc8b3dd6fb	247942
3	S03A	94d3d8f8ef6743d020e34ac0c4f1debf	1733261
4	S04A	78af7c6128d9904c5cd7bb4df36a2140	283890
4	S04A	e3122035af627e17b0e56cd207f08bbb	1758460
5	S05A	58bc42a721b5f00a01033b12b0bd245c	330046
5	S05A	e3122035af627e17b0e56cd207f08bbb	1758460
6	S11A	0e1563214162f3405d789226eafe70bf	327774
6	S11A	f3ff68980fe1420ca138fe98d1412a08	1829439
7	S11B	c2d15127558abe5b6dcb2ddb29bda028	342758
7	S11B	b1066638d277943ca2faeedd4a20d6b4	1836183
8	S12A	f33535a92d675d2ba10c26698c68e749	343292
8	S12A	156275bb3f77155e5f8d7b28e9626502	1850019

Table 5: Hashes and sizes of the libraries comprising the SmartSensors implementations, denoted by S. The hash values are intended to support version control and verification, and are meaningful only to the supplier of the SDK. The library sizes may have some relevance to deployers, for example on architectures where memory is limited.

T	SDK	MD5 Hash	Size (Bytes)
1	T01A	43eae94dc5d409f0d14e3eb494c5002c	188830
2	T01B	6cb0bfc4d26518f3bb71e52597553399	187262
3	T02A	4a0361a78adebfe0b4758afd6b229b0e	191152
4	T02B	062848811458a6b6639b8b4c99c3c5c1	193376
5	T03A	3b8ff6b836ee86b329a4998d59e606c1	192752
6	T03B	9d2e42418f28f5c0ad81d93e1c4791a4	194864
7	T04A	d9e1ae487791255c262734ed47b0f065	199752
8	T11A	f8fbffdbd4e556fedcde91d06d08e2e5	203082
9	T11B	8c3e2e0da6cbe2ff79a77b89885e9dfd	194344
10	T12B	88819a9ed90642c5ac2940531277063c	204050

Table 6: Hashes and sizes of the libraries comprising the Cambridge implementations, denoted by T. The hash values are intended to support version control and verification, and are meaningful only to the supplier of the SDK. The library sizes may have some relevance to deployers, for example on architectures where memory is limited.

U	SDK	MD5 Hash	Size (Bytes)
1	U01A	9817f2d1a934e6265472a6ab88f4524f	1355538
2	U01B	01fe584b2b6222d8cd1824102776c583	1356234
3	U02A	072428ebae3c9c5743653dbb3fde324c	1355018
4	U03A	b3eeb918adb79d6b93f10e0dab757243	1311008
5	U03B	257b5411b1873c30d125767b5fe7e9e1	1312104
6	U04A	db7ed90f8db8c2071a2c826b4cb3f544	1311912
7	U04B	58702c2af7ea4ce80998e6e16c4b963f	1313008
8	U11A	9cdf89e6cc59272cf48f6c0e893db69e	2766624
9	U11B	0e23478fba2b8f48e13251a380e926fa	2767578
10	U12A	876b4e8469fb00b64bce88ed611f2a88	2767578
11	U12B	f591c603a94672ac950f798b0719f20b	2768290

Table 7: Hashes and sizes of the libraries comprising the L1 implementations, denoted by U. The hash values are intended to support version control and verification, and are meaningful only to the supplier of the SDK. The library sizes may have some relevance to deployers, for example on architectures where memory is limited.

V	SDK	MD5 Hash	Size (Bytes)
1	V01A	1213e7439dc1ad8c6a2ef8655552adb8	3218992
1	V01A	6d8b4c89644543c2f2a2dd41e121695a	1571879
1	V01A	3af89fd10a25a68a7d977ad850d2c585	2379370
2	V02A	4a270ee1f473859d8f222776684b93ea	4047915
2	V02A	8b3f4c61f1680e766c68e91db1ff1715	2101061
2	V02A	3af89fd10a25a68a7d977ad850d2c585	2379370
3	V03A	4743bb03c60e7c14c9414ac262dc58d9	4084254
3	V03A	809735790a0c3678db67a9bd7781a83f	2625237
3	V03A	b3951fd2e6cfb326d8c70b059d76c751	2387576
4	V03B	3dc84837d13d6c5761c3e133c11751f1	4084382
4	V03B	809735790a0c3678db67a9bd7781a83f	2625237
4	V03B	8b47c6a564442b6245217aaddea68606	2387576
5	V04A	02e8f0487cd7c47f270b91ef7a8532bd	4065951
5	V04A	fd594ac03ce33fbdd1f08e014c34e091	2132206
5	V04A	ee70b5d8d249bcde933f3d2f1719526d	2380874
6	V11A	24afd755ecf4640e949ed258ca9e5ed4	4088337
6	V11A	d55558b080c3c7d8ab232a9a6187ab11	2625237
6	V11A	b3951fd2e6cfb326d8c70b059d76c751	2387576
7	V11B	47a22913b3d0e148b18af9936f04dc56	4088977
7	V11B	d55558b080c3c7d8ab232a9a6187ab11	2625237
7	V11B	8b47c6a564442b6245217aaddea68606	2387576
8	V12A	e36528b2efe48db6cb70bdaf2699cafa	4089138
8	V12A	d55558b080c3c7d8ab232a9a6187ab11	2625237
8	V12A	b3951fd2e6cfb326d8c70b059d76c751	2387576
9	V12B	760212de3f74d050ed513c933c09bd95	4652234
9	V12B	d55558b080c3c7d8ab232a9a6187ab11	2625237
9	V12B	8b47c6a564442b6245217aaddea68606	2387576

Table 8: Hashes and sizes of the libraries comprising the Morpho implementations, denoted by V. The hash values are intended to support version control and verification, and are meaningful only to the supplier of the SDK. The library sizes may have some relevance to deployers, for example on architectures where memory is limited.

W	SDK	MD5 Hash	Size (Bytes)
1	W01A	d8adb94cf6b2c760128c766c05d5a3db	699714
1	W01A	c95fd3fe720af365c00538437cecf887	171856
2	W01B	262b9174e46c416aed89a02ed1e12a06	68384
2	W01B	5e329e78f56e3c0f92b394cf86150e4d	181231
3	W02A	1f8e1ecc5755268cc1f51351fa1e350f	116080
3	W02A	5e329e78f56e3c0f92b394cf86150e4d	181231
4	W02B	807a4a1c2161f9f5247e69fa83d33814	116080
4	W02B	5e329e78f56e3c0f92b394cf86150e4d	181231
5	W03A	aff765fee12a1a15411796f1866ce495	68384
5	W03A	5e329e78f56e3c0f92b394cf86150e4d	181231
6	W04A	3f1d3a78c8d7b0e0b15704dab7599aa2	116080
6	W04A	5e329e78f56e3c0f92b394cf86150e4d	181231
7	W05A	7084c2999667838ca7401ba070e6067e	68384
7	W05A	5e329e78f56e3c0f92b394cf86150e4d	181231
8	W11A	15b57b39c635af8ece4f486806036ad4	72448
8	W11A	160b8ca77bccf948067a00cfb368d444	184775
9	W11B	0dfa7e6cdd27d39d4eb461dfa0a91218	68864
9	W11B	160b8ca77bccf948067a00cfb368d444	184775
10	W12A	96a32a33385925ada95b76a03967d032	72526
10	W12A	03dac0560cb51ef088d3248875ddfcad	184775

Table 9: Hashes and sizes of the libraries comprising the IrisID implementations, denoted by W. The hash values are intended to support version control and verification, and are meaningful only to the supplier of the SDK. The library sizes may have some relevance to deployers, for example on architectures where memory is limited.

X	SDK	MD5 Hash	Size (Bytes)
1	X02A	3465e23f8f41984e96143d8fba7f4154	2645152
2	X03A	ad8e103a8c6341eaf8a7eb6f90c87da3	2646724
3	X04A	f87352f4c29482e73f51da34a90ec127	2646724
4	X11A	4be75e2cc2ac3e6e7b996f5efee7dfca	2647116
5	X11B	9d4be2da54381634b02bd6154cf44f84	2647116

Table 10: Hashes and sizes of the libraries comprising the Crossmatch implementations, denoted by X. The hash values are intended to support version control and verification, and are meaningful only to the supplier of the SDK. The library sizes may have some relevance to deployers, for example on architectures where memory is limited.

Y	SDK	MD5 Hash	Size (Bytes)
1	Y02A	83defd1fc0aaa1ff3ce04e679fe9dc20	10343578
2	Y02B	efc2a5bc276d96b604ac8ae3fa60ce0d	10343578
3	Y03A	4ace8f98b1613f6e8c3046dde262e6cd	10531738
4	Y03B	a01cf56e00d0eca81164c5fced65dc20	10531730

Table 11: Hashes and sizes of the libraries comprising the Kynen implementations, denoted by Y. The hash values are intended to support version control and verification, and are meaningful only to the supplier of the SDK. The library sizes may have some relevance to deployers, for example on architectures where memory is limited.